CODEN: JASMAN

The Journal of the Acoustical Society of America

ISSN: 0001-4966

Vol. 115, No. 6, June 2004

(Continued)

THE JOURNAL OF THE ACOUSTICAL SOCIETY OF AMERICA VOL. 115, NO. 6, JUNE 2004

CONTENTS—*Continued from preceding page*

(Continued)

THE JOURNAL OF THE ACOUSTICAL SOCIETY OF AMERICA VOL. 115, NO. 6, JUNE 2004

CONTENTS—*Continued from preceding page*

ACOUSTICAL MEASUREMENTS AND INSTRUMENTATION [58]

ACOUSTIC SIGNAL PROCESSING [60]

PHYSIOLOGICAL ACOUSTICS [64]

PSYCHOLOGICAL ACOUSTICS [66]

SPEECH PRODUCTION [70]

SPEECH PERCEPTION [71]

(Continued)

THE JOURNAL OF THE ACOUSTICAL SOCIETY OF AMERICA VOL. 115, NO. 6, JUNE 2004

CONTENTS—*Continued from preceding page*

SPEECH PROCESSING AND COMMUNICATION SYSTEMS [72]

BIOACOUSTICS [80]

ERRATA

INDEX TO VOLUME 115

ACOUSTICAL NEWS—USA

Elaine Moran
Acoustical Society of America, Suite 1NO1, 2 Huntington Quadrangle, Melville, NY 11747-4502

Editor's Note: *Readers of this Journal are encouraged to submit news items on awards, appointments, and other activities about themselves or their colleagues. Deadline dates for news items and notices are 2 months prior to publication.*

Catgut Acoustical Society joins the Violin Society of America

The Violin Society of America and the Catgut Acoustical Society recently announced that the Catgut Acoustical Society (CAS) will join the Violin Society of America (VSA) as the CAS Forum and will continue its distinguished research in musical acoustics.

The VSA is an international organization of more than 1500 members whose mission is to advance the art and science of making stringed instruments and bows. The CAS is an international organization of more than 500 members dedicated to acoustic research and its application to the construction of fine stringed instruments.

The two groups have shared goals and interests and have many members in common. Recent VAS-CAS collaborative efforts have resulted in the addition of a violin acoustic workshop to the VSA-Oberlin summer workshop program.

USA Meetings Calendar

Listed below is a summary of meetings related to acoustics to be held in the U.S. in the near future. The month/year notation refers to the issue in which a complete meeting announcement appeared.

2004

12–14 July	Noise-Con 2004, Baltimore, MD [Institute of Noise Control Engineering of the USA, Inc., INCE/USA Business Office, 212 Marston Hall, Iowa State Univ., Ames, IA 50011-2153; Tel.: 515-294-6142; Fax: 515-294-3528; E-mail: ibo@inceusa.org; WWW: http://www.inceusa.org/NoiseCon04call.pdf].
3–7 Aug.	8th International Conference of Music Perception and Cognition, Evanston, IL [School of Music, Northwestern Univ., Evanston, IL 60201; WWW: www.icmpc.org/conferences.html].
16–18 Sept.	Twelfth Annual Conference on the Management of the Tinnitus Patient. For professionals and tinnitus patients. The University of Iowa, Iowa City, Iowa. [Contact Rich Tyler, (319)356-2471, E-mail: rich-tyler@uiowa.edu, WWW: www.uihealthcare.com/depts/med/otolaryngology/conferences/index.html].
20–24 Sept.	ACTIVE 2004—The 2004 International Symposium on Active Control of Sound and Vibration, Williamsburg, VA [INCE Business Office, Iowa State Univ., 212 Marston Hall, IA 50011-2153; Fax: 515-294-3528; E-mail: ibo@ince.org; WWW: inceusa.org].
15–19 Nov.	148th Meeting of the Acoustical Society of America, San Diego, CA [Acoustical Society of America, Suite 1NO1, 2 Huntington Quadrangle, Melville, NY 11747-4502; Tel.: 516-576-2360; Fax: 516-576-2377; E-mail: asa@aip.org; WWW: http://asa.aip.org].

2005

16–19 May	Society of Automotive Engineering Noise & Vibratin Conference, Traverse City, MI [Patti Kreh, SAE International, 755 W. Big Beaver Rd., Ste. 1600, Troy, MI 48084, Tel.: 248-273-2474; E-mail: pkreh@sae.org].

Cumulative Indexes to the *Journal of the Acoustical Society of America*

Ordering information: Orders must be paid by check or money order in U.S. funds drawn on a U.S. bank or by Mastercard, Visa, or American Express credit cards. Send orders to Circulation and Fulfillment Division, American Institute of Physics, Suite 1NO1, 2 Huntington Quadrangle, Melville, NY 11747-4502; Tel.: 516-576-2270. Non-U.S. orders add $11 per index.

Some indexes are out of print as noted below.

Volumes 1–10, 1929–1938: JASA and Contemporary Literature, 1937–1939. Classified by subject and indexed by author. Pp. 131. Price: ASA members $5; Nonmembers $10.

Volumes 11–20, 1939–1948: JASA, Contemporary Literature, and Patents. Classified by subject and indexed by author and inventor. Pp. 395. Out of Print.

Volumes 21–30, 1949–1958: JASA, Contemporary Literature, and Patents. Classified by subject and indexed by author and inventor. Pp. 952. Price: ASA members $20; Nonmembers $75.

Volumes 31–35, 1959–1963: JASA, Contemporary Literature, and Patents. Classified by subject and indexed by author and inventor. Pp. 1140. Price: ASA members $20; Nonmembers $90.

Volumes 36–44, 1964–1968: JASA and Patents. Classified by subject and indexed by author and inventor. Pp. 485. Out of Print.

Volumes 36–44, 1964–1968: Contemporary Literature. Classified by subject and indexed by author. Pp. 1060. Out of Print.

Volumes 45–54, 1969–1973: JASA and Patents. Classified by subject and indexed by author and inventor. Pp. 540. Price: $20 (paperbound); ASA members $25 (clothbound); Nonmembers $60 (clothbound).

Volumes 55–64, 1974–1978: JASA and Patents. Classified by subject and indexed by author and inventor. Pp. 816. Price: $20 (paperbound); ASA members $25 (clothbound); Nonmembers $60 (clothbound).

Volumes 65–74, 1979–1983: JASA and Patents. Classified by subject and indexed by author and inventor. Pp. 624. Price: ASA members $25 (paperbound); Nonmembers $75 (clothbound).

Volumes 75–84, 1984–1988: JASA and Patents. Classified by subject and indexed by author and inventor. Pp. 625. Price: ASA members $30 (paperbound); Nonmembers $80 (clothbound).

Volumes 85–94, 1989–1993: JASA and Patents. Classified by subject and indexed by author and inventor. Pp. 736. Price: ASA members $30 (paperbound); Nonmembers $80 (clothbound).

Volumes 95–104, 1994–1998: JASA and Patents. Classified by subject and indexed by author and inventor. Pp. 632. Price: ASA members $40 (paperbound); Nonmembers $90 (clothbound).

Revision List

New Associates

Baddorf, Brian C., Globe Motors, Inc., Engineering, 2275 Stanley Ave., Dayton, OH 45404

Barber, Christopher, NSWC Carderock Div., Characterization and Analysis Dept., 9500 MacArthur Blvd., West Bethesda, MD 20817-5700

Barrass, Andrew N., Ctr. of Excellence for Field Biology, Austin Peay State Univ., P.O. Box 4718, Clarksville, TN 37044

Benzel, Steven M., Dept. of Mathematics, Berry College, P.O. Box 5014, Mount Berry, GA 30149-5014

Bertsch, Matthias, Inst. for Musical Acoustics, Music Univ. Vienna, Singerstrasse 26A, Vienna, Wien 1010, Austria

Bird, Sonya F., Linguistics, Univ. of British Columbia, 1866 Main Mall, Buchanan E270, Vancouver, BC V6T 1Z1, Canada

Bossy, Emmanuel, Aerospace and Mech. Eng., Boston Univ., 110 Cummington St., Boston, MA 02215

Brandes, T. Scott, 2812 27th St., NW, Washington, DC 20008

Bresin, Roberto, Speech, Music, Hearing, KTH, Stockholm 10044, Sweden

Brown, Timothy G., Charles M. Salter Associates, Inc., 130 Sutter St., #500, San Francisco, CA 94104

Carr, Scott A., 10 Hillcrest Ave., Wolfville, NS B4P 1T4, Canada

 0001-4966/2004/115(6)/2677/6/$20.00 © 2004 Acoustical Society of America

Cartagena, Claro F., 34 Los Felis Dr., Phillips Ranch, CA 91766
Chandler, Ray L., Anshen + Allen Los Angeles, 5055 Wilshire Blvd., Ste. 900, Los Angeles, CA 90036
Cherry, Peter V., 47 Railroad Ave., Beverly, MA 01915
Coleman, K. A., 430 Wileray Dr., Miamisburg, OH 45342
Crow, Daniel P., 477 Hillcrest Cir., Verona, WI 53593
Cummings, Jim, Acoustic Ecology Inst., 45 Cougar Canyon, Santa Fe, NM 87508
Dallinga, Kurtis D., Spectrum Engineers, 175 S. Main St., Ste. 300, Salt Lake City, UT 84111
Dias, Antonio, Rua De Santarem, Lote 18, 4 Direito, 2755-292 Alcabideche, Portugal di Francescantonio, Paolo, STS, Via Dalmazi 30, Varese VA 21100, Italy
Dong, Hefeng, Telecommunications/Acoustics, Norwegian Univ. of Science and Technology, O.S. Bragstads Plass 2B, Trondheim N-7491, Norway
Driesch, Patricia L., United Technologies Research Ctr., 411 Silver Ln., East Hartford, CT 06108
Duhamel, Denis, Ecole Nationale des Ponts et Chausses, Lab. Analyze des Matriaux et Ident., 6 et 8 Ave. Blaise Pascal, Cit Descartes, Champs sur Marne, Eadie, Tanya L., Univ. of Washington, Speech and Hearing Sci., 1417 NE 42nd St., Seattle, WA 98105
Edelmann, Geoffrey F., Scripps Inst. of Oceanography, Marine Physical Lab., 9500 Gilman Dr., San Diego, CA 92093-0238
Edwards, Sharry K., South Health, Research Sauber Research Ctr., Lake Snowden Dr., Albany, OH 45710
Eide, Nathan T., 2186 Hartford Ave., St. Paul, MN 55116
Ellis, Martha A., Box 719, Keene Valley, NY 12943
Elsberry, Wesley R., 3027 Macaulay St., San Diego, CA 92106
Fiedler, Steven F., URS Corporation, 1615 Murray Canyon Rd., San Diego, CA 92108
Flaherty, Jeremiah J., 8029 West 160th St., Tinley Park, IL 60477
Folegot, Thomas, Marine Sciences and Technology, ATLANTIDE, Tech. Brest-Iroise CS 23866 Brest, Cedex 3 29238, France
Foulkes, John T., Cavanaugh Tocci Associates, 327F Boston Post Rd., Sudbury, MA 01776
Fraas, Michael R., Communication Sciences and Disorders, Univ. of New Hampshire, 4 Library Way, Durham, NH 03824
Fruhmann, Markus, Fehwiesenstrasse 37, Munich 81673, Germany
Gibbons, Steven J., NORSAR, Seismology, Postboks 53, Instituttveien 25, N-2027 Kjeller, Norway
Gill, Chip C., IAGC, 2550 North Loop West, Ste. 104, Houston, TX 77092
Gonzalez, Roberto A., Acoustic Sonic Inc., Design, 2520 NW 112 Ave., Miami, FL 33172
Gregg, Helen L., Ridge Corp./Management, 2917 University Blvd., Dallas, TX 75205
Griffin, Rowland A., Monadnock Non-Wovens LLC, Industrial Park Dr. at Park Ct., Mount Pocono, PA 18344
Grinnip, Roger S., 10 Prospect Rd., Lake Zurich, IL 60047
Grothe, Benedikt, Dept. of Biology II, Univ. of Munich, Luisenstr. 14, Muenchen, Bavaria
Hachmeister, Jorge E., Baylor College of Medicine, Otolaryngology, 6501 Fannin St. 1237, Houston, TX 77030
Haines, Garrett, Treelady Studios, 937 William Penn Ct., Pittsburgh, PA 15221
Hales, L. Paul, QSC Audio Products, Inc., Loudspeaker R&D, 1675 MacArthur Blvd., Costa Mesa, CA 92626
Hall, Carl M., 65 Kings Oak Park, Walnut Creek, CA 94596
Hawker, Larry E., Audio and Display Development, Research in Motion, 305 Philip St., Waterloo, ON N2L 3W8, Canada
Henry, Belinda A., Dept. of Communicative Disorders, Univ. of Wisconsin—Madison, 373 Goodnight Hall, 1975 Willow Dr., Madison, WI 53706
Hess, Wolfgang G., Ruhr-Universitaet, Inst. fuer Kommunikationsakustik (IKA), Universitaetsstr. 150, Bochum NRW 44780, Germany
Hodge, Colin G., Ohmeda Medical, 8880 Gorman Rd., Laurel, MD 20723
Holt, Rachel F., Otolaryngology Head and Neck Surgery, Indiana Univ., Riley Res. Wing 044, 699 West Dr., Indianapolis, IN 46202
Hongbin, Wang, Eaton Corporation, 26201 Northwestern Highway, Southfield, MI 48076
Horesco, Joseph F., Lewis S. Goodfriend & Assoc., 760 Revere Ct., Whippany, NJ 07981
Horonjeff, Richard D., 81 Liberty Square Rd. #20-B, Boxborough, MA 01719
Hufnagle, Jr., Lawrence C., 10040 Springwood Ln., NE, Bainbridge Island, WA 98110
Iannelli, Gerald R., Sarnoff Corp., 201 Washington Rd., Princeton, NJ 08540
Jiang, Xiaoai, 1414 McIntyre Dr., Ann Arbor, MI 48105
Jo, Cheolwoo, Mechatronics, Changwon Natl. Univ., #9 Sarimdong, Changwon, Gyeongnam 641773
Johnson, Tiffany A., Boys Town Natl. Res. Hosp., Hearing Research, 555 N. 30th St., Omaha, NE 68131
Jun, Ogura, Japan Defense Agency, Tech. Res. & Dev. Inst., Fifth Research Ctr., Nagase 3-13-1, Japan
Kadlec, Frantisek, Serikova 2129, Nymburk, 28802, Czech Rep.
Kergomard, Jean, CNRS-Lab. de Mecanique et d'Acoustique, 31 Chemin Joseph Aiguier, 13402 Marseille, Cedex 20, France
King, Wayne M., Speech and Hearing Sciences, Ohio State Univ., 1070 Carmack Rd., Columbus, OH 43210
Kjellin, Olle, Brantosa, Moheda 34036, Sweden
Kresge, James K., 246 Kennedy Dr., Severna Park, MD 21146
Kulmann, Charles A., 7415 Gum Grove Ln., Vacaville, CA 95688-9653
Kumaresan, Jeevith I., 295 Triplicane High Rd., Chennai, Tamil Nadu 600 005, India
Lally, Jonathan P., 197 E. 3rd, #16, New York, NY 10009
Lang, Thomas N., 21 Terrace Dr., Ottawa, ON K2H 9N3, Canada
Lee, Peng, HomeSafe Inspection, Inc., 604 South 16th St., Oxford, MS 38655
Lee, Soyoung, 1636 Kimble Dr., Carrollton, TX 75010
Leistner, Philip, Hanne-Schorp-Pflumm-weg 7, Stuttgart Baden, 70569 Wurttemberg, Germany
Leurer, Klaus C., Dept. of Earth and Ocean Sci., Natl. Univ. of Ireland, Galway, University Rd., Galway, Republic of Ireland
Liu, Chang, Communicative Disorders and Sciences, 122 Cary Hall, 3435 Main St., Buffalo, NY 14214
Majer, Bruce W., 14 Fairway Dr., Plymouth Meeting, PA 19462
Markham, Benjamin E., Acentech Inc., 33 Moulton St., Cambridge, MA 02138
Masi, John A., Shropshire Associates, LLC, 709 Stokes Rd., Medford, NJ 08055
Maye, Jessica, Communication Sciences and Disorders, Northwestern Univ., 2240 Campus Dr., Evanston, IL 60208-3540
Menard, Lucie, Univ. Au Quebec A Montreal, Linguistique et Didactique des Langues, Case Postalle 8888, Succursale Center-Ville, France
Miller, Lee A., Biology Dept., Univ. of Southern Denmark, Campusvej 55, Odense DK5230, Denmark
Millot, Laurent P., 9 rue Charles Peguy, Les Lilas 93260, France
Mocaby, Shawn J., 567 W. Rams Hill St., Kuna, ID 83634
Mora, Mario A., Environmental Acoustics Ltda., Avenida Echenique 5499-D, Nunoa, Santiago 56211, Chile
Mosheh, Moskowitz T., 406 Stonington Rd., Silver Spring, MD 20902
Myers, Scott P., Linguistics, Univ. of Texas, 1 University Station, B5100, Austin, TX 78712-0198
Nakagawa, Seiichi, 138-10 makino-cho, Toyohashi, Aichi 441-8112, Japan
Neal, Edgar H., Neal Research Assoc. Inc., 11809 Collins Dr., Germantown, MD 20876
Newton, Jessica E., The Talaske Group, Inc., 105 N. Oak Park Ave., Oak Park, IL 60301
Niedzielski, Nancy A., Linguistics, Rice Univ., MS-23, Houston, TX 77005
Ogletree, Tim J., MediaMerge, Inc., 12585 Old Hwy. 280, Ste. 105, Chelsea, AL 35043
O'Neill, Kevin F., NSWCCD, Code 713 Self Noise, 9500 MacArthur Blvd., West Bethesda, MD 20817-5700
Ostrovskii, Igor V., Physics and Astronomy, Univ. of Mississippi, 108 Lewis Hall, University, MS 38677
Oswood, Robert, Synergistic Design Assoc., LLC, 4001 Stinson Blvd., Ste. 319, Minneapolis, MN 55112
O'Ulainn, Seamus P., 2107 Dexter Ave., Silver Spring, MD 20902
Padgett, Robert B., EMS, 1515 Larimer St., Denver, CO 80202
Paeng, Dong-Guk, Cheju National Univ., Faculty of Marine Industrial Eng., 1 Ara 1-dong, Jeju, 690-756 Korea
Paige, Gary D., Neurobiology and Anatomy, Univ. of Rochester, 601 Elmwood Ave., Box 603, Rochester, NY 14642

Pastore, Robert A., 132 Pin Oak Rd., Freehold, NJ 07728
Pelizzone, Marco F., ORL, Center Romand d'Implants Cochleaires, Hospital cantonal Universitaire, Geneva CH-1211, Switzerland
Penner, Matthew G., MCW/AGE Consult. Prof. Eng., Electrical, 210-1821 Wellington Ave., Winnipeg, MB R3H 0G4, Canada
Peterson, Chris E., 1505 Drake Ave., Austin, TX 78704
Pishchalnikov, Yuri A., Anatomy and Cell Biology, Indiana Univ., 635 Barnhill Dr., MS 5055U, Indianapolis, IN 46202
Pitermann, Michel, CNRS-Universite de Provence, Lab. Parole et Langage, 29 av. Robert Schuman, Aix-en-Provence, 13621, France
Pitre, Richard, RobTre Consulting Group, L.L.C., 11846 Simpson Rd., Clarksville, MD 21029
Poletti, Mark A., Industrial Research Ltd., Communications and Sensors, P.O. Box 31-310, Lower Hutt, Wellington, United Kingdom
Prentice, Scott C., 10298 Huron Terrace, New Market, MD 21774
Quene, Hugo, Utrecht Univ., Linguistics, Trans 10, Utrecht, NL 3571 GK, The Netherlands
Ramani, Deepak V., Submaroine Sonar Department, Naval Undersea Warfare Ctr., 1176 Howell St., Newport, RI 02841
Reams, Robert W., Neural Audio, 10544 5th Ave., NE, Seattle, WA 98125
Rollings, Tom D., 13413 Sunset Meadows Ln., St. Louis, MO 63128
Ross, Tetjana, Woods Hole Ocean. Inst., Appl. Ocean Phys. & Eng., MS #9, Woods Hole, MA 02543
Russell, Todd, 15 Orchard Ct., Roslyn Heights, NY 11577
Sadek, Ramy S., Univ. of Southern California, Inst. for Creative Technology, 13274 Fiji Way, Marina Del Rey, CA 90292
San Souci, Sooch, 35 bis rue de Fay, St. Pierre Les Nemours PA 77140, France
Scholik, Amy R., GEO-Marine, Inc., 11846 Rock Landing Dr. Ste. C, Newport News, VA 23606
Sekimoto, Sotaro, Graduate Medical School, Speech and Cognitive Science, Univ. of Tokyo, 7-3-1
Hongo, Bunkyo-ku, Tokyo 113-0033, Japan
Serridge, Mark, Bruel & Kjaer North America, Inc., 2815A Colonnades Ct., Norcross, GA 30071
Short, Patrick J., 15 Western Ave., Woodley, Reading, Berkshire RG5 3BJ, England
Smith, Desmond A., Acoustimed (Pty) Ltd., P.O. Box 909, Auckland Park, Gauteng, 2006 South Africa
Snieder, Roel K., Geophysics, Colorado School of Mines, 1500 Illinois St., Golden, CO 80401
Soeta, Yoshiharu, Natl. Inst. of Adv. Indust. Sci. & Tech., Life Electronics Lab., 1-8-31
Midorigaoka, Ikeda, Osaka, 563-8577, Japan
Song, Hyunkyung, Samsung Engineering & Construction, Research Dept., CPO Box 1008, Seoul, 100-610 South Korea
Stone, Michael A., 38 Silverdale Ave., Coton, Cambridgeshire CB3 7PP, United Kingdom
Sun, Xiao-Ming, Speech Pathology & Audiology, Univ. of South Alabama, 2000 University Commons, Mobile, AL 36688-0002
Tan, Cheah Heng, Motorola Technology Sdn. Bhd., Plot 2, Bayan Lepas Technoplex Indust. Park, Mukim 12, S.W.D., Penang 11900, Malaysia
Tan, Mung Sar, Pertac Res. Sdn. Bhd., 27, Jalan 5/76B, Desa Pandan, Kuala Lumpur, Fed. Terr., 55100, Malaysia
Thompson, Quay, 106 Aster Dr., Horseheads, NY 14845
Thorpe, Sonya J., Metropolitan Acoustics, Ste. 108, 40 W. Evergreen Ave., Philadelphia, PA 9118
Traweek, Charles M., 4216 Crosswick Turn, Bowie, MD 20715
Tuss, Joel R., ANP Laboratory, The Boeing Company, P.O. Box 3707, Seattle, WA 98124
Van Doorn, Janis L., Dept. of Clinical Sciences, Umea Univ., Imea 90187, Sweden
van Munster, Bjorn, SIAP B. V., P.O. Box 720, Uden, 5400 AS, The Netherlands
Varfolomeev, Anton L., Pavlov Inst. of Physiology, Grp. of Hearing Physiology, Makarova emb. 6, St. Petersburg, 199034, Russia
Vos, Joos, TNO Human Factors, Kampweg 5, Soesterberg 3769 DE, The Netherlands
Vosbein, Heidi A., Naval Research Lab., Code 7180, Bldg. 1005, Stennis Space Center, MS 39529
Walsh, Kenneth M., 51 Bayberry Ln., Middletown, RI 02842
Walters, Honey L., Edaw Inc., Air Quality/Noise, 2022 ''J'' St., Sacramento, CA 95814
Wear, Keith A., Ctr. for Devices and Radiological Health, Food and Drug Administration, HFZ-142, 12720 Twinbrook Parkway, Rockville, MD 20852
Wenneman, Wayne F., The Boeing Company, Noise Lab., 7755 E. Marginal Way South, Seattle, WA 98108
Whiteford, William D., 320 Honeylocust Ct., Bel Air, MD 21015
Whitfield, James, Liebherr Mining Equipment, 4100 Chestnut Ave., Newport News, VA 23607
Wu, Xiangfa, Univ. of Nebraska—Lincoln, Dept. of Eng. Mech., 900N 17th St., Lincoln, NE 68588-0526
Yang, Wen-Bin, Naval Research Lab., Code 7120, 4555 Overlook Ave., SW, Washington, DC 20375
Zhang, Jiping, Environmental Impact Assessment Ctr., Zhejiang Research and Design Inst. of Environmental Protection, 111 Tian Mu Shan Rd., Hangzhou, Zhjiang, PROC

New Students

Adams, Norman H., Elect. Eng. and Comp. Sci., Univ. of Michigan, 1101 Beal Ave., ATL, Ann Arbor, MI 48109-2110
Aden, Eric, Audio Arts and Acoustics, Columbia College, 600 South Michigan, Chicago, IL 60605
Agarwal, Anurag, Aerospace Engineering, Penn State Univ., 233 Hammond Bldg., University Park, PA 16801
Aguilar, Aucensio A., Columbia College, 600 South Michigan Ave., Chicago, IL 60605
Alam, Iftekhar, Naval EMC Center, c/o F.M.O., Mumbai-400001, India
Almansouri, Ali L., 1615 Ellis Dr., #2, Lawrence, KS 66044
Anderson, Kate T., 1140 West Hancock Ave., Athens, GA 30606
Astrom, Robert B., 8045 Clark's Chapel, Athens, OH 45701
Atwood, Steven G., P.O. Box 65, East Wilton, ME 04234
Austin, Kimberly, 2506 Ashmore Cir., #24, Thousand Oaks, CA 91362
Badertscher, Jeff W., Mechanical Eng., Georgia Inst. of Technology, 771 Ferst Dr., Rm. 122, Atlanta, GA 30332
Bahang, Junghwa, Univ. of Tennessee, Audiology & Speech Pathology, 578 South Stadium, Knoxville, TN 37919
Baik, Kyungmin, Washington State Univ., P.O. Box 642814, Dept. of Physics, Washington State Univ., Pullman, WA 99164-2814
Bailey, Helen R., Biological Sciences, Univ. of Aberdeen, Lighthouse Field Station, Cromarty, Ross-shire, United Kingdom
Baker, Brendan J., 154 Didbrook St., Robertson, Qld 4109, Australia
Bedard, Magella, 1480 Laterriere app. 13, Sherbrooke, QC J1K 3A9, Canada
Berbee, Matthew W., 3715 Newhaven Rd., Pasadena, CA 91107
Bier, Peter J., Bioengineering Inst., Univ. of Auckland, Level 7, 70 Symonds St., Auckland 1001, New Zealand
Bigelow, Timothy A., 1601 Willow Dr., #205, Urbana, IL 61801
Boeser, Sebastian, DESY Zeuthen, AMANDA, Platanenallee 6, Zeuthen, Berlin, Germany
Bogacka, Ann, ul. Plonowa 19, Poznan, Wielkopolska, 61-312, Poland
Brasher, Anthony, Univ. of Michigan, Linguistics, 4080 Frieze Bldg., 105 S. State St., Ann Arbor, MI 48109-1285
Brogan, Daniel S., 4 Russell St., Concord, NH 03301-5315
Brugman, Johanna C., 206 Farm St., Apt. 2W, Ithaca, NY 14850
Buchan, Julie N., Psychology, Queen's Univ., 62 Arch St., Kingston, ON K7L 3N6, Canada
Caldecott, Marion G., Linguistics, Univ. of British Columbia, 1866 Main Mall, Buchanan E270, Vancouver, BC V6T 1Z1, Canada
Camin, John H., 9400 W. Parmer Ln., Apt. 324, Austin, TX 78717
Campbell, Fiona M., Univ. of British Columbia, Linguistics, 1866 Main Mall, Buchanan E270, Vancouver, BC V6T 1Z1, Canada
Cardoso de Cardoso, Guilherme, 920 Symphony Dr., Aurora, IL 60504
Chen, Quan, Medical Physics, UW—Madison, 1530 MSC, 1300 University Ave., Madison, WI 53706
Chester, Scott M., 208 Purlington Rd., Timonium, MD 21093
Choquette, Patrice P.C., Groupe d'Acoust. de l'Univ. de Sherbrooke, Genie Mecanique, Dept. de Genie Mecanique, 2500 Boulv. Universite, Sherbrooke, QC J1K 2R1, Canada
Clarke, Clyde C., Morgan State Univ., Electrical Eng., 5200 Perring Pkwy., Baltimore, MD 21251

Coffin, Allison, Biology, Univ. of Maryland, Biology-Psychology Bldg., College Park, MD 20742
Cohen, Penny D., Applied Marine Physics, 4600 Rickenbacker Causeway, Miami, FL 33149
Conklin, Wade F., Graduate Program in Acoustics, Penn State Univ., P.O. Box 30, State College, PA 16804
Corbley, Shawn M., 100 N. State St., Marengo, IL 60152
Costantino, Anthony, Box 327, 1200 Main St., Bethlehem, PA 18018
Cotte, Benjamin, 0306C White Course A, University Park, PA 16802-6821
Cox, Ethan A., Psychology Dept., Univ. of Arizona, 1503 East Univ., Bldg. 68, Tucson, AZ 85721-0068
Davidson, Greg, 845 E. 57th, #2, Chicago, IL 60637
Denis, Max F., 25 Nesmith St., Lowell, MA 01852
Di Iorio, Lucia, Univ. of Zurich, Zoology-Behavioural Biology, Winterthurerstrasse 190, Zurich 8057, Switzerland
Dillon, Caitlin, 418 E. 17th St., Apt. 11, Bloomington, IN 47408
Dorffner, Kerry, Audiology and Speech Pathology, Bloomsburg Univ., 400 East 2nd St., Bloomsburg, PA 17815
Du, Jikai, Engineering Science and Mechanics, Pennsylvania State Univ., 212 Earth and Engineering Sci. Bldg., University Park, PA 16802
Duke, Connor R., Physics Dept., Brigham Young Univ., 788 North 700 East, Provo, UT 84606
Eichfeld, Jahn D., 1209 Saint Paul St., Baltimore, MD 20202
El-Kady, Mona A., Communication Science and Disorders, Univ. of Pittsburgh, 4019 Forbes Tower, Pittsburgh, PA 15260
Epstein, Michael J., P.O. Box 230338, Boston, MA 02123-0338
Espinoza, German A., Armada de Chile, Escuela de submarinos, Av. Jorge Montt s/n Base Naval, Talcahuano 4260000, Chile
Everhard, Ian L., 1403 Wicker Park Ave., Apt. B, Chicago, IL 60622
Faszer, Andrew C., Flat 41, Churchill Collee Storey's Way, Cambridge CB3 0DS, United Kingdom
Faulkner, Katie F., 912 Lordshill, St. Louis, MO 63119
Federici, Jovi P., Sarah Lawrence College, 1 Mead Way, Bronxville, NY 10708,
Felty, Robert A., Germanic Linguistics, Univ. of Michigan, 3110 MLB, 812 East Washington St., Ann Arbor, MI 48109-1275
Flurie, Alexander D., Swarthmore College, 500 College Ave., Swarthmore, PA 19081
Foxwell, Adam R., Pennsylvania State Univ., P.O. Box 30, 202 Applied Science Bldg., State College, PA 16804
Francoeur, Dany, 2019 Galt ouest #4, Sherbrooke, QC J1K 1J9, Canada
Gant, Valdez L., Math/Eng., Southern Univ. and A&M College, T. T. Allain Hall, Rm. #201, Baton Rouge, LA 70813
Garber, Ben, ICOLAF Records, Box 2306, Providence, RI 02906
Garcia-Sierra, Adrian, 3456 North Hills Dr. #207C, Austin, TX 78731
Giannini, Roberto, Faculty of Elect. Eng. and Computing, Electronic Syst. and Information Process., Unska 3, Zagreb 1000, Croatia
Giessler, Kurt E., 3 Winding Way, Plymouth, MA 02360
Gilcrist, Laura E., 110 Lyrae Dr., Getzville, NY 14068
Glasbrenner, Merete M., 6052 Central Ave., New Port Richey, FL 34653
Grace, Angela, 201 G. Millville Rd., Bloomsburg, PA 17815
Gratke, Jesse T., Applied Research Lab., Pennsylvania State Univ., P.O. Box 30, State College, PA 16803
Gregan, Melanie J., 3434 Colfax Ave. S., #204, Minneapolis, MN 55408
Guerra, Melania, Scripps Inst. of Oceanography, Marine Phys. Lab., 8820 Shellback Way, OAR Bldg. Off. 231, La Jolla, CA 92093-0238
Haberman, Michael R., Mechanical Engineering, Georia Tech Lorraine, 2-3 rue Marconi, Metz, Lorraine 57070, France
Hacihabiboglu, Huseyin, Sonic Arts Reserach Ctr., Queen's Univ. Belfast, University Rd., Belfast BT7 1NN, United Kingdom
Hall, Jessica M., Architectural Engineering, Univ. of Nebraska, 1110 South 67th St., Omaha, NE 68182
Harb, Hadi, Ecole Centrale de Lyon, 36, av Guy de Collongue, Ecully, Rhone Alpes, France, 69130
Harris, Michael C., 2052 South California Ave., #8, Provo, UT 84606
Hartnett, Chris A., 1550 Greenleaf Ave., Lakeforest, IL 60045
Hedin, Clare L., 1603 Oxford St., Berkeley, CA 94709
Heiman, Catherine P., 452 Lewis Pl., Mineola, NY 11501
Hettler, Steffen, Brennerstr. 54, Leonberg, 71229 Germany
Hilt, Matthew G., 3 Graduate Cir., Apt. K, State College, PA 16801
Hoyt, Kenneth, Drexel Univ., Biomed. Eng. Sci. & Health Syst., 3141 Chestnut St., Philadelphia, PA 19104
Huber, Terese, Audiology, Atlanta Area School for the Deaf, 890 N. Indian Creek Dr., Clarkston, GA 30021
Hudson, Harvey D., Speech and Hearing Science, Ohio State Univ., 1070 Carmack Rd., Columbus, OH 43210
Hughes, Eli M., 1621 Ashwicken Ct., State College, PA 16801
Hwang, Yongsin, Graduate Program in Acoustics, Pennsylvania State Univ., 202 Applied Science Bldg., University Park, PA 16802
Jesse, Alexandra, Univ. of California, Santa Cruz, Dept. of Psychology, Social Sciences 2, 1156 High St., Santa Cruz, CA 95064
Johnson, Sean P., Peabody Inst. of Johns Hopkins, Recording Arts & Acoustics, 1 East Mount Vernon Pl., Baltimore, MD 21202
Jung, Youngsook, Jangan 2 dong 316-17, 2nd Floor, Tongdaemoon, Seoul 130-102, South Korea
Kalyanapasupathy, Vijayaraghavan, Electrical Eng. and Computer Sci., IIS Vanderbilt Univ., 2015 Terrace Pl., Nashville, TN 37212
Kan, Alan, 87 Shaftsbury Rd., Denistone, Sydney, NSW 2114, Australia
Kang, A. Min, Haskins Laboratories, 270 Crown St., New Haven, CT 06511
Kang, Soyoung, Ohio State Univ., Linguistics, 1712 Neil Ave., #222 Oxley Hall,
Kluk, Karolina, Experimental Psychology, Univ. of Cambridge, Downing St., Cambridge CB2 3EB, England
Kozasa, Tomoko, Linguistics, Univ. of Hawaii at Manoa, 1890 East-West Rd., Honolulu, HI 96822
Kreider, Wayne E., Univ. of Washington, Appl. Phys. Lab., Bioengineering, 1035 NE 40th St., Box 355640, Seattle, WA 98105
Kubo, Norio, Eichelkamp 23, 3, OGR, Wolfsburg, Niedersachen 38440, Germany
Kurz, Anja, chez Mlle Arnaudova, 161 av. Felix Faure, Lyon, France 69003
Labuda, Cecille, 751 Shady Oaks Cir., Oxford, MS 38655
Lande, Rolf H., Dept. of Engineering, Univ. of Cambridge, Trumpington St., Cambridge, CB2 1PZ, United Kingdom
Lee, Jae Hee, 2451 E. 10th St., #704, Bloomington, IN 47408
Lee, Leo J., 310-106 Seagram Dr., Waterloo, ON N2L 3B8, Canada
Lee, Linda-Eling, Harvard Univ., Sherman Hall, Soldiers Field, Boston, MA 02114
Lee, Ok Kyun J., 418 West Nittany Ave., State College, PA 16801
Levy, Erika S., 220 W. 98th St. #8J, New York, NY 10025
Lewis, Johnathan C., 181 Heritage Dr., Mackinaw, IL 61755
Li, Anxiang, Iowa State Univ., Ctr. for Nondestructive Evaluation, 137 ASC III, 1915 Scholl Rd., Ames, IA 50011
Londono, Jairo, c/o Ultrabox, Ste. 5401, 6910 N.W. 50th St., Miami, FL 33166
Luis, Joseph M., 601 Marjorie Mae St., State College, PA 16803
Lulich, Steven M., 129 Franklin St., #120, Cambridge, MA 02139
Mamou, Jonathan, Univ. of Illinois at Urbana—Champaign, Bioacoustics Research Laboratory, 405 North Mathews, Urbana, IL 61801
Manis, Matthew K., 13 Appletree Ln., Carle Place, NY 11514-1320
Martin, Eric J., Ocean Engineering, Univ. of Rhode Island Bay Campus, South Ferry Rd., Narragansett, RI 02882
Matthis, Kyle J., 3510 North Pine Grove, Apt. 324, Chicago, IL 60657
Midam, Kim, 320-1 Sajik-dong, Jongno-gu, Seoul 110-054, Korea
Miksis, Jennifer L., URI Grad. School of Oceanography, Biol. Ocean., South Ferry Rd., Box 200, Narragansett, RI 02882
Millman, Rebecca E., School of Neurology, Neurobiology and Psychiatry, Univ. of Newcastle upon Tyne, The Medical School, Framlington Pl., Newcastle NE2 4HH, United Kingdom
Mohammadi, Saeed, EE, Georgia Inst. of Technology, 777 Atlantic Dr. NW, Atlanta, GA 30332
Monson, Brian B., Physics and Astronomy, Brigham Young Univ., N203 ESC BYU, Provo, UT 84602
Montealto, Ramil J., Greenfields, Banilad, Mandaue City, Cebu 6014, Philippines
Moran, Cheryl L., 32031/2 Cherrywood Rd., Austin, TX 78722
Morgan, Andrew J., Wheaton College, Physics, CPO 1901, Wheaton, IL 60187
Noriega, Lauren E., Communication Disorders, Lamar Univ. Speech and Hearing, P.O. Box 10076, Beaumont, TX 77710
Norris, Molly K., Rensselaer Polytechnic Inst., Architectural Acoustics, 110 8th St., Troy, NY 12180
Novak, Barbra J., 2303 Blue Bonnet Blvd., Houston, TX 77030
Otero, Sebastian, 2439 22nd St., Apt. 4, Troy, NY 12180
Pai, Nitin, Wayne State Univ., 5050 Anthony Wayne Dr., Detroit, MI 48202

Peng, Shu-Chen, Speech Pathol. & Audiol., Univ. of Iowa, 309 WJSHC, Iowa City, IA 52246
Pestka, Kenneth A., 460 Waupelani Dr., Apt. 205, State College, PA 16801
Phan, Ha T., 78 Mundy Ave., Staten Island, NY 10310
Pinsonnault, Jerome, 17355 Philharmonique, Saint-Hyacinthe, QC J2T 4Z4, Canada
Playfair, David M., Univ. of Iowa, Voxman Music Bldg., Iowa City, Iowa 52242
Pleckham, Jay M., Audio Arts and Acoustics, Columbia College Chicago, 600 S. Michigan Ave., Chicago, IL 60605
Popolo, Peter S., National Ctr. for Voice and Speech, Univ. of Iowa, Hawkins Dr., Bldg. SHC, Room 332, Iowa City, IA 52242
Puckett, Anthony D., Univ. of Maine, Mechanical Eng., 5711 Boardman Hall, Orono, ME 04469
Rabbitt, Alicia A., 86 Great Rd., North Smithfield, RI 02896-7008
Rankin, Summer K., Florida Atlantic Univ., Ctr. for Complex Systems & Brain Sciences, 777 Glades Rd., Boca Raton, FL 33431
Rathsam, Jonathan, Architectural Engineering, Univ. of Nebraska, 247 Peter Kiewit Inst., Omaha, NE 68182-0681
Rosales, Paola, 61 Willowcrest Ln., Phillips Ranch, CA 91766
Rowland, Daniel C., 725 Riceville Rd., #13, Asheville, NC 28805
Saenz, Michael K., 829 N. Dodge St., Iowa City, IA 52245
Sagastegui, Maria M., 3429 Organdy Ln., Chino Hills, CA 91709
Saire, Javier A., Serrano 129, Dpt. 43, Santiago 56, Chile
Salameh, Amjad, 8415 Dynasty Dr., Boca Raton, FL 33433
Scarborough, Rebecca A., Linguistics Dept., UCLA, 3125 Campbell Hall, Los Angeles, CA 90095
Scarpaci, Jacob W., Biomedical Engineering, Boston Univ., 44 Cummington St., Boston, MA 02215
Schuepbach, Matthew R., 14310 Millchester Cir., Chesterfield, MO 63017
Shapiro, Peter J., 440 West Foster Ave., Apt. 6, State College, PA 16801
Shepherd, Paul D., 502 Elmwood Pl. #201, Austin, TX 78705
Silbert, Noah, 1208 S. Woodlawn Ave., Bloomington, IN 47401
Skovenborg, Esben, Kildegaarden 10, 1.th, Aarhus DK-8000 Denmark
Smolenski, Brett Y., 2433 Forest Ln., Schwenksville, PA 19473
So, Connie K., Simon Fraser Univ., Dept. of Linguistics, 8888 University Dr., Burnaby, BC V5A 1S6, Canada
Sodnik, Jaka, Univ. of Ljubljana, Faculty of Electrical Eng., Trzaska 25, Ljubljana, 1000 Slovenia
Son, Minjung, Linguistics, Yale Univ., 370 Temple, #204, New Haven, CT 06520
Songer, Jocelyn, Speech and Hearing Bioscience and Tech., MIT, Room E25-303, 77 Massachusetts Ave., Cambridge, MA 02139
Spiewla, Jacek K., 218 Hubbell St., Apt. 3, Houghton, MI 49931
Steppat, Michael, Erlenweg 17, Nuthetal-Saarmund, Brandenburg 14558, Germany
Sutor, Malinda, 289 Clara Dr., Baton Rouge, LA 70808
Swick, Andrew H., 11900 Hobby Horse Ct., Austin, TX 78758
Tillery, Candice, 2937 N. Dawson, Apt. 2, Chicago, IL 60618
Trenton, John, 975 Shady Ln., Somerset, PA 15501
Truett, Amanda A., Montgomery College, Biology, Takoma Park, MD 20912-4197
Utami, Sentagi S., Physics and Astronomy, Brigham Young Univ., Eyring Science Ctr. (ESC), Provo, UT 84602
Valentine, Louis W., 2001 Linglebach Ln., Bloomington, IN 47408
Vannoni, Elisabetta, Dept. of Animal Behavior, Univ. of Zurich, Winterthurestrasse 190, Zurich 8057, Switzerland
Vidal, Miguel A., 4012 Grant St., Hollywood, FL 33021
Wallace, Rik, 1028 Glenmere Rd., Vista, CA 92084
Walsh, Bridget M., 451 Littleton St., West Lafayette, IN 47906
Wang, Weifang, Rensselaer Polytechnic Inst., 110 8th St., Troy, NY 12180
Wang, Xin, 1900 East 10th St., Eigenmann Hall 1136, Bloomington, IN 47406-7512
Wang, Yong, Chiba Univ., Dept. of Info. & Image Sci., Hachiya Lab., 1-33 Yayoi-cho, Inage-ku, Chiba 263-8522, Japan
Warren, Laura J., 1684 Linden St., Des Plaines, IL 60018
Whitehouse, Andrew M., 45 Mount St., Derby, Derbyshire DE1 2HH, United Kingdom
Wieberg, Kimberly M., Psychology, Univ. of Nevada, Las Vegas, 4505 Maryland Parkway, Las Vegas, NV 89154-5030
Wilcox, Mark A., Univ. of Hartford, Box 3632, 200 Bloomfield Ave., West Hartford, CT 06117
Wise, Jason A., 720 Penn Ave., Apt. #3, Atlanta, GA 30308
Yang, Dan, Systems Science, Univ. of Ottawa, 115 Seraphin Marion St., Ottawa, ON K1N 6N5, Canada
Yang, Liyong, Engineering Mechanics, Univ. of Nebraska, W317.4 Nebraska Hall, Lincoln, NE 68588
Yun, Gwanhi, Univ. of Arizona, Dept. of Linguistics, P.O. Box 210028, Tucson, AZ 85721-0028
Zeitler, Berndt, Technical Acustics, Technical Univ. of Berlin, Einsteinufer 25, Berlin 10587, Germany

New Electronic Associates

Acker-Mills, Barbara, 247 Green St., Auburn, AL 36830
Bal Kocyigit, Filiz, Kocyigit Bldg. Elect. Tur., Imrahor M. 42/b/Ilker, Ankara 06700, Turkey
Beddoes, Michael P., Univ. of British Columbia, Electrical and Computer Eng., 2356 Mail Mall. UBC., Vancouver, BC V6T 1Z4, Canada
Berkley, Terence J., Canadian Forces Maritime Test Ranges, P.O. Box 188, Nanoose Bay, BC V9P 9J9, Canada
Brueckner, Raymond C., Ulmer Str. 14, Blaustein 89134, Germany
Burnett, Ian S., Academic SECTE/Informatics, Univ. of Wollongong, Northfields Ave., Wollongong, NSW 2522, Australia
Busch, Christopher K., Busch Design Group, 2106 Woodland Ave., Raleigh, NC 27608, Carroll, Raymond, 78A Lawrence Rd., Boxford, MA 01921
Carter, Samuel, Rannoch Corp., Airport Noise Monitoring, 1800 Diagonal Rd., Ste. 430, Alexandria, VA 22314
Champagne, Claude, 10998 Waverly St., Montreal, QC H3L 2X1, Canada
Davison, Deborah S., Stanford Univ., Research Compliance, 1215A Welch Rd., Mod. A MC 5401, Stanford, CA 94305
de Blok, Kees, Aster Thermoakoestische Systemen, Smeestraat 11, Veessen, Gelderland, NL 8394 LG, the Netherlands
Dreini, Marco, Pro Soft Professional Software S.r.L., Via Privata O.T.O 3/5, La Spezia, La Spezia, 19136, Italy
Drew, Teresa, Golder Associates Ltd., Calgary Air Group, 1000, 940 6th Ave., SW, Calgary, AB T2Y 3T1, Canada
Edouard, Nesvijski G., 2335 Woodbridge, #255, Roseville, MN 55113
Gladden, Mark, Signature Sight and Sound, P.O. Box 23567, Charlotte, NC 29227
Heimann, Dietrich, DLR Institut fuer Physik der Atmosphaere, Oberpfaffenhofen, Wessling, Bavaria D-82234, Germany
Ingram, Ian L. H., 22 Juniper Ridge Rd., Exeter, NH 03833
Ingrisano, Dennis, Manhattan Bioacoustics, LLC, 1607 Poyntz Ave., Ste. B, Manhattan, KS 66502
Kim, Kang, Univ. of Michigan, Biomedical Engineering, 2200 Bonisteel Blvd., Ann Arbor, MI 48109-2099
Lane, Courtney C., ECE Dept., MS 380, Rice Univ., P.O. Box 1892, Houston, TX 77251-1892
Lang, Albert-Georg, Ludgerusstrasse 3, Duesseldorf, NRW 40225, Germany
Manning, Stephen, Cambridge Collaborative, 689 Concord Ave., Cambridge, MA 02138-1002
Mather, Melissa L., Univ. of Nottingham, Electrical & Electronic Engineering, Rm. 1007 Tower Bldg., University Park, Nottingham NG7 2RD, England
McBride, Dennis K., Potomac Inst., 901 N. Stuart St., 200, Arlington, VA 22203
McPherson, Geoff R., Dept. of Primary Industries, Queensland Fisheries Services, P.O. Box 5396, Queensland 4870, Australia
Moksnes, Knut, Dept. of Engineering, Nord-Trndelag Univ. College, Rostad, Levanger N-7600, Norway
Molero Alonso, Adriana, IMS/IS, CTBTO, P.O. Box 1200, Vienna A-1400, Austria
Nam, Yang-Hee, Div. of Digital Media, Ewha Womans Univ., 11-1 Daehyun-dong, Seodaemungu, Seoul 120-750, Korea
Nedwell, Jeremy, Subacoustech, Chase MIll, Winchester Rd., Bishops Waltham, Southampton SO32 1AH, United Kingdom
Noon, Blake C., Eckel Industries of Canada, P.O. Box 776, 15 Allison Ave., Morrisburg, ON K0C 1X0, Canada
Oyarzun, Miguel F., Digital System Sciences, 184 John Clarke Rd., Middletown, RI 02842
Pietrzyk, John, Biomimetic Connections, Inc., 5066 Anaheim Loop, Union City, CA 94587
Plain, Simon, 68A Allan St. West, Waterloo, ON N2L 1C8, Canada

Quinn, Robert P., 25 Lake Concord Rd., Concord, NC 28025
Randolph, Patricia, Howard Univ. Hospital, 2041 Georgia Ave. NW 4B27, Washington, DC 20060
Rogan, Marshall J., 12 Indian Hill Rd., Medfield, MA 02052
Sassaroli, Elisabetta, 31 Winslow Rd., Apt. #4, Brookline, MA 02446
Schmerr, Lester W., Ctr. for NDE, Iowa State Univ., 1915 Scholl Rd., Ames, IA 50011
Schreiner, Christoph E., Otolaryngology, HSE 824, Univ. of California, San Francisco, 513 Parnassus Ave., San Francisco, CA 94143-0732
Shropshire, David R., Shropshire Associates, LLC, 709 Stokes Rd., Medford, NJ 08055
Soltis, Joseph M., Disney's Animal Kingdom, P.O. Box 10000, Orlando, FL 32830
Spiegelberg, Scott C., School of Music, DePauw Univ., 600 S. Locust, Greencastle, IN 46135
Strelioff, David, Head & Neck Surgery, UCLA School of Medicine, 10833 Le Conte Ave., Los Angeles, CA 90095
Suzuki, Mikio, MediLab, Technical Ctr., 3-41-16 Sengoku Bunkyo-ku, Tokyo, 112-0011 Japan
Taylor, Lawrence S., Biomedical Engineering, Univ. of Rochester, P.O. Box 270168, Hopeman Hall 310, Rochester, NY 14627
Walker, Steven J., Audio Designs Multimedia, 13110 Ransom St., Holland, MI 49424
William, Michaels L., Natl. Marine Fisheries Serv., U.S. Dept. Commerce, 166 Water St., Woods Hole, MA 02543
Yapura, Carlos L., G-Systems, Engineering, 860 Ave. F, Ste. 100, Plano, TX 75074
Yegor, Sinelnikov D., Transurgical, Inc., 220 Belle Meade Rd., Setauket, NY 11733
Yin, Chuan, Apache Corporation, 2000 Post Oak Blvd., Ste. 100, Houston, TX 77056
Zastoupil, Greg, 3734 Ashford Dunwood Rd., Apt. S, Atlanta, GA 30319
Zechmann, Edward L., 5535 Columbia Pike, #704, Arlington, VA 22204-3189

New Corresponding Electronic Associates

Arslan, Burak R., Agah Efendi Sok Esen AP 3/5, Istanbul, Erenkoy, 81070 Turkey
Cutanda Henriquez, Vicente, Vibrations and Acoustics, Centro Nacional de Metrologia, km 4.5
Carretera a los Cues, Municipio del Marques, Queretaro 76241, Mexico
Legorreta, Jaramillo, Armando Martin, Av. Ruiz 1812 e/18 y Ambar, Zona Centro, Ensenada, Baja California, Mexico
Loske, Achim M., UNAM, Centro de Fisica Aplicada y Tecnologia Avanzada, A.P. 1-1010, Queretaro 76000, Mexico
Marzano, Eduardo L., Alameda dos Uapos 945, Sao Paulo, SP 04067-032, Brazil
Pimentel, Jamie A., Juan N Frias 48, Queretaro 76147, Mexico
Shahin, Kimary N., Effat College of Al Faisal Univ. Language & Translation, P.O. Box 34689, Jeddah, Saudi Arabia, 21478
Smirnov, Nickolay A., Simeonovskaya-30, App. 14, Tver 170000, Russia

Reinstated

R. R. Gawtry, L. R. Moss, R. E. van Doeren, D. C. Walton—*Members*

A. G. DeLoach, W. K. Holliday, D. N. Honorof, S. Smith, P. H. Szeto—*Associates*

X. Mou—*Student*

Deceased

W. S. Cramer, C. R. Moe, R. W. Morse, J. E. White—*Fellows*

E. V. Carlson, R. F. Dixon, T. L. Finch, W. J. Finney, H. Levinson, O. R. Woods—*Members*

T. W. Dawson—*Associate*

Members Elected Fellows

A. Alwan, R. O. Cleveland, D. H. Chambers, G. J. Heald,, J. Kang, A. J. Oxenham, D. Rouseff, D. K. Wilson, E. W. Wood

Associates Elected Fellows

A. de Cheveigne, L. Deng, C. J. Plack, C. L. Talmadge

Members to Electronic Associates

T. A. Holden, R. A. Hunt, A. H. Koenig, T. N. Lawrence

Students to Associates

P. Bonaventura, A. L. Butler, M. M. Brimer, B. A. Carter, T. Chi, M. Cleary, J. L. Cooper, V. B. Deecke, E. L. Dugan, C. C. Dunn, B. R. Dzikowicz, S. D. Frank, S. S. Goodman, H. A. Griffin, W. G. Hess, N. Iyer, Y. E. Kim, I. E. Lampropoulos, J. P. Larue, D. Li, J. H. Lowenstein, C. T. McLennan, A. B. Nagy, K. Nishi, J. J. O'Donovan, G. Petculescu, M. Pouplier, J. S. Queen, J. R. Sanchez, N. O. Schiller, V. Shafiro, P. Torre III, P. N. Vassilakis, R. S. Wakeland, X. Yang, X. Zhao, D. N. Zotkin

Students to Electronic Associates

T. L. Arbogast, R. M. Bello, D. Brown, F. J. Gallun, R. L. Hayes, A. Hojen, S. E. Parks, M. Pierson, A. Protopapas

Associates to Students

P. D. Cohen, M. Gregan

Associates to Electronic Associates

T. Akamatsu, J. E. Ament, S. N. Backhaus, G. A. Barth, K. B. Christensen, P. D. Corl, J. A. Dunne, M. Hankard, L. L. Holt, J. E. Lane, D. A. Lindwall, M. D. Manning, J. D. McAuley, W. Metzner, J. L. Miller, A. Okalidou, T. J. Plsek, M. T. Schiff, P. A. Stucky, M. M. Taiwo, E. J. Tucholski, M. Yamashita, S. Dance, S. Oh, G. T. Silva

Electronic Associate to Associate

S. Kouzoupis

Resigned

H. E. Boemmel, G. Manley, B. H. Repp, G. Zweig—*Fellows*

A. A. Aburto, Jr., C. Bean, A. Bostrom, R. F. Coombs, W. J. Cunningham, D. Fucci, T. C. Hundley, D. Y-J. Kim, E. E. Teal, D. Spain, N. Williams, M. S. Vlaming—*Members*

I. J. Ballmann, P. Carkner, J. R. Fricke, J. D. Judege, J. B. Kreijger, M. Markowitz, S. Maxwell, T. M. Nakra, J. M. Quinn, W. R. Rust, R. Schallock, M. Stanzani, D. L. Stover, A. M. Szyhowski, K. Van de Rostyne, B. Wallander, J. M. Flanders, M. Willatzen—*Associates*

I. Sow—*Student*

Fellows	897
Members	2372
Associates	2588
Students	821
Electronic Associates	258
Total	6936

ACOUSTICAL NEWS—INTERNATIONAL

Walter G. Mayer
Physics Department, Georgetown University, Washington, DC 20057

International Meetings Calendar

Below are announcements of meetings and conferences to be held abroad. Entries preceded by an * are new or updated listings.

June 2004

6–9 **13th International Conference on Noise Control**, Gdynia, Poland (Web: www.ciop.pl/noise_04).

8–10 **Joint Baltic–Nordic Acoustical Meeting**, Mariehamn, Åland, Finland (Fax: +358 09 460 224; e-mail: asf@acoustics.hut.fi).

8–10 **Transport Noise and Vibration 2004**, St. Petersburg, Russia (Web: webcente.ru/~eeaa/tn04).

July 2004

5–7 ***International Conference on Modeling and Simulation (MS'2004-France)**, Lyon, France (Web: www.MS2004-france.org).

5–8 **7th European Conference on Underwater Acoustics (ECUA 2004)**, Delft, The Netherlands (Fax: +31 70 322 9901; web: www.ecua2004.tno.nl).

5–8 **11th International Congress on Sound and Vibration (ICSV11)**, St. Petersburg, Russia (Web: www.iiav.org).

11–16 **12th International Symposium on Acoustic Remote Sensing (ISARS)**, Cambridge, UK (Fax: +44 161 295 3815; web: www.isars.org.uk).

August 2004

23–27 **2004 IEEE International Ultrasonics, Ferroelectrics, and Frequency Control 50th Anniversary Conference**, Montréal, Canada (Fax: +1 978 927 4099; web: www.ieee-uffc.org/index2-asp).

22–25 **Inter-noise 2004**, Prague, Czech Republic (Web: www.internoise2004.cz).

30–1 **Low Frequency 2004**, Maastricht, The Netherlands (G. Leventhall, 150 Craddlocks Avenue, Ashtead, Surrey KT 21 1NL, UK; web: www.lowfrequency2004.org.uk).

September 2004

1–3 **Subjective and Objective Assessment of Sound**, Poznań, Poland (Institute of Acoustics, Adam Mankiewicz University, Poznań, Poland. Fax: +48 61 8295 123; web: www.soas.amu.edu.pl/soas.html).

6–10 **51st Open Seminar on Acoustics**; **9th School on Acoustooptics and Applications**; **Ultrasound in Biomeasurements**, Gdańsk, Poland (University of Gdańsk, Institute of Experimental Physics, 80-952 Gdańsk, Poland; fax: +48 58 341 31 75; web: univ.gda.pl/~osa).

13–17 **4th Iberoamerican Congress on Acoustics**, **4th Iberian Congress on Acoustics**, **35th Spanish Congress on Acoustics**, Guimarães, Portugal (Fax: +351 21 844 3028; web: www.spacustica.pt/novidades.htm).

14–16 **International Conference on Sonar Signal Processing and Symposium on Bio-Sonar Systems and Bioacoustics**, Loughboro, UK [Fax: +44 1509 22 7053 (c/o D. Gordon); web: ioa2004.lboro.ac.uk].

15–17 **26th European Conference on Acoustic Emission Testing**, Berlin, Germany (DGZIP, Max-Planck-Str. 26, 12489 Berlin, Germany; web: www.ewgae2004.de).

20–22 **International Conference on Noise and Vibration Engineering (ISMA2004)**, Leuven, Belgium (Fax: +32 16 32 29 87; web: www.isma-isaac.be/fut_conf/default_en.phtml).

20–22 **9th International Workshop "Speech and Computer" (SPECOM'2004)**, St. Petersburg, Russia (Web: www.spiiras.nw.ru/speech).

28–30 **Autumn Meeting of the Acoustical Society of Japan**, Naha, Japan (Fax: +81 3 5256 1022; web: wwwsoc.nii.ac.jp/asj/index-e.html).

October 2004

4–8 **8th Conference on Spoken Language Processing (Interspeech)**, Jeju Island, Korea (Web: www.icslp2004.org).

6–8 **Acoustics Week in Canada**, Ottawa, ON, Canada (J. Bradley, NRC Institute for Research on Construction [Acoustics Section], Ottawa, Ontario, K1A 0R6; fax: +1 613 954 1495; web: caa-aca.ca/ottawa-2004.html).

6–7 ***Autumn Conference of the Institute of Acoustics**, Oxford, UK (Web: www.ioa.org.uk).

8–9 **Reproduced Sound 20**, Oxford, UK (Web: www.ioa.org.uk).

November 2004

3–5 **Australian Acoustical Society Conference—Transportation Noise & Vibration**, Surfers Paradise, Queensland, Australia (Fax: +61 7 6217 0066; web: www.acoustics.asn.au/conference/index.htm).

4–5 **Autumn Meeting of the Swiss Acoustical Society**, Rapperswil, Switzerland (Fax: +41 419 62 13; web: www.sga-ssa.ch).

15–18 ***15th Meeting of the Russian Acoustical Society**, Nizhny Novgorod, Russia (Fax: +7 95 126 0100; web: www.akin.ru).

17–19 ***7th National Congress of the Turkish Acoustical Society**, Nevsehir-Cappadocia, Turkey (Web: www.tak-.der.org).

April 2005

18–21 **International Conference on Emerging Technologies of Noise and Vibration Analysis and Control**, Saint Raphaël, France (Fax: +33 4 72 43 87 12; e-mail: goran.pavic@insa-lyon.fr).

May 2005

16–20 **149th Meeting of the Acoustical Society of America**, Vancouver, British Columbia, Canada (ASA, Suite 1NO1, 2 Huntington Quadrangle, Melville, NY 11747-4502; fax: +1 516 576 2377; web: asa.aip.org).

June 2005

28–1 ***International Conference on Underwater Acoustic Measurements**: **Technologies and Results**, Heraklion, Crete, Greece (Web: UAmeasurements2005.iacm.forth.gr).

July 2005

11–14 ***12th International Congress on Sound and Vibration**, Lisbon, Portugal (Web: www.iiav.org).

August 2005

6–10 **Inter-Noise**, Rio de Janeiro, Brazil (Web: www.internoise2005.ufsc.br).

 0001-4966/2004/115(6)/2683/2/$20.00 © 2004 Acoustical Society of America

28–2 **EAA Forum Acusticum Budapest 2005**, Budapest, Hungary (I. Bába, OPAKFI, Fö u. 68, Budapest 1027, Hungary; fax: +36 1 202 0452; web: www.fa2005.org).

September 2005

4–8 **9th Eurospeech Conference (EUROSPEECH'2005)**, Lisbon, Portugal (Fax: +351 213145843; web: www.interspeech2005.org).

5–9 **Boundary Influences in High Frequency**, **Shallow Water Acoustics**, Bath, UK (Web: acoustics2005.bath.ac.uk).

11–15 ***6th World Congress on Ultrasonics**, Beijing, China (Secretariat of WCU 2005, Institute of Acoustics, Chinese Academy of Sciences, P.O. Box 2712 Beijing, 100080 China; fax: +86 10 62553898; web: www.ioa.ac.cn/wcu2005).

14–16 ***Autumn Meeting of the Japanese Acoustical Society**, Sendai, Japan (Web: www.asj.gr.jp/index-en.html).

October 2005

19–21 **36th Spanish Congress on Acoustics Joint with 2005 Iberian Meeting on Acoustics**, Terrassa (Barcelona), Spain (Sociedad Española de Acústica, Serrano 114, 28006 Madrid, Spain; fax: +34 914 117 651; web: www.ia.csic.es/sea/index.html).

June 2006

26–28 **9th Western Pacific Acoustics Conference (WESPAC 9)**, Seoul, Korea (Web: www.wespac8.com/WespacIX.html).

July 2007

9–12 ***14th International Congress on Sound and Vibration (ICSV14)**, Cairns, Australia (E-mail: n.kessissoglou@unsw.edu.au).

September 2007

2–7 **19th International Congress on Acoustics (ICA2007)**, Madrid, Spain (SEA, Serrano 144, 28006 Madrid, Spain; web: www.ia.csic.es/sea/index.html).

Preliminary Announcement

June 2008

23–27 **Joint Meeting of European Acoustical Association (EAA)**, **Acoustical Society of America (ASA)**, **and Acoustical Society of France (SFA)**, Paris, France (details to be announced later).

BOOK REVIEWS

P. L. Marston
Physics Department, Washington State University, Pullman, Washington 99164

These reviews of books and other forms of information express the opinions of the individual reviewers and are not necessarily endorsed by the Editorial Board of this Journal.

Editorial Policy: *If there is a negative review, the author of the book will be given a chance to respond to the review in this section of the Journal and the reviewer will be allowed to respond to the author's comments. [See "Book Reviews Editor's Note," J. Acoust. Soc. Am.* ***81****, 1651 (May 1987).]*

Specification Development, Vol. 5 of Mechanical Vibration & Shock

Christian Lalanne

Taylor & Francis, New York, 2002.
Price: $150.00 (hardcover), ISBN: 1-56032-990-4.

During the past half century there has been increasing interest in the detection, measurement, and analysis of sound generated by equipment and systems. Principal purposes of the measurements included development of required maintenance intervals and procedures, prediction of life, determination of effect of noises on people, and interference with electrical and electronic systems. The earliest measurements used battery powered sound level meters equipped probes. Broadband measurements were made of displacement, velocity, and acceleration. Later developments initially included proportional bandwidth analyzers, which permitted one-third octave band analysis through the frequency range of interest. This was followed by the use of very narrow band analyzers, fast Fourier transform (FFT) analyzers, etc. Readings using the probe varied widely because of angles with respect to the surface, hand tremors, and applied pressure. They were eventually replaced by accelerometers attached to the machinery surface.

The above described measurement procedures were used by the Navy to guide maintenance procedures for equipment and machinery systems used on ships and submarines. The use of the probe was developed and taught by R. Y. Chapman of the New London, Connecticut Submarine base. These measurements were referred to as Chapman numbers. Concurrently studies were conducted of machinery system generated airborne and structureborne noise transmission aboard ships and submarines to determine acceptable maximum acceleration levels. Those levels formed the basis of Military Standard MIL-STD-740, which rather recently was slightly modified and formed the basis for ANSI S2.26-2501, Vibration Testing Requirements and Acceptance Criteria for Shipboard Equipment. During the same recent time frame, there was started ISO Technical Committee 108, Condition Monitoring and Diagnostics of Machines. Lelanne's book provides a useful discussion of relevant issues.

Lalanne in the introduction to his book notes that mechanical environment standards were taken directly from written standards developed many years ago from measurements of equipment and systems of now obsolete design. The instrumentation was long ago succeeded by modern analysis instruments and procedures. With the development of solid state electronics, more sophisticated analysis techniques with narrow measurement bands, various rise times, and averaging times became available. Early standards which are still in use are, by necessity, quite conservative, and resulted in overly costly and complex designs.

Lalanne's book is divided into two major parts. The first six chapters deal with various spectra types including (1) extreme response spectra (ERS) of sinusoidal vibration, (2) first passage at a given level of response of a single-degree-of-freedom linear system to a random vibration, (3) the ERS of a random vibration, (4) fatigue damage spectra (FDS) of sinusoidal vibration, (5) FDS of a random vibration, and (6) FDS of a shock.

The second section of the book actually deals with specification development. Chapter 7 discusses specifications in general, and the several uses of tests including evaluation and determination of equipment characteristics, qualification and prequalification testing, etc. It also discusses derivation of specifications derived from standards. There is also a brief description of the derivation of several presently used standards such as MIL-STD 810. In this chapter he discusses tailoring specifications to be more realistic.

Chapter 8 discusses the uncertainty or safety factor. It explains the reasons such factors are needed: measurement errors, effects of real life environments, variation of measurement locations, and equipment aging. Effects of aging both due to system use and extended storage are discussed in detail in Chap. 9 and aging factors are given. Lalanne points out that care must be used to not use an aging factor if the equipment has undergone accelerated usage prior to the testing.

Chapter 10 contains a discussion of qualification tests to demonstrate that the equipment meets its requirements at the time of its design. Chapter 11, titled ''Specification development,'' explains tailoring, which is divided into four main stages: analysis of life cycle profile, collection of data in real environment, synopsis of data, and establishment of test program. Chapter 12 gives some other uses of ERS and FDS.

The book discusses and summarizes hundreds of studies on the subject from this country and many European sources. The techniques should be useful to both scientists and engineers in updating presently used standards and specifications. They should result in greater precision in actual equipment requirements and likely savings in equipment and system cost and weight.

LOUIS A. HERSTEIN III
2722 Hanson Avenue
Baltimore, Maryland 21209-3911

 0001-4966/2004/115(6)/2686/1/$20.00 © 2004 Acoustical Society of America

REVIEWS OF ACOUSTICAL PATENTS

Lloyd Rice
11222 Flatiron Drive, Lafayette, Colorado 80026

The purpose of these acoustical patent reviews is to provide enough information for a Journal reader to decide whether to seek more information from the patent itself. Any opinions expressed here are those of reviewers as individuals and are not legal opinions. Printed copies of United States Patents may be ordered at $3.00 each from the Commissioner of Patents and Trademarks, Washington, DC 20231. Patents are available via the Internet at http://www.uspto.gov.

Reviewers for this issue:

GEORGE L. AUGSPURGER, *Perception, Incorporated, Box 39536, Los Angeles, California 90039*
JOHN ERDREICH, *Ostergaard Acoustical Associates, 200 Executive Drive, West Orange, New Jersey 07052*
DAVID PREVES, *Starkey Laboratories, 6600 Washington Ave. S., Eden Prarie, Minnesota 55344*
DANIEL R. RAICHEL, *2727 Moore Lane, Fort Collins, Colorado 80526*
CARL J. ROSENBERG, *Acentech Incorporated, 33 Moulton Street, Cambridge, Massachusetts 02138*
ERIC E. UNGAR, *Acentech, Incorporated, 33 Moulton Street, Cambridge, Massachusetts 02138*
ROBERT C. WAAG, *Univ. of Rochester, Department of Electrical and Computer Engineering, Rochester, New York 14627*

6,651,484

43.35.Zc DEVICE FOR MEASURING THE SPECIFIC DENSITY OF A GASEOUS OR LIQUID MEDIUM

Klaus-Dieter Fiebelkorn and Alf Puettmer, assignors to Siemens Aktiengesellschaft
25 November 2003 (Class 73/32 A); filed in Germany 23 September 1999

Cylindrical delay paths of different lengths, made of quartz glass, are epoxied to the sides of a two-sided circular acoustic transducer. Cylindrical containers are affixed to the sides of the delay paths that are remote from the transducer. One of these containers holds a reference fluid, such as air, and the other holds the test fluid. The density of the test fluid is determined by comparing the round-trip time of a pulse in it to that of a pulse in the reference fluid.—EEU

6,651,502

43.35.Zc METHOD FOR ACOUSTIC IMAGING OF A TUBULAR SHAPE

William R. Davis, assignor to The United States of America as represented by the Secretary of the Navy
25 November 2003 (Class 73/606); filed 3 April 2002

An ultrasound beam is directed through a focusing lens so that it penetrates the outer surface of a tube being inspected. The beam is reflected from the inner surface, passes back through the outer surface, and through another lens to an imaging camera chip. This chip converts the beam into an image of the inner surface, the outer surface, and the internal volume.—EEU

6,658,376

43.38.Ar DETERMINATION OF VIBRATION FREQUENCY CHARACTERISTICS OF ELECTRODED CRYSTAL PLATE

Ji Wang *et al.*, assignors to Seiko Epson Corporation
2 December 2003 (Class 703/13); filed 30 November 1999

This patent pertains to an analytical method for analyzing the vibration characteristics of crystal plates with attached electrodes in the design stage. The method is based on third-order Mindlin plate theory and applies correction factors to make the cutoff frequencies exact. The method is supposedly able to determine, for example, the fundamental thickness-shear frequency, coupling between the thickness-shear mode and other modes (such as a flexural mode), and coupling between the thickness-stretch mode and other modes.—EEU

6,674,215

43.38.Ar ELASTIC WAVE DEVICE

Kenji Yoshida *et al.*, assignors to Mitsubishi Denki Kabushiki Kaisha
6 January 2004 (Class 310/313 R); filed in Japan 16 November 1999

This patent relates to an apparatus for propagating acoustic waves, used in circuits for communication equipment. The apparatus consists of a piezoelectric substrate containing primarily lithium tantalate and an interdigital transducer formed on the substrate. The surface of the substrate is a surface rotated a certain amount (34° to 41°) from the crystal *Y* axis about the crystal *X* axis. The ratio of the electrode finger thickness to the wavelength of the surface acoustic wave is set between 0.01 and 0.05. The ratio of the electrode finger width to the finger's spatial period is set between 0.6 and a little less than 1.—EEU

6,669,644

43.38.Fx MICRO-MACHINED ULTRASONIC TRANSDUCER (MUT) SUBSTRATE THAT LIMITS THE LATERAL PROPAGATION OF ACOUSTIC ENERGY

David G. Miller, assignor to Koninklijke Philips Electronics N.V.
30 December 2003 (Class 600/459); filed 31 July 2001

The device is a micro-machined ultrasonic transducer (MUT) substrate that is designed to limit the lateral propagation of acoustic energy. The MUT incorporates holes, usually referred to as vias, in the substrate and proximate to a MUT element. These vias are said to reduce or eliminate the propagation of acoustic energy traveling laterally in the substrate. The vias may also be doped to provide an electrical connection between the MUT element and circuitry on the surface of an integrated circuit substrate to which the MUT substrate is attached.—DRR

 0001-4966/2004/115(6)/2689/19/$20.00 © 2004 Acoustical Society of America

6,668,062

43.38.Hz FFT-BASED TECHNIQUE FOR ADAPTIVE DIRECTIONALITY OF DUAL MICROPHONES

Fa-Long Luo *et al.*, assignors to GN ReSound AS
23 December 2003 (Class 381/122); filed 9 May 2000

The power of digital processing allows adaptively steered microphone arrays to be used in mobile communications systems and even in hearing aids. In practice, the array's null zone is steered toward a source of unwanted noise while at the same time adequate sensitivity along the preferred axis is maintained. This patent describes a different approach. There is no preferred direction as such. Given two microphones located some distance apart, the only additional requirements are that the preferred source and the noise source lie in different directions and that the power response of the noise source is greater than that of the preferred source. When these conditions are met, a noise-attenuated signal can be realized by performing two FFTs and one inverse FFT for each frame of data. In cases where the power levels of the two sources are roughly equal, data can be gathered during speech pauses and used to obtain necessary phase information about the noise signal.—GLA

6,665,412

43.38.Ja SPEAKER DEVICE

Akio Mizoguchi, assignor to Sony Corporation
16 December 2003 (Class 381/336); filed 23 August 1999

This patent runs to almost 50 pages, includes 34 illustrations, and is garnished with a sprinkling of math. Its basic premise seems to be that two-channel stereo reproduction can be improved by using directional loudspeakers (not a new idea) and that the most practical way to achieve the desired directionality ''down to ultra low frequencies'' is through ''a combination of omnidirectionality and bidirectionality.'' The latter phrase simply defines a cardioid sound source, so it too is not a new idea. The implementation shown consists of loudspeaker **22** in box **21** which has a ''sound wave radiation port'' **23** covered with acoustic resistance material **24**. The radiation port is located on one of the sides of the box rather than the rear panel. This configuration was patented by LTV-Altec in 1973, so it can hardly be considered new either. In fact, there is a substantial body of prior art, not referenced in the patent, relating to gradient source loudspeakers and their application to stereo reproduction.—GLA

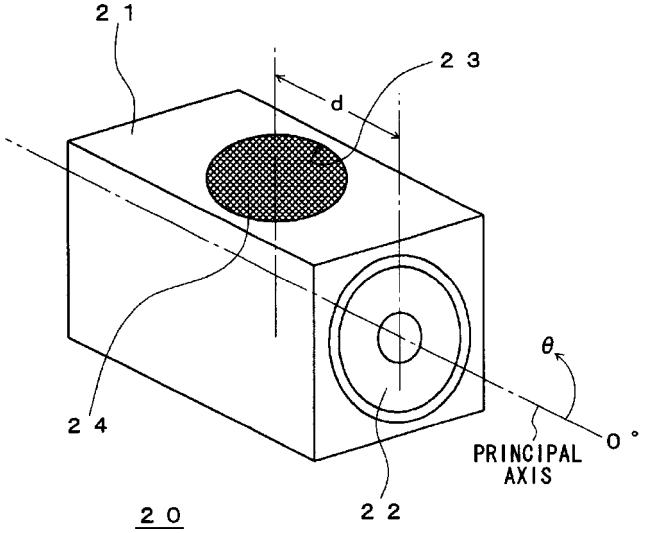

6,654,475

43.38.Ja ELECTRICITY-TO-SOUND TRANSDUCER

Jiro Nakaso, assignor to Victor Company of Japan, Limited
25 November 2003 (Class 381/396); filed in Japan 29 September 2000

Tall, thin loudspeakers can be driven by elongated voice coils similar to the illustration. The idea goes back at least 40 years and commercial versions have appeared from time to time. This patent describes a design that includes several improvements over prior art. The most significant feature is ''reinforcing beam'' **13**, which is said to suppress unwanted vibrational modes.—GLA

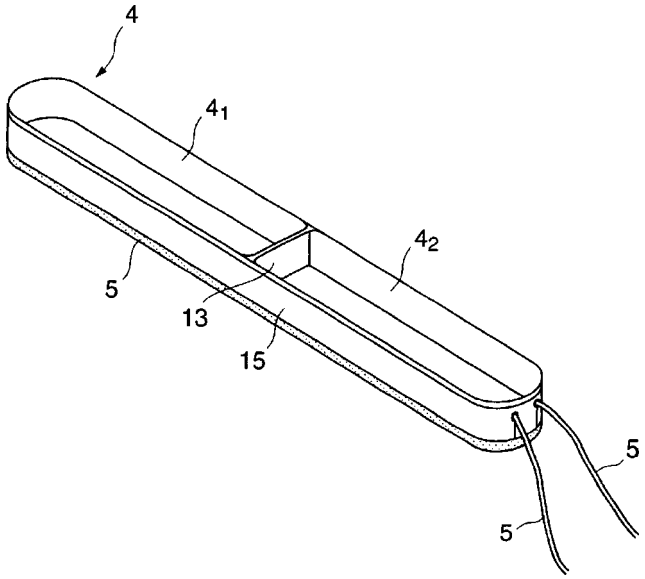

6,655,495

43.38.Ja LOUDSPEAKER DAMPER AND LOUDSPEAKER

Mitsukazu Kuze *et al.*, assignors to Matsushita Electric Industrial Company, Limited
2 December 2003 (Class 181/171); filed in Japan 16 October 2001

In almost all conventional loudspeakers, while voice coil **1a** moves up and down it is kept centered in magnetic gap **9** by outer suspension **4** and centering spider **3A**. (Japanese speaker manufacturers prefer to use the term ''damper.'') The spider usually takes the form of a corrugated disk. However, this patent argues that a central flat portion as shown improves linearity and resists rocking modes.—GLA

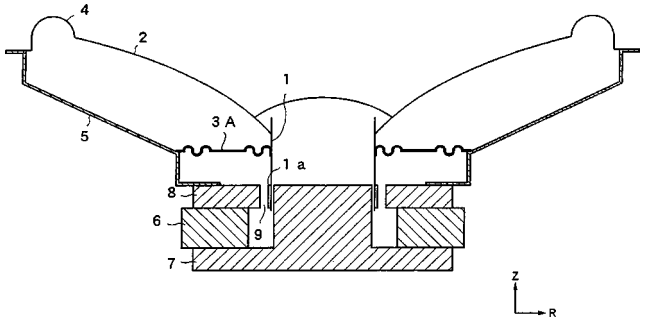

6,658,128

43.38.Ja HORN LOUDSPEAKER

Tsutomu Yoshioka *et al.*, assignors to TOA Corporation
2 December 2003 (Class 381/340); filed in Japan 30 April 1998

A sectoral horn driven by a right-angle throat section can be designed to produce relatively uniform coverage over a wide frequency range. The horn described in this patent is, in a sense, a 180° variant of the original

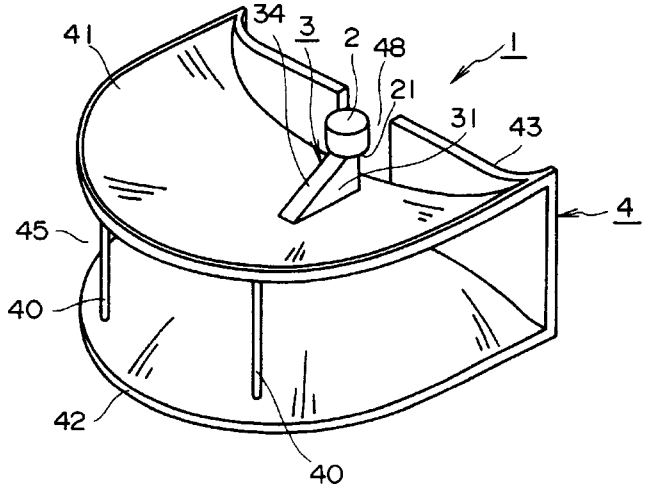

Western Electric 31A, but its right-angle throat is quite different. Throat **34** takes the form of a narrow wedge, terminating in a slot-shaped transition. Multiple-driver variants are also described in the patent.—GLA

6,661,903

43.38.Ja LOUDSPEAKER

Kazuaki Tamura and Shoji Tanaka, assignors to Matsushita Electric Industrial Company, Limited
9 December 2003 (Class 381/423); filed in Japan 28 April 1998

This high-frequency loudspeaker uses a shallow, clamped-edge cone to minimize cavity resonances and thereby provide more accurate reproduction. The patent briefly describes more than a dozen preferred embodiments

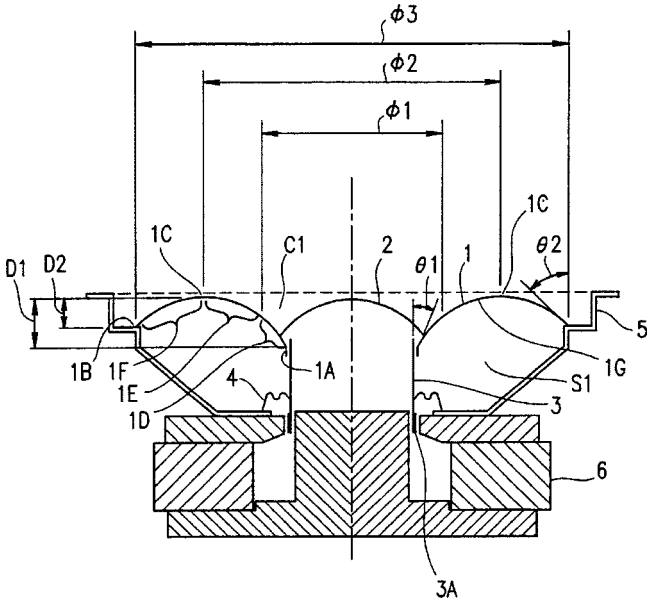

covering almost every possible permutation and combination of features. It also includes curves showing impressively smooth frequency response over a range from about 1500 Hz to more than 20 kHz.—GLA

6,654,468

43.38.Kb APPARATUS AND METHOD FOR MATCHING THE RESPONSE OF MICROPHONES IN MAGNITUDE AND PHASE

Stephen C. Thompson, assignor to Knowles Electronics, LLC
25 November 2003 (Class 381/92); filed 16 November 1998

Although this invention is intended mainly for use with hearing aid microphone arrays, it might well find other applications. For any kind of transducer array to operate as intended the individual transducers must be closely matched. In today's high-tech world, electronic signal processing

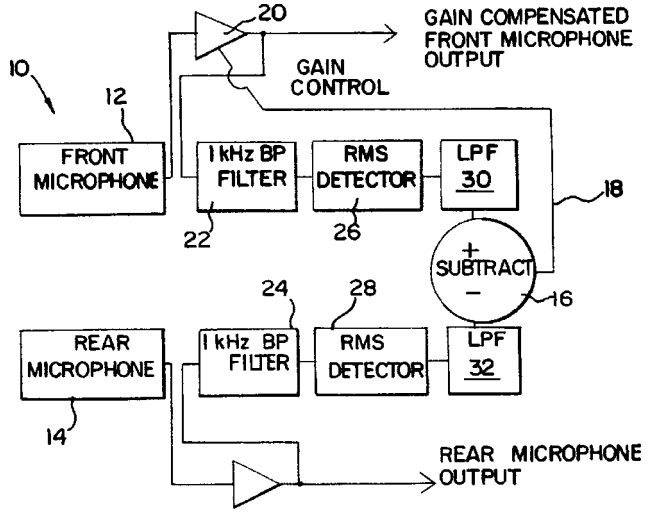

may be more practical than selecting matched transducers. The three claims of this short patent seem to cover the basic idea of electronically matching the signals from two microphones by subtracting one signal from the other, then using the resulting error signal to adjust the gain and response contour of one microphone.—GLA

6,651,501

43.38.Lc ADAPTIVE EQUALIZER FOR VARIABLE LENGTH SOUND TUBES UTILIZING AN ELECTRICAL IMPEDANCE MEASUREMENT

Richard Lance Willis, assignor to Motorola, Incorporated
25 November 2003 (Class 73/589); filed 30 December 2002

In one common type of lightweight headset, sound is conducted from a transducer to the ear through a tube. Standing waves in the tube produce severe peaks and dips in response. If these peaks and dips are electrically equalized, sound quality is improved and the threshold of feedback is raised. However, some users prefer a short accessory tube while others use a longer tube that partly enters the ear canal, requiring different equalization for different combinations of equipment. A suitable adaptive equalizer might be designed using measurement of acoustic response, delay, or electrical impedance. The inventor has investigated all three methods. In each case, an automated test procedure estimates the effective length of the tube, and this information is used to create an inverse equalizer.—GLA

6,665,411

43.38.Lc DVE SYSTEM WITH INSTABILITY DETECTION

Shawn K. Steenhagen, assignor to Digisonix LLC
16 December 2003 (Class 381/93); filed 21 February 2001

DVE stands for ''digital voice enhancement'' and the problem addressed is that of identifying incipient acoustic feedback, or howling. This is

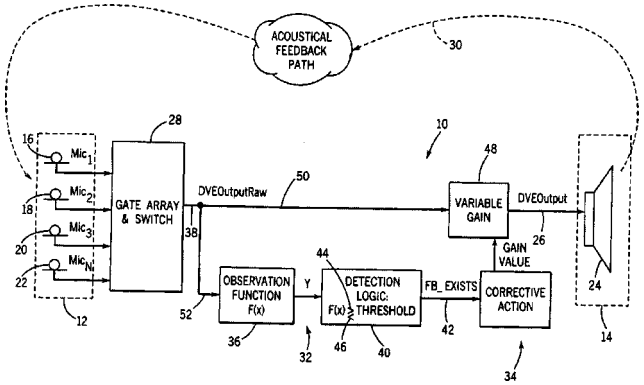

accomplished by continually modeling the signal at point **38** as a second-order all-pole filter and monitoring one of the filter coefficients. ''Under normal conditions, the variation of such a filter coefficient is large. At the onset of feedback, the DVE output at **38** becomes sinusoidal, and the variation of the filter coefficient becomes very small.'' The patent explains this process in some detail and is not difficult to follow.—GLA

6,584,182

43.38.Si METHOD AND APPARATUS FOR COMMUNICATING DATA OVER A TELEPHONE LINE USING AN ACOUSTIC MODEM

Donald E. Brodnick, assignor to GE Medical Systems Information Technologies, Incorporated
24 June 2003 (Class 379/93.37); filed 27 August 2001

Although essentially obsolete for computer communications, acoustic modems are still used in certain remote monitoring, doctor/patient situations, where a patient at home may wish to transmit certain data, such as electrocardiogram readings, to the doctor. An elderly, sick, feeble, intimidated, or confused patient may have to begin with a voice interaction, then place the handset properly in a cradle, start the transmission, and then determine somehow whether the data transmission has succeeded, when it is complete, and when the phone may again be picked up. This device is expected to help in that process by accepting the handset in either direction. Both ends of the device include transducers suitable for coupling to either the microphone or the earpiece of the handset.—DLR

6,661,901

43.38.Si EAR TERMINAL WITH MICROPHONE FOR NATURAL VOICE RENDITION

Jarle Svean *et al.*, assignors to Nacre AS
9 December 2003 (Class 381/328); filed 1 September 2000

The invention described in this patent is a sophisticated in-the-ear terminal for use in noisy environments. It is designed to provide hearing protection and improved electronic communication, including natural sounding sidetone to the user. Moreover, the device can be programmed to

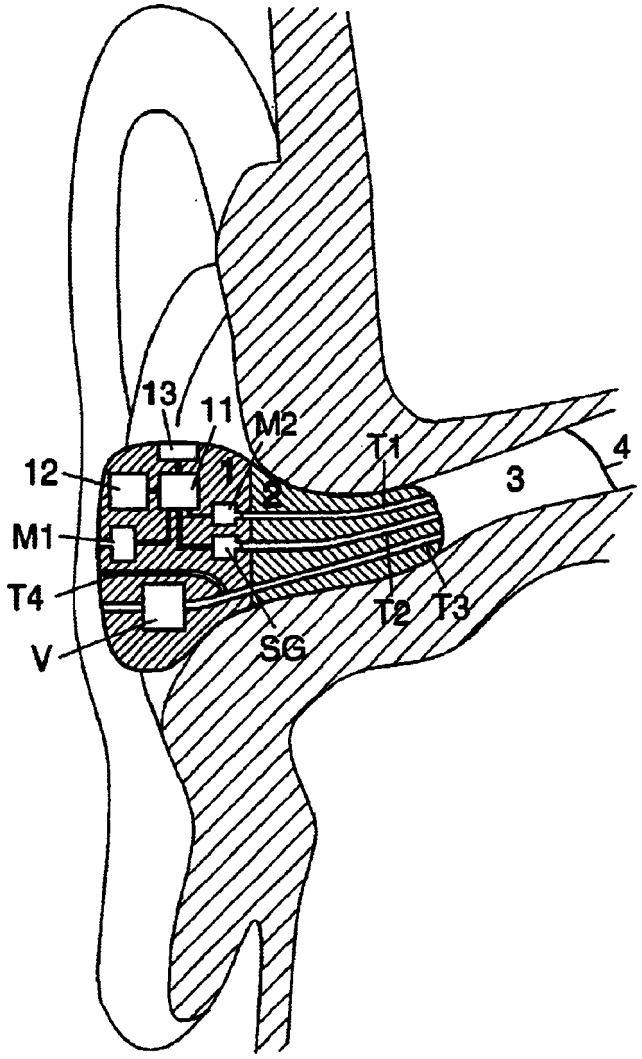

act as an accurate noise exposure meter (dosimeter) and to verify that it has been inserted correctly and is functioning properly. The terminal contains two microphones **M1** and **M2**, a receiver **SG**, and elaborate digital audio circuitry in component **11**.—GLA

6,668,065

43.38.Si BONE-CONDUCTION TRANSDUCER AND BONE-CONDUCTION SPEAKER HEADSET THEREWITH

Sang Chul Lee and Bon Youn Koo, assignors to Dowumitec Corporation
23 December 2003 (Class 381/380); filed in the Republic of Korea 18 April 2000

Bone conduction transducers can be used under certain conditions where headsets or in-the-ear receivers are not practical. However, it is difficult to design a small, lightweight, efficient, wide-range bone conduction

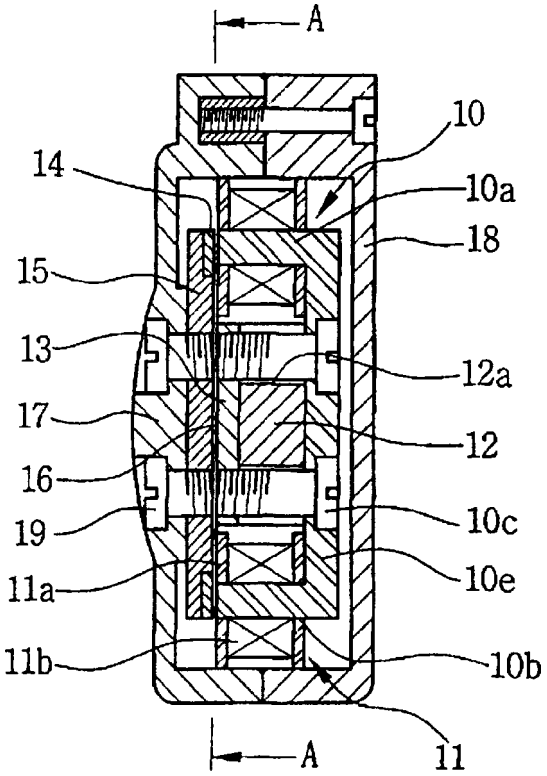

transducer. This patent describes an improved design utilizing twin (fixed) voice coils **11a** and **11b**, a magnet **12** located between the coils, and a diaphragm **15** made of low magnetic resistance material. These are nested to form a small, rectangular assembly.—GLA

6,651,513

43.40.Le VIBRATION METER AND METHOD OF MEASURING A VISCOSITY OF A FLUID

Alfred Wenger *et al.*, assignors to Endress & Hauser Flowtec AG
25 November 2003 (Class 73/861.357); filed in Germany 27 April 2000

This patent pertains to a means for measuring the mass flow rate, density, and viscosity of a fluid. A flexible pipe element is excited at a constant frequency in one plane perpendicular to the pipe, and the motion that results in the orthogonal direction (due to the Coriolis effect) is measured. The mass flow rate is determined from this measurement. The pipe element also is subjected to a vibratory torque about its axis and the resulting torsional motion is sensed. The ratio of the torque to the angular motion is used to determine the viscosity of the liquid in the tube.—EEU

6,655,215

43.40.Tm INVERSE CORNER CUBE FOR NON-INTRUSIVE THREE AXIS VIBRATION MEASUREMENT

George D. Hadden, assignor to Honeywell International Incorporated
2 December 2003 (Class 73/657); filed 15 June 2001

One face of a regular tetrahedron **2** is attached to vibrating object **1**. The other three faces have mirrored surfaces. A light beam **14** is directed onto the apex, so that a portion of it is reflected from each mirrored surface,

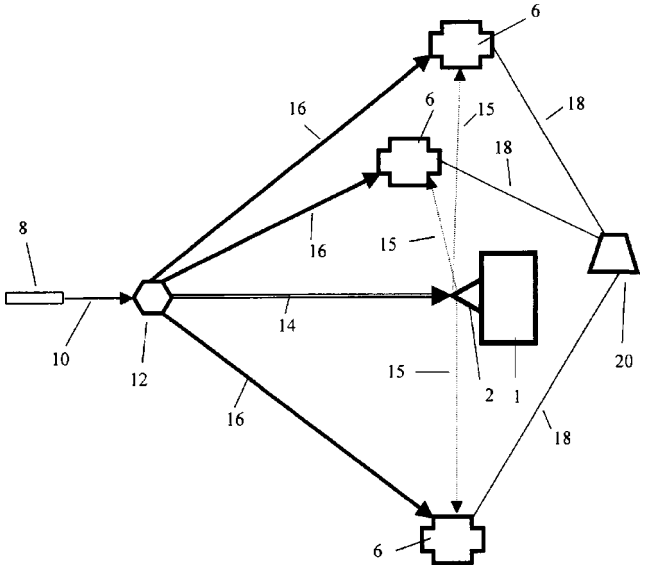

sending beams in three directions to three light sensors. The magnitude of the vibrations in three orthogonal directions are determined by measuring the difference in movements of position between the reflected beams and a reference beam **16**.—EEU

6,655,668

43.40.Tm UNIVERSAL VIBRATION DAMPER

Paul J. Wakeen, Woodville and Larry W. Jacoby, Downing, both of Wisconsin
2 December 2003 (Class 267/195); filed 4 September 2002

The dampers described in this patent make use of steel balls such as are used in ball bearings. One layer of balls is supported on a flat surface and constrained horizontally. A second layer of different sized balls is placed atop the first, so that the balls of the second layer rest in depressions between adjacent balls of the first layer. Additional layers are added similarly until the top layer consists of a single ball, and the whole arrangement is enclosed in a housing. Typically, several of these assemblies are used to protect an item; for example, the flat bases of the assemblies may be attached to a vibrating surface and the item that is to be protected is supported on the assemblies' top balls.—EEU

6,669,309

43.40.Tm VIBRATION DAMPER FOR DAMPING FLUID VIBRATIONS IN A HYDRAULIC SYSTEM

Georg Gierer *et al.*, assignors to ZF Friedrichshafen AG
30 December 2003 (Class 303/87); filed in Germany 9 December 1998

An essentially cup-shaped elastomeric element is located within a cylindrical cavity in a housing, whose top is closed off by a cover plate. Hydraulic fluid communicates with the volume within the elastomeric cup via a small opening in the cover plate. A second, smaller, elastomeric cup is positioned between the first cup and a pressure release orifice at the bottom of the aforementioned cavity in order to seal the release orifice in case of a failure of the first cup, thus avoiding leaks in the hydraulic circuit.—EEU

6,676,101

43.40.Tm VIBRATION ISOLATION SYSTEM

David L. Platus, assignor to Minus K. Technology, Incorporated
13 January 2004 (Class 248/603); filed 28 May 2002

This isolation system, intended to achieve low transmission in the horizontal direction, in essence consists of two plates that are interconnected by columns perpendicular to the plates. The columns are connected to each plate by flexures, which permit the columns to rotate easily relative to the planes of the plates, but which are stiff in the directions of the column axes.—EEU

6,679,295

43.40.Tm VIBRATION ABSORBING RUBBER HOSE

Eiichi Daikai *et al.*, assignors to Tokai Rubber Industries, Limited
20 January 2004 (Class 138/126); filed in Japan 9 August 2001

This hose, intended for use in automotive coolers or air conditioners, consists of a lamination of an inner layer of butyl rubber, a reinforcing layer, and an outer layer of an ethylene-propylene copolymer.—EEU

6,680,591

43.40.Vn APPARATUS FOR PHASE ANGLE MONITORING OF A PLURALITY OF VIBRATING MACHINES

Rusty Roger Knutson and Edward Charles Steffes, Jr., assignors to General Kinematics Corporation
20 January 2004 (Class 318/114); filed 1 November 2002

This phase angle monitoring system for monitoring a vibratory system consists of a controller **36** that produces a phase angle control signal representing the lead or lag between the vibratory movement of two separate vibrating masses. The phase angle control signal is relayed to at least one of

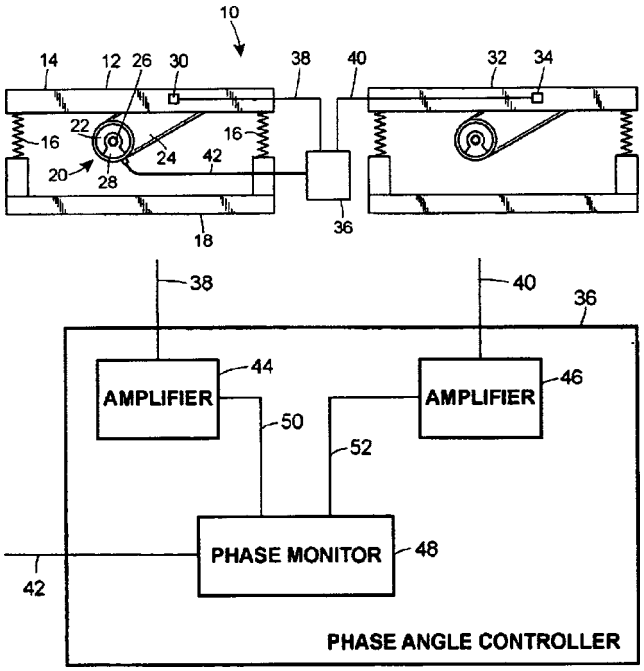

the vibrating masses to adjust the vibration of the mass to generate a desired phase angle, e.g., 180°. An accelerometer **30**, **34** senses the vibratory movement and generates a signal that is transmitted to a control that is capable of modifying the amplitude or the frequency of the vibratory movement.—DRR

6,661,737

43.40.Yq ACOUSTIC LOGGING TOOL HAVING PROGRAMMABLE SOURCE WAVEFORMS

Laurence Wisniewski *et al.*, assignors to Halliburton Energy Services, Incorporated
9 December 2003 (Class 367/25); filed 2 January 2002

An oil well acoustic logging tool may include a combination of monopole and crossed dipole transmitters plus an array of receivers. The transmitters are fired in a predetermined sequence at each depth—every few inches—and digitized waveforms are retrieved from the receivers and sent to the surface for analysis. This patent discloses an improved dipole source excitation mechanism which is ''...fully programmable in all its aspects including frequency, amplitude, emitted wave signature, and wave duration.'' The patent describes eight improved logging methods made possible by this feature.—GLA

6,668,234

43.40.Yq METHOD AND APPARATUS FOR CALCULATING THE AMPLITUDE OF A COMPLEX WAVEFORM ASSOCIATED WITH A ROTATING MACHINE SHAFT AFTER REMOVING THE RUNNING SPEED FREQUENCY

Anthony M. DiTommaso *et al.*, assignors to ABB Incorporated
23 December 2003 (Class 702/66); filed 22 March 2002

What we have here is a set of computer flow charts showing how the procedure set forth in the patent's title can be implemented. The approach is straightforward and the patent is easy to follow.—GLA

6,668,621

43.40.Yq VISCOSITY MEASUREMENT BY MEANS OF DAMPED RESONANT VIBRATION NORMAL TO AN APPROXIMATE RIGID PLATE

Hubert Arthur Wright, Winchester, Massachusetts
30 December 2003 (Class 73/54.25); filed 13 June 2002

A fixed flat surface is located near the tip of a cantilever reed so that fluid in the small gap between that surface and the reed is subjected to shear when the reed vibrates. The reed is made to oscillate by means of an electromagnet and then its vibration is permitted to decay freely. The viscosity of the fluid is determined from the rate of decay of this vibration.—EEU

6,671,425

43.40.Yq METHOD AND SYSTEM FOR ACOUSTICALLY TUNING A LIGHT SOURCE

Jacob B. Khurgin *et al.*, assignors to CeLight
30 December 2003 (Class 385/7); filed 18 June 2002

The light sources to which this patent pertains apply to optical communication systems. Light at a given frequency is transmitted from one waveguide to another, but only light that satisfies a frequency-dependent coupling condition is accepted by the second waveguide. The frequency of the light reaching this waveguide is modified by subjecting the first waveguide to high-frequency longitudinal vibrations.—EEU

6,674,030

43.40.Yq INTELLIGENT SURGICAL FOOTPEDAL WITH LOW NOISE, LOW RESISTANCE VIBRATION FEEDBACK

Jerry S. J. Chen and Dung Ma, assignors to Advanced Medical Optics
6 January 2004 (Class 200/86.5); filed 19 September 2001

When a surgeon depresses this foot pedal by a specific amount, signals are activated to control an associated surgical apparatus. A vibrator deployed on the treadle vibrates the treadle at selected depression points. This provides a sensory warning to the user that further treadle depression will cause a given event to occur. A bracket attaches the vibrator to the treadle and causes resonant vibration of the treadle and vibrator.—DRR

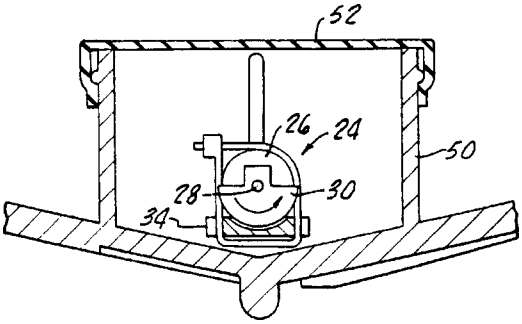

6,675,653

43.40.Yq METHOD AND SYSTEM FOR DETECTING DRIVE TRAIN VIBRATIONS

Liming Chen, assignor to Robert Bosch Corporation
13 January 2004 (Class 73/650); filed 17 August 2001

Data on the rotational behavior of the wheels of a vehicle are obtained from wheel-mounted sensors. The data are processed to obtain a signal corresponding to the rigid-body motions of the wheels and a superposed signal related to the drive train vibrations.—EEU

6,659,223

43.50.Gf SOUND ATTENUATING MATERIAL FOR USE WITHIN VEHICLES AND METHODS OF MAKING SAME

Timothy J. Allison and Carroll Owenby, assignors to Collins & Aikman Products Company
9 December 2003 (Class 181/290); filed 5 October 2001

Atop a layer of fiber batting or acoustic foam material there is fused a thin layer of a thermoplastic material. Another layer of a thermoplastic is fused atop the former and this second thermoplastic layer is topped by a layer of woven or unwoven fibers. The four-layer assembly can be heated, shaped, and compressed locally so as to obtain regions of modified acoustical impedance.—EEU

6,668,970

43.50.Gf ACOUSTIC ATTENUATOR

Peng Lee, assignor to Acoustic Horizons, Incorporated
30 December 2003 (Class 181/224); filed 6 June 2001

This device is intended for reducing noise in a heating and air-conditioning system. The attenuator consists of intake air duct **14** (also referred to as a return air duct) that connects to an outside environment and an opening that leads to blower fan **13**. Air is sucked through the intake air duct and conducted towards the fan. In one embodiment, the acoustic attenuator **18**, consisting of a noise-reflecting panel or shield with an appropriate amount of acoustic absorptive padding, is installed in the duct by attaching it directly under the lower section of the fan. It is asserted that significant broad-band noise reduction will be achieved.—DRR

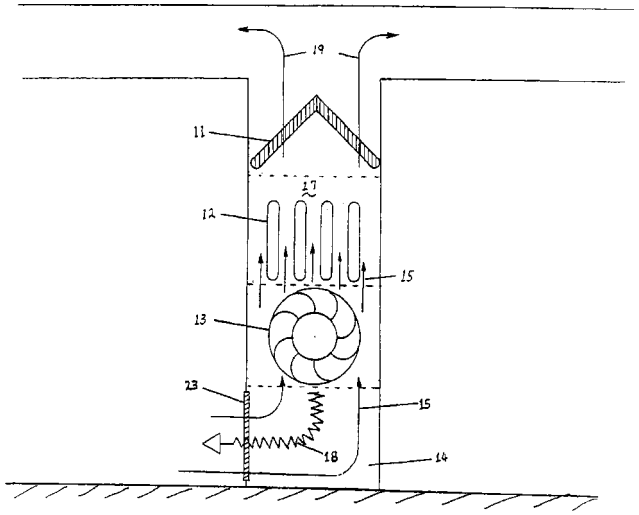

6,669,436

43.50.Gf GAS COMPRESSION APPARATUS AND METHOD WITH NOISE ATTENUATION

Zheji Liu, assignor to Dresser–Rand Company
30 December 2003 (Class 415/1); filed 28 February 2002

An array of Helmholtz resonators is provided on the rotor, between each pair of adjacent vanes. These resonators are made integral with the rotor disc and communicate via small openings with the fluid that is being compressed.—EEU

6,679,296

43.50.Gf DUCTING

Diane Gibson, assignor to Smiths Group PLC
20 January 2004 (Class 138/131); filed in the United Kingdom 15 March 2002

This sound-attenuating duct features an inner layer and an outer layer formed by strips of a foamed thermoplastic rubber material. An inner helical wire supports these layers. Axial and helical reinforcing yarns extend along the duct between the layers. A manufacturing process is also described whereby the two strips are fabricated by extrusion, the extrusion rate of the inner strip being less than that of the outer strip so that the inner strip is stretched to become the more porous structure of the two. The patent asserts that the inner layer would be more efficient in absorbing orifice noise within the duct and the outer layer would be more efficacious in containing radiated noise.—DRR

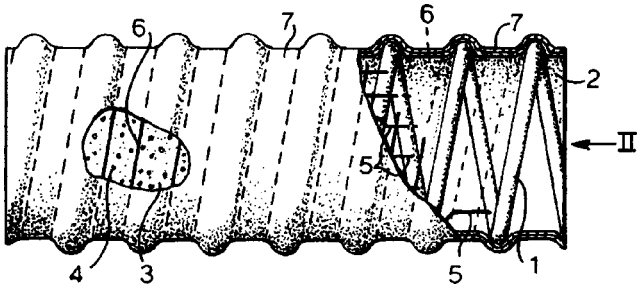

6,678,897

43.50.Hg HEARING PROTECTION DEVICE

Mats Lindgren, assignor to Ab Kompositprodukter Vikmanshyttan
20 January 2004 (Class 2/209); filed in Sweden 15 February 2000

While hearing protector design does not evolve, there are a myriad of different headband designs. This patent describes a one-piece headband de-

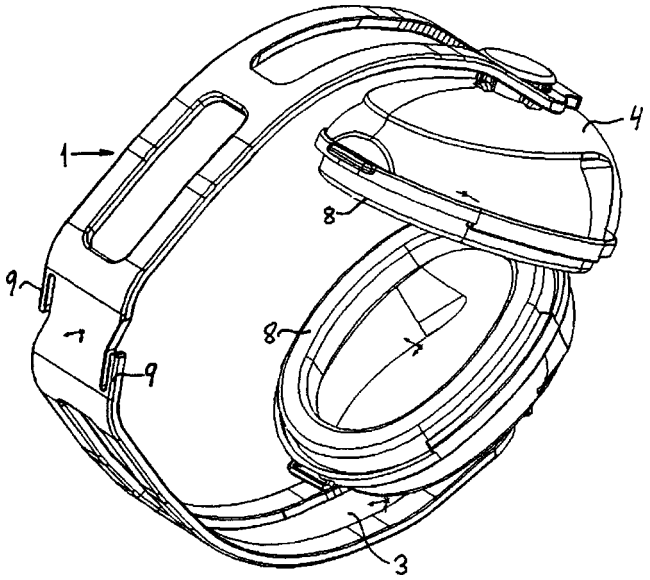

sign that permits the protector to be folded into a pocket. It also includes integral clips **9** to permit storing the device on one's belt.—JE

6,658,117

43.55.Lb SOUND FIELD EFFECT CONTROL APPARATUS AND METHOD

Kiyoshi Hasebe, assignor to Yamaha Corporation
2 December 2003 (Class 381/61); filed in Japan 12 November 1998

Creating electronic reverberation that sounds natural continues to be a major field of endeavor in musical engineering. By accurately modeling early reflections in addition to later reverberant decay, the acoustical characteristics of specific halls can be convincingly reproduced by contemporary

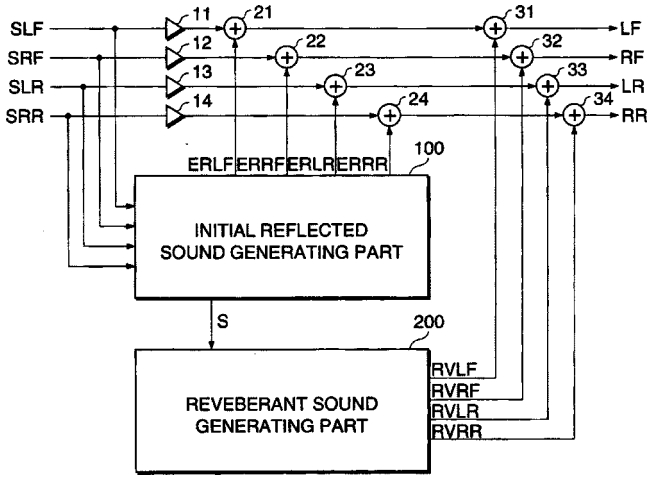

reverberation generators. This patent points out that by utilizing the capabilities of multi-channel playback (surround sound), an even more realistic illusion can be created if early reflections are localized as they would be heard from a sound source at a given location in a given acoustic environment.—GLA

6,669,553

43.55.Ti NOISE SUPPRESSION AND SOUND PROOF CHAMBER

Albert G. Adams, Mississauga, Canada
30 December 2003 (Class 454/237); filed 18 December 2002

This sound-proof chamber is pieced together from prefabricated panels. There is a sealed cavity within all walls, roof, and optionally even the

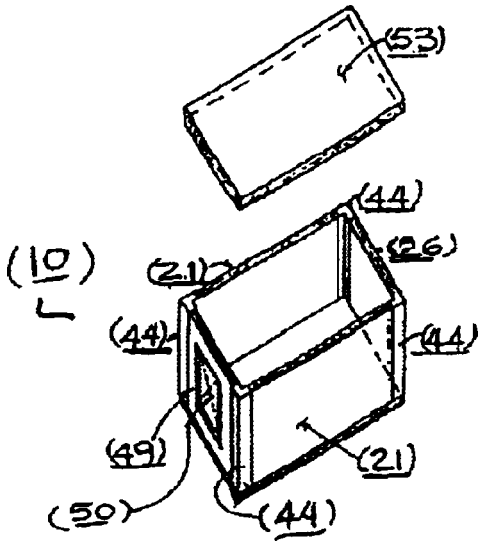

floor, that is kept under a partial vacuum to improve noise isolation capabilities.—CJR

6,668,980

43.55.Vj ELEVATOR CAR ISOLATION SYSTEM AND METHOD

Rory Smith, assignor to Thyssen Elevator Capital Corporation
30 December 2003 (Class 187/401); filed 6 July 2001

This method of supporting an elevator platform within a sling includes suspending the cab with tension elements made of aramid fibers (e.g., Kevlar rope) that improve low frequency isolation.—CJR

6,672,165

43.58.Kr REAL-TIME THREE DIMENSIONAL ACOUSTOELECTRONIC IMAGING AND CHARACTERIZATION OF OBJECTS

John D. G. Rather *et al.*, assignors to Barbara Ann Karmanos Cancer Center
6 January 2004 (Class 73/603); filed 25 February 2002

The object to be imaged is insonified and the acoustic signals scattered from the object are collected and digitized. The resulting digital data are used in both direct imaging and holographic methods to produce a three-dimensional representation of the object from which images and characterizations can be generated.—EEU

6,675,140

43.60.Lq MELLIN-TRANSFORM INFORMATION EXTRACTOR FOR VIBRATION SOURCES

Toshio Irino and Roy D. Patterson, assignors to Seiko Epson Corporation
6 January 2004 (Class 704/203); filed in Japan 28 January 1999

This patent relates to time-sequential data analysis and is said to be applicable to tone recognition, speech and speaker recognition, as well as signal analysis, encoding, and enhancement of voice or music. The method described in the patent provides a means of extracting a signal feature invariant regardless of the size and periodicity of the signal source or reduction or expansion of the time axis. The Mellin transform is a type of integral transform. It has the property that the absolute value of the profile obtained by the transform is invariant (except for a multiplicative constant) as the response of a signal is expanded or contracted in time. The patent realizes corresponding signal processing, for example, to allow speech recognition regardless of differences in spectral structures and pitch periods.—EEU

6,655,212

43.60.Qv SOUND FIELD MEASURING APPARATUS AND METHOD

Yoshiki Ohta, assignor to Pioneer Corporation
2 December 2003 (Class 73/586); filed in Japan 23 October 2000

Consider the plight of a solo listener whose favorite chair is located some distance away from the centerline between his stereo loudspeakers. Prior art suggests that electronic delay can be used to synchronize the signals from the two speakers. However, to set the delay properly, the relative arrival times of the two signals must be measured. An exponential pulse generator, a threshold detector, and a little digital processing can be combined to perform the chore automatically.—GLA

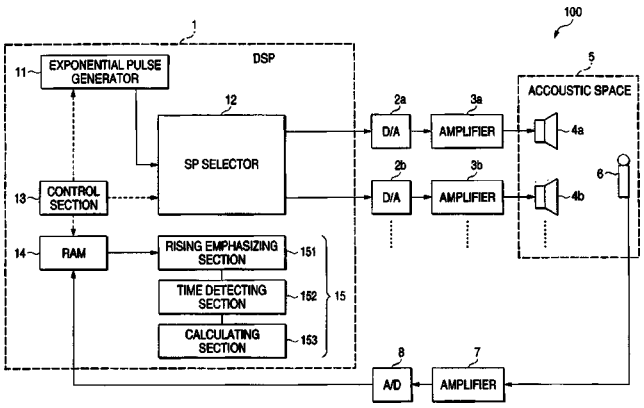

6,542,857

43.60.Uv SYSTEM AND METHOD FOR CHARACTERIZING SYNTHESIZING AND/OR CANCELING OUT ACOUSTIC SIGNALS FROM INANIMATE SOUND SOURCES

John F. Holzrichter *et al.*, assignors to The Regents of the University of California
1 April 2003 (Class 703/2); filed 2 December 1998

This patent essentially argues that sounds from inanimate objects, including most musical instruments, as well as ''windowpanes, automobile road noise, [and] air duct noise,'' can be anaylzed for description, synthesis, or cancellation more accurately than previously possible by applying the source/filter model to such sounds. The patent also maintains that such models have not been so applied in the past. The ''filter'' model applied here is essentially a sum-of-sinusoids model, accounting for phase and amplitude changes on a frequent frame-to-frame basis. Several prior-art analysis methods are discussed. In many cases, a separate electromagnetic pickup attached to a source object would be able to pick up source excitations independently from later filtering effects.—DLR

6,542,869

43.60.Uv METHOD FOR AUTOMATIC ANALYSIS OF AUDIO INCLUDING MUSIC AND SPEECH

Jonathan Foote, assignor to Fuji Xerox Company, Limited
1 April 2003 (Class 704/500); filed 11 May 2000

This is a method for automatically finding points of significant change over a wide range of time scales in a recording of speech or music. The method begins with a standard frame analysis, such as FFT, cepstrum, or linear prediction. Measures of self-similarity and cross-similarity are then computed for each frame based on frames in both the past and future of the

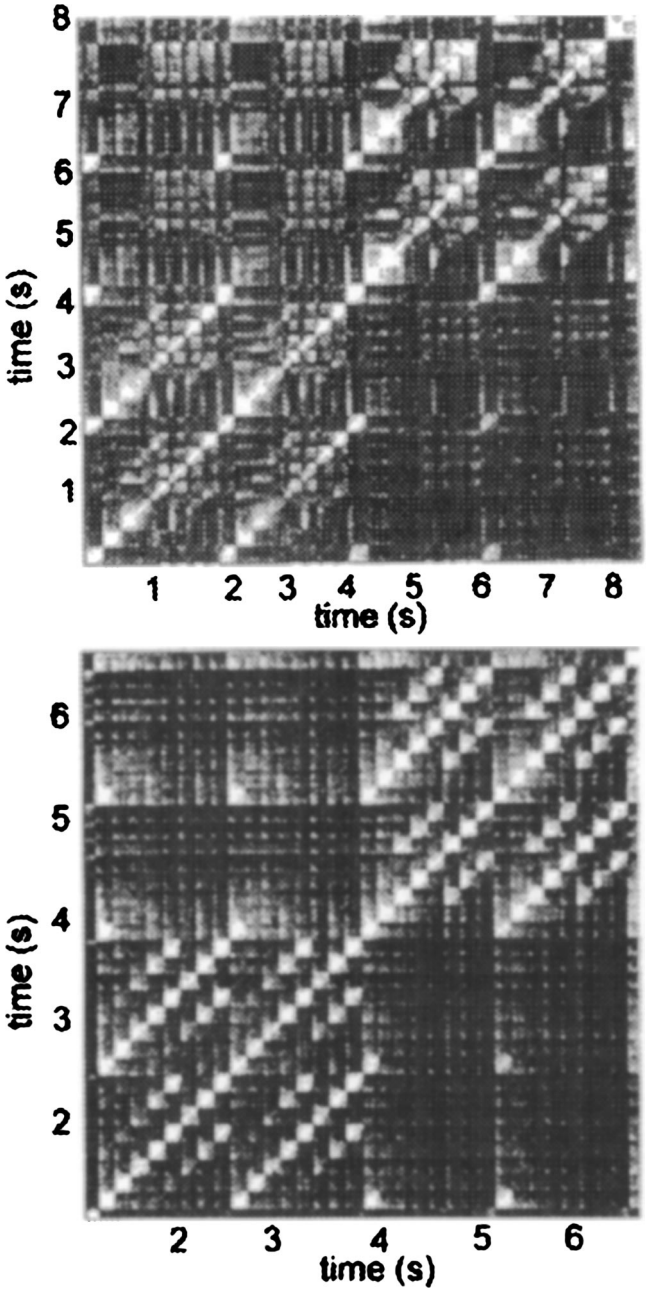

frame at hand. Analysis parameters between frames are compared using any of several methods, including Euclidean distance, dot product, or various normalized or windowed versions of those. The figures compare two analyses of Bach's Prelude No. 1 as performed by Glenn Gould (upper figure) and the same piece in a MIDI realization (lower figure).—DLR

6,676,489

43.64.Ri SOUND ENHANCED LAPPING APPARATUS

Bettina M. Fitzgerald *et al.*, assignors to SEH America, Incorporated
13 January 2004 (Class 451/41); filed 25 February 2002

The preparation of semiconductor devices made from silicon, gallium-arsenide, and the like begins with growing a monocrystalline boule. The boule is sliced into thin disks called wafers, which are then circumferentially ground, lapped, chemically etched, polished, and cleaned. Improvements in the lapping step are offered here. Sounds generated during the lapping process are transmitted to a receiver, allowing the operator to discern problems in the lap processes. The disclosed apparatus includes a microphone and transmitter placed within the confines of the safety shield and oriented in such a manner so as to capture and transmit sounds generated within the lapping machine. A receiver placed outside the shield picks up the sounds generated by the lapping machine. An amplifier and filter may be included to allow the operator to selectively screen for particular sounds. It is apparent that some training and experience on the part of the operator may be required to correctly interpret these sounds.—DRR

6,671,559

43.66.Ts TRANSCANAL, TRANSTYMPANIC COCHLEAR IMPLANT SYSTEM FOR THE REHABILITATION OF DEAFNESS AND TINNITUS

Miles Manning Goldsmith and Byron Lee Boylston, assignors to Microphonics, Incorporated
30 December 2003 (Class 607/57); filed 22 January 2002

A single-electrode receiver device is advocated for reasons of simplicity, cost, good performance, and safety over a multi-electrode approach for a transcanal, transtympanic cochlear implant system. An external sound processor with at least one microphone and transmitting coil, located in a molded insert conforming to the ear canal, couples via electromagnetic or rf energy to an implanted component in the middle ear that contains an insulated receiver coil and electrode. The electrode carries electrical signals through the round window into the cochlea.—DAP

6,671,643

43.66.Ts METHOD FOR TESTING A HEARING AID, AND HEARING AID OPERABLE ACCORDING TO THE METHOD

Manfred Kachler and Fred Zoels, assignors to Siemens Audiologische Technik GmbH
30 December 2003 (Class 702/116); filed in Germany 18 September 2000

Described is a method for performing a self-test on a hearing aid without need for the traditional hearing aid analyzer and test chamber. The

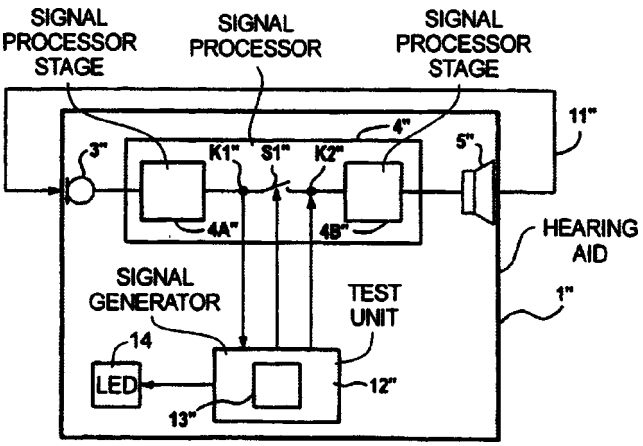

electrical path of the hearing aid is broken and a test signal, which may be stored in the hearing aid, is injected. The acoustic output of the hearing aid is coupled to the hearing aid microphone inlet.—DAP

6,674,867

43.66.Ts NEUROFUZZY BASED DEVICE FOR PROGRAMMABLE HEARING AIDS

Stavros Photios Basseas, assignor to Belltone Electronics Corporation
6 January 2004 (Class 381/314); filed 13 October 1998

A method for programming hearing aids using a neural net and fuzzy logic is said to be independent of the specific hearing aid circuitry utilized. Target frequency responses as a function of input sound level are stored

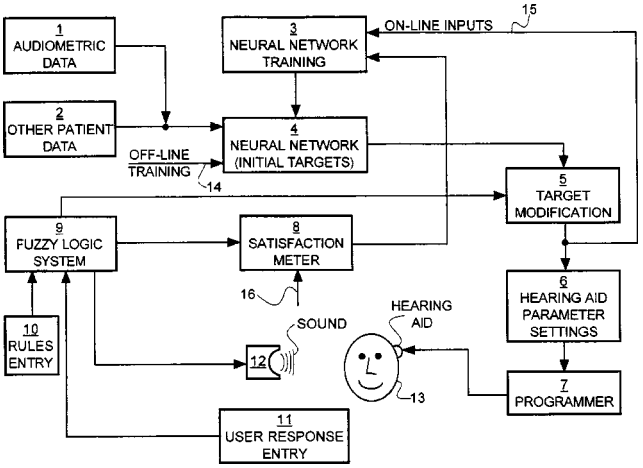

a priori with fuzzy rules. A fine tuning process is implemented with known stimuli using comments from the hearing aid wearer to train the system.—DAP

6,678,385

43.66.Ts COMPACT MODULAR IN-THE-EAR HEARING AID

Jørgen Mejner Olsen, assignor to Widex A/S
13 January 2004 (Class 381/322); filed in Denmark 15 April 1997

To facilitate repair or replacement of the hearing aid electronics, a modular design allows nondestructive removal of an electronic module from a custom hearing aid without adding significantly to the faceplate size. A

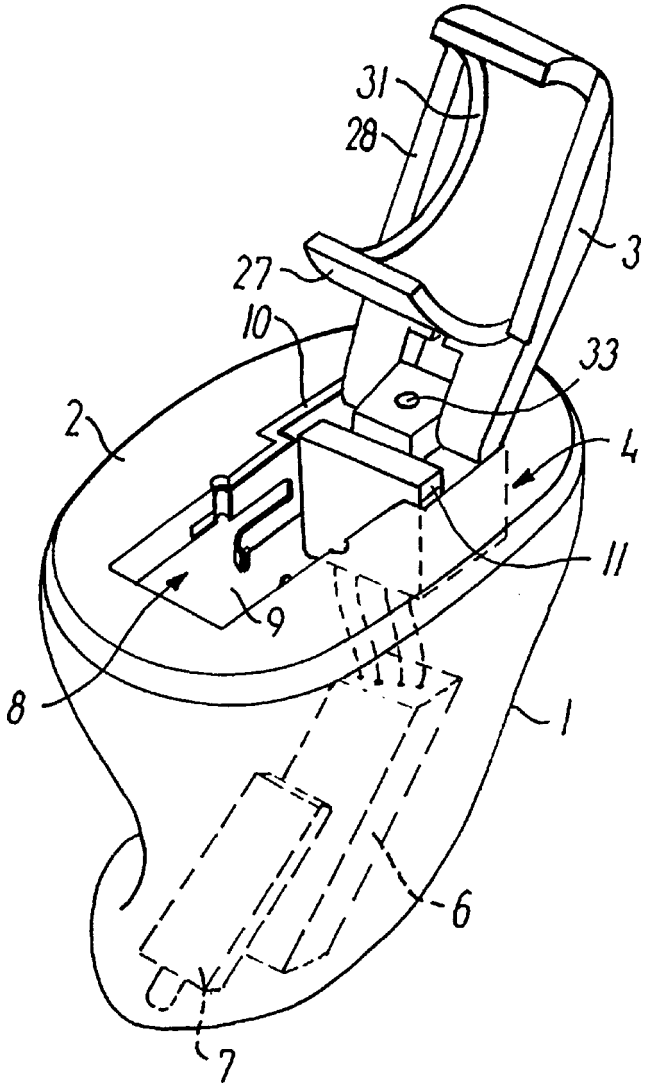

recess in the faceplate has an opening for the battery compartment. A second region located below the battery compartment within the hearing aid contains a socket that the electronics module plugs into. The electronics module may be removed when the battery compartment is removed.—DAP

6,584,440

43.66.Yw METHOD AND SYSTEM FOR RAPID AND RELIABLE TESTING OF SPEECH INTELLIGIBILITY IN CHILDREN

Ruth Y. Litovsky, assignor to Wisconsin Alumni Research Foundation
24 June 2003 (Class 704/271); filed 4 February 2002

This is a device for testing whether a child can perceive speech intelligibly in a variety of competing acoustic situations. Various objects and situations are presented visually, on a computer screen, and a word is presented audibly, while competing sounds, speech, speech-shaped noise, time-reversed speech, etc., are played over speakers at various locations around the subject. The child is to point to one of several pictures associated with the word. A set of rules determines repetitions, playback volume, and progression through the sequence based on the analysis of the child's responses. A goal of the system is to make a rapid analysis before the child's attention wanders.—DLR

6,585,517

43.66.Yw PHONOLOGICAL AWARENESS, PHONOLOGICAL PROCESSING, AND READING SKILL TRAINING SYSTEM AND METHOD

Janet M. Wasowicz, assignor to Cognitive Concepts, Incorporated
1 July 2003 (Class 434/167); filed 20 July 2001

This is an interactive game device designed to test one or more of an individual's auditory processing, phonological awareness, phonological processing, and reading skills. Several different games are available, constructed in such a way that crucial items or situations may be auditorily

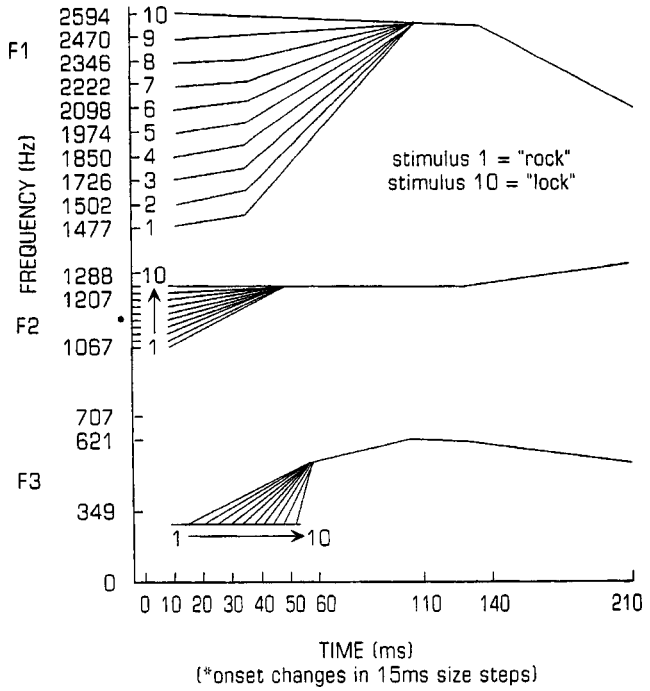

confusible. Formant patterns are then manipulated by the device during the play, to test the perceptual limits of the subject. The patent places a heavy emphasis on the levels of difficulty of the various tests and how the results are affected by those factors.—DLR

6,675,144

43.72.Gy AUDIO CODING SYSTEMS AND METHODS

Roger Cecil Ferry Tucker *et al.*, assignors to Hewlett–Packard Development Company, L.P.
6 January 2004 (Class 704/264); filed in the European Patent Office 15 May 1997

A system is described for encoding and decoding an audio signal utilizing lower and upper subbands over a bandwidth of 5.5 kHz with a bit rate less than 4.8 kbits/s. The lower subband may contain a mechanism for

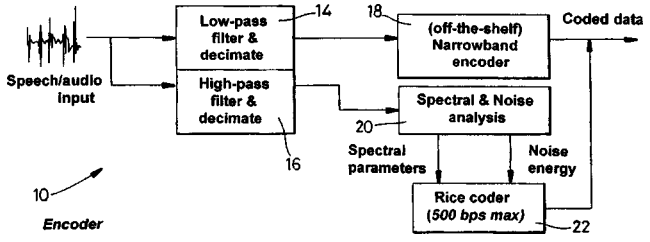

making a voicing decision. A source filter model is used to encode the nonperiodic components of the upper subband into one or more second-order LPC coefficients. An excitation containing synthesized noise is used for decoding the upper subband.—DAP

6,539,354

43.72.Ja METHODS AND DEVICES FOR PRODUCING AND USING SYNTHETIC VISUAL SPEECH BASED ON NATURAL COARTICULATION

Stephen Sutton and Pieter Vermeulen, assignors to Fluent Speech Technologies, Incorporated
25 March 2003 (Class 704/260); filed 24 March 2000

This is a method for creating synthetic video talking heads to go with synthesized speech. The process of producing the video display, as proposed here, would have a great deal in common with current concatenative methods of speech synthesis. Segments of facial display features, known as

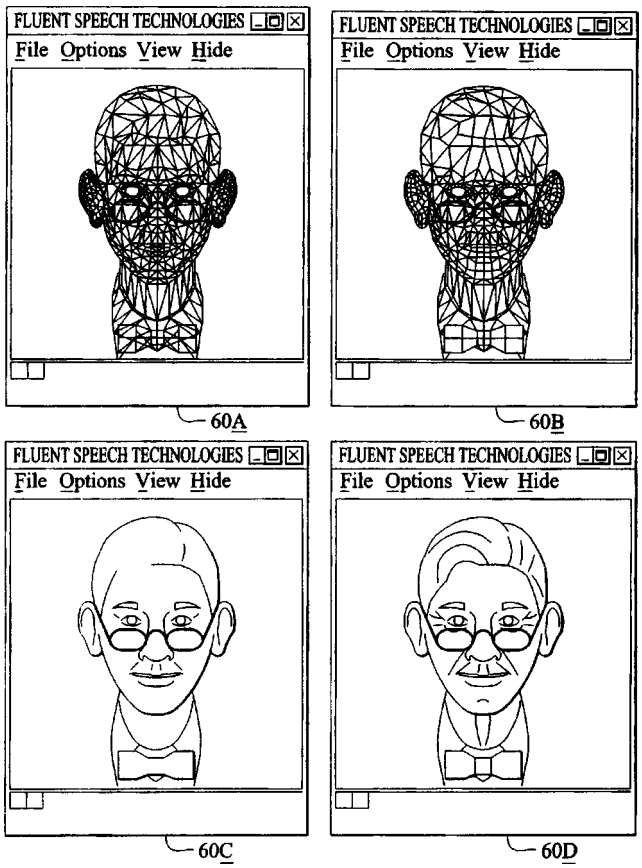

visemes, are concatenated much as are the speech segments, diphones, triphones, etc. These segments are then joined together using video morphing technology to produce a smooth video sequence showing the talking face.—DLR

6,542,867

43.72.Ja SPEECH DURATION PROCESSING METHOD AND APPARATUS FOR CHINESE TEXT-TO-SPEECH SYSTEM

Shih Chang Sun and Chin Yun Hsieh, assignors to Matsushita Electric Industrial Company, Limited
1 April 2003 (Class 704/260); filed 28 March 2000

A new model for Chinese syllable durations is described. Intrinsic durations are stored for each of 408 distinct syllable types. These durations are then modified according to the tone, phrase construction, location of the syllable in the phrase, location of the phrase in the sentence, and the classes of connected phonemes. Formulas are given in the patent for the computation of durations using multiplicative and weighted additive adjustments. Weights and parameters for the model are based on the collection and analysis of ''a large amount'' of natural speech.—DLR

6,546,366

43.72.Ja TEXT-TO-SPEECH CONVERTER

David Randall Ronca and Stephen Francis Ruhl, assignors to Mitel, Incorporated
8 April 2003 (Class 704/260); filed 26 February 1999

Speech synthesis can be performed using a wide variety of hardware, ranging from a single, small CPU to a more elaborate DSP-based system, with resulting differences in the speed of the synthesis. This patent is concerned entirely with a buffering technique which can be used in a message retrieval system so as to minimize the delays caused by the smaller and cheaper synthesis hardware.—DLR

6,546,367

43.72.Ja SYNTHESIZING PHONEME STRING OF PREDETERMINED DURATION BY ADJUSTING INITIAL PHONEME DURATION ON VALUES FROM MULTIPLE REGRESSION BY ADDING VALUES BASED ON THEIR STANDARD DEVIATIONS

Mitsuru Otsuka, assignor to Canon Kabushiki Kaisha
8 April 2003 (Class 704/260); filed in Japan 10 March 1998

This is a model of phoneme durations for the synthesis of Japanese speech, with the specific goal of being able to adjust the overall rate of speaking while maintaining a natural pattern of phoneme durations. The model is based entirely on statistical data in that all durations are initially set to be a fixed fraction of the desired overall utterance duration and are then adjusted according to the averages, variances, and minima observed for each phoneme type from the analysis of natural speech. Formulas are given for the application of the observed statistics to the duration adjustments. Additional factors, such as syntactic or semantic context, are not mentioned.—DLR

6,546,369

43.72.Ja TEXT-BASED SPEECH SYNTHESIS METHOD CONTAINING SYNTHETIC SPEECH COMPARISONS AND UPDATES

Peter Buth and Frank Dufhues, assignors to Nokia Corporation
8 April 2003 (Class 704/275); filed in Germany 5 May 1999

This speech synthesis system, described using a few examples of German city names, is intended to handle irregular pronunciations without resorting to the method of inserting a human-spoken recording of the variant item into the synthetic speech stream. Phrases to be synthesized, such as train destinations, are originally spoken into the system and reduced to a phonetic respresentation. At the same time, a resynthesis is attempted and the result is compared with the original human version of the phrase. If a significant difference is detected between the natural and synthetic versions, then the system will generate a sequence of variations in the phonetic spelling of the differing item. After resynthesis of the generated variations, the best matching phonetic form is stored in the phonetic sequence to be used for synthesis.—DLR

6,553,343

43.72.Ja SPEECH SYNTHESIS METHOD

Takehiko Kagoshima and Masami Akamine, assignors to Kabushiki Kaisha Toshiba
22 April 2003 (Class 704/262); filed in Japan 4 December 1995

This patent describes a method of speech analysis to obtain parameters for speech synthesis. A body of natural speech is inverse filtered through a linear prediction filter and, during voiced portions, the exact moments of the

quasiperiodic excitation are recovered from the residual signal. From this point, the emphasis is on the resonant spectral charactistics of the filter, with no further mention of the periodicity structure of the residual signal. Most of the discussion is concerned with producing the intended spectral shape as the synthesis pitch is varied. All of this is expanded into 23 embodiments and then captured in a single, short claim.—DLR

6,553,344

43.72.Ja METHOD AND APPARATUS FOR IMPROVED DURATION MODELING OF PHONEMES

Jerome R. Bellegarda and Kim Silverman, assignors to Apple Computer, Incorporated
22 April 2003 (Class 704/267); filed 22 February 2002

A system is described for modeling phoneme durations for use in a speech synthesizer. The basic duration model is described as a sum-of-products model, that is, a sum of weighted factors. However, this basic idea is modified in that the resulting sum is transformed by a cosine-based functional, such as shown in the figure. From the analysis of a large body of natural speech, a number of contributing factors are considered. The raw

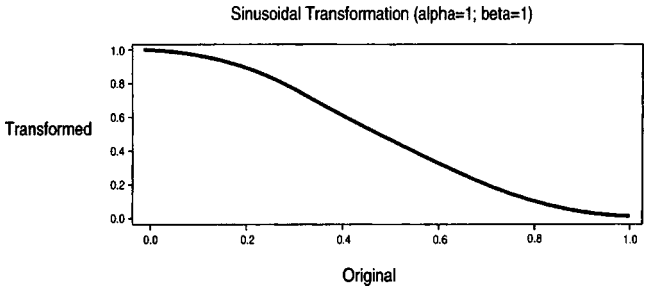

duration measurements are inverse transformed through the functional before the weights are determined by using a standard procedure, such as regression. The functional parameters, alpha and beta, allow compression to be applied at various parts of the scale, either at the center or toward the limits, which are set based on the observed factor's minima and maxima. Different functional parameters may be used with each factor, if enough data is available to justify the fit of such a model.—DLR

6,556,972

43.72.Ne METHOD AND APPARATUS FOR TIME-SYNCHRONIZED TRANSLATION AND SYNTHESIS OF NATURAL-LANGUAGE SPEECH

Raimo Bakis *et al.*, assignors to International Business Machines Corporation
29 April 2003 (Class 704/277); filed 16 March 2000

This ambitious patent describes a system supposedly able to perform simultaneous, realtime translation of spoken input into a number of target languages. On the input side, a recognizer would identify phrases based on a limited number of specific reference phrases. In a template embodiment, the recognized phrases are immediately passed to a translation unit. An understanding embodiment allows an extra step, wherein the meaning of a phrase is identified and used to select one of a set of formal, language-independent meanings. These are passed to the translation unit to be synthesized in various target languages. Throughout the description of this improbable system, there is a curious emphasis on an ability to synchronize the output translations with certain external events, perhaps referred to in the original input. The last sentence of the abstract meekly admits that the success of the system may depend upon application to a limited subject domain—DLR

6,567,778

43.72.Ne NATURAL LANGUAGE SPEECH RECOGNITION USING SLOT SEMANTIC CONFIDENCE SCORES RELATED TO THEIR WORD RECOGNITION CONFIDENCE SCORES

Eric I. Chao Chang and Eric G. Jackson, assignors to Nuance Communications
20 May 2003 (Class 704/257); filed 23 June 1999

This is a description of a speech recognizer organized around a slot grammar for a specific target domain, for example, an airline flight reservation system. As words in the input speech stream are recognized, they are identified with specific slots in the grammar and assigned a confidence score that the word correctly fits the identified slot. Based on the resulting scores, the system may ask for a repeat of specific information, avoiding the need to request that the entire input be repeated. The patent includes a discussion of the relationship between the confidence scores and the semantic content in a specific application domain.—DLR

6,671,226

43.80.Gx ULTRASONIC PATH GUIDANCE FOR VISUALLY IMPAIRED

Joel L. Finkel and Jiping He, assignors to Arizona Board of Regents
30 December 2003 (Class 367/116); filed 31 May 2002

This system emits ultrasound pulses and detects obstacles in the path of the visually impaired. An array of directionally-aimed ultrasound transmitters is positioned on the torso of the individual user. One or more receivers detect echoes from obstacles upon which the emitted ultrasound impinges. An audible tone is generated each time an echo is received. The

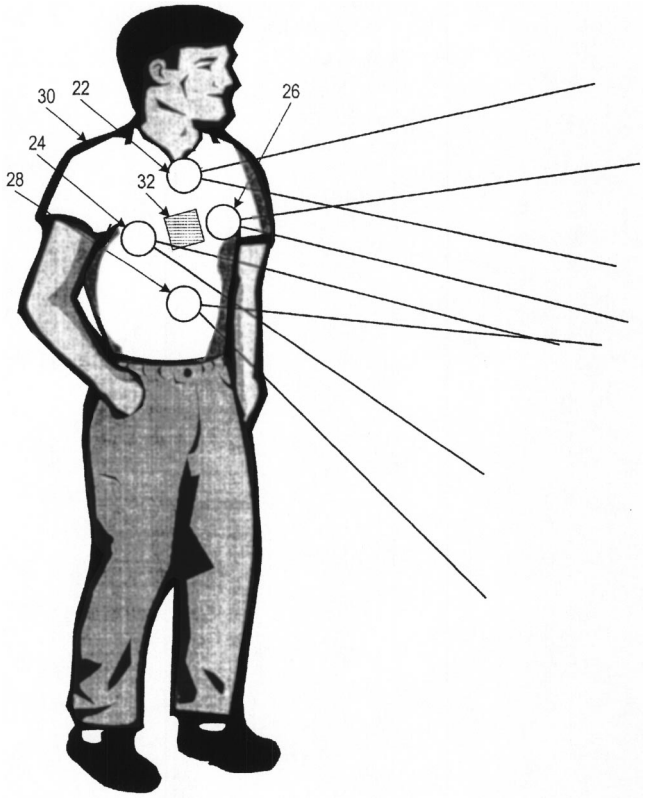

tone's frequency depends on which transducer emitted the original ultrasound pulse that resulted in the detected echo. This yields an indication of the location of the detected obstacle(s), and the elapsed time from emission of the ultrasound to reception of its echo indicates the distance to the obstacle.—DRR

6,669,636

43.80.Qf ULTRASOUND TRANSMITTER AND/OR RECEIVER SYSTEM

Jeroen Martin van Klooster, assignor to Krohne A.G.
30 December 2003 (Class 600/437); filed in Germany 14 September 2001

The objective of this apparatus is to provide an ultrasound transmitting and receiving system in which undesirable cross coupling or crosstalk can be largely avoided. This is purportedly achieved by introducing an impedance step between the ultrasound transducer and the side of its jacket facing away from the transducer. In one embodiment the jacket is positioned at a distance from the transducer, with the result that an air gap is created next to the end of the jacket facing the transducer. The gap is filled with a material that has an acoustic impedance different from that of the jacket and of the transducer.—DRR

6,671,550

43.80.Qf SYSTEM AND METHOD FOR DETERMINING LOCATION AND TISSUE CONTACT OF AN IMPLANTABLE MEDICAL DEVICE WITHIN A BODY

Paul A. Iaizzo and Timothy G. Laske, assignors to Medtronic, Incorporated
30 December 2003 (Class 607/27); filed 14 September 2001

This is a system for monitoring the status of an implantable medical device (IMD) within a body. The IMD can be a lead, guidewire, stylet, catheter, or other IMD device which contains a microphone for detecting acoustic signals in the body. The IMD connects to an amplifier that generates an audible signal indicating the status of the IMD, such as its location and pertinent tissue-contact data. A processing circuit may be included to assist in the analysis of the data.—DRR

6,673,018

43.80.Qf ULTRASONIC MONITORING SYSTEM AND METHOD

Zvi M. Friedman, assignor to GE Medical Systems Global Technology Company LLC
6 January 2004 (Class 600/440); filed 28 June 2002

This ultrasound diagnostic system provides a multi-window display for live ultrasound images. One window displays live ultrasound images and a second window displays a reference cine image that was captured prior to the currently displayed live images. The images of these two windows are synchronized by ECG gating. This system may be employed to monitor the heart and to detect subtle changes in heart condition from the time the reference image was captured.—DRR

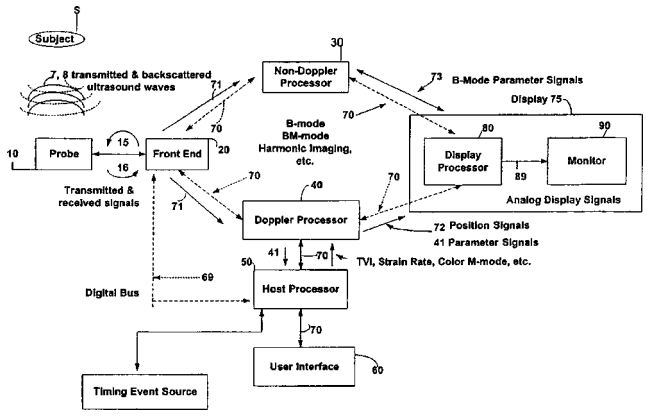

6,673,019

43.80.Qf DIAGNOSTIC ULTRASOUND IMAGING BASED ON RATE SUBTRACTION IMAGING (RSI)

Naohisa Kamiyama, assignor to Kabushiki Kaisha Toshiba
6 January 2004 (Class 600/443); filed in Japan 31 January 2000

This is apparently a diagnostic ultrasound imaging system that is based on a contrast echo technique for an object into which a contrast agent is administered. The main constituent of the contrast agent is microbubbles. The diagnostic imaging uses rate subtraction imaging (RSI) to detect transient signals caused by the microbubbles, thereby distinguishing minute blood flows from tissue surrounding those flows. In the procedure, an ultrasound pulse is sent two times in each of the rasters on a region undergoing

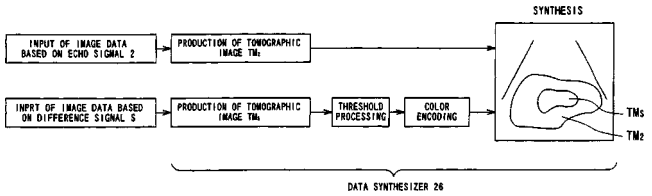

the scanning. Subtraction between echo signals is conducted for each time of transmission to yield a difference signal. One of the echo signals and one of the difference signals are converted into individual tomographic images, independently of each other. The resulting individual tomographic images are displayed in a superimposed fashion or on a side-by-side basis. This contrast echo imaging, based on the RSI technique, thus permits blood flows to be discerned from the surrounding tissue in the region.—DRR

6,673,020

43.80.Qf ULTRASONIC DIAGNOSTIC APPARATUS

Takashi Okada and Akimitsu Harada, assignors to Aloka Company, Limited
6 January 2004 (Class 600/454); filed in Japan 10 February 2000

Intended for measuring blood flow diameter, blood flow velocity, or the like, this apparatus transmits an ultrasonic pulse and obtains echo data for measurements of displacement of a blood vessel wall and of the blood velocity, respectively. A tomogram of a blood vessel results from the echo data and a measurement line relative to the vessel axis is automatically or manually set in the tomogram. When the position of a vessel wall on the measurement line is specified, that position is tracked in order to calculate displacement of the vessel wall. Using the measurement line as reference, a sample gate is set within the blood vessel to extract Doppler information from the echo data. The speed of blood stream flow in the sample gate is calculated, then an evaluation value is computed on the basis of the displacement of the blood vessel wall and the blood velocity.—DRR

6,676,600

43.80.Qf SMART PHYSIOLOGIC PARAMETER SENSOR AND METHOD

Ronald S. Conero and Stuart L. Gallant, assignors to Tensys Medical, Incorporated
13 January 2004 (Class 600/438); filed 31 August 2000

A sensor assembly is provided for measurement of one or more physiological parameters of a living subject. In a preferred embodiment, the sensor assembly consists of a disposable combined pressure and ultrasonic sensor that incorporates an electronically erasable programmable read-only memory (EEPROM). The assembly is used for the noninvasive measurement of arterial blood pressure. The sensor EEPROM contains a variety of

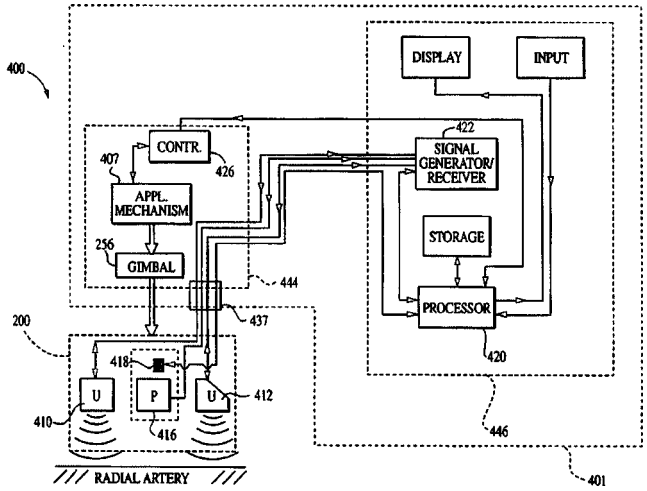

information relating to the manufacture, run time, calibration, and operation of the sensor, in addition to application-specific data such as patient or health care facility identification. Portions of the data are encrypted to prevent tampering. In another embodiment, one or more additional EEPROMs are included within the host system to allow the storage of system data and to accommodate a variety of different sensors. In a third embodiment, one or more of the individual transducer elements within the assembly are made detachable and disposable, thereby allowing for replacement of certain components that may degrade or become contaminated.—DRR

6,676,605

43.80.Qf BLADDER WALL THICKNESS MEASUREMENT SYSTEM AND METHODS

Bill Barnard and Stephen Dudycha, assignors to Diagnostic Ultrasound
13 January 2004 (Class 600/449); filed 7 June 2002

The device incorporates a three-dimensional ultrasound transceiver to scan a patient's bladder. Data collected in the ultrasound scan are analyzed to calculate the bladder mass. Bladder mass information is then used to assess bladder dysfunction. In the preferred embodiment of the device, a microprocessor-based ultrasound transceiver placed on the exterior of the patient's bladder scans the bladder in multiple planes, receives echoes along each plane, and transforms the echoes to analog signals which are then digitized and downloaded to a computer system.—DRR

6,676,606

43.80.Qf ULTRASONIC DIAGNOSTIC MICRO-VASCULAR IMAGING

David Hope Simpson *et al.*, assignors to Koninklijke Philips Electronics N.V.
13 January 2004 (Class 600/458); filed 11 June 2002

Contrast agents are used in this ultrasonic imaging system for imaging microvascular systems. The microbubbles in the contrast agent serve as a beacon to their location as they move through blood vessels. These images are temporally processed to distinguish the moving microbubbles and then persistence processed to present images that display the tracks generated by the microbubbles through the blood vessels.—DRR

6,669,643

43.80.Sh METHOD AND APPARATUS FOR SONOGRAPHIC EXAMINATION, BIOPSY, AND EXCISION

Theodore J. Dubinsky, Seattle, Washington
30 December 2003 (Class 600/459); filed 13 October 2000

This device relates particularly to sonographic examination, biopsy, and excision within multi-chambered cavities of human and other bodies. In one embodiment, the apparatus consists of a sonographic transducer for examination and incorporates a substantially tubular catheter and any one of a wide variety of biopsy devices for performing biopsies within a vaginal or uterine chamber. In another embodiment, sonographic or fluoroscopic imaging is used in combination with an apparatus for examining the cavities under study and for guiding the apparatus during a biopsy procedure.—DRR

6,669,690

43.80.Sh ULTRASOUND TREATMENT SYSTEM

Mitsumasa Okada *et al.*, assignors to Olympus Optical Company, Limited
30 December 2003 (Class 606/40); filed in Japan 6 April 1995

The objects of this system are (a) an ultrasonic treatment that can provide endoscopic observation or the like with good maneuverability, treatment through ultrasonic vibrations, and/or a high-frequency current with safety, preventing a treatment member from touching normal tissue unnecessarily and (b) a means via ultrasound of incising and coagulating tissue and evacuating the crushed tissue out of the body using ultrasonic coagulation and incision. A handpiece incorporates an ultrasonic transducer and serves as an operation unit. A probe connected to the transducer serves to transmit vibrations to a distal member. The operation unit can be manipulated to clamp the tissue with the clamping member and to free the tissue therefrom. A suction end is formed at the back of the handpiece and communicates through a hole bored through the center axis of the probe and the transducer. The perfusion base is formed on the outer surface of the handpiece and communicates with the lumen of the sheath.—DRR

6,676,601

43.80.Sh APPARATUS AND METHOD FOR LOCATION AND TREATMENT USING ULTRASOUND

Francois Lacoste and Dominique Cathignol, assignors to Technomed Medical Systems, S.A.; Institut National de la Sante et de la Recherche Medicale (Inserm)
13 January 2004 (Class 600/439); filed in France 26 May 1999

Apparatus is disclosed for the location and focused ultrasound treatment of myoma or other types of tumor having a pedicle. The device consists of a probe that accesses myomas by a vaginal route. The probe delivers focused ultrasound and Doppler echography locates the region to be treated. The therapeutic operational modes may include sweeping the myoma with the focused spot of the therapy probe in order to provoke necrosis of the myoma or coagulate the mass of myoma and/or sweeping the myoma pedicle with the focused spot of the therapy probe in order to provoke necrosis or coagulation of blood vessels composing it. In this latter case, tissue mass necrosis proceeds by ischemia. Small myomas are exposed spontaneously. In other cases, it may be necessary to remove the myoma mass. As this is coagulated tissue, the operation is facilitated with no bleeding occurring and the amount of mass to be removed has been reduced.—DRR

6,676,607

43.80.Sh INTRAOPERATIVE MICROSURGICAL ULTRASONIC DEVICE AND METHODS RELATED THERETO

Eugene de Juan, Jr. and Patrick S. Jensen, assignors to The Johns Hopkins University
13 January 2004 (Class 600/461); filed 3 January 2001

This device provides mechanisms for imaging structure and/or tissue at a surgical site during and after microsurgical (mainly ophthalmic) procedures. A high-frequency ultrasonic imaging mechanism is deployed in close proximity to the surgical site of interest so that the surgeon obtains high-quality and high-resolution images. A typical embodiment of the intraoperative imaging device includes a probe member having a specific length and

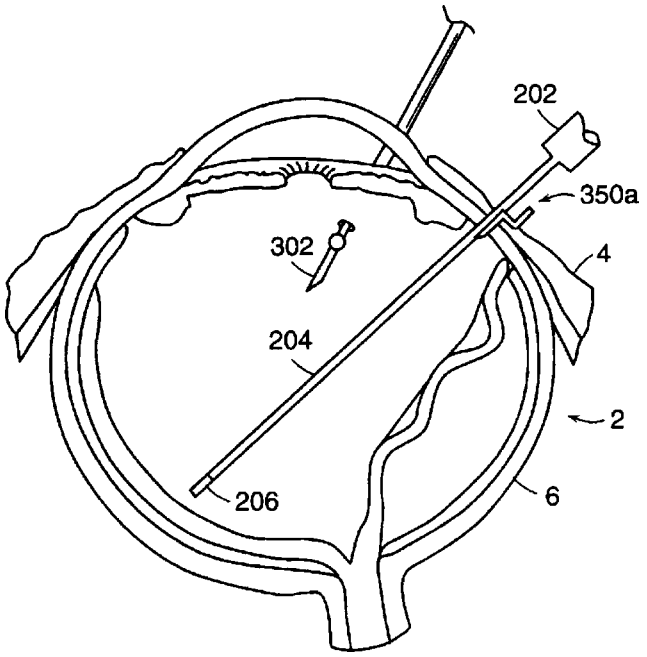

an ultrasonic signal transmitting and receiving transducer secured to the probe member. The specific length is established to facilitate the placement of the probe in the proximity of the surgical site and the frequency of the ultrasonic signals is chosen to provide the desired amount of imaging detail.—DRR

6,679,855

43.80.Sh METHOD AND APPARATUS FOR THE CORRECTION OF PRESBYOPIA USING HIGH INTENSITY FOCUSED ULTRASOUND

Gerald Horn, Deerfield, Illinois and Gene Zdenek, West Hills, California
20 January 2004 (Class 601/2); filed 29 May 2001

The device, intended for correcting vision, applies laser energy or ultrasound to treat presbyopia, hyperopia, primary open angle glaucoma, and ocular hypertension. Energy in the form of high-intensity focused ultrasound (HIFU) is directed at the eye so as to generate discrete heating within the eye. This results in a contraction of the impacted area and increases the tension on components connected to the lens, thereby correcting or preventing presbyopia.—DRR

6,679,899

43.80.Sh METHOD FOR DETECTING TRANSVERSE VIBRATIONS IN AN ULTRASONIC HAND PIECE

Eitan T. Wiener and William T. Donofrio, assignors to Ethicon Endo-Surgery, Incorporated
20 January 2004 (Class 606/169); filed 14 September 2001

One of the problems with surgical ultrasonic cutting instruments is uncontrolled or undamped vibrations and the resultant heat and material fatigue. A method for detecting transverse mode vibrations in an ultrasonic handpiece/blade is provided by monitoring the power delivered to the handpiece. If the measured power exceeds an established pass/fail threshold level, a determination is made that the handpiece manifests transverse mode

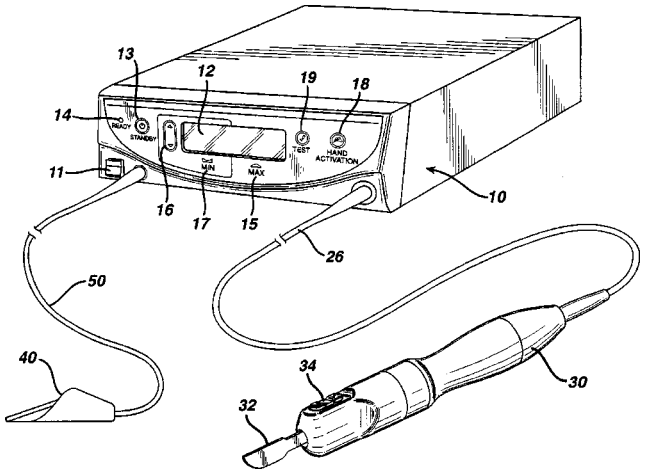

behavior. If such is the case, operation of the generator is inhibited and a ''Transverse Mode Vibrations Present'' error message is displayed on a liquid crystal display on the generator console. The transverse vibration is also detected if an extraordinary power increase occurs as the drive frequency is shifted upward or downward from a primary resonant operating frequency.—DRR

6,669,633

43.80.Vj UNITARY OPERATOR CONTROL FOR ULTRASONIC IMAGING GRAPHICAL USER INTERFACE

Michael Brodsky *et al.*, assignors to TeraTech Corporation
30 December 2003 (Class 600/437); filed 30 March 2001

An ultrasonic imaging operation is selected with one control and then a parameter is selected using another control. The selected operation and parameter are used for imaging. The selections can be made using one hand while the other hand can be used to position the ultrasonic imaging system probe.—RCW

6,669,635

43.80.Vj NAVIGATION INFORMATION OVERLAY ONTO ULTRASOUND IMAGERY

Paul Kessman *et al.*, assignors to Surgical Navigation Technologies, Incorporated
30 December 2003 (Class 600/437); filed 14 January 2002

The tip of a surgical instrument and the trajectory of the tip are represented by an icon, which is overlaid on a real-time ultrasound image. The format of the instrument trajectory is changed when the surgical instrument crosses the plane of the image.—RCW

6,669,637

43.80.Vj PARAMETRIC TRANSMIT WAVEFORM GENERATOR FOR MEDICAL ULTRASOUND IMAGING SYSTEM

Albert Gee, assignor to Acuson Corporation
30 December 2003 (Class 600/437); filed 6 January 2003

Stored parameters are used to produce a transmit waveform. Sets of the parameters define envelope and modulation functions that are combined

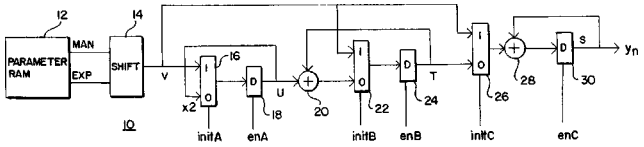

in a piecewise fashion. Separate transmit waveforms can also be combined before being applied to transducer elements.—RCW

6,669,638

43.80.Vj IMAGING ULTRASOUND TRANSDUCER TEMPERATURE CONTROL SYSTEM AND METHOD

David Miller *et al.*, assignors to Koninklijke Philips Electronics N.V.
30 December 2003 (Class 600/438); filed 10 October 2002

The temperature of a transducer is controlled by changing the operation of an ultrasonic imaging system to which the probe is connected. In one mode of operation, feedback from temperature sensors in the transducer is used to switch from high- to low-power imaging. In other modes of operation, the system switches from high- to low-power imaging after a predetermined period of time, or the system cycles rapidly between imaging power settings.—RCW

6,669,640

43.80.Vj ULTRASOUND IMAGING SYSTEM USING MULTI-STAGE PULSE COMPRESSION

Moo Ho Bae, assignor to Medison Company, Limited
30 December 2003 (Class 600/447); filed in the Republic of Korea 5 September 2001

Groups of transducer array elements are formed and signals from the

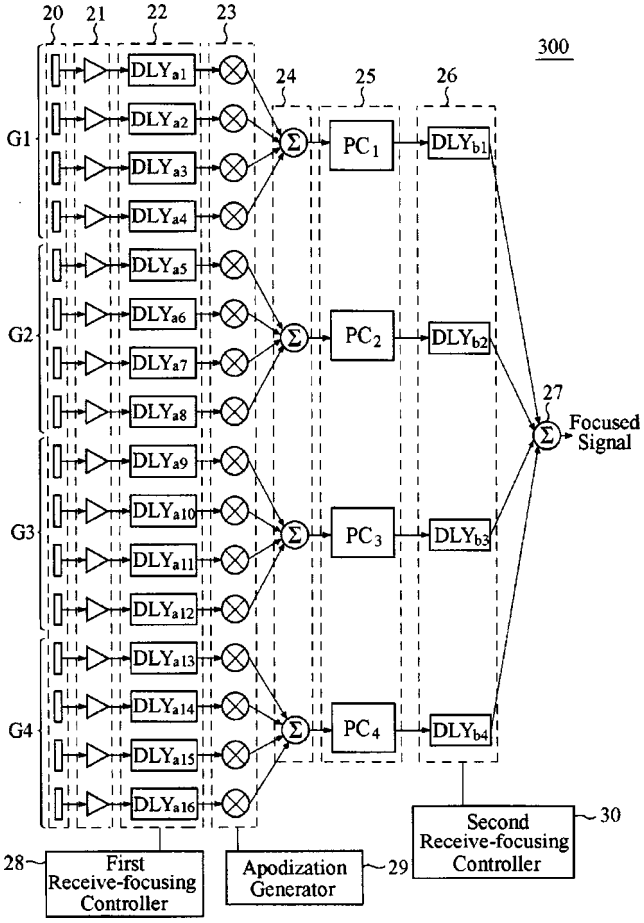

groups are processed hierarchically using multiple stages of pulse compression and time delay to produce a receive focus.—RCW

6,669,641

43.80.Vj METHOD OF AND SYSTEM FOR ULTRASOUND IMAGING

McKee Dunn Poland *et al.*, assignors to Koninklijke Philips Electronics N.V.
30 December 2003 (Class 600/447); filed 10 October 2002

A volume is visualized using biplane images. One of the biplane images has a fixed orientation relative to the transducer. The plane of the other biplane image can be varied relative to the fixed image. Together with the two biplane images, an image orientation icon is displayed to depict the relative orientation of the two planar images.—RCW

6,673,016

43.80.Vj ULTRASOUND SELECTABLE FREQUENCY RESPONSE SYSTEM AND METHOD FOR MULTI-LAYER TRANSDUCERS

Mirsaid Bolorforosh *et al.*, assignors to Siemens Medical Solutions USA, Incorporated
6 January 2004 (Class 600/437); filed 14 February 2002

Piezoelectric layers are stacked to form a transducer. Signals from each of the layers are processed independently during a transmit event, a receive event, and both transmit and receive events. Signals from the transducer are filtered to isolate harmonics for imaging. The configuration has a wide bandwidth for harmonic imaging and also avoids a low response often associated with the second harmonic of a fundamental frequency.—RCW

6,673,017

43.80.Vj TEMPORAL RESOLUTION METHOD AND SYSTEMS FOR ULTRASOUND IMAGING

John I. Jackson, assignor to Acuson Corporation
6 January 2004 (Class 600/437); filed 28 August 2002

Temporal indicators are used to interleave frames from ECG cycles. The interleaved frames result in a higher effective frame rate with improved temporal resolution. Average velocity waveforms calculated from frames in each of the cycles are fit together.—RCW

6,673,021

43.80.Vj ULTRASOUND PROBE FOR ULTRASOUND EXAMINATION SYSTEM

Hiromu Itoi, assignor to Fuji Photo Optical Company, Limited
6 January 2004 (Class 600/466); filed in Japan 28 September 2001

A guide is attached to the proximal end of a deformable probe. A flexible wiring film coiled into a helical roll extends inside the probe from the guide to the distal end of the probe. On the surface of the wiring film at the distal end are connection points for signal lines from ultrasound transducer elements. An external relay unit allows the signal lines to be disconnected from the ultrasound imaging system.—RCW

6,675,038

43.80.Vj METHOD AND SYSTEM FOR RECORDING PROBE POSITION DURING BREAST ULTRASOUND SCAN

Tommy Earl Cupples *et al.*, assignors to U-Systems, Incorporated
6 January 2004 (Class 600/424); filed 14 May 2001

A probe icon is manipulated relative to a breast icon and text describing the position of an ultrasound probe is automatically produced to reduce user error and fatigue by avoiding manual keying.—RCW

6,676,599

43.80.Vj METHOD AND APPARATUS FOR PROVIDING REAL-TIME CALCULATION AND DISPLAY OF TISSUE DEFORMATION IN ULTRASOUND IMAGING

Hans Torp *et al.*, assignors to G. E. Vingmed Ultrasound AS
13 January 2004 (Class 600/437); filed 22 January 2002

Velocity is estimated by filtering a received ultrasonic signal at three frequencies related to the second harmonic of the ultrasound signal. A reference velocity estimated from signals filtered at the upper and lower frequencies is used to choose a velocity from values estimated using the middle frequency. Strain rate in any direction, not necessarily along the ultrasound beam, is estimated. Tissue deformation parameters may be presented as functions of time or spatial position for applications such as stress echocardiography.—RCW

6,676,602

43.80.Vj TWO DIMENSIONAL ARRAY SWITCHING FOR BEAMFORMING IN A VOLUME

Stephen R. Barnes *et al.*, assignors to Siemens Medical Solutions USA, Incorporated
13 January 2004 (Class 600/443); filed 25 July 2002

Elements associated with essentially the same time delay are connected to form a macro element and reduce the number of independent elements used in beamformation. To form a beam, the macro elements are configured to operate as a phased array or along lines in two dimensions on the face of the transducer. Various configurations such as 1.25D, 1.5D, or 1.75D arrays are possible.—RCW

6,676,603

43.80.Vj METHOD AND APPARATUS FOR BEAM COMPOUNDING

Manfred Aichhorn and Franz Steinbacher, assignors to Kretztechnik AG
13 January 2004 (Class 600/447); filed 9 November 2001

A set of receive beams is formed to intersect at a location in a sample volume. A compound echo is produced from the set of beams and a compound image is formed from echoes compounded in this way. A frame rate acceptable for abdominal scanning in real time is achieved.—RCW

6,676,626

43.80.Vj ULTRASOUND ASSEMBLY WITH INCREASED EFFICACY

Frederick J. Bennett and James E. Rodriguey, assignors to EKOS Corporation
13 January 2004 (Class 604/22); filed 16 August 1999

This version of an ultrasound catheter system features a catheter body incorporating a chamber containing a low impedance medium and an ultrasound transducer. The transducer is positioned on the external surface of an elongated body so that one end of the transducer is adjacent to the chamber. Two different mediums are positioned at the two ends of the transducers. The more pliant medium is located at the end of the transducer next to the chamber and a harder medium placed at the opposite end. This is to ensure flexibility at the end near the chamber and efficient transmission of ultrasound energy from the external side of the transducer.—DRR

6,679,843

43.80.Vj ADAPTIVE ULTRASOUND IMAGE FUSION

Qinglin Ma *et al.*, assignors to Siemens Medical Solutions USA, Incorporated
20 January 2004 (Class 600/441); filed 25 June 2002

B-mode and Doppler signals are combined nonlinearly. Portions of the B-mode signal associated with stationary tissue are used while portions of the B-mode signal associated with flow are suppressed. To avoid artifacts, the suppression is gradual rather than abrupt. Suppression of the B-mode signals where flow exists permits better identification of small vessels. Small vessel or other small structure information associated with moving fluid is inserted within the B-mode image. Anatomic features are kept intact by the presence of echoes that show stationary tissue while added visibility of small vessels provides detail about tissue morphology.—RCW

6,679,846

43.80.Vj DIAGNOSTIC ULTRASOUND IMAGING METHOD AND SYSTEM WITH IMPROVED FRAME RATE

David J. Napolitano *et al.*, assignors to Acuson Corporation
20 January 2004 (Class 600/447); filed 21 February 2002

This system forms receive beams from spatially distinct transmit beams. The receive beams alternate in type across the regions being imaged. The types differ in at least one parameter other than transmit and receive line geometry. The difference can be in transmit phase, transmit or receive aperture, system frequency, transmit focus, complex phase angle, transmit code, or transmit gain. The receive beams associated with spatially distinct transmit beams are then combined. This allows multiple-pulse techniques that include phase inversion, synthetic aperture, synthetic frequency, and synthetic focusing to be used simultaneously without the frame rate penalty normally associated with them.—RCW

6,679,845

43.80.Vj HIGH FREQUENCY SYNTHETIC ULTRASOUND ARRAY INCORPORATING AN ACTUATOR

Timothy Adam Ritter *et al.*, assignors to The Penn State Research Foundation
20 January 2004 (Class 600/444); filed 13 August 2001

This array is connected to a mechanism that translates the array to

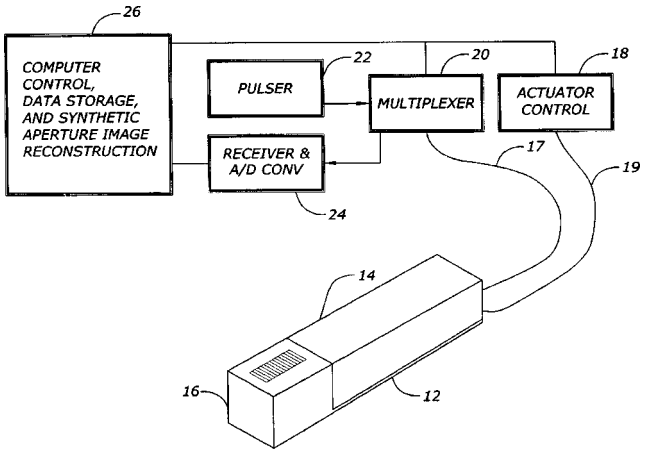

increase the spatial sampling of the array.—RCW

6,679,847

43.80.Vj SYNTHETICALLY FOCUSED ULTRASONIC DIAGNOSTIC IMAGING SYSTEM FOR TISSUE AND FLOW IMAGING

Brent S. Robinson and Clifford Cooley, assignors to Koninklijke Philips Electronics N.V.
20 January 2004 (Class 600/447); filed 30 April 2002

Individual elements in a transducer array are excited to sonify a region to be imaged and echoes are received by the elements. The echoes are used to produce motion maps for different velocity vectors over the imaged

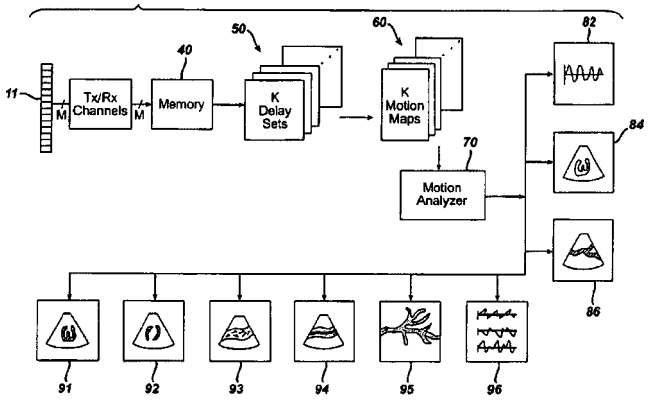

region. The motion maps are used to produce a variety of ultrasound images that include gray-scale images, colorflow images, and spectral flow displays.—RCW

6,679,849

43.80.Vj ULTRASONIC TEE PROBE WITH TWO DIMENSIONAL ARRAY TRANSDUCER

David G. Miller *et al.*, assignors to Koninklijke Philips Electronics N.V.
20 January 2004 (Class 600/463); filed 13 December 2002

A two-dimensional transducer array is mounted on the distal end of an elongated probe. The transmit beamformer is connected to the transducer array and is used to transmit several ultrasound beams defined by orientations in azimuth and elevation. The receive beamformer is also connected to the transducer array and is used to acquire echoes from a selected tissue volume defined by the azimuthal and elevation orientations and by a selected scan range. An image is synthesized from the pulse-echo ultrasound data.—RCW

A uniqueness theorem for the time-domain elastic-wave scattering in inhomogeneous, anisotropic solids with relaxation

Adrianus T. de Hoop[a)]
Laboratory of Electromagnetic Research, Faculty of Information Technology and Systems, Delft University of Technology, 4 Mekelweg, 2628 CD Delft, the Netherlands

(Received 16 March 2003; revised 11 June 2003; accepted 23 February 2004)

A uniqueness theorem for the (analytic or computational) time-domain modeling of the elastic wave motion in a scattering configuration that consists of inhomogeneous, anisotropic solids with arbitrary relaxation properties, occupying a bounded subdomain in an unbounded homogeneous, isotropic, perfectly elastic embedding, is presented. No direct time-domain uniqueness proof seems to exist for this kind of configuration. As an intermediate step, the one-to-one correspondence between the causal time-domain wavefield components and the constitutive material response functions on the one hand, and their time Laplace-transform counterparts for (a sequence of) real, positive values of the transform parameter on the other hand, seems a necessary tool. It is shown that such an approach leads to simple, explicit, sufficiency conditions on the inertial loss and compliance relaxation tensors describing the solid's constitutive behavior for uniqueness to hold. In it, the property of causality plays an essential role. In Christensen [*Theory of Viscoelasticity—An Introduction* (Academic, New York, 1971)] a similar approach is applied to the problem of uniqueness of the elastodynamic initial-/boundary-value problem associated with a viscoelastic object of bounded extent, the surface of which is subject to an admissible set of explicit boundary values. In the scattering configuration of unbounded extent, no explicit boundary values occur and the far-field compressional and shear wave radiation characteristics at ''infinity'' in the embedding play a key role in the proof. © *2004 Acoustical Society of America.* [DOI: 10.1121/1.1710876]

PACS numbers: 43.20.Bi, 43.20.Px [JJM] Pages: 2711–2715

I. INTRODUCTION

One of the issues one is confronted with in the mathematical modeling—be it with analytical or numerical techniques—of elastodynamic wave phenomena is the question about the uniqueness of the solution of the problem as it is formulated mathematically. Such a uniqueness should be expected on account of the underlying physics. When investigating wave propagation and scattering problems, the pertaining partial differential equations, constitutive relations, boundary conditions at interfaces, excitation conditions at exciting sources, initial values at the time window one considers, and the causal relationship that is to exist between the exciting sources and the generated wavefield are expected to play a role. For simple solids with instantaneous constitutive relations, i.e., for lossless solids, the elastodynamic time-domain power balance provides a tool to prove uniqueness. This is also the case when simple loss mechanisms (such as the Kelvin–Voigt relaxation model and frictional force losses) are incorporated. A uniqueness proof for the case of arbitrary relaxation effects in the solids seems to withstand such a direct time-domain approach. Since for the class of linear, time-invariant, causally reacting solids the constitutive relations are expressed via time convolutions (Christensen, 1971, Chap. I; Achenbach, 1973, pp. 399–402), the time Laplace transformation (under which transformation the convolution operation transforms into a simple product of the relevant constituents) can be expected to provide a useful tool. In Christensen (1971) such an approach is applied to the problem of uniqueness of the elastodynamic initial-/boundary-value problem associated with a viscoelastic object of bounded extent, the surface of which is subject to an admissible set of explicit boundary values. In the present paper the method is applied to a scattering configuration that consists of inhomogeneous, anisotropic solids with arbitrary relaxation properties, occupying a bounded subdomain in an unbounded homogeneous, isotropic, perfectly elastic embedding. In such a configuration no explicit boundary values occur and the far-field compressional and shear wave radiation characteristics at ''infinity'' in the embedding play a key role in the proof. Simple, explicit, sufficiency conditions on the inertial loss and compliance relaxation tensors describing the solid's constitutive behavior in the inhomogeneous subdomain of the scattering configuration are derived. In view of Lerch's theorem of the one-sided (=causal) Laplace transformation (Widder, 1946), they are to hold at a sequence of equidistant, real, positive values of the time Laplace transform parameter.

II. DESCRIPTION OF THE CONFIGURATION

The configuration for which the uniqueness of the elastodynamic wavefield problem is proved consists of a linear, time-invariant, locally reacting, inhomogeneous, anisotropic solid with arbitrary inertia and compliance relaxation properties and of bounded support $\mathcal{D}\subset\mathcal{R}^3$. This part of the configuration is embedded in a linear, time-invariant, locally reacting, homogeneous, isotropic, instantaneously reacting solid with volume density of mass ρ^∞ and Lamé stiffness

a)Electronic mail: a.t.dehoop@its.tudelft.nl

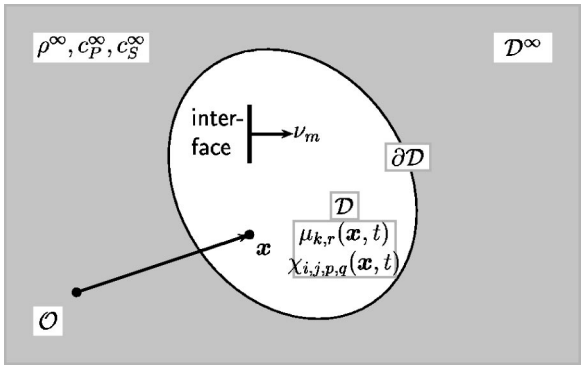

FIG. 1. Scattering configuration with inhomogeneous, anisotropic solid with relaxation (with bounded support $\mathcal{D}$) embedded in a homogeneous, isotropic, lossless solid (with unbounded support $\mathcal{D}^\infty$).

coefficients λ^∞ and μ^∞. These constitutive coefficients satisfy the conditions $\rho^\infty>0$, $\lambda^\infty>-2\mu^\infty/3$ and $\mu^\infty>0$. The corresponding compressional or *P*-wave speed is $c_P^\infty=[(\lambda^\infty+2\mu^\infty)/\rho^\infty]^{1/2}$, and the corresponding shear or *S*-wave speed is $c_S^\infty=(\mu^\infty/\rho^\infty)^{1/2}$. The unbounded domain occupied by the embedding is denoted as $\mathcal{D}^\infty$. The common boundary of $\mathcal{D}$ and $\mathcal{D}^\infty$ is the bounded closed surface $\partial\mathcal{D}$ (Fig. 1). The configuration thus defined is typical for the modeling of elastodynamic wave scattering problems. The constitutive relaxation functions in $\mathcal{D}$ vary piecewise continuously with position, with finite jump discontinuities at a finite number of piecewise smooth, bounded surfaces (interfaces). Position in the configuration is specified by the coordinates $\{x_1,x_2,x_3\}$ with respect to an orthogonal Cartesian reference frame with the origin $\mathcal{O}$ and the three mutually perpendicular base vectors $\{\mathbf{i}_1,\mathbf{i}_2,\mathbf{i}_3\}$ of unit length each. In the indicated order, the base vectors form a right-handed system. The subscript notation for Cartesian vectors and tensors is used and the summation convention for repeated subscripts applies. Whenever appropriate, vectors are indicated by boldface symbols, with $\mathbf{x}$ as the position vector. The time coordinate is t. Partial differentiation with respect to x_m is denoted by ∂_m; ∂_t is a reserved symbol indicating partial differentiation with respect to t. Volume source distributions of force and of deformation rate, with bounded supports, excite a transient elastodynamic wavefield in the configuration. Without loss of generality we locate the sources in $\mathcal{D}$. They start to act at the instant $t=0$. The field that is causally related to the action of these sources, then vanishes throughout the configuration for $t<0$.

III. FORMULATION OF THE ELASTODYNAMIC WAVEFIELD PROBLEM

At any point in the configuration where the elastodynamic wavefield quantities are differentiable they satisfy the linearized, coupled, first-order elastic wave equations (De Hoop, 1995, pp. 311, 314, and 320)

$$\Delta^+_{k,m,p,q}\partial_m\tau_{p,q}-\partial_t(\mu_{k,r}\overset{(t)}{*}v_r)=-f_k, \tag{1}$$

$$\Delta^+_{i,j,n,r}\partial_n v_r-\partial_t(\chi_{i,j,p,q}\overset{(t)}{*}\tau_{p,q})=h_{i,j}, \tag{2}$$

where $\tau_{p,q}$=dynamic stress (Pa), v_r=particle velocity (m/s), f_k=volume source density of force (N/m^3), $h_{i,j}$=volume source density of deformation rate (s^{-1}), $\mu_{k,r}$=inertia relaxation tensor (kg/m^3·s), and $\chi_{i,j,p,q}$=compliance relaxation tensor (Pa/s).

The symbol $\overset{(t)}{*}$ denotes time convolution and $\Delta^+_{k,m,p,q}$ is the symmetrical unit tensor of rank four: $\Delta^+_{k,m,p,q}=(\delta_{k,p}\delta_{m,q}+\delta_{k,q}\delta_{m,p})/2$, with $\delta_{k,p}=\{1,0\}$ for $\{k=p,\ k\neq p\}$ as the symmetrical unit tensor of rank two (Kronecker tensor). The symmetrical unit tensor of rank four extracts out of any tensor of rank two with which it has contracted its symmetrical part. So, $\Delta^+_{k,m,p,q}\tau_{p,q}=(\frac{1}{2})(\tau_{k,m}+\tau_{m,k})$ and $\Delta^+_{i,j,n,r}\partial_n v_r=(\frac{1}{2})(\partial_i v_j+\partial_j v_i)$. The constitutive relaxation tensors are piecewise continuous functions of position in $\mathcal{D}$, while in the embedding (De Hoop, 1995, pp. 320–321)

$$\mu_{k,r}=\rho^\infty\delta_{k,r}\delta(t) \quad \text{for } \mathbf{x}\in\mathcal{D}^\infty, \tag{3}$$

$$\chi_{i,j,p,q}=[\Lambda^\infty\delta_{i,j}\delta_{p,q}+M^\infty(\delta_{i,p}\delta_{j,q}+\delta_{i,q}\delta_{j,p})]\delta(t) \quad \text{for } \mathbf{x}\in\mathcal{D}^\infty, \tag{4}$$

in which $\Lambda^\infty=-\lambda^\infty/(3\lambda^\infty+2\mu^\infty)2\mu^\infty$ and $M^\infty=1/4\mu^\infty$.

Across any interface Σ of jump discontinuity in constitutive properties the boundary conditions of the continuity type (De Hoop, 1995, pp. 322–323)

$$\Delta^+_{k,m,p,q}\nu_m\tau_{p,q}=\text{continuous across } \Sigma, \tag{5}$$

$$v_r=\text{continuous across } \Sigma, \tag{6}$$

hold, where ν_m is the unit vector along the normal to Σ. This implies that the dynamic traction (=the normal component of the dynamic stress) and all components of the particle velocity are continuous across the interface. The constitutive relaxation functions are subject to the causality condition

$$\mu_{k,r}(\mathbf{x},t)=0 \quad \text{for } t<0 \quad \text{and all } \mathbf{x}\in\mathcal{D}, \tag{7}$$

$$\chi_{i,j,p,q}(\mathbf{x},t)=0 \quad \text{for } t<0 \quad \text{and all } \mathbf{x}\in\mathcal{D}. \tag{8}$$

Further conditions to be laid upon them with regard to the uniqueness of the elastodynamic wavefield problem are investigated further on.

In the embedding, the Green's tensors (dynamic stress and particle velocity due to point-sources of force and of deformation rate) can be determined analytically (De Hoop, 1995, Secs. 15.8 and 15.12). From the corresponding surface source representations over $\partial\mathcal{D}$ it follows that the outgoing fields in $\mathcal{D}^\infty$ admit the far-field expansion

$$\{\tau_{p,q},v_r\}(\mathbf{x},t)=\left[\frac{\{T^P_{p,q},V^P_r\}(\boldsymbol{\theta},t-|\mathbf{x}|/c_P^\infty)}{4\pi|\mathbf{x}|}+\frac{\{T^S_{p,q},V^S_r\}(\boldsymbol{\theta},t-|\mathbf{x}|/c_S^\infty)}{4\pi|\mathbf{x}|}\right]\times[1+O(|\mathbf{x}|^{-1})] \quad \text{as } |\mathbf{x}|\to\infty, \tag{9}$$

where $\mathbf{x}$ is the position vector from the chosen far-field reference center to the point of observation and $\boldsymbol{\theta}=\mathbf{x}/|\mathbf{x}|$ is the unit vector in the direction of observation. The far-field radiation characteristics $T^{P,S}_{p,q}$ for the dynamic stress and $V^{P,S}_r$ for the particle velocity are mutually related via

$$V_k^P = -(\rho^\infty c_P^\infty)^{-1}\Delta^+_{k,m,p,q}\theta_m T^P_{p,q}, \tag{10}$$

$$V_k^S = -(\rho^\infty c_S^\infty)^{-1}\Delta^+_{k,m,p,q}\theta_m T^S_{p,q}, \tag{11}$$

while

$$V_k^P = (V_r^P\theta_r)\theta_k, \tag{12}$$

$$V_k^S = V_k^S - (V_r^S\theta_r)\theta_k, \tag{13}$$

implying that the *P*-wave far-field particle velocity is longitudinal with respect to its radial direction of propagation and the *S*-wave far-field particle velocity is transverse with respect to its radial direction of propagation.

In the following it is shown that the problem thus formulated has at most one solution, assuming that, for each type of excitation, at least one solution exists. The proof puts restrictions on the relaxation functions representing the inertia and complicance properties of the solid in $\mathcal{D}$. For the medium in $\mathcal{D}^\infty$ the conditions simply are $\rho^\infty > 0$, $\lambda^\infty > -2\mu^\infty/3$ and $\mu^\infty > 0$ (as indicated already).

IV. THE ELASTODYNAMIC WAVEFIELD PROBLEM IN THE TIME LAPLACE-TRANSFORM DOMAIN

The general type of solids with relaxation properties as considered in the present paper withstands, as far as is known, a direct uniqueness proof in the space/time domain based on energy considerations as is the case for media with simple constitutive behavior (Achenbach, 1973, pp. 80–82). However, taking into account the causality of both the solid's passive constitutive response and the wavefield's relation to its activating sources, the time Laplace transformation with real, positive transform parameter yields a tool to specify certain conditions to be imposed on the constitutive relaxation functions in order that the wavefield problem has a unique solution. The relevant transformation is given by

$$\{\hat\tau_{p,q},\hat v_r\}(\mathbf{x},s) = \int_{t=0}^{\infty}\exp(-st)\{\tau_{p,q},v_r\}(\mathbf{x},t)\,\mathrm{d}t. \tag{14}$$

For the case of physical interest of excitation functions and relaxation functions that are bounded in space and at most show a Dirac delta distribution time behavior, the time Laplace transforms of the wavefield quantities and the relaxation tensors exist for all $\{s\in\mathcal{C};\mathrm{Re}(s)>0\}$, i.e., for all values of the transform parameter in the right half of the complex *s*-plane. Furthermore, since all time functions involved are real-valued, their Laplace transforms take on real values for real values of *s*. In relation to our uniqueness proof we now take *s* to be a *Lerch sequence*: $\{s\in\mathcal{R};\ s=s_0+nh,\ s_0>0,\ h>0,\ n=0,1,2,...\}$. Lerch's theorem (Widder, 1946, p. 63) states that if the transformation expressed by Eq. (14) is to hold for all *s* belonging to such a sequence, only one (causal) time-domain original corresponds to its related transform. Recalling that under the transformation the time derivative is replaced with a multiplication by *s* (if zero-value initial conditions apply, as is the case) and that the time convolution transforms into the product of the constituents, Eqs. (1)–(4) lead, upon time Laplace transformation, to

$$\Delta^+_{k,m,p,q}\partial_m\hat\tau_{p,q} - s\hat\mu_{k,r}\hat v_r = -\hat f_k \quad \text{for } \mathbf{x}\in\mathcal{D}, \tag{15}$$

$$\Delta^+_{i,j,n,r}\partial_n\hat v_r - s\hat\chi_{i,j,p,q}\hat\tau_{p,q} = \hat h_{i,j} \quad \text{for } \mathbf{x}\in\mathcal{D}, \tag{16}$$

and

$$\Delta^+_{k,m,p,q}\partial_m\hat\tau_{p,q} - s\rho^\infty\hat v_k = 0 \quad \text{for } \mathbf{x}\in\mathcal{D}^\infty, \tag{17}$$

$$\Delta^+_{i,j,n,r}\partial_n\hat v_r - s[\Lambda^\infty\delta_{i,j}\hat\tau_{p,p} + M^\infty(\hat\tau_{i,j}+\hat\tau_{j,i})] = 0 \quad \text{for } \mathbf{x}\in\mathcal{D}^\infty. \tag{18}$$

The interface continuity conditions (5) and (6) are upon Laplace transformation replaced by

$$\Delta^+_{k,m,p,q}\nu_m\hat\tau_{p,q} = \text{continuous across } \Sigma, \tag{19}$$

$$\hat v_r = \text{continuous across } \Sigma, \tag{20}$$

and the far-field expansion (9) by

$$\{\hat\tau_{p,q},\hat v_r\}(\mathbf{x},t) = \left[\{\hat T^P_{p,q},\hat V^P_r\}(\boldsymbol{\theta},s)\frac{\exp(-s|\mathbf{x}|/c_P^\infty)}{4\pi|\mathbf{x}|} + \{\hat T^S_{p,q},\hat V^S_r\}(\boldsymbol{\theta},s)\frac{\exp(-s|\mathbf{x}|/c_S^\infty)}{4\pi|\mathbf{x}|}\right] \times[1+O(|\mathbf{x}|^{-1})] \ \text{as}\ |\mathbf{x}|\to\infty. \tag{21}$$

Upon contracting Eqs. (15) and (17) with $\hat v_k$ and Eqs. (16) and (18) with $\hat\tau_{i,j}$ and combining the results, the relations

$$-\partial_m\Delta^+_{m,r,p,q}(\hat\tau_{p,q}\hat v_r) + s\hat v_k\hat\mu_{k,r}\hat v_r + s\hat\tau_{i,j}\hat\chi_{i,j,p,q}\hat\tau_{p,q} = \hat v_k\hat f_k - \hat\tau_{i,j}\hat h_{i,j} \quad \text{for } \mathbf{x}\in\mathcal{D}, \tag{22}$$

and

$$-\partial_m\Delta^+_{m,r,p,q}(\hat\tau_{p,q}\hat v_r) + s\hat v_k\rho^\infty\hat v_k + s\hat\tau_{i,j}[\Lambda^\infty\delta_{i,j}\hat\tau_{p,p} + M^\infty(\hat\tau_{i,j}+\hat\tau_{j,i})] = 0 \quad \text{for } \mathbf{x}\in\mathcal{D}^\infty \tag{23}$$

are constructed. Integration of Eq. (22) over $\mathcal{D}$ and application of Gauss' divergence theorem yields

$$-\int_{\partial\mathcal{D}}\nu_m\Delta^+_{m,r,p,q}\hat\tau_{p,q}\hat v_r\,\mathrm{d}A(\mathbf{x}) + \int_{\mathcal{D}}(s\hat v_k\hat\mu_{k,r}\hat v_r + s\hat\tau_{i,j}\hat\chi_{i,j,p,q}\hat\tau_{p,q})\mathrm{d}V(\mathbf{x}) = \int_{\mathcal{D}}(\hat v_k\hat f_k - \hat\tau_{i,j}\hat h_{i,j})\mathrm{d}V(\mathbf{x}), \tag{24}$$

where ν_m is the outward unit vector along the normal to $\partial\mathcal{D}$. Next, Eq. (23) is integrated over the domain that is bounded internally by $\partial\mathcal{D}$ and externally by the sphere $\mathcal{S}_\Delta$ of radius Δ and center at the far-field reference center, where Δ is chosen so large that $\mathcal{S}_\Delta$ completely surrounds $\partial\mathcal{D}$ (Fig. 2). Subsequent application of Gauss' divergence theorem leads to

$$-\int_{\mathcal{S}_\Delta}\nu_m\Delta^+_{m,r,p,q}\hat\tau_{p,q}\hat v_r\,\mathrm{d}A(\mathbf{x}) + \int_{\partial\mathcal{D}}\nu_m\Delta^+_{m,r,p,q}\hat\tau_{p,q}\hat v_r\,\mathrm{d}A(\mathbf{x}) + \int_{\mathcal{D}^\infty\cap\mathcal{D}_\Delta}\{s\hat v_k\rho^\infty\hat v_k + s\hat\tau_{i,j}[\Lambda^\infty\delta_{i,j}\hat\tau_{p,p} + M^\infty(\hat\tau_{i,j}+\hat\tau_{j,i})]\}\mathrm{d}V(\mathbf{x}) = 0, \tag{25}$$

where $\mathcal{D}_\Delta$ is the domain interior to $\mathcal{S}_\Delta$. Using the far-field representation (21) in the integration over $\mathcal{S}_\Delta$ and taking the

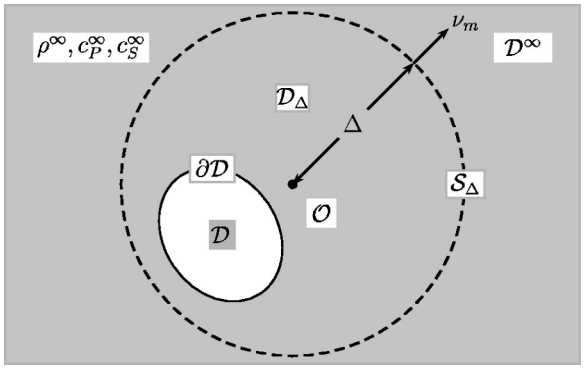

FIG. 2. Configuration used in the derivation of the time Laplace-transform domain uniqueness criterion. (The limit $\Delta\to\infty$ is taken.)

limit $\Delta\to\infty$, Eq. (25) leads to (note that the integral over $\mathcal{S}_\Delta$ goes to zero as $\Delta\to\infty$)

$$\int_{\partial\mathcal{D}} \nu_m \Delta^+_{m,r,p,q}\hat{\tau}_{p,q}\hat{v}_r\,\mathrm{d}A(\mathbf{x}) + \int_{\mathcal{D}^\infty}\{s\hat{v}_k\rho^\infty\hat{v}_k + s\hat{\tau}_{i,j}[\Lambda^\infty\delta_{i,j}\hat{\tau}_{p,p} + M^\infty(\hat{\tau}_{i,j}+\hat{\tau}_{j,i})]\}\mathrm{d}V(\mathbf{x}) = 0. \tag{26}$$

Addition of Eqs. (24) and (26) finally yields

$$\int_{\mathcal{D}}(s\hat{v}_k\hat{\mu}_{k,r}\hat{v}_r + s\hat{\tau}_{i,j}\hat{\chi}_{i,j,p,q}\hat{\tau}_{p,q})\mathrm{d}V(\mathbf{x}) + \int_{\mathcal{D}^\infty}\{s\hat{v}_k\rho^\infty\hat{v}_k + s\hat{\tau}_{i,j}[\Lambda^\infty\delta_{i,j}\hat{\tau}_{p,p} + M^\infty(\hat{\tau}_{i,j}+\hat{\tau}_{j,i})]\}\mathrm{d}V(\mathbf{x}) = \int_{\mathcal{D}}(\hat{v}_k\hat{f}_k - \hat{\tau}_{i,j}\hat{h}_{i,j})\mathrm{d}V(\mathbf{x}), \tag{27}$$

where the surface integrals over $\partial\mathcal{D}$ have canceled in view of the continuity of $\nu_m\Delta^+_{m,r,p,q}\hat{\tau}_{p,q}\hat{v}_r$ across $\partial\mathcal{D}$. Equation (27) is the basis for the construction of the uniqueness proof.

V. THE UNIQUENESS PROOF

The uniqueness proof follows the standard procedure (see, for example, Christensen, 1971, Sec. 5.1). It starts by assuming that in the given configuration, for one and the same source excitation, there exist at least two nonidentical wavefield solutions, which are distinguished by the superscripts $^{[1]}$ and $^{[2]}$. Then, $f_k^{[1]}=f_k^{[2]}=f_k$ and $h_{i,j}^{[1]}=h_{i,j}^{[2]}=h_{i,j}$. Consider the differences in value in the field quantities $\Delta\tau_{p,q}=\tau_{p,q}^{[2]}-\tau_{p,q}^{[1]}$ and $\Delta v_r=v_r^{[2]}-v_r^{[1]}$. Their time Laplace transforms then satisfy the equations [cf. Eqs. (15)–(18)]

$$\Delta^+_{k,m,p,q}\partial_m\Delta\hat{\tau}_{p,q} - s\hat{\mu}_{k,r}\Delta\hat{v}_r = 0 \quad \text{for } \mathbf{x}\in\mathcal{D}, \tag{28}$$

$$\Delta^+_{i,j,n,r}\partial_n\Delta\hat{v}_r - s\hat{\chi}_{i,j,p,q}\Delta\hat{\tau}_{p,q} = 0 \quad \text{for } \mathbf{x}\in\mathcal{D}, \tag{29}$$

and

$$\Delta^+_{k,m,p,q}\partial_m\Delta\hat{\tau}_{p,q} - s\rho^\infty\Delta\hat{v}_k = 0 \quad \text{for } \mathbf{x}\in\mathcal{D}^\infty, \tag{30}$$

$$\Delta^+_{i,j,n,r}\partial_n\Delta\hat{v}_r - s[\Lambda^\infty\delta_{i,j}\Delta\hat{\tau}_{p,p} + M^\infty(\Delta\hat{\tau}_{i,j}+\Delta\hat{\tau}_{j,i})] = 0 \quad \text{for } \mathbf{x}\in\mathcal{D}^\infty. \tag{31}$$

The same operations that have led to Eq. (27) now lead to

$$\int_{\mathcal{D}}(s\Delta\hat{v}_k\hat{\mu}_{k,r}\Delta\hat{v}_r + s\Delta\hat{\tau}_{i,j}\hat{\chi}_{i,j,p,q}\Delta\hat{\tau}_{p,q})\mathrm{d}V(\mathbf{x}) + \int_{\mathcal{D}^\infty}\{s\Delta\hat{v}_k\rho^\infty\Delta\hat{v}_k + s\Delta\hat{\tau}_{i,j}[\Lambda^\infty\delta_{i,j}\Delta\hat{\tau}_{p,p} + M^\infty(\Delta\hat{\tau}_{i,j}+\Delta\hat{\tau}_{j,i})]\}\mathrm{d}V(\mathbf{x}) = 0. \tag{32}$$

By observing that

$$\Delta\hat{\tau}_{i,j}[\Lambda^\infty\delta_{i,j}\Delta\hat{\tau}_{p,p} + M^\infty(\Delta\hat{\tau}_{i,j}+\Delta\hat{\tau}_{j,i})] = (\Lambda^\infty+2M^\infty/3)\Delta\hat{\tau}_{i,i}\Delta\hat{\tau}_{p,p} + M^\infty(\Delta\hat{\tau}_{i,j}-\Delta\hat{\tau}_{p,p}\delta_{i,j}/3) \times(\Delta\hat{\tau}_{i,j}-\Delta\hat{\tau}_{q,q}\delta_{i,j}/3), \tag{33}$$

and taking into account that $\Lambda^\infty+2M^\infty/3>0$ and $M^\infty>0$ in view of the conditions laid upon λ^∞ and μ^∞, it follows that for real, positive values of s the integrand in the integral over $\mathcal{D}^\infty$, and hence the integral itself, is positive for any nonidentically vanishing $\Delta\hat{\tau}_{p,q}$ and/or any nonidentically vanishing $\Delta\hat{v}_r$ throughout $\mathcal{D}^\infty$. The integral over $\mathcal{D}$ shares this property if we impose on $\hat{\mu}_{k,r}$ and $\hat{\chi}_{i,j,p,q}$ the condition that throughout $\mathcal{D}$ they are positive definite tensors of ranks two and four, respectively, for all real, positive values of s. Under this condition, also the integral over $\mathcal{D}$ is positive for any nonidentically vanishing $\Delta\hat{\tau}_{p,q}$ and/or any nonidentically vanishing $\Delta\hat{v}_r$ throughout $\mathcal{D}$. For nonidentically vanishing $\Delta\hat{\tau}_{p,q}$ and/or nonidentically vanishing $\Delta\hat{v}_r$ throughout $\mathcal{D}\cup\mathcal{D}^\infty$ Eq. (32) leads, in view of the value zero of the right-hand side, to a contradiction. Under the given conditions we therefore have $\Delta\hat{\tau}_{p,q}=0$ and $\Delta\hat{v}_r=0$ for $\mathbf{x}\in\{\mathcal{D}\cup\mathcal{D}^\infty\}$, which implies $\hat{\tau}_{p,q}^{[2]}=\hat{\tau}_{p,q}^{[1]}$ and $\hat{v}_r^{[2]}=\hat{v}_r^{[1]}$ for $\mathbf{x}\in\{\mathcal{D}\cup\mathcal{D}^\infty\}$. In view of Lerch's uniqueness theorem of the one-sided Laplace transformation this implies that $\tau_{p,q}^{[2]}=\tau_{p,q}^{[1]}$ and $v_r^{[2]}=v_r^{[1]}$ for $\mathbf{x}\in\{\mathcal{D}\cup\mathcal{D}^\infty\}$ and all $t\geqslant 0$, i.e., there is only one elastodynamic wavefield in the scattering configuration that is causally related to the action of its exciting sources.

It is noted that the conditions imposed on the constitutive relaxation functions are specified through their time Laplace transforms. Strictly speaking the pertaining conditions need only hold on a Lerch sequence. In view of the analyticity of the transforms in $\{s\in\mathcal{C};\mathrm{Re}(s)>0\}$, however, they hold for all real, positive values of s. The conditions thus specified are *sufficient ones*, but at present no weaker conditions seem to be in existence. Also, a simple time-domain counterpart does not seem to exist. This, however, is the same situation as in general linear, time-invariant, causal, passive system's theory.

VI. EXAMPLES OF RELAXATION FUNCTIONS

Some examples of relaxation functions that are in use to model elastic wave propagation in dissipative solids are given below. They all apply to the simple case of isotropic solids. Their dependence on $\mathbf{x}$ is not indicated explicitly.

A. Frictional-force and Maxwell-type viscosity

For an isotropic solid with frictional-force and Maxwell-type viscosity loss terms the constitutive coefficients are of the form (Kolsky, 1964, p. 107)

$$\hat{\mu}_{k,r} = \rho(1+1/s\tau_\mathrm{f})\delta_{k,r}, \tag{34}$$

$$\hat{\chi}_{i,j,p,q}=[\Lambda\delta_{i,j}\delta_{p,q}+M(\delta_{i,p}\delta_{j,q}+\delta_{i,q}\delta_{j,p})]\times(1+1/s\tau_{\mathrm{M}}), \tag{35}$$

in which ρ is the volume density of mass of the solid, $\Lambda=-\lambda/(3\lambda+2\mu)\mu$, and $M=1/4\mu$, with λ and μ the Lamé stiffness coefficients of the solid, τ_{f} the frictional-force relaxation time and τ_{M} the Maxwell viscosity relaxation time. The coefficients satisfy the conditions $\rho>0$, $\lambda>-2\mu/3$, $\mu>0$, $\tau_{\mathrm{f}}>0$ and $\tau_{\mathrm{M}}>0$. The corresponding time-domain relaxation functions are

$$\mu_{k,r}=\rho[\delta(t)+\tau_{\mathrm{f}}^{-1}H(t)]\delta_{k,r}, \tag{36}$$

$$\chi_{i,j,p,q}=[\Lambda\delta_{i,j}\delta_{p,q}+M(\delta_{i,p}\delta_{j,q}+\delta_{i,q}\delta_{j,p})]\times[\delta(t)+\tau_{\mathrm{M}}^{-1}H(t)], \tag{37}$$

where $\delta(t)$ is the Dirac delta distribution and $H(t)$ is the Heaviside unit step function.

B. The standard linear solid with creep/relaxation loss mechanism

For the standard linear solid with creep/relaxation loss mechanism, or Zener solid, the constitutive coefficients are of the form (Carcione, 2001; Mainardi 2002)

$$\hat{\mu}_{k,r}=\rho\delta_{k,r}, \tag{38}$$

$$\hat{\chi}_{i,j,p,q}=[\Lambda\delta_{i,j}\delta_{p,q}+M(\delta_{i,p}\delta_{j,q}+\delta_{i,q}\delta_{j,p})]\times\left(1+\frac{1/\tau_{\sigma}-1/\tau_{\epsilon}}{1/\tau_{\epsilon}+s}\right), \tag{39}$$

in which $\tau_{\sigma}>0$ is the stress relaxation time and $\tau_{\epsilon}>0$ is the strain relaxation time. On account of the physical condition of creep yield, the condition

$$\tau_{\sigma}<\tau_{\epsilon} \tag{40}$$

holds. The corresponding time-domain relaxation functions are

$$\mu_{k,r}=\rho\delta(t)\delta_{k,r}, \tag{41}$$

$$\chi_{i,j,p,q}=[\Lambda\delta_{i,j}\delta_{p,q}+M(\delta_{i,p}\delta_{j,q}+\delta_{i,q}\delta_{j,p})]\times[\delta(t)+(1/\tau_{\sigma}-1/\tau_{\epsilon})\exp(-t/\tau_{\epsilon})H(t)]. \tag{42}$$

It is observed that the relaxation functions shown here do satisfy the conditions for uniqueness discussed in Sec. V.

VII. CONCLUSION

A time-domain uniqueness theorem for elastodynamic wavefield scattering in a configuration consisting of inhomogeneous, anisotropic solids with arbitrary relaxation properties, occupying a bounded subdomain in an unbounded homogeneous, isotropic, perfectly elastic embedding, is presented. Sufficient conditions for the uniqueness to be laid upon the tensorial relaxation functions are formulated in the (causal) time Laplace-transform domain for real, positive values of the transform parameter. Some simple relaxation functions that are in use in the modeling of wave phenomena in nonperfectly elastic solids are shown to be in accordance with the criteria developed.

ACKNOWLEDGMENT

The author wishes to express his sincere thanks to an (anonymous) reviewer for bringing to his attention the most valuable reference to Christensen (1971). For some inexplicable reason, this reference had hitherto escaped the author's attention.

Achenbach, J. D. (**1973**). *Wave Propagation in Elastic Solids* (North-Holland (Elsevier), Amsterdam).

Carcione, J. M. (**2001**). *Waves in Real Media: Wave Propagation in Anisotropic, Anelastic and Porous Media* (Pergamon, Oxford).

Christensen, R. M. (**1971**). *Theory of Viscoelasticity—An Introduction* (Academic, New York); also (Dover, New York, 2003).

De Hoop, A. T. (**1995**). *Handbook of Radiation and Scattering of Waves* (Academic, London).

Kolsky, H. (**1964**). *Stress Waves in Solids* (Dover, New York).

Mainardi, F. (**2002**). ''Linear Viscoelasticiy,'' Chap. 4 in *Acoustic Interactions with Submerged Elastic Structures*, edited by A. Guran, A. Boström, O. Leroy, and G. Maze (World Scientific, Singapore).

Widder, D. V. (**1946**). *The Laplace Transform* (Princeton U.P., Princeton).

Comparison of a finite element model with a multiple-scales solution for sound propagation in varying ducts with swirling flows

Fabien Treyssède[a] and Mabrouk Ben Tahar
Université de Technologie de Compiègne, Laboratoire Roberval UMR 6066, Secteur Acoustique, BP 20529, 60205 Compiègne Cedex, France

(Received 5 September 2003; revised 5 January 2004; accepted 26 February 2004)

A multiple-scales (MS) solution is proposed to study sound propagation in slowly varying ducts with mean swirling flows. Instead of the standard linearized Euler equations, the MS method is applied to the so-called Galbrun's equation. This equation is based on an Eulerian–Lagrangian description and corresponds to a wave equation written only in terms of the Lagrangian perturbation of the displacement. This yields simpler differential equations to solve for the MS model as well as simpler boundary conditions. In this paper, Galbrun's equation is also solved by a mixed pressure-displacement finite element method (FEM). The proposed FEM model has already been tested in authors' previous papers. This model is quite general and is extended here to arbitrary mean flows, including compressibility and swirling flow effects. Some MS and FEM solutions are then compared in order to validate both models. © *2004 Acoustical Society of America.*
[DOI: 10.1121/1.1707084]

PACS numbers: 43.20.Bi, 43.28.Py, 43.20.Mv [MO]

Pages: 2716–2730

NOMENCLATURE

D, C, P, $\mathbf{V}$	Mean flow variables
p, $\mathbf{w}$	Acoustic variables
ω	Pulsation
$d(\cdot)/dt$	Material derivative
(r,θ,z)	Cylindrical coordinates
$\mathbf{n}$	Outward normal
Z_1, Z_2	Inner and outer wall impedances
R_1, R_2	Inner and outer duct radii
$Z=\epsilon z$	Slow axial scale
k_z	Local axial wave number
m	Azimuthal mode number
D_0, C_0, P_0, $\mathbf{V}_0$	zeroth-order mean flow variables
p_0, $\mathbf{w}_0$	zeroth-order acoustic variables
Ω	Flow modified pulsation
L, $L^\dagger$	Acoustic operator and its adjoint
ψ_0, $\psi_0^\dagger$	zeroth-order eigenfunction and its adjoint
Ω_a	Fluid domain
Γ_i	Wall boundary
Γ_w	Forced displacement boundary
p^*, $\mathbf{w}^*$	Trial fields
L^*, C^*	Characteristic length and sound speed
M_0, Ω_0	Axial and azimuthal Mach number
$\mathbf{i}$	Time-averaged intensity ($\mathrm{W\,m^{-2}}$)
μ	Total duct attenuation (dB)

I. INTRODUCTION

Mean swirling flows may have a significant impact upon sound propagation in ducts, particularly when turbomachines are involved. For instance, the fan of an aeroengine duct is likely to generate a significant rotating flow, for which the azimuthal velocity can even be comparable to the axial component. It is then obvious that the effects of swirl on acoustic wave propagation cannot be neglected.

Almost all analyses taking into account such effects deal with the study of a mode propagating inside a simple straight duct.[1–5] This work has notably provided a meaningful understanding of coupling that occurs between the so-called acoustic and rotational waves.

Recently, Cooper and Peake[6] extended Golubev and Atassi's study[4] to slowly varying lined ducts by applying a multiple-scales (MS) method. Results outlined the influence of mean flow swirl, which produces a large difference in axial wave number and moves co-rotating modes closer to cut-off (counter-rotating modes are moved further). One consequence is that, when a lining is present at walls, co-rotating modes are always much more damped than those in a non-swirling flow (counter-rotating modes may be amplified).

In order to describe sound propagation in swirling flows, all the above-mentioned references are based on the linearized Euler equations (note that the standard full-potential equation, which assumes that both acoustics and aerodynamics are irrotational, cannot be considered). However, there exists another wave equation, the so-called Galbrun's equation[7] also derived by Godin,[8] which is a reformulation of the linearized Euler equations using an Eulerian–Lagrangian description. Galbrun's equation constitutes a second-order partial differential equation, which has the particularity to be written only in terms of the Lagrangian perturbation of the displacement vector (itself expressed with Eulerian variables). Theoretical details about this equation are given in Refs. 8 and 9.

Few works deal with this equation, but it may have the

[a]Electronic mail: fabien.treyssede@utc.fr

 0001-4966/2004/115(6)/2716/15/$20.00 © 2004 Acoustical Society of America

following several advantages: a gain of one to two unknowns compared to the linearized Euler equations, availability of exact expressions of intensity and energy,[8,10] simple expressions of boundary conditions (compared to Myers' condition[11]). Studying a single mode propagating in a straight duct with swirling flows, Poirée[12] derived a differential equation from Galbrun's equation that is satisfied by the radial component of the Lagrangian displacement.

In this paper, a MS method based on Galbrun's equation is proposed to solve sound propagation in slowly varying lined ducts with swirling flows. The overall method is inspired from Rienstra's[13] and Cooper and Peake's[6] papers. The proposed model does not *a priori* provide some great insights from a physical point of view compared to Cooper and Peake's, but equations are much easier to solve and the mean flow being considered is not necessarily homentropic (though no such flows are considered for the numerical results presented in this paper).

A second part of the paper consists in proposing a quite general finite element method (FEM) to solve Galbrun's equation in the harmonic case, for any arbitrary mean flow whether it is sheared, swirling and/or compressible. It has to be emphasized that some work has been made to solve the general linearized equations of fluid mechanics using a FEM. This work concerns the linearized Euler equations in the late 1970s,[14–16] as well as Galbrun's equation more recently.[10,17–19] Unfortunately, the effects of swirling flows have not yet been specifically studied in those analyses.

Here, the proposed FEM is applicable to any type of flow. The choice of a mixed pressure-displacement variational formulation combined with a finite element satisfying the inf-sup condition avoids the well-known locking phenomenon, which usually occurs with a purely displacement based formulation. The developed FEM model has already been successfully tested in the present authors' recent papers for sound propagation in sheared flows[18] and vibro-acoustic interactions.[19] The slight difference with those references comes from the fact that the variational formulation is now quite general because it includes the additional terms inherent to mean flow compressibility effect, which were not previously considered.

The last part of the paper gives some numerical results in the axisymmetric case, obtained with the MS and FEM models. The main goal of this part is to validate both models and to verify that they adequately include the effects of swirl upon acoustic propagation.

II. MULTIPLE-SCALES SOLUTION FOR ACOUSTICS

This section only gives the multiple-scales solution for acoustics, based on Galbrun's equation. A multiple-scales solution for the mean flow has already been considered in Ref. 6 and will not be detailed here. More insight about Galbrun's equation can be found in Refs. 8, 9, 10, and 19.

The multiple-scales methodology (see for instance Refs. 20–22) may be divided into three main parts. First, a slowly varying parameter is defined and used to rewrite governing equations. Second, a local eigenvalue problem is solved at each duct cross-section (zeroth-order solution). Third, a solvability condition is derived from the first-order problem in order to get the axially varying factor of the solution.

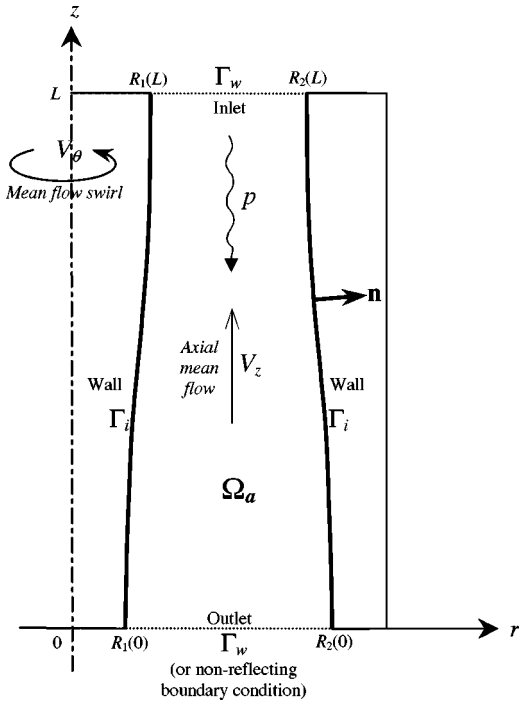

FIG. 1. Geometry of a slowly varying duct carrying flow with swirl. The acoustic inlet being located at the top section $z=0$ m, the sketched duct is expanding from the acoustical point of view.

A. Problem formulation

In order to simplify calculations in the remainder, Galbrun's equation is first rewritten in its mixed pressure-displacement form:

$$D\frac{d^2\mathbf{w}}{dt^2}+\nabla p+(\nabla\cdot\mathbf{w})\nabla P-{}^T\nabla\cdot\mathbf{w}\nabla P=0,$$
$$p+DC^2\nabla\cdot\mathbf{w}=0. \tag{2.1}$$

Upper and lower case letters, respectively, denote mean flow and acoustic variables. In the following, the adjective ''acoustic'' may be a misnomer because it will be used to qualify any disturbance, although a perturbation wave is likely to be of vortical type also. D, C, P, and $\mathbf{V}$ are the density, sound celerity, pressure, and velocity of the mean flow. p and $\mathbf{w}$ are the pressure and displacement Lagrangian perturbations (this kind of perturbation is associated with the same particle, unlike standard Eulerian perturbations). In the harmonic case, assuming an $e^{-i\omega t}$ dependence, the material derivative is given by $d/dt=-i\omega+\mathbf{V}\cdot\nabla$. An axisymmetric duct geometry is assumed. Cylindrical coordinates (r,θ,z) will be used, where z is the duct axis. Figure 1 represents a slowly varying annular duct in the (r,z) cutting plane.

Based on the continuity of normal displacement,[8] the general boundary conditions at walls is given by

$$p=-i\omega Z_i\mathbf{w}\cdot\mathbf{n} \quad \text{at } r=R_i, \quad i=1,2. \tag{2.2}$$

$\mathbf{n}$ is the outward normal from the fluid point of view. R_1 and R_2 denote the inner and outer duct radii. Z_1 and Z_2 are the

wall impedances at $r=R_1$ and R_2, respectively. R_i and Z_i may vary slowly along the duct axis.

The assumption of a slowly varying duct geometry suggests the use of a multiple-scales method, which first consists in defining the following slow spatial scale:

$$Z=\epsilon z, \quad \partial/\partial z=\epsilon\partial/\partial Z. \tag{2.3}$$

ϵ is a small parameter that can be quantified by the maximum axial slope of duct walls. Moreover, approximate solutions of the acoustic fields are sought of the following form:

$$\varphi(r,\theta,z,t)=\varphi(r,z)\exp\left(i\int^z k_z(\alpha)d\alpha\right)\exp[i(m\theta-\omega t)]. \tag{2.4}$$

k_z represents the local axial wave number (unlike for a straight duct, k_z is slowly varying along the axis). m is the azimuthal mode number. Suppressing the exponential, derivation rules with respect to z become formally

$$\frac{\partial\varphi}{\partial z}=ik_z\varphi+\epsilon\frac{\partial\varphi}{\partial Z}. \tag{2.5}$$

Concerning the mean flow, stationarity and θ independence are supposed. Then, the application of a multiple-scales method to the basic equations of fluid mechanics shows that mean flow variables have the following expansions (see Refs. 6 and 13):

$$\begin{cases} D(r,Z;\epsilon)=D_0(r,Z)+O(\epsilon^2) \\ C(r,Z;\epsilon)=C_0(r,Z)+O(\epsilon^2), \\ P(r,Z;\epsilon)=P_0(r,Z)+O(\epsilon^2) \end{cases}$$

$$\begin{cases} V_r(r,Z;\epsilon)=\epsilon V_{r_1}(r,Z)+O(\epsilon^3) \\ V_\theta(r,Z;\epsilon)=V_{\theta_0}(r,Z)+O(\epsilon^2) \\ V_z(r,Z;\epsilon)=V_{z_0}(r,Z)+O(\epsilon^2) \end{cases}. \tag{2.6}$$

In the remainder of this section, indices will denote the expansion order. Mean flow variables are supposed to have been calculated beforehand.

Then, using Eq. (2.5) and the mean flow mass conservation $\nabla\cdot D\mathbf{V}=0$ to leading order (order ϵ^1), it can be shown that the material second derivatives can be written, after some calculations:

$$D_0\frac{d^2\varphi}{dt^2}=-D_0\Omega^2\varphi-i\epsilon\frac{1}{\varphi}\left\{\frac{\partial(D_0V_{z_0}\Omega\varphi^2)}{\partial Z}+\frac{1}{r}\frac{\partial(rD_0V_{r_1}\Omega\varphi^2)}{\partial r}\right\}+O(\epsilon^2) \tag{2.7}$$

with $\Omega=\omega-k_zV_{z_0}-\frac{m}{r}V_{\theta_0}$.

Finally, reporting Eqs. (2.5)–(2.7) into Eq. (2.1) yields the following system, up to first order:

$$\begin{aligned}
&-D_0\Omega^2w_r+\frac{\partial p}{\partial r}+\frac{\partial P_0}{\partial r}\left(\frac{w_r}{r}+\frac{im}{r}w_\theta+ik_zw_z\right)\\
&\quad=i\epsilon\frac{1}{w_r}\left\{\frac{\partial(D_0V_{z_0}\Omega w_r^2)}{\partial Z}+\frac{1}{r}\frac{\partial(rD_0V_{r_1}\Omega w_r^2)}{\partial r}\right\}\\
&\qquad+\epsilon\left\{\frac{\partial P_0}{\partial Z}\frac{\partial w_z}{\partial r}-\frac{\partial P_0}{\partial r}\frac{\partial w_z}{\partial Z}\right\},\\
&-D_0\Omega^2w_\theta+\frac{im}{r}p-\frac{\partial P_0}{\partial r}\left(\frac{im}{r}w_r-\frac{w_\theta}{r}\right)\\
&\quad=i\epsilon\frac{1}{w_\theta}\left\{\frac{\partial(D_0V_{z_0}\Omega w_\theta^2)}{\partial Z}+\frac{1}{r}\frac{\partial(rD_0V_{r_1}\Omega w_\theta^2)}{\partial r}\right\}\\
&\qquad+\epsilon\frac{\partial P_0}{\partial Z}\frac{im}{r}w_z,\\
&-D_0\Omega^2w_z+ik_zp-\frac{\partial P_0}{\partial r}ik_zw_r\\
&\quad=i\epsilon\frac{1}{w_z}\left\{\frac{\partial(D_0V_{z_0}\Omega w_z^2)}{\partial Z}+\frac{1}{r}\frac{\partial(rD_0V_{r_1}\Omega w_z^2)}{\partial r}\right\}\\
&\qquad+\epsilon\left\{-\frac{\partial p}{\partial Z}-\frac{\partial P_0}{\partial Z}\left(\frac{1}{r}\frac{\partial}{\partial r}(rw_r)+\frac{im}{r}w_\theta\right)+\frac{\partial P_0}{\partial r}\frac{\partial w_r}{\partial Z}\right\},\\
&p+D_0C_0^2\left(\frac{1}{r}\frac{\partial}{\partial r}(rw_r)+\frac{im}{r}w_\theta+ik_zw_z\right)=-\epsilon D_0C_0^2\frac{\partial w_z}{\partial Z}.
\end{aligned} \tag{2.8}$$

Concerning the boundary condition (2.2), the outward normal is

$$\mathbf{n}_i=\mp\frac{1}{\sqrt{1+\left(\frac{dR_i}{dz}\right)^2}}\left(\mathbf{e}_r-\frac{dR_i}{dz}\mathbf{e}_z\right), \quad i=1,2, \tag{2.9}$$

where the minus (respectively, plus) sign is associated to $i=1$ (respectively, $i=2$). Then, applying Eq. (2.3), condition (2.2) becomes

$$p=\pm i\omega Z_i\left(w_r-\epsilon\frac{dR_i}{dZ}w_z\right) \quad \text{at } r=R_i, \quad i=1,2. \tag{2.10}$$

In order to obtain an approximate solution of $\mathbf{w}$ and p, acoustic variables are now expanded in powers of ϵ such that

$$\begin{Bmatrix} w_r \\ w_\theta \\ w_z \\ p \end{Bmatrix}=\begin{Bmatrix} w_{r_0} \\ w_{\theta_0} \\ w_{z_0} \\ p_0 \end{Bmatrix}+\epsilon\begin{Bmatrix} w_{r_1} \\ w_{\theta_1} \\ w_{z_1} \\ p_1 \end{Bmatrix}+O(\epsilon^2). \tag{2.11}$$

B. Local solution at the order $O(1)$

Applying the expansion (2.11) to system (2.8), we obtain to leading order (order ϵ^0)

$$
\begin{aligned}
&-D_0\Omega^2 w_{r_0}+\frac{\partial p_0}{\partial r}+\frac{\partial P_0}{\partial r}\left(\frac{w_{r_0}}{r}+\frac{im}{r}w_{\theta_0}+ik_z w_{z_0}\right)=0,\\
&-D_0\Omega^2 w_{\theta_0}+\frac{im}{r}p_0-\frac{\partial P_0}{\partial r}\left(\frac{im}{r}w_{r_0}-\frac{w_{\theta_0}}{r}\right)=0,\\
&-D_0\Omega^2 w_{z_0}+ik_z p_0-\frac{\partial P_0}{\partial r}ik_z w_{r_0}=0,\\
&p_0+D_0C_0^2\left(\frac{1}{r}\frac{\partial}{\partial r}(rw_{r_0})+\frac{im}{r}w_{\theta_0}+ik_z w_{z_0}\right)=0.
\end{aligned}
\tag{2.12}
$$

The azimuthal and axial components of the displacement may be expressed in terms of the pressure and radial displacement, thanks to the second and third equations of the above system:

$$
w_{\theta_0}=\frac{im}{r}\frac{p_0-\dfrac{\partial P_0}{\partial r}w_{r_0}}{D_0\Omega^2-\dfrac{1}{r}\dfrac{\partial P_0}{\partial r}},\qquad w_{z_0}=ik_z\frac{p_0-\dfrac{\partial P_0}{\partial r}w_{r_0}}{D_0\Omega^2}.
\tag{2.13}
$$

Now, the system (2.12) can be simplified to a system of two differential equations by replacing the azimuthal and axial displacements (2.13) into the first and fourth equations of Eq. (2.12). This leads to

$$
\begin{aligned}
&\alpha\frac{1}{r}\frac{\partial}{\partial r}(rw_{r_0})+\beta\frac{\partial P_0}{\partial r}w_{r_0}+\left\{\frac{\alpha}{D_0C_0^2}-\beta\right\}p_0=0,\\
&\alpha\frac{\partial p_0}{\partial r}-\beta\frac{\partial P_0}{\partial r}p_0+\left\{\beta\left(\frac{\partial P_0}{\partial r}\right)^2-\alpha^2\right\}w_{r_0}=0,
\end{aligned}
\tag{2.14}
$$

with

$$
\alpha=D_0\Omega^2-\frac{1}{r}\frac{\partial P_0}{\partial r},\qquad \beta=\frac{m^2}{r^2}+k_z^2-\frac{1}{rD_0\Omega^2}\frac{\partial P_0}{\partial r}k_z^2.
$$

Boundary condition (2.10) to leading order is simply given by

$$
p_0=\pm i\omega Z_i w_{r_0}\quad \text{at } r=R_i\quad (i=1,2).
\tag{2.15}
$$

Equations (2.14) and (2.15) constitute an eigenvalue problem (k_z is the eigenvalue) of two first-order differential equations with two eigenfunctions, p_0 and w_{r_0}. However, this problem is unidimensional (r-dependent only) and is obviously not sufficient to give a complete solution of our problem. In fact, Eqs. (2.14) and (2.15) must be solved for each cross section of the duct (the duct axis being discretized) in order to obtain the radial profiles of the acoustic fields $\mathbf{w}_0(r)$ and $p_0(r)$. As explained in the following, the z dependence of the acoustic variables will be obtained by means of a solvability condition derived from the first-order problem.

It has to be outlined that system (2.14) can be further transformed into a single differential equation written in terms of p_0 only (see the Appendix). Nevertheless, this does not really simplify the equations to solve because the single differential equation becomes of second order and the boundary condition, which would then have to be expressed in terms of pressure only, has a more complex form.

C. Solvability condition

Applying Eq. (2.11) to Eq. (2.8), the problem to first order ϵ^1 is given by

$$
L\psi_1=f_0
\tag{2.16}
$$

with the following notations:

$$
L=\begin{bmatrix}
-D_0\Omega^2+\dfrac{1}{r}\dfrac{\partial P_0}{\partial r} & i\dfrac{m}{r}\dfrac{\partial P_0}{\partial r} & ik_z\dfrac{\partial P_0}{\partial r} & \dfrac{\partial}{\partial r}\\
-i\dfrac{m}{r}\dfrac{\partial P_0}{\partial r} & -D_0\Omega^2+\dfrac{1}{r}\dfrac{\partial P_0}{\partial r} & 0 & i\dfrac{m}{r}\\
-ik_z\dfrac{\partial P_0}{\partial r} & 0 & -D_0\Omega^2 & ik_z\\
-\dfrac{1}{r}\dfrac{\partial(r(\cdot))}{\partial r} & -i\dfrac{m}{r} & -ik_z & -\dfrac{1}{D_0C_0^2}
\end{bmatrix},\qquad
\psi_1=\begin{Bmatrix} w_{r_1}\\ w_{\theta_1}\\ w_{z_1}\\ p_1\end{Bmatrix},
$$

$$
f_0=\begin{Bmatrix}
i\dfrac{1}{w_{r_0}}\left\{\dfrac{\partial(D_0V_{z_0}\Omega w_{r_0}^2)}{\partial Z}+\dfrac{1}{r}\dfrac{\partial(rD_0V_{r_1}\Omega w_{r_0}^2)}{\partial r}\right\}+\dfrac{\partial P_0}{\partial Z}\dfrac{\partial w_{z_0}}{\partial r}-\dfrac{\partial P_0}{\partial r}\dfrac{\partial w_{z_0}}{\partial Z}\\
i\dfrac{1}{w_{\theta_0}}\left\{\dfrac{\partial(D_0V_{z_0}\Omega w_{\theta_0}^2)}{\partial Z}+\dfrac{1}{r}\dfrac{\partial(rD_0V_{r_1}\Omega w_{\theta_0}^2)}{\partial r}\right\}+\dfrac{\partial P_0}{\partial Z}\dfrac{im}{r}w_{z_0}\\
i\dfrac{1}{w_{z_0}}\left\{\dfrac{\partial(D_0V_{z_0}\Omega w_{z_0}^2)}{\partial Z}+\dfrac{1}{r}\dfrac{\partial(rD_0V_{r_1}\Omega w_{z_0}^2)}{\partial r}\right\}-\dfrac{\partial p_0}{\partial Z}-\dfrac{\partial P_0}{\partial Z}\left(\dfrac{1}{r}\dfrac{\partial}{\partial r}(rw_{r_0})+\dfrac{im}{r}w_{\theta_0}\right)+\dfrac{\partial P_0}{\partial r}\dfrac{\partial w_{r_0}}{\partial Z}\\
\dfrac{\partial w_{z_0}}{\partial Z}
\end{Bmatrix}.
\tag{2.17}
$$

To first order, the boundary condition (2.10) is now

$$p_1 \mp i\omega Z_i w_{r_1} = \mp i\omega Z_i \frac{dR_i}{dZ} w_{z_0} \quad \text{at } r=R_i, \quad i=1,2. \tag{2.18}$$

L is not a self-adjoint operator. Thus, we must solve the adjoint problem, denoted by the exponent †, and which satisfies the following identity:

$$\langle \psi_0^\dagger, L\psi_0 \rangle = \langle L^\dagger \psi_0^\dagger, \psi_0 \rangle, \tag{2.19}$$

where the inner product is suitably defined by

$$\langle A,B \rangle = \int_{R_1}^{R_2} \sum_{n=1}^{4} A_n^* B_n r\, dr. \tag{2.20}$$

The exponent * denotes the complex conjugate. The following notations have been chosen for the eigenfunction and its adjoint:

$$\psi_0 = \langle w_{r_0}, w_{\theta_0}, w_{z_0}, p_0 \rangle, \quad \psi_0^\dagger = \langle w_{r_0}^\dagger, w_{\theta_0}^\dagger, w_{z_0}^\dagger, p_0^\dagger \rangle. \tag{2.21}$$

Then, after integrating by part terms in r derivatives of the left-hand side of Eq. (2.19), and taking into account the fact that $L\psi_0 = 0$—see Eq. (2.12)—and of Eq. (2.15), it can be shown that the adjoint problem is given explicitly by

$$L^{\dagger *}\psi_0^{\dagger *} = 0, \quad p_0^{\dagger *} = \pm i\omega Z_i w_{r_0}^{\dagger *} \quad \text{at } r=R_i \quad (i=1,2), \tag{2.22}$$

where the adjoint operator $L^\dagger$ is

$$L^\dagger = \begin{bmatrix} -D_0\Omega^{*2} + \frac{1}{r}\frac{\partial P_0}{\partial r} & i\frac{m}{r}\frac{\partial P_0}{\partial r} & ik_z^* \frac{\partial P_0}{\partial r} & \frac{\partial}{\partial r} \\ -i\frac{m}{r}\frac{\partial P_0}{\partial r} & -D_0\Omega^{*2} + \frac{1}{r}\frac{\partial P_0}{\partial r} & 0 & i\frac{m}{r} \\ -ik_z^* \frac{\partial P_0}{\partial r} & 0 & -D_0\Omega^{*2} & ik_z^* \\ -\frac{1}{r}\frac{\partial (r(\cdot))}{\partial r} & -i\frac{m}{r} & -ik_z^* & -\frac{1}{D_0 C_0^2} \end{bmatrix}. \tag{2.23}$$

Solution of the adjoint problem (2.22) is then simply given by

$$w_{r_0}^{\dagger *} = w_{r_0}, \quad w_{\theta_0}^{\dagger *} = -w_{\theta_0}, \quad w_{z_0}^{\dagger *} = -w_{z_0}, \quad p_0^{\dagger *} = p_0. \tag{2.24}$$

This can be easily verified by reporting Eq. (2.24) into Eq. (2.22) and by verifying that the system thus obtained is strictly equivalent to Eqs. (2.12) and (2.15).

Then, the solvability condition is obtained by integrating by part the inner product between $\psi_0^\dagger$ and $L\psi_1$, which gives

$$\langle \psi_0^\dagger, L\psi_1 \rangle = \underbrace{\langle L^\dagger \psi_0^\dagger, \psi_1 \rangle}_{=0} + [-rp_0^{\dagger *} w_{r_1} + rw_{r_0}^{\dagger *} p_1]_{R_1}^{R_2}. \tag{2.25}$$

Making use of Eq. (2.24) and of the boundary condition to leading order (2.15), as well as to first order (2.18), the equality (2.25) becomes

$$\langle \psi_0^\dagger, L\psi_1 \rangle = i\omega Z_2 R_2 \frac{dR_2}{dZ} w_{r_0} w_{z_0}\Big|_{r=R_2} + i\omega Z_1 R_1 \frac{dR_1}{dZ} w_{r_0} w_{z_0}\Big|_{r=R_1}. \tag{2.26}$$

The left-hand side of the above equation can also be explicitly calculated, knowing that $L\psi_1 = f_0$ and relations (2.24). After some rearrangements, this yields

$$\begin{aligned} \langle \psi_0^\dagger, L\psi_1 \rangle = \int_{R_1}^{R_2} \Bigg\{ & i\Bigg[\frac{\partial}{\partial Z}\{D_0 V_{z_0}\Omega(w_{r_0}^2 - w_{\theta_0}^2 - w_{z_0}^2)\} \\ & + \frac{1}{r}\frac{\partial}{\partial r}\{rD_0 V_{r_1}\Omega(w_{r_0}^2 - w_{\theta_0}^2 - w_{z_0}^2)\}\Bigg] \\ & + \frac{\partial}{\partial Z}(p_0 w_{z_0}) + \frac{1}{r}\frac{\partial}{\partial r}\left(\frac{\partial P_0}{\partial Z} r w_{r_0} w_{z_0} \right) \\ & - \frac{\partial}{\partial Z}\left(\frac{\partial P_0}{\partial r} w_{r_0} w_{z_0} \right) \Bigg\} r\, dr. \end{aligned} \tag{2.27}$$

Terms in $\partial/\partial r$ are integrated in a straightforward way. For terms in $\partial/\partial Z$, the Leibniz formula is used:

$$\int_{R_1(Z)}^{R_2(Z)} \frac{\partial}{\partial Z} f(r,Z)\, dr = \frac{d}{dZ}\int_{R_1(Z)}^{R_2(Z)} f(r,Z)\, dr - \left[\frac{dR(Z)}{dZ} f(Z,R) \right]_{R_1(Z)}^{R_2(Z)}. \tag{2.28}$$

Using Eq. (2.28) in (2.27), and using Eq. (2.15), again leads to

$$\langle \psi_0^\dagger, L\psi_1 \rangle = \frac{d}{dZ}\int_{R_1}^{R_2}\left\{ iD_0 V_{z_0}\Omega(w_{r_0}^2 - w_{\theta_0}^2 - w_{z_0}^2) + p_0 w_{z_0} - \frac{\partial P_0}{\partial r} w_{r_0} w_{z_0}\right\} r\, dr$$
$$+\left[iD_0 r\Omega\left(V_{r_1} - \frac{dR}{dZ} V_{z_0}\right)(w_{r_0}^2 - w_{\theta_0}^2 - w_{z_0}^2)\right]_{R_1}^{R_2} + i\omega Z_2 R_2 \frac{dR_2}{dZ} w_{r_0} w_{z_0}\Big|_{r=R_2} + i\omega Z_1 R_1 \frac{dR_1}{dZ} w_{r_0} w_{z_0}\Big|_{r=R_1}$$
$$+\left(R_2 w_{r_0} w_{z_0}\left\{ \frac{\partial P_0}{\partial Z} - \frac{dR_2}{dZ}\frac{\partial P_0}{\partial r}\right\}\right)\Big|_{r=R_2} - \left(R_1 w_{r_0} w_{z_0}\left\{ \frac{\partial P_0}{\partial Z} - \frac{dR_1}{dZ}\frac{\partial P_0}{\partial r}\right\}\right)\Big|_{r=R_1}. \tag{2.29}$$

Now, the boundary condition for the mean flow is $\mathbf{V}\cdot\mathbf{n}=0$ at $r=R_i$, which gives to leading order (order ϵ^1):

$$V_{r_1} - \frac{dR_i}{dZ} V_{z_0} = 0 \quad \text{at } r=R_i \quad (i=1,2). \tag{2.30}$$

The above-mentioned condition makes the first term of the second line of Eq. (2.29) vanish. Then, it has to be noted that the radial mean flow velocity completely disappears from expression (2.29), which renders its calculation unnecessary.

Finally, combining equalities (2.26) and (2.29) leads to the following rather simple solvability condition:

$$\frac{d}{dZ}\int_{R_1}^{R_2}\left\{ iD_0 V_{z_0}\Omega(w_{r_0}^2 - w_{\theta_0}^2 - w_{z_0}^2) + p_0 w_{z_0} - \frac{\partial P_0}{\partial r} w_{r_0} w_{z_0}\right\}$$
$$\times r\, dr + \left(R_2 w_{r_0} w_{z_0}\left\{ \frac{\partial P_0}{\partial Z} - \frac{dR_2}{dZ}\frac{\partial P_0}{\partial r}\right\}\right)\Big|_{r=R_2}$$
$$-\left(R_1 w_{r_0} w_{z_0}\left\{ \frac{\partial P_0}{\partial Z} - \frac{dR_1}{dZ}\frac{\partial P_0}{\partial r}\right\}\right)\Big|_{r=R_1} = 0. \tag{2.31}$$

D. Multiple-scales solution

Mode-like displacement and pressure variables that we are looking for are rewritten as follows:

$$p_0(r,Z) = A_0(Z) p_0(r), \quad w_{r_0}(r,Z) = A_0(Z) w_{r_0}(r),$$
$$w_{\theta_0}(r,Z) = A_0(Z) w_{\theta_0}(r), \quad w_{z_0}(r,Z) = A_0(Z) w_{z_0}(r), \tag{2.32}$$

where $p_0(r)$ and $\mathbf{w}_0(r)$ correspond to the local eigenfunctions obtained from Eqs. (2.14) and (2.15). $A_0(Z)$ is an axial amplitude function to solve. Replacing acoustic variables (2.32) in the solvability condition (2.31) and making use of expression (2.13) gives the following differential equation for the unknown $A_0(Z)^2$:

$$\frac{d}{dZ}[\gamma(Z) A_0(Z)^2] = \lambda(Z) A_0(Z)^2, \tag{2.33}$$

where γ and λ only depend upon Z, and are given by

$$\gamma(Z) = \int_{R_1}^{R_2} iD_0 V_{z_0}\Omega\left[w_{r_0}^2 + \frac{1}{D_0^2\Omega^4}\left(p_0 - \frac{\partial P_0}{\partial r} w_{r_0}\right)^2 \times\left\{ \frac{m^2}{r^2}\left(1 - \frac{1}{rD_0\Omega^2}\frac{\partial P_0}{\partial r}\right)^{-2} + k_z^2 + k_z\frac{\Omega}{V_{z_0}}\right\}\right] r\, dr, \tag{2.34}$$

$$\lambda(Z) = \sum_{i=1}^{2}\left(\frac{R_i k_z}{\omega Z_i D_0\Omega^2} p_0\left(p_0 - \frac{\partial P_0}{\partial r} w_{r_0}\right)\times\left\{ \frac{\partial P_0}{\partial Z} - \frac{dR_i}{dZ}\frac{\partial P_0}{\partial r}\right\}\right)\Big|_{r=R_i}.$$

The general solution of Eq. (2.33) is

$$A_0(Z)^2 = N_0^2 \exp\int^Z \frac{\lambda(x) - \gamma'(x)}{\gamma(x)} dx, \tag{2.35}$$

where N_0^2 denotes a normalization factor (constant of integration).

From a computational point of view, the solving method is as follows. Equations are adimensionalized. First, the local eigenvalue problem given by Eqs. (2.14) and (2.15) is solved for each duct cross section by an iterative Runge–Kutta algorithm. Then, knowing $p_0(r)$, $\mathbf{w}_0(r)$, and $k_z(Z)$, a numerical one-dimensional (1D) integration with respect to r is used to compute $\gamma(Z)$ from Eq. (2.34). Finally, given $\gamma(Z)$ and $\lambda(Z)$, another 1D integration (with respect to Z this time) is computed in order to obtain $A_0(Z)$ from Eq. (2.35). The complete solution is provided by Eq. (2.32) multiplied by the exponential factors of Eq. (2.4).

As stated earlier, this section has assumed that the mean flow was initially computed. Except for some physical and realistic conditions the mean flow has to satisfy—Eq. (2.30) and mass conservation used for Eq. (2.7)—the proposed multiple-scales solution is valid for any arbitrary mean flow. In particular, it remains also valid for nonhomentropic flows, unlike Cooper and Peake's solution.[6] Moreover, the local eigenvalue problem consists in solving two differential equations, instead of four for Cooper and Peake's solution, and the solvability condition seems to be simpler to compute.

However, for conciseness and clarity, no turning points analysis has been included here, the main point of the paper being to compare the MS solution with a FEM model. Turning points occur when a mode changes from cut-on to cut-off

inside the duct. For this peculiar case, the proposed MS approximation breaks down and the method needs some adaptation (see for instance Ref. 6).

III. FEM MODEL

In this section, the FEM proposed to study sound propagation in arbitrary flows is briefly recalled. The numerical method has already been developed in the present authors' recent papers,[18,19] to which the reader is referred for more details. Unlike the multiple-scales model, the developed FEM is valid for any varying duct geometry (not necessarily slowly varying).

A. Problem formulation

A typical duct is depicted in Fig. 1. The geometry is axisymmetric and sketched on the (r,z) cutting plane. Ω_a denotes the fluid domain. Boundary notations correspond to different types of boundary conditions, as defined in the following.

Differential equations governing acoustics in Ω_a have already been given by Eq. (2.1). An $e^{-i\omega t}$ harmonic regime is assumed. The mean flow is supposed to be stationary. Two kinds of boundary conditions may be defined: a prescribed displacement condition and an absorbing wall condition. The former may be imposed at both the inlet and the outlet. These conditions are, respectively, given by

$$\mathbf{w}=\overline{\mathbf{w}} \quad \text{on } \Gamma_w, \tag{3.1}$$

$$\mathbf{w}\cdot\mathbf{n}=-\frac{1}{i\omega Z}p \quad \text{on } \Gamma_i. \tag{3.2}$$

Note that the above impedance condition is based on the normal Lagrangian displacement continuity.[8] For a perfectly rigid wall, i.e., $Z\to\infty$, Eq. (3.2) reduces to $\mathbf{w}\cdot\mathbf{n}=0$.

It must be emphasized that a prescribed outlet displacement implies that we already know the solution at the outlet, which is not very satisfying from a physical point of view. Indeed, as explained in Sec. IV, a modal decomposition will be preferred at the duct outlet in order to simulate a multimodal nonreflecting boundary condition.

B. Variational formulation

Though a purely displacement formulation can be derived from Eq. (2.1) (see for instance Ref. 10 or 23), a mixed pressure-displacement variational formulation is preferred in order to avoid spurious numerical solutions, known in the literature as a ''locking'' phenomenon.[24]

The equations in (2.1) are, respectively, multiplied by two trial fields, $\mathbf{w}^*$ and p^*, and integrated over Ω_a. Integrating by parts and applying boundary conditions (3.1) and (3.2) yields the following variational problem, which consists in solving the acoustic variables $\{\mathbf{w},p\}$ verifying $\{\mathbf{w}|_{\Gamma_w}=\overline{\mathbf{w}}\}$ and

$$\begin{aligned}
&-\int_{\Omega_a}\frac{1}{DC^2}p^*p\,dV+\int_{\Omega_a}\nabla p^*\cdot\mathbf{w}\,dV+\int_{\Omega_a}\mathbf{w}^*\cdot\nabla p\,dV-\omega^2\\
&\times\int_{\Omega_a}D\mathbf{w}^*\cdot\mathbf{w}\,dV-i\omega\int_{\Omega_a}D\mathbf{w}^*\cdot(\mathbf{V}\cdot\nabla\mathbf{w})dV+i\omega\\
&\times\int_{\Omega_a}D(\mathbf{V}\cdot\nabla\mathbf{w}^*)\cdot\mathbf{w}\,dV-\int_{\Omega_a}D(\mathbf{V}\cdot\nabla\mathbf{w}^*)\cdot(\mathbf{V}\cdot\nabla\mathbf{w})dV\\
&+\int_{\Omega_a}(\mathbf{w}^*\cdot\nabla P)(\nabla\cdot\mathbf{w})dV-\int_{\Omega_a}\mathbf{w}^*\cdot({}^T\nabla\mathbf{w}\cdot\nabla P)dV\\
&-\int_{\Gamma_w}p^*(\mathbf{w}\cdot\mathbf{n})dS+\frac{1}{i\omega}\int_{\Gamma_i}\frac{1}{Z}p^*p\,dS=0,\\
&\forall\mathbf{w}^*,p^*/\{\mathbf{w}^*|_{\Gamma_w}=0\}.
\end{aligned} \tag{3.3}$$

The four first terms represent the no-flow acoustic operators, the three following terms give the additional operators when flow is present. The last line is a boundary integral, on which boundary conditions are imposed. Note that impermeable walls have been assumed so that $\mathbf{V}\cdot\mathbf{n}=0$ on Γ_i.

The third line corresponds to operators that have to be included when the mean pressure is not spatially constant. For simplicity, those operators were not considered in previous papers[10,18] because they do not *a priori* represent any difficulty from a numerical point of view. In this paper, results tend to prove that this statement is actually true. Unlike Refs. 18 and 19, it is important to note that no assumption is made here for the mean flow (except its stationarity), so that formulation (3.3) is quite general and, in particular, takes into account compressibility effects of the mean flow. Thus, mean density, sound celerity, pressure, and velocity can arbitrarily vary inside the duct.

C. Finite element discretization

The geometry is assumed to be axisymmetric. Without loss of generality, fluctuating variables can be rewritten in the following form:

$$(\mathbf{w},p)(r,\theta,z,t)=(\mathbf{w},p)(r,z)e^{i(m\theta-\omega t)}. \tag{3.4}$$

Trial functions are given by

$$(\mathbf{w}^*,p^*)(r,\theta,z,t)=(\mathbf{w}^*,p^*)(r,z)e^{-i(m\theta-\omega t)}. \tag{3.5}$$

In order to avoid locking and spurious solutions, interpolations for displacement and pressure variables must also be adequately chosen. Though not necessary, a criterion that ensures convergence and stability of the finite element is given by the inf-sup condition, well known for incompressible media (see for instance Ref. 24). This kind of finite element has already been successfully applied to the variational formulation (3.3) in the constant P case, when testing the effect of shear flows.[18,19]

The element chosen in this paper, referred to as the "$P_1^+-P_1$," "4/3c" or "MINI" element in the literature, is a three-node triangle with an internal degree of freedom for each component of the displacement. Its interpolating functions are, on the reference element:

$$\mathbf{w}(u,\nu)=(1-u-\nu)\mathbf{w}_1+u\mathbf{w}_2+\nu\mathbf{w}_3+(1-u-\nu)u\,\nu\mathbf{a},$$
$$p(u,\nu)=(1-u-\nu)p_1+up_2+\nu p_3, \tag{3.6}$$

where the subscripts i ($i=1,2,3$) denote node number. **a** is a generalized variable corresponding to an internal degree of freedom, which can be condensed out before the elements are assembled. As a side remark, the overall method presented in this paper is easily applicable to the three-dimensional case because elements satisfying the inf-sup condition also exists in three dimensions.[24]

After assembling and applying boundary conditions, the global discretized variational formulation yields an algebraic system of the $\mathbf{Ku}=\mathbf{f}$ form, where **u** contains all the acoustic nodal unknowns (displacement and pressure). The matrix **K** is ω dependent, unsymmetrical, complex and band. A sparse storage is chosen. For a fixed ω, the unknown nodal vector **u** is finally obtained by using a LU decomposition.

IV. RESULTS

In the following, both MS and FEM models are compared. Acoustic computations are made for perfectly rigid and lined ducts, in the presence of compressible flows with swirl.

A. Preliminary remarks

Boundary conditions used for FEM calculations are shown in Fig. 1. At the duct inlet (from an acoustical point of view), Lagrangian displacement calculated from the MS solution is prescribed. In the following, the acoustic inlet will always be at the top section $z=2$ m. At the outlet ($z=0$ m), a multimodal decomposition technique is used. This technique consists in recasting the nodal acoustic variables located at the duct outlet via an eigenmode expansion (see, for example, Refs. 25 and 26). This technique was also satisfyingly used in Refs. 18 to simulate a multimodal nonreflecting boundary condition, with nonswirling flows. Here, the method is extended to swirling flows. In this paper, five radial modes have been used for the decomposition, which is far enough given that higher order modes are strongly cut-off for the considered test cases (it must be noted that no azimuthal decomposition is needed because m is a fixed parameter in the axisymmetric FEM code).

The reason why a multimodal nonreflecting condition is used at the outlet comes from reflection and scattering into other modes that may occur when the launched mode propagates along the duct. The FEM model naturally includes any reflection and scattering. This is not the case for the MS model, which implicitly assumes a one-way propagating mode, neglecting reflection and scattering.[18,25] Thus, forcing the Lagrangian displacement (calculated from the MS model) at the outlet too would not be very satisfying from a physical point of view, nor would be a monomodal nonreflecting condition.

However, applying a modal decomposition technique raises the problem of mode orthogonality and completeness. For nonswirling flows, modes are orthogonal if the axial mean flow is uniform at the duct section being considered (as well as mean density, celerity, and pressure). For swirling flows, as shown in Appendix, the flow must also be in rigid-body rotation. For our purpose, this means that the mean flow at the outlet must be uniform in its axial direction, in rigid-body rotation and that density, celerity, and pressure remains also constant.

Consequently, mean flows considered in this paper are restricted to this particular form at the outlet. They are calculated from the aerodynamic MS model of Cooper and Peake.[6] This model provides aerodynamic solutions for slowly varying ducts in the fully compressible case with the assumption of homentropy (yet, we recall that the acoustic MS model proposed in this paper remains valid even for nonhomentropic mean flows). Solutions have the particularity to be nearly uniform at the computing starting point, here at the outlet $z=0$ m, and hence to satisfy all the requiring conditions needed to use the above-mentioned nonreflecting condition. To be quantitatively more precise, for results presented in the following, mean flow density, celerity, and pressure vary up to 5% from their respective mean at the outlet. Variations of the axial velocity and rotation are almost of 0%. Then, the MS model yields acoustic modes which axial wave numbers have a 4% maximum difference from the uniform flow case, with quasi-identical pressure profiles.

Inputs of Cooper and Peake's aerodynamic MS model are the outlet axial Mach number $M_0=V_z/C^*$ and the outlet azimuthal Mach number defined as $\Omega_0=V_\theta L^*/rC^*$, where C^* and L^* denote, respectively, the characteristic sound speed and length. In this paper, $C^*=340\,\mathrm{m\,s^{-1}}$ and $L^*=1$ m. In all test cases given in the following, the computed density D remains about $1.2\,\mathrm{kg\,m^{-3}}$ throughout the fluid, C and P are about $340\,\mathrm{m\,s^{-1}}$ and 10^5 Pa.

The geometry considered is the same as in Ref. 6. This is a slowly varying duct, contracting or expanding, defined by its inner and outer radii as

$$R_1(z)=0.5482\pm 0.05\tanh(2z-2),$$
$$R_2(z)=1.1518\mp 0.05\tanh(2z-2). \tag{4.1}$$

In the following, iso-pressure contours are given in Pa in order not to minimize errors. Propagation and axial flow directions are also sketched in order to explicitly show if wave propagation is upstream or downstream. Test cases sweep a nondimensional frequency range up to about $kL^*=30$ and the duct geometry is generally meshed with a $\lambda/10$ finite element length. Figure 2 exhibits two examples of $\lambda/10$ meshes used in this paper.

B. Comparison for perfectly rigid ducts

The first example is that of a $(-5,1)$ mode propagating in a perfectly rigid and expanding duct with $M_0=-0.21$ and $\Omega_0=+0.30$ at the outlet ($z=0$). A negative product $m\Omega_0$ means that the mode is counter-rotating. Figure 3 depicts all mean flow variables but radial velocity, which is negligible and not needed for acoustic MS solutions. At $z=0$ m, it can be observed that the axial velocity is uniform and that the azimuthal velocity profile varies linearly, indicating a rigid-body rotation. Besides, density, celerity, and pressure vary slowly. Thus, at $z=0$, a modal decomposition can be accurately made. At the inlet $z=2$ m (from the acoustical point of

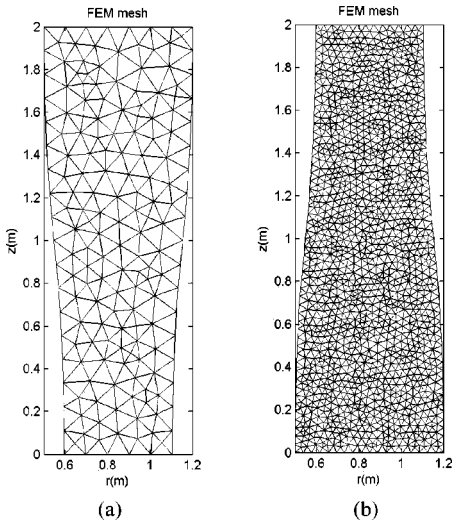

FIG. 2. λ/10 FEM meshes for a duct: (a) slowly contracting at $f=300$ Hz, (b) slowly expanding at $f=850$ Hz.

view), the mean flow is not uniform anymore, cross-sectional means of M_0 and Ω_0 are -0.30 and $+0.30$, respectively.

Figure 4 shows the acoustic results for both models and for $f=350$, 500, and 650 Hz. A good agreement is found for every frequency. In particular, the $(-5,1)$ mode is strongly attenuated at $f=350$ Hz, indicating a cut-off. Cut-off frequencies can be approximated by the analytical expression (A8) valid in the uniform case (if not uniform, the flow has then to be averaged at each section). This expression gives a local cut-off frequency of 361 and 391 Hz at $z=0$ and 2 m, respectively, which confirms that the mode is evanescent throughout the duct (no turning point occurs).

Small discrepancies can be observed in Fig. 4(e) near the modal pressure node (at $r\simeq 1.0$ m). As shown in Fig. 5, they almost disappear when the mesh is refined (λ/10 and λ/20 meshes have been used for Figs. 4(e) and 5, respectively). In the remainder of this paper, analyses of convergence of the FEM implementation will not be pursued and are left for further studies. However, mesh refinements have been done for every test case of the present paper (though not shown for conciseness) in order to determine if the differences observed between solutions are physical or numerical. FEM results presented in this paper are given with a sufficiently small meshing (generally a λ/10 mesh), which prevents discrepancies due to a convergence lack and truly enables a physical interpretation.

The second test case concerns a $(+20,0)$ mode propagating in a contracting duct at $f=1250$, 1500, and 1750 Hz (see Fig. 6). At $z=0$, the flow is nearly uniform, with $M_0=+0.30$ and $\Omega_0=+0.30$ (at $z=2$ m, their means are, respectively, $+0.21$ and $+0.30$). For conciseness, mean flow variables are not depicted anymore in the following.

Both models converge in a satisfying way. A very slight difference may be seen at 1750 Hz, which can be explained by some little reflections occurring inside the duct (not taken into account by the MS model). As previously, the mode being considered is cut-off for the lowest frequency $f=1250$ Hz. The analytical cut-off frequency goes from 1304 Hz at $z=2$ m to 1367 Hz at $z=0$ m, which confirms the evanescence observed.

Figure 7 shows the axial time-averaged intensity for the three frequencies. The time-averaged intensity is postprocessed from the FEM solution, and explicitly given by

$$\overline{\mathbf{i}}=-\frac{\omega}{2}\mathrm{Im}\left\{(p-\mathbf{w}\cdot\nabla P)\mathbf{w}^*+D\left(\frac{d\mathbf{w}}{dt}\cdot\mathbf{w}^*\right)\mathbf{V}\right\}. \qquad (4.2)$$

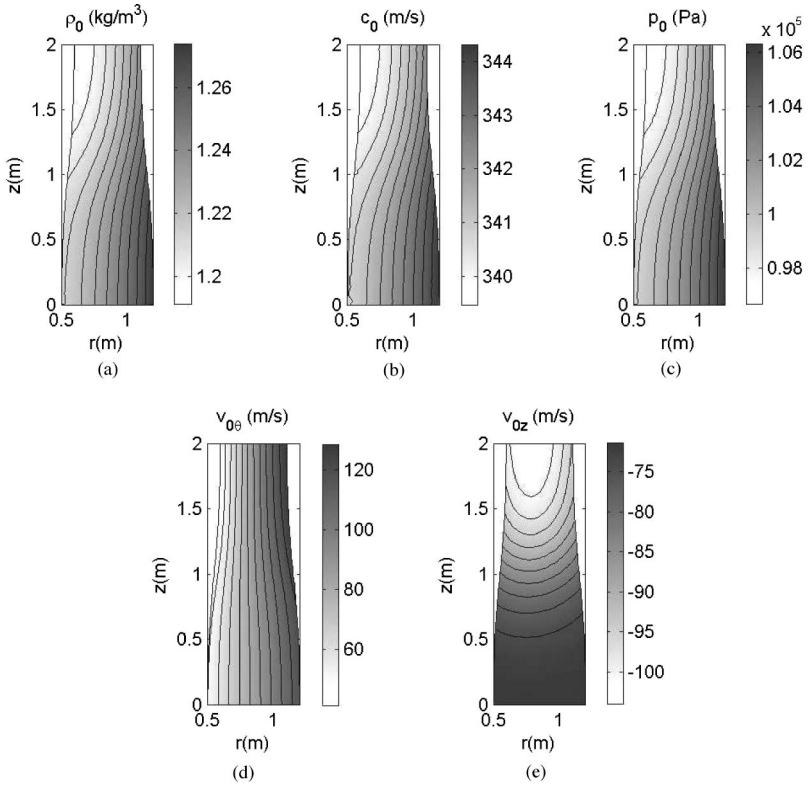

FIG. 3. Mean flow variables calculated from the aerodynamic MS model of Cooper and Peake, with $M_0=-0.21$ and $\Omega_0=+0.30$ at the acoustic outlet ($z=0$ section): (a) density, (b) celerity, (c) pressure, (d) azimuthal velocity, and (e) axial velocity.

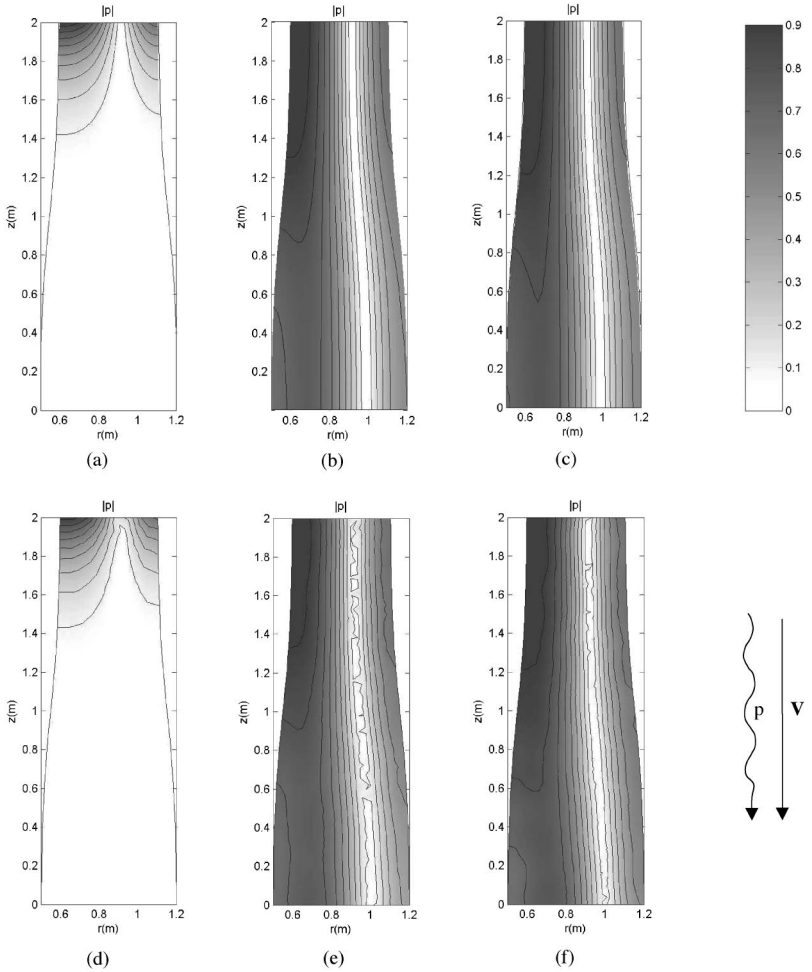

FIG. 4. Pressure modulus in Pa of the $(-5,1)$ mode launched in an expanding rigid-wall duct, with $M_0=-0.21$ and $\Omega_0=+0.30$ at the acoustic outlet ($z=0$ m): (a), (b), (c) MS solutions for $f=350$, 500, and 650 Hz, respectively, (d)–(f) FEM solutions.

In Eq. (4.2), $\mathbf{w}^*$ denotes the complex conjugate of $\mathbf{w}$ and must not be confused with the trial field of Eq. (3.3). Equation (4.2) derives from the intensity expression obtained from Galbrun's equation in Refs. 8 and 10. This expression is exact and quite general (but not unique).

The cut-off occurring at 1250 Hz is well characterized by a negligible axial intensity compared to the two other frequencies. Note that this intensity is not equal to zero (but strongly decreases from the inlet) because, when flow is present, cut-off modes have a small propagative part (the axial wave number is not purely imaginary). Besides, as expected, axial intensity is slightly increased from 1500 to 1750 Hz, because of the axial wave number increase with frequency.

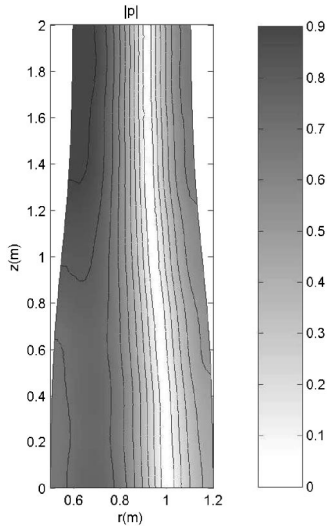

FIG. 5. Pressure modulus in Pa of the $(-5,1)$ mode at $f=500$ Hz (rigid-wall duct, with $M_0=-0.21$ and $\Omega_0=+0.30$). FEM solution with mesh refinement.

It must be noted that, without swirl, the mode would be completely cut-on, even at 1250 Hz (analytical cut-off frequency would be of about 1000 Hz): what is seen at $f=1250$ Hz is one of the swirl effects, which increases cut-off frequencies for co-rotating modes (i.e., with positive product $m\Omega_0$). This effect is thus correctly included in both MS and FEM models.

C. Comparison for lined ducts

In this section, lined ducts are considered. In the presence of treatment at walls, modes are not orthogonal in the usual sense, which may affect the efficiency of the nonreflecting boundary condition. The duct must then be perfectly rigid at the outlet $z=0$. However, in fact, the transition from impedance to rigid wall can be initiated at an arbitrarily small distance from the outlet, as stated in Ref. 25.

The third example gives a comparison for the $(\pm 3,0)$ modes propagating at $f=200$ and 300 Hz, inside a contract-

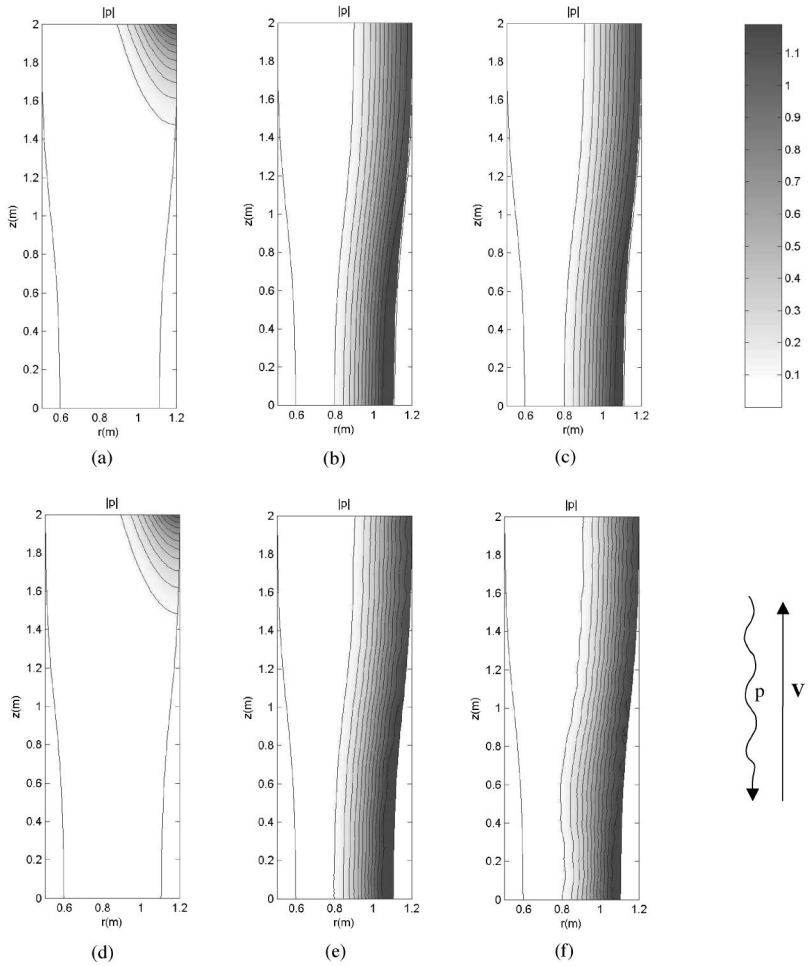

FIG. 6. Pressure modulus in Pa of the (+20,0) mode launched in a contracting rigid-wall duct, with $M_0=+0.30$ and $\Omega_0=+0.30$ at the acoustic outlet ($z=0$ m): (a), (b), (c) MS solutions for $f=1250$, 1500, and 1750 Hz respectively, (d), (e), (f) FEM solutions.

ing duct, with $M_0=+0.52$ and $\Omega_0=+0.20$ at $z=0$ m (at $z=2$ m, averaged M_0 and Ω_0 are, respectively, $+0.35$ and $+0.20$). Walls are lined with impedances $Z_1=Z_2=408-408i$. As shown in Fig. 8, the agreement between both models is very good for every case. In particular, axial attenuation satisfyingly converges (at 300 Hz and for $m=-3$, the FEM model gives a very little smaller attenuation, probably due to some reflection inside the duct). This attenuation, denoted by μ in dB, can be explicitly computed with the following definition:

$$\mu=10\log_{10}\left(\int_{R_1(0)}^{R_1(0)}|p(r,z=0)|^2 r\,dr \Big/ \int_{R_1(L)}^{R_1(L)}|p(r,z=L)|^2 r\,dr\right). \tag{4.3}$$

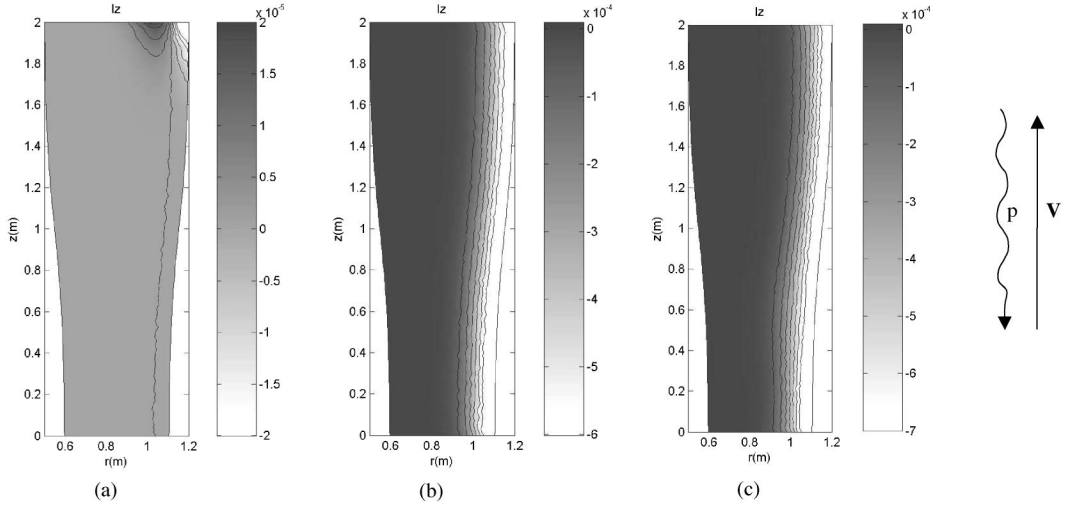

FIG. 7. Axial intensity in W/m^2 (postprocessed from FEM solutions) of the (+20,0) mode at: (a) $f=1250$ Hz, (b) $f=1500$ Hz; (c) $f=1750$ Hz.

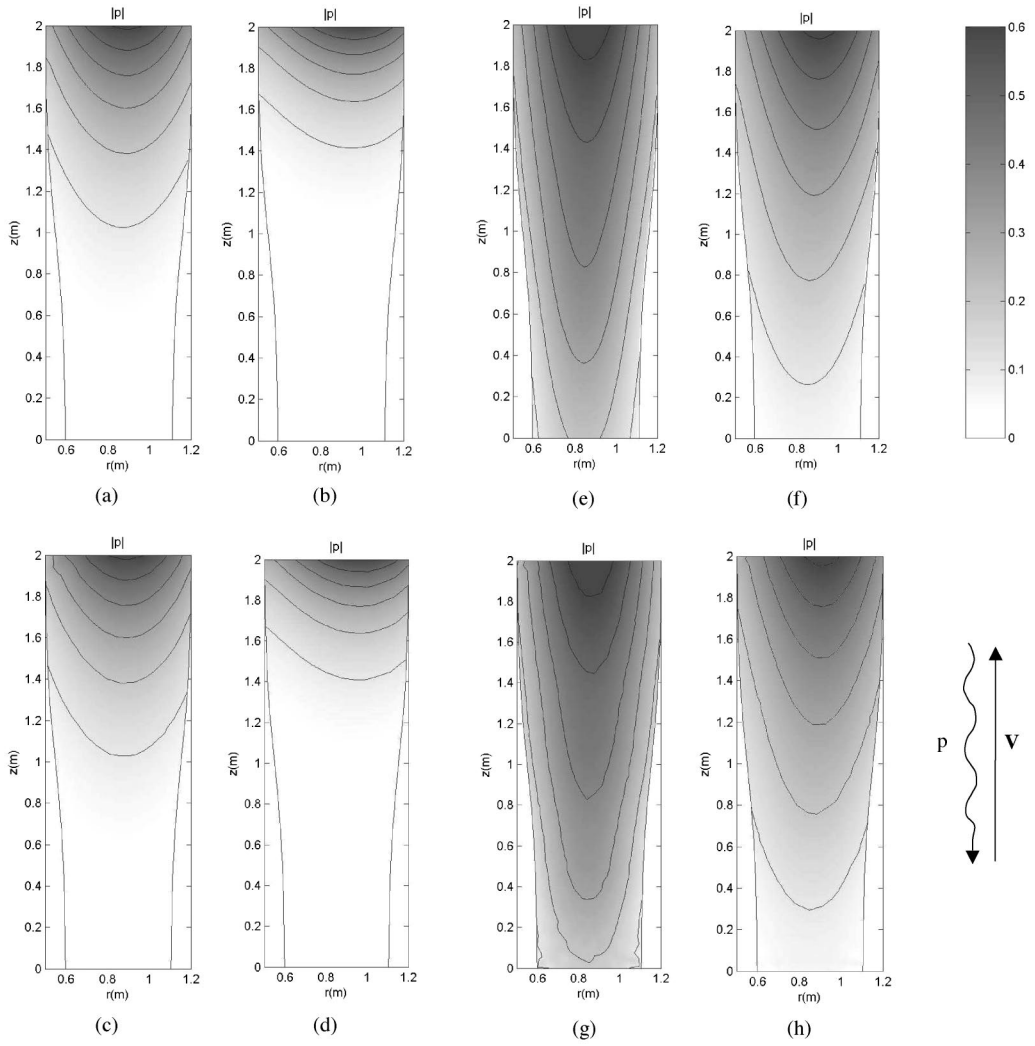

FIG. 8. Pressure modulus in Pa of the $(\pm 3,0)$ mode launched in a contracting lined duct ($Z_1 = Z_2 = 408 - 408i$), with $M_0 = +0.52$ and $\Omega_0 = +0.20$ at the acoustic outlet ($z = 0$ m): (a), (b) MS solutions at 200 Hz for $m = -3$ and $m = +3$, (c), (d) respective FEM solutions, (e), (f) MS solutions at 300 Hz for $m = -3$ and $m = +3$, (g), (h) respective FEM solutions.

At 200 Hz, the attenuation is about 40 and 60 dB for $m = -3$ and $m = +3$, respectively. At 300 Hz, it decreases to about 10 and 20 dB. Those results confirm the general trend found by Cooper and Peake,[6] indicating that co-rotating modes are always more damped than counter-rotating ones. This difference in damping may be important, as shown by the presented results. It becomes lower as frequency increases, going further and further from cut-off (cut-off frequencies for counter- and co-rotating modes are about 130 and 195 Hz, respectively).

Figure 9 exhibits the last test case: a $(\pm 10,1)$ mode propagating in a lined expanding duct at 850 Hz. Flow parameters at $z = 0$ m are given by $M_0 = -0.35$ and $\Omega_0 = +0.2$ (this yields averages of -0.52 and $+0.2$ at $z = 2$ m). Wall impedances are $Z_1 = Z_2 = 1020 - 1020i$. In order to explicitly show the effect of swirl, Fig. 9 gives a comparison between the three following modes: $m = -10$ (with swirl), $m = 10$ without swirl, $m = +10$ (with swirl). Note that without swirl, the sign of m has no consequence upon the solution, and that the MS solution corresponds to Rienstra's solution[13] (mean flow variables do not depend upon r and are uniform upon each section).

The convergence between both models is rather good but some wiggles can be observed for FEM solutions, which are probably due to reflection and/or scattering into other modes. As explained earlier, it has been verified that the differences between MS and FEM solutions are not mesh related (refinements may yield some smoother profiles but they do not modify the overall results presented in this paper). For $m = +10$, almost no wiggles appear because this mode is near its cut-off frequency (about 800 Hz): the axial wave number k_z is then lower, which makes the effect of geometry axial variations less important upon acoustic wave propagation (reflections are negligible).

This example shows the effect of the presence of swirl compared to the no swirl case. Attenuation equals about 6, 7, and 15 dB for $m = -10$, $m = 10$ without swirl, and $m = +10$, respectively. Here again, the conclusion agrees with Cooper and Peake's results.

Figure 10 depicts the axial intensity postprocessed from FEM solutions for the three modes. It can be observed that intensity is gradually decreased from $m = -10$ to $m = +10$. For $m = +10$, the axial intensity is very low because this mode is near its cut-off frequency (about 800 Hz), which is

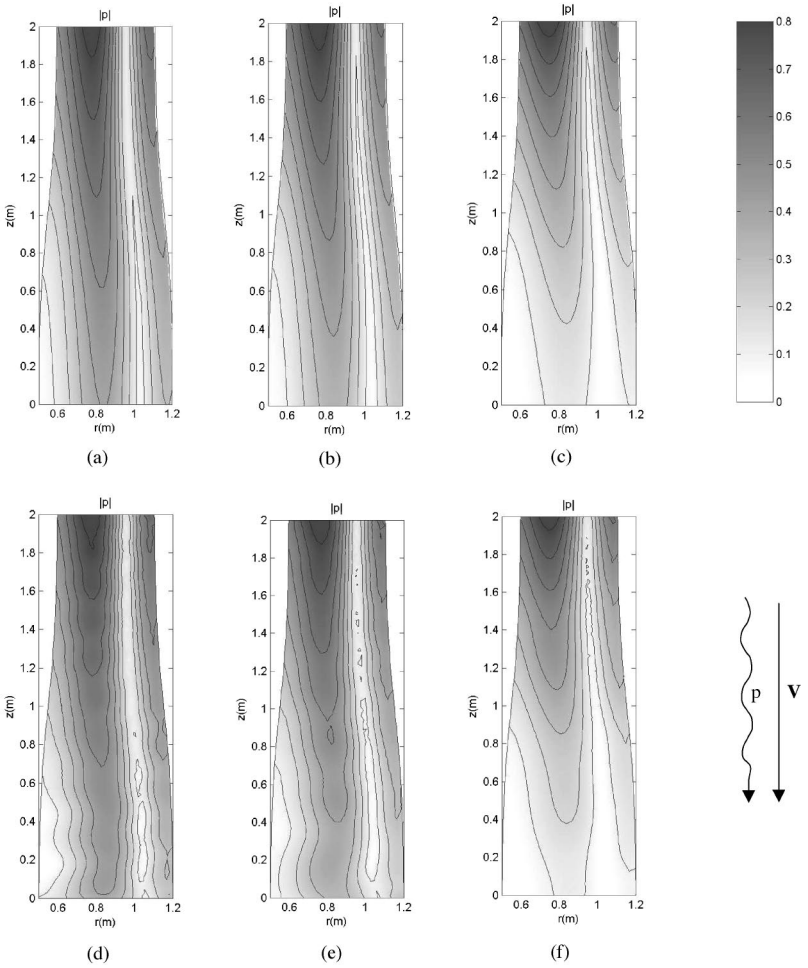

FIG. 9. Pressure modulus in Pa of the $(\pm 10,1)$ mode launched in an expanding lined duct ($Z_1 = Z_2 = 1020 - 1020i$) at 850 Hz, with $M_0 = -0.35$ and $\Omega_0 = +0.20$ at the acoustic outlet ($z = 0$ m): (a), (b), (c) MS solutions for $m = -10$, $m = 10$ with no swirl, and $m = +10$, respectively, (d), (e), (f) FEM solutions.

not the case of modes $m = -10$ and $m = 10$ without swirl (their respective cut-off occurs at about 570 and 690 Hz). Moreover, an enlargement of intensity vector is also given, which shows that it is not parallel to the wall, meaning that some energy is absorbed. Note that the vector penetrates more into the walls for $m = -10$. Those energy considerations are coherent with the fact that attenuation is higher (respectively lower) for co-rotating (respectively, counter-rotating) modes than in the no-swirl case.

V. CONCLUSION

In this paper, a MS method and a FEM have been proposed to study sound propagation in ducts with compressible

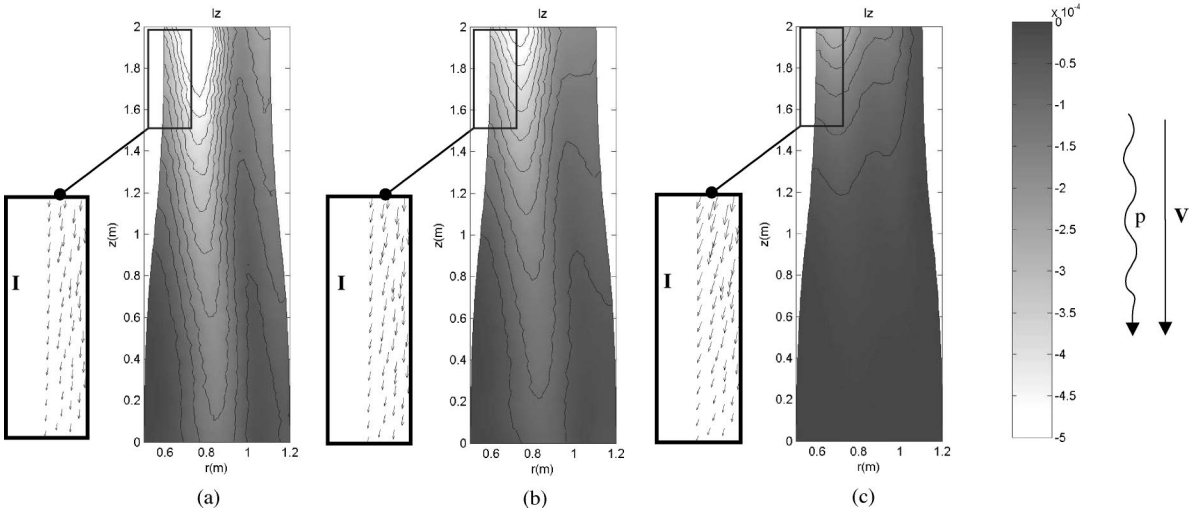

FIG. 10. Axial intensity in W/m^2 (computed from FEM solutions) of the $(\pm 10,1)$ mode at $f = 850$ Hz for: (a) $m = -10$, (b) $m = 10$ with no swirl, (c) $m = +10$. Enlargements of intensity vectors are also shown at walls.

and swirling flows. Both methods are based on Galbrun's equation, which provides some interesting aspects. Boundary conditions at lined walls have a simplified form, and exact expressions of intensity and energy are available. For the MS model, equations are easier to solve than those based on the standard linearized Euler equations. For the FEM model, a mixed pressure-displacement based formulation allows the direct application of the inf-sup condition, well known for incompressible media.

The MS method applies for slowly varying duct, whereas the FEM model is quite general. In order to validate both models, a comparison between MS and FEM solutions has been realized for a slowly varying duct, expanding or contracting. A good agreement has been found. Results presented in this paper show that both models are able to take into account the effects of swirl upon acoustic propagation, and that neglecting swirl in acoustics with flows may lead to significant errors. In particular, co-rotating (respectively, counter-rotating) modes are likely to be cut-off (respectively, cut-on) or, if the duct is lined, more (respectively, less) damped compared to the no-swirl case. The importance that those effects may have shows the limitations inherent to a full-potential formulation, which assumes that both acoustic and aerodynamic velocities are irrotational. This justifies the use of more general equations, such as the linearized Euler equations or Galbrun's equation.

However, concerning FEM computations, the nonreflecting boundary condition used in this paper assumes a uniform and rigid-body rotation flow at the outlet (or nearly). Because its efficiency may be affected by stronger flow nonuniformities, the proposed nonreflecting boundary condition would *a priori* need some adaptation in order to be applied to any kind of flows.

APPENDIX: LOCAL EIGENPROBLEM

System (2.14) can be reduced to a single differential equation written in terms of p_0. From the second equation of (2.14), the radial displacement is

$$w_{r_0}=\frac{\alpha\dfrac{\partial p_0}{\partial r}-\beta\dfrac{\partial P_0}{\partial r}p_0}{\alpha^2-\beta\left(\dfrac{\partial P_0}{\partial r}\right)^2}. \tag{A1}$$

After some tedious calculations, replacing the radial displacement into the first equation of Eq. (2.14) leads to the following single differential equation for p_0:

$$\frac{\partial^2 p_0}{\partial r^2}+\left\{\frac{1}{r}+\frac{-\alpha\alpha'+(\beta'+2\beta P_0'-\alpha'\beta/\alpha)P_0'^2}{\alpha^2-\beta P_0'^2}\right\}\frac{\partial p_0}{\partial r}+\left\{\left(\frac{\alpha}{D_0C_0^2}-\beta\right)\left(1-\frac{\beta}{\alpha^2}P_0'^2\right)+\frac{(2\alpha'\beta-\alpha\beta')P_0'-\alpha\beta(rP_0')'/r-(\alpha^2\beta-\beta^2P_0'^2+\alpha\beta r(P_0'/r)')\beta P_0'^2/\alpha^2}{\alpha^2-\beta P_0'^2}\right\}p_0=0, \tag{A2}$$

where primes refer to first and second partial derivatives (with respect to r) of the equation coefficients. Boundary condition (2.15) has also to be expressed in terms of p_0:

$$\frac{\partial p_0}{\partial r}=\mp\frac{i}{\omega Z_i\alpha}\{\alpha^2-\beta P_0'^2\pm i\omega Z_i\beta P_0'\}p_0 \quad \text{at } r=R_i \quad (i=1,2). \tag{A3}$$

In the specific case of a uniform flow defined by the fact that D_0, C_0, P_0, V_{z_0}, and V_{θ_0}/r do not depend upon r (i.e., uniform axial velocity and rigid-body rotation), Eq. (A2) reduces to

$$\frac{\partial^2 p_0}{\partial r^2}+\frac{1}{r}\frac{\partial p_0}{\partial r}+\left\{\frac{\Omega^2}{C_0^2}-\frac{m^2}{r^2}-k_z^2\right\}p_0=0, \tag{A4}$$

where Ω is now constant. Solutions of Eq. (A4) are thus a combination of Bessel's functions:

$$p_{0_{mn}}(r)=AJ_m(k_{r_{mn}}r)+BY_m(k_{r_{mn}}r), \tag{A5}$$

where the radial wave number is given by the dispersion equation:

$$k_{r_{mn}}^2=\Omega^2/C_0^2-k_{z_{mn}}^2. \tag{A6}$$

As for the no-flow case, the (m,n) modes are orthogonal when walls are perfectly rigid.

Furthermore, it can be shown from Eq. (A6) that

$$k_{z_{mn}}^{\pm}=\frac{-M_0(k-mk_0)\pm\sqrt{(k-mk_0)^2-(1-M_0^2)k_{r_{mn}}^2}}{1-M_0^2}, \tag{A7}$$

where $k=\omega/C_0$, $M_0=V_{z_0}/C_0$, and $k_0=V_{\theta_0}/rC_0$. This relation is the same that in Kerrebrock's analysis.[1] Cut-off frequencies of the (m,n) mode correspond to the value of k for which term inside the square root vanishes (when perfectly rigid walls are considered). After some calculations, this leads to

$$f_{c_{mn}}=\sqrt{1-M_0^2}\,f_{0_{mn}}+\frac{m\omega_0}{2\pi}, \tag{A8}$$

where $\omega_0=V_{\theta_0}/r$. $f_{0_{mn}}=c_0k_{r_{mn}}/2\pi$ is the no-flow cut-off frequency. This relation shows that cut-off frequencies are modulated by a $\sqrt{1-M_0^2}$ factor (for any direction of the axial flow) and incremented by $m\omega_0/2\pi$ (cut-off frequencies of counter-rotating modes are decreased, and vice-versa for co-rotating modes). This basic result is experienced in Sec. IV.

Assumptions used to obtain Eq. (A4) may not be realistic from the mean flow point of view, because the mean pressure gradient is directly related to the presence of swirl[27] (if swirl is present, then the mean pressure cannot be constant). Nevertheless, for acoustic computations, small mean pressure gradient may be neglected. Then, orthogonal properties of solution (A5) and Eq. (A8) may be very useful for acoustic computations and physical understanding, as proved in Sec. IV.

[1] J. L. Kerrebrock, ''Small disturbances in turbomachine annuli with swirl,'' Am. Inst. Aeronautics Astron. J. **15**, 794–803 (1977).
[2] M. Roger and H. Arbey, ''Champ de pression dans un conduit annulaire en présence d'un écoulement tournant de rotation solide'' (''Pressure field in a fluid in solid body rotation''), Rev. Acoust. **16**, 240–242 (1983).
[3] M. Roger and H. Arbey, ''Relation de dispersion des ondes de pression dans un écoulement tournant'' (''Dispersion relation of pressure waves in a swirling flow''), Acustica **59**, 95–101 (1985).
[4] V. Golubev and H. M. Atassi, ''Acoustic-vorticity waves in swirling flows,'' J. Sound Vib. **209**, 203–222 (1998).
[5] C. K. W. Tam and L. Auriault, ''The wave modes in ducted swirling flows,'' J. Fluid Mech. **371**, 1–20 (1998).
[6] J. Cooper and N. Peake, ''Propagation of unsteady disturbances in a slowly varying duct with mean swirling flow,'' J. Fluid Mech. **445**, 207–234 (2001).
[7] H. Galbrun, *Propagation d'Une Onde Sonore Dans l'Atmosphère et Théorie des Zones de Silence (Propagation of an Acoustic Wave in the Atmosphere and Theory of Zones of Silence)* (Gauthier-Villars, Paris, 1931).
[8] O. A. Godin, ''Reciprocity and energy theorems for waves in a compressible inhomogeneous moving fluid,'' Wave Motion **25**, 143–167 (1997).
[9] B. Poirée, ''Les équations de l'acoustique linéaire et non linéaire dans un écoulement de fluide parfait'' (''Equations of linear and non linear acoustics in a perfect fluid flow''), Acustica **57**, 5–25 (1985).
[10] C. Peyret and G. Elias, ''Finite-element method to study harmonic aeroacoustics problems,'' J. Acoust. Soc. Am. **110**, 661–668 (2001).
[11] M. K. Myers, ''On the acoustic boundary condition in the presence of flow,'' J. Sound Vib. **71**, 429–434 (1980).
[12] B. Poirée, ''Petites perturbations d'un écoulement tournant'' (''Small perturbations in a rotating flow''), Acustica **59**, 85–94 (1985).
[13] S. W. Rienstra, ''Sound transmission in slowly varying circular and annular lined ducts with flow,'' J. Fluid Mech. **380**, 279–296 (1999).
[14] L. Abrahamson, ''A finite element algorithm for sound propagation in axisymmetric ducts containing compressible mean flow,'' AIAA Fourth Aeroacoustics Conference, Atlanta, 1977.
[15] R. J. Astley and W. Eversman, ''Acoustic transmission in non-uniform ducts with mean flow. II. The finite element method,'' J. Sound Vib. **74**, 103–121 (1981).
[16] R. J. Astley and W. Eversman, ''A finite element formulation of the eigenvalue problem in lined ducts with flow,'' J. Sound Vib. **65**, 61–74 (1979).
[17] S. Bonnet-Ben Dhia, G. Legendre, and E. Luneville, ''Analyse mathématique de l'équation de Galbrun en écoulement uniforme'' (''Mathematical analysis of Galbrun's equation with uniform flow''), C. R. Acad. Sci., Ser. IIb: Mec., Phys., Chim., Astron. **329**, 601–606 (2001).
[18] F. Treyssède, G. Gabard, and M. Ben Tahar, ''A mixed finite element method for acoustic wave propagation in moving fluids based on an Eulerian-Lagrangian description,'' J. Acoust. Soc. Am. **113**, 705–716 (2003).
[19] G. Gabard, F. Treyssède, and M. Ben Tahar, ''A numerical method for vibro-acoustic problems with sheared mean flows,'' J. Sound Vib. (to be published).
[20] A. H. Nayfeh, *Introduction to Perturbation Techniques* (Wiley, New York, 1981).
[21] E. J. Hinch, *Perturbation Methods* (Cambridge University Press, New York, 1991).
[22] A. H. Nayfeh and D. P. Telionis, ''Acoustic propagation in ducts with varying cross sections,'' J. Acoust. Soc. Am. **54**, 1654–1661 (1973).
[23] M. Ben Tahar and E. Goy, ''Resolution of a vibroacoustic problem in the presence of a nonuniform mean flow,'' Fourth AIAA Joint Aeroacoustics Conference Paper No. 98-2215, 1998.
[24] K. J. Bathe, *Finite Element Procedures* (Prentice–Hall, Englewood Cliffs, NJ, 1996).
[25] S. W. Rienstra and W. Eversman, ''A numerical comparison between the multiple-scales and finite-element solution for sound propagation in lined flow ducts,'' J. Fluid Mech. **437**, 367–384 (2001).
[26] W. Eversman, ''A reverse flow theorem and acoustic reciprocity in compressible potential flows in ducts,'' J. Sound Vib. **246**, 71–95 (2001).
[27] G. K. Batchelor, *An Introduction To Fluid Dynamics* (Cambridge University Press, New York, 1967).

Elimination of internal resonance problem associated with acoustic scattering by three-dimensional rigid body

B. Chandrasekhar and Sadasiva M. Rao[a)]
Supercomputer Education and Research Centre, Indian Institute of Science, Bangalore-560 012, India

(Received 1 August 2003; revised 13 February 2004; accepted 17 February 2004)

In this work, a simple and stable numerical method is presented, utilizing the method of moments (MoM), to eliminate the internal resonance problem associated with acoustic scattering by three-dimensional rigid body subjected to a plane wave incidence. The numerical method is based on the potential theory and combines the single layer formulation (SLF) and the double layer formulation (DLF). The scattering body is approximated by planar triangular patches. For the MoM solution of SLF and DLF, the basis functions have been defined with respect to the edges to approximate the unknown source distribution. These basis functions along with an efficient testing procedure generate accurate results at all frequencies, including the characteristic frequencies. Finally, the new solution method is validated with several representative examples. © *2004 Acoustical Society of America.* [DOI: 10.1121/1.1703537]

PACS numbers: 43.20.Fn [LLT] Pages: 2731–2737

I. INTRODUCTION

Acoustic scattering from an arbitrary shaped rigid body, although a classical problem, received considerable attention recently owing to the developments in digital computer technology. There exist several numerical algorithms to solve the acoustic scattering problem, viz., (a) the T-matrix approach,[1–4] (b) the boundary integral equation method,[5–8] and (c) the method of moments (MoM).[9–14] Further, we note that, although all these formulations work well with varying degrees of complexity, one problem common to all these methods is the so-called internal resonance problem. The internal resonance problem refers to the nonuniqueness of the solution when the incident field frequency coincides with the resonance frequency of the cavity of the same shape as that of the scattering body. In fact, this problem is quite severe because of the following reasons.

(1) The numerical solution starts deteriorating in the vicinity of the characteristic frequency and it is difficult to estimate the accuracy of the given solution, even away from the resonance.

(2) These resonance frequencies occur more frequently as we extend the methods into the high-frequency regime, thereby making the method virtually useless.

Several remedies have been proposed to overcome this problem. Notable among them are the following (a) the Combined Helmholtz Integral Equation Formulation (CHIEF) procedure[15] and (b) the Burton and Miller (BM) procedure.[16] The CHIEF method, although very popular, is somewhat heuristic and prone to inaccuracies, especially at high frequencies. On the other hand, the BM solution is more elegant and mathematically guaranteed to be stable.

The BM procedure basically suggests developing two separate formulations, viz., (a) the Helmholtz formulation and (b) its normal derivative, also known as single and double layer formulations (SLF and DLF), respectively. The required integral equation is then obtained by combining them with an appropriate weighting parameter to generate a single equation. Burton and Miller proved mathematically that in the resulting equation, the breakdown phenomenon is completely eliminated.[16]

Several researchers have attempted to use the BM procedure[17–19] to overcome the internal resonance problem. Obviously, the main focus in these attempts is to solve the DLF, which is much more involved than the SLF. This is because the DLF procedure involves hypersingular kernels and an accurate numerical solution of such problems requires careful evaluation of the integrals involved. The usual procedure has been to regularize the kernel or to evaluate complex integrals, which, unfortunately, resulted in rather unattractive/complicated algorithms. At this stage we also note that, as far as our knowledge is concerned, all the numerical methods available are, in fact, node-based methods (i.e., the unknown quantities have been evaluated at the junction points of the basic elements in finite element/boundary element scheme) that compounded the problem.

In this work, we adopt the idea proposed in Ref. 16 and develop a simple numerical scheme based on the MoM. In the solution scheme, as reported earlier,[20] we utilize the edge-based basis functions to approximate the unknown quantities. Here we note that the DLF has been successfully implemented in Ref. 20, and in this work we report the evaluation of SLF and then combine both the SLF and the DLF to eliminate the internal resonance problem.

This paper is organized as follows.

In the next section, we describe the mathematical derivation of the SLF and the DLF. Since the DLF numerical solution is reported elsewhere,[20] we only mention the essential features here for the sake of completeness. Next, in Sec. III, we describe the edge-based numerical solution procedure of solving the SLF using MoM. In Sec. IV, we describe the procedure to combine the SLF and the DLF to obtain a combined layer formulation (CLF) that is free of an internal reso-

[a)]Corresponding Author: Sadasiva M. Rao, Supercomputer Education and Research Center, Indian Institute of Science, Bangalore—560 012, India. Electronic mail: smrao@serc.iisc.ernet.in; Telephone: 91-80-360 0086.

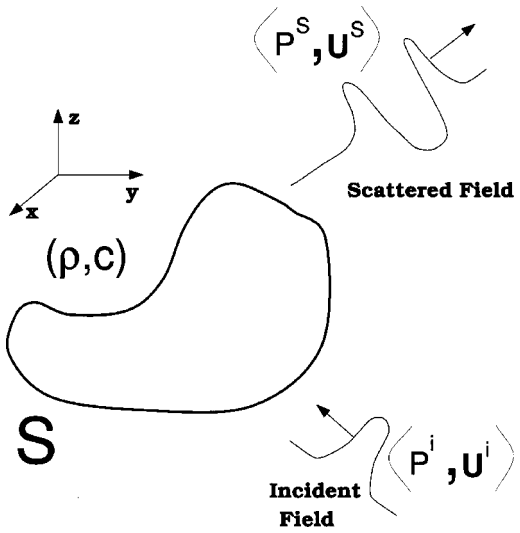

FIG. 1. Arbitrary body excited by an acoustic plane wave.

nance problem. Several representative examples are presented to illustrate the efficacy of the present approach in Sec. V. Last, in Sec. VI, we present some important conclusions drawn from this work.

II. SINGLE AND DOUBLE LAYER FORMULATIONS

Consider an arbitrarily shaped three-dimensional acoustically rigid body surrounded by an infinite, homogeneous, nonviscous medium, such as air, as shown schematically in Fig. 1. Let S represent the surface of the body, and ρ and c be the density and speed of sound in the surrounding medium, respectively. Let $(p^i,\mathbf{u}^i)$ and $(p^s,\mathbf{u}^s)$ represent the incident and scattered pressure and velocity fields, respectively. It is important to note that the incident fields are defined in the absence of the scatterer. It is customary to introduce a velocity potential Φ such that $\mathbf{u}=\nabla\Phi$ and $p=-j\omega\rho\Phi$, assuming a harmonic time variation.

Let σ represent the simple source distribution on the scatterer. Using the potential theory and the free space Green's function, the scattered velocity potential may be defined as

$$\Phi^s=\int_S \sigma(\mathbf{r}')G(\mathbf{r},\mathbf{r}')ds' \tag{1}$$

and

$$\Phi^s=\int_S \sigma(\mathbf{r}')\frac{\partial G(\mathbf{r},\mathbf{r}')}{\partial n'}ds', \tag{2}$$

for the SLF and the DLF, respectively. In Eqs. (1) and (2),

$$G(\mathbf{r},\mathbf{r}')=\frac{e^{-jkR}}{4\pi R}, \tag{3}$$

and

$$R=|\mathbf{r}-\mathbf{r}'|, \tag{4}$$

$\mathbf{r}'$, $\mathbf{r}$, and k represent the locations of the source point, the location of the observation point, and the wave number, respectively. Both $\mathbf{r}$ and $\mathbf{r}'$ are defined with respect to a global coordinate origin O. Also, note that in Eq. (2), $\partial/\partial n'$ represents the normal derivative with respect to the source point $\mathbf{r}'$. Noting that, at the surface of the hard scatterer, normal derivative of the total velocity potential, which is the sum of the incident and the scattered potentials must vanish, the SLF and the DLF integral equations may be derived, given by

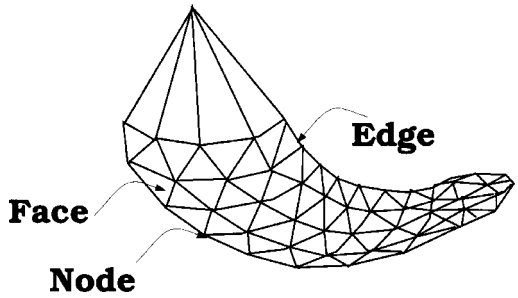

FIG. 2. Arbitrarily shaped closed body modeled by triangular patches.

$$\int_S \sigma(\mathbf{r}')\frac{\partial G(\mathbf{r},\mathbf{r}')}{\partial n}ds'=-\frac{\partial \Phi^i(\mathbf{r})}{\partial n}, \tag{5}$$

and

$$\frac{\partial}{\partial n}\int_S \sigma(\mathbf{r}')\frac{\partial G(\mathbf{r},\mathbf{r}')}{\partial n'}ds'=-\frac{\partial \Phi^i(\mathbf{r})}{\partial n}, \tag{6}$$

respectively. In Eqs. (5) and (6), $\partial/\partial n$ represents the normal derivative with respect to the observation point $\mathbf{r}$. Also, in Eqs. (5) and (6), Φ^i represents the incident velocity potential that is related to the incident pressure field p^i by the relation $p^i=-j\omega\rho\Phi^i$.

In the next section, we develop the numerical solution using edge-based basis functions to solve Eq. (5). As mentioned earlier, the details of the numerical solution of Eq. (6) are available in Ref. 20 and hence not included here.

It is important to note that the edge-based MoM solution procedure is *not* the most efficient algorithm in terms of computational resources, as compared to an earlier method, viz., the face-based solution.[9] However, it is difficult to extend the face-based solution procedure to solve the DLF.

III. NUMERICAL SOLUTION OF SLF

Let the given arbitrary body be represented by N_n nodes, N_e edges, and N_f triangular patches, as shown in Fig. 2. Here, we note that the SLF is valid for closed bodies only, and thus we have $N_n-N_e+N_f=2$.[21] We note that in the following solution scheme, the number of unknowns N, i.e., the dimension of the moment matrix, is equal to N_e. For the MoM solution procedure, we use the same basis functions, defined in Ref. 20 and included here for the sake of clarity, to represent the unknown source distribution σ.

Let T_n^+ and T_n^- represent two triangles connected to edge n of the triangulated surface model, as shown in Fig. 3. The plus or minus designation of the triangles is arbitrary and of no consequence in the numerical solution scheme. We define the basis function associated with the nth edge as

$$f_n(\mathbf{r})=\begin{cases}1, & \mathbf{r}\in S_n;\\ 0, & \text{otherwise};\end{cases} \tag{7}$$

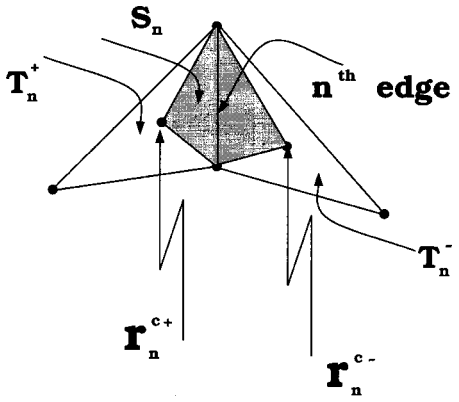

FIG. 3. Geometrical parameters associated with an interior edge.

where S_n represents the region obtained by connecting the centroids of triangles $T_n^{\pm}$, denoted by position vectors $\mathbf{r}_n^{c\pm}$, to the nodes of edge *n*. Note that this area is shown shaded in Fig. 3. Using these basis functions, the unknown source distribution σ may be approximated as

$$\sigma(\mathbf{r}) = \sum_{n=1}^{N} \alpha_n f_n(\mathbf{r}), \tag{8}$$

where α_n represents the unknown coefficient to be determined.

The next step in the MoM is to select a testing procedure. For the sake of simplicity, we select the testing functions as delta functions defined at the centroids of $S_n^{\pm}$, given by

$$f_n(\mathbf{r}) = \begin{cases} \delta(\mathbf{r}-\mathbf{r}_n^{c+}), & \mathbf{r}\in S_n^{+}; \\ \delta(\mathbf{r}-\mathbf{r}_n^{c-}), & \mathbf{r}\in S_n^{-}; \\ 0, \quad \text{otherwise}; \end{cases} \tag{9}$$

where $\mathbf{r}_n^{c\pm}$ represents the position vector to the centroid of region $S_n^{\pm}$. We note here that, since the testing of the integral equation is done at the centroid of $S_n^{\pm}$, which is always a flat region for the planar triangular patch modeling, the extraction of principal value term in Eq. (5) becomes trivial. Thus, we can rewrite Eq. (5) as

$$\frac{\sigma(\mathbf{r})}{2} - \int_S \sigma(\mathbf{r}') \frac{\partial G(\mathbf{r},\mathbf{r}')}{\partial n} ds' = -\frac{\partial \Phi^i(\mathbf{r})}{\partial n}, \tag{10}$$

where $\int_S$ represents the integration over the surface, excluding the principal value term, i.e., $\mathbf{r}=\mathbf{r}'$. Thus, we note that the $\int_S$ represents a well-behaved integral, although rapidly varying, which can be evaluated using standard integration algorithms, as explained in the following.

The testing procedure begins with defining the symmetric product as

$$\langle f_1, f_2 \rangle = \int_S f_1 f_2 \, ds, \tag{11}$$

where f_1 and f_2 are two scalar functions defined over a surface *S*. Thus, the testing equation may be written as

$$\left\langle f_m, \frac{\sigma}{2} \right\rangle - \left\langle f_m, \int_S \sigma(\mathbf{r}') \frac{\partial G(\mathbf{r},\mathbf{r}')}{\partial n} ds' \right\rangle = -\langle f_m, \mathbf{a}_n \cdot \nabla \Phi^i \rangle \tag{12}$$

where $\mathbf{a}_n$ represents the outward unit normal vector.

We observe that

$$\left\langle f_m, \frac{\sigma}{2} \right\rangle \approx \frac{1}{2}\left[\frac{A_m^+ \sigma(\mathbf{r}_m^{c+}) + A_m^- \sigma(\mathbf{r}_m^{c-})}{3}\right] \tag{13}$$

and

$$\begin{aligned} &\left\langle f_m, \int_S \sigma(\mathbf{r}') \frac{\partial G(\mathbf{r},\mathbf{r}')}{\partial n} ds' \right\rangle \\ &\quad \approx \int_S \int_S \sigma(\mathbf{r}') \frac{\partial G(\mathbf{r},\mathbf{r}')}{\partial n} ds' \, ds \\ &\quad = \frac{A_m^+}{3} \int_S \sigma(\mathbf{r}') \frac{\partial G(\mathbf{r}_m^{c+},\mathbf{r}')}{\partial n^+} ds' \\ &\qquad + \frac{A_m^-}{3} \int_S \sigma(\mathbf{r}') \frac{\partial G(\mathbf{r}_m^{c-},\mathbf{r}')}{\partial n^-} ds', \end{aligned} \tag{14}$$

where $A_m^{\pm}$ and $\mathbf{r}_m^{c\pm}$ represent the area and the position vector to the centroid of $S_m^{\pm}$ connected to the *m*th edge, respectively. We also note that the surface integration over the testing functions in Eqs. (13) and (14) is approximated by the integrand at the centroid of $S_m^{\pm}$ and multiplying by the area of the subdomain patch. This approximation is justified because the subdomains are sufficiently small, which is a necessary requirement to obtain an accurate solution using the MoM.

Next, using the same logic and assuming the incident field to be a slowly varying function, we approximate the right-hand side of Eq. (12) as

$$\begin{aligned} \langle f_m, \mathbf{a}_n \cdot \nabla \Phi^i \rangle &= \int_S f_m(\mathbf{r}) \mathbf{a}_n \cdot \nabla \Phi^i(\mathbf{r}) ds \\ &\approx \left(\frac{A_m^+}{3} \mathbf{a}_m^+ + \frac{A_m^-}{3} \mathbf{a}_m^- \right) \cdot \nabla \Phi^i(\mathbf{r}_m), \end{aligned} \tag{15}$$

where $\mathbf{r}_m$ and $\mathbf{a}_m^{\pm}$ represent the midpoint of the *m*th edge and the outward unit normal vector to $S_m^{\pm}$, respectively.

Thus, using Eqs. (13), (14), and (15), the testing equation may be written as

$$\begin{aligned} &\frac{1}{2}\left[\frac{A_m^+ \sigma(\mathbf{r}_m^{c+}) + A_m^- \sigma(\mathbf{r}_m^{c-})}{3}\right] \\ &\qquad - \frac{A_m^+}{3} \int_S \sigma(\mathbf{r}') \frac{\partial G(\mathbf{r}_m^{c+},\mathbf{r}')}{\partial n^+} ds' \\ &\qquad - \frac{A_m^-}{3} \int_S \sigma(\mathbf{r}') \frac{\partial G(\mathbf{r}_m^{c-},\mathbf{r}')}{\partial n^-} ds' \\ &\quad = -\left(\frac{A_m^+}{3} \mathbf{a}_m^+ + \frac{A_m^-}{3} \mathbf{a}_m^- \right) \cdot \nabla \Phi^i(\mathbf{r}_m), \end{aligned} \tag{16}$$

for $m = 1,2,...,N$.

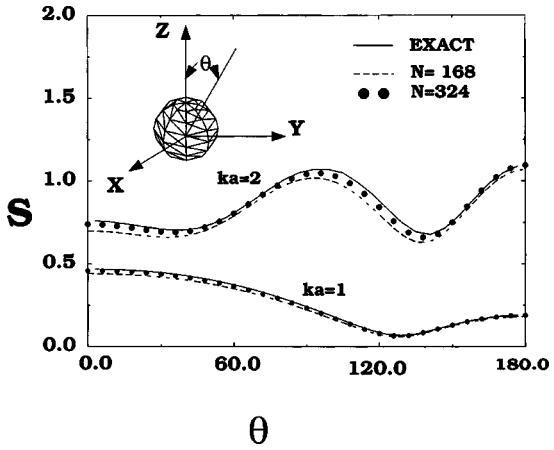

FIG. 4. Scattering cross section versus polar angle for an acoustically hard sphere subjected to an axially incident plane wave.

Substituting the source expansion Eq. (8) into Eq. (16) yields an $N\times N$ system of linear equations, which may be written in matrix form as

$$\mathbf{ZX}=\mathbf{Y}, \tag{17}$$

where $\mathbf{Z}=[Z_{mn}]$ is an $N\times N$ matrix and $\mathbf{X}=[\alpha_n]$ and $\mathbf{Y}=[Y_m]$ are column vectors of length N. Elements of $\mathbf{Z}$ and $\mathbf{Y}$ are given by

$$Z_{mn}=\begin{cases}\dfrac{1}{2}\left[\dfrac{A_m^+ + A_m^-}{3}\right]+G_{mm}^+ + G_{mm}^-, & m=n;\\ -\left[\dfrac{A_m^+ G_{mn}^+}{3}+\dfrac{A_m^- G_{mn}^-}{3}\right], & m\neq n;\end{cases} \tag{18}$$

$$Y_m=\left(\frac{A_m^+}{3}\mathbf{a}_m^+ + \frac{A_m^-}{3}\mathbf{a}_m^-\right)\cdot\nabla\Phi^i(\mathbf{r}_m), \tag{19}$$

where

$$G_{mn}^{\pm}=\int_{S_n^+}\frac{\partial G(\mathbf{r}_m^{c\pm},\mathbf{r}')}{\partial n^{\pm}}ds'+\int_{S_n^-}\frac{\partial G(\mathbf{r}_m^{c\pm},\mathbf{r}')}{\partial n^{\pm}}ds', \tag{20}$$

$$\frac{\partial G(\mathbf{r}_m^{c\pm},\mathbf{r}')}{\partial n^{\pm}}=(1+jkR_m^{c\pm})\frac{e^{-jkR_m^{c\pm}}}{4\pi R_m^{c\pm 3}}\mathbf{a}_{m^{\pm}}\cdot(\mathbf{r}_m^{c\pm}-\mathbf{r}'), \tag{21}$$

$$R_m^{c\pm}=|\mathbf{r}_m^{c\pm}-\mathbf{r}'|. \tag{22}$$

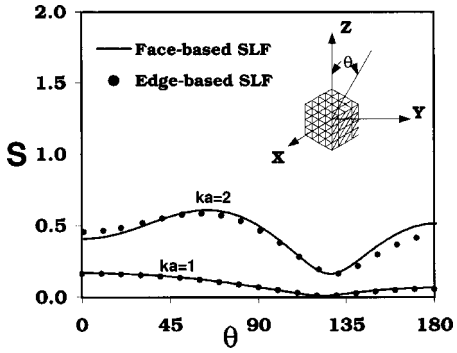

FIG. 5. Scattering cross section versus polar angle for an acoustically hard cube subjected to an axially incident plane wave.

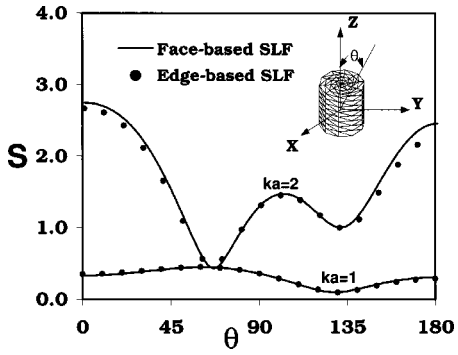

FIG. 6. Scattering cross section versus polar angle for an acoustically hard cylinder subjected to an axially incident plane wave.

Integrals appearing in Eq. (20) are straightforward integrals over a triangular region. Here we note that the integrals do not have singular kernels because of the extraction of the principal value term wherein the self-patch integral is deleted. Thus, $G_{mn}=0$ if both the mth-edge and the nth edge belong to the same planar triangle. However, the intgrand in Eq. (20) can vary rapidly and, hence, the integrals may be evaluated using the methods described in Refs. 22, 23 for an accurate solution.

For the plane wave incidence, we set

$$\Phi^i=e^{jk\mathbf{k}\cdot\mathbf{r}}, \tag{23}$$

where the propagation vector $\mathbf{k}$ is

$$\mathbf{k}=\sin\theta_0\cos\phi_0\mathbf{a}_x+\sin\theta_0\sin\phi_0\mathbf{a}_y+\cos\theta_0\mathbf{a}_z, \tag{24}$$

and (θ_0,ϕ_0) defines the angle of arrival of the plane wave in terms of the usual spherical coordinate convention.

Once the elements of the moment matrix $\mathbf{Z}$ and the forcing vector $\mathbf{Y}$ are determined, one may solve the resulting system of linear equations, Eq. (17), for the unknown column vector $\mathbf{X}$.

IV. COMBINED LAYER FORMULATION

In this section, we present the combined layer formulation (CLF) which is a general formulation applicable to both open and closed bodies. Further, as suggested in Ref. 16, the solution of CLF is also free of an interior resonance problem, as described in the following.

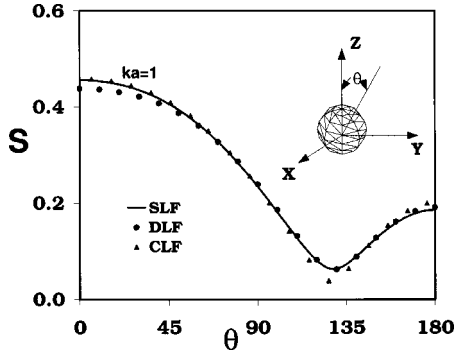

FIG. 7. A comparison of different formulations for the scattering cross section versus the polar angle for an acoustically hard sphere.

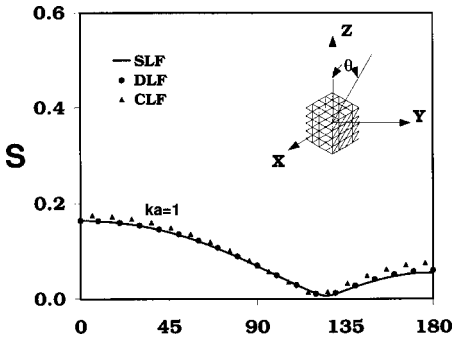

FIG. 8. A comparison of different formulations for the scattering cross section versus the polar angle for an acoustically hard cube.

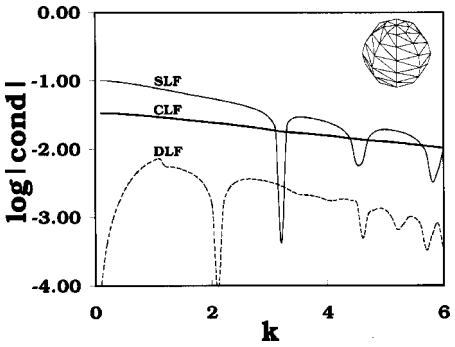

FIG. 10. A comparison of SLF, DLF, and CLF as a function of frequency for the scattering by a rigid sphere.

For the CLF case, let σ represent the simple source distribution on the scatterer. Using the potential theory and the free space Green's function, the scattered velocity potential may be defined as

$$\Phi^s = \int_S \sigma(\mathbf{r}') \left[G(\mathbf{r},\mathbf{r}') + \alpha \frac{\partial G(\mathbf{r},\mathbf{r}')}{\partial n'} \right] ds', \tag{25}$$

where α is a complex additive constant. Noting that, at the surface of the hard scatterer, the normal derivative of the total velocity potential, which is the sum of the incident and scattered potentials must vanish, the CLF integral equation may be derived, given by

$$\int_S \sigma(\mathbf{r}') \left[\frac{\partial G(\mathbf{r},\mathbf{r}')}{\partial n} + \alpha \frac{\partial}{\partial n} \frac{\partial G(\mathbf{r},\mathbf{r}')}{\partial n'} \right] ds' = - \frac{\partial \Phi^i(\mathbf{r})}{\partial n}. \tag{26}$$

From Eq. (26) we note that the integral equation is a combination of the SLF, discussed so far, and the DLF discussed in Ref. 20. Following the numerical procedures developed for these formulations, we can develop a numerical solution to the CLF by simply combining the matrices developed for the SLF and the DLF cases with an additive constant α. Further, numerical tests have shown that for a given surface mesh the best accuracy solutions are obtained by choosing $\alpha = 1/jk$, where k is the wave number.[24–26]

V. NUMERICAL RESULTS

In this section, numerical results are presented for several canonical shapes and compared with other solutions whereever possible. The numerical results are presented for the following cases: (i) To validate the edge-based SLF; (ii) To validate the edge-based CLF, and (iii) To check for the ill-conditioning of the moment matrix at characteristic frequencies for SLF and DLF methods and eliminate this problem using CLF.

For all these cases, we consider plane wave excitation.

A. Validation of the edge-based SLF

In this section, we validate the edge-based solution of SLF, discussed so far in this work, by comparing with the patch-based solution presented in Ref. 9. The geometries considered are a sphere, a cube, and a finite cylinder. For all cases, the body is placed at the center of the coordinate system and the plane wave is traveling along the Z axis with wave number $k=1$. In all cases the scattering cross section S is given by

$$S = 4\pi r^2 \left| \frac{\Phi^s}{\Phi^i} \right|^2. \tag{27}$$

Figure 4 shows the scattering cross section S as a function of the polar angle θ for a hard sphere, radius 1 m, excited by an incident plane wave traveling along the polar axis. The sphere is modeled by a coarse and a finer grid scheme having 112 and 216 patches, which results in a matrix size of 168 and 324, respectively. For comparison, we also present the exact solution. Here, we note that the numerical solution compares very well with the exact solution. Furthermore, the finer solution shows a better comparison than the coarser

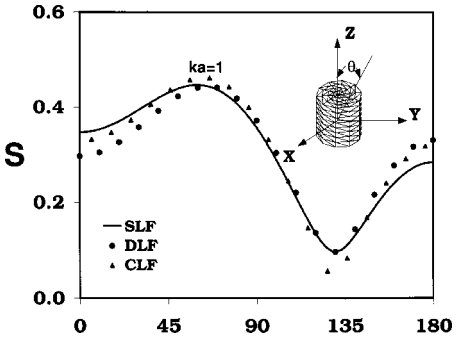

FIG. 9. A comparison of different formulations for the scattering cross section versus the polar angle for an acoustically hard cylinder.

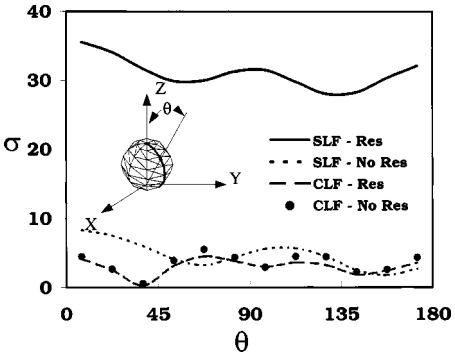

FIG. 11. The source distribution versus the polar angle for SLF and CLF for a sphere excited by an axially incident plane wave.

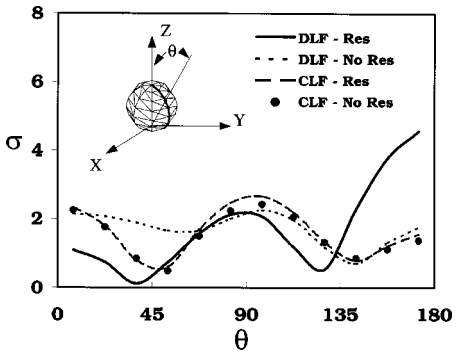

FIG. 12. The source distribution versus the polar angle for DLF and CLF for a sphere excited by an axially incident plane wave.

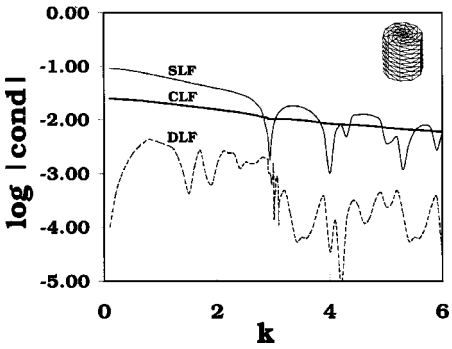

FIG. 14. A comparison of SLF, DLF, and CLF as a function of frequency for the scattering by a rigid cylinder.

scheme, indicating the convergence of the results to the exact solution.

Next, Fig. 5 shows the scattering cross section S as a function of θ for the case of a cube, length 1 m, placed such that the origin of the coordinate system coincides with the center of the cube. The cube is modeled by 96 square patches of equal area. By joining the diagonal of each square patch, the planar triangular patch model of the cube can be generated with 192 triangular patches and 288 edges. Once again, we notice an excellent comparison between edge-/patch-based results.

As a last example, we consider the case of a finite cylinder closed at both ends, radius 1 m and length 2 m, excited by an axially incident plane wave. The cylinder is modeled by 300 triangular patches and 450 edges. Figure 6 shows the scattering cross section S as a function of θ. For this case also, we note good comparison between edge-based SLF and patch-based SLF results.

B. Validation of edge-based CLF

In this section, we present the scattering cross section as a function of the polar angle θ using solutions for SLF, DLF, and CLF for several canonical shapes.

The rigid sphere, cube, and cylinder have been modeled using planar triangular patches, as shown in the inset of Figs. 4, 5, and 6, respectively, and excited by an axially incident plane wave. Figures 7–9 show the scattering cross section S as a function of θ for all the three formulations. For the CLF solution, we have set $\alpha = -j0.16$, although this value is not critical. From the figures, we notice that the CLF solution compares well with both SLF and DLF methods.

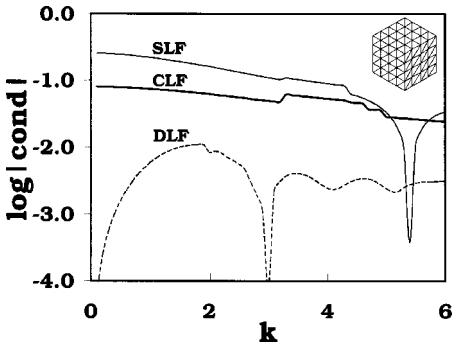

FIG. 13. A comparison of SLF, DLF, and CLF as a function of frequency for the scattering by a rigid cube.

C. Elimination of ill-conditioning problem

In this section, we present the numerical results to support the claim that the CLF method is free from the ill-conditioning problem. Here, we consider a sphere, a cube, and a cylinder, which are closed bodies, and check for the ill-conditioning problem at characterestic frequencies. We note that such a problem exists for both the SLF and the DLF methods.

Figure 10 shows the plot of the logarithm of the reciprocal of the condition number of the **Z** matrix versus wave number k for the case of a rigid sphere of radius 1 m excited by an axially incident plane wave. The sphere is modeled as in the previous example. It may be noted that the matrices for the SLF and the DLF cases become highly ill-conditioned at $k=3.1926$ and $k=2.1$, respectively. We note that the theoretical values, obtained as the roots of the spherical Bessel function for the Dirichlet and Neumann problems, are 3.14 and 2.08, respectively.[27] The slight difference in the numerical and theoratical values may be explained by noting that the triangulated sphere is, in reality, not an exact sphere. Obviously, when the body is excited by an incident field at these values, the numerical solution is erroneous, resulting in a large and unphysical solution, as demonstrated in Figs. 11 and 12. However, in both cases the CLF solution is stable and provides a reasonable solution.

In Fig. 11, we show the source distribution as a function of the polar angle θ for two cases, viz., $ka=2.9$ (nonresonant case) and 3.1926 (SLF resonance case). We note that, from Fig. 11 at $ka=3.1926$, the source distribution results in very large and unphysical values. Obviously, this suggests an erroneous solution. However, CLF algorithm generates reasonable and similar results for both values of ka.

Similarly, Fig. 12 represents the situation when the DLF algorithm generates erroneous results. Here, we select two frequencies, viz., $ka=1.99$ (nonresonance case) and $ka=2.1$ (resonance case). From the figure, it is evident that the DLF formulation exhibits widely different solutions at these two frequencies whereas the CLF generates very similar results.

Finally, we present the comparison of SLF, DLF, and CLF for two more cases, viz., a rigid cube of 1 m side length and a cylinder with radius 1 m and length 2 m, in Figs. 13

and 14, respectively. We note that for the case of a cube, the SLF and the DLF fail around $k=5.399$ and 2.99, respectively. In a similar way, for the case of a cylinder, the SLF and the DLF fail around $k=2.94$ and 4.2, respectively. However, the CLF solution exhibits smooth variation throughout the frequency range.

VI. CONCLUSIONS

In this work, we have presented a general method to obtain the scattered acoustic fields from an arbitrarily shaped body subjected to a plane wave incidence. Further, we have a presented a simple solution method to eliminate the troublesome internal resonance problem. The numerical solution is obtained via the method of moments solution procedure. The numerical solution of CLF is applicable to both open as well as closed bodies. Obviously, for open bodies the CLF is same as the DLF presented in Ref. 20. However, for the case of closed bodies, the CLF represents a combination both the DLF and the SLF. This combination is necessary in order to ensure a stable solution for all frequencies of the incident field. Last, work is in progress to apply the CLF formulation to a more complex fluid-body problem.

[1] *Acoustic, Electromagnetic and Elastic Wave Scattering-Focus on the T-Matrix Approach*, edited by V. K. Varadan and V. V. Varadan (Pergamon, New York, 1980).

[2] V. V. Varadan, A. Lakathia, and V. K. Varadan, ''Comments on recent criticism of the T-Matrix method,'' J. Acoust. Soc. Am. **84**, 2280–2284 (1988).

[3] W. Tobocman, ''Calculation of acoustic wave scattering by means of the Helmholtz integral equation I,'' J. Acoust. Soc. Am. **76**, 595–607 (1984).

[4] W. Tobocman, ''Calculation of acoustic wave scattering by means of the Helmholtz integral equation II,'' J. Acoust. Soc. Am. **76**, 1549–1554 (1984).

[5] G. T. Schuster and L. C. Smith, ''A comparison and four direct boundary integral methods,'' J. Acoust. Soc. Am. **77**, 850–864 (1985).

[6] G. T. Schuster, ''A hybrid BIE+Born series modeling scheme: Generalized Born series,'' J. Acoust. Soc. Am. **77**, 865–879 (1985).

[7] A. F. Seybert, B. Soenarko, F. J. Rizzo, and D. J. Shippy, ''An advanced computation method for radiation and scattering acoustic waves in three dimensions,'' J. Acoust. Soc. Am. **77**, 362–368 (1985).

[8] P. Malbequi, S. M. Candel, and E. Rignot, ''Boundary integral calculations of scattered fields: Application of spacecraft launcher,'' J. Acoust. Soc. Am. **82**, 1771–1781 (1987).

[9] S. M. Rao and P. K. Raju, ''Application of Method of moments to acoustic scattering from multiple bodies of arbitrary shape,'' J. Acoust. Soc. Am. **86**, 1143–1148 (1989).

[10] P. K. Raju, S. M. Rao, and S. P. Sun, ''Application of the method of moments to acoustic scattering from multiple infinitely long fluid filled cylinders,'' Comput. Struct. **39**, 129–134 (1991).

[11] S. M. Rao and B. S. Sridhara, ''Application of the method of moments to acoustic scattering from arbitrary shaped rigid bodies coated with lossless, shearless materials of arbitrary thickness,'' J. Acoust. Soc. Am. **90**, 1601–1607 (1991).

[12] S. M. Rao, P. K. Raju, and S. P. Sun, ''Application of the method of moments to acoustic scattering from fluid-filled bodies of arbitrary shape,'' Commun. Appl. Numer. Methods **8**, 117–128 (1992).

[13] S. M. Rao and B. S. Sridhara, ''Acoustic scattering from arbitrarily shaped multiple bodies in half-space: Method of moments solution,'' J. Acoust. Soc. Am. **91**, 652–657 (1992).

[14] S. P. Sun and S. M. Rao, ''Application of the method of moments to acoustic scattering from multiple infinitely long fluid-filled cylinders using three different formulation,'' Comput. Struct. **43**, 1147–1153 (1992).

[15] H. A. Schenck, ''Improved integral formulation for acoustic radiation problems,'' J. Acoust. Soc. Am. **44**, 41–58 (1968).

[16] A. J. Burton and G. F. Miller, ''The application of integral equation methods to the numerical solution of some exterior boundary value problems,'' Proc. R. Soc. London, Ser. A **323**, 601–618 (1971).

[17] S. Amini and D. T. Wilton, ''An investigation of boundary element methods for the exterior acoustic problem,'' Comput. Methods Appl. Mech. Eng. **54**, 49–65 (1986).

[18] W. L. Meyer, W. A. Bell, B. T. Zinn, and M. P. Stallybras, ''Boundary integral solutions of three dimensional acoustic radiation problems,'' J. Sound Vib. **59**, 245–262 (1978).

[19] C. C. Chien, H. Raliyah, and S. N. Alturi, ''An effective method for solving the hyper singular integral equations in 3-D acoustics,'' J. Acoust. Soc. Am. **88**, 918–937 (1990).

[20] B. Chandrasekhar and S. M. Rao, ''Acoustic scattering from rigid bodies of arbitrary shape—Double layer formulation,'' submitted to J. Acoust. Soc. Am. **115**, 1926–1933 (2004).

[21] B. O'Neill, *Elementary Differential Geometry* (Academic, New York, 1966).

[22] D. R. Wilton, S. M. Rao, A. W. Glisson, D. H. Schaubert, O. M. Al-Bundak, and C. M. Bulter, ''Potential integrals for uniform and linear source distributions on polygons and polyhedra domains,'' IEEE Trans. Antennas Propag. **AP-32**, 276–281 (1984).

[23] P. C. Hammer, O. P. Marlowe, and A. H. Stroud, ''Numerical integration over simplxes and cones,'' Math. Tables Aids Comput. **10**, 130–138 (1956).

[24] Z. Reut, ''On the boundary integral methods for the exterior acoustic problem,'' J. Acoust. Soc. Am. **103**, 297–298 (1985).

[25] S. Amini, P. J. Harris, and D. T. Wilton, *Coupled Boundary and Finite Element Methods for the Solution of the Dynamic Fluid-Structure Interaction Problem*, Lecture Notes in Engineering (Springer-Verlag, New York, 1992), Vol. 77.

[26] Demkowicz, ''Asymptotic convergence in finite and boundary element methods: Part 2: The LLB constant for rigid and elastic scattering problems,'' Comput. Math. Appl. **28**, 93–109 (1994).

[27] L. E. Kinsler, A. R. Frey, A. B. Coppens, and J. V. Sanders, *Fundamentals of Acoustics* (Wiley, New York, 2000).

Effect of viscosity on acoustic diffraction by a circular disk

Anthony M. J. Davis
Mathematics Department, University of Alabama, Tuscaloosa, Alabama 35487-0350

Raymond J. Nagem[a)]
Aerospace and Mechanical Engineering Department, Boston University, Boston, Massachusetts 02115

(Received 19 December 2003; revised 2 March 2004; accepted 3 March 2004)

A complete solution is obtained for the diffraction of a time-harmonic acoustic plane wave by a circular disk in a viscous fluid. Arbitrary disk radius size and arbitrary angle of incidence are considered. The linearized equations of viscous flow and the no-slip condition on the rigid disk are used to derive sets of dual integral equations for the fluid velocity and pressure. The dual integral equations are solved by analytic reduction to sets of linear algebraic equations. An asymptotic approximation for the far-field scattered pressure is given, and this approximation is compared to results of previous inviscid acoustic analyses. It is shown that our results for the force on the disk and the far-field scattered pressure are consistent with the prediction of the theory of aerodynamic sound. Numerical results are presented for the fluid velocity field in the case of tangential incidence. The velocity field near the disk is shown to contain vortices that are swept along the disk with the passage of the incident plane wave. © *2004 Acoustical Society of America.*
[DOI: 10.1121/1.1736650]

PACS numbers: 43.20.Fn, 43.28.Ra [MSH] Pages: 2738–2748

I. INTRODUCTION

Acoustic diffraction by a circular disk is a problem of both theoretical and practical importance. Theoretically, the disk can be used to investigate orientation and edge effects for a finite body in an analytically tractable setting. A review of analytic results for diffraction by a disk is given in Ref. 1; some more recent results are cited in Refs. 2 and 3. The analyses in Refs. 1–3, like most acoustic analyses, assume an inviscid fluid medium. It is shown in Ref. 4 that viscosity can be of practical importance in diffraction by a circular aperture, and similar effects can be expected for the disk. An approximate expression for the viscous correction in diffraction by a sphere is given in Ref. 5, but no such expression is available for the disk. For diffraction by a thin disk at grazing incidence, viscous effects represent not a correction, but rather the primary mechanism of diffraction.

In this paper, we consider in detail the effects of fluid viscosity on the diffraction of sound by a circular disk. As in Refs. 4 and 6, we assume an incident time-harmonic plane wave, and seek the scattered field due to the imposition of the no-slip condition on the surface of the disk. Arbitrary angle of incidence and arbitrary disk radius are considered.

With the inclusion of viscosity, the disk scattering problem comprises a rich variety of fluid flow phenomena. The various flow regimes may be parametrized in terms of the maximum velocity v_0 of the incident plane wave, the radius R of the disk, the frequency ω of the time-harmonic acoustic field, the acoustic wave number k_0 of the incident plane wave, and the fluid kinematic viscosity ν. We assume here that the Reynolds number Rv_0/ν is small, so that the fluid equations can be linearized. With this assumption, the remaining parameters can be grouped into the two dimensionless quantities k_0R and $(\nu/\omega)^{1/2}/R$. The parameter space defined by these two dimensionless quantities is shown in Fig. 1. The horizontal axis (region I) in Fig. 1 corresponds to the assumption of an inviscid fluid; standard acoustic diffraction analyses, including all those cited in Ref. 1, are restricted to this region. The vertical axis (region II) in Fig. 1 corresponds to the case $k_0=0$, or, equivalently, the assumption of incompressible viscous fluid flow. Linearized time-harmonic incompressible viscous flow (oscillatory Stokes flow) in the presence of a circular disk is discussed in Ref. 7. In the hatched region III, the disk radius R is large compared to the viscous diffusion length $(\nu/\omega)^{1/2}$, and viscous effects are therefore confined to a thin spatial region near the disk. Region III may thus be called the acoustic boundary layer region. In the hatched region IV, the acoustic wavelength is large compared to the disk radius, so that flow near the disk is quasi-incompressible. Region V in Fig. 1 may be described as general linear viscous compressible flow.

The analysis in this paper spans the entire parameter space in Fig. 1, from inviscid acoustics to incompressible Stokes flow. In Secs. II and III, we derive general expressions for the complete velocity and pressure fields. The force on the disk and the vorticity field are derived in Sec. IV, and an asymptotic approximation for the far-field scattered pressure is given in Sec. V. Section VI presents specific numerical results that show the effects of viscosity on this far-field scattered acoustic pressure. We compare these results to those of previous inviscid acoustic analyses, and show that our results for the force on the disk and the far-field scattered pressure are consistent with the prediction of the theory of aerodynamic sound. We also give numerical results in Sec. VI for the fluid velocity field near the disk when the direction of propagation of the incident plane wave is parallel to the plane of the disk. In standard inviscid acoustics, the scattered field vanishes completely for this case of tangential inci-

a)Electronic mail: nagem@bu.edu

 0001-4966/2004/115(6)/2738/11/$20.00 © 2004 Acoustical Society of America

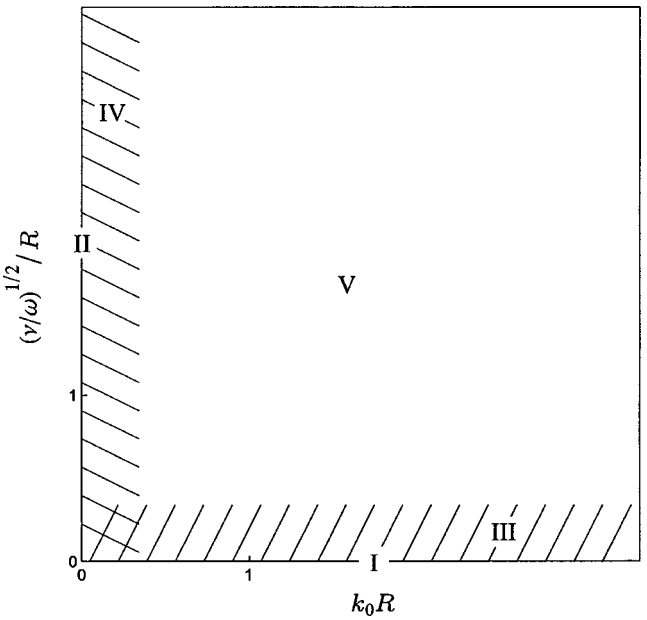

FIG. 1. Parameter space for disk diffraction problem. Region I: inviscid acoustics; region II: oscillatory Stokes flow; region III: acoustic boundary layer region; region IV: quasi-incompressible flow; region V: general compressible viscous flow.

dence. The scattered field (including a propagating acoustic field far from the disk) that we compute for tangential incidence is thus due solely to the viscous effects on the surface of the disk. Our results for the velocity field near the disk show the presence of vortices that are formed in the regions corresponding to the velocity nodes of the incident plane wave, and which are swept along the disk as the velocity node of the incident plane wave propagates. The linear analysis here is thus able to account for the initial generation of the vortices that are normally associated with high amplitude nonlinear acoustics or the presence of a convective mean flow.

II. THEORY

The standard acoustic equations for linearized flow in a homogeneous viscous fluid medium are the continuity equation

$$\frac{\partial \rho}{\partial t}+\rho_0 \nabla\cdot\mathbf{v}=0, \tag{1}$$

the momentum equation

$$\frac{\partial \mathbf{v}}{\partial t}=-\frac{1}{\rho_0}\nabla p+\nu\nabla^2\mathbf{v}+\frac{\nu}{3}\nabla(\nabla\cdot\mathbf{v}), \tag{2}$$

and the equation of state

$$\frac{dp}{d\rho}=c_0^2, \tag{3}$$

in which $\mathbf{v}$ is the fluid velocity vector, ρ_0 is the ambient fluid density, ρ is the density perturbation, p is the fluid pressure, and ν is the kinematic viscosity. Equation (2) assumes a Stokesian fluid for which the viscous forces are expressed in terms of the shear coefficient of viscosity $\eta=\rho_0\nu$.[8] It may be deduced from Eqs. (1) to (3) that the vorticity $\mathbf{\Omega}$ satisfies

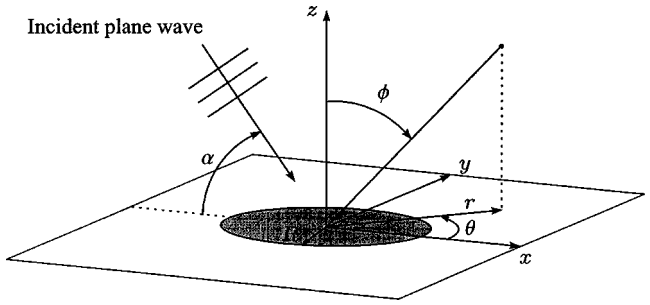

FIG. 2. Geometric configuration for disk diffraction problem.

$$\frac{\partial \mathbf{\Omega}}{\partial t}=\nu\nabla^2\mathbf{\Omega}, \tag{4}$$

as in unsteady creeping flow, while ρ and $\nabla\cdot\mathbf{v}$ satisfy an acoustic wave equation with viscous damping, namely

$$\frac{\partial^2}{\partial t^2}[\rho,\nabla\cdot\mathbf{v}]=\left(c_0^2+\frac{4\nu}{3}\frac{\partial}{\partial t}\right)\nabla^2[\rho,\nabla\cdot\mathbf{v}]. \tag{5}$$

In particular, an irrotational plane wave has velocity field of the form

$$\mathbf{v}=v_0\frac{c_0}{\omega}\nabla\{\exp[i(k_a\mathbf{e}\cdot\mathbf{r}-\omega t)]\},\quad k_a^{-2}=\frac{c_0^2}{\omega^2}-i\frac{4\nu}{3\omega}, \tag{6}$$

where $\mathbf{e}$ denotes a unit vector.

The geometric configuration for the disk diffraction problem is illustrated in Fig. 2. A rigid disk, at which the no-slip condition $\mathbf{v}=\mathbf{0}$ is imposed, is at $z=0, 0\leqslant r<R$ and generates a three-dimensional disturbance to an incident plane wave of period $2\pi/\omega$. Define

$$k_0=\frac{\omega}{c_0},\quad \epsilon^2=\frac{\nu}{\omega}k_0^2, \tag{7}$$

and suppress the time factor $e^{-i\omega t}$. Then Eq. (6) yields

$$k_a=\frac{k_0}{\left(1-\frac{4i}{3}\epsilon^2\right)^{1/2}}, \tag{8}$$

which lies just above the positive real axis, and an incident wave given by

$$\mathbf{v}_{\text{inc}}=(\mathbf{i}\cos\alpha-\mathbf{k}\sin\alpha)v_0\exp[ik_a(x\cos\alpha-z\sin\alpha)] \tag{9}$$

in which $0\leqslant\alpha\leqslant\pi/2$. Thus the scattered field $\mathbf{v}_{\text{sc}}$ generated by the disk must cancel $\mathbf{v}_{\text{inc}}$ on the disk, to satisfy the no-slip condition, and be such that the stress discontinuities are confined to the disk. It is calculated by using the modal structure generated by the expansion

$$\exp[ik_a x\cos\alpha]=J_0(k_a r\cos\alpha)+2\sum_{n=1}^{\infty} i^n J_n(k_a r\cos\alpha)\cos n\theta, \tag{10}$$

where J_n is the Bessel function of the first kind of order n.[9] From Eqs. (1) to (3), $\mathbf{v}_{\text{sc}}$ is governed by

$$\frac{i\omega}{\rho_0 c_0^2} p_{sc} = \nabla \cdot \mathbf{v}_{sc}, \tag{11}$$

$$\left(\nabla^2 + \frac{i\omega}{\nu}\right)\mathbf{v}_{sc} = \frac{1 - \frac{i}{3}\epsilon^2}{\rho_0 \nu} \nabla p_{sc}. \tag{12}$$

It is assumed that, at infinity, $\mathbf{v}_{sc}$ has only diffracted waves. Define the dimensionless Fourier coefficients

$$\begin{bmatrix} \mathbf{i}\cdot\mathbf{v}_{sc}/v_0 \\ \mathbf{k}\cdot\mathbf{v}_{sc}/v_0 \\ p_{sc}/\rho_0 c_0 v_0 \end{bmatrix} = \begin{bmatrix} U_0(r,z) \\ W_0(r,z) \\ P_0(r,z) \end{bmatrix} + 2\sum_{n=1}^{\infty} i^n \begin{bmatrix} U_n(r,z) \\ W_n(r,z) \\ P_n(r,z) \end{bmatrix} \cos n\theta,$$

$$\mathbf{j}\cdot\mathbf{v}_{sc}/v_0 = 2\sum_{n=1}^{\infty} i^n V_n(r,z) \sin n\theta, \tag{13}$$

which, according to Eqs. (11) and (12), are such that

$$\frac{i\omega}{c_0} P_0 = \frac{i}{r}\frac{\partial}{\partial r}[r(U_1 + V_1)] + \frac{\partial W_0}{\partial z},$$

$$\frac{i\omega}{c_0} P_1 = \frac{1}{2i}\frac{\partial U_0}{\partial r} + \frac{i}{2r^2}\frac{\partial}{\partial r}[r^2(U_2 + V_2)] + \frac{\partial W_1}{\partial z}, \tag{14}$$

$$\frac{i\omega}{c_0} P_n = \frac{r^{n-1}}{2i}\frac{\partial}{\partial r}\left(\frac{U_{n-1} - V_{n-1}}{r^{n-1}}\right) + \frac{i}{2r^{n+1}}\frac{\partial}{\partial r} \times [r^{n+1}(U_{n+1} + V_{n+1})] + \frac{\partial W_n}{\partial z} \quad (n > 1),$$

and

$$\left(\frac{\partial^2}{\partial r^2} + \frac{1}{r}\frac{\partial}{\partial r} + \frac{\partial^2}{\partial z^2} + \frac{i\omega}{\nu}\right)\begin{bmatrix} U_0 \\ W_0 \end{bmatrix} = \frac{i\omega}{c_0 k_a^2}\left(k_a^2 - \frac{i\omega}{\nu}\right)\begin{bmatrix} \frac{i}{r}\frac{\partial}{\partial r}(rP_1) \\ \frac{\partial P_0}{\partial z} \end{bmatrix},$$

$$\left(\frac{\partial^2}{\partial r^2} + \frac{1}{r}\frac{\partial}{\partial r} - \frac{n^2}{r^2} + \frac{\partial^2}{\partial z^2} + \frac{i\omega}{\nu}\right)\begin{bmatrix} U_n \\ V_n \\ W_n \end{bmatrix} = \frac{i\omega}{c_0 k_a^2}\left(k_a^2 - \frac{i\omega}{\nu}\right) \times \begin{bmatrix} \frac{r^{n-1}}{2i}\frac{\partial}{\partial r}\left(\frac{P_{n-1}}{r^{n-1}}\right) + \frac{i}{2r^{n+1}}\frac{\partial}{\partial r}(r^{n+1}P_{n+1}) \\ \frac{r^{n-1}}{2i}\frac{\partial}{\partial r}\left(\frac{P_{n-1}}{r^{n-1}}\right) - \frac{i}{2r^{n+1}}\frac{\partial}{\partial r}(r^{n+1}P_{n+1}) \\ \frac{\partial P_n}{\partial z} \end{bmatrix} \quad (n \geq 1). \tag{15}$$

Since $(\nabla^2 + k_a^2)p_{sc} = 0$, with k_a defined by Eq. (6), the solution for P_n that vanishes as $|z| \to \infty$ is

$$P_n = \int_0^{\infty} k^{-1}[A_n(k) + B_n(k)\mathrm{sgn}(z)] \times e^{-(k^2 - k_a^2)^{1/2}|z|} J_n(kr)\,dk \quad (n \geq 0). \tag{16}$$

The solution (16) allows the possibility that P_n or its first derivative with respect to z may be discontinuous at $z = 0$, and is more convenient than the alternative of writing one solution for $z > 0$ and a second solution for $z < 0$. Then the solution of Eq. (15) that ensures continuity of $\mathbf{V}$ at $z = 0$ is now

$$W_n = \frac{i\omega}{c_0 k_a^2}\int_0^{\infty} \frac{\sqrt{k^2 - k_a^2}}{k}\{[A_n(k)\mathrm{sgn}(z) + B_n(k)] \times e^{-(k^2 - k_a^2)^{1/2}|z|} - [A_n(k)\mathrm{sgn}(z) + C_n(k)] \times e^{-(k^2 - i\omega/\nu)^{1/2}|z|}\} J_n(kr)\,dk \quad (n \geq 0), \tag{17}$$

$$U_n \pm V_n = \frac{\omega}{c_0 k_a^2}\int_0^{\infty}\{[A_{n\mp1}(k) + B_{n\mp1}(k)\mathrm{sgn}(z)] \times e^{-(k^2 - k_a^2)^{1/2}|z|} - [D_n^{\pm}(k) + B_{n\mp1}(k)\mathrm{sgn}(z)] \times e^{-(k^2 - i\omega/\nu)^{1/2}|z|}\} J_n(kr)\,dk \quad (n \geq 1), \tag{18}$$

$$U_0 = \frac{\omega}{c_0 k_a^2}\int_0^{\infty}\{[A_1(k) + B_1(k)\mathrm{sgn}(z)]e^{-(k^2 - k_a^2)^{1/2}|z|} - [D_0^{-}(k) + B_1(k)\mathrm{sgn}(z)] \times e^{-(k^2 - i\omega/\nu)^{1/2}|z|}\} J_0(kr)\,dk. \tag{19}$$

In Eq. (18), the upper signs and the function D_n^+ are used in the equation for $U_n + V_n$, while the lower signs and the function D_n^- are used in the equation for $U_n - V_n$. When these expressions are substituted into Eqs. (14), it follows that

$$\begin{bmatrix} D_1^+(k) \\ B_0(k) \end{bmatrix} = \frac{1}{k^2}(k^2 - k_a^2)^{1/2}\left(k^2 - \frac{i\omega}{\nu}\right)^{1/2}\begin{bmatrix} A_0(k) \\ C_0(k) \end{bmatrix},$$

$$\begin{bmatrix} \frac{1}{2}[D_{n-1}^-(k) + D_{n+1}^+(k)] \\ B_n(k) \end{bmatrix} = \frac{1}{k^2}(k^2 - k_a^2)^{1/2}\left(k^2 - \frac{i\omega}{\nu}\right)^{1/2} \times \begin{bmatrix} A_n(k) \\ C_n(k) \end{bmatrix} \quad (n \geq 1).$$

Hence

$$C_n(k) = \left[1 - \frac{K(k)}{(k^2 - k_a^2)^{1/2}}\right]B_n(k) \quad (n \geq 0),$$

$$D_1^+(k) = \left[1 + \frac{\left(k^2 - \frac{i\omega}{\nu}\right)^{1/2}}{k^2}K(k)\right]A_0(k),$$

where

$$K(k) = (k^2 - k_a^2)^{1/2} - \frac{k^2}{\left(k^2 - \frac{i\omega}{\nu}\right)^{1/2}}. \tag{20}$$

Since the sum $(D^{-}_{n-1}+D^{+}_{n+1})$ is given above in terms of the function A_n, it is convenient to introduce the function E_n $(n\geqslant 1)$ by setting

$$\left.\begin{matrix} D^{-}_{n-1}(k) \\ D^{+}_{n+1}(k) \end{matrix}\right\} = \left[1+\frac{\left(k^2-\frac{i\omega}{\nu}\right)^{1/2}}{k^2}K(k)\right]A_n(k)\pm E_n(k) \quad (n\geqslant 1).$$

When these relations are substituted into Eqs. (17)–(19), the latter can be rearranged as

$$W_n=\frac{i\omega}{c_0k_a^2}\int_0^\infty\Bigg\{\frac{\sqrt{k^2-k_a^2}}{k}[A_n(k)\mathrm{sgn}(z)+B_n(k)] \times[e^{-(k^2-k_a^2)^{1/2}|z|}-e^{-(k^2-i\omega/\nu)^{1/2}|z|}] + \frac{K(k)}{k}B_n(k)e^{-(k^2-i\omega/\nu)^{1/2}|z|}\Bigg\}J_n(kr)\,dk \quad (n\geqslant 0), \tag{21}$$

$$U_0=\frac{\omega}{c_0k_a^2}\int_0^\infty\Bigg\{[A_1(k)+B_1(k)\mathrm{sgn}(z)][e^{-(k^2-k_a^2)^{1/2}|z|} -e^{-(k^2-i\omega/\nu)^{1/2}|z|}]-\Bigg[\frac{\left(k^2-\frac{i\omega}{\nu}\right)^{1/2}}{k^2}K(k)A_1(k) +E_1(k)\Bigg]e^{-(k^2-i\omega/\nu)^{1/2}|z|}\Bigg\}J_0(kr)\,dk, \tag{22}$$

$$U_n-V_n=\frac{\omega}{c_0k_a^2}\int_0^\infty\Bigg\{[A_{n+1}(k)+B_{n+1}(k)\mathrm{sgn}(z)] \times[e^{-(k^2-k_a^2)^{1/2}|z|}-e^{-(k^2-i\omega/\nu)^{1/2}|z|}] -\Bigg[\frac{\left(k^2-\frac{i\omega}{\nu}\right)^{1/2}}{k^2}K(k)A_{n+1}(k)+E_{n+1}(k)\Bigg] \times e^{-(k^2-i\omega/\nu)^{1/2}|z|}\Bigg\}J_n(kr)\,dk \quad (n\geqslant 1), \tag{23}$$

$$U_1+V_1=\frac{\omega}{c_0k_a^2}\int_0^\infty\Bigg\{[A_0(k)+B_0(k)\mathrm{sgn}(z)] \times[e^{-(k^2-k_a^2)^{1/2}|z|}-e^{-(k^2-i\omega/\nu)^{1/2}|z|}] -\frac{\left(k^2-\frac{i\omega}{\nu}\right)^{1/2}}{k^2}K(k)A_0(k)e^{-(k^2-i\omega/\nu)^{1/2}|z|}\Bigg\} \times J_1(kr)\,dk, \tag{24}$$

$$U_n+V_n=\frac{\omega}{c_0k_a^2}\int_0^\infty\Bigg\{[A_{n-1}(k)+B_{n-1}(k)\mathrm{sgn}(z)] \times[e^{-(k^2-k_a^2)^{1/2}|z|}-e^{-(k^2-i\omega/\nu)^{1/2}|z|}] -\Bigg[\frac{\left(k^2-\frac{i\omega}{\nu}\right)^{1/2}}{k^2}K(k)A_{n-1}(k)-E_{n-1}(k)\Bigg] \times e^{-(k^2-i\omega/\nu)^{1/2}|z|}\Bigg\}J_n(kr)\,dk \quad (n\geqslant 2). \tag{25}$$

The sets of unknown functions $\{A_n(k),B_n(k);n\geqslant 0\},\{E_n(k);n\geqslant 1\}$ are now determined by requiring zero velocity on the disk and no net stress discontinuities at $z=0, r>R$. Let the total velocity field be $\mathbf{v}_{\mathrm{inc}}-\mathbf{v}_{\mathrm{sc}}$, with associated pressure field $p_{\mathrm{inc}}-p_{\mathrm{sc}}$. It is readily seen from Eqs. (21) to (25) that $\mathbf{v}_{\mathrm{sc}}=\mathbf{v}_{\mathrm{inc}}$ on the disk provided

$$\int_0^\infty\frac{K(k)}{k}B_n(k)J_n(kr)\,dk=\frac{c_0k_a^2}{\omega}i\sin\alpha J_n(k_ar\cos\alpha) \quad (r<R,n\geqslant 0), \tag{26}$$

$$\int_0^\infty\Bigg[\frac{\left(k^2-\frac{i\omega}{\nu}\right)^{1/2}}{k^2}K(k)A_n(k)\pm E_n(k)\Bigg]J_{n\mp 1}(kr)\,dk =-\frac{c_0k_a^2}{\omega}\cos\alpha J_{n\mp 1}(k_ar\cos\alpha) \quad (r<R,n\geqslant 1), \tag{27}$$

$$\int_0^\infty\frac{\left(k^2-\frac{i\omega}{\nu}\right)^{1/2}}{k^2}K(k)A_0(k)J_1(kr)\,dk =-\frac{c_0k_a^2}{\omega}\cos\alpha J_1(k_ar\cos\alpha) \quad (r<R). \tag{28}$$

Equations valid for $r>R$ are obtained in the following by considering the normal and tangential stresses at the plane $z=0$. The normal stress at a $z=$constant plane is given[10] by

$$-p+2\rho_0\nu\left(\frac{\partial v_z}{\partial z}-\frac{1}{3}\boldsymbol{\nabla}\cdot\mathbf{v}\right).$$

However, if $\mathbf{v}$ is continuous, then the normal derivative is equal to the divergence and hence, in virtue of Eq. (11), continuity of pressure suffices to ensure continuity of normal stress. According to the Fourier expansions (10),(13) and the solution (16), the pressure discontinuity in the scattered field is confined to the disk provided

$$\int_0^\infty k^{-1}B_n(k)J_n(kr)\,dk=\frac{1}{2}[P_n]^{0+}_{z=0-} =0 \quad (r>R,n\geqslant 0). \tag{29}$$

Equations (26) and (29) furnish, for each $n\geqslant 0$, a pair of dual integral equations for $B_n(k)$ that are disjoint from the other equations.

The tangential stress discontinuities in the scattered field are, according to the Fourier expansions (10),(13) and the solution (22)–(25), similarly confined to the disk provided

$$\int_0^\infty \left[\frac{(k^2-k_a^2)^{1/2}}{k^2} A_n(k) \pm (-i\omega/\nu)^{-1} \left(k^2 - \frac{i\omega}{\nu} \right)^{1/2} E_n(k) \right] \times J_{n\mp 1}(kr)\,dk = 0 \quad (r>R, n\geqslant 1), \tag{30}$$

$$\int_0^\infty \frac{(k^2-k_a^2)^{1/2}}{k^2} A_0(k) J_1(kr)\,dk = 0 \quad (r>R). \tag{31}$$

Equations (28) and (31) provide a pair of dual integral equations for $A_0(k)$ that are disjoint from the other equations. However, for each $n\geqslant 1$, Eqs. (27) and (30) are identified as coupled pairs of dual integral equations for $A_n(k), E_n(k)$.

III. THE SCATTERED FIELD: SOLUTION BY TRANTER'S METHOD

Such groups of dual integral equations can be converted into coupled integral equations, defined on $r<R$ or $r>R$. But their numerical solution requires discretization and, when rapidly oscillating forcing occurs, as here, the direct reduction to algebraic equations given by Tranter[11] is expected to be preferable. This method starts with the key observation that

$$A(u) = u^\alpha \sum_{m=0}^\infty a_m J_{\nu-\alpha+2m+1}(u)$$

satisfies

$$\int_0^\infty A(u) J_\nu(xu)\,du = 0 \quad (x>1)$$

for $|\alpha|<1$. Explicit expressions for the coefficients are available when the integrand for the interval $x<1$ has only the additional factor $u^{-2\alpha}$. Otherwise, the choice of α is determined by the behavior of the additional factor as $u\to\infty$. So, since the velocities introduce a factor $\sim K(k)=O(k^{-1})$ as $k\to\infty$, $\alpha=1/2$ here. Thus Eqs. (29)–(31) are satisfied by writing

$$\frac{1}{k} B_n(k) = (kR)^{1/2} \sum_{m=0}^\infty b_{nm} J_{n+2m+1/2}(kR) \quad (n\geqslant 0), \tag{32}$$

$$\frac{(k^2-k_a^2)^{1/2}}{k^2} A_0(k) = (kR)^{1/2} \sum_{m=1}^\infty a_{0m} J_{2m-1/2}(kR), \tag{33}$$

$$\frac{(k^2-k_a^2)^{1/2}}{k^2} A_n(k) \pm (-i\omega/\nu)^{-1} \left(k^2 - \frac{i\omega}{\nu} \right)^{1/2} E_n(k) = (kR)^{1/2} \sum_{m=0}^\infty (a_{nm} \pm e_{nm}) J_{n+2m-1/2}(kR) \quad (a_{n0}=e_{n0}, n\geqslant 1). \tag{34}$$

After substituting Eq. (32) and writing $u=kR$, $r=R\xi$, Eq. (26) becomes

$$\sum_{m=0}^\infty b_{nm} \int_0^\infty \frac{K(u/R)}{R} u^{1/2} J_{n+2m+1/2}(u) J_n(u\xi)\,du = \frac{c_0 k_a^2}{\omega} i \sin\alpha J_n(k_a R\xi\cos\alpha) \quad (\xi<1, n\geqslant 0).$$

Tranter's method, described by Sneddon[12] in Sec. 4.6, now transforms this functional identity into linear algebraic equations by multiplying by

$$\frac{2^{1/2}\Gamma(n+l+1)}{\Gamma(n+1)\Gamma(l+1/2)} \frac{\xi^{n+1}}{(1-\xi^2)^{1/2}} \mathcal{F}_l(n+1/2, n+1, \xi^2)$$

and integrating over $0<\xi<1$ to obtain

$$\sum_{m=0}^\infty b_{nm} \int_0^\infty \frac{K(u/R)}{R} J_{n+2m+1/2}(u) J_{n+2l+1/2}(u)\,du = \frac{c_0 k_a^2}{\omega} i \sin\alpha (k_a R\cos\alpha)^{-1/2} J_{n+2l+1/2}(k_a R\cos\alpha) \quad (l,n\geqslant 0). \tag{35}$$

Here $\mathcal{F}_l$ is a Jacobi polynomial, defined by

$$\mathcal{F}_l(a,b,\xi) = {}_2F_1(-l, a+l; b; \xi) = \frac{\Gamma(l+1)\Gamma(b)}{\Gamma(l+b)} P_l^{(b-1,a-b)}(1-2\xi) = \frac{\Gamma(l+1)\Gamma(b)}{\Gamma(l+a)} \sum_{s=0}^l \frac{\Gamma(l+s+a)(-\xi)^s}{\Gamma(s+b)(l-s)!\,s!}, \tag{36}$$

in which the definition,

$$P_n^{(\alpha,\beta)}(x) = \frac{(-1)^n}{2^n n!} (1-x)^{-\alpha} (1+x)^{-\beta} \times \frac{d^n}{dx^n} [(1-x)^{\alpha+n} (1+x)^{\beta+n}],$$

is an obvious extension of Rodrigues' formula for $P_n(x)$.

A set of linear equations for the coefficients in $A_0(k)$ is similarly obtained by substituting Eq. (33) into Eq. (28), multiplying by

$$\frac{2^{1/2}\Gamma(l+2)}{\Gamma(l+1/2)} \frac{\xi^2}{(1-\xi^2)^{1/2}} \mathcal{F}_l(3/2, 2, \xi^2)$$

and integrating over $0<\xi<1$. Thus

$$\sum_{m=1}^\infty a_{0m} \int_0^\infty \left[\frac{u^2 - \frac{i\omega}{\nu} R^2}{u^2 - (k_a R)^2} \right]^{1/2} \times \frac{K(u/R)}{R} J_{2m-1/2}(u) J_{2l+3/2}(u)\,du = -\frac{c_0 k_a^2}{\omega} \cos\alpha (k_a R\cos\alpha)^{-1/2} J_{2l+3/2}(k_a R\cos\alpha) \quad (l\geqslant 0). \tag{37}$$

Further, for each $n \geqslant 1$, coupled sets of linear equations for the coefficients in $A_n(k), E_n(k)$ are obtained by substituting Eq. (34) into Eq. (27), multiplying by

$$\frac{2^{1/2}\Gamma(n+l)}{\Gamma(n)\Gamma(l+1/2)} \frac{\xi^n}{(1-\xi^2)^{1/2}} \mathcal{F}_l(n-1/2, n, \xi^2)$$

and

$$\frac{2^{1/2}\Gamma(n+l+2)}{\Gamma(n+2)\Gamma(l+1/2)} \frac{\xi^{n+2}}{(1-\xi^2)^{1/2}} \mathcal{F}_l(n+3/2, n+2, \xi^2),$$

respectively, and integrating over $0<\xi<1$. Thus

$$\int_0^\infty \sum_{m=0}^\infty \left\{ \frac{K(u/R)}{R} \left[\frac{u^2 - \frac{i\omega}{\nu}R^2}{u^2-(k_aR)^2} \right]^{1/2} a_{nm} + \frac{\left(-\frac{i\omega}{\nu}\right)}{\left(u^2 - \frac{i\omega}{\nu}R^2\right)^{1/2}} e_{nm} \right\} \times J_{n+2m-1/2}(u) J_{n+2l-1/2}(u)\, du$$
$$= -\frac{c_0 k_a^2}{\omega} \cos\alpha (k_aR\cos\alpha)^{-1/2} J_{n+2l-1/2}(k_aR\cos\alpha) \quad (l \geqslant 0, n \geqslant 1), \tag{38}$$

$$\int_0^\infty \sum_{m=0}^\infty \left\{ \frac{K(u/R)}{R} \left[\frac{u^2 - \frac{i\omega}{\nu}R^2}{u^2-(k_aR)^2} \right]^{1/2} a_{nm} - \frac{\left(-\frac{i\omega}{\nu}\right)}{\left(u^2 - \frac{i\omega}{\nu}R^2\right)^{1/2}} e_{nm} \right\} \times J_{n+2m-1/2}(u) J_{n+2l+3/2}(u)\, du$$
$$= -\frac{c_0 k_a^2}{\omega} \cos\alpha (k_aR\cos\alpha)^{-1/2} J_{n+2l+3/2}(k_aR\cos\alpha) \quad (l \geqslant 0, n \geqslant 1). \tag{39}$$

It may be noted that the function $K(k)$ given by Eq. (20) appeared as the Wiener–Hopf kernel in the half-plane diffraction analysis in Ref. 6, and also appeared in the circular aperture diffraction analysis in Ref. 4. This function evidently plays a key role in the acoustic/viscous interaction associated with diffraction problems. It might be described here as the "kernel" of Eq. (35). Note that the right-hand sides of Eqs. (35) and (37)–(39) have been exactly evaluated since integrals of the same type appeared on the corresponding left-hand sides. This simplification was overlooked in Ref. 4.

For later numerical evaluation of the semi-infinite integrals in Eq. (35) and Eqs. (37)–(39), it is advantageous to identify the dominant behavior of the integrands as $u \to \infty$ and to evaluate the integrals corresponding to this asymptotic form using the identity

$$\int_0^\infty \frac{J_{n+2m+1/2}(u) J_{n+2l+1/2}(u)}{u}\, du = \frac{\delta_{ml}}{2n+4m+1}.$$

It is also convenient to rescale the coefficients a_{mn}, b_{mn}, and e_{mn} so as to remove common factors from the right-hand sides. Thus, on writing

$$[a_{nm}, e_{nm}] = \frac{c_0 k_a^2}{\omega} \cos\alpha (2n+4m-1) \left[\frac{2\alpha_{nm}}{k_a^2 + \frac{i\omega}{\nu}}, \frac{\gamma_{nm}}{\frac{i\omega}{\nu}} \right],$$
$$b_{nm} = -\frac{c_0 k_a^2}{\omega} i \sin\alpha (2n+4m+1) \frac{2\beta_{nm}}{k_a^2 + \frac{i\omega}{\nu}}, \tag{40}$$

and substituting for K from Eq. (20), Eqs. (35), (37)–(39) reduce to

$$\beta_{nl} - \sum_{m=0}^\infty (2n+4m+1)\beta_{nm} \times \int_0^\infty J_{n+2m+1/2}(u) J_{n+2l+1/2}(u) \times \left[\frac{2(u^2 - k_a^2R^2)^{1/2} - 2u^2(u^2 - iR^2\omega/\nu)^{-1/2}}{(k_a^2 + i\omega/\nu)R^2} + \frac{1}{u} \right] du$$
$$= (k_aR\cos\alpha)^{-1/2} J_{n+2l+1/2}(k_aR\cos\alpha) \quad (l,n \geqslant 0), \tag{41}$$

$$\alpha_{0,l+1} - \sum_{m=1}^\infty (4m-1)\alpha_{0m} \int_0^\infty J_{2m-1/2}(u) J_{2l+3/2}(u) \times \left[\frac{2}{(k_a^2 + i\omega/\nu)R^2} \left\{ (u^2 - iR^2\omega/\nu)^{1/2} - \frac{u^2}{(u^2 - k_a^2R^2)^{1/2}} \right\} + \frac{1}{u} \right] du$$
$$= (k_aR\cos\alpha)^{-1/2} J_{2l+3/2}(k_aR\cos\alpha) \quad (l \geqslant 0), \tag{42}$$

$$\alpha_{nl} - \sum_{m=0}^\infty (2n+4m-1)\alpha_{nm} \int_0^\infty J_{n+2m-1/2}(u) J_{n+2l-1/2}(u) \times \left[\frac{2}{(k_a^2 + i\omega/\nu)R^2} \left\{ (u^2 - iR^2\omega/\nu)^{1/2} - \frac{u^2}{(u^2 - k_a^2R^2)^{1/2}} \right\} + \frac{1}{u} \right] du + \gamma_{nl} - \sum_{m=0}^\infty (2n+4m-1)\gamma_{nm} \times \int_0^\infty J_{n+2m-1/2}(u) J_{n+2l-1/2}(u) \times \left[\frac{1}{u} - \frac{1}{(u^2 - iR^2\omega/\nu)^{1/2}} \right] du$$
$$= (k_aR\cos\alpha)^{-1/2} J_{n+2l-1/2}(k_aR\cos\alpha) \quad (l \geqslant 0, n \geqslant 1). \tag{43}$$

$$\alpha_{n,l+1}-\sum_{m=0}^{\infty}(2n+4m-1)\alpha_{nm}$$
$$\times\int_0^{\infty}J_{n+2m-1/2}(u)J_{n+2l+3/2}(u)$$
$$\times\left[\frac{2}{(k_a^2+i\omega/\nu)R^2}\left\{(u^2-iR^2\omega/\nu)^{1/2}-\frac{u^2}{(u^2-k_a^2R^2)^{1/2}}\right\}+\frac{1}{u}\right]du-\gamma_{n,l+1}+\sum_{m=0}^{\infty}(2n+4m-1)\gamma_{nm}$$
$$\times\int_0^{\infty}J_{n+2m-1/2}(u)J_{n+2l+3/2}(u)$$
$$\times\left[\frac{1}{u}-\frac{1}{(u^2-iR^2\omega/\nu)^{1/2}}\right]du$$
$$=(k_aR\cos\alpha)^{-1/2}J_{n+2l+3/2}(k_aR\cos\alpha)\quad(l\geqslant 0,n\geqslant 1). \tag{44}$$

For $n\geqslant 1$, $a_{n0}=e_{n0}$ implies $2\alpha_{n0}=(1-ik_a^2\nu/\omega)\gamma_{n0}$, which ensures that the number of equations matches the number of unknown coefficients. Note that the forcing terms (right-hand sides) depend on only k_aR while the matrices on the left-hand sides depend on both k_aR and $(\omega/\nu)^{1/2}R$, with emphasis dictated by the magnitudes of these parameters.

In the inviscid limit, only $\{B_n(k);n\geqslant 0\}$ and hence one set of equations are required. However, the additional factor in the integral over (0,1) now behaves like u, corresponding to the pressure now playing the role of velocity potential instead of normal stress. Thus, with $\alpha=-1/2$, Eq. (32) is modified to

$$\frac{1}{k}B_n(k)=(Rk)^{-1/2}\sum_{m=0}^{\infty}\hat{b}_{nm}J_{n+2m+3/2}(kR)\quad(n\geqslant 0), \tag{45}$$

and the resulting system, corresponding to Eq. (35), is

$$\sum_{m=0}^{\infty}\hat{b}_{nm}\int_0^{\infty}\frac{(u^2-k_0^2R^2)^{1/2}}{R^2u^2}J_{n+2m+3/2}(u)J_{n+2l+3/2}(u)du$$
$$=k_0i\sin\alpha(k_0R\cos\alpha)^{-3/2}J_{n+2l+3/2}(k_0R\cos\alpha)$$
$$(l,n\geqslant 0), \tag{46}$$

with the right-hand side evaluated exactly, in contrast to the presentation in Ref. 4.

IV. FORCE ON DISK: VORTICITY

The normal stress discontinuity at the disk is, on taking account of the dilatation as described earlier, $[-p_{sc}]k_0^2/k_a^2$. Equation (13) shows that the normal force exerted by the fluid motion $-\mathbf{v}_{sc}$ on the disk is

$$-2\pi\mathbf{k}\frac{\rho_0\omega k_0v_0}{k_a^2}\int_0^R[-P_0]_{z=0-}^{0+}\,r\,dr,$$

while the tangential stress yields a side force

$$-2\pi\mathbf{i}\rho_0\nu v_0\int_0^R\left[\frac{\partial U_0}{\partial z}\right]_{z=0-}^{0+}r\,dr.$$

On substitution of Eqs. (16),(19) and then Eqs. (32),(34), the total force $\mathbf{F}$ is given by

$$\mathbf{F}=4\pi\frac{\rho_0\omega k_0Rv_0}{k_a^2}\left(\frac{2}{\pi}\right)^{1/2}[2ia_{10}\mathbf{i}+b_{00}\mathbf{k}]. \tag{47}$$

Finally, substitution of Eq. (40) gives the force formula

$$\mathbf{F}=16\frac{\rho_0\omega Rv_0i}{k_a^2+\dfrac{i\omega}{\nu}}\left(\frac{\pi}{2}\right)^{1/2}[2\alpha_{10}\cos\alpha\mathbf{i}-\beta_{00}\sin\alpha\mathbf{k}]$$
$$=16\frac{\rho_0\nu v_0R}{1-\dfrac{ik_a^2\nu}{\omega}}\left(\frac{\pi}{2}\right)^{1/2}[2\alpha_{10}\cos\alpha\mathbf{i}-\beta_{00}\sin\alpha\mathbf{k}]. \tag{48}$$

This does not imply no normal force in the limit $\nu\to 0$ because the solution structure is different in the inviscid case.

The calculation of the vorticity requires that $\mathbf{v}_{sc}$, given by Eq. (13), be expressed in cylindrical polar form by use of the unit vectors $\hat{\mathbf{r}}$, $\hat{\boldsymbol{\theta}}$, $\hat{\mathbf{z}}$. After substituting Eqs. (21)–(25) and using the definition (20) of $K(k)$, the simplest procedure is to first construct the gradient and curl decomposition:

$$\mathbf{v}_{sc}=\boldsymbol{\nabla}\left\{-\frac{ik_0v_0}{k_a^2}\int_0^{\infty}\left[(A_0+B_0\,\mathrm{sgn}\,z)J_0(kr)+2\sum_1^{\infty}i^n(A_n+B_n\,\mathrm{sgn}\,z)J_n(kr)\cos n\theta\right]\times e^{-(k^2-k_a^2)^{1/2}|z|}\frac{dk}{k}\right\}+\boldsymbol{\nabla}\times\left\{\frac{i\omega}{k_a^2}\int_0^{\infty}\left\langle\hat{\boldsymbol{\theta}}J_0'(kr)\times\left[\frac{(k^2-k_a^2)^{1/2}}{k}A_0\,\mathrm{sgn}\,z+\frac{kB_0}{(k^2-i\omega/\nu)^{1/2}}\right]+2\sum_1^{\infty}i^n\left[\frac{n}{kr}\hat{\mathbf{r}}J_n(kr)\sin n\theta+\hat{\boldsymbol{\theta}}J_n'(kr)\cos n\theta\right]\times\left[\frac{(k^2-k_a^2)^{1/2}}{k}A_n\,\mathrm{sgn}\,z+\frac{kB_n}{(k^2-i\omega/\nu)^{1/2}}\right]+2\hat{\mathbf{z}}\sum_1^{\infty}i^nE_nJ_n(kr)\sin n\theta\right\rangle e^{-(k^2-i\omega/\nu)^{1/2}|z|}\frac{dk}{k}\right\}, \tag{49}$$

in which the scalar and vector potentials satisfy Helmholtz equations with respective wave numbers k_a and $(i\omega/\nu)^{1/2}$. The vorticity $\boldsymbol{\Omega}=-\boldsymbol{\nabla}\times\mathbf{v}_{sc}$ is readily found from Eq. (49) to be given by

$$\boldsymbol{\Omega}=\frac{ik_0v_0}{k_a^2}\int_0^\infty\Bigg[\Bigg[-\frac{i\omega}{\nu}\hat{\boldsymbol{\theta}}J_0'(kr)\times\left[\frac{(k^2-k_a^2)^{1/2}}{k}A_0\,\mathrm{sgn}\,z+\frac{kB_0}{(k^2-i\omega/\nu)^{1/2}}\right]+2\sum_1^\infty i^n\Bigg\langle-\frac{i\omega}{\nu}\Bigg[\frac{n}{kr}\hat{\mathbf{r}}J_n(kr)\sin n\theta+\hat{\boldsymbol{\theta}}J_n'(kr)\cos n\theta\Bigg]\times\left[\frac{(k^2-k_a^2)^{1/2}}{k}A_n\,\mathrm{sgn}\,z+\frac{kB_n}{(k^2-i\omega/\nu)^{1/2}}\right]+E_n\Bigg\{-k\hat{\mathbf{z}}J_n(kr)\sin n\theta+\left(k^2-\frac{i\omega}{\nu}\right)^{1/2}\times\mathrm{sgn}\,z\left[\hat{\mathbf{r}}J_n'(kr)\sin n\theta+\frac{n}{kr}\hat{\boldsymbol{\theta}}J_n(kr)\cos n\theta\right]\Bigg\}\Bigg\rangle\Bigg]\Bigg]\times e^{-(k^2-i\omega/\nu)^{1/2}|z|}\frac{dk}{k}. \tag{50}$$

V. PRESSURE AT INFINITY

According to Eqs. (13) and (16), the scattered pressure is given by

$$\begin{aligned}\frac{p_{\mathrm{sc}}}{\rho_0c_0v_0}&=\int_0^\infty k^{-1}e^{-(k^2-k_a^2)^{1/2}|z|}\Bigg\{[A_0(k)+B_0(k)\mathrm{sgn}(z)]J_0(kr)+2\sum_{n=1}^\infty i^n[A_n(k)+B_n(k)\mathrm{sgn}(z)]J_n(kr)\cos n\theta\Bigg\}dk\\&=\int_0^\infty\frac{ke^{-(k^2-k_a^2)^{1/2}|z|}}{(k^2-k_a^2)^{1/2}}(kR)^{1/2}\times\Bigg\{J_0(kr)\sum_{m=1}^\infty a_{0m}J_{2m-1/2}(kR)+2\sum_{n=1}^\infty i^nJ_n(kr)\cos n\theta\sum_{m=0}^\infty a_{nm}J_{n+2m-1/2}(kR)\Bigg\}dk\\&\quad+\mathrm{sgn}(z)\int_0^\infty e^{-(k^2-k_a^2)^{1/2}|z|}(kR)^{1/2}\times\Bigg\{J_0(kr)\sum_{m=0}^\infty b_{0m}J_{2m+1/2}(kR)+2\sum_{n=1}^\infty i^nJ_n(kr)\cos n\theta\sum_{m=0}^\infty b_{nm}J_{n+2m+1/2}(kR)\Bigg\}dk,\end{aligned} \tag{51}$$

after insertion of the series (32)–(34). Evidently the first term in Eq. (51) is even in z while the second is an odd function of z. Thus it is sufficient to evaluate each term in the half space $z>0$. Since $(\boldsymbol{\nabla}^2+k_a^2)p_{\mathrm{sc}}=0$, the awkward dependence on z can be circumvented by using Green's theorem with Neumann or Dirichlet conditions at $z=0$ for the first and second terms, respectively. The vanishing of the second term when $r>R$ is immaterial in the subsequent calculation for $z>0$.

The Green's functions with unit point source and image point source or sink are given by

$$G_\pm[r^2+r_0^2-2rr_0\cos(\theta-\theta_0),z,z_0]=-\frac{e^{ik_a|\mathbf{r}-\mathbf{r}_0|}}{4\pi|\mathbf{r}-\mathbf{r}_0|}\pm\frac{e^{ik_a|\mathbf{r}-\mathbf{r}_0'|}}{4\pi|\mathbf{r}-\mathbf{r}_0'|}, \tag{52}$$

where $\mathbf{r}_0=(r_0,\theta_0,z_0)$, $\mathbf{r}_0'=(r_0,\theta_0,-z_0)$. Since p_{sc} and $G_\pm$ satisfy the same radiation condition, an application of Green's theorem in the half space $z>0$ yields

$$p_{\mathrm{sc}}(r_0,\theta_0,z_0)=\int_0^\infty\int_{-\pi}^\pi\left[G_\pm\frac{\partial p_{\mathrm{sc}}}{\partial z}-p_{\mathrm{sc}}\frac{\partial G_\pm}{\partial z}\right]_{z=0}r\,dr\,d\theta, \tag{53}$$

for the respective Dirichlet and Neumann cases. The far field behavior is deduced by letting $|\mathbf{r}_0|\to\infty$ and inserting into $G_\pm$ the estimate

$$\begin{aligned}\frac{e^{ik_a|\mathbf{r}-\mathbf{r}_0|}}{|\mathbf{r}-\mathbf{r}_0|}&\sim\frac{e^{ik_a|\mathbf{r}_0|}}{|\mathbf{r}_0|}\exp\left\{-ik_a\left[\frac{rr_0\cos(\theta-\theta_0)+zz_0}{\sqrt{r_0^2+z_0^2}}\right]\right\}\\&=\frac{e^{ik_a|\mathbf{r}_0|}}{|\mathbf{r}_0|}\exp\{-ik_a[r\sin\phi_0\cos(\theta-\theta_0)+z\cos\phi_0]\},\end{aligned}$$

in which the spherical polar angle ϕ_0 has been introduced for subsequent convenience in notation. This yields, from Eq. (52),

$$G_-[r^2+r_0^2-2rr_0\cos(\theta-\theta_0),0,z_0]\sim-\frac{e^{ik_a|\mathbf{r}_0|}}{2\pi|\mathbf{r}_0|}e^{-ik_ar\sin\phi_0\cos(\theta-\theta_0)}, \tag{54}$$

$$\frac{\partial G_+}{\partial z}[r^2+r_0^2-2rr_0\cos(\theta-\theta_0),0,z_0]\sim ik_a\cos\phi_0\frac{e^{ik_a|\mathbf{r}_0|}}{2\pi|\mathbf{r}_0|}e^{-ik_ar\sin\phi_0\cos(\theta-\theta_0)}. \tag{55}$$

But the Fourier coefficients of $e^{-ik_ar\sin\phi_0\cos(\theta-\theta_0)}$ are determined by Eq. (10) and application of a recurrence relation to Eq. (3), Sec. 6.512 of Ref. 13 yields

$$\int_0^\infty J_n(kr)J_n(k_ar\sin\phi_0)r\,dr=k^{-1}\delta(k-k_a\sin\phi_0)\quad(n\geqslant0).$$

Thus, by use of G_- and G_+ in Eq. (53) for the first and second terms, respectively, in Eq. (51), the far field estimates (54) and (55) yield two amplitudes in terms of triple integrals which can be evaluated exactly. Thus the scattered pressure at infinity is given asymptotically by

$$p_{sc}(r_0,\theta_0,z_0)$$
$$\sim \rho_0 c_0 v_0 \frac{e^{ik_a|\mathbf{r}_0|}}{|\mathbf{r}_0|}(k_a R\sin\phi_0)^{1/2}$$
$$\times\left\{\sum_{m=1}^{\infty} a_{0m}J_{2m-1/2}(k_a R\sin\phi_0)\right.$$
$$+2\sum_{n=1}^{\infty}\cos n\theta_0\sum_{m=0}^{\infty} a_{nm}J_{n+2m-1/2}(k_a R\sin\phi_0)$$
$$-i\frac{z_0}{r_0}\left[\sum_{m=0}^{\infty} b_{0m}J_{2m+1/2}(k_a R\sin\phi_0)\right.$$
$$\left.\left.+2\sum_{n=1}^{\infty}\cos n\theta_0\sum_{m=0}^{\infty} b_{nm}J_{n+2m+1/2}(k_a R\sin\phi_0)\right]\right\}, \tag{56}$$

valid for positive or negative z_0 after replacing $\cot\phi_0$ by z_0/r_0. At this stage, the suffix "0" can be dropped from this simple modal expansion of the far field pressure in terms of the computed coefficients. When $k_0 R \ll 1$, Eq. (56) yields the estimate

$$p_{sc}(r,\theta,z)\sim \rho_0 c_0 v_0 \frac{e^{ik_a|\mathbf{r}|}}{|\mathbf{r}|}(k_a R\sin\phi)^{1/2}$$
$$\times\left\{a_{01}J_{3/2}(k_a R\sin\phi)+2a_{10}J_{1/2}(k_a R\sin\phi)\right.$$
$$\times\cos\theta - i\frac{z}{r}[b_{00}J_{1/2}(k_a R\sin\phi)$$
$$\left.+2b_{10}J_{3/2}(k_a R\sin\phi)\cos\theta]\right\}$$
$$\sim \rho_0 c_0 v_0 e^{ik_a|\mathbf{r}|}\left(\frac{2}{\pi}\right)^{1/2}\left[k_a R\frac{2a_{10}x - ib_{00}z}{|\mathbf{r}|^2}\right.$$
$$\left.+\frac{(k_a R)^2}{3}\frac{a_{01}r^2 - 2ib_{10}xz}{|\mathbf{r}|^3}\right], \tag{57}$$

where $|\mathbf{r}|^2 = r^2+z^2$. The leading term on the right-hand side of Eq. (57) can be interpreted as the combination of a dipole source oriented in the z direction perpendicular to the plane of the disk and a dipole source oriented in the x direction parallel to the plane of the disk. Inviscid scattering theory gives only the dipole in the direction perpendicular to the disk.

Our result for the far-field scattered pressure can be compared to the prediction of the theory of aerodynamic sound. For a stationary acoustically compact body, $k_0 R \ll 1$ in our case, this theory[8] gives the far-field pressure estimate

$$p(\mathbf{r},t)\sim \frac{1}{4\pi c_0|\mathbf{r}|^2}\mathbf{r}\cdot\frac{\partial}{\partial t}\mathbf{F}\left(t-\frac{|\mathbf{r}|}{c_0}\right), \tag{58}$$

where $\mathbf{F}(t)$ is the force exerted on the fluid by the body. In our linearized theory, this result can be easily obtained by solving Eqs. (1)–(3), forced by adding $\mathbf{F}(t)\delta(x)\delta(y)\delta(z)$ to the right-hand side of Eq. (2) and with viscosity neglected. In Ref. 8, however, Eq. (58) is derived for a much more general class of fluid flow phenomena. Our viscous results can be used to verify Eq. (58) in a case where viscosity is included rigorously. In our case, the force on the fluid is

$$-\mathbf{F}e^{-i\omega t} = 4\pi\frac{\rho_0\omega k_0 R v_0}{k_a^2}\left(\frac{2}{\pi}\right)^{1/2}[2ia_{10}\mathbf{i}+b_{00}\mathbf{k}]e^{-i\omega t},$$

after using Eq. (47). This suggests, according to Eq. (58), that our scattered pressure field has the far-field behavior

$$-p_{sc}e^{-i\omega t}\sim -\frac{\rho_0\omega R v_0}{|\mathbf{r}|^2}\left(\frac{2}{\pi}\right)^{1/2}[2ia_{10}x - ib_{00}z]$$
$$\times e^{i(k_0|\mathbf{r}|-\omega t)}. \tag{59}$$

Despite the viscous contribution to $\mathbf{F}$, this is remarkably the case because, for small values of the viscosity parameter ϵ, we may neglect the difference between k_0 and k_a in the far-field scattered pressure given by Eq. (57) and observe agreement of the leading terms with Eq. (59). At grazing incidence (angle of incidence $\alpha=0$), the force on the fluid is due solely to viscous friction at the surface of the disk, yet Eq. (58) still holds. The far-field prediction of the theory of aerodynamic sound, derived for a general class of acoustically compact objects, is thus satisfyingly consistent with our analysis for the disk. This is because, no matter how the force exerted by the body on the fluid is created, its influence in the far field is primarily acoustic.

VI. NUMERICAL RESULTS

Numerical results for the coefficients β_{nl}, α_{nl}, and γ_{nl} are obtained by truncating the systems of Eqs. (41)–(44) at a finite value M of l and m. The truncation limit M is increased until the coefficients become negligibly small with increasing l. It is also necessary to choose the maximum number N of angular modes corresponding to the index n. In general, the required values of M and N increase with increasing values of the disk radius R and with decreasing values of the viscosity parameter $\epsilon = k_0\sqrt{\nu/\omega}$. For large R and small ϵ, the viscous effects are confined to a small boundary layer near the edge of the disk, and the modal summations (13) require several terms in order to resolve the velocity and pressure fields in this boundary layer.

A. Far-field pressure

Following Kristensson,[2] we define the far-field amplitude S of the scattered pressure as

$$S = \lim_{|\mathbf{r}|\to\infty}\left[\frac{p_{sc}}{\rho_0 c_0 v_0}\left(\frac{e^{ik_a|\mathbf{r}|}}{k_a|\mathbf{r}|}\right)^{-1}\right]. \tag{60}$$

For small $k_a R$, Ref. 2 gives the far-field amplitude S for inviscid scattering as, in our notation,

$$S = \frac{2}{3\pi}\sin\alpha\cos\phi(k_a R)^3, \tag{61}$$

while our result in Eq. (57) gives

$$S = \left(\frac{2}{\pi}\right)^{1/2} ik_a R(2a_{10}(k_a R,\alpha,\epsilon)\sin\phi\cos\theta$$
$$-b_{00}(k_a R,\alpha,\epsilon)\cos\phi). \tag{62}$$

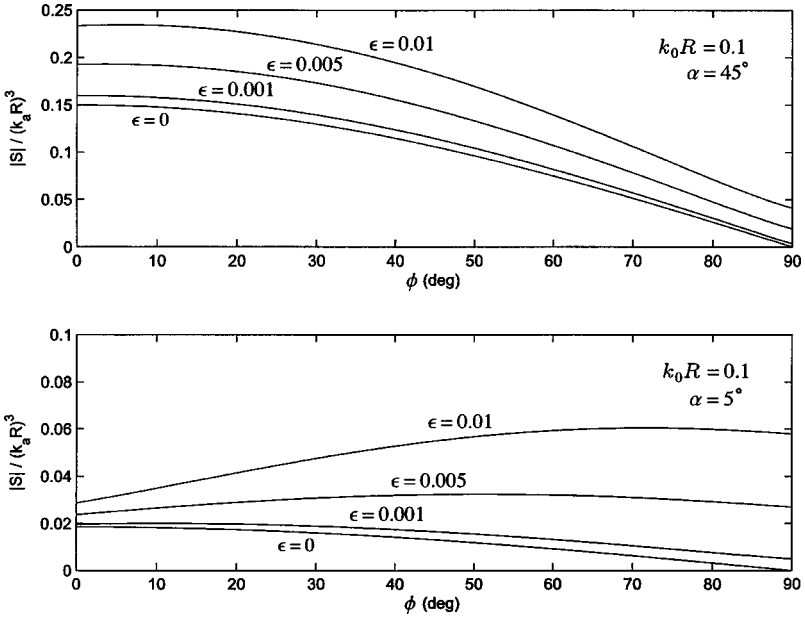

FIG. 3. Far-field forward scattering amplitude as function of polar angle ϕ and viscosity parameter ϵ for angles of incidence $\alpha=45°$ and $\alpha=5°$.

Figure 3 shows the magnitude $|S|/(k_aR)^3$ as a function of the polar angle ϕ for the forward scattering direction $\theta=0$ and for the angles of incidence $\alpha=45°$ and $\alpha=5°$. The curves marked $\epsilon=0$ are obtained using Eq. (61), while the curves for nonzero ϵ are obtain using Eq. (62). It is seen that the presence of viscosity always increases the amplitude of the scattered pressure. The increase in the scattered field is due to the additional viscous force, given explicitly in Eq. (48), that the disk exerts on the fluid. The relative effects of viscosity are largest in the plane of the disk ($\phi=90°$), and become increasingly significant as the angle α approaches the tangential limit $\alpha=0$.

B. Velocity field for tangential incidence

In the limiting case of tangential incidence ($\alpha=0$), the incident field has the simple form $\mathbf{v}_{\text{inc}}=v_0\mathbf{i}e^{ik_ax}$ and the lack of forcing in Eq. (26) ensures that $\{B_n(k)=0;n\geqslant 0\}$, consis-

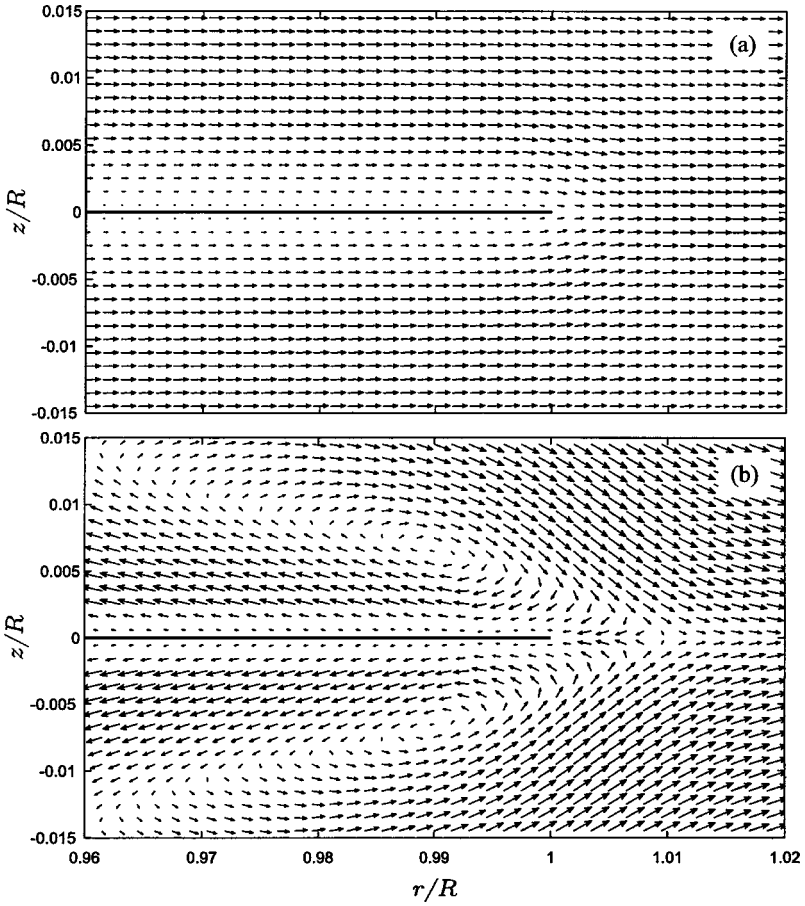

FIG. 4. Instantaneous fluid velocity field near the edge of the disk for the case of tangential incidence.

tent with the expectation of continuous pressure across the disk. Tangential incidence is especially interesting because an inviscid acoustic diffraction analysis predicts that the scattered field completely vanishes in this case. As mentioned in Sec. I, the scattered field (including the propagating acoustic field far from the disk) that is predicted by our viscous diffraction analysis for tangential incidence is due solely to the viscous effects on the surface of the disk.

Instantaneous values of the velocity components are obtained from the quantities

$$\Re(\mathbf{i}\cdot\mathbf{v}e^{-i\omega t}), \quad \Re(\mathbf{j}\cdot\mathbf{v}e^{-i\omega t}), \quad \Re(\mathbf{k}\cdot\mathbf{v}e^{-i\omega t}),$$

at specific values of the time t. The total velocity $\mathbf{v}=\mathbf{v}_{\text{inc}}-\mathbf{v}_{\text{sc}}$ is defined by Eqs. (9) and (13).

An illustration of the instantaneous velocity field near the edge of the disk in the plane $y=0$ is shown in Fig. 4 at two particular instants of time. For $y=0$, the velocity field has components only in the x and z directions. Figure 4 is obtained using the parameters $k_0R=2\pi$ and $\epsilon=0.02$. Thus $(\nu/\omega)^{1/2}/R=\epsilon/(k_0R)\approx 0.003$, so that Fig. 4 corresponds to a point in the acoustic boundary layer region III of Fig. 1. At the instant of time portrayed in the upper plot (a) of Fig. 4, the incident plane wave over the illustrated section of the disk is essentially a uniform flow in the positive x direction. The velocity field near the disk displays the characteristic boundary layer profile of viscous flow over a flat plate. The lower plot (b) of Fig. 4 shows the same region of the flow at a later instant of time, when a velocity node of the incident plane wave is passing over the illustrated section of the disk. The flow field now displays a vortex motion near the disk. The magnitude of the vortex flow is small compared to the amplitude of the incident plane wave; the velocity components in Fig. 4(b) have been magnified so that the vortex can be seen more clearly. Numerical results at additional instants of time show that this vortex is formed when a velocity node of the incident plane wave approaches the leading of the disk. The vortex is swept along the disk as the velocity node of the incident plane wave propagates. Although vorticity in the fluid propagates according to the diffusion equation (4), vorticity is generated at the surface of the disk by the boundary interaction with the incident plane wave. It is this boundary interaction that carries the vortex in Fig. 4(b) along the surface of the disk with the velocity node of the incident field. The vortex disappears when it leaves the edge of the disk. The linear analysis here is thus able to predict the formation and propagation of the vortices normally associated with high amplitude nonlinear acoustics or with a convective mean flow. In the presence of a mean flow, the vortices formed on the surface of the disk would presumably be carried into the free field downstream of the disk.

VII. CONCLUSIONS

A complete solution has been derived for the problem of linear acoustic diffraction by a circular disk in a viscous fluid. We have compared our results for the far-field scattered pressure to the corresponding results for the standard inviscid diffraction problem, and have shown that our results for the force on the disk and the far-field scattered pressure are consistent with the prediction of the theory of aerodynamic sound. Our results for the instantaneous velocity field near the disk show that the linear analysis considered here is capable of predicting the initial formation and propagation of the vortices that are important in high amplitude nonlinear acoustics and in unsteady convective flows.

[1] F. B. Sleator, "The disc," in *Electromagnetic and Acoustic Scattering by Simple Shapes*, edited by J. J. Bowman, T. B. A. Senior, and P. L. E. Uslenghi (North-Holland, Amsterdam, 1969).

[2] G. Kristensson and P. C. Waterman, "The *T* matrix for acoustic and electromagnetic scattering by circular disks," J. Acoust. Soc. Am. **72**, 1612–1625 (1982).

[3] C.-C. Coussios, "The significance of shape and orientation in single-particle weak-scatterer models," J. Acoust. Soc. Am. **112**, 906–915 (2002).

[4] A. M. J. Davis and R. J. Nagem, "Influence of viscosity on the diffraction of sound by a circular aperture in a plane screen," J. Acoust. Soc. Am. **113**, 3080–3090 (2003).

[5] H. Lamb, *Hydrodynamics*, 6th ed. (Dover, New York, 1945), pp. 657–659.

[6] A. M. J. Davis and R. J. Nagem, "Acoustic diffraction by a half plane in a viscous acoustic medium," J. Acoust. Soc. Am. **112**, 1288–1296 (2002).

[7] W. Zhang and H. A. Stone, "Oscillatory motions of circular disks and nearly spherical particles in viscous flows," J. Fluid Mech. **367**, 329–358 (1998).

[8] M. S. Howe, *Theory of Vortex Sound* (Cambridge University Press, Cambridge, 2003), pp. 3, 129.

[9] G. N. Watson, *A Treatise on the Theory of Bessel Functions*, 2nd ed. (Cambridge University Press, Cambridge, 1995), Sec. 2.

[10] G. K. Batchelor, *An Introduction to Fluid Dynamics* (Cambridge University Press, Cambridge, 1967).

[11] C. J. Tranter, *Integral Transforms in Mathematical Physics* (Wiley, New York, 1966).

[12] I. N. Sneddon, *Mixed Boundary Problems in Potential Theory* (North-Holland, Amsterdam, 1966).

[13] I. S. Gradshteyn and I. M. Ryzhik, *Tables of Integrals, Series and Products*, enlarged ed. editor A. Jeffrey (Academic, London, 1980).

A model for wave propagation in a composite solid matrix saturated by a single-phase fluid

Juan E. Santos[a)]
CONICET-Facultad de Ciencias Astronómicas y Geofísicas, Universidad Nacional de La Plata, Paseo del Bosque, S/N, (1900) La Plata, Argentina and Department of Mathematics, Purdue University, 150 N. UniversityStreet, West Lafayette, Indiana 47907-2067

Claudia L. Ravazzoli
CONICET-Facultad de Ciencias Astronómicas y Geofísicas, Universidad Nacional de La Plata, Paseo del Bosque, S/N, (1900) La Plata, Argentina

José M. Carcione
Istituto Nazionale di Oceanografia e di Geofisica Sperimentale (OGS), Borgo Grotta Gigante 42c, 34010 Sgonico, Trieste, Italy

(Received 19 June 2003; accepted for publication 1 March 2004)

This paper presents a theory to describe wave propagation in a porous medium composed of two solids saturated by a single-phase fluid for spatially variable porosity. This problem has been previously solved for constant porosity when one of the solids is ice or clay, but that model is not useful for most realistic situations. The equations for variable porosity are derived from the virtual work principle, where the generalized coordinates are identified as the displacements of the two solid phases and a new variable associated with the relative fluid flow, whose divergence is the change in fluid content. The generalized forces are the fluid pressure and combinations of the stress tensor of each solid phase and the fluid pressure. The Lagrangian equations of motion are derived for the isotropic case and a theorem on the existence and uniqueness of their solution is given. The plane wave analysis reveals the existence of three compressional and two shear waves. The theory is applied to wave propagation in shaley sandstones showing that phase velocities of the faster P and S waves agree very well with experimental data for varying porosity and clay content. A simulation through a plane interface separating two frozen sandstones of different ice contents is presented. © *2004 Acoustical Society of America.* [DOI: 10.1121/1.1710500]

PACS numbers: 43.20.Gp, 43.20.Jr [JJM] Pages: 2749–2760

I. INTRODUCTION

Wave propagation in composite porous materials has applications in many branches of science and technology, such as seismic methods in the presence of shaley sandstones,[1] permafrost,[2,3] gas-hydrate concentration in ocean-bottom sediments,[4] and evaluation of the freezing conditions of foods by ultrasonic techniques.[5]

Leclaire *et al.*[6] have developed a theory for describing wave propagation in frozen porous media in which solid substrate, ice, and water coexist, under the assumption of the existence of a layer of unfrozen water around the solid particles isolating them from ice. This model, valid for uniform porosity, predicts the existence of three compressional and two shear waves; the verification that additional (slow) waves can be observed in laboratory experiments was published by Leclaire *et al.*[7]

Later, this theory was generalized by Carcione and Tinivella[4] to include the interaction between the solid and ice particles and grain cementation with decreasing temperature. Also, Carcione *et al.*[1] have applied this theory to study the acoustic properties of shaley sandstones, assuming that sand and clay are *nonwelded* and form a continuous and interpenetrating porous composite skeleton.

Both frozen porous media and shaley sandstones are two examples of porous materials where the two solid phases are *weakly coupled* or *nonwelded*. Similar *weakly coupled* formulations have previously been proposed. For instance, McCoy[8] explicitly assumed the weak coupling and phase connectivity conditions over macro-scale distances. He proposed a mixture theory appropriate for the combination of two *acoustic phases*.

This work generalizes the theory developed in Refs. 6 and 4 to the case of nonuniform porosity so that the differential equations can be used to perform numerical experiments or fit laboratory data related to heterogeneous media. The *nonwelding* condition between the two solid phases is assumed when the potential and kinetic energies are defined, with proper interaction terms among the solid and fluid phases. If the two solid phases would be welded, then additional slow waves would not be present.[9] Our approach is based on the energy formulation used by Biot,[10] rather than on volume averaging or homogenization methods used, for instance, by Burridge and Keller.[11]

In this paper the virtual work principle for the composite material is stated and the strains in the two solid phases and the change in fluid content are identified as the state variables to represent the variation in strain energy $\delta \mathcal{W}$, consequently identifying the generalized forces. These are the total

a)Electronic mail: santos@fcaglp.fcaglp.unlp.edu.ar

stress tensors in both solid phases, denoted by $\sigma^{1,T}$ and $\sigma^{3,T}$, respectively, and the fluid pressure p_f.

The kinetic energy density and the dissipation function are defined in terms of the generalized coordinates, which are the two solid displacement vectors and the new variable w, associated with the fluid flow relative to the solid composite matrix, whose divergence is the change in fluid content.

The Lagrangian formulation of the equations of motion is a generalization of the approach of Biot,[10] Santos *et al.*,[12] and Carcione.[13] It is shown that in the case of uniform porosity, the known theories[6,4] are recovered. The plane wave analysis shows the existence of three compressional and two shear modes of propagation, in agreement with the original theory derived by Leclaire *et al.*[6]

An existence and uniqueness result for a general initial boundary value problem is given, showing that for each time t each component of the solid displacements belongs to the Sobolev space $H^1(\Omega)$, while the fluid displacement lies in the space $H(\mathrm{div},\Omega)$.

The theory is applied to wave propagation in shaley sandstones showing that the phase velocities of the faster waves (the seismic P and S waves) agree very well with experimental data for varying porosity and clay content. Moreover, in a simulation of waves travelling through a plane interface separating two frozen sandstones of different porosity is performed. The numerical solver is a modification of the pseudospectral modeling algorithm used by Carcione and Seriani[3] to model propagation in frozen porous media with uniform porosity.

II. THE STRAIN ENERGY OF THE COMPOSITE SYSTEM

Let Ω be an elementary cube of porous material composed of two solid phases, referred to by the subscripts or superscripts 1 and 3, saturated by a fluid phase indicated by the subscript or superscript 2. Thus, $\Omega=\Omega_1\cup\Omega_2\cup\Omega_3$. Let V_i denote the volume of the phase Ω_i and V_b and V_{sm} the bulk volume of Ω and the solid matrix $\Omega_{\mathrm{sm}}=\Omega_1\cup\Omega_3$, so that

$$V_{\mathrm{sm}}=V_1+V_3, \quad V_b=V_1+V_2+V_3.$$

Let $S_1=V_1/V_{\mathrm{sm}}$ and $S_3=V_3/V_{\mathrm{sm}}$ denote the two solid fractions of the composite matrix and define the effective porosity as $\phi=V_2/V_b$. Let $u^{(1)}$, $u^{(2)}$, and $u^{(3)}$ be the averaged solid and fluid displacements over the bulk material. Here $u^{(2)}$ is defined such that on any face F of the cube Ω,

$$\int_F \phi u^{(2)}\nu\, d\sigma$$

is the amount of fluid displaced through F, while

$$\int_F S_1 u^{(1)}\nu\, d\sigma, \quad \int_F S_3 u^{(3)}\nu\, d\sigma$$

represent the displacements in the two solid parts of F, respectively. Here $\nu=(\nu_j)$ denotes the unit outward normal to F and $d\sigma$ the surface measure on F.

Let $\sigma_{ij}^{(1)}$ and $\sigma_{ij}^{(3)}$ denote the stress tensors in Ω_1 and Ω_3 averaged over the bulk material Ω, respectively, and let p_f denote the fluid pressure. These quantities describe small changes with respect to reference values corresponding to an initial equilibrium state. Let us also introduce the tensors

$$\sigma_{ij}^{(1,T)}=\sigma_{ij}^{(1)}-S_1\phi p_f\delta_{ij}, \quad \sigma_{ij}^{(3,T)}=\sigma_{ij}^{(3)}-S_3\phi p_f\delta_{ij}, \tag{2.1}$$

associated with the total stresses in Ω_1 and Ω_3, respectively, so that the total stress tensor in the bulk material Ω is given by

$$\sigma_{ij}=\sigma_{ij}^{(1,T)}+\sigma_{ij}^{(3,T)}. \tag{2.2}$$

Next the stress–strain relations for our system shall be derived using the virtual work principle, following the derivation of Biot[10] for the case of a single solid phase. In what follows the Einstein convention is used, i.e., sum on repeated indices. Let $\mathcal{W}$ be the strain energy density and $\mathcal{V}$ the total potential energy. Also let $\mathcal{V}_d$ denote the total potential energy density. Then, if $f_i^{(1)}$, $f_i^{(3)}$, $f_i^{(2)}$ represent the surface forces acting on the solid and fluid parts of the boundary of Ω, denoted by $\partial\Omega$, we have that

$$\mathcal{V}=\int_\Omega \mathcal{V}_d\, dx=\int_\Omega \mathcal{W}\, dx-\int_{\partial\Omega}(f_i^{(1)}u_i^{(1)}+f_i^{(2)}u_i^{(2)}+f_i^{(3)}u_i^{(3)})\,d\sigma, \tag{2.3}$$

and the virtual work principle for the composite fluid–solid system can be stated in the form:

$$\delta\mathcal{V}=0=\int_\Omega \delta\mathcal{W}\, dx-\int_{\partial\Omega}(f_i^{(1)}\delta(u_i^{(1)})+f_i^{(2)}\delta(u_i^{(2)})+f_i^{(3)}(\delta u_i^{(3)}))\,d\sigma, \tag{2.4}$$

where

$$f_i^{(1)}=\sigma_{ij}^{(1)}\nu_j, \quad f_i^{(3)}=\sigma_{ij}^{(3)}\nu_j, \quad f_i^{(2)}=-\phi p_f\delta_{ij}\nu_j, \tag{2.5}$$

and δ denotes virtual changes in the different quantities. Using Eqs. (2.1) and (2.5) in Eq. (2.4) yields

$$\delta\mathcal{V}=0=\int_\Omega \delta\mathcal{W}\, dx-\int_{\partial\Omega}(\sigma_{ij}^{(1,T)}\nu_j\delta(u_i^{(1)})+\sigma_{ij}^{(3,T)}\nu_j\delta(u_i^{(3)})-p_f\delta_{ij}\nu_j\delta w_i)\,d\sigma. \tag{2.6}$$

where

$$w_i=\phi(u_i^{(2)}-S_1u_i^{(1)}-S_3u_i^{(3)}). \tag{2.7}$$

Then, transforming the surface integral in Eq. (2.6) into a volume integral gives

$$\delta\mathcal{V}=0=\int_\Omega \delta W\, dx-\int_\Omega \frac{\partial}{\partial x_j}[\sigma_{ij}^{(1,T)}\delta(u_i^{(1)})+\sigma_{ij}^{(3,T)}\delta(u_i^{(3)})-p_f\delta_{ij}\delta w_i]dx. \tag{2.8}$$

Since Ω remains in equilibrium under the action of the virtual displacements, it follows that

$$\frac{\partial}{\partial x_j}\sigma_{ij}^{(1,T)}=\frac{\partial}{\partial x_j}\sigma_{ij}^{(3,T)}=\frac{\partial}{\partial x_j}p_f\delta_{ij}=0,$$

and consequently, using the symmetry of the stress tensors $\sigma_{ij}^{(1,T)}$ and $\sigma_{ij}^{(3,T)}$ we obtain

$$\delta\mathcal{V}=0=\int_\Omega \delta\mathcal{W}-\int_\Omega(\sigma_{ij}^{(1,T)}\delta(\epsilon_{ij}(u^{(1)}))+\sigma_{ij}^{(3,T)}\delta(\epsilon_{ij}(u^{(3)}))+p_f\delta\zeta)dx, \tag{2.9}$$

where $\zeta=-\nabla\cdot w$ represents the change in fluid content and

$$\epsilon_{ij}(u^{(m)})=\frac{1}{2}\left(\frac{\partial u_i^{(m)}}{\partial x_j}+\frac{\partial u_j^{(m)}}{\partial x_i}\right),\quad m=1,3,$$

denotes the strain tensor in Ω_m with linear invariant $\theta_m=\epsilon_{ii}(u^{(m)})$.

Thus from Eqs. (2.1) and (2.9) the following expression for the variation in strain energy density δW is finally obtained:

$$\delta\mathcal{W}=(\sigma_{ij}^{(1)}-S_1\phi p_f\delta_{ij})\,\delta(\epsilon_{ij}(u^{(1)}))+(\sigma_{ij}^{(3)}-S_3\phi p_f\delta_{ij})\,\delta(\epsilon_{ij}(u^{(3)}))+p_f\delta\zeta. \tag{2.10}$$

Consequently, since $\delta\mathcal{W}$ is an exact differential of the variables $\epsilon_{ij}(u^{(1)})$, $\epsilon_{ij}(u^{(3)})$, and ζ we have that

$$\frac{\partial\mathcal{W}}{\partial\epsilon_{ij}(u^{(m)})}=\sigma_{ij}^{(m)}-S_m\phi p_f\delta_{ij},\quad m=1,3,\quad \frac{\partial\mathcal{W}}{\partial\zeta}=p_f. \tag{2.11}$$

Also, it follows from Eq. (2.10) that

$$\mathcal{W}=\tfrac{1}{2}[(\sigma_{ij}^{(1)}-S_1\phi p_f\delta_{ij})(\epsilon_{ij}(u^{(1)}))+(\sigma_{ij}^{(3)}-S_3\phi p_f\delta_{ij})(\epsilon_{ij}(u^{(3)}))+p_f\zeta]. \tag{2.12}$$

Next, to obtain the expression for the *potential energy* of our system, let us consider perturbations of the system from the equilibrium state. Using Eq. (2.3), the argument leading to Eq. (2.8) and expression (2.10) for $\delta\mathcal{W}$ yields

$$\delta\mathcal{V}_d=-\frac{\partial}{\partial x_j}[\sigma_{ij}^{(1)}-S_1\phi p_f\delta_{ij}]\delta u_i^{(1)}-\frac{\partial}{\partial x_j}[\sigma_{ij}^{(3)}-S_3\phi p_f\delta_{ij}]\delta u_i^{(3)}+\frac{\partial}{\partial x_i}p_f\delta w_i. \tag{2.13}$$

If $u_i^{(1)}$, $u_i^{(3)}$, w_i are chosen as generalized coordinates to describe our composite system, since the system is assumed to be conservative it follows that

$$\frac{\partial\mathcal{V}_d}{\partial u_i^{(m)}}=-\frac{\partial}{\partial x_j}[\sigma_{ij}^{(m)}-S_m\phi p_f\delta_{ij}],\quad m=1,3,\quad \frac{\partial\mathcal{V}_d}{\partial w_i}=\frac{\partial}{\partial x_i}p_f. \tag{2.14}$$

III. THE LINEAR ISOTROPIC STRESS–STRAIN RELATIONS

Let us denote the deviatoric strain tensor in Ω_m as

$$d_{ij}^{(m)}=\epsilon_{ij}(u^{(m)})-\tfrac{1}{3}\theta_m\delta_{ij},\quad m=1,3.$$

In the linear isotropic case the strain energy density $\mathcal{W}$ in Eq. (2.12) is a quadratic positive definite form in the invariants θ_1, θ_3, ζ, $(d_1)^2=d_{ij}^{(1)}d_{ij}^{(1)}$, $(d_3)^2=d_{ij}^{(3)}d_{ij}^{(3)}$ and $d_{1,3}=d_{ij}^{(1)}d_{ij}^{(3)}$. Note that

$$(d_m)^2=\epsilon_{ij}(u^{(m)})\epsilon_{ij}(u^{(m)})-\tfrac{1}{3}(\theta_m)^2,\quad m=1,3,$$

$$d_{1,3}=\epsilon_{ij}(u^{(1)})\epsilon_{ij}(u^{(3)})-\tfrac{1}{3}\theta_1\theta_3.$$

Then,

$$\mathcal{W}=\tfrac{1}{2}H_1(\theta_1)^2+\mu_1(d_1)^2+\tfrac{1}{2}H_3(\theta_3)^2+\mu_3(d_3)^2-B_1\theta_1\zeta-B_2\theta_3\zeta+B_3\theta_1\theta_3+\tfrac{1}{2}K_{av}(\zeta)^2+\mu_{1,3}d_{1,3}. \tag{3.1}$$

Remark: The B_3 and μ_{13} terms represent elastic interaction between the two solid phases.

Thus,

$$\frac{\partial\mathcal{W}}{\partial\epsilon_{ij}(u^{(1)})}=\sigma_{ij}^{(1)}-S_1\phi p_f\delta_{ij}=[H_1\theta_1-B_1\zeta+B_3\theta_3]\delta_{ij}+2\mu_1 d_{ij}^{(1)}+\mu_{1,3}d_{ij}^{(3)}, \tag{3.2}$$

$$\frac{\partial\mathcal{W}}{\partial\epsilon_{ij}(u^{(3)})}=\sigma_{ij}^{(3)}-S_3\phi p_f\delta_{ij}=[H_3\theta_3-B_2\zeta+B_3\theta_1]\delta_{ij}+2\mu_3 d_{ij}^{(3)}+\mu_{1,3}d_{ij}^{(1)}, \tag{3.3}$$

$$\frac{\partial\mathcal{W}}{\partial\zeta}=p_f=-B_1\theta_1-B_2\theta_3+K_{\mathrm{av}}\zeta. \tag{3.4}$$

Equations (3.2)–(3.4) express the generalized stresses $\sigma_{ij}^{(1)}-S_1\phi p_f\delta_{ij}$, $\sigma_{ij}^{(3)}-S_3\phi p_f\delta_{ij}$ and p_f in terms of the strains $\epsilon_{ij}(u^{(1)})$, $\epsilon_{ij}(u^{(3)})$, and ζ.

IV. DETERMINATION OF THE COEFFICIENTS IN THE STRESS–STRAIN RELATIONS

This section presents a procedure to determine the coefficients in the stress–strain relations (3.2)–(3.4) for the variable porosity case. It is assumed that the moduli for the case of uniform porosity can be obtained from known expressions given in a previous formulations.[4] First note that setting $\theta_2=\nabla\cdot u^{(2)}$, for the case of uniform porosity we have that

$$\zeta=\phi(S_1\theta_1+S_3\theta_3-\theta_2) \tag{4.1}$$

and consequently, from Eq. (3.4) we get

$$-\phi p_f=(B_1\phi-K_{\mathrm{av}}\phi^2S_1)\theta_1+(B_2\phi-K_{\mathrm{av}}\phi^2S_3)\theta_3+K_{\mathrm{av}}\phi^2\theta_2. \tag{4.2}$$

Next, combining Eqs. (3.2), (4.1), and (4.2) yields

$$\sigma_{ij}^{(1)}=\{[H_1+(S_1\phi)^2K_{\rm av}-2S_1\phi B_1]\theta_1+[S_1S_3\phi^2K_{\rm av}-S_3\phi B_1-S_1\phi B_2+B_3]\theta_3-(\phi^2S_1K_{\rm av}-\phi B_1)\theta_2\}\delta_{ij}+2\mu_1 d_{ij}^{(1)}+\mu_{1,3}d_{ij}^{(3)}. \tag{4.3}$$

Also, it follows from Eqs. (3.3), (4.1), and (4.2) that

$$\sigma_{ij}^{(3)}=\{[H_3+(S_3\phi)^2K_{\rm av}-2S_3\phi B_2]\theta_3+[S_3S_1\phi^2K_{\rm av}-S_3\phi B_1-S_1\phi B_2+B_3]\theta_1-(\phi^2S_3K_{\rm av}-\phi B_2)\theta_2\}\delta_{ij}+2\mu_3 d_{ij}^{(3)}+\mu_{1,3}d_{ij}^{(1)}. \tag{4.4}$$

Set

$$\begin{aligned}
&K_2=K_{\rm av}\phi^2,\quad C_{12}=B_1\phi-K_{\rm av}\phi^2S_1,\\
&C_{23}=B_2\phi-K_{\rm av}\phi^2S_3,\\
&K_1=H_1+(S_1\phi)^2K_{\rm av}-2S_1\phi B_1,\\
&K_3=H_3+(S_3\phi)^2K_{\rm av}-2S_3\phi B_2,\\
&C_{13}=S_1S_3\phi^2K_{\rm av}-S_3\phi B_1-S_1\phi B_2+B_3.
\end{aligned} \tag{4.5}$$

Then, the stress–strain relations (4.2)–(4.4) for constant porosity can be stated as follows:

$$\sigma_{ij}^{(1)}=(K_1\theta_1+C_{13}\theta_3+C_{12}\theta_2)\delta_{ij}+2\mu_1 d_{ij}^{(1)}+\mu_{1,3}d_{ij}^{(3)}, \tag{4.6}$$

$$\sigma_{ij}^{(3)}=(K_3\theta_3+C_{13}\theta_1+C_{23}\theta_2)\delta_{ij}+2\mu_3 d_{ij}^{(3)}+\mu_{1,3}d_{ij}^{(1)}, \tag{4.7}$$

$$-\phi p_f=C_{12}\theta_1+C_{23}\theta_3+K_2\theta_2. \tag{4.8}$$

Relations similar to Eqs. (4.6)–(4.8) were derived by Leclaire *et al.*[6] for the case of uniform porosity and when one of the solid phases is ice; it is also assumed in that paper that there is no contact between the solid and ice phases. This situation corresponds to the particular case in which $C_{13}=\mu_{1,3}=0$. Carcione and Tinivella[4] generalized the model of Leclaire *et al.*[6] to include interaction between the solid and ice phases and grain cementation with temperature and obtained stress–strain relations in the form given in Eqs. (4.6)–(4.8).

The nonsingular linear system of equations (4.5) yields the following expressions for the coefficients of the variable porosity formulation:

$$\begin{aligned}
&H_1=K_1+(S_1)^2K_2+2S_1C_{12},\\
&H_3=K_3+(S_3)^2K_2+2S_3C_{23},\\
&B_1=\frac{S_1K_2+C_{12}}{\phi},\quad B_2=\frac{S_3K_2+C_{23}}{\phi},\\
&B_3=(C_{13}+S_3C_{12}+S_1C_{23}+S_3S_1K_2),\quad K_{\rm av}=\frac{K_2}{\phi^2}.
\end{aligned} \tag{4.9}$$

In Appendix A the ideas presented in Refs. 6 and 4 are used to obtain formulas for the computation of the coefficients K_1, K_2, K_3, C_{12}, C_{13}, C_{23}, μ_1, μ_3, $\mu_{1,3}$, which combined with Eq. (4.9) allows for the evaluation of the moduli H_1, H_3, B_1, B_2, B_3, $K_{\rm av}$, needed for this new formulation. However, it must be remarked that appropriate theoretical (*gedanken*) experiments should be devised for a rigorous determination of these coefficients.

V. A LAGRANGIAN FORMULATION OF THE EQUATIONS OF MOTION

A. The kinetic energy density

Let $\mathcal{T}$ denote the kinetic energy density on Ω and let ρ_m, $m=1, 2, 3$ denote the mass density of each solid and fluid constituent in Ω. Also let $\phi_m=V_m/V_b$, $m=1, 3$ be the fractions of the two solid phases in the bulk material.

Let us consider the kinetic energy density in the solid parts Ω_1 and Ω_3. Here the argument follows the ideas presented in Ref. 4. Let us introduce the relative macrovelocity of each solid phase with respect to the other:

$$q_i^{(1,3)}=\phi_1(u_i^{(1)}-u_i^{(3)}),\quad q_i^{(3,1)}=\phi_3(u_i^{(3)}-u_i^{(1)}), \tag{5.1}$$

and denote $s_i^{(1,3)}$ and $s_i^{(3,1)}$ the corresponding relative microvelocity fields. Assuming that the relative flows of the solid phases are of laminar type, it follows that

$$s_i^{(1,3)}=\beta_{ij}^{(1,3)}\dot{q}_j^{(1,3)},\quad s_i^{(3,1)}=\beta_{ij}^{(3,1)}\dot{q}_j^{(3,1)}. \tag{5.2}$$

Note that by their definition,

$$\frac{1}{V_b}\int_{\Omega_1}s_i^{(1,3)}\,dx=\dot{q}_i^{(1,3)},\quad \frac{1}{V_b}\int_{\Omega_3}s_i^{(3,1)}\,dx=\dot{q}_i^{(3,1)}. \tag{5.3}$$

Then the kinetic energy densities $\mathcal{T}_1$ and $\mathcal{T}_3$ in Ω_1 and Ω_3 are given by

$$\mathcal{T}_1=\frac{1}{2}\frac{1}{V_b}\int_{\Omega_1}\rho_1(\dot{u}_i^{(3)}+s_i^{(1,3)})(\dot{u}_i^{(3)}+s_i^{(1,3)})dx=\frac{1}{2}\rho_1\phi_1\dot{u}_i^{(3)}\dot{u}_i^{(3)}+\rho_1\dot{u}_i^{(3)}\dot{q}_i^{(1,3)}+\frac{1}{2}n_{ij}^{(1,3)}\dot{q}_i^{(1,3)}\dot{q}_j^{(1,3)}, \tag{5.4}$$

$$\mathcal{T}_3=\frac{1}{2}\frac{1}{V_b}\int_{\Omega_3}\rho_3(\dot{u}_i^{(1)}+s_i^{(3,1)})(\dot{u}_i^{(1)}+s_i^{(3,1)})dx=\frac{1}{2}\rho_3\phi_3\dot{u}_i^{(1)}\dot{u}_i^{(1)}+\rho_3\dot{u}_i^{(3)}\dot{q}_i^{(3,1)}+\frac{1}{2}n_{ij}^{(3,1)}\dot{q}_i^{(3,1)}\dot{q}_j^{(3,1)}, \tag{5.5}$$

where

$$n_{ij}^{(1,3)}=\rho_1\frac{1}{V_b}\int_{\Omega_1}\beta_{ki}^{(1,3)}\beta_{kj}^{(1,3)}dx,$$

$$n_{ij}^{(3,1)}=\rho_3\frac{1}{V_b}\int_{\Omega_3}\beta_{ki}^{(3,1)}\beta_{kj}^{(3,1)}dx.$$

In terms or the original variables $u_i^{(1)}$, $u_i^{(3)}$ and for the case of statistical isotropy, (i.e., $n_{ij}^{(1,3)}=n^{(1,3)}\delta_{ij}$, $n_{ij}^{(3,1)}=n^{(3,1)}\delta_{ij}$), we can rewrite $\mathcal{T}_1$ and $\mathcal{T}_3$ in the form

$$\mathcal{T}_1=\tfrac{1}{2}((\phi_1)^2n^{(1,3)}-\rho_1\phi_1)\dot{u}_i^{(3)}\dot{u}_i^{(3)}+(\rho_1\phi_1-(\phi_1)^2n^{(1,3)})\dot{u}_i^{(1)}\dot{u}_i^{(3)}+\tfrac{1}{2}(\phi_1)^2n^{(1,3)}\dot{u}_i^{(1)}\dot{u}_i^{(1)}, \tag{5.6}$$

and

$$\mathcal{T}_3=\tfrac{1}{2}((\phi_3)^2 n^{(3,1)}-\rho_3\phi_3)\dot{u}_i^{(1)}\dot{u}_i^{(1)}+(\rho_3\phi_3 -(\phi_3)^2 n^{(3,1)})\dot{u}_i^{(1)}\dot{u}_i^{(3)}+\tfrac{1}{2}(\phi_3)^2 n^{(3,1)}\dot{u}_i^{(3)}\dot{u}_i^{(3)}. \quad (5.7)$$

Next, let us define the macroscopic relative velocities of the fluid with respect to the two solid phases:

$$w_i^{(m)}=\phi(u_i^{(2)}-u_i^{(m)}), \quad m=1,3. \quad (5.8)$$

Then if $v_i^{(1)}$ and $v_i^{(3)}$ denote the corresponding relative microvelocity fields, the assumption that the relative fluid flow is of laminar type yields

$$v_i^{(l)}=\alpha_{ij}^{(l,2)}\dot{w}_j^{(l)}, \quad l=1,3. \quad (5.9)$$

Since $(1/V_b)\int_{\Omega_2} v_i^{(l)}dx=\dot{w}_i^{(l)}$, $l=1$, 3, the kinetic energy density $\mathcal{T}_2$ in the fluid part Ω_2 is given by

$$\begin{aligned}\mathcal{T}_2=&\frac{1}{2}\frac{1}{V_b}\int_{\Omega_2}\rho_2(\dot{u}_i^{(1)}+v_i^{(1)})(\dot{u}_i^{(1)}+v_i^{(1)})dx\\&+\frac{1}{2}\frac{1}{V_b}\int_{\Omega_2}\rho_2((\dot{u}_i^{(3)}+v_i^{(3)}))(\dot{u}_i^{(3)}+v_i^{(3)}))\\&-\frac{1}{2}\rho_2\phi\dot{u}_i^{(2)}\dot{u}_i^{(2)}\\=&\frac{1}{2}\rho_2\phi\dot{u}_i^{(1)}\dot{u}_i^{(1)}+\rho_2\dot{u}_i^{(1)}\dot{w}_i^{(1)}+\frac{1}{2}m_{ij}^{(1,2)}\dot{w}_i^{(1)}\dot{w}_j^{(1)}\\&+\frac{1}{2}\rho_2\phi\dot{u}_i^{(3)}\dot{u}_i^{(3)}+\rho_2\dot{u}_i^{(3)}\dot{w}_i^{(3)}+\frac{1}{2}m_{ij}^{(3,2)}\dot{w}_i^{(3)}\dot{w}_j^{(3)}\\&-\frac{1}{2}\rho_2\phi\dot{u}_i^{(2)}\dot{u}_i^{(2)}, \end{aligned} \quad (5.10)$$

where

$$m_{ij}^{(l,2)}=\rho_2\frac{1}{V_b}\int_{\Omega_2}\alpha_{ki}^{(l,2)}\alpha_{kj}^{(l,2)}dx, \quad l=1,3.$$

Next, using that $u_i^{(2)}=w_i/\phi+S_1u_i^{(1)}+S_3u_i^{(3)}$ in Eq. (5.8) gives

$$\begin{aligned}w_i^{(1)}&=w_i+S_3\phi(u_i^{(3)}-u_i^{(1)}),\\w_i^{(3)}&=w_i+S_1\phi(u_i^{(1)}-u_i^{(3)}),\end{aligned} \quad (5.11)$$

and

$$\begin{aligned}w_i^{(1)}w_i^{(1)}&=w_iw_i+2S_3\phi w_i(u_i^{(3)}-u_i^{(1)})\\&\quad+(S_3\phi)^2(u_i^{(3)}-u_i^{(1)})(u_i^{(3)}-u_i^{(1)}),\\w_i^{(3)}w_i^{(3)}&=w_iw_i+2S_1\phi w_i(u_i^{(1)}-u_i^{(3)})\\&\quad+(S_1\phi)^2(u_i^{(3)}-u_i^{(1)})(u_i^{(3)}-u_i^{(1)}),\\w_i^{(1)}w_i^{(3)}&=w_iw_i+(S_3-S_1)\phi w_i(u_i^{(3)}-u_i^{(1)})\\&\quad-S_1S_3(\phi)^2(u_i^{(3)}-u_i^{(1)})(u_i^{(3)}-u_i^{(1)}).\end{aligned} \quad (5.12)$$

Using Eqs. (5.11) and (5.12) in Eq. (5.10), for the isotropic case the following expression for $\mathcal{T}_2$ is obtained:

$$\begin{aligned}\mathcal{T}_2=&[\tfrac{1}{2}\rho_2\phi+\tfrac{1}{2}(\phi)^2((S_3)^2m^{(1,2)}+(S_1)^2m^{(3,2)})-S_3\rho_2\phi-\tfrac{1}{2}(S_1)^2\rho_2\phi]\dot{u}_i^{(1)}\dot{u}_i^{(1)}\\&+[\rho_2+\phi(S_1m^{(3,2)}-S_3m^{(1,2)})-S_1\rho_2]\dot{u}_i^{(1)}\dot{w}_i+[\rho_2\phi-(\phi)^2((S_3)^2m^{(1,2)}+(S_1)^2m^{(3,2)})-S_1S_3\rho_2\phi]\dot{u}_i^{(1)}\dot{u}_i^{(3)}\\&+\frac{1}{2}\left[m^{(1,2)}+m^{(3,2)}-\frac{\rho_2}{\phi}\right]\dot{w}_i\dot{w}_i+[\rho_w+\phi(S_3m^{(1,2)}-S_1m^{(3,2)})-S_3\rho_2]\dot{w}_i\dot{u}_i^{(3)}\\&+[\tfrac{1}{2}\rho_2\phi+\tfrac{1}{2}(\phi)^2((S_3)^2m^{(1,2)}+(S_1)^2m^{(3,2)})-S_1\rho_2\phi-\tfrac{1}{2}(S_3)^2\rho_2\phi]\dot{u}_i^{(3)}\dot{u}_i^{(3)}.\end{aligned} \quad (5.13)$$

The kinetic energy density $\mathcal{T}$ in Ω is therefore

$$\mathcal{T}=\mathcal{T}_1+\mathcal{T}_2+\mathcal{T}_3. \quad (5.14)$$

Remark: The third term on the right-hand side of Eq. (5.13) represents dynamic interaction between the two solid phases.

B. Dissipation function

Here it is assumed that the dissipation function $\mathcal{D}$ is a quadratic non-negative form in the variables $(\dot{u}_i^{(3)}-\dot{u}_i^{(1)})$ and $\dot{w}_i$. Then, if η denotes the fluid viscosity, in the statistically isotropic case the dissipation function has the form

$$\mathcal{D}=\tfrac{1}{2}f_{11}(\dot{u}_i^{(3)}-\dot{u}_i^{(1)})(\dot{u}_i^{(3)}-\dot{u}_i^{(1)})+\tfrac{1}{2}f_{22}\dot{w}_i\dot{w}_i+f_{12}(\dot{u}_i^{(3)}-\dot{u}_i^{(1)})\dot{w}_i. \quad (5.15)$$

Remark: Appendix B contains the derivation of formulas to compute the mass and dissipation coefficients in the kinetic energy density $\mathcal{T}$ and the dissipation function $\mathcal{D}$ so that for the case of uniform porosity the model presented in Ref. 4 is obtained. Thus, this new model is a generalization to the nonuniform porosity case of the previous models proposed in Refs. 6 and 4.

C. The differential equations of motion

Set $u=(u_j)=(u_i^{(1)},w_i,u_i^{(3)})$, $1\leqslant i\leqslant 3$, $1\leqslant j\leqslant 9$. The Lagrangian formulation of the equations of motion for our system is

$$\frac{d}{dt}\left(\frac{\partial\mathcal{T}}{\partial\dot{u}_j}\right)+\frac{\partial\mathcal{D}}{\partial\dot{u}_j}=-\frac{\partial\mathcal{V}_d}{\partial u_j}, \quad 1\leqslant j\leqslant 9. \quad (5.16)$$

Next, combine Eqs. (2.13), (5.6), (5.7), (5.13)–(5.16) to conclude that the equations of motion can be written in the form:

$$p_{11}\ddot{u}_i^{(1)}+p_{12}\ddot{w}_i+p_{13}\ddot{u}_i^{(3)}+f_{11}\dot{u}_i^{(1)}-f_{12}\dot{w}_i-f_{11}\dot{u}_i^{(3)}$$
$$=\frac{\partial}{\partial x_j}[\sigma_{ij}^{(1)}-S_1\phi p_f\delta_{ij}], \tag{5.17}$$

$$p_{12}\ddot{u}_i^{(1)}+p_{22}\ddot{w}_i+p_{23}\ddot{u}_i^{(3)}-f_{12}\dot{u}_i^{(1)}+f_{22}\dot{w}_i+f_{12}\dot{u}_i^{(3)}=-\frac{\partial p_f}{\partial x_i}, \tag{5.18}$$

$$p_{13}\ddot{u}_i^{(1)}+p_{23}\ddot{w}_i+p_{33}\ddot{u}_i^{(3)}-f_{11}\dot{u}_i^{(1)}+f_{12}\dot{w}_i+f_{11}\dot{u}_i^{(3)}$$
$$=\frac{\partial}{\partial x_j}[\sigma_{ij}^{(3)}-S_3\phi p_f\delta_{ij}], \quad i=1,2,3. \tag{5.19}$$

The mass coupling coefficients in Eqs. (5.17)–(5.19) are given by

$$\begin{aligned}
p_{11}&=\rho_2\phi+(\phi)^2((S_3)^2m^{(1,2)}+(S_1)^2m^{(3,2)})-2S_3\rho_2\phi\\
&\quad-(S_1)^2\rho_2\phi+(\phi_1)^2n^{(1,3)}+(\phi_3)^2n^{(3,1)}-\phi_3\rho_3,\\
p_{12}&=p_{21}=\rho_2+\phi(S_1m^{(3,2)}-S_3m^{(1,2)})-S_1\rho_2,\\
p_{13}&=p_{31}=\rho_2\phi-(\phi)^2((S_3)^2m^{(1,2)}+(S_1)^2m^{(3,2)})\\
&\quad-S_1S_3\rho_2\phi+\rho_1\phi_1-(\phi_1)^2n^{(1,3)}+\rho_3\phi_3\\
&\quad-(\phi_3)^2n^{(3,1)},\\
p_{22}&=m^{(1,2)}+m^{(3,2)}-\frac{\rho_2}{\phi},\\
p_{23}&=p_{32}=\rho_w+\phi(S_3m^{(1,2)}-S_1m^{(3,2)})-S_3\rho_2,\\
p_{33}&=\rho_2\phi+(\phi)^2((S_3)^2m^{(1,2)}+(S_1)^2m^{(3,2)})-2S_1\rho_2\phi\\
&\quad-(S_3)^2\rho_2\phi+(\phi_1)^2n^{(1,3)}+(\phi_3)^2n^{(3,1)}-\phi_1\rho_1.
\end{aligned} \tag{5.20}$$

The coefficients p_{ij} in Eq. (5.20) can be written in terms of the tortuosities a_{13}, a_{31}, a_{12}, and a_{32} defined in Refs. 4 and 6 as follows:

$$\begin{aligned}
&n^{(1,3)}=a_{13}\frac{\rho_1}{\phi_1}, \quad n^{(3,1)}=a_{31}\frac{\rho_3}{\phi_3},\\
&m^{(1,2)}=a_{12}\frac{\rho_2}{\phi}, \quad m^{(3,2)}=a_{32}\frac{\rho_2}{\phi},\\
&a_{12}=\frac{\phi_1\rho}{\phi\rho_2}r_{12}+1, \quad a_{32}=\frac{\phi_3\rho'}{\phi\rho_2}r_{32}+1,\\
&a_{13}=\frac{\phi_3\rho'}{\phi_1\rho_1}r_{13}+1, \quad a_{31}=\frac{\phi_1\rho}{\phi_3\rho_3}r_{31}+1,
\end{aligned} \tag{5.21}$$

where r_{ij} are the geometrical aspects of the boundaries separating the phases i and j (equal to $\frac{1}{2}$ for spheres) and

$$\rho=\frac{\phi\rho_2+\phi_3\rho_3}{\phi+\phi_3}, \quad \rho'=\frac{\phi\rho_2+\phi_1\rho_1}{\phi+\phi_1}.$$

Using the relations (5.21) in Eq. (5.20) yields

$$\begin{aligned}
p_{11}&=\rho_2\phi(1+(S_1)^2a_{32}+(S_3)^2a_{12}-2S_3-(S_1)^2)\\
&\quad+a_{13}\rho_1\phi_1+(a_{31}-1)\rho_3\phi_3,\\
p_{12}&=\rho_2(S_3(1-a_{12})+S_1a_{32}),\\
p_{13}&=\rho_2\phi(1-(S_1)^2a_{32}-(S_3)^2a_{12}-S_1S_3)\\
&\quad+\rho_1\phi_1(1-a_{13})+\rho_3\phi_3(1-a_{31}),\\
p_{22}&=\frac{\rho_2}{\phi}(a_{12}+a_{32}-1),\\
p_{23}&=\rho_2(S_1(1-a_{32})+S_3a_{12}),\\
p_{33}&=\rho_2\phi(1+(S_1)^2a_{32}+(S_3)^2a_{12}-2S_1-(S_3)^2)\\
&\quad+a_{31}\rho_3\phi_3+(a_{13}-1)\rho_1\phi_1.
\end{aligned} \tag{5.22}$$

In Appendix B the mass coefficients p_{ij} are related to the mass coefficients of the previous formulations in Refs. 6 and 4.

VI. PLANE WAVE ANALYSIS

Let ω denote the angular temporal frequency and let us define the matrices $\mathcal{M}\in\mathbf{R}^{7\times7}$, $\mathcal{E}\in\mathbf{R}^{7\times7}$ be defined by

$$\mathcal{M}=\begin{bmatrix}
m_{11} & 0 & 0 & m_{12} & m_{13} & 0 & 0\\
0 & q_1 & 0 & 0 & 0 & q_2 & 0\\
0 & 0 & q_1 & 0 & 0 & 0 & q_2\\
m_{12} & 0 & 0 & m_{22} & m_{33} & 0 & 0\\
m_{13} & 0 & 0 & m_{23} & m_{33} & 0 & 0\\
0 & q_2 & 0 & 0 & 0 & q_3 & 0\\
0 & 0 & q_2 & 0 & 0 & 0 & q_3
\end{bmatrix},$$

and

$$\mathcal{E}=\begin{bmatrix}
H_1+\frac{4}{3}\mu_1 & 0 & 0 & B_1 & B_3+\frac{2}{3}\mu_{13} & 0 & 0\\
0 & \mu_1 & 0 & 0 & 0 & \frac{1}{2}\mu_{13} & 0\\
0 & 0 & \mu_1 & 0 & 0 & 0 & \frac{1}{2}\mu_{13}\\
B_1 & 0 & 0 & K_{av} & B_2 & 0 & 0\\
B_3+\frac{2}{3}\mu_{13} & 0 & 0 & B_2 & H_3+\frac{4}{3}\mu_3 & 0 & 0\\
0 & \frac{1}{2}\mu_{13} & 0 & 0 & 0 & \mu_3 & 0\\
0 & 0 & \frac{1}{2}\mu_{13} & 0 & 0 & 0 & \mu_3
\end{bmatrix},$$

where

$$\begin{aligned}
&m_{11}=p_{11}-i\frac{f_{11}}{\omega}, \quad m_{12}=p_{12}+i\frac{f_{12}}{\omega}, \quad m_{13}=p_{13}+i\frac{f_{11}}{\omega},\\
&m_{22}=p_{22}-i\frac{f_{22}}{\omega}, \quad m_{23}=p_{23}+i\frac{f_{12}}{\omega}, \quad m_{33}=p_{33}+i\frac{f_{11}}{\omega},\\
&q_1=m_{11}-\frac{(m_{12})^2}{m_{22}}, \quad q_2=m_{13}-\frac{m_{12}m_{23}}{m_{22}},\\
&q_3=m_{33}-\frac{(m_{23})^2}{m_{22}}.
\end{aligned}$$

Set

$$\mathcal{S}=\mathcal{E}^{-1}\mathcal{M}. \tag{6.1}$$

Then a generalization of the argument using plane waves given by Santos *et al.*[14] shows that after finding the complex eigenvalues $1/(c_m)^2$, $m=1,...,7$ of the matrix $\mathcal{S}$ by solving

$\det(\mathcal{S}-(1/c^2)I)=0$, the phase velocities α_m and the attenuation coefficients d_m (in dB) of the compressional and shear waves are obtained in terms of c_m from

$$\alpha_m=\frac{1}{\mathrm{Re}(c_m)}, \quad d_m=2\pi 8.685\,889\left|\frac{\mathrm{Im}(c_m)}{\mathrm{Re}(c_m)}\right|. \tag{6.2}$$

Three of the eigenvalues of the matrix $\mathcal{S}$, associated with the first, fourth, and fifth rows and columns are related with the compressional modes, while of the other four eigenvalues only two of them are different and they are related with the two shear modes of propagation. These wave modes are in agreement with those predicted previously in Refs. 6, 7, and 4.

The experimental observation of the additional (slow) waves was reported by Leclaire *et al.*[7] The slow wave modes are important to explain attenuation and dispersion effects observed on the faster modes associated with scattering phenomena due to the presence of heterogeneities inside the composite poroelastic materials being analyzed.

VII. AN EXISTENCE AND UNIQUENESS RESULT

Let the positive definite mass matrix $\mathcal{P}\in\mathbf{R}^{9\times 9}$ and the non-negative dissipation matrix $\mathcal{C}\in\mathbf{R}^{9\times 9}$ be defined by

$$\mathcal{P}=\begin{bmatrix} p_{11}I & p_{12}I & p_{13}I \\ p_{12}I & p_{22}I & p_{23}I \\ p_{13}I & p_{23}I & p_{33}I \end{bmatrix},$$

$$\mathcal{C}=\begin{bmatrix} f_{11}I & -f_{12}I & -f_{11}I \\ -f_{12}I & f_{22}I & f_{12}I \\ -f_{11}I & f_{12}I & f_{11}I \end{bmatrix},$$

where I denotes the identity matrix in $\mathbf{R}^{3\times 3}$. Also, let $\mathcal{L}(u)$ be the second-order differential operator defined by

$$\mathcal{L}(u)=\{\boldsymbol{\nabla}\cdot[\sigma_{ij}^{(1)}(u)-S_1\phi p_f(u)\,\delta_{ij}], -\boldsymbol{\nabla}p_f(u), \boldsymbol{\nabla}\cdot[\sigma_{ij}^{(3)}(u)-S_3\phi p_f(u)\,\delta_{ij}]\}.$$

Then the equations of motion (5.17)–(5.19) can be stated in the form

$$\mathcal{P}\frac{\partial^2 u}{\partial t^2}+\mathcal{C}\frac{\partial u}{\partial t}-\mathcal{L}(u)=f(x,t),$$

$$(x,t)\in\Omega\times(0,T)\equiv\Omega\times J. \tag{7.1}$$

Let us consider the solution of Eq. (7.1) with initial conditions

$$u(x,0)=u^0, \quad \frac{\partial u}{\partial t}(x,0)=v^0, \quad x\in\Omega, \tag{7.2}$$

and boundary conditions

$$(\sigma_{ij}^{(1)}(u)-S_1\phi p_f(u)\,\delta_{ij})\nu_j=-g^{(1)}, \quad (x,t)\in\partial\Omega\times J, \tag{7.3}$$

$$(\sigma_{ij}^{(3)}(u))-S_3\phi p_f(u)\,\delta_{ij})\nu_j=-g^{(3)}, \quad (x,t)\in\partial\Omega\times J, \tag{7.4}$$

$$p_f(u)=g^{(2)}, \quad (x,t)\in\partial\Omega\times J. \tag{7.5}$$

To state a weak form of problem (7.1)–(7.5) some notation needs to be introduced. Let $(\cdot,\cdot)$ and $\langle\cdot,\cdot\rangle$ denote the usual inner products in $L^2(\Omega)$ and $L^2(\partial\Omega)$, respectively. Also, for any real number s and $E=\Omega$, $\partial\Omega$ let $H^s(E)$ denote the usual Sobolev space with corresponding norm $\|\cdot\|_{s,E}$. Let

$$H(\mathrm{div},\Omega)=\{v\in[L^2(\Omega)]^3:\boldsymbol{\nabla}\cdot v\in L^2(\Omega)\},$$
$$V=[H^1(\Omega)]^3\times H(\mathrm{div},\Omega)\times[H^1(\Omega)]^3, \tag{7.6}$$

with the natural norm

$$\|v\|_V=[\|v^{(1)}\|_{1,\Omega}^2+\|v^{(3)}\|_{1,\Omega}^2+\|v^{(2)}\|_{H(\mathrm{div},\Omega)}^2]^{1/2},$$

$$v=(v^{(1)},v^{(2)},v^{(3)})\in V.$$

Set

$$\Lambda(u,v)=(\sigma_{ij}^{(1)}(u)-S_1\phi p_f(u)\,\delta_{ij},\epsilon_{ij}(v^{(1)})+(\sigma_{ij}^{(3)}(u)-S_3\phi p_f(u)\,\delta_{ij},\epsilon_{ij}(v^{(3)})-(p_f(u),\boldsymbol{\nabla}\cdot v^2). \tag{7.7}$$

Next recall that the strain energy density $\mathcal{W}$ in Eq. (3.1) is a positive definite quadratic form in the variables $\epsilon_{ij}(u^{(1)})$, $\epsilon_{ij}(u^{(3)})$, and ζ, which implies that

$$\mathcal{W}(u)\geq M\left[\sum_{ij}((\epsilon_{ij}(u^{(1)}))^2+(\epsilon_{ij}(u^{(3)}))^2)+\zeta^2\right], \tag{7.8}$$

and consequently applying Korn's second inequality[15,16] it follows that

$$\begin{aligned}\Lambda(u,u)&\geq M\int_\Omega\left[\sum_{ij}((\epsilon_{ij}(u^{(1)}))^2+(\epsilon_{ij}(u^{(3)}))^2)+(\boldsymbol{\nabla}\cdot w)^2\right]d\Omega\\ &\geq M_1[\|u^{(1)}\|_{1,\Omega}^2+\|u^{(3)}\|_{1,\Omega}^2+\|w\|_{H(\mathrm{div},\Omega)}^2]-M_2\|u\|_{0,\Omega}^2, \quad \forall u\in V.\end{aligned} \tag{7.9}$$

In Eqs. (7.8) and (7.9) M, M_1, and M_2 denote positive constants depending only on the upper and lower bounds of the coefficients of our differential problem and the domain Ω.

Next, the weak form of problem (7.1)–(7.5) is obtained as usual by multiplying Eq. (7.1) by $v\in V$ and integrating the result over Ω, using integration by parts in the $(\mathcal{L}(u),v)$-term and applying the boundary conditions (7.3)–(7.5). Thus a variational form for our problem can be formulated as follows: find the map u: $J\to V$ such that

$$\left(\mathcal{P}\frac{\partial^2 u}{\partial t^2},v\right)+\left(\mathcal{C}\frac{\partial u}{\partial t},v\right)+\Lambda(u,v)+\langle g^{(1)},v^{(1)}\rangle+\langle g^{(3)},v^{(3)}\rangle+\langle v^{(2)}\cdot\nu,g^{(2)}\rangle=(f,v), \quad v\in V, \quad t\in J. \tag{7.10}$$

Set

$$Q_r^2=\left\|\frac{\partial^r f}{\partial t^r}\right\|_{L^2(J,[L^2(\Omega)]^9)}+\left\|\frac{\partial^r g^{(1)}}{\partial t^r}\right\|_{L^\infty(J,[H^{-1/2}(\partial\Omega)]^3)}+\left\|\frac{\partial^{r+1} g^{(1)}}{\partial t^{r+1}}\right\|_{L^2(J,[H^{-1/2}(\partial\Omega)]^3)}+\left\|\frac{\partial^r g^{(3)}}{\partial t^r}\right\|_{L^\infty(J,[H^{-1/2}(\partial\Omega)]^3)}+\left\|\frac{\partial^{r+1} g^{(3)}}{\partial t^{r+1}}\right\|_{L^2(J,[H^{-1/2}(\partial\Omega)]^3)}+\left\|\frac{\partial^r g^{(2)}}{\partial t^r}\right\|_{L^\infty(J,H^{1/2}(\partial\Omega))}+\left\|\frac{\partial^{r+1} g^{(2)}}{\partial t^{r+1}}\right\|_{L^2(J,H^{1/2}(\partial\Omega))},\tag{7.11}$$

$$P^2=\|u^0\|_{2,\Omega}^2+\|v^0\|_{1,\Omega}^2+\|f(x,0)\|_{0,\Omega}^2+1.\tag{7.12}$$

Let us state a theorem about the existence, uniqueness, and regularity of the solution u of problem (7.1)–(7.5). The proof is similar to that given by Santos *et al.*[17] for the case in which the porous solid matrix consists of only one solid phase and is omitted.

Theorem 1: *Let* f, $g^{(1)}$, $g^{(2)}$, $g^{(3)}$, u^0, v^0 *be given and such that* $Q_0<\infty$, $Q_1<\infty$, $P<\infty$. *Then there exists a unique solution* $u(x,t)$ *of (7.1)–(7.5) such that* u, $\partial u/\partial t\in L^\infty(J,V)$ *and* $\partial^2 u/\partial t^2\in L^\infty(J,[L^2(\Omega)]^9)$.

VIII. EXAMPLES

A. Shaley sandstones

The theory can be applied to various composite media, such as shaley sandstones,[1] permafrost,[3,18] gas-hydrate bearing sediments,[4] and frozen foods.[5] Let us consider a shaley sandstone, and denote the sand fraction by S_1 and the clay fraction by S_3. As stated previously, the theory predicts three compressional waves (P waves) and two shear waves (S waves), whose phase velocities can be obtained by solving the eigensystem resulting from the equation of motion as indicated in Sec. VI [cf. Eq. (6.2)]; see also Ref. 1. In this example, we consider the faster P and S waves.

The bulk and shear moduli of the sand and clay (dry) matrices versus porosity ϕ are obtained from a relationship proposed by Krief *et al.*[19] using formulas (A6) and (A7) in Appendix A. We consider the data set published by Han *et al.*[20] obtained at a confining pressure of 40 MPa. Han and his co-workers provide ultrasonic measurements of P- and S-wave velocities for 75 sandstone samples with porosities ranging from 2% to 30% and clay content from 0 to 50%. One feature of this data set is that a small amount of clay significantly softens the rock moduli, leading to reduced velocities. Table I shows the properties of the different constituents. The friction coefficients and permeabilities are calculated by using the equations given in Appendix B. Moreover, the mass coefficients are $r_{12}=r_{32}=r_{13}=r_{31}=1/2$. The predictions of the theory against the measurements obtained by Han *et al.*[20] are shown in Figs. 1(a) and (b), where $A=2$ and $a=0.5$ [see Eqs. (A6) and (A7)]. To fit the experimental data a frequency of 5 kHz was assumed. Strictly speaking, this is not correct since the data have been acquired at ultrasonic frequencies of the order of hundreds of kilohertz. However, it is well known that Biot-type dissipation mechanisms alone do not account for the level of attenuation observed in rocks. A correct description of this phenomenon would require the generalization of the different stiffness moduli to relaxation functions.[10] However, this fact reflects the robustness of the model for this particular example. The figure shows the compressional and shear velocities versus porosity, where each curve corresponds to a dif-

TABLE I. Material properties of the clay-bearing sandstone.

Solid grain	Bulk modulus, K_{s1}	39 GPa
	Shear modulus, μ_{s1}	39 GPa
	Density, ρ_1	2650kg/m^3
	Average radius, R_{s1}	50 μm
Clay	Bulk modulus, K_{s3}	20 GPa
	Shear modulus, μ_{s3}	10. GPa
	Density, ρ_3	2650kg/m^3
	Average radius, R_{s3}	1 μm
Fluid	Bulk modulus, K_f	2.4 GPa
	Density, ρ_2	1000kg/m^3
	Viscosity, η	1.798cP

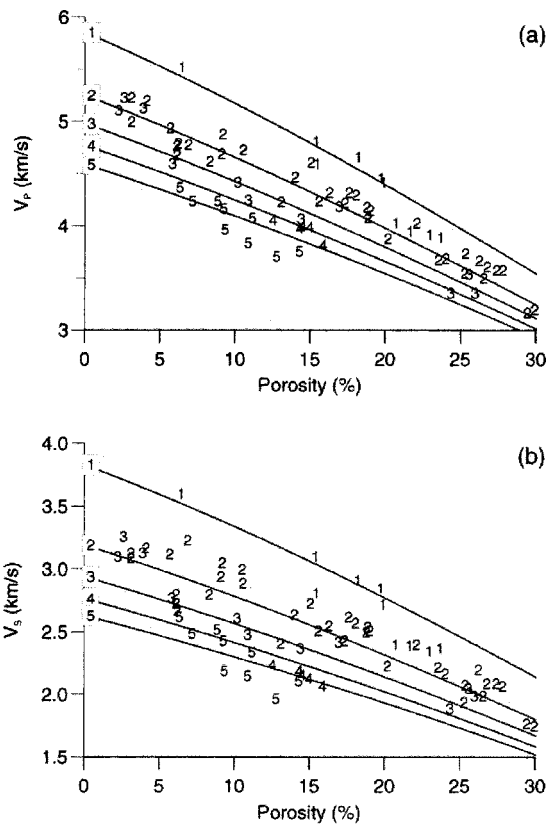

FIG. 1. Velocities of the faster compressional (a) and shear (b) waves vs porosity ϕ for different values of clay content S_3, indicated by the numbers inside the boxes (1: $S_3=0\%$, 2: $S_3=10\%$, 3: $S_3=20\%$, 4: $S_3=30\%$ and 5: $S_3=40\%$). The experimental data, represented with numbers, correspond to the data set published by Han *et al.* (Ref. 20). In this case, 1, 2, 3, 4, and 5 correspond to S_3 values in the ranges $[S_3,S_3+5\%]$, $S_3=0,...,40\%$. The frequency is 5 kHz.

ferent value of the clay content S_3. The root-mean-square deviation computed for all samples, apart from five outliers for P waves and seven outliers for S waves, is 93 m/s for the P-wave velocity and 100 m/s for the S-wave velocity.

B. Permafrost

To illustrate the use of the variable-porosity differential equations, let us consider wave propagation through an interface separating two sandstones with different ice content. Basically, the model consists of two homogeneous half spaces separated by a plane boundary. The upper medium is the sandstone used in the examples of Carcione and Seriani,[18] with no ice in the pores. It has a porosity of 20% when the medium is unfrozen. The lower media has 90% ice content in the pores. In this case the bulk and shear moduli of the sandstone and ice matrices are computed using a percolation model as indicated in Appendix A. We omit the properties of the sandstone (including the ice and water properties) since they are given in Ref. 18 [the properties correspond to those of Figs. 2(b) and 3(c) of that paper].

The time stepping method is a Runge–Kutta fourth-order algorithm, and the spatial derivatives are calculated with the Fourier method by using the fast Fourier transform.[13] This spatial approximation is infinitely accurate for band-limited periodic functions with cutoff spatial wave numbers which are smaller than the cutoff wave numbers of the mesh. Since the presence of quasistatic modes makes the differential equations stiff, a time-splitting integration algorithm is used to solve the stiff part analytically. Due to the splitting algorithm, the modeling is second-order accurate in the time discretization. The method is illustrated in detail in Carcione and Helle[21] for a two-phase medium and in Carcione and Seriani[18] for a three-phase medium.

A 357×357 mesh is used, with square cells and a grid spacing of 14 m (the model has a dimension of approximately 5×5 km). The source is a vertical force with a dominant frequency of 12 Hz, applied at 380 m above the interface. The time step required by the Runge–Kutta algorithm is 0.5 ms. Snapshots of the wave field at 0.6 s are shown in Fig. 2. The faster P and S waves and planar head waves can be seen in the snapshots. Strong converted waves, interpreted as slow waves, can be observed in the lower medium. The high amplitudes of the slow waves at low frequencies can be due to the very high permeability of the ice frame ($5\times10^{-4}\,\mathrm{m}^2$).

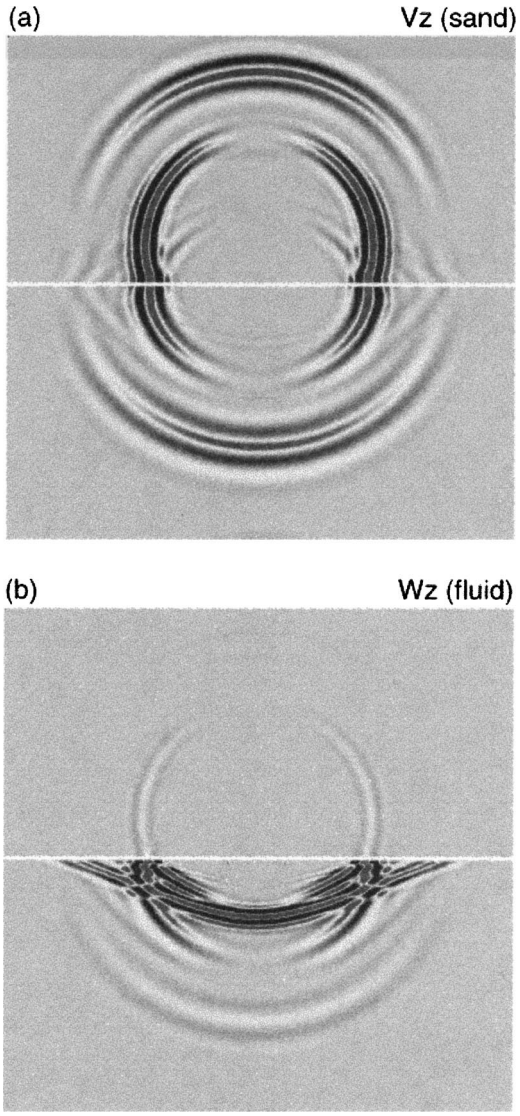

FIG. 2. Snapshots of the particle velocities of the frame (a) and particle velocity of the fluid relative to the solid phases (b) at 0.6 s. The upper medium is unfrozen and the lower medium has an ice content of 90%. The source is a vertical force in the frame with a central frequency of 12 Hz. Its location is 380 m above the interface. The ratio maximum amplitude in (a) to maximum amplitude in (b) is 547.

IX. CONCLUSIONS

A theory was developed to study the processes of deformation and wave propagation in porous media composed of three interacting phases (two solids and one fluid), for the case of spatially variable porosity. The model, based on first principles, can be generalized to the case of multiple solid constituents. Appropriate constitutive relations were established, and equivalence between the elastic moduli and those corresponding to the uniform porosity case, given in previous formulations, was found, which can also be related to known petrophysical models. Using the classical Lagrangian approach, the differential equations of motion were obtained and the problem of existence and uniqueness of the solution under appropriate initial and boundary conditions was analyzed. It was shown that five wave modes can propagate in this composite medium (three compressional and two shear waves).

The model was applied to the study of two geophysical problems. First, the phase velocities of the faster waves in a shaley sandstone were computed for different values of water saturation and clay content. The predictions of our model agree very well with the observations. The second application consists of the numerical simulation of the wave fields generated by a point source within a frozen sandstone with variable ice content. The simulation reveals strong wave-mode conversions, indicating that the model can be useful to study the freezing conditions of porous media.

In future works simulations in heterogeneous media will be performed and the effects that the slow waves (modes)

have on the faster modes will be analyzed. The present paper has been written to obtain (and justify) the differential equations for such media.

ACKNOWLEDGMENT

This work was funded in part by CONICET, Argentina (PIP 0363/98).

APPENDIX A: A FORM OF COMPUTING THE COEFFICIENTS IN THE CONSTITUTIVE RELATIONS

This section presents a form of evaluating the coefficients in the stress–strain relations (4.6)–(4.8), which combined with Eq. (4.9) yield the values of the coefficients for this new variable porosity formulation.

Let $K_{s1,m}$, $K_{s3,m}$, $\mu_{s1,m}$, and $\mu_{s3,m}$ denote the bulk and shear modulus of the two solid (dry) frames, respectively. In Appendices A1 and A2 it is indicated how to determine these moduli for the two examples presented in this paper. Also, let K_{s1}, μ_{s1}, K_{s3}, μ_{s3} denote the bulk and shear moduli of the grains in the two solid phases, respectively, and let K_f denote the bulk modulus of the fluid phase. For the coefficients μ_1, μ_3, and μ_{13} the formulas given in Ref. 4 were used:

$$\mu_j=[(1-g_j)\phi_j]^2\mu_{\rm av}+\mu_{sj,m},\quad g_j=\frac{\mu_{sj,m}}{\phi_j\mu_{sj}},\quad j=1,3,$$
$$\mu_{13}=(1-g_1)(1-g_3)\phi_1\phi_3\mu_{\rm av}, \tag{A1}$$
$$\mu_{\rm av}=\left[\frac{(1-g_1)\phi_1}{\mu_{s1}}+\frac{\phi}{2\omega\eta}+\frac{(1-g_3)\phi_3}{\mu_{s3}}\right]^{-1},$$

where g_1 and g_3 are the so-called shear consolidation coefficients of the solid frames 1 and 3.[6] The symbol ω in the definition of $\mu_{\rm av}$ above denotes the angular frequency.

Also, since $K_2=\phi^2K_{\rm av}$, [cf. Eq. (4.5)], to determine K_2 the following expression for $K_{\rm av}$ given in Ref. 4 is used:

$$K_{\rm av}=\left[(1-c_1)\frac{\phi_1}{K_{s1}}+\frac{\phi}{K_f}+(1-c_3)\frac{\phi_3}{K_{s3}}\right]^{-1}. \tag{A2}$$

The remaining elastic coefficients are given by[4]

$$K_j=[(1-c_j)\phi_j]^2K_{\rm av}+K_{sj,m},\quad c_j=\frac{K_{sj,m}}{\phi_jK_{sj}},\quad j=1,3,$$
$$C_{12}=(1-c_1)\phi_1\phi K_{\rm av}, \tag{A3}$$
$$C_{13}=(1-c_1)(1-c_3)\phi_1\phi_3K_{\rm av},$$
$$C_{23}=(1-c_3)\phi\phi_3K_{\rm av},$$

where c_1, c_3 are the bulk consolidation coefficients of the solid frames 1 and 3.

These elastic moduli for constant porosity can be rewritten in terms of a set of coefficients analogous to those given by Gassmann[22] as follows:

$$K_j=K_{Gj}-2\alpha_jS_j\phi K_{\rm av}+(S_j\phi)^2K_{\rm av},\quad j=1,3,$$
$$C_{12}=\phi K_{\rm av}(\alpha_1-S_1\phi),\quad C_{23}=\phi K_{\rm av}(\alpha_3-S_3\phi), \tag{A4}$$
$$C_{13}=K_{\rm av}(\alpha_1-S_1\phi)(\alpha_3-S_3\phi),$$

where

$$K_{Gj}=K_{sj,m}+(\alpha_j)^2K_{\rm av},\quad \alpha_j=S_j-\frac{K_{sj,m}}{K_{sj}},\quad j=1,3. \tag{A5}$$

The moduli K_{G1} and K_{G3} are analogous to Gassmann's modulus (a calculation shows that $K_{Gj}=H_j$, H_j, $j=1,3$), while the coefficients α_1 and α_3 correspond to the effective stress coefficients in the classic Biot theory.[10,13] The bulk and shear moduli $K_{s1,m}$, $K_{s3,m}$, $\mu_{s1,m}$ and $\mu_{s3,m}$ in Eqs. (A1) and (A5) can be determined in several fashions. In some cases, they can be obtained from the measurements of compressional and shear wave velocities on the empty rock or alternatively, they can be estimated using known petrophysical models. The procedure used in this paper to determine those moduli for the cases of shaley sandstones and frozen porous media is indicated in the following.

1. The case of shaley sandstones

The porosity dependence of the sand and clay (dry) matrices is consistent with the concept of critical porosity, since the moduli should vanish above a certain value of the porosity (usually from 0.4 to 0.5). This dependence is determined by the empirical coefficient A in Eq. (A6). In some rocks there is an abrupt change of rock matrix properties with the addition of a small amount of clay, attributed to softening of cements, clay swelling, and surface effects.[23] That is, the wave velocities decrease significantly when the clay content increases from 0 to a few percentages. In order to model this effect, the shear modulus of the sand matrix is multiplied by a factor depending on the empirical coefficient a in Eq. (A7) (this factor tends to 1 when $a\to\infty$). If Ω_1 represents the sand and Ω_3 the clay minerals, then the bulk and shear moduli of the sand and clay (dry) matrices are assumed to satisfy

$$K_{sj,m}=S_jK_{sj}(1-\phi)^{1+A/(1-\phi)},\quad j=1,3, \tag{A6}$$
$$\mu_{s1,m}=\exp\{-[(1-S_3)S_3)]^a\}K_{s1,m}\mu_{s1}/K_{s1},$$
$$\mu_{s3,m}=K_{s3,m}\mu_{s3}/K_{s3}. \tag{A7}$$

2. The case of frozen porous media

Following Refs. 6 and 4 it is assumed that $K_{s1,m}$ is known, and that the other modulus may be computed using a percolation-type model with critical exponent 3.8.[24] As explained by Leclaire *et al.*,[6] the percolation theory is used here to describe the transition of a system from the continuous to the discontinuous state, which is governed by a power law independent of the system material. Hence, $\mu_{s1,m}$, $\mu_{s3,m}$ and $K_{s3,m}$ are obtained using

$$\mu_{sj,m}=[\mu_{sj,m}^{(\max)}-\mu_{sj,m}^0]\left[\frac{\phi_3}{1-\phi_1}\right]^{3.8}+\mu_{sj,m}^0,\quad j=1,3,$$
$$K_{s3,m}=[K_{s3,m}^{(\max)}-K_{s3,m}^0]\left[\frac{\phi_3}{1-\phi_1}\right]^{3.8}+K_{s3,m}^0, \tag{A8}$$

where $\mu_{s1,m}^{(\max)}$, $\mu_{s3,m}^{(\max)}$, and $K_{s3,m}^{(\max)}$ are computed using Kuster and Toksöz's model,[25] taking the known values of K_{s1}, μ_{s1}, K_{s3}, μ_{s3} for the background medium with inclusions of air, with properties K_a, μ_a. For the solid matrix Ω_1 the concentration of inclusions is $c=1-\phi_1$ and for the ice matrix Ω_3

we consider that the water is totally frozen, i.e., $c=\phi_1$. The moduli $\mu^0_{s1,m}$, $\mu^0_{s3,m}$, and $K^0_{s3,m}$ are appropriate reference values. Here it is assumed that[4]

$$K^0_{s3,m}=\mu^0_{s3,m}=0. \tag{A9}$$

For variable temperatures, the porosity (or water proportion) may be computed as function of temperature using the expressions given in Refs. 6 and 4.

APPENDIX B: IDENTIFICATION OF THE MASS AND DISSIPATIVE COEFFICIENTS FROM PREVIOUS FORMULATIONS

In this section it is shown that under the assumption of uniform porosity from Eqs. (5.17) to (5.19) the equations of motion in the form presented in Refs. 6 and 4 are obtained.

First, use Eqs. (2.7) and (5.18) in Eq. (5.17) to obtain

$$\begin{aligned}\frac{\partial}{\partial x_j}\sigma^{(1)}_{ij}=&(p_{11}-2S_1\phi p_{12}+(S_1\phi)^2p_{22}))\ddot{u}^{(1)}_i+\phi(p_{12}\\&-S_1\phi p_{22})\ddot{u}^{(2)}_i+(p_{13}-S_1\phi p_{23}-S_3\phi p_{12}\\&+S_1S_3(\phi)^2p_{22})\ddot{u}^{(3)}_i-\phi(f_{12}+S_1\phi f_{22})\\&\times(\dot{u}^{(2)}_i-\dot{u}^{(1)}_i)-(f_{11}+(S_1-S_3)\phi f_{12}\\&-S_1S_3(\phi)^2f_{22})(\dot{u}^{(3)}_i-\dot{u}^{(1)}_i).\end{aligned} \tag{B1}$$

Next, setting $\sigma=-\phi p_f$, it follows from Eq. (5.18) that

$$\begin{aligned}\frac{\partial}{\partial x_i}\sigma=&\phi(p_{12}-S_1\phi p_{22}))\ddot{u}^{(1)}_i+(\phi)^2p_{22}\ddot{u}^{(2)}_i+\phi(p_{23}\\&-S_3\phi p_{22})\ddot{u}^{(3)}_i+\phi(f_{12}+S_1\phi f_{22})(\dot{u}^{(2)}_i-\dot{u}^{(1)}_i)\\&+\phi(S_3\phi f_{22}-f_{12})(\dot{u}^{(2)}_i-\dot{u}^{(3)}_i).\end{aligned} \tag{B2}$$

Also, using Eqs. (2.7) and (5.18) in Eq. (5.19) yields

$$\begin{aligned}\frac{\partial}{\partial x_j}\sigma^{(3)}_{ij}=&(p_{13}-S_1\phi p_{23}-S_3\phi p_{12}+S_1S_3(\phi)^2p_{22})\ddot{u}^{(1)}_i\\&+\phi((p_{23}-S_3\phi p_{22})\ddot{u}^{(2)}_i+(p_{33}-2S_3\phi p_{23}\\&+(S_3\phi)^2p_{22})\ddot{u}^{(3)}_i-\phi(S_3\phi f_{22}-f_{12})\\&\times(\dot{u}^{(2)}_i-\dot{u}^{(3)}_i)+(f_{11}+(S_1-S_3)\phi f_{12}\\&-S_1S_3(\phi)^2f_{22})(\dot{u}^{(3)}_i-\dot{u}^{(1)}_i).\end{aligned} \tag{B3}$$

Using the expressions given in Eq. (5.22) a calculation shows the following equivalence between the mass coefficients defined in Ref. 4 and the new coefficients p_{ij}:

$$\begin{aligned}\rho_{11}\equiv&p_{11}-2S_1\phi p_{12}+(S_1\phi)^2p_{22}\\&=\rho_1\phi_1a_{13}+\rho_2\phi_2(a_{12}-1)+\rho_3\phi_3(a_{31}-1),\\\rho_{12}\equiv&\phi(p_{12}-S_1\phi p_{22})=-\rho_2\phi(a_{12}-1)),\\\rho_{13}\equiv&p_{13}-S_1\phi p_{23}-S_3\phi p_{12}+S_1S_3(\phi)^2p_{22}\\&=-\rho_1\phi_1(a_{13}-1)-\rho_3\phi_3(a_{31}-1),\\\rho_{22}\equiv&(\phi)^2p_{22}=\rho_2\phi_2(a_{12}+a_{32}-1),\\\rho_{23}\equiv&\phi(p_{23}-S_3\phi p_{22})=-\rho_2\phi(a_{32}-1),\\\rho_{33}\equiv&p_{33}-2S_3\phi p_{23}+(S_3\phi)^2p_{22}\\&=\rho_1\phi_1(a_{13}-1)+\rho_2\phi_2(a_{32}-1)+\rho_3\phi_3a_{31}.\end{aligned} \tag{B4}$$

The expressions for the mass-coupling coefficients ρ_{ij} in Eq. (B4) coincide with those given by Carcione and Tinivella.[4]

Next let us give a procedure to choose the dissipation coefficients f_{11}, f_{22}, and f_{12}. For the case of frozen porous media, following Ref. 4, the dissipation coefficients b_{12}, b_{23}, and b_{13} are defined as follows:

$$\begin{aligned}&b_{12}=(\phi)^2\frac{\eta}{\kappa_1},\quad b_{23}=(\phi)^2\frac{\eta}{\kappa_3},\\&b_{13}=\text{friction coefficient between the ice}\\&\qquad\text{and the solid frames,}\end{aligned} \tag{B5}$$

where η denotes the fluid viscosity and the permeability coefficients κ_1, κ_3 are defined in terms of the absolute permeabilities $\kappa_{1,0}$, $\kappa_{3,0}$ of the two solid frames by (see also Ref. 6)

$$\kappa_1=\kappa_{1,0}\frac{(\phi)^3}{(1-\phi_1)^3},\quad \kappa_3=\kappa_{3,0}\frac{(1-\phi_1)^2}{\phi_3^2}\left(\frac{\phi}{\phi_1}\right)^3. \tag{B6}$$

For the case of shaley sandstones, following Ref. 1 the coefficient b_{13} can be assumed to be zero and the friction coefficients b_{12} and b_{23} are taken to be of the form:

$$\begin{aligned}b_{12}&=45\eta R^{-2}_{s1}\phi^{-1}(1-\phi)\phi_1,\\b_{23}&=45\eta R^{-2}_{s3}\phi^{-1}(1-\phi)\phi_3,\end{aligned} \tag{B7}$$

where R_{s1}, R_{s3} denote the average radii of the sand and clay particles, respectively. These expressions are given in Appendix B3 of Carcione *et al.*[1] (but in that paper the viscous drag coefficients are respectively denoted by b_{11} and b_{33}).

It follows from Eqs. (B1) to (B3) that to recover the uniform porosity formulation in Ref. 4 the coefficients f_{11}, f_{22}, and f_{12} must be taken to satisfy the following nonsingular system of equations:

$$\begin{aligned}&f_{11}+(S_1-S_3)\phi f_{12}-S_1S_3(\phi)^2f_{22}=b_{13},\\&\phi(S_3\phi f_{22}-f_{12})=b_{23},\\&\phi(f_{12}+S_1\phi f_{22})=b_{12}.\end{aligned} \tag{B8}$$

The coefficients f_{11}, f_{12}, and f_{22} are determined by Eq. (B8) with the coefficient b_{13} left as a free parameter chosen so that the condition

$$f_{11}f_{22}-f^2_{12}\geqslant 0 \tag{B9}$$

is satisfied, which is needed in order to have a non-negative dissipation function $\mathcal{D}$ in the variables $(\dot{u}^{(3)}_i-\dot{u}^{(1)}_i)$, and $\dot{w}_i$. Since the coefficient b_{13} takes into account friction between the two solid phases, a proper model based, for example, in Coulomb's friction theory may be used, but this problem is beyond the scope of this work. For simplicity in all the numerical examples presented in this article the coefficient b_{13} was set to be zero.

[1] J. M. Carcione, B. Gurevich, and F. Cavallini, ''A generalized Biot-Gassmann model for the acoustic properties of shaley sandstones,'' Geophys. Prospect. **48**, 539–557 (2000).
[2] J. L. Morack and J. C. Rogers, ''Seismic evidence of shallow permafrost beneath the islands in the Beafort Sea,'' Arctic **3**, 166–174 (1981).
[3] J. M. Carcione and G. Seriani, ''Seismic velocities in permafrost,'' Geophys. Prospect. **46**, 441–454 (1998).
[4] J. M. Carcione and U. Tinivella, ''Bottom-simulating reflectors: Seismic velocities and AVO effects,'' Geophysics **65**, 54–67 (2000).
[5] S. Lee, L. J. Pyrak-Nolte, P. Cornillon, and O. Campanella, ''Characterization of frozen orange juice by ultrasound and wavelet analysis,'' J. Sci. Food Agric. (to be published).
[6] Ph. Leclaire, F. Cohen-Tenoudji, and J. Aguirre Puente, ''Extension of Biot's theory of wave propagation to frozen porous media,'' J. Acoust. Soc. Am. **96**, 3753–3767 (1994).
[7] Ph. Leclaire, F. Cohen-Tenoudji, and J. Aguirre Puente, ''Observation of two longitudinal and two transverse waves in a frozen porous medium,'' J. Acoust. Soc. Am. **97**, 2052–2055 (1995).
[8] J. J. McCoy, ''Conditionally averaged response formulation for two-phase random mixtures,'' J. Appl. Mech. **58**, 973–981 (1991).
[9] R. J. S. Brown and J. Korringa, ''On the dependence of the elastic properties of a porous rock on the compressibility of a pore fluid,'' Geophysics **40**, 608–616 (1975).
[10] M. A. Biot, ''Mechanics of deformation and acoustic propagation in porous media,'' J. Appl. Phys. **33**, 1482–1498 (1962).
[11] R. Burridge and J. B. Keller, ''Poroelasticity equations derived from microstructure,'' J. Acoust. Soc. Am. **70**, 1140–1146 (1981).
[12] J. E. Santos, J. Douglas, Jr., M. E. Morley, and O. M. Lovera, ''A model for wave propagation in a porous medium saturated by a two-phase fluid,'' J. Acoust. Soc. Am. **87**, 1439–1448 (1990).
[13] J. M. Carcione, *Wave Fields in Real Media: Wave Propagation in Anisotropic, Anelastic and Porous Media*, Handbook of Geophysical Exploration Vol. 31 (Pergamon, New York, 2001).
[14] J. E. Santos, J. Douglas, Jr., J. Corberó, and O. M. Lovera, ''Finite element methods for a model for full waveform acoustic logging,'' IMA J. Numer. Anal. **8**, 415–433 (1988).
[15] G. Duvaut and J. L. Lions, *Inequalities in Mechanics and Physics* (Springer, Berlin, 1976).
[16] J. A. Nitsche, ''On Korn's second inequality,'' RAIRO: Anal. Numer. **15**, 2337–248 (1981).
[17] J. E. Santos, ''Elastic wave propagation in fluid-saturated porous media. I. The existence and uniqueness theorems,'' Math. Modell. Numer. Anal. **20**, 113–128 (1986).
[18] J. M. Carcione and G. Seriani, ''Wave simulation in frozen porous media,'' J. Comput. Phys. **170**, 676–695 (2001).
[19] M. Krief, J. Garat, J. Stellingwerff, and J. Ventre, ''A petrophysical interpretation using the velocities of P and S waves (full waveform sonic),'' Log Analyst **31**, 355–369 (1990).
[20] D. H. Han, A. Nur, and D. Morgan, ''Effects of porosity and clay content on wave velocities in sandstones,'' Geophysics **51**, 2093–2107 (1986).
[21] J. M. Carcione and H. B. Helle, ''Numerical solution of the poroviscoelastic wave equation on a staggered mesh,'' J. Comput. Phys. **154**, 520–527 (1999).
[22] F. Gassmann, ''Über die elastizität poröser medien'' (''On the elasticity of porous media''), CHE 1856-1999 246 Vierteljahrsschrift der Naturforschenden Gessellschaft in Zurich **96**, 1–23 (1951).
[23] I. Goldberg and B. Gurevich, ''A semi-empirical velocity-porosity-clay model for petrophysical interpretation of P- and S-velocities,'' Geophys. Prospect. **46**, 271–285 (1998).
[24] D. Deptuck, J. P. Harrison, and P. Zawadzki, ''Measurement of elasticity and conductivity in a three-dimensional percolation system,'' Phys. Rev. Lett. **54**, 913–916 (1985).
[25] G. T. Kuster and M. N. Toksöz, ''Velocity and attenuation of seismic waves in two-phase media. 1. Theoretical formulations,'' Geophysics **39**, 587–606 (1974).

Plane wave solution for elastic wave scattering by a heterogeneous fracture

Seiji Nakagawa,[a] Kurt T. Nihei, and Larry R. Myer
Earth Sciences Division, Lawrence Berkeley National Laboratory, Berkeley, California 94720

(Received 22 March 2003; revised 6 March 2004; accepted 15 March 2004)

A plane-wave method for computing the three-dimensional scattering of propagating elastic waves by a planar fracture with heterogeneous fracture compliance distribution is presented. This method is based upon the spatial Fourier transform of the seismic displacement-discontinuity (SDD) boundary conditions (also called linear slip interface conditions), and therefore, called the wave-number-domain SDD method (wd-SDD method). The resulting boundary conditions explicitly show the coupling between plane waves with an incident wave number component (specular component) and scattered waves which do not follow Snell's law (nonspecular components) if the fracture is viewed as a planar boundary. For a spatially periodic fracture compliance distribution, these boundary conditions can be cast into a linear system of equations that can be solved for the amplitudes of individual wave modes and wave numbers. We demonstrate the developed technique for a simulated fracture with a stochastic (correlated) surface compliance distribution. Low- and high-frequency solutions of the method are also compared to the predictions by low-order Born series in the weak and strong scattering limit. © *2004 Acoustical Society of America.* [DOI: 10.1121/1.1739483]

PACS numbers: 43.20.Gp, 43.20.Px, 43.58.Ta [LLT] Pages: 2761–2772

I. INTRODUCTION

At microscales, fractures in rocks, metals, and ceramics can take many different forms including aligned open cracks, two surfaces in imperfect contact and a planar, thin zone filled with materials more compliant than the background medium.[1] Since a fracture scatters propagating elastic waves as a function of the microscale structure and resulting mechanical properties, they can be detected and characterized from the scattering behavior of the waves. The microscale properties, including surface roughness and aperture distribution, and connectivity and permeability of the cracks and gouge material, can also have a large impact on the hydraulic properties of a fracture.

Unfortunately, the microscale geometry and spatial property variations of a fracture is difficult to resolve using elastic waves if these heterogeneous features are much smaller than the wavelengths. Instead, these heterogeneities are likely to affect the scattering behavior of the waves through static, effective mechanical properties of the fracture that are determined at some subwavelength scale larger than the heterogeneities themselves. This is one of the basic principles of the seismic displacement–discontinuity (SDD) boundary conditions (also known as linear-slip interface conditions) commonly used for examining elastic wave scattering by fractures.

The SDD conditions assume a linear relationship between the wave-introduced, small relative displacement and stress across a fracture, via material parameters called fracture stiffness and its inverse, fracture compliance.[2] Since the SDD model is incapable of discriminating the detailed local geometry of a fracture, the fracture compliance does not directly reflect the hydraulic properties. However, in general, a large compliance value suggests a more open, permeable fracture. Baik and Thompson (1984)[3] showed that the fracture compliance can be determined analytically for fractures consisting of sparsely distributed, co-planar circular cracks and of contact patches between half-spaces. Angel and Achenbach (1985)[4] showed that elastic wave scattering off a fracture, consisting of aligned microcracks, can be modeled by the SDD conditions for long wavelengths. From laboratory ultrasonic transmission tests across a synthetic fracture with known, regular geometry, Myer *et al.* (1985)[5] found good agreement between measured waves and theoretical prediction by the SDD model.

Theoretical studies based upon the SDD model on the elastic wave scattering by fractures are limited to, or assume, fractures with a homogeneous distribution of fracture compliance on the fracture plane.[2,6–8] This is because the conventional SDD model, when used with plane wave theory, requires a ''range-independent'' (material properties do not vary along the fracture plane) fracture compliance distribution. Naturally occurring fractures are, however, heterogeneous, with the microscale properties varying along the fracture plane. This gives rise to fracture compliance that is spatially heterogeneous and, possibly, correlated. Since the heterogeneity of a fracture has a great impact on the hydraulic and mechanical properties of the fracture,[9–12] understanding the effect of the heterogeneity on the scattering of elastic waves can provide valuable tools for geophysical and nondestructive characterization of the fracture properties.

In this paper, we present analytical and numerical techniques to examine the elastic wave scattering by a heterogeneous fracture, based on the ''local'' SDD boundary conditions and the plane wave theory. This is achieved by

[a]Author to whom correspondence should be addressed; electronic mail: snakagawa@lbl.gov

applying a spatial Fourier transform to the SDD conditions with ''local'' fracture compliance that is a function in space. For this reason, this method is called the wave number domain seismic displacement discontinuity method (wd–SDD method). Previously, the local SDD model was used in geometric ray approximations. Pyrak-Nolte and Nolte (1992)[13] examined the apparent, scattering induced frequency dependence of fracture compliance assuming that the compliance varied much more slowly compared to the wavelength (high-frequency ray approximation). Nihei (1989)[14] and Oliger *et al.* (2003)[15] used Kirchhoff approximations to take into account the diffraction of waves transmitted across a heterogeneous fracture. In the Kirchhoff approximations, the amplitudes and phases of the transmitted waves across a fracture are computed at each location on the fracture, assuming that the fracture is planar and has a single value of fracture compliance assigned to that location. In contrast, the wd–SDD method is not limited to high frequencies and takes into account the interactions between different locations on the fracture. Although numerical methods such as the boundary element method[16] and the finite difference method[17,18] can also be used to examine the scattering of elastic waves at full range of frequencies, applications of these methods to three-dimensional problems results in high computational costs, particularly large computer memory. Further, the analytical nature of the introduced method can provide clearer insights into the mechanism of wave scattering by a heterogeneous fracture.

II. THEORY

A. Plane wave analysis

We first hypothesize that the ''local fracture compliance'' can be defined for a fracture. This means that the dynamic behavior of a real fracture is well approximated by the behavior of an interface between half-spaces with a heterogeneous distribution of compliance which is measured locally at some length scale much smaller than the seismic (elastic wave) wavelengths. This approach is commonly taken to numerically simulate wave scattering by fractures with heterogeneous surface contacts using the boundary element method and the finite difference method.

In our model, we also assume that the dimension of a fracture in the fracture-normal direction, such as the surface roughness and waviness, is much smaller than considered seismic wavelengths, and therefore, the fracture can be treated as a plane. For the local fracture compliance model, the SDD boundary conditions are specified at each spatial location on the fracture on the x, y plane as (Fig. 1)

$$\boldsymbol{\sigma}(x,y;z\rightarrow+0)=\boldsymbol{\sigma}(x,y;z\rightarrow-0)\equiv\boldsymbol{\sigma}(x,y), \tag{1}$$

$$\boldsymbol{\eta}(x,y)\,\boldsymbol{\sigma}(x,y)=[\mathbf{u}](x,y), \tag{2}$$

where the displacement–discontinuity vector $[\mathbf{u}]$, stress traction vectors $\boldsymbol{\sigma}$, and the compliance matrix $\boldsymbol{\eta}$ are defined as

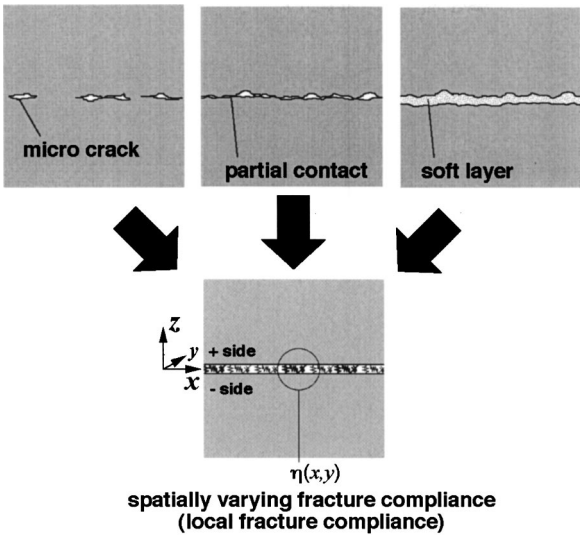

FIG. 1. Heterogeneous fractures with a variety of microstructures are modeled as a planer interface between half-spaces with spatially varying fracture compliance (springs in the figure).

$$[\mathbf{u}](x,y)\equiv\mathbf{u}(x,y;z\rightarrow+0)-\mathbf{u}(x,y;z\rightarrow-0)$$
$$=\begin{bmatrix}u_x\\u_y\\u_z\end{bmatrix}_{z\rightarrow+0}-\begin{bmatrix}u_x\\u_y\\u_z\end{bmatrix}_{z\rightarrow-0}, \tag{3}$$

$$\boldsymbol{\sigma}(x,y;z\rightarrow\pm0)=\begin{bmatrix}\sigma_{xz}\\\sigma_{yz}\\\sigma_{zz}\end{bmatrix}_{z\rightarrow\pm0}, \tag{4}$$

$$\boldsymbol{\eta}(x,y)\equiv\begin{bmatrix}\eta_{xx}&\eta_{xy}&\eta_{xz}\\\eta_{yx}&\eta_{yy}&\eta_{yz}\\\eta_{zx}&\eta_{zy}&\eta_{zz}\end{bmatrix}. \tag{5}$$

It is noted that the stress traction vector is defined via components of stress on planes parallel to the x, y plane rather than components of traction the sign of which depends on the orientation of the surface. However, without confusion, we shall call this ''traction (vector).'' We assume that the incident waves insonify the fracture on the $z<0$ side. By directly applying the spatial 2D Fourier transform to these ''local'' SDD conditions given in Eqs. (1) and (2), we get

$$\tilde{\boldsymbol{\sigma}}(k_x,k_y;z\rightarrow+0)=\tilde{\boldsymbol{\sigma}}(k_x,k_y;z\rightarrow-0)\equiv\tilde{\boldsymbol{\sigma}}(k_x,k_y), \tag{6}$$

$$(\tilde{\boldsymbol{\eta}}^{*}\tilde{\boldsymbol{\sigma}})(k_x,k_y)=[\tilde{\mathbf{u}}](k_x,k_y). \tag{7}$$

Tilde ''~'' indicates transformed variables, and ''*'' indicates a convolution. It is noted that for a uniform fracture, $\boldsymbol{\eta}(x,y)$ is a constant matrix, and the convolution is reduced to a multiplication, i.e., the same relationship as in the x, y domain.

In this paper, we assume a single plane fracture embedded within a homogeneous background medium with a stiffness tensor $\mathbf{C}=[C_{ijkl}]$ and a density ρ. For a given frequency ω and fracture-parallel wave numbers k_x and k_y, the Christoffel equation is solved to obtain six z-direction wave numbers $k_z^{1\pm}$, $k_z^{2\pm}$, $k_z^{3\pm}$, where 1, 2, 3 indicate the three modes of plane waves, and corresponding unit particle displacement vectors $\hat{\mathbf{u}}_1^{\pm}$, $\hat{\mathbf{u}}_2^{\pm}$, $\hat{\mathbf{u}}_3^{\pm}$. Hereafter, the superscripts

"$-$" and "$+$" indicate waves propagating in the negative z direction (reflected waves) and in the positive z direction (incident and transmitted waves), respectively. For plane waves, the displacement and stress can be related to each other via single vector variables $\mathbf{a}^{\pm}$ containing the displacement amplitudes of three plane wave modes. Using the wave numbers and unit displacement vectors defined in the above, a single wave number component of the plane wave displacement is given by

$$\begin{aligned}\mathbf{u}^{\pm}(x,y;z) &= \begin{bmatrix} u_x^{\pm} \\ u_y^{\pm} \\ u_z^{\pm} \end{bmatrix} (=\tilde{\mathbf{u}}^{\pm}(k_x,k_y;z)) = \{\hat{\mathbf{u}}_1^{\pm} \quad \hat{\mathbf{u}}_2^{\pm} \quad \hat{\mathbf{u}}_3^{\pm}\} \\ &\times \begin{bmatrix} e^{ik_z^{1\pm}z} & & \\ & e^{ik_z^{2\pm}z} & \\ & & e^{ik_z^{3\pm}z} \end{bmatrix} \\ &\times \begin{bmatrix} a_1^{\pm} \\ a_2^{\pm} \\ a_3^{\pm} \end{bmatrix} e^{i(k_x x+k_y y-\omega t)} \\ &\equiv \mathbf{U}^{\pm}(k_x,k_y)\mathbf{E}^{\pm}(k_x,k_y;z)\mathbf{a}^{\pm}(k_x,k_y)e^{i(k_x x+k_y y-\omega t)}, \quad (8)\end{aligned}$$

where ω is the circular frequency. The traction is computed from the displacement vector using the Hooke's law as

$$\begin{aligned}\boldsymbol{\sigma}^{\pm}(x,y;z)(=\tilde{\boldsymbol{\sigma}}^{\pm}(k_x,k_y;z)) &= \begin{bmatrix} \sigma_{xz}^{\pm} \\ \sigma_{yz}^{\pm} \\ \sigma_{zz}^{\pm} \end{bmatrix} \\ &= i\omega\mathbf{S}^{\pm}(k_x,k_y)\mathbf{E}^{\pm}(k_x,k_y;z)\mathbf{a}^{\pm}(k_x,k_y)e^{i(k_x x+k_y y-\omega t)}. \quad (9)\end{aligned}$$

Dependence on the phase term, $e^{i(k_x x+k_y y-\omega t)}$, is understood and omitted from the following equations. We will define $\mathbf{S}^{\pm}$ shortly.

For an isotropic background medium, the three modes of wave propagation are two shear (S) waves and one compressional (P) wave. We label these modes as $1=Sv$ wave, $2=Sh$ wave, and $3=P$ wave, where a convention is taken such that the Sh wave has the particle displacement parallel to the fracture (or z) plane. For a plane-parallel wave number $k_r=\sqrt{k_x^2+k_y^2}$, the z-direction wave numbers are $k_z^{1,2\pm}=\pm k_z^S \equiv \pm\sqrt{k_S^2-k_r^2}$ and $k_z^{3\pm}=\pm k_z^P \equiv \pm\sqrt{k_P^2-k_r^2}$, where $k_P=\omega/c_P$ and $k_S=\omega/c_S$ are the P- and S-wave wave numbers with velocities c_P and c_S, respectively. The displacement and stress matrices in Eqs. (8) and (9) take the forms

$$\mathbf{U}^{\pm}=\mathbf{R}^T\begin{bmatrix} \mp k_z^S/k_S & & k_r/k_P \\ & 1 & \\ k_r/k_S & & \pm k_z^P/k_P \end{bmatrix}, \quad (10)$$

$$\mathbf{S}^{\pm}=\rho c_S\mathbf{R}^T\begin{bmatrix} -(1-2(k_r/k_S)^2) & 0 & \pm 2k_r k_z^P/k_P k_S \\ 0 & \pm k_z^S/k_S & 0 \\ \pm 2k_r k_z^S/k_S^2 & 0 & (1-2(k_r/k_S)^2)(k_S/k_P) \end{bmatrix}, \quad (11)$$

where $\mathbf{R}$ is the rotation matrix around the z axis given by

$$\mathbf{R}\equiv\begin{bmatrix} k_x/k_r & k_y/k_r & \\ -k_y/k_r & k_x/k_r & \\ & & 1 \end{bmatrix}. \quad (12)$$

The superscript "T" indicates matrix transposition. It is noted that the matrices $\mathbf{U}^{\pm}$ and $\mathbf{R}$ are dimensionless, and $\mathbf{S}^{\pm}$ has the dimension of acoustic impedance. Also, all of these matrices are frequency independent for a given wave propagation direction (or a fracture-parallel slowness) because wave numbers in the expressions appear only as a ratio between two wave numbers.

Using Eqs. (8) and (9), the displacement and traction introduced by an incident plane wave propagating in the positive z direction are $\tilde{\mathbf{u}}_{\mathrm{Inc}}=\mathbf{U}^+\mathbf{E}^+\mathbf{a}_{\mathrm{Inc}}$ and $\tilde{\boldsymbol{\sigma}}_{\mathrm{Inc}}=i\omega\mathbf{S}^+\mathbf{E}^+\mathbf{a}_{\mathrm{Inc}}$, respectively, where $\mathbf{a}_{\mathrm{Inc}}$ contains the displacement amplitudes of the individual plane wave modes. Using Eq. (8), and noting that there are no waves propagating in the negative z direction on the $z>0$ side of the fracture, the transformed-domain displacement–discontinuity vector on the fracture is computed from Eqs. (3), (8), and (10) as

$$\begin{aligned}[\tilde{\mathbf{u}}] &\equiv \tilde{\mathbf{u}}(z\to+0)-\tilde{\mathbf{u}}(z\to-0) \\ &= [\tilde{\mathbf{u}}^+-(\tilde{\mathbf{u}}^-+\tilde{\mathbf{u}}_{\mathrm{Inc}})]_{z=0} \\ &= \mathbf{U}^+\mathbf{a}^+-(\mathbf{U}^-\mathbf{a}^-+\mathbf{U}^+\mathbf{a}_{\mathrm{Inc}}). \quad (13)\end{aligned}$$

The traction vectors are given by Eqs. (9) and (11) as

$$\begin{aligned}\tilde{\boldsymbol{\sigma}}(z\to+0) &= (\tilde{\boldsymbol{\sigma}}^+)_{z=0}=i\omega\mathbf{S}^+\mathbf{a}^+, \\ \tilde{\boldsymbol{\sigma}}(z\to-0) &= (\tilde{\boldsymbol{\sigma}}^-+\tilde{\boldsymbol{\sigma}}_{\mathrm{Inc}})_{z=0}=i\omega(\mathbf{S}^-\mathbf{a}^-+\mathbf{S}^+\mathbf{a}_{\mathrm{Inc}}). \quad (14)\end{aligned}$$

Using Eqs. (13) and (14), Eqs. (6) and (7) are rewritten, respectively, as

$$i\omega\mathbf{S}^+\mathbf{a}^+=i\omega(\mathbf{S}^-\mathbf{a}^-+\mathbf{S}^+\mathbf{a}_{\mathrm{Inc}})\equiv\tilde{\boldsymbol{\sigma}}(k_x,k_y), \quad (15)$$

$$\tilde{\boldsymbol{\eta}}^*(i\omega\mathbf{S}^+\mathbf{a}^+)=\mathbf{U}^+\mathbf{a}^+-\mathbf{U}^-\mathbf{a}^--\mathbf{U}^+\mathbf{a}_{\mathrm{Inc}}. \quad (16)$$

To simplify the above equations, we choose to use the traction vector $\tilde{\boldsymbol{\sigma}}$ as our primary variable. This choice leads to an

efficient implementation of a numerical algorithm, which we will discuss later. Using the equalities in the first equation,

$$\mathbf{a}^+ = (i\omega \mathbf{S}^+)^{-1}\tilde{\boldsymbol{\sigma}},$$
$$\mathbf{a}^- = (i\omega \mathbf{S}^-)^{-1}(\tilde{\boldsymbol{\sigma}} - i\omega \mathbf{S}^+ \mathbf{a}_{\mathrm{Inc}}). \tag{17}$$

These are used to eliminate the variables $\mathbf{a}^-$ and $\mathbf{a}^+$ from Eq. (16), resulting in

$$\begin{aligned}\tilde{\boldsymbol{\eta}}^* \tilde{\boldsymbol{\sigma}} &= \mathbf{U}^+ (i\omega \mathbf{S}^+)^{-1} \tilde{\boldsymbol{\sigma}} - \mathbf{U}^- (i\omega \mathbf{S}^-)^{-1} (\tilde{\boldsymbol{\sigma}} - i\omega \mathbf{S}^+ \mathbf{a}_{\mathrm{Inc}}) \\ &\quad - \mathbf{U}^+ \mathbf{a}_{\mathrm{Inc}} \\ &= (i\omega)^{-1} [\mathbf{U}^+ (\mathbf{S}^+)^{-1} - \mathbf{U}^- (\mathbf{S}^-)^{-1}] (\tilde{\boldsymbol{\sigma}} - i\omega \mathbf{S}^+ \mathbf{a}_{\mathrm{Inc}}) \\ &\equiv (i\omega)^{-1} \mathbf{H} (\tilde{\boldsymbol{\sigma}} - \tilde{\boldsymbol{\sigma}}_{\mathrm{Inc}}). \end{aligned} \tag{18}$$

or

$$[(i\omega)^{-1}\mathbf{H} - \tilde{\boldsymbol{\eta}}^*]\tilde{\boldsymbol{\sigma}} = (i\omega)^{-1}\mathbf{H}\tilde{\boldsymbol{\sigma}}_{\mathrm{Inc}}. \tag{19}$$

Note that the stress introduced by the incident wave is evaluated on the fracture $(z=0)$. The matrix $\mathbf{H}$ is defined as

$$\begin{aligned}\mathbf{H} &\equiv \mathbf{U}^+ (\mathbf{S}^+)^{-1} - \mathbf{U}^- (\mathbf{S}^-)^{-1} \\ &= \frac{2}{\rho c_S \cdot R} \mathbf{R}^T \begin{bmatrix} k_z^S/k_S & & \\ & k_S R/k_z^S & \\ & & k_z^P/k_S \end{bmatrix} \mathbf{R}, \end{aligned} \tag{20}$$

where R is the dimensionless Rayleigh function

$$R \equiv [1 - 2(k_r/k_S)^2]^2 + 4(k_r/k_S)^2 (k_z^P k_z^S / k_S^2). \tag{21}$$

It is noted that $\mathbf{H}$ has the dimension of inverse acoustic impedance, and both R and $\mathbf{H}$ are frequency independent for a fixed wave propagation direction.

Equation (19) is a Fredholm integral equation of the second kind for the total stress $\tilde{\boldsymbol{\sigma}}$ on the fracture, which can be given explicitly as

$$\begin{aligned}\tilde{\boldsymbol{\sigma}}(k_x, k_y) &= \tilde{\boldsymbol{\sigma}}_{\mathrm{Inc}}(k_x, k_y) + i\omega \mathbf{H}^{-1}(k_x, k_y) \\ &\quad \times \int_{-\infty}^{+\infty} \int_{-\infty}^{+\infty} \tilde{\boldsymbol{\eta}}(k_x - k_x', k_y - k_y') \\ &\quad \times \tilde{\boldsymbol{\sigma}}(k_x', k_y') dk_x' \, dk_y'. \end{aligned} \tag{22}$$

The first term on the right-hand side of the equation is the incident wave field, and the second term is the scattered wave field. The second term shows that, for a heterogeneous fracture compliance distribution, different wave number components are coupled through the convolution with the Fourier transformed fracture compliance, resulting in nonspecular transmission and reflection of an incident plane wave. For simplicity, we define 3×3 matrix operators $\overline{\mathbf{H}}^{-1}$ and $\bar{\tilde{\boldsymbol{\eta}}}$. $\overline{\mathbf{H}}^{-1}$ is a "diagonal" multiplication operator (performs multiplication by the matrix $\mathbf{H}^{-1}$), and $\bar{\tilde{\boldsymbol{\eta}}}$ is a convolution operator [performs convolution in Eq. (12) with multiplication by the matrix $\tilde{\boldsymbol{\eta}}$]. The formal solution of Eq. (22) is obtained (Neumann series) by rewriting Eq. (22) using these operators as

$$\tilde{\boldsymbol{\sigma}} = \tilde{\boldsymbol{\sigma}}_{\mathrm{Inc}} + i\omega \overline{\mathbf{H}}^{-1} \bar{\tilde{\boldsymbol{\eta}}} \tilde{\boldsymbol{\sigma}} \equiv \tilde{\boldsymbol{\sigma}}_{\mathrm{Inc}} + i\overline{\boldsymbol{\Omega}} \tilde{\boldsymbol{\sigma}}, \tag{23}$$

where $\overline{\boldsymbol{\Omega}} \equiv \omega \overline{\mathbf{H}}^{-1} \bar{\tilde{\boldsymbol{\eta}}}$, and then by applying Eq. (23) recursively to itself as

$$\tilde{\boldsymbol{\sigma}} = [\overline{\mathbf{I}} + i\overline{\boldsymbol{\Omega}} + (i\overline{\boldsymbol{\Omega}})^2 + \cdots] \tilde{\boldsymbol{\sigma}}_{\mathrm{Inc}} = (\overline{\mathbf{I}} - i\overline{\boldsymbol{\Omega}})^{-1} \tilde{\boldsymbol{\sigma}}_{\mathrm{Inc}}. \tag{24}$$

$\overline{\mathbf{I}}$ is the identity operator. If the scattering is weak so that the stress field on the fracture can be approximated by the stress introduced by the incident wave, the (first-order) Born approximation can be used in Eq. (23), resulting in

$$\tilde{\boldsymbol{\sigma}} = \tilde{\boldsymbol{\sigma}}_{\mathrm{Inc}} + i\overline{\boldsymbol{\Omega}} \tilde{\boldsymbol{\sigma}}_{\mathrm{Inc}} = (\overline{\mathbf{I}} + i\overline{\boldsymbol{\Omega}}) \tilde{\boldsymbol{\sigma}}_{\mathrm{Inc}}, \tag{25}$$

which can also be obtained by keeping the first two terms in the Neumann series (Born series) in Eq. (24). It is noted that an alternative approximation that is valid for the strong-scattering limit can be obtained if the stiffness of the fracture, instead of compliance, is used. The derivation of this approximation is shown in the Appendix.

Introducing higher-order terms in the Born series increases the applicable range of the approximation for stronger scattering, as long as the series is convergent. However, the series may converge very slowly, or even may not converge for moderately to strongly scattering fractures (for weakly to moderately scattering fractures if the formulation in Appendix is used). For these cases, the original system equation (19) has to be solved numerically.

B. Numerical analysis

In order to solve the integral equation (19) numerically, the equation is discretized in wave number to obtain a linear system of equations by applying the discrete Fourier transforms instead of the continuous Fourier transforms. This indicates that both the two-dimensional fracture compliance distribution and the resulting waves are treated as periodic, though the waves are periodic in the dynamic sense as in the Floquet boundary condition (i.e., a phase shift is included in the periodic boundary condition). Also, for the linear system of equations to be finite in size, the spectra of the transformed fracture compliance need to be band limited (decay away from the origin sufficiently fast). The discrete form of Eq. (19) is [for computational efficiency, Eqs. (22) and (23) are not used]

$$\begin{aligned}&\sum_{m'=0}^{M-1} \sum_{n'=0}^{N-1} [(i\omega)^{-1} \delta_{mm'} \delta_{nn'} \mathbf{H}_{mn} - \tilde{\boldsymbol{\eta}}_{m-m',n-n'}] \tilde{\boldsymbol{\sigma}}_{m'n'} \\ &\quad = (i\omega)^{-1} \mathbf{H}_{mn} \tilde{\boldsymbol{\sigma}}_{\mathrm{Inc},mn} \\ &\quad\quad (m = 0,1,...,M-1 \quad \text{and} \quad n = 0,1,...,N-1). \end{aligned} \tag{26}$$

$\delta_{mm'}$ and $\delta_{nn'}$ are the Kronecker deltas. All vectors and matrices are evaluated at discrete wave numbers, $k_{xm} = 2m\pi/L_x$ and $k_{yn} = 2n\pi/L_y$, with indices m and n. Note that all these indices are periodic with periods M and N, and the compliance distribution is spatially periodic with periods L_x and L_y. The length of the periods given by M and N should be sufficiently long to avoid spectral leakage in the solution. By grouping the two indices (m,n) and (m',n') to the vectors and matrices into single indices l and l' $(l,l' = 0,1,...,MN-1)$, respectively, Eq. (26) are assembled into a single matrix equation

$$[(i\omega)^{-1} \overline{\mathbf{H}} - \bar{\tilde{\boldsymbol{\eta}}}] \overline{\boldsymbol{\sigma}} = (i\omega)^{-1} \overline{\mathbf{H}} \overline{\boldsymbol{\sigma}}_{\mathrm{Inc}}, \tag{27}$$

where

$$\overline{\mathbf{H}} \equiv \begin{bmatrix} \mathbf{H}_0 & & & \\ & \mathbf{H}_1 & & \\ & & \ddots & \\ & & & \mathbf{H}_{MN-1} \end{bmatrix},$$

$$\bar{\bar{\boldsymbol{\eta}}} \equiv \begin{bmatrix} \tilde{\boldsymbol{\eta}}_0 & \tilde{\boldsymbol{\eta}}_{-1} & \cdots & \tilde{\boldsymbol{\eta}}_{-MN+1} \\ \tilde{\boldsymbol{\eta}}_{+1} & \tilde{\boldsymbol{\eta}}_0 & \cdots & \tilde{\boldsymbol{\eta}}_{-MN+2} \\ \vdots & \vdots & \ddots & \vdots \\ \tilde{\boldsymbol{\eta}}_{MN-1} & \tilde{\boldsymbol{\eta}}_{MN-2} & \cdots & \tilde{\boldsymbol{\eta}}_0 \end{bmatrix},$$

$$\overline{\boldsymbol{\sigma}} = \begin{bmatrix} \tilde{\boldsymbol{\sigma}}_0 \\ \tilde{\boldsymbol{\sigma}}_1 \\ \vdots \\ \tilde{\boldsymbol{\sigma}}_{MN-1} \end{bmatrix}, \quad \overline{\boldsymbol{\sigma}}_{\mathrm{Inc}} = \begin{bmatrix} \tilde{\boldsymbol{\sigma}}_{\mathrm{Inc},0} \\ \tilde{\boldsymbol{\sigma}}_{\mathrm{Inc},1} \\ \vdots \\ \tilde{\boldsymbol{\sigma}}_{\mathrm{Inc},MN-1} \end{bmatrix}. \tag{28}$$

$\overline{\mathbf{H}}$ and $\bar{\bar{\boldsymbol{\eta}}}$ here are the inverse of multiplication operator $\overline{\mathbf{H}}^{-1}$ and convolution operator $\bar{\bar{\boldsymbol{\eta}}}$ in Eq. (23), respectively, defined for a finite number of wave numbers. Once the stress vector $\overline{\boldsymbol{\sigma}}$ is determined, by solving Eq. (27), the coefficient vectors for each wave number and wave mode component are computed via

$$\mathbf{a}^{+}_{mn} = (i\omega \mathbf{S}^{+}_{mn})^{-1} \tilde{\boldsymbol{\sigma}}_{mn}, \tag{29}$$

$$\mathbf{a}^{-}_{mn} = (i\omega \mathbf{S}^{-}_{mn})^{-1} (\tilde{\boldsymbol{\sigma}}_{mn} - \tilde{\boldsymbol{\sigma}}_{\mathrm{Inc}}), \tag{30}$$

for transmitted and reflected waves, respectively. From these, the displacement vectors for the transmitted and reflected waves are

$$\mathbf{u}^{+}(x,y;z>0) = \sum_{m=0}^{M-1} \sum_{n=0}^{N-1} \mathbf{U}^{+}_{mn} \mathbf{E}^{+}_{mn} \mathbf{a}^{+}_{mn} e^{i(k_{xm}x + k_{yn}y - \omega t)}, \tag{31}$$

$$\mathbf{u}^{-}(x,y;z<0) = \sum_{m=0}^{M-1} \sum_{n=0}^{N-1} (\mathbf{U}^{-}_{mn} \mathbf{E}^{-}_{mn} \mathbf{a}^{-}_{mn} + \mathbf{U}^{+}_{mn} \mathbf{E}^{+}_{mn} \mathbf{a}_{\mathrm{Inc},mn}) e^{i(k_{xm}x + k_{yn}y - \omega t)}, \tag{32}$$

where $\mathbf{E}^{\pm}_{mn} = \mathbf{E}^{\pm}(k_{mx}, k_{ny}; z)$ are the discrete forms of the phase-shift matrices defined in Eq. (8).

C. Computational considerations

The system matrix has a size $\mathrm{M_{mat}} \times \mathrm{M_{mat}}$ where $\mathrm{M_{mat}} = \mathrm{M} \times \mathrm{N} \times \mathrm{DOF}$ (degrees of freedom, three for three-dimensional problems) which grows rapidly as the number of wave number components increases. However, unique properties of the equation allow an efficient implementation of the method in a computer program, which leads to significant savings in the computer time and memory.

First, we discuss the memory considerations. From Eqs. (26), (27), and (28), notice that the system matrix consists of two parts: the 3×3 block diagonal part $\overline{\mathbf{H}}$, and the fully populated part $\bar{\bar{\boldsymbol{\eta}}}$. The latter matrix has the same structure as the Toeplitz matrix: each element of the matrix, a 3×3 submatrix, appears recursively, with the first entry of the compliance matrix $\tilde{\boldsymbol{\eta}}_{00} = \tilde{\boldsymbol{\eta}}_0$ in the diagonal. This is the direct consequence of expressing a convolution operation with a periodic function using a matrix. Therefore, for this system matrix, if an iterative solver such as the stabilized bi-conjugate gradient method[19] or the GMRES method[20] is used, it is sufficient to store only the block diagonal part of the matrix $\mathbf{H}$ and the transformed fracture compliance matrices corresponding to the first $3 \times \mathrm{M_{mat}}$ part of the matrix $\bar{\bar{\boldsymbol{\eta}}}$.

An iterative solver requires both fast computation of matrix-vector products (mat-vecs) and effective preconditioning of the system matrix. The fully populated structure of the system matrix is usually not suited for fast computation of mat-vecs. Fortunately, Eq. (26) reveals that the matrix-vector product between $\bar{\bar{\boldsymbol{\eta}}}$ and $\overline{\boldsymbol{\sigma}}$ is essentially a single convolution between $\tilde{\boldsymbol{\eta}}_{m,n} (= \tilde{\boldsymbol{\eta}}_l)$ and $\tilde{\boldsymbol{\sigma}}_{m,n} (= \tilde{\boldsymbol{\sigma}}_l)$. Therefore, this computation can be carried out efficiently by transforming the vectors to the spatial domain and then transforming back the products between the vectors and the local compliance matrices to the wave number domain, using fast Fourier transforms. The preconditioning of the matrix is carried out in the spatial domain using the Kirchhoff approximation of the scattered waves. This involves first computing the scattering matrix for the incident plane wave at each location on the fracture, assuming the fracture is homogeneous and the compliance distribution is uniform. Subsequently, the resulting 3×3 block diagonal matrix is transformed in the wave number domain, and then LU decomposition is applied to the band-diagonal part of the matrix using a small bandwidth (3–9 are used). This LU-decomposed matrix is used for preconditioning the system matrix during each mat-vec operation.

Finally, for a plane incident wave with a wave number vector $(k_x^{\mathrm{Inc}}, k_y^{\mathrm{Inc}})$, the definition of the wave numbers is changed to $(k_{xm}, k_{yn}) = (k_x^{\mathrm{Inc}} + 2m\pi/L_x, k_y^{\mathrm{Inc}} + 2n\pi/L_y)$, so that the nonspecular wave number components close to the incident wave wave number are preferentially used to represent the scattered waves. This is a reasonable choice because the partial waves with wave numbers close to the source wave number are more strongly excited due to the coupling introduced by the diagonally dominant kernel of the convolution integral in Eq. (22). The expression for the stress vector also changes as

$$\tilde{\boldsymbol{\sigma}}_{\mathrm{Inc},mn} \rightarrow \delta_{m0} \delta_{n0} \tilde{\boldsymbol{\sigma}}_{\mathrm{Inc}}. \tag{33}$$

III. EXAMPLES

A. Comparison with a boundary element code

In order to check the performance of the numerical technique, we compared the numerical results of the wd-SDD technique developed in the preceding sections to the results from a two-dimensional, frequency-domain elastodynamic boundary element (BE) method of Hirose and Kitahara (1991).[21] In this test, the results from the two methods were compared for an incident plane *P* wave propagating in the *z* direction. For the wd-SDD, we assumed a fracture with sinusoidal compliance distribution, $\boldsymbol{\eta}(x,y) = \eta_0 \mathbf{I}(1 - \cos 2\pi x/\lambda)/2$ where $\mathbf{I}$ is a 3×3 identity matrix, $\eta_0 = 1.33 \times 10^{-10}$ m/Pa, and period $\lambda = 4$ m. In contrast, the two-dimensional fracture in the BE model is finite in extent from -28 m to $+28$ m.

z-direction displacement waveforms computed for receivers located on both sides of the fracture are shown in Fig.

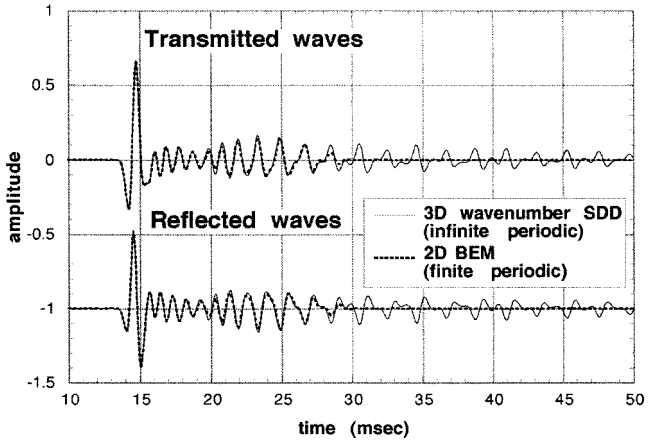

FIG. 2. Comparison between waveforms computed using the BEM and the wd-SDD method. A plane *P* wave is normally incident on the fractures. The first-arriving parts of the waves show very good agreement. The results of the wd-SDD method show long-lasting reverberations (''coda'') due to the waves scattered a long distance away from the receiver.

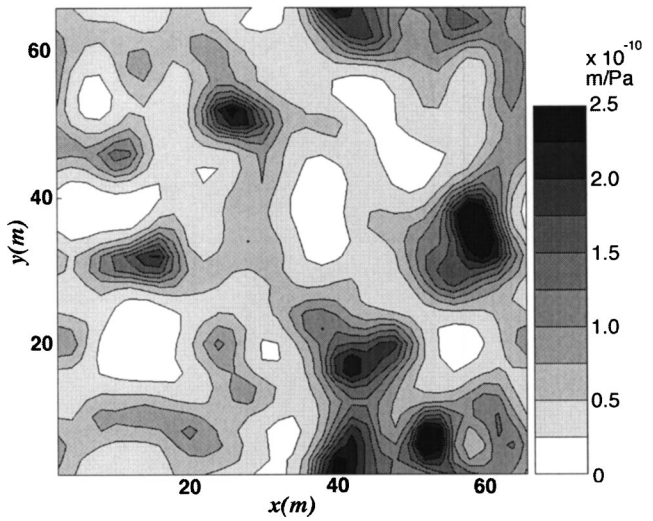

FIG. 3. Single periodic cell for the compliance distribution of a simulated fracture. The distribution is periodic in both *x* and *y* directions. The correlation length of the distribution is 4 m (single standard deviation of a fitted Gaussian distribution), and the compliance values vary by about an order of magnitude.

2. The distance of the receivers from the fracture is 20 m, the incident wave is a plane *P* wave Ricker wavelet (second derivative of a Gaussian wavelet) with a central frequency corresponding to 4 m which is also the spatial period of the compliance distribution. Compared to the SDD results, the BE results show much shorter, more compact waveforms, because the fracture in the BE model is finite. However, the waveforms are in good agreement until about 28 ms, for both reflected and transmitted waveforms, which indicates that the scattering of the waves can be accurately modeled using the wave-number-domain SDD technique. The secondary arrivals that also show rather good agreement are due to the *S* waves converted by the fracture.

B. Numerical models of a heterogeneous fracture

In the following examples, we used a fracture with a numerically simulated stochastic compliance distribution. For simplicity, the fracture compliance matrix was assumed to be proportional to an identity matrix, i.e., normal and shear compliances are the same, and $\boldsymbol{\eta}(x,y)=\eta(x,y)\mathbf{I}$. A distribution of logarithmic compliance, $\ln \eta(x,y)$, was generated from a Gaussian correlation function with a correlation length (one standard deviation) of 4 m and uncorrelated phase between the Fourier components.[22] The range of a single periodic cell is $(L_x,L_y)=(64\,\mathrm{m},64\,\mathrm{m})$. The resulting compliance $\eta(x,y)$, shown in Fig. 3, has a log-normal distribution with a mean and a standard deviation of the compliance of 6.74×10^{-11} m/Pa and 4.87×10^{-11} m/Pa, respectively. The correlation length of the distribution (one standard deviation of a fitted Gaussian profile) is approximately 4 m.

C. Exact solutions

Waves scattered by the heterogeneous fracture in Fig. 3 were computed for a plane incident *P* wave, using a Ricker wavelet (second derivative of a Gaussian function) with a central frequency, 750 Hz, corresponding to the correlation length of the fracture. The velocities and density of the homogeneous, isotropic, elastic background were $c_p=3000$ m/s, $c_s=1731$ m/s, and $\rho=2100$ kg/m^3, respectively. If the fracture had a homogeneous fracture compliance distribution, the mean compliance value of 6.74×10^{-11} m/Pa would give the same normal incidence *P* wave transmission and reflection coefficients of amplitudes of $\sqrt{2}/2\sim0.71$. The condition for this to occur is that frequency$=\rho c_p/\pi$.

The snapshots in Figs. 4(a) and 4(b) were computed for both a normally incident *P* wave and an obliquely incident *P* wave with a unit propagation vector $(v_x,v_y,v_z)=(1/\sqrt{3},1/\sqrt{3},1/\sqrt{3})$, respectively. To emphasize the scattered waves with small amplitudes, the amplitude scale was magnified by a factor of 4, which caused the saturation of scale for a part of transmitted and reflected waves. In both snapshots, it can be seen that patches of large and small compliance scatter the incident waves, creating circular (spherical) diffraction patterns in both sides of the fracture. For the normal incidence case, the amplitude and phase fluctuations in the both transmitted and reflected waves can be seen. It is also noted that incoherent *S* waves were generated. For the oblique incidence case, the diffracted waves generated horizontally propagating *P* waves in later times, part of which was critically refracted as head waves propagating away from the fracture (multiple, faint oblique wave fronts propagating symmetrically across the fracture).

Figure 5 shows the amplitude distribution of individual wave number components for a given frequency (750 Hz) and angles of incidence (normal and oblique) of incident plane *P* waves. The axes of the plots show the integral numbers (m,n) corresponding to the wave number components $(k_{xm},k_{yn})=(k_x^{\mathrm{Inc}}+2m\pi/L_x,k_y^{\mathrm{Inc}}+2n\pi/L_y)$. Remember that the components of wave numbers used in the numerical simulations were distributed around the incident wave number $(k_x^{\mathrm{Inc}},k_y^{\mathrm{Inc}})$. These diagrams can be used to see if the spectrum leakage occurs due to a premature truncation of the wave number series (or undersampling in the spatial do-

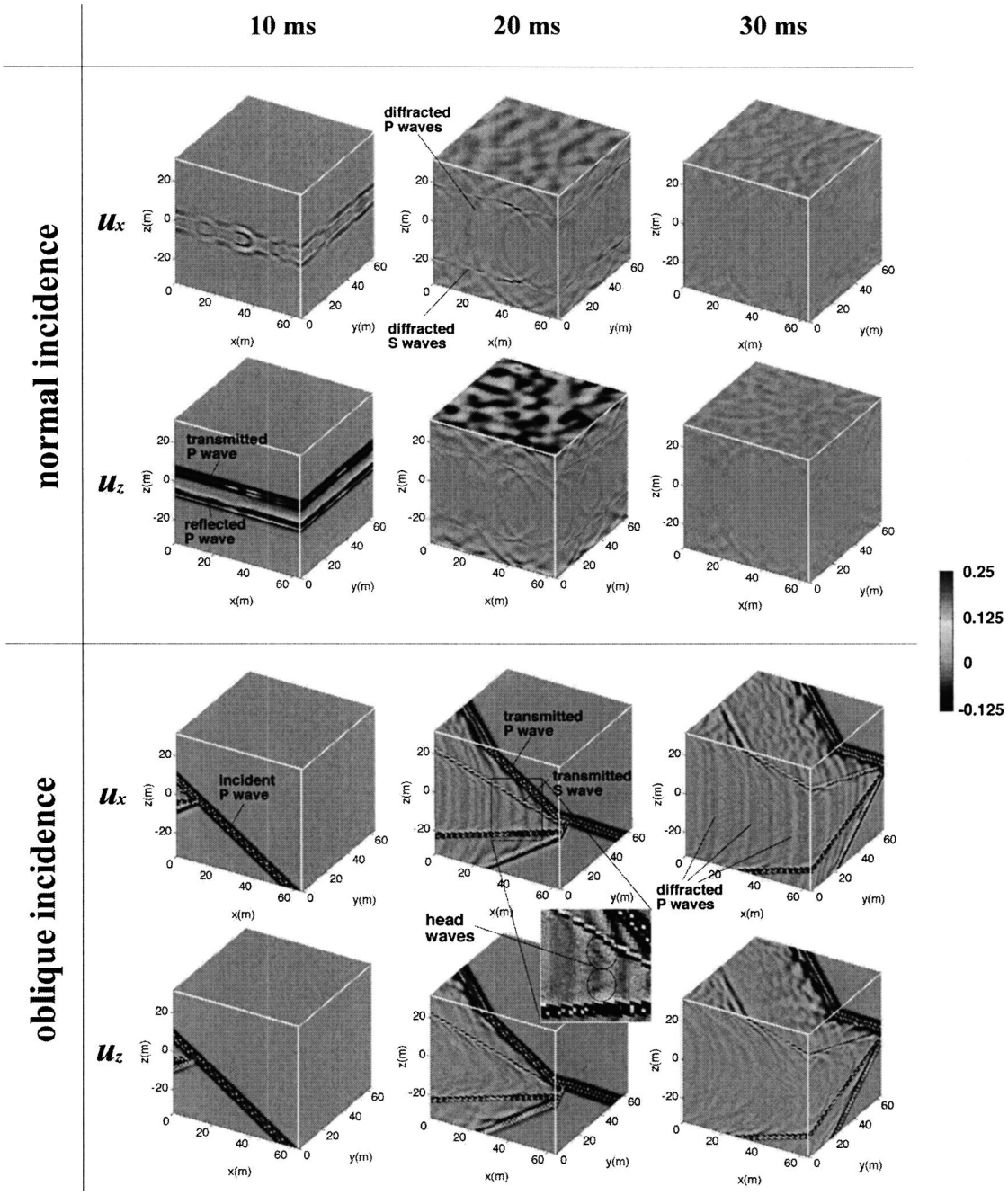

FIG. 4. Three-dimensional snapshots of the waves scattered by a single plane fracture at $z=0$, with the heterogeneous fracture compliance distribution shown in Fig. 4. Both x and z direction particle displacements are shown on the surfaces of a cube cut out of an infinite medium containing the fracture. The top two rows are for a normally incident P wave propagating from the bottom of the plots, and the bottom two rows are for an obliquely incident P waves propagating from the bottom left corner of the cube, in the $(1/\sqrt{3},1/\sqrt{3},1/\sqrt{3})$ direction.

main). For this example, although the length of the wave number series was rather short $[(M,N)=(32,32)]$, the amplitudes of the scattered waves became significantly small at the edge of the diagram, showing *a posteori* that the selected length of the series was sufficiently long. It is also noted that while the normal-incidence case showed no coupling between the incident P wave and Sh waves, the oblique-incidence case showed small Sh waves.

D. Born approximations and low- and high-frequency asymptotic solutions

If the compliance distribution is uniform, only the specular wave number component needs to be examined. This is because the convolution matrix, $\bar{\bar{\boldsymbol{\eta}}}$, and therefore the system matrix in Eq. (27), becomes block diagonal due to the lack of coupling between different wave number components. For a plane incident wave, using the vectors and matrices in Eq. (28), the ''exact'' equation (27) reduces to

$$[(i\omega)^{-1}\mathbf{H}_0-\tilde{\boldsymbol{\eta}}_0]\tilde{\boldsymbol{\sigma}}=(i\omega)^{-1}\mathbf{H}_0\tilde{\boldsymbol{\sigma}}_{\mathrm{Inc}} \quad \text{or}$$

$$(\mathbf{I}-i\omega\mathbf{H}_0^{-1}\tilde{\boldsymbol{\eta}}_0)\tilde{\boldsymbol{\sigma}}_0\equiv(\mathbf{I}-i\boldsymbol{\Omega}_0)\tilde{\boldsymbol{\sigma}}_0=\tilde{\boldsymbol{\sigma}}_{\mathrm{Inc}}. \tag{34}$$

For a diagonal fracture compliance matrix $\tilde{\boldsymbol{\eta}}_0 \equiv \mathrm{diag}[\eta_{xx},\eta_{yy},\eta_{zz}]$, $\boldsymbol{\Omega}_0$ is

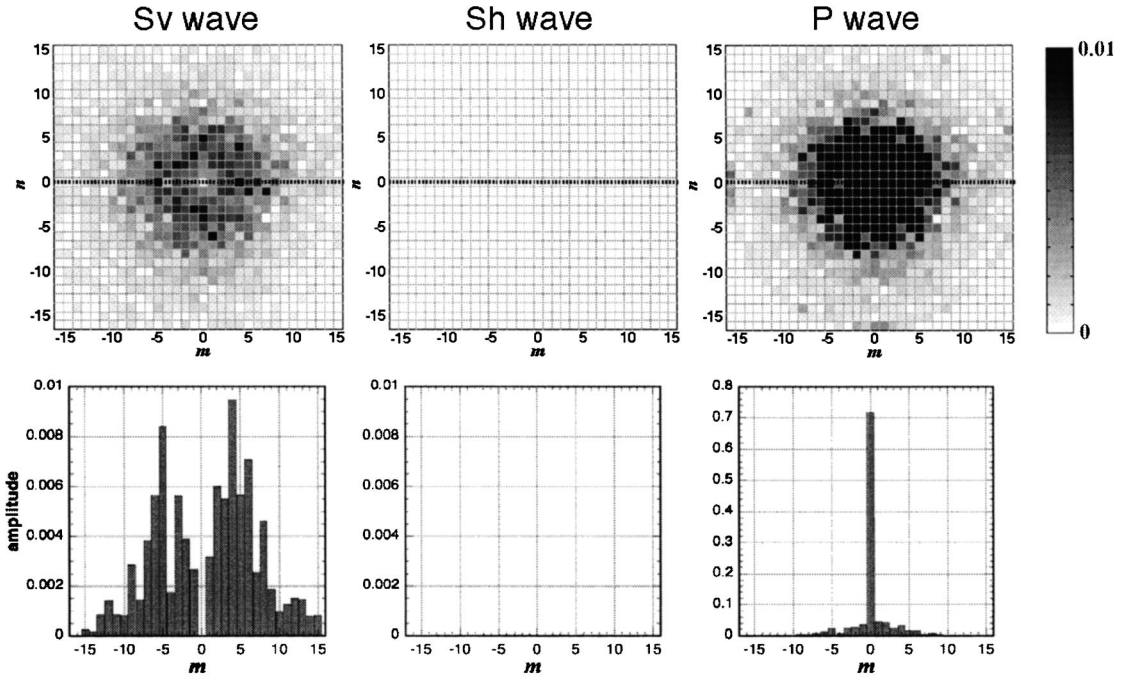

(a) Wave number diagrams for a normally incident P wave

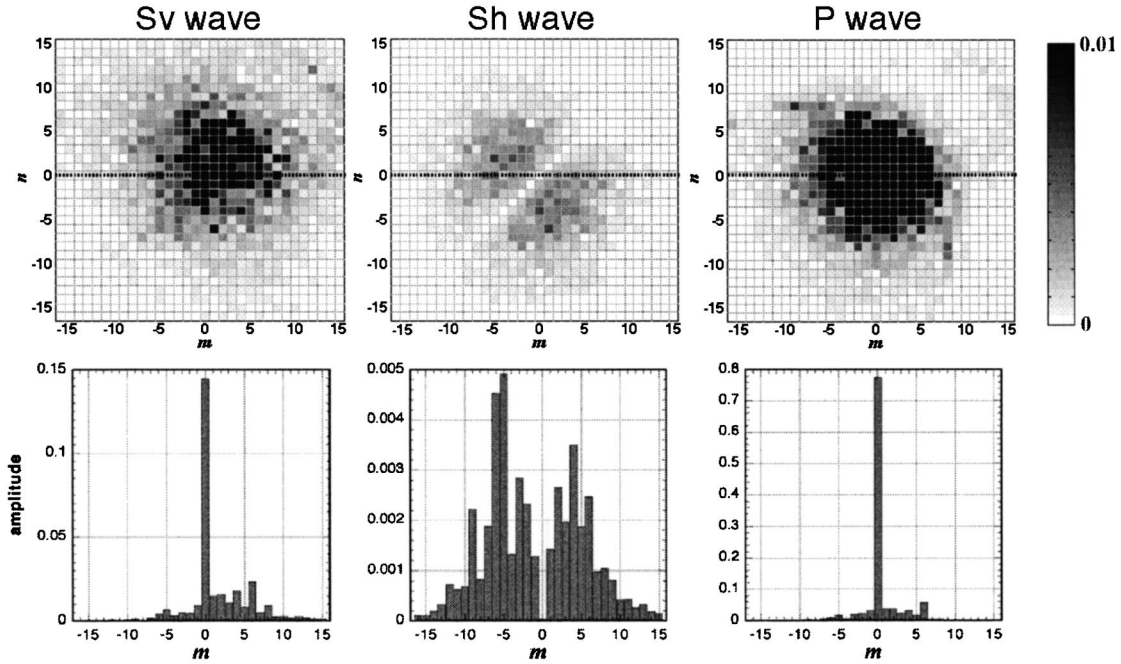

(b) Wave number diagrams for an obliquely incident P wave

FIG. 5. *Sv*, *Sh*, and *P*-wave amplitude distributions of wave number components around a unit amplitude, incident *P* wave ($m=n=0$). Both the normal incidence case (a) and oblique incidence case (b) are shown. The frequency of the waves is 750 Hz. The color scale is saturated for components with an amplitude larger than 0.01. The line diagrams are the profiles of the distributions cut along the line, $m=0$ (shown as a dotted line). The amplitudes of the wave number components decay quickly away from the center (incident wave).

$$\mathbf{\Omega}_0 = \mathrm{Diag}\left[\frac{\omega\rho c_S \eta_{xx}}{2}\ \frac{\omega\rho c_S \eta_{yy}}{2}\ \frac{\omega\rho c_P \eta_{zz}}{2}\right] \equiv \mathrm{Diag}[\Omega_{Sv}\ \ \Omega_{Sh}\ \ \Omega_P]. \tag{35}$$

Therefore the components of this matrix are the dimensionless frequencies defined by Haugen and Schoenberg (2000).[23] The stiffness based equations (defined in Appendix) also reduces to

$$(i\omega\mathbf{H}_0^{-1} - \tilde{\boldsymbol{\kappa}}_0)[\tilde{\mathbf{u}}] = i\omega\mathbf{H}_0^{-1}[\tilde{\mathbf{u}}]_{\mathrm{Inc}} \quad \text{or}$$

$$[\mathbf{I} - (i\omega)^{-1}\mathbf{H}_0\tilde{\boldsymbol{\kappa}}_0][\tilde{\mathbf{u}}]_0 \equiv (\mathbf{I} + i\mathbf{T}_0)[\tilde{\mathbf{u}}]_0 = [\tilde{\mathbf{u}}]_{\mathrm{Inc}}. \tag{36}$$

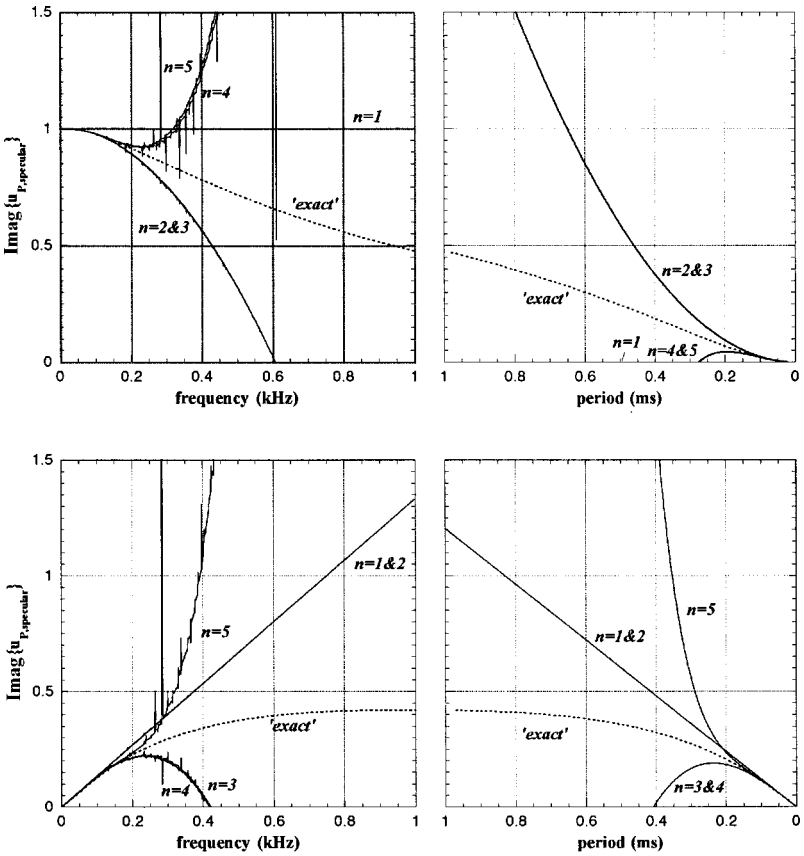

FIG. 6. Real (top) and imaginary (bottom) parts of the transmission coefficients (the most dominant specular components of *P* wave are compared) computed using the Born approximations of different orders up to $n=5$. For comparison, the "exact" numerical solutions are also plotted. The low-frequency (left) approximations are computed using the compliance-based Born series while the high-frequency (right) approximations are obtained from the stiffness-based Born series.

Since both $\tilde{\boldsymbol{\eta}}_0$ and $\tilde{\boldsymbol{\kappa}}_0$ are constant and diagonal, and $\mathbf{H}_0$ is also diagonal for normally incident waves, $\tilde{\boldsymbol{\kappa}}_0=\tilde{\boldsymbol{\eta}}_0^{-1}$, and $\mathbf{T}_0=\boldsymbol{\Omega}_0^{-1}$. Therefore, the two Born series are

$$\tilde{\boldsymbol{\sigma}}_0=\sum_{n=0}^{\infty} i^n \boldsymbol{\Omega}_0^n \cdot \tilde{\boldsymbol{\sigma}}_{\mathrm{Inc}}, \tag{37}$$

$$[\tilde{\mathbf{u}}]_0=\sum_{n=0}^{\infty} (-i)^n \boldsymbol{\Omega}_0^{-n} \cdot [\tilde{\mathbf{u}}]_{\mathrm{Inc}}. \tag{38}$$

Since the eigenvalues of the matrices $\boldsymbol{\Omega}_0$ and $\boldsymbol{\Omega}_0^{-1}$ are the Haugen and Schoenberg's dimensionless frequencies and their inverse, the above Born series converge for $|\Omega_{Sv,Sh,P}|<1$ for compliance based series, and $|\Omega_{Sv,Sh,P}|>1$ for the stiffness based series. Therefore compliance and stiffness-based Born approximations can be applied in the low- and high-frequency limits, respectively. Physically, the compliance-based Born series can be viewed as a perturbation of the totally transmitted waves across a welded fracture in the static limit by small reflection of nonzero-frequency wave energy. In contrast, the stiffness-based Born series is a perturbation of the totally reflected waves for an open fracture in the high-frequency limit by small transmission of finite-frequency wave energy.

For heterogeneous fracture compliance and stiffness distributions, these relationships are more complicated due to the nonspecular scattering of waves. The matrix-vector form of the Born series is obtained from Eq. (23) as

$$\overline{\boldsymbol{\sigma}}=\sum_{n=0}^{\infty} (i\omega \overline{\mathbf{H}}^{-1} \tilde{\bar{\boldsymbol{\eta}}})^n \overline{\boldsymbol{\sigma}}_{\mathrm{Inc}} \equiv \sum_{n=0}^{\infty} i^n \overline{\boldsymbol{\Omega}}^n \overline{\boldsymbol{\sigma}}_{\mathrm{Inc}}. \tag{39}$$

Also, from the Appendix, the stiffness-based Born series is

$$[\overline{\mathbf{u}}]=\sum_{n=0}^{\infty} [(i\omega)^{-1} \overline{\mathbf{H}} \tilde{\bar{\boldsymbol{\kappa}}}]^n [\overline{\mathbf{u}}]_{\mathrm{Inc}} \equiv \sum_{n=0}^{\infty} (-i)^n \overline{\mathbf{T}}^n [\overline{\mathbf{u}}]_{\mathrm{Inc}}. \tag{40}$$

These series are convergent if $\|\overline{\boldsymbol{\Omega}}\|<1$ and $\|\overline{\mathbf{T}}\|<1$, i.e., the magnitude of the eigenvalues of the matrices are smaller than unity. It is desirable to interpret these conditions as the low- and high-frequency limits, as we saw for a homogeneous fracture, so that we can apply the Born approximations to the low- and high-frequency scattering problems for a heterogeneous fracture. We will examine these possibilities using numerical simulations.

For the fracture model used in the preceding section, we can compute the scattered wavefield from the (generalized) Born series. For simplicity, we assume normally incident, monochromatic transmitted *P* waves, and examine only the specular component of the waves. The "exact" solutions are also computed from Eq. (27) for a range of frequencies, and compared to the Born approximations of different orders. Figures 6 shows the comparisons of transmission coefficient amplitudes computed from the *z*-direction particle motions of *P* waves. Each curve in the plots is labeled with the order of Born approximation. The low-frequency approximations were computed using the compliance-based Born series, and the high-frequency approximations were computed using the stiffness-based Born series. As can be seen from the plots, the Born approximations appear to be valid in both low- and high-frequency limits, respectively, and including higher-order terms in the Born series does improve the applicability

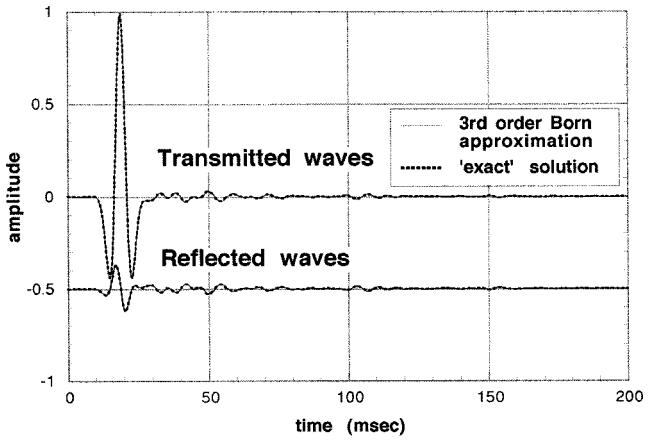

FIG. 7. Comparison between z-direction particle motions computed by solving the matrix equation in Eq. (27) and by the third-order, compliance-based Born approximation. The central frequency of the incident Ricker wavelet (P wave) is 100 Hz, and the receivers are located on both sides, 32 m away from the fracture. The results are nearly identical.

of the approximations. For the fracture and background properties used for this example, the low-frequency approximation is valid below 150 Hz, and the high-frequency approximation is valid above 10 kHz. In Fig. 7, z-direction particle displacements are compared for both third-order Born approximation and the exact numerical solution. The receivers are located at $z=32\,\mathrm{m}$ (transmitted waves) and $z=-32\,\mathrm{m}$ (reflected waves), and a low frequency (a central frequency of 100 Hz) Ricker wavelet was used. For this example, the results of the two methods are indistinguishable.

However, these results do not necessarily guarantee that the first two terms in the Born series (first-order Born approximations) are exactly the leading terms in the series, i.e., low- and high-frequency asymptotes of the exact solutions. We examined the low- and high-frequency limit behavior of the two Born series more in detail by plotting the displacement amplitudes computed from the individual terms of both series as a function of frequency [Figs. 8 left and right, respectively]. It is noted that the lowest order term of the stiffness-based Born series is $O(1/\omega)$, because the transmitted wave's displacement computed from the displacement is computed via a relationship $\tilde{\mathbf{u}}^{+}=[\tilde{\mathbf{u}}]-[\tilde{\mathbf{u}}]_{\mathrm{Inc}}$ which removes the 0th order term from the original Born series.

From Fig. 8 left, the second and the higher-order terms of the compliance-based Born series all exhibit $O(\omega)$ dependence, instead of the expected $O(\omega^n)$ dependence for a homogeneous fracture in Eq. (37), where n is the order of the term. This indicates that, although it is still a good approximation due to small magnitudes of the terms higher than $n>2$, the compliance-based Born approximation does not give the exact low-frequency asymptotic solution. In contrast, from Fig. 8 right, the terms in the stiffness-based Born approximation are $O(1/\omega^n)$, giving correct high-frequency asymptotes.

Since the frequency-independent $\mathbf{H}$ matrices should result in $O(\omega^n)$ dependence of the compliance-based Born series from Eq. (39), the above result seems to be incorrect. This apparent discrepancy is due to the wave number convolution involving both $\mathbf{H}=\mathbf{H}(k_r/\omega)$ and $\tilde{\boldsymbol{\eta}}=\tilde{\boldsymbol{\eta}}(k_r)$ for twice or more scattered waves in the compliance-based Born series. $\mathbf{H}$ is frequency independent only if the plane parallel wave number k_r is viewed as a function of frequency ($k_r/\omega=p$, p is the plane parallel slowness). However, this exchange of independent variables does not make the convolution integral frequency independent, because $\tilde{\boldsymbol{\eta}}$, which originally is dependent upon only k_r, is now frequency dependent: $\tilde{\boldsymbol{\eta}}=\tilde{\boldsymbol{\eta}}(k_r)=\tilde{\boldsymbol{\eta}}(\omega p)$. Therefore, the resulting convolution operators (or matrices) $\bar{\boldsymbol{\Omega}}^n\equiv(\omega\bar{\mathbf{H}}^{-1}\bar{\tilde{\boldsymbol{\eta}}})^n$ are not $O(\omega^n)$. In contrast, for high-frequencies and the stiffness-based Born series, $\mathbf{H}$ is frequency independent without exchanging the variables, because $\mathbf{H}=\mathbf{H}(k_r/\omega)=\mathbf{H}(k_z^P/k_S,k_z^S/k_S)\rightarrow\mathbf{H}(c_S/c_P,1)$, which yields $\mathbf{T}^n\sim O(\omega^{-n})$.

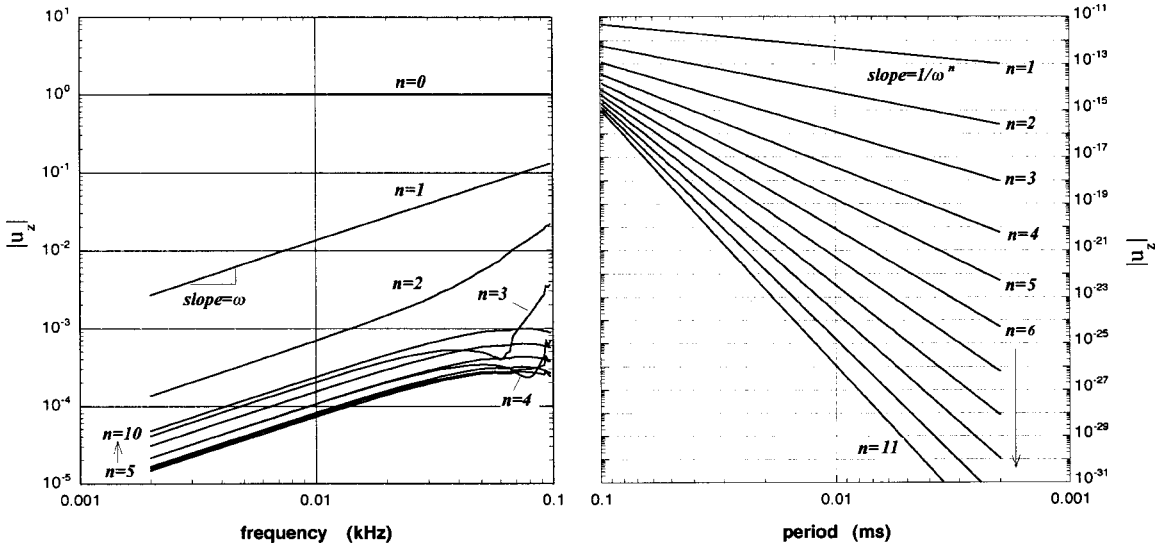

FIG. 8. Displacement amplitude computed from individual terms in the Born series for a unit-amplitude, plane incident P wave. The z-direction particle displacements of transmitted P wave are shown. The nth-order term of the high-frequency Born series (right) scales as $O(1/\omega^n)$. In contrast, all the terms except for the 0th-order term (incident wave) in the low-frequency Born series (left) scale as $O(\omega)$. The absolute magnitudes of the higher order terms, however, are small for this example.

IV. CONCLUSIONS

We developed a plane wave method to compute the three-dimensional scattering of plane elastic waves by a fracture with a heterogeneous stiffness (compliance) distribution. This technique allows us to examine the relationships between the characteristics of scattered elastic waves and the microstructural variations along the fracture plane (e.g., surface contact and crack distribution, gouge layer thickness variation) that are modeled as heterogeneities in the fracture compliance distribution.

This method is a straightforward extension of the commonly used seismic displacement discontinuity (SDD) method for a homogeneous fracture, to a fracture with a heterogeneous fracture compliance distribution. Even though the developed technique is a full-waveform technique and successfully models a variety of wave phenomena involving a fracture, such as mode converted waves, head waves (refracted waves), surface waves and diffracted waves, it does not require massive parallel computers as finite difference methods and boundary element methods would do.

The current numerical technique can be applied to nonplanar incident waves by simply modifying the incident wave vector. In this case, however, a larger number of wave number components need to be used in the matrix equation. It should also be noted that this technique is difficult to apply to extremely heterogeneous fractures, because such fractures typically results in a large linear system of equations to solve for nonspecular components of scattered waves with wave numbers far different from the incident wave. Further, the compliance-based equations break down for open cracks and voids (infinite compliance) and the stiffness-based equations break down for welded surfaces (infinite stiffness), because the Fourier transforms cannot be performed.

Last, we demonstrated that two types of Born series can be used to examine the low- and high-frequency limit behavior of the wave scattering by a heterogeneous fracture. The low-frequency Born series (compliance-based formulation), however, should be used with a caution, because the lowest-order term does not provide the exact low-frequency asymptotic solution. In contrast, the high-frequency Born series (stiffness-based formulation) is the exact high-frequency asymptote, although, in practice, the local SDD conditions used as a basis of the theory may not be valid for such high frequencies.

ACKNOWLEDGMENTS

This research has been supported by the Office of Science, Office of Basic Energy Sciences, Division of Chemical Sciences of the U.S. Department of Energy under Contract No. DE-AC76SF00098. Also, the authors would like to thank Dr. Michael Schoenberg for his helpful comments and suggestions.

APPENDIX

As an alternative to using the compliance-based equations, we can use equations based on fracture stiffness $\boldsymbol{\kappa}(x,y)=\boldsymbol{\eta}^{-1}(x,y)$. In this case, Eq. (7) in the text is replaced by

$$(\tilde{\boldsymbol{\kappa}}^{*}[\tilde{\mathbf{u}}])(k_x,k_y)=\tilde{\boldsymbol{\sigma}}(k_x,k_y). \tag{A1}$$

$\tilde{\boldsymbol{\kappa}}$ is the Fourier transformed fracture stiffness matrix. By using the displacement discontinuity vector $[\tilde{\mathbf{u}}]$ as the primary variable, the traction vector $\tilde{\sigma}$ is eliminated from Eq. (A1), resulting in

$$(i\omega\mathbf{H}^{-1}-\tilde{\boldsymbol{\kappa}}^{*})[\tilde{\mathbf{u}}]=i\omega\mathbf{H}^{-1}[\tilde{\mathbf{u}}]_{\mathrm{Inc}}, \tag{A2}$$

where the incident term for the displacement–discontinuity vector is defined as

$$[\tilde{\mathbf{u}}]_{\mathrm{Inc}}\equiv-\mathbf{H}\mathbf{S}^{+}\mathbf{a}_{\mathrm{Inc}}. \tag{A3}$$

Equation (A3) is the displacement–discontinuity vector for an open fracture (free surface). The integral equation corresponding to Eq. (22) is

$$[\tilde{\mathbf{u}}](k_x,k_y)=[\tilde{\mathbf{u}}]_{\mathrm{Inc}}(k_x,k_y)+(i\omega)^{-1}\mathbf{H}(k_x,k_y)\times\int_{-\infty}^{+\infty}\int_{-\infty}^{+\infty}\tilde{\boldsymbol{\kappa}}(k_x-k_x',k_y-k_y')[\tilde{\mathbf{u}}]\times(k_x',k_y')dk_x'\,dk_y', \tag{A4}$$

and the Neumann series (Born series) corresponding to Eq. (24) is

$$[\tilde{\mathbf{u}}]=[\overline{\mathbf{I}}-i\overline{\mathbf{T}}+(-i\overline{\mathbf{T}})^{2}+\cdots][\tilde{\mathbf{u}}]_{\mathrm{Inc}}=(\overline{\mathbf{I}}+i\overline{\mathbf{T}})^{-1}[\tilde{\mathbf{u}}]_{\mathrm{Inc}}, \tag{A5}$$

where the operator $\overline{\mathbf{T}}$ is defined as $\overline{\mathbf{T}}\equiv\omega^{-1}\overline{\mathbf{H}}\bar{\bar{\boldsymbol{\kappa}}}$. Note that, in general, the fracture stiffness convolution operator $\bar{\bar{\boldsymbol{\kappa}}}$ is not the inverse of the compliance operator $\bar{\bar{\boldsymbol{\eta}}}$. Equation (A4) can be written in a matrix form to be solved numerically. The resulting matrix equation is equivalent to the compliance-based equation (26) but shows faster convergence of iterative solutions at higher frequencies. This property can be used to efficiently implement the computer program to solve for the "exact" solutions: the compliance formulation is used at low frequencies and the stiffness formulation at high frequencies.

[1] E. Liu, J. A. Hudson, and T. Pointer, "Equivalent medium representation of fractured rock," J. Geophys. Res., [Solid Earth] **105**, 2981–3000 (2000).

[2] M. A. Schoenberg, "Elastic wave behavior across linear slip interfaces," J. Acoust. Soc. Am. **68**, 1516–1521 (1980).

[3] J. Baik and R. B. Thompson, "Ultrasonic scattering from imperfect interfaces: a quasi-static model," J. Nondestruct. Eval. **4**, 177–196 (1984).

[4] Y. C. Angel and J. D. Achenbach, "Reflection and transmission of elastic waves by a periodic array of cracks," J. Appl. Mech. **52**, 33–41 (1985).

[5] L. R. Myer, D. Hopkins, and N. G. W. Cook, "Effects of contact area of an interface on acoustic wave transmission," Proceedings of the 26th US Symposium on Rock Mechanics, Rapid City, Ed.: E. Ashworth, Balkema, Rotterdam, Boston, 549–556 (1985).

[6] L. J. Pyrak-Nolte and N. G. W. Cook, "Elastic interface waves along a fracture," Geophys. Res. Lett. **14**, 1107–1110 (1987).

[7] S. I. Rokhlin and Y. J. Wang, "Analysis of boundary conditions for elastic wave interaction with an interface between two solids," J. Acoust. Soc. Am. **89**, 503 (1991).

[8] S. Nakagawa, K. T. Nihei, and L. R. Myer, "Elastic wave propagation along a set of parallel fractures," Geophys. Res. Lett., DOI 10 1029/2002 GLO14925 (2002).

[9] L. J. Pyrak-Nolte, L. R. Myer, N. G. W. Cook, and P. A. Witherspoon, "Hydraulic and mechanical properties of natural fractures in low permeability rock," Proceedings of the 6th International Congress of Rock Mechanics, Montreal, I, Eds: G. Herget and S. Vongpaisal, Balkema, Rotterdam, Boston, I, 225–232 (1987).

[10] O. Buck, D. K. Rehbein, and R. B. Thompson, "Crack tip shielding by

asperity contact as determined by acoustic measurements,'' Eng. Fract. Mech. **28**, 413 (1987).
[11] A. Oliger, L. J. Pyrak-Nolte, and D. D. Nolte, ''Scismic focusing by a single planar fracture,'' Geophys. Res. Lett. **30**, DOI 10 1029/2002GL014925 (2003).
[12] E. Hakami and E. Larsson, ''Aperture measurement and flow experiments on a single natural fracture,'' Int. J. Rock Mech. Min. Sci. Geomech. Abstr. **33**, 395–404 (1996).
[13] L. J. Pyrak-Nolte and D. D. Nolte, ''Frequency dependence of fracture stiffness,'' Geophys. Res. Lett. **19**, 325–328 (1992).
[14] K. T. Nihei, ''Modeling elastic waves in fractured rock with the Kirchhoff method,'' M.S. thesis, University of California at Berkeley, 1989.
[15] A. Oliger, L. J. Pyrak-Nolte, and D. D. Nolte, ''Seismic focusing by a single planar fracture,'' Geophys. Res. Lett. (in press).
[16] Y. Mikata and J. D. Achenbach, ''Interaction of harmonic waves with a periodic array of inclined cracks,'' Wave Motion **10**, 59–72 (1988).
[17] M. Punjani and L. J. Bond, ''Scattering of plane waves by a partially closed crack,'' Rev. Prog. Quant. Nondestr. Eval. **5A**, 61–71 (1986).
[18] R. T. Coates and M. A. Schoenberg, ''Finite-difference modeling of faults and fractures,'' Geophysics **60**, 1514–1526 (1995).
[19] H. Van der Vorst, ''Bi-CGSTAB: A fast and smoothly converging variant of Bi-CG for the solution of nonsymmetric linear equations,'' SIAM (Soc. Ind. Appl. Math.) J. Sci. Stat. Comput. **13**, 631–644 (1992).
[20] Y. Saad and M. H. Schultz, ''GMRES: A generalized minimum residual algorithm for solving unsymmetric linear systems,'' SIAM (Soc. Ind. Appl. Math.) J. Sci. Stat. Comput. **7**, 856–869 (1986).
[21] S. Hirose and M. Kitahara, ''Scattering of elastic waves by a crack with spring-mass contact,'' Int. J. Numer. Methods Eng. **31**, 789–801 (1991).
[22] E. Pardo-Iguzquiza and M. Chica-Olmo, ''The Fourier Integral Method: An efficient spectral method for simulation of random fields,'' Math. Geol. **25**, 177–217 (1993).
[23] G. U. Haugen and M. A. Schoenberg, ''The echo of a fault or fracture,'' Geophysics **65**, 176–189 (2000).

Scattering of an elastic wave by a single dislocation

Agnès Maurel[a)]
Laboratoire Ondes et Acoustique, UMR CNRS 7587, Ecole Supérieure de Physique et de Chimie Industrielles, 10 rue Vauquelin, 75005 Paris, France

Jean-François Mercier
Laboratoire de Simulation et de Modélisation des Phénomènes de Propagation, URA 853, Ecole Nationale Supérieure des Techniques Avancées 32 bd Victor, 75015 Paris, France

Fernando Lund
Departamento de Física, Facultad de Ciencias Físicas y Matemáticas, Universidad de Chile, Casilla 487-3, Santiago, Chile and Centro para la Investigación Interdisciplinaria Avanzada en Ciencias de los Materiales (CIMAT), Santiago, Chile

(Received 29 June 2003; revised 18 January 2004; accepted 26 January 2004)

The scattering amplitude for the scattering of anti-plane shear waves by screw dislocations, and of in-plane shear and acoustic waves by edge dislocations are computed within the framework of elasticity theory. The former case reproduces well-known results obtained on the basis of an electromagnetic analogy. The latter case involves four scattering amplitudes in order to fully take into account mode conversion, and an adequately generalized optical theorem for vector waves is provided. In contrast to what happens for scattering by obstacles, the scattering amplitude increases with wavelength, and, in general, mode conversion in the forward direction does not vanish. © *2004 Acoustical Society of America.* [DOI: 10.1121/1.1687735]

PACS numbers: 43.20.GP, 43.35.Cg, 43.40.Fz [ANN] Pages: 2773–2780

I. INTRODUCTION

The interaction of an elastic wave with inclusion-like defects has received quite a bit of attention, starting with work in the 1950s concerning the scattering of acoustical waves by spherical obstacles that may be empty, fluid filled, or elastic, embedded in an elastic medium.[1–3] Further works consider the case of transverse incident wave both for two-dimensional cylindrical cavities[4,5] and for three-dimensional spherical cavities[6–8] as well as for more complicated inclusion shapes.[9–12]

In addition to inclusions and flaws, which are static obstacles to elastic wave propagation in a solid, and whose interaction provide the underpinning for nondestructive testing,[13–17] dislocations are also defects that interact with acoustic waves. Edge dislocations were introduced as defects in a crystal by Orowan, Polanyi, and Taylor,[18–20] and screw dislocations were introduced by Burgers.[21] Although they play a central role in the understanding of plasticity, it is very difficult to quantitatively measure their properties, a standard tool being electron microscopy. Would it be possible to develop acoustical diagnostic techniques to make quantitative dislocation measurements? A first step in that direction would involve a full understanding of the interaction between elastic waves and dislocations, about which surprisingly little can be found in the literature.

Again in the 1950s, the interaction of elastic waves with dislocations was studied by Nabarro,[22] who noted that waves would be scattered by a dislocation because the motion induced by the incoming wave would generate the emission of a scattered wave. Thus, a description of this mechanism involves two steps: the motion of a dislocation in the presence of an incident wave has to be known as well as a representation for the elastic field generated by a moving dislocation. Eshelby[23,24] and Nabarro[22] used an electromagnetic analogy to tackle the case of a two-dimensional screw dislocation, which reduces to a scalar problem when the interaction is with an anti-plane shear wave. However, this analogy is no longer valid for edge dislocations when both in-plane shear and compressional waves are involved, each one with its own propagation velocity. In 1963, Mura[25] derived from the Navier equations an integral representation for the elastic field generated by a dislocation loop in three dimensions in arbitrary motion, of which two-dimensional cases can be obtained as special cases. Kiusalaas[26] considered the special case of an edge dislocation oscillating with an arbitrary velocity. Also, the expression of the total scattering cross section of an elastic shear wave incident at right angles with the Burgers vector of the dislocation can be found in the conclusion of this paper, suggesting that the authors have used some equation of motion for the edge dislocation. Unfortunately, no calculations are given, the authors indicating that they are too lengthy to be reproduced.

The derivation from the Navier equation of the equation of motion for a dislocation in the presence of an external, time-dependent, stress field has been obtained by Lund.[27] This work, together with the integral representation of Mura,[25] allows for a full description of the scattering of elastic waves by dislocations. This paper carries out this program for both screw and edge dislocations in two dimensions. In the former case, the problem reduces to a scalar problem for the anti-plane (shear) wave. The results obtained are in agreement with those obtained in Ref. 22 using the electromagnetic analogy. The latter case leads to a vector problem

a)Electronic mail: agnes.maurel@espci.fr

for the two in-plane (shear and compressional) waves. Thus, accounting for mode conversions, four scattering functions are determined.

In three dimensions, the interaction of sound waves with dislocation segments has been described by the vibrating string model[28–31] based on the formulation of Koehler[32] in which the dislocation is modeled as a scalar string driven by a scalar time dependent stress. This model is very simple, a fact that allows for many applications, and it certainly captures the essence of the physics of the elastic wave–dislocation interaction. It has been quite successful in explaining a wealth of data in acoustics and thermal conductivity experiments.[33] However, it does not consider the many complexities of this interaction. For example, it does not differentiate between edge and screw dislocations, or among the various polarizations available to an elastic wave. The present work presents a full vector treatment of the elastic wave–dislocation interaction in two dimensions.

The paper is organized as follows. Section II presents briefly the integral representation of the scattered wave due to the motion of the dislocation and the equation of motion for a dislocation in the presence of an incident wave. Simplified expressions for the bidimensional problem and in the case of small amplitude and small velocity (well below the speed of sound) motion of the dislocation are given. Sections III and IV treat, respectively, the anti-plane and in-plane cases and the derivation of the scattering functions are presented, as well as the resulting cross sections. It is found in both cases that the scattering strength of a dislocation increases when increasing the wavelength of the incident wave. The explanation for this unusual behavior comes from the particular mechanism of the scattering which differs from the mechanism responsible for the scattering by static inhomogeneity such as inclusions and voids, where a vanishing scattering cross section is expected at long wavelengths. As previously noted, the scattering by a dislocation is a consequence of a dynamic interaction with the incident wave and there is no reason to expect similar results here. Rather, the scattering cross section is linked to the equation of motion of the dislocation in the presence of an incoming wave, a motion whose amplitude does increase with the wavelength in the dynamical models of Refs. 24 and 27. A complete description of the interaction of an elastic wave with a dislocation would also consider the interaction with the core of the dislocation. This would need an atomistic description of the dislocation core. However, this effect can be neglected for elastic wavelengths that are long compared to core size, as is the case for externally generated waves even at the highest ultrasonic frequencies available.

II. BASIC EQUATIONS

The mechanism for the scattering of an elastic incident wave by a dislocation is quite simple: The incident wave hits the dislocation, causing it to oscillate in response. The ensuing oscillatory motion will generate outgoing (from the dislocation position) elastic waves.

The goal of this section is to briefly derive the integral representation of the scattered wave due to the motion of a dislocation (2.4) and the equation of motion of a dislocation (2.5). Equation (2.4) comes from Ref. 25 written in two dimensions and under the hypothesis of small amplitude motion. Equation (2.5) comes from Ref. 27 under the same hypothesis.

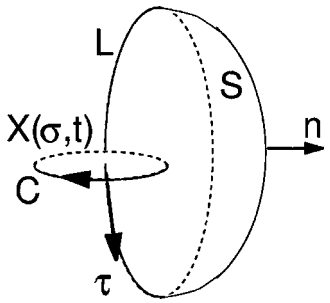

FIG. 1. Definition of the Burgers vector.

In Secs. III and IV, these equations will be used when the dislocation motion is induced by an incident wave.

A. Scattered wave by a moving dislocation

We consider a dislocation loop $\mathbf{X}(\sigma,t)$, where σ is the coordinate along the loop L in the three-dimensional space with the current coordinates $\mathbf{x}=(x_1,x_2,x_3)$. $\mathbf{b}$ is the Burgers vector, defined by a discontinuity of the displacement field $\mathbf{u}$: $\oint_{\mathcal{C}} d\mathbf{u} \equiv -\mathbf{b}$, formally written $[\mathbf{u}]=\mathbf{b}$, where $\mathcal{C}$ is a closed curve around the dislocation with a direct orientation with respect to $\boldsymbol{\tau}=\partial\mathbf{X}/\partial\sigma$ (Fig. 1).

A homogeneous, linearly elastic solid containing a dislocation loop L is described by displacements $\mathbf{u}(\mathbf{x},t)$ away from an equilibrium position, and the equations of elastodynamics are

$$\rho \frac{\partial^2}{\partial t^2} u_i(\mathbf{x},t) - c_{ijkl} \frac{\partial^2}{\partial x_j \partial x_k} u_l(\mathbf{x},t) = 0 \tag{2.1}$$

with boundary conditions

$$[u_i] = b_i, \quad \left[c_{ijkl} \frac{\partial u_l}{\partial x_k} n_j \right] = 0 \tag{2.2}$$

across a surface S bounded by the dislocation loop. We consider an isotropic solid, where the elastic constants are $c_{ijkl} = \lambda \delta_{ij}\delta_{kl} + \mu(\delta_{ik}\delta_{jl} + \delta_{il}\delta_{jk})$ with (λ,μ) the Lamé coefficients and ρ is the density. Using the Green function in the three-dimensional free space $G^{0(3\mathrm{D})}$, defined by

$$\rho \frac{\partial^2}{\partial t^2} G^{0(3\mathrm{D})}_{im}(\mathbf{x}-\mathbf{x}',t-t') - c_{ijkl} \frac{\partial^2}{\partial x_j \partial x_k} G^{0(3\mathrm{D})}_{lm}(\mathbf{x}-\mathbf{x}',t-t')$$
$$= \delta(\mathbf{x}-\mathbf{x}')\,\delta(t-t')\,\delta_{im},$$

the displacement u_m generated by a dislocation loop $\mathbf{X}(\sigma,t)$ undergoing arbitrary motion can be written as an integral representation,

$$u_m(\mathbf{x},t) = c_{ijkl} \int \int_{S(t')} dt'\, dS\, b_l n_k \frac{\partial}{\partial x_j} G^{0(3\mathrm{D})}_{im}(\mathbf{x}-\mathbf{x}',t-t'),$$

where $\mathbf{n}$ denotes the normal vector to $S(t)$, the surface of discontinuity for the displacement [$S(t)$ is time dependent since the dislocation line that defines $\mathbf{X}(\sigma,t)$ moves]. Since this surface does not have a special physical significance, it

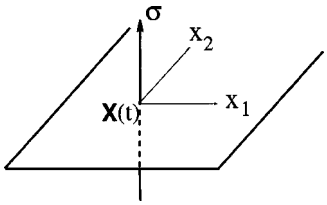

FIG. 2. Configuration of the two-dimensional (2D) problem.

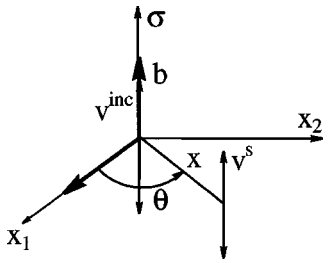

FIG. 3. Shear wave propagating along x_1 (velocity v^{inc}) interacting with a 2D screw dislocation.

should be possible to express physically meaningful quantities in terms of a source that is localized along the loop L. This was done by Mura[25] taking the time derivative of the preceding expression. Using $\int_{\Delta S} dS\, n_k = \epsilon_{knh} \oint_L d\sigma\, \dot{X}_n \tau_h \Delta t$, where ΔS is an increment of $S(t)$ with respect to a time increment Δt, ϵ_{knh} is the usual completely antisymmetric tensor and an overdot means time derivative. Thus, the velocity $v_m \equiv \dot{u}_m$ is found to satisfy the integral representation:

$$v_m(\mathbf{x},t) = \epsilon_{knh} c_{ijkl} \int \oint_L dt'\, d\sigma\, b_l \dot{X}_n(\sigma,t')\, \tau_h(\sigma)\, \frac{\partial}{\partial x_j} \times G_{im}^{0(3\mathrm{D})}(\mathbf{x} - \mathbf{X}(\sigma,t'), t-t'). \tag{2.3}$$

In addition to the interest of deriving an integral representation over a curve that has a physical meaning, note that the displacement **u** (for which no such integral can be found) is not particularly relevant contrary to its time and space derivatives which appear in expressions of energy and momentum.

We consider now the bidimensional case of a dislocation line along the x_3 axis moving in the plane (x_1, x_2) (Fig. 2). Equation (2.3) takes the form

$$v_m(\mathbf{x},t) = \epsilon_{kn} c_{ijkl} \int dt'\, b_l \dot{X}_n(t')\, \frac{\partial}{\partial x_j} G_{im}^0(\mathbf{x} - \mathbf{X}(t'), t-t'),$$

where $\epsilon_{ij} \equiv \epsilon_{ij3}$ and $G^0 \equiv \int dx_3\, G^{0(3\mathrm{D})}$ is the Green function in two dimensions. For small amplitude motion of a dislocation near the origin, we have at dominant order $G^0(\mathbf{x} - \mathbf{X}(t'), t-t') \simeq G^0(\mathbf{x}, t-t')$. Since v_m appears as a convolution product, we obtain in the frequency domain

$$v_m(\mathbf{x},\omega) = \epsilon_{kn} c_{ijkl} b_l \dot{X}_n(\omega)\, \frac{\partial}{\partial x_j} G_{im}^0(\mathbf{x},\omega). \tag{2.4}$$

In order to complete the description of the problem, the motion of the dislocation, $\dot{\mathbf{X}}(t)$, needs to be known.

B. Equation of motion of a dislocation in two dimensions

A method of finding an equation of motion for a dislocation loop can be found in Ref. 27. It is based on the observation that the equations of dynamic elasticity follow from a variational principle, and assumes low accelerations so that the backreaction of the radiation on the dislocation dynamics can be neglected. In two dimensions and under the hypothesis of subsonic bidimensional motion $\dot{X} \ll \alpha, \beta$, where $\alpha = \sqrt{(\lambda + 2\mu)/\rho}$ and $\beta = \sqrt{\mu/\rho}$ are the shear and compressional velocities, it takes the form:

$$\frac{\partial}{\partial t}\left(\frac{\partial \mathcal{L}}{\partial \dot{X}_a} \right) = \epsilon_{ab} b_i \Sigma_{ib}, \tag{2.5}$$

where $\Sigma_{ib} = c_{ibkl}(\partial/\partial x_l) u_k$ is the stress tensor [in Eq. (2.5), Σ_{ib} is evaluated at the dislocation position] and $\mathcal{L}$ is the Lagrangian density,

$$\mathcal{L} = -\frac{\mu}{4\pi} \ln\left(\frac{\delta}{\epsilon}\right) \left\{ b_\parallel^2 \left(1 - \frac{\dot{X}^2}{2\beta^2} \right) + b_\perp^2 \left[2(1-\gamma^{-2}) - \frac{\dot{X}^2}{2\beta^2}(1+\gamma^{-4}) \right] + \frac{(b_\perp \wedge \dot{\mathbf{X}})^2}{\beta^2}(1-\gamma^{-4}) \right\},$$

with $\gamma = \alpha/\beta$ and δ, ϵ are the long- and short-distance cut-off lengths, respectively. $b_\parallel$ and $b_\perp$ are the components of the Burgers vector parallel and perpendicular to the dislocation line. Equation (2.5) represents typically an equation for a string endowed with mass forced by the usual Peach–Koehler force.[34] In a more general case, say for oblique wave incidence, there would be additional terms arising from the line tension associated with the dislocation line curvature. A more realistic case would also consider the dislocation's viscosity. Here we neglect this effect for simplicity. Note, however, that even in the absence of an intrinsic dissipation by a single dislocation, the multiple scattering by many dislocations will damp an acoustic wave.[35]

In Secs. III and IV, the response $\dot{\mathbf{X}}(t)$ of screw ($b_\perp = 0$), and edge ($b_\parallel = 0$), dislocations to an external elastic wave is derived from Eq. (2.5).

III. THE ANTI-PLANE CASE: SCATTERING BY A SCREW DISLOCATION

Here we consider the two-dimensional problem of the scattering of an elastic wave by a screw dislocation, for which $b_\perp = 0$, interacting with an incident anti-plane shear wave (no interaction with in-plane waves occurs). This is a scalar problem, which is easy to deal with.

A. Derivation of the scattering function

A screw dislocation corresponds to a Burgers vector parallel to the dislocation line $b_i = b\,\delta_{i3}$ (Fig. 3). In the presence of an incident wave $\mathbf{v}^{\mathrm{inc}}$ of frequency Ω, Eq. (2.4) concerns the wave scattered by the dislocation $\mathbf{v}^s = \mathbf{v} - \mathbf{v}^{\mathrm{inc}}$ and simplifies in

$$v^s(\mathbf{x},\omega)=\mu b\,\epsilon_{ab}\dot{X}_b(\omega)\frac{\partial}{\partial x_a}G^0(\mathbf{x},\omega), \tag{3.1}$$

where v denotes v_3 and $G^0\equiv G^0_{33}$ is the scalar Green function for the shear wave. Since $G^0_{31}=G^0_{32}=0$, the anti-plane case corresponds to the scalar case of the interaction of the anti-plane shear wave with a screw dislocation. As previously said, the integral representation has to be completed with the law for the dislocation motion $\dot{\mathbf{X}}(\omega)$ to be self-consistent. In the case of a screw dislocation, the Lagrangian density reduces to $\mathcal{L}=(\mu b^2/4\pi\beta^2)\ln(\delta/\epsilon)(\dot{X}^2/2-\beta^2)$. Equation of motion (2.5) takes the form

$$M\ddot{X}_b(t)=-\mu b\,\epsilon_{bc}\frac{\partial u}{\partial x_c}(\mathbf{X}(t),t),$$

with $M=(\mu b^2/4\pi\beta^2)\ln(\delta/\epsilon)$ the usual effective mass per unit length of dislocation.[36,37] For a weak scattering strength, we use the Born approximation ($u=u^{\mathrm{inc}}$ in the term on the right-hand side) and we use the hypothesis of small amplitude motion [$\mathbf{X}(t)$ is taken equal to zero at dominant order for $\Omega X/\beta\ll 1$]. The previous expression takes the following form in the frequency domain:

$$\dot{X}_b(\omega)=-\frac{\mu b}{M\omega^2}\epsilon_{bc}\frac{\partial v^{\mathrm{inc}}}{\partial x_c}(\mathbf{0},\omega). \tag{3.2}$$

The Born approximation is valid for weak interaction, i.e., when the scattered wave is a small correction to the incident wave. That this is a realistic assumption is demonstrated by recent experiments of acoustic waves interacting with dislocations[38–40] where it can be seen that the incident plane wave is only slightly distorted when crossing a dislocation.

Finally, Eqs. (3.1) and (3.2) lead to

$$v^s(\mathbf{x},\omega)=\frac{\mu^2b^2}{M\omega^2}\frac{\partial v^{\mathrm{inc}}}{\partial x_a}(\mathbf{0},\omega)\frac{\partial}{\partial x_a}G^0(\mathbf{x},\omega). \tag{3.3}$$

At the distance x far from the dislocation, the scattering function $f(\theta)$ is defined as the angular dependence of the scattered wave $v^s(\mathbf{x},t)=f(\theta)(e^{i\Omega x/\beta}/\sqrt{x})v^{\mathrm{inc}}(\mathbf{0},t)$ for an incident plane wave $v^{\mathrm{inc}}(\mathbf{x},t)$ of frequency Ω, propagating, say along the x_1 axis, and of unit amplitude $v^{\mathrm{inc}}(\mathbf{x},t)=e^{i\Omega(x_1/\beta-t)}$, with $\theta=(\widehat{Ox_1,\mathbf{x}})$. Using the asymptotic behavior of the Green function $G^0(\mathbf{x},\omega)=(i/4\mu)\dot{H}_0^{(1)}(\omega x/\beta)\simeq(i/4\mu)\sqrt{(2\beta/\pi\omega)}e^{-i\pi/4}(e^{i\omega x/\beta}/\sqrt{x})$, we obtain from Eq. (3.3)

$$v^s(\mathbf{x},t)=\int d\omega\, e^{-i\omega t}\frac{\mu^2b^2}{M\omega^2}\left(\frac{i\Omega}{\beta}\delta(\omega-\Omega)\right)\times\left(-\frac{1}{4\mu}\sqrt{\frac{2\beta}{\pi\omega}}e^{-i\pi/4}\frac{\omega x_1}{\beta x}\frac{e^{i\omega x/\beta}}{\sqrt{x}}\right),$$

from which it is easy to obtain

$$f(\theta)=-\frac{\mu b^2}{2M}\frac{e^{i\pi/4}}{\sqrt{2\pi\Omega\beta^3}}\cos\theta. \tag{3.4}$$

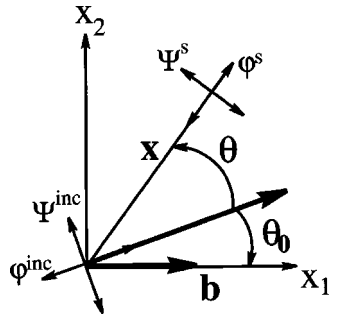

FIG. 4. Acoustic wave (velocity potential φ^{inc}) and in-plane shear-wave (velocity potential ψ^{inc}) interacting with a 2D gliding edge dislocation.

B. Total cross section

The total cross section is classically defined starting from the time averaged total energy flux across a cylinder around the dislocation $\sigma^a=\frac{1}{2}\Re(\int \mathbf{dS}\,\Sigma\mathbf{v}^*)$ and decomposing Σ and $\mathbf{v}$ into a sum of the incident part and scattered part. Then, the scattered and total cross sections are defined, with $\sigma^s=-\frac{1}{2}\Re(\int \mathbf{dS}\,\Sigma^s\mathbf{v}^{s*})$ and $\sigma^t=\sigma^a+\sigma^s$. In the scalar case, $\Sigma\mathbf{v}^*$ reduces to $\mu(\partial u/\partial x)v^*$. Normalizing the fluxes with the energy flux $\sigma_0=\mu\Omega^2/2\beta$ of the incident plane wave across a unit surface leads to

$$\frac{d\tilde{\sigma}^s}{d\theta}=|f(\theta)|^2, \tag{3.5}$$

$$\tilde{\sigma}^t=2\Im\left(\sqrt{\frac{2\pi\beta}{\Omega}}f(0)e^{-i\pi/4}\right), \tag{3.6}$$

where $\tilde{\sigma}=\sigma/\sigma_0$. The first relation gives the scattering cross-section $\tilde{\sigma}^s$ and we obtain

$$\tilde{\sigma}^s=\frac{\mu^2b^4}{8M^2\Omega\beta^3}, \tag{3.7}$$

in agreement with Ref. 26. Note that the behavior of the scattering cross section versus frequency Ω, first observed in Refs. 22–24, is unusual since it indicates that the strength of the scatterer increases with wavelength, as opposed to what happens with fixed inclusions. This is discussed further in Sec. V. The second relation is known as the optical theorem.

IV. THE IN-PLANE CASE: SCATTERING OF AN ELASTIC WAVE BY AN EDGE DISLOCATION

We consider in the following the two-dimensional problem of the scattering of an elastic wave by an edge dislocation interacting with incident in-plane compressional and shear waves (Fig. 4). In this case, no interaction with anti-plane wave occurs. The mechanism for such scattering is the same as in the anti-plane case: The dislocation oscillates under the action of the incident wave, producing the emission of scattered waves. The differences come from the vectorial nature of the considered waves: Due to mode conversions, an incident compressional wave produces both compressional and shear scattered waves and the same occurs for an incident shear wave. Thus, in a general case, four scattering functions have to be calculated.

A. Derivation of the scattering functions

The in-plane case corresponds to the interaction of an edge dislocation, for which $b_\parallel = 0$, with the in-plane waves, propagating at velocities α and β. We restricted ourselves to the case of gliding edge dislocations, for which the line dislocation moves only along its Burgers vector. Dislocation climb is not considered in this paper as it involves diffusive mass transport and cannot be treated within a purely elastic framework.

The velocity of the wave scattered by a gliding edge along the x_1 axis can be expressed using Eq. (2.4), with $b_i = b\,\delta_{i1}$ and $\dot{X}_i = \dot{X}\,\delta_{i1}$,

$$v_m^s(\mathbf{x},\omega) = -b\mu\dot{X}(\omega)\left(\frac{\partial}{\partial x_2}G_{1m}^0(\mathbf{x},\omega) + \frac{\partial}{\partial x_1}G_{2m}^0(\mathbf{x},\omega)\right), \tag{4.1}$$

The motion $\dot{\mathbf{X}}(t) = (\dot{X}(t),0,0)$ of a gliding edge along the x_1 axis submitted to the wave displacement field $\mathbf{u}$ is given by Ref. 27, using Eq. (2.5) with $b_\parallel = 0$ and $b_\perp \wedge \dot{\mathbf{X}} = 0$. In this case, the Lagrangian density reduces to $\mathcal{L} = (\mu b^2/4\pi\beta^2)(1+\gamma^{-4})\ln\,(\delta/\epsilon)(\dot{X}^2/2 - 2\beta^2(1-\gamma^{-2})/(1+\gamma^{-4}))$ and we get

$$M\ddot{X}(t) = \Sigma_{12} b, \tag{4.2}$$

where $M = (\mu b^2/4\pi\beta^2)(1+\gamma^{-4})\ln(\delta/\epsilon)$ is the effective mass per unit length of edge dislocation. As for the case of the screw dislocation, we use the Born approximation to express $\dot{X}(\omega)$ as a function of the incident potentials (for weak scattering). At dominant order, the small parameter being $\Omega X/\alpha,\beta$, we get

$$\dot{X}(\omega) = -\frac{b\mu}{M\omega^2}\left(\frac{\partial v_1^{\mathrm{inc}}}{\partial x_2}(\mathbf{0},\omega) + \frac{\partial v_2^{\mathrm{inc}}}{\partial x_1}(\mathbf{0},\omega)\right), \tag{4.3}$$

so we have

$$v_m^s(\mathbf{x},\omega) = K_m(\mathbf{x},\omega)\frac{b^2\mu^2}{M\omega^2}\left(\frac{\partial v_1^{\mathrm{inc}}}{\partial x_2}(\mathbf{0},\omega) + \frac{\partial v_2^{\mathrm{inc}}}{\partial x_1}(\mathbf{0},\omega)\right), \tag{4.4}$$

with

$$K_m(\mathbf{x},\omega) = \frac{\partial}{\partial x_2}G_{1m}^0(\mathbf{x},\omega) + \frac{\partial}{\partial x_1}G_{2m}^0(\mathbf{x},\omega). \tag{4.5}$$

It now becomes convenient to introduce longitudinal (φ) and shear (ψ) velocity potentials:

$$\mathbf{v} = \boldsymbol{\nabla}\varphi + \boldsymbol{\nabla}\times\boldsymbol{\psi} \tag{4.6}$$

with $\boldsymbol{\psi} = (0,0,\psi)$. The incident wave, propagating in a direction θ_0 with the x_1 axis (Fig. 4), is described by its potentials

$$\begin{aligned}\varphi^{\mathrm{inc}}(\mathbf{x},t) &= A_\alpha e^{i(\Omega/\alpha)(x_1\cos\theta_0 - x_2\sin\theta_0)}e^{-i\Omega t},\\ \psi^{\mathrm{inc}}(\mathbf{x},t) &= A_\beta e^{i(\Omega/\beta)(x_1\cos\theta_0 - x_2\sin\theta_0)}e^{-i\Omega t}.\end{aligned} \tag{4.7}$$

Far from the dislocation, the scattered potentials are defined by

$$\begin{pmatrix}\varphi^s(\mathbf{x},t)\\ \psi^s(\mathbf{x},t)\end{pmatrix} = \frac{1}{\sqrt{x}}\begin{pmatrix} f_{\alpha\alpha}(\theta)e^{i(\Omega x/\alpha)} & f_{\alpha\beta}(\theta e^{i(\Omega x/\alpha)}\\ f_{\beta\alpha}(\theta)e^{i(\Omega x/\beta)} & f_{\beta\beta}(\theta)e^{i(\Omega x/\beta)}\end{pmatrix} \times\begin{pmatrix}\varphi^{\mathrm{inc}}(\mathbf{0},t)\\ \psi^{\mathrm{inc}}(\mathbf{0},t)\end{pmatrix}, \tag{4.8}$$

where the scattering functions f_{ab}, with $a,b = \alpha,\beta$ denote the a wave resulting from an incident b wave and angle θ is the angle between $\mathbf{x}$ and the direction of propagation of the incident wave (Fig. 4).

To derive the scattering functions, the matrix in Eq. (4.8) has to be found. To do this, we use the following relations:

$$\begin{pmatrix}\varphi^s(\mathbf{x},\omega)\\ \psi^s(\mathbf{x},\omega)\end{pmatrix} = N^s\begin{pmatrix}v_1^s(\mathbf{x},\omega)\\ v_2^s(\mathbf{x},\omega)\end{pmatrix}, \tag{4.9}$$

$$\begin{pmatrix}v_1^s(\mathbf{x},\omega)\\ v_2^s(\mathbf{x},\omega)\end{pmatrix} = N^{s,\mathrm{inc}}(\mathbf{x},\omega)\begin{pmatrix}v_1^{\mathrm{inc}}(\mathbf{x},\omega)\\ v_2^{\mathrm{inc}}(\mathbf{x},\omega)\end{pmatrix}, \tag{4.10}$$

$$\begin{pmatrix}v_1^{\mathrm{inc}}(\mathbf{x},\omega)\\ v_2^{\mathrm{inc}}(\mathbf{x},\omega)\end{pmatrix} = N^{\mathrm{inc}}\begin{pmatrix}\varphi^{\mathrm{inc}}(\mathbf{x},\omega)\\ \psi^{\mathrm{inc}}(\mathbf{x},\omega)\end{pmatrix}, \tag{4.11}$$

where Eqs. (4.9) and (4.11) are simply the relations between velocity and potentials deduced from Eq. (4.6), with

$$N^s = \frac{1}{i\Omega}\begin{pmatrix}\alpha\cos(\theta-\theta_0) & \alpha\sin(\theta-\theta_0)\\ \beta\sin(\theta-\theta_0) & -\beta\cos(\theta-\theta_0)\end{pmatrix} \tag{4.12}$$

and

$$N^{\mathrm{inc}} = i\Omega\begin{pmatrix}\cos\theta_0/\alpha & -\sin\theta_0/\beta\\ -\sin\theta_0/\alpha & -\cos\theta_0/\beta\end{pmatrix}. \tag{4.13}$$

Equation (4.10) is equivalent to Eq. (4.4) with

$$N^{s,\mathrm{inc}}(\mathbf{x},\omega) = \frac{\mu^2 b^2}{M\omega^2}\begin{pmatrix} K_1(\mathbf{x},\omega)\left.\frac{\partial}{\partial x_2}\right|_{\mathbf{x}=\mathbf{0}} & K_1(\mathbf{x},\omega)\left.\frac{\partial}{\partial x_1}\right|_{\mathbf{x}=\mathbf{0}}\\ K_2(\mathbf{x},\omega)\left.\frac{\partial}{\partial x_2}\right|_{\mathbf{x}=\mathbf{0}} & K_2(\mathbf{x},\omega)\left.\frac{\partial}{\partial x_1}\right|_{\mathbf{x}=\mathbf{0}}\end{pmatrix}, \tag{4.14}$$

where K_m is defined in Eq. (4.5). In the next step, we use now that the differential operators

$$\left.\frac{\partial}{\partial x_i}\right|_{\mathbf{x}=\mathbf{0}}$$

in the product of matrices $N^{s,\mathrm{inc}}(\mathbf{x},\omega)N^{\mathrm{inc}}$ act on the potentials $\varphi^{\mathrm{inc}}(\mathbf{x},\omega)$ and $\psi^{\mathrm{inc}}(\mathbf{x},\omega)$. It is sufficient to use

$$\begin{aligned}\frac{\partial}{\partial x_i}\varphi^{\mathrm{inc}}(\mathbf{x},\omega)\big|_{\mathbf{x}=\mathbf{0}} &= \frac{i\Omega}{\alpha}(\cos\theta_0;-\sin\theta_0)\varphi^{\mathrm{inc}}(\mathbf{0},\omega),\\ \frac{\partial}{\partial x_i}\psi^{\mathrm{inc}}(\mathbf{x},\omega)\big|_{\mathbf{x}=\mathbf{0}} &= \frac{i\Omega}{\beta}(\cos\theta_0;-\sin\theta_0)\psi^{\mathrm{inc}}(\mathbf{0},\omega)\end{aligned} \tag{4.15}$$

to write the set of Eqs. (4.10) and (4.11) as

$$\begin{pmatrix}v_1^s(\mathbf{x},\omega)\\ v_2^s(\mathbf{x},\omega)\end{pmatrix} = M^{s,\mathrm{inc}}(\mathbf{x},\omega)\begin{pmatrix}\varphi^{\mathrm{inc}}(\mathbf{0},\omega)\\ \psi^{\mathrm{inc}}(\mathbf{0},\omega)\end{pmatrix} \tag{4.16}$$

and we find

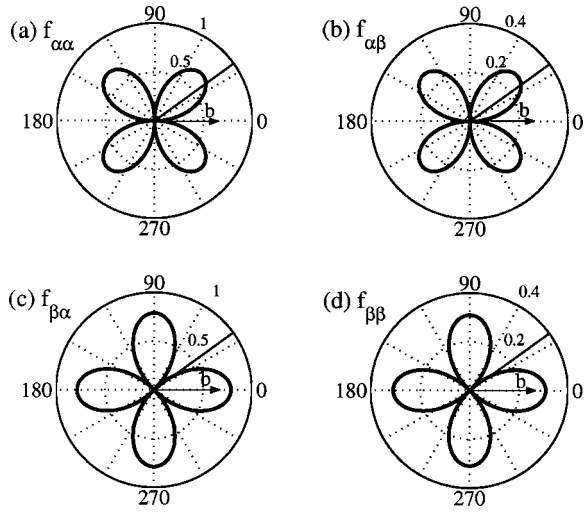

FIG. 5. Scattering function vs θ for an angle between the Burgers vector (along the horizontal axis) and the incident wave direction $\theta_0=\pi/5$ (the direction of the incident wave is indicated in plain line).

$$M^{s,\mathrm{inc}}(\mathbf{x},\omega) = \frac{\mu^2 b^2 \Omega^2}{M\omega^2}\begin{pmatrix} \dfrac{K_1(\mathbf{x},\omega)}{\alpha^2}\sin 2\theta_0 & \dfrac{K_1(\mathbf{x},\omega)}{\beta^2}\cos 2\theta_0 \\ \dfrac{K_2(\mathbf{x},\omega)}{\alpha^2}\sin 2\theta_0 & \dfrac{K_2(\mathbf{x},\omega)}{\beta^2}\cos 2\theta_0 \end{pmatrix}. \tag{4.17}$$

Finally, with $\varphi^{\mathrm{inc}}(\mathbf{0},\omega)$, $\psi^{\mathrm{inc}}(\mathbf{0},\omega)\propto\delta(\omega-\Omega)$, we have

$$\begin{pmatrix}\varphi^s(\mathbf{x},t)\\ \psi^s(\mathbf{x},t)\end{pmatrix} = N^s M^{s,\mathrm{inc}}(\mathbf{x},\Omega)\begin{pmatrix}\varphi^{\mathrm{inc}}(\mathbf{0},t)\\ \psi^{\mathrm{inc}}(\mathbf{0},t)\end{pmatrix}. \tag{4.18}$$

Far from the dislocation, the asymptotic values of K_m are calculated (see the Appendix) and the scattering functions are found by identification between Eqs. (4.8) and (4.18),

$$\begin{aligned} f_{\alpha\alpha}(\theta) &= \frac{\mu b^2}{2M}\frac{e^{i\pi/4}}{\sqrt{2\pi\Omega\alpha^3}}\left(\frac{\beta}{\alpha}\right)^2\sin 2\theta_0\sin(2\theta-2\theta_0),\\ f_{\alpha\beta}(\theta) &= \frac{\mu b^2}{2M}\frac{e^{i\pi/4}}{\sqrt{2\pi\Omega\alpha^3}}\cos 2\theta_0\sin(2\theta-2\theta_0),\\ f_{\beta\alpha}(\theta) &= -\frac{\mu b^2}{2M}\frac{e^{i\pi/4}}{\sqrt{2\pi\Omega\beta^3}}\left(\frac{\beta}{\alpha}\right)^2\sin 2\theta_0\cos(2\theta-2\theta_0),\\ f_{\beta\beta}(\theta) &= -\frac{\mu b^2}{2M}\frac{e^{i\pi/4}}{\sqrt{2\pi\Omega\beta^3}}\cos 2\theta_0\cos(2\theta-2\theta_0), \end{aligned} \tag{4.19}$$

whose shapes are given in Fig. 5. From Fig. 5 and related formulas (4.19), important features of the elastic wave scattering can be seen: (i) no interaction occurs between the incident wave and the dislocation in the case of an incident longitudinal α wave propagating in a direction parallel or perpendicular to the Burgers vector ($\theta_0=0,\pi/2$); similarly no interaction occurs in the case of an incident shear β wave propagating in directions with angle $\pi/4$ with the Burgers vector. (ii) The scattered longitudinal wave is always zero in the direction of the Burgers vector ($\theta=\theta_0$) and in the direction orthogonal to the Burgers vector while the shear wave reaches its maximum in these directions. Similarly, the shear scattered wave vanishes in directions with angle $\pi/4$ with the Burgers vector (directions where the longitudinal wave reaches its maximum).

However, in a general case, there is no particular behavior of the cross-coupled scattered waves in the incident direction, contrary to the case of scattering by an inhomogeneity studied in Ref. 41, where the cross-coupled scattered waves remain always apart from the incident direction. An important consequence is that there is no simple argument to neglect mode conversion in a pure forward scattering problem.

B. The optical theorem with polarized waves

The cross sections are defined as in the scalar case. Here, the term $\Sigma\mathbf{v}^*\,\mathbf{dS}$ reduces to

$$x\,d\theta\rho\left(\alpha^2\frac{\partial u_r}{\partial x}v_r^* + \beta^2\frac{\partial u_\theta}{\partial x}v_\theta^*\right).$$

It is easy to find that $\tilde{\sigma}^s$ and $\tilde{\sigma}^t$, normalized with the energy flux $\sigma_0=\rho\Omega^2/2(A_\alpha^2/\alpha+A_\beta^2/\beta)$ of the incident plane wave across a unit surface, verify

$$\begin{aligned} \frac{d\tilde{\sigma}^s}{d\theta} &= \frac{1}{\dfrac{A_\alpha^2}{\alpha}+\dfrac{A_\beta^2}{\beta}}\left(\frac{|f_{\alpha\alpha}(\theta)A_\alpha+f_{\alpha\beta}(\theta)A_\beta|^2}{\alpha}\right.\\ &\quad\left.+\frac{|f_{\beta\alpha}(\theta)A_\alpha+f_{\beta\beta}(\theta)A_\beta|^2}{\beta}\right), \end{aligned} \tag{4.20}$$

$$\begin{aligned} \tilde{\sigma}^t &= \frac{1}{\dfrac{A_\alpha^2}{\alpha}+\dfrac{A_\beta^2}{\beta}}\left\{2\Im\left(\sqrt{\frac{2\pi\alpha}{\Omega}}f_{\alpha\alpha}(0)\frac{A_\alpha^2}{\alpha}e^{-i\pi/4}\right)\right.\\ &\quad+2\Im\left(\sqrt{\frac{2\pi\beta}{\Omega}}f_{\beta\beta}(0)\frac{A_\beta^2}{\beta}e^{-i\pi/4}\right)\\ &\quad\left.+2\Im\left[A_\alpha A_\beta\left(\frac{f_{\alpha\beta}(0)}{\sqrt{\alpha}}+\frac{f_{\beta\alpha}(0)}{\sqrt{\beta}}\right)\sqrt{\frac{2\pi}{\Omega}}e^{-i\pi/4}\right]\right\}. \end{aligned} \tag{4.21}$$

The scattering cross-section $\tilde{\sigma}^s$ is deduced from Eq. (4.20),

$$\begin{aligned} \tilde{\sigma}^s &= \frac{1}{\dfrac{A_\alpha^2}{\alpha}+\dfrac{A_\beta^2}{\beta}}\left(\frac{\mu b^2}{2M}\right)^2\frac{1}{2\Omega}\left(1+\frac{\beta^4}{\alpha^4}\right)\\ &\quad\times\left(\sin 2\theta_0\frac{A_\alpha}{\alpha^2}+\cos 2\theta_0\frac{A_\beta}{\beta^2}\right)^2. \end{aligned} \tag{4.22}$$

This expression is in agreement with Ref. 26 where the calculation was performed in the particular case $A_\alpha=0$, $\theta_0=\pi/2$, with a shear wave incident along the Burgers vector. Note that the scattered and total cross sections cannot be split in longitudinal and shear wave portions, because of the mode

conversion. Such coupling has already been observed in the case of scattering of ultrasound by flaws in elastic materials[42] or in the case of the scattering of sound by an elastic inclusion.[43] As in the scalar case, it is found that the scattering strength increases with wavelength (see Sec. V). The second relation (4.21) corresponds to the optical theorem for coupled vector waves.

V. CONCLUDING REMARKS

The scattering by a dislocation investigated in this paper is related to a particular interaction that an elastic wave experiences with a dislocation. In addition to the scattering by the dislocation core, which is negligible at wavelength large compared with core size, the incident wave forces the dislocation to move. This motion involves not only the material close by the dislocation core, but also material at a distance from it comparable to the range of the dislocation deformation field. It is this mechanism that is investigated here. As the dislocation moves with an amplitude proportional to the frequency of the incident wave, it is found that the scattering strength increases with the wavelength (the scattering cross section is proportional to Ω^{-1}).

The limit $\Omega \to 0$, in which the scattering cross section diverges, is outside the framework of the present study. This is mainly because two-dimensional analysis assumes that the typical length in the third direction (here the length of the dislocation line) is large compared to the typical in-plane lengths, which fall off for infinite wavelength. In our calculations, the wavelength thus has an explicit lower limit b and an implicit upper limit that three-dimensional analysis would make appear.

This mechanism, although unusual, has been previously observed for an acoustic wave incident on a fluid vortex;[44] solving Navier–Stokes makes appear a motion of the vortex core due to the incident wave, producing scattering of the acoustic wave.

The vector case of coupled longitudinal and shear waves has been investigated here and it is, to the best of our knowledge, the first time that the complete calculation is reported.

In the recent years, experimental works[38–40] have shown pictures of the wave scattered by an individual dislocation in $LiNbO_3$ thanks to x-ray imaging. Comparison with these experimental results would necessitate extracting from the images quantitative information which is still not available.

Also, a natural extension of the present study would be to describe the modification of the wave propagation in the presence of multiple dislocations.[35] A recent experiment suggests that ultrasounds may be used to determine changes in the attenuation and the acoustic velocity due to dislocations.[45] Another possible experiment in this case would be to measure the modification of the resonant frequencies of a sample of material due to the presence of such scatterers. Work is in progress in that direction.

Finally, one can intend to describe the scattering by the dislocation core, i.e., due to the local microstructure near the dislocation line. As previously said, such scattering has a vanishing strength at long wavelengths (for instance, a discussion on this mechanism can be found in Ref. 22 where the author estimates the scattering cross section of order $b^2\Omega/\beta$). Since long means large compared with the core size b, usual situations are always in the range $\lambda \gg b$. Nevertheless, if interest is in that description, care has to be taken when considering the lattice as a continuum and a better description has to be sought with atomistic modeling, as done for instance numerically in Refs. 46 and 47.

ACKNOWLEDGMENTS

We gratefully acknowledge the support of the framework of a French/Chilean collaboration on ''Propagation of wave in continuous disordered media,'' and FONDAP Grant No. 11980002.

APPENDIX: ASYMPTOTIC BEHAVIOR OF THE GREEN FUNCTIONS FOR THE TWO-DIMENSIONAL NAVIER EQUATION

The asymptotic behavior of the Green functions $G^0(\mathbf{x},\omega)$ for $x \to \infty$ can be calculated starting from $G^0(\mathbf{k},\omega)$. With

$$\rho \frac{\partial^2}{\partial t^2} G^0_{im}(\mathbf{x}-\mathbf{x}',t-t') - c_{ijkl} \frac{\partial^2}{\partial x_j \partial x_k} G^0_{lm}(\mathbf{x}-\mathbf{x}',t-t') = \delta(\mathbf{x}-\mathbf{x}')\,\delta(t-t')\,\delta_{im},$$

we obtain

$$G^0(\mathbf{k},\omega) = \frac{1}{\rho\alpha^2} \frac{1}{\gamma^2(k^2-k_\alpha^2)(k^2-k_\beta^2)} \times \begin{pmatrix} k^2-k_\beta^2+(\gamma^2-1)k_2^2 & -(\gamma^2-1)k_1k_2 \\ -(\gamma^2-1)k_1k_2 & k^2-k_\beta^2+(\gamma^2-1)k_1^2 \end{pmatrix}. \tag{A1}$$

It is now sufficient to take the asymptotic form for large x (dominant terms in $1/\sqrt{x}$) of the $\mathbf{k}$-Fourier transform of $G^0(\mathbf{k},\omega)$. After some calculations, we find

$$G^0_{11}(\mathbf{x},\omega) \simeq \frac{1}{4\rho}\sqrt{\frac{2}{\pi\omega}}\, e^{i\pi/4} \times \left(\frac{\cos^2\theta}{\alpha^{3/2}} \frac{e^{i\omega x/\alpha}}{\sqrt{x}} + \frac{\sin^2\theta}{\beta^{3/2}} \frac{e^{i\omega x/\beta}}{\sqrt{x}} \right), \tag{A2}$$

$$G^0_{22}(\mathbf{x},\omega) \simeq \frac{1}{4\rho}\sqrt{\frac{2}{\pi\omega}}\, e^{i\pi/4} \times \left(\frac{\sin^2\theta}{\alpha^{3/2}} \frac{e^{i\omega x/\alpha}}{\sqrt{x}} + \frac{\cos^2\theta}{\beta^{3/2}} \frac{e^{i\omega x/\beta}}{\sqrt{x}} \right), \tag{A3}$$

$$G^0_{12}(\mathbf{x},\omega) \simeq \frac{1}{4\rho}\sqrt{\frac{2}{\pi\omega}}\, e^{i\pi/4} \sin\theta\cos\theta \times \left(\frac{1}{\alpha^{3/2}} \frac{e^{i\omega x/\alpha}}{\sqrt{x}} - \frac{1}{\beta^{3/2}} \frac{e^{i\omega x/\beta}}{\sqrt{x}} \right). \tag{A4}$$

The asymptotic behaviors of K_1 and K_2 defined in Eq. (4.5) are thus deduced

$$
\begin{aligned}
K_1 &= \frac{\partial}{\partial x_2} G_{11}^0(\mathbf{x},\omega) + \frac{\partial}{\partial x_1} G_{21}^0(\mathbf{x},\omega) \\
&\simeq \frac{i\omega}{4\rho}\sqrt{\frac{2}{\pi\omega}}\, e^{i\pi/4}\left(\sin 2\theta \cos\theta \frac{e^{i\omega x/\alpha}}{\alpha^{5/2}\sqrt{x}} \right. \\
&\quad \left. - \cos 2\theta \sin\theta \frac{e^{i\omega x/\beta}}{\beta^{5/2}\sqrt{x}} \right), \\
K_2 &= \frac{\partial}{\partial x_2} G_{12}^0(\mathbf{x},\omega) + \frac{\partial}{\partial x_1} G_{22}^0(\mathbf{x},\omega) \\
&\simeq \frac{i\omega}{4\rho}\sqrt{\frac{2}{\pi\omega}}\, e^{i\pi/4}\left(\sin 2\theta \sin\theta \frac{e^{i\omega x/\alpha}}{\alpha^{5/2}\sqrt{x}} \right. \\
&\quad \left. + \cos 2\theta \cos\theta \frac{e^{i\omega x/\beta}}{\beta^{5/2}\sqrt{x}} \right),
\end{aligned}
\tag{A5}
$$

where we have used $(\partial/\partial x_i)(x_i/x)$ for large x.

[1] C. F. Ying and R. Truell, "Scattering of a plane longitudinal wave by a spherical obstacle in an isotropically elastic solid," J. Appl. Phys. **27**, 1086–1097 (1956).
[2] N. G. Einspruch and R. Truell, "Scattering of a plane longitudinal wave by a spherical fluid obstacle in an elastic medium," J. Acoust. Soc. Am. **32**, 214–220 (1960).
[3] Y. H. Pao and C. C. Mow, "Scattering of plane compressional waves by a spherical obstacle," J. Appl. Phys. **34**, 493–499 (1963).
[4] R. M. White, "Elastic wave scattering at a cylindrical discontinuity in a solid," J. Acoust. Soc. Am. **30**, 771–785 (1958).
[5] T. S. Lewis and D. W. Kraft, "Mode conversion relation for elastic wave scattered by a cylindrical obstacle in a solid," J. Acoust. Soc. Am. **56**, 1899–1901 (1974).
[6] N. G. Einspruch, E. J. Witterholt, and R. Truell, "Scattering of a plane transverse wave by a spherical obstacle in an elastic medium," J. Appl. Phys. **31**, 806–818 (1960).
[7] D. W. Kraft and M. C. Franzblau, "Scattering of elastic waves from a spherical cavity in a solid medium," J. Appl. Phys. **42**, 3019–3024 (1971).
[8] R. J. McBride and D. W. Kraft, "Scattering of a transverse elastic wave by an elastic sphere in a solid medium," J. Appl. Phys. **43**, 4853–4861 (1972).
[9] S. K. Datta, "Propagation of SH-waves through a fiber-reinforced composite-elliptic cylindrical fibers," J. Appl. Mech. **42**, 165–170 (1975).
[10] V. K. Varadan, V. V. Varadan, and Y. A. Pao, "Multiple scattering of elastic waves by cylinders of arbitrary cross section," J. Acoust. Soc. Am. **63**, 1310–1319 (1978).
[11] V. K. Varadan, "Scattering of elastic waves by randomly distributed and oriented scatterers," J. Acoust. Soc. Am. **65**, 655–657 (1979).
[12] B. Peterson, V. K. Varadan, and V. V. Varadan, "Scattering of elastic waves by a fluid inclusion," J. Acoust. Soc. Am. **73**, 1487–1493 (1983).
[13] L. W. Schmerr, Jr., *Fundamentals of Ultrasonic Nondestructive Evaluation: A modelling Approach* (Plenum, New York, 1996).
[14] R. K. Ing and M. Fink, "Time recompression of dispersive Lamb wave using time reversal mirror applications to flaw detection in thin plates," IEEE Ultrasonics Symposium Proceedings, San Antonio, 1996, pp. 659–664.
[15] M. Fink, "Ultrasound puts material to the test," Phys. World **11**, 41–45 (1998).
[16] J. C. Aldrin and J. D. Achenbach, "Model and methodology for crack detection on a cylindrical hole containing an elastic insert," AIP Conf. Proc. **615**, 181–188 (2002).
[17] J. D. Achenbach, "Modeling for quantitative non-destructive evaluation," Ultrasonics **40**, 1–10 (2002).
[18] E. Orowan, "Zür Kristallplastizität I-III," Z. Phys. **89**, 605–634 (1934).
[19] M. Polanyi, "Über eine Art Gitterstörung, die einem Kristall plastisch machen könnte," Z. Phys. **89**, 660–664 (1934).
[20] G. I. Taylor, "The mechanism of plastic deformation of crystals I-II," Proc. R. Soc. London, Ser. A **145**, 362–388 (1934).
[21] J. M. Burgers, "Some considerations on the fields of stress connected with dislocations in a regular crystal lattice," Proc. K. Ned. Akad. Wet. **42**, 293–378 (1939).
[22] F. R. N. Nabarro, "The interaction of screw dislocations and sound wave," Proc. R. Soc. London, Ser. A **209**, 278–290 (1951).
[23] J. D. Eshelby, "Dislocation as a cause of mechanical damping in metals," Proc. R. Soc. London, Ser. A **197**, 396–416 (1949).
[24] J. D. Eshelby, "The equation of motion of a dislocation," Phys. Rev. **90**, 248–255 (1953).
[25] T. Mura, "Continuous distribution of moving dislocations," Philos. Mag. **8**, 843–857 (1963).
[26] J. Kiusalaas and T. Mura, "On the elastic field around an edge dislocation with application to dislocation vibration," Philos. Mag. **9**, 1–7 (1963).
[27] F. Lund, "Response of a stringlike dislocation loop to an external stress," J. Mater. Res. **3**, 280–297 (1988).
[28] A. V. Granato and K. Lücke, in *Physical Acoustics*, edited by W. P. Mason (Academic, New York, 1966), Vol. 4A.
[29] A. V. Granato and K. Lücke, J. Appl. Phys. **27**, 583 (1956); **27**, 789 (1956).
[30] K. Lücke and A. V. Granato, Phys. Rev. B **24**, 6991 (1981); A. V. Granato and K. Lücke, *ibid.* **24**, 7007 (1981).
[31] G. A. Kneezel and A. V. Granato, Phys. Rev. B **25**, 2851 (1982).
[32] J. S. Koehler, in *Imperfections in Nearly Perfect Crystals*, edited by W. Schockley *et al.* (Wiley, New York, 1952).
[33] A. C. Anderson, in *Dislocations in Solids*, edited by F. R. N. Nabarro (North-Holland, Amsterdam, 1983), Chap. 29.
[34] M. O. Peach and J. S. Koehler, "The forces exerted on dislocations and the stress fields produced by them," Phys. Rev. **80**, 436–439 (1950).
[35] A. Maurel, J.-F. Mercier, and F. Lund, "Elastic wave propagation through a random array of dislocations," Phys. Rev. B. (submitted).
[36] J. P. Hirth and J. Lothe, *Theory of Dislocations* (McGraw–Hill, New York, 1982).
[37] F. R. N. Nabarro, *Theory of Crystal Dislocations* (Oxford University Press, Oxford, 1967), as well as reviews by A. M. Kosevich in *Dislocations in Solids*, edited by F. R. N. Nabarro (North-Holland, Amsterdam, 1980), Vol. 1.
[38] E. Zolotoyabko, D. Shilo, and E. Lakin, "X-ray imaging of acoustic wave interaction with dislocations," Mater. Sci. Eng., A **309**, 23–27 (2001).
[39] D. Shilo and E. Zolotoyabko, "Visualization of acoustic wave scattering by dislocations," Ultrasonics **40**, 921–925 (2002).
[40] D. Shilo and E. Zolotoyabko, "Stroboscopic x-ray imaging of vibrating dislocations excited by 0.58 GHz phonons," Phys. Rev. Lett. **91**, 115506/1–4 (2003).
[41] R.-S. Wu, "The perturbation method in elastic wave scattering," Pure Appl. Geophys. **131**, 605–637 (1989).
[42] J. E. Gubernatis, E. Domany, and J. A. Krumhansl, "Formal aspects of the theory of the scattering of ultrasound by flows in elastic materials," J. Appl. Phys. **48**, 2804–2811 (1977).
[43] V. A. Korneev and L. R. Johnson, "Fluctuations of elastic waves due to random scattering from inclusions," J. Comput. Acoust. **9**, 973–991 (2001).
[44] F. Lund and C. Rojas, "Ultrasound as a probe of turbulence," Physica D **37**, 508–514 (1989).
[45] S. Kenderian, T. P. Berndt, R. E. Green, and B. B. Djordjevic, "Ultrasonic monitoring of dislocations during fatigue of pearlitic rail steel," Mater. Sci. Eng., A **338**, 90–99 (2003).
[46] H. Koizumi and H. O. K. Kirchner, "Lattice wave emission from a moving dislocation," Phys. Rev. B **65**, 214104 (2002).
[47] P. Gumbsh and H. Gao, "Dislocations faster than the speed of sound," Science **283**, 965–968 (1999).

Quantifying elasticity and viscosity from measurement of shear wave speed dispersion

Shigao Chen, Mostafa Fatemi, and James F. Greenleaf[a)]
Basic Ultrasound Research Laboratory, Department of Physiology and Biomedical Engineering, Mayo Clinic College of Medicine, Rochester, Minnesota 55905

(Received 25 April 2003; revised 6 March 2004; accepted 19 March 2004)

The propagation speed of shear waves is related to frequency and the complex stiffness (shear elasticity and viscosity) of the medium. A method is presented to solve for shear elasticity and viscosity of a homogeneous medium by measuring shear wave speed dispersion. Harmonic radiation force, introduced by modulating the energy density of incident ultrasound, is used to generate cylindrical shear waves of various frequencies in a homogeneous medium. The speed of shear waves is measured from phase shift detected over the distance propagated. Measurements of shear wave speed at multiple frequencies are fit with the theoretical model to solve for the complex stiffness of the medium. Experiments in gelatin phantoms show promising results validated by an independent method. Practical considerations and challenges in possible medical applications are discussed. © *2004 Acoustical Society of America.* [DOI: 10.1121/1.1739480]

PACS numbers: 43.20.Jr, 43.25.Qp, 43.35.Mr, 43.35.Zc, 43.80.Vj [FD] Pages: 2781–2785

I. INTRODUCTION

Pathological changes are usually correlated with changes in mechanical properties of soft tissues, such as shear elasticity (stiffness). *In vitro* and *in vivo* studies show that normal breast tissue is approximately four times softer than fibroadenoma tissue, which is approximately eight times softer than carcinomas [Ophir *et al.*, 1996]. Palpation fails in many cases, despite the difference in stiffness, due to the small size of a lesion and/or its deep location in the body. The lesion may or may not possess echogenic properties that make it ultrasonically detectable. For example, prostate and breast tumors can be much harder than the surrounding tissue, yet be invisible in standard ultrasound examinations [Garra *et al.*, 1997]. In addition to pathology, the shear elasticity of various *normal* tissues spans over orders of magnitude, providing very high inherent contrast for medical imaging [Sarvazyan *et al.*, 1998]. Kallel *et al.* (1998) have shown strain images of a kidney with easily discernible contrast between the cortex and the medullary pyramids. Therefore, noninvasive and quantitative measurement of mechanical properties of tissue can be very useful in medical diagnosis.

Many methods have been proposed to image tissue elasticity. The general approach is to measure the response of a tissue to an excitation force and use it to infer some mechanical parameters of the tissue. The excitation force can be applied externally by static compression [Ophir *et al.*, 1991], dynamic vibration [Lerner *et al.*, 1988], or internally by ultrasound radiation force [Sarvazyan *et al.*, 1998]. The response of the tissue can be detected by ultrasound [Ophir *et al.*, 1991], magnetic resonance imaging [Muthupillai *et al.*, 1995], or an acoustic hydrophone [Fatemi and Greenleaf, 1999].

Despite all the techniques mentioned above, there are still problems to be explored in this field. First, many of these methods are not truly quantitative. For example, some methods only provide images of *relative* stiffness, where the absolute value of a lesion's stiffness is unknown, although one can tell that it is softer or stiffer than its surroundings. In some other methods, the imaged parameter is not truly stiffness. Strain or displacement is used as a surrogate for stiffness. Absolute measurement of stiffness would help to identify pathology despite observer and subject variations. Second, characterization of tissue viscosity is rarely studied. Very little is known about its value in medical diagnosis and measurement techniques.

In this paper, we explore the possibility of *quantifying* both tissue *elasticity* and *viscosity* from measured shear wave speed dispersion (change of speed vs frequency). Shear wave propagation speed has been used in a number of studies to quantify tissue elasticity. Yamakoshi *et al.* (1990) used shear wave speed, estimated from displacement measured with ultrasound Doppler, as a parameter for tissue characterization. The same concept was employed in magnetic resonant elastography [Muthupillai *et al.*, 1995], where MRI was used as a detection method for displacement. Sarvazyan *et al.* (1998) used a short pulse of ultrasound radiation force to introduce shear waves remotely within the object. Shear wave speed was then estimated by tracking the propagation of the wave front. However, viscosity was ignored in these investigations because the dispersion of shear wave propagation speed was not studied.

We propose a new method to evaluate the complex stiffness of a homogeneous medium by measuring its shear wave speed dispersion. Ultrasound radiation force is used to generate monochromatic shear waves of various frequencies within the object. Oscillatory radiation force is produced by mixing two ultrasound beams with slightly different frequencies, as demonstrated by Fatemi and Greenleaf (1999). In contrast to Sarvazyan's method, the shear waves introduced within the object are narrow band rather than broadband.

a)Electronic mail: jfg@mayo.edu

Therefore, we determine the propagation speed by tracking the phase delay ($\Delta\varphi$) over the distance traveled (Δx) by the shear wave. For a monochromatic wave, the ratio $\Delta\varphi/\Delta x$ is equal to the wave number of the shear wave, which can be used to calculate the speed if the frequency of motion is known. The dispersion of the shear wave speed is measured at several frequencies and used to estimate the complex stiffness of the medium. The paper is organized as follows. The method and its related theory are presented in Sec. II. Section III describes the details of experiments. The results are presented in Sec. IV. Section V discusses some practical application issues of this research. The last section is the summary.

II. METHOD

Section II A presents the formula relating the shear elasticity and viscosity to the shear wave speed. The details of the measurement technique and the theory of shear wave generation are explained in Sec. II B. The formula used to solve for the shear wave speed from measurement of phase delay is also provided. Section II C explains a technique used to validate the method proposed in this paper.

A. Shear wave speed formula

The Voigt and Maxwell models are linear descriptions of a viscoelastic medium. They consist of a spring and a dashpot, either in parallel (Voigt) or in series (Maxwell) [Fung, 1993]. We use the Voigt model in the following derivations because it seems to produce satisfactory results for soft materials such as gelatin phantoms [Chen *et al.*, 2002a, b; Royston *et al.*, 1999]. The equation relating the propagation speed of a *plane* shear wave and the mechanical properties of a homogeneous isotropic Voigt body is given by Yamakoshi *et al.* (1990)

$$c_s = \sqrt{\frac{2(\mu_1^2+\omega^2\mu_2^2)}{\rho(\mu_1+\sqrt{\mu_1^2+\omega^2\mu_2^2})}}, \tag{1}$$

where ρ is the density of the medium, ω is the angular frequency of vibration, and μ_1 and μ_2 are the shear elasticity and shear viscosity. Therefore, given the mechanical properties of the medium and the frequency of vibration, one can compute the shear wave speed. On the other hand, if one can measure the shear wave speed for several values of ω in an unknown medium, the complex stiffness of the medium can be calculated, assuming ρ is known. For a pure elastic medium, μ_2 is equal to zero, and according to Eq. (1), shear wave speed is constant over all frequencies. For viscoelastic media, such as soft tissues, shear wave speed increases monotonically with frequency ω. The slope of such dispersion is controlled by the viscosity of the medium: higher viscosity leads to higher slope. Therefore, one needs to measure shear wave speed at several frequencies in order to solve for both shear elasticity and viscosity.

B. Measurement method

Acoustic radiation force is caused by a change in the energy density of the incident acoustic field. Thus, an object in the wave path that absorbs or reflects sound energy is subjected to an acoustic radiation force. This force is a steady force if the intensity of the incident sound field does not change over time. Fatemi *et al.* (1999) interfered two ultrasound beams of slightly different frequency to modulate the energy density sinusoidally at the beat frequency. This produces an oscillatory radiation force on the object. An alternative approach for generating oscillatory radiation force is to modulate the amplitude (AM) of a single incident ultrasound beam. We use the AM approach in this paper due to its simplicity in instrumentation.

Near the focus of the transducer, the ultrasound has a very narrow beamwidth, which is relatively uniform along the beam axis. Therefore, the oscillatory radiation force is mainly along the beam axis. The force varies strongly in the transverse direction, decreasing with distance from the axis. The force weakly depends on the axial coordinate. Therefore, the ultrasound radiation force produces an approximate cylindrical shear wave in the medium [Andreev *et al.*, 1997]. We present a brief theory about cylindrical shear wave propagation in this section. A complete treatment of this problem is out of the scope of this paper. Therefore, only analysis illustrative to the application of our method is presented below.

For a pure elastic medium, the cylindrical shear wave produced by a harmonic force concentrated along the z axis of the cylindrical coordinates is [Graff, 1991]

$$u_z(r,t) = \frac{i}{4}H_0^{(1)}(hr)e^{-i\omega t}, \tag{2}$$

where u_z is the displacement along the z axis, the z axis is the axis of the cylindrical coordinate coinciding with the axis of the acoustic beam, $H_0^{(1)}$ is the first kind of Hankel function of order zero, $h=\sqrt{\rho\omega^2/\mu_1}$ is the shear wave number, and r is the radial distance. At large distance from the z axis ($hr \gg 0$), Eq. (2) can be approximated by

$$u_z(r,t) \approx \frac{i}{4}\sqrt{\frac{2}{\pi hr}}e^{i(hr-\omega t+\pi/4)}. \tag{3}$$

Therefore, phase of the cylindrical shear wave changes linearly with distance traveled in the r direction. For a Voigt viscoelastic medium, we follow the approach by Oestreicher (1951) to introduce the complex stiffness in the expression of wave number $\tilde{h}=\sqrt{\rho\omega^2/(\mu_1-i\omega\mu_2)}$. Equations (2) and (3) can be extended to include the medium's viscosity simply by replacing h with $\tilde{h}$. The speed of shear wave in this case is $\omega/\mathrm{Re}[\tilde{h}]$, which also leads to the result in Eq. (1).

The linear relationship between phase delay and r, shown in Eq. (3), comes from an approximation for large r. Simulations based on Eq. (2) show that this linearity holds when r is greater than one-tenth of the shear wavelength, which is about 1 millimeter in our typical application. These simulations are not presented here because they are not the focus of this paper. Under this approximation, one can measure the speed of the cylindrical shear wave from the phase shift $\Delta\varphi$ caused by propagation over a distance Δr

$$c_s = \frac{\omega\Delta r}{\Delta\varphi}. \tag{4}$$

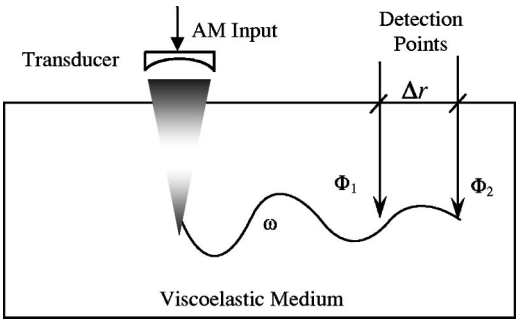

FIG. 1. Concept of speed estimation from phase detection. Phase of a monochromatic shear wave generated by radiation force is measured at two locations Δr apart laterally. The speed of the shear wave can be calculated from the phase shift $(\varphi_1-\varphi_2)$, the frequency of the shear wave ω, and Δr.

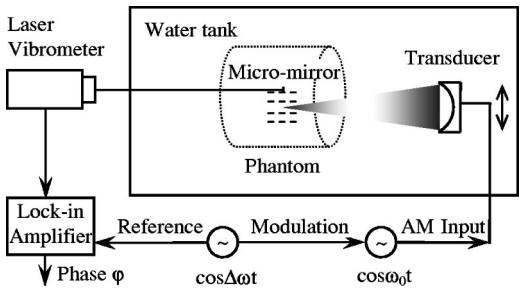

FIG. 2. Diagram of experimental setup. A shear wave generated at the focus of the transducer propagates to the micromirror, is detected by the laser vibrometer, and fed through the lock-in amplifier to extract the phase.

In this paper, Eq. (4) is used to determine the shear wave speeds at multiple frequencies. These measurements are then fit with Eq. (1) to solve for the shear elasticity (μ_1) and viscosity (μ_2) of the medium.

The concept of the proposed method is illustrated in Fig. 1. Amplitude-modulated ultrasound is used to introduce harmonic radiation force within the medium. The shear waves propagate away from the focus of the transducer and are detected at two locations Δr apart laterally. Based on the measured phase difference $\Delta\varphi$, the shear wave speed is then estimated by Eq. (4). The frequency of the generated shear wave can be varied by controlling the modulation frequency of the input signal that drives the transducer. Therefore, shear wave speed at various frequencies can be obtained to solve for the shear elasticity and shear viscosity by Eq. (1).

C. Validation

We use a method proposed by Chen *et al.* (2002a) to validate the estimations of shear elasticity and viscosity in this paper. This method solves for the complex shear modulus of a medium by characterizing the resonant behavior of an embedded sphere. Theoretical analysis shows that the motion of an oscillating sphere is controlled by its radiation impedance, which depends on the elastic and viscous properties of its surrounding medium. The vibration magnitude of the sphere exhibits resonance vs frequency, which provides a unique signature for the surrounding medium. In practice, the sphere is vibrated by oscillatory radiation force at various frequencies. The vibration magnitude is measured at each frequency of vibration by laser velocimeter or ultrasound Doppler. The measurements are then combined with the vibration theory to solve for the complex stiffness of the medium. The accuracy of this method has been studied and the typical error is around 5% [Chen *et al.*, 2002b]. Therefore, we use this method as an independent validation for the new method proposed in this paper.

III. EXPERIMENTS

The following experiments are designed to measure the shear elasticity and viscosity of two different gel phantoms. An optical vibrometry system is used to detect motions in the gel phantoms. This method provides excellent motion sensitivity for our experiment. Transparent gelatin phantoms of different stiffness are made. A small, reflective plastic mirror (Meadowbrook Inventions Inc., Bernardsville, NJ) and a steel sphere (New England Miniature Ball LLC, Norfolk, CT) are embedded in each phantom. The mirror provides a reflective surface for the optical vibrometry measurement and the sphere is used in the validation measurement. The phantoms are of cylindrical shape, with a diameter of 65 mm and a length of 65 mm. The diameter of the sphere is 0.85 mm and the plastic mirror has a diameter of 200 μm and a thickness of 12.7 μm. The sphere and the mirror are placed at the center of the phantom, about 15 mm apart.

Figure 2 is a schematic of the experiment. The transducer has a diameter of 45 mm and a focal length of 70 mm. Continuous shear waves generated at the transducer focus propagate to the micromirror whose vibration is detected by the laser vibrometer (Polytec GmbH, Waldbronn, Germany). The micromirror is very small and its mass is negligible; thus, it is considered to follow the medium's motion caused by the shear waves. Though the motion is of very small magnitude, we are able to achieve accurate phase measurements with a lock-in amplifier (PerkinElmer Instruments, Oak Ridge, TN). The lock-in amplifier recovers the phase and amplitude of the motion at each selected frequency. The frequency of the signal to be measured is set by the reference which is the sinusoidal signal that modulates the amplitude of ultrasound. During the experiments the transducer is moved to several values of r, at 1-mm intervals, to vary the distance traveled by the shear wave from the focus to the micromirror. At each position, phases for shear waves are measured at frequencies between 300 and 900 Hz. The phases measured by the lock-in amplifier are relative to the reference signal. Therefore, the measured phase is the ''true'' phase of the motion plus an unknown constant. The phase difference between any two positions is only due to the propagation speed of the wave because the unknown constant cancels out.

In the validation experiments using Chen's method (2002a), the laser and the ultrasound are both focused on the embedded sphere (not shown in Fig. 2 for the sake of clarity). The frequency of the oscillatory radiation force is swept from 100 to 2000 Hz. The magnitude of the vibration at each frequency is measured by the laser vibrometer. The recorded data are fit with the theoretical model to solve for the shear elasticity and viscosity of the phantom. Results are used to validate the estimation from the dispersion method.

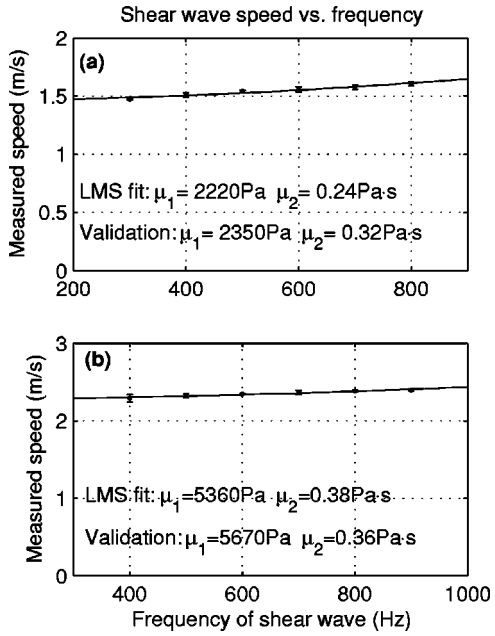

FIG. 3. Measured shear wave speed in two different phantoms. The shear elasticity and viscosity estimated by embedded spheres are $\mu_1=2350$ and $\mu_2=0.321$ for (a), and $\mu_1=5670$ and $\mu_2=0.358$ for (b). Bars represent 1 standard deviation for six measurements. Solid lines represent LMS fit to the data according to Eq. (1).

IV. RESULTS

Figure 3 shows results for two gelatin phantoms of different stiffness. Phantom (a) was made with Bloom 75 gelatin powder (from Sigma-Aldrich), whereas phantom (b) was made with Bloom 300 gelatin powder (also Sigma-Aldrich). Both had a concentration of 12% by volume. Phases of shear waves at several different frequencies were measured at six positions from 3 to 9 mm away from the transducer focus, at 1-mm intervals. Shear wave velocity at each frequency was then calculated from the phase shifts for $\Delta r=1$ mm. This procedure yields six estimations at each frequency. The error bar in Fig. 3 at each data point represents 1 standard deviation from the mean value. The mean values of estimated speeds at various frequencies were used with Eq. (1) to solve for the shear elasticity and viscosity for the phantoms. The least mean square (LMS) fit, with 95% confidence bounds, for phantom (a) yields $\mu_1=2220\pm80$ Pa and $\mu_2=0.24\pm0.03$ Pa·s. The same parameters estimated from the embedded sphere are $\mu_1=2350$ Pa and $\mu_2=0.32$ Pa·s. Because the variance of estimation is small for the sphere method, one set of data is assumed to be enough for comparison. The results for phantom (b) are $\mu_1=5360\pm130$ Pa and $\mu_2=0.38\pm0.06$ Pa·s, while the embedded sphere yields $\mu_1=5670$ Pa and $\mu_2=0.36$ Pa·s.

V. DISCUSSION

Our theory is based on a cylindrical shear wave generated by a line source. This is only an approximation because the radiation force from a transducer is more like a "cigar" than a line source. Therefore, diffraction effects may modify the relative phase of the vibration field at different points.

In this paper, we used shear wave speed dispersion to estimate the complex stiffness of a medium. Another possibility to estimate complex stiffness is through the shear wave attenuation. Attenuation is usually measured by the decrease of wave amplitude vs propagation distance. The amplitude of a cylindrical wave decreases due to both geometric effect [$\sim 1/\sqrt{r}$ in Eq. (3)] and attenuation. Therefore, one must correct for the geometric effect first in order to estimate attenuation. In addition, the cylindrical shear wave caused by radiation force is very weak. Therefore, estimation of complex stiffness from attenuation measurement may be less reliable than that from shear wave speed dispersion.

A laser vibrometer was used in this study to measure shear wave motion. For medical applications, where tissues are generally opaque, ultrasound can be used as an alternative detection method. In our experiments, the transducer was operated at continuous wave (cw) mode. The intensity at its focus was equivalent to 1 w/cm^2 in tissue. The measured vibration amplitude ranged from 5 to 35 μm/s, depending on the frequency of the shear wave and the propagation distance. The gelatin phantoms used in our experiments have very little attenuation for ultrasound. Therefore, we expect the vibration amplitude in tissue to increase by an order of magnitude because radiation force is proportional to attenuation coefficient of the medium [Nightingale *et al.*, 2001]. Motion of such magnitude is still difficult to detect by conventional ultrasonic methods. One possible solution is to use ultrasound of higher intensity to increase the tissue motion. For safety reasons, the FDA has recommended the output intensity of diagnostic ultrasound devices to be limited to 0.72 w/cm^2. However, we can operate the transducer in tone-burst mode to increase the shear wave magnitude, while keeping the average intensity below the FDA limit. Another possibility is to increase the sensitivity of ultrasound detection method, using the fact that the motion is harmonic and its frequency is known. Taking advantage of such *a priori* knowledge, we are able to measure harmonic vibration down to 90 μm/s with a novel ultrasound pulse–echo method [Zheng *et al.*, 2003].

Equation (1) assumes that the medium is homogeneous. In medical applications, tissues are usually inhomogeneous. However, Eq. (1) is still applicable under the assumption of piecewise homogeneity, given that we can accurately measure the local shear wave speed. The experiments presented in this paper show that shear wave speed can be estimated with measurements at two locations 1 mm apart. Therefore, we believe that this method can detect the shear elasticity and viscosity of a region a few millimeters in diameter. Of course, measurements over longer distance will yield more precise results. According to Eq. (4), speed estimation over larger Δr results in smaller percentage error, assuming similar uncertainty in the phase measurement $\Delta\varphi$.

Another potential problem that can be caused by tissue inhomogeneity is the reflection of shear waves. Under such situations, shear wave speed estimated by Eq. (4) will not be applicable. The viscosity of tissue is fairly high (about an order of magnitude larger than that of the phantoms used in this paper). Therefore, shear waves die out quickly within a short distance and standing waves caused by tissue inhomo-

geneity will be less of a problem. In addition, to reduce the effect of standing waves, we can use shear waves of higher frequencies, which have higher attenuation. However, this requires the shear wave speed to be estimated over a shorter distance, resulting in less precision. The frequency of shear waves, and the propagation range over which the phase will be tracked, can and should be carefully selected to benefit different applications.

VI. SUMMARY

We present a new method to estimate the complex stiffness of a viscoelastic medium by measuring shear wave speed at multiple frequencies. The uniqueness of this method lies in its ability to measure *viscosity*, as well as elasticity, in a truly *quantitative* sense. Ultrasound radiation force is used to generate cylindrical shear waves of various frequencies in an object. The formula relating the complex stiffness of the medium and the shear wave speed, and the formula for calculating the speed from phase shift, are given. The shear wave speeds in the medium are measured from displacement phase shift vs the distance traveled. The speeds measured at multiple frequencies are then fit with the theoretical formula of shear wave speed to solve for the complex stiffness of the medium. Experiments in phantoms show very promising results that were validated by an independent method. Practical considerations and challenges in possible medical applications are also discussed.

ACKNOWLEDGMENTS

The authors are grateful to Randall R. Kinnick for his help on experiments. This work was supported by Grants EB-02640 and EB-02167 from National Institutes of Health, and IMG0100744 from the Susan G. Komen Breast Cancer Foundation.

Andreev, V. G., Dmitriev, V. N., Pischalnikov, Y. A., Rudenko, O. V., Sapozhnikov, O. A., and Sarvazyan, A. P. (**1997**). ''Observation of shear waves excited by focused ultrasound in rubber-like medium,'' Acoust. Phys. **43**(2), 123–128.

Chen, S., Fatemi, M., and Greenleaf, J. F. (**2002a**). ''Remote measurement of material properties from radiation force induced vibration of an embedded sphere,'' J. Acoust. Soc. Am. **112**, 884–889.

Chen, S., Fatemi, M., and Greenleaf, J. F. (**2002b**). ''Shear property characterization of viscoelastic media using vibrations induced by ultrasound radiation force,'' Proc. 2003 Ultrason. Symp., 1827–1831.

Fatemi, M., and Greenleaf, J. F. (**1999**). ''Vibro-acoustography: An imaging modality based on ultrasound-stimulated acoustic emission,'' Proc. Natl. Acad. Sci. U.S.A. **96**, 6603–6608.

Fung, Y. C. (**1993**). *Biomechanics*, 2nd ed. (Springer, New York), pp. 41–42.

Garra, B. S., Cespedes, E. I., Ophir, J., Spratt, R. S., Zuurbier, R. A., Magnant, C. M., and Pennanen, M. F. (**1997**). ''Elastography of breast lesions: Initial clinical results,'' Radiology **202**, 79–86.

Graff, K. F. (**1991**). *Wave Motion in Elastic Solids* (Dover, New York), pp. 284–286.

Kallel, F., Ophir, J., Magee, K., and Krouskop, T. (**1998**). ''Elastographic imaging of low-contrast elastic modulus distributions in tissue,'' Ultrasound Med. Biol. **24**, 409–425.

Lerner, R. M., Parker, K. J., Holen, J., Gramiak, R., and Waag, R. C. (**1988**). ''Sono-elasticity: Medical elasticity images derived from ultrasound signals in mechanically vibrated targets,'' in *Acoustical Imaging*, edited by L. J. Kessler (Kluwer Academic, New York), **16**, pp. 317–327.

Muthupillai, R., Lomas, D. J., Rossman, P. J., Greenleaf, J. F., Manduca, A., and Ehman, R. L. (**1995**). ''Magnetic resonance elastography by direct visualization of propagating acoustic strain waves,'' Science **269**, 1854–1857.

Nightingale, K. R., Palmeri, M. L., Nightingale, R. W., and Trahey, G. E. (**2001**). ''On the feasibility of remote palpation using acoustic radiation force,'' J. Acoust. Soc. Am. **110**, 625–634.

Oestreicher, H. L. (**1951**). ''Field and impedance of an oscillating sphere in a viscoelastic medium with an application to biophysics,'' J. Acoust. Soc. Am. **23**, 707–714.

Ophir, J., Cespedes, I., Ponnekanti, H., Yazdi, Y., and Li, X. (**1991**). ''Elastography: A quantitative method for imaging the elasticity of biological tissues,'' Ultrason. Imaging **13**, 111–134.

Ophir, J., Cespedes, I., Garra, B., Ponnekanti, H., Huang, Y., and Maklad, N. (**1996**). ''Elastography: Ultrasonic imaging of tissue strain and elastic modulus *in vivo*,'' Eur. J. Ultrasound **3**, 49–70.

Royston, T. J., Mansy, H. A., and Sandler, R. H. (**1999**). ''Excitation and propagation of surface waves on a viscoelastic half-space with application to medical diagnosis,'' J. Acoust. Soc. Am. **106**, 3678–3686.

Sarvazyan, A. P., Redenko, O. V., Swanson, S. D., Fowlkers, J. B., and Emelianov, S. Y. (**1998**). ''Shear wave elasticity imaging: A new ultrasonic technology of medical diagnostics,'' Ultrasound Med. Biol. **24**, 1419–1435.

Yamakoshi, Y., Sato, J., and Sato, T. (**1990**). ''Ultrasonic imaging of internal vibration of soft tissue under forced vibration,'' IEEE Trans. Ultrason. Ferroelectr. Freq. Control **37(2)**, 45–53.

Zheng, Y., Chen, S., Tang, W., and Greenleaf, J. F. (**2003**). ''Kalman filter motion detection for vibro-acoustography using pulse echo ultrasound,'' Proc. 2003 Ultrason. Symp., 1812–1815.

A two-field hybrid formulation for multilayers involving poroelastic, acoustic, and elastic materials

Stéphane Rigobert and Franck C. Sgard[a)]
Laboratoire des Sciences de l'Habitat, DGCB URA CNRS 1652, Ecole Nationale des Travaux Publics de l'Etat, 69518 Vaulx-en-Velin CEDEX, France

Noureddine Atalla
Groupe d'Acoustique de l'Université de Sherbrooke, Department of Mechanical Engineering, Univ. de Sherbrooke, Sherbrooke, QC J1K 2R1, Canada

(Received 15 August 2003; revised 7 February 2004; accepted 8 February 2004)

Recently, an implementation of the mixed pressure displacement $\{u,P\}$ formulation for poroelastic materials using the theory of hierarchical elements has been proposed. It has been shown that poroelastic hierarchical elements allow for an important reduction of the number of degrees of freedom required for the modeling of a porous material in three dimensions, compared to linear finite elements. In this paper, the coupling of a porous material modeled with hierarchical elements and an elastic domain modeled with finite elements or a fluid modeled with hierarchical elements is presented. Non-coincident meshes are assumed. Continuity of the fields is ensured by using a two-field hybrid formulation. The paper is organized as follows. The theory is first presented. The computation of fluid-structure coupling integrals over non-coincident meshes is then tackled. Numerical results are produced to show the accuracy and the performance of the proposed model for the modeling of an elastic-porous or a porous-fluid coupled system. Comparisons between numerical simulations and experiments are also presented in the case of a porous coated plate. © *2004 Acoustical Society of America.* [DOI: 10.1121/1.1698758]

PACS numbers: 43.20.Jr, 43.50.Gf, 43.55.Wk [ADP] Pages: 2786–2797

I. INTRODUCTION

Due to their dissipative properties, porous materials are extensively used in building acoustics as well as in the automotive industry or in aeronautics for the purpose of passive noise control. In practical applications, poroelastic materials are involved in multilayered structures comprising elastic and acoustic media. These systems may have complex geometries, and are subjected to various kinds of boundary conditions and loadings. To calculate the low frequency response of such multilayered structures, the use of numerical methods such as the finite element method becomes necessary.

In the past, several 2-D and 3-D finite element models based on Biot-Allard theory have been proposed for the computation of the forced response of a poroelastic material. The first models use the displacement **u** in the solid phase and the displacement **U** in the fluid phase as unknowns.[1–4] These {**u**,**U**} formulations are accurate but lead to large frequency-dependent systems. Hence, cumbersome calculations are required for complex structures. A {**u**,**P**} finite element formulation for a porous material in three dimensions was proposed by Atalla *et al.*[5] The boundary and coupling conditions for this formulation were presented by Debergue *et al.*[6] The proposed {**u**,**P**} formulation presents several interesting features. First, it is exact since the equations used are those from Biot's theory of poroelasticity without any new assumption. Also, the coupling conditions with an elastic or an acoustic medium are easily handled. Compared to classical {**u**,**U**} formulations, 4 degrees of freedom per node are used instead of 6, allowing for an important saving of computational ressources.

Classical finite elements based on the latter formulations have a slow convergence for real 3-D deformations because of, among other things, numerical locking of 3-D linear elements.[7] To alleviate this problem, the theory of hierarchical elements has been recently used for the implementation of a weak {**u**,**U**}[8] or a weak {**u**,**P**}[9,10] formulation. The use of high-order polynomials for the interpolation of the fields allows for an increase of the convergence rate of the solution and solves the problems of numerical locking. As a result, the so-called hierarchical poroelastic elements bring an important reduction of the number of degrees of freedom required for the modeling of a porous domain in comparison with classical linear poroelastic elements. The connection of the finite element models of two subdomains requires the satisfaction of continuity equations at their common interface and, in some instances, the computation of coupling integrals. These two steps are achieved without any difficulty if compatible meshes are used, namely if the nodes of the mesh for the two subdomains coincide at the common interface. However, using compatible meshes may require a number of degrees of freedom uncessarily large. For instance, consider the coupling of an elastic domain to a fluid with compatible meshes. The wavelengths in the fluid and the structure are usually very different. The common mesh at the interface is related to the smaller wavelength and hence is not optimal for one of the two components of the coupled system. Thus, the use of non-coincident meshes is interesting in practical applications, especially when porous materials are involved

[a)]Author to whom correspondence should be addressed. Electronic mail: franck.sgard@entpe.fr

 0001-4966/2004/115(6)/2786/12/$20.00 © 2004 Acoustical Society of America

since they need to be discretized along their thickness.

Few published works deal with the computation of fluid-structure coupling integrals on non-coincident meshes. A method proposed by Coyette *et al.*[11] is based on the projection of the nodes of one of the domains on the mesh of the other domain. However, it leads to a loss of information regarding the coupling between the fluid and the structure. The approach presented by Guerich and Hamdi[12] overcomes this problem by considering a common mesh for the geometry on the interface from which new meshes are constructed independently for the structure and the fluid. Cubic spline functions are then used for the approximation of the modes shape for the structure and the fluid on their respective new mesh. The coupling integrals are then computed on the common mesh of the interface.

On the other hand, the connection of non-coincident meshes have been tackled by several authors dealing with the static or dynamic analysis of structures. For these problems, the continuity of displacements has to be satisfied. Node collocation is the simplest method to account for the continuity of displacement.[13] This technique is based on the following principle. For each of the two subdomains, the displacement at each node of the mesh lying on the interface is expressed as a function of a reference displacement field. This amounts to verifying a set of linear constraints, involving the degrees of freedom for each subdomain related to the interpolation of the displacement at the interface. A weaker form of these constraints can be obtained by establishing a discrete least square formulation based on the same principle.[14] These linear relations are then classically enforced in the discretized weak formulation of the problem using discrete Lagrange multipliers. Aminpour[14] notes that the collocation method and the discrete least square compatibility are not suitable since these methods do not pass the interface patch test. The uniform strain approach for finite elements was used by Dohrmann[15] to ensure the displacement continuity in the case of nonconforming geometries. This method allows one to overcome the difficulties met in the application of the collocation method but its implementation is not straightforward. Non-coincident meshes can also be connected using two fields[16,13] or three fields[14] hybrid formulations. Both of these techniques consist in ensuring a weak continuous compatibility of displacement on the interface, which is enforced in the weak formulation of the problem using continuous Lagrange multipliers. In two-field formulations, the variables of interest are the displacement at the interface for each subdomain and the Lagrange multipliers. When using a three-field formulation, a reference displacement field is introduced in addition. Both of these methods are efficient but the use of Lagrange multipliers leads to nonpositive definite linear systems to be solved.

In this paper, the coupling of hierarchical poroelastic elements with the finite element model of an elastic or an acoustic domain is presented. Non-coincident meshes are assumed in order to benefit fully from the important reduction of the number of degrees of freedom allowed by the use of the former elements for the modeling of a poroelastic domain in comparison with classical finite elements. The problem tackled herein is summarized in Fig. 1. In the first part of this paper, the classical weak formulation for an elastic and an acoustical domain are recalled together with the {**u**,**P**} formulation. The coupling conditions at the interface between a porous material and an elastic domain or a fluid are presented. Second, a two-field hybrid formulation is constructed for the coupled porous-elastic and porous-fluid coupled system, taking into account the essential coupling conditions to be satisfied for these two configurations. The numerical implementation of these formulations is then presented assuming non-coincident meshes. In particular, a simple technique is proposed for the computation of the fluid-structure coupling integral appearing in the case of a porous material coupled to a fluid. Validation results are then presented for the configurations of a porous material coupled to a cavity and a porous coated plate. Comparison with measurements performed on the plate for the latter configuration is also provided.

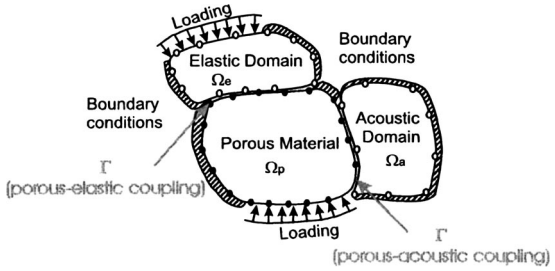

FIG. 1. Elasto-poro-acoustic system with complex geometry submitted to various kinds of excitations and boundary condition. Subdomains are assumed to have non-coincident meshes.

II. THEORY

In the following subsections, a harmonic time dependence is assumed for the fields in an elastic, poroelastic or acoustic domain. Namely, considering a harmonic excitation, any field x of interest writes $x(t)=\hat{x}(\omega)\cdot e^{j\omega t}$ in the time domain. ω is the angular frequency related to the frequency f by the formula $w=2\pi f$. The work presented in this paper is based on theoretical developments in the frequency domain.

A. Weak formulation for an elastic domain

The weak integral form of the equation of motion for an elastic domain Ω_{el} is classical and reads[17]

$$\int_{\Omega_{el}} \underset{\approx}{\sigma}^{el}(\mathbf{u}^{el}):\underset{\approx}{\epsilon}^{el}(\delta\mathbf{u}^{el})\,d\Omega - \int_{\Omega_{el}} \rho_{el}\omega^2\mathbf{u}^{el}\cdot\delta\mathbf{u}^{el}\,d\Omega - \int_{\partial\Omega_{el}} [\underset{\approx}{\sigma}^{el}\cdot\mathbf{n}]\cdot\delta\mathbf{u}^{el}\,dS = 0, \tag{1}$$

where $\underset{\approx}{\sigma}^{el}$, $\underset{\approx}{\epsilon}^{el}$ are the stress and strain tensors related to the elastic domain. $\mathbf{u}^{el}$ is the displacement vector and $\delta\mathbf{u}^{el}$ is its admissible variation. ρ_{el} is the mass density. $\partial\Omega_{el}$ is the boundary of the elastic domain, and $\mathbf{n}$ is the outward normal vector to $\partial\Omega_{el}$.

B. Weak formulation for a fluid

The propagation of waves in an acoustical medium Ω_a is governed by Helmholtz equation. The associated weak formulation is given by[17]

$$\int_{\Omega_a}\left[\frac{1}{\omega^2\rho_a}\boldsymbol{\nabla}p^a\,\delta\boldsymbol{\nabla}p^a-\frac{1}{\rho_a c_a^2}p^a\,\delta p^a\right]d\Omega - \frac{1}{\omega^2\rho_a}\int_{\partial\Omega_a}\frac{\partial p^a}{\partial n}\,\delta p^a\,dS=0, \tag{2}$$

where p^a and δp^a are the pressure in the fluid and its admissible variation. ρ_a is the fluid density and c_a is the sound speed in the fluid.

C. Weak {u,P} formulation for a porous material

The weak formulation used in this paper and derived from the poroelasticity equations of Biot–Allard theory is a variant of the original {**u**,**P**} formulation for a porous material initially established by Atalla *et al.*[5] Compared to the latter formulation, the variant used herein couples naturally with elastic, acoustic, and porous media and handles naturally acoustic and mechanical loads. It reads[18]

$$\begin{aligned}\int_{\Omega_p}\tilde{\underline{\underline{\sigma}}}^s(\mathbf{u}^s):\underline{\underline{\epsilon}}^s(\delta\mathbf{u}^s)\,d\Omega-\tilde{\rho}\omega^2\int_{\Omega_p}\mathbf{u}^s\cdot\delta\mathbf{u}^s\,d\Omega\\ +\int_{\Omega_p}\left[\frac{\phi^2}{\omega^2\tilde{\rho}_{22}}\boldsymbol{\nabla}p\cdot\boldsymbol{\nabla}\delta p-\frac{\phi^2}{\tilde{R}}p\,\delta p\right]d\Omega\\ -\int_{\Omega_p}\left[\tilde{\gamma}+\phi\left(1+\frac{\tilde{Q}}{\tilde{R}}\right)\right]\delta(\boldsymbol{\nabla}p\cdot\mathbf{u}^s)\,d\Omega-\phi\left(1+\frac{\tilde{Q}}{\tilde{R}}\right)\\ \times\int_{\Omega_p}\delta(p\,\mathrm{div}(\mathbf{u}^s))\,d\Omega-\int_{\partial\Omega_p}[\underline{\underline{\sigma}}^t\cdot\mathbf{n}]\cdot\delta\mathbf{u}^s\,dS\\ -\int_{\partial\Omega_p}\phi(U_n^f-u_n^s)\,\delta p\,dS=0,\end{aligned} \tag{3}$$

where $\tilde{\underline{\underline{\sigma}}}^s$ and $\underline{\underline{\epsilon}}^s$ are the strain and stress tensor related to the solid phase of the porous material *in vacuo*. $\underline{\underline{\sigma}}^t$ is the total strain tensor in the porous material. $\mathbf{u}^s$ and p are respectively the displacement vector of the solid phase and the pressure in the pores. $\delta\mathbf{u}^s$ and δp are their admissible variations. U_n^f is the component of the fluid displacement normal to the boundary of the poroelastic domain. $\tilde{\rho}_{22}$ is the modified Biot's density of the fluid phase accounting for viscous dissipation. $\tilde{\rho}$ is a modified density given by $\tilde{\rho}=\tilde{\rho}_{11}-\tilde{\rho}_{12}/\tilde{\rho}_{22}$ where $\tilde{\rho}_{11}$ is the modified Biot's density of the solid phase accounting for viscous dissipation. $\tilde{\rho}_{12}$ is the modified Biot's density which accounts for interaction between inertia forces of the solid and fluid phase together with viscous dissipation. ϕ denotes the porosity. $\tilde{\gamma}$, $\tilde{Q}$, and $\tilde{R}$ are poroelastic coefficients.[6]

D. Coupling conditions

This section recalls the coupling conditions to be satisfied at the interface Γ between a porous material and an elastic or an acoustic domain.

1. Poroelastic-elastic coupling conditions

At the interface Γ between a poroelastic and an elastic domain, the following relations hold:[4]

$$\underline{\underline{\sigma}}^t\cdot\mathbf{n}=\underline{\underline{\sigma}}^{el}\cdot\mathbf{n},\quad U_n^f-u_n^s=0,\quad \mathbf{u}^s=\mathbf{u}^{el}, \tag{4}$$

where $\mathbf{n}$ is the normal vector pointing into the elastic domain. The first equation allows for the continuity of the forces acting at the interface between the two subdomains. The second equation indicates that there is no relative mass flux across the interface. The third equation ensures the continuity of displacement.

2. Poroelastic-acoustic coupling conditions

The coupling conditions at the interface Γ between a poroelastic domain and an acoustic domain are the following:[4]

$$\underline{\underline{\sigma}}^t\cdot\mathbf{n}=-p^a\mathbf{n},\quad \frac{1}{\rho_a\omega^2}\frac{\partial p^a}{\partial n}=(1-\phi)u_n^s+\phi U_n^f,\quad p^a=p, \tag{5}$$

where $\mathbf{n}$ is the normal vector pointing outward the poroelastic domain. The first equation transcribes the continuity of stresses at the interface. The second equation corresponds to the continuity of normal displacements. The third equation ensures the continuity of pressures.

E. Weak formulation for the coupled system

In this paragraph, the weak formulation for a coupled system made up of a porous material and an elastic or an acoustic domain is presented. It is obtained in two steps. First, a weak formulation for the system is established from the weak formulation of each of the two components of the multilayer, and the natural coupling conditions (e.g., continuity of stresses) are implicitly taken into account. Next, continuous Lagrange multipliers are introduced to enforce the essential coupling conditions, such as the continuity of displacement for the case of a porous material coupled to an elastic domain, leading to a two-field hybrid formulation for the coupled system.

1. Porous material-elastic domain coupled system

The porous-elastic coupled formulation is obtained by summing Eqs. (1) and (3) and by considering the first and the second equations in Eq. (4):

$$\int_{\Omega el} \underset{\approx}{\sigma}^{el}(\mathbf{u}^{el}):\underset{\approx}{\epsilon}^{el}(\delta\mathbf{u}^{el})d\Omega - \rho_{el}\omega^2\int_{\Omega el}\mathbf{u}^{el}\cdot\delta\mathbf{u}^{el}\,d\Omega + \int_{\Omega p}\underset{\approx}{\sigma}^{s}(\mathbf{u}^{s}):\underset{\approx}{\epsilon}^{s}(\delta\mathbf{u}^{s})d\Omega - \tilde{\rho}\omega^2\int_{\Omega p}\mathbf{u}^{s}\cdot\delta\mathbf{u}^{s}\,d\Omega$$
$$+\int_{\Omega p}\left[\frac{\phi^2}{\omega^2\tilde{\rho}_{22}}\nabla p\cdot\nabla\delta p - \frac{\phi^2}{\tilde{R}}p\,\delta p\right]d\Omega - \int_{\Omega p}\left[\tilde{\gamma}+\phi\left(1+\frac{\tilde{Q}}{\tilde{R}}\right)\right]\delta(\nabla p\cdot\mathbf{u}^{s})d\Omega - \phi\left(1+\frac{\tilde{Q}}{\tilde{R}}\right)$$
$$\times\int_{\Omega p}\delta(p\,\mathrm{div}(\mathbf{u}^{s}))d\Omega - \int_{\partial\Omega_{el}\backslash\partial\Omega_p}[\underset{\approx}{\sigma}^{el}\cdot\mathbf{n}^1]\cdot\delta\mathbf{u}^{el}\,dS - \int_{\partial\Omega_p\backslash\partial\Omega_{el}}[\underset{\approx}{\sigma}^{t}\cdot\mathbf{n}^2]\,\delta\mathbf{u}^{s}\,dS - \int_{\partial\Omega_p\backslash\partial\Omega_{el}}\phi(U^f_{n^2}-u^s_{n^2})\,\delta p\,dS = 0, \tag{6}$$

where $\mathbf{n}^1$ and $\mathbf{n}^2$ denote the normal outward vector to $\partial\Omega_{el}$ and $\partial\Omega_p$, respectively. $\partial\Omega_{el}\backslash\partial\Omega_p$ (resp. $\partial\Omega_p\backslash\partial\Omega_{el}$) stands for the part of the boundary of the elastic (resp. poroelastic domain) which is not adjacent to the poroelastic (resp. elastic) domain. It may be adjacent to an acoustical medium, for example, or subjected to boundary conditions or excitations. Only the two latter cases are considered in this paper.

In the following, the external fluid loading on the plate or on unconstrained boundaries of the porous material is not accounted for. To be precise this is taken into account in the weak $\{\mathbf{u},\mathbf{P}\}$ of a porous material by setting $p=0$ on the concerned boundary (see Ref. 6). Considering the configuration of a porous coated plate immerged in a surrounding fluid, Dauchez *et al.*[7] indicate that this lack may have an influence on the quality of the predictions for the vibroacoustics indicators. Horoshenkov *et al.*[19] presented an analytical model taking into account the influence of the vibrations of the skeleton of a porous material on a surrounding fluid medium. However, this model does not take into account the coupling between the two phases of the porous material, which phenomenon was proved to be important in some cases in the low frequency range.[9] Actually, accounting for the radiation of a poroelastic material in an infinite fluid is of great interest in many fields including geophysics, underwater, architectural acoustics, etc., but is still a subject of research in the context of the finite element method.

The weak formulation given by Eq. (6) implicitly accounts for the continuity of stresses and the equality of the solid and fluid normal displacement (zero displacement flux) in the porous material along the interface Γ. Namely, the first and third equations of system (4) stand for the continuity of stresses and displacements on the common interface, which the latter condition also applies to the variational fields in the elastic and poroelastic domains. Hence, one gets

$$\int_\Gamma[\underset{\approx}{\sigma}^{el}\cdot\mathbf{n}^1]\cdot\delta\mathbf{u}^{el}\,dS + \int_\Gamma[\underset{\approx}{\sigma}^{t}\cdot\mathbf{n}^2]\cdot\delta\mathbf{u}^{s}\,dS = 0 \tag{7}$$

with $\mathbf{n}^1=-\mathbf{n}^2$ on Γ. This explains why the surface integrals on Γ related to the description of elastic and poroelastic domain vanish. Equation (6) is equivalent to the minimization of an energy functional Π_{pel} depending on the admissible variables $\mathbf{u}^{el}$, $\mathbf{u}^{s}$, and p. In order to enforce the continuity of displacement, an energy functional Π'_{pel} is introduced:

$$\Pi'_{pel}=\Pi_{pel}+\int_\Gamma\boldsymbol{\lambda}\cdot(\mathbf{u}^{el}-\mathbf{u}^{s})dS, \tag{8}$$

where $\boldsymbol{\lambda}$ is a continuous Lagrange multiplier. Π_{pel} depends on the admissible variables $\mathbf{u}^{el}$, $\mathbf{u}^{s}$, p, and λ. Perfoming the variation of Π'_{pel} leads to

$$\delta\Pi'_{pel}=\delta\Pi_{pel}+\underbrace{\int_\Gamma\delta\boldsymbol{\lambda}\cdot\mathbf{u}^{el}\,dS}_{I_1}+\underbrace{\int_\Gamma\boldsymbol{\lambda}\cdot\delta\mathbf{u}^{el}\,dS}_{I'_1}$$
$$-\underbrace{\int_\Gamma\delta\boldsymbol{\lambda}\cdot\mathbf{u}^{s}\,dS}_{I_2}-\underbrace{\int_\Gamma\boldsymbol{\lambda}\cdot\delta\mathbf{u}^{s}\,dS}_{I'_2}=0. \tag{9}$$

$\delta\Pi_{pel}$ is given by the left-hand side of Eq. (6) augmented by the term

$$-\int_\Gamma[\underset{\approx}{\sigma}^{el}\cdot\mathbf{n}^1]\cdot\delta\mathbf{u}^{el}\,dS-\int_\Gamma[\underset{\approx}{\sigma}^{t}\cdot\mathbf{n}^2]\cdot\delta\mathbf{u}^{s}\,dS, \tag{10}$$

which was previously disregarded as it was proved to be equal to 0 [see Eq. (7)]. The solution to the problem satisfies $\delta\Pi'_{pel}=0$ for any admissible variation $\delta\mathbf{u}^{\mathrm{el}}$, $\delta\mathbf{u}^{\mathrm{s}}$, δp and $\delta\boldsymbol{\lambda}$. Hence, Eq. (6) has to be satisfied together with

$$\int_\Gamma\delta\boldsymbol{\lambda}\cdot(\mathbf{u}^{el}-\mathbf{u}^{s})dS+\int_\Gamma(\boldsymbol{\lambda}-\underset{\approx}{\sigma}^{el}\cdot\mathbf{n}^1)\cdot\delta\mathbf{u}^{el}\,dS$$
$$-\int_\Gamma(\boldsymbol{\lambda}-\underset{\approx}{\sigma}^{t}\cdot\mathbf{n}^1)\cdot\delta\mathbf{u}^{s}\,dS=0, \tag{11}$$

which must be true for all variations $\delta\mathbf{u}^{el}$, $\delta\mathbf{u}^{s}$ and $\delta\boldsymbol{\lambda}$. First, this leads to

$$\mathbf{u}^{el}=\mathbf{u}^{s}\quad\text{on }\Gamma, \tag{12}$$

namely the continuity of displacements at the interface between the elastic material and the poroelastic medium. Second, it defines $\boldsymbol{\lambda}$ as

$$\boldsymbol{\lambda}=\underset{\approx}{\sigma}^{el}\cdot\mathbf{n}^1=\underset{\approx}{\sigma}^{t}\cdot\mathbf{n}^1. \tag{13}$$

This equation indicates that the Lagrange multipliers can be physically interpreted as the interface forces allowing for the continuity of displacements.

Integrals I_1 and I'_1 (resp. I_2 and I_2) appearing in Eq. (9) are discretized on the mesh of the elastic domain (resp. porous domain). The meshes for the elastic and the porous

domain are thus not required to be compatible. The shape functions used for the approximation of $\mathbf{u}^{el}$ and $\mathbf{u}^s$ in the computation of these equations are those used in the finite element model for the elastic and the porous domains, respectively. Moreover, a discretization for the Lagrange multipliers is also required. This point is discussed further later in the paper.

2. Porous material-acoustic domain coupled system

The methodology is similar to the previous case. The weak formulation for the porous material given by Eq. (3) and the weak formulation for the fluid given by Eq. (2) are summed. Taking into account the first and second equations of system (5), one gets

$$\int_{\Omega_p} \tilde{\underline{\underline{\sigma}}}^s(\mathbf{u}^s) : \underline{\underline{\epsilon}}^s(\mathbf{u}^s)\, d\Omega - \tilde{\rho}\omega^2 \int_{\Omega_p} \mathbf{u}^s \cdot \delta\mathbf{u}^s\, d\Omega + \int_{\Omega_p} \left[\frac{\phi^2}{\omega^2 \tilde{\rho}_{22}} \nabla p \cdot \nabla \delta p - \frac{\phi^2}{\tilde{R}} p\, \delta p \right] d\Omega - \int_{\Omega_p} \left[\tilde{\gamma} + \phi\left(1 + \frac{\tilde{Q}}{\tilde{R}}\right) \right] \delta(\nabla p \cdot \mathbf{u}^s) d\Omega$$

$$- \phi\left(1 + \frac{\tilde{Q}}{\tilde{R}}\right) \int_{\Omega_p} \delta(p\ \mathrm{div}(\mathbf{u}^s)) d\Omega + \int_{\Omega_a} \left[\frac{1}{\omega^2 \rho_a} \nabla p^a \delta \nabla p^a - \frac{1}{\rho_a c_a^2} p^a \delta p^a \right] d\Omega + \underbrace{\int_\Gamma \delta p^a u_{n^2}^s\, dS}_{I_3} + \underbrace{\int_\Gamma p^a \delta u_{n^2}^s\, dS}_{I_3'}$$

$$- \frac{1}{\omega^2 \rho_a} \int_{\partial\Omega_a \setminus \partial\Omega_p} \frac{\partial p^a}{\partial n^1} \delta p^a\, dS - \int_{\partial\Omega_p \setminus \partial\Omega_a} [\underline{\underline{\sigma}}^t \cdot \mathbf{n}^2] \delta\mathbf{u}^s\, dS - \int_{\partial\Omega_p \setminus \partial\Omega_a} \phi(U_{n^2}^f - u_{n^2}^s)\, \delta p\, dS = 0, \tag{14}$$

where $\mathbf{n}^1$ and $\mathbf{n}^2$ are the normal vector pointing out of the acoustic and the poroelastic domain, respectively. Equation (14) is equivalent to the minimization of an energy functional Π_{pa} and implicitly takes into account the continuity of normal stresses and normal displacements leading to the fluid-structure coupling integrals I_3 and I_3'. The computation of these two terms is detailed in the following section. A new energy functional Π_{pa}' is defined in order to enforce the continuity of pressure at the interface between the porous material and the fluid. It is given by

$$\Pi_{pa}' = \Pi_{pa} + \int_\Gamma \lambda (p - p^a) dS, \tag{15}$$

where λ is a scalar continuous Lagrange multiplier. The minimization of Π_{pa}' leads to

$$\delta\Pi_{pa}' = \delta\Pi_{pa} + \underbrace{\int_\Gamma \delta\lambda p\, dS}_{I_4} + \underbrace{\int_\Gamma \lambda\, \delta p\, dS}_{I_4'} - \underbrace{\int_\Gamma \delta\lambda p^a\, dS}_{I_5} - \underbrace{\int_\Gamma \lambda\, \delta p^a\, dS}_{I_5'} \tag{16}$$

which has to be satisfied for any admissible variable $\delta\mathbf{u}^s$, δp, δp^a, $\delta\lambda$, which leads to

$$\delta\Pi_{pa} = 0, \quad p = p^a \quad \text{on } \Gamma, \quad \lambda = \phi(u_{n^2}^s - U_{n^2}^f). \tag{17}$$

It follows that Eq. (14) is satisfied and that the continuity of pressure is ensured. In this configuration, the Lagrange multiplier corresponds to the relative flux across the interface Γ allowing for the continuity of pressure.

Integrals I_4 and I_5, together with I_4' and I_5', are discretized on the mesh of the porous domain and the fluid domain, respectively. In consequence, these two meshes are not required to be coincident. The shape functions used for the approximation of p and p^a are the same as the ones used in the finite element model of the porous and the acoustic domain.

III. NUMERICAL IMPLEMENTATION

In this section, the numerical implementation of the proposed approach is presented. First, the theoretical developments leading to the construction of hierarchical poroelastic elements are briefly recalled. More details are available in Ref. 9. Second, the interpolation on the interface Γ of the Lagrange multipliers introduced in the two-field hybrid formulations presented in the previous section is discussed. A simple technique is then presented for the computation of fluid-structure coupling integrals assuming non-coincident meshes.

A. Hierarchical poroelastic elements

In the following, a porous domain is considered and the weak $\{\mathbf{u},\mathbf{P}\}$ formulation given by Eq. (3) is used. The poroelastic domain is discretized using eight-node brick elements. The theoretical foundations of hierarchical elements lie in the way the pressure in the pores and the displacement of the solid phase are interpolated at any point of the subdomain. The pressure in the pores is given by[9]

$$p(\xi,\eta,\zeta)=\sum_i \mathcal{N}_i q_i^{ph}+\sum_j \mathcal{G}_j q_j^{gen}, \tag{18}$$

where ξ, η, ζ are the coordinates on the parent element. $\mathcal{N}_i$ and $\mathcal{G}_j$ are polynomial shape functions defined on the parent element. The associated variables q_i^{ph} and q_j^{gen} stand for the amplitude of these functions. Amplitudes q_i^{ph} $(1<j<8)$ are the amplitudes of the pressure in the pores at the element nodes, and $\mathcal{N}_i$ are the classical shape functions used in finite elements. Amplitudes q_j^{gen} denote generalized coordinates. The associated generalized functions $\mathcal{G}_j$ are divided in several categories: side modes, face modes, and internal modes. These functions are selected to make complete polynomials of ascending order. Namely, the basis functions of the hierarchical variables are constructed using Legendre polynomials. Their number depend on the interpolation order. For further details on the selection process, the reader is invited to refer to Szabò and Babuška.[20]

Equation (18) can be rewritten:

$$p=\{N_f\}^T\cdot\{p_n\}^e, \tag{19}$$

where $\{N_f\}$ is the columun vector containing the polynomial shape functions and $\{p_n\}^e$ is the column vector including the amplitudes q_i^{ph} and q_j^{gen} associated to each shape function. The approximation of the variation δp of p as well as the solid phase displacement and its variation is achieved in the same way.

Hierarchical poroelastic elements are obtained from the coupling of a solid element and an equivalent fluid element. A hierarchical finite element model for fluids is therefore available and will be used in the result section for the modeling of acoustic media.

B. Interpolation of Lagrange multipliers

Vector or scalar Lagrange multipliers have been introduced to enforce the continuity of solid displacement or pressure on the interface Γ between a porous material and an elastic material or a fluid. The discretization of the two-field hybrid formulation used to describe the problem implies the computation of surface integrals along Γ involving these Lagrange multipliers. These unknowns thus need to be interpolated on the interface. This point is the subject of the present section.

To illustrate the used methodology, the porous-acoustic medium coupled system is considered. The subdomains are assumed to have planar geometries. Any point lying on the interface Γ is located by its x and y coordinates. The continuous scalar Lagrange multiplier λ used in Eq. (15) to ensure the continuity of pressure is defined globally on the interface by

$$\lambda=\sum_{j=1}^{p_x}\sum_{k=1}^{p_y} A_{jk}\cdot L_j(x)\cdot L_k(y), \tag{20}$$

where L_j is the Legendre polynomial of order j. p_x and p_y are the maximum orders for that polynomial in the directions x and y. Equation (20) can be rewritten as

$$\lambda=\{N_\lambda\}^T\cdot\{A_{jk}\}, \tag{21}$$

where $\{N_\lambda\}$ is the column vector of the shapes functions $L_j(x)\cdot L_k(y)$ associated to the amplitudes A_{jk}.

The choice of the values for p_x and p_y is an important issue. Farhat *et al.*[16] indicate that in order to avoid the stiffening of the most refined mesh, the number of unknowns associated to the interpolation of λ should remain lower than the number of degrees of freedom (d.o.f.) n_p and n_a related to the approximation of pressure in the fluid phase of the porous material and in the acoustic medium, respectively.[16] This leads to

$$(p_x+1)(p_y+1)\leqslant\min(n_p,n_a). \tag{22}$$

Surface integrals in Eq. (16) are discretized on the porous and the acoustic domain meshes. Consider for instance I_4. This integral is expressed as the sum of integrals I_4^e evaluated on each element of the mesh for the poroelastic domain having a side lying on $\Gamma=\partial\Omega_p\cap\partial\Omega_p$. On element e, the use of the expressions of λ and p given by Eqs. (21) and (19) gives

$$\begin{aligned} I_4^e&=\{\delta A_{jk}\}^T\left(\int_{\partial\Omega_e}\{N_\lambda\}\cdot\{N_f\}^T\,dS\right)\{p_n^e\}\\ &=\{\delta A_{jk}\}^T\cdot([C_{pp}]^e)^T\cdot\{p_n^e\}, \end{aligned} \tag{23}$$

where the amplitudes $\{p_n^e\}$ are related to the approximation of the interstitial pressure on the face of the element lying on Γ. $\{\delta A_{jk}\}$ is the vector containing the unknowns related to the interpolation of the variation of the Lagrange multiplier λ. Summing the integrals I_4^e for all e amounts to proceeding to the assembly of element matrices $[C_{pp}]^e$ into a global matrix $[C_{pp}]$ to write

$$I_4=\{\delta A_{jk}\}^T[C_{pp}]^T\{p_n\}, \tag{24}$$

where $\{p_n\}$ is the vector of the degrees of freedom related to the approximation of the pressure in the porous medium. Using the same methodology for the computation of I_4', I_5 and I_5' leads to the following expressions:

$$I_4'=\{\delta p_n\}^T[C_{pp}]\{A_{jk}\}, \tag{25}$$

$$I_5=\{\delta A_{jk}\}^T[C_{pa}]^T\{p_n^a\}, \tag{26}$$

$$I_5'=\{\delta p_n^a\}^T[C_{pa}]\{A_{jk}\}, \tag{27}$$

where $\{p_n^a\}$ is the vector containing the degrees of freedom related to the approximations of the pressure in the acoustic medium. $\{A_{jk}\}$ is the vector containing the unknowns related to the interpolation of the variation of the Lagrange multiplier λ. The matrices $[C_{pp}]$ and $[C_{pa}]$ may be very ill-conditioned for high values of p_x and p_y. The use of an orthogonal basis does not completely overcome the problem but allows for a minimization of these effects. This justifies the use of Legendre polynomials.

In the case of a porous material coupled to an elastic domain, each component $\boldsymbol{\lambda}_i$ of the Lagrange multiplier vector $\boldsymbol{\lambda}$ used to enforce the continuity of displacements is interpolated using a formula similar to Eq. (20). One writes

$$\boldsymbol{\lambda}_i=\sum_{j=1}^{p_x^i}\sum_{k=1}^{p_y^i} B_{jk}^i\cdot L_j(x)\cdot L_k(y). \tag{28}$$

The maximum degree for the Legendre polynomials used for the interpolation of $\boldsymbol{\lambda}_i$ must satisfy Eq. (22), replacing n_a by n_e which is the number of dof related to the approximation of the ith component of $\mathbf{u}^{el}$.

Surface integrals I_1 and I_2 in Eq. (9) are discretized together with integrals I_1' and I_2' on the meshes used for the elastic domain and the porous domain, respectively. Proceeding the same way as in the acoustic-porous material configuration, one gets

$$I_1=\{\delta B_{jk}\}^T[C_{uel}]^T\{u_n^{el}\}, \quad I_1'=\{\delta u_n^{el}\}^T[C_{uel}]\{B_{jk}\}, \tag{29}$$

$$I_2=\{\delta B_{jk}\}^T[C_{up}]^T\{u_n^{s}\}, \quad I_2'=\{\delta u_n^{s}\}^T[C_{up}]\{B_{jk}\}, \tag{30}$$

where $\{u_n^{el}\}$ and $\{u_n^{s}\}$ are the degrees of freedom used for the approximation of $\mathbf{u}^{\mathrm{el}}$ and $\mathbf{u}^{\mathrm{s}}$. $\{B_{jk}\}$ is the vector containing the unknowns related to the interpolation of $\mathbf{u}^{el}$.

C. Fluid-structure coupling integral

Fluid-structure coupling integrals appear in Eq. (14) related to the weak formulation for the porous material-acoustic medium coupled system. The computation of these integrals is not straightforward if the meshes for the two subdomains are non-coincident. The following technique is used here in the case of a planar interface.

A mesh, denoted m_Γ, is constituted for the interface Γ. m_Γ is the union of the mesh m_p and m_a used on the interface for Ω_p and Ω_a respectively, as indicated in Fig. 2. Integrals I_3 and I_3' [see Eq. (14)] are then discretized on m_Γ. By construction, each element i_Γ of m_Γ is embedded into an element j_p of m_p and j_a of m_a. The coupling integral on i_Γ is then computed using the shape functions on j_p and j_a of the hierarchical finite element model for the porous material and the fluid. The proposed technique allows for an easy evaluation of the elementary fluid-structure integrals. Using the same methodology as for the computation of I_4, one finally gets

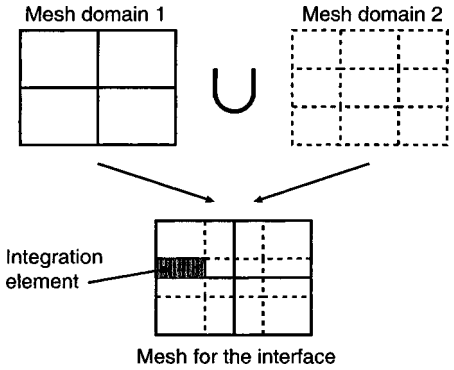

FIG. 2. Construction of a specific mesh for the interface.

$$I_3'=\{\delta u_n^{s}\}[C_{fs}]\{p_n^{a}\}, \tag{31}$$

$$I_3=\{\delta p_n^{a}\}[C_{fs}]^T\{u_n^{s}\}, \tag{32}$$

where $\{u_n^{s}\}$ and $\{p_n^{a}\}$ are the vectors containing the degrees of freedom used for the interpolation of $\mathbf{u}^{s}$ and p^{a}. $[C_{fs}]$ is a "global" coupling matrix between the solid phase of the porous material and the acoustic medium.

D. Linear coupled systems

1. Porous material-elastic domain coupled system

The system composed of a porous material coupled to an elastic material is considered. The excitation is a mechanical force applied on the elastic domain. The discretization of the weak formulation given by $\delta\Pi_{pel}'=0$ [see Eq. (9)] leads to the following linear system:

$$\begin{bmatrix} [K_{el}]-\omega^2[M_{el}] & 0 & 0 & [C_{uel}] \\ 0 & [K_s]-\omega^2[\tilde{M}_s] & -[\tilde{C}] & -[C_{up}] \\ 0 & -[\tilde{C}] & \dfrac{[\tilde{H}]}{\omega^2}-[\tilde{Q}] & 0 \\ [C_{uel}]^T & -[C_{up}]^T & 0 & 0 \end{bmatrix} \begin{Bmatrix} \{u_n^{el}\} \\ \{u_n^{s}\} \\ \{p_n\} \\ \{B_{jk}^{i}\} \end{Bmatrix} = \begin{Bmatrix} \{F_n^{el}\} \\ \{0\} \\ \{0\} \\ \{0\} \end{Bmatrix}, \tag{33}$$

where $[K_{el}]$ and $[M_{el}]$ are the stiffness and mass matrix for the elastic domain. $[K_{el}]$ is a complex valued matrix taking into account structural damping in the elastic domain. $[K_s]$ and $[\tilde{M}_s]$ are the stiffness and mass matrix for the solid phase of the porous material. $[\tilde{H}]$ and $[\tilde{Q}]$ are the kinematic and compression matrix for the fluid phase of the porous material. $[\tilde{C}]$ is a coupling matrix between the two phases of the porous material. $[C_{uel}]$ and $[C_{up}]$ are the matrices related to the use of Lagrange multipliers to ensure the continuity of solid displacements at the interface between the two subdomains. These matrices are defined by Eqs. (29) and (30), respectively. $\{F_n^{el}\}$ is the force vector corresponding to the excitations on the elastic domain. $[\tilde{}]$ means that matrices are frequency dependent.

2. Porous material-acoustic domain coupled system

The case of a porous material coupled to an acoustical fluid is now considered. The porous material is assumed to be subjected to an acoustical excitation, namely an imposed pressure condition with amplitude p_0. This kind of excitation leads to linear constraints on the degrees of freedom for the fluid phase, which are expressed by

$$[C_p]\{p_n\}=\{F_0^p\}. \tag{34}$$

These constraints are enforced in the discretized weak formulation using a set of discrete Lagrange multipliers $\{\lambda_p^u\}$.[9] In addition, a surface force acting on the solid phase has to be accounted for. This is achieved by considering a forcing vector $\{F_1^p\}$.

The discretization of the weak formulation given by $\delta\Pi'_{pa}=0$ [see Eq. (16)] leads to the following system:

$$\begin{bmatrix} [K_s]-\omega^2[\tilde{M}_s] & -[\tilde{C}] & [C_{fs}] & 0 & 0 \\ -[\tilde{C}] & \dfrac{[\tilde{H}]}{\omega^2}-[\tilde{Q}] & 0 & -[C_{pp}] & [C_p]^T \\ [C_{fs}]^T & 0 & \dfrac{1}{\rho_a\omega^2}[H_a]-\dfrac{1}{\rho_a c_a^2}[Q_a] & [C_{pa}] & 0 \\ 0 & -[C_{pp}]^T & [C_{pa}]^T & 0 & 0 \\ 0 & [C_p] & 0 & 0 & 0 \end{bmatrix} \begin{Bmatrix} \{u_n^s\} \\ \{p_n\} \\ \{p_n^a\} \\ \{A_{jk}\} \\ \{\lambda_n^p\} \end{Bmatrix} = \begin{Bmatrix} \{F_1^p\} \\ \{0\} \\ \{0\} \\ \{0\} \\ \{F_0^p\} \end{Bmatrix}, \tag{35}$$

where $[H_a]$ and $[Q_a]$ are the kinematic and compression matrices for the acoustic medium. $[C_{fs}]$ is defined by Eq. (31) and corresponds to the discretization of the fluid-structure coupling integral between the poroelastic domain and the acoustic domain. $[C_{pp}]$ and $[C_{pa}]$ are the matrices related to the use of Lagrange multipliers to ensure the continuity of pressure on the interface between the two subdomains.

IV. VALIDATION RESULTS

In this section, numerical results are presented in order to validate the proposed approach in the case of a porous material modeled with hierarchical elements coupled to an elastic or an acoustic domain assuming non-coincident meshes. A comparison is performed with the results obtained with a classical finite element code using linear poroelastic elements and coincident meshes.

A. The studied configurations

1. Elastic plate-porous material

The configuration of a porous coated plate, depicted in Fig. 3, is considered. The plate is made of aluminum and is simply supported. The coating is a mineral wool bonded on the plate. Free edges conditions are applied on the lateral faces of the porous subdomain (see Ref. 6 for details). The characteristics of the materials are given in Table I. The plate and the porous coating are 1 mm and 2 cm thick, respectively. The lateral dimensions are $L_x=0.35$ m and $L_y=0.22$ m. The excitation is a point force with amplitude 1 N normal to the plate. This force is located at the point with coordinates $X=0.04375$ m and $Y=0.0275$ m.

In the following, the plate is modeled with the same four-node quadrilateral plate classical finite elements in both the classical finite element code and the presented method.

2. Porous material-fluid cavity

The coupling between a porous material and an acoustic domain is validated through the study of the configuration of a fluid cavity backed by a porous material, as represented in Fig. 4. The fluid in the cavity is air ($\rho_0=1.213$ kg/m^3 and $c_0=342.3$ m/s). The porous material is a 2-cm-thick foam, denoted foam A in the following, and its lateral edges are bonded. Its characteristics are given in Table I. The dimensions of the cavity are $0.35\times0.22\times0.2$ m^3. The excitation is an imposed pressure condition with amplitude 1 Pa applied on the porous material (see Fig. 4).

As indicated previously, hierarchical fluid elements are used for the modeling of the cavity since these elements are easily obtained from poroelastic hierarchical elements.

B. The vibroacoustic indicators

In the following, the effect of a porous material on the vibrations of the plate or on the pressure levels in the cavity is studied. The indicators of interest are the mean square

TABLE I. Properties of the materials.

Material	E (kPa)	ν	η	ρ_s (kg/m^3)	ϕ	α_∞	σ (kN·s/m^4)	Λ (μm)	Λ' (μm)
Aluminum	6.9×10^7	0.33	0.01	2700	⋯	⋯	⋯	⋯	⋯
Steel	2.35×10^8	0.29	0.01	7842	⋯	⋯	⋯	⋯	⋯
Foam A	540	0.35	0.1	1500	0.98	1.7	13.5	80	160
Foam B	29.4	0.3	0.18	928	0.906	1.68	25.15	58.9	147.2
Mineral wool	42	0	0.05	600	0.95	1.4	25	93.2	93.2

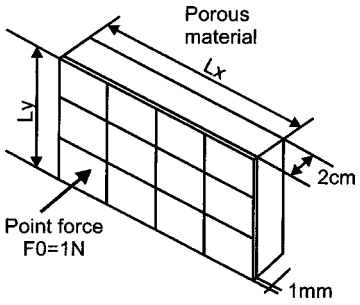

FIG. 3. Porous coated plate excited by a point force.

velocity of the plate and the mean square pressure in the cavity. The definition and the computation of these indicators are now recalled.

1. Mean square velocity of the plate

The mean square velocity $\langle V_z^2 \rangle$ of the plate is defined by

$$\langle V_z^2 \rangle = \frac{\omega^2}{2\Omega_{el}} \int_{\Omega_{el}} |u_z^{el}|^2 \, d\Omega, \tag{36}$$

where ω is the angular frequency and Ω_{el} denotes the volume occupied by the plate. u_z^{el} is the plate displacement along the thickness. Considering the discretization of the displacement field in the plate, this indicator is computed using the following formula:

$$\langle V_z^2 \rangle = \frac{\omega^2}{2S_{pl}} \{w_n\}^T [M_z] \{w_n\}^*, \tag{37}$$

where $\{w_n\}$ is the vector containing the degrees of freedom used for the interpolation of the deflection of the plate. $[M_z]$ contains the coefficients of $[M_{el}]$ divided by ρ_{el} related to the degrees of freedom of interest. S_{pl} is the surface of the plate. (*) means complex conjugate.

2. Mean square pressure in the cavity

The mean square pressure $\langle P^2 \rangle$ in the fluid cavity is defined by

$$\langle P^2 \rangle = \frac{1}{2\Omega_a} \int_{\Omega_a} |p^a|^2 \, d\Omega, \tag{38}$$

where Ω_a is the volume of the cavity. Given the approximation of the pressure in the fluid, this indicator is obtained by the following formula:

$$\langle P^2 \rangle = \frac{1}{2\Omega_a} \{p_n^a\}^T [Q] \{p_n^a\}^*, \tag{39}$$

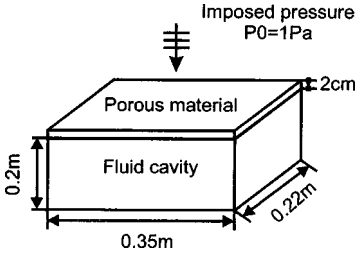

FIG. 4. Porous material coupled to a fluid cavity acoustical excited.

where $[Q]$ is the real-valued compression energy matrix of the fluid multiplied by $\rho_a c_a^2$.

C. Results

1. Porous coated plate

The values of plate mean square velocity [Eq. (37)] computed using the present approach is compared to the results given by MNS/Nova™,[21] a finite element code developed at the Université de Sherbrooke for the modeling of elasto-poro acoustic multilayers. This latter code, validated both numerically and experimentally,[5,6] is based on classical linear poroelastic elements and coincident meshes and is referred to as the classical approach in the following. The classical code uses a 28×18-node mesh in the lateral dimensions and two elements along the thickness for the porous material, which suffices to ensure the convergence of the vibroacoustic indicators.

The present approach uses a 16×11 node mesh for the plate. The poroelastic domain is discretized with a 3×2×1-brick element mesh. The convergence of the present approach, as far as the modeling of the porelastic material is concerned, is obtained by applying *p-method*, namely by increasing the interpolation order in the solid phase and in the fluid phase, respectively. This method leads to an interpolation order equal to 6 in the solid phase and 4 in the fluid phase. A coarser mesh for the porous domain would have required higher interpolation orders for convergence. Increasing interpolation orders leads to an increase of the computational time devoted to the calculation of the elementary mass and stiffness matrices related to the porous domain. In practice, the use of interpolation orders greater than 9 induces too important a time overhead. Hence, a 3×2×1-element mesh rather than a mesh composed of a single element was used for the application of the *p-method*.

As indicated above, the determination of the interpolation orders for the convergence of the *p-method* in the studied configuration is done iteratively using successive richer interpolation orders. The same remarks hold when modeling a single poroelastic domain with hierarchical elements. The convergence of poroelastic materials has been investigated by Rigobert.[22] This study has been performed for a mineral wool and a polymer foam. It indicates that a general convergence criterion seems to be difficult to establish for poroelastic hierarchical elements. These difficulties are consistent with the fact that the behaviors of the two materials considered in this study depend on the excitation and the boundary conditions.

The results of the comparison between the classical and the present approach are given in Fig. 5 for a frequency domain ranging from 10 to 500 Hz. Figure 5 shows an excellent agreement between the two approaches. Besides, the present approach allows for a significant reduction of the number of d.o.f. required for an accurate description of the multilayer. Actually, 2701 d.o.f. are sufficient to ensure convergence instead of 10 232 d.o.f. for the classical approach.

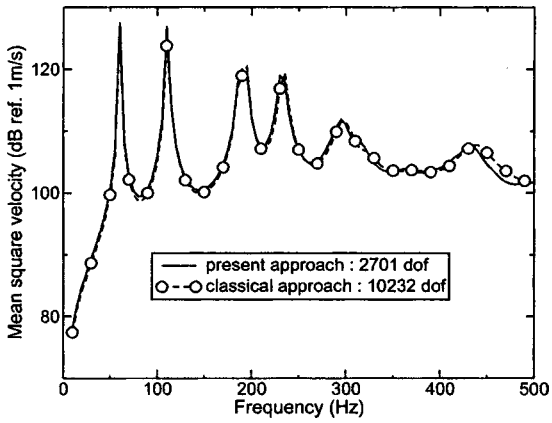

FIG. 5. Mean square velocity of a plate coated with a mineral wool. Comparison between the present approach and the classical approach.

2. Porous material coupled to a fluid cavity

As indicated in the previous section, a hierarchical acoustic element is easily derived from a poroelastic hierarchical element. Hence, hierarchical acoustic elements are used to model the cavity. A $2\times1\times2$-element mesh is provided for that subdomain with an interpolation order equal to 4, which is sufficient to ensure the convergence of the model. $4\times3\times2$ elements are used for the poroelastic domain with an interpolation order equal to 5 for the solid phase and 1 for the fluid phase. The results obtained with the present approach for the prediction of the mean square pressure in the cavity are given in Fig. 6 for the frequency band [10 Hz; 500 Hz]. The results given by the classical code are also shown. For the latter approach, the porous material and the fluid cavity are modeled with linear poroelastic elements and linear fluid elements, respectively, using two different sets of compatible meshes for the multilayer. Mesh 1 contains 26×16 elements in the lateral dimensions, 2 elements along thickness for the porous material, and 5 elements along the thickness for the cavity. Mesh 2 contains 35×22 elements in the lateral dimensions, 4 elements along thickness for the porous material, and 5 elements along thickness for the cavity. Note that a number of elements greater than 5 along thickness for the cavity does not improve the accuracy of the prediction.

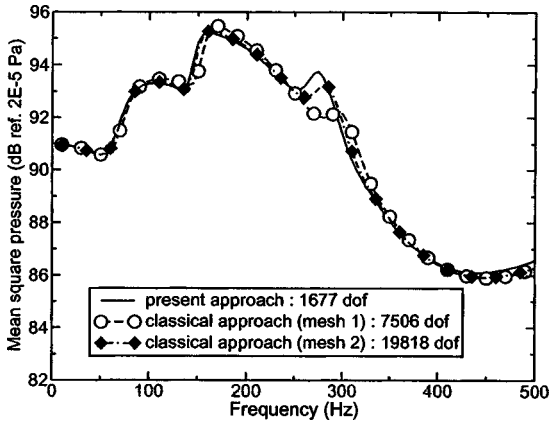

FIG. 6. Porous material coupled to a fluid cavity. Computation of the mean quadratic pressure in the cavity. Comparison between the present approach and the classical approach.

According to Fig. 6, the predictions made with the classical approach with mesh 1 show small discrepancies compared to the results obtained with the present approach. In particular, this is noticeable around the peak located at 275 Hz associated with a resonance of the skeleton in the foam. Mesh 2 alleviates these differences. The convergence of the classical code is thus obtained using a very refined mesh for the poroelastic domain.

The number of d.o.f. required for the convergence of the model is about 11 times less for the present approach (1677 d.o.f.) compared to the classical approach with mesh 2 (19 818 d.o.f.). Note that the convergence of the model presented herein is obtained using very different interpolation orders for the solid and the fluid phases of the porous material, namely 5 and 1, respectively. Actually, the ability of chosing these two parameters independently enables one to optimize the number of d.o.f. From a physical viewpoint, this indicates that a good prediction of the pressure levels in the cavity is closely related to a good description of the solid phase. The peak noticed in Fig. 6 at 275 Hz and associated with a resonance of the skeleton of the foam shows the great influence of the solid phase motion on the pressure levels in the cavity.

Considering the latter remarks, the reasons for the slow convergence of the classical approach can be explained. One notices that a number of elements greater than 4 in the thickness of the porous material does not improve the predictions for $\langle P^2\rangle$ in the fluid cavity whatever the mesh in the lateral dimensions (these results are not produced here). The convergence of the classical code, which is related to an accurate description of the solid phase material, hence requires a refinement of the mesh in the lateral dimensions. The slow convergence of linear poroelastic elements is therefore probably due to shear locking related to the bending motion of the porous material and the used boundary conditions (bonded edges). This phenomenon has already been underlined in the literature for a similar configuration in which the porous material has a bending motion.[7]

V. COMPARISON WITH EXPERIMENTS

In this section, the presented approach is confronted to experimental results in the case of a porous coated plate.

An 0.8-mm-thick steel plate (see Table I for the characteristics of steel) with clamped edges is considered. Its lateral dimensions are $L_x=0.5$, $L_y=0.38$ m. This plate is coated with a 2-cm-thick porous material. The coating is a foam, denoted as foam B in the following, with the characteristics given in Table I. A measurement grid is constituted on the plate as shown in Fig. 7. The plate is excited with a hammer at point 27 of this grid. The excitation is modeled as a point force with 1-N amplitude in numerical simulations. The frequency response function (FRF) associated to the acceleration of the plate is measured at different points of this grid with an accelerometer.

The modeling of this configuration is achieved considering the following assumptions. First, the coupling between the porous material and the surrounding acoustic medium is not accounted for as discussed in Sec. II. As an approximation, a ''free face'' condition (see Ref. 6 for details) has been

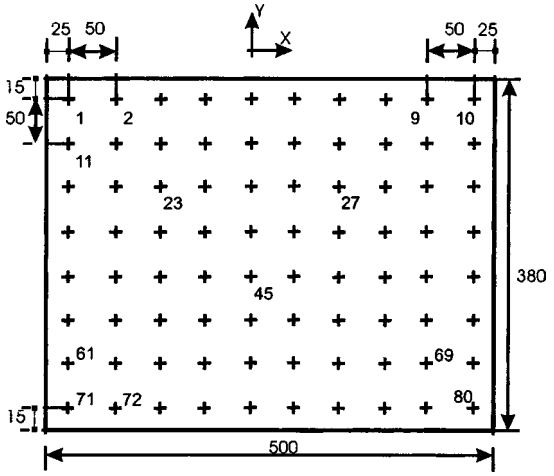

FIG. 7. Representation of the experimental setup. Excitation at point 27. Measurements at point 69.

imposed on the edges and the rear face of the coating. In addition, the effects of the surrounding acoustic medium on the plate vibrations (mass effect, damping related to the radiation of the plate) are not taken into account.

The present approach is compared to the measured FRF at point 69 for frequencies ranging from 0.5 to 350 Hz. At first, the comparison between measurements and simulations has been performed considering the mechanical properties of the foam measured in the laboratory. No good agreement could be obtained on the whole frequency band using these values in the numerical simulations (results not presented). In order to get a better match between numerical and experimental results, the frequency band of interest was split into several intervals. For each of them, the Young's modulus of the solid phase of the porous material was fitted to get the best agreement possible between measurements and simulations. The Young's modulus initially measured is referred to as E in the following. From 0.5 to 160 Hz, a value equal to $0.5E$ was used. For the frequency band [160 Hz; 250 Hz], Young's modulus was chosen to be equal to E. The value $1.9E$ was used beyond 225 Hz. Figure 8 represents the numerical predictions for the FRF obtained with the present approach. 21×16 quadrilateral plate elements were used for the plate. A $8\times6\times2$-brick element mesh was provided for the porous material with an interpolation order equal to 3 for the solid and the fluid phase.

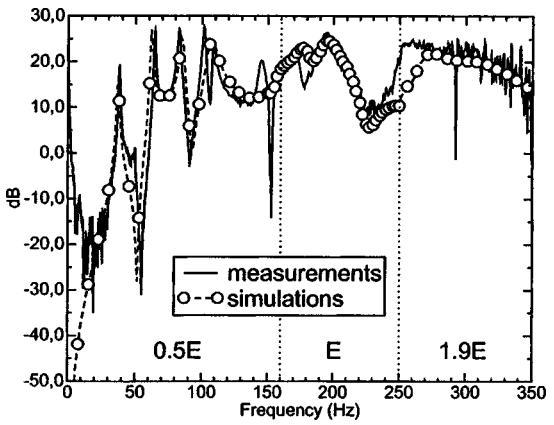

FIG. 8. Clamped plate coated with a polymer foam. FRF of the acceleration at point 69. Comparison between measurement and simulation.

A good agreement is observed between simulation and measurement. These results demonstrate the utility and validity of the presented approach. Equally important, they underline the frequency dependence of the mechanical properties of the foam used for the coating of the plate. (This is usually neglected in the published methods used to measure the mechanical properties of foams.) In particular, the viscoelastic behavior of the solid phase is highlighted, which is a known property of polymer foams.[23]

VI. CONCLUSION

The coupling of a poroelastic material modeled with hierarchical elements and an elastic domain modeled with classical finite elements or an acoustic domain modeled with hierarchical elements has been presented. The meshes for the subdomains coupled have been assumed to be non-coincident at their common interface. A two-field hybrid formulation has been constructed for the coupled system. In this weak formulation, continuous Lagrange multipliers are used to enforce the essential coupling conditions, such as the continuity of pressure or solid displacements, and natural coupling conditions are implicitly accounted for. A simple technique has been presented for the computation of fluid-structure coupling integrals over incompatible meshes at the interface between a porous material and an acoustic domain.

The present approach has been validated through a comparison with a finite element code using linear poroelastic elements and coincident meshes. The configurations of a porous coated plate and a porous material coupled to a fluid cavity have been considered. Numerical locking of linear poroelastic elements has been underlined and overcome by the use of poroelastic hierarchical elements. The latter elements allow for an increase of the convergence rate of the solution and thus an important reduction of the number of degrees of freedom required for the modeling of the multilayer. This feature of the proposed model is enhanced by the use of non-coincident meshes. A comparison between simulation and experiment has also been presented for the configuration of a porous coated plate mechanically excited. The results given by the present approach were found to be in good agreement with measurement and underlined the frequency dependence of the Young's modulus of the solid phase of the porous coating.

[1] Y. Kang and J. Bolton, "Finite element modeling of isotropic porous materials coupled with acoustical finite elements," J. Acoust. Soc. Am. **98**, 635–643 (1995).
[2] Y. Kang and J. Bolton, "A finite element model for sound transmission through foam-lined double-panel structures," J. Acoust. Soc. Am. **99**, 2755–2765 (1996).
[3] R. Panneton and N. Atalla, "Numerical prediction of sound transmission through finite multilayer systems with poroelastic materials," J. Acoust. Soc. Am. **100**, 346–354 (1996).
[4] R. Panneton and N. Atalla, "An efficient finite element scheme for solving the three-dimensional poroelasticity problem in acoustics," J. Acoust. Soc. Am. **101**, 3287–3298 (1997).
[5] N. Atalla, R. Panneton, and P. Debergue, "A mixed displacement-pressure formulation for poroelastic materials," J. Acoust. Soc. Am. **104**, 1444–1452 (1998).
[6] P. Debergue, R. Panneton, and N. Atalla, "Boundary conditions for the

weak formulation of the mixed (u,p) poroelasticity problem,'' J. Acoust. Soc. Am. **106**, 2383–2390 (1999).
[7] N. Dauchez, S. Sahraoui, and N. Atalla, ''Convergence of poroelastic finite elements based on biot displacement formulation,'' J. Acoust. Soc. Am. **109**, 33–40 (2001).
[8] N. Hörlin, M. Nordström, and P. Göranson, ''A 3-d hierarchical FE formulation of Biot's equations for elasto-acoustic modelling of porous media,'' J. Sound Vib. **245**, 633–652 (2001).
[9] S. Rigobert, N. Atalla, and F. Sgard, ''Investigation of the convergence of the mixed displacement-pressure formulation for three-dimensional poroelastic materials using hierarchical elements,'' J. Acoust. Soc. Am. **114**, 2607–2617 (2003).
[10] S. Rigobert, N. Atalla, and F. Sgard, ''Numerical modeling of porous-elastic materials using hierarchical elements,'' in *5th French Congress on Acoustics* (2000), pp. 1125–1128.
[11] J. Coyette and Y. Pelerin, ''An efficient coupling procedure for handling large size interior structural-acoustic problems,'' in *ISMA 19: Tools for Noise and Vibration Analysis* (1994), pp. 729–738.
[12] M. Guerich and M. Hamdi, ''A numerical method for vibro-acoustic problems with incompatible finite elements meshes using b-spline functions,'' J. Acoust. Soc. Am. **105**, 1682–1694 (1999).
[13] L. Quiroz, ''Connexion des maillages hétérogènes dans la méthode des éléments finis,'' Ph.D. thesis, Université de Liège, 1993.
[14] M. Aminpour, J. Ransom, and S. McCleary, ''A coupled analysis method for structures with independently modelled finite element subdomains,'' Int. J. Numer. Methods Eng. **38**, 3695–3718 (1995).
[15] C. Dohrmann, S. Key, and M. Heinstein, ''Methods for connecting dissimilar three-dimensional finite element meshes,'' Int. J. Numer. Methods Eng. **47**, 1057–1080 (2000).
[16] C. Farhat and M. Géradin, ''On a component mode synthesis method and its application to imcompatible meshes,'' Comput. Struct. **51**, 459–473 (1994).
[17] H. Morand and R. Ohayon, *Fluid-structure Interactions* (Masson, Paris, 1992).
[18] N. Atalla and R. Panneton, ''Enhanced weak integral formulation of the mixed (u,p) poroelastic equations,'' J. Acoust. Soc. Am. **109**, 3065–3068 (2001).
[19] K. Horoshenkov and K. Sakagami, ''A method to calculate the acoustic response of a thin, baffled, simply supported poroelastic plate,'' J. Acoust. Soc. Am. **110**, 904–917 (2001).
[20] B. Szabò and I. Babuška, *Finite Element Analysis* (Wiley, New York, 1991).
[21] MNS/Nova, *Theoretical manual*, Tech. Rep., G.A.U.S., Département de génie mécanique, Université de Sherbrooke (1999).
[22] S. Rigobert, ''Modélisation par éléments finis des systèmes élasto-poro-acoustiques couplés: éléments hiérarchiques, maillages incompatibles, modèles simplifiés,'' Ph.D. thesis, INSA Lyon, France, École doctorale M.E.G.A., 2001.
[23] L. Gibson and M. Ashby, *Cellular Solids. Structure and Properties*, 2nd ed. (Cambridge U.P., Cambridge, 1997).

Evolution of nonlinear Rayleigh waves in a coated substrate

Won-Suk Ohm[a] and Mark F. Hamilton
Department of Mechanical Engineering, The University of Texas at Austin, Austin, Texas 78712-1063

(Received 25 August 2003; revised 12 March 2004; accepted 21 March 2004)

Nonlinear Rayleigh waves propagating in a substrate coated with a thin elastic film are studied numerically. The evolution model consists of the nonlinear spectral equations of Zabolotskaya [J. Acoust. Soc. Am. **91**, 2569–2575 (1992)] augmented *ad hoc* to include film dispersion. The dispersion relation is obtained from linear theory but is otherwise exact. Both loading and stiffening films are considered. Computations are performed for nonlinear evolution of an initially sinusoidal Rayleigh wave under three distinct dispersion regimes corresponding to different film thicknesses. The validity of the evolution model is also examined. © *2004 Acoustical Society of America.*
[DOI: 10.1121/1.1738837]

PACS numbers: 43.25.Fe [ANN] Pages: 2798–2806

I. INTRODUCTION

Over the past decade, interest in thin-film characterization have led to a resurgence of surface acoustic wave (SAW) spectroscopy as a tool for nondestructive testing. Presence of a thin film on the surface of an elastic half-space can introduce significant dispersion. By observing dispersion characteristics of SAWs in a thin-film system, one can determine parameters such as film thickness, adhesion strength, and mechanical properties of the film.[1,2] Because the intensities involved in traditional SAW spectroscopy are relatively low, linear theory is often sufficient to describe SAW propagation under such circumstances. However, a series of experimental investigations[3–7] has emerged on high-intensity SAWs in thin-film systems, where nonlinearity as well as dispersion were pronounced. Nayanov,[3] Cho *et al.*,[4] and Kavalerov *et al.*[5] observed evolution of a sinusoidal input wave in coated $LiNbO_3$ substrates. Recently, Lomonosov *et al.*[6,7] reported that laser-excited SAW pulses in coated silicon and fused quartz can exhibit soliton-like behavior that is characteristic of wave propagation in dispersive nonlinear systems. The analysis of SAWs in such systems requires provision for both nonlinearity and dispersion.

One of the most common approaches to modeling dispersive nonlinear waves is to augment an existing nonlinear evolution equation (initially derived for nondispersive waves) by adding a dispersion term *ad hoc*. Here, the characterization ''*ad hoc*'' refers to a tacit assumption that introduction of dispersion *per se* does not perturb the preexisting nonlinear mechanism. For example, in order to study the effects of a thin film on nonlinear surface wave propagation, one may add to a nonlinear evolution equation an appropriate dispersion term that is either assumed or obtained from the exact linear boundary value problem. Adler and Nassar[8] were among the first investigators who adopted this modeling scheme to describe dispersive nonlinear SAWs. They modified a nonlinear evolution equation of Adler *et al.*[9] to include dispersion and calculated the generation of higher harmonics. Ewen *et al.*[10] later proposed Benjamin–Ono (BO) and Korteweg–de Vries (KdV) equations as possible evolution models for nonlinear SAWs in film-coated substrates. Mayer[11] showed in his extensive review article that the models of Adler *et al.* and Ewen *et al.* could be viewed as simplifications of a more comprehensive evolution model. Recently, Eckl *et al.*[12,13] studied numerical and analytical solutions for solitary nonlinear SAWs in coated substrates. Using the nonlinear evolution model of Mayer that includes a dispersion term of the BO type, they obtained stable numerical solutions for periodic pulse trains that become solitary waves in the limit of infinite periodicity. Most recently, Lomonosov *et al.*[7] reported experimental corroboration of Mayer's theoretical model.

Although there is a growing body of literature on nonlinear SAWs in thin-film systems, no extensive parametric studies on the topic appear to have been performed or reported. Moreover, despite the general acceptance of the *ad hoc* approach employed in the aforementioned theoretical investigations, its validity remains to be examined on a more rigorous theoretical basis. In this context, the present article provides a comprehensive numerical study of nonlinear SAWs in a film-coated half-space, conducted with an appropriate validity criterion in place. Unlike the earlier studies that assumed dispersion laws of the BO or KdV type, the current work employs the exact film-dispersion relation derived from the linear theory.[14] The dispersion relation is incorporated into the nonlinear evolution model of Zabolotskaya[15] for the study of SAW propagation in different dispersion regimes (weak, moderate, and strong in relation to nonlinearity). Because there is a myriad of possible combinations of film-substrate materials, surface cuts, and propagation directions for crystals, our attention is devoted to Rayleigh waves propagating in two representative isotropic material pairs (gold film on fused-quartz substrate for loading dispersion, and alumina film on fused quartz for stiffening dispersion). The relative simplicity brought by the assumption of isotropy does not come at the expense of generality; Rayleigh waves have been shown to possess many of the salient features of SAWs in crystals.

[a]Current address: Acoustical Standards, Institute for National Measurement Standards, National Research Council, Ottawa, Ontario K1A 0R6, Canada. Electronic mail: wonsuk.ohm@nrc-cnrc.gc.ca

 0001-4966/2004/115(6)/2798/9/$20.00 © 2004 Acoustical Society of America

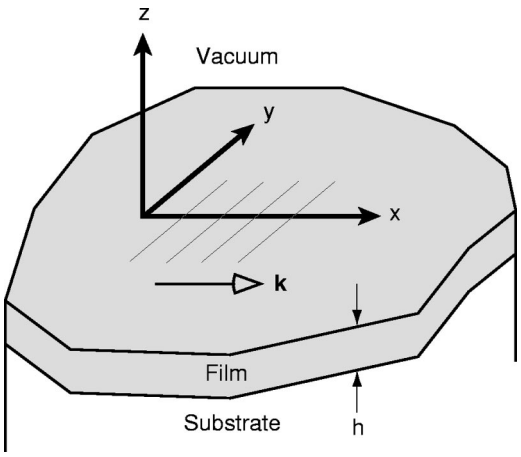

FIG. 1. Propagation geometry of a thin-film system.

II. LINEAR THEORY

Consider an inhomogeneous plane wave propagating in an isotropic elastic half-space coated with a single layer of a second isotropic elastic material (Fig. 1). The direction of propagation (taken as the $+x$ direction) is parallel to the free surface. The film-substrate interface is located at $z=0$ and the traction-free surface at $z=h$. The film is assumed to be perfectly bonded to the substrate so that continuity of particle displacements and stresses at the interface is satisfied at all times.

Because the substrate and film are isotropic, both the equations of motion and the boundary conditions decouple into the sagittal-plane (spanned by the x and z axes) and transverse (the y axis) components. This results in two independent modes of propagation; solutions with sagittal-plane components only are called Rayleigh modes while the ones with transverse components only are called Love modes. Here, we consider only the Rayleigh modes of propagation.

Rayleigh-mode solutions in the form of particle displacement components are given by

$$u_x=[iC_t^-\xi_t e^{\xi_t kz}+C_l^- e^{\xi_l kz}]e^{ik(x-c_{\mathrm{ph}}t)}, \tag{1}$$

$$u_z=[C_t^- e^{\xi_t kz}-iC_l^-\xi_l e^{\xi_l kz}]e^{ik(x-c_{\mathrm{ph}}t)} \tag{2}$$

in the substrate. Here, $u_{x,z}$ are horizontal (x) and vertical (z) displacement components, c_{ph} is the phase speed, k is the wave number, $\xi_{l,t}=(1-c_{\mathrm{ph}}^2/c_{l,t}^2)^{1/2}$, and $c_{l,t}$ are the longitudinal (l) and transverse (t) bulk wave speeds of the substrate. Parameters $\xi_{l,t}$ determine the amplitude variation as a function of depth ($-z$ direction). The corresponding particle displacement components in the film are

$$\hat{u}_x=[-i\hat{C}_t^+\hat{\xi}_t e^{-\hat{\xi}_t kz}+\hat{C}_l^+ e^{-\hat{\xi}_l kz}+i\hat{C}_t^-\hat{\xi}_t e^{\hat{\xi}_t kz}+\hat{C}_l^- e^{\hat{\xi}_l kz}]e^{ik(x-c_{\mathrm{ph}}t)}, \tag{3}$$

$$\hat{u}_z=[\hat{C}_t^+ e^{-\hat{\xi}_t kz}+i\hat{C}_l^+\hat{\xi}_l e^{-\hat{\xi}_l kz}+\hat{C}_t^- e^{\hat{\xi}_t kz}-i\hat{C}_l^-\hat{\xi}_l e^{\hat{\xi}_l kz}]e^{ik(x-c_{\mathrm{ph}}t)}, \tag{4}$$

where circumflexes are used to designate quantities in the film. Note that the solutions in the substrate consist solely of terms that decay exponentially into the substrate, while both decaying and growing terms are allowed within the film of finite thickness.

Six weighting factors ($C_{l,t}^-$ for the substrate and $\hat{C}_{l,t}^{\pm}$ for the film) in Eqs. (1)–(4) are chosen in such a way as to satisfy the boundary conditions. Upon substitution of Eqs. (1)–(4) into six boundary condition equations (continuity of sagittal displacements and stresses at the interface and zero sagittal stresses at the free surface), a system of six linear homogeneous equations is produced.[16] The determinant of the resulting boundary-condition matrix must be zero to ensure nontrivial solutions. In general, for a given dimensionless wave number kh, the boundary-condition determinant will not be zero for an arbitrary choice of c_{ph}. Numerical iteration is necessary to find the value of c_{ph} that renders the boundary-condition determinant zero. Repeating the iterative search procedure over a range of kh leads to the desired dispersion curve of the phase speed c_{ph} as a function of kh.

It has been shown by Tiersten[17] that two classes of dispersion can be observed depending on the ratio of transverse bulk wave speeds of the film and substrate. When the transverse bulk wave speed of the film is less than that of the substrate, the phase speed of a Rayleigh mode decreases with frequency and the film is said to ''load'' the substrate. On the other hand, a film whose transverse bulk wave speed is greater than that of the substrate increases the phase speed and is said to ''stiffen'' the substrate. Sufficient conditions for loading and stiffening dispersion are

$$\hat{c}_t/c_t<1/\sqrt{2}, \quad \text{loading dispersion,} \tag{5}$$

$$\hat{c}_t/c_t>\sqrt{2}, \quad \text{stiffening dispersion,} \tag{6}$$

where $\hat{c}_t$ and c_t are transverse bulk wave speeds of the film and substrate, respectively.

With the above criterion in mind, we choose two representative material pairs as follows. We select fused quartz[18] ($c_t=3754$ m/s, $\rho=2203$ kg/m^3) as the substrate because it is a readily available material that has been used in a number of experimental and numerical studies.[7,18] With fused quartz as the substrate, polycrystalline gold[19] ($\hat{c}_t=1200$ m/s, $\hat{\rho}=19\,300$ kg/m^3) and alumina[20] ($\hat{c}_t=6401$ m/s, $\hat{\rho}=3978$ kg/m^3) are chosen as film materials for their respective loading and stiffening behaviors.

A. Loading dispersion

The dispersion curves for the loading-dispersion pair (gold film on fused-quartz substrate) are shown in Fig. 2. A noticeable feature of loading dispersion is the existence of an unlimited number of Rayleigh modes. The phase speed of the first Rayleigh mode (R1) starts at the Rayleigh speed of the substrate ($c=3401$ m/s) for $kh=0$ and decreases monotonically with increasing kh. For large kh the phase speed asymptotically approaches the Rayleigh speed of the film ($\hat{c}=1134$ m/s). In contrast, each of the higher-order Rayleigh modes has a low-frequency cutoff at which the phase speed is equal to the transverse bulk wave speed of the substrate ($c_t=3754$ m/s). All higher-order modes eventually approach the transverse bulk wave speed of the film ($\hat{c}_t=1200$ m/s) with increasing kh. (We note that the Stoneley wave mode cannot exist at the interface between gold and fused quartz.)

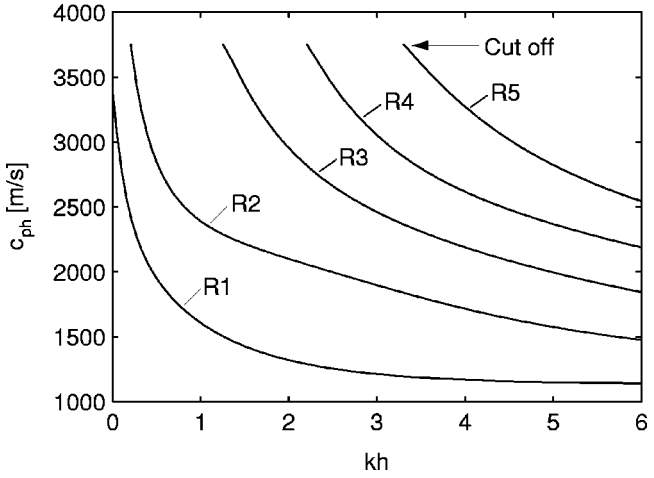

FIG. 2. Dispersion curves for the Rayleigh modes in polycrystalline gold on fused quartz. The first Rayleigh mode is designated by R1, the second R2, and so on.

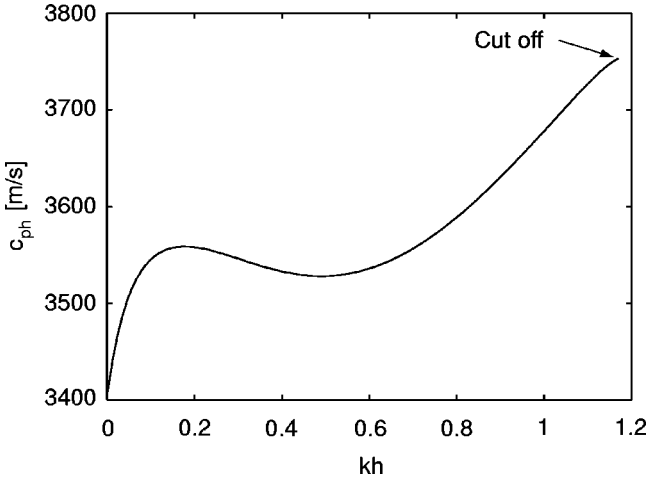

FIG. 4. Dispersion curve for the Rayleigh mode in polycrystalline alumina on fused quartz. The cutoff of the Rayleigh mode occurs near $kh=1.18$.

Due to the large phase speed variation of the first Rayleigh mode near $kh=0$, a substantial amount of dispersion can be introduced with relatively small film thickness. Throughout our numerical simulation of nonlinear Rayleigh waves with loading dispersion, the film thickness is restricted to be considerably smaller than any wavelengths associated with significant energy in the signal. Thus, our practical upper limit of kh becomes very small compared to unity, and we may ignore nonlinear mode coupling with the higher-order Rayleigh modes, which occurs only for $kh \gtrsim 0.2$. For convenience, the first Rayleigh mode is hereafter referred to as simply ''the Rayleigh mode'' without ambiguity.

Variation in amplitudes of the displacement components [the terms inside brackets in Eqs. (1)–(4)] is shown in Fig. 3. The amplitude of each displacement component is normalized to its value at the free surface ($z=h$) and is plotted against the dimensionless vertical coordinate kz. If the medium consists of the substrate only and is therefore nondispersive, Rayleigh waves not only propagate at the same phase speed but also have the same depth profile versus kz regardless of frequency; the depth profile at any frequency is represented by the curve for $kh=0$. However, if the substrate is layered with a film, the substrate depth profile of any frequency component differs increasingly from the profile for $kh=0$ as frequency is increased. This change in mode shapes imposes limits on the validity of the nonlinear evolution model, as discussed below in Sec. III A.

B. Stiffening dispersion

For the stiffening material combination (alumina film on fused-quartz substrate), only one Rayleigh mode can exist. As shown in Fig. 4, the dispersion curve for the Rayleigh mode starts at the substrate Rayleigh speed ($c=3401$ m/s) and increases until it reaches the transverse bulk wave speed of the substrate ($c_t=3754$ m/s) at $kh=1.18$. The fractional increase in phase speed from $kh=0$ to 0.1 is only about 4%, whereas the phase speed for loading dispersion (Fig. 2) undergoes 18% fractional change over the same range of kh. Therefore, in order to introduce dispersion comparable to that of the loading film, relatively large film thickness is necessary for the stiffening film.

Shown in Fig. 5 is the depth dependence of the particle displacement. Again, the displacement amplitude normalized to its value at the free surface is plotted against the dimensionless vertical coordinate kz. As in Fig. 3, the depth profiles for any frequencies collapse into the curve for $kh=0$ if the substrate is not layered with a film. With a film of finite

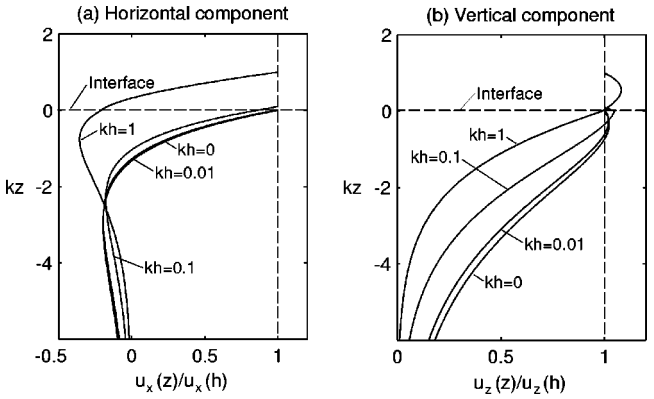

FIG. 3. Particle displacement depth profiles for polycrystalline gold on fused quartz.

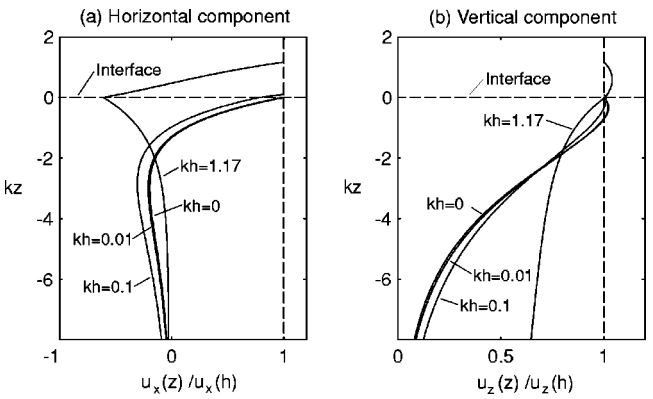

FIG. 5. Particle displacement depth profiles for polycrystalline alumina on fused quartz.

thickness, however, the depth profile deviates from the curve for $kh=0$ with increasing frequency.

One striking contrast to the loading counterpart [Fig. 3(b)] is the behavior of the vertical component at large penetration depth with increasing frequency [Fig. 5(b)]. The depth profile near cutoff (the $kh=1.17$ curve) shows very slow decay into the substrate, portending the onset of the transverse bulk mode that exists above the cutoff frequency. This can also be observed from Eq. (2). As kh nears the cutoff, the phase speed c_{ph} approaches the substrate shear speed c_t. The parameter ξ_t approaches zero, and the term $C_t^- e^{\xi_t kz}$ in Eq. (2) becomes dominant with a very slow decay rate. Because the transverse bulk waves radiate into the substrate at grazing angles, they may manifest themselves through unusually high attenuation of a signal detected at the free surface when there is significant mode coupling between the Rayleigh and transverse bulk waves.

III. EFFECTS OF DISPERSION ON NONLINEAR RAYLEIGH WAVES

A. Evolution model

The dispersion law described above is introduced *ad hoc* in the model equation of Zabolotskaya[15] to constitute our evolution equation for nonlinear Rayleigh waves in a coated substrate. It should be pointed out that Zabolotskaya's theory is derived for an uncoated medium; the effect of thin-film coating enters into our model only through a dispersion term. This way, the problem is transformed into that of surface waves propagating in a fictitious homogeneous half-space possessing a dispersion law equivalent to that for a film on the same substrate.

In Zabolotskaya's model, the following Fourier series representation is used for the particle velocity components of a Rayleigh wave in an isotropic half-space:

$$v_x(x,z,\tau)=\frac{i}{2}\sum_{n=1}^{\infty} v_n(x)(\xi_t e^{\xi_t n k_1 z}+\eta e^{\xi_l n k_1 z})e^{-in\omega_1\tau}+\text{c.c.}, \tag{7}$$

$$v_z(x,z,\tau)=\frac{1}{2}\sum_{n=1}^{\infty} v_n(x)(e^{\xi_t n k_1 z}+\xi_l \eta e^{\xi_l n k_1 z})e^{-in\omega_1\tau}+\text{c.c.} \tag{8}$$

Here, $\tau=t-x/c$ is a retarded time, c is the nondispersive Rayleigh speed, ω_1 is the fundamental (or repetition) angular frequency, $k_1=\omega_1/c$ is the associated wave number, $\xi_{l,t}=(1-c^2/c_{l,t}^2)^{1/2}$, and $\eta=-2\xi_t/(1+\xi_t^2)$. The terms in parentheses describe the depth dependence of the velocity components and are collectively depicted by the $kh=0$ curves as in Figs. 3 and 5. The spectral amplitude of the nth harmonic component is denoted by $v_n(x)$.

The dependence of v_n on x is due to nonlinearity, dispersion, and absorption. The coupled evolution equations[15,21] for the harmonic amplitudes v_n as functions of propagation distance x are

$$\frac{dv_n}{dx}+(\alpha_n+i\delta_n)v_n=-\frac{n^2\omega_1\mu}{2\zeta\rho c^4}\left(\sum_{m=1}^{n-1} R_{m,n-m}v_m v_{n-m}-2\sum_{m=n+1}^{\infty} R_{m,n-m}v_m v_{m-n}^*\right), \tag{9}$$

where ρ is the density of the substrate material, μ is the shear modulus, and $\zeta=\xi_t+\xi_t^{-1}+(\xi_l+\xi_l^{-1})\eta^2+4\eta$. The nonlinearity matrix R_{lm} determines the strength of nonlinear interaction between the lth and mth harmonics leading to the generation of the nth harmonic. The matrix is defined by

$$\begin{aligned}R_{lm}=&\frac{\alpha'}{|n|\xi_l+|l|\xi_t+|m|\xi_t}+\frac{\alpha'}{|n|\xi_t+|l|\xi_t+|m|\xi_l}\\&+\frac{\alpha'}{|n|\xi_t+|l|\xi_l+|m|\xi_t}+\frac{\beta'}{|n|\xi_t+|l|\xi_l+|m|\xi_l}\\&+\frac{\beta'}{|n|\xi_l+|l|\xi_t+|m|\xi_l}+\frac{\beta'}{|n|\xi_l+|l|\xi_l+|m|\xi_t}\\&+\frac{3\gamma'}{|n|\xi_l+|l|\xi_l+|m|\xi_l},\end{aligned} \tag{10}$$

where $n=l+m$, and the material-dependent coefficients α', β', and γ' are found in Ref. 15. The nonlinearity matrix is based only on material properties of the substrate. Equation (9), without the second term on the left-hand side, was derived by Zabolotskaya[15] using Hamiltonian formalism. The evolution equation was obtained using averaging to eliminate asynchronous, weakly coupled spectral interactions, leaving only nonlinear terms describing resonant spectral interactions in progressive waves.

Both absorption and dispersion are taken into account *ad hoc* by the term $(\alpha_n+i\delta_n)v_n$ in Eq. (9), where α_n and δ_n are, respectively, absorption and dispersion coefficients for the nth harmonic. The dispersion coefficient δ_n is given by

$$\delta_n=n\omega_1\left(\frac{1}{c}-\frac{1}{c_n}\right) \tag{11}$$

and quantifies the difference between the nondispersive Rayleigh wave speed c and the phase speed c_n for the nth harmonic. For waves in a thin-film system, the phase speed c_n is obtained from the dispersion relation described in the preceding section. The purpose of the absorption coefficient α_n is twofold. First, it models the attenuation of surface waves in solids. Second, it provides numerical stability when computations of Eq. (9) are to be extended into a region of shock formation.

To judge the validity of the above evolution model it is instructive to recall from linear theory the effects of a film on the propagation of Rayleigh waves. First, a film introduces dispersion. Second, a film causes the depth profiles for particle displacement in the substrate to deviate from those for an uncoated, nondispersive substrate. The latter effect dictates the range of applicability of the evolution model, because the nonlinear theory[15] is derived for mode shapes corresponding to an uncoated medium. (Other nonlinear evolution models based upon these same depth profiles[11,22] are all subject to this restriction when augmented *ad hoc* to

include film-dispersion.) Therefore, the following criterion is proposed to determine the accuracy of our numerical calculation. From Figs. 3 and 5 it can be seen that the deviation of depth profiles from those for an uncoated medium is reasonably small for $kh<0.1$. Because the waveforms under consideration have broad spectra, particularly following nonlinear distortion and shock formation, a frequency that characterizes the upper end of the spectrum has to be identified. We define this upper frequency to be that above which the energy is always 40 dB below the peak in the spectrum. The corresponding value of kh is designated $(kh)_{\max}$. If $(kh)_{\max}<0.1$, we suggest that our simulation is accurate.

The evolution equations [Eq. (9)] are solved numerically. For this purpose, it is convenient to introduce the dimensionless quantities

$$V_n=v_n/v_0, \quad X=x/\overline{x}, \quad A_n=\alpha_n\overline{x}, \quad D_n=\delta_n\overline{x}, \tag{12}$$

where v_0 is a characteristic velocity amplitude and[23]

$$\overline{x}=\frac{\rho c^4\zeta}{4\mu\omega_1 v_0|R_{11}|} \tag{13}$$

is a length scale that approximates the shock formation distance for a surface wave radiated at angular frequency ω_1 with amplitude $|v_1(0)|=v_0$. The evolution equations then take the following dimensionless form:

$$\frac{dV_n}{dX}+(A_n+iD_n)V_n=-\frac{n^2}{8|R_{11}|}\left(\sum_{m=1}^{n-1}R_{m,n-m}V_mV_{n-m}-2\sum_{m=n+1}^{N}R_{m,n-m}V_mV_{m-n}^*\right), \tag{14}$$

where N is the number of harmonics retained in the calculation. The above spectral equations are integrated by way of a second-order Runge-Kutta method with a fixed step size. We use 400 harmonics ($N=400$) for all calculations but retain only 390 harmonics in the waveform reconstruction (to reduce Gibbs-type oscillations). For calculation of the nonlinearity matrix R_{lm} we use the values of third-order elastic constants for fused quartz measured by Bogardus.[24] These third-order elastic constants are $A=-42$ GPa, $B=93$ GPa, and $C=26$ GPa in the notation of Landau and Lifshitz.[25] A quadratic absorption law $A_n=n^2A_1$ is assumed, which is a reasonable model for attenuation of surface waves in solids.[26] We choose $A_1=0.01$ for all calculations because at the propagation distances of interest, effects of absorption are significant only at the shocks. For appreciably lower values of A_1, computations require unreasonably large numbers of harmonics in order to accurately describe the shocks.

In Secs. III B–D, numerical results for the evolution of an initially monochromatic wave are presented. The source condition at $X=0$ corresponding to a pure sinusoid is given by $V_1=-1$, and $V_n=0$ for $n>1$. To provide a benchmark, we first discuss nonlinear Rayleigh wave propagation in an uncoated medium. Then, the propagation under both loading and stiffening dispersion is addressed.

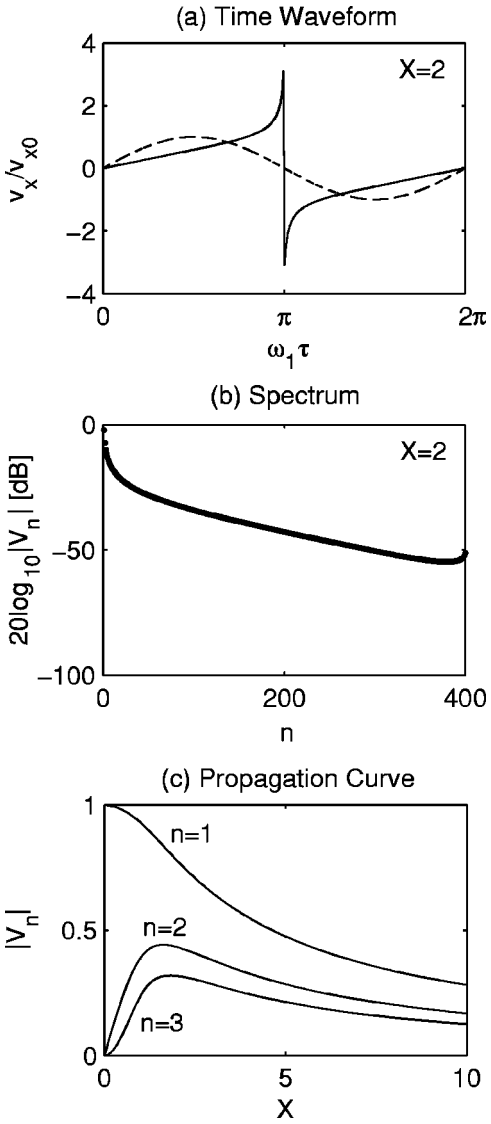

FIG. 6. Nonlinear evolution of an initially monochromatic Rayleigh wave. No dispersion.

B. Nondispersive propagation

Depicted in Fig. 6 is the nonlinear evolution of an initially sinusoidal Rayleigh wave in an uncoated fused-quartz substrate. In Fig. 6(a), one period of the horizontal velocity waveform at the free surface ($z=0$), normalized by the horizontal source amplitude $v_{x0}=-v_0(\xi_t+\eta)$, is shown in the dimensionless retarded time frame $\omega_1\tau$. The waveform at distance $X=2$ (solid line) is compared with the source waveform (dashed line). The corresponding frequency spectrum at $X=2$ is shown in Fig. 6(b). The horizontal velocity waveform exhibits a typical feature of nonlinear surface wave distortion; the waveform develops a shock with cusps.[15] Fused quartz possesses negative nonlinearity in the sense that the negative portions of the horizontal velocity waveform advance on the zero crossings and positive portions recede (e.g., the opposite occurs in velocity waveforms for sound waves in fluids).

The dependence of the first three harmonic amplitudes on propagation distance is displayed in Fig. 6(c). The fundamental component decreases monotonically in magnitude,

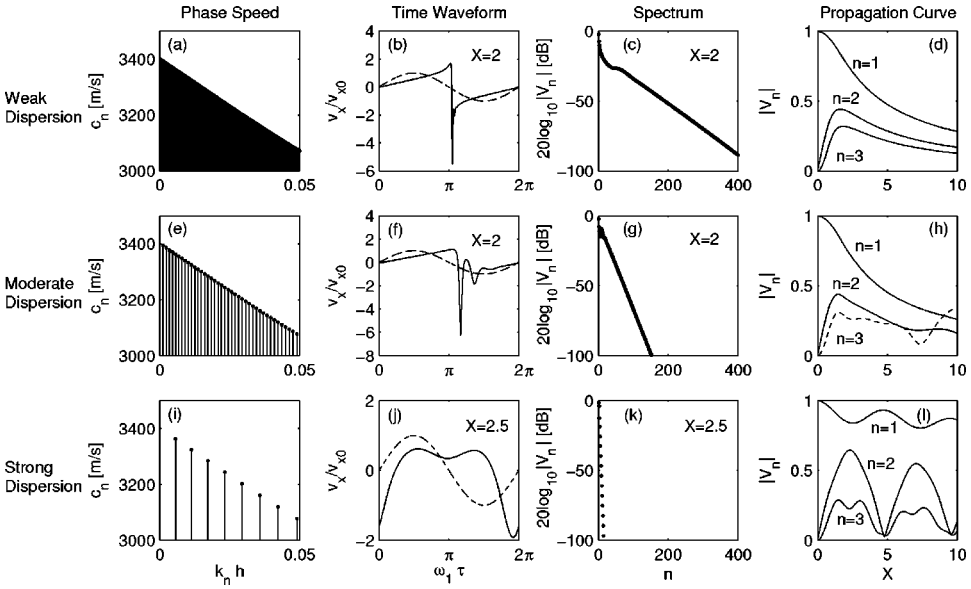

FIG. 7. Summary of nonlinear Rayleigh wave propagation with loading dispersion.

whereas the second and third harmonics ramp up initially and then gradually decay with propagation distance.

C. Propagation with loading dispersion

The propagation medium considered here is a fused-quartz substrate coated with a gold film. The dispersion coefficient D_n in Eq. (14) is calculated via Eqs. (11) and (12), where the phase speed c_n for the nth harmonic is determined by the dispersion curve labeled R1 in Fig. 2. In so doing, it is necessary to specify the fundamental frequency (the source frequency) ω_1 and the nonlinear length scale $\bar{x}$. We choose the fundamental frequency to be $f_1 = 30\,\mathrm{MHz}$ and the nonlinear length scale $\bar{x} = 1\,\mathrm{mm}$ in the absence of the film ($h = 0$), which are values typical for the experiments of Lomonosov *et al.*[6,7] The corresponding peak horizontal strain is $\epsilon_x \equiv v_{x0}/c = 0.0084$. Three different film thicknesses, representing weak, moderate, and strong dispersion in relation to nonlinearity, are considered because the features of waveform distortion turn out to be very distinct in these dispersion regimes.

We start with Rayleigh wave propagation with weak loading dispersion, produced by a film thickness of 5 nm. Shown in the first row of Fig. 7 are (a) phase speeds of the harmonic components, (b) the horizontal velocity waveform, (c) the corresponding frequency spectrum, and (d) propagation curves for the first three harmonics under the condition of weak dispersion. Because the film considered here is relatively thin, the values of kh for the participating harmonics are correspondingly small. Hence, the spectral lines are densely packed near the origin in Fig. 7(a) and are indistinguishable from one another.

A comparison of Figs. 7(b) and 6(a) reveals that in the presence of a film, waveforms are no longer antisymmetric about $\omega_1 \tau = \pi$. The dispersion is sufficiently weak that a shock still forms in v_x, although different in appearance and slightly farther back in the waveform (i.e., at later retarded time) than when there is no dispersion. This lag in retarded time is because under loading dispersion, high-frequency components responsible for the formation of a shock possess lower phase speeds than the nondispersive Rayleigh speed c. Dispersion also causes the spectral amplitude to taper off relatively fast with frequency [Fig. 7(c)] compared to the nondispersive case [Fig. 6(b)].

The propagation curves for the three lowest harmonics [Fig. 7(d)] are virtually identical to those for the nondispersive case shown in Fig. 6(c). This is because for the given film thickness ($h = 5\,\mathrm{nm}$), the dispersion is not strong enough to change the dependence of the lowest several harmonics on propagation distance.

Increasing the film thickness to 20 nm produces a moderate dispersion regime. The second row of Fig. 7 contains (e) phase speeds of the harmonic components, (f) the horizontal waveform, (g) the corresponding spectrum, and (h) propagation curves for the first three harmonics under moderate dispersion. Due to the increased dispersion and phase mismatch among higher harmonic components, the coupling and generation of higher harmonics are not as strong as in the previous case. [Compare Figs. 7(c) and (g).] Therefore, the horizontal velocity waveform no longer develops a shock. Instead, ''impulse shedding'' occurs in the time waveform [Fig. 7(f)]; a train of well-defined impulses emerges gradually as the waveform evolves from the initial sinusoid. A similar behavior was observed by Zabusky *et al.*[27] in the numerical solution of the KdV equation, who solved the periodic boundary value problem for an initially sinusoidal profile. For loading dispersion, the direction of impulse shedding is toward later time (to the right). In other words, emerging impulses travel at speeds lower than the nondispersive Rayleigh speed c. Among the impulses, the larger ones propagate faster than the smaller ones, i.e., the larger waves appear before the smaller ones in retarded time.

In Fig. 7(h), crossing of the harmonic propagation curves is observed. The propagation curve for the fundamental component decreases monotonically while the second harmonic shows a slight upward turn near $X = 8$. The curve for the third harmonic (dashed line) exhibits rather an erratic behavior, crossing the propagation curves of the first two harmonics. The undulation of the third harmonic amplitude

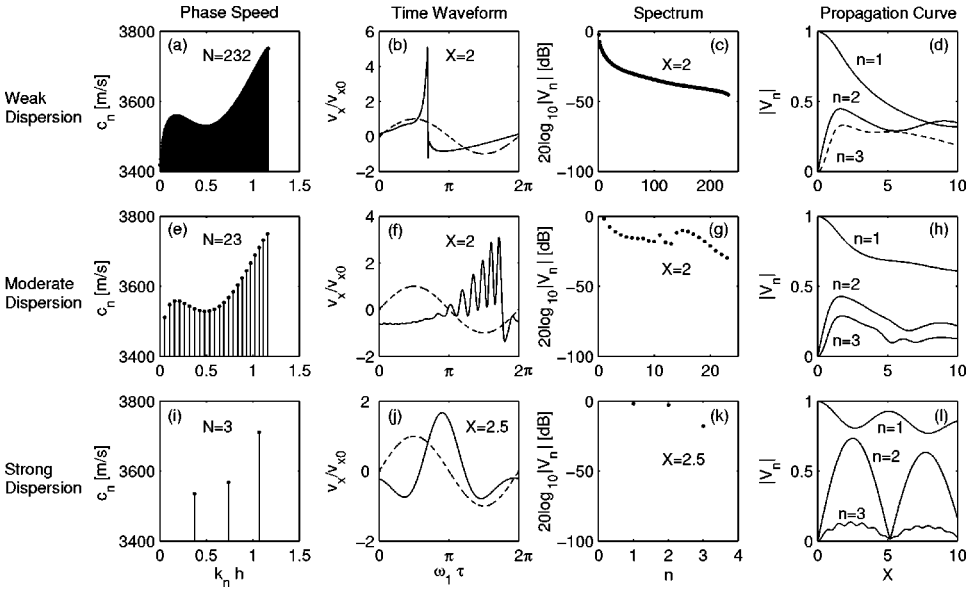

FIG. 8. Summary of nonlinear Rayleigh wave propagation with stiffening dispersion.

forecasts the growth-decay cycle that occurs under strong dispersion.

The strong dispersion regime is encountered for $h = 100$ nm (the third row in Fig. 7). When dispersion is strong in relation to nonlinearity, the velocity waveform [Fig. 7(j)] assumes a drastically different shape from those of the two preceding cases; the waveform is smooth because it is composed mainly of the first few harmonics.

For understanding the relevant nonlinear distortion process for strong dispersion, propagation curves are more convenient than the time waveform. Shown in Fig. 7(l) are the propagation curves for the lowest three harmonics. Note the growth-decay cycle of each harmonic component, which is a common occurrence in the presence of strong dispersion. The large variations in phase speeds prevent efficient coupling of the interacting harmonics, and therefore the acoustic energy tends to be exchanged between the source frequency component and the lowest several harmonics. One interesting aspect of nonlinear wave propagation under conditions of strong dispersion is the recurrence of the initial waveform. As shown in Fig. 7(l), the fundamental component has a local maximum near $X = 5$, where the second and third harmonic amplitudes are smallest. Since most of the energy is channeled back to the source frequency component, the waveform almost recovers its initial profile, apart from slightly reduced amplitude due to absorption (waveform not shown).

We conclude this section by mentioning that all calculations shown here meet our proposed validity criterion. That is, the maximum effective kh for any of the weak, moderate, and strong dispersion cases turns out to be less than 0.1. For example, the number of harmonic components participating effectively in the evolution process under strong dispersion is $n = 7$ according to the aforementioned -40 dB cutoff in spectral amplitude. The corresponding value of $(kh)_{\max}$ is 0.04 and thus the calculation is deemed accurate according to our validity criterion.

D. Propagation with stiffening dispersion

We now consider a fused-quartz substrate layered with an alumina film. As in the previous section, the fundamental component is set at $f_1 = 30$ MHz and the shock formation distance in the absence of the film ($h = 0$) is $\bar{x} = 1$ mm. The dispersion coefficients D_n are obtained from the corresponding dispersion curve (Fig. 4).

A film thickness of $h = 0.1\ \mu$m is chosen to introduce weak stiffening dispersion. Because of the cutoff of the Rayleigh mode (recall Fig. 4), only 232 harmonics can propagate, and only those harmonics are retained in the calculation [Fig. 8(a)]. Figure 8(b) shows the waveform distortion process. In contrast to the case of weak loading dispersion [Fig. 7(b)], the shock in the horizontal component displays a leftward shift in the retarded time frame. High-frequency components having greater speeds than the nondispersive Rayleigh speed c manifest themselves in the form of a shock that advances in retarded time. The accompanying spectrum and harmonic propagation curves are shown in Figs. 8(c) and (d), respectively.

Moderate stiffening dispersion is obtained for $h = 1\ \mu$m. In this case, the cutoff occurs just below the 24th harmonic and therefore only the lowest 23 harmonics can propagate [Fig. 8(e)]. The corresponding waveform distortion [Fig. 8(f)] is characterized by impulse shedding similar to that found in Fig. 7(f). However, the direction of impulse shedding for stiffening dispersion is opposite to that for loading dispersion, i.e., it is earlier in retarded time (to the left). [Note that the impulses shown in Fig. 8(f) have already moved past $\omega_1 \tau = 0$ and wrapped around in the retarded time frame.] Also, impulses emerging from a monochromatic horizontal velocity waveform are positive in polarity under stiffening dispersion, whereas negative impulses form from a sinusoid under loading dispersion. This is characteristic of impulse shedding in the film-substrate pair, where the substrate possesses negative nonlinearity, as in fused quartz. If a substrate exhibits positive nonlinearity (as in most solids), the impulses that are shed in an initially mono-frequency

horizontal waveform assume opposite polarities depending on the dispersion; negative impulses emerge for stiffening dispersion while positive impulses appear for loading dispersion.

A simple argument can be made to explain the direction and polarity of the impulse shedding. Take a fused-quartz substrate as an example. Since fused quartz possesses negative nonlinearity, the positive side of an initially sinusoidal horizontal velocity waveform gradually steepens to the right in the retarded time frame, while the negative side steepens to the left. Just before shock formation, dispersion comes into play and a train of impulses composed mainly of high-frequency components emerges. The location of the emergence of impulses relative to the near-shock front is determined by the sign of the dispersion at hand. If the film stiffens the substrate, impulses emerge on the left-hand side of the near-shock front because higher-frequency components travel faster than the front, which moves at roughly the phase speed of the fundamental component. On the left-hand side of the front exists the positive portion of the velocity waveform, which eventually dictates the polarity of the emerging impulses; if any impulse is to emerge from the positive portion, it must possess positive polarity. Under loading dispersion, however, impulses appear from the negative portion on the right-hand side of the near-shock front and hence must carry the negative sign. A similar logic can be used to predict the polarity of the impulses emerging under conditions of positive nonlinearity and the accompanying dispersion.

Waveform distortion for strong stiffening dispersion is shown in Fig. 8(j). Here, the film thickness is 7 μm, and, due to the cutoff, only the first three harmonics participate in the nonlinear interaction [Fig. 8(i)]. The waveform distortion is reminiscent of the loading counterpart in Fig. 7(j). Figure 8(l) shows the propagation curves for the first three harmonics. As expected, each propagation curve follows its own growth-decay cycle. Near $X=5$, the fundamental harmonic achieves its local maximum, while the second and third harmonics reach their local minima, resulting in the recurrence of the initial wave profile (waveform not shown).

With strong loading dispersion the large variations in phase speeds are responsible for the periodic undulation of propagation curves. For strong stiffening dispersion, however, the grow-decay cycle of propagation curves can be attributed chiefly to the abrupt truncation of the frequency spectrum. Since the cutoff for stiffening dispersion limits the number of interacting harmonic components, the acoustic energy must be shared among the participating three harmonics regardless of the variations in phase speeds (if one does not account for the nonlinear mode coupling with the bulk waves).

As pointed out in Sec. II B, due to the relatively small changes in phase speed associated with stiffening dispersion, relatively large film thicknesses are required to create a degree of waveform distortion comparable to the loading counterpart shown in Fig. 7. This implies that $(kh)_{\max}$ is correspondingly large for stiffening dispersion. Indeed, the values of $(kh)_{\max}$ for the weak, moderate, and strong stiffening dispersion cases in Fig. 8 are, respectively, 0.9, 1.2, and 1.1, all

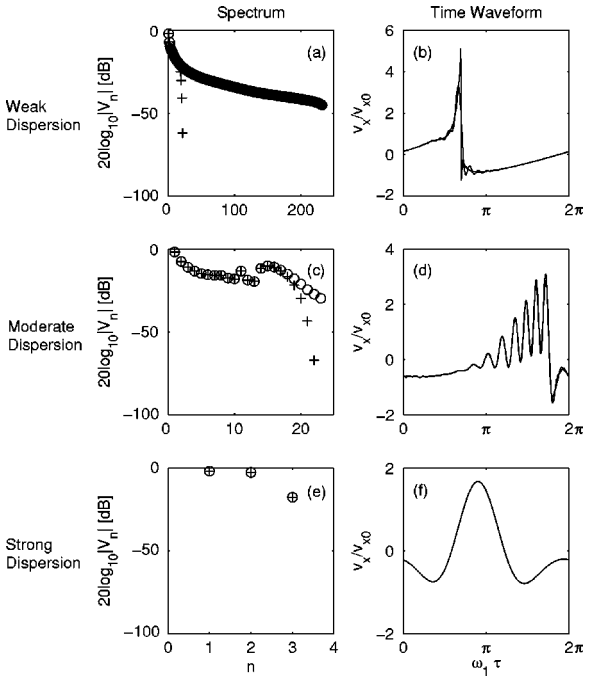

FIG. 9. Effects of spectral amplitude shading for the case of stiffening dispersion. Spectra before (○) and after (+) shading in the first column are followed by the corresponding horizontal velocity waveforms in the second column. The pairs of waveforms in (d) and (f) are virtually indistinguishable.

of which are well above the proposed tolerance limit of 0.1.

Nonetheless, we propose that the violation of the validity criterion may not necessarily invalidate our numerical results. Note that it is mostly higher harmonic components whose predicted contributions may be erroneous due to their large values of kh. The effects of higher harmonics can be diminished by applying a spectral amplitude shading function similar to that used by Kumon:[28]

$$W(n)=\exp[-(n/M)^{16}], \tag{15}$$

where M is the harmonic number that corresponds to the effective bandwidth. Spectra obtained from running the propagation algorithm [Eq. (14)] keeping all harmonics ($N=232$, 23, and 3 for the cases of weak, moderate, and strong stiffening dispersion, respectively) are multiplied by the weighting function [Eq. (15)]. Waveforms reconstructed from spectra with and without shading are then compared to judge the influence of the higher harmonics. Results of the spectral amplitude shading with $M=20$, applied to the frequency spectra of Fig. 8, are displayed in Fig. 9. Spectral amplitudes before (○) and after (+) the shading are shown in the first column and the corresponding horizontal velocity waveforms are found in the second column. For the case of weak stiffening dispersion, the shading function dramatically reduces the number of harmonics [Fig. 9(a)]. The value of $(kh)_{\max}$ for the shaded spectrum is 0.1, indicating that the waveform is constructed only with harmonics for which $kh<0.1$. The waveforms before and after shading are quite similar, apart from oscillations due to the truncation [Fig. 9(b)]. For moderate and strong stiffening dispersion, however, most, if not all, harmonics are unaffected by shading [Figs. 9(c) and (e)] and the values of $(kh)_{\max}$ thus remain

greater than 0.1. Whereas the phase speeds of all modes are correct, the mode shapes are inaccurate for large kh, and therefore simulations presented in the second and third rows of Fig. 8 should be viewed as qualitative descriptions of the actual wave process.

Although undertaken above as a mathematical exercise, spectral amplitude shading has a practical ramification when comparisons are to be made between computations and measurements; spectral amplitude shading can be used to simulate the bandwidth limitation inherent in experiments and therefore to facilitate a fairer comparison of computed waveforms with measurements.[28] For example, given the fundamental frequency at 30 MHz, Eq. (15) with $M=20$ yields a bandwidth of approximately 500 MHz, which is a typical bandwidth of the experimental setup used by Lomonosov *et al.*[6]

IV. SUMMARY

Nonlinear Rayleigh wave propagation in an isotropic substrate coated with a film of a second isotropic material is investigated numerically. Two representative isotropic material pairs are chosen for loading and stiffening dispersion. Linear solutions of the problem are presented in terms of dispersion relations and depth profiles of the particle displacement components. It is suggested that the deviation of the depth profiles from those of the nondispersive case can be used to judge the error associated with the nonlinear evolution model. Based on this, a criterion for assessing the accuracy of the numerical calculation is proposed. Nonlinear distortion of an initially sinusoidal waveform is considered for three different dispersion strengths: weak, moderate, and strong. The features of the nonlinear waveform distortion differ drastically among different dispersion regimes; graphical summaries are provided in Figs. 7 and 8.

ACKNOWLEDGMENTS

The authors gratefully acknowledge discussions with Yu. A. Ilinskii, E. A. Zabolotskaya, and R. E. Kumon.

[1] A. Neubrand and P. Hess, "Laser generation and detection of surface acoustic waves: Elastic properties of surface layers," J. Appl. Phys. **71**, 227–238 (1992).
[2] R. Kuschnereit, P. Hess, D. Albert, and W. Kulisch, "Density and elastic constants of hot-filament-deposited polycrystalline diamond films: methane concentration dependence," Thin Solid Films **312**, 66–72 (1998).
[3] V. I. Nayanov, "Surface acoustic cnoidal waves and solitons in a $LiNbO_3$-(SiO film) structure," JETP Lett. **44**, 314–317 (1986).
[4] Y. Cho and N. Miyagawa, "Surface acoustic wave soliton propagating on the metallic grating waveguide," Appl. Phys. Lett. **63**, 1188–1190 (1993).
[5] V. Kavalerov, H. Katoh, N. Kasaya, M. Inoue, and T. Fujii, "Experimental studies on nonlinear dispersive surface acoustic waves for solitons," Jpn. J. Appl. Phys., Part 1 **34**, 2653–2659 (1995).
[6] A. Lomonosov and P. Hess, "Effects of nonlinear elastic surface pulses in anisotropic silicon crystals," Phys. Rev. Lett. **83**, 3876–3879 (1999).
[7] A. M. Lomonosov, P. Hess, and A. P. Mayer, "Observation of solitary elastic surface pulses," Phys. Rev. Lett. **88**, 076104 (2002).
[8] E. L. Adler and A. A. Nassar, "Effect of dispersion on harmonic generation of acoustic surface waves," in *Proceedings of the IEEE Ultrasonics Symposium, 1973*, pp. 268–270.
[9] E. L. Adler, E. Bridoux, G. Coussot, and E. Dieulesaint, "Harmonic generation of acoustic surface waves in $Bi_{12}GeO_{20}$ and $LiNbO_3$," IEEE Trans. Sonics Ultrason. **20**, 13–16 (1973).
[10] J. F. Ewen, R. L. Gunshor, and V. H. Weston, "An analysis of solitons in surface acoustic wave devices," J. Appl. Phys. **53**, 5682–5688 (1982).
[11] A. P. Mayer, "Surface acoustic waves in nonlinear elastic media," Phys. Rep. **256**, 237–366 (1995).
[12] C. Eckl, A. P. Mayer, and A. S. Kovalev, "Do surface acoustic solitons exist?" Phys. Rev. Lett. **81**, 983–986 (1998).
[13] C. Eckl, J. Schöllmann, A. P. Mayer, A. S. Kovalev, and G. A. Maugin, "On the stability of surface acoustic pulse trains in coated elastic media," Wave Motion **34**, 35–49 (2001).
[14] G. W. Farnell and E. L. Adler, "Elastic wave propagation in thin layers," in *Physical Acoustics*, edited by W. P. Mason and R. N. Thurston (Academic, New York, 1972), Vol. 9, pp. 35–127.
[15] E. A. Zabolotskaya, "Nonlinear propagation of plane and circular Rayleigh waves in isotropic solids," J. Acoust. Soc. Am. **91**, 2569–2575 (1992).
[16] In the equivalent equation of Ref. 14 [Eq. (18)], a typo is found at row 5, column 4. The following correction should be made: replace $-2b^{(5)}\exp(-ikb^{(6)}h)$ by $-2b^{(6)}\exp(-ikb^{(6)}h)$.
[17] H. F. Tiersten, "Elastic surface waves guided by thin films," J. Appl. Phys. **40**, 770–789 (1969).
[18] A. Lomonosov, V. G. Mikhalevich, P. Hess, E. Yu. Knight, M. F. Hamilton, and E. A. Zabolotskaya, "Laser-generated nonlinear Rayleigh waves with shocks," J. Acoust. Soc. Am. **105**, 2093–2096 (1999).
[19] R. C. Weast (ed.), *Handbook of Chemistry and Physics*, 53rd ed. (CRC, Cleveland, 1972).
[20] O. L. Anderson, "Determination and some uses of isotropic elastic constants of polycrystalline aggregates using single-crystal data," in *Physical Acoustics*, edited by W. P. Mason (Academic, New York, 1965), Vol. 3, pp. 43–95.
[21] D. J. Shull, M. F. Hamilton, Yu. A. Il'insky, and E. A. Zabolotskaya, "Harmonic generation in plane and cylindrical nonlinear Rayleigh waves," J. Acoust. Soc. Am. **94**, 418–427 (1993).
[22] D. F. Parker, "Waveform evolution for nonlinear surface acoustic waves," Int. J. Eng. Sci. **26**, 59–75 (1988).
[23] E. Yu. Knight, M. F. Hamilton, Yu. A. Il'inskii, and E. A. Zabolotskaya, "On Rayleigh wave nonlinearity, and analytical approximation of the shock formation distance," J. Acoust. Soc. Am. **102**, 2529–2535 (1997).
[24] E. H. Bogardus, "Third-order elastic constants of Ge, MgO, and fused SiO_2," J. Appl. Phys. **36**, 2504–2513 (1965).
[25] L. D. Landau and E. M. Lifshitz, *Theory of Elasticity*, 3rd ed. (Pergamon, New York, 1986), p. 107.
[26] E. Salzmann, T. Plieninger, and K. Dransfeld, "Attenuation of elastic surface waves in quartz at frequencies of 316 MHz and 1047 MHz," Appl. Phys. Lett. **13**, 14–15 (1968).
[27] N. J. Zabusky and M. D. Kruskal, "Interaction of 'solitons' in a collisionless plasma and the recurrence of initial states," Phys. Rev. Lett. **15**, 240–243 (1965).
[28] R. E. Kumon, "Nonlinear surface acoustic waves in cubic crystals," Ph.D. dissertation, The University of Texas at Austin, 1999.

Broadband performance of a time reversing array with a moving source[a)]

Karim G. Sabra[b)] and David R. Dowling[c)]
Department of Mechanical Engineering, University of Michigan, Ann Arbor, Michigan 48109-2133

(Received 12 September 2002; accepted for publication 9 February 2004)

The automatic spatial and temporal focusing properties of a time-reversing array (TRA) make it an attractive technology for active and passive sonar systems that may be deployed in unknown multipath environments. However, in these and other potential underwater applications of TRAs, either the source, the array, or both are likely to be moving. In this paper we present broadband-signal TRA performance predictions that include the influence of the Doppler effect on the time-reversal process for broadband signals transmitted from an arbitrarily moving source to a stationary vertical TRA through a shallow ocean environment. Here, the impact of source motion on TRA performance is predicted from analysis and numerical simulations using a formulation of the Doppler shifted field based on Fourier superposition of stationary but spatially distributed time-harmonic sources. Quantitative results for the size and location of the TRA's retrofocus are presented as well as the correlation of the TRA retrofocus signal with the time-reversed original signal for various source motions in range-independent and range-dependent shallow water sound channels. Overall, source motion is predicted to have little effect on TRA operations with source speeds less than 20 m/s for signals having a center frequency of 500 Hz at source–array ranges of a few kilometers. © *2004 Acoustical Society of America.* [DOI: 10.1121/1.1703539]

PACS numbers: 43.30.Es, 43.30.Vh, 43.30.Yj [WLS] Pages: 2807–2817

I. INTRODUCTION

Active acoustic time reversal is the process of recording a signal from a remote source with an array of transducers, and then replaying the signal in a time-reversed fashion from the same array to retrodirect the sound back to where it came from to form a retrofocus. A successful time-reversing array (TRA) retrofocus may be formed without any prior knowledge of the environment, the source location, or the array's transducer locations. A TRA may be of nearly any size or shape and may operate in any frequency range. Moreover, TRAs with sufficient aperture perform well in multipath environments in the absence of acoustic absorption losses and temporal changes in the environment. The robust focusing and pulse compression provided by time-reversal techniques may be exploited for active sonar [Kuperman *et al.*, 1998; Lingevitch *et al.*, 2002] and by coherent [Rouseff *et al.*, 2001; Edelmann *et al.*, 2002; Yang *et al.*, 2003] and incoherent [Smith *et al.*, 2003; Heinemann *et al.*, 2003] underwater communication systems deployed in unknown multipath environments.

However, array motion, medium motion, and source motion can each influence the time-reversal process because they alter the reciprocity on which the technique relies. In fact, prior work on scattering from a moving source (Lai and Makris, 2003) suggests that time-reversal techniques may not be applicable when the source or the array or both are moving. Yet, the effects of array motion on time reversal in an ocean waveguide may be mild at low towing speeds, depending on the source–array geometry and the array orientation (Sabra and Dowling, 2003a). Medium motion may also mildly influence the effectiveness of time reversal with similar speed and geometry dependencies (Dowling, 1993; Sabra and Dowling, 2003b).

In this paper we cover the remaining topic of how source motion and the Doppler effect influence the time-reversal process. Both analytical and simulation results that describe the impact of source motion on TRA performance in ocean waveguides are presented. These results are developed from extension and simplification of the Doppler formulation found in Schmidt and Kuperman (1994, hereafter referred to as SK94) for sources and receivers moving in a range-independent ocean waveguide. This prior formulation is extended in this paper to arbitrarily moving sources and range-dependent waveguides via computations, and to the two-way propagation scenario of time reversal. The prior formulation is simplified for zero receiver velocity because the TRA is assumed stationary. In addition, the current formal results are simplified for low Mach number source motion to analytical formulas.

The effects of source motion on time reversal and on one-way propagation of sound in a waveguide have been the subjects of prior studies; in this paper we combine the two. In free space the effect of a moving source is well known (see Morse and Ingard, 1968), and early time-reversal work for ideal continuous closed TRAs (Jackson and Dowling, 1991) utilized these classical results. In an ocean sound channel, the Doppler shifts created by source or receiver motion are more complex because of multipath propagation. A variety of studies of one-way propagation (from a moving source to an array) are available for small Mach number source

[a)]Portions of this work were presented at the 142nd ASA meeting in Chicago, IL, June 2001.
[b)]Currently employed by the Marine Physical Laboratory, Scripps Institution of Oceanography.
[c)]Corresponding author. Electronic mail: drd@umich.edu

motion. Ray-acoustic approaches have been reported for an isospeed channel (Jacyna *et al.*, 1976) and a bounded deep ocean channel (Clark *et al.*, 1976). An early normal-mode-based formulation for long-range sound propagation is provided in Neubert (1977). Another normal-mode-based formulation was introduced (Hawker, 1979) and then exploited to analyze the performance of source localization schemes based on matched-mode processing (Song and Baggeroer, 1990; Chen and Lu, 1992; Song, 1993). Another waveguide Doppler formulation was developed in terms of retarded times for range-independent environments (Lim and Ozard, 1994a) and weakly range-dependent environments via the adiabatic mode approximation (Lim and Ozard, 1994b). These formulations are equivalent at small Mach number. A parabolic equation (PE) approach has been reported (Howell *et al.*, 1993), but these simple PE results differ from recent spectral and modal formulations (SK94), where the source and receiver dynamics are shown to be inherently nonreciprocal. The work reported here utilizes elements of the one-way spectral and PE formulations mentioned above for simulations of TRA performance.

The remainder of this paper is divided into four sections. A broadband formulation of the Doppler-shifted field from an arbitrarily moving point source is presented in the next section. This general description is simplified for short signal pulses and low source Mach number to highlight the important phenomena leading to changes in TRA performance. In the third section we extend the broadband formulation to the time-reversal process with a moving source and a stationary array, and shows that time reversal remains an optimum spatial–temporal matched filter when the source is moving. In the fourth section we illustrate the impact of a moving source on TRA performance through simulations of various source motions in range-independent and range-dependent shallow water sound channels. A summary of findings and the conclusions drawn from this study are presented in the final section.

II. DOPPLER EFFECT FORMULATION

A. General solution for arbitrary source motion

The acoustic pressure field, $p(\mathbf{r},t)$, at location $\mathbf{r}$ at time t, produced by a point source moving along a trajectory $\mathbf{r}_s(t)$, can be obtained as the solution of the forced wave equation in a time-independent environment (cf. Morse and Ingard, 1968):

$$\frac{1}{c^2(\mathbf{r})}\frac{\partial^2 p(\mathbf{r},t)}{\partial t^2}-\nabla^2 p(\mathbf{r},t)=S(t)\,\delta(\mathbf{r}-\mathbf{r}_s(t)), \tag{1}$$

where $c(\mathbf{r})$ is the speed of sound, $S(t)$ is the signal emitted by the moving source, and bold characters indicate vectors. The formal solution of Eq. (1),

$$p(\mathbf{r},t)=\int_{-\infty}^{+\infty}\int_{\text{all } r'} G(\mathbf{r},\mathbf{r}';t-t')S(t') \times \delta(\mathbf{r}'-\mathbf{r}_s(t'))d^3r'\,dt', \tag{2}$$

involves the time-dependent Green's function, $G(\mathbf{r},\mathbf{r}';t-t')$ for the same environment that solves

$$\frac{1}{c^2(\mathbf{r})}\frac{\partial^2 G(\mathbf{r},\mathbf{r}';t-t')}{\partial t^2}-\nabla^2 G(\mathbf{r},\mathbf{r}';t-t') = \delta(\mathbf{r}-\mathbf{r}')\,\delta(t-t'), \tag{3}$$

and satisfies the same boundary conditions as $p(\mathbf{r},t)$ (Pierce, 1989). Here, the solution domain is presumed to be semi-infinite below the ocean surface with spatial variations in $c(\mathbf{r})$ arising from the ocean's water column and bottom properties. Thus, a radiation condition applies as $|\mathbf{r}|\to\infty$ below the ocean surface, and the usual pressure release boundary condition, $p=0$ and $G=0$, applies on the ocean surface. Under these circumstances the possible boundary integral contribution to Eq. (2) is absent (Pierce, 1989; Jensen *et al.*, 1994).

Two simplifications of Eq. (2) are possible that facilitate further analytical and numerical work. The volume integration over r' may be evaluated through the sifting property of the Dirac δ function:

$$p(\mathbf{r},t)=\int_{-\infty}^{+\infty} G(\mathbf{r},\mathbf{r}_s(t');t-t')S(t')dt'. \tag{4}$$

The application of a temporal Fourier transform,

$$\tilde{p}(\mathbf{r},\omega)=\int_{-\infty}^{+\infty} p(\mathbf{r},t)e^{i\omega t}\,dt, \tag{5}$$

to Eq. (4) produces the intended result:

$$\tilde{p}(\mathbf{r},\omega)=\int_{-\infty}^{+\infty} \tilde{G}(\mathbf{r},\mathbf{r}_s(t');\omega)S(t')e^{i\omega t'}\,dt'. \tag{6}$$

Here, the time-shift invariance in $G(\mathbf{r},\mathbf{r}';t-t')$ and the definition

$$\tilde{G}(\mathbf{r},\mathbf{r}';\omega)=\int_{-\infty}^{+\infty} G(\mathbf{r},\mathbf{r}';\tau)e^{i\omega\tau}\,d\tau, \tag{7}$$

have been used to reach Eq. (6) from Eq. (4). An inverse Fourier transform of Eq. (6) recovers $p(\mathbf{r},t)$ from $\tilde{p}(\mathbf{r},\omega)$.

B. Consistency with prior Doppler formulation

At first glance, Eq. (6) may seem to be inconsistent with Eq. (16) in SK94. Our intent in this short subsection is to show that the two formulations are equivalent when each is evaluated for the same conditions within its stated limitations. The overlap domain requires a range-independent environment, a stationary receiver ($\boldsymbol{\nu}_r=0$), and a steady horizontal source velocity $\boldsymbol{\nu}_s$. For this situation, define $\mathbf{r}=(\mathbf{r}_0,z)$ where $\mathbf{r}_0$ is two-dimensional vector composed of the horizontal components of $\mathbf{r}$, and z is the vertical coordinate. Using the current notation, Eq. (16) from SK94 becomes

$$\tilde{p}(\mathbf{r}_0,z,\omega)=\frac{1}{2\pi}\int \tilde{S}(\omega-\mathbf{k_r}\cdot\boldsymbol{\nu}_s)G_{\text{SK94}}(|\mathbf{k_r}|,z;\omega) \times\exp\{i\mathbf{k_r}\cdot\mathbf{r_0}\}d^2k_r, \tag{8}$$

where G_{SK94} is the depth-dependent wave number–domain Green's function that solves

$$\frac{d^2}{dz^2}G_{\mathrm{SK94}}(|\mathbf{k_r}|,z;\omega)+\left[\frac{\omega^2}{c^2(z)}-|\mathbf{k_r}|^2\right]G_{\mathrm{SK94}}(|\mathbf{k}_r|,z;\omega)$$
$$=-\frac{1}{2\pi}\delta(z-z_s), \tag{9}$$

and $\mathbf{k_r}$ is the two-dimensional horizontal wave number (see Jensen *et al.*, 1994). The relationship between G_{SK94} and the Helmholtz equation Green's function $\tilde{G}$ defined by Eq. (7) can be obtained by applying a temporal Fourier transform and a two-dimensional horizontal wave number transform to Eq. (3). The relationship is

$$\tilde{G}(\mathbf{r_0},z,\mathbf{r_{0s}},z_s;\omega)=\frac{1}{2\pi}\int_{\text{all }\mathbf{k_r}}G_{\mathrm{SK94}}(|\mathbf{k_r}|,z;\omega)\times\exp\{+i\mathbf{k_r}\cdot(\mathbf{r_0}-\mathbf{r_{0s}})\}d^2k_r, \tag{10}$$

where the additional notation change $\mathbf{r_s}=(\mathbf{r_{0s}},z_s)$ has been made. Substituting Eq. (10) into the main result of the prior subsection, Eq. (6), produces

$$\tilde{p}(\mathbf{r_0},z,\omega)=\int_{-\infty}^{+\infty}\left[\frac{1}{2\pi}\int_{\text{all }\mathbf{k_r}}G_{\mathrm{SK94}}(|\mathbf{k_r}|,z;\omega)\times\exp\{+i\mathbf{k_r}\cdot(\mathbf{r_0}-\boldsymbol{\nu_s}t')\}d^2k_r\right]S(t')e^{i\omega t'}\,dt', \tag{11}$$

where the replacement $\mathbf{r_{0s}}=\boldsymbol{\nu_s}t'$ specifies the horizontal source motion.

The goal here is to show that Eq. (11) is identical to Eq. (8). First, regroup the various factors in Eq. (11) and swap the order of the integrations to find

$$\tilde{p}(\mathbf{r_0},z,\omega)=\frac{1}{2\pi}\int_{\text{all }\mathbf{k_r}}G_{\mathrm{SK94}}(|\mathbf{k_r}|,z;\omega)\exp\{+i\mathbf{k_r}\cdot\mathbf{r_0}\}\times\left[\int_{-\infty}^{+\infty}S(t')\exp\{+i(\omega-\mathbf{k_r}\cdot\boldsymbol{\nu_s})t'\}dt'\right]d^2k_r. \tag{12}$$

Performing the t' integration (equivalent to a Fourier transform) reduces the contents of the [,] brackets to $\tilde{S}(\omega-\mathbf{k_r}\cdot\boldsymbol{\nu_s})$ and renders Eq. (12) equivalent to Eq. (8). Thus, the moving source formulation provided by Eq. (6) is consistent with the formulation in SK94 when environmental and geometric factors are matched.

C. Numerical implementation

The formal Doppler-field solution embodied in Eq. (6) is applicable to arbitrary source motion in a time-independent environment containing the lone sound source at $\mathbf{r_s}$. If the signal $S(t)$ is zero outside of the time interval $[t_i,t_f]$, the integration in Eq. (6) is finite and can be approximated by a sum:

$$\tilde{p}(\mathbf{r},\omega)\cong\sum_{t_k=t_i}^{t_k=t_f}\tilde{G}(\mathbf{r},\mathbf{r_s}(t_k),\omega)S(t_k)\exp(i\omega t_k), \tag{13}$$

where the t_k are discrete sample times spaced finely enough to ensure that $S(t)$ and $\mathbf{r_s}(t)$ are well represented $S(t_k)$ and $\mathbf{r_s}(t_k)$. For this effort, the Fourier-domain Green's function was numerically computed at the discretized source locations $\mathbf{r_s}(t_k)$ at all the frequencies of interest. The spatial sampling rate of the source trajectory was set to achieve accurate signal reconstructions; the distance between spatial evaluation points, $|\mathbf{r_s}(t_{k+1})-\mathbf{r_s}(t_k)|$, did not exceed 1/10th of a wavelength at radian frequency ω. A numerical inverse Fourier transform recovered the time–domain pressure signal from Eq. (13). This approach allows arbitrary source motion within a range-dependent sound channel without limitations on Mach number. Unfortunately, it becomes computationally burdensome when $S(t)$ is broadband and the source moves many characteristic wavelengths λ_c in the time interval $[t_i,t_f]$. Here, λ_c may be defined as c_c/f_c, where c_c is a representative water column sound speed and f_c is the center frequency of the signal.

D. Approximation for short signal pulses and low-Mach number source motion

When the signal duration is short or when the source is slowly moving, i.e., when $\max|\mathbf{r_s}(t)-\mathbf{r_s}(t_i)|\ll\lambda_c$, then the frequency domain Green's function in Eq. (6) may be expanded around the average source position:

$$\tilde{G}(\mathbf{r},\mathbf{r_s}(t');\omega)\approx\tilde{G}(\mathbf{r},\mathbf{r_s}(0);\omega)+(\mathbf{r_s}(t')-\mathbf{r_s}(0))\cdot\boldsymbol{\nabla}_s\tilde{G}(\mathbf{r},\mathbf{r_s}(0);\omega), \tag{14}$$

where $\boldsymbol{\nabla}_s$ implies spatial differentiation with respect to the $\mathbf{r_s}(0)$ coordinates. In this paper, the chosen source trajectories were centered on the origin of the range axis with the transmitted pulses lying in a symmetric interval about $t=0$, i.e., $t_i=-T_s/2$ and $t_f=+T_s/2$. Consistent with the approximation inherent in Eq. (14) is an expansion of the source trajectory itself:

$$\mathbf{r_s}(t)=\mathbf{r_s}(0)+\boldsymbol{\nu_s}(0)t+\mathbf{a_s}(0)t^2/2+\cdots, \tag{15}$$

where $\boldsymbol{\nu_s}$ and $\mathbf{a_s}$ are the source's velocity and acceleration. Although it is possible to carry the source acceleration through this analytical development (see Sabra, 2003), source acceleration and higher-order terms are typically unimportant in underwater acoustics and are dropped from the following development for simplicity. Therefore, the substitution of Eq. (14) and the first two terms of Eq. (15) into Eq. (6) produces

$$\tilde{p}(\mathbf{r},\omega)\approx\tilde{G}(\mathbf{r},\mathbf{r_s}(0);\omega)\tilde{S}(\omega)+[\boldsymbol{\nu_s}(0)\cdot\boldsymbol{\nabla}_s\tilde{G}(\mathbf{r},\mathbf{r_s}(0);\omega)]\times\int_{-\infty}^{+\infty}t'S(t')e^{i\omega t'}\,dt', \tag{16}$$

where $\tilde{S}(\omega)$ is the Fourier transform of $S(t)$. The integral in Eq. (16) can be evaluated in terms of the frequency derivative of $\tilde{S}(\omega)$, so that

$$\tilde{p}(\mathbf{r},\omega)\approx\tilde{G}(\mathbf{r},\mathbf{r_s}(0);\omega)\tilde{S}(\omega)-i\boldsymbol{\nu_s}(0)\cdot\boldsymbol{\nabla}_s\tilde{G}(\mathbf{r},\mathbf{r_s}(0);\omega)\frac{d\tilde{S}(\omega)}{d\omega}. \tag{17}$$

A further evaluation is possible by specifying the environment and the direction of source motion. For source motion that lies in a vertical r-z plane intersecting the origin and the receiver location, a normal mode expansion of $\tilde{G}$ can be made in a range-independent sound channel (Jensen *et al.*, 1994):

$$\tilde{G}(r,z,r_s,z_s;\omega)=\frac{e^{i\pi/4}}{\rho(z_s)\sqrt{8\pi}}\sum_{m=1}^{M}\Psi_m(z)\Psi_m(z_s)\times\frac{\exp(ik_m(r-r_s))}{\sqrt{k_m(r-r_s)}}, \tag{18}$$

where r and z are the usual range and depth coordinates, r_s and z_s are the range and depth of the source, ρ is the water column density, Ψ_m is the vertical mode shape of the mth mode, and k_m is the horizontal wave number of the mth mode. This form for $\tilde{G}$ is valid when $k_m(r-r_s)\gg 1$.

In this environment, horizontal and vertical source motions are the two simplest possibilities. For horizontal source motion, $\mathbf{r_s}(t)=(\nu_s t,z_s^0)$, Eqs. (17) and (18) produce

$$\tilde{p}(r,z,\omega)=\frac{e^{i\pi/4}}{\rho(z_s^0)\sqrt{8\pi}}\sum_{m=1}^{M}\Psi_m(z)\Psi_m(z_s^0)\times\frac{\exp(ik_m r)}{\sqrt{k_m r}}\left[\tilde{S}(\omega)-k_m\nu_s\frac{d\tilde{S}(\omega)}{d\omega}\right]. \tag{19}$$

Similarly, for vertical source motion, $\mathbf{r_s}(t)=(0,z_s^0+\nu_s t)$, Eqs. (17) and (18) produce

$$\tilde{p}(r,z,\omega)=\frac{e^{i\pi/4}}{\rho(z_s^0)\sqrt{8\pi}}\sum_{m=1}^{M}\Psi_m(z)\frac{\exp(ik_m r)}{\sqrt{k_m r}}\times\left[\tilde{S}(\omega)\Psi_m(z_s^0)-\left(\frac{d\Psi_m}{dz}-\frac{\Psi_m}{\rho}\frac{d\rho}{dz}\right)_{z=z_s^0}\times\left(i\nu_s\frac{d\tilde{S}(\omega)}{d\omega}\right)\right]. \tag{20}$$

These final expressions for $\tilde{p}$ represent the first-order Doppler effect for low source Mach numbers and short signal pulses. As seen in the next section, they allow analytic predictions of TRA performance with moving sources.

III. THE TIME-REVERSAL PROCESS FOR A MOVING SOURCE AND A STATIONARY ARRAY

A. Retrofocused signal at a stationary point

Time reversal involves two-way propagation. Here, the recording step of time reversal takes place at a vertical array of N transducers located at $\mathbf{r_n}=(r_a,z_n)$. During the playback step of time reversal, each transducer replays the signal it recorded backwards. The array transducers are stationary so all Doppler effects occur during the recording step only. The usual monopole formulation of the TRA-produced pressure field (Jackson and Dowling, 1991) at frequency ω and location r_f is

$$\tilde{P}_{\mathrm{TRA}}(\mathbf{r_f},\omega)=\sum_{n=1}^{N}[\tilde{p}(\mathbf{r_n},\omega)]^*e^{i\omega T_c}\tilde{G}(\mathbf{r_f},\mathbf{r_n},\omega), \tag{21}$$

where the "*" denotes a complex conjugate, and T_c is a time delay that ensures causality. Equations (6), (13), and (19)–(21) allow formal, numerical, and approximate predictions of TRA performance with a moving source. Inserting the form of $\tilde{p}$ given by Eq. (6) yields

$$\tilde{P}_{\mathrm{TRA}}(\mathbf{r_f},\omega)=\sum_{n=1}^{N}\int_{-\infty}^{+\infty}\tilde{G}^*(\mathbf{r_n},\mathbf{r_s}(t');\omega)\times\tilde{G}(\mathbf{r_f},\mathbf{r_n},\omega)S(t')e^{i\omega(T_c-t')}\,dt'. \tag{22}$$

The application of an inverse Fourier transform produces the formal result for the time–domain field produced by the TRA:

$$P_{\mathrm{TRA}}(\mathbf{r_f},t)=\frac{1}{2\pi}\sum_{n=1}^{N}\int_{-\infty}^{+\infty}\int_{-\infty}^{+\infty}\tilde{G}^*(\mathbf{r_n},\mathbf{r_s}(t');\omega)\times\tilde{G}(\mathbf{r_f},\mathbf{r_n},\omega)S(t')e^{-i\omega(t+t'-T_c)}\,dt'\,d\omega. \tag{23}$$

A numerical evaluation of Eqs. (21)–(23) may proceed directly from the scheme outlined below, Eq. (13).

At the average source location, $\mathbf{r_s}(0)$, the first-order approximation, Eq. (17), allows Eq. (21) to be simplified to

$$\tilde{P}_{\mathrm{TRA}}(\mathbf{r_s}(0),\omega)=e^{i\omega T_c}\sum_{n=1}^{N}\left[\tilde{S}^*(\omega)|\tilde{G}(\mathbf{r_n},\mathbf{r_s}(0),\omega)|^2+i\boldsymbol{\nu_s}(0)\cdot\boldsymbol{\nabla}_s\tilde{G}^*(\mathbf{r_n},\mathbf{r_s}(0);\omega)\times\frac{d\tilde{S}^*(\omega)}{d\omega}\tilde{G}(\mathbf{r_n},\mathbf{r_s}(0),\omega)\right], \tag{24}$$

where reciprocity of has been used to swap the spatial arguments of $\tilde{G}$. For a sound channel with a vertical or horizontal moving source, Eq. (18) may be used in Eq. (24). If the TRA is vertical with sufficient element density and length, then mode orthogonality can be used to simplify the final results (see Kuperman *et al.*, 1998). Thus, for a horizontally-moving source, Eq. (24) becomes

$$\tilde{P}_{\mathrm{TRA}}(\mathbf{r_s}(0),\omega)=\frac{e^{i\omega T_c}}{8\pi\rho(z_s^0)R}\left[\tilde{S}^*(\omega)\sum_{m=1}^{M}\frac{\Psi_m^2(z_s^0)}{k_m}-\left(\nu_s\frac{d\tilde{S}^*(\omega)}{d\omega}\right)\sum_{m=1}^{M}\Psi_m^2(z_s^0)\right], \tag{25}$$

where $r=R$ is the range to the vertical array, while for a vertically moving source it becomes

$$\tilde{P}_{\mathrm{TRA}}(\mathbf{r_s}(0),\omega)=\frac{e^{i\omega T_c}}{8\pi\rho(z_s^0)R}\left[\tilde{S}^*(\omega)\sum_{m=1}^{M}\frac{\Psi_m^2(z_s^0)}{k_m}+\left(i\nu_s\frac{d\tilde{S}^*(\omega)}{d\omega}\right)\times\sum_{m=1}^{M}\frac{1}{k_m}\left(\frac{1}{2}\frac{d\Psi_m^2}{dz}-\frac{\Psi_m^2}{\rho}\frac{d\rho}{dz}\right)_{z=z_s^0}\right]. \tag{26}$$

These equations can be used to analytically assess the sensitivity of time reversal to source motion for harmonic signals when the mode shapes and wave numbers are known. Note that the modal factor in the Doppler term in Eq. (25) is always positive definite, while the same factor in Eq. (26) is composed of terms that may be of either sign. Thus, horizontal source motion should influence time reversal more strongly than vertical source motion at the same speed.

B. Time-reversal process as the optimal matched filter

Stationary TRAs responding to stationary sound sources provide optimal spatial–temporal matched filtering (Kuperman *et al.*, 1998; Roux and Fink, 2000; Tanter *et al.*, 2000). This subsection shows that this concept can be extended to time reversal with moving sources. Here, source motion couples the spatial and temporal variables so the TRA retrofocus reverse traces the trajectory followed by the source during its broadcast. The derivation starts from Eq. (4) for the field $p(\mathbf{r_n},t)$ broadcast by the source and received at the array element locations, $\mathbf{r_n}$,

$$p(\mathbf{r_n},t)=\int_{-\infty}^{+\infty} G(\mathbf{r_n},\mathbf{r_s}(t');t-t')S(t')dt'. \tag{27}$$

To accomplish time reversal, $p(\mathbf{r_n},t)$ is delayed (to ensure causality) and the sign of its time argument is changed before the TRA's transmission. Thus, $p(\mathbf{r_n},T_c-t)$ is broadcast from each element, and the TRA-produced field along an arbitrary listening trajectory $\mathbf{r_f}(t)$ is

$$P_{\mathrm{TRA}}(\mathbf{r_f}(t),t)=\sum_{n=1}^{N}\int_{-\infty}^{+\infty} G(\mathbf{r_f}(t),\mathbf{r_n};t-t'')p(\mathbf{r_n},T_c-t'')dt''. \tag{28}$$

The appropriate matched filter, $C(\tau)$, for P_{TRA} can be constructed as a correlation with $S(-t)$,

$$C(\tau)=\int_{-\infty}^{+\infty} P_{\mathrm{TRA}}(\mathbf{r}_f(t'''),t''')S(\tau-t''')dt'''. \tag{29}$$

The listening trajectory that maximizes $C(\tau)$ is best. To deduce this optimum trajectory, combine Eqs. (27)–(29):

$$C(\tau)=\sum_{n=1}^{N}\int_{-\infty}^{+\infty}\int_{-\infty}^{+\infty}\int_{-\infty}^{+\infty} G(\mathbf{r_f}(t'''),\mathbf{r_n};t'''-t'')\times G(\mathbf{r_n},\mathbf{r_s}(t');T_c-t''-t')S(\tau-t''')\times S(t')dt'\,dt''\,dt'''. \tag{30}$$

This relationship for $C(\tau)$ can be recast as sum of integrals with perfect-square integrands when (i) $C(\tau)$ is evaluated at $\tau=T_c$; (ii) the t'-integration variable is changed, $t'=T_c-\hat{t}$; (iii) spatial reciprocity is used to swap $\mathbf{r_n}$ and $\mathbf{r_f}$ in the first Green's function under the triple integral; and (iv) the arbitrary listening trajectory is chosen to trace the source trajectory backwards at a later time, $r_f(t''')=r_s(T_c-t''')$. With these conditions, Eq. (30) becomes

$$C(T_c)=\sum_{n=1}^{N}\int_{-\infty}^{+\infty}\left[\int_{-\infty}^{+\infty} G(\mathbf{r_n},\mathbf{r_s}(T_c-\hat{t});\hat{t}-t'')\times S(T_c-\hat{t})d\hat{t}\right]^2 dt''. \tag{31}$$

The Cauchy–Schwartz inequality and the form of Eq. (31) ensure that $C(T_c)$ is maximal. Thus, the listening trajectory with the highest correlation occurs on the path that reverse traces the source's broadcast trajectory, and this completes the proof.

The above result also specifies a limitation of time reversal: TRAs can only focus sound back to where it originated; they do not anticipate where an evasive moving source will go next. A TRA will retrofocus the received signal correctly but the retrofocus will occur at a *past* source location because of the time required for sound propagation and signal recording. If the source continues moving after its signal broadcast, the source location at the time of the retrofocus is not necessarily known and the source may not be in the TRA's focal region when the retrofocus forms.

This limitation of time reversal may not always be important. A slowly moving source that broadcasts a short-duration signal at short source–array ranges may still be within the TRA's main lobe at the time of the retrofocus (estimates of TRA retrofocus sizes in waveguides are available in Roux and Fink, 2000; and Kim *et al.*, 2001). TRA aperture shading may be a benign way to achieve focal broadening while maintaining side lobe control. For higher source speeds, longer transmissions, or larger source–array ranges, retrofocusing on the source may require a tracking scheme, and a means for range (Song *et al.*, 1998) and depth (Conti *et al.*, 2002) retrofocus shifting.

IV. NUMERICAL SIMULATIONS

In this section we present numerical results for the pressure field generated by a moving source using Eqs. (6) and (13). The simulations cover horizontal and vertical source motions in range-independent and range-dependent shallow ocean waveguides. Results for signals of variable bandwidth and duration are shown. In all cases, the array is linear and vertical. The sound channel results are based on propagation calculations using the wide-angle parabolic-equation code RAM (Collins, 1993, 1994, 1999) or the normal-mode code KRAKEN (Porter and Reiss, 1984). The computational parameters within RAM were set to ensure reciprocity for both amplitude and phase in the computed pressure fields: eight Padé terms, a range step of at most one wavelength, and a depth step of at most one-thirtieth of a wavelength for each frequency component of the signal. Such parametric choices were similarly conservative for the KRAKEN calculations. Time–domain signals were generated by Fourier superposition of single-frequency results.

A. Signal parameters

The simulated signals were Gaussian-windowed sine waves:

$$S(t)=e^{-t^2/\sigma^2}\sin(\omega_c t), \tag{32}$$

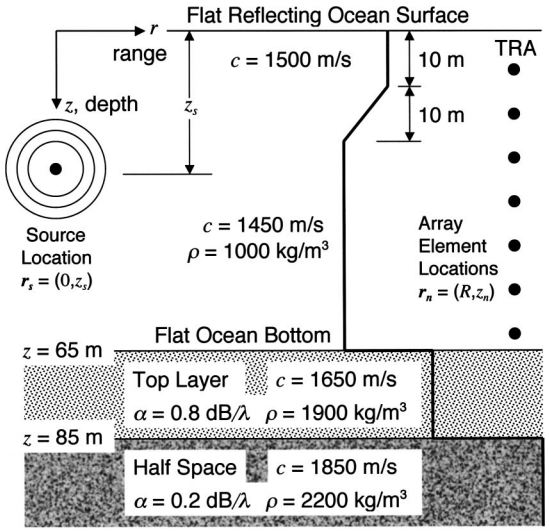

FIG. 1. Computational range-independent shallow water sound channel. Here, ρ=density, α=attenuation coefficient (with λ=wavelength), and c=sound speed and is indicated by the heavier black line.

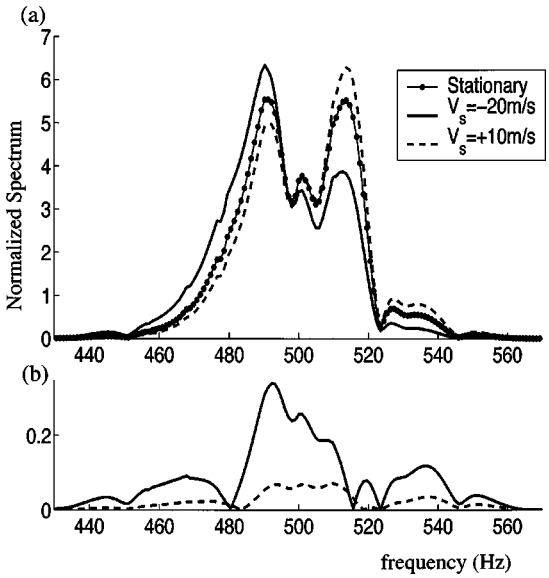

FIG. 2. (a) The received signal spectrum at a source array range of 1 km when the source moves horizontally at a depth of 18 m at speeds of −20, 0, and +10 m/s in the sound channel of Fig. 1. The original source signal is a Gaussian windowed sine wave with a center frequency of 500 Hz and a 99%-energy bandwidth of 64.5 Hz. (b) The difference between the numerical solution plotted in (a) and the first-order approximation provided by Eq. (19) for the same source velocities. The vertical axes for (a) and (b) have the same units.

where σ sets the signal duration of the pulse and $\omega_c = 2\pi f_c$ is the center frequency, with f_c chosen to be 500 Hz for these simulations. Here, the signal bandwidth, $B=(\omega_2 - \omega_1)/2\pi$, is the smallest range of positive frequencies that contains 99% of the signal energy:

$$\int_{\omega_1}^{\omega_2} |\tilde{S}(\omega)|^2 \, d\omega = 0.99 \int_0^{\infty} |\tilde{S}(\omega)|^2 \, d\omega. \tag{33}$$

Similarly, the signal duration, $T_s = t_2 - t_1$, is defined as the smallest time interval that contains 99% of the signal energy:

$$\int_{t_1}^{t_2} S^2(t) dt = 0.99 \int_{-\infty}^{+\infty} S^2(t) dt. \tag{34}$$

The Fourier period for the simulations of single pulses was 0.256 s (a frequency spacing of 3.91 Hz), while for pulse trains it was 1.024 s (a frequency spacing of 0.98 Hz). The window durations were sufficient to contain the sound channel spread signals at the source–array ranges of interest, 1 and 3.072 km. The number of frequencies used in the computations was chosen to fully cover the signal bandwidth B. The single pulse simulations were conducted at four bandwidths: $B=64.5$, 129, 258, and 516 Hz. The pulse train simulations were conducted at $B=258$ Hz.

B. Horizontally moving source in a range-independent environment

The geometry and parameters for the generic range-independent oceanic waveguide used for the simulations are shown in Fig. 1. The channel has a downward refracting sound speed profile, a depth of 65 m, and first bottom layer parameters representative of sand. The range coordinate, r, runs in the horizontal direction, and the vertical z coordinate increases downward and has its origin at the water surface. The speed of sound, bottom layer densities, and bottom attenuation coefficients are all specified in Fig. 1. The array is centered in the sound channel and has 21 elements with 3 m vertical spacing.

The Doppler effect for a source moving horizontally in the Fig. 1 sound channel is illustrated by the signal spectra shown in Fig. 2(a) for speeds of $\nu_s = -20$ m/s and $\nu_s = +10$ m/s. Here, the + implies decreasing source–array range and $r=0$ defines the center of the source trajectory, the source depth is 18 m, and the signal is defined by Eq. (32) with $f_c = 500$ Hz and $\sigma = 40/\omega_c$ ($B=64.5$ Hz). The signal spectra shown in Fig. 2(a) occur at a depth of $z_s^0 = 18$ m and a source–array range of $r=1$ km based on Eq. (13). The Doppler effect is clearly visible and related to the sign of the source velocity but is not a simple frequency shift of the stationary source spectrum in this multipath shallow water sound channel since $BT_r > M$ (Kilfoyle and Baggeroer, 2000) where BT_r is the time–bandwidth product of the signal at the receiver location and $M = \nu_s/c_c = 0.013$ is the Mach Number with $c_c = 1475$ m/s in this case. The absolute difference between the numerical solution plotted in Fig. 2(a) and the first-order approximate solution, given by Eq. (19), for the same source velocities are plotted in Fig. 2(b). The differences are small compared to the peak spectral levels shown in Fig. 2(a). Thus, the first-order approximation shows good agreement (±1%) with the numerical solutions for a source velocity of 10 m/s, and is still reasonably accurate (±5%) for a source velocity of −20 m/s.

Overall the retrofocus field changes produced by source motion are small for realistic source velocities, more than 20 dB below the signal energy peak for $\nu_s = -20$ m/s, as illustrated in Figs. 3 and 4. Figure 3 shows the retrofocused energy, $\int_{-\infty}^{+\infty} |P_{\mathrm{TRA}}(\mathbf{r},t)|^2 \, dt$, in depth versus range coordinates when the TRA is located 1 km from a stationary source at a depth of 18 m, and the broadcast signal is the same as the one used to create Fig. 2. Figure 4 shows the difference in the retrofocused energy distribution in the array's response to

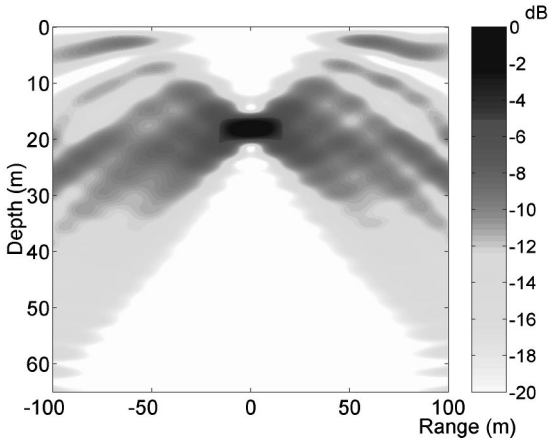

FIG. 3. The TRA retrofocused energy distribution (in dB relative to the peak) in depth versus range coordinates in the Fig. 1 sound channel for a stationary source. The signal and sound channel parameters are the same as for Fig. 2. A cylindrical spreading correction has been made to visually balance the contrast up- and down-range from the source location.

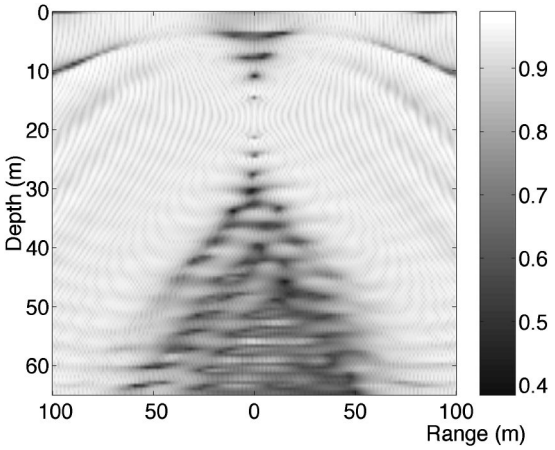

FIG. 5. Spatial distribution of the maximum temporal correlation, $\hat{C}(\mathbf{r_f})$ from Eq. (35), between the retrofocused signal and $S(-t)$ in depth and range coordinates near the retrofocus location when the source is moving horizontally away from the array at a speed of 20 m/s. The signal and sound channel parameters are the same as Fig. 2.

a stationary source and a source moving away from the TRA at $\nu_s=-20$ m/s, normalized by the stationary source retrofocus peak energy and converted to decibels. The low decibel values in Fig. 4 indicate that the retrofocused energy distribution changes little at this source speed. This situation remains true for other source speeds and broadcast-signal durations as long as the signal energy is emitted while the source moves only a small fraction of a center-frequency wavelength (i.e., $T_s\nu_s \ll \lambda_c = c_c/f_c$). Under this condition, the TRA retrofocuses the signal energy correctly along the short source–broadcast trajectory.

Another performance requirement for TRA retrofocusing is that the retrofocused signal at the intended retrofocus location must be well correlated to a time-reversed version of the original signal. This is especially important for potential applications of TRAs in phase-coherent underwater communication. The appropriate correlation, $\hat{C}(\mathbf{r_f})$, can be built by normalizing a stationary-listener version of Eq. (29) and evaluating it at $\tau = T_c$,

$$\hat{C}(\mathbf{r_f}) = \frac{\int_{-\infty}^{+\infty} \tilde{S}(\omega)\tilde{P}_{\mathrm{TRA}}(\mathbf{r_f},\omega)e^{-i\omega T_c}\,d\omega}{\left[\int_{-\infty}^{+\infty}|\tilde{S}(\omega)|^2\,d\omega\right]^{1/2}\left[\int_{-\infty}^{+\infty}|\tilde{P}_{\mathrm{TRA}}(\mathbf{r_f},\omega)|^2\,d\omega\right]^{1/2}}, \tag{35}$$

where $\tilde{P}_{\mathrm{TRA}}(\mathbf{r_f},\omega)$ is defined by Eq. (21) or Eq. (22) and $\mathbf{r_f}$ is stationary. Figure 5 shows the $\hat{C}(\mathbf{r_f})$ field close to the retrofocus location ($r=0$, $z_s^0=18$ m) when the source is moving horizontally at $\nu_s=-20$ m/s, for the same signal pulse and source–array geometry used for Fig. 2. Here the signal correlation is well above 95% throughout most of the field near the TRA retrofocus. For longer pulses and higher source speeds, a stationary listener located at the center of the source track hears an increasingly distorted version of the initial pulse because the source was closer to the array when it started its broadcast and farther from the array when it finished. Consequently, the correlation field values drop but the spatial distribution of the correlation field remains similar to that shown in Fig. 5.

The effect of source motion on the correlation of the retrofocused field can also be predicted using the first-order expansion given by Eq. (25). Figure 6 illustrates this variation of the maximum value of the temporal correlation at the average source broadcast position ($r=0$, $z_s^0=18$ m) for increasing Mach number, for both the direct numerical simulations and the first-order expansion (lines with dots) for the four different signal pulses ($B=516$ Hz with $T_s=4.1$ ms, $B=258$ Hz with $T_s=8.3$ ms, $B=129$ Hz with $T_s=16.5$ ms, and $B=64.5$ Hz with $T_s=32.7$ ms). The correlation of the shortest pulse remains almost constant and near unity for Mach numbers exceeding 0.1, supercavitating torpedo speeds (Ashley, 2001). When the signal pulse is longer, the correlation drops faster with the Mach number because the source track lengthens relative to λ_c. For the highest source speed considered ($M\approx 0.1$), the source moves more than four center-frequency wavelengths during transmission, while for the shortest pulse at the same speed the source moves only half a wavelength. The theoretical first-order predictions (dotted lines) based on Eq. (25) match the direct simulations well up to source speeds of 40 m/s ($M\approx 0.027$,

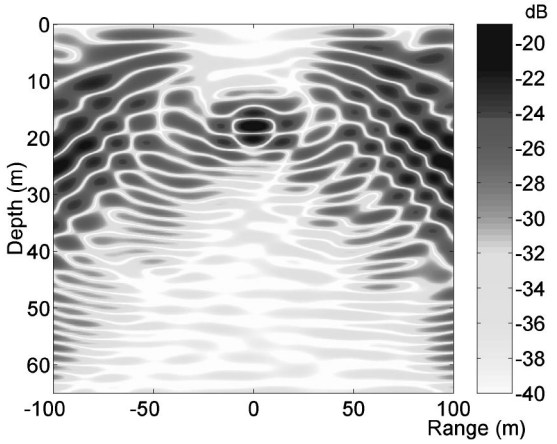

FIG. 4. The difference in TRA retrofocused energy distribution (in dB relative to the peak energy in Fig. 3) between the array's responses to a source moving horizontally away from the array at a speed of 20 m/s and a stationary source. The signal and sound channel parameters are the same as Fig. 2.

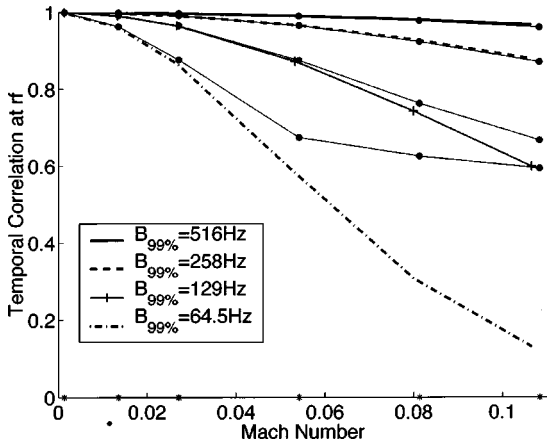

FIG. 6. The maximum temporal correlation, $\hat{C}(\mathbf{r_f})$ from Eq. (35), between the retrofocused signal and $S(-t)$ at the average location of the source during its broadcast versus the Mach number of the source motion for single pulses with different bandwidths from the numerical evaluation of Eq. (23). The sound channel parameters are the same as Fig. 2. The thin lines with the black dots are approximate analytical results from Eq. (25). The *'s on the horizontal axis indicate the Mach numbers at which the calculations were performed.

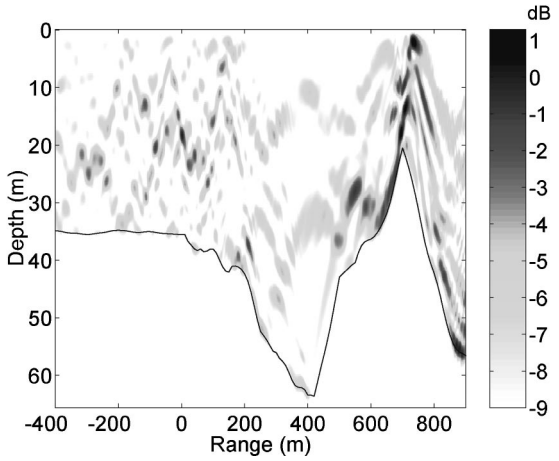

FIG. 7. The TRA retrofocused energy distribution (in dB relative to the retrofocus peak at zero range and 18 m depth) in depth versus range coordinates in a range-dependent sound channel. The signal parameters are the same as for Fig. 2. The source is moving horizontally away from the array at a speed of 20 m/s at a depth of 18 m. The array is linear, vertical, spans the water column, and is located at a range of 1 km, just off the right edge of the figure. The black line marks the bottom contour. A cylindrical spreading correction has been made to visually balance the contrast up- and down-range from the source location.

~80 knots). Therefore, the approximation, Eq. (25), may provide a sufficiently accurate assessment of TRA sensitivity to source motion for nearly all underwater TRA applications.

C. Horizontally moving source in a range-dependent environment

The results presented in this subsection for a range-dependent environment parallel those in the previous subsection. Here, the environment includes a seamount, trench, and plateau added on top of the flat bottom of the Fig. 1 sound channel. At the array location, $r=1$ km, the environment has the same depth, 65 m, bottom properties, and speed of sound profile as the Fig. 1 sound channel. The sound source also has the same depth, 18 m, but now moves in shallower water, ~35 m. The bottom contour, $z=H(r)$, for this range-dependent environment, is shown in Fig. 7 as a black line. Bottom properties for depths shallower than 65 m are similar to those of the top layer of the Fig. 1 sound channel. The speed of sound profile at any range is similar to the speed of sound profile of the Fig. 1 environment but is truncated for depths larger than $H(r)$. To facilitate comparisons, the signal characteristics, source depth, source–array range, and array parameters for the simulations in this environment are the same as those used for Fig. 3.

Figure 7 shows the distribution of the retrofocused energy (in dB relative to the peak energy in Fig. 3) for nearly the whole range between the source and the array with $\nu_s = -20$ m/s. These results were generated using Eq. (13) and RAM calculations. The retrofocus is correctly centered at the initial source location ($r=0$, $z_s^0=18$ m), but sidelobe levels are higher than in the range-independent case. The high-amplitude features near the tip of the sea mount are created by the near-field interference pattern of the array, independently of source motion.

Similarly to the range-independent case, the effects of source motion in the range-dependent environment are illustrated by comparing Fig. 8, which shows the retrofocus generated by a stationary source, and Fig. 9, which displays the difference in the retrofocused energy distribution between a stationary source and a source moving with $\nu_s=-20$ m/s. As in Fig. 4, this energy difference is normalized by the stationary source retrofocus peak energy and converted to decibels. Although the decibel values in Fig. 9 are larger than those in Fig. 4, they do indicate that the retrofocused energy distribution at this source speed remains close to the stationary source case.

The correlation between the retrofocused signal returned to the center of the source track and the time-reversed original signal in the range-dependent environment is shown in Fig. 10 for the same four pulse signals used to generate Fig. 6. At the lowest source speeds, differences in attenuation cause the correlation to be slightly less for the broader-band pulses. Here, the range dependency of the environment causes the acoustic waves to interact more strongly with the

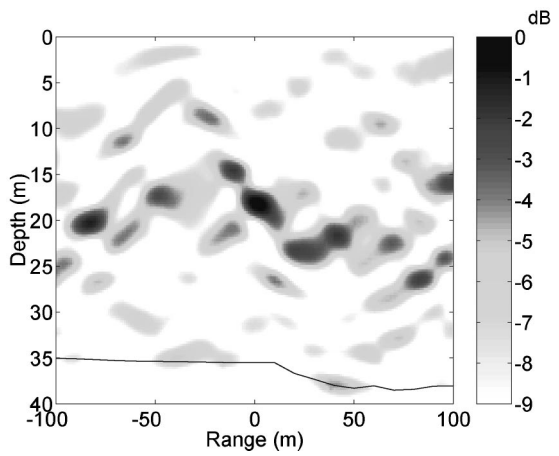

FIG. 8. The same as Fig. 3 for the range-dependent sound channel of Fig. 7. The black line marks the bottom contour.

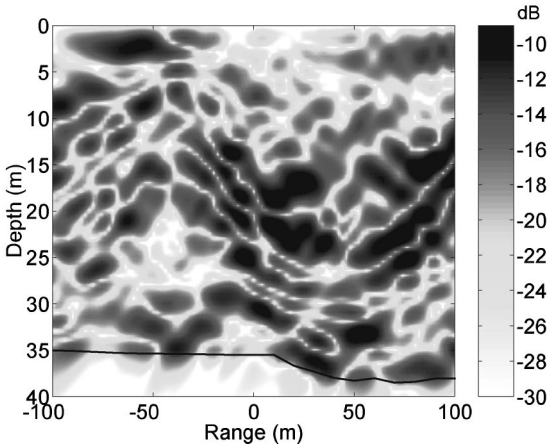

FIG. 9. The same as Fig. 4 for the range-dependent sound channel of Fig. 7 with the dB normalization drawn from the peak energy in Fig. 8. The black line marks the bottom contour.

absorbing bottom, leading to higher attenuation at high frequencies and thereby causing more retrofocus degradation for the shorter (higher bandwidth) pulses. This phenomena implies that an overall positive Doppler frequency shift (source moving closer to the array) will lead to more rapid decorrelation compared to an overall negative Doppler frequency shift (source moving farther from the array) when both sources have the same speed. In addition, these range-dependent-environment results are similar to range-independent ones, in that the correlation of the shorter pulse is the greatest at higher source speeds. However, compared to the range-independent-environment results, the correlation drops faster in the range-dependent environment with increasing source speed when the signal pulse is longer.

D. Vertically moving source in a range-independent environment

In an oceanic time-reversal experiment a tethered or float-suspended source may oscillate vertically because of surface or internal waves. The analysis presented in Sec. II allows the potential importance of such oscillations to be assessed. In this subsection we present TRA simulations for a vertically oscillating source in the range-independent shallow-water sound channel shown in Fig. 1. Only one simple case is considered: sinusoidal vertical motion with amplitude $A_0(=2\ \mathrm{m})$ at a frequency $\omega_0(=5\ \mathrm{rad/s})$ centered around an average source position of $z_s^0=15\ \mathrm{m}$ (within the thermocline). These chosen parameters correspond to an extreme case of large and rapid oscillations (peak source velocity of 10 m/s) to test the robustness of time reversal to vertical source motion.

For the shallower source, the main results are illustrated in Figs. 11 and 12. Figure 11 shows a close-up of the distribution of the retrofocused signal energy for a stationary shallow source. Figure 12 displays the signal-energy difference between the stationary and a vertically oscillating source. Here, the signal is a sequence of 38 equally spaced Gaussian-windowed sine pulses with $f_c=500\ \mathrm{Hz}$ and $B=258\ \mathrm{Hz}$ [see

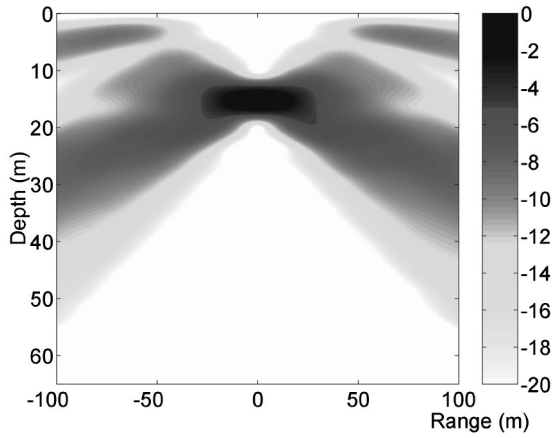

FIG. 11. The TRA retrofocused energy distribution (in dB relative to the retrofocus peak at zero range and 15 m depth) in depth versus range coordinates in the Fig. 1 sound channel for a stationary source at a depth of 15 m. A cylindrical spreading correction has been made to visually balance the contrast up- and down-range from the source location. The array is linear, vertical, spans the water column, and is located at a range of 3.072 km. The signal is a pulse train of 38 Gaussian-windowed sine pulses with a center frequency of 500 Hz and a 99% energy bandwidth of 258 Hz [see Fig. 13(a)].

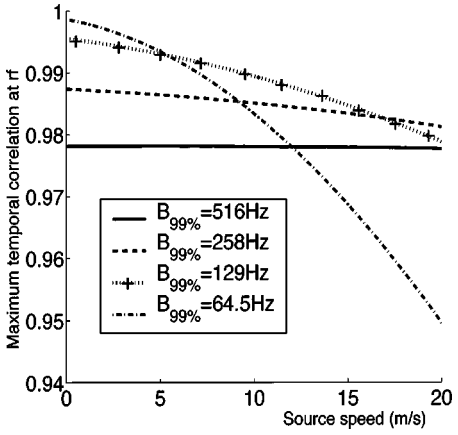

FIG. 10. Maximum temporal correlation, $\hat{C}(\mathbf{r}_f)$ from Eq. (35), between the retrofocused signal and $S(-t)$ at the average location of the source during its broadcast versus the source speed for single pulses with different bandwidths from numerical evaluation of Eq. (23) in the range-dependent sound channel of Fig. 7.

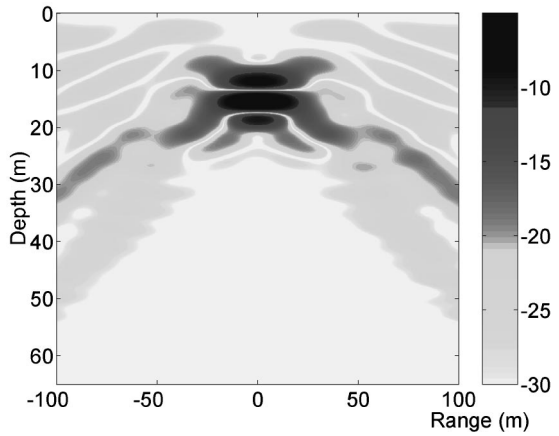

FIG. 12. The difference in the TRA retrofocused energy distribution (in dB relative to the peak energy in Fig. 11) between the array's responses to a source oscillating vertically (amplitude=2 m, oscillation frequency=5 rad/s) about an average depth of 15 m and a stationary source. The signal, array, and sound channel parameters are the same as for Fig. 11.

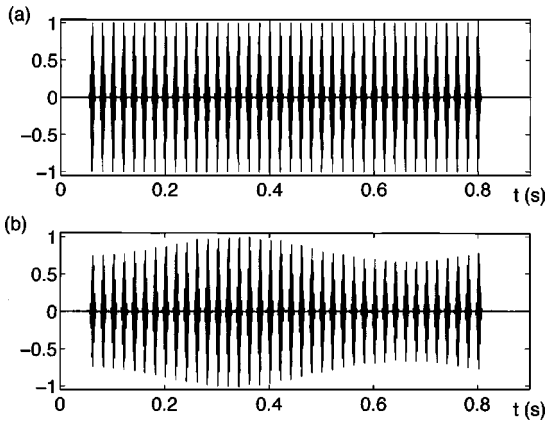

FIG. 13. (a) The pulse train broadcast by the source. (b) A retrofocused signal at the average source position (zero range, 15 m depth) when the source oscillates vertically as in Fig. 12. The array, and sound channel parameters are the same as for Fig. 11.

Fig. 13(a)]; the TRA is vertical, linear, and located at $r = 3072$ m; and signal energies are normalized by the retrofocus peak energy value in Fig. 11. Figure 12 shows that the TRA retrofocuses energy correctly despite the rapid oscillations of the source in the thermocline. The main change from the stationary source case is a slight broadening of the focal spot due to the spatial extent of the oscillating source trajectory during the pulse train broadcast. A time–domain comparison between the broadcast signal sequence and the received signal sequence at the average location of the source is shown in Fig. 13. The primary difference between these signals is ± 2 dB amplitude modulation in the case of the oscillating source [see Fig. 13(b)].

When the source is placed in the lower half of the sound channel (not shown), the retrofocus is slightly louder, larger, and less sensitive to source motion than the shallow source case illustrated in Figs. 11–13. The decreased sensitivity to source motion deeper in the sound channel comes from the deeper source more strongly exciting the lower-order modes that are less attenuated and have broader antinodes.

V. SUMMARY AND CONCLUSIONS

In this paper we describe the results of theoretical and numerical investigations of time-reversing array performance in a shallow ocean sound channel with a moving source. The four main conclusions drawn from this study are presented and discussed below.

First of all, the limitations imposed on TRA performance by source motion can be understood in terms of the distance that the source travels during the signal broadcast compared to the center-frequency acoustic wavelength of the signal. When the source path covers a tiny fraction of a wavelength, TRA performance will be essentially identical to that with a stationary source. When the source covers several wavelengths, the TRA retrofocus will move backwards over the source track so that any stationary receiver will record a distorted signal compared to the stationary source case. This effect may be important for synchronization and demodulation in underwater communication systems. Fortunately, at least for underwater applications where the speed of sound is approximately 1500 m/s, the parametric range where source motion clearly becomes important lies somewhat beyond the propulsion speed limit for most underwater vehicles. However, when the source moves rapidly, it may easily pass beyond the edges of the TRA retrofocus main lobe by the time the signal has traveled to, and returned from, the TRA. Thus, time reversal alone is unlikely to provide a means for tracking or illuminating evasive high-speed sources, but it may be part of an overall solution involving other technologies.

Second, the simple approximations given by Eq. (17) and the subsequent expressions, Eqs. (25) and (26), can provide accurate assessments of TRA sensitivity to source motion for nearly all underwater TRA applications with a moving source when the environment is range independent or nearly so. The accuracy of these approximations increases as the source velocity decreases.

Third, TRA performance is more strongly influenced by source motion in range-dependent sound channels than in range-independent ones. This is clearly an effect of enhanced sound interaction with the bottom in the simulations presented here.

And, finally, the time-reversal process in a shallow water sound channel appears to be robust to both horizontal and vertical source motions, even for a source moving in the thermocline.

ACKNOWLEDGMENT

The research was sponsored by the Ocean Acoustics Program of the Office of Naval Research under Grant No. N00014-96-1-0040.

Ashley, S. (**2001**). ''Warp drive underwater,'' Sci. Am. **283**, 70–79.
Chen, H.-Y., and Lu, I.-T. (**1992**). ''Matched-mode processing schemes of a moving point source,'' J. Acoust. Soc. Am. **92**, 2039–2050.
Clark, J. G., Flanagan, R. P., and Weinberg, N. L. (**1976**). ''Multipath acoustic propagation with a moving source in a bounded deep ocean channel,'' J. Acoust. Soc. Am. **60**, 1274–1284.
Collins, M. D. (**1993**). ''A split-step Padé solution for parabolic equation method,'' J. Acoust. Soc. Am. **93**, 1736–1742.
Collins, M. D. (**1994**). ''Generalization of the split-step Padé solution,'' J. Acoust. Soc. Am. **96**, 382–385.
Collins, M. D. (**1999**). ''The stabilized self-starter,'' J. Acoust. Soc. Am. **106**, 1724–1726.
Conti, S., Roux, P., and Fink, M. (**2002**). ''Depth and range shifting of a focal spot using a time-reversal mirror in an acoustic waveguide,'' Appl. Phys. Lett. **80**, 3647–3649.
Dowling, D. R. (**1993**). ''Phase-conjugate array focusing in a moving medium,'' J. Acoust. Soc. Am. **94**, 1716–1718.
Edelmann, G. F., Akal, T., Hodgkiss, W. S., Kim, S., Kuperman, W. A., and Song, H. C. (**2002**). ''An initial demonstration of underwater acoustic communication using time reversal,'' IEEE J. Ocean. Eng. **27**, 602–609.
Hawker, K. E. (**1979**). ''A normal mode theory of acoustic Doppler effects in the oceanic waveguide,'' J. Acoust. Soc. Am. **65**, 675–681.
Heinemann, M., Larraza, A., and Smith, K. B. (**2003**). ''Experimental studies of applications of time reversal acoustics to noncoherent underwater communications,'' J. Acoust. Soc. Am. **113**, 3111–3116.
Howell, K. J., Jacobson, M. J., and Siegman, W. L. (**1993**). ''Parabolic approximation predictions of underwater acoustic effects due to source and receiver motions,'' J. Acoust. Soc. Am. **94**, 293–301.
Jackson, D. R., and Dowling, D. R. (**1991**). ''Phase-conjugation in underwater acoustics,'' J. Acoust. Soc. Am. **89**, 171–181.
Jacyna, G. M., Jacobson, M. J., and Clark, J. G. (**1976**). ''General treatment of source motion on the total acoustic field with application to an isospeed channel,'' J. Acoust. Soc. Am. **60**, 815–824.

Jensen, F. B., Kuperman, W. A., Porter, M. B., and Schmidt, H. (**1994**). *Computational Ocean Acoustics* (American Institute of Physics Press, Woodbury, NY), pp. 86–90, 272–275.

Kilfoyle, D. B., and Baggeroer, A. B. (**2000**). ''The state of the art in underwater acoustic telemetry,'' IEEE J. Ocean. Eng. **25**, 4–27.

Kim, S., Edelmann, G. F., Kuperman, W. A., Hodgkiss, W. S., Song, H. C., and Akal, T. (**2001**). ''Spatial resolution of time-reversing arrays in shallow water,'' J. Acoust. Soc. Am. **110**, 820–829.

Kuperman, W. A., Hodgkiss, W. S., Song, H. C., Akal, T., Ferla, C., and Jackson, D. R. (**1998**). ''Phase-conjugation in the ocean: experimental demonstration of an acoustic time reversal mirror,'' J. Acoust. Soc. Am. **103**, 25–40.

Lai, Y.-S., and Makris, N. C. (**2003**). ''Spectral and modal formulations of the Doppler-shifted field scattered by an object moving in a stratified medium,'' J. Acoust. Soc. Am. **113**, 223–244.

Lim, P. H., and Ozard, J. M. (**1994a**). ''On the underwater acoustic field of a moving point source. I. Range-independent environment,'' J. Acoust. Soc. Am. **95**, 131–137.

Lim, P. H., and Ozard, J. M. (**1994b**). ''On the underwater acoustic field of a moving point source. II. Range-dependent environment,'' J. Acoust. Soc. Am. **95**, 138–151.

Lingevitch, J. F., Song, H. C., and Kuperman, W. A. (**2002**). ''Time reversed reverberation focusing in a waveguide,'' J. Acoust. Soc. Am. **111**, 2609–2614.

Morse, P. M., and Ingard, K. U. (**1968**). *Theoretical Acoustics* (Princeton University Press, Princeton, NJ), pp. 715–731.

Neubert, J. A. (**1977**). ''The effect of Doppler on long-range sound propagation,'' J. Acoust. Soc. Am. **62**, 1404–1411.

Pierce, A. D. (**1989**). *Acoustics* (AIP Press, Woodbury, NY), pp. 163–165, 177–183.

Porter, M., and Reiss, E. L. (**1984**). ''A numerical method for ocean-acoustic normal modes,'' J. Acoust. Soc. Am. **76**, 244–252.

Rouseff, D., Jackson, D. R., Fox, W. L. J., Jones, C. D., Ritcey, J. A., and Dowling, D. R. (**2001**). ''Underwater acoustic communication by passive phase conjugation: theory and experimental results,'' IEEE J. Ocean. Eng. **26**, 821–831.

Roux, P., and Fink, M. (**2000**). ''Time reversal in a waveguide: Study of the termporal and spatial focusing,'' J. Acoust. Soc. Am. **107**, 2418–2429.

Sabra, K. G. (**2003**). ''Broadband performance of time reversing arrays in shallow water,'' Ph.D. thesis (University of Michigan, Ann Arbor, MI).

Sabra, K. G., and Dowling, D. R. (**2003a**). ''Broadband performance of a moving time reversing array,'' J. Acoust. Soc. Am. **114**, 1395–1405.

Sabra, K. G., and Dowling, D. R. (**2003b**). ''Effect of ocean currents on the performance of a time reversing array in shallow water,'' J. Acoust. Soc. Am., to appear.

Schmidt, H., and Kuperman, W. A. (**1994**). ''Spectral and modal representations of the Doppler-shifted field in ocean waveguides,'' J. Acoust. Soc. Am. **96**, 386–395.

Smith, K. B., Abrantes, A. A., and Larraza, A. (**2003**). ''Examination of time-reversal acoustics and applications to noncoherent underwater communications,'' J. Acoust. Soc. Am. **113**, 3095–3110.

Song, H. C. (**1993**). ''Performance bounds for passively locating a moving source of a known frequency in oceanic waveguide using a vertical array,'' IEEE J. Ocean. Eng. **18**, 189–198.

Song, H. C., and Baggeroer, A. B. (**1990**). ''The resolution of modal Doppler shifts in a dispersive oceanic waveguide,'' J. Acoust. Soc. Am. **88**, 268–282.

Song, H. C., Kuperman, W. A., and Hodgkiss, W. S. (**1998**). ''A time-reversal mirror with variable range focusing,'' J. Acoust. Soc. Am. **103**, 3234–3240.

Tanter, M., Thomas, J. L., and Fink, M. (**2000**). ''Time reversal and the inverse filter,'' J. Acoust. Soc. Am. **108**, 223–234.

Yang, T. C. (**2003**). ''Temporal resolutions of time-reversal and phase conjugation for underwater acoustic communications,'' IEEE J. Ocean. Eng. **28**, 229–245.

High-frequency scattering from saturated sand sediments

Charles F. Greenlaw,[a] D. V. Holliday, and Duncan E. McGehee
BAE SYSTEMS, Applied Technologies, Inc., 4669 Murphy Canyon Road, Suite 102, San Diego, California 92123

(Received 30 September 2003; revised 13 February 2004; accepted 23 February 2004)

Measurements of bottom scattering strengths were made with a multi-frequency echo sounder mounted on a tower on a sandy bottom off West Destin, FL. Data were measured at five frequencies in the range 265–1850 kHz, at subcritical grazing angles ranging from 9° to 20° and at azimuths up to ±90° around the tower. Scattering strength increased at about $f^{1.4}$ up to >400 kHz, peaked between 700 and 1100 kHz, and decreased at higher frequencies. © *2004 Acoustical Society of America.* [DOI: 10.1121/1.1707085]

PACS numbers: 43.30.Gv, 43.30.Ma, 43.20.Fn, 43.20.Px [SLB] Pages: 2818–2823

I. INTRODUCTION

Reported measurements of bottom scattering are largely confined to low (hundreds of Hz up to 300 kHz) frequencies.[1–8] Relatively few measurements of bottom scattering strengths in higher frequency ranges have been reported.[9] The general consensus of these and other field studies of bottom scattering includes the following: (1) bottom scattering generally follows a Lambert's rule form of dependence upon grazing angle; (2) for sand bottoms, scattering strength tends to increase with frequency at f^k, where $1<k<2$; (3) within the broad classifications of silt, sand, gravel, and rock, there is little or no correlation with mean particle size; and (4) at shallow grazing angles and for frequencies above about 10 kHz, backscattering is primarily controlled by surface roughness and sound penetration into the sediment decreases with increasing frequency.

A multi-investigator experiment was conducted in 1999 to examine anomalous acoustic penetration into a near-shore sandy sea bottom (Sediment Acoustics Experiment, SAX-99[10,11]). During this experiment, the opportunity was taken to obtain acoustic backscattering data from a well-characterized shallow sandy bottom at frequencies from 265 kHz to 1.85 MHz. The results of this experiment are reported here.

II. FIELD EXPERIMENT

The SAX-99 experiment was conducted approximately 2 km offshore of West Destin, FL during October–November of 1999.[10,11] The research vessel R/V Seward Johnson was moored in 18–19 m of water over a medium sand bottom, providing a platform and power to support several experiments simultaneously.

A small (3.5 m high) tower was deployed on the bottom in the near vicinity of APL/UW's Benthic Acoustic Measurement System.[10,12,13] A pan-tilt mechanism on this tower mounted an 8-frequency echo integrator system (TAPS-8) previously developed for bioacoustics research.[14–17] The TAPS-8 used eight separate piston transducers driven by individual transceivers to measure acoustic backscattering intensities at discrete frequencies from 104 to 3000 kHz. Beamwidths were similar at 6°–8° (half-power). An imbedded computer, responding to external commands, controlled transmissions and digitized the detected echo envelopes to 12 bit resolution, computing and storing the mean-squared echo profiles internally. Cables for power and data transfer led from the tower and TAPS-8 to the ship.

TAPS-8 was originally designed to measure volume scattering strengths from zooplankton distributions. The channel gains were reduced for this experiment based upon estimates of the bottom scattering strength from previous measurements in this general area at lower frequencies (M. Richardson, private communication) and the unit recalibrated. The gains of the two lowest channels (104 and 165 kHz) were reduced to the point that backscattering data had very low signal-to-noise ratio. They are not included in the data presented here. The highest-frequency channel (3 MHz) similarly did not have sufficient signal levels to permit estimation of bottom scattering strengths, in part due to the high absorption over the ranges involved. The data presented here range in frequency from 265 to 1850 kHz.

A computer located aboard ship controlled both the pan-tilt mechanism and the TAPS-8. Scripts were written to control data collection: ordering the pan-tilt to specified azimuths and depression/elevation angles (DE) and commanding TAPS-8 to measure and average acoustic backscattering intensity profiles over a selected number of pings. Transmitted pulse lengths were fixed at 336 μs and echo envelope values were sampled at 84 μs intervals, giving 4 samples per pulse length. The number of samples per ping could be varied, changing the maximum range, depending upon the depression angle. For the data presented here (DE $=-15°$), 480 samples per ping were recorded for approximately 31 m of range extent. Echo amplitude samples were squared and summed into sequential range bins. Subsequent scaling and division by the number of pings produced the mean backscattered intensity versus range.

Sound speed was computed from CTD casts at the ship and the value at the bottom was used to compute actual ranges from the time intervals between samples. Similarly, the bottom water temperature and salinity measured by the periodic CTD casts from the ship were used to compute ab-

[a]Electronic-mail: charles.greenlaw@baesystems.com

 0001-4966/2004/115(6)/2818/6/$20.00 © 2004 Acoustical Society of America

sorption coefficients. Spreading and absorption corrections were applied to the data in post-processing.

Some 35 scans of the bottom were made with TAPS-8 over a 24 day period (17 October–10 November). With few exceptions, all data were taken during daylight hours. Most of the scans ensonified a $\pm 45°$ azimuthal swath at 5° increments. Depression angles included 15°, 20°, 25°, and 30°. The data from the 15° depression angle sets provided the largest range of grazing angles and are the data analyzed here.

A. Environmental factors

The weather was generally benign during the experiment except for a few days at the end of October where the wind speed forecasts exceeded the safe limits for the ship in its moored configuration. The ship cast off from the moorings on 30 October, returning on 3 November.

The bottom consisted of a large expanse of well-sorted medium sand with a mean surficial grain size of 1.27 ϕ (0.41 mm diameter) and a mean porosity of 36.6%.[11] Sediment sound speeds were in the range of 1.14–1.16 times the bottom seawater sound speed, which averaged about 1530 m/s. Calculations of the critical angle, presuming the water-saturated sand bottom acted as a fluid half-space, were approximately 28°–32°.

The bottom topography was initially characterized as consisting of irregular, sharp-crested ripples. Over the duration of SAX99, these ripples were eroded by hydrodynamic and biological processes. At the end of the experiment, the bottom topography consisted largely of a relatively smooth bottom cratered with pockmarks created by fish foraging on the bottom fauna. The spectrum of wave heights obtained from stereo photographs had a steep slope, indicating a lack of high-spatial-frequency wave structure. The wind event that caused the ship to depart restored the initial ripple conditions briefly but the effects of currents and fish foraging were observed very shortly thereafter.[11]

B. Data analysis

A typical echo from the TAPS-8 is shown in Fig. 1. Each such profile was obtained by summing echo intensity samples in fixed range bins over 24 pings. Incoherent processing is ideal for volume scattering measurements, the original purpose of the TAPS-8. Although most of the historical measurements of bottom scattering have used incoherent processing, the current trend in measuring bottom scattering strengths is to average echo wave forms to extract the coherent part of the scattering; incoherent scattering represents a noise signal and tends to cancel over several ping cycles. If random scatterers such as fish are present, incoherent summation of echoes can lead to bias errors in the sum. Fish were attracted to the tower, thus the potential existed that the TAPS-8 data could overestimate the actual bottom scattering strengths. Practical measurements of bottom scattering taken from a moving platform, such as an AUV, might not be processed coherently, however, so the sort of measurements taken in this field experiment are representative of many realistic remote sensing applications.

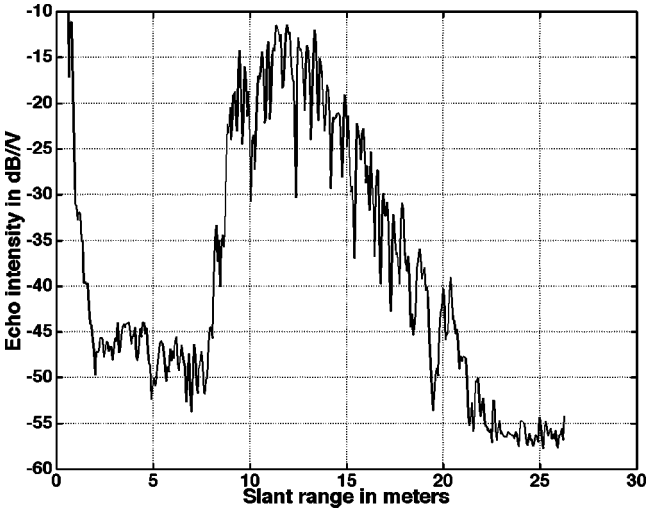

FIG. 1. Echo intensity vs range at 700 kHz for a depression angle of $-15°$. This profile is an average of echo intensities over 24 successive pings. The peak at about 2.5 m range is probably volume reverberation from the fish that were attracted to the tower. Some of the variability in the echo structure may also be due to interference from fish; most is thought to arise from bottom relief due to the high spatial resolution of the acoustic system, which was comparable to the scales of the sand ripple structure.

A video camera co-located with the TAPS-8 made it abundantly clear that fish were attracted to the tower. The scattering at short range in Fig. 1 is undoubtedly largely due to fish since the acoustic pulse cannot reach the bottom until a range of 3.5 m (the height of TAPS-8 above the bottom). Fish were observed feeding on the bottom and, in fact, were determined to be a significant contributor to the erosion of sand waves created by storm events. It is therefore reasonable to ascribe some of the variability in the echo intensity to interference from fish. Other sources of variability, such as sound speed inhomogeneities in the water column, are thought to be negligible in relation to these fluctuations.

Several sets of data were collected with the possibility of volume scattering contamination in mind, recording eight repetitions of the 24-ping averages at fixed azimuths and depression angles to estimate the impact of fish on the bottom scattering data. Over-plotting the echo intensities made it clear that many of the fluctuations were deterministic, i.e., resulting from features on or in the bottom. Moreover, the relatively high spatial resolution of this acoustic system ($\sim 0.4\ \mathrm{m}^2$ effective ensonified area at the intersection of the MRA with the bottom) would be expected to generate more fluctuation in the echo data than might be produced by a wider-beam or longer-pulse-length system.

By comparing echo data sets with the video recordings, a subset of data were selected that appeared to be largely unaffected by fish. Out of 35 data sets covering a 14 day period, 25 were selected for further processing.

Data processing proceeded in two ways. For some data sets we used the sonar equation (adapted from Urick[18]):

$$\mathrm{EL} = (\mathrm{SL} + \mathrm{RS} + G) - 40\log(r) - 2\alpha r + S_s + 10\log(\Phi), \tag{1}$$

where

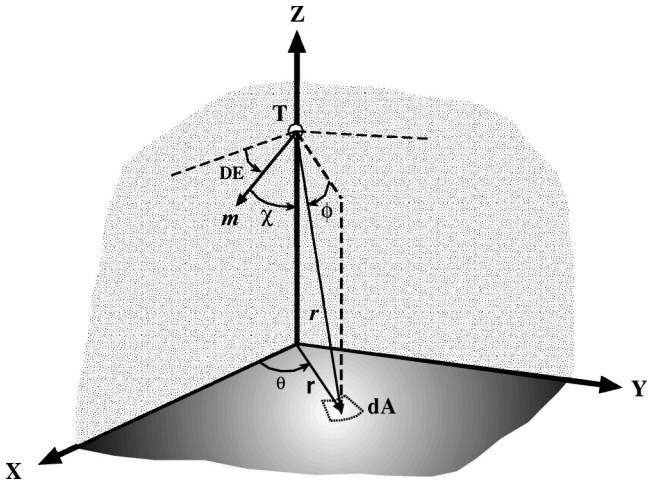

FIG. 2. Geometry for bottom reverberation. **r** is the vector from the transducer to the area element dA on the circular annulus ensonified at time t. **m** is the unit vector in the $X-Z$ plane describing the MRA of the transducer, T, which is depressed in elevation by the angle DE. χ is the angle between **r** and **m**, the angle needed to calculate the value of the (circularly symmetric) beam pattern function in the direction of the differential area element on the bottom.

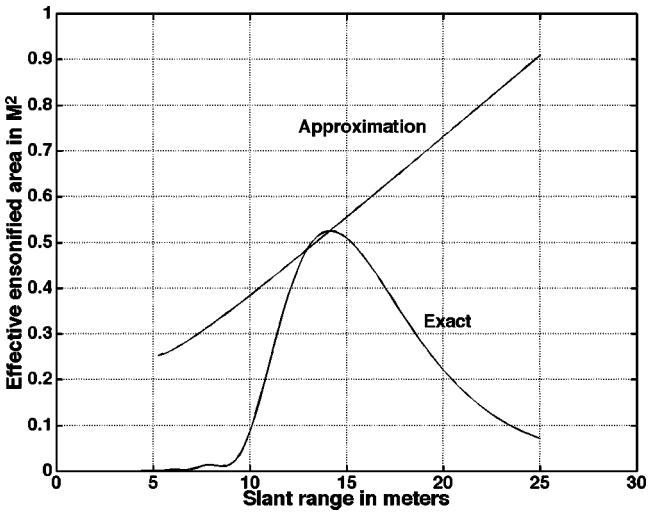

FIG. 3. Effective ensonified areas for a typical TAPS-8 piston transducer at a depression angle of $-15°$ comparing the integral equation for the area with the approximate formula. Note that the effective ensonified areas agree only in a limited region, at the point where the MRA strikes the bottom. The ensonified areas are also relatively small, even in the region of the main lobe. The horizontal dimensions of the effective ensonified area are comparable to or smaller than the wavelength of the sand ripples at this site (70 cm). The likely range of useful data for this transducer and geometry extends from about 10 to 22 m, corresponding to grazing angles of 20° to 9°.

$$\Phi = \int b^2(\theta,\phi)\,dA \tag{2}$$

and EL is the measured echo level in dB‖V_{rms}, SL+RS+G is the system response (source level+receiving sensitivity +gain) in dB, r is the slant range in meters, α is absorption in dB/m, S_s is the bottom scattering strength in dB, $b(\theta,\phi)$ is the one-way directivity function (intensity versus off-axis angles θ,ϕ) for the transducer, and Φ is the effective ensonified area on the bottom. The area integral is over a circular annulus with center below the transducer and at the slant range r (see Fig. 2). For symmetric transducers, such as the circular piston elements used here, this integral can be approximated by[18]

$$\Phi = \frac{c\tau}{2} r \int_{-\pi}^{\pi} b^2(\chi)\,d\varphi, \tag{3}$$

where c is the sound speed, τ is the pulse length, b is now a function of only one angle, χ, which is the angle between the major response axis (MRA) of the transducer and the vector from the transducer to the differential area, dA, on the bottom at angle φ and range r. The cosine of the angle χ can be found from the dot product of the vector **r**, pointing to the differential area on the bottom, and **m**, a unit vector pointing along the MRA of the transducer. The result is

$$\cos(\chi) = \frac{\sqrt{r^2-H^2}\cos(\varphi)\cos(\mathrm{DE}) + H\sin(\mathrm{DE})}{r}, \tag{4}$$

which is a function of the range, r, and depression angle DE (which is negative in this instance) and the height off the bottom, H. An example of the effective ensonified area obtained from numerical integration of the area integral is shown in Fig. 3.

The sonar equation can be solved for S_s as

$$S_s = \mathrm{EL} - (\mathrm{SL}+\mathrm{RS}+G) + 40\log(r) + 2\alpha r - 10\log(\Phi) \tag{5}$$

or

$$S_s = \mathrm{EL} - (\mathrm{SL}+\mathrm{RS}+G) + 40\log(r) + 2\alpha r - 10\log\left(\frac{c\tau}{2} r\right) - 10\log(X), \tag{6}$$

where X denotes the beam pattern integral in Eq. (3). This solution is valid for any geometry and (symmetric) beam pattern function. In practice, however, plausible values are seldom recovered from the sidelobe region so estimates of S_s are limited to the region scanned by the main lobe (10–22 m in the example, Fig. 3).

Alternatively, one can limit the region of interest to only that portion of the bottom where the grazing angle is approximately equal to the transducer depression angle—the intersection of the MRA with the bottom. In this case, the effective ensonified area can be approximated by[4,7,9]

$$\Phi \approx \frac{c\tau}{2} r \phi_H \sec(\theta_g), \tag{7}$$

where ϕ_H is the effective transducer beam width (in radians) and θ_g is the grazing angle ($\approx -\mathrm{DE}$). This function is also plotted in Fig. 3. It can be seen that this approximation is only useful in a limited region around the point of intersection of the MRA with the bottom. It is, however, much simpler and quicker to calculate than the integral expression. These data were processed using both of these methods.

Backscattering from the seabed often approximately follows Lambert's rule for diffuse surfaces, which postulates backscattering to be proportional to the square of the sine of the grazing angle,[2,18] viz.

$$S_s = 10\log\mu + 10\log(\sin^2\theta_g). \tag{8}$$

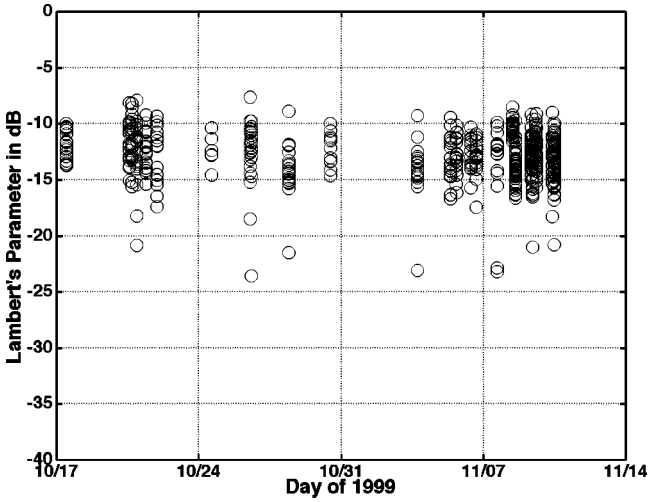

FIG. 4. Estimates of Lambert's parameter measured at 1100 kHz over the duration of the SAX99 experiment. Individual points are estimates at a depression angle of $-15°$ and at various azimuths calculated using the approximate area method. The data gap following 10/31/99 marks the storm event that caused the ship to leave the test area. All but two data sets were obtained during daylight hours.

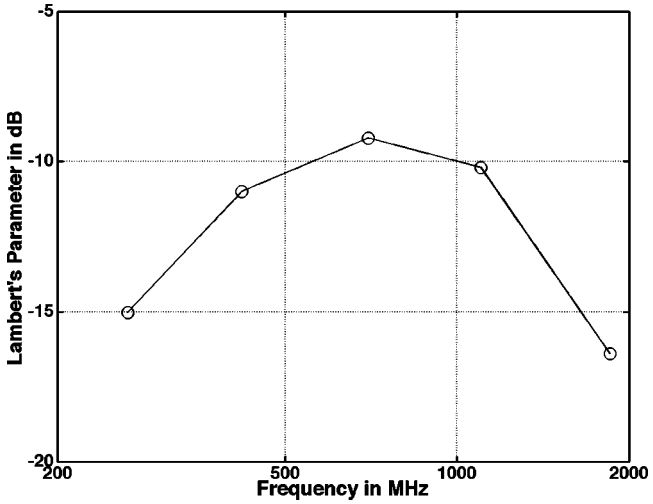

FIG. 5. Mean values of measurements of Lambert's parameter vs frequency from a repetitive series at four azimuths using the sonar equation method to extract Lambert's Parameter over the range of grazing angles. Data are from a single day: 8 November 1999. Numbers of data points in these averages range from 2976 at the low frequencies to 1488 at the highest frequency.

If this sine-squared dependence is removed from the bottom scattering strength estimate, S_s, the scattering strength reduces to a single parameter independent of grazing angle. MacKenzie[2] simply refers to this term as $10 \log \mu$. Boehme and Chotiros[6] call it the mean normalized backscattering strength. It will be referred to here as Lambert's parameter. Since the grazing angles covered by TAPS-8 range over $9°-20°$, where Lambert's rule is often found to apply, the field experiment results have been converted to this measure. Note also that all of these data are for grazing angles below the critical angle (approximately $28°-32°$).

C. Field experiment results

Preliminary inspection of the bottom scattering data involved quickly estimating Lambert's parameter for the entire data set to get a sense for the degree of variability encountered over space and time. One such result is shown in Fig. 4 where individual point estimates of Lambert's parameter at 1100 kHz at the various azimuths are plotted versus time. The spread of data versus azimuth in this data set is 5 dB or so but there is no obvious trend over time. This was true for all frequencies examined.

A special data set taken with high azimuthal resolution was examined as well, using the exact areal calculation to obtain a larger number of data points. Areal variability tended to be somewhat higher than that shown in Fig. 4 (see Fig. 15 in Thorsos *et al.*[10]).

Data from a repetitive series were analyzed using the sonar equation method. These data consisted of 8 replicates of 24 pings each at depression angle of $-15°$ and four azimuths ($-25°$, $-20°$, $-15°$, and $-10°$). By repeating the measurements at fixed azimuths over time, it was hoped that the effects of scattering from fish would be reduced when the data were averaged. The results of this analysis are summarized in Fig. 5. This plot shows both the mean values and 99% confidence interval. It should be noted that different numbers of points were averaged at each frequency as the range interval over which the signal-to-noise ratio was adequate tended to decrease with frequency. Examination of these estimates of Lambert's parameter versus slant range showed no consistent trends with range, suggesting that the assumption of Lambert's law scattering was valid for this range of grazing angles.

Historical data for backscattering from sandy bottoms are available in the literature[3,6] and suggest that the frequency dependence of Lambert's parameter varies from f^0 to $f^{1.5}$. Most data are for frequencies from 1 to 200 kHz. Comparable data on sandy bottoms were extracted from published studies and corrected for grazing angles where necessary. These historical values are compared to the present results in Fig. 6. It can be seen that the new high-frequency data are consistent with historical measurements at low fre-

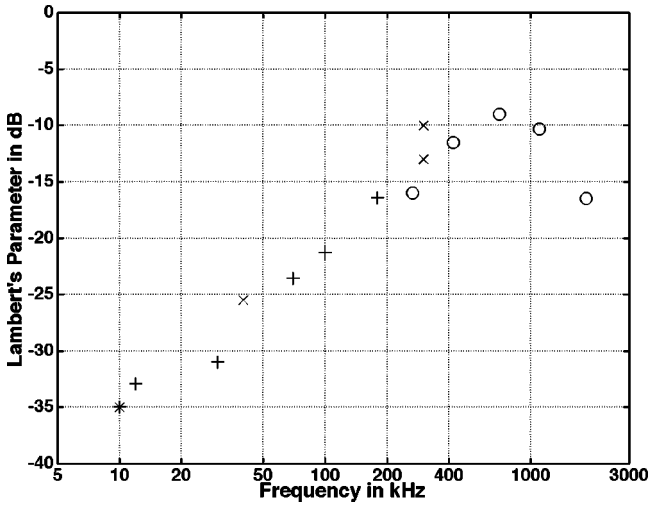

FIG. 6. Mean values of Lambert's parameter vs frequency for similar sandy seabeds. Data key: (○) these data; (×) BAMS data from SAX-99 (K. Williams, private communication); (*) Muir, as reported by Boehme and Chotiros—Ref. 6; (+) medium sand data from McKinney and Anderson (Ref. 3). The TAPS-8 data are those of Fig. 4.

quencies but exhibit a resonance-like behavior at the higher frequencies.

III. DISCUSSION

Williams *et al.*[19] measured high-frequency broad-band scattering from beds of glass beads and sand in the laboratory. This work found the spectral peaks to be approximately related to grain size. Data from glass beads showed spectral peaks around $ka=1$ (where a is the mean grain radius and k is the wave number) while the sand data peaked at about $ka=0.73$ (1.1 MHz peak for sand of mean diameter 0.32 mm). The sand grain sizes for the SAX99 field experiment were somewhat larger (0.40–0.42 mm diameter). Scaling from the Williams *et al.* laboratory data predicts a peak in scattering for the field data at around 825–860 kHz, consistent with the observed peak in the TAPS-8 field data between 700 and 1100 kHz.

Models for scattering from individual sand grains[20–22] tend to peak at values of $ka\approx 2.5-3$. For the sand in this experiment, this would imply a peak in backscattering at about 2.9–3.5 MHz, above the frequency range of the field measurements. These models are useful only for volume scattering from relatively diffuse concentrations of sand particles, however, and are not directly applicable to dense layers of sand grains as found on the ocean bottom.

A more likely explanation might be a transition from large-scale roughness caused by sand waves and bioturbation to a roughness regime produced by the shapes and sizes of the sand grains themselves. The wavelength at the (inferred) peak scattering frequency was about 1.74 mm, which is of the order of the mean grain size (0.41 mm). So far as can be determined, however, the existing models[23,24] for roughness-controlled scattering from ocean bottoms have not been exercised in this regime of frequency and roughness scales. Moreover, a description of sand-grain-controlled roughness would have to include both irregular topography and randomly oriented facets of varying sizes.

Another potential explanation is the possible presence of small bubbles on or in the bottom sediment. The effects of contained gas bubbles can be occasionally dramatic.[25–27] Direct measurements[11] of sediment gas content from diver cores around the ship produced small but detectable gas contents in the sediments. Near the BAMS tower, the volume fraction of gas was measured at 0.000 15. All of the estimates were below the lower design limit of the apparatus, however so all estimates of gas content were constrained to $<0.000\,15$ volume fraction. Indirect measurements[11] demonstrated that the benthic algae were photosynthetically active and produced oxygen on and within the sediment cores. Laboratory incubations produced oxygen supersaturation in these cores at atmospheric pressures; whether these algae could have produced similar O_2 profiles at the 17 m depth of the bottom is difficult to assess.

Boyle and Chotiros[28] proposed a model for volume scattering from free air bubbles trapped in the interstices of sand grains. In reviewing data from the literature, they found that some data sets showed one or more peaks in scattering strength which they ascribed to resonances from interstitial bubbles. The radius of a free bubble that would resonate at 877 kHz at a depth of 17 m is about 6 μm,[29] rather large for the grain sizes of the SAX99 sediments (see their Fig. 4). However, lab experiments (unpublished) have shown that surficial bubbles produced by benthic algae can form and reside on the surface for considerable periods. Some bubbles attain sufficient size to break free and rise to the surface. Others fail to achieve buoyant escape before algal respiration ceases (some hours after dark) and are slowly resorbed. Divers looked for evidence of bubbles[11] on the bottom but bubbles of this small size are not easily detected.

The fact that bottom scattering strengths showed no discernible trends over time while the weather changed radically over the experiment argues against this explanation as one would expect O_2 production to depend upon solar insolation. Withal, this explanation cannot be wholly discounted.

ACKNOWLEDGMENTS

This work was conducted with the sponsorship of the Office of Naval Research (under Contract Nos. N00014-98-C-0442 and N00014-00-D-0122), which also supported the SAX-99 experiment. We wish to acknowledge the important role that APL/UW played in handling the logistics for this entire experiment; Eric Thorsos and Kevin Williams, Le Olson, Eric Boget, Kate Bader, Paul Aquilar, and Tom Lehman. We thank the crews of the R/V Pelican and R/V Seward Johnson for their able assistance in rigging, deploying, and removing our equipment and Liko Self and Jill Schmidt for substantial support underwater. David Thistle and Peter Jumars provided insight into benthic fauna and the critical role they play in creating the physical properties of the sediments. Kerry Commander and the staff of NCSC, Panama City provided crucial on-site logistical support, without which this experiment could never have happened.

[1] R. J. Urick, "The backscattering of sound from a harbor bottom," J. Acoust. Soc. Am. **26**, 231–235 (1954).
[2] K. V. MacKenzie, "Bottom reverberation for 530- and 1030-cps sound in deep water," J. Acoust. Soc. Am. **33**, 1498–1504 (1961).
[3] C. M. McKinney and W. D. Anderson, "Bottom backscattering near grazing incidence in shallow water," J. Acoust. Soc. Am. **36**, 158–163 (1964).
[4] H. N. Boehme, N. P. Chotiros, L. D. Rolleigh, S. P. Pitt, A. L. Garcia, T. G. Goldsberry, and R. A. Lamb, "Acoustic backscattering at low grazing angles from the ocean bottom. I. Bottom backscatter strength," J. Acoust. Soc. Am. **77**, 962–974 (1985).
[5] D. R. Jackson, A. M. Baird, J. J. Crisp, and P. A. G. Thomason, "High-frequency bottom backscattering measurements in shallow water," J. Acoust. Soc. Am. **80**, 1188–1199 (1986).
[6] H. N. Boehme and N. P. Chotiros, "Acoustic backscattering at low grazing angles from the ocean bottom," J. Acoust. Soc. Am. **84**, 1018–1029 (1988).
[7] S. Stanic, K. B. Briggs, P. Fleischer, R. I. Ray, and W. B. Sawyer, "Shallow-water high-frequency bottom scattering off Panama City, Florida," J. Acoust. Soc. Am. **83**, 2132–2144 (1988).
[8] S. Stanic, K. B. Briggs, P. Fleischer, W. B. Sawyer, and R. I. Ray, "High-frequency acoustic backscattering from a coarse shell ocean bottom," J. Acoust. Soc. Am. **85**, 125–136 (1989).
[9] A. W. Nolle, W. A. Hoyer, J. F. Mifsud, W. R. Runyan, and M. B. Ward, "Acoustical properties of water-filled sands," J. Acoust. Soc. Am. **35**, 1394–1408 (1963).
[10] E. I. Thorsos, K. L. Williams, N. P. Chotiros, J. T. Christoff, K. W. Commander, C. F. Greenlaw, D. V. Holliday, D. R. Jackson, J. L. Lopes, D. E. McGehee, J. E. Piper, M. D. Richardson, and D. Tang, "An overview of SAX99: Acoustic measurements," IEEE J. Ocean. Eng. **26**, 4–25 (2001).
[11] M. D. Richardson, K. B. Briggs, L. D. Bibee, P. A. Jumars, W. B. Sawyer, D. B. Albert, R. H. Bennett, T. K. Berger, M. J. Buckingham, N. P.

Chotiros, P. H. Dahl, N. T. Dewitt, P. Fleisher, R. Flood, C. F. Greenlaw, D. V. Holliday, M. H. Hurlbert, M. P. Hutnak, P. D. Jackson, J. S. Jaffe, H. P. Johnson, D. L. Lavoie, A. P. Lyons, C. S. Martens, D. E. McGehee, K. D. Moore, T. H. Orsi, J. N. Piper, R. I. Ray, A. H. Reed, R. F. L. Self, J. L. Schmidt, S. G. Schock, F. Simonet, R. D. Stoll, D. Tang, D. E. Thistle, E. I. Thorsos, D. J. Walter, and R. A. Wheatcroft, ''Overview of SAX99: Environmental considerations,'' IEEE J. Ocean. Eng. **26**, 26–53 (2001).

[12] D. R. Jackson and K. B. Briggs, ''High-frequency bottom backscattering: Roughness versus sediment volume scattering,'' J. Acoust. Soc. Am. **92**, 962–977 (1992).

[13] D. Tang, G. Jin, D. R. Jackson, and K. L. Williams, ''Analyses of high-frequency bottom and subbottom backscattering for two distinct shallow water environments,'' J. Acoust. Soc. Am. **96**, 2930–2936 (1994).

[14] C. A. Barans, B. W. Stender, D. V. Holliday, and C. F. Greenlaw, ''Variation in the vertical distribution of zooplankton and fine particles in an estuarine inlet of South Carolina,'' Estuaries **20**, 467–482 (1997).

[15] D. V. Holliday, R. E. Pieper, C. F. Greenlaw, and J. K. Dawson, ''Acoustical sensing of small-scale vertical structures in zooplankton assemblages,'' Oceanography **11**, 18–23 (1988).

[16] D. E. McGehee, C. F. Greenlaw, and D. V. Holliday, ''Multifrequency acoustical volume backscattering patterns in the Arabian Sea—265 kHz to 3 MHz,'' J. Acoust. Soc. Am. **107**, 193–200 (2000).

[17] K. Kringel, P. A. Jumars, and D. V. Holliday, ''A shallow scattering layer: High-resolution acoustic analysis of nocturnal vertical migration from the seabed,'' Limnol. Oceanogr. **48**, 1223–1234 (2003).

[18] R. J. Urick, *Principles of Underwater Sound for Engineers* (McGraw–Hill, New York, 1967).

[19] K. L. Williams, R. H. Hackman, and D. H. Trivett, ''High-frequency scattering from liquid/porous sediment interfaces,'' J. Acoust. Soc. Am. **84**, 760–770 (1988).

[20] D. V. Holliday, ''Acoustic determination of suspended particle size spectra,'' in *Coastal Sediments '87* (WW Div./ASCE, New York, 1987) Vol. 1, pp. 260–272.

[21] J. Sheng, ''Remote deterimination of suspended sediment size and concentration by multi-frequency acoustic backscatter,'' Ph.D. thesis, Department of Physics, Memorial University of Nfld., 1991.

[22] A. M. Crawford and A. E. Hay, ''Determining suspended sand size and concentration from multifrequency acoustic backscatter,'' J. Acoust. Soc. Am. **94**, 3312–3324 (1993).

[23] D. R. Jackson, D. P. Winebrenner, and A. Ishimaru, ''Application of the composite roughness model to high-frequency bottom backscattering,'' J. Acoust. Soc. Am. **79**, 1410–1422 (1986).

[24] P. D. Mourad and D. R. Jackson, ''High frequency sonar equation models for bottom backscatter and forward loss,'' in *Proceedings of OCEANS'89* (IEEE, New York, 1989), pp. 1168–1175.

[25] A. P. Lyons, M. D. Duncan, and A. L. Anderson, ''Predictions of the acoustic scattering response of free-methane bubbles in muddy sediments,'' J. Acoust. Soc. Am. **99**, 163–172 (1996).

[26] A. L. Anderson and L. D. Hampton, ''Acoustics of gas-bearing sediments I. Background,'' J. Acoust. Soc. Am. **67**, 1865–1889 (1980).

[27] A. L. Anderson and L. D. Hampton, ''Acoustics of gas-bearing sediments. II. Measurements and models,'' J. Acoust. Soc. Am. **67**, 1890–1903 (1980).

[28] F. A. Boyle and N. P. Chotiros, ''A model for high-frequency acoustic backscatter from gas bubbles in sandy sediments at shallow grazing angles,'' J. Acoust. Soc. Am. **98**, 531–541 (1995).

[29] H. Medwin and C. S. Clay, *Fundamentals of Acoustical Oceanography* (Academic, New York, 1998), pp. 294–295.

The derivative of a waveguide acoustic field with respect to a three-dimensional sound speed perturbation[a)]

Aaron Thode[b)]
Marine Physical Laboratory, Scripps Institution of Oceanography, San Diego, California 92093-0205

(Received 11 July 2003; accepted for publication 15 March 2004)

Semianalytic expressions are derived for the first-order derivative of a pressure field in a laterally homogeneous waveguide, with respect to an arbitrary three-dimensional refractive index perturbation in either the water column or ocean bottom. These expressions for the ''environmental derivative,'' derived using an adjoint method, require a three-dimensional spatial correlation between two Green's functions, weighted by an environmental parameter basis function, with the Green's functions expressed in terms of normal modes. When a particular set of orthogonal spatial basis functions is chosen, the three-dimensional spatial integral can be converted into a set of one-dimensional integrations over depth and azimuth. The use of the orthogonal basis permits environmental derivatives to be computed for an arbitrary sound-speed perturbation. To illustrate the formulas, a simple sensitivity study is presented that explores under what circumstances three-dimensional plane-wave and cylindrical perturbations produce non-negligible horizontal refraction effects, for a fixed source/receiver geometry. Other potential applications of these formulas include benchmarking three-dimensional propagation codes, and computing Cramer–Rao bounds for three-dimensional environmental parameter estimates, including internal wave components. © *2004 Acoustical Society of America.* [DOI: 10.1121/1.1736651]

PACS numbers: 43.30.Pc; 43.30.Bp [WLS] Pages: 2824–2833

I. INTRODUCTION

The full-field inversion of ocean acoustic data for water-column sound speed and bottom geoacoustic properties requires adequate understanding of the sensitivity of a modeled acoustic field to various kinds of environmental perturbations. If the field is relatively insensitive to a particular parameter, then attempts to invert the parameter will yield estimates with large variances and biases for a given signal-to-additive-noise ratio (SANR). One quantitative measure of this sensitivity is the derivative of an acoustic field with respect to an environmental parameter, or ''environmental pressure derivative.'' More rigorous measures of the minimum possible variance and bias of a parameter estimate, including the Cramer–Rao lower bound (CRLB)[1,2] and related higher-order tensor terms,[3–5] still require environmental pressure derivatives. Whenever actual acoustic data are available to be compared with a model output, environmental pressure derivatives can also be used to compute the gradient of the local error surface.

Environmental pressure derivatives are typically estimated using a finite-difference numerical scheme involving small environmental perturbations, which can lead to stability and convergence problems. An alternate approach that has been often employed in the control theory,[6] geophysics,[7–11] and physical oceanography,[12] literature is the ''adjoint'' or ''costate'' Green's function technique. Several independent derivations of this method[9–11] have shown that by solving two forward problems in the same propagation environment, the environmental pressure derivative with respect to an environmental perturbation can be derived by spatially correlating the two solutions over all space, weighted by the environmental perturbation. The resulting formulas are very similar to those used in diffraction tomography.[13,14]

The application of these expressions to acoustic propagation in a waveguide has been fairly recent.[15] Adjoint parabolic equation (PE) models have been used to estimate the environmental pressure derivatives of two-dimensional refractive index perturbations in a vertical plane connecting an acoustic source and receiver.[16,17] More recently, a normal-mode formulation of the acoustic pressure field was combined with adjoint techniques to derive analytical expressions for first- through third-order environmental pressure derivatives of laterally homogeneous (depth-dependent only) sound speed and density perturbations in a laterally homogeneous waveguide.[18]

In Sec. II the adjoint normal-mode formulation introduced in Ref. 18 is extended to incorporate environmental pressure derivatives with respect to an arbitrary three-dimensional perturbation in a laterally homogeneous waveguide, a situation that would normally require finite-difference computations of a three-dimensional coupled mode or parabolic equation code. The contribution of the paper is to illustrate how, for the restricted geometry of an acoustic waveguide, the three-dimensional spatial integration required by the adjoint method can be analytically simplified into a bounded two-dimensional integral, which can be evaluated numerically with relatively coarse grid sizes. The simplification is attained by using a normal-mode formulation for the Green's function, related in spirit to recent work on a Born scatterer in a waveguide.[15]

To illustrate one application of these formulas, Sec. III

[a)]Portions of this work have been presented at the Oceans 2003 Conference in San Diego, CA.

[b)]Electronic mail: thode@mpl.ucsd.edu

 0001-4966/2004/115(6)/2824/10/$20.00 © 2004 Acoustical Society of America

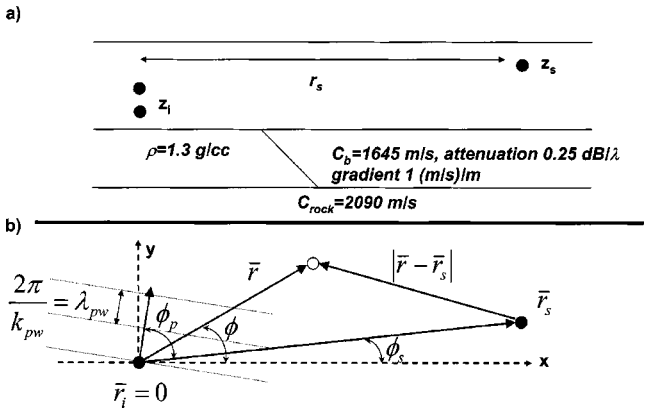

FIG. 1. Geometry used to illustrate adjoint formulas. (a) A 48-element vertical array, with 2-m spacing and first element at 1-m depth, is positioned in a 100-m isovelocity waveguide with bottom speed of 1645 m/s, bottom speed gradient of 1 m/s per m, density 1.3 g/cc, and attenuation of 0.25 dB/wavelength. A rock half-space lies 100 m below the sediment/water interface, with compressional speed of 2090 m/s. The acoustic source is positioned at 3-km horizontal range at 50-m depth. The bottom density is uniform in both the sediment and half-space. (b) View of geometry looking down onto the ocean. The receiver is placed at the coordinate origin. An example of a horizontal plane wave with wave number k_{pw} and propagation azimuth ϕ_p is shown.

presents a simple sensitivity study of horizontal refraction effects produced by plane-wave and compact cylindrical perturbations. A body of literature extending over two decades has examined the issue of horizontal refraction through eddies[19–22] and other features[23–25] in detail; the motivation of Sec. III is not to extend these studies, but to illustrate how the formulas derived here can quickly identify situations where horizontal refraction might be a non-negligible issue, given a particular source/receiver geometry. The first example presented here uses horizontally propagating plane waves as a simple model for internal waves, while the second example uses compact vertical cylindrical perturbations as a model for small eddies or gyres.

II. THEORY

A. General adjoint expression for environmental derivative

Density perturbations are not discussed in this particular paper, but their incorporation should follow similar lines of development as below. However, the spatial gradient of the Green's function would be required as well as the Green's function itself.[18]

A Green's function $g(\bar{r},\bar{r}_s,\omega)$ describes an acoustic field of frequency ω generated at location $\bar{r}_s$ that propagates through an unknown environment to location $\bar{r}$. The explicit dependence of g on frequency is now dropped. The source and receiver positions are expressed in terms of cylindrical coordinates, with the receivers r_i lying on the origin, and the source placed along the x axis, so that $\phi_s=0$ (Fig. 1). The propagation of the field is governed by the density-dependent inhomogeneous Helmholtz equation

$$\rho(\bar{r})\nabla\cdot\left(\frac{1}{\rho(\bar{r})}\nabla g(\bar{r},\bar{r}_s)\right)+k_{\mathrm{ref}}^2\eta(\bar{r})g(\bar{r},\bar{r}_s)=-\delta(\bar{r}-\bar{r}_s). \tag{1}$$

Here, k_{ref} is a spatially invariant reference medium wave number, and $\eta(\bar{r},\omega)\equiv k(\mathbf{r})^2/k_{\mathrm{ref}}^2=c_{\mathrm{ref}}^2/c(\mathbf{r})^2$ is the spatially dependent refractive index squared that, along with the spatially dependent density $\rho(\bar{r})$, defines the propagation environment. The linear operator L_0 provides a shorthand way of writing this differential equation.

This refractive-index term can be written as the sum of a laterally homogeneous (but potentially depth-dependent) "background" square refractive index η_0, and a perturbative expansion based on an *infinitesimal* nondimensional sound-speed perturbation magnitude ε

$$\eta(\bar{r})\equiv\eta_0(z)+\varepsilon\,\eta_\varepsilon(\bar{r})+\cdots, \tag{2}$$

where $\varepsilon\equiv\delta c/c_{\mathrm{ref}}$, with δc being a compressional sound-speed magnitude in (m/s). The quantity $\eta_\varepsilon\equiv\partial\eta/\partial\varepsilon|_{\varepsilon=0}$ is an order-one term in the perturbative expansion, and represents the derivative of a three-dimensional square index of refraction distribution with respect to the sound-speed perturbation magnitude, and will be subsequently referred to as the "refractive index derivative." If the functional dependence of the square-refractive index is such that higher-order derivatives are both physically relevant and non-negligible, Eq. (2) can be expanded to higher-order terms.

The Green's function $g(\bar{r},\bar{r}_s)$ of the perturbed environment can be expressed as a similar expansion

$$g(\bar{r},\bar{r}_s)\equiv g_0(\bar{r},\bar{r}_s)+\varepsilon g_\varepsilon+\cdots. \tag{3}$$

Here, $g_\varepsilon\equiv\partial g/\partial\varepsilon|_{\varepsilon=0}$ is the derivative of the Green's function with respect to the environmental parameter magnitude, and is assumed to be of order one in this series solution as well. Having expressed the new Green's function as an expansion of the nondimensional ε, a solution can now be found for the Green's function derivative g_ε. The final derivative formula can then be expressed in terms of the dimensional differential δc.

A rigorous derivation of how g_ε can be linearly related to η_ε is reviewed elsewhere,[7,9,11,18] however, a brief heuristic argument can be derived from the Born approximation[14,15]

$$g(\bar{r}_i,\bar{r}_s)\approx g_0(\bar{r}_i,\bar{r}_s)+k_{\mathrm{ref}}^2\rho(\bar{r}_i)\times\int_V\int\int\left[\{\varepsilon\,\eta_\varepsilon(\bar{r})\}\frac{g_0(\bar{r},\bar{r}_i)}{\rho(\bar{r})}g_0(\bar{r},\bar{r}_s)\right]\mathbf{d}^3\mathbf{r}. \tag{4}$$

By rearranging this expression, dividing by ε, and taking the limit as $\varepsilon\to0$, the approximate equality of Eq. (4) converges to an *exact* solution, which, when multiplied by a appropriate source strength and converted to dimensional units, becomes the acoustic adjoint equation for the derivative of acoustic pressure with respect to compressional speed magnitude

$$\frac{\partial p(\bar{r}_i,\bar{r}_s)}{\partial c}=\left(\frac{S}{S_0}\right)S_0k_{\mathrm{ref}}^2\rho(\bar{r}_i)\times\int_V\int\int\left[\eta_c(\bar{r})\frac{g(\bar{r},\bar{r}_i)}{\rho(\bar{r})}g(\bar{r},\bar{r}_s)\right]\mathbf{d}^3\mathbf{r}. \tag{5}$$

Here, $S_0=\rho\omega^2 V_0$, with V_0 being a volume injection sufficient to generate a pressure level of 1 Pa at 1 m range (120 dB re: 1 μPa @ 1 m source level). This choice of V_0 sets $S_0=1$ Pa-m, while S is the actual source level of the pressure field in Pa-m. From Eq. (5) onwards the environmental pressure derivative will be written with respect to sound-speed magnitude in dimensional units of m/s, and the zero subscript for the unperturbed Green's function is dropped, with the understanding that the term ''Green's function'' in subsequent discussion will always refer to the *unperturbed* Green's function.

Two comments must be made concerning the validity and practicality of Eq. (5). First, even though it was derived via the Born approximation, Eq. (5) is an *exact* expression for the environmental derivative, as more complete derivations demonstrate. However, if a *finite* perturbation changes the sound-speed magnitude by an amount δc, Eq. (5) can only provide an *approximate* estimate of the perturbed pressure field, in the form of $p(\bar{r}_i,\bar{r}_s)\approx p_0(\bar{r}_i,\bar{r}_s)+\delta c([\partial p(\bar{r}_i,\bar{r}_s)]/\partial c)$, and only if δc is extremely small. Thus, Eq. (5) would be of limited use for full-field inversion procedures, without further information about higher-order derivatives of p like $p_{cc}\equiv\partial^2 p/\partial c^2|_{\varepsilon=0}$, which can be shown to correspond to higher-order terms in the Born approximation.[7]

Second, while the adjoint expression in Eq. (5) does not require a finite differencing scheme, it does so at the cost of requiring a spatial integration of the Green's functions, which must be performed numerically under general geometries, e.g., Ref 8. Without further simplification the evaluation of Eq. (5) faces the same issues with computational speed and convergence as finite-difference approaches. The key result of this paper is that the particular geometry of a laterally homogeneous waveguide permits this integration to be reduced analytically to a numerically stable two-dimensional intergal over azimuth and depth. Furthermore, it will be shown how an appropriate choice of refractive index basis functions permits one to compute a large number of environmental derivatives with only a single set of computations.

B. Orthogonal decomposition of refractive index perturbation

A standard technique in linear inversion theory is to model perturbations as a linear sum of basis functions,[26] i.e., $\eta_c(\bar{r})=\Sigma_p a_p \eta_p(\bar{r})$.

In a similar spirit, in cylindrical coordinates the refractive index derivative can be expressed as a sum of a set of orthogonal basis functions, exploiting an orthogonality relationship between Bessel functions of the first kind J_ν

$$\eta_c(\bar{r},z)=\sum_{q=1}^{Q}\eta_q(z)\sum_{\nu=-\infty}^{\infty}e^{-i\nu\phi}\times\int_0^\infty a(k_p,\nu,q)J_\nu(k_p r)k_p\,dk_p, \tag{6a}$$

with

$$a(k_p,\nu,q)\equiv a_{pq\nu}=\frac{1}{2\pi}\int_0^{2\pi}e^{i\nu\phi}d\phi\times\int_0^\infty dz\int_0^\infty\eta_c(\bar{r},z)\,\eta_q(z)J_\nu(k_p r)r\,dr. \tag{6b}$$

Here, J_ν is a Bessel function of the first kind of order ν. The functions η_q are a set of Q orthonormal vertical basis functions, such as sine and cosine waves, empirical orthogonal functions (EOFs) derived directly from data, acoustic normal modes, or even internal wave modal functions.[27]

Equation (6) suggests that if a set of ''fundamental'' basis functions

$$\eta_{pq\nu}(\bar{r},z)=\eta_q(z)e^{-i\nu\phi}J_\nu(k_p|r|), \tag{7}$$

is inserted into Eq. (5) for $\eta_\varepsilon(\bar{r})$ and evaluated, the result would provide a general solution for the environmental pressure derivative

$$\frac{\partial g(\bar{r}_i,\bar{r}_s)}{\partial c}=\sum_{q=1}^{Q}\sum_{\nu=-\infty}^{\infty}\int_0^\infty a_{p\nu q}\frac{\partial g(\bar{r}_i,\bar{r}_s)}{\partial c_{pq\nu}}k_p\,dk_p$$
$$\frac{\partial g(\bar{r}_i,\bar{r}_s)}{\partial c_{pq\nu}}\equiv\left(\frac{S}{S_0}\right)S_0k_{\mathrm{ref}}^2\rho(\bar{r}_i)\int_V\int\int\left[\eta_q(z)e^{-i\nu\phi}J_\nu(k_p r)\times\frac{g(\bar{r},\bar{r}_i)}{\rho(\bar{r})}g(\bar{r},\bar{r}_s)\right]\mathbf{d}^3\mathbf{r}. \tag{8}$$

For the special case of the horizontally propagating complex plane wave illustrated in Fig. 1(b), with horizontal wave number k_{pw} and propagation direction ϕ_p with respect to the x axis, the basis function decomposition has the form

$$e^{-i\bar{k}_{pw}\cdot\bar{r}}=e^{-ik_{pw}r\cos(\phi-\phi_p)}=\sum_{\nu=0}^{\infty}\beta_\nu(-i)^\nu\cos[\nu(\phi-\phi_p)]J_\nu(k_{pw}r), \tag{9}$$

where $\beta_\nu=2$, except for $\beta_0=1$. Thus, from Eq. (6b)

$$a_{pq\nu}=(-i)^\nu e^{i\nu\phi_p}\frac{\delta(k_{pw}-k_p)}{k_p}\int_0^\infty\eta_q(z)dz, \tag{10}$$

and Eq. (8) becomes

$$\frac{\partial g(\bar{r}_i,\bar{r}_s)}{\partial c_{\text{plane-wave}}}=\sum_{q=1}^{Q}\int_0^\infty\eta_q(z)dz\times\sum_{\nu=-\infty}^{\infty}(-i)^\nu e^{i\nu\phi_p}\frac{\partial g(\bar{r}_i,\bar{r}_s)}{\partial c_{(k_{pw})q\nu}}. \tag{11}$$

All the examples shown in this paper use a single vertical basis function, so Q is restricted to 1.

C. Adjoint solution for basis function in a constant-depth waveguide

Solving the adjoint Eq. (8) requires two Green's functions, one describing propagation from the source r_s to an arbitrary point r, and one describing propagation from the receiver r_i to the same point r [see Fig. 1(b)].

In the geophysics community the Green's functions are typically computed numerically over a set of grid points, and the subsequent spatial correlation is achieved by numerical integration over the grid. Because of computational costs the numerical integration is often restricted to a 2D plane incorporating the source and receiver.[8,28] However, for the case of a laterally homogeneous waveguide the Green's function can be expressed as a sum of normal modes $U_n(z)$, which permits some analytical simplification. To begin, the Green's function between a location r and receiver location centered at the origin is

$$g(\overline{r,r_i})=\frac{i}{4\rho(z_i)}\sum_f U_f(z)U_f(z_i)H_0^{(1)}(k_{rf}|\overline{r}|), \tag{12}$$

and the Green's function between the source at r_s and location r is

$$\begin{aligned} g(\overline{r,r_s})&=\frac{i}{4\rho(z_s)}\sum_g U_g(z)U_g(z_s)H_0^{(1)}(k_{rg}|\overline{r_s}-\overline{r}|)\\ &=\frac{i}{4\rho(z_s)}\sum_g\sum_{\nu'=0}^{\infty}\beta_{\nu'}U_g(z)U_g(z_s)\cos\nu'(\phi-\phi_s)\\ &\quad\times\begin{cases}J_{\nu'}(k_{rg}\overline{r})H_{\nu'}^{(1)}(k_{rg}\overline{r_s}), & |r|<|r_s|\\ J_{\nu'}(k_{rg}\overline{r_s})H_{\nu'}^{(1)}(k_{rg}\overline{r}), & |r|>|r_s|\end{cases}, \end{aligned} \tag{13}$$

where $H_\nu^{(1)}$ is the νth-order outgoing Hankel function of the first kind. In the second line of Eq. (13), Graf's addition theorem for Bessel functions has been used.[29] Combining Eqs. (7), (12), and (13) into Eq. (8) and performing the azimuthal integration yields nonzero terms only when $\nu'=\pm\nu$.

The final result expresses the environmental pressure derivative as a sum of one-dimensional depth integrals

$$\begin{aligned}\frac{\partial p(\overline{r_i},\overline{r_s})}{\partial a_{pq\nu}}&=\left(\frac{S}{S_0}\right)\left[\frac{-S_0\pi}{8\rho(z_s)}\sum_{f,g}Z_{qfg}U_f(z_i)U_g(z_s)\right.\\ &\quad\left.\times\sum_{\nu=-\infty}^{\infty}R_{p\nu fg}(r_s)e^{-i\nu\phi_s}\right],\end{aligned} \tag{14}$$

$$Z_{qfg}\equiv k_{\mathrm{ref}}^2\int_0^\infty\frac{\eta_q(z')}{\rho_0(z')}U_f(z')U_g(z')dz', \tag{15}$$

$$\begin{aligned}&R_{p\nu fg}(r_s)\\ &=\begin{cases}H_\nu^{(1)}(k_{rg}r_s)\displaystyle\int_0^{r_s}rJ_\nu(k_pr)J_\nu(k_{rg}r)H_0^{(1)}(k_{rf}r)dr\\ +J_\nu(k_{rg}r_s)\displaystyle\int_{r_s}^{\infty}rJ_\nu(k_pr)H_\nu^{(1)}(k_{rg}r)H_0^{(1)}(k_{rf}r)dr\end{cases}.\end{aligned} \tag{16}$$

Note that while Eq. (15) is symmetric with respect to f and g, Eq. (16) is *not*. The first term of Eq. (16) represents contributions to the spatial correlation from regions where $|r|<|r_s|$, while the second term represents contributions from spatial regions where $|r|>|r_s|$; i.e., a "backscattering" regime.

This integral is highly oscillatory, and the large-argument asymptotic expressions for the Bessel functions cannot be used, because they are only valid whenever $k_{rg}r\gg\nu$. However, Eq. (16) can be simplified in a manner analogous to previous work modeling ocean ambient noise in range-dependent environments.[30] First, note that the triple product within the integrand can be reduced to a two-term integrand using a Bessel addition theorem

$$J_\nu(k_pr)B_\nu(k_{rg}r)=\frac{1}{\pi}\int_0^\pi d\phi B_0(k_{rpg}r)\cos\nu\phi, \tag{17a}$$

$$k_{rpg}^2=k_{rg}^2+k_p^2-2k_{rg}k_p\cos\phi, \tag{17b}$$

where B_ν is either J_ν or $H_\nu^{(1)}$. The range integral can then be solved

$$\begin{aligned}\int_0^{r_s}rJ_0(k_{rpg}r)H_0^{(1)}(k_{rf}r_s)dr&=\frac{k_{rpg}r_sH_0^{(1)}(k_{rf}r_s)J_1(k_{rpg}r_s)-k_{rf}r_sH_1^{(1)}(k_{rf}r_s)J_0(k_{rpg}r_s)-2i/\pi}{k_{rpg}^2-k_{rf}^2},\\ \int_{r_s}^{\infty}rH_0^{(1)}(k_{rpg}r)H_0^{(1)}(k_{rf}r_s)dr&=-\frac{k_{rpg}r_sH_0^{(1)}(k_{rf}r_s)H_1^{(1)}(k_{rpg}r_s)-k_{rf}r_sH_1^{(1)}(k_{rf}r_s)H_0^{(1)}(k_{rpg}r_s)}{k_{rpg}^2-k_{rf}^2}.\end{aligned} \tag{18}$$

The constant $2i/\pi$ arises from evaluating the limit at $r=0$, using the small argument approximations for $H_1^{(1)}$ and J_0. Since k_p is always real and k_{rg} and k_{rf} will have imaginary components due to bottom attenuation, the upper limit of the integral will always vanish, and the denominator of (18) will always be nonzero.

Combining Eqs. (16)–(18) creates a numerically stable bounded integral that can be solved with a relatively coarse integration step

$$R_{p\nu fg}(r_s)=\frac{r_s}{\pi}\int_0^\pi\frac{\cos[\nu\phi]d\phi}{k_{rpg}^2-k_{rf}^2}\begin{Bmatrix}k_{rpg}H_0^{(1)}(k_{rf}r_s)[H_\nu^{(1)}(k_{rg}r_s)J_1(k_{rpg}r_s)-H_1^{(1)}(k_{rpg}r_s)J_\nu(k_{rg}r_s)]\\ -k_{rf}H_1^{(1)}(k_{rf}r_s)[H_\nu^{(1)}(k_{rg}r_s)J_0(k_{rpg}r_s)-H_0^{(1)}(k_{rpg}r_s)J_\nu(k_{rg}r_s)]\\ -2iH_\nu^{(1)}(k_{rg}r_s)/\pi\end{Bmatrix}. \tag{19}$$

For the special case $k_p=0$ (range-independent perturbation), all azimuthal terms vanish except for $\nu=0$, and $R_{p\nu fg}$ reduces to a form similar to that obtained in Ref. 18

$$R_{00fg}(r_s)=\begin{cases} -\dfrac{2i}{\pi}\dfrac{H_0^{(1)}(k_{rf}r_s)-H_0^{(1)}(k_{rg}r_s)}{k_{rf}^2-k_{rg}^2} & f\neq g \\ \dfrac{ir_sH_1^{(1)}(k_{rf}r_s)}{\pi k_{rf}} & f=g \end{cases}. \tag{20}$$

Equation (19) requires a numerical integration over ϕ for each basis function desired. Practically it was found that the integrand need only be evaluated at around 1000 pts to achieve the needed precision. While the form of Eq. (19) may be intuitively unenlightening, substituting the large-argument asymptotic expansions for the Bessel functions indicates that the integral should produce large values whenever $k_p=k_{rf}\pm k_{rg}$, an observation that is verified in the following section.

Note that $R_{p\nu fg}$ is unequal to $R_{p\nu gf}$; i.e., switching the source and receiver does not produce the same environmental derivative, i.e., reciprocity does not hold. The reason for this asymmetry is that the perturbation origin of Eqs. (12) and (13) has been changed. Thus, swapping source and receiver creates a situation where the basis functions are centered at the source, and not the receiver, as in the original problem.

III. NUMERICAL EXAMPLES

A. Modeled waveguide environment

Here, Eqs. (14), (15), and (19) are demonstrated in a sensitivity study using a simple waveguide environment. An omnidirectional 20-Hz source is placed in a isovelocity waveguide 100 m deep, with a bottom speed of 1645 m/s, and standard values for a linear bottom gradient, density, and attenuation (Fig. 1, caption). A bottom half-space with a compressional speed of 2090 m/s begins 100 m below the water/sediment interface. At 20 Hz this waveguide supports six propagating modes. The source/receiver separation in the following examples has been set to either 1 or 3 km, with the source always placed at 50-m depth, and 48 receivers aligned in a vertical array with 2-m spacing.

B. Properties of range integral $R_{p\nu fg}$

The expression in Eq. (19) does not lend itself to physical insight, so Fig. 2 plots the integral as a function of perturbation wave number k_p and ν, using values of k_{rf} and k_{rg} computed from the environment presented above. In the top subplot $k_{rf}=k_{rg}$, and in the bottom subplot they are different. While the numerical computation of Eq. (19) is straightforward, some numerical instability issues arise for large orders of ν. While an asymptotic expansion of Eq. (19) for high-order ν demonstrates that the integral must converge to zero as ν grows large, the numerical evaluation becomes unstable and diverges from zero whenever $\nu>k_{rf}|r_s|$. Therefore, in all computations presented here $R_{p\nu fg}$ is set to zero whenever ν satisfies the above inequality.

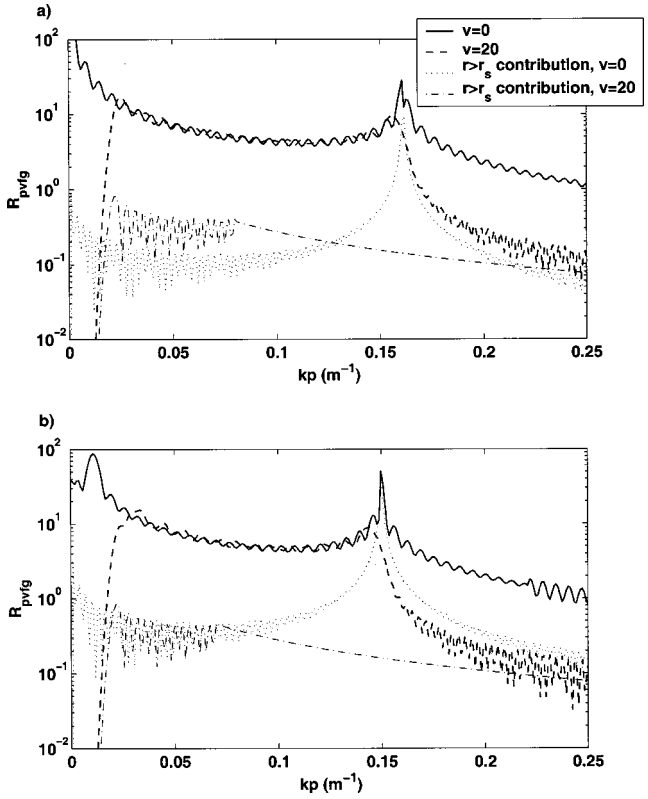

FIG. 2. Plot of $R_{p\nu fg}$ as a function of perturbation wavelength k_p and azimuthal index ν, using modal wave numbers computed from the environment described in Fig. 1, and for a source/receiver separation of 1 km. Solid line: $\nu=0$ (azimuthally symmetric case), dashed line, $\nu=20$. Dotted line: contribution of second term of Eq. (15) for $\nu=0$, where $r>r_s$. Dash-dot line: contribution of second term when $\nu=20$. (a) $k_{rf}=k_{rg}=0.0806$; (b) $k_{rf}=0.0806$, $k_{rg}=0.069\,392$.

The most obvious feature of both Figs. 2(a) and (b) is that $R_{p\nu fg}$ only has significant values whenever $k_{rf}-k_{rg}<k_p<k_{rf}+k_{rg}$. Since $k_{rf}\sim k_{\mathrm{ref}}$, the medium wave number, one can conclude that the propagating acoustic field is only sensitive to perturbation spatial wavelengths that are larger than half of the medium acoustic wavelength, a result well-known from diffraction tomography,[14,31] a procedure that also makes extensive use of the Born approximation. For the case of an azimuthally symmetric perturbation component ($\nu=0$), one sees that whenever k_p is equal to the sum or difference of a set of horizontal wave numbers, $R_{p\nu fg}$ attains a peak, indicating that a propagating acoustic field is especially sensitive to perturbation components with a spatial wave number that matches the sum or differences of pairs of modal wave numbers. Azimuthally dependent perturbation components ($\nu>0$) also display similar peaks, but they occur at slightly different perturbation wave numbers, as can be seen for the case of $\nu=20$ in Fig. 2. The peak associated with the difference between modal wave numbers migrates to a k_p slightly greater than $k_{rf}-k_{rg}$, while the peak associated with the sum of modal wave numbers shifts to a value slightly lower than $k_{rf}+k_{rg}$.

As the range separation r_s between source and receiver increases, these peaks become larger and narrower, indicating that at large ranges and for azisymmetric perturbations, the acoustic field becomes sensitive only to perturbation

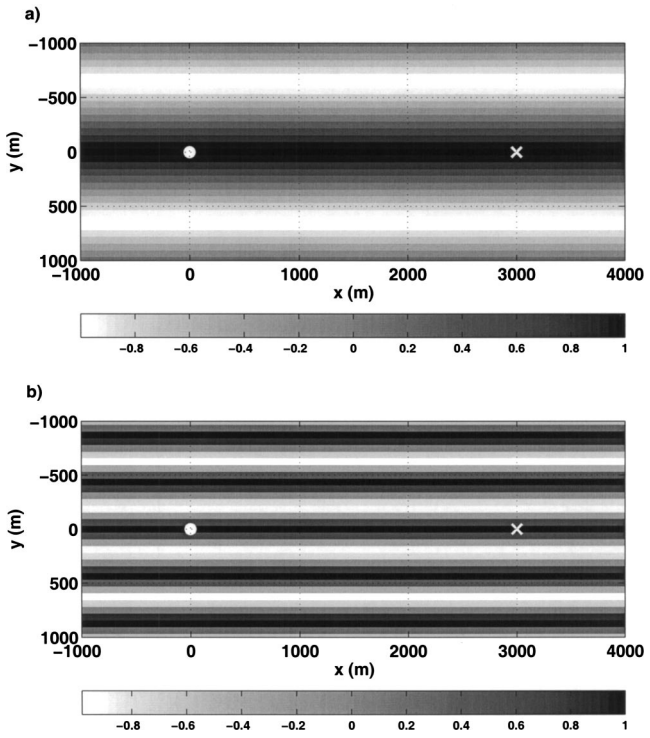

FIG. 3. Examples of plane-wave perturbations that yield the same two-dimensional range–depth perturbation in the vertical plane between acoustic source and receiver. The white circle marks the receiving array location, while the white cross marks the source location at 3-km horizontal range: (a) 1.28-km wavelength perturbation oriented along the y axis ($\phi_p = 90°$); (b) 426-m wavelength perturbation oriented along the y axis.

wavelengths quantized at $k_{rf} \pm k_{rg}$, a result obtained independently by another analysis.[15] It is also interesting to separate the integral contributions into the first and second terms visible in Eq. (16). Whenever $\nu = 0$ contributions from regions where $r > r_s$ (''backscatter region'') cannot be neglected, but for $\nu > 0$ this upper range integral contributions become relatively small—i.e., 10% of the amplitude at the peak in the figure shown.

C. Effect of a horizontal plane-wave perturbation on pressure derivative

As suggested by Eq. (11), it should be straightforward to compute the environmental pressure derivative with respect to horizontally propagating plane wave. As illustrated in Fig. 1(b), one simply evaluates Eqs. (14)–(15) and (19) for $k_p = k_{pw}$ and $\phi_s = \phi_p$, for all values of ν up to $\nu_{\max} = k_{rf} r_s$. The results can then be combined via Eq. (11).

In this section a set of horizontally propagating three-dimensional plane waves has been computed, each one with the same values along the vertical cross section connecting the source and receiver shown in Fig. 1(a), for a source–range separation of 3 km. Two examples of these perturbations are plotted in Fig. 3, looking down onto the ocean surface from above. Two types of depth dependence are modeled: one where the perturbation has a constant value in the water column, and is zero in the ocean bottom, and one where the perturbation has a constant value in the ocean bottom, but is zero in the ocean column. In other words, the horizontal cross sections visible in Fig. 3 would have the same appearance if cut across a different depth, provided that depth is in the same medium (water or ocean bottom).

These perturbations are cosine waves with $\phi_p = 90°$. Therefore, the perturbation values in the vertical plane between the source and receiver are always unity, a situation that was checked via numerical synthesis of the perturbations. This particular perturbation set thus provides a simple opportunity to explore the circumstances under which perturbation components from outside the vertical plane connecting the source and receiver cannot be neglected. In other words, at what perturbation wavelength scale do horizontal refraction effects become non-negligible?

Figure 4 illustrates the magnitude and phase of the environmental pressure derivative across the vertical receiving array as a function of the plane-wave perturbation number k_{pw}, for the case where the perturbation exists only in the water column. A perturbation wave number of 0 indicates a

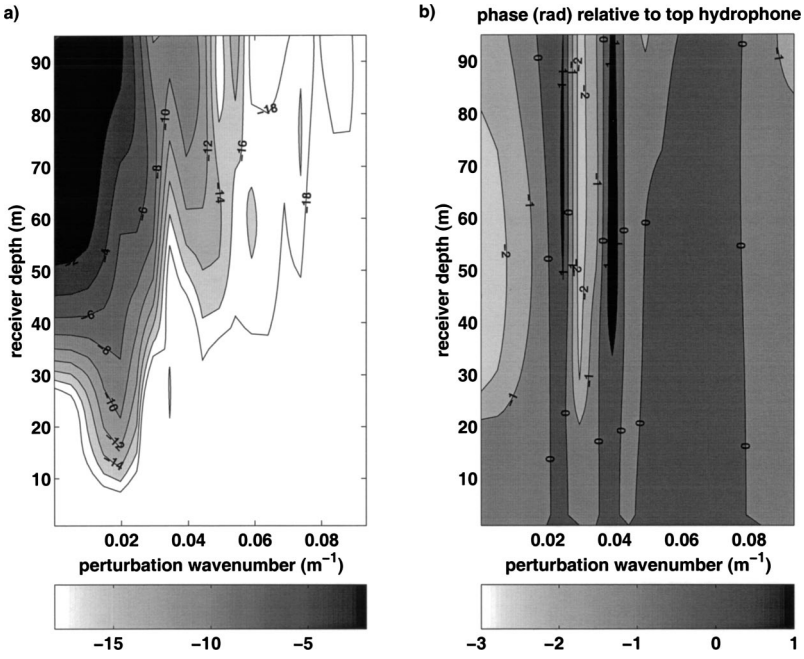

FIG. 4. Effect of plane-wave water-column perturbations on environmental pressure derivative for a 20-Hz field with source level of 120 dB re: 1 μPa @ 1 m, derived from source and receiver geometries shown in Figs. 1 and 3. All perturbations would appear identical in a 2D range–depth slice between source and receiver array. (a) Magnitude in dB of pressure derivative as a function of receiving element depth and perturbation wave number, relative to the maximum environmental pressure derivative of 1.12×10^{-7} Pa/(m/s) attained by the azimuthally symmetric (''range-independent'') result at the x-axis origin. The right limit of the x axis corresponds to a 62-m wavelength. (b) Phase of the environmental derivative, relative to the top receiving hydrophone, as a function of perturbation wave number.

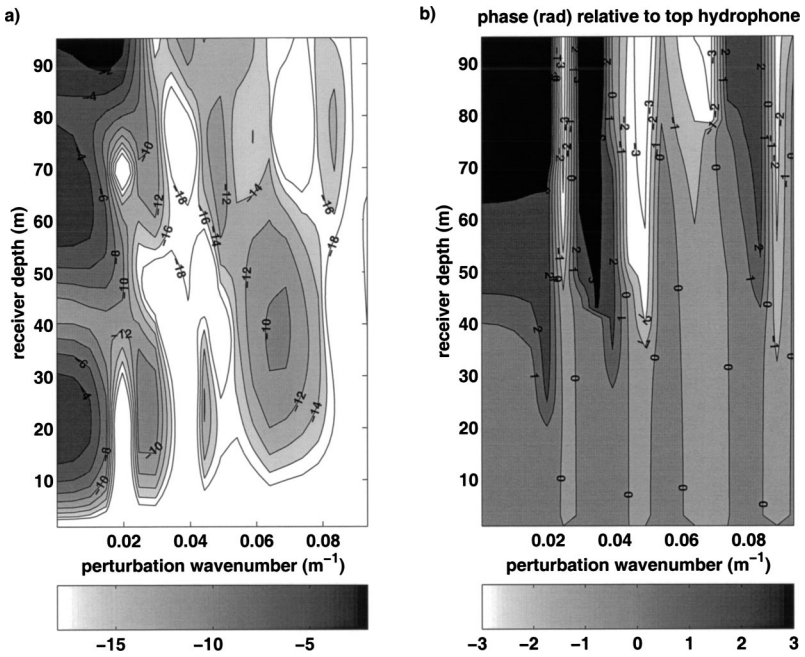

FIG. 5. Same as Fig. 4, but with the plane-wave perturbation restricted to the bottom half-space. Environmental derivative magnitude is displayed in dB relative to the maximum environmental pressure derivative of 6.31×10^{-8} Pa/(m/s).

constant perturbation value over all space (range-independent perturbation). For large wavelengths (small perturbation wave numbers) the environmental pressure derivative is very similar to the range-independent case, but starting at perturbation wavelengths of about 400 m (5 wavelengths of a 20-Hz signal) the phase and magnitude of the derivative change markedly, with a noticeable trend to smaller magnitudes at higher perturbation wavelengths. Figure 5 illustrates a similar computation, but with the perturbation restricted to the ocean bottom. A similar result is seen, in that the environmental pressure derivative changes markedly once the perturbation wavelength decreases below 400 m. An actual plane-wave ocean perturbation, such as those generated by internal waves,[27] would not generate a uniform perturbation with depth, but is generally restricted to a certain portion of the water column. Thus, the horizontal refraction effects produced by realistic plane-wave perturbations, which would be a simple extension of the computations shown here, may not be as large.

D. Effect of a compact cylindrical perturbation on pressure derivative

A second three-dimensional perturbation that can be evaluated analytically is a vertical cylinder with a circular horizontal cross section, which provides a convenient means for investigating the effect of a localized perturbation on the modal field. The perturbation might be considered a very simple model of an eddy.[19,21,32] The geometry of the cylindrical perturbation is illustrated in Fig. 6, from both a top view (a) and a perspective view (b). As with the plane-wave perturbation, the perturbation can be restricted to the water column, below the ocean bottom, or both.

By exploiting Graf's addition theorem one can derive the basis coefficients [Eq. (6b)] needed to construct a circle with radius a displaced from the receiver origin by a distance r_{shift} and by a rotation angle ϕ_{shift} from the x axis [Fig. 6(a)], for the basis functions in Eq. (7)

$$a_{pq\nu}=\frac{aJ_1(k_pa)}{k_p}J_\nu(k_pr_{\text{shift}})e^{-i\nu\phi_{\text{shift}}}. \tag{21}$$

Thus, once a set of derivatives with respect to a set of basis function perturbations has been computed, it is straightforward to compute environmental derivatives for cylindrical perturbations of various diameters at any location.

To illustrate Eq. (21), two cylindrical perturbations with respective radii of 150 and 600 m were inserted into the waveguide environment of Fig. 1, with 1-km horizontal range between the vertical receiving array and perturbation center, and with the 50-m-deep acoustic source remaining at 3-km range. To approximate the continuous integral implied by Eq. (8), k_p was evaluated at 512 points between 0 and 0.251 m^{-1}, or three times the medium wave number. This sampling provided sufficient spacing between the discrete values of k_p so that any artifacts generated appear at ranges much greater than the source range r_s. A convergence test determined that a value of $\nu=60$ was sufficient to reproduce the perturbation at these ranges.

The question of the sensitivity of the environmental pressure derivative to a localized out-of-plane perturbation

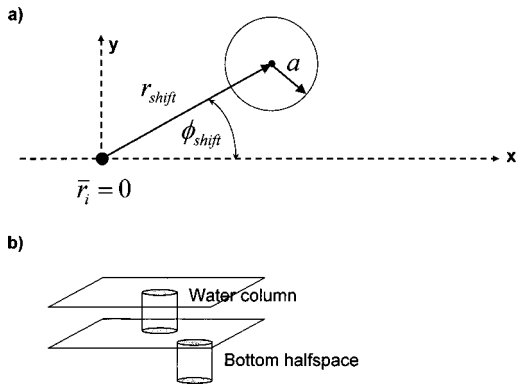

FIG. 6. Geometry of offset cylindrical perturbation: (a) top view; (b) perspective view.

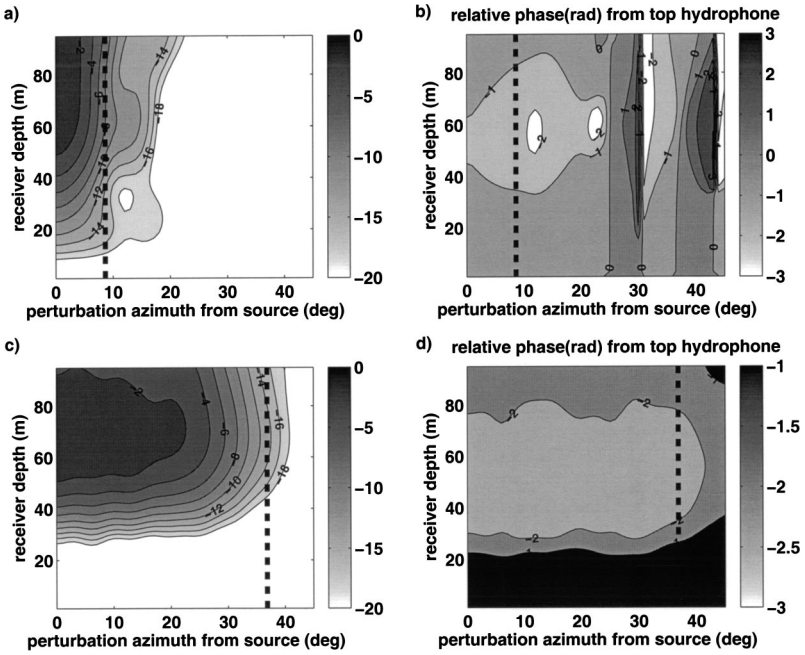

FIG. 7. Effect of a cylindrical (''eddy'') perturbation in water column on 20-Hz acoustic field with source level of 120 dB re: 1 μPa @ 1 m, as a function of perturbation azimuth ϕ_{shift}. The center of the perturbation r_{shift} lies 1 km from the origin. (a) $a=150$-m radius perturbation: environmental pressure derivative magnitude in dB re: the maximum magnitude of 1.58×10^{-8} Pa/(m/s); and (b) relative phase of environmental derivative; (c) $a=600$-m radius perturbation: environmental pressure derivative magnitude in dB re: the maximum magnitude of 7.94×10^{-8} Pa/(m/s) and (d) relative phase.

can be explored by systematically changing the rotation angle ϕ_{shift} in Eq. (21), thus rotating the perturbation around the origin. Beyond some geometric angle $\phi_{\text{extent}}=\sin^{-1}(a/r_{\text{shift}})$ the physical boundaries of the perturbation will no longer intersect the vertical plane intersecting the source and receiver array.

Figures 7 and 8 show a plot similar to Figs. 4 and 5, in that the magnitude and relative phases of the environmental pressure derivative of a 20-Hz signal are shown across the vertical receiving array. This time, however, the horizontal axis represents the rotation angle ϕ_{shift}, and the vertical dashed lines mark ϕ_{extent}. The color map scale has been normalized and plotted on a log scale, so that the maximum magnitude of the environmental pressure derivative across the receiving array when $\phi_{\text{shift}}=0$ has been defined as 0 dB. This value will be subsequently referred to as the ''in-plane maximum.''

Figure 7 shows the effect of a cylindrical perturbation placed in the water column only, with the top row showing the effect of the 150-m radius perturbation, and the bottom row the effect of the 600-m perturbation. The figures show that the environmental pressure derivative still exists even when the perturbations lie completely outside the vertical source–receiver plane ($\phi_{\text{shift}}>\phi_{\text{extent}}$), but with a magnitude at least 8 dB less than the in-plane maximum. The smaller the perturbation radius, the larger the relative magnitudes the out-of-plane results tend to be. This observation is consistent with the expectation that the greater curvature of small-radii perturbations should have relatively larger horizontal refraction effects.

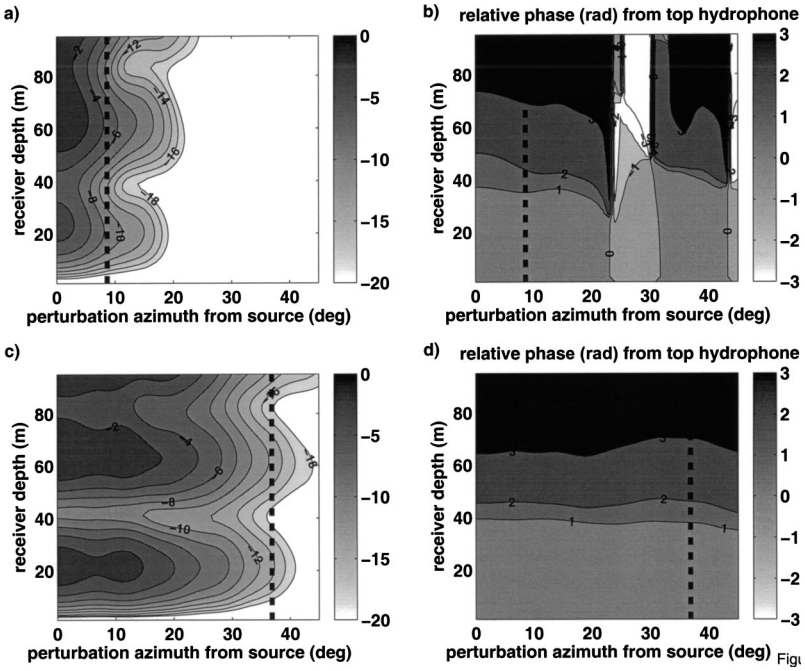

FIG. 8. Effect of cylindrical perturbation in ocean bottom on 20-Hz acoustic field, as a function of ϕ_{shift}, for $r_{\text{shift}}=1$ km. (a) $a=150$-m radius perturbation: environmental pressure derivative magnitude in dB re: the maximum magnitude of 6.31×10^{-9} Pa/(m/s); and (b) relative phase of environmental derivative; (c) $a=600$-m radius perturbation: environmental pressure derivative magnitude in dB re: the maximum magnitude of 2.24×10^{-8} Pa/(m/s) and (d) relative phase.

Figure 8 shows an identical situation, except with the cylindrical perturbations existing only beneath the ocean bottom. As with Fig. 7, derivatives with respect to out-of-plane perturbations exist, with larger relative magnitudes produced by perturbations with smaller radii. Furthermore, the out-of-plane results can be non-negligible when compared with the in-plane maximum. For example, in subplot (a) a 150-m radius perturbation produces environmental pressure derivatives that are within 10 dB of the in-plane maximum out to rotation angles of 15 deg, if the receiver depth is 50 m. This angle is nearly twice the value of ϕ_{extent}.

The results of this simple sensitivity study on this particular deployment configuration indicate that while neglecting out-of-plane refraction effects may be a safe assumption for certain cylindrical perturbations in the water column, it may not be a valid assumption for small-radii perturbations in the ocean bottom.

As the environmental pressure field can be interpreted as a field ''scattered'' from an infinitesimal perturbation via the Born approximation, some further physical insight into these results can be obtained by computing how an incident acoustic plane wave diffracts from an aperture with the same lateral dimensions as the perturbation.[33,34] As a normal mode consists of two plane waves propagating nearly horizontally, the assumption of an incident plane wave in the diffraction analysis is valid. For a perturbation radius of 600 m, a point 2-km range from the perturbation center lies within the Fresnel diffraction region ($r \approx a^{1/3}\sqrt{ka/2} = 1700\,\text{m}$).[14] Treating the perturbation as a rectangular aperture 1.2 km wide, an analysis of the resulting Fresnel diffraction pattern using a Cornu spiral finds that the boundaries of the geometric shadow are quite sharp. Thus, for the 600-m radius perturbation the apparent angular half-width of the diffracted field would be very close to the geometric half-width of 36° for ϕ_{extent} at this range, as was found to be the case.

By contrast, a perturbation radius of 150 m places the 2-km range receiver location in the Fraunhofer region ($r > 4a^2/\lambda = 1200\,\text{m}$), and diffraction effects are found to be prominent. Given a total perturbation ''aperture'' of 300 m, the azimuthal angle at which the diffraction mainlobe attains its first null is $\phi_{\text{null}} = \lambda/2a = 14.4°$ from the mainlobe center, close to the angular extent of the observed pressure derivatives in Figs. 7(a) and 8(a), and nearly twice as large as the geometrical angle ϕ_{extent}. Thus, the predictions of simple plane-wave diffraction theory are consistent with the results from the expressions derived here.

IV. CONCLUSION

A semianalytic set of expressions has been derived for the derivative of an acoustic pressure field in a laterally homogeneous waveguide, with respect to an arbitrary three-dimensional refractive index perturbation anywhere within that waveguide, using a normal-mode formulation. The expressions, which were derived using an adjoint Green's function formalism, require two sets of one-dimensional numerical integrations over a set of spatial basis functions. Once these integrations have been computed, a wide variety of perturbations can be rapidly synthesized. The extension of these expressions to density perturbations, although not presented here, should follow a similar route, although the spatial gradient of the Green's function, and thus the gradient of Eqs. (12) and (13), would be required.[18]

These expressions have been demonstrated in simple sensitivity studies that illustrate how both plane-wave and cylindrical perturbations can influence the received pressure field, even when the perturbation does not physically intersect the vertical plane connecting the source and receiver. Whether realistic ocean perturbations produce similar out-of-plane effects has been a question of practical interest.[19,23–25,35,36] Many realistic perturbations, especially those of internal linear waves,[27] can be expressed as straightforward combinations of the basis functions of Eq. (7), so these expressions may be useful in more sophisticated sensitivity studies.

In practical terms the expressions used here could be used to check whether significant horizontal refraction effects might be expected under various experimental deployment geometries, before applying tomographic algorithms that neglect out-of-plane refraction effects. These expressions might also serve as benchmarks for three-dimensional propagation codes, such as a three-dimensional parabolic equation code.[37,38]

These expressions have some theoretical interest as well, as they can be used to compute the Cramer–Rao bounds for environmental parameters related to three-dimensional structures in an ocean waveguide, a rigorous approach for estimating the sensitivity of an acoustic field to a perturbation. For example, the minimum variance of internal wave spectrum estimates extracted from acoustic data could be derived as a function of input sample size and signal-to-noise ratio.

ACKNOWLEDGMENTS

The author wishes to thank Paul Hursky, Bruce Cornelle, Peter Gerstoft, and Bill Kuperman for helpful discussions on adjoint theory. Michael Buckingham and William Siegmann provided advice and references on Bessel addition theorems and perturbative expansions, respectively, while Peter Gerstoft helped provide references to the geoacoustic inversion literature. The ONR Uncertainty Program [ONR Contract No. N00014-00-F-0395] provided support for the authors of this paper, and the ONR Acoustic Entry-Level Faculty Award [ONR Contract No. N00014-03-1-0215] provided supplemental support.

[1] L. L. Van Trees, *Detection, Estimation and Modulation Theory* (Wiley, New York, 1970).
[2] A. B. Baggeroer, W. A. Kuperman, and H. Schmidt, ''Matched field processing: Source localization in correlated noise as an optimum parameter estimation problem,'' J. Acoust. Soc. Am. **83**, 571–587 (1988).
[3] E. Naftali and N. C. Makris, ''Necessary conditions for a maximum-likelihood estimate to become asymptotically unbiased and attain the Cramer–Rao lower bound. I. General approach with an application to time-delay and Doppler shift estimation,'' J. Acoust. Soc. Am. **110**, 1917–1930 (2001).
[4] A. M. Thode, M. Zanolin, E. Naftali, P. Ratilal, and N. C. Makris, ''Necessary conditions for a maximum likelihood estimate to become asymptotically unbiased and attain the Cramer–Rao lower bound. II. Range and depth localization of a sound source in an ocean waveguide,'' J. Acoust. Soc. Am. **112**, 1890–1910 (2002).
[5] M. Zanolin, I. Ingram, A. M. Thode, and N. C. Makris, ''Asymptotic

accuracy of geoacoustic inversions,'' J. Acoust. Soc. Am. (submitted).
[6] D. E. Kirk, *Optimal Control Theory* (Prentice-Hall, Englewood Cliffs, NJ, 1970).
[7] P. R. McGillivray and D. W. Oldenburg, ''Methods for calculation of Frechet derivatives and sensitivities for the nonlinear inverse problem: A comparative study,'' Geophys. Prospect. **38**, 499–524 (1990).
[8] R. G. Pratt, C. Shin, and G. J. Hicks, ''Gauss–Newton and full Newton methods in frequency-space seismic waveform inversion,'' J. Geophys. Int. **133**, 341–362 (1998).
[9] A. Tarantola, ''Inversion of seismic reflection data in the acoustic approximation,'' Geophysics **49**, 1259–1266 (1984).
[10] M. S. Zhdanov, *Geophysical Inverse Theory and Regularization Problems* (Elsevier, Amsterdam, 2002).
[11] S. J. Norton, ''Iterative inverse scattering algorithms: Methods of computing Frechet derivatives,'' J. Acoust. Soc. Am. **106**, 2653–2660 (1999).
[12] C. Wunsch, *The Ocean Circulation Inverse Problem* (Cambridge University Press, Cambridge, MA, 1996).
[13] R.-S. Wu and M. N. Toksoz, ''Diffraction tomography and multisource holography applied to seismic imaging,'' Geophysics **52**, 11–25 (1987).
[14] M. Born and E. Wolf, *Principles of optics* (Cambridge University Press, Cambridge, 1999).
[15] D. N. G. Roy and G. J. Orris, ''A Born scatterer in an acoustical waveguide,'' J. Acoust. Soc. Am. **114**, 626–633 (2003).
[16] P. Hursky, M. B. Porter, B. Cornuelle, W. S. Hodgkiss, and W. A. Kuperman, ''Adjoint modeling for acoustic inversion,'' J. Acoust. Soc. Am. **115**, 607–619 (2003).
[17] J.-C. L. Gac, Y. Stephan, M. Asch, P. Helluy, and J.-P. Hermand, ''A variational approach for geoacoustic inversion using adjoint modeling of a PE approximation model with nonlocal impedance conditions,'' in *Sixth International Conference on Theoretical and Computational Acoustics*, edited by A. Tolstoy, E.-C. Shang, and Y.-C. Teng (World Scientific, Naval Undersea Warfare Center Division, Singapore, 2003).
[18] A. M. Thode and K. Kim, ''Multiple-order derivatives of a waveguide acoustic field with respect to sound speed, density, and frequency,'' J. Acoust. Soc. Am. (accepted).
[19] R. N. Baer, ''Calculations of sound propagation through an eddy,'' J. Acoust. Soc. Am. **67**, 1180–1185 (1980).
[20] M. V. Hall and M. A. Irving, ''Application of adiabatic mode theory to the calculation of horizontal refraction through a mesoscale ocean eddy,'' J. Acoust. Soc. Am. **86**, 1465–1477 (1989).
[21] W. H. Munk, ''Horizontal deflection of acoustic paths by mesoscale eddies,'' J. Phys. Oceanogr. **10**, 596–604 (1980).
[22] W. H. Munk and F. Zachariasen, ''Refraction of sound by islands and seamounts,'' J. Atmos. Ocean. Technol. **8**, 554–574 (1991).
[23] S. Finette and R. Oba, ''Horizontal array beamforming in an azimuthally anisotropic internal wave field,'' J. Acoust. Soc. Am. **114**, 131–144 (2003).
[24] O. A. Godin, ''A 2D description of sound propagation in a horizontally inhomogeneous ocean,'' J. Comput. Acoust. **10**, 123–151 (2002).
[25] A. Tolstoy, ''3D propagation issues and models,'' J. Comput. Acoust. **4**, 243–271 (1996).
[26] R. L. Parker, *Geophysical Inverse Theory* (Princeton University Press, Princeton, NJ, 1994).
[27] T. C. Yang and K. Yoo, ''Internal wave spectrum in shallow water: Measurement and comparison with Garrett-Munk model,'' IEEE J. Ocean. Eng. **24**, 333–345 (1999).
[28] R. G. Pratt and M. H. Worthington, ''Inverse theory applied to multisource cross-hole tomography. I. Acoustic wave-equation method,'' Geophys. Prospect. **38**, 287–310 (1990).
[29] M. Abramowitz and I. A. Stegun, *Handbook of Mathematical Functions* (Dover, New York, 1972).
[30] J. S. Perkins, W. A. Kuperman, F. Ingenito, L. T. Fialkowski, and J. Glattetre, ''Modeling ambient noise in three-dimensional ocean environments,'' J. Acoust. Soc. Am. **93**, 739–752 (1993).
[31] T.-W. Lo, G. L. Duckworth, and M. N. Toksoz, ''Minimum cross entropy seismic diffraction tomography,'' J. Acoust. Soc. Am. **87**, 748–756 (1990).
[32] R. N. Baer, ''Propagation through a three-dimensional eddy including effects on an array,'' J. Acoust. Soc. Am. **69**, 70–75 (1981).
[33] E. G. Williams, *Fourier Acoustics* (Academic, London, 1999).
[34] J. J. Bowman, T. B. A. Senior, and P. L. E. Uselenghi, *Electromagnetic and Acoustic Scattering by Simple Shapes* (Hemisphere, New York, New York, 1987).
[35] J. C. Preisig and T. F. Duda, ''Coupled acoustic mode propagation through continental-shelf internal solitary waves,'' IEEE J. Ocean. Eng. **22**, 256–269 (1997).
[36] S. Finette, M. H. Orr, A. Turgut, J. R. Apel, J. Badiey, C. S. Chiu, R. H. Headrick, J. N. Kemp, J. F. Lynch, A. E. Newhall, K. von der Heydt, B. Pasewark, S. N. Wolf, and D. Tielbuerger, ''Acoustic field variability induced by time evolving internal wave fields,'' J. Acoust. Soc. Am. **108**, 957–972 (2000).
[37] W. L. Siegmann, G. A. Kriegsmann, and D. Lee, ''A wide-angle three-dimensional parabolic wave equation,'' J. Acoust. Soc. Am. **78**, 659–664 (1985).
[38] K. B. Smith, ''A three-dimensional propagation algorithm using finite azimuthal aperture,'' J. Acoust. Soc. Am. **106**, 3231–3239 (1999).

Localization of marine mammals near Hawaii using an acoustic propagation model

Christopher O. Tiemann and Michael B. Porter
Center for Ocean Research, Science Applications International Corporation, 10260 Campus Point Dr, San Diego, California 92121

L. Neil Frazer
Department of Geology & Geophysics, University of Hawaii at Manoa, Honolulu, Hawaii 96822

(Received 18 April 2002; accepted for publication 1 December 2003)

Humpback whale songs were recorded on six widely spaced receivers of the Pacific Missile Range Facility (PMRF) hydrophone network near Hawaii during March of 2001. These recordings were used to test a new approach to localizing the whales that exploits the time-difference of arrival (time lag) of their calls as measured between receiver pairs in the PMRF network. The usual technique for estimating source position uses the intersection of hyperbolic curves of constant time lag, but a drawback of this approach is its assumption of a constant wave speed and straight-line propagation to associate acoustic travel time with range. In contrast to hyperbolic fixing, the algorithm described here uses an acoustic propagation model to account for waveguide and multipath effects when estimating travel time from hypothesized source positions. A comparison between predicted and measured time lags forms an ambiguity surface, or visual representation of the most probable whale position in a horizontal plane around the array. This is an important benefit because it allows for automated peak extraction to provide a location estimate. Examples of whale localizations using real and simulated data in algorithms of increasing complexity are provided. © *2004 Acoustical Society of America.* [DOI: 10.1121/1.1643368]

PACS numbers: 43.30.Sf, 43.30.Wi [WMC] Pages: 2834–2843

I. INTRODUCTION

Passive acoustic methods of observing marine mammals have been of interest for many years for censusing, behavioral studies, and more recently for ensuring mammals are not present in acoustic ranges during operations which might disturb them.[1–5] The acoustic characteristics of whale songs make them detectable at long ranges using hydrophones.[5–9] For example, low-frequency blue and fin whale sounds can be detected 1600 km away.[10,11] When received over an array of hydrophones, whale songs can be used to estimate a singer's position. Unlike difficult radio tagging, passive acoustic observation methods are unobtrusive; a whale's behavior is unlikely to change because of the observation.[12] Acoustic techniques can observe many individuals at once and are suitable for continuous monitoring applications. In addition, acoustic localization also works when animals are hidden from view, such as at night or when submerged.[4]

This paper will describe a new passive acoustic technique for localizing sound sources based on acoustic propagation modeling with an illustration of the technique to localizing marine mammals using widely spaced receivers. The localization algorithm also provides a novel graphical display of marine mammal location that conveys the confidence of the localization and allows for automatic extraction of location estimates. To demonstrate the benefits of this model-based approach, examples of localizations using both real and simulated data in algorithms of increasing complexity will be provided.

A common technique for localizing marine mammals is that of hyperbolic fixing.[4,5,12–17] The measured difference in arrival time of a whale call recorded on multiple hydrophone pairs produces intersecting hyperbolas indicating the animal's position. When the hydrophone pairs are very closely spaced such as on a short towed array or vertical line array (VLA), hyperbolic fixing is no longer practical. Alternative model-based techniques that exploit either the temporal or spatial structure of the received field are then needed. For instance, the arrival times and amplitudes on a single phone can be used to estimate a whale's range.[9] Alternatively, the interphone phase relationships on a VLA (representing the arrival angles of the multipath) can also be exploited.[18]

The technique described here has several advantages over other localization methods. It uses an acoustic propagation model to account for variations in soundspeed and bathymetry, thus eliminating errors from constant soundspeed and straight-line propagation assumptions inherent to hyperbolic fixing.[16] It can be applied to data from widely spaced individual receivers rather than line arrays. Robustness against environmental variability and acoustic multipath may come from performing some processing in the spectral domain,[12,14] but a formal environmental mismatch study has not been performed. The output of the algorithm is a graphical display that easily conveys mammal location and confidence, and despite the algorithm's added computational complexity, it is suitable for real-time implementation without user interaction.

Acoustic data from the Pacific Missile Range Facility (PMRF) hydrophone network off the western coast of Kauai were used to develop this model-based algorithm.[19] In this data set, the species of interest are humpback whales (*Megaptera novaeangliae*) which are known to congregate

 0001-4966/2004/115(6)/2834/10/$20.00 © 2004 Acoustical Society of America

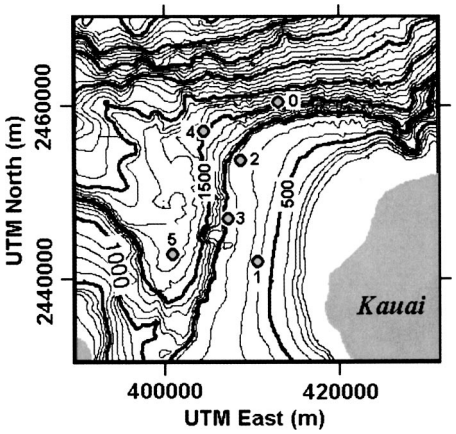

FIG. 1. Bathymetry contours (depths in meters) and hydrophone locations (0–5) at the Pacific Missile Range Facility. Axes are for Universal Transverse Mercator (UTM) Zone 4 coordinates.

near Kauai to breed in winter through spring months after a long migration from the Gulf of Alaska.[20] After describing the available acoustic data set in Sec. II, the localization technique is discussed in Sec. III. Comparisons of localization methods of increasing complexity are presented in Sec. IV.

II. ACOUSTIC DATA

The Pacific Missile Range Facility is an underwater array of over 100 hydrophones in the waters near Kauai, Hawaii. Personnel at PMRF have implemented a near real-time system for transmitting acoustic data from six broadband hydrophones to the Maui High-Performance Computing Center (MHPCC) for analysis. Acoustic data files are posted to MHPCC in 1-min increments. The hydrophones available for use are located 5–20 km apart and are deployed on the sea floor at the locations and depths shown in Fig. 1 and Table I.

Two days of continuous acoustic data from the six hydrophones during March 22 and 23, 2001 were used for algorithm development. Originally sampled at 10 or 20 kHz, the data were low-pass filtered and downsampled to 2 kHz to isolate the frequency band containing most of the energy of the humpback whale songs. Songs are heard on every hydrophone and at all times of day. In many cases, the sounds of multiple marine mammals can be heard simultaneously. While viewing spectrograms of the acoustic data, spectral patterns similar to those associated with humpback whales[21,22] are frequently observed. While it is not practical to listen to every channel of the entire data set duration,

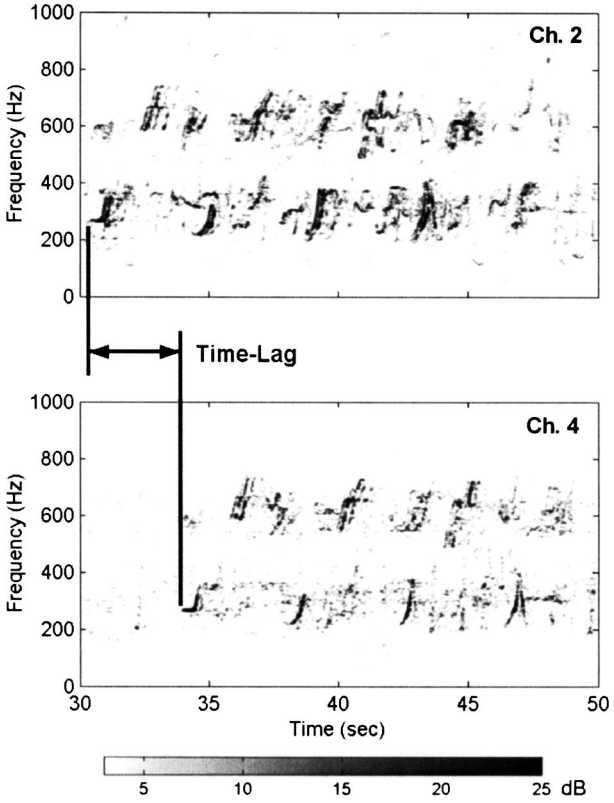

FIG. 2. Spectrograms of acoustic data from hydrophones 2 (top) and 4 (bottom) starting at time 20:16:30 on 3/22/01. A 3.5-s time lag for spectral transients is apparent between the two spectrograms. Spectral patterns resemble those of humpback whale calls.

spectrograms can be examined quickly to confirm that all recordings contained the patterns expected of humpback whale songs.

When spectrograms from all hydrophones for the same time segment are viewed concurrently, similar spectral patterns are often recognized in two or more spectrograms, but offset in time. In such cases, the same whale call is being recorded on multiple receivers, but the time of arrival at the receiver varies according to range from the singer. As an example, Fig. 2 shows spectrograms from hydrophones 2 and 4 for a 20-s segment of data from minute 20:16 on March 22, 2001; the spectrograms were made using 512-point fast Fourier transforms (FFT's) with 90% overlap. A call pattern can be seen repeated on hydrophone 4 approximately 3.5 s after the same pattern on hydrophone 2. It is this difference in arrival times (or time lag) for the same call on two different channels that will be used in the localization process.

TABLE I. Hydrophone positions in geodetic and Universal Transverse Mercator coordinates (Zone 4, WGS84 datum).

Hydrophone No.	Latitude (deg)	Longitude (deg)	UTM North (m)	UTM East (m)	Depth (m)
0	22.246158	−159.842556	2460315.3	413179.3	1638
1	22.080938	−159.867735	2442040.5	410480.1	649
2	22.191175	−159.886739	2454254.8	408590.6	777
3	22.125975	−159.897757	2447044.0	407412.1	843
4	22.215686	−159.929232	2456994.3	404226.6	1560
5	22.091847	−159.957723	2443303.8	401203.5	1768

III. LOCALIZATION ALGORITHM

The model-based localization algorithm consists of two main components: spectral pattern correlation to calculate time lags and ambiguity surface construction to generate a location estimate. Ambiguity surfaces are probabilistic indicators of source location and are constructed through comparison of measured time lags (''data'') to predicted time lags (''replicas''). Replica generation has a hierarchy of increasing modeling complexity, and one goal of this study was to determine how much modeling sophistication is necessary for a correct localization. Example localizations from three techniques using both real and simulated data are presented below to address that question.

A. Spectrogram correlation

Measuring time lags between whale call arrivals at different hydrophones is a critical step in the localization algorithm. The standard method for determining time lags between two signals is through cross correlation, but whether the correlation should be performed on the original wave forms or their spectrograms is open to debate and could depend upon the peculiarities of the signals being processed. Spectrogram correlations are commonly used in whale localization efforts,[4,5,12,14] perhaps because the signal structure remains obvious even in the presence of interferers. Spectrogram correlation may also be more robust than wave form correlation against multipath acoustic arrivals.[12] However, wave forms containing whale calls have been successfully used in both matched-filter[13] and cross correlation[14,16,17] processes. Proponents of wave form approaches argue that the resulting measurements of time lag are more precise.[12,14] Because no formal arguments exist regarding the superiority of a correlation method, both spectral and wave form correlation methods were applied to short segments of the data set in order to determine which method is best for measuring pairwise time lags in the PMRF environment.

The pairwise spectral shape correlations follow an example described by Seem and Rowe.[23] Spectrograms from two hydrophones are digitized, i.e., converted to two levels of intensity (on or off) based on a data-adaptive threshold that guarantees a minimum number of ''on'' pixels per time window. In doing so, the loudest spectral content remains visible in the digitized spectrogram while low-level spectral patterns are hidden, thus adding some robustness against multiple sources. Correlation is done very quickly by performing a logical AND operation on the overlapping region as two digitized spectrograms are shifted past each other. Summing the overlapping pixels provides a correlation score, in units of pixels, whose maximum determines the time lag between channels as well as providing a confidence level of the measurement.

A mathematical description of both the wave form and spectral correlators follows. It assumes that two receivers are separated by a distance d in waters with mean sound speed c. Time series from the two receivers are sampled with a period of Δt and are described by

$$r_i = r(t_i) \quad \text{and} \quad s_i = s(t_i) \quad \text{where} \quad t_i = i \cdot \Delta t. \tag{1}$$

A frame length in seconds, τ_{frame}, is chosen that is slightly longer than a typical whale call from the species of interest. (A 10-s frame length was used with humpback whale calls.) Each frame will contain N samples defined by

$$N = \tau_{\text{frame}} / \Delta t. \tag{2}$$

The mth frame is extracted from each time series:

$$r_i^m = r_{m \cdot N + i} \quad \text{and} \quad s_i^m = s_{m \cdot N + i}, \quad i = 1,...,N. \tag{3}$$

The wave form correlation score at each lag bin l for the mth frame is calculated by

$$c_l^m = \sum_{i=1}^{N} r_i^m \cdot s_{i-l}^m. \tag{4}$$

The lag bin l with the highest wave form correlation score designates the time lag T_w between the two time series for frame m according to

$$T_w^m = l \cdot \Delta t. \tag{5}$$

The spectral correlation is based on the short-time Fourier transform of a time series:

$$R(t, f; \tau_{\text{snap}}) = \int_{-\tau_{\text{snap}}/2}^{\tau_{\text{snap}}/2} r(t-\tau) \cdot e^{-i 2 \pi f \tau} d\tau. \tag{6}$$

Spectrogram R is computed using a FFT to produce a discretized spectrogram. Each spectrogram frame is of length τ_{frame} and has dimensions of N_{freq} frequency bins (256 in this example) and N_{snap} time bins or ''snapshots'' where

$$N_{\text{snap}} = \frac{N}{2 \cdot N_{\text{freq}}} \tag{7}$$

(assume N_{freq} divides N exactly). It follows that the time resolution of the snapshots is

$$\tau_{\text{snap}} = 2 \cdot N_{\text{freq}} \cdot \Delta t \tag{8}$$

and the frequency resolution is

$$\Delta f = \frac{1}{\tau_{\text{snap}}}. \tag{9}$$

Given the notation

$$R_{ij} = R(t_i^{\text{snap}}, f_j) \quad \text{where} \quad i_i^{\text{snap}} = i \cdot \tau_{\text{snap}} \quad \text{and} \quad f_j = j \cdot \Delta f \tag{10}$$

the mth frame is defined as

$$R_{ij}^m = R_{m \cdot N_{\text{snap}} + i, j} \quad \text{where} \quad i = 1,...,N_{\text{snap}} \quad \text{and} \quad j = 1,...,N_{\text{freq}}. \tag{11}$$

A repeat of the above for time series s makes an analogous definition for frame S_{ij}^m. Also calculated is the number of snapshots needed when the maximum possible time lag between sensors is added to the desired frame length:

$$N_{\text{max lag}} = \frac{\tau_{\text{frame}} + d/c}{\tau_{\text{snap}}}. \tag{12}$$

Next, each receiver's spectrogram frame will be digitized or ''pixilated,'' i.e., each time/frequency bin in the spectrogram will be assigned a 0 or 1 according to an adap-

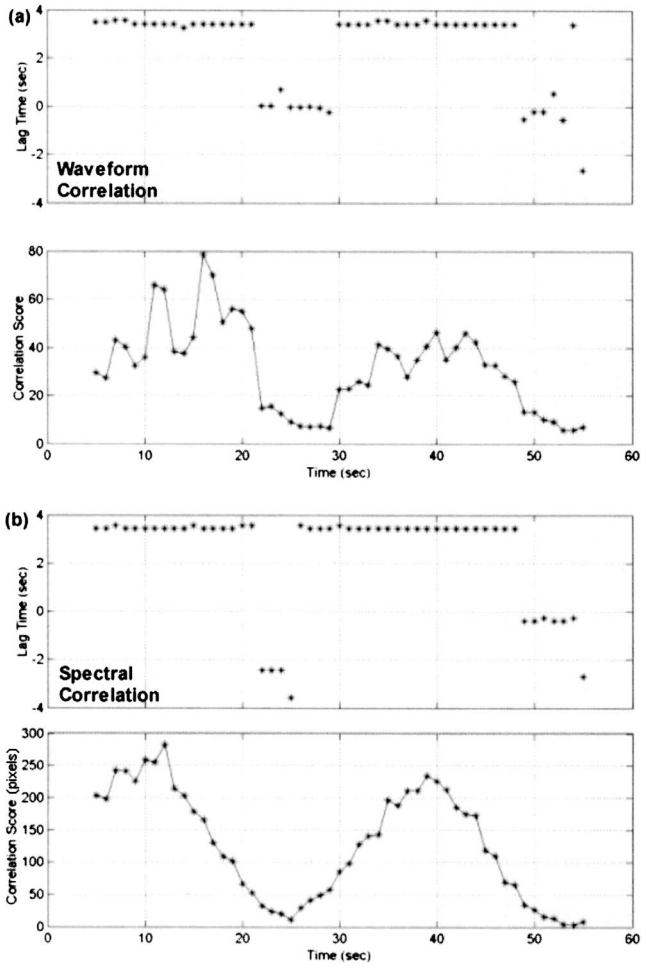

FIG. 3. Time lags and correlation scores output by the cross correlator using wave forms (a) and digitized spectrograms (b). Cross correlations use data from hydrophones 2 and 4 for minute 20:16 on 3/22/01. The 3.5-s time-lag measurement from the correlators agrees with that visually observed in Fig. 2.

tive threshold. A unit step function provides the digitization mechanism:

$$u(x)=\{1 \quad \text{if} \quad x>0$$
$$\{0 \quad \text{if} \quad x\leqslant 0. \tag{13}$$

For each frame R_{ij}^m, a spectral power threshold σ_R^m is calculated that guarantees a minimum number N_{pixels} of "1" pixels (40 per second in this example), such that

$$\sum_i \sum_j u(R_{ij}'''-\sigma_R^m)\geqslant N_{\text{pixels}}. \tag{14}$$

A different threshold σ is calculated for each receiver, and the mth frames are pixelated to make the digitized frames D and E:

$$D_{ij}^m=u(R_{ij}^m-\sigma_R^m) \quad \text{and} \quad E_{ij}^m=u(S_{ij}^m-\sigma_S^m). \tag{15}$$

The spectral correlation score at each lag bin l for the mth frame is calculated by

$$C_l^m=\sum_{i=1}^{N_{\text{snap}}}\sum_{j=1}^{N_{\text{freq}}} D_{ij}^m\cdot E_{i-l,j}^m$$
$$\text{where} \quad l=-N_{\text{max lag}},\ldots,N_{\text{max lag}}. \tag{16}$$

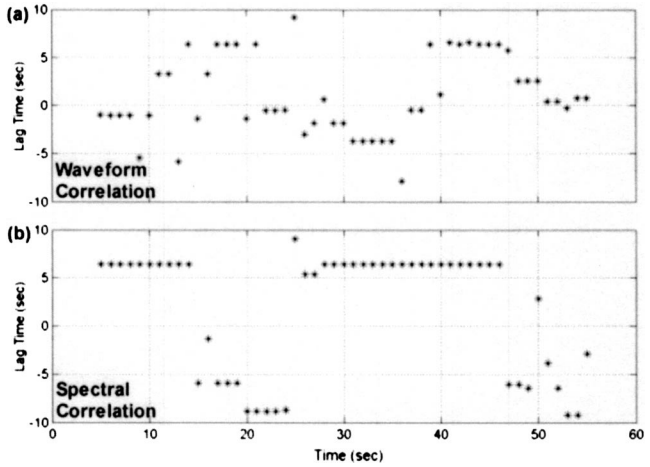

FIG. 4. Time lags output by the cross correlator using wave forms (a) and digitized spectrograms (b). Cross correlations use data from hydrophones 2 and 5 for minute 20:16 on 3/22/01. The consistency of the spectral correlator made it the preferred method for time-lag measurement.

The lag bin l with the highest spectral correlation score designates the time lag T_s between the two mth frames according to

$$T_s^m=l\cdot N_{\text{freq}}\cdot \Delta T. \tag{17}$$

An example of cross correlator output is shown in Fig. 3, where results from both wave form correlation [Fig. 3(a)] and digitized spectral correlation [Fig. 3(b)] are presented for comparison. Data are from hydrophones 2 and 4 for minute 20:16 on March 22, 2001; this time segment includes the data shown in Fig. 2. A time window 10 s long extracts data subsets (frames) to use with each correlation, and the window advances in 1-s increments through the entire minute, calculating a time-lag and correlation score at each step. (Note that correlation scores indicate relative correlation strength among time steps, are in different units, and should not be compared between the two techniques.) In this example, both the wave form and spectrogram correlation methods correctly extract the interchannel time lag of 3.5 s during periods when the whale is singing. Furthermore, the correlator scores drop when the animal stops singing (around 25 s). By setting thresholds on the correlation score, only the most confident of the time-lag estimates are passed to the localization process, thus freeing the correlation output from human examination. A spectrogram correlation score threshold of 100 pixels was used in this processing, and if no correlation score exceeded the threshold for a given time window, no localization was attempted.

Agreement between the two correlation methods is not always as good as that shown in Fig. 3. Typically, the spectral correlator time-lag measurements were more consistent. To illustrate this, Fig. 4 shows output from both the wave form and spectral correlators for the same minute as that in Fig. 3 but for the hydrophone pair 2 and 5. Time-lag measurements from the wave form correlator are quite variable over the minute while the spectral correlation process provides a more stable measurement. Perhaps the scattering in the wave form correlator's output is due to interferers such as other distant animals singing simultaneous songs,[12] but de-

termining the criteria for when one correlation method is better than another remains an interesting area of study which will not be addressed further here. Because of the more consistent measurements provided by the spectral correlator in this environment, it was used in all further analysis to provide time-lag data to the ambiguity surface constructor.

B. Replica generation

The second input needed for ambiguity surface generation is the replica. In this application, the replica is a prediction of time lags that would be measured by every receiver pair combination from a source at every location within a grid of candidate positions around the array. In order to calculate time lags, acoustic travel times from each possible source location to each receiver must be calculated first, but the model complexity used during travel-time calculation can sometimes affect the accuracy of the resulting localization. In efforts to compare the effects of modeling complexity, three replicas were made within a hierarchy of modeling sophistication. Replica computation time increases with added complexity.

Common to all the replicas is the resolution of the candidate source locations. Simulated sources are spaced every 200 m in latitude and longitude in a 30-km square grid around the array. Source frequency is set at 500 Hz, the center of the frequency band of interest, and source depth is assumed to be 10 m, within the range of expected depths for singing humpbacks near Hawaii.[24] While only one source depth is used in the replica generation to follow, the search grid can be expanded to include multiple source depths if needed. Average historical soundspeed profiles for the region were taken from the Generalized Digital Environmental Model (GDEM), and PMRF provided bathymetry data for the range. Geoacoustic properties of the sea floor are those typical of sand:[25] density 1.9 g/cm^3, compressional wave speed 1650 m/s, compressional wave attenuation .8 dB/wavelength. (Values are from Table 1.3 of Ref. 26, based on the work of Hamilton.[27]) The Gaussian beam acoustic propagation model BELLHOP was used to calculate travel times as it can account for depth-dependent sound speed profiles and range-dependent bathymetry.[28,29] Given the small variation in sound speed profiles over the area of study, the assumption of range-independent sound speeds inherent to BELLHOP was acceptable, and refractive effects outside of the plane of propagation were not considered in the modeling.

The simplest replica uses assumptions equivalent to three-dimensional hyperbolic fixing techniques. Sound speed is assumed to be constant at 1510 m/s, and only the direct acoustic path from the shallow source to the true receiver depths determines the acoustic travel time. No bathymetric effects are considered. After travel times from every candidate source position to every receiver position are calculated, the appropriate travel time pairs are subtracted to create a replica matrix of time lags indexed by source position and hydrophone pair.

The next replica in this hierarchy adds a depth-dependent sound speed profile to the acoustic modeling, but bathymetric effects are still ignored; this will be called the ''range-independent'' replica. To illustrate the effect of the downward-refracting sound speed profile on acoustic paths, Fig. 5 shows both the average sound speed profile used in the calculation and the resulting direct acoustic ray paths between the shallow source and hydrophone 0 at several ranges. The mean acoustic sound speed varies with range from the receiver, so travel time will not increase linearly with range. The travel time is still that of the direct acoustic path.

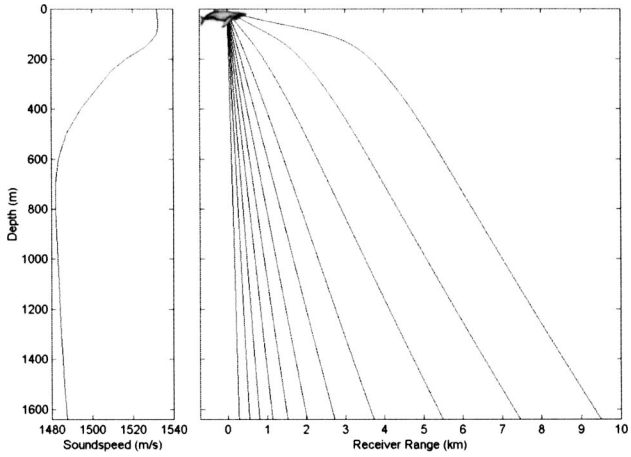

FIG. 5. Average soundspeed profile and predicted direct acoustic ray paths between a shallow whale and hydrophone 0 (1638-m depth) at several ranges. The predicted mean acoustic soundspeed varies with range from the receiver, and no bathymetric effects are included. Travel times from such simulations constitute the ''range-independent'' replica.

Lastly, the ''range-dependent'' replica adds range-dependent bathymetric effects to the acoustic modeling. Note that sound speed profiles are still range independent. The addition of bathymetry contours to the acoustic model allow for multipath arrivals from bottom-reflected paths to be included in the travel time calculation. Figure 6 shows the predicted acoustic ray paths from a shallow source to hydrophones 2 and 5 along two perpendicular bathymetry slices.

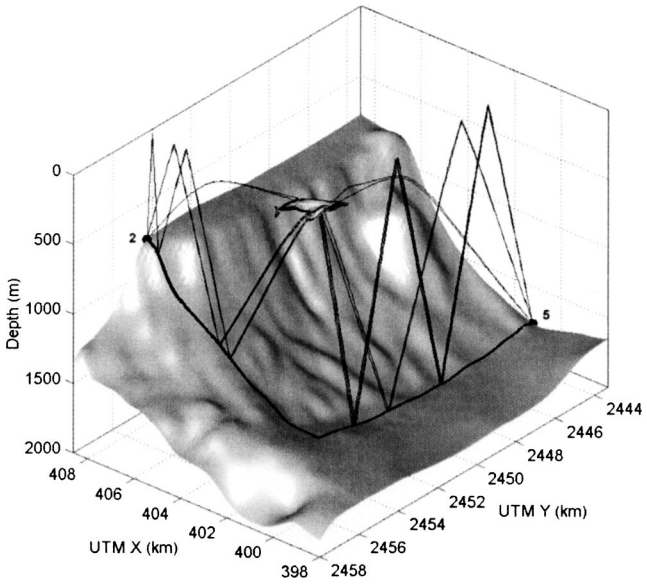

FIG. 6. Predicted direct and reflected acoustic ray paths between a shallow whale and hydrophones 2 and 5 along two perpendicular bathymetry slices. Whale not drawn to scale. The ''range-dependent'' replica allows for both direct and reflected ray paths to be included in the travel time calculation.

While both slices in this example contain both direct and reflected ray paths, in some long-range cases, there is no direct acoustic ray path between a candidate source position and a receiver; only reflected ray paths will connect the two. Because every ray path has a different travel time τ, an average travel time τ_{avg} from all N_{arr} arrivals, weighted by the ray paths' predicted amplitudes a, is used as the single travel time value from a given source location:

$$\tau_{\text{avg}} = \sum_{i=1}^{N_{\text{arr}}} \frac{|a_i| \cdot \tau_i}{a_{\text{sum}}} \quad \text{where} \quad a_{\text{sum}} = \sum_{i=1}^{N_{\text{arr}}} |a_i|. \tag{18}$$

To complete the replica generation process, the replica time lag T_r is made by taking the difference in average travel times for a given receiver pair p from a hypothesized source at search grid position $\overline{x_s} = (x_s, y_s, z_s)$. Like the other replicas, the range-dependent time-lag replica is precalculated for all receiver pair/source position combinations:

$$T_r^p(\overline{x_s}) = \tau_{\text{avg}}^{p_1}(\overline{x_s}) - \tau_{\text{avg}}^{p_2}(\overline{x_s}), \tag{19}$$

where p_1 and p_2 are the two hydrophones making up receiver pair p.

For every replica type, the BELLHOP propagation model also provides an estimate of acoustic intensity $P_n(\overline{x_s})$ for acoustic paths between every source position $\overline{x_s}$ and receiver n. Degradation of the source amplitude, or transmission loss, is saved as part of the replica as well and will be used in scaling the ambiguity surface to follow.

C. Ambiguity surface construction

A singing whale is localized through the construction of an ambiguity surface that is generated in the same way regardless of the type of replica (range independent or range dependent) used. The ambiguity surface is a two-dimensional plan view of the area around the array containing the same latitude/longitude locations as the candidate source positions assumed during replica construction. Although each surface assumes a constant source depth, a different surface can be made for each hypothesized source depth. One input to the localization process is the spectrogram-measured time lags T_s^{mp} and correlation score for frame m and each receiver pair p. Only those measurements with high spectral correlation scores (over 100 pixels) are passed to the localization process. This ensures a high confidence in the resulting location estimates. The replicas of predicted time lags $T_r^p(\overline{x_s})$ and transmission loss $P_n(\overline{x_s})$ serve as another input. Note that replicas are time independent; they only need to be calculated once provided the environment or receiver positions do not change.

For each source position $\overline{x_s}$ and receiver pair combination, the difference between the predicted time lag from the replica and the measured time lag is normalized by the maximum possible time lag between receiver pair p separated by distance d_p. The resulting likelihood scores for each pair form a surface with a minimum where the replica and data agree best. The contours of the surface are accentuated by taking the square root of the likelihood scores to make the new surface L for the mth frame:

$$L_p^m = \sqrt{\frac{|T_r^p(\overline{x_s}) - T_s^{mp}|}{d_p / c}}. \tag{20}$$

In order to represent increased localization uncertainty at long range, the contribution to a localization from a distant receiver pair is diminished; close receiver pairs will contribute more in the ambiguity surface construction. This is done by scaling the likelihood scores by the predicted acoustic intensity. The acoustic transmission loss in dB, α, is calculated for the two acoustic paths from a source to a pair of receivers and summed:

$$\alpha_p(\overline{x_s}) = 20 \log_{10}(P_{p_1}(\overline{x_s}) \cdot P_{p_2}(\overline{x_s})). \tag{21}$$

When an α is found for every candidate source position $\overline{x_s}$, it will form a transmission loss surface of the same dimensions as the likelihood surface L. The likelihood surfaces for all contributing receiver pairs are scaled by their corresponding α and summed to complete construction of the ambiguity surface A for the mth frame:

$$A^m = \sum_p L_p^m \cdot \alpha_p. \tag{22}$$

The surface A represents a planview of the waters around the array for a single source depth, and source location estimates common to many receiver pairs will sum to form a peak indicating the best estimate of source position.

IV. LOCALIZATION COMPARISONS

Because of the added computational complexity required of each level of the replica generation hierarchy, a comparison of localization results from different replicas, plus comparisons to standard hyperbolic fixing techniques, would examine whether any added benefits are worth the additional computational costs. However, that answer depends on the environment under study and the source position. The following sections provide an example in which all localization methods perform equally well plus another example in which only the most sophisticated modeling will produce the correct answer. In the comparisons to follow, time-lag measurements are provided to three localization techniques: two-dimensional hyperbolic fixing, range-independent model-based localization, and range-dependent model-based localization.

A. Real-data localization

The first set of localization comparisons uses time-lag measurements from the same data exhibited in Figs. 2, 3, and 4: recordings of minute 20:16 on March 22, 2001. From one frame of time-lag measurements extracted from that minute, six hydrophone pairs have correlation scores exceeding the score threshold, and their time lags are passed to the localization algorithms. Output from the three localization techniques is presented in Fig. 7 in order of increasing computational complexity. Each frame of Fig. 7 represents a 30-km-square area of ocean around the PMRF array, with hydrophone positions labeled (0–5).

Figure 7(a) represents the traditional technique of plotting intersecting hyperbolic trajectories of possible source

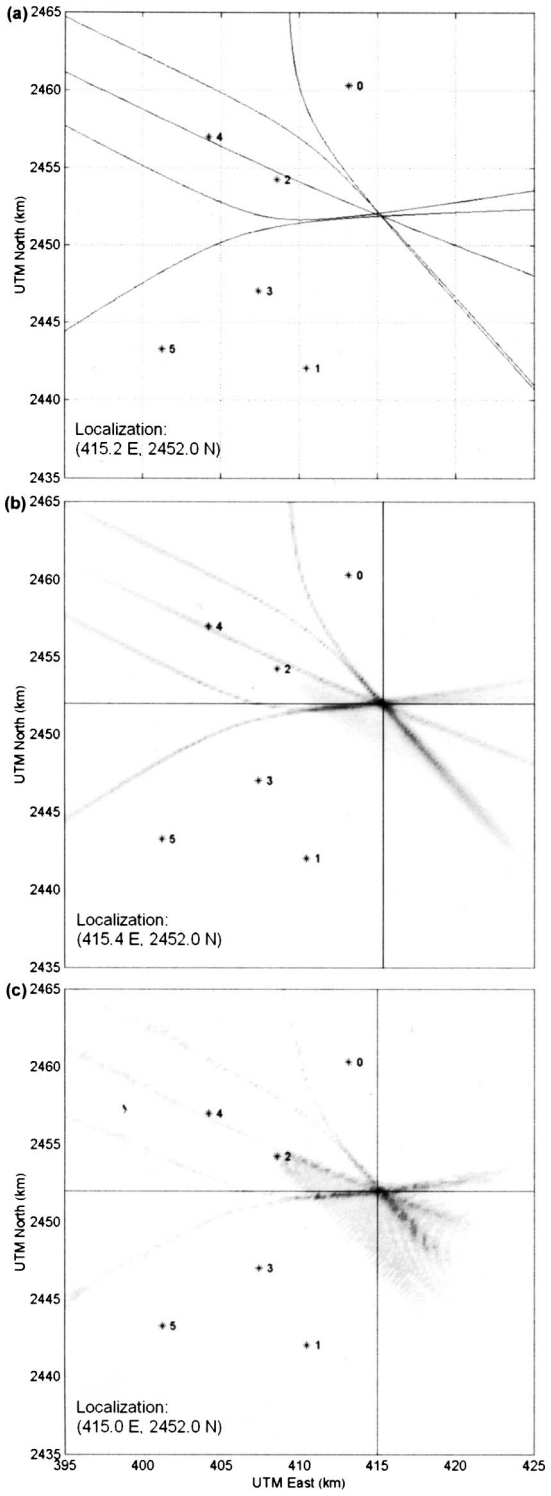

FIG. 7. Plan views of the waters around the PMRF array with hydrophone positions (0–5) indicated. Axes are for UTM Zone 4. Curves from hyperbolic fixing (a) intersect at possible whale positions. Ambiguity surfaces from range-independent (b) and range-dependent (c) model-based localizations indicate whale position estimates with high intensities and crosshairs. Coordinates of the location estimates indicated in figure. Data is from minute 20:16 on 3/22/01.

positions based on time lags. This technique uses no acoustic modeling other than the assumption of a constant soundspeed of 1510 m/s, although the mean horizontal propagation speed versus range from source to hydrophone could vary from 1300 m/s to 1520 m/s depending upon range and depth of the receiver. Note that not all hyperbolic paths intersect precisely at the same point, perhaps due to the errors associated with the constant soundspeed assumption. Nevertheless there is a tight clustering of intersections at approximately 415.2 km east, 2452.0 km north, which is then regarded as the estimate of whale location.

Figures 7(b) and (c) demonstrate the strengths of ambiguity surface visualization. Using the time-lag data and range-independent [7(b)] or range-dependent [7(c)] replicas, ambiguity surfaces were constructed as described in Sec. III C. On these surfaces, areas of peak intensity represent the most confident whale position estimates and are marked with crosshairs. The location estimates from the model-based approaches agree well with each other and the hyperbolic estimate; exact localization coordinates are indicated within each figure frame. Note that ambiguity surfaces still reveal patterns resembling hyperbolas, but the curves have effectively been thickened and stacked in such a way that automatic identification of the most probable source location is possible. The jaggedness of the range-dependent curves is due to variability in travel time and transmission loss predictions caused by bathymetry effects. Furthermore, the narrowness of the ambiguity surface peak convey high confidence in the localization. A sharp peak implies that many receiver paris had the same location estimate in common; a broad peak suggests greater uncertainty in the localization as several pairs' location estimates failed to overlap at a common point.

In this localization example, all techniques agree well, and localizations are in close proximity regardless of replica complexity. The agreement between all techniques is probably due to the relatively short ranges from source to receiver and deepness of the water; direct acoustic paths to all receivers exist, so accounting for bathymetric effects is not necessary for a correct answer. Unfortunately, no independent visual surveys are available during the times of the acoustic recordings, so location estimates cannot be verified through other means.

The analysis described here was applied to many other short time segments throughout the two days of acoustic data. Localization using the constant-soundspeed replica, not shown in the comparisons above, was included as well. In every case, a source was confidently localized by the model-based techniques through a contribution of four or more receiver pairs. The acoustic data from those times were then played back to verify the presence of a marine mammal. However, when using hyperbolic fixing methods, the tight grouping of intersections like those in the example above was not always seen, sometimes making source location difficult to determine. It was hypothesized that any advantages of the most sophisticated range-dependent replica over the other replicas would best be seen in localizations of sources at long range from the receivers. This could best be tested by placing a simulated whale at the extent of the search grid.

B. Simulated localization

To demonstrate a situation when the full complexity of the range-dependent model-based replica is necessary for a correct localization, a simulated source is placed in the

southwest corner of the search grid very near the border (396 km east, 2436 km north, 10 m depth) and the acoustic model BELLHOP used to simulate travel times from the source to all receivers. The difference in simulated travel times became the simulated time-lag data passed to the localization algorithms.

Figure 8 shows the resulting source location estimates from three techniques. The hyperbolic fixing method, shown in Fig. 8(a), has many hyperbola intersections, each indicating a possible source location. Because the intersections are scattered over several square kilometers, determining a single location estimate is difficult. The range-independent model output, shown in Fig. 8(b), shows some increases in intensity on the ambiguity surface indicating likely source positions. However, the contributions from individual receiver pairs do not stack up correctly to form a single peak at the true source location. Instead, a coincidental intersection of ambiguity surface curves puts a peak 15.3 km away from the true source location. The ambiguity surface from the range-dependent model, Fig. 8(c), correctly identifies the true source position, but it is expected to do so since the data and replica in this test will have perfect agreement at the source location. This one simulation illustrates that at ranges where refractive and bathymetric effects are important the assumptions inherent to hyperbolic fixing and the range-independent replica break down, leading to an incorrect localization.

In efforts to quantitatively compare the localization errors of the different techniques, a simulation like the one above was repeated many times while moving the simulated source through every search grid position around the array. The distance between the resulting location estimate and the source was recorded for each source position. The localization errors were then assembled to make an error map like those of Fig. 9. The three replicas of increasing complexity as described in Sec. III B were used in the localization process, each generating its own error map. Figure 9(a) shows the error map for the simplest replica which uses assumptions equivalent to hyperbolic fixing techniques: constant soundspeed and straight-line, direct acoustic paths with no bathymetric effects. Figure 9(b) shows the error map when the range-independent replica is used in the localization. Note that an error map for the range-dependent replica is not shown because it always correctly identifies the source location; the simulated data and replica are identical.

Of interest in Fig. 9 is that localization is almost perfect regardless of replica type when the source is close enough to the receivers for a direct acoustic path to exist. In cases where bathymetric effects can be ignored, even the assumptions of the simplest hyperbolic fixing method are still suitable for a correct localization. The advantages of using the full range-dependent replica are apparent at the outer limits of the search grid where localization errors from using simple models can be as high as 25 km. Only the range-dependent replica that accounts for bottom interactions correctly locates the source. Therefore, when trying to extend target localization far beyond array boundaries, one must balance the increased accuracy of the more sophisticated replica model against the increased costs of longer calculation time and higher environmental characterization requirements.

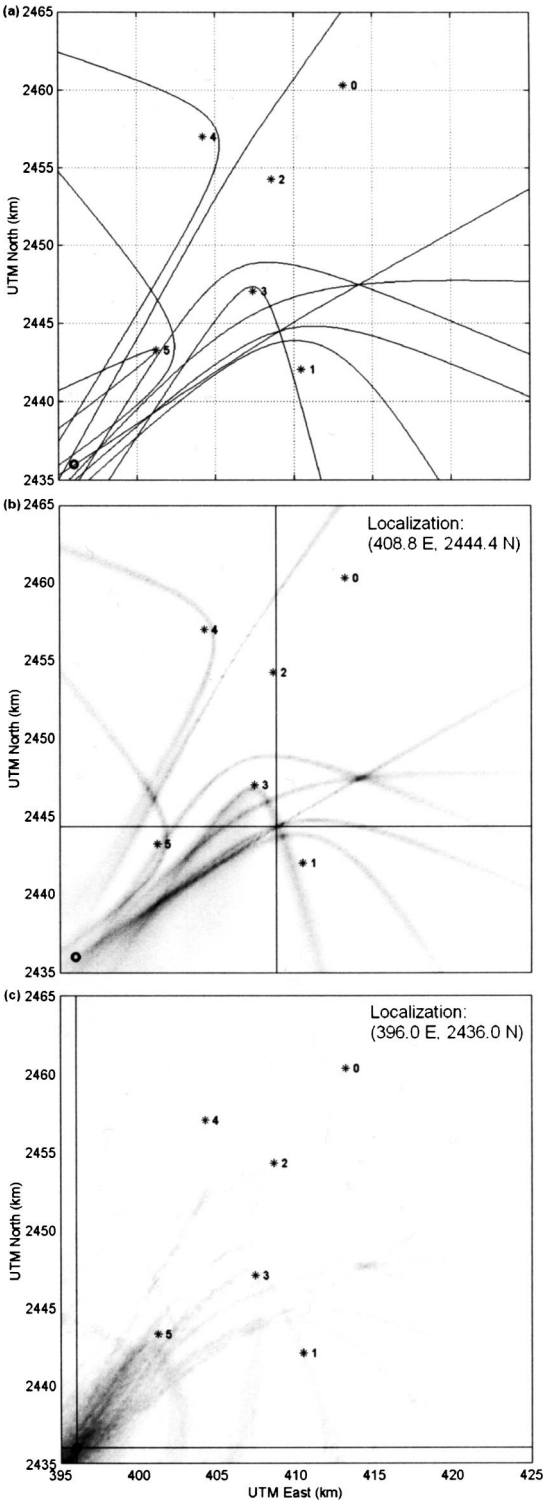

FIG. 8. Plan views of the waters around the PMRF array with hydrophone positions (0–5) indicated. Axes are for UTM Zone 4. Curves from hyperbolic fixing (a) intersect at many possible whale positions. Ambiguity surfaces from range-independent (b) and range-dependent (c) model-based localizations indicate whale position estimates with high intensities and crosshairs. Data are from a simulated whale at 396 km east, 2436 km north with position indicated by circle. Coordinates of the model-based location estimates indicated in figure.

The error maps of Fig. 9 are an example of how one can quantify errors associated with the different techniques

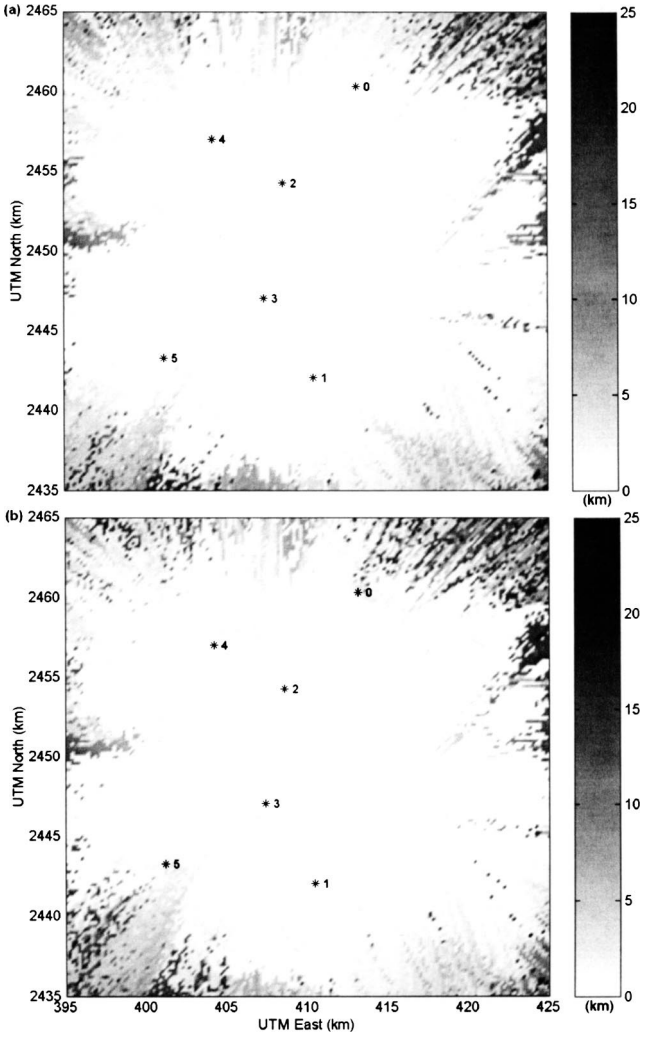

FIG. 9. Maps of localization error on plan views of the waters around the PMRF array with hydrophone positions (0–5) indicated. Axes are for UTM Zone 4. Maps indicate distance in kilometers between source and location estimate for a simulated source at the map coordinates. Results from simple hyperbolic replica shown in (a); range-independent replica shown in (b). Errors increase when far outside array as bathymetric effects become more important with increased range.

through simulation, but to truly measure the error an experiment localizing a controlled source of known location is required. However, any error measurements, real or simulated, will be specific to the environment and receiver geometries used and thus are not easily generalized. It is also difficult to get formal bounds on uncertainties in the localization, such as those resulting from environmental mismatch or the correlation process for example. One strategy for measuring uncertainty could involve adding mismatch in a Monte Carlo fashion to the environment used in replica and simulated data generation and then repeating the localization process.

V. DISCUSSION

The purpose of this work is to introduce a new passive acoustic technique, with advantages over traditional methods, for localizing singing marine mammals, humpback whales in particular. Based on acoustic propagation modeling, it claims increased accuracy in geometries where acoustic bottom interaction becomes important. The algorithm also provides a visual display of whale location that is easy to interpret and allows for automatic location extraction. While the few localization examples shown here, plus many others not presented, build confidence in the algorithm, it is recognized that the algorithm has yet to be verified with other independent methods such as by visual observation or controlled source localization.

One question that arises is what amount of acoustic modeling complexity is really necessary for localizations of a desired accuracy. Each level of the modeling hierarchy has its advantages and disadvantages. For example, the range-independent replica used in this work can be quickly calculated in minutes and requires no prior knowledge of an environment's bathymetry or geoacoustic properties. The range-dependent replica can improve localization accuracy, particularly at long ranges, but it requires 100 times more computation time. The advantages of the range-dependent replica may drastically increase in areas with complicated bathymetry or in shallow water. Ultimately, the choice of model lies with the user to balance environmental definition and replica precalculation time versus localization accuracy and range, and even traditional hyperbolic fixing methods should remain an option in some geometries.

It should be stressed that although replica precalculation can be a several-hour process, this step needs to be repeated only as often as the environment or array geometry changes; the remaining spectrogram correlation and localization calculations are relatively simple. In the analysis of data from PMRF, the localization could be completed within the data update period of 1 min. The algorithm can run without operator oversight by requiring high localization scores, such as over 75% of maximum possible score, be met before declaring a localization in order to minimize false alarms. It is also rapid enough for near real-time processing. Both of these qualities make it a good candidate for continuous, long-term monitoring of marine mammal activity, provided the animals are vocalizing.

To demonstrate how this algorithm could be a tool for behavioral studies, Fig. 10 shows the most confident whale location estimates from the 24 hours of March 23, 2001. The locations of ambiguity surface peaks that were over 75% of the maximum score are shown as points on this plan view. From this plot, one could conclude that on this day singing whales preferred to stay near the shore of Kauai instead of venturing out into deeper water. Through acoustic studies over longer time periods and ranges, common travel routes may become apparent, especially when used in conjunction with other complementary techniques such as visual observation and tagging.

The algorithm presented here has a modular design that adds to its flexibility and facilitates advancement. For example, should wave form cross correlations offer advantages over spectrogram correlations, it is easy to substitute that step in the processing. Because replica generation is independent of the visualization process, it does not have to be limited to ray theory; full wave acoustic models may easily be substituted for still further improvements in accuracy. Lastly, while the algorithm described here was used in a two-

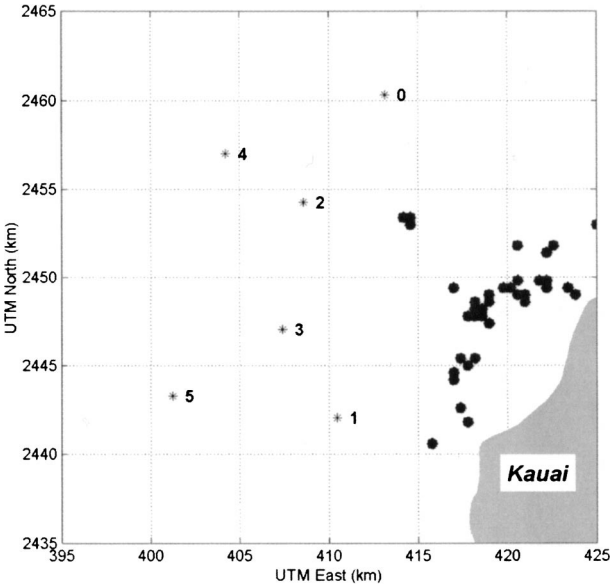

FIG. 10. Plan view of the waters around the PMRF array with hydrophone positions (0–5) indicated. Axes are for UTM Zone 4. Points show locations of the most confident whale location estimates during the 24 hours of 3/23/01. Such continuous, long term monitoring can provide clues to animal behavior.

dimensional search (latitude/longitude) it has an immediate generalization to a full three-dimensional volumetric search.

ACKNOWLEDGMENTS

We gratefully acknowledge the support of the Pacific Missile Range Facility (Jim Hager) and the Maui High-Performance Computing Center (Robert Desonia and D. J. Fabozzi) in establishing the real-time monitoring facility. Several colleagues at SAIC were also instrumental in this work. In particular, thanks to Dave Gever for implementing the web-based control software and Richard Bachman for environmental characterization of the site. Thanks to Paul Hursky for preparing all the raw acoustic data for use. Finally, we thank Herb Freese for general discussions. This work was supported by the National Defense Center of Excellence for Research in Ocean Sciences (CEROS Contract No. 47316). Additional support was provided by the Office of Naval Research (ONR Contract No. N00014-00-D-0115).

[1] H. E. Winn, R. K. Edel, and A. G. Taruski, ''Population estimate of the humpback whale (*Megaptera novaeangliae*) in the West Indies by visual and acoustic techniques,'' J. Fish. Res. Board Can. **32**, 499–506 (1975).
[2] W. A. Watkins, ''Activities and underwater sounds of fin whales,'' Sci. Rep. Whales Res. Inst. **33**, 83–117 (1981).
[3] P. O. Thompson, W. C. Cummings, and S. J. Ha, ''Sounds, source levels, and associated behavior of humpback whales, Southeast Alaska,'' J. Acoust. Soc. Am. **80**, 735–740 (1986).
[4] C. W. Clark, W. T. Ellison, and K. Beeman, ''Acoustic tracking of migrating bowhead whales,'' IEEE Oceans 1986 Conference Proceedings, pp. 341–346.
[5] A. S. Frankel, C. W. Clark, L. M. Herman, and C. M. Gabriele, ''Spatial distribution, habitat utilization, and social interactions of humpback whales, *Megaptera novaeangliae*, off Hawai'i determined using acoustic and visual techniques,'' Can. J. Zool. **73**, 1134–1146 (1995).
[6] T. F. Norris, M. McDonald, and J. Barlow, ''Acoustic detections of singing humpback whales (*Megaptera novaeangliae*) in the eastern North Pacific during their northbound migration,'' J. Acoust. Soc. Am. **106**, 506–514 (1999).
[7] J. A. Thomas, S. R. Fisher, and L. M. Ferm, ''Acoustic detection of cetaceans using a towed array of hydrophones,'' Rep. Int. Whal. Commn. **8**, 139–148 (1986).
[8] H. E. Winn and L. K. Winn, ''The song of the humpback whale (*Megaptera novaeangliae*) in the West Indies,'' Mar. Biol. (Berlin) **47**, 97–114 (1978).
[9] M. A. McDonald, J. A. Hildebrand, and S. C. Webb, ''Blue and fin whales observed on a seafloor array in the Northeast Pacific,'' J. Acoust. Soc. Am. **98**, 712–721 (1995).
[10] C. W. Clark, ''Application of the U.S. Navy underwater hydrophone arrays for scientific research on whales,'' Sci. Rep. Int. Whal. Comm. **44**, 1–12 (1994).
[11] C. W. Clark, ''Acoustic behaviors of blue and fin whales,'' paper presented at the 24th International Ethology Conference, Honolulu, HI, 1995.
[12] V. M. Janik, S. M. Van Parijs, and P. M. Thompson, ''A two-dimensional acoustic localization system for marine mammals,'' Marine Mammal Sci. **16**, 437–447 (2000).
[13] K. M. Stafford, C. G. Fox, and D. S. Clark, ''Long-range acoustic detection and localization of blue whale calls in the northeast Pacific Ocean,'' J. Acoust. Soc. Am. **104**, 3616–3625 (1998).
[14] C. W. Clark and W. T. Ellison, ''Calibration and comparison of acoustic location methods used during the spring migration of the bowhead whale, *Balaena mysticetus*, off Pt. Barrow, Alaska, 1984–1993,'' J. Acoust. Soc. Am. **107**, 3509–3517 (2000).
[15] F. Desharnais, M. Laurinolli, A. Hay, and J. A. Theriault, ''A scenario for right whale detection in the Bay of Fundy,'' MTS/IEEE Oceans 2000 Conference Proceedings, Providence, Rhode Island, September 11–14, 2000 (Holland Publications, Escondido, California, 2000), pp. 1735–1741.
[16] J. L. Spiesberger and K. M. Fristrup, ''Passive localization of calling animals and sensing of their acoustic environment using acoustic tomography,'' Am. Nat. **135**, 107–153 (1990).
[17] S. Mitchell and J. Bower, ''Localization of animal calls via hyperbolic methods,'' J. Acoust. Soc. Am. **97**, 3352–3353 (1995).
[18] A. M. Thode, G. L. D'Spain, and W. A. Kuperman, ''Matched-field processing, geoacoustic inversion, and source signature recovery of blue whale vocalizations,'' J. Acoust. Soc. Am. **107**, 1286–1300 (2000).
[19] C. O. Tiemann, M. B. Porter, and L. Neil Frazer, ''Automated model-based localization of marine mammals near Hawaii,'' MTS/IEEE Oceans 2001 Conference Proceedings, Honolulu, Hawaii, November 5–8, 2001 (Holland Publications, Escondido, California, 2001), pp. 1395–1400.
[20] C. S. Baker, L. M. Herman, A. Perry, W. S. Lawton, J. M. Straley, A. A. Wolman, G. D. Kaufman, H. E. Winn, J. D. Hall, J. M. Reinke, and J. Ostman, ''Migratory movement and population structure of humpback whales (*Megaptera novaeangliae*) in the central and eastern North Pacific,'' Mar. Ecol.: Prog. Ser. **31**, 105–119 (1986).
[21] P. O. Thompson and W. A. Friedl, ''A long term study of low frequency sounds from several species of whale off Oahu, Hawaii,'' Cetology **45**, 1–19 (1982).
[22] D. J. McSweeney, K. C. Chu, W. F. Dolphin, and L. N. Guinee, ''North Pacific humpback whale songs: A comparison of southeast Alaskan feeding ground songs with Hawaiian wintering ground songs,'' Marine Mammal Sci. **5**, 139–148 (1989).
[23] D. A. Seem and N. C. Rowe, ''Shape correlation of low-frequency underwater sounds,'' J. Acoust. Soc. Am. **95**, 2099–2103 (1994).
[24] J. D. Darling, ''Migration, abundance, and behavior of Hawaiian humpback whales (*Megaptera novaeangliae*),'' Ph.D. dissertation, University of California, Santa Cruz, 1983.
[25] P. J. Fischer and D. R. Thor, ''A preliminary oceanographic-environmental evaluation of the BSURE area, northwest of Kauai, Hawaii,'' California State Univ. Northridge report CSUN-MS-75-1, p. 31 (1975).
[26] F. B. Jensen, W. A. Kuperman, M. B. Porter, and H. Schmidt, *Computational Ocean Acoustics* (American Institute of Physics, Woodbury, NY, 1999), p. 41.
[27] E. L. Hamilton, ''Geoacoustic modeling of the sea floor,'' J. Acoust. Soc. Am. **68**, 1313–1340 (1980).
[28] M. B. Porter, ''The KRAKEN normal mode program,'' SACLANT Undersea Research Centre Memorandum (SM-245)/Naval Research Laboratory Mem. Rep. 6920 (1991).
[29] M. B. Porter and Y. C. Liu, ''Finite-Element Ray Tracing,'' Proceedings of the International Conference on Theoretical and Computational Acoustics, Eds. D. Lee and M. H. Schultz (World Scientific, Singapore 1994), pp. 947–956.

Effects of time-reversing array deformation in an ocean wave guide

Karim G. Sabra and David R. Dowling[a)]
Department of Mechanical Engineering, University of Michigan, Ann Arbor, Michigan 48109-2133

(Received 16 May 2003; revised 13 February 2004; accepted 1 March 2004)

Active acoustic time reversal is a technique for focusing sounds recorded in complex unknown environments back to their remote point(s) of origin. It can be accomplished with a transducer array—a time-reversing array (TRA)—that sends and receives sound. Nearly all prior work on TRA performance has involved stationary arrays. This letter describes how random array deformation influences TRA retrofocusing in shallow ocean environments. For harmonic signals, randomly drifting array elements degrade TRA performance by ~20% when the average horizontal wavenumber times the root-mean-square horizontal element displacement approaches 0.5. TRA focusing should be less sensitive to vertical element drift. © *2004 Acoustical Society of America.* [DOI: 10.1121/1.1710502]

PACS numbers: 43.30.Vh, 43.30.Yj, 43.30.Bp [WLS] Pages: 2844–2847

I. INTRODUCTION

Acoustic time reversal is a means for focusing sound in unknown environments. It is based on the invariance of the lossless wave equation to changes in the sign of the time variable. Active acoustic time reversal may be accomplished by recording sounds with an array of transducers—a time-reversing array (TRA)—and then replaying the recorded sounds from the same array to produce back-propagating waves that converge at the location(s) of the remote sound source(s). TRAs may be of nearly any size or shape and can operate in any frequency range without knowledge of the source location(s), transducer locations, or environmental characteristics. TRAs perform well in the absence of acoustic absorption losses and temporal changes in the environment when the array possesses sufficient aperture. Future active sonar and underwater communication systems suitable for use in unknown shallow ocean waters may be developed from the automatic spatial and temporal focusing properties of TRAs.

For many array-signal processing techniques, it is important to know the relative positions of the sensors (or, equivalently, the shape of the array) to maximize the array-processing gain (Hinch and Rule, 1975; Hodgkiss, 1983, 1989; Hodgkiss *et al.*, 1996). The time-reversal process does not require knowledge of the array shape as long as the array shape does not change between the signal reception and time-reversed transmission (Jackson and Dowling, 1991; Kuperman *et al.*, 1998), an important advantage over conventional array-processing techniques. However, in practice, cable dynamics, tow ship maneuvers, and shear and currents in the ocean water column may cause array dynamic deformation (Carey *et al.*, 1998; Caveny *et al.*, 1999) in the time interval between signal reception and time-reversed transmission.

This work presents a study of TRA performance when the array is composed of drifting elements each having an uncorrelated zero-mean random displacement between the recording and broadcast steps of the time reversal process. This simple model holds for mild array deformations when the array elements move independently, i.e., when the stiffness of the array mounting system or cable is neglected. This model could be used to estimate for how long or under which deformations a field of drifting sonobuoys (see Dosso and Collison, 2002) could be used as a temporary TRA. The case of coherent TRA element motion is covered in a separate study (Sabra and Dowling, 2003).

This article reports the results of a theoretical and computational investigation into how random array deformation and array orientation influence TRA retrofocusing in shallow ocean environments. The main findings are that array performance degradation is similar for both vertical and horizontal array orientations and this degradation increases monotonically with the product of the average horizontal (vertical) wavenumber and the root-mean-square horizontal (vertical) element displacement. Here, the main performance metric examined is the field amplitude produced by the TRA at the source location. TRA focus size in ocean waveguides can be deduced from an appropriate method of images construction (Kim *et al.*, 2001).

II. ANALYTICAL FORMULATION

A time-reversing array both receives and sends acoustic signals. When the array's elements are displaced between the receiving and transmitting steps of time reversal, its performance will be degraded because the transmitted time-reversed signals will no longer be precisely matched to the measured propagation characteristics that were established during the array's recording step. Here, it is assumed that the element displacements are random and that the elements only move between, and not during, the recording and transmitting steps. If the recording and broadcasting locations of the jth array element are $\vec{r}_j$ and $\vec{r}_j + \vec{\Delta}_j$, respectively, then the

[a)]Author to whom correspondence should be addressed. Electronic mail: drd@umich.edu

 0001-4966/2004/115(6)/2844/4/$20.00 © 2004 Acoustical Society of America

usual harmonic-signal monopole TRA formulation (Jackson and Dowling, 1991; Kuperman *et al.*, 1998) produces

$$P(\vec{r},\vec{\Delta}_j,\omega)=A\sum_{j=1}^{N} G(\vec{r},\vec{r}_j+\vec{\Delta}_j,\omega)e^{i\omega T_c}G^*(\vec{r}_j,\vec{r}_s,\omega), \tag{1}$$

where $P(\vec{r},\vec{\Delta}_j,\omega)$ is the TRA-produced acoustic field at frequency ω, N is the number of array elements, $\vec{r}_s$ is the source location, G is the Helmholtz equation Green's function, T_c is a time delay that ensures causality for the array's operations, and A is an the overall gain constant determined by the characteristics of the array's elements. In this work, the impact of the random displacements $\vec{\Delta}_j$ are illustrated through the mean normalized TRA field amplitude at the source location $\vec{r}_s$,

$$\frac{\langle P(\vec{r}_s,\vec{\Delta}_j,\omega)\rangle}{P(\vec{r}_s,0,\omega)}=\frac{\langle \Sigma_{j=1}^{N} G(\vec{r},\vec{r}_j+\vec{\Delta}_j,\omega)G^*(\vec{r}_j,\vec{r}_s,\omega)\rangle}{\Sigma_{j=1}^{N}|G(\vec{r}_j,\vec{r}_s,\omega)|^2}, \tag{2}$$

where the angle brackets denote the expected value for the random variables $\vec{\Delta}_j$. When this ratio is near unity, element drift is predicted to have little or no influence on array performance. When it approaches zero, TRA retrofocusing is lost.

The statistical model for the element displacements is chosen to be as simple as possible to extract analytical results from Eq. (2). The range, depth, and azimuthal components of $\vec{\Delta}_j=(\Delta r_j,\Delta z_j,\Delta x_j)$ are assumed to be small, $|\vec{\Delta}_j| \ll |\vec{r}_j|$, independent, and identically distributed from element to element with zero mean. This corresponds to the case of a loose or an elastic array (Caveny *et al.*, 1999) whose elongational and lateral stiffnesses are ignored. In a typical ocean waveguide, when the source is placed at the origin of the range coordinate $\vec{r}_s=(0,z_s,0)$, azimuthal displacements (Δx_j) of the array's elements tend to occur along lines of constant source signal phase. Therefore, Δx_j is not expected to degrade TRA performance and is not considered further. However, TRA element displacements in range (Δr_j) and depth (Δz_j) remain important and are taken to have variances of σ_r^2 and σ_z^2, respectively.

With these simple statistics for the element displacements, progress can be made in evaluating Eq. (2) when a modal sum form of the Green's function (see Jensen *et al.*, 1994) is employed. Here, the range independent form is used with $\vec{r}_s=(0,z_s,0)$,

$$G(\vec{r}_j,\vec{r}_s,\omega)=\frac{ie^{-i\pi/4}}{\rho(z_s)\sqrt{8\pi}}\sum_{m=1}^{M}\frac{\Psi_m(z_s)\Psi_m(z_j)}{\sqrt{k_m r_j}}e^{ik_m r_j}, \tag{3}$$

where $\rho(z)$ is the water density, the M propagating modes have vertical profiles $\Psi_m(z)$, and k_m is the horizontal wavenumber of the mth mode. Combining Eqs. (2) and (3) produces

$$\frac{\langle P(\vec{r}_s,\vec{\Delta}_j,\omega)\rangle}{P(\vec{r}_s,0,\omega)}=\frac{\Sigma_{j=1}^{N}\Sigma_{n=1}^{M}\Sigma_{m=1}^{M}\left\langle\frac{\Psi_n(z_j+\Delta z_j)e^{ik_n\Delta r_j}}{\rho(z_j+\Delta z_j)\sqrt{k_n(r_j+\Delta r_j)}}\right\rangle\frac{\Psi_n(z_s)\Psi_m(z_s)\Psi_m(z_j)}{\rho(z_s)\sqrt{k_m r_j}}e^{i(k_n-k_m)r_j}}{\Sigma_{j=1}^{N}\Sigma_{n=1}^{M}\Sigma_{m=1}^{M}\frac{\Psi_n(z_j)\Psi_n(z_s)\Psi_m(z_s)\Psi_m(z_j)}{\rho(z_j)\rho(z_s)\sqrt{k_n r_j}\sqrt{k_m r_j}}e^{i(k_n-k_m)r_j}}. \tag{4}$$

When Δr_j and Δz_j are independent, their joint distribution function factors, so that their impact in Eq. (4) can be assessed separately. Consider Δz_j first. When the vertical density gradient is mild, a Taylor series expansion can be used to determine

$$\begin{aligned}\left\langle\frac{\Psi_m(z_j+\Delta z_j)}{\rho(z_j+\Delta z_j)}\right\rangle &\approx \frac{1}{\rho(z_j)}\left[\Psi_m(z_j)+\frac{\sigma_z^2}{2}\frac{d^2\Psi_m(z_j)}{dz^2}\right]\\ &\approx \frac{\Psi_m(z_j)}{\rho(z_j)}\left[1-\left(\frac{\omega^2}{c^2(z)}-k_m^2\right)\frac{\sigma_z^2}{2}\right]\\ &\approx \frac{\Psi_m(z_j)}{\rho(z_j)}\left[1-\frac{k_{z,m}^2\sigma_z^2}{2}\right],\end{aligned} \tag{5}$$

where the second approximate equality follows from the differential equation for the mode shapes $\Psi_m(z)$, $c(z)$ is the sound speed profile at the array, the depth-averaged value of $\sqrt{(\omega/c(z))^2-k_m^2}$ is $k_{z,m}$, and the linear term in the expansion is missing because $\langle\Delta z_j\rangle=0$. The third approximate equality in Eq. (5) is convenient because it removes the depth dependence from the multiplier of σ_z^2. Similarly for Δr_j, when the source-element distances are large, the influence of Δr_j will be primarily felt through the complex exponential factor. Thus, when Δr_j is Gaussian distributed—as is assumed here—the random range factors produce

$$\left\langle\frac{e^{ik_n\Delta r_j}}{\sqrt{k_n(r_j+\Delta r_j)}}\right\rangle\approx\frac{\exp\{-k_n^2\sigma_r^2/2\}}{\sqrt{k_n r_j}}. \tag{6}$$

Equations (4)–(6) provide a formal prediction of the normalized mean field amplitude produced by a TRA with randomly drifting elements.

These formal results can be evaluated in a reasonably compact form when the TRA is linear and vertical with sufficient aperture and element density so that the sums in Eq. (4) are simplified via mode orthogonality (see Kuperman *et al.*, 1998):

$$\frac{\langle P(\vec{r}_s,\vec{\Delta}_j,\omega)\rangle}{P(\vec{r}_s,0,\omega)} \cong \frac{\Sigma_{m=1}^{M}[\Psi_m^2(z_s)\exp\{-k_m^2\sigma_r^2/2\}/\rho(z_s)k_mR][1-k_{z,m}^2\sigma_z^2/2]}{\Sigma_{m=1}^{M}[\Psi_m^2(z_s)/\rho(z_s)k_mR]}, \tag{7}$$

where R is the source-array range. Bottom losses prevent the modes from forming a complete orthogonal set so Eq. (7) is approximate. However, the discrepancy is small and is unlikely to affect this analysis. For a horizontal array, all elements at depth z_a, there is no general simplification. However, horizontal arrays are commonly analyzed by considering only the diagonal terms in the double modal sums in Eq. (4) (Bogart and Yang, 1994; Dungan and Dowling, 2002) because the off-diagonal terms will tend to cancel with each other while the diagonal terms will tend to reinforce each other. Thus, for a horizontal array,

$$\frac{\langle P(\vec{r}_s,\vec{\Delta}_j,\omega)\rangle}{P(\vec{r}_s,0,\omega)} \approx \frac{\Sigma_{m=1}^{M}[\Psi_m^2(z_s)\Psi_m^2(z_a)\exp\{-k_m^2\sigma_r^2/2\}/\rho(z_s)\rho(z_a)k_mR][1-k_{z,m}^2\sigma_z^2/2](\Sigma_{j=1}^{N}(R/r_j))}{\Sigma_{m=1}^{M}[\Psi_m^2(z_s)\Psi_m^2(z_a)/\rho(z_s)\rho(z_a)k_mR](\Sigma_{j=1}^{N}(R/r_j))}, \tag{8}$$

where R is the average source-array range. In Eqs. (7) and (8), the additional factors in the numerators compared to the denominators are the same, so random element displacement should have similar effects on both vertical and horizontal arrays. In addition, $k_{z,m}$ will typically be much smaller than k_m, so that a given level of range-direction element displacement should cause more degradation than an equal amount of vertical element displacement.

III. NUMERICAL SIMULATIONS

Numerical simulations based directly on Eq. (2) were performed for both vertical and horizontal (endfire) arrays in a generic range-independent shallow water sound channel (Fig. 1). The normal mode program KRAKEN (Porter and Reiss, 1984) was used to compute the mode shapes and k_m's, for this sound channel. The expected value in Eq. (2) was computed by averaging 100 realizations of random array deformation starting from an initially straight linear configuration. For the vertical array simulations, the array had 21 elements and was centered in the sound channel with a 3-m vertical spacing. For the horizontal array simulations, the array also had 21 elements but was placed at a depth of 32.5 m with a range spacing between elements of 25 m to ensure proper sampling of the modes (see Dungan and Dowling, 2002). For both array orientations, the source depth was 27 m and the average source-array range R was 5 km.

Figure 2 shows a comparison of the mean normalized field amplitude for vertical and horizontal arrays along with the predictions of Eqs. (7) and (8) for a frequency of 500 Hz when the TRA's elements drift randomly in the range (horizontal) direction alone. Here all the results collapse well within the 95% confidence limits shown by the error bars on the simulation results when the root-mean-square (rms) element drift distance, σ_r, is scaled by $k_{av}=2\pi f/c_{av}$ where c_{av} is the average sound speed through the water column depth. Simulation results at 250 and 750 Hz (not shown for clarity) collapse with similarly fidelity to $\exp\{-k_{av}^2\sigma_r^2/2\}$. These simulation results confirm the accuracy of Eqs. (7) and (8) for random range-direction element drift.

Figure 3 shows a comparison of the mean normalized field amplitude for vertical and horizontal arrays along with the predictions of Eqs. (7) and (8) for a frequency of 500 Hz when the TRA's elements drift randomly in the vertical direction alone. To at least partially account for the differences in vertical and horizontal modal wavenumbers, the results are presented with the rms element drift distance, σ_z, scaled by the average vertical wavenumber, $k_{z,av}$, of the first ten propagating modes. The Fig. 1 sound channel supports 21 propagating modes but the first ten carry most of the signal energy. The collapse of the simulation results shown on Fig.

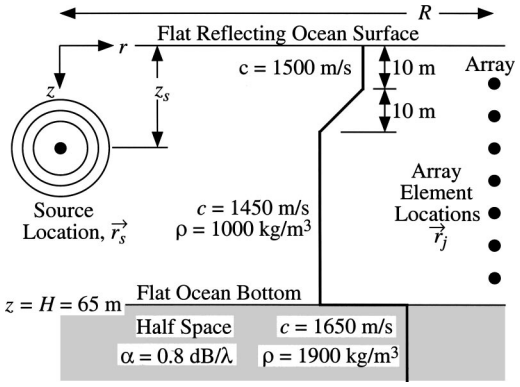

FIG. 1. Computational sound channel with environmental parameters. The heavier line indicates the speed of sound profile.

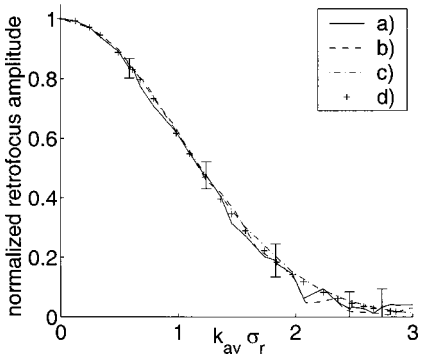

FIG. 2. Normalized mean TRA retrofocus amplitude versus the product of the average horizontal wavenumber $k_{av}=2\pi f/c_{av}$ (c_{av}=depth averaged speed of sound) and the root-mean-square range-direction horizontal element displacement, σ_r, at a frequency 500 Hz. The solid curve (a) is an average result of 100 simulations for a vertical array with different random element displacements. The dashed curve (b) is a similar average of simulation results for a horizontal array. The (a) and (b) curves have error bars that extend to plus and minus two standard deviations of the mean (95% confidence interval). The dash-dot curve (c) represents Eqs. (7) and (8). The pluses (d) are the average amplitude decay $\exp\{-k_{av}^2\sigma_r^2/2\}$.

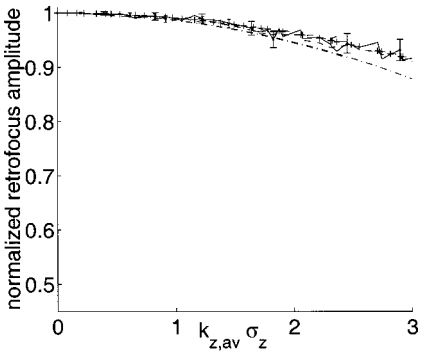

FIG. 3. Normalized mean TRA retrofocus amplitude versus the product of the average vertical wavenumber, $k_{z,av}$, for the first ten propagating modes and the root-mean-square vertical element displacement, σ_z, at a frequency of 500 Hz. The (a)–(c) curves are the same as Fig. 2. The pluses (d) represent $1-k_{z,av}^2\sigma_z^2/2$.

3 is not as good as that on Fig. 2. The poorer Fig. 3 collapse can be traced to the fact that each mode has its own distinct vertical wavenumber and $k_{z,av}$ does not fully capture this variability. Plus, the Taylor series expansion leading to Eqs. (7) and (8) loses its validity as σ_z increases. However, there is little loss of TRA focus amplitude for $k_{z,av}\sigma_z$ less than unity. Simulations results at frequencies of 250 to 750 Hz (not shown) were essentially identical to those shown on Fig. 3. As a final point, Fig. 3 shows that conservative (i.e., pessimistic) predictions of TRA focusing performance are provided by Eqs. (7) and (8), so they do provide a means of bounding TRA performance when the elements drift vertically.

IV. SUMMARY AND CONCLUSIONS

Deformation of a time-reversing array between the receiving and transmitting steps of the time reversal process degrades TRA performance. There are two main conclusions to be drawn from this study. First of all, TRA-field amplitude loss worsens with increasing frequency and root-mean-square element displacement. For range-direction horizontal displacements, a 20% amplitude loss will occur when the product of the average horizontal wavenumber and the rms element displacement reaches $\sim\frac{1}{2}$. For vertical element displacements to cause the same level of amplitude loss, the product of the average vertical wavenumber and the rms displacement must be approximately an order of magnitude larger. And, second, when comparing a vertical array that spans the water column and a horizontal array that is long enough for adequate sampling of the propagating modes, the orientation of the array does not play an important role in determining the extent of drifting element degradation. In practice, the effects of array deformation and motion on TRA performance should be cumulative when the array is towed. Therefore devices that limit dynamic deformation of the array or techniques that permit array shape compensation may be needed when TRAs are towed, especially for applications at high frequencies (e.g., underwater communications). Experimental measurements could be used to determine the importance of element drift on TRA performance for any particular TRA deployment.

ACKNOWLEDGMENTS

The research was sponsored by the Ocean Acoustics Program of the Office of Naval Research under Grant No. N00014-96-1-0040.

Bogart, C. W., and Yang, T. C. (**1994**). ''Source localization with horizontal arrays in shallow water: Spatial sampling and effective aperture,'' J. Acoust. Soc. Am. **96**, 1677–1686.

Carey, W., Reese, J., and Bucker, H. (**1998**). ''Environmental acoustic influences on array beam response,'' J. Acoust. Soc. Am. **104**, 133–140.

Caveny, D. M., Del Balzo, D. R., Leclere, J. H., and Ioup, G. E. (**1999**). ''Performance of sinusoidally deformed hydrophone line arrays,'' J. Acoust. Soc. Am. **105**, 2203–2209.

Dosso, S. E., and Collison, N. E. B. (**2002**). ''Acoustic tracking of a freely drifting sonobuoy field,'' J. Acoust. Soc. Am. **111**, 2166–2177.

Dungan, M. R., and Dowling, D. R. (**2002**). ''Orientation effects on linear time reversing array retrofocusing in shallow water,'' J. Acoust. Soc. Am. **112**, 1842–1852.

Hinch, M. J., and Rule, W. (**1975**). ''Bearing estimation using a towed array,'' J. Acoust. Soc. Am. **58**, 1023–1029.

Hodgkiss, W. (**1983**). ''The effects of array shape perturbation on beamforming and passive ranging,'' IEEE J. Ocean. Eng. **8**, 120–130.

Hodgkiss, W. S. (**1989**). ''Shape determination of a shallow-water bottomed array,'' in *OCEANS'89* (IEEE, New York), pp. 1199–1204.

Hodgkiss, W. S., Ensberg, D. E., Murray, J. J., D'Spain, G. L., Booth, N. O., and Schey, P. W. (**1996**). ''Direct measurement and matched-field inversion approaches to array shape estimation,'' IEEE J. Ocean. Eng. **21**, 393–401.

Jackson, D. R., and Dowling, D. R. (**1991**). ''Phase-conjugation in underwater acoustics,'' J. Acoust. Soc. Am. **89**, 171–181.

Jensen, F. B., Kuperman, W. A., Porter, M. B., and Schmidt, H. (**1994**). *Computational Ocean Acoustics* (American Institute of Physics, New York).

Kim, S., Edelmann, G., Hodgkiss, W. H., Kuperman, W. A., Song, H. C., and Akal, T. (**2001**). ''Spatial resolution of time reversal arrays in a shallow water,'' J. Acoust. Soc. Am. **110**, 820–829.

Kuperman, W. A., Hodgkiss, W. S., Song, H. C., Akal, T., Ferla, C., and Jackson, D. R. (**1998**). ''Phase-conjugation in the ocean: experimental demonstration of an acoustic time reversal mirror,'' J. Acoust. Soc. Am. **103**, 25–40.

Porter, M., and Reiss, E. L. (**1984**). ''A numerical method for ocean-acoustic normal modes,'' J. Acoust. Soc. Am. **76**, 244–252.

Sabra, K. G., and Dowling, D. R. (**2003**). ''Broadband performance of a moving time reversing array,'' J. Acoust. Soc. Am. **114**, 1395–1405.

Acoustic performance of a large-aperture, seabed, fiber-optic hydrophone array

G. A. Cranch[a)]
SFA Inc., 9315 Largo Drive West, Suite 200, Largo, Maryland 20774

R. Crickmore
QinetiQ, Winfrith Technology Center, Winfrith Newburgh, Dorchester, Dorset, DT2 8XJ, United Kingdom

C. K. Kirkendall
Naval Research Laboratory, Code 5674, 4555 Overlook Avenue SW, Washington, DC 20375

A. Bautista, K. Daley, S. Motley, and J. Salzano
SFA Inc., 9315 Largo Drive West, Suite 200, Largo, Maryland 20774

J. Latchem and P. J. Nash
QinetiQ, Winfrith Technology Centre, Winfrith Newburgh, Dorchester, Dorset, DT2 8XJ, United Kingdom

(Received 24 July 2003; accepted for publication 1 March 2004)

A large-aperture, seabed mounted, fiber-optic hydrophone array has been constructed and characterized. The system is designed for use as a large area surveillance array for deployment in shallow water regions. The underwater portion comprises two arrays of 48 hydrophones separated by a 3 km fiber-optic link, which are connected to a shore station by 40 km of single-mode optical fiber. The hydrophone is based on a fiber-optic Michelson interferometer and the acoustic transduction mechanism is a fiber-wrapped mandrel design. No electrical power is required in the underwater portion. The performance of the system is described, characterized during laboratory measurements and during a recent sea trial. Specifically, measurements of the acoustic resolution, array shape, beam patterns, array gain, and target tracking capability of this array. The system demonstrates self-noise levels up to 20 dB (typically 10 dB) lower than the ambient acoustic noise experienced in the sea trial and array gains close to the theoretical maximum. The system telemetry and electronics have been designed to be expandable to accommodate several hundred hydrophones.
© *2004 Acoustical Society of America.* [DOI: 10.1121/1.1710504]

PACS numbers: 43.30.Wi, 43.30.Yj, 43.38.Zp [RAS] Pages: 2848–2858

I. INTRODUCTION

Optical fiber acoustic sensors are being developed for a variety of passive sonar applications. Since their inception in the late 1970s,[1] this technology has been developed to a level of maturity such that prototype systems have been successfully demonstrated in realistic sea trials.[2] One area of particular interest is shallow water acoustic surveillance. This application requires acoustic arrays comprising in some cases several hundred sensors, which may be located several kilometers from the receiving station. These installations may be deployed for between a few months to several years. For this application the all-optical system offers several advantages. These systems contain no electrical components in the wet-end portion and are therefore light-weight and less susceptible to water ingress, improving reliability. The high multiplexing capability of the optical fiber systems allows several hundred sensors to be interrogated through two fibers or less; requiring only a small diameter cable to link the underwater array to the shore. The underwater portion is also immune to electro-magnetic interference.

Described here is the performance of a large-scale fiber-optic seabed hydrophone array that has been characterized during laboratory tests and during an open water sea-trial. The system comprises 96 hydrophones in total, which are divided into two arrays of 48 hydrophones separated by 3 km. The arrays are designed for conventional plane-wave beamforming. The hydrophones are linearly spaced at 1.51 m intervals, yielding a design frequency, f_d, equal to 488 Hz, where $f_d = c_w/2d$ (here, d is the hydrophone spacing and the sound speed in water, $c_w = 1475$ m/s). Data from the two arrays are processed separately. The arrays are separated by a 3 km fiber-optic cable and connected to the shore by a 40 km fiber-optic link.

The detailed design of this system has been reported elsewhere,[3,4] and emphasis is placed on analyzing the performance of the individual sensors and the array; however, a brief explanation of the operating principle and system design is given in Sec. II. The fiber-optic system contains several different noise sources, compared with electro-ceramic based systems; it is therefore important to accurately characterize each noise source and determine its relative contribution to the total noise. This will allow an accurate prediction of the performance of the system during field use. These noise sources and the correlation of the noise sources between sensors are discussed, followed by the effect on the array detection performance when array beamforming is per-

[a)]Present address: Naval Research Laboratory, Code 5674, 4555 Overlook Avenue SW, Washington, DC 20375; electronic mail: geoff.cranch@nrl.navy.mil

formed. In Sec. III, measurements of the self-noise of the sensors and data from the field trial are presented. In Sec. IV, the method of determining the array shape after deployment is described and the results are presented. This information is then used to perform shape-corrected conventional beamforming, which allows the beam patterns and array gain to be determined. In Sec. V, the acoustic emission tracking capability of the system is demonstrated. Finally, a summary is given in the concluding section.

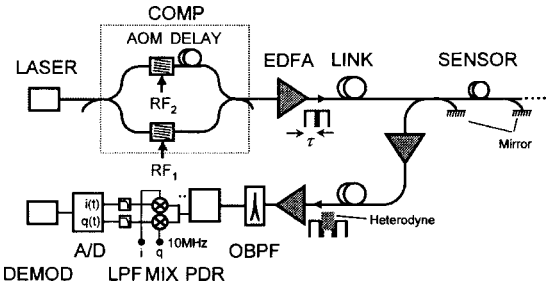

FIG. 1. Sensor configuration.

II. PRINCIPLE OF OPERATION

A. Background and sensor configuration

A fiber-optic hydrophone operates by converting the acoustically induced strain within an optical fiber placed within the acoustic field into a phase shift in the light propagating in the fiber. This phase shift is converted into intensity modulation by incorporating the fiber into one arm of a fiber-optic interferometer. To enhance the strain induced in the fiber, an amplification mechanism is usually incorporated. The technique used in this system is based on a fiber wrapped air-backed mandrel design.[5] The physical change in the diameter of a plastic mandrel, around which the fiber is wrapped, under the influence of a time varying pressure field induces a strain in the fiber. The air backing increases the compliance of the structure and therefore increases the induced strain within the fiber. An omni-directional hydrophone response is obtained when the acoustic wavelength is much greater than the maximum hydrophone dimension. Multiplexing is achieved by serial concatenation of sensors and using the time of flight of injected optical pulses to sequentially address each sensor. Wavelength division multiplexing is incorporated with the time division multiplexing to permit signals from several time division multiplexed sensor arrays to be combined onto a single optical fiber. Sixteen sensors are multiplexed with time (expandable to 64) and six wavelengths are used to allow 96 hydrophones to be interrogated through two optical fibers. To achieve high phase resolution from the interferometric sensor, a high coherence laser is required that emits a stable single optical frequency. Six erbium doped distributed feedback fiber lasers are used in this system with emission wavelengths ranging from 1541.35 to 1549.32 nm spaced by 1.6 nm. The transfer function of the interferometer is cosinusoidal and therefore an interrogation method is required to linearize the response of the sensor. A heterodyne based method is employed, where by the frequency of the light from each arm of the interferometer is shifted. When the two beams interfere on the detector, a beat frequency equal to the difference in frequency between the two beams is generated. A strain imposed on the fiber will modulate the phase of the light, which will appear as phase modulation sidebands around the beat frequency. The beat frequency is then mixed with a phase locked local oscillator, and the phase information of interest is retrieved using a trigonometric method. A simplified example of a single sensor in this multiplexed configuration is shown in Fig. 1.

The optical emission from the laser is injected into a path-imbalanced interferometer or compensator (COMP). Acousto-optic modulators in each arm frequency shift and amplitude modulate the light when driven by a pulsed radio frequency source. The output from one acousto-optic modulator is delayed with a fiber delay line before being combined with the other arm. The compensator thus generates two delayed pulses with a frequency difference, $\Delta f = RF_2 - RF_1$, which are repeated at a frequency, f_{rep}. The pulses are amplified with an erbium doped fiber amplifier (EDFA) and launched into the sensor array. The sensing region of the fiber is defined by splicing two reflective directional couplers at each end. The fiber length in-between the coupler forms one arm of a Michelson interferometer, and is set to give an optical path length equal to half the optical path length of the delay line in the compensator. Therefore, the reflection of the first pulse from the mirror after the sensor arrives back at the detector at the same time as the reflection of the second pulse from the mirror before the sensor. The total phase of this interferometer configuration is the difference in phase between the compensator and the Michelson interferometer sensor,

$$\phi_{\text{tot}} = (2\pi n/\lambda)\cdot(L_{\text{COMP}} - 2L_{\text{MI}}), \tag{1}$$

where n is the effective index of the fiber core, λ is the free-space optical wavelength, and L_{COMP} and L_{MI} are the fiber path imbalances in the compensator and Michelson interferometer, respectively. In the ideal case $(L_{\text{COMP}} - 2L_{\text{MI}}) = 0$ and $\phi_{\text{tot}} = 0$; however, imperfect matching of optical fiber paths and thermally induced fluctuations in the fiber lengths result in a small effective imbalance and hence a nonzero total phase. At the detector, the two pulses reflected from each directional coupler overlap and generate the heterodyne beat frequency. Assuming that equal power is reflected from each directional coupler, then the intensity in the heterodyne pulse is given by

$$I = I_{\text{inc}}(1 + V\cos(2\pi\Delta f t + \phi_s(t))), \tag{2}$$

where I_{inc} is the total mean intensity in the heterodyne pulse and $\phi_s(t)$ is the phase modulation containing the acoustic information. V is a fringe visibility term, ranging from zero to unity, that depends on the relative orientations of the polarization of the light from each interferometer arm. Removing the dc component from Eq. (2) and mixing with in-phase (i) and quadrature (q) components of a stable local oscillator yields

$$i(t) = A\cos(\phi_s(t)), \tag{3a}$$

$$q(t) = A\sin(\phi_s(t)), \tag{3b}$$

TABLE I. Definition of terms.

Parameter	Value	Description
$f_{\text{rep}}(=1/T)$	120 kHz	Sensor interrogation rate
τ		Pulse width/sample time
L		Sensor fiber length
$D(=\tau/T)$		Duty cycle
Δf	10 MHz	Heterodyne frequency
f_d	488 Hz	Array design frequency
c_w	1475 m/s	Sound speed in water
d	1.51 m	Hydrophone spacing
λ	1550 nm	Free-space optical wavelength
n	1.465	Effective refractive index of fiber core
ϕ		Optical phase
V		Fringe visibility
RIN		Relative intensity noise
P		Optical power
I		Optical intensity
$S_{\delta P}$		Spectral density
γ_{xy}^2		Ordinary coherence function
G_{xy}		Cross-spectra function
N		Number of sensors

where A is proportional to the fringe visibility, photodiode responsivity, received power, and gain in the mixing process. The signal phase of interest is then obtained by taking the arctangent of the ratio of Eqs. (3b) and (3a). Prior to detection, the pulse train is amplified by a second EDFA. An optical bandpass filter (OBPF) is placed at the output to remove amplified spontaneous emission, generated by the EDFAs, that lies outside the optical bandwidth of the signal interrogating the sensor. The effect of polarization induced signal fading is alleviated with a polarization diversity receiver (PDR), discussed in the following. The two outputs of the PDR are each mixed with the local oscillator, low-pass filtered and digitally sampled (A/D). The phase measurement and tracking is then performed digitally by the demodulator. Phase locking the local oscillator to the oscillators driving the acousto-optic modulators allows the phase of the interferometer to be tracked. Although the phase will drift due to thermally induced fluctuations in the fiber lengths and laser wavelength, these effects are usually very slow, and in most cases very low frequency pressure fluctuations ($\ll$1 Hz) can be resolved.

A third EDFA is located at the output of the sensor array. It is powered with an optical pump signal, at a wavelength of 1480 nm, delivered through a separate fiber and is called a remotely pumped EDFA. The gain provided by this amplifier compensates for signal attenuation in the return fiber, and therefore allows the fiber link to be extended.

The definition of terms and values of various parameters used in this paper are given in Table I.

B. Optical sensor noise sources

A noise source refers to any effect that generates a signal, which is unrelated to the acoustic signal of interest and interferes with its precise measurement. In the remotely interrogated optical hydrophone sensor, there are several optical noise sources that can contribute significantly to the total sensor noise. These are: (i) laser frequency noise, (ii) laser intensity noise, (iii) amplified spontaneous emission noise, and (iv) coherent double Rayleigh scattering noise.[6] Other noise sources, such as optical shot noise, detector noise, oscillator phase noise, single Rayleigh backscattering,[7] fiber thermal noise,[8] and input polarization noise[9] are also present but are generally less significant and will be ignored.

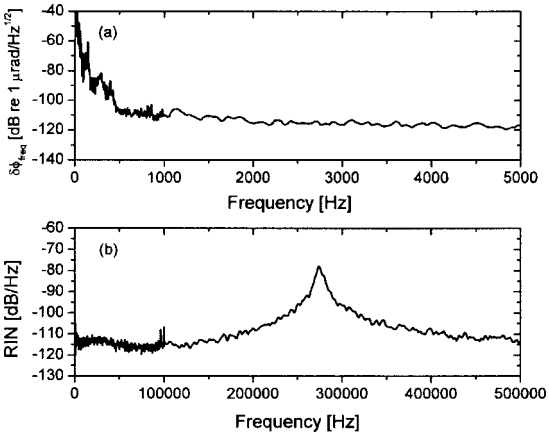

FIG. 2. Laser noise: (a) frequency induced phase noise in a Michelson interferometer with a 1 m fiber path-imbalance and (b) relative intensity noise.

Laser frequency induced phase noise arises from the small path imbalance present in each sensor. An imbalanced interferometer converts input frequency fluctuations into intensity fluctuations, which are proportional to the path imbalance. The frequency induced phase noise, $\delta\phi_{\text{freq}}$, for one laser isolated from environmental noise is shown in Fig. 2(a) scaled to a fiber path-imbalance of 1 m in a Michelson interferometer. Fluctuations in the intensity of the laser also contribute to the sensor noise and generate a noise current on detection indistinguishable from the sensor phase signal. This is characterized in terms of the relative intensity noise spectral density (RIN) where

$$\text{RIN}=\frac{S_{\delta P}}{\overline{P}^2}. \tag{4}$$

$S_{\delta P}$ is the spectral density of the optical power fluctuations and $\overline{P}$ is the mean optical power. A typical RIN spectrum is shown in Fig. 2(b). For the case when the RIN occupies a bandwidth much less than the heterodyne beat frequency, the RIN induced phase noise is given by $\delta\phi_{\text{RIN}}=\sqrt{\text{RIN}}$. RIN appears in the parameter, A, in Eqs. (3a) and (3b) and is therefore common mode to these two signals. Thus, by careful balancing of signal levels during the process of extracting the phase, first-order rejection of the RIN can be achieved. Optical amplifiers in the system generate amplified spontaneous emission (ASE). ASE occupies an optical spectrum approximately 30 nm in width centered on ~1545 nm, most of which is filtered prior to detection. However, ASE noise within the bandwidth of the optical filter (approximately 0.5 nm) will contribute a significant noise source. On detection, two noise contributions arise: noise due to beating of the ASE with the signal, $\delta\phi_{s\text{-}sp}$, and noise due to beating of the ASE with itself, $\delta\phi_{sp\text{-}sp}$. Expressions for these noise sources can be found in Ref. 10 and only their relative mag-

nitudes are considered here. In an optimized system the ASE generated by the remotely pumped amplifier dominates the total noise contribution due to ASE.[10] Coherent double Rayleigh scattering generated in the input fiber also contributes a significant noise source when the input fiber is many kilometers long. This noise source appears as an additional intensity noise and can therefore be reduced by common mode rejection. It is considered here only in terms of the laser RIN.

Finally, another source of noise that has been found to degrade the sensor performance is due to leakage light from the acousto-optic modulators. This is generated when the extinction of the frequency shifted light is not sufficiently high. This continuous leakage light forms multiple imbalanced parasitic interferometers, which generate frequency induced phase noise. In the system presented here the optical extinction ratio of the acousto-optic modulators at the shift frequency is in excess of 100 dB and no degradation in the sensor noise has been observed due to leakage light.

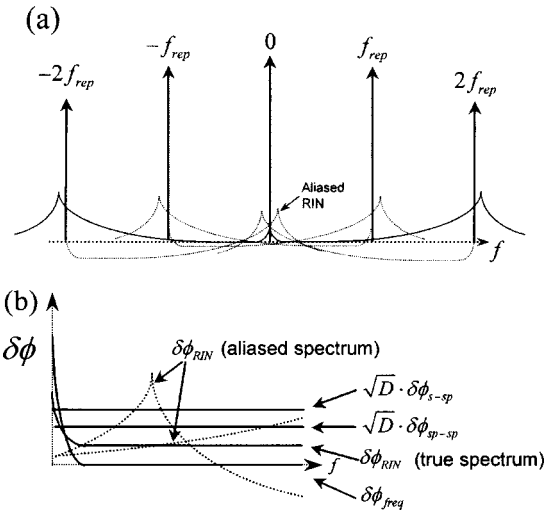

FIG. 3. (a) Fourier spectral content of the signal prior to digitization and (b) sampled spectrum of sensor showing relative levels of noise sources.

C. Noise in multiplexed systems: Noise aliasing and correlation

The effects of the above-described noise sources are now considered in the case of the multiplexed sensor system. The sensor signals [labeled "$i(t)$" and "$q(t)$" in Fig. 1] consist of a pulse train with each pulse proportional to the function given by Eq. (3a) or (3b). An individual sample is taken during each pulse corresponding to a sample of each sensor. The signal to be sampled contains the phase information of interest as well as noise components that may occupy a bandwidth much greater than the effective sensor sampling frequency, f_{rep}. For the general case of sampling an arbitrary wave form, the Fourier transform of the sampled spectrum is given by the convolution of the Fourier transform of the wave form with the Fourier transform of the sampling function. Consequently, when the wave form occupies a bandwidth greater than the sampling frequency, the components of the wave form at frequencies greater than the sampling frequency will be aliased (or folded) into the true spectrum. The result of this effect can be understood by considering the case of sampling bandwidth limited white noise that occupies a bandwidth much greater than the sampling frequency. In this case, the aliased noise will add incoherently with the spectral components in the true spectrum. This, if bandwidth limited white noise with a power spectral density, $\overline{\eta^2}$, is sampled with a periodic rectangular pulse train of period, T, and pulse width, τ, then the sampled signal will exhibit a noise spectral density equal to $\sqrt{D}\overline{\eta^2}$, where $D=\tau/T$ is the sampling duty cycle. For bandwidth-limited white noise the effect of aliasing is to increase the noise power in the true spectrum by $\sqrt{D}$. Noise sources such as amplified spontaneous emission noise closely resemble bandwidth-limited white noise and will contribute aliased terms. However, if the spectral density of the noise source decreases for frequencies above the sampling frequency then the aliased noise contribution can be neglected. Conversely, if the noise exhibits a spectral density that increases for frequencies above the sampling frequency, then the aliased noise contribution will be greater than $\sqrt{D}$. This is the case for RIN, shown in Fig. 2(b), which exhibits a noise spectrum resembling an under damped harmonic oscillator.

Shown in Fig. 3(a) is the convolution of the sampling function with the RIN spectrum, which illustrates the components that are aliased into the true spectrum as dotted lines. The sampling rate is chosen such that the aliased RIN corresponding to the peak in the RIN spectrum (also know as the relaxation oscillation frequency) does not fall within the acoustic bandwidth of the sensor.

The digitized noise spectrum of the sensor therefore comprises contributions from all the noise sources described in Sec. II B and also aliased contributions from the noise sources whose spectral density either remains constant or increase for frequencies above the sampling frequency. The aliased noise contribution cannot be suppressed, since it is not possible to incorporate anti-alias filters prior to the analogue to digital conversion process.

Having determined the significant noise sources in the sensor, it is necessary to consider the effect of noise correlation. Correlated noise may degrade the beamforming process, since the effectiveness of beamforming relies on the implicit assumption that the correlation of the noise between sensors is very low. It is generally valid to assume that the above-described noise sources are statistically unrelated to one another and are therefore uncorrelated. However, optical noise sources that have a common origin, with a weak aliased component, exhibit a high degree of correlation between sensors, particularly at the low frequencies of interest in acoustic sensing. For example, for the case of white noise existing between 0 Hz and f_0 Hz, the degree of correlation of this noise source between two adjacent sensors is given by its normalized autocorrelation function,

$$\hat{R}(\tau)=\sin(2\pi f_0\tau)/(2\pi f_0\tau), \tag{5}$$

where τ is the time between sampling two consecutive sensors. Thus, for the case when $f_0=f_{\mathrm{rep}}/2$ (i.e., the noise bandwidth meets the Nyquist sampling condition) then $\hat{R}(\tau)=0$ (i.e., no correlation) when $\tau=1/(2f_{\mathrm{rep}})$. However, for an

array of N sensors, $\tau \approx 1/(N+1)f_{\text{rep}}$ and in most cases, $\hat{R}(\tau) \neq 0$ (i.e., noise is partially correlated). As the bandwidth of the white noise decreases, then $\hat{R}(\tau)$ tends to unity. This example is also a good approximation for noise sources whose spectral density decreases for frequencies increasing above f_0. In this fiber-optic system, noise sources that fit this criteria are laser frequency noise and double Rayleigh scattering noise. Conversely, when the noise has a strong aliased component the correlation is low, since the aliased noise adds incoherently with the true noise spectrum. This case corresponds to amplified spontaneous emission noise. An example of the relative contributions of the noise sources is illustrated in Fig. 3(b). The exact level of each noise source will depend on the system configuration; however, in most systems of this type the sensor noise will be limited by ASE noise generated by the optical amplifiers.

To quantify the correlation of noise between sensors, the ordinary coherence function, γ^2, is employed, where

$$\gamma_{xy}^2(f) = \frac{G_{xy}(f)F_{xy}^*(f)}{G_{xx}(f)G_{yy}(f)}. \tag{6}$$

Here, G_{xy} is the cross-spectral density between signals x and y, G_{xx} is the power spectral density, and* indicates complex conjugation. This quantity must be calculated by averaging over several records, since for a single average γ_{xy}^2 equals unity. The effect of correlated noise on the array performance is observed when the array data are beamformed. For our analysis, a conventional phase shift and add beamformer is employed. The beamforming process provides an enhancement in signal-to-noise ratio (SNR) in the direction of the acoustic emission, when the array is in an isotropic noise field. The enhancement in SNR is known as the array gain and correlated noise reduces the array gain obtained by the beamforming process, in the broadside direction.

D. Polarization diversity receiver

The visibility term, V, in Eq. (2) includes components for the laser coherence, optical loss, and polarization of the light from each arm of the interferometer. The coherence lengths of the lasers used in this system are several orders of magnitude larger than the differential path mismatch in the Michelson interferometer and this effect can be ignored. The loss component includes the effects of the coupler coefficients, mirror reflectivity, and other optical losses, which can imbalance the return powers from each arm of the interferometer. The intrinsic visibility component resulting from an imbalance in received intensities is given by $V_i = 2\sqrt{I_1 I_2}/(I_1+I_2)$, where I_1 and I_2 are the optical intensities at the detector from arms 1 and 2 of the interferometer, respectively. This establishes the maximum achievable visibility and is effectively set at manufacture of the array with some small thermal and aging related variation. The polarization component of the visibility accounts for the state of polarization (SOP) of the light from each arm of the interferometer. If the polarization states are aligned they will optimally interfere but if they are orthogonal to one another there will be no interference, resulting in what is referred to as a polarization induced fade. This causes an increase in the sensor noise. Without the use of a PDR, the polarization induced visibility component is given by $V_p = \cos(\eta)$ where η is the angle between the two SOPs. Environmentally induced perturbations on the fiber cause the SOP of the light from each arm to vary randomly with time and η can vary between 0 and 90°. Typically this is not acceptable and some method to either eliminate or manage the polarization induced fading must be incorporated.

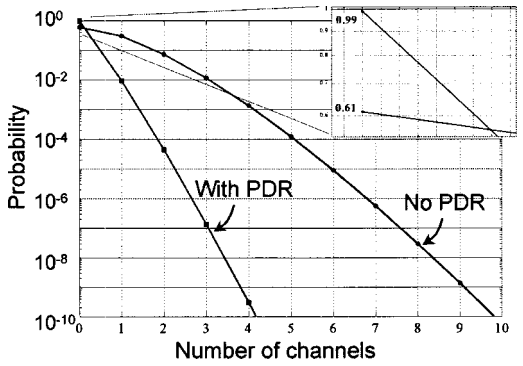

FIG. 4. Probability that N channels of a 48-element array experience a polarization induced signal fade of less than 10% (i.e., $V_p < 0.1$).

The use of a polarizer based PDR is a common technique to overcome polarization induced fading and a "bi-cell" configuration is used in this system. Polarizer-based PDRs interfere the return signal across multiple polarizers with different angular orientations and select the output with the largest interference signal for further processing. Systems incorporating three linear polarizers angularly spaced by 60° can be shown to eliminate the possibility of a complete signal fade.[11] Bi-cell configurations, which incorporate two orthogonal polarizers, do not eliminate the possibility of a complete signal fade but they do significantly reduce the possibility of it occurring to an acceptable level. Figure 4 shows the probability that a given number of channels in a 48-element array have a polarization induced visibility term less than 10% (i.e., $V_p < 0.1$), for both the bi-cell PDR and the no PDR cases. The magnitude of the signal fade that can be accommodated is dependent on the noise and dynamic range of the detector as well as the above-given intrinsic visibility. Referring to Fig. 4, the probability that none of the 48 channels have faded below the 10% level is 99% when the bi-cell PDR is present and 61% when no PDR is present (i.e., 99% of the time, no channels in a 48-element array will have faded below 10% of their maximum value when a bi-cell PDR is used). The probability that two channels have faded below 10% is only 0.004% for the bi-cell PDR. Thus, during an 8 h acquisition one channel will fade by greater that 10% over approximately 5 min and two or more channels will fade for a little more than 1 s. Losing one channel in the array does not seriously degrade performance and is deemed acceptable for this application. The bi-state PDR reduces the electronics and signal processing requirements by one-third, compared to a three polarizer based PDR approach.

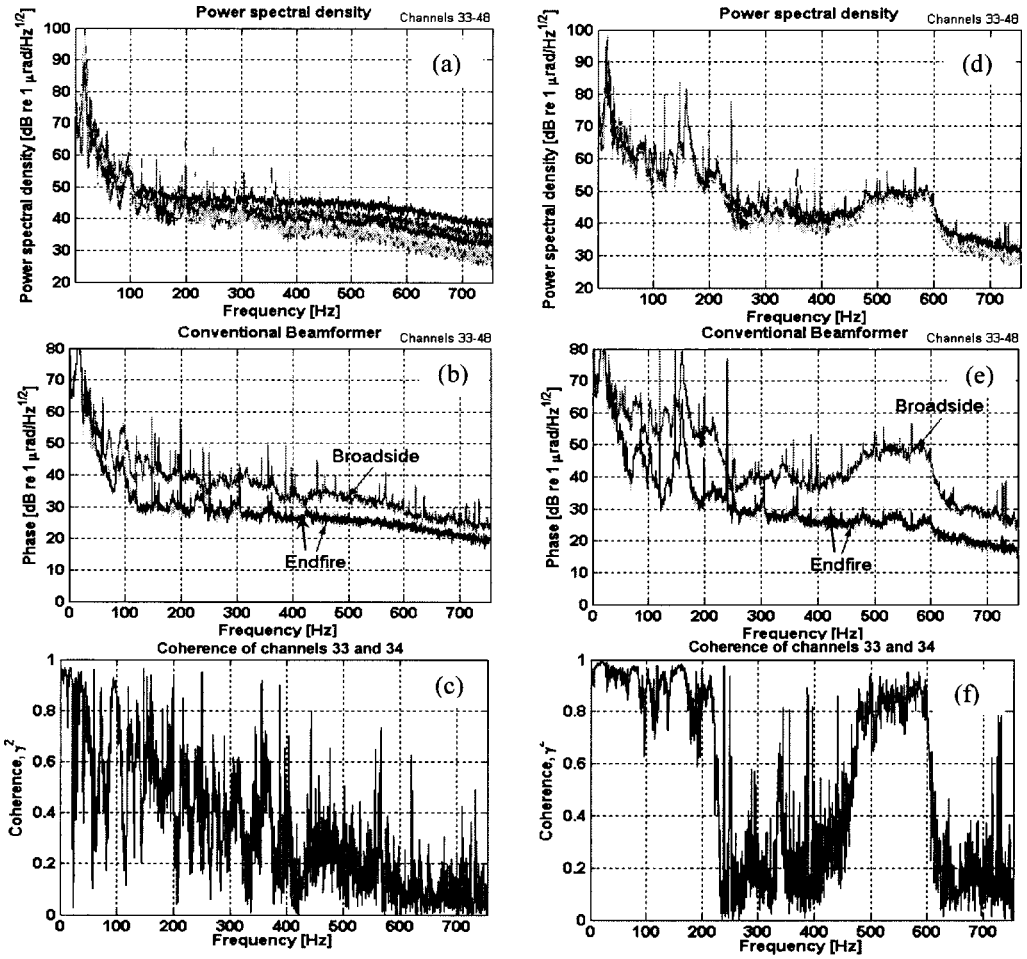

FIG. 5. System self-noise power spectral density, beamformed data, and adjacent channel coherence. Array 1, 35 km link: (a) power spectral density, (b) beamformer, (c) coherence; array 2, 35 km link: (d) power spectral density, (e) beamformer, (f) coherence.

III. SYSTEM PERFORMANCE

A. Laboratory measurements

The system noise is characterized by replacing the hydrophone sensors with a ''simulator'' array. This consists of 16 sensors arranged in the same in-line Michelson configuration, but with the fiber for each sensor wound onto a piezoceramic (PZT) cylinder. This ''simulator'' array is placed into an acoustically isolated box. The measured sensor noise is now limited by system noise and not ambient acoustic noise. Driving the PZT cylinders allows signals to be individually injected onto a sensor. During these tests, all six wavelengths interrogated the same simulator array, and thus the self-noise at each wavelength can be directly compared. The phase resolution is expressed in units of dB re 1 μrad/Hz$^{1/2}$ and can be converted to a noise equivalent sound pressure level by subtracting the hydrophone responsivity (-7.5 dB re 1 rad/Pa).

The sampled data are filtered and decimated to yield an acoustic bandwidth of $\sim$750 Hz. The frequency response of the digital filter exhibits a roll-off of $\sim$7 dB for frequencies greater than 500 Hz, which is reflected in the following phase spectra.

The arrays are denoted array 1 and array 2. The phase noise spectral density for sensors 33–48 in arrays 1 and 2 are shown in Figs. 5(a) and (d), respectively, and have been chosen to illustrate best and worst case examples of sensor noise. These measurements were taken with a 35 km fiber link on the input and output. The variation in total noise between the sensors is due to the combined effects of variation in received power from each sensor and polarization induced signal fading. The phase resolution obtained was $\sim$40 dB re 1 μrad/Hz$^{1/2}$ at 500 Hz, which corresponds to a pressure resolution of 47.5 dB re 1 μPa/Hz$^{1/2}$. In both arrays, at frequencies below $\sim$100 Hz, the noise is limited by laser frequency fluctuations. In array 2, a significant elevation in the noise is present for frequencies between 100 and 200 Hz and between 400 and 600 Hz (some narrowband tones originating from the power supplies are also present in the noise spectra). This is due to laser frequency fluctuations induced by the environmental sensitivity of the laser. The packaging in which the lasers used to interrogate array 1 were incorporated provided better isolation to environmental disturbances than that used for the lasers interrogating array 2. The detrimental effect of this laser noise is shown by the beamformed data, which are given in Figs. 5(b) and (e). (These are calculated with a conventional beamformer, a Hann time window, and no aperture shading.) Three beams are shown for each array, corresponding to each endfire direction and broadside. The noise at broadside is greater than the noise at endfire for both arrays; however, the increase in noise is much greater

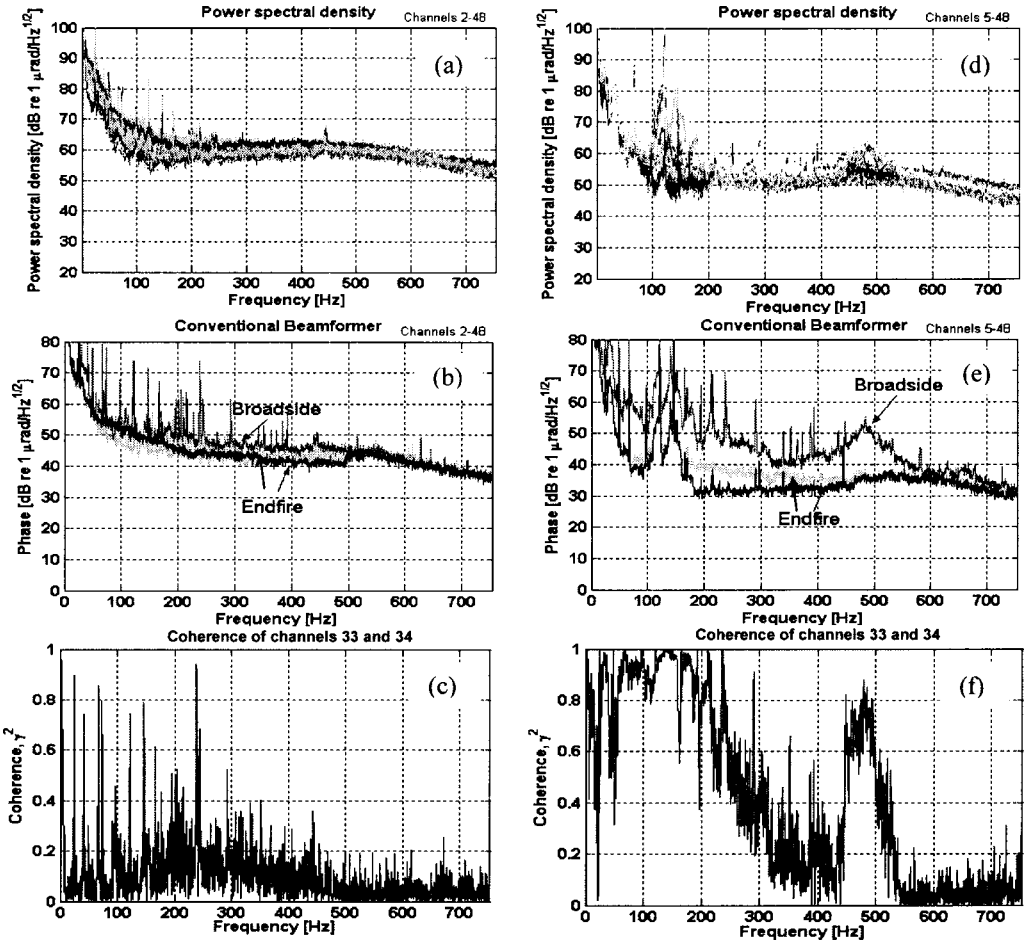

FIG. 6. At-sea ambient noise. Array 1, 35 km link: (a) power spectral density, (b) beamformer, (c) coherence; array 2, 35 km link: (d) power spectral density, (e) beamformer, (f) coherence.

for array 2, particularly at frequencies between 400 and 600 Hz. This shows that the sensor self-noise adds coherently, rather than incoherently, when the data are beamformed in the broadside direction. The correlation between sensor noise is quantified by calculation of the coherence between two adjacent sensors, which is shown in Figs. 5(c) and (f) for arrays 1 and 2, respectively (these plots are typical of the coherence between two adjacent sensors). The coherence is close to unity for frequencies less than 100 Hz for array 1 and frequencies less than 200 Hz and between 500 and 600 Hz for array 2. Consequently, at frequencies where the coherence is high the beamforming process yields little improvement in signal to noise ratio at broadside. In the presence of an incoming acoustic signal at broadside, if the sensor noise is highly correlated and the ambient sea-state induced phase noise is comparable to the sensor self-noise, then the array gain will be significantly degraded. Therefore, the sensor self-noise must be sufficiently lower than the ambient noise to ensure that correlated sensor noise does not degrade the beamforming process.

Injecting narrowband tones onto a single sensor and measuring the signal amplitude on adjacent sensors allows cross-talk to be characterized. This was found to range between -39 and -66 dB at 100 Hz depending on the sensor location relative to the test sensor.

B. Sea-trial measurements

Arrays 1 and 2 were deployed a few kilometers from the coast of a major military and commercial shipping port. A 3 km fiber-optic cable joined each array and a 5 km cable connected array 1 to the shore station. For the majority of the tests, an extra 35 km of optical fiber wound onto spools was added to the input and output fibers, to increase the effective array standoff to 40 km. Array 1 was deployed at a depth of 57 m and array 2 at a depth of 73 m. Shown in Figs. 6(a) and (d) are the phase noise spectral density for all useable channels from data taken during the sea trial. The region where the array was deployed experienced a lot of marine traffic and there were few opportunities when no marine traffic was present. However, these plots represent ''quiet'' periods and allow the spatial filtering ability of the array to be examined. The ambient acoustic noise at this time was close to sea state 3 for array 1 and sea state 1 for array 2. This results in an ambient acoustic induced phase noise approximately 20 dB higher than the mean sensor self-noise at 488 Hz for array 1 and up to 10 dB higher than the sensor self-noise for array 2 (it is assumed that the environmentally induced laser noise level during the laboratory measurements is similar to that during the sea trial). The beamformed data, calculated with no aperture shading and shown in Figs. 6(b) and (e), demonstrates that for array 1 the noise adds incoherently. Thus,

with an acoustic signal present an array gain of ~15 dB would be obtainable at all steer angles (beamforming the data also reveals a weak target in one of the endfire directions). However, for array 2 the noise is coherent, which results in an increase in the beamformed noise by up to ~15 dB in the broadside direction compared with the endfire directions. The array gain for a 48-hydrophone array with no aperture shading and linear spacing, in an isotropic noise field at the design frequency is given by $10\log_{10}(N)$, which for $N=48$ yields 16.8 dB. Thus, during this data acquisition, close to the maximum array gain would be obtainable from array 1; however, coherent noise from the lasers would degrade the array gain for array 2 in the direction of broadside. The correlation of the noise is confirmed by examining the coherence between two adjacent hydrophones as shown in Figs. 6(c) and (f). The frequencies at which coherent noise addition is observed in array 2 corresponds to regions of high signal coherence, indicating that a highly correlated component is present in the sensor signals. It should be emphasized that the correlated noise level between different sensors in array 2 was found to be rather variable. The data shown here represent a period when the correlation was above average.

IV. ARRAY BEAM PATTERNS AND ARRAY GAIN

A. Shape measurement

During the deployment procedure the aim is to lay the hydrophones in a straight line with no slack in the cable between them. Although the arrays were deployed under tension as they entered the sea, the effect of ocean currents at various depths can affect how the array is deposited onto the sea bottom. Therefore, measurements must be performed to determine the actual positions of the hydrophones within each array.

These experiments were conducted by deploying an acoustic source at eight different positions around each array. At each position chirp signals were transmitted across the band 50–2000 Hz. The length of the chirp was 2 s and it was repeated continuously over a period of about 1 min. The Global Positioning System (GPS) data of the boat from which the source was deployed were recorded at the start and end of the chirp transmissions.

The hydrophone locations are calculated using the following procedure: replica correlation functions are calculated between the transmitted signal and the received signals for each of the hydrophones in the array. Relative travel times are then calculated between the sensors from the correlation data for each of the propagating paths. A propagation model is used to predict relative travel times for each path. Sensor and source positions are determined by minimizing the residual error between the measured and modeled delays using a technique similar to that described in Ref. 12. When calculating the delays, a sound speed equal to 1475 m/s at all depths is assumed.

The inverse problem of estimating sensor positions from time delay information is nonunique and ill conditioned. An iterative linearized inversion is employed, which determines the optimum solution by including *a priori* information about the problem. A two-stage process has been adopted to determine the positions of the sensors and sources. In the first stage an optimization procedure is performed to determine the absolute location of the array (relative to the nominal source positions). To achieve this, the positions of the sources are fixed at their nominal positions obtained from the GPS measurements made during deployment. The depths of the sensors are also fixed at their initial positions (interpolated from the water depth at the array). In the second stage, a further inversion procedure is performed to determine the optimum positions and depths of both the sensors and sources. In the second inversion, the position of sensor 24 in the array is fixed and the positions of the remaining sensors relative to it are determined.

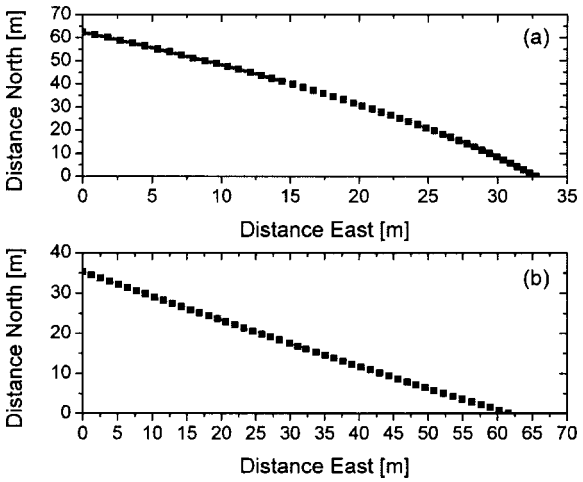

FIG. 7. Derived shape of (a) array 1 and (b) array 2.

Figures 7(a) and (b) show the derived shapes for the two arrays. Array 1 is slightly curved, with the headings at each end of the array differing by 17°. Array 2 is much straighter with the heading at each end differing by only 4°. The curvature of array 1 is beneficial and will be utilized to resolve the left/right ambiguity in the beam pattern.

B. Beam patterns and sidelobe suppression

In order to test the beamforming capabilities of the array, measurements are made using a signal transmitted by an acoustic source towed behind a surface ship. For these experiments, the signal consisted of broadband noise and a number of tonals at known frequencies. In order to track the towed source it is necessary to beamform the data. This has been done using a conventional shape corrected beamformer with the hydrophone positions obtained from the hydrophone localization measurements. For the following data analysis, a Hann window is used in the temporal domain, while in the spatial domain a Kaiser–Bessel window is used, designed to give a maximum side lobe suppression of −36 dB.

An important feature of a hydrophone array is the level of the sidelobes in the beam pattern, which affects the ability of a system to detect a weak signal in the presence of a larger one on a different bearing. Beam patterns at 445 Hz for both arrays have been calculated at a time when the towed source was relatively close to the arrays and so there was a strong signal from a particular direction. For a perfectly straight array an acoustic signal arriving on opposite sides of the

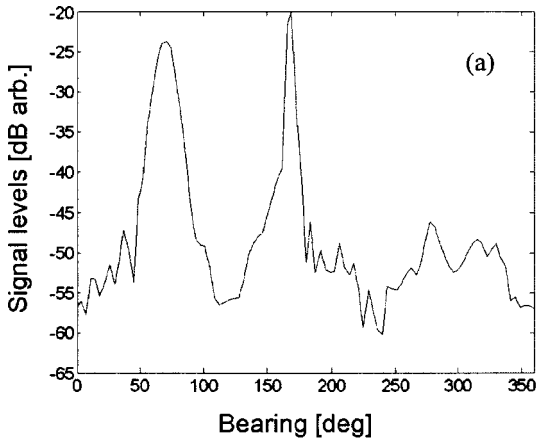

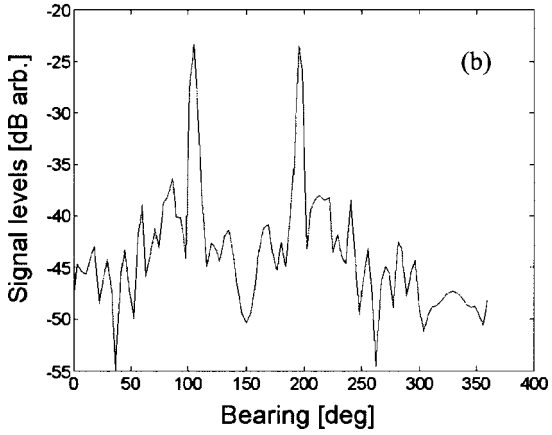

FIG. 8. Beam pattern for (a) array 1 and (b) array 2.

array but at the same angle to broadside, will result in exactly the same phase differences between the signals detected by each hydrophone. It would therefore not be possible to determine which was the actual direction of arrival and this effect is known as the left/right ambiguity. Figure 8(a) shows the beam pattern from array 1 for a towed source range of 1.0 km on a bearing of 170°. The main peaks are at the true bearing and the corresponding bearing on the other side of the array. The curvature in this array results in the peak at the true bearing being sharper and higher than the false one, thus allowing the left/right ambiguity to be resolved. The highest sidelobe is ~26 dB lower than the main peak. A similar ratio is obtained at a latter time when the towed source is at a range of 4.7 km and the signal is 17 dB lower. This suggests that the sidelobe level is determined by leakage from the main peak rather than the background noise level. The array shading used in the beam pattern should give a maximum sidelobe level of −36 dB for a straight array. The higher sidelobe level is partly due to the array curvature, and partly to a number of other effects including variation in responsivity of the hydrophones, and errors in their calculated positions.

Figure 8(b) shows the beam pattern for array 2 when the towed source was at a range of 2.3 km and a bearing of 195°. Due to the straightness of this array, the two peaks are almost identical and it cannot be determined from the beam pattern which peak corresponds to the true bearing. The maximum sidelobe level in this case is only ~15 dB below the main peak although they are lower at greater separations from the peak.

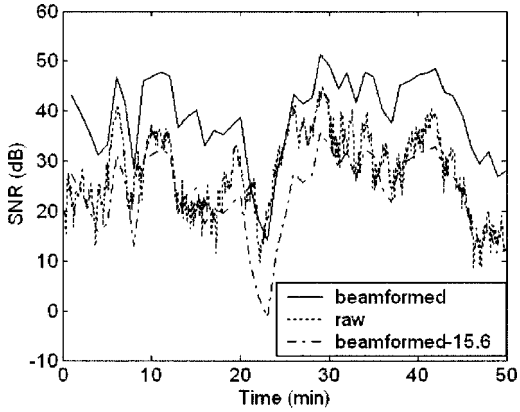

FIG. 9. SNRs of beamformed and raw data.

The sidelobe suppression in array 2 is expected to be lower than array 1 since four of the hydrophones were damaged during manufacture of the array and produced no acoustic signal. To try and minimize the effect of this missing data on the beam pattern, the analysis program estimates the missing hydrophone signal by interpolating values from the remaining hydrophones. However, the interpolation cannot perfectly reconstruct the missing data and the errors introduced by the interpolation have the effect of increasing the sidelobe levels. It may also be the case that the hydrophone responsivity is more variable in array 2 or that the errors in the calculated hydrophone positions are greater than estimated.

In order to compare the width of the peak in the beam pattern with the predicted value, the same beamforming procedure is used to process ideal simulated data. The simulated data corresponds to a signal of 445 Hz incident on a straight array with the same number of hydrophones and spacing. Although, due to its idealized nature, the sidelobe levels are lower for the simulated data, it is found that the width of the two peaks down to 20 dB below their maxima is very similar. This demonstrates that any variation between the hydrophone responsivities and uncertainties in their positions do not adversely affect the width of the peak.

C. Array gain

As discussed earlier, the gain of an array is defined as the increase in the SNR that is obtained by beamforming in the direction of the source. To demonstrate this effect the SNR of the signal at 445 Hz is used, this being defined as the ratio between the 445 Hz signal and the mean noise level in the frequency bands within 50 Hz on either side of the peak.

The SNRs, which are shown in Fig. 9, have been calculated with 50 min of data collected by array 1. To obtain the SNR from the raw data, the power spectrum from each hydrophone in the array is calculated followed by the mean value over all hydrophones. Since the mean is calculated using the power spectrums, the phase information of the hydrophones is lost and no increase occurs in the SNR when the signals from all the hydrophones are combined. For the

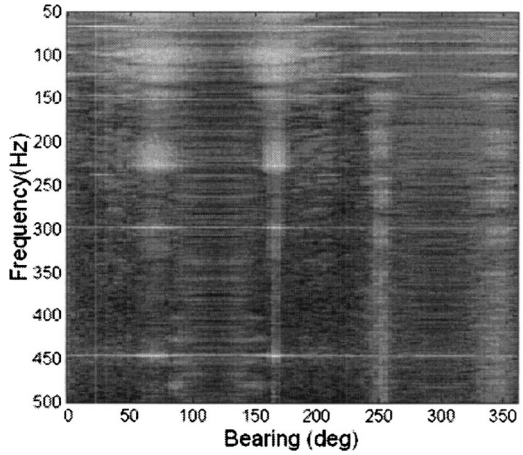

FIG. 10. Beam pattern image of towed source.

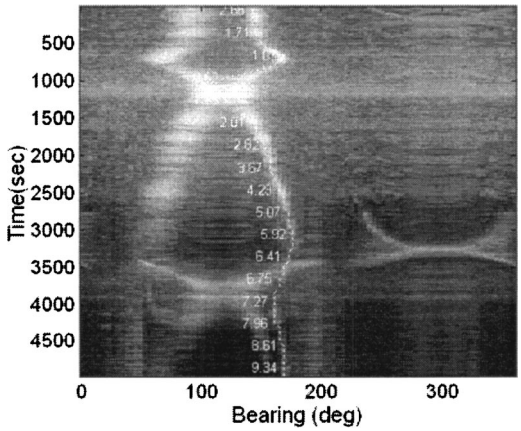

FIG. 11. Tracking pattern using array 1 data.

beamformed data the SNR is calculated using the frequency spectrum of the beam in the direction of the towed source.

The predicted value of the array gain depends on the number of hydrophones in the array and the weighting function used in the beamforming, and for this configuration is 15.6 dB. The dot-dash line in Fig. 9 shows the beamformed SNR minus 15.6 dB, which if the array gain is as predicted should overlap with the dotted line showing the raw SNR. Although there is short term variability in the two lines their general levels agree, showing that the array can achieve the predicted gain. The main discrepancy is between 20 and 30 min and this is due to the nature of the noise in this period. The calculation of the array gain assumes that the noise on each hydrophone is isotropic; however, inspection of the data between 20 and 30 min shows that the noise mainly originates from the ship towing the towed source, which during this period was quite close to the array. Under these circumstances the array gain should be less than the optimum value, which is the situation that is observed.

V. ACOUSTIC EMISSION TRACKING

Figure 10 shows the results of beamforming data from array 1 during one of the towed source runs, when the source was at a bearing of 168°. The gray scale shows the amplitude of the signal as a function of bearing and frequency. The strongest signals occur at both the true bearing and at 80°, which would be a signal arriving at the same angle to broadside but from the other side of the array. Again, the true bearing is higher and has a smaller angular width than the false one and so the left–right ambiguity can be resolved. As well as the vessel with the towed source there also appears to be a second vessel present on a bearing of 255°, which accounts for the broadband signal at that bearing and the ''mirrored'' signal at 340°. The presence of coherent noise in the array would generate an apparent signal at the two broadside directions of 26° and 206°. The lack of any such signal demonstrates that the coherent noise is low enough not to have any observable effect.

The towed source transmitted a number of discrete frequencies and since the angular resolution of an array increases with frequency, tracking is most accurately achieved using the highest of the discrete frequencies, which is 445 Hz. To show the capability of the system to track the towed source only the section of the beam pattern at 445 Hz is used, and this is combined with the same section from subsequent beam patterns. This enables an image to be created that shows how the bearing and strength of the signal at 445 Hz varies as the towed source moves. Such an image, shown in Fig. 11, has been created from 4900 s of data from array 1.

At times up to 2500 s the strongest signal detected is from the towed source; however, as it moves further away its signal strength decreases and the signal from another nearby vessel becomes higher.

As before there are normally two maxima on the trace due to the left/right ambiguity. When the towed source moves near the endfire position (which happens around 1200 s), the angular resolution of the beam pattern becomes worse and the two traces merge. The right-hand trace is narrower and more intense, which shows that this represents the true bearing. The dotted white line in this figure shows the actual bearing of the towed source calculated from the log of its GPS positions. The numbers beside this line show the range in kilometers of the towed source from the array at that time. There is clearly very good agreement between the actual and measured bearing out to a range of around 5.5 km (3000 s) after which time the signal from another vessel temporarily masks the signal from the towed source. After 4200 s, when the other vessel has moved away, there is still a faint trace that follows the dotted line, which shows that the towed source is being detected to a range of ~9 km.

VI. CONCLUSIONS

This paper describes the design and acoustic performance of a large-aperture, seabed mounted, fiber-optic hydrophone array. The system comprises two arrays of 48 hydrophones separated by a 3 km fiber-optic link, which are connected to the interrogation electronics at a shore station through 40 km of optical fiber. The sensors are multiplexed using time and dense wavelength division multiplexing. An erbium doped fiber amplifier is incorporated into the underwater array, which is optically powered by a pump laser located within the interrogation electronics. The system has been characterized by tests carried out in the laboratory and during a sea-trial. During the sea-trial, the array was de-

ployed a few miles from the coast of a major military and commercial port. The portion of the array deployed in the sea is entirely passive and requires no electrical power. The hydrophones in the array are linearly spaced at 1.51 m intervals. An element localization method has been used to determine the shape of the array after deployment. Processing the acoustic data with a shape corrected conventional beamformer has demonstrated successful tracking of a towed acoustic source by a surface vessel. Other passing vessels can also be simultaneously tracked. The width of the main lobe in the beam patterns and the array gain achieved agrees with the theoretically predicted values. One of the arrays was laid on the seabed with a small amount of curvature. This has enabled the left–right ambiguity in the bearing of a target, which exists for a perfectly straight array, to be resolved.

The ambient acoustic noise measured with the arrays on the seabed is typically 10 dB higher than that measured in the laboratory, thus the sensor noise is generally limited by ambient acoustic noise. Correlation of the noise between sensors has been characterized. The noise correlation for sensors interrogated by the same laser is generally higher than between sensors interrogated by different lasers and is found to be due to the environmental sensitivity of the lasers. Isolation of the lasers from environmental noise greatly reduces this noise correlation.

The optical architecture permits the number of multiplexed hydrophones to be significantly increased without increasing the number of optical fibers in the link cable. Thus, this system is suitable as a rapidly deployable, large-area surveillance array.

ACKNOWLEDGMENTS

This work was carried out as part of a collaboration between the Naval Research Laboratory, U.S. and Defense Science and Technology Laboratory, U.K. This project was funded by the US Office of Naval Research, Naval International Programs Office and the U.K. Ministry of Defense. The authors would like to gratefully acknowledge N. Goddard (QinetiQ) for calculating the array shapes and thank G. Cogdell (NRL) for assistance in arranging this collaboration. QinetiQ, UK and Cogent Defense Systems, UK designed and constructed the underwater portion of this system.

[1] J. A. Bucaro, N. Lagakos, J. Cole, and T. Giallorenzi, ''Fiber optic acoustic transduction,'' Phys. Acoust. **XVI**, 385–457 (1982).
[2] A. Dandridge, ''Fiber-optic sensors for acoustic array applications,'' J. Acoust. Soc. Am. **102**, 3168 (1997).
[3] G. A. Cranch, C. K. Kirkendall, K. Daley, S. Motley, A. Bautista, J. Salzano, P. J. Nash, J. Latchem, and R. Crickmore, ''Large-scale, remotely pumped and interrogated fiber-optic interferometric sensor array,'' IEEE Photonics Technol. Lett. **15**, 1579–1581 (2003).
[4] G. A. Cranch and P. J. Nash, ''Large-scale arrays of fiber-optic interferometric sensors using TDM and DWDM,'' IEEE J. Light. Tech. **19**, 697–699 (2001).
[5] P. J. Nash and J. Keen, ''Design and construction of practical optical fibre hydrophones,'' Proc. Inst. of Acoustics **12**, 201–212 (1990).
[6] G. A. Cranch, A. Dandridge, and C. K. Kirkendall, ''Suppression of double Rayleigh scattering induced excess noise in remotely interrogated fiber-optic interferometric sensors,'' IEEE Photonics Technol. Lett. **15**, 1582–1584 (2003).
[7] M. J. Marrone, A. D. Kersey, C. A. Villarruel, C. K. Kirkendall, and A. Dandridge, ''Elimination of coherent Rayleigh backscatter induced noise in fibre Michelson interferometers,'' Electron. Lett. **28**, 1803–1804 (1992).
[8] K. H. Wanser, ''Fundamental phase noise limit in optical fibers due to temperature fluctuations,'' Electron. Lett. **28**, 53–54 (1992).
[9] A. D. Kersey, M. J. Marrone, and A. Dandridge, ''Observation of input-polarization-induced phase noise in interferometric fiber-optic sensors,'' Opt. Lett. **13**, 847–849 (1988).
[10] G. A. Cranch, P. J. Nash, and C. K. Kirkendall, ''Large-scale remotely interrogated arrays of fiber-optic interferometric sensors for underwater acoustic applications,'' IEEE Sensors J. **3**, 19–30 (2003).
[11] N. J. Frigo, A. Dandridge, and A. B. Tveten, ''Technique for elimination of polarization fading in fiber interferometers,'' Electron. Lett. **20**, 319–320 (1984).
[12] S. E. Dosso, B. J. Sotirin, and J. L. Newton, ''Array element localization for horizontal arrays via Occam's inversion,'' J. Acoust. Soc. Am. **104**, 846 (1998).

Temperature dependence of ultrasonic propagation speed and attenuation in excised canine liver tissue measured using transmitted and reflected pulses

U. Techavipoo
Department of Medical Physics and Department of Electrical and Computer Engineering, The University of Wisconsin–Madison, Madison, Wisconsin 53706

T. Varghese[a)]
Department of Medical Physics and Department of Biomedical Engineering, The University of Wisconsin—Madison, Madison, Wisconsin 53706

Q. Chen and T. A. Stiles
Department of Medical Physics, The University of Wisconsin—Madison, Madison, Wisconsin 53706

J. A. Zagzebski
Department of Medical Physics and Department of Radiology, The University of Wisconsin—Madison, Madison, Wisconsin 53706

G. R. Frank
Department of Medical Physics, The University of Wisconsin—Madison, Madison, Wisconsin 53706

(Received 27 October 2003; revised 13 March 2004; accepted 19 March 2004)

Previous reported data from our laboratory demonstrated the temperature dependence of propagation speed and attenuation of canine tissue *in vitro* at discrete temperatures ranging from 25 to 95 °C. However, concerns were raised regarding heating the same tissue specimen over the entire temperature range, a process that may introduce irreversible and, presumably, cumulative tissue degradation. In this paper propagation speed and attenuation vs temperature are measured using multiple groups of samples, each group heated to a different temperature. Sample thicknesses are measured directly using a technique that uses both transmitted and reflected ultrasound pulses. Results obtained using 3 and 5 MHz center frequencies demonstrate a propagation speed elevation of around 20 m/s in the 22–60 °C range, and a decrease of 15 m/s in the 60–90 °C range, in agreement with previous results where the same specimens were subjected to the entire temperature range. However, sound speed results reported here are slightly higher than those reported previously, probably due to more accurate measurements of sample thickness in the present experiments. Results also demonstrate that while the propagation speed varies with temperature, it is not a function of tissue coagulation. In contrast, the attenuation coefficient depends on both tissue coagulation effects and temperature elevation. © *2004 Acoustical Society of America.*
[DOI: 10.1121/1.1738453]

PACS numbers: 43.35.−c, 43.35.Cg, 43.35.Yb [FD] Pages: 2859–2865

I. INTRODUCTION

Numerous articles on ultrasonic propagation speed and attenuation in soft tissue can be obtained from the retrievable literature. Several papers, for example by Wells,[1] Goss,[2,3] and Duck[4] have summarized data on ultrasonic propagation speeds and attenuation coefficients in human and animal tissues. However, previously reported data on the temperature dependence of the propagation speed and attenuation in tissues generally are limited to maximum temperatures of about 65 °C.[5–9] The emerging use of thermal ablative therapies necessitates the acquisition of information on the variation in these parameters at a higher temperature. As tissue is heated during ablation, it expands as well as undergoes changes in the ultrasonic propagation speed and attenuation. These changes introduce time shifts in backscattered ultrasound echo signals from the heated region. The variations in these parameters during heating have been used to compute the temperature distribution in tissue during ablative procedures.[10–16]

Conventional transabdominal ultrasound imaging is presently used during rf ablation procedures for guidance, monitoring, and placement of the electrodes.[17,18] Advantages of ultrasound include widespread availability, real-time guidance for electrode placement, and accurate, convenient needle puncture guides. However a significant drawback of current ultrasonic methods is that the zone of necrosis produced during rf, microwave or high-intensity focused ultrasound (HIFU) ablation is not easily visualized by transabdominal sonography because of the low intrinsic contrast between normal and ablated liver. The poor visualization of the ablated region has prompted clinicians to seek other methods such as x-ray CT to guide the ablation procedure.[19]

Ultrasound guidance of ablation therapy could be im-

a)Electronic mail: tvarghese@wisc.edu

proved if changes in echo arrival time or other temperature related parameters during heating could be used to monitor heating patterns and estimate temperature distributions. Several ultrasonic methods have been proposed to estimate temperature. These include monitoring attenuation,[16] backscattered power,[20] and propagation speed[21] changes with temperature. Thermal expansion either without[11] or with propagation speed variations[11–16] have also been monitored. Several of these techniques are based on tracking the echo-shift in the time-domain, and differentiating the time-shift estimates along the axial direction to obtain a temperature profile.[11–16] Although promising, none of the ultrasonic methods proposed above[12,13] has been applied to measure temperature changes larger than a few degrees, with Simon *et al*. estimating the largest temperature rise—from 23 to 43 °C over 208 minutes.[12] Our preliminary results both *in-vitro* and *in-vivo* suggest the possibility to provide real-time tracking of 2-D temperature changes over the large range of temperatures traditionally used in ablative therapy (40–100 °C) during the procedure.[14]

We have previously reported the temperature dependence of propagation speed and attenuation of canine tissue samples *in vitro* at discrete temperatures, ranging from 25 to 95 °C.[22] The procedure used in Techavipoo *et al.*[22] involved raising the same tissue sample to all measurement temperatures. This procedure where the same tissue sample was raised to all the temperatures in the measurement protocol, however, may introduce an irreversible and presumably cumulative degradation of the tissue structure, thereby altering the values of the propagation speed and attenuation obtained. In this paper, the measurement protocol was changed such that each tissue specimen was raised to a single elevated temperature. The results obtained in this paper demonstrate that any tissue degradation incurred by subjecting samples to the entire range of temperature elevations did not significantly affect the propagation speed or attenuation coefficient changes in tissue.

II. MATERIALS AND METHODS

The method used to measure the propagation speed and attenuation coefficient is similar to the one discussed by Techavipoo *et al.*[22] However, information obtained from reflected pulses off the sample walls is used here for an accurate estimation of tissue sample thickness in the direction of insonification.[23] In addition, the experimental protocol was modified such that sound speeds and attenuation in each tissue specimen was measured at only one temperature.

A. Apparatus

The equipment used is shown in Fig. 1. Two water baths are shown: one for performing acoustical measurements (measurement bath) and the other for heating and retaining the sample (heating bath). Ultrasound pulses were generated by a computer-controlled pulser/receiver (Panametrics model 5800, Waltham, MA) driving a single element, unfocused transducer (Panametrics V309). The acoustic signal was transmitted through a tissue sample positioned within a tissue holder and received by a second transducer (Aerotech Delta PN2794-3, Krauthkramer Inc., Lewistown, PA). In addition, ultrasound echoes from the interfaces at the front and the back of the tissue holder were detected by the Panametrics transducer, operated in a pulse-echo mode. Both transducers have a 5 MHz center frequency. The signals from the receiving transducer as well as the echo signals from the pulse-echo transducer were amplified in the pulser/receiver, and each was digitized at a 100 MHz sampling rate using a 12 bit data acquisition board (Gage Applied Sciences Inc., Lachine, QUE, Canada). Signals were stored for offline processing.

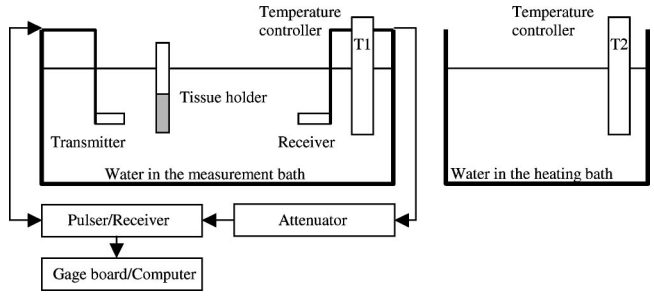

FIG. 1. The apparatus used for the experimental measurements of the propagation speed and attenuation coefficient.

B. Tissue preparation

Canine livers were obtained from 10-month old male hounds available from unrelated studies in an adjoining lab. The excised liver tissues were obtained from animals that do not undergo any procedures on the liver, and hence were considered to be normal specimens. Each individual liver was cut into samples in approximate dimension of $1.6\times5\times5$ cm. Samples did not contain large blood vessels or bile ducts. Five samples (S1, S2, S3, S4, S5) were obtained from each excised liver for the five different temperature elevations in the measurement protocol. Each of these specimens was placed into a sample holder (shown in Fig. 1) along with a degassed saline buffer. Ultrasound propagation measurement was initiated less than 5 hours after excision of the liver. The experiment was repeated using tissues from 10 different animals to obtain the mean and standard deviation of the propagation speed and attenuation over different animals.

C. Data acquisition

Propagation speeds and attenuations for all five liver samples (S1, S2, S3, S4, S5) in each group were first measured at temperatures of 22 °C and 37 °C. The temperature of 37 °C was used since this temperature is close to the animal body temperature *in-vivo*. The samples in their holders were heated by placing them into the heating bath with a preset measured water temperature for duration of 20 minutes. We assumed that the tissue temperature within the holder would reach the preset temperature of the heating bath within the 20 minute interval. The five different tissue samples (from the same excised liver) were heated to different preset temperatures, i.e., S1 to 50 °C, S2 to 60 °C, S3 to 70 °C, S4 to 80 °C, and S5 to 90 °C in our measurement protocol. The propagation speeds and attenuations of the samples were also measured again at 37 °C after the tissue

was cooled. For the measurements at 22 and 37 °C, the temperature in the measurement bath was set to the target temperature, and every sample was equilibrated to the measurement temperature. In contrast, for the measurements at the higher target temperatures, the temperature in the measurement bath was held at 37 °C while samples were heated and retained in the heating bath at the target temperature. Propagation speed and attenuation of the tissue specimen in the sample holder was then immediately measured in the measurement bath. The measurements were done in the order of lowest to highest temperatures. Because of the temperature difference between the temperatures of the tissue sample and the water in the measurement bath, care was taken to ensure that time shifts and transmitted amplitudes were recorded within 5 seconds after transferring the sample to the measurement bath. The variations in the tissue temperatures were limited to the amount of heat transferred between the tissue and the water in the measurement bath during the measurement.

D. Method

The propagation speed and attenuation coefficient were determined using the substitution technique.[22,23] For each measurement four signals were recorded, as described below, with and without the sample inserted into the ultrasound path. We record four pulses, namely the transmission pulse through water without the sample present $P_w(t)$, the transmission pulse with the sample inserted $P_s(t)$, and echoes from the proximal and distal sample windows, $P_1(t)$ and $P_2(t)$, respectively. Note that $t=0$ corresponds to the time when the pulser/receiver transmits the corresponding pulse.

Propagation speeds in tissue samples were calculated[23] using the equation

$$V_p(f)=c_w\left[1+2\times\frac{\phi_w(f)-\phi_s(f)+2\pi f(t_w-t_s)}{\phi_2(f)-\phi_1(f)+2\pi f(t_2-t_1)}\right], \quad (1)$$

where c_w is the sound speed in water, ϕ denotes the phase spectrum of a pulse that was shifted from its center to zero, and t is the corresponding time-shift. The subscripts w and s refer to the water reference and the sample, respectively. The sample thickness along the beam propagation path was estimated using

$$\hat{L}=\frac{c_w}{4\pi f}[\phi_2-\phi_1+2\phi_w-2\phi_s+2\pi f(t_2-t_1+2t_w-2t_s)]. \quad (2)$$

The frequency dependence of the phase spectra on the right side of Eq. (2) cancels out making $\hat{L}$ a constant. However, $\hat{L}$ estimated from the experimental data may vary with the frequency. The variance of $\hat{L}$ can be used to ascertain the reliability of the experiment.[23]

The measurement of propagation speed and sample thickness involves the utilization of the absolute phase spectra of the pulses. The phase information from Fourier transforms wraps around zero, making it difficult to recover the absolute phase spectra. Before implementing Eqs. (1) and (2), the center of each pulse was shifted to $t=0$; therefore the absolute phase evolves slowly with frequency and is easier to track and unwrap. However, the transducers used in the experiment have a 60% bandwidth, with phase information outside the bandwidth not suitable for tracking the phase evolution with frequency.

We defined the center of the pulse at the position of the maximum of its envelope, and we unwrapped the phase starting at 4-MHz frequency for 5 MHz center frequency pulses. Since the transducer used in the experiment was narrowband, phase unwrapping could not be initiated starting at zero frequency. The magnitude spectra of pulses at frequencies lower than 4 MHz were very small, resulting in high uncertainty in the phase spectra. Assuming that the maximum phase evolution from 0 to 4 MHz lies within $\pm 2\pi$, the possible phase after shifting the center to zero can be written as

$$\phi(f)=\phi_{\text{unwrap}}(f)\pm 2n\pi, \quad \text{for } n=0 \text{ or } 1, \quad (3)$$

where ϕ_{unwrap} is the phase after unwrapping. We obtained phase estimates by substituting the phase spectra in Eq. (2) using Eq. (3) and selecting the combination of the phases that provided the lowest thickness variation. The standard deviation of the thickness estimates for each measurement at the frequencies between 4 MHz and 6 MHz after this process is less than 0.05 mm. This combination of the phases was then substituted into Eq. (1) to obtain the propagation speed.

The attenuation coefficients in units of dB/cm were calculated from the magnitude spectra of $P_w(t)$ and $P_s(t)$ using

$$\alpha(f)=(20/\hat{L})\log_{10}[A_w(f)T_{\text{total}}(f)/A_s(f)], \quad (4)$$

where A_w and A_s are the magnitude spectra, and T_{total} is the combined amplitude transmission coefficient through the sample windows.[24] T_{total} is calculated using

$$T_{\text{total}}(f)=\frac{4Z_1Z_3}{(Z_1+Z_3)^2\cos^2(2\pi fl/c_2)+(Z_2+Z_1Z_3/Z_2)^2\sin^2(2\pi fl/c_2)}, \quad (5)$$

where the subscripts 1, 2, and 3 refer to the properties of the water in the measurement bath, the thin layer material, and the tissue sample, respectively; Z denotes the acoustic impedance, l is the thin layer thickness of the tissue holder; and c_2 is the sound speed in the thin layer. We assume that the thin layer properties are constant with temperature, $Z_2=4.25\times10^6$ kg/m^2 s, $c_2=2540$ m/s, and $l=25\ \mu$m.[24] The acoustic impedances of the tissue samples and water are cal-

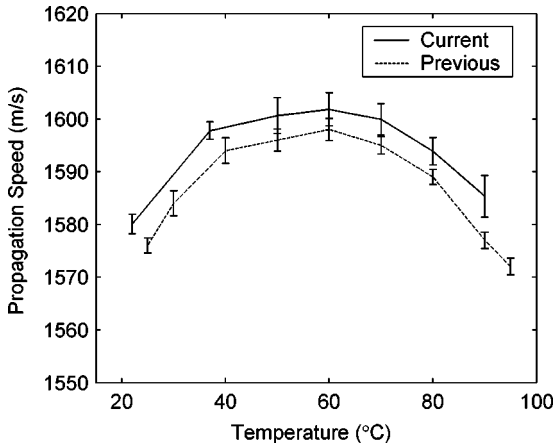

FIG. 2. Plots of mean propagation speed in canine liver tissue measured at different temperatures compared to the previous results reported in Techavipoo *et al.* (Ref. 22). Note that error bars are plus and minus one standard error across 10 different animals.

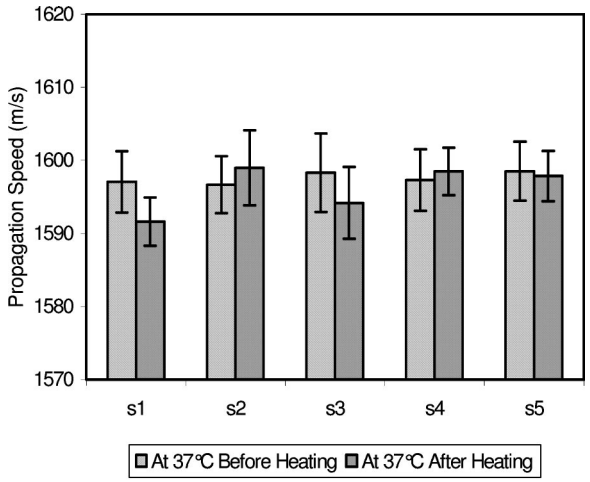

FIG. 3. Bar plots comparing the propagation speeds in canine liver tissue measured at 37 °C before and after the tissue samples were heated to the elevated target temperatures. Tissue sample S1 was raised to a single target temperature of 50 °C, S2 to 60 °C, S3 to 70 °C, S4 to 80 °C, and S5 to 90 °C, respectively.

culated from the multiplication of their densities and sound speeds. Canine liver tissue density is assumed to be equal to that of human liver, 1.050×10^3 kg/m^3,[4] and constant with temperature. The sound speeds in water and the water densities at different temperatures were adopted from Greenspan and Tschegg[25] and Gill,[26] respectively. Using these constants and the mean values over the 4 MHz to 6 MHz range for the propagation speed in samples and their thicknesses, the attenuation coefficient can be estimated using Eq. (4).

III. RESULTS

Figure 2 presents the speed of sound vs temperature for samples evaluated in this experiment. The solid line denotes the results obtained here, while the dashed line illustrates our previous results heating each sample to all measurement temperatures, as reported in Techavipoo *et al.*[22] These values are also shown in Table 1. Both plots demonstrate the same trend in the results, with the propagation speed increasing with temperature below 60 °C, reaching a maximum value at 60 °C, and then decreasing with a further temperature increase.

TABLE I. A comparison between the current and previous measurements of the propagation speeds in canine liver tissue at different temperatures.

	Current propagation speed (m/s)		Previous propagation speed (m/s)	
Temperature (°C)	Mean	Standard error	Mean	Standard error
22	1580	1.85	-	-
25	-	-	1576	1.40
30	-	-	1584	2.38
37	1598	1.66	-	-
40	-	-	1594	2.44
50	1601	3.39	1596	2.10
60	1602	3.16	1598	2.08
70	1600	2.97	1595	1.68
80	1594	2.61	1589	1.45
90	1585	3.95	1577	1.54
95	-	-	1572	1.58

All sound speeds measured in this experiment are about 5 m/s larger than our previous results. The cause of this difference likely can be explained as follows. In our previous experiment, propagation speed in tissue was calculated using $c_m = c_w/(1-c_w\,\Delta t/d)$, where c_w, Δt, and d are the sound speed in water, time-shift between the pulses with and without sample insertion, and sample thickness, respectively. The sample thickness was measured using a caliper outside the water tank, but the time-shift was measured while the sample was under water. Water pressure may have caused the sample windows to adhere more closely to the tissue sample in the measurement path than in air. Therefore, the real sample thickness for the time-shift measurement was smaller than the sample thickness measured using a caliper. As a result, the term in the parentheses in the above equation should be smaller, and c_m should be larger, assuming that the Δt is positive. In addition the thickness measurement is more accurate using the technique described in this paper since the measurement is performed at the same site where the sound speed is measured.

Comparisons between the propagation speeds in tissue measured at 37 °C before and after the samples heated to the target temperatures are shown in Fig. 3. These data evaluate whether tissue coagulation introduces irreversible changes in the propagation speed after the tissue is returned to body temperature. Observe from the figure that all the speeds of sound in all samples before and after heating lie between 1590 and 1600 m/s. No statistically significant differences are observed in the propagation speed at 37 °C measured before vs after tissue coagulation. These results demonstrate that the changes observed in the propagation speed are entirely due to the elevated temperature in tissue.

Attenuation coefficients (dB/cm) vs tissue temperature for three ultrasound frequencies are shown in Fig. 4. The attenuation coefficients vary within a 1-dB/cm range over the temperatures spanned and reach a minimum at a temperature of around 50 to 60 °C. Data for each frequency show the same trend with heating, while variations between frequen-

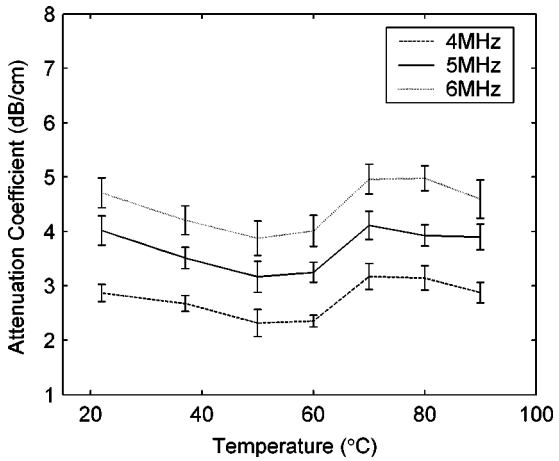

FIG. 4. Attenuation coefficients in canine liver tissue measured at different temperatures for center frequencies of 4, 5, and 6 MHz.

cies are consistent with attenuation being proportional to frequency. The attenuation coefficients obtained at 5 MHz are compared to the results obtained using the previous experimental protocol[22] in Fig. 5. These values are also provided in Table II. Note that the attenuation coefficient curves in both experiments are in the range of 3 to 4 dB/cm, and that the errorbars overlap. These results again demonstrate that attenuation coefficients derived using the two experimental protocols are nearly identical, and any differences between these and our previous results are not statistically significant.

However, the plots in Fig. 6 comparing the attenuation coefficient at 5 MHz obtained at 37 °C for the same tissue sample before and after temperature elevation indicates that there is an increase in the attenuation coefficient of the cooled tissue following coagulation. The difference between pre- and post-heating attenuation coefficients is greater for the tissues elevated to 80 °C and 90 °C (S4 and S5) than for the tissues whose target temperatures were lower (S1, S2, and S3). The third bar in each group in Fig. 6 represents the difference between the first and second measurements. The attenuation coefficient after heating increases almost linearly from 3 to 6 dB/cm when the target temperature increases

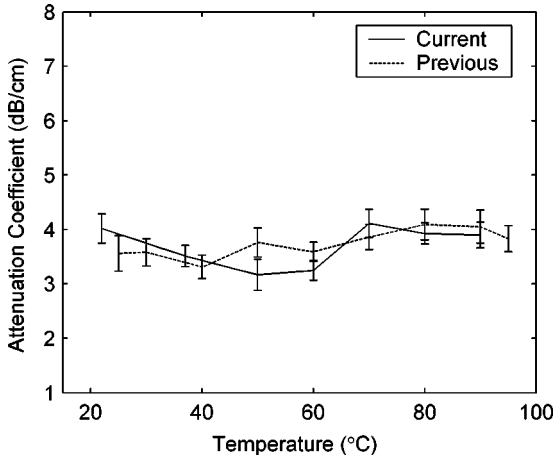

FIG. 5. Plots of the attenuation coefficients at 5-MHz frequency in canine liver tissue measured at different temperatures compared to the previous results reported in Techavipoo *et al.* (Ref. 22). Note that error bars are plus and minus one standard error across 10 different animals.

TABLE II. A comparison between the current and previous measurements of the attenuation coefficients at 5 MHz in canine liver tissue at different temperatures.

	Current attenuation (dB/cm)		Previous attenuation (dB/cm)	
Temperature (°C)	Mean	Standard error	Mean	Standard error
22	4.01	0.269	-	-
25	-	-	3.56	0.326
30	-	-	3.58	0.250
37	3.51	0.195	-	-
40	-	-	3.31	0.215
50	3.17	0.285	3.76	0.269
60	3.25	0.185	3.59	0.177
70	4.11	0.258	3.86	0.231
80	3.93	0.194	4.09	0.285
90	3.90	0.237	4.05	0.304
95	-	-	3.83	0.237

from 50 to 90 °C. These results depict that an irreversible change occurs, likely caused by tissue coagulation that occurs with increasing temperature. Another interesting facet that can be gleaned from comparing Figs. 5 and 6 is that the large increase in the attenuation coefficient is not present while the tissues are still at the elevated temperature.

Figure 7 illustrates this further, comparing the attenuation coefficient for each temperature group measured at 37 °C before heating to the attenuation at the elevated temperature. Again, the third bar in each group of three represents the difference between the first and second measurements, denoting the contributions of both the temperature elevation and tissue coagulation effects. Finally we attempt to decouple the individual contributions of tissue coagulation and temperature elevation in Fig. 8. Shown for each temperature group are differences in 37 °C attenuation before and after heating (B–A); differences between attenuation results when measured at the target temperature and when measured at 37 °C (C–A); and differences between attenuation results

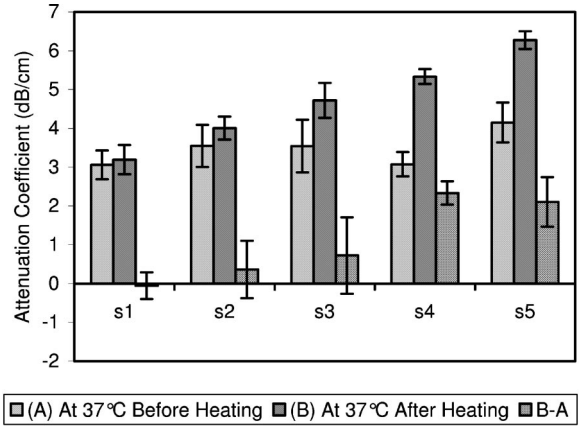

FIG. 6. Bar plots comparing the attenuation coefficients in tissue measured at 37 °C before and after the tissue samples were heated to the elevated target temperatures. The third bar-plot in each set represents the difference between the first and second measurements (B–A), demonstrating the increased attenuation due to tissue coagulation. Tissue sample S1 was raised to a single target temperature of 50 °C, S2 to 60 °C, S3 to 70 °C, S4 to 80 °C, and S5 to 90 °C, respectively.

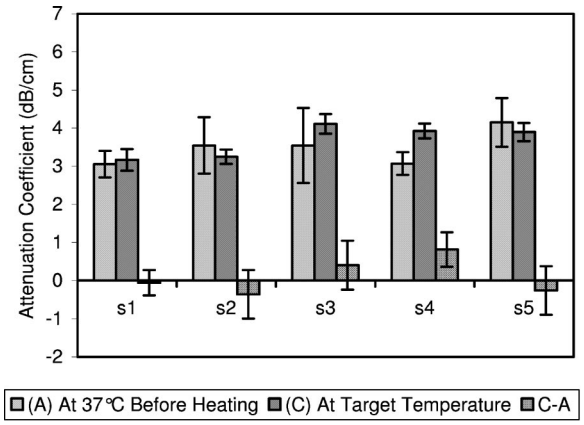

FIG. 7. Bar plots comparing the attenuation coefficients in tissue measured at 37 °C before heating and at the elevated target temperature. The third bar plot in each set represents the difference between the first and second measurements (C–A), demonstrating the increased attenuation due to both tissue coagulation and temperature elevation. Tissue sample S1 was raised to a single target temperature of 50 °C, S2 to 60 °C, S3 to 70 °C, S4 to 80 °C, and S5 to 90 °C, respectively.

when measured at the target temperature and when measured after heating but at 37 °C (C–B). Some of the larger differences in the (C–B) results in Fig. 8 is observed for the 80 °C and 90 °C temperatures (where the errorbars do not overlap), pointing out that temperature elevation itself introduces changes in the attenuation coefficient that negates the increase in the attenuation coefficient caused by tissue coagulation.

IV. DISCUSSION AND CONCLUSIONS

The propagation speed and attenuation coefficient in canine liver tissue measured in this paper agree with our previous results (Techavipoo *et al.*[22]). This implies that continuously heating and measuring properties for the same tissue samples over the entire temperature range produces similar results for both attenuation and propagation speed as the results from applying a single target temperature to each specimen. The only other difference between the measurement procedures is the more accurate measurement of specimen thickness in this paper.

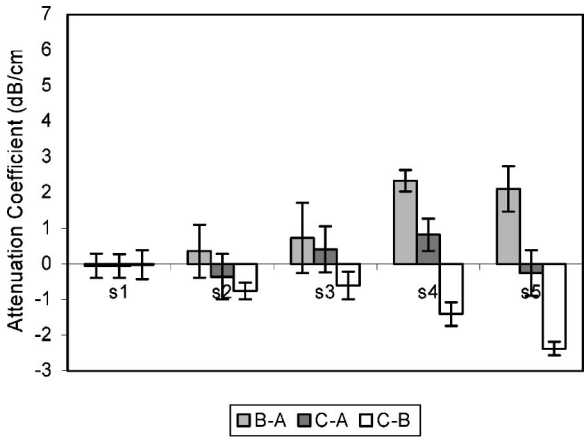

FIG. 8. Bar plots comparing the components of the attenuation coefficient due to tissue coagulation (B–A) both tissue coagulation and temperature elevation (C–A) and the component due to temperature elevation only (C–B). Note that the variation in the attenuation coefficient due to temperature elevation is opposite to that die to tissue coagulation.

In addition, we also demonstrate that no statistically significant changes in propagation speed estimates are observed before and after temperature elevation on the same tissue specimens measured at 37 °C. The higher temperatures reached almost certainly lead to tissue coagulation. The results indicate that variations in propagation speed with temperature are not a function of tissue coagulation effects that are induced with temperature elevation. Thus, it appears that tissue denaturation does not have an appreciable impact on the propagation speed. Therefore, the resultant shape of the propagation speed curve depends primarily on the temperature elevation, thereby making it an ideal parameter to measure temperature elevation in tissue.

On the other hand, the attenuation coefficient depends on both tissue coagulation and temperature elevation. By measuring the attenuations at 37 °C before and after heating, the tissue coagulation effect could be observed. The attenuation coefficient increases with the temperature that was used to heat the tissue. An increase in the temperature produces a concomitant increase in tissue coagulation and a subsequent increase in the attenuation coefficient upon cooling. In addition, temperature elevation and coagulation appear to have opposite effects on attenuation, thereby accounting for relatively unchanged values for the attenuation coefficients measured at the elevated temperatures. These results suggest that attenuation coefficients are probably not suitable for monitoring tissue temperature. However, the quantifiable and statistically significant increases in the attenuation obtained after heating (to a level that induces coagulation) followed by cooling of the tissue clearly demonstrate the potential of using the local maps of attenuation coefficients to demarcate the ablated regions. It also shows the possibility of ascertaining the degree of thermal damage by the change or the increase of the attenuation coefficient.

ACKNOWLEDGMENTS

The authors thank Mr. Larry Whitesell and Ms. Jennifer Puck for providing canine liver tissue samples and Mr. Ashish V. Thakkar for collecting some of the data used in this paper. This work was supported in part by start-up funds from the Department of Medical Physics, Medical School and Graduate School at the University of Wisconsin—Madison, NIH Grant No. 1 R01CA39224 and funds from the Wisconsin Alumni Research Foundation.

[1] P. N. T. Wells, *Biomedical Ultrasonics* (Academic, London, 1977).
[2] S. A. Goss, R. L. Johnston, and F. Dunn, "Comprehensive compilation of empirical ultrasonic properties of mammalian tissues," J. Acoust. Soc. Am. **64**, 423–457 (1978).
[3] S. A. Goss, R. L. Johnston, and F. Dunn, "Compilation of empirical ultrasonic properties of mammalian tissues. II," J. Acoust. Soc. Am. **68**, 93–108 (1980).
[4] F. A. Duck, *Physical Properties of Tissue: A Comprehensive Reference Book* (Academic, San Diego, 1990).
[5] T. Bowen, W. G. Connor, R. L. Nasoni, A. E. Pifer, and R. R. Sholes, *Measurement of the Temperature Dependence of the Velocity of Ultrasound in Soft Tissues*, Ultrasonic Tissue Characterization II (National Bureau of Standards Washington, DC, 1979), p. xi+362.

[6] K. A. Wear, ''Temperature dependence of ultrasonic attenuation in human calcaneus,'' Ultrasound Med. Biol. **26**, 469–472 (2000).
[7] A. E. Worthington and M. D. Sherar, ''Changes in ultrasound properties of porcine kidney tissue during heating,'' Ultrasound Med. Biol. **27**, 673–682 (2001).
[8] J. C. Bamber and C. R. Hill, ''Ultrasonic attenuation and propagation speed in mammalian tissues as a function of temperature,'' Ultrasound Med. Biol. **5**, 149–157 (1979).
[9] M. O'Donnell, J. W. Mimbs, B. E. Sobel, and J. G. Miller, ''Ultrasonic attenuation of myocardial tissue: dependence on time after excision and on temperature,'' J. Acoust. Soc. Am. **62**, 1054–1057 (1977).
[10] C. A. Damianou, N. T. Sanghvi, F. J. Fry, and R. Maass-Moreno, ''Dependence of ultrasonic attenuation and absorption in dog soft tissues on temperature and thermal dose,'' J. Acoust. Soc. Am. **102**, 628–634 (1997).
[11] R. Seip and E. S. Ebbini, ''Noninvasive estimation of tissue temperature response to heating fields using diagnostic ultrasound,'' IEEE Trans. Biomed. Eng. **42**, 828–839 (1995).
[12] C. Simon, P. VanBaren, and E. S. Ebbini, ''Two-dimensional temperature estimation using diagnostic ultrasound,'' IEEE Trans. Ultrason. Ferroelectr. Freq. Control **45**, 1088–1099 (1998).
[13] R. Maass-Moreno, C. A. Damianou, and N. T. Sanghvi, ''Noninvasive temperature estimation in tissue via ultrasound echo-shifts. Part II. In vitro study,'' J. Acoust. Soc. Am. **100**, 2522–2530 (1996).
[14] T. Varghese, J. A. Zagzebski, Q. Chen, U. Techavipoo, G. Frank, C. Johnson, A. Wright, and F. T. Lee, ''Ultrasound monitoring of temperature change during radiofrequency ablation: preliminary in-vivo results,'' Ultrasound Med. Biol. **28**, 321–329 (2002).
[15] N. R. Miller, J. C. Bamber, and P. M. Meaney, ''Fundamental limitations of noninvasive temperature imaging by means of ultrasound echo strain estimation,'' Ultrasound Med. Biol. **28**, 1319–1333 (2002).
[16] S. Ueno, M. Hashimoto, H. Fukukita, and T. Yano, *Ultrasound Thermometry in Hyperthermia*, 1990, pp. 1645–1652.
[17] L. Solbiati, S. N. Goldberg, T. Ierace, T. Livraghi, F. Meloni, M. Dellanoce, S. Sironi, and G. S. Gazelle, ''Hepatic metastases: percutaneous radio-frequency ablation with cooled-tip electrodes,'' Radiology **205**, 367–373 (1997).
[18] L. Solbiati, T. Ierace, S. N. Goldberg, S. Sironi, T. Livraghi, R. Fiocca, G. Servadio, G. Rizzatto, P. R. Mueller, A. Del Maschio, and G. S. Gazelle, ''Percutaneous US-guided radio-frequency tissue ablation of liver metastases: treatment and follow-up in 16 patients,'' Radiology **202**, 195–203 (1997).
[19] C. H. Cha, F. T. Lee, Jr., J. M. Gurney, B. K. Markhardt, T. F. Warner, F. Kelcz, and D. M. Mahvi, ''CT versus sonography for monitoring radiofrequency ablation in a porcine liver,'' AJR, Am. J. Roentgenol. **175**, 705–711 (2000).
[20] W. L. Straube and R. M. Arthur, ''Theoretical estimation of the temperature dependence of backscattered ultrasonic power for noninvasive thermometry,'' Ultrasound Med. Biol. **20**, 915–922 (1994).
[21] R. L. Nasoni, ''Temperature corrected speed of sound for use in soft tissue imaging,'' Med. Phys. **8**, 513–515 (1981).
[22] U. Techavipoo, T. Varghese, J. A. Zagzebski, T. Stiles, and G. Frank, ''Temperature dependence of ultrasonic propagation speed and attenuation in canine tissue,'' Ultrason. Imaging **24**, 246–260 (2002).
[23] P. He, ''Measurement of acoustic dispersion using both transmitted and reflected pulses,'' J. Acoust. Soc. Am. **107**, 801–807 (2000).
[24] E. L. Madsen, F. Dong, G. R. Frank, B. S. Garra, K. A. Wear, T. Wilson, J. A. Zagzebski, H. L. Miller, K. K. Shung, S. H. Wang, E. J. Feleppa, T. Liu, W. D. O'Brien, Jr., K. A. Topp, N. T. Sanghvi, A. V. Zaitsev, T. J. Hall, J. B. Fowlkes, O. D. Kripfgans, and J. G. Miller, ''Interlaboratory comparison of ultrasonic backscatter, attenuation, and speed measurements,'' J. Ultrasound Med. **18**, 615–631 (1999).
[25] M. Greenspan and C. E. Tschegg, ''Tables of the speed of sound in water,'' J. Acoust. Soc. Am. **31**, 75–76 (1959).
[26] A. E. Gill, *Properties of Seawater* (Academic, New York, 1982).

Air-coupled, focused ultrasonic dispersion spectrum reconstruction in plates

Stephen D. Holland[a] and Sorin V. Teles
Center for Nondestructive Evaluation, Iowa State University, Ames, Iowa 50011

D. E. Chimenti
Department of Aerospace Engineering and Center for Nondestructive Evaluation, Iowa State University, Ames, Iowa 50011

(Received 1 July 2003; accepted for publication 1 March 2004)

This paper presents and demonstrates a noncontact method for measuring the Lamb wave dispersion spectrum of a plate. Noncontact air-coupled source and receive transducers are used with line-focus mirrors and 50–700 kHz broadband apparatus for simultaneous measurement over a broad spectrum of refractive angles and multiple guided modes. Broadband, wide-angle wave forms are measured as a function of position. The Fourier transform of these wave forms from the $t-x$ domain to the $\omega-k$ domain gives an approximate spectrum of the dispersion relation. We measure the dispersion spectra of Lucite™, aluminum, balsa wood, and a carbon fiber epoxy laminate, and show that the measured spectra agree well with the dispersion relation calculated from Lamb wave theory. © *2004 Acoustical Society of America.* [DOI: 10.1121/1.1710501]

PACS numbers: 43.35.Cg, 43.35.Ns, 43.20.Gp, 43.35.Zc [RLW] Pages: 2866–2872

I. INTRODUCTION

Air-coupled ultrasonic materials characterization has been in use since the 1970s, but has not been widely used until recently because of the unavailability of commercial systems. Modern air-coupled ultrasonics began with the development of the capacitive ultrasonic transducer by Kuhl *et al.*[1] in 1954. Luukkala *et al.*[2] in 1971 used capacitive transducers to infer the dispersion of guided modes in plates by identifying peaks in transmission as a function of incident angle. While this led to an approximate estimation of dispersion, it was limited in its precision by interference from sidelobes of the transducer. Safaeinili *et al.*[3] in 1995 introduced both synthetic aperture scanning, which factors out sidelobe interference, and model-based prediction to yield a precision measurement of the dispersion relation of a sample. By 1995, air-coupled ultrasound was established as a qualitative tool for defect imaging, with development culminating in the release of a commercial air-coupled ultrasonic system,[4] which made narrowband air-coupled ultrasonic measurement broadly accessible as a research tool. Schindel *et al.*[5] developed in 1995 broadband micromachined capacitive air-coupled transducers, making truly broadband air-coupled measurements possible. In 1996 Ladabaum and Khuri-Yakub[6] introduced high frequency micromachined air-coupled transducers with sensitivity as high as 11.4 MHz. In 2002 Hosten and Castaings[7] used a parabolic mirror and chirp excitation for measuring the phase velocity of Lamb modes.

We apply the water-coupled two-dimensional Fourier transform method of Fei and Chimenti[8] and the parabolic mirror of Hosten and Castaings[7] to air-coupled measurements of dispersion spectra. We provide theoretical justification for our method and show that, unlike previously used air-coupled dispersion methods, it decouples transducer artifacts from the measured data.

We present a method for the reconstruction of the transmission coefficient of a plate and its related guided wave mode dispersion spectrum using highly focused, broadband air-coupled ultrasound both for generation and detection. We apply pulse compression techniques to maximize signal-to-noise ratio, but insonify with a novel burst of temporally and spectrally tailored random phase noise rather than the more conventional chirp excitation. Stepwise scanning of the transmitted field, followed by a spatial-temporal two-dimensional Fourier transform, yields a reconstruction of the plate transmission coefficient. In the following we summarize our theory and procedure and present measured transmission coefficient results, displayed as grayscale image data, from samples of aluminum, Lucite™, carbon fiber epoxy laminate, and wood plates. Corresponding guided wave mode curves calculated from known geometric, density, and elastic parameters are compared to the experimental data and found to be in close agreement.

II. THEORY

Previous papers analyzing air-coupled plate mode propagation, such as Safaeinili *et al.*,[3] model the plate as a transmission coefficient that operates on the plane wave spectrum of piston transducers. Safaeinili *et al.* showed that a pair of piston transducers can be very closely modeled with a pair of Gaussian transducers, and therefore it is common to model piston transducers as Gaussian. A Gaussian transducer model allows the use of the complex transducer point[9] to mathematically replace a distributed Gaussian transducer with a point transducer spatially displaced into the complex plane.

[a]Author to whom all correspondence should be addressed; electronic mail: sdh4@cornell.edu

 0001-4966/2004/115(6)/2866/7/$20.00 © 2004 Acoustical Society of America

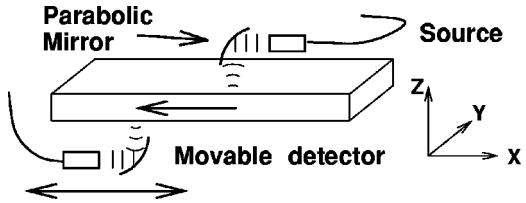

FIG. 1. Diagram of plate with air-coupled transducers and focusing mirrors.

Transducer modeling has been very important because wave form predictions have been used in prior work to calibrate and verify the measurements. In contrast, the results of our dispersion spectra measurements can be directly compared with calculations of Lamb wave modes, because air is a very tenuous coupling medium and only minutely perturbs the Lamb mode dispersion. Since there is no need to include transducer characteristics in those calculations, an empirical transducer model is sufficient for our purposes. We treat our transducer systems (the transducers themselves coupled to focusing mirrors) as sound producing units. Each transducer system is modeled as an arbitrary continuum of point transducers, or equivalently as a generator or detector of an arbitrary spectrum of plane waves. The transducer characteristic, which will be denoted $H(k_x,k_y,k_z,\omega)$, is left as an unknown in the model, and can be measured experimentally.

Our measurement apparatus consists of planar air-coupled thin-film transducers[5] focused by a cylindrical parabolic mirror to create a focused sheet beam incident on the plate, as illustrated in Fig. 1. The beam can be considered as a spectrum of plane waves containing a broad range of spatial frequencies. At the surface, the plane waves couple into guided modes within the plate. Each mode propagates along the plate and leaks energy into the air. The reradiated field below the plate is measured by a nominally identical detector through another line focus mirror. The detector is scanned stepwise in x parallel to the surface, and the transmitted signal is measured as a function of position and time.

Consider an acoustic point source located at coordinates (x',y',z') in the air. An impulse generated by this point source will, satisfying the wave equation, create a transient spherical pressure wave propagating outward in the surrounding air,

$$f(x,y,z,t)=\frac{1}{r}\,\delta(r-c_a t)\otimes_t h_s(t), \tag{1}$$

where $r=\sqrt{(x-x')^2+(y-y')^2+(z-z')^2}$, c_a is the air wave speed, $h_s(t)$ is the impulse response of the source transducer and electronics, and $\otimes_t$ denotes temporal convolution.

We represent our source transducer system, the transducer and mirror, by a spatial continuum of point sources. The shape of the continuum will be the shape of the source transducer itself distorted into a curve by reflection in the mirror. We give each point in the continuum source a separate impulse response, $h_s(x,y,z,t)$. The pressure wave in the air is then the integral of the effects of each infinitesimal point source, that is the convolution over space and time of the effect of a single source with the source distribution,

$$f(x,y,z,t)=\delta(\sqrt{(x-x')^2+(y-y')^2+(z-z')^2}-c_a t)\otimes_{x,y,z,t} h_s(x,y,z,t). \tag{2}$$

This expression for $f(x,y,z,t)$ in Eq. (2) is the pressure wave in the air resulting from the arbitrary source characteristic $h_s(x,y,z,t)$. For our line-focus system of transducer and mirror, we assume that the source transducer has a uniform response over a length l in y, normal to the incident plane as shown in Fig. 1. That is, $h_s(x,y,z,t)=h_s(x,z,t)(u(y+l/2)-u(y-l/2))/\sqrt{2\pi l}$, where $u(y)$ is the spatial unit step in the y direction.

Spectral decomposition [four-dimensional (4D) Fourier transform] of $f(x,y,z,t)$ yields

$$F(k_x,k_y,k_z,\omega)=\frac{4\pi^2}{ik_r c_a}[\,\delta(\omega/c_a-k_r)-\delta(\omega/c_a+k_r)]\times H_s(k_x,k_z,\omega)\sqrt{\frac{l}{2\pi}}\,\mathrm{sinc}\left(\frac{k_y l}{2}\right)\times e^{-ik_x x'-ik_y y'-ik_z z'}, \tag{3}$$

where k_x, k_y, and k_z are the x, y, and z spatial wave numbers respectively, $H_s(k_x,k_z,\omega)$ is the Fourier transform of $h_s(x,z,t)$, ω/c_a is the spatial wave number of a plane wave of frequency ω in air, and $k_r\equiv\sqrt{k_x^2+k_y^2+k_z^2}$. Equation (3) can be understood very easily by looking at its parts. The 4D Fourier transform of a spherical wave propagating outward from the origin is $4\pi^2/ik_r c_a[\,\delta(\omega/c_a-k_r)-\delta(\omega/c_a+k_r)]$. The transform of $h_s(x,z,t)$ is $H_s(k_x,k_z,\omega)$. The width and shape of the source transducer in the y (focal line) direction transforms to $\sqrt{l/2\pi}\,\mathrm{sinc}(k_y l/2)$, and the spatial shift of the source transducer location from the origin to coordinates (x',y',z') is represented by $\exp(-ik_x x'-ik_y y'-ik_z z')$.

Equation (3) allows us to analyze our source as an infinite sum of plane waves, i.e., as a spectral decomposition. It is the spectrum of the acoustic field anywhere in space above the plate. The acoustical effect of the plate is to introduce into this expression a transmission coefficient.[10] The transmission coefficient is the complex ratio of the transmitted pressure divided by the incident pressure of a plane wave. The effect of the transmission coefficient is an amplitude reduction and phase change in the transmitted wave. In particular, it encompasses the effect of resonant guided modes within the plate.[3] The pressure wave spectrum below the plate is therefore

$$\frac{4\pi^2}{ik_r c_a}\left[\delta\left(\frac{\omega}{c_a}-k_r\right)-\delta\left(\frac{\omega}{c_a}+k_r\right)\right]\times T(k_x,k_y,k_z,\omega)H_s(k_x,k_z,\omega)\times\sqrt{\frac{l}{2\pi}}\,\mathrm{sinc}\left(\frac{k_y l}{2}\right)e^{-ik_x x'-ik_y y'-ik_z z'}, \tag{4}$$

where $T(k_x,k_y,k_z,\omega)$ is the transmission coefficient.

As with the source transducer shape and impulse response, the line focus detector transducer can, by reciprocity, be modeled by convolution of the field with the transducer's temporal-spatial response, $h_d(x,y,z,t)$, which yields the measured voltage wave form. Equivalently, spectral domain

multiplication with the Fourier transform of the response, $H_d(k_x,k_y,k_z,\omega)$, provides the spectrum of the measured voltage wave form. As in the case of the source system, we model the detector transducer and line-focus mirror as a single unit with uniform response over its spatial extent l in y, $h_d(x,y,z,t)=h_d(x,z,t)(u(y+l/2)-u(y-l/2))/\sqrt{2\pi l}$, or equivalently in the spectral domain, $H_d(k_x,k_y,k_z,\omega)=H_d(k_x,k_z,\omega)\sqrt{l/2\pi}\,\mathrm{sinc}(k_y l/2)$.

The spectrum measured by the detector transducer is therefore the pressure wave spectrum of Eq. (4) multiplied by the detector response,

$$V(k_x,k_y,k_z,\omega)$$
$$=\frac{4\pi^2}{ik_r c_a}\left[\delta\left(\frac{\omega}{c_a}-k_r\right)-\delta\left(\frac{\omega}{c_a}+k_r\right)\right]$$
$$\times T(k_x,k_y,k_z,\omega)H_s(k_x,k_z,\omega)H_d(k_x,k_z,\omega)\frac{l}{2\pi}$$
$$\times\mathrm{sinc}^2\left(\frac{k_y l}{2}\right)e^{-ik_x x'-ik_y y'-ik_z z'}. \tag{5}$$

From hereon, for the sake of simplicity we will assume infinite transducer extent in y. As the length l of the transducers along the focal axis goes to infinity (perfect line focus), the k_y dependence can be simplified to a delta function, leaving

$$V(k_x,k_y,k_z,\omega)$$
$$=\frac{4\pi^2}{ik_r c_a}\left[\delta\left(\frac{\omega}{c_a}-k_r\right)-\delta\left(\frac{\omega}{c_a}+k_r\right)\right]$$
$$\times T(k_x,k_y,k_z,\omega)H_s(k_x,k_z,\omega)H_d(k_x,k_z,\omega)$$
$$\times\delta(k_y)e^{-ik_x x'-ik_y y'-ik_z z'}. \tag{6}$$

The voltage measured by the detector transducer at location (x,y,z) is the four-dimensional inverse Fourier transform of Eq. (6),

$$v(x,y,z,t)$$
$$=\frac{1}{4\pi^2}\int_\omega\int_{k_x}\int_{k_y}\int_{k_z}\frac{1}{ik_r c_a}\left[\delta\left(\frac{\omega}{c_a}-k_r\right)-\delta\left(\frac{\omega}{c_a}+k_r\right)\right]$$
$$\times T(k_x,k_y,k_z,\omega)H(k_x,k_z,\omega)\delta(k_y)$$
$$\times e^{ik_x(x-x')+ik_y(y-y')+ik_z(z-z')+i\omega t}dk_z dk_y dk_x d\omega. \tag{7}$$

Here we have combined $H_s(k_x,k_z,\omega)H_d(k_x,k_z,\omega)$ into a single composite function $H(k_x,k_z,\omega)$ that represents the combined response of the source and detector transducer systems. Equation (7) gives the time domain signal recorded by our detector in response to an impulse excitation. Because of the presence of delta functions, it is straightforward to perform two of the integrals in Eq. (7). We choose to perform the k_y and k_z integrals, yielding

$$V(x,y,z,t)=\frac{1}{4\pi^2}\int_\omega\int_{k_x}\frac{1}{ik_{z0}c_a}T(k_x,0,k_{z0},\omega)H(k_x,k_{z0},\omega)$$
$$\times e^{ik_x(x-x')+ik_{z0}(z-z')+i\omega t}dk_x d\omega \tag{8}$$

where $k_{z0}\equiv\sqrt{\omega^2/c_a^2-k_x^2}$, the z component of the air wave vector.

In the processing of our measured data, we will perform a two-dimensional forward discrete Fourier transform in x and t. In the model, we approximate that discrete transform with a two-dimensional forward continuous Fourier transform, leading to

$$V(k_x,y,z,\omega)=\frac{1}{ik_{z0}c_a}T(k_x,0,k_{z0},\omega)H(k_x,k_{z0},\omega)$$
$$\times e^{-ik_x x'+ik_{z0}(z-z')}. \tag{9}$$

The final step in our processing will be taking the complex magnitude of V,

$$|V(k_x,y,z,\omega)|=\frac{1}{c_a k_{z0}}|T(k_x,0,k_{z0},\omega)||H(k_x,k_{z0},\omega)|, \tag{10}$$

which is conveniently independent of both vertical transducer positions, z' and z. It is also independent of the transducer positions along the focal line, y' and y because we have assumed the transducers to be infinitely long. Finally, k_{z0}, as defined earlier, is dependent only on ω, k_x, and c_a, so its dependence can be subsumed into the other parameters. We can write

$$|V(k_x,\omega)|=\frac{1}{c_a k_{z0}}|T(k_x,\omega)||H(k_x,\omega)|, \tag{11}$$

where $T(k_x,\omega)\equiv T(k_x,0,k_{z0},\omega)$ and $H(k_x,\omega)\equiv H(k_x,k_{z0},\omega)$. Therefore, the measured $V(x,t)$, discrete Fourier transformed to $V(k,\omega)$, is the magnitude of the spectral transmission coefficient T, windowed by the response of the transducers $H(k_x,\omega)=H_s H_d$ and scaled by the reciprocal of the z component of the air wave vector. The simplicity of Eq. (11) allows for very simple analysis. Since maxima in the transmission coefficient correspond to portions of the spectral domain where the plate is in transverse resonance,[11] i.e., guided wave modes in the plate, and these maxima thereby indicate the plate dispersion relation,[3] we will interpret ridges in $|V(k_x,\omega)|$ as the dispersion curves of guided wave modes. Moreover, Eq. (11) shows that the combined effect of the transducers and mirrors is purely that of a multiplicative window in the (k,ω) domain. In contrast with previous models, this analysis identifies the two-dimensional Fourier transform of the measured voltage to be the transmission coefficient without assuming a particular beam profile, such as Gaussian. Instead it allows either an empirically measured model of the transducer or a calculated model based on the spatial Fourier transform of the shape of the active area. In addition, this analysis can be readily extended to three dimensions, yielding a modified Eq. (11) with k_y dependence added to V, T, and H.

The above-presented analysis is limited by a few assumptions. We implicitly assume an infinite plate, but the real plates we measure are finite. We assume infinitely long line focus transducers, but the transducer assemblies are actually rather narrow. We ignore reflections and reverberations between the transducers and the plate, because these can be eliminated through time windowing. Despite these limita-

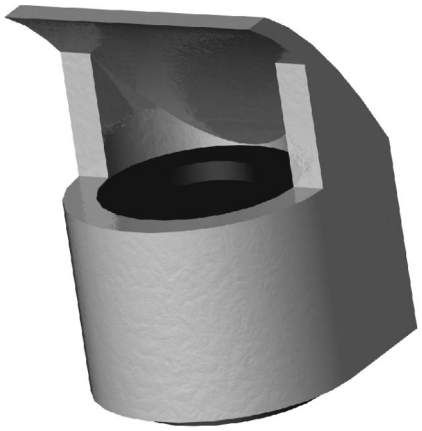

FIG. 2. Line-focus mirror (gray) and transducer (black).

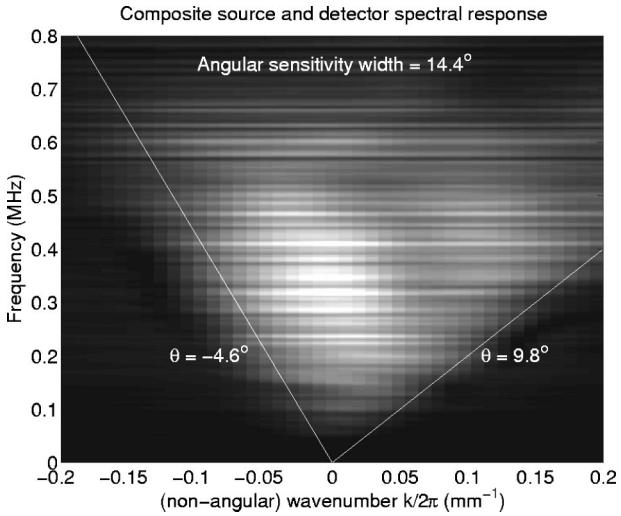

FIG. 3. Spectral sensitivity window of air-coupled transducers and mirrors, $H(k_x,0,\sqrt{\omega^2/c_a^2-k_x^2},\omega)$. Lines are drawn to reflect the beam width.

tions, in practice we have found the above-given analysis to be quite satisfactory for interpreting measured data and matching theoretically calculated dispersion curves to experiment.

III. EXPERIMENTAL METHOD

We measure the transmission coefficient of a medium in the geometry shown schematically in Fig. 1 using an effective impulse source (explained later) and a 10 MSPS 12 bit wave form recorder. Time wave forms are recorded as the position x is stepped over a range wide enough for the signal to disappear in noise, giving $V(x,t)$. The measured, windowed transmission function, $|V(k_x,\omega)|$ is calculated from the two-dimensional discrete Fourier transform of $V(x,t)$. The reciprocal of the step size in x determines the largest k_x that can be measured without aliasing. The range traveled in x determines the resolution in k_x, and zero-padding the $V(x,t)$ data reduces pixelation in the $V(k_x,\omega)$ spectrum through interpolation.

The actual transducers that we use are planar (piston radiators). To create line-focus source and detector systems, the planar transducers are coupled to line-focus mirrors. The mirrors, shown in Fig. 2, have been designed with a CAD tool to have the required parabolic shape and are manufactured from Duraform GF (glass-filled polyamide) using a rapid prototyping method to a surface finish better than 5 μm. These mirrors have a sufficient beam angle to excite a 14.4° slice of the useful region of (k_x,ω) space. Because of the low velocity ratio between air and almost any solid, both shear and longitudinal critical angles occur at relatively low values, so a 14.4° beam acceptance angle is sufficient for most measurements. Figure 3 shows the result of the measurement procedure below with vertically aligned transducers and no plate in place. This is the empirical transducer and mirror response window $H(k_x,\omega)$ of Eq. (11). No contrast stretching or histogram equalization has been performed on this or any other image reported in this paper. As seen in Fig. 3, the transducers have a spectral sensitivity width of 14.4° and wideband frequency response. We have measured the system response, including the effects of both transducers, to be centered at 380 kHz with −10 dB points at 169 and 657 kHz. The dispersion measurements themselves tend to be limited to a somewhat reduced bandwidth because the sensitivity of the measurement drops off with $1/k_{z0}$ [Eq. (11)] which is equivalent to it dropping off with $1/\omega$. The asymmetry visible in Fig. 3 comes from the reflection of the diffraction from the edge of the transducer in the inherently asymmetric parabolic mirror.

Unlike previous methods, we have not had to assume in our analysis a particular physical shape and directivity function of the transducer, except that it is line focus. Instead, we subsumed the transducer shape and directivity into the spectral characteristic of the transducers, $H(k_x,\omega)$, that we empirically measured in Fig. 3. As shown in Eq. (11), $H(k_x,\omega)$ windows the transmission coefficient $T(k_x,\omega)$ in the measurement. The transducer shape and directivity thereby determine which region in (k_x,ω) space is probed by the measurement. In general for a focused transducer, $H(k_x,\omega)$ has the approximate shape of a slice in (k_x,ω) with an angular width that corresponds to the beam acceptance angle of the mirrors and transducers. While we will not attempt to divide out H from our results, this empirical measurement informs us of the effect of the transducer shape on our results, and all measurements are subject to this sensitivity window.

In most of our experiments, we rotate the mirrors about their focal line. Rotating the mirror rotates and stretches the measurement sensitivity window in (k_x,ω) space and allows more modes to be simultaneously excited and measured than possible with unrotated transducers. If the rotated slice is still not large enough to measure all the modes of interest, measurements can be repeated at multiple mirror angles to provide a complete picture of the modal structure built from the sum of rotated copies of the measurement window of Fig. 3.

To maximize the signal-to-noise ratio (SNR), we use a pulse compression technique that simulates an impulse source, equivalent to the autocorrelation of the long, broadband excitation signal. Others have demonstrated similar SNR improvements,[12] but we have developed a random phase excitation wave form to use in place of the usual chirp (linear frequency sweep). The random phase wave form is constructed to have both a desired frequency spectrum and

desired temporal envelope. The wave form is constructed in the frequency domain with the desired amplitude spectrum, but with phases selected using a pseudorandom number generator. The temporal envelope is then applied in the time domain. The desired amplitude spectrum and temporal envelope are inherently contradictory requirements. We apply the two criteria iteratively until a wave form is obtained that very nearly satisfies both. The random phase wave form is transmitted using a Ritec RAM-10000 ultrasonic system, modified to accept arbitrary wave form excitation and perform automatic digital cross correlation on the measured response. A distinct advantage of the random phase signal over the chirp is that our signal transforms any system nonlinearity into time-domain noise that can be reduced by windowing. To obtain the impulse response of the ultrasonic system, the measured wave form from the detector is cross correlated with a stored replica of the transmitted excitation wave form. The correlated signal is equivalent to the response of the ultrasonic system to an elastic wave transient, and therefore can be treated like a conventional pulse wave form.

The measured time-domain wave forms $V(x,t)$ always contain interference signals not predicted by the above-given simplified analysis. At minimum, there are reflections and echos in the air between the transducers and the sample. In addition, our measurement system has a small, but detectable, leakage of the excitation signal into the detector circuit. Sound scattered from the source transducer can reflect from the measurement apparatus around the sample and appear at the detector. All of these interference signals are separated temporally from the desired plate mode wave forms. A key advantage of our time-domain measurement is our ability to eliminate interference by performing time-domain windowing.

The final step of our measurement procedure is to plot the two-dimensional spatial-temporal discrete Fourier transform of all of the correlated windowed time-domain wave forms. This step gives $V(k_x,\omega)$, our windowed measurement of the transmission coefficient. The magnitude of $V(k_x,\omega)$, plotted as a gray scale as a function of (k_x,ω) (or equivalently f and $k_x/2\pi$), is a spectrum of the transmission maxima of the medium. Because air is so tenuous, the transmission maxima essentially coincide with the Lamb modes of the medium, so the experimental result $V(k_x,\omega)$ is effectively a dispersion spectrum.

IV. RESULTS

We have reconstructed the dispersion relations of a wide variety of materials, but show only a few here for illustrative purposes. Figure 4 shows the dispersion relation of 6.68 mm 6061-T6 aluminum. The image is produced from a 300 mm scan in 2 mm steps in x with 3600 averages and the source and detector assemblies each rotated 2° to allow phase matching into as many modes as possible. Bright traces correspond to propagating Lamb modes. The lower frequency bound of the experiment is about 100 kHz and this can be seen in Fig. 4 as a sharp cutoff in the image background. The dashed curves in Fig. 4 are calculated from waveguide theory[10] using nominal values for the elastic parameters of aluminum. Each curve corresponds to a different mode.

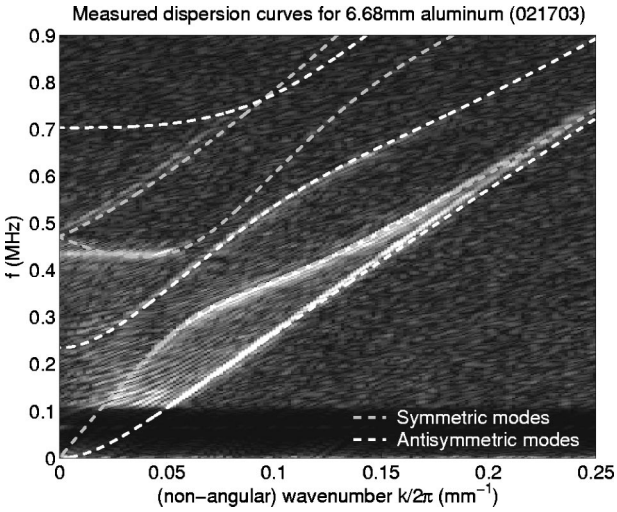

FIG. 4. Image of measured dispersion spectrum for aluminum, with superimposed dashed curves calculated from nominal elastic parameters. The horizontal axis, $k/2\pi$, is equivalent to $1/\lambda$.

Phase velocity of a mode at a particular frequency and wave number is ω/k or equivalently $f/(k/2\pi)$ and is determined by measuring the slope of the line from the origin to $(f,k/2\pi)$. Group velocity at a particular frequency and wave number is determined by measuring the slope of the dispersion curve $d\omega/dk$ [or equivalently $df/(dk/2\pi)$]. The dispersion curves shown in Fig. 4 correspond to, from bottom to top, the lowest order antisymmetric (A_0) and symmetric (S_0) modes, the first-order antisymmetric (A_1), first- and second-order symmetric $(S_1$ and $S_2)$, and the second-order antisymmetric mode (A_2). Figure 4 shows the lowest order antisymmetric and symmetric modes very clearly. The first-order antisymmetric mode is clearly present, and the second-order symmetric mode is also clearly present in the measured data.

This scan was time consuming. Our equipment achieves a repetition rate of 15 Hz; this scan took approximately 10 h. Long scans and substantial averaging are required to achieve fine detail and optimum signal-to-noise ratio in the measured image. Nevertheless, even short scans with few averages can provide an adequate dispersion spectrum. We have achieved recognizable dispersion spectra in as little as 10 min.

Figure 5 shows the measured dispersion relation image for Lucite (poly methyl methacrylate), generated from a 160 mm scan in 2 mm steps with the transducers rotated to an angle of 7° with 4000 averages. Curves calculated from waveguide theory using nominal elastic parameters for Lucite[13] are superimposed upon the curves shown in Fig. 5. These correspond to, from bottom to top, the A_0, S_0, A_1, S_1, S_2, A_2, S_3, and A_3 modes. Every measured mode shows good alignment with the calculated curves. All of the modes except for the second-order antisymmetric and the third-order symmetric mode are visible in the measured dispersion relation image. Some portions of some modes appear brighter than others. Modes with large out-of-plane surface displacements will couple more efficiently to a pressure wave in the air. This fact explains why the upper portion of the S_0 mode beyond 0.07 mm^{-1} is so bright and almost disappears below 0.05 mm^{-1}. In addition, the transducer bandwidth and the spectral directivity of the rotated trans-

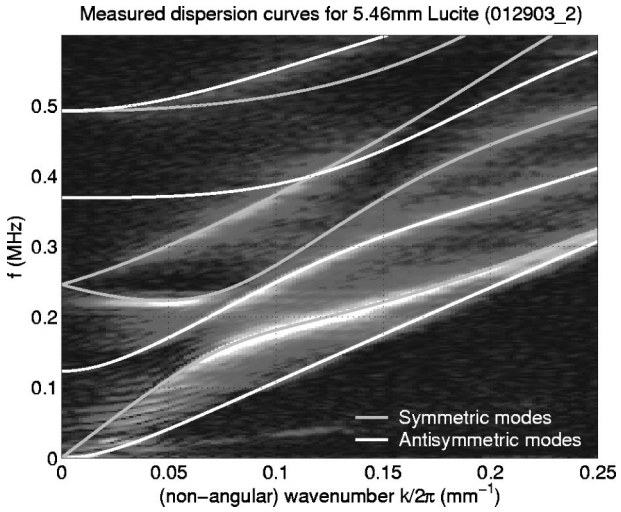

FIG. 5. Image of measured dispersion relation for Lucite, with superimposed curves calculated from nominal elastic parameters.

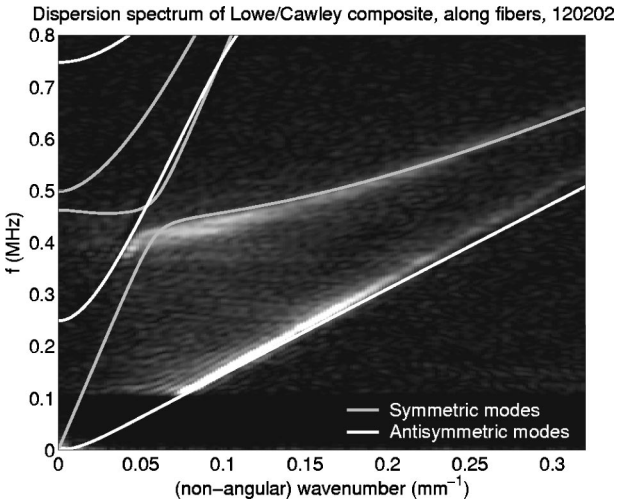

FIG. 7. Measured dispersion spectrum of uniaxial carbon fiber, parallel to fiber direction.

ducer limit the measurement region and thereby affect the intensities of the measured modes. Both Figs. 4 and 5 show the measured dispersion of the S_1 mode below 0.05 mm^{-1} to be nearly horizontal, whereas the theoretical curve increases toward the axis. This phenomenon is the well-known negative group velocity mode. In fact, a full three-dimensional reconstruction of the dispersion spectrum, utilizing spatial scanning in both x and y, yields curves which follow precisely the calculation. The horizontal segment that appears in Figs. 4 and 5 is therefore an artifact caused by the finite extent in y of the line source. This interesting effect has significant implications for scanned imaging, and we have taken this up in another publication.[14]

Figure 6 shows a synthetic dispersion spectrum analogous to the 5.46 mm Lucite of Fig. 5 calculated using Eq. (11). It is the transmission coefficient, calculated using well-known theory,[10] and multiplied by the transducer response, similar to Fig. 3, but measured with a transducer rotation angle of 6°. The calculation was done based on the same elastic parameters used to calculate the dispersion curves of Fig. 3, and with published viscoelastic attenuation values.[3] More modes are visible here than in Fig. 3 because of the perfect signal-to-noise ratio, but they appear in the same places and many have similar intensity ratios. We note that the flat spot in the S_1 mode discussed earlier does not appear. That is because this calculation is based on a two-dimensional model that assumes the transducer to be infinite in y. The flat spot was caused by using a three-dimensional transducer in a two-dimensional model.

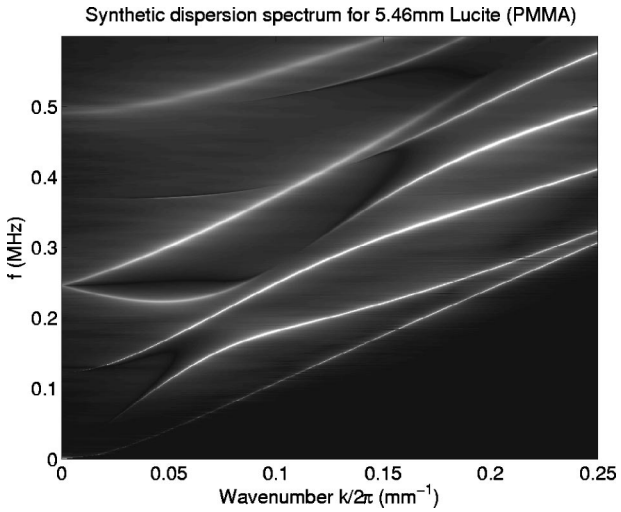

FIG. 6. Synthetic dispersion spectrum for Lucite, calculated according to Eq. (11).

We can measure dispersion spectra of anisotropic materials as well. In this case, the measured spectra will depend on the selected direction of propagation. Figure 7 shows a measured dispersion spectrum (1500 averages) for propagation along the fibers of a sample of 3.3-mm-thick uniaxial carbon fiber epoxy laminate. For this measurement the transducer assemblies have been rotated to 6°. Superimposed on the data are dispersion curves calculated from independently measured elastic constants. The A_0 and S_0 modes are clearly visible, although the lower frequencies and initial slope of the S_0 are not, for reasons pointed out earlier. The sharp knee in the S_0 at around 0.06 mm^{-1} and 0.4 MHz is a consequence of the high elastic anisotropy typical of these materials. Figure 8 shows the measured spectrum for propagation normal to the fiber direction of the same sample, this time with the transducer assemblies again rotated to 6°, and again with 1500 averages. Here, A_0, S_0, A_1, and S_2 modes are all clearly visible in the locations predicted by the theoretical calculations. The modal structure in this case is indicative of an isotropic sample, because we are measuring in the composite's plane of isotropy.

Figure 9 shows a dispersion spectrum for a 9.53-mm-thick balsa wood plate, measured with 2400 averages. In this case we have been able to image both the zeroth-order and many higher order modes. The effect of anisotropy of the wood is also clearly visible in these curves, as it was in the case of the composite. Because wood is a natural fiber, elastic property variations can occur from point to point. Therefore, the data in Fig. 9 are less well defined than for the engineering materials presented earlier. Nonetheless, the structure of the higher order modes is clear and both the

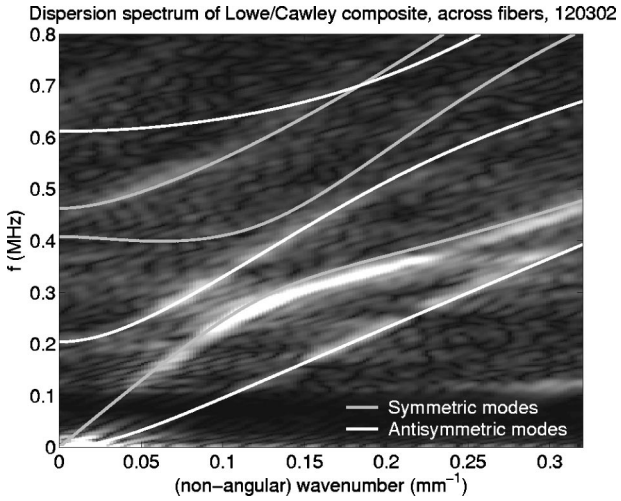

FIG. 8. Measured dispersion spectrum of uniaxial carbon fiber, perpendicular to fiber direction.

longitudinal wave speed and Rayleigh wave asymptote are clearly visible in the data of Fig. 9

V. CONCLUSIONS

We have demonstrated in this paper a noncontact method using air-coupled focused ultrasound to deduce the dispersion characteristics of isotropic and anisotropic plates. By combining random phase excitation and correlation with synthetic aperture scanning we can reconstruct entire portions of a dispersion spectrum in a single scan. The large number of inflection points in the dispersion curves visible in the images shown in Sec. IV allow a robust and reliable fitting procedure. The high sensitivity of certain dispersion curve segments to particular elastic constants is well established.[8,15] Unlike many previous methods, our results can be compared directly with calculations from waveguide theory. Assumptions (except for line-focus) about the acoustic beam function of the transducers are not required.

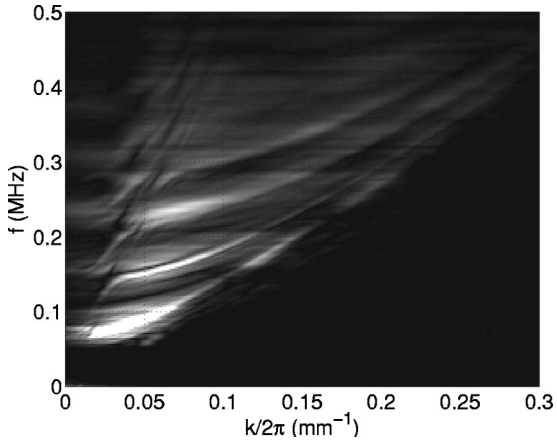

FIG. 9. Experimental dispersion spectrum of 9.53 mm balsa wood, measured along the grain.

The several examples shown here serve to illustrate the capability of this technique. We have reconstructed the dispersion relations of a wide variety of materials, including anisotropic composites and even wood. There is nothing in principle that limits applicability of this method to measuring guided Lamb waves in plates; the dispersion characteristic of any leaky ultrasonic guided mode can be measured in this way. The noncontact nature of the procedure presented here opens possibilities for examining materials which cannot be immersed in coupling liquids.

[1] W. Khul, G. R. Schodder, and F. K. Schröder, ''Condenser transmitters and microphones with solid dielectric for airborne ultrasonics,'' Acustica **4**, 519–532 (1954).
[2] M. Luukkala, P. Heikkila, and J. Surakka, ''Plate wave resonance—A contactless test method,'' Ultrasonics **9**, 201–208 (1971).
[3] A. Safaeinili, O. I. Lobkis, and D. E. Chimenti, ''Air-coupled ultrasonic estimation of viscoelastic stiffness in plates,'' IEEE Trans. Ultrason. Ferroelectr. Freq. Control **43**, 1171–1180 (1996).
[4] W. A. Grandia and C. M. Fortunko, ''NDE applications of air-coupled ultrasonic transducers,'' Proceedings of the 1995 IEEE Ultrasonics Symposium, pp. 697–709.
[5] D. W. Schindel, D. A. Hutchins, L. Zou, and M. Sayer, ''The design and characterization of micromachined air-coupled capacitance transducers,'' IEEE Trans. Ultrason. Ferroelectr. Freq. Control **42**, 42–50 (1995).
[6] I. Ladabaum and B. T. Khuri-Yakub, ''Micromachined ultrasonic transducers: 11.4 MHz transmission in air and more,'' Appl. Phys. Lett. **68**, 7–9 (1996).
[7] B. Hosten and M. Castaings, ''Parabolic mirror and air-coupled transducer for multimodal plate wave detection,'' in *Review of Progress in Quantitative Nondestructive Evaluation*, edited by D. O. Thompson and D. E. Chimenti (AIP Press, New York, 2002), Vol. 22, pp. 1243–1250.
[8] D. Fei and D. E. Chimenti, ''Single-scan elastic property estimation in plates,'' Acoustics Res. Lett. Online **2**, 49–54 (2001).
[9] G. A. Deschamps, ''Gaussian beam as a bundle of complex rays,'' Electron. Lett. **7**, 684–685 (1971).
[10] A. N. Nayfeh, *Wave Propagation in Layered Anisotropic Media* (Elsevier, Amsterdam, 1995).
[11] B. A. Auld, *Acoustic Fields and Waves in Solids*, 2nd ed. (Krieger, Malabar, FL, 1990), Vol. II.
[12] T. H. Gan, D. A. Hutchins, D. R. Billson, and D. W. Schindel, ''The use of broadband acoustic transducers and pulse-compression techniques for air-coupled ultrasonic imaging,'' Ultrasonics **39**, 181–194 (2001).
[13] B. Hartmann and J. Jarzynski, ''Immersion apparatus for ultrasonic measurements in polymers,'' J. Acoust. Soc. Am. **56**, 1469–1477 (1974).
[14] S. D. Holland and D. E. Chimenti, ''Air-coupled acoustic imaging with zero-group-velocity Lamb modes,'' Appl. Phys. Lett. **83**, 2704–2706 (2003).
[15] D. E. Chimenti and D. Fei, ''Scattering coefficient reconstruction in plates using focused acoustic beams,'' Int. J. Solids Struct. **39**, 5495–5513 (2002).

Effectiveness of parallel-plate heat exchangers in thermoacoustic devices

Ray Scott Wakeland and Robert M. Keolian[a)]
The Pennsylvania State University, Graduate Program in Acoustics and Applied Research Laboratory, P. O. Box 30, State College, Pennsylvania 16804-0030

(Received 29 July 2003; revised 14 February 2004; accepted 1 March 2004)

Measurements are made of the heat transferred between two identical parallel-plate heat exchangers under conditions of oscillating flow over a range of frequencies and amplitudes. The results are analyzed and summarized in terms of heat-exchanger effectiveness, the ratio of the actual heat transfer rate to the maximum possible heat transfer rate. Measured results are compared to the DELTAE model that is often used in the design of conventional thermoacoustic devices, and possible improvements to the model are offered. © *2004 Acoustical Society of America.*
[DOI: 10.1121/1.1710503]

PACS numbers: 43.35.Ud, 44.27.+g [RR] Pages: 2873–2886

I. INTRODUCTION

Heat exchangers are important components of thermoacoustic engines and refrigerators. This paper reports measurements of heat transfer between identical heat exchangers in oscillating flow. The results are analyzed in a way that is intended to be useful in the design of thermoacoustic devices.

The authors are not aware of any previously published experiments on the performance of heat exchangers in purely oscillatory flow without externally imposed pressure oscillations. Cooper, Yang, and Nee[1] carried out a review of ''fluid mechanics of oscillatory and modulated flows,'' resulting in 63 references in the category ''convective heat transfer.'' Almost all of the cited studies, however, concern ''modulated flows,'' i.e., steady flows with small oscillatory components superimposed. Most of these papers are concerned with the use of flow pulsations as an enhancement mechanism. Of the papers cited in their review, the only experimental investigation of a situation similar to that encountered in thermoacoustics is the reviewers' own study.[2] In this experimental paper they note that, ''to the knowledge of the authors, no papers have been published dealing strictly with heat transfer to oscillatory flows [with no mean flow].'' Details of their experiment, however, make it difficult to apply their results to heat exchangers for thermoacoustics. In particular, Cooper *et al.* used a complicated system of ''doors'' and ''back flow preventers'' in order ''to provide fresh air every half oscillation cycle,'' so that their experiment is more like the repeated measurement of a time-varying unidirectional flow than a true oscillatory flow. One paper on heat exchange in oscillating flow that escaped the attention of Cooper *et al.* is that of Hwang and Dybbs.[3] Once again, however, the details are such that we have not yet found a way to relate Hwang and Dybbs's results to the results of the present study.

A conventional method of testing a heat exchanger is depicted in Fig. 1(a). Fluid at a well-defined temperature T_{in} flows down a duct and through a heat exchanger that is held at temperature T_{hx}. The fluid exits the exchanger at a different temperature T_{out}. Meanwhile, the rate at which heat is delivered to the exchanger is monitored. A heat-transfer coefficient is then determined in terms of the temperatures and heat.

The situation is not so straightforward for the case of oscillating flow. Consider a single heat exchanger in an oscillating flow in a duct, shown in Fig. 1(b). The exchanger is at temperature T_{hx}, and the fluid in the duct is initially at T_{∞}. After a few passes through the exchanger, however, all the fluid near the exchanger approaches T_{hx}. At this point, the temperature of the fluid entering the exchanger is not well known, and the rate of heat delivery to the fluid has more to do with the way heat is transported along the length of the duct than it has to do with the characteristics of the exchanger itself. This configuration has been studied experimentally by Peattie and Budwig.[4] The interaction between the oscillating boundary layer and the temperature gradient along the duct causes a type of thermoacoustic heat pumping examined in several papers by Kurzweg and collaborators (Refs. 5 and 6, and references therein). While there are applications for this type of transport, it is not particularly relevant to the study of heat exchanger performance in thermoacoustics.

By outfitting an exchanger and a stack (or regenerator) with temperature sensors, it is possible to study heat exchangers in the context of a thermoacoustic device, as in Fig. 1(c), where a heat exchanger is seen placed adjacent to a stack. Brewster, Raspet, and Bass[7] report some results from this sort of measurement, as do Braun *et al.*,[8] and a particularly careful study of this type was undertaken recently by Mozurkewich.[9] For all measurements of this sort, the experimental situation is complicated, and interpretation of the results is difficult. In particular, the stack only functions in the presence of pressure oscillations. As discussed in Sec. VIII B, however, we believe that the temperature oscillations caused by these pressure swings may significantly alter the heat transfer within the heat exchanger. Furthermore, the way in which heat transfer occurs at the end of the stack is no better understood than within the heat exchanger, and

a)Electronic mail: keolian@psu.edu

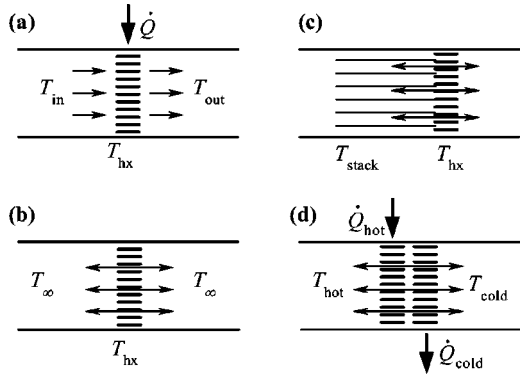

FIG. 1. Heat exchanger measurement configurations: (a) a heat exchanger tested under steady-flow conditions; (b) a single heat exchanger in oscillating flow; (c) a heat exchanger adjacent to a thermoacoustic stack; (d) two heat exchangers at different temperatures in oscillating flow.

may be different in nature. These phenomena are, of course, part of the reality of heat exchanger performance within real thermoacoustic devices. However, it is important to know the isolated effects of oscillating flow on the exchanger itself, without additional complications.

The approach taken in the present measurement is to place two exchangers at different temperatures close together, and to move fluid in an oscillatory manner between the two exchangers, as depicted in Fig. 1(d). The situation is now well defined, and involves only heat exchangers; if the duct is insulated, then, in steady state, this is a measurement of the exchangers, not of transport in the duct. Furthermore, if the exchangers are identical, then the average temperature in the plane centered between the exchangers is known to be $(T_h+T_c)/2$.

II. EXPERIMENTAL APPARATUS

The core of the measurement apparatus is shown in Fig. 2. A test section, consisting of two test heat exchangers separated by a spacer, is inserted into the middle of the apparatus, which is vertically symmetrical about the test section except for the shaker at the bottom. An APS Dynamics[10] shaker moves a metal end-plate that is connected to the stationary parts of the duct via a square polyurethane bellows. Just above the bellows is a heat exchanger, which we call a ''guard heat exchanger'' discussed in the following. Next is a 185-mm-long square-sided diffuser section that matches the inside dimensions of the bellows and guard heat exchanger to those of the test duct. Between the diffuser and the test duct are two layers of window screen to reduce the possibility of turbulence from the bellows entering the test duct. The test duct, made of acrylic, has square 292 mm$\times$292 mm inner cross-sectional dimensions. The half of the test duct below the test section is 305 mm long, with a flange at the top for mounting test sections. Above the test section, the parts are repeated in reverse order. The top and bottom end plates are coupled by rigid connecting rods, so that the end plates go up and down together, driven by the single shaker. The test section, ducts, and diffusers are held fixed relative to the base of the shaker (and the lab) by a large support frame (not

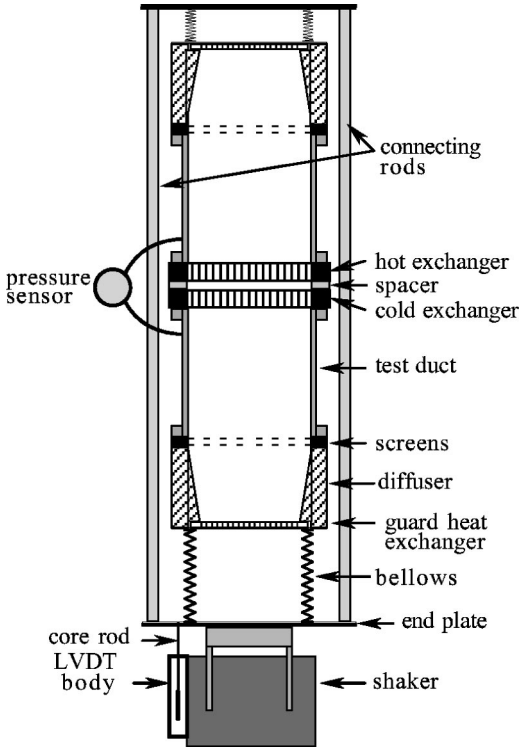

FIG. 2. Schematic of the measurement apparatus. The connecting rods, end plates, and LVDT core rod are driven up and down by the shaker armature, with the rest of the apparatus held stationary by a strut structure (not shown). The moving parts are shown here in their lowest position, so that the upper bellows is compressed and the lower bellows is expanded. Also not shown are springs attached to the shaker armature that raise the resonance frequency of the moving parts to around 4 Hz.

shown). In Fig. 2, the end plates are at their lowest point, so that the upper bellows is compressed and the lower bellows is expanded.

Also attached to the shaker (but not shown in the diagram) is a strut structure that supports suspension springs. The spring stiffness combines with the mass of the moving parts to give a resonance frequency around 4 Hz. This choice of spring stiffness allows the shaker to oscillate the end plates to its full stroke at up to 5 Hz while still allowing the full stroke at 0.125 Hz. The amplitude diminishes as the frequency is increased above 5 Hz due to amplifier limitations.

All experiments are conducted in air at ambient atmospheric pressure, which is measured with a mercury barometer for determination of the air density ρ_m. The thermal conductivity k_0 and dynamic viscosity μ of air are calculated from the mean temperature of the gas in the duct using formulas from Pierce,[11] and the kinematic viscosity is $\nu=\mu/\rho_m$. The specific heat of air is $c_p=1005\,\mathrm{J\,kg^{-1}\,K^{-1}}$.

The position of the end plates is measured with a linear variable differential transformer (LVDT). The gas displacement is inferred from the end-plate position measurement. The maximum peak gas displacement amplitude is 70 mm, which at 5 Hz gives a maximum air speed of 2.2 m/s. The pressure drop across the test section is also measured, but pressure measurements are not reported in the present paper. Data acquisition, validation, and error analysis of the pressure and position sensors are described in detail in Ref. 12.

A. Flow loops, chillers, and pumps

The primary goal of the experiments is the measurement of the amount of heat transferred between two heat exchangers in oscillating flow for various conditions of oscillation amplitude and frequency. The heat transferred between the two exchangers is found by measuring the amount of temperature change of water flowing though the heat exchanger tubes. There are two flow loops, one for the hot exchanger and one for the cold. In each loop, the temperature is maintained by a ''recirculating chiller.'' The ''chiller'' on the hot side includes an electric heater so that it may be used above room temperature. In each loop, water is pumped from the chiller through a reference heater (described in the following), the heat exchanger, a filter, a turbine flow meter, the guard heat exchanger, and back to the chiller. The flow rate is adjusted to produce a reasonable temperature increase as the water passes through the heat exchanger, with flow rates of about 0.3–0.6 kg/min. Distilled water is used for all measurements, with the addition of a few drops of a biocide and a few grams of corrosion inhibitor.

The guard heat exchangers are off-the-shelf units intended for the cooling of truck transmission fluid. Their form is similar to that of a car radiator. The primary function of the guard heat exchangers is to insulate the air inside the duct from the room. Almost all of the core of the test apparatus is well insulated with 2.5–10 cm of polystyrene foam, but it is impossible to insulate the bellows. The guard heat exchanger acts as a substitute for insulation, holding the air that passes from the bellows into the test duct at a temperature that is near to that of the nearest heat-exchanger-under-test. The guard exchanger also acts to straighten the flow of the air coming into the duct from the compressing bellows.

B. Temperature sensors

Water temperatures are measured with thermistor probes manufactured by RDP Corporation.[13] Each probe contains a 2252 Ω YSI[14] series 55000 glass-encapsulated thermistor, sheathed in a stainless steel tube that is 15 cm long and 3.175 mm in diameter. Attached to each heat exchanger are two 6.35-mm-o.d. tubes for connecting the hoses for entering and exiting water. These tubes are made quite long, about 13 cm. The long sheath of a thermistor probe is inserted through the straight leg of a Swagelok tee-fitting and into a connecting tube. Water enters through the side branch of the tee, so that water flows past the entire length of the probe sheath on its way into the exchanger (and vice versa for exiting water). By this connection method, the probe is effectively immersed in the water to a depth of 15 cm. Tests in the recirculating chiller bath show that 10 cm of immersion is sufficient to eliminate any detectable effect from heat leak down the sheath. An additional advantage of this arrangement, in which the water plumbing connections are made far from the exchanger, is that insulation can be tightly and permanently attached to the heat exchanger connecter tube right up to the exchanger manifold, while at the same time allowing the thermistor, which is at the tip of the long probe, to be placed very close to the exchanger entrance or exit. This is especially important for the cold heat exchanger, since the circulating cold water is sometimes cold enough to condense moisture from the ambient air. Additional insulation is placed over the Swagelok tee-fitting after the water connections are made.

The present measurements are not very sensitive to absolute temperature accuracy, but are extremely sensitive to the accuracy of temperature *differences*. Response differences between the probes are corrected to within 2 mK by calibrating them simultaneously in a variable-temperature water bath.

C. Flow meters and reference heaters

A DigiFlow DFS-2W turbine flow meter[15] is placed in each flow loop to measure the rate of water flow. Temperatures and flow rates are combined to give heat transfer rates. For the determination of heats based on the flow meters, $\dot{Q}_{\mathrm{raw}}=\dot{m}_w c_w|\Delta T_{\mathrm{hx}}|$, where $\dot{m}_w$ is the mass flow rate of the water, $c_w=4180\ \mathrm{J\,kg^{-1}\,K^{-1}}$ is the specific heat of water, which is constant within the accuracy of these measurements, and ΔT_{hx} is the change of temperature of the water as it passes through the exchanger.

An electric heating element inserted in the flow loop provides a second method of measuring the heats. The method is to measure the temperature increase in the circulating fluid due to a well-known rate of heating, provided by an electric heating element, and to compare the temperature change at the test exchanger to that at the reference heater, measured with probes like those used to measure the heat–exchanger temperature differences (see Ref. 16, Sec. 9.2.2). The heater-method uses $\dot{Q}_{\mathrm{raw}}=\dot{Q}_{\mathrm{ref}}|\Delta T_{\mathrm{hx}}|/\Delta T_{\mathrm{ref}}$, where ΔT_{ref} is the temperature increase of the water as is passes through the heater and $\dot{Q}_{\mathrm{ref}}$, the known electrical heat supplied to the reference heater, is calculated from the resistance of the heater element and the voltage at the heater measured by four-wire technique.

III. THE PARALLEL-PLATE HEAT EXCHANGERS

The parallel-plate heat exchangers used in these measurements are made from flat extruded aluminum tubing of a type used in automotive air-conditioner condensers. The tubes are 2.0 mm×22.0 mm in external cross section, having rounded ends. The interior of the tube is divided into nine rectangular channels, as shown in Fig. 3. Interior and side walls are all 0.50 mm thick. These tubes are analogous to the parallel fins of a tube-and-fin heat exchanger, with nearly 100% fin efficiency (no conduction loss) due to the water flowing through them. That is, in these exchangers, the ''tubes'' and the ''plates'' are the same.

Each 292 mm×292 mm exchanger is made up of 35 of these tubes separated by 6.35 mm gaps, for a center-to-center tube spacing of 8.35 mm and hydraulic radius of $r_h=y_0=3.175$ mm. (The hydraulic radius for parallel plates is half of the plate separation. This half spacing is often referred to as y_0 in thermoacoustics, following the notation of Swift.[16]) The total wetted perimeter of the tubes[17] is $\Pi=20.45$ m. The tubes are mounted at each end into a manifold made from 25.4 mm square aluminum tube. The tubes are centered on the manifolds, so that each tube is set $(25.4-22.0)/2$

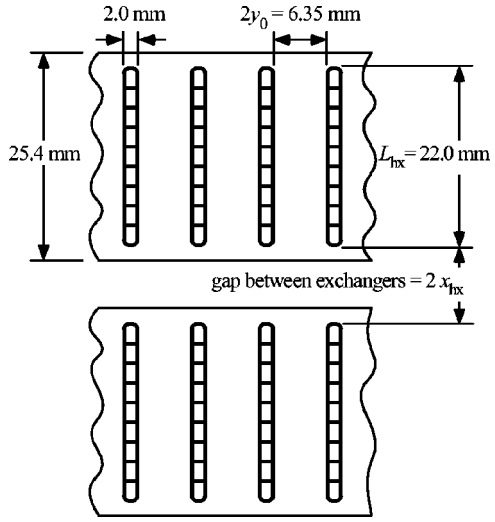

FIG. 3. Cross-sectional drawing of a portion of the two heat exchangers, with dimensions. The portion shown includes, for each exchanger, four of the hollow tubes that are the ''plates'' of the parallel plate heat exchangers.

$=1.7$ mm back from the edges of the manifold. That is, when the two heat exchangers are brought together with their manifolds touching, there is a 3.4 mm gap between the two sets of tubes. This 3.4 mm is then the minimum possible value of the distance between the edges of the tubes of the two exchangers, which is the distance that is meant by the term ''heat exchanger separation'' and indicated by the symbol $2x_{\mathrm{hx}}$.

When the exchangers are installed in the test rig, each is placed into a mounting structure made from polystyrene foam board of the type used to insulate houses. This mounting insulates the exchangers from the test duct and from the outside air, and also forms the two sides of each exchanger that are perpendicular to the manifolds. An additional piece of foam is the ''spacer,'' used to insulate the exchanger manifolds from each other, and to establish the exchanger separation spacing.

The hot exchanger is placed above the cold exchanger for gravitational stability of the air inside the duct. Care is taken to align the exchangers so that, if one could look axially down the duct, the tubes of the closer exchanger would lie directly in front of the tubes of the far exchanger, with a maximum amount of ''free flow area.'' Water passes through the exchangers in counter-flow with respect to each other, so that the temperature difference between the exchangers should be nearly the same at each location along the length of the tubes.

The adjustment of oscillation amplitude x_1 and frequency f (and angular frequency $\omega=2\pi f$) is under computer control. The control program reads a desired oscillation amplitude from a list and adjusts the shaker drive level until the measured amplitude is within about 1% of the prescribed value. The temperature difference across each exchanger is measured, and then measured again about 1 min later. If either ΔT has changed by more than 3 mK (the smallest practical noise-limited value), the process is repeated until both heat exchangers meet the 3 mK tolerance during a single measurement cycle, after which the computer records

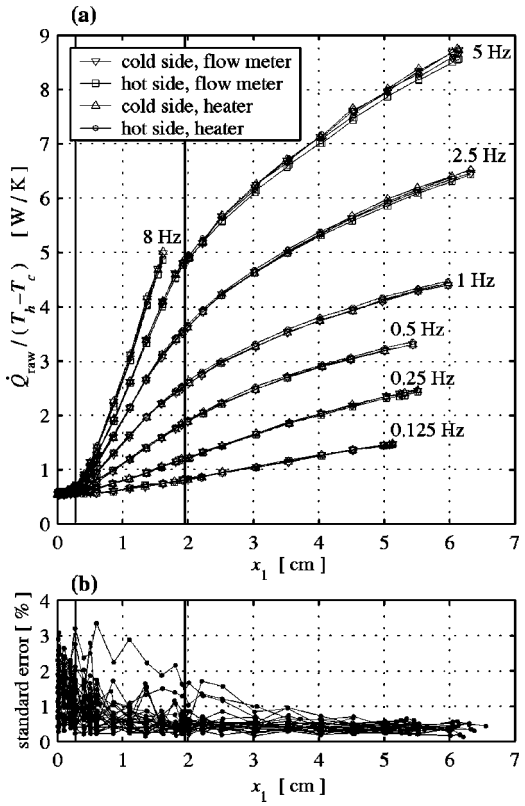

FIG. 4. (a) Parallel-plate heat exchange data collected using the smallest practical separation of 5.5 mm. (b) The standard error of the four measurements of heat made at each amplitude. This is an estimate of the uncertainty of the water flow rates.

all measured values and moves to the next desired amplitude or frequency.

IV. RAW RESULTS AND UNCERTAINTIES

Measurements at several sample frequencies are shown in Fig. 4. In this measurement, the exchangers are placed as close together as possible: the insulating spacer between the manifolds is 2.1 mm thick, so that the separation of the exchanger tubes is $2x_{\mathrm{hx}}=5.5$ mm. Plotted along the horizontal axis is x_1, the peak displacement amplitude of the oscillating gas. The two solid vertical lines are aids to the eye that show the ''position'' of the edges of the exchanger. The first is at x_{hx}, the amplitude at which a parcel of gas that begins at the center of the inter-exchanger gap barely enters each exchanger at the limits of its excursion. The second line represents the amplitude at which this parcel barely *traverses* both exchangers. This occurs when $x_1=x_{\mathrm{hx}}+\sigma L_{\mathrm{hx}}$, where L_{hx} is the length of each exchanger in the oscillation direction (22 mm) and σ is the porosity (void volume divided by total volume) of the exchangers (0.760).

The curve for each frequency in Fig. 4(a) is actually a cluster of four curves, one for each measurement method, as indicated by the legend. A significant difference between these would indicate a problem either with a flow meter or with one or both of the temperature sensors in a reference heater, or with the reference heater insulation. The flowmeter and reference-heat methods of measuring the heat are not completely independent, however, since both depend

ΔT_{hx}. These are basically two ways of measuring mass flow rate,[18] though the reference heater is actually measuring *heat capacity* rate. The spread in these four curves is an indication of the uncertainty of the flow measurements. The standard error in the mean[19] of the four measurements is plotted in Fig. 4(b). The error is generally about 0.5% for amplitudes that take the gas beyond both exchangers, 1% for amplitudes within the exchangers, growing to as much as 3% for the smallest amplitudes.

Any systematic offset in the measured temperature differences can be detected by reversing the direction of the flow through both exchangers and then repeating the measurements. (The direction of flow through the reference heaters is not reversed.) Once again, typical discrepancies are about 0.5% for large amplitudes, 1% for medium amplitudes, and 3% for the smallest amplitudes. The mean of all of these points is -0.2%, indicating that the overall systematic discrepancy of the temperature differences measured across the exchangers is small.

The objective of the experiment is to measure the heat transfer between the heat exchangers due to oscillating flow. In the absence of oscillation, however, there is still some heat transfer between the exchangers due to simple conduction through the air, and between the manifolds of the exchangers through the spacer. There is an additional heat leak out of the hot exchanger into the room and from the room onto the cold exchanger, via the foam that insulates the sides of the exchangers from the room air. After reducing heat leaks as much as practical with insulation, the strategy has been to make the hot and cold heat leaks equal by putting the hot exchanger above room temperature and the cold exchanger an equal amount below room temperature, typically 10–15 K. The baseline heat $\dot{Q}_0$, which is observed, for example, as the nonzero value of the heat at zero amplitude in Fig. 4(a) is then subtracted from all measured heats $\dot{Q}_{raw}$ to give the amount of heat flow attributed to oscillating flow advection, $\dot{Q}=\dot{Q}_{raw}-\dot{Q}_0$, before subsequent analysis.

The temperature of the room fluctuates over the course of the measurement. It took 4.75 days to collect the small-gap data, during which time the room temperature varied over a range of ± 2 K. The variation in the small-amplitude heat leak over this time, however, was only ± 0.02 W/K.

The oscillating flows within the exchangers are very likely laminar. The *peak* Reynolds number based on hydraulic diameter ($=4r_h$), $\mathrm{Re}_{hx}=\omega x_1 4r_h/\nu$, has a maximum value of 2020. The acoustic, oscillating-flow Reynolds number, $\mathrm{Re}_{ac}=\omega x_1 \delta_\nu/\nu$, depends on frequency, since the viscous penetration depth is $\delta_\nu=\sqrt{2\nu/\omega}$. Its maximum value for any of these measurements is 160. With this combination of Re_{hx} and Re_{ac}, the flow within the exchanger would be expected to be strictly laminar if the exchangers were long (see Ref. 16, Sec. 7.2). The shortness of the exchangers puts this conclusion in some doubt, but the low value of $\mathrm{Re}_{hx}<2020$ itself also suggests that laminar conditions are likely.

In this paper, measured heats are normalized by such quantities as thermal penetration depth $\delta_\kappa=\sqrt{2k_0/\rho_m c_p \omega}$ and heat capacity rate $\dot{m}c_p$. The reader should keep in mind that in the experiments, only two quantities were varied, amplitude and frequency. Thus, normalization by "δ_κ" is really normalization by $f^{-0.5}$, for example. Additional factors involving ρ_m, c_p, y_0, and L_{hx} are included to nondimensionalize the results, and there is reason to believe that the results should be scalable to other gases at other pressures. In the present study, however, no experiments were carried out using gases of different properties or exchangers of different geometries.

V. NORMALIZED RESULTS

Normalized results are shown in Fig. 5 for small, medium, and large exchanger separations. In these plots, the results of the different measurement methods have been averaged together, four measurements for each point in Figs. 5(a) and (b), and two measurements each in Fig. 5(c), for which reference-heater data are not available. The baseline heats have been subtracted. The average $\dot{Q}$ for each amplitude and frequency is divided by $\Delta T_{ave}=(T_h-T_c)/2$, where T_h and T_c are the temperatures of the hot exchanger and of the cold exchanger (that is, each is the average of the inlet and the outlet temperature for that exchanger.) This ΔT_{ave} is the difference between either exchanger and the average temperature in the plane that is halfway between the two exchangers.

Besides division by ΔT_{ave}, $\dot{Q}$ is nondimensionalized by normalizing by k_0 and $\Pi=20.45$ m, the wetted perimeter of the exchanger tubes. Since the hydraulic radius r_h is related to the minimum free-flow area A_c and the total frontal (duct) area A_{fr} by $r_h=A_c/\Pi=\sigma A_{fr}/\Pi$, normalizing by Π is equivalent to normalizing by $\sigma A_{fr}/r_h$.

The oscillation amplitude x_1 on the abscissa is normalized two ways: on the bottom axis x_1 is normalized by $y_0=r_h$. On the top axis, the oscillation amplitude is normalized in terms of exchanger length. The dotted vertical line represents the center of the exchanger. The factor of σ has been included in this normalization so that an increase in normalized amplitude of 1.0 causes the fluid *within the exchanger* to oscillate an additional exchanger length in each direction. This complication is unavoidable in any real exchanger, which necessarily has porosity less than 1.0.

The curves for different frequencies are labeled in terms of the nondimensional ratio $y_0/\delta_\kappa=r_h/\delta_\kappa$. Researchers in other fields use Valensi number (usually taken to be $4r_h^2\omega/\nu=8r_h^2/\delta_\nu^2$) or Womersley number (usually $\sqrt{2}r_h/\delta_\nu$ or $2\sqrt{2}r_h/\delta_\nu$) in conjunction with Prandtl number ($\mathrm{Pr}=\delta_\nu^2/\delta_\kappa^2$). The 5 Hz curve ($y_0/\delta_\kappa=2.65$) in Fig. 5(a) appears more jagged than the others because it includes points from two separate sweeps of amplitude at this frequency that were separated in time by 28 h.

VI. THE DELTAE HEAT EXCHANGER MODEL

The *de facto* standard for designing thermoacoustic devices is a piece of software called DELTAE.[20] One of the major reasons for carrying out the heat exchanger measurements has been to test, examine, and possibly improve upon DELTAE's parallel-plate heat exchanger model, a very simple model that is probably the weakest aspect of the software. Before analyzing the data, it is useful to review DELTAE's

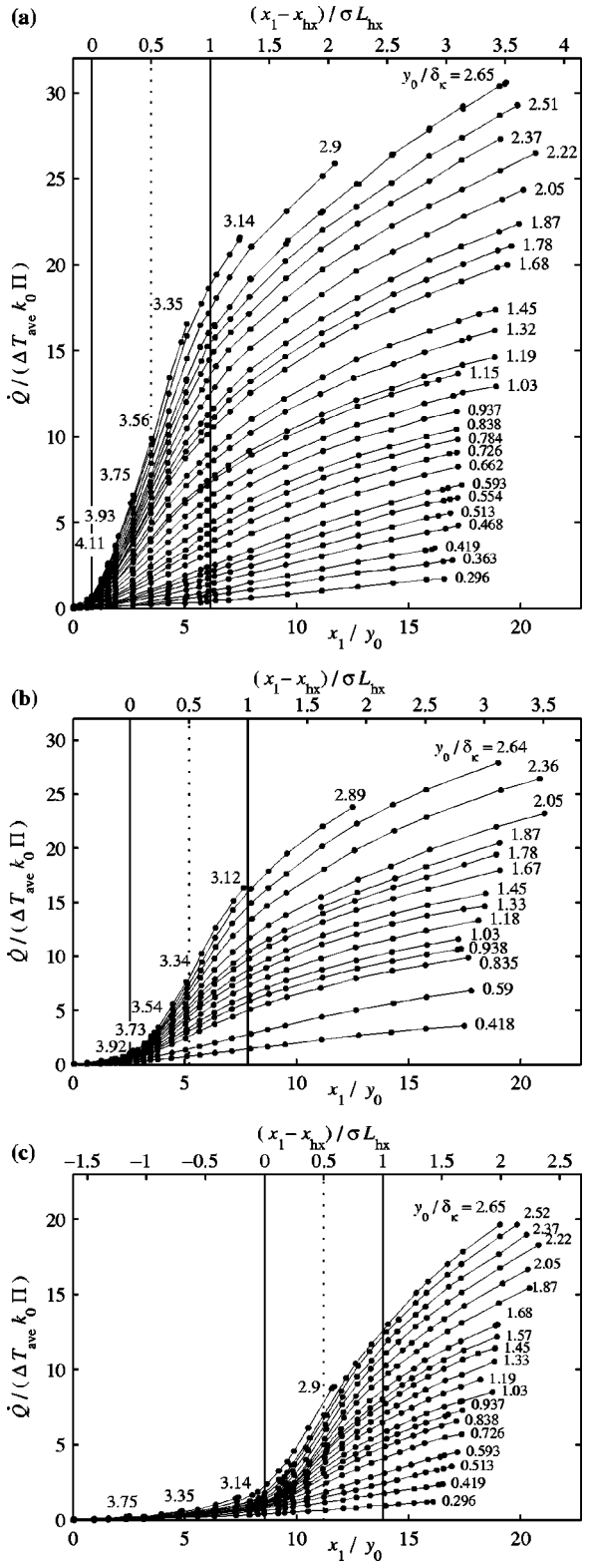

FIG. 5. Normalized parallel-plate heat transfer. The results of the different measurement methods have been averaged together. Data for (a) small gap $2x_{hx}=5.5$ mm, (b) medium gap $2x_{hx}=16.3$ mm, (c) large gap $2x_{hx}=54.4$ mm (with a different scale on the ordinate).

parallel-plate heat exchanger model to provide context and motivate the type of analysis that is carried out.

The DELTAE model for parallel-plate heat exchangers (Ref. 20, p. 113) can be cast in terms of the present notation as

$$\dot{Q}_{\mathrm{DELTAE}}=(\Delta T_{\mathrm{ave}}k_0\Pi)C\frac{x_{\mathrm{eff}}}{y_{\mathrm{eff}}}, \tag{1}$$

with

$$x_{\mathrm{eff}}=\min\{2(x_1-x_{\mathrm{hx}})/\sigma, L_{\mathrm{hx}}\}, \tag{2}$$

$$y_{\mathrm{eff}}=\min\{\delta_\kappa, y_0\}, \tag{3}$$

where the constant C, which is 1 in the DELTAE model, has been added as a parameter to adjust. The general form of Eqs. (1)–(3) was postulated by Swift.[21]

DELTAE assumes that the exchanger is directly adjacent to a stack or regenerator. In the present experiment, the exchangers are separated by a distance $2x_{\mathrm{hx}}$, and oscillation within this gap does not contribute to the effective transfer area, hence the use of $2(x_1-x_{\mathrm{hx}})/\sigma$ rather than $2x_1/\sigma$ in Eq. (2). The analysis will concentrate on the small-gap data, so that the situation is as much like that in a thermoacoustic device as possible.

At high frequencies ($y_0/\delta_\kappa>1$), $\dot{Q}_{\mathrm{DELTAE}}$ is inversely proportional to $\delta_\kappa\propto f^{-1/2}$; at low frequencies ($y_0/\delta_\kappa<1$), $\dot{Q}_{\mathrm{DELTAE}}$ is independent of frequency. Specifically, for $y_0/\delta_\kappa>1$,

$$\left(\frac{\dot{Q}_{\mathrm{DELTAE}}}{\Delta T_{\mathrm{ave}}k_0\Pi}\right)\frac{\delta_\kappa}{L_{\mathrm{hx}}}=2C\frac{x_1-x_{\mathrm{hx}}}{\sigma L_{\mathrm{hx}}}, \tag{4}$$

which indicates that, when plotted against $(x_1-x_{\mathrm{hx}})/\sigma L_{\mathrm{hx}}$, $(\delta_\kappa/L_{\mathrm{hx}})\dot{Q}_{\mathrm{DELTAE}}/\Delta T_{\mathrm{ave}}k_0\Pi$ gives a straight line with slope $2C$ for all y_0/δ_κ, whereas for $y_0/\delta_\kappa<1$, $\dot{Q}_{\mathrm{DELTAE}}/\Delta T_{\mathrm{ave}}k_0\Pi$ is the quantity that produces a single straight line, in this case with slope $2CL_{\mathrm{hx}}/y_0$, which for these exchangers is $13.9C$. The DELTAE model is shown together with data for these two normalizations in Fig. 6. Figure 6(a) shows the small-gap data at the twelve highest frequencies ($y_0/\delta_\kappa>2$) using the $\delta_\kappa\dot{Q}$ normalization. The curves are all nearly the same shape, and are remarkably straight in the region between the vertical lines that indicate amplitudes corresponding to the edges of the exchangers. The dashed line is the prediction of the DELTAE model, with $C=1$. The heavy solid line shows the DELTAE model with $C=0.45$. If the frequency range of the data is extended down to $y_0/\delta_\kappa=1$, these lower-frequency curves have the same slope and straight-line shape up to about $(x_1-x_{\mathrm{hx}})/\sigma L_{\mathrm{hx}}=1$, above which they diverge (upward) somewhat from the higher frequency data.

Figure 6(b) shows the DELTAE model together with the small-gap data for all frequencies low enough that $y_0/\delta_\kappa<1$. The amplitude coordinate is the same as in Fig. 6(a), but $\dot{Q}$ is normalized by $\Delta T_{\mathrm{ave}}k_0\Pi$, independent of frequency. The result is disturbing: even in the low-amplitude region, the data curves decrease with frequency, but the DELTAE model does not. As a consequence, even with $C=0.45$ the model seriously over-predicts heat transfer at the lowest frequencies.

It turns out that there is a fundamental problem with the model defined by Eqs. (1)–(3). The problem is revealed by considering the case of perfect heat exchange, for which all of the working gas undergoes the full temperature swing

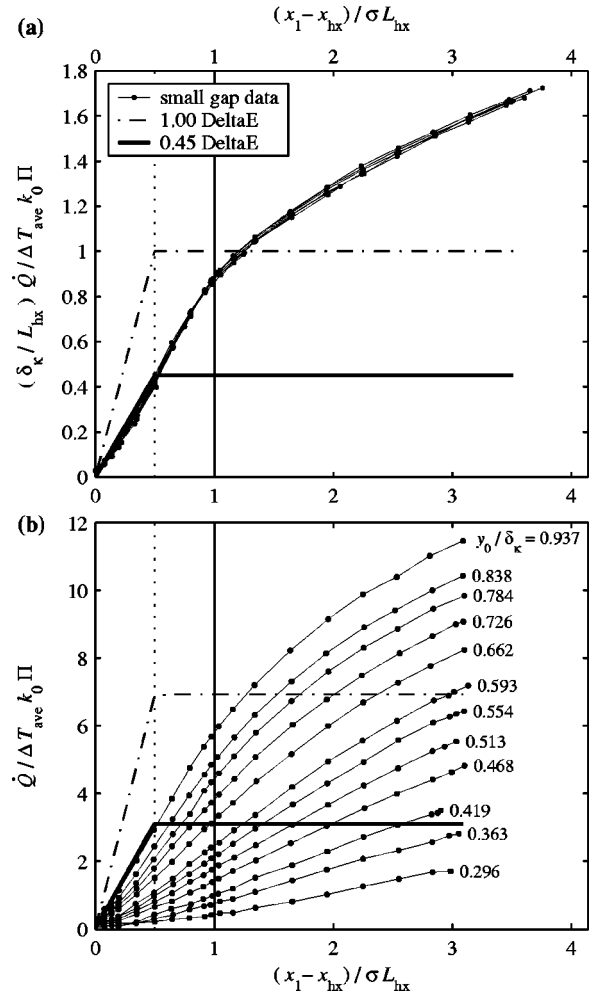

FIG. 6. Comparison of the DELTAE model to present data: (a) high-frequency $\dot{Q}$ normalized with δ_κ; (b) low-frequency data without δ_κ in the normalization.

$(T_h-T_c)=2\Delta T_{\text{ave}}$. Since the rate at which mass oscillates between the exchangers is $\dot{m}=\rho_m x_{\text{eff}} A_c f$, the maximum heat transfer rate is

$$\dot{Q}_{\text{perfect}}=\dot{m}c_p(T_h-T_c) \tag{5}$$

$$=\rho_m c_p x_{\text{eff}} A_c f 2\Delta T_{\text{ave}} \tag{6}$$

$$=(\Delta T_{\text{ave}} k_0 \Pi)\frac{x_{\text{eff}}}{y_{\text{eff}}}\frac{2}{\pi}\frac{y_0 y_{\text{eff}}}{\delta_\kappa^2}. \tag{7}$$

Comparing Eq. (1) to Eq. (7) we see that

$$\frac{\dot{Q}_{\text{DELTAE}}}{\dot{Q}_{\text{perfect}}}=C\frac{\pi}{2}\frac{\delta_\kappa^2}{y_0 y_{\text{eff}}}. \tag{8}$$

For $y_0 \geqslant \delta_\kappa$ (large plate spacing or high frequency), $y_{\text{eff}}=\delta_\kappa$, so

$$\left[\frac{\dot{Q}_{\text{DELTAE}}}{\dot{Q}_{\text{perfect}}}\right]_{y_0\geqslant\delta_\kappa}=C\frac{\pi}{2}\frac{\delta_\kappa}{y_0}. \tag{9}$$

However, for $y_0 \leqslant \delta_\kappa$ (small plate spacing or low frequency), $y_{\text{eff}}=y_0$, so

$$\left[\frac{\dot{Q}_{\text{DELTAE}}}{\dot{Q}_{\text{perfect}}}\right]_{y_0\leqslant\delta_\kappa}=C\frac{\pi}{2}\frac{\delta_\kappa^2}{y_0^2}. \tag{10}$$

The problem is now evident. For any exchanger plate spacing tighter than $y_0/\delta_\kappa=\pi/2=1.57$, the DELTAE model with $C=1$ predicts $\dot{Q}_{\text{DELTAE}}/\dot{Q}_{\text{perfect}}>1$, a greater rate of heat transfer than can possibly occur with fluid of this heat capacity at this frequency. While a value of $C=0.45$ shifts the value at which this problem occurs down to $y_0/\delta_\kappa=0.71$, for sufficiently tight spacings this problem will arise for any constant value of C. This problem was pointed out six years ago by Brewster *et al.*,[7] but the importance of this result does not seem to have been appreciated by the thermoacoustics community.

If one defines a sort of "effective heat transfer coefficient" h_{eff} by

$$\dot{Q}_{\text{DELTAE}}=h_{\text{eff}}x_{\text{eff}}\Pi\Delta T_{\text{ave}}, \tag{11}$$

then $h_{\text{eff}}=Ck_0/y_{\text{eff}}$. With $C=1$,

$$h_{\text{eff}}=\frac{k_0}{\delta_\kappa} \quad \text{for} \quad \frac{y_0}{\delta_\kappa}\geqslant 1, \tag{12}$$

and

$$h_{\text{eff}}=\frac{k_0}{y_0} \quad \text{for} \quad \frac{y_0}{\delta_\kappa}\leqslant 1. \tag{13}$$

We know from Eq. (10) that there is some error in Eqs. (11) and (13). The form $h_{\text{eff}}=k_0/y_0$ for $y_0/\delta_\kappa<1$ appears quite reasonable, however. After all, how can the effective film thickness be greater than half the plate spacing? The problem is not in h_{eff} *per se*. Rather, it is with the notion that a heat transfer coefficient can be used in conjunction with an *initial* temperature difference such as ΔT_{ave}. In heat exchangers with $y_0/\delta_\kappa<1$, the instantaneous gas-to-exchanger temperature difference $\Delta T(t)$ becomes small enough that the rate of heat transfer is small even though the heat transfer coefficient is large. In cases where $\Delta T(t)$ is not approximately constant, use of the concept of "heat transfer coefficient" requires detailed knowledge of the time history of $\Delta T(t)$. An alternative approach that allows us to retain use of ΔT_{ave} is to use the concept of "effectiveness," discussed next.

VII. EFFECTIVENESS

Effectiveness ε is[22] "the ratio of the actual heat transfer rate for a heat exchanger to the maximum possible heat transfer rate,"

$$\varepsilon\equiv\frac{\dot{Q}}{\dot{Q}_{\text{perfect}}}. \tag{14}$$

In Fig. 7, $\dot{Q}$ is normalized by $2\Delta T_{\text{ave}}\rho_m c_p A_{\text{fr}}\sigma L_{\text{hx}} f$. This heat-capacity-based normalization results in the plot of $\dot{Q}_{\text{perfect}}$ vs $(x_1-x_{\text{hx}})/\sigma L_{\text{hx}}$ having a constant slope of 2, shown by the heavy line. At the lowest frequency, $y_0/\delta_\kappa=0.418$, the exchangers are nearly perfectly effective, even for amplitudes that take the gas well beyond both exchangers. At $y_0/\delta_\kappa=0.835$, the effectiveness is still quite high at

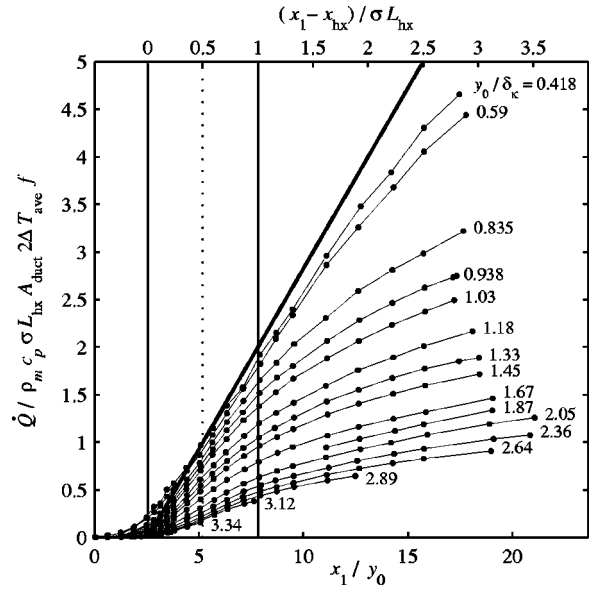

FIG. 7. $\dot{Q}/\Delta T_{ave}$ normalized by dividing by frequency and other quantities related to oscillating heat capacity rate. With this normalization, perfect exchanger effectiveness is single straight line, independent of frequency, shown by the heavy solid line. The data curves begin near $\dot{Q}_{perfect}$ at the lowest frequency and decrease steadily with increasing frequency. This is medium-gap data.

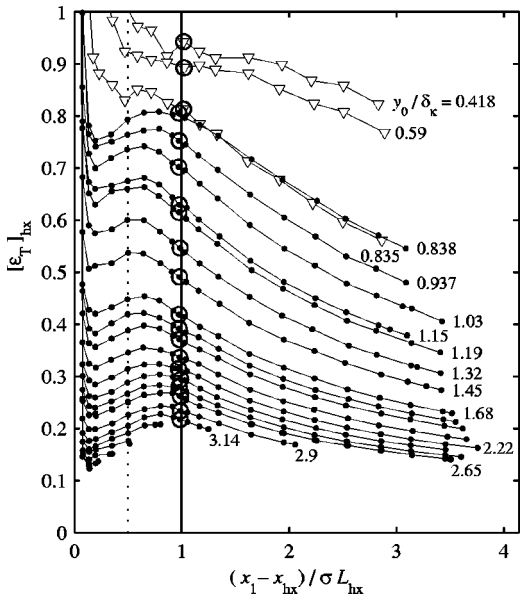

FIG. 8. Effectiveness as a function of amplitude for various frequencies. The curves with triangle markers are medium-gap data; the rest are small-gap data. For each frequency, the circled point near $(x_1-x_{hx})/\sigma L_{hx}=1$ is selected to represent the low-amplitude effectiveness at that frequency. These points appear in Fig. 9.

low amplitudes, around 80%, but drops to 60% for the highest amplitude. At $y_0/\delta_\kappa=2.05$, the effectiveness is never more than about 30%, even at low amplitudes.

A model based on effectiveness, rather than on an effective heat transfer coefficient, would have the advantage that it would naturally incorporate heat capacity into the heat transfer model, and is attractive because the oscillating heat capacity rate is well known. In the following, the data are cast in terms of effectiveness, fits are made, and an effectiveness-based heat transfer model is proposed for use in design. Such a model might form the basis of an improved DELTAE parallel-plate heat exchanger segment.

A. Low-amplitude conduction enhancement

Before completing the analysis, it is necessary to discuss a difficulty arising from the fact that $x_{hx}>0$. In Eq. (6), which is the simplest possible model of "perfect" heat transfer between the exchangers, $\dot{Q}=0$ for any $x_1<x_{hx}$, since no gas actually enters *both* exchangers. In Fig. 5, however, we see that in fact $\dot{Q}>0$ for $x_1=x_{hx}$. Even when there is an oscillation that is too small to carry any gas over the full distance between the exchangers, gas that has its equilibrium position barely within one exchanger spends some time *closer* to the other exchanger than it would have had there been no oscillation. The effect is actually not so much one of increased effective conductivity as of *decreased effective exchanger separation*. Since this phenomenon is not understood quantitatively, no attempt has been made to correct for it. Unfortunately, this "low-amplitude enhancement effect" causes the measured effectiveness to exceed unity at the lowest amplitudes.

The small-amplitude enhancement effect becomes more important as x_{hx} is increased, as can be seen by comparing Figs. 5(a)–(c). Collecting data using the smallest practical gap reduces the effect, but does not eliminate it. Using a tiny gap introduces its own problems, however, since it increases the baseline (zero-amplitude) heat that is subtracted from all data. At the lowest frequencies, for which the oscillation-induced $\dot{Q}$ is very small, this means subtracting a very large fraction of the total measured heat, resulting in errors. We judge the lowest-frequency data for the small gap configuration to be unreliable except at the very highest amplitudes. For this reason, medium-gap data are used in the ensuing analysis for determination of the low-amplitude effectiveness at the lowest frequencies. Medium-gap data are indicated by triangular markers. A complete discussion of this issue is found in Ref. 23.

B. Effectiveness data and low-amplitude fit

In the present oscillating flow study, where two exchangers interact, the notation must distinguish between the effectiveness of a single exchanger and that of a two-exchanger system. In the analysis carried out later, the symbol ε_{hx} is used to indicate the effectiveness of a single exchanger of type "hx," the symbol ε_T refers to the total effectiveness of a two-exchanger system, and the symbol $[\varepsilon_T]_{hx}$ refers to the total effectiveness of two identical exchangers of type "hx." The measured effectiveness of the experimental parallel-plate exchangers is of this last type, so the results are referred to using the $[\varepsilon_T]_{hx}$ notation, for compatibility with the later analysis.

The measured effectiveness of the heat transfer between the two exchangers $[\varepsilon_T]_{hx}$ is plotted in Fig. 8 for many different frequencies. This plot includes all of the small-gap data above 0.5 Hz ($y_0/\delta_\kappa \geqslant 0.838$), plus medium-gap at 0.5 Hz and two lower frequencies, indicated with triangles.

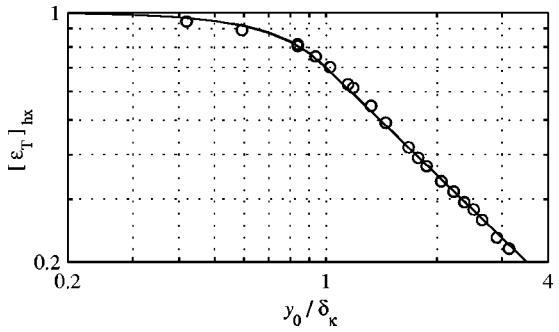

FIG. 9. Circled data points from Fig. 8, together with a bipartite fit function (solid curve) defined by Eqs. (15) and (16).

Below $(x_1-x_{hx})/\sigma L_{hx}=1$, the effectiveness at each frequency is at least roughly constant, but because $\dot{Q}_{perfect}$ goes to zero at $(x_1-x_{hx})/\sigma L_{hx}=0$, the measured $[\varepsilon_T]_{hx}$ is not very stable in this region. For the purposes of proceeding with the analysis, the value of $[\varepsilon_T]_{hx}$ nearest $(x_1-x_{hx})/\sigma L_{hx}=1$ is chosen as representative of the low-amplitude effectiveness. This is a somewhat arbitrary choice, and it probably underestimates $[\varepsilon_T]_{hx}$ slightly, but we have concluded that the values of $[\varepsilon_T]_{hx}$ at lower amplitudes are simply less reliable, even when considering some scheme of averaging. The points selected for analysis are highlighted with circles.

The selected points are collected into a single plot of $[\varepsilon_T]_{hx}$ vs y_0/δ_κ in Fig. 9. The log–log rendering reveals a very straight line connecting the points at the higher frequencies.

The function chosen to fit the data, indicated by the curve, has two parts. At high frequencies the fit is

$$[\varepsilon_T]_{hx}=\frac{0.7}{y_0/\delta_\kappa}$$

$$\text{for } y_0/\delta_\kappa \geqslant 1 \text{ and } \frac{x_1-x_{hx}}{\sigma L_{hx}}<1. \tag{15}$$

This is not actually new information, corresponding as it does to the fact that $\dot{Q}\propto\delta_\kappa^{-1}$ at high frequencies, as established by Fig. 6(a), and to be discussed further in Sec. VII C. The new information to come out of Fig. 9 is the low-frequency fit,

$$[\varepsilon_T]_{hx}\simeq 1-0.3(y_0/\delta_\kappa)^{2.5}$$

$$\text{for } y_0/\delta_\kappa \leqslant 1 \text{ and } \frac{x_1-x_{hx}}{\sigma L_{hx}}<1. \tag{16}$$

Unfortunately, there are few reliable data points in this region, and Eq. (16) is both strictly empirical and not very tightly constrained by the data. Fortunately, having the exact power in Eq. (16) is not particularly important, because $[\varepsilon_T]_{hx}$ is so close to 1.0 in this region. Equation (16) simply provides a convenient way of connecting the known zero frequency limit, $[\varepsilon_T]_{hx}=1$, and the physically motivated high-frequency form $[\varepsilon_T]_{hx}\propto(y_0/\delta_\kappa)^{-1}$, which has the measured value $[\varepsilon_T]_{hx}=0.7$ at $y_0/\delta_\kappa=1$.

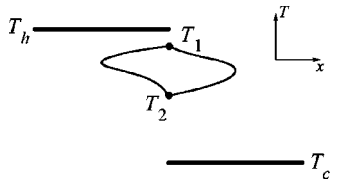

FIG. 10. Temperatures used in defining the effectiveness of heat exchangers in oscillating flow. Gas oscillates between a hot heat exchanger (on the left) at temperature T_h and a cold exchanger at T_c. Gas enters the cold exchanger at T_1 and exits the cold exchanger at T_2. In this diagram, the hot exchanger is more effective than the cold exchanger, so that on the average the gas is closer in temperature to T_h than to T_c.

C. Effectiveness in oscillating flow

In this section, the measured effectiveness is related to ΔT_{ave}, so that we can use the measurements in a model that has the same form as the existing DELTAE model. The derivation is greatly simplified by the fact that the heat capacity of an exchanger is effectively infinite compared to that of the oscillating gas. Under these circumstances, and if the specific heat of the gas is constant, effectiveness can be expressed simply in terms of temperatures,

$$\varepsilon_{hx}=\frac{T_{in}-T_{out}}{T_{in}-T_s}, \tag{17}$$

where T_{in} is the temperature of the gas as it enters the exchanger, T_{out} is the temperature of the gas as it exits the exchanger, and T_s is the (constant) exchanger surface temperature.

Figure 10 shows a sketch of temperature versus position for a parcel of gas as it oscillates between hot and cold exchangers at temperatures T_h and T_c. Gas enters the cold exchanger at $T_{in}=T_1$ and exits at $T_{out}=T_2$, so the effectiveness ε_c of the cold exchanger is

$$\varepsilon_c=\frac{T_1-T_2}{T_1-T_c}. \tag{18}$$

Similarly, for the hot exchanger,

$$\varepsilon_h=\frac{T_2-T_1}{T_2-T_h}=\frac{T_1-T_2}{T_h-T_2}. \tag{19}$$

Now consider a combined system of hot and cold heat exchangers. If both exchangers were perfect, then the gas would cover the full span between T_h and T_c as it oscillated, so for the nonideal exchangers of Fig. 10, the total effectiveness ε_T is

$$\varepsilon_T=\frac{T_1-T_2}{T_h-T_c}. \tag{20}$$

The relationship between the effectiveness of the individual exchangers and the effectiveness of the two exchanger system is, then,

$$\frac{1}{\varepsilon_h}+\frac{1}{\varepsilon_c}=\frac{1}{\varepsilon_T}+1. \tag{21}$$

For the case of two identical heat exchangers, each with effectiveness ε_{hx}, the total effectiveness is

$$[\varepsilon_T]_{\mathrm{hx}}=\frac{\varepsilon_{\mathrm{hx}}}{2-\varepsilon_{\mathrm{hx}}}. \tag{22}$$

For purposes of comparing to the DELTAE model, it is useful to put these results in terms of T_{ave}, the average temperature of the gas at the interface between a stack (or regenerator) and a heat exchanger. Consider Fig. 10, interpreting the heavy line labeled T_h to be the end of a stack or regenerator of unknown effectiveness ε_h. This unknown effectiveness affects the average temperature of the gas at the interface, and thus the amount of heat transfer. For example, if the line T_h represents a regenerator in good thermal contact with the gas, the higher ε_h of the regenerator will result in an average temperature closer to T_h, and more total heat transfer for a given ε_c, than would the lower ε_h of a stack. The average temperature of the gas at the interface T_{ave} is

$$T_{\mathrm{ave}}=\frac{T_1+T_2}{2}. \tag{23}$$

The difference between T_{ave} and T_c is

$$[\Delta T_{\mathrm{ave}}]_c=T_{\mathrm{ave}}-T_c. \tag{24}$$

Using Eqs. (18), (22), and (24) it can be seen that

$$[\Delta T_{\mathrm{ave}}]_c 2[\varepsilon_T]_c=T_1-T_2. \tag{25}$$

Similar algebra results in a similar expression of the hot exchanger, so that, in general,

$$[\Delta T_{\mathrm{ave}}]_{\mathrm{hx}} 2[\varepsilon_T]_{\mathrm{hx}}=T_1-T_2, \tag{26}$$

where $[\Delta T_{\mathrm{ave}}]_{\mathrm{hx}}$ is the difference between the average gas temperature at the interface and the *heat exchanger* temperature, whether the exchanger is hotter or colder than the stack. That is, $[\Delta T_{\mathrm{ave}}]_{\mathrm{hx}}$ is the very "ΔT_{ave}" used in the DELTAE model. Equation (26) is the desired relationship between ΔT_{ave}, the total effectiveness of two identical exchangers $[\varepsilon_T]_{\mathrm{hx}}$, which is the effectiveness measured in the present experiment, and T_1-T_2, which is necessary to calculate the amount of heat transferred.

The rate of heat transfer in Fig. 10 is

$$\dot{Q}=\dot{m}c_p(T_1-T_2) \tag{27}$$

$$=\rho_m c_p \frac{2(x_1-x_{\mathrm{hx}})}{\sigma} A_c f 2\Delta T_{\mathrm{ave}}[\varepsilon_T]_{\mathrm{hx}} \tag{28}$$

$$=(\Delta T_{\mathrm{ave}} k_0 \Pi)\frac{2[\varepsilon_T]_{\mathrm{hx}}}{\pi}\frac{x_{\mathrm{EFF}} y_0}{\delta_\kappa^2}, \tag{29}$$

where x_{EFF} is different from x_{eff} in that

$$x_{\mathrm{EFF}}\equiv\frac{2(x_1-x_{\mathrm{hx}})}{\sigma} \quad \text{for all } x_1, \tag{30}$$

whereas the x_{eff} from DELTAE has an upper limit of L_{hx}. Below L_{hx}, x_{eff} and x_{EFF} are the same.

From Eq. (15), we have $[\varepsilon_T]_{\mathrm{hx}}=0.7/(y_0/\delta_\kappa)$ at high frequencies, so

$$\dot{Q}=(\Delta T_{\mathrm{ave}} k_0 \Pi)\left[\frac{2}{\pi}0.7\right]\frac{x_{\mathrm{EFF}}}{\delta_\kappa}$$

$$\text{for } y_0/\delta_\kappa \geqslant 1 \text{ and } \frac{x_1-x_{\mathrm{hx}}}{\sigma L_{\mathrm{hx}}}<1. \tag{31}$$

Comparing Eq. (31) to Eq. (1), we see that we have recovered the high-frequency, low-amplitude DELTAE model, with $C=0.7(2/\pi)=0.45$. The result applies up to $x_{\mathrm{EFF}}=2L_{\mathrm{hx}}$, not just to $x_{\mathrm{EFF}}=L_{\mathrm{hx}}$, however.

With the effectiveness-based model of $\dot{Q}$, in the form of either Eq. (28) or Eq. (29), and the low-frequency effectiveness fit of Eq. (16), we can immediately extend the model to low frequencies,

$$\dot{Q}=(\Delta T_{\mathrm{ave}} k_0 \Pi)\frac{2}{\pi}[1-0.3(y_0/\delta_\kappa)^{2.5}]\frac{x_{\mathrm{EFF}} y_0}{\delta_\kappa^2}$$

$$\text{for } y_0/\delta_\kappa \leqslant 1 \text{ and } \frac{x_1-x_{\mathrm{hx}}}{\sigma L_{\mathrm{hx}}}<1. \tag{32}$$

with the assurance that the result will not exceed that which is physically possible.

VIII. EXTENDING TO HIGHER AMPLITUDES

A. Empirical fit

So far, we have a model that works well at the lower amplitudes ($x_{\mathrm{EFF}}\leqslant 2L_{\mathrm{hx}}$). One of the more important features observed in the data is that heat transfer continues to increase significantly as the amplitude increases beyond $x_{\mathrm{EFF}}=2L_{\mathrm{hx}}$. For design purposes, it would be very useful to have a fit that follows the data into the high amplitude region. This fit is to be used to calculate $\dot{Q}$ in the form

$$\dot{Q}_{\mathrm{fit}}=\rho_m c_p x_{\mathrm{EFF}} \Pi y_0 f 2\Delta T_{\mathrm{ave}} \varepsilon_0 F_\varepsilon, \tag{33}$$

or

$$\dot{Q}_{\mathrm{fit}}=(\Delta T_{\mathrm{ave}} k_0 \Pi)\frac{x_{\mathrm{EFF}} y_0}{\delta_\kappa^2}\frac{2}{\pi}\varepsilon_0 F_\varepsilon, \tag{34}$$

where x_{EFF} is defined in Eq. (30), ε_0 is the low-amplitude effectiveness fit of Eqs. (15) and (16), namely

$$\varepsilon_0=1-0.3(y_0/\delta_\kappa)^{2.5} \quad \text{if } y_0/\delta_\kappa \leqslant 1, \tag{35}$$

$$\varepsilon_0=0.7(y_0/\delta_\kappa)^{-1} \quad \text{if } y_0/\delta_\kappa \geqslant 1, \tag{36}$$

and F_ε is a function of x_{EFF} that will fit the data at high amplitudes. A fit that works fairly well is

$$F_\varepsilon=1 \quad \text{if } x_{\mathrm{EFF}}<2L_{\mathrm{hx}}, \tag{37}$$

$$F_\varepsilon=\frac{1+0.7(y_0/\delta_\kappa)}{1+0.7(y_0/\delta_\kappa)(x_{\mathrm{EFF}}/2L_{\mathrm{hx}})^{0.7}} \quad \text{if } x_{\mathrm{EFF}}>2L_{\mathrm{hx}}. \tag{38}$$

Data curves are shown in Fig. 11, together with $\dot{Q}_{\mathrm{fit}}$ curves determined from Eqs. (33) to (38). Not all frequencies are shown in Fig. 11 to make it easier to distinguish which fit curve goes with which data. An encouraging aspect of the fit is the lowest curve on the plot, $y_0/\delta_\kappa=0.296$, measured at 1/16 Hz using the small gap. Recall that these data were excluded from the fit to $[\varepsilon_T]_{\mathrm{hx}}$, because they are deemed unreliable below $x_{\mathrm{EFF}}=2L_{\mathrm{hx}}$. The fit curve does, however, approach the data at the highest amplitude, where these data

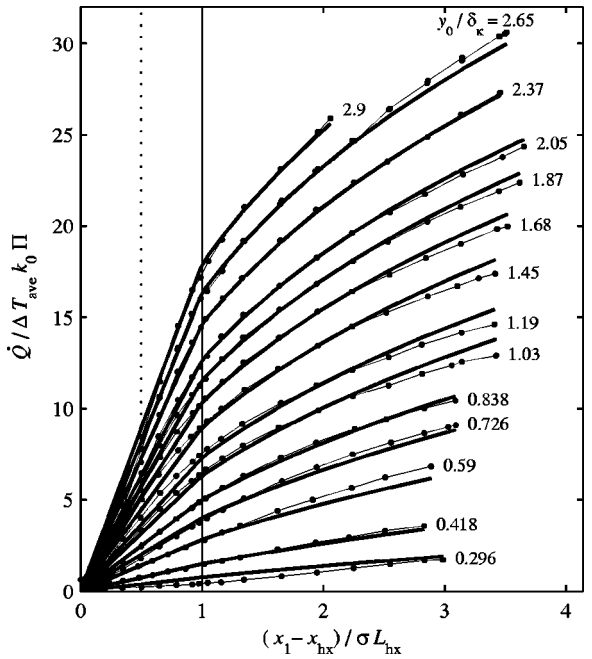

FIG. 11. Fit curves for each frequency (heavy curves) are calculated using Eqs. (33)–(38). Only a few frequencies are shown to improve readability.

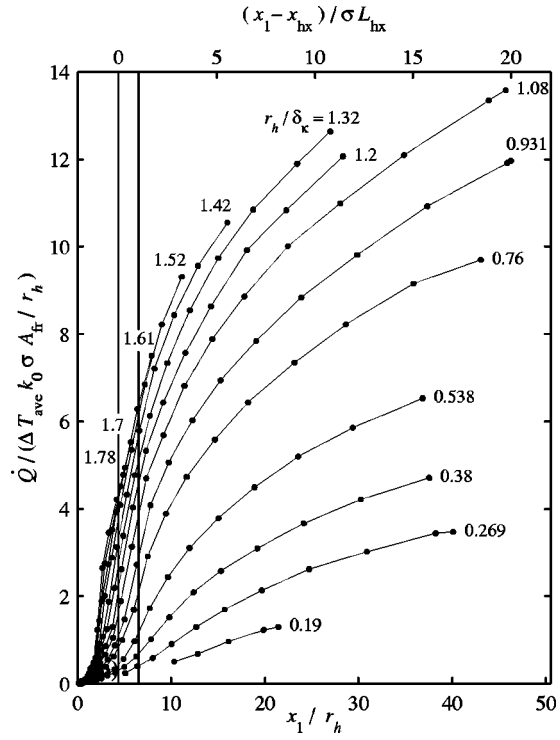

FIG. 12. Measured heat transfer between heat exchangers made from 6.350 mm tubes separated by 3.175 mm spaces. At the highest frequencies, there is an abrupt increase in heat transfer at an amplitude of around $r_h/\delta_\kappa = 2$.

are most reliable. Generally speaking, the fits are within 10% of the data for amplitudes above $(x_1 - x_{hx})/\sigma L_{hx} = 0.5$ (which is $x_{EFF} = L_{hx}$), below which the low-amplitude enhancement effect causes the errors to grow and eventually to blow up at $x_1 - x_{hx} = 0$.

The proposed form of Eq. (38), which is basically a variation on $1/(1+x^a)$ with $0 < a < 1$, while empirical, is not entirely arbitrary. We have endeavored to find a function that is physically plausible at higher amplitudes, i.e., that results in a $\dot{Q}_{fit}$ that does not turn over and go to zero (or even negative!) at amplitudes just above the limits of the fitted data. This rules out most forms involving exponential decays and most power laws. The function in Eq. (38) becomes proportional to $x_{EFF}^{-0.7}$ at high amplitudes. When multiplied by x_{EFF} in Eq. (33) or (34), the result is $\dot{Q} \propto x_{EFF}^{0.3}$ for large x_{EFF}. The search for a function with a high-amplitude limit of x_{EFF}^b with $0 < b < 1$ was motivated by the thought that at high amplitudes the heat transfer should be dominated by the high-velocity portion of the cycle when the boundary layer is similar to the steady-flow entrance-region result. The velocity dependence of Nusselt number for the steady-flow problem depends on the boundary conditions. For constant wall temperature under steady laminar flow, ''thermal entry length'' conditions give $\mathrm{Nu} \propto \mathrm{Re}^{1/3}$ and ''simultaneously developing'' thermal and hydrodynamic boundary layers[24] give $\mathrm{Nu} \propto \mathrm{Re}^{1/2}$. The power 0.7 in Eq. (38) results in $\mathrm{Nu} \propto \mathrm{Re}^{0.3}$, which may not be exactly correct, but it is probably the right idea. This power sets the rate of curvature at the higher amplitudes. Referring to Fig. 11, the choice of 0.7 was obviously a compromise, with the middle frequencies exhibiting sharper curvature than either of the frequency extremes. The remaining details of Eq. (38) were chosen simply to improve the fit. Presumably, it is mere coincidence that the coefficient 0.7 on the factors $0.7(y_0/\delta_\kappa)$ is equal to the power 0.7 on the factor $(x_{EFF}/2L_{hx})^{0.7}$. The coefficients, as well as the power 1 on (y_0/δ_κ), help match the slopes of the curves at $(x_1 - x_{hx})/\sigma L_{hx} = 1$. It seems likely that some or all of these parameters depend in some way on the ratio $\sigma L_{hx}/y_0$. The test heat exchangers are fairly ''short'' compared to exchangers in some devices, with $\sigma L_{hx}/y_0 = 5.3$. Measurements on heat exchangers with different dimensions would be necessary to clarify this matter.

B. Discussion

Hofler carried out an effectiveness analysis eight years ago[25] and concluded that ''Heat exchangers with $[x_1/L_{hx}]$ in the range of 4 to 8 can be thermally effective if y_0/δ_κ is in the range 0.75 to 0.5,'' where ''thermally effective'' means that ''thermal effectiveness is between 77% and 93%.'' Hofler was concerned about minimizing both thermal and viscous losses in the heat exchangers. ''Thermal losses'' peak when the plate spacing is around $y_0/\delta_\kappa = 1$ for the same reason that stacks operate in this range. Of course, viscous losses simply increase as y_0/δ_κ decreases. Based on this reasoning, Hofler concluded that ''it is apparent that some appropriate 'figure of merit' function used in optimizing heat exchanger geometries would peak strongly at a value of about $y_0/\delta_\kappa = 0.5$.'' Hofler, then, advocated exchangers that had smaller y_0/δ_κ and shorter L_{hx} than the dimensions $y_0/\delta_\kappa \simeq 1$ and $L_{hx} \simeq 2x_1/\sigma$ that tend to emerge from designs developed with DELTAE.

For the most part, the present measurements support the viewpoint put forward by Hofler in 1994. In particular, the effectiveness of tightly spaced plates is quite high, and heat transfer does continue to increase even as the amplitude increases to take the gas well beyond the far edges of both

exchangers. Two factors unknown to the thermoacoustics community at the time of Hofler's analysis may result in modifying his conclusion. These are the importance of minor losses and the effect of externally imposed pressure oscillations.

Minor losses[16,26] result from flow past abrupt changes in geometry, such as the sudden change in cross-sectional area between a heat exchanger and the adjacent duct. The pressure loss from the acoustic oscillation due to this type of loss depends roughly on $(1-\sigma)^2$ and on the square of the velocity within the exchanger, which is greater than that outside the exchanger by $1/\sigma^2$. The result is that the minor loss goes up sharply as porosity decreases. It is difficult to make a heat exchanger with small y_0/δ_κ that does not also have a small porosity. This is partly due to the difficulty manufacturing very thin fins, and also due to problems getting heat off the fins and onto a secondary flow loop (i.e., a problem with fin efficiency).

The other consideration, the influence on heat exchangers of the temperature oscillations that are caused by the oscillating pressure in thermoacoustic devices, is more speculative. We have carried out numerical studies that indicate that, for spacings typical of parallel-plate heat exchangers used in thermoacoustic devices ($y_0/\delta_\kappa \simeq 2/3$) and pressure amplitudes of 5% of mean pressure, the pressure-driven temperature oscillations in standing-wave devices might increase or decrease heat transfer by as much as 30% for refrigerators and engines, respectively. There is some experimental evidence for this idea. Mozurkewich[9] measured heat transfer between a thermoacoustic stack and a tube heat exchanger within a thermoacoustic refrigerator. The test heat exchanger was the one nearer the velocity node, the ''hot heat exchanger'' in a standing-wave refrigerator, which exhausts heat from the stack. Mozurkewich measured the amount of exhaust heat, the temperature T_{hhx} of the heat exchanger, and the temperature T_H of the stack material at the end of the stack adjacent to the exchangers. One of his interesting observations was of significant heat transfer when $T_H - T_{hhx}$ was *zero*. In Mozurkewich's experiments, this ''heat flow at zero temperature difference'' grew linearly with amplitude, as in his Fig. 2. (In this standing-wave type of device, displacement amplitude and pressure amplitude increase together.) By adjusting the temperature of the heat exchanger at the opposite end of the stack, he could bring the heat transfer to zero by forcing the temperature of the stack to be many degrees *below* that of the exchanger to which it was exhausting heat. Clearly, a heat transfer model where $\dot{Q}$ is proportional to ΔT_{ave} cannot account for this type of phenomenon, even when calibrated against oscillating-flow heat transfer experiments like the ones in this paper, which do not include pressure oscillations.

This effect depends on plate spacing, disappearing as $y_0/\delta_\kappa \to 0$, and, of course, it depends upon the gas's being within the exchanger. Thus, pressure-oscillation-driven enhancement or degradation of heat transfer would be considerably less in a ''Hofler-style'' (short, tight) exchanger. While this would appear to be an advantage in a standing-wave engine, it might be a disadvantage in an standing-wave refrigerator. We have yet to study how this effect would manifest itself in the exchangers of a regenerator-based device, for which the oscillations at the heat exchangers have a mixture of standing- and traveling-wave phasing.

IX. CONCLUSIONS

Measurements of the heat transferred between two identical parallel-plate heat exchangers, made under conditions of oscillating flow over a range of frequencies and amplitudes, have been analyzed with the goal of producing an improved model for use in the design of thermoacoustic devices. The proposed model is summarized by Eqs. (30) and (33)–(38). Qualitative conclusions are:

(1) For $(x_1 - x_{\text{hx}})/\sigma L_{\text{hx}} \leqslant 0.5$ and $y_0/\delta_\kappa \geqslant 1$, the idea that $\dot{Q} \propto \delta_\kappa^{-1}$ seems to be correct.
(2) Figure 6(a) makes it appear that for $y_0/\delta_\kappa > 2$, the product $\dot{Q}\delta_\kappa$ collapses to a single curve, independent of frequency, even at high amplitudes. This may be an illusion, however, since the upper amplitude limit decreases with frequency. It could be that the high frequency transport is actually frequency dependent at higher amplitudes.
(3) The idea that $\dot{Q} \propto x_1 - x_{\text{hx}}$ for $(x_1 - x_{\text{hx}})/\sigma L_{\text{hx}} \leqslant 0.5$ seems to be correct.
(4) The value of the constant C indicated by the present measurements is 0.45. This value may depend on parameters not varied in these measurements, such as the porosity. Recall also that the leading edges of the parallel plates used in these heat exchangers are rounded, unlike the blunt-edged fins that have often been used in thermoacoustic devices, which may affect $\dot{Q}$. Mozurkewich studied heat exchange in oscillating flow analytically[27] using an eigenfunction approach. His analysis concluded by suggesting the value $C = 0.61$.
(5) The form $h_{\text{eff}} \propto k_0/y_0$ for $y_0/\delta_\kappa \leqslant 1$ is incorrect, at least when used in conjunction with an equation like $\dot{Q} = h_{\text{eff}} x_{\text{eff}} \Pi \Delta T_{\text{ave}}$. For $y_0/\delta_\kappa \leqslant 1$ the cycle-averaged heat transfer is limited by heat capacity, not by the heat transfer coefficient.
(6) As a result, it is not correct that ''you can always increase the heat transfer by decreasing the plate spacing.'' One *can* always make the effectiveness close to 1 by decreasing plate spacing. In this limit, the amount of heat transferred for a given temperature difference is set by the oscillating heat capacity rate, the calculation of which might be useful in making design decisions.
(7) It is quite clear that the idea that x_{eff} has a maximum value of L_{hx} is not correct. The slope of $\dot{Q}$ is nearly constant up to an amplitude of about $2(x_1 - x_{\text{hx}}) = 2\sigma L_{\text{hx}}$ [rather than $2(x_1 - x_{\text{hx}}) = \sigma L_{\text{hx}}$], and has a significant positive value well beyond this value. That is, effectiveness decreases as the amplitude exceeds $x_{\text{EFF}} = 2L_{\text{hx}}$, but not abruptly. This suggests that it might be possible to get almost equal performance from exchangers that are only half as long as what has conventionally been suggested. A relatively simple empirical fit function [Eqs. (37) and (38)] describes the performance of the present experimental heat exchangers fairly well. This fit

can probably be used in a general model to give approximate results, but it is likely that the fit parameters depend on $\sigma L_{hx}/y_0$ or some other geometrical parameter that was not varied in the present measurements.

(8) The concept of "effectiveness" is useful in the study of oscillating-flow heat exchangers, in part because it incorporates heat capacity into the analysis.

(9) The total combined effectiveness of two identical heat exchangers (separated by little or no gap) in oscillating flow, as measured in the present experiments, can be incorporated easily and directly into an effectiveness-based oscillating flow model.

ACKNOWLEDGMENTS

This work was supported by the Office of Naval Research, the Penn State Applied Research Laboratory, and the Pennsylvania Space Grant Consortium. Thanks to Stefan Turneaure for work on the earliest heat exchanger measurements, and insight gained from his work on no-stack prime movers. Thanks also to Ralph Webb for information on heat-exchanger manifolds.

APPENDIX: ROUND TUBE HEAT EXCHANGERS

In addition to the parallel-plate heat exchanger measurements that are analyzed in detail in the main body of the text, earlier measurements were carried out on round tube heat exchangers, some of which are presented here, in Fig. 12. These measurements are relegated to an appendix because we have less confidence in them, and also because it is not at all evident what sort of analysis should be carried out on these data.

Each round tube heat exchanger is made up of a single row of hollow circular brass tubes with an external diameter of 6.35 mm, separated by spaces of 3.175 mm, for a center-to-center spacing of 9.525 mm. It takes 30 such tubes to span the 292.1 mm duct, with 6.35 mm of extra space left at the end. Results are normalized by the "length" L_{hx} of an exchanger, taken to be the tube external diameter, and hydraulic radius r_h, defined by

$$r_h \equiv \frac{V_{void}}{A}, \tag{A1}$$

where V_{void} is the void volume (of the air) and A is the total wetted area. For the heat exchangers examined in this appendix, where the space between tubes is half the tube diameter, $r_h = 0.227\, D_{tube}$, or 1.44 mm.

For these exchangers, the low-amplitude conduction enhancement effect (see Sec. VII A) is very large. At the highest frequencies, there is a noticeable sudden increase in heat transfer at around $x_1/r_h = 2$, about half the amplitude required for any parcel of the gas to traverse the full inter-exchanger gap. Apparently some additional mechanism, such as jet formation, is further enhancing conduction at the higher frequencies. This unknown but interesting phenomenon makes these curves particularly difficult to analyze.

One problem with the round tube exchangers is that the manifolds are too small to provide for an even flow of water through all of the tubes. Fortunately, we were alerted to this issue before construction of the parallel plate exchangers, which were made to have much larger manifolds as a result. The manifolds on the round tube exchangers are 9.525 mm square tubes. The inlet and outlet are also at opposite corners, with the intention of equalizing the lengths of the various paths through the exchanger. This turns out to be a bad idea because of Bernoulli pressure changes in the manifolds.[28,29] Evidence that uneven flow distribution is a problem in the tube heat exchangers but not in the parallel plate heat exchangers comes from reversing the flow direction through both exchangers in each case. The reversal should not change the total amount of heat transfer, and it does not in the parallel plate exchangers. Reversing the flow direction through both of the round tube exchangers, in contrast, reduces the measured heat transfer by as much as 10%. Because of this, and because the entire set of validation tests was never completed for these exchangers, we place the uncertainty on these results at +10%, −20%.

[1] W. L. Cooper, K. T. Yang, and V. W. Nee, "Fluid mechanics of oscillatory and modulated flows and associated applications in heat and mass transfer—A review," J. Energy Heat Mass Trans. **15**, 1–19 (1993).
[2] W. L. Cooper, V. W. Nee, and K. T. Yang, "An experimental investigation of convective heat transfer from the heated floor of a rectangular duct to a low frequency, large tidal displacement oscillatory flow," Int. J. Heat Mass Transfer **37**, 581–592 (1994).
[3] M. F. Hwang and A. Dybbs, "Heat transfer in a tube with oscillatory flow," Tech. Rep. 83-WA/HT-90, ASME, 1983.
[4] R. A. Peattie and R. Budwig, "Heat transfer in laminar, oscillatory flow in cylindrical and conical tubes," Int. J. Heat Mass Transfer **32**, 923–934 (1989).
[5] U. H. Kurzweg and L. D. Zhao, "Heat transfer by high-frequency oscillations: A new hydrodynamic technique for achieving large effective thermal conductivities," Phys. Fluids **27**, 2624–2627 (1984).
[6] U. H. Kurzweg and J. Chen, "Heat transport along an oscillating flat plate," J. Heat Transfer **110**, 789–790 (1988).
[7] J. R. Brewster, R. Raspet, and H. E. Bass, "Temperature discontinuities between elements of thermoacoustic devices," J. Acoust. Soc. Am. **102**, 3355–3360 (1997).
[8] J. E. Braun, L. Mongeau, B. Minner, A. Alexander, and I. Paek, "Evaluating the performance of thermoacoustic cooling," Tech. Rep. ARTI-21CR/610-10040-01, Air-Conditioning and Refrigeration Technology Institute, 2000.
[9] G. Mozurkewich, "Heat transfer from transverse tubes adjacent to a thermoacoustic stack," J. Acoust. Soc. Am. **110**, 841–847 (2001).
[10] APS Dynamics, Inc., 5371 Palmer Way, Suite A, Carlsbad, CA 92008, www.apsdynamics.com
[11] A. D. Pierce, *Acoustics: An Introduction to Its Physical Principles and Applications* (Acoustical Society of America, Melville, NY, 1989).
[12] R. S. Wakeland and R. M. Keolian, "Measurements of resistance of individual square-mesh screens to oscillating flow at low and intermediate Reynolds numbers," J. Fluids Eng. **125**, 851–862 (2003).
[13] RDP Corp., 5877 Huberville Ave., Dayton, OH 45431, www.rdp-corp.com
[14] YSI Inc., Yellow Springs, OH 45387, www.ysi.com
[15] DigiFlow Systems, 781 Clifton Blvd., Mansfield, OH 44907, www.digiflowsys.com
[16] G. Swift, *Thermoacoustics: A Unifying Perspective for Some Engines and Refrigerators* (Acoustical Society of America, Melville, NY, 2002).
[17] This is the air-to-tube wetted perimeter in the part of the exchanger that is constant in cross section. In this approximation, the hydraulic diameter is simply $4y_0 = 0.5$ in. $= 12.7$ mm. This does not take into account the transverse surface area at the round ends of the tubes. If the total gas volume on the gas side of the exchanger is divided by the total surface area of the tubes, the resulting hydraulic diameter is 5% smaller. Where the tubes enter the manifold, there are 6.35 mm sections of aluminum manifold between each pair of tubes, which add an additional 0.44 m, or 2%, to the total exchange perimeter.
[18] Turbine flow meters are often considered to measure *volume* flow rate. However, in our lab these meters are always calibrated by *weighing* the

water passing through the meter in some time interval, so the calibration is actually of mass flow rate.
[19] Also called ''the standard deviation of the mean,'' the standard error is the square root of the variance divided by the $\sqrt{N}$, where N is the number of samples ($N=4$ in this case). See Eqs. (4.9) and (4.14) in J. R. Taylor, *An Introduction to Error Analysis* (University Science Books, Mill Valley, CA, 1982).
[20] B. Ward and G. Swift, ''DELTAE: Design Environment for Low-amplitude ThermoAcoustic Engines: User's Guide and Tutorial,'' Los Alamos National Laboratory, LA-CC-93-8, 1996. Note: the DELTAE software (Version 5.1) and the User's Guide (Revision 6/1/2001) are now available on the CD-ROM included with Swift's text (Ref. 16), or online at www.lanl.gov/thermoacoustics/
[21] G. W. Swift, ''Analysis and performance of a large thermoacoustic engine,'' J. Acoust. Soc. Am. **92**, 1551–1563 (1992).
[22] F. P. Incropera and D. P. DeWitt, *Fundamentals of Heat and Mass Transfer*, 4th ed. (Wiley, New York, 1996).
[23] R. S. Wakeland, ''Heat exchangers in oscillating flow, with application to thermoacoustic devices that have neither stack nor regenerator,'' Ph.D. thesis, The Pennsylvania State University, 2003.
[24] R. K. Shah and A. L. London, *Laminar Flow Forced Convection in Ducts*, Advances in Heat Transfer Suppl. 1, edited by T. F. Irvine, Jr. and J. P. Harnett (Academic, New York, 1978).
[25] T. J. Hofler, ''Annual summary report for improved efficiency and power density for thermoacoustic coolers,'' Tech. Rep. Navy Environmentally Safe Ships Program, Office of Naval Research, 1994.
[26] R. S. Wakeland and R. M. Keolian, ''Influence of velocity profile nonuniformity on minor losses for flow exiting thermoacoustic heat exchangers,'' J. Acoust. Soc. Am. **112**, 1249–1252 (2002).
[27] G. Mozurkewich, ''Time-average temperature distribution in a thermoacoustic stack,'' J. Acoust. Soc. Am. **103**, 380–388 (1998).
[28] R. A. Bajura and E. H. Jones, Jr., ''Flow distribution manifolds,'' J. Fluids Eng. **98**, 654–666 (1976).
[29] A. B. Datta and A. K. Majumdar, ''Flow distribution in parallel and reverse flow manifolds,'' Int. J. Heat Mass Transfer **2**, 253–262 (1980).

Transient temperature rise due to ultrasound absorption at a bone/soft-tissue interface

Matthew R. Myers
Center for Devices and Radiological Health, HFZ-132, U. S. Food and Drug Administration, Rockville, Maryland 20852

(Received 3 November 2003; revised 20 February 2004; accepted 26 February 2004)

Thermal effects due to high ultrasound absorption in bone pose an ongoing safety issue. Of considerable concern is the heating of the soft tissue adjacent to the bone surface. Mathematical models can be useful in predicting the transient temperature near the interface during insonation. This paper develops a model that provides the temperature field in terms of simple expressions that convey the functional dependence of the material properties, and are easily incorporated into standards and ultrasound machine software, yet are able to incorporate the material properties of both bone and soft tissue. The model contains an asymptotic theory based upon a ''high-attenuation'' assumption: the distance diffused by heat over the time of interest is large compared to the ultrasound attenuation length. Model predictions of temperature rise and location of maximum temperature were in close agreement with finite-element calculations, using parameters appropriate for radiation-force imaging and focused-ultrasound surgery. © *2004 Acoustical Society of America.*
[DOI: 10.1121/1.1707091]

PACS numbers: 43.35.Wa [FD] Pages: 2887–2891

I. INTRODUCTION

In the safety evaluation of medical ultrasound technologies, an important consideration is the thermal effect arising from insonation of bone. Ultrasound energy incident upon the bone from a soft-tissue medium is attenuated strongly, resulting in potentially hazardous temperature rises within the bone or surrounding soft tissue. Of particular value in the assessment of thermal effects is the transient temperature field, since the time-temperature relationship dictates the ''thermal-dose'' equivalent related to thermal damage (Herman and Harris, 2002). Mathematical models of heat transfer near the interface can provide useful estimates of this temperature field.

Thermal models applied to ultrasound heating at a bone/soft-tissue interface include finite-difference and finite-element solutions of the bioheat equation (Chan *et al.*, 1973; Doody *et al.*, 2000). These models provide a high level of flexibility in incorporating different material properties and geometries. More analytical models are typically derived from integrals of basic thermal point sources (Nyborg, 1988; Carstensen *et al.*, 1990; Wu and Du, 1990). These methods are advantageous in that they elucidate the functional dependence of the critical parameters, and are often simple and readily incorporated into standards and ultrasound-machine software. An example is the representation of the absorbing region in the bone as a two-dimensional heated disk. This heated-disk model has been incorporated in steady-state form into both AIUM/NEMA (AIUM/NEMA, 1998) and IEC (IEC, 2001) standards for medical equipment and displayed on ultrasound scanners. A drawback of the analytical models available to date is that only a single set of thermal properties (e.g., soft tissue or bone but not both) can be incorporated. Hence, our understanding of the actual transient temperature field based upon these models is limited.

In the present paper, the high ultrasound absorption in bone is used to develop an asymptotic model that retains the simplicity of the point-source based models, yet possesses the ability of the fully numerical models to handle two sets of material properties. The essential requirement of the asymptotic model is that the attenuation length (over which the intensity decays by a factor of $1/e$) for the ultrasound beam be short compared to the distance heat diffuses during the time of interest. The model utilizes a Laplace transform in the time variable, and contains a solution to the heat-conduction equations in the form of an inverse transform. The ''high attenuation'' assumption is used to convert the complicated inverse-transform integral into a relatively simple asymptotic series.

The following section presents the assumptions of the model and develops the asymptotic series. In the subsequent section, model predictions are compared with those of a finite-element approach using parameter values appropriate for two emerging ultrasound technologies, radiation-force imaging (Nightingale *et al.*, 2001; Walker 1999) and focused ultrasound surgery (ter Haar, 2001). The final section examines the results and discusses the range of applicability of the model.

II. METHOD

We consider an ultrasound beam of uniform cross section incident from a soft-tissue medium onto a bone surface, with the beam axis perpendicular to the bone surface. The beam width is assumed small compared to the radii of curvature of the bone surface, so that the interface may be considered planar. The distance that the heat diffuses over the time of interest, in addition to being large compared with the attenuation length, is assumed to be less that the thickness of the outer (cortical) layer of bone. In this way, the bone and soft-tissue layers may be considered semi-infinite. The simplified geometric model is shown in Fig. 1.

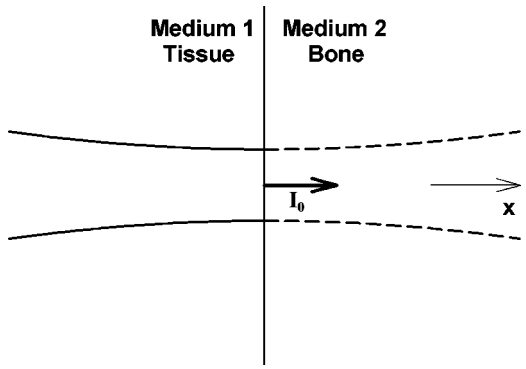

FIG. 1. Ultrasound beam incident upon planar interface between soft-tissue and bone. Transmitted intensity is denoted by I_0.

As will be seen subsequently, of primary importance is the region on the beam axis very near the interface. In this region axial variations in the temperature field greatly exceed radial ones, and the beam may be considered infinite in the radial direction. As discussed in the final section, this assumption is expected to hold up to the time it takes heat to diffuse the radius of the ultrasound beam. The relevant time intervals are also assumed short enough that perfusion may be ignored (Herman and Harris, 2002; Walker, 1999).

The intensity of the beam is taken to be constant, representing the temporal average of a time-varying pulse. We denote the intensity transmitted into the bone by I_0. The intensity is assumed to be small enough for linear acoustics to adequately describe the propagation. In this case the transmitted intensity can be easily related to the incident intensity through the transmission coefficient. For typical properties of soft tissue and bone, approximately 70% of the incident intensity is transmitted into the bone (Wu and Du, 1990). The attenuation within the bone may be described in terms of an intensity attenuation coefficient μ, with attenuation length $1/\mu$. Since the attenuation coefficient in soft tissues is between one and two orders of magnitude smaller than that of cortical bone (ICRU, 1998), attenuation within the soft-tissue medium is neglected over the short axial distances of interest.

Under the assumptions just described, the temperature rise T within soft tissue (medium 1) is determined by axial diffusion of heat away from the interface:

$$\frac{\partial T_1}{\partial t}-\kappa_1\frac{\partial^2 T_1}{\partial x^2}=0, \tag{1}$$

where x denotes axial distance measured from the interface, t is time, and κ is the thermal diffusivity. In bone (medium 2) ultrasound absorption is significant along with axial diffusion, and the temperature is described by

$$\frac{\partial T_2}{\partial t}-\kappa_2\frac{\partial^2 T_2}{\partial x^2}=\frac{\mu I_0}{\rho_2 c_2}e^{-\mu x}, \tag{2}$$

where ρ is the density and c is the specific heat. The boundary conditions include continuity of temperature and heat flux across the interface:

$$T_1(0,t)=T_2(0,t), \tag{3}$$

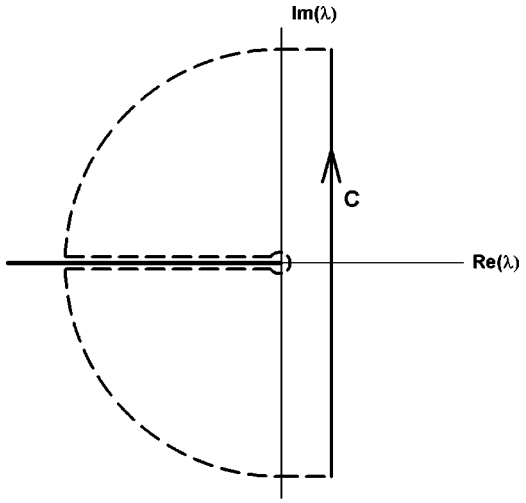

FIG. 2. Inversion contours for the Laplace transform solution, in the complex λ plane.

$$k_1\frac{\partial T_1}{\partial x}(0,t)=k_2\frac{\partial T_2}{\partial x}(0,t). \tag{4}$$

Here $k=\kappa\rho c$ is the thermal conductivity.

To solve the system of equations (1)–(4), we employ a Laplace transform in time. We first transform (1) and (2), solve the resulting ordinary differential equations, then require that the solutions far from the interface ($x=\pm\infty$) decay to zero. We focus attention upon the bone medium, where the maximum temperature rise occurs. After enforcing the transformed versions of (3) and (4), we obtain the following solution for the temperature rise in the bone:

$$T_2=\frac{\mu I_0}{2\pi i\rho_2 c_2}\int_C\frac{d\lambda e^{\lambda t}}{\lambda(\lambda-\mu^2\kappa_2)}\times\left\{e^{-\mu x}-\frac{1+\mu(k_2/k_1)\sqrt{\kappa_1/\lambda}}{1+(k_2/k_1)\sqrt{\kappa_1/\kappa_2}}e^{-\sqrt{\lambda/\kappa_2}x}\right\}. \tag{5}$$

The inversion contour C in the complex λ plane is shown in Fig. 2. We next close the contour in the left half plane, along the dashed contour shown in Fig. 2. The singular behavior at the origin is treated using a circle of small radius ϵ; we momentarily defer the limiting process. After including the contributions from the integrals along the top and bottom of the branch cut (singularity at $\lambda=\kappa_2\mu^2$ is removable), we obtain

$$T_2=\lim_{\epsilon\to 0}\frac{-I_0}{\rho_2 c_2\mu\kappa_2}[-e^{-\mu x}+S_\epsilon+S_s+S_c], \tag{6}$$

$$S_\epsilon=\frac{1}{2\pi(1+\beta)}\int_{-\pi}^{\pi}\left(1+\frac{\mu\beta}{\sqrt{\epsilon/\kappa_2}e^{i\theta/2}}\right)e^{-\sqrt{\epsilon/\kappa_2}e^{i\theta/2}x}d\theta, \tag{7}$$

$$S_s=\frac{\mu^2\kappa_2 t}{\pi(1+\beta)}\int_{\epsilon t}^{\infty}\frac{\sin(s^{1/2}x/\sqrt{\kappa_2 t})}{s(s+\mu^2\kappa_2 t)}e^{-s}ds, \tag{8}$$

$$S_c=\frac{\beta}{\pi(1+\beta)}(\mu^2\kappa_2 t)^{3/2}\int_{\epsilon t}^{\infty}\frac{\cos(s^{1/2}x/\sqrt{\kappa_2 t})}{s^{3/2}(s+\mu^2\kappa_2 t)}e^{-s}ds. \tag{9}$$

Here

$$\beta=\frac{k_2}{k_1}\sqrt{\frac{\kappa_1}{\kappa_2}}=\sqrt{\frac{k_2\rho_2 c_2}{k_1\rho_1 c_1}}. \tag{10}$$

Equations (6)–(9) apply for all axial locations and all times. We now make the assumptions

$$\sqrt{\kappa_2 t}\gg\mu^{-1}, \tag{11}$$

$$\sqrt{\kappa_2 t}\gg x. \tag{12}$$

Physically, the first assumption states that over the time of interest, heat diffuses a distance which is large compared to the ultrasound attenuation length. In the second assumption, the distance that the heat diffuses is large relative to the distance from the interface to the observation point. We shall see subsequently that the location of maximum temperature is of order of magnitude $1/\mu$ [$x_{\max}=O(1/\mu)$] in distance from the interface, so that for the purposes of determining maximum temperature inequalities (11) and (12) are equivalent.

Employing assumptions (11) and (12) in the integrals of (7)–(9) and letting $\epsilon\to 0$ gives

$$T_2=\frac{I_0}{\mu k_2}\left[\frac{2\beta}{\sqrt{\pi}(1+\beta)}M+F_0(x;\mu,\beta)+\frac{1}{M}F_1(x;\mu,\beta)+O(1/M^2)\right], \tag{13}$$

where

$$M=\sqrt{\mu^2\kappa_2 t}\gg 1, \tag{14}$$

$$F_0=-e^{-\mu x}+\frac{1-\mu\beta x}{1+\beta}, \tag{15}$$

and

$$F_1=\frac{2\beta-2\mu x+\beta\mu^2x^2}{2\sqrt{\pi}(1+\beta)}. \tag{16}$$

The location of maximum temperature rise $x_{\max}$ can be obtained by differentiating (13) with respect to x and setting the result equal to zero. We then obtain

$$\mu x_{\max}=\ln\frac{1+\beta}{\beta}+\frac{1}{M}\left(\ln\frac{1+\beta}{\beta}-\frac{1}{\beta}\right)+O\left(\frac{1}{M^2}\right). \tag{17}$$

The maximum temperature rise $T_{\max}$ is obtained by inserting $x_{\max}$ from (17) into (13), and ignoring terms of magnitude $1/M^2$ or smaller. The result will be investigated numerically below.

III. RESULTS

The asymptotic values (13) and (17) for the temperature rise and location of maximum temperature were compared with a numerical solution to the heat-conduction equations (1)–(4), for a simulated insonation of bone. The Galerkin finite-element formulation as implemented in the FIDAP (Fluent Inc., Lebanon, NH) commercial code was used in the numerical calculations. Parameters were chosen to be in the range appropriate for radiation-force imaging or focused ultrasound surgery. Thus we consider pulse lengths up to 16 s (ter Haar, 2001; Walker, 1999). We also concentrate on a frequency of 10 MHz, which is on the upper end of the clinical range (ter Haar, 2001; Walker, 1999), and of highest importance from a safety perspective due to the high attenuation. Lower frequencies are considered in one set of calculations.

TABLE I. Location of maximum temperature rise, as a function of time, determined by the asymptotic series and the finite-element method. Ultrasound frequency is 10 MHz and the transmitted intensity is 1.0 W/m^2.

		Location of Maximum Temperature Rise (mm from interface)		
t (sec.)	$(\mu^2\kappa_2\ t)^{1/2}$	Finite Element	1-term Asymptotic	2-term Asymptotic
0.25	1.84	.109	.121	.102
0.35	2.18	.111	.121	.105
0.5	2.61	.112	.121	.108
1.0	3.69	.115	.121	.112
2.0	5.22	.117	.121	.114
4.0	7.36	.118	.121	.116
8.0	10.43	.119	.121	.118
16.0	14.75	.120	.121	.119

At high ultrasonic frequencies there is little data available regarding the attenuation coefficient of cortical bone. The range of values reported by the ICRU (ICRU, 1998) for 1 MHz was linearly extrapolated to 10 MHz, resulting in an attenuation coefficient of $3.1\ \text{mm}^{-1}<\mu<5.1\ \text{mm}^{-1}$. We take $\mu=4.0\ \text{mm}^{-1}$ as the attenuation coefficient at 10 MHz. The corresponding attenuation length is $1/\mu=0.25$ mm. The attenuation coefficient at lower frequencies was linearly extrapolated in a similar manner, so that the coefficients at 3 and 6 MHz are 1.2 and 2.4 mm^{-1}, respectively.

Values of density, heat capacity, and thermal conductivity for the soft-tissue and bone media are (NCRP, 1992) $[\rho_1,c_1,k_1]=[1000\ \text{kg/m}^3,\ 4000\ \text{J/(kg K)},\ 0.6\ \text{W/(m K)}]$ and $[\rho_2,c_2,k_2]=[1700\ \text{kg/m}^3,\ 1600\ \text{J/(kg K)},\ 2.3\ \text{W/(m K)}]$. The resulting thermal diffusivities for soft tissue and cortical bone are $\kappa_1=0.15\times10^{-6}\ \text{m}^2/\text{s}$ and $\kappa_2=0.85\times10^{-6}\ \text{m}^2/\text{s}$. The dimensionless parameter β [Eq. (10)] attains a value of 1.6. An intensity of 1.0 W/cm^2 (Walker, 1999) was used in the calculations. Since the governing equations are assumed linear in the acoustic intensity, predictions based upon other intensities of interest may be obtained through a simple rescaling.

Table I displays the location of maximum temperature rise in the bone for various insonation times, as determined by both the finite-element method and the asymptotic theory. The frequency is 10 MHz ($\mu=4.0\ \text{mm}^{-1}$). The parameter $M=(\mu^2\kappa_2 t)^{1/2}$, representing the ratio of the diffusion length to the attenuation length and assumed large in the asymptotic theory, is displayed in the second column. The location of maximum temperature rise (column 3) shifts slightly away from the interface with time, to an asymptotic value of approximately half of the attenuation length. The one-term

TABLE II. Maximum temperature rise as a function of time, determined by the asymptotic series and the finite-element method. Ultrasound frequency is 10 MHz and the transmitted intensity is 1.0 W/m2

		Maximum Temperature Rise (K)			
t (sec.)	$(\mu^2\kappa_2\ t)^{1/2}$	Finite Element	1-term Asymptotic	2-term Asymptotic	3-term Asymptotic
0.25	1.84	0.96	1.40	0.82	0.98
0.35	2.18	1.19	1.65	1.07	1.21
0.5	2.61	1.50	1.97	1.39	1.51
1.0	3.69	2.28	2.79	2.21	2.30
2.0	5.22	3.40	3.95	3.37	3.43
4.0	7.36	5.01	5.58	5.00	5.04
8.0	10.43	7.30	7.89	7.31	7.34
16.0	14.75	10.55	11.20	10.58	10.60

asymptotic prediction of $x_{\max}$ (column 4) is independent of time, and within 10% of the finite-element prediction for the lowest time (lowest M value). The accuracy of the one-term prediction improves as time (M value) increases, to within 1% of the finite-element prediction at the largest time value. The two-term asymptotic result reflects the increases in $x_{\max}$ with time. The agreement between the finite-element and two-term asymptotic predictions increases with time, from about 7% to 1% over the range of times considered.

The $x_{\max}$ locations of Table I correspond to the maximum temperature values shown in Table II. The one-term asymptotic series has an error of approximately 45% at the lowest time and 6% at the largest time. The range of agreement for the two-term asymptotic series is 15% to 0.3%, while the three-term series is within about 2% for all times considered.

Lower ultrasound frequencies are considered in Table III. The three-term asymptotic model agrees with the finite-element model within 10% accuracy for M values above approximately 1.1, and within 20% accuracy for M values greater than about 0.9.

IV. DISCUSSION

The asymptotic model demonstrates good accuracy over the range of parameters considered, as judged by agreement between the three-term series and the finite-element approach. Somewhat surprisingly, good accuracy for the three-term series is maintained for values of the large parameter M below 1, providing a wider range of applicability for the model than the condition $M \gg 1$ would suggest. Use of just the first term in the series requires an M value of perhaps 4 or greater.

TABLE III. Maximum temperature predicted by the 3-term asymptotic series and the finite-element method, for a variety of frequencies and exposure times. Transmitted intensity is 1.0 W/cm

			Maximum Temperature Rise (K)	
Frequency (MHz)	t (sec.)	$(\mu^2\kappa_2\ t)^{1/2}$	Finite Element	3-term Asymptotic
6	1.0	2.21	2.04	2.06
6	0.5	1.56	1.30	1.33
6	0.25	1.11	0.80	0.89
6	0.17	0.90	0.59	0.73
3	1.0	1.11	1.60	1.78
3	0.5	0.78	0.96	1.33
3	0.25	0.55	0.56	1.25

For fixed heat-conduction properties (β values), the temperature normalized by $I_0/\mu k_2$ [see (13)] depends only upon the dimensionless length M. Hence, in terms of normalized maximum temperatures, a 6 MHz exposure for 0.25 s is equivalent to a 3 MHz exposure for an exposure time yielding the same M value, i.e., 1.0 s (third and fifth entries of Table III). This exclusive dependence upon M, which can be seen by inserting (17) into (13)–(16), compactly portrays how the accuracy of the model increases with increased attentuation (ultrasound frequency), exposure time, and thermal diffusivity in bone.

The first term in the asymptotic series (13) can be rewritten

$$T_2 = \frac{I_0}{\frac{1}{2}\left(\sqrt{k_1\rho_1 c_1} + \sqrt{k_2\rho_2 c_2}\right)} \sqrt{\frac{t}{\pi}}. \tag{18}$$

When the thermal properties of medium 1 and medium 2 are the same, this expression reduces to the expression arising naturally from thermal-point-source approaches for a heated disk in a single medium (Herman and Myers, 2003):

$$T = I_0 \sqrt{\frac{t}{\pi k \rho c}}. \tag{19}$$

Equation (18) can thus be thought of as an extension of the heated-disk model to a two-layered medium. It can be seen that the optimal approximation to the two-medium model using a single, ''effective'' medium is one for which the square root of the product of the thermal properties $(k_{\text{eff}}\rho_{\text{eff}}c_{\text{eff}})^{1/2}$ is equal to the average of the square roots for the two media. Since the product of the thermal properties of bone exceeds that of soft tissue, a soft-tissue-only model will result in an overestimate of the actual temperature rise and a bone-only model will result in an underestimate. Thus, between the two single media, soft tissue is preferable from a safety standpoint due to the conservative prediction. However, due to the rather weak (square-root) dependence of the temperature rise upon material properties, neither the uniform-bone nor the uniform-soft-tissue approximation deviates excessively from the two-medium result [Eq. (18)]—about 20% for both based upon property values from the previous section. It is important to note additionally that Eq. (18) is in error relative to the finite-element or three-term asymptotic result by the amounts exemplified in Table II (about 40% for $M = 1.84$).

The model requires that the distance over which heat diffuses in bone in the time of interest be large relative to both the attenuation length and the distance from the interface to the observation point [Eqs. (11) and (12)]. From Table I and Eq. (17), it is seen that the position of maximum temperature is located roughly one-half of an attenuation length from the interface [assuming β (Eq. 10) equal to 1.6 for a combination of soft tissue and bone]. Thus, provided that attention is restricted to distances comparable to the lo-

cation of maximum temperature rise, the primary assumption of the model may be summarized in the ''high-attenuation'' requirement described by Eq. (11).

In the model development, radial variations in the ultrasound beam profile and the resulting temperature field were neglected. This was partially justified on the grounds that the location of maximum temperature is along the beam axis, very near ($\sim 1/2\mu$) the interface. Axial variations in the temperature field occur on this scale, while radial variations vary on a much larger scale (the beam width). Radial heat-conduction can then be logically neglected relative to axial conduction. For sufficiently large times, however, the presence of the outer edge of the beam will be felt on the beam axis, due to diffusion of heat across the entire beam. This time is roughly a^2/κ_2, where a is the beam radius. Thus, provided $a > (\kappa_2 t)^{1/2}$, the present theory is expected to apply. For a time of 0.35 s and a bone diffusivity of $\kappa_2 = 0.85\ \text{mm}^2/\text{s}$, the required condition is $a > 0.5$ mm. Even at times for which radial variations in the temperature field become important, the asymptotic series (13) is useful from a safety standpoint, in that it provides a conservative estimate of the temperature rise for a given intensity (no temperature reduction due to radial conduction of heat).

In the present theory the beam width is assumed to be small compared to the radii of curvature of the bone surface, in order to justify a planar interface. This requirement can be difficult to support in applications such as fetal imaging, or a beam incident upon the tip of a rib. If the ultrasound beam incident upon a curved bone surface is modeled as a ray tube, some of the rays will encounter the surface at non-normal incidence and be transmitted with reduced intensity relative to the case of normal incidence. The planar interface case can then be thought of as conservative, in the sense of highest transmitted sound intensity. However, rays at non-normal incidence will give rise to shear waves, which are more highly attenuated than compressional waves. Treatment of shear waves, and curved bone surfaces, awaits a more sophisticated model than the one presented here.

Another geometric simplification of the model was the treatment of the cortical bone layer as a semi-infinite medium. This assumption is reasonable if the beam is highly attenuated in the layer, and heat diffuses axially a distance less than the cortical layer over the time of interest. As with the radial variations, the diffusion length $(\kappa_2 t)^{1/2}$ must be comparable to the cortical thickness for finite-thickness effects to appear in axial heat conduction. Photographs of human rib cross sections (Granik and Stein, 1973) show the cortical bone thickness h to be on the order of 1 mm. The ultrasound beam is highly attenuated in a layer this size, at least at high frequencies. Heat conduction is also confined primarily to the layer for times less than roughly $(h^2/\kappa_2)^{1/2}$, about 1 s.

Derivation of the asymptotic series was performed within the bone medium, since the heat source and location of maximum temperature are located within the bone. Model formulation within the soft tissue medium proceeds similarly to that in bone. However, the location of maximum temperature rise for soft tissue is the interface, and the temperature rise there may be computed from Eq. (13) by setting $x = 0$. Temperature rises at the interface were found to agree with finite-element results with the same level of accuracy as the maximum temperatures of Table II. For the cases considered in Table II, interface temperatures were lower than maximum temperatures by less than 5%, with the difference decreasing with increasing M. It is also worth noting that, to first order, the tissue temperature and bone temperature are independent of location [Eq. (18)], and depend only upon material properties and the square root of the time.

The theory presented in this paper assumes a constant intensity and applies to pulses only in a temporally averaged sense. The theory can be extended to treat short-duration pulses, with the primary assumption being $\mu^2\kappa(t-\delta) \gg 1$, δ being the pulse duration. Ultrasound pulses will be addressed in a subsequent report.

ACKNOWLEDGMENTS

The author wishes to thank Bruce Herman and Gerald Harris of the US FDA/CDRH for suggesting this problem, providing valuable references, and engaging in interesting discussions of the results.

AIUM/NEMA (**1998**). ''Standard for real-time display of thermal and mechanical acoustic output indices on diagnostic ultrasound equipment, Revision 1,'' American Institute of Ultrasound in Medicine, Laurel, MD; National Electrical Manufacturers Association, Rosslyn, VA.

Carstensen, E. L., Child, S. Z., Norton, S., and Nyborg, W. (**1990**). ''Ultrasonic heating of the skull,'' J. Acoust. Soc. Am. **87**, 1310–1317.

Chan, A. K., Rubens, A. S., Guy, A. W., and Lehmann, J. F. (**1973**). ''Calculation by the method of finite differences of the temperature distribution in layered tissues,'' IEEE Trans. Biomed. Eng. **20**, 86–90.

Doody, C., Duck, F. A., and Humphrey, V. F. (**2000**). ''Comparison of finite-element and heated disk models of tissue heating by ultrasound,'' Ultrasound Med. Biol. **26**, 1347–1355.

Granik, G., and Stein, I. (**1973**). ''Human ribs: static testing as a promising medical application,'' J. Biomech. **6**, 237–240.

Herman, B. A., and Harris, G. R. (**2002**). ''Models and regulatory considerations for transient temperature rise during diagnostic ultrasound pulses,'' Ultrasound Med. Biol. **28**, 1217–1224.

Herman, B. A., and Myers, M. R. (**2003**). ''An analytical derivation for the transient temperature rise during an ultrasound pulse focused on bone,'' Ultrasound Med. Biol. **29**, 771–773.

ICRU (**1998**). *Tissue Substitutes, Phantoms and Computational Modelling in Medical Ultrasound*, International Commission on Radiation Units and Measurements Report 61.

IEC (**2001**). ''Medical electrical equipment—Part 2-37: Particular requirements for the safety of ultrasonic medical diagnostic and monitoring equipment,'' IEC 60601-2-37 (IEC, Geneva).

NCRP (**1992**). *Exposure criteria for medical diagnostic ultrasound: I. Criteria based on thermal mechanisms*, National Council on Radiation Protection and Measurements Report No. 113, p. 53.

Nightingale, K. R., Palmeri, M. L., Nightingale, R. W., and Trahey, G. E. (**2001**). ''On the feasibility of remote palpation using acoustic radiation force,'' J. Acoust. Soc. Am. **110**, 625–634.

Nyborg, W. L. (**1988**). ''Solutions of the bio-heat transfer equation,'' Phys. Med. Biol. **33**, 785–792.

ter Haar, G. R. (**2001**). ''Acoustic Surgery,'' Phys. Today **54**, 29–34.

Walker, W. F. (**1999**). ''Internal deformation of a uniform elastic solid by acoustic radiation force,'' J. Acoust. Soc. Am. **105**, 2508–2518.

Wu, J., and Du, G. (**1990**). ''Temperature elevation generated by a focused Gaussian ultrasonic beam at a tissue-bone interface,'' J. Acoust. Soc. Am. **87**, 2748–2755.

Amplitude and phase calibration of hydrophones up to 70 MHz using broadband pulse excitation and an optical reference hydrophone

Volker Wilkens[a] and Christian Koch
Physikalisch-Technische Bundesanstalt, Department 1.6, Sound, Bundesallee 100, 38116 Braunschweig, Germany

(Received 2 December 2003; revised 26 February 2004; accepted 27 February 2004)

A substitution calibration technique for piezoelectric ultrasonic hydrophones is presented that uses an optical multilayer hydrophone as the reference receiver. Broadband nonlinearly distorted focused pulses are first measured with the reference hydrophone and then with the hydrophone to be calibrated. By Fourier transformation of the time wave forms and division of the frequency spectra, the complex-valued frequency response of the hydrophone under test is obtained in a broad frequency range in a very fast and efficient way and with high frequency resolution. The results obtained for a membrane hydrophone and a needle-type hydrophone are compared with those obtained by independent calibration techniques such as primary calibration using optical interferometry and secondary calibration using time-delay spectrometry, and good agreement is found. The calibration data obtained are apt to improve the results of ultrasound exposure measurements using broadband voltage-to-pressure conversion. This is demonstrated for standard pulse parameter determination from exemplar exposure measurements on a commercial diagnostic ultrasound machine. For the membrane hydrophone, the evaluation method commonly used leads to an overestimation of the positive peak pressure by up to 50%, an underestimation of the rarefactional peak pressure by up to 11%, and an overestimation of the pulse intensity integral by up to 28%. © *2004 Acoustical Society of America.* [DOI: 10.1121/1.1707087]

PACS numbers: 43.35.Yb, 43.30.Yj, 43.58.Vb [YHB] Pages: 2892–2903

I. INTRODUCTION

For precise and reliable measurements of medical and technical ultrasound fields calibrated hydrophones are required. To process the results of exposure measurements with calibrated hydrophones it has become a standard practice to use the voltage-pressure transfer factor M at the acoustic working frequency f_{awf} of the device under test rather than the broadband frequency dependent transfer function $M(f)$ of the hydrophone. This is a consistent approach if the ultrasonic field is of narrow bandwidth, or if the hydrophone provides a sufficiently flat frequency response covering the whole frequency range of interest. So international guidelines for exposure measurements of diagnostic ultrasound machines,[1,2] for instance, state requirements and recommendations for the hydrophone bandwidths which should extend up to several (up to eight) times f_{awf} of the pulses to be measured to account for the presence of harmonics due to nonlinear sound propagation.[3,4] On the low frequency side, the bandwidth should extend down to at least half f_{awf} to account for the impact of low frequency components on the maximum rarefactional pressure and mechanical/cavitation indices.[5,6] For measurements on current diagnostic ultrasound machines with working frequencies up to 10 MHz and even beyond, it seems to be very hard to find hydrophones that meet these flatness criteria, since the frequency responses of common hydrophones suffer more or less from thickness-mode resonances, diffraction effects, radial resonances, and a roll-off at high frequencies due to electronic restrictions.[7–10] An alternative to the demand for a flat frequency response may be an adequate correction procedure. Correct pressure wave forms $p(t)$ and the respective standard pulse parameters can be obtained for broadband pulses by deconvolution of the voltage–time signals $u(t)$ with the nonideal impulse response $m(t)$ of the hydrophone. The calculation can, in principle, be easily performed in the frequency domain by complex division of the voltage spectrum $U(f)$ by the voltage–pressure transfer function $M(f)$ of the hydrophone. In contrast to the usual conversion method described earlier, the transfer function has to be known here in amplitude and phase, and the data have to cover the whole frequency range where a significant content of the voltage spectrum $U(f)$ is expected.

Various calibration techniques are commonly applied to determine the frequency response of piezoelectric hydrophones. Primary calibration techniques based on reciprocity[11,12] or optical interferometry[13–15] provide calibrated reference hydrophones suitable for secondary substitution calibration techniques. In these techniques, different kinds of ultrasound wave forms are used: quasi-single frequency tone bursts for calibration at discrete frequency points, nonlinearly distorted tone bursts together with an evaluation at multiple harmonics of the fundamental frequency,[16] swept frequency bursts together with time-delay spectrometry (TDS) for fast, quasicontinuous calibration,[12,17] and broadband pulses together with Fourier transformation to obtain the information in the frequency domain.[18–21] While in the past great efforts were made to obtain the amplitude

[a]Electronic mail: volker.wilkens@ptb.de

 0001-4966/2004/115(6)/2892/12/$20.00 © 2004 Acoustical Society of America

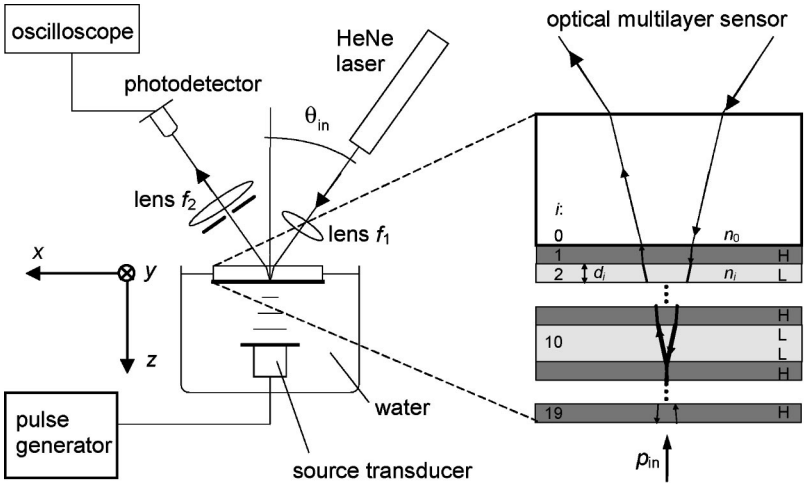

FIG. 1. Optical multilayer hydrophone setup; insert: optical multilayer system deposited onto a plane glass substrate; $i=0$: substrate, $i=1,...,19$: dielectric layers, H, L: high-index and low-index optical quarter-wave layer, respectively, p_{in}: incident pressure wave, n_i: refractive index, and d_i: thickness of the ith medium.

response and to extend the frequency ranges of calibrations,[14,15,22] the determination of experimental phase responses has been dealt with only recently. Using two alternative extensions of TDS—gated time-delay spectrometry and heterodyne time-delay spectrometry (HTDS)—phase data could be obtained by substitution calibration against a standard hydrophone.[23]

In this paper an alternative method for amplitude and phase calibration is described that has previously been used to determine the complex frequency responses of fiber-optic hydrophones.[24,25] An optical multilayer hydrophone with constant-amplitude frequency response from at least 1 to 75 MHz serves as the reference. This large bandwidth confirmed by primary interferometric calibration is made possible by the optical detection technique, the very small thickness of the sensing element (1.9 μm), and the exclusion of lateral resonances.[26,27] The subresonant operation mode is expected to extend to frequencies even beyond 75 MHz, but absolute calibration and verification has not been possible up to now since independent references and primary calibration were not available. Due to the flat amplitude response, the system is expected to provide also a flat phase response, and it is suggested for use as a primary phase standard. The application of broadband pulse excitation enables the complete relevant phase response to be measured instantaneously, i.e., basically within the pulse length of about 2 μs. This is an important advantage over other excitation types with longer measurement times that require much effort for the stabilization of the acoustic path length and elimination of temperature drifts to obtain reliable phase response data. The method described provides the complex-valued voltage–pressure transfer function of hydrophones in a very broad frequency range and with high frequency resolution. The results can be used to effectively improve the determination of standard pulse parameters such as positive peak pressure p_+ and rarefactional peak pressure p_- using common piezoelectric hydrophones. This is demonstrated by exemplar exposure measurements on a commercial diagnostic ultrasound machine using the broadband complex-valued calibration data obtained for wave form deconvolution.

II. CALIBRATION METHOD

The optical multilayer hydrophone used as a reference receiver in the secondary calibration technique has been calibrated and characterized previously.[27] Due to its flat frequency response in a very broad frequency range, it is most suitable for this purpose. The calibration method is based on the successive measurement of broadband nonlinearly distorted pulses of a focusing source transducer with the reference and the hydrophone to be calibrated using the same excitation conditions. By Fourier transformation of the time wave forms and division of the respective frequency spectra, the complex-valued frequency response of the hydrophone under test is obtained.

A. Optical multilayer reference hydrophone

Since a detailed characterization of the optical multilayer hydrophone is given in Ref. 27, a brief description will be sufficient here. The sensor element of the optical multilayer hydrophone consists of a dielectric layer system acting as a microinterferometer deposited onto a plane glass substrate (Fig. 1). The ultrasound measurement is based on the elastic deformation of the layer system by the incident pressure wave p_{in}. The change in the thicknesses d_i and the refractive indices n_i of the layers cause modulation of the optical intensity reflectance ΔR, which is measured by a simple optical detection setup comprising a HeNe laser (Polytec GmbH, Waldbronn, Germany, wavelength: 633 nm, output power: ~2 mW), two lenses, and a photodetector (photodiode: Siemens BPX 65, amplifier: manufactured in-house). Adjustment to the optimum acoustic operation point of the individual layer system sample for the given optical wavelength of the laser is achieved by appropriate choice of the light incidence angle θ_{in} (here: $\theta_{\text{in}} \approx 35°$). The interference filter structure used combines high optical finesse of the microinterferometer with a very small overall thickness of about 1.9 μm for 19 layers, and good acoustic sensitivity as well as a large acoustic detection bandwidth are obtained. As described in Ref. 27, the frequency response is constant at least in the range from 1 to 75 MHz within the uncertainty of the primary calibration (typ.: ~11% at 20 MHz, 95% confidence level) if a correction for the photodetector frequency

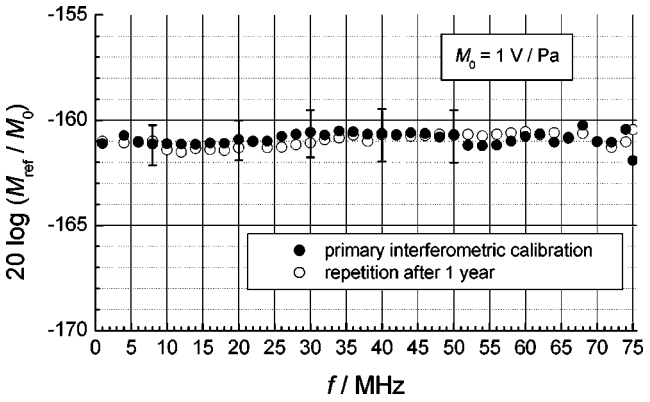

FIG. 2. Frequency response of the optical multilayer hydrophone as determined by primary interferometric calibration (uncertainties displayed relate to 95% confidence level; from Ref. 27, revised).

response is applied (Fig. 2). The voltage–pressure transfer factor obtained is $M_{\mathrm{ref}}=8.9\,\mathrm{mV/MPa}$. Due to the subresonant operation in this broad frequency range which is confirmed by the constant-amplitude response, a flat phase response is expected as well. The sensitivity in terms of noise equivalent pressure amplitude is $p_{\mathrm{min}}=30\,\mathrm{kPa}$ without signal averaging using an analog detection bandwidth of ~25 MHz of the oscilloscope (72 kPa using 250 MHz bandwidth). By signal averaging, the signal-to-noise ratio can be considerably enhanced. According to calculations, pressure amplitude linearity is achieved up to 37 MPa with deviations below 5%. The restriction in linearity is due to the dependence of the optical reflectance of the microresonator on the layer thicknesses deviating from a linear dependence for large thickness changes (cf. Ref. 27). The lateral resolution capability is determined by the spot size of the focused light beam within the layer system. The experimentally determined full widths at $1/e$ of the maximum of the Gaussian intensity profile are ~60 μm in the x direction and ~45 μm in the y direction (asymmetry due to oblique light incidence).

B. Pulse measurement and calculation of frequency response

For the substitution calibration, broadband pulses from a focusing source transducer (Karl Deutsch GmbH, Hürth, Germany, single element PZT, acoustic focusing, frequency range: 3–12 MHz, diameter: 12 mm, nominal focal length: 50 mm) driven by a pulse generator were successively measured with the optical multilayer hydrophone and the hydrophone to be calibrated under the same excitation conditions in de-ionized and degassed water (Fig. 3). The pulse generator customized in-house provided high voltage spikes by sudden discharge of a capacitor (peak voltage: 350 V, rise time measured with 50 Ω load: 18 ns). The output signals $u(t)$ from the photodetector and the hydrophone amplifier were recorded, displayed, and saved by a digital oscilloscope (Tektronix TDS 744 A). The analog bandwidth of the oscilloscope was set to 250 MHz and the pulses were sampled with 1000 data points in a time period of $T=4$ μs, giving a Nyquist frequency of 125 MHz. Signal averaging (100 pulses) was applied to improve the signal-to-noise ratio. The distance between transducer and hydrophones was adjusted using the same delay time of 32 μs for the two measurements. Lateral adjustment was carried out by searching for the maximum peak voltage. An example of the wave forms obtained is depicted in Fig. 4. The conversion to the pressure–time wave form $p(t)$ in the case of the reference measurement was performed using the frequency independent voltage–pressure transfer factor M_{ref} (cf. Sec. II A). The time window for undistorted measurements of the present optical multilayer hydrophone is restricted to 2.2 μs, because afterwards acoustic reflections from the rear side of the glass substrate arrive at the sensing element.[27] To avoid artifacts, all data points of the reference time wave form 2.2 μs after the beginning of the pulse were set to zero to eliminate the backreflection while it was ensured that the original pulse was already abated within these 2.2 μs. In addition, to minimize global phase offsets, the cross-correlation function of both wave forms $u(t)$ was calculated and one wave form was shifted in time by cutting and pasting zeros at the end and at the beginning, so the maximum correlation was obtained afterwards for zero shift in time. Typically, a shift of the wave form of zero, one, or two time steps of $\Delta t=4$ ns was necessary. It should be noted that this procedure is not absolutely necessary to obtain the relevant phase data required for impulse deconvolution, but it simplifies comparison of different phase responses. Otherwise, a phase offset linearly increasing or decreasing with frequency is added to the phase response of the hydrophone calibrated. In a deconvolution procedure, this phase offset, in turn, only induces a shift in time of the complete time–pressure wave form, whereas none of the pressure pulse parameters itself is affected.

By numerical discrete Fourier transformation $\mathcal{F}$ the pressure frequency spectrum $P(f)$ (reference) and the voltage frequency spectrum $U(f)$ (hydrophone) were calculated from the time wave forms using the Mathcad™ software. Here the Singleton method was used, which offers the ad-

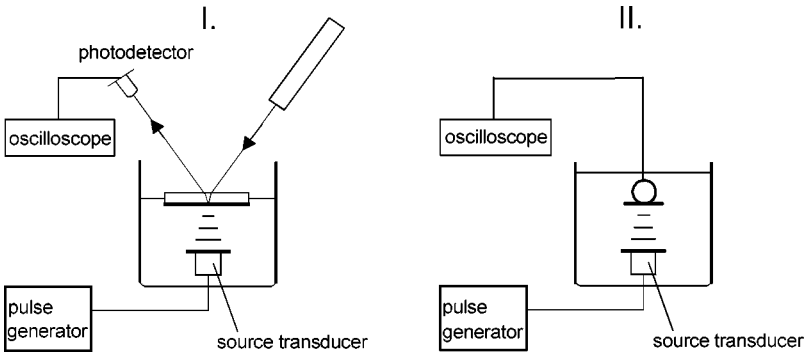

FIG. 3. Hydrophone substitution calibration procedure: (I) measurement of a broadband focused ultrasound pulse with the optical reference hydrophone; (II) measurement with the hydrophone to be calibrated after topping up the water tank.

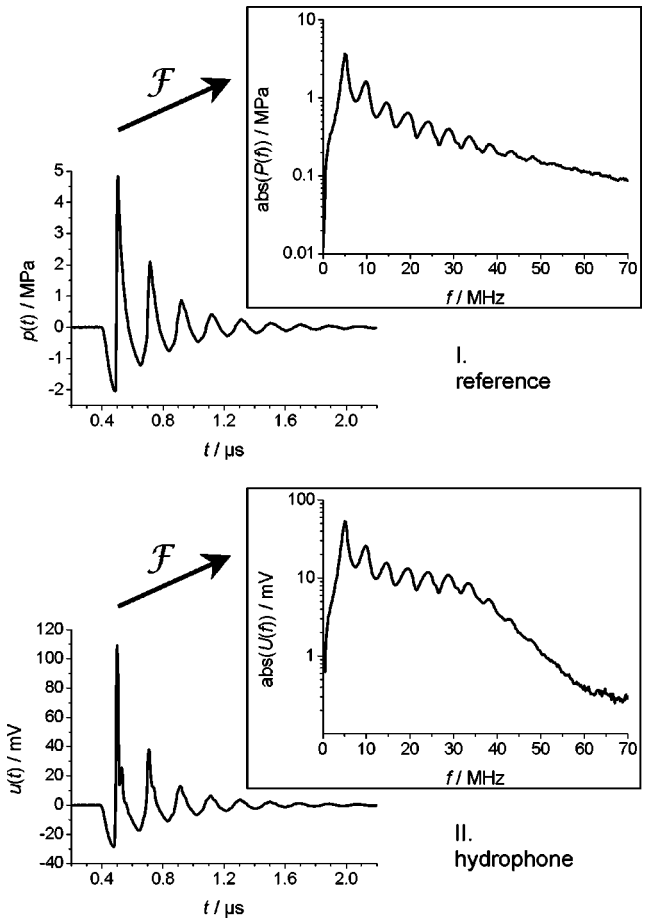

FIG. 4. Example of a pressure–time wave form $p(t)$ of the reference measurement (I) and voltage–time wave form $u(t)$ of a membrane hydrophone measurement (II) and associated amplitude spectra $|P(f)|$ and $|U(f)|$ obtained by numerical Fourier transformation $\mathcal{F}$.

vantage to be free from the restriction of other fast Fourier transformation algorithms to data point numbers of $N=2^n$, $n=1,2,3,\ldots$.[28] Since the hydrophone measurements to be corrected by deconvolution within the exposimetry application (cf. Sec. IV) will be sampled with $N=2500$ to allow a longer pulse duration of $T=10\,\mu$s to be recorded, it is appropriate here to use the same N for the calculation of the frequency responses. For the calibration pulse measurement it is sufficient to ensure the same time increment Δt as in the measurements to be corrected by deconvolution, since it is possible to add an arbitrary number of zeros to the end of the time wave forms. Here, 1500 zero-valued data points were added to the wave forms acquired. The frequency spectra obtained (frequency increment: $\Delta f=100\,$kHz) contain the fundamental and the higher harmonics, and also in between there is significant information (Fig. 4). Due to the short excitation voltage pulse and the nonlinear propagation of the sound wave, particularly emphasized by the large pressure amplitude and focusing with a relatively long propagation path length ($\sim$47 mm), the broad frequency range from 1 up to 70 MHz is covered using this transducer-pulse generator combination. Division of the complex-valued voltage frequency spectrum of the hydrophone measurement $U(f)$ by the complex-valued pressure frequency spectrum of the reference measurement $P(f)$ provides the frequency response

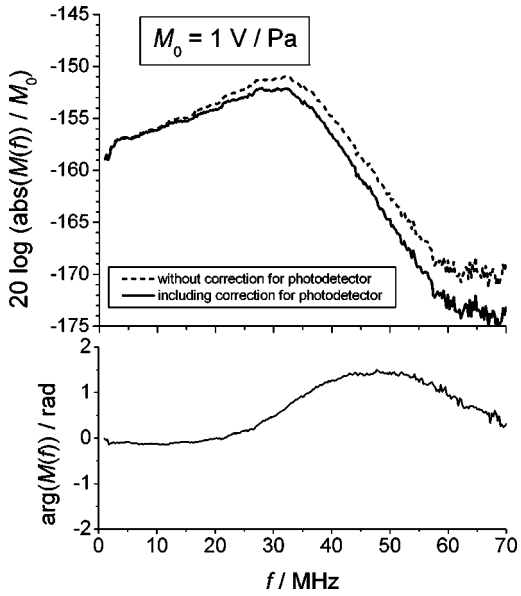

FIG. 5. Amplitude and phase of the voltage–pressure transfer function $M(f)$ obtained by complex division of the spectra depicted in Fig. 4; correction of the amplitude response for the impact of the photodetector frequency response of the optical hydrophone; here the signal-to-noise ratio above 57 MHz is quite low, particularly due to the strongly decreasing frequency response of the hydrophone example shown.

of the hydrophone $M(f)$ in amplitude and phase (Fig. 5). Compensation of the monotonously decreasing frequency response of the photodetector determined in a separate optical mixing experiment[14] was performed in the case of the amplitude of the transfer function abs($M(f)$). No additional information about the phase response of the photodetector was available, but only small deviations from a constant phase response are expected in consideration of the smooth amplitude decrease. No correction was, therefore, applied for the phase of the transfer function arg($M(f)$).

C. Lateral pulse field characterization

In hydrophone substitution calibration, spatial averaging over the sensor element has to be considered when hydrophones with different diameters are compared and, in particular, if focusing source transducers are used. For single frequency tone bursts simple sound field calculations can provide the necessary correction data.[14] If nonlinear sound propagation is employed, the sound field has to be modeled in a more complex way to obtain adequate correction factors for the calibration data at the fundamental frequency and the higher harmonics.[29–31] For the investigation of spatial averaging effects in the calibration technique presented here using broadband, focused, and nonlinearly distorted pulses, an experimental approach was applied similar to that described in Ref. 15 for the evaluation at the harmonics of nonlinearly distorted unfocused tone bursts. Taking advantage of the high lateral resolution capability of the reference receiver (cf. Sec. II A) a lateral line scan along the y axis (cf. Fig. 1) through the focus of the pulse field was performed using the same excitation conditions as for calibration. The pressure–time wave forms $p(t)$ were captured in 51 positions with 20 μm separation by translation of the water tank including the

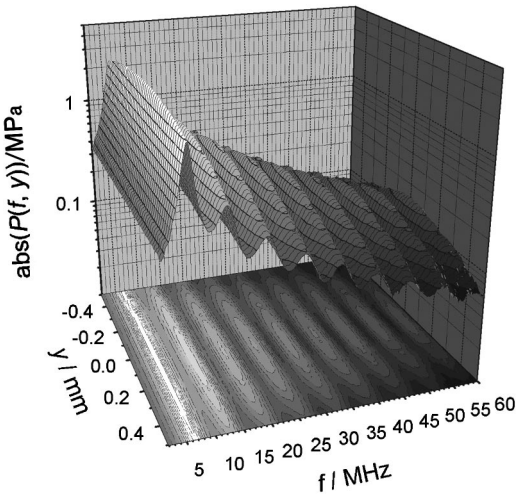

FIG. 6. Amplitude spectrum $|P(f,y)|$ determined by a lateral line scan along the y axis through the focus of the pulse field showing beam profiles vs frequency. Gaussian profiles were obtained at the fundamental and harmonic frequencies, whereas local minima occur on the sound field axis in between the harmonics.

source transducer. The wave forms were then Fourier transformed to provide the pressure amplitude spectra $P(f,y)$ (Fig. 6). For each frequency value f the amplitude spectra was then evaluated as a function of position $P(y)$. While the experimental beam profiles at the fundamental frequency and the harmonics can be represented very well by simple Gaussian profiles, the profiles belonging to the frequencies in between show a different shape mostly accentuated in the minima of the spectrum, where two maxima occur symmetric about the sound field axis (Fig. 6). The basic generation principle of this characteristic is not completely understood up to now but a similar effect can be observed in the results of Ref. 32, where the nonlinearly distorted pulse field of a planar transducer with a fundamental frequency of 2 MHz was investigated and off-axis maxima occurred in the beam profile at 3 MHz. Intended future investigations including nonlinear sound propagation modeling may provide more insight and may lead to an optimization, i.e., an enlargement of the width of the sound field to be used for the hydrophone calibration. To take the experimental finding into account here, a more general double-peak Gaussian formula was used to describe the beam profiles:

$$|P(y)| = P_0\left[\exp\left[-2\left(\frac{y-y_0-y_s}{w}\right)^2\right] + \exp\left[-2\left(\frac{y-y_0+y_s}{w}\right)^2\right]\right], \quad (1)$$

where the magnitude P_0, the Gaussian width w, the center position y_0, and the distance between the two peaks y_s were determined by a four-dimensional least-squares fitting procedure for each frequency point from 1 to 70 MHz (frequency increment: 0.25 MHz). The case of simple Gaussian profiles at the fundamental and the harmonics (and the respective vicinities) is covered by Eq. (1) by $y_s=0$, and the experimental data at the other frequencies were represented by this approach very well, too (Fig. 7). The profiles were normalized with the center pressure value abs$(P(y=y_0))$, and assuming radial symmetry of the sound field, spatial averaging factors were obtained by integration of the profiles over the circle area pertaining to the nominal diameter d of the hydrophone to be calibrated. The results for $d=0.2$ mm and $d=0.5$ mm are depicted in Fig. 8. At the fundamental and the harmonics, the amplitude is underestimated by spatial averaging of the hydrophone, whereas in between, at the minima of the spectra, the amplitude is overestimated due to the local minimum of the spot profiles on the sound field axis. However, for $d=0.2$ mm, the alternating deviations are smaller than $\pm 2\%$, even for the very high frequencies. Since these systematic deviations are of the order of or smaller than other uncertainties, a correction was dispensed with. Instead, improvement of the calibration results was achieved by averaging the results of multiple pulse measurements as described in the following. As expected, the deviations are much greater for larger hydrophone diameters, up to -13% for $d=0.5$ mm. Therefore the technique in its current realization is restricted to the calibration of small diameter hydrophones.

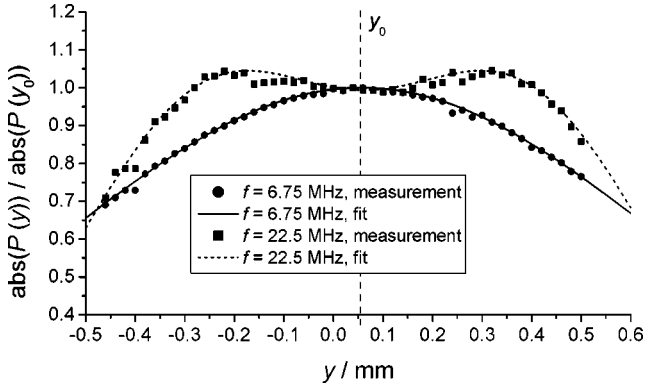

FIG. 7. Normalized beam profile experimentally determined at the fundamental frequency ($f=6.75$ MHz) and at the spectral minimum between the second and third harmonic; fit of double-peak Gaussian profiles centered around y_0.

D. Multiple pulse measurements

To improve the signal-to-noise ratio of the calibration for the frequencies at the minima of the pressure frequency spectra in particular, multiple pulse measurements were performed with the reference and the hydrophone to be

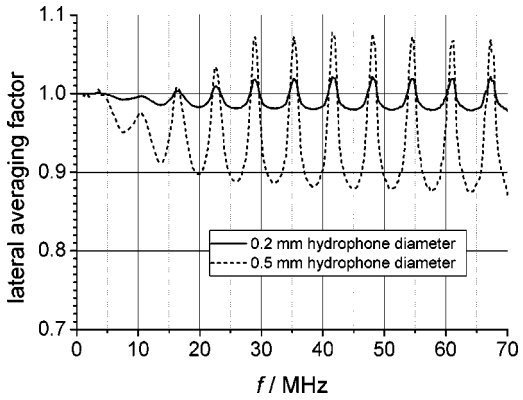

FIG. 8. Spatial averaging factor vs frequency for two different hydrophone sensor diameters derived from the experimental lateral pulse field characterization.

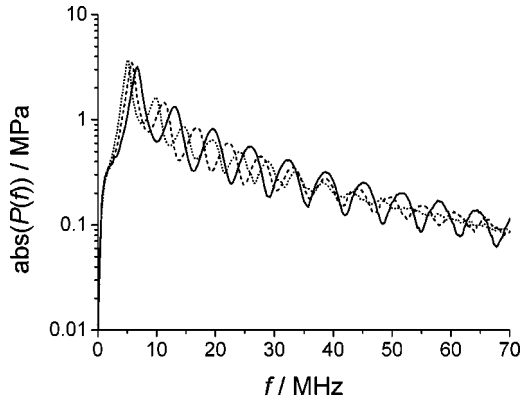

FIG. 9. Pressure amplitude spectra for three different pulse measurements with the optical reference hydrophone; frequency shifts produced by variation of the electrical load at the pulse generator.

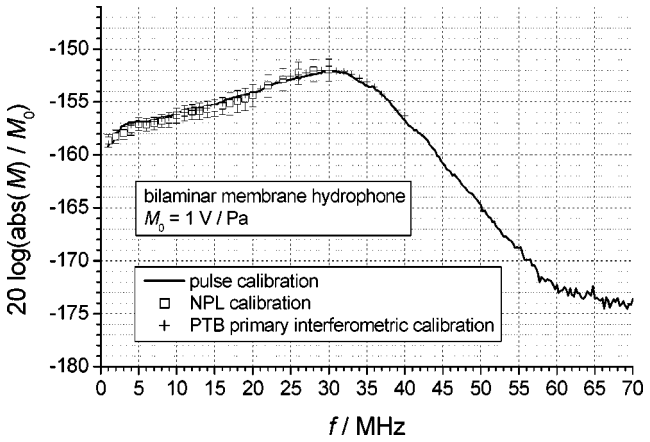

FIG. 10. Amplitude response of a PVDF bilaminar membrane hydrophone with 15 μm layer thickness; comparison of results obtained by broadband pulse calibration and other techniques (uncertainties displayed relate to 95% confidence level).

calibrated.[33] Different pulse wave forms could be generated by modification of the electrical load at the pulse generator which was implemented here through three different cable lengths between pulse generator and transducer. In this way, the fundamental frequency and the harmonics were shifted in frequency, and the frequency regions with low pressure amplitude giving a low signal-to-noise ratio (Fig. 9) as well as the regions with possible over- or underestimation of the frequency response due to spatial averaging are shifted, too. The final frequency responses shown in Sec. III were then obtained by averaging the three respective frequency responses.

In addition, the application of multiple pulse measurements described can serve to control the proper alignment of the hydrophone. If the lateral adjustment is carefully performed, the three frequency response results obtained for each excitation condition differ very little for the hydrophones investigated with 0.2 mm nominal diameter. If deviations significantly greater than indicated by Fig. 8 occur, the adjustment is not optimized.

III. CALIBRATION RESULTS

The calibration result for a bilaminar membrane hydrophone (Precision Acoustics Ltd., Dorchester, UK) with a built-in broadband preamplifier, a nominal diameter of 0.2 mm, and a PVDF layer thickness of 15 μm is shown in Fig. 10. The amplitude response increases monotonously up to the thickness mode resonance at ~31 MHz and decreases at higher frequencies. Very good agreement is found with results of a primary interferometric calibration at discrete frequencies in the range from 1 to 40 MHz (rms deviation of the pulse calibration data from the primary calibration data: 2.5%). Also, the calibration data from an independent calibration laboratory (National Physical Laboratory, Teddington, UK) using a different technique shows very good agreement in the range from 1 to 30 MHz (rms deviation of the pulse calibration data from the NPL data: 4.4%).

The second exemplar calibration relates to a needle-type PVDF hydrophone (Precision Acoustics Ltd., Dorchester, UK) with a nominal diameter of the sensing element of 0.2 mm, an outer diameter of the needle of 0.5 mm, a foil thickness of 9 μm, and a built-in broadband preamplifier. This sample shows very strong variations in the amplitude response in the frequency range from 1 to 20 MHz and the thickness mode resonance peak can be observed at ~38 MHz (Fig. 11). However, this hydrophone is expected to provide limited results for exposure measurements, but here it confirms the high frequency resolution and broadband capabilities of the calibration method investigated and the effectiveness of the deconvolution procedure described in Sec. IV.

The uncertainty of the amplitude calibration is mostly determined by the primary calibration uncertainty of the optical reference hydrophone including the uncertainty of the photodetector frequency response, the lateral adjustment uncertainty of the hydrophones in combination with the spatial averaging effect, and the signal-to-noise ratio in the pulse measurements. An overview of the relevant uncertainty contributions for the needle-type hydrophone calibration is given in Table I for $f=20$ MHz and $f=50$ MHz (95% confidence level). The overall uncertainty ranges versus frequency are specified in Table II and indicated at several frequencies in Fig. 11. An increase in uncertainty below ~2 MHz is mainly caused by a decrease in the signal-to-noise ratio in the optical hydrophone pulse measurement. An increase in uncertainty beyond ~60 MHz is caused by a decreasing signal-to-noise ratio in the needle-type hydrophone pulse measurement together with increasing positioning and spatial averaging correction uncertainties in the primary calibration of the optical hydrophone.

Comparison with the result of an HTDS substitution calibration performed as described in Ref. 23 in the frequency range from 1 to 50 MHz shows excellent agreement between both quasicontinuous amplitude responses, whereas large deviations occur only at the narrow dip at 5.6 MHz. The rms deviation of the pulse calibration data from the HTDS calibration data calculated from 1 to 50 MHz, with the exception of the range from 3.8 to 6.8 MHz, is 4.8%. During pulse calibrations repeated several times it was observed that the local minimum value at 5.6 MHz strongly varied with time, so the deviations in the range excluded in

TABLE I. Example of systematic uncertainty contributions in percent for the impulse calibration results depicted in Fig. 11 at $f=20$ MHz and $f=50$ MHz (95% confidence level).

	20 MHz	50 MHz
Primary calibration of the optical reference hydrophone		
Frequency response of photodetector, interferometer	6.8%	6.8%
Frequency response of photodetector, optical hydrophone	6.8%	6.8%
Signal-to-noise ratio, interferometer	0.2%	0.6%
Signal-to-noise ratio, optical hydrophone	3.0%	2.2%
Voltage at source transducer	1.4%	1.4%
Signal voltage measurement	4.0%	4.0%
Sound field geometry, positioning, and spatial averaging correction	0.6%	9.4%
Subtotal	10.9%	14.3%
Impulse calibration		
Sound field geometry, positioning, and spatial averaging	3.6%	4.0%
Stability of laser and impulse generator	2.3%	2.3%
Signal-to-noise ratio, optical hydrophone (3 pulse spectra averaged, cf. Sec. II D)	0.7%	3.9%
Signal-to-noise ratio, needle-type hydrophone (3 pulse spectra averaged, cf. Sec. II D)	0.6%	1.8%
Subtotal	4.4%	6.3%
Overall uncertainty	11.7%	15.6%

the above-given calculation seem to be caused by a possible instability of the hydrophone itself.

In Fig. 12 the phase responses of both the membrane and the needle-type hydrophone are depicted. For the membrane hydrophone the phase response is flat up to ~22 MHz and shows some variation at higher frequencies with the first inflection point at the resonance peak frequency of the amplitude response. Similar to the respective amplitude response variations, the phase response for the needle-type hydrophone shows strong variations in the frequency range from 1 to 20 MHz and smoother changes at higher frequencies. As already mentioned, the HTDS calibration method recently developed can provide phase responses of hydrophones relative to a reference. Therefore, the difference between the needle-type hydrophone and the membrane hydrophone phase response as determined by the pulse calibration technique was calculated and can be compared with the result of the relative HTDS calibration of the needle-type hydrophone using the membrane hydrophone as the reference (Fig. 12). The curves of both phase responses show very good agreement after a linear term has been subtracted from the latter phase response, which is necessary because of slight path length deviations in the HTDS measurements.[23] Note that this fact does not mean any limitation of the methods (cf. Sec. II B). The deviations are less than $\pm 5°$ and somewhat larger (up to $\pm 8°$) in the frequency range close to 50 MHz where the signal-to-noise ratio of the HTDS measurement becomes low, and in the vicinity of 5.6 MHz according to the larger deviations in the amplitude frequency responses mentioned earlier (rms deviation of the pulse calibration phase data from the HTDS calibration phase data calculated from 1 to 3.8 MHz and 6.8 to 50 MHz: 2.4°).

IV. APPLICATION TO IMPULSE DECONVOLUTION

To investigate the applicability and importance of the broadband complex-valued hydrophone calibration data obtained, exemplar exposure measurements on a commercial diagnostic ultrasound machine were performed using both hydrophones calibrated. Pulse measurements were made in degassed water at distances $z=30$ mm and $z=100$ mm from the linear array transducer for two different nonscanning beam modes to cover both very short broadband pulses (M mode) and more narrow-band bursts (pulse-Doppler mode). For each measurement the focus and the flow measurement window (for pulse-Doppler mode) were set to the distance z, and the hydrophone was adjusted to the lateral position with maximum pulse integral calculated from the squared voltage–time signal. Simultaneous B-mode imaging was deactivated during the pulse measurements. The analog bandwidth of the oscilloscope was set to 250 MHz, and 2500 data points spanning $T=10\,\mu$s were acquired for each pulse. This ensured both the complete time wave form lying in the time interval acquired and the same time and frequency sampling increments as in the calibration procedure data sets (cf. Sec. II B). Pressure–time wave forms were obtained from the voltage data by both methods for comparison: (A) common conversion using the factor $M(f_{\mathrm{awf}})$, where f_{awf} was determined as the mean value of the two -3 dB points in the impulse amplitude spectrum already corrected for the hydrophone frequency response, and (B) deconvolution of the voltage–time signals $u(t)$ with the hydrophone impulse response $m(t)=\mathcal{F}^{-1}(M(f))$ performed in the frequency domain using the complex-valued broadband transfer function $M(f)$:

TABLE II. Overall systematic uncertainty ranges vs frequency f in percent for the impulse calibration results depicted in Fig. 11 (95% confidence level).

Frequency (MHz)	1–2	2–5	5–20	20–30	30–50	50–60	60–70
Overall uncertainty (%)	13.6–16.5	13.2–13.5	11.7–11.8	13.7–13.9	15.1–15.6	15.6–17.1	16.9–22.0

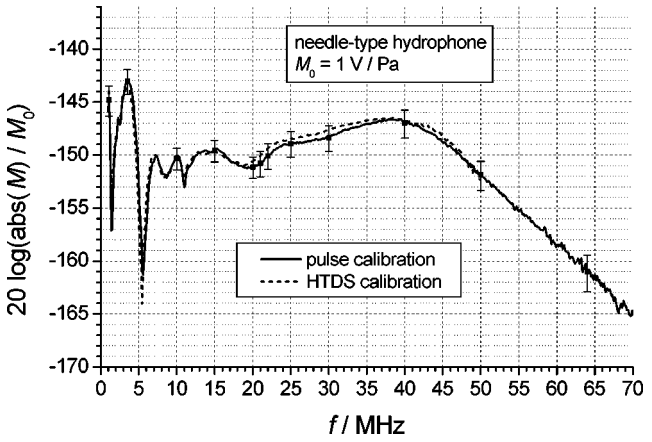

FIG. 11. Amplitude response of a PVDF needle-type hydrophone with 9 μm layer thickness; comparison of results obtained by broadband pulse calibration and HTDS substitution calibration (uncertainties displayed relate to 95% confidence level).

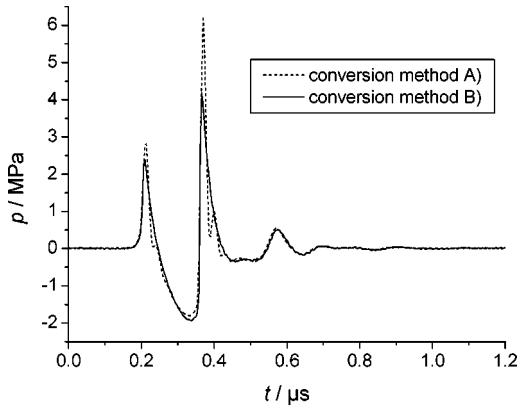

FIG. 13. M-mode pressure–time wave form produced by a commercial diagnostic ultrasound machine ($z=30$ mm); membrane hydrophone measurement; voltage-to-pressure conversion as commonly applied using $M(f_{\mathrm{awf}})$ (method A), and using the broadband complex-valued frequency response $M(f)$ as determined by pulse calibration (method B).

$$p(t)=\mathcal{F}^{-1}(\mathcal{F}(u(t))/M(f)). \tag{2}$$

Here $M(f)$ was determined by pulse calibration using M_{ref} and without correction for the photodetector frequency response of the optical reference hydrophone, since the respective phase data were not available (cf. Sec. II B). The complete data set of $M(f)$ relating to the whole frequency range up to 125 MHz with steps of 0.1 MHz was used without additional window filtering. The lower signal-to-noise ratio of the calibration data below 1 MHz and beyond 70 MHz does not involve any serious shortcoming here, since the respective spectral content of the diagnostic pulses measured is small, and in the case of the upper limit, the hydrophone frequency responses are already very low providing hardly any spectral contribution anyway.

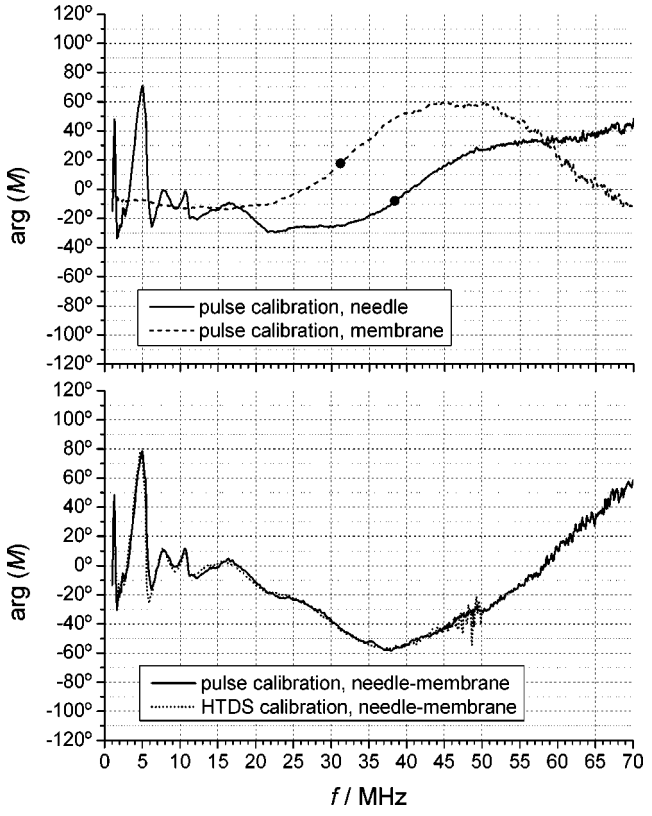

FIG. 12. Phase responses of the needle-type and the membrane hydrophone as determined by broadband pulse calibration using the optical multilayer hydrophone as the reference [upper plot; inflection points (●) at resonance peak frequencies of the respective amplitude responses]; comparison of the difference of both phase responses with the result of an HTDS phase calibration of the needle-type hydrophone using the membrane hydrophone as the reference (lower plot).

An example of the pressure wave forms for M-mode operation measured with the membrane hydrophone at $z=30$ mm is shown in Fig. 13 where a typical property of the membrane hydrophone can be observed. Due to the transfer function increasing with increasing frequency up to the thickness mode resonance, the positive peak pressure value $p_+=\mathrm{maximum}\{p(t)\}$ is strongly overestimated and the rarefactional peak pressure $p_-=\mathrm{minimum}\{p(t)\}$ slightly underestimated when using conversion method A in comparison to the results obtained by conversion method B. Here the oscillations in the decreasing parts of the positive voltage peaks are corrected very well, and a much more reasonable pressure wave form is obtained because the weighting effect of the above-described hydrophone frequency response is numerically compensated. Similar effects were observed with the membrane hydrophone for the larger distance and also for the pulse-Doppler mode at two different possible working frequencies f_{awf}. The results for p_+, p_-, and the pulse intensity integral:

$$\mathrm{PII}=\int_{t_1}^{t_2}\frac{p(t)^2}{\rho c}dt, \tag{3}$$

with ρ the density, c the sound velocity in water, and the complete pressure–time wave form $p(t)\neq 0$ lying in the time interval $[t_1,t_2]$, are listed in Table III for the different parameter settings. In these exemplar measurements, p_+ is overestimated by up to ~50%, p_- is underestimated by up to ~11%, and PII is overestimated by up to ~28% when using conversion method A in comparison to the broadband evaluation method B. For the measurements performed, maximum PII occurs in the pulse-Doppler mode, for the lower frequency setting, and at $z=30$ mm which is close to the fixed elevational focus of the transducer. It is appropriate to re-

TABLE III. Pulse parameters derived from measurements with a membrane hydrophone using A transfer factor $M(f_{awf})$ and B broadband complex-valued transfer function $M(f)$ for different settings of a diagnostic ultrasound machine; numbers in percent: deviations of results after conversion method A from results after B.

Mode	z (mm)	f_{awf} (MHz)	$M(f_{awf})$ (mV/MPa)	Method A $M(f_{awf})$ p_+ (MPa)	Method A $M(f_{awf})$ p_- (MPa)	Method A $M(f_{awf})$ PII (J m^{-2})	Method B $M(f)$ p_+ (MPa)	Method B $M(f)$ p_- (MPa)	Method B $M(f)$ PII (J m^{-2})
M	30	5.5	14.37	6.27	1.76	0.562	4.19	1.93	0.438
				+50%	−9%	+28%			
M	100	4.8	14.49	1.79	0.57	0.064	1.23	0.64	0.053
				+46%	−11%	+21%			
pD	30	5.3	14.38	3.53	1.27	1.858	2.62	1.32	1.674
				+35%	−4%	+11%			
pD	100	5.2	14.39	1.71	0.40	0.326	1.19	0.43	0.266
				+44%	−7%	+23%			
pD	30	6.9	14.58	4.58	1.59	1.783	3.11	1.76	1.476
				+47%	−10%	+18%			

mark that p_+ is of less importance than p_- and PII for output characterization of diagnostic ultrasound equipment according to current standards.[34]

It should be noted that, unlike p_+ and p_-, PII fundamentally does not depend on phase data of the impulse pressure spectra and therefore is independent of the hydrophone phase response due to the pressure quadrature. It can be calculated by summation of $|P(f)|^2$ in the frequency domain before backtransformation to the time domain as well.

Table IV shows the results obtained with the needle-type hydrophone for the same parameter settings of the diagnostic ultrasound machine. For comparison, the deviations (numbers given in percent beneath the acoustic quantities) from the results of the membrane hydrophone measurements obtained by the broadband conversion method B (Table III), that are expected to be the most reliable values, are given. Conversion method A leads to very large deviations, since the needle-type hydrophone frequency response shows very strong variations in the frequency range of interest (cf. Fig. 11) leading to much stronger wave form distortions than with the membrane hydrophone. For the same reason, the results strongly depend on the accuracy of the determination of f_{awf} that sensitively influences $M(f_{awf})$ to be used for voltage-to-pressure conversion. Here p_+ is overestimated by up to ~150%, p_- is overestimated by up to 274%, and PII is overestimated by up to 767%. In general, the results seem to be less predictable than for the membrane hydrophone due to the much stronger variations of the frequency response. But even for this most nonideal hydrophone, the results can be improved so as to arrive at more reasonable values using the broadband conversion method B. In this case, the deviations from the results of the respective membrane hydrophone measurements using broadband conversion method B range from −5% to +22% for p_+, from +3% to +30% for p_-, and from +8% to +28% for PII. An example for the pressure–time wave forms for pulse-Doppler mode operation ($z=30$ mm, $f=5.3$ MHz) obtained by the needle-type hydrophone using both conversion methods A and B and comparison with the respective result of the membrane hydrophone measurement using conversion method B is depicted in Fig. 14. Although improvement has been achieved using method B for all settings of the diagnostic ultrasound machine, for pulse-Doppler mode with $f_{awf}=6.9$ MHz a deviation of 30% remains for p_- (Table IV). The reason for this particular poor result is not understood up to now and future investigations using a larger variety of hydrophones and more measurement data to be compared than in this first examples may give more information about the improvement achievable in practice for different types of hydrophones. However, apart from numerical limitations, three main aspects are expected to impede perfect compensation of the needle-type hydrophone frequency response as indicated by

TABLE IV. Pulse parameters derived from measurements with a nonideal needle-type hydrophone using A transfer factor $M(f_{awf})$ and B broadband complex-valued transfer function $M(f)$ for different settings of a diagnostic ultrasound machine; numbers in percent: deviations from results of membrane hydrophone measurements evaluated after B (Table III).

Mode	z (mm)	f_{awf} (MHz)	$M(f_{awf})$ (mV/MPa)	Method A $M(f_{awf})$ p_+ (MPa)	Method A $M(f_{awf})$ p_- (MPa)	Method A $M(f_{awf})$ PII (J m^{-2})	Method B $M(f)$ p_+ (MPa)	Method B $M(f)$ p_- (MPa)	Method B $M(f)$ PII (J m^{-2})
M	30	5.8	11.57	10.47	6.81	3.798	3.97	2.03	0.474
				+150%	+253%	+767%	−5%	+5%	+8%
M	100	5.3	14.41	2.36	2.18	0.437	1.20	0.66	0.061
				+92%	+241%	+725%	−2%	+3%	+15%
pD	30	5.3	14.41	5.71	3.76	4.547	3.20	1.41	2.014
				+118%	+185%	+172%	+22%	+7%	+20%
pD	100	5.3	14.41	2.55	1.61	0.805	1.31	0.46	0.286
				+114%	+274%	+203%	+10%	+7%	+8%
pD	30	6.9	29.23	4.60	2.38	2.005	3.29	2.28	1.895
				+48%	+35%	+36%	+6%	+30%	+28%

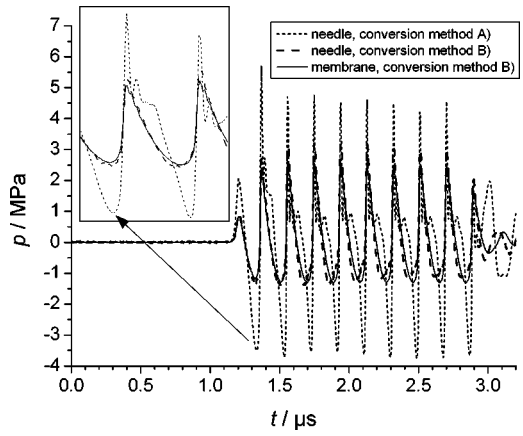

FIG. 14. Pulse-Doppler mode pressure–time wave form produced by a commercial diagnostic ultrasound machine ($z=30$ mm, $f=5.3$ MHz); needle-type hydrophone measurement; voltage-to-pressure conversion using $M(f_{\mathrm{awf}})$ (method A), and using the broadband complex-valued frequency response $M(f)$ as determined by pulse calibration (method B); comparison with membrane hydrophone measurement; voltage-to-pressure conversion method B.

this data: first, inaccuracy when repositioning the hydrophones can induce additional deviations in the comparison of results between the needle-type and the membrane hydrophone and, second, the hydrophone calibration uncertainties also affect this comparison. The third source of systematic errors which might restrict the quality of the deconvolution results here may lie in the inadequate time-dependent properties of the needle-type hydrophone that were observed to have an impact on the frequency response around 5.6 MHz (cf. Sec. III).

V. CONCLUSIONS

A secondary hydrophone calibration technique using an optical multilayer hydrophone as the reference receiver was described. The optical hydrophone offers high lateral resolution, good stability, and a constant frequency response in a remarkably broad frequency range from at least 1 to 75 MHz, which is why the system is very well suitable for use as a reference. Due to the flat amplitude response, the system is expected to also provide a flat phase response, and it is suggested for use as a primary phase standard. Broadband nonlinearly distorted focused pulses were measured successively with the optical reference hydrophone and with the hydrophone to be calibrated using the same excitation conditions. By Fourier transformation of the time wave forms and division of the frequency spectra, the complex-valued frequency response of the hydrophone under test was obtained in a very fast, simple, and efficient way with high and adjustable frequency resolution (increment used here: 0.1 MHz) in a broad frequency range (1–70 MHz). The technique was applied to calibrate both a piezoelectric membrane and a needle-type hydrophone with small sensor element diameter. The amplitude responses obtained were compared with the results of independent calibration techniques such as primary calibration using optical interferometry and secondary calibration using time-delay spectrometry. Within the measurement uncertainties good agreement was achieved (rms deviations: 2.5% and 4.8%, respectively). The phase responses obtained were compared with results of an HTDS calibration which furnished the phase response of the needle-type hydrophone relative to the membrane hydrophone up to 50 MHz, and again very good agreement was found (rms deviation: 2.4°).

The calibration results obtained can be applied to significantly improve the hydrophone measurement results. This was demonstrated by exemplar exposure measurements on a typical diagnostic ultrasound machine in two different operation modes and at various parameter settings. The pulse parameters obtained by the evaluation method commonly applied using the voltage-to-pressure transfer factor at the acoustic working frequency $M(f_{\mathrm{awf}})$ were compared with those obtained by pulse deconvolution using the broadband complex-valued transfer function $M(f)$. The membrane hydrophone was shown to systematically overestimate the positive peak pressure p_+ by up to ~50%, underestimate the rarefactional peak pressure p_- by up to ~11%, and overestimate the pulse intensity integral PII by up to ~28% if no broadband conversion is applied. Using the nonideal needle-type hydrophone all pulse parameters were dramatically overestimated due to the strong variations of the frequency response, but the results could be improved to a large extent using the broadband conversion method whose application was made possible by the pulse calibration data.

The broadband voltage-to-pressure conversion method suggested increases the usable bandwidth of real nonideal hydrophones to a large extent by numerical means. It will not raise the technical expense of exposure measurements very much if the complex-valued transfer function is supplied in an appropriate form, since the calculation of frequency spectra by Fourier transformation should already be implemented for the calculation of the working frequency f_{awf} from the pulses measured. Unlike in the present investigation, the broadband voltage-to-pressure conversion should be performed automatically during the exposure measurements by the data acquisition computer program to allow for correct maximum search procedures when scanning the ultrasound fields.[35–38] It should be noted that current mechanical/cavitation and thermal exposure indices according to the output display standard for diagnostic ultrasound machines are based on measurements of pulse parameters as investigated here (p_-, PII, f_{awf}) along with additional geometrical parameters.[39]

Although theoretical membrane hydrophone models have been suggested which provide complex-valued transfer functions,[14,40] the experimental determination of individual phase responses should be preferred for the same reasons which are widely accepted for individual amplitude calibration of hydrophones: in addition to individual material parameters and manufacturing tolerances, individual geometry parameters are taken into account in the case of needle-type hydrophones in particular.

Due to the dimension and structure of the sound field used, the calibration method described is restricted to hydrophones with 0.2 mm diameter or smaller if no additional corrections for spatial averaging effects are applied. For larger diameters, the uncertainty increases to ranges larger

than commonly achieved by other substitution calibration techniques (in the frequency range where those are available). Improvement may be achievable with other source transducers. Otherwise, the phase data for larger diameter hydrophones may be determined in a form appropriate for impulse deconvolution applications by HTDS substitution calibration using the optical multilayer hydrophone as the primary phase standard and a small diameter hydrophone for transfer. It would also be desirable to reduce and validate the lower limit of the calibration frequency range to 0.5 MHz or even less to fully accomplish the recommendations of measurement guidelines for ultrasound exposimetry, particularly when ultrasound pulses with lower f_{awf} than in this study have to be evaluated.[5,6] This requires first, a larger time window for undisturbed measurements with the optical reference hydrophone to be realized, for instance, by a thicker glass substrate of the sensor element, and second, an appropriate pulse sound field for calibration. Optionally, calibration data obtained with more than one source transducer could be synthesized to obtain a frequency response that covers the complete frequency range in question. Finally, the frequency response of the photodetector of the optical reference hydrophone may be enhanced so that a correction can be dispensed with without accuracy being lost in the deconvolution procedure.

ACKNOWLEDGMENT

The authors wish to thank Walter Molkenstruck for constructing and assembling the pulse generator that causes the source transducer to produce the ultrasound pulses with remarkable broad frequency spectra.

[1] IEC, ''Measurement and characterisation of ultrasonic fields using hydrophones in the frequency range 0.5 MHz to 15 MHz,'' International Electrotechnical Commission Publ. No. 61102, Geneva, 1991.
[2] AIUM/NEMA, ''Acoustic output measurement standard for diagnostic ultrasound equipment,'' NEMA Standards Publ. No. UD 2-1998, 1998.
[3] R. A. Smith, ''The importance of the frequency response of a hydrophone when characterising medical ultrasonic fields,'' Proc. Inst. Acoust. **8**, 119–128 (1986).
[4] G. R. Harris, ''A model of the effects of hydrophone and amplifier frequency response on ultrasound exposure measurements,'' IEEE Trans. Ultrason. Ferroelectr. Freq. Control **38**, 413–417 (1991).
[5] G. R. Harris, ''Pressure pulse distortion by hydrophones due to diminished low frequency response,'' IEEE Trans. Ultrason. Ferroelectr. Freq. Control **42**, 989–992 (1995).
[6] G. R. Harris, ''Are current hydrophone low frequency response standards acceptable for measuring mechanical/cavitation indices?,'' Ultrasonics **34**, 649–654 (1996).
[7] D. R. Bacon, ''Characteristics of a PVDF membrane hydrophone for use in the range 1–100 MHz,'' IEEE Trans. Sonics. Ultrason. **29**, 18–25 (1982).
[8] B. Fay, P. A. Lewin, G. Ludwig, G. M. Sessler, and G. Yang, ''The influence of spatial polarization distribution on spot poled PVDF membrane hydrophone performance,'' Ultrasound Med. Biol. **18**, 625–635 (1992).
[9] B. Fay, G. Ludwig, C. Lankjaer, and P. A. Lewin, ''Frequency response of PVDF needle-type hydrophones,'' Ultrasound Med. Biol. **20**, 361–366 (1994).
[10] Y. Nakamura and T. Otani, ''Study of surface elastic wave induced on backing material and diffracted field of a piezoelectric polymer film hydrophone,'' J. Acoust. Soc. Am. **94**, 1191–1199 (1993).
[11] K. Brendel and G. Ludwig, ''Calibration of ultrasonic standard probe transducers,'' Acustica **36**, 203–208 (1976).
[12] G. Ludwig and K. Brendel, ''Calibration of hydrophones based on reciprocity and time delay spectrometry,'' IEEE Trans. Ultrason. Ferroelectr. Freq. Control **35**, 168–174 (1988).
[13] D. R. Bacon, ''Primary calibration of ultrasonic hydrophones using optical interferometry,'' IEEE Trans. Ultrason. Ferroelectr. Freq. Control **35**, 152–161 (1988).
[14] C. Koch and W. Molkenstruck, ''Primary calibration of hydrophones with extended frequency range 1 to 70 MHz using optical interferometry,'' IEEE Trans. Ultrason. Ferroelectr. Freq. Control **46**, 1303–1314 (1999).
[15] T. J. Esward and S. P. Robinson, ''Extending the frequency range of the NPL primary standard laser interferometer for hydrophone calibration to 60 MHz,'' IEEE Trans. Ultrason. Ferroelectr. Freq. Control **46**, 737–744 (1999).
[16] R. A. Smith and D. R. Bacon, ''A multiple-frequency hydrophone calibration technique,'' J. Acoust. Soc. Am. **87**, 2231–2243 (1990).
[17] P. A. Lewin, ''Calibration and performance evaluation of miniature ultrasonic hydrophones using time delay spectrometry,'' Proceedings of the 1981 IEEE Ultrasonics Symposium, 1981, pp. 660–664.
[18] P. Pesqué and C. Méquio, ''A new and fast calibration method for ultrasonic hydrophones,'' Proceedings of the 1984 IEEE Ultrasonics Symposium, 1984, pp. 743–747.
[19] R. Reibold and W. Molkenstruck, ''Investigation of pulse-excited hydrophones for ultrasonic field measurements using laser interferometry,'' Ultrasonics **25**, 114–118 (1987).
[20] H. Djelouah, J. C. Baboux, and M. Perdrix, ''Pulsed calibration technique of miniature ultrasonic receivers using a wideband laser interferometer,'' Ultrasonics **27**, 80–85 (1989).
[21] G. R. Harris and P. M. Gammell, ''Sensitivity measurements of piezoelectric polymer hydrophones from 0.2 to 2 MHz using a broadband pulse technique,'' J. Acoust. Soc. Am. **105**, 725–731 (1999).
[22] E. G. Radulescu, P. A. Lewin, J. Wójcik, and A. Nowicki, ''Calibration of ultrasonic hydrophone probes up to 100 MHz using time gating frequency analysis and finite amplitude waves,'' Ultrasonics **41**, 247–254 (2003).
[23] C. Koch, ''Amplitude and phase calibration of hydrophones by heterodyne and time-gated time-delay spectrometry,'' IEEE Trans. Ultrason. Ferroelectr. Freq. Control **50**, 344–348 (2003).
[24] V. Wilkens, C. Koch, and W. Molkenstruck, ''Frequency response of a fiber-optic dielectric multilayer hydrophone,'' Proceedings of the 2000 IEEE Ultrasonics Symposium, San Juan, Puerto Rico, 2000, pp. 1113–1116.
[25] V. Wilkens, ''Characterization of an optical multilayer hydrophone for use as broadband ultrasound reference receiver—Comparison with PVDF membrane hydrophones,'' Proceedings of the 2002 IEEE Ultrasonics Symposium, Munich, Germany, 2002, pp. 752–755.
[26] V. Wilkens and C. Koch, ''Optical multilayer detection array for fast ultrasonic field mapping,'' Opt. Lett. **24**, 1026–1028 (1999).
[27] V. Wilkens, ''Characterization of an optical multilayer hydrophone with constant frequency response in the range from 1 to 75 MHz,'' J. Acoust. Soc. Am. **113**, 1431–1438 (2003).
[28] R. C. Singleton, ''Algol procedures for the fast Fourier transform,'' Commun. ACM **11**, 773–776 (1968).
[29] B. Zeqiri and A. D. Bond, ''The influence of waveform distortion on hydrophone spatial-averaging corrections—Theory and measurement,'' J. Acoust. Soc. Am. **92**, 1809–1821 (1992).
[30] H. J. Bleeker and P. A. Lewin, ''A novel method for determining calibration and behaviour of PVDF ultrasonic hydrophone probes in the frequency range up to 100 MHz,'' IEEE Trans. Ultrason. Ferroelectr. Freq. Control **47**, 1354–1362 (2000).
[31] E. G. Radulescu, P. A. Lewin, and A. Nowicki, ''1–60 MHz measurements in focused fields using spatial averaging corrections,'' Ultrasonics **40**, 497–501 (2002).
[32] A. C. Baker and V. F. Humphrey, ''Distortion and high-frequency generation due to nonlinear propagation of short ultrasonic pulses from a plane circular piston,'' J. Acoust. Soc. Am. **92**, 1699–1705 (1992).
[33] V. Wilkens, ''Dielektrische optische Interferenzschichthydrophone zur zeitlich und räumlich hochauflösenden Messung von Ultraschallfeldern,'' Ph.D. dissertation, University of Oldenburg, Germany, 2001, and PTB Report No. PTB-MA-67, 2001, ISBN 3-89701-750-4 (in German).
[34] IEC, ''Requirements for the declaration of the acoustic output of medical diagnostic ultrasonic equipment,'' International Electrotechnical Commission Publ. No. 61157, Geneva, 1992.
[35] G. R. Harris, ''Hydrophone measurements in diagnostic ultrasound fields,'' IEEE Trans. Ultrason. Ferroelectr. Freq. Control **35**, 87–101 (1988).
[36] R. C. Preston, D. R. Bacon, and R. A. Smith, ''Calibration of medical

ultrasonic equipment—Procedures and accuracy assessment,'' IEEE Trans. Ultrason. Ferroelectr. Freq. Control **35**, 110–121 (1988).
[37] M. E. Schafer and P. A. Lewin, ''A computerized system for measuring the acoustic output from diagnostic ultrasound equipment,'' IEEE Trans. Ultrason. Ferroelectr. Freq. Control **35**, 102–109 (1988).
[38] T. L. Szabo, H. E. Melton, Jr., and P. Hempstead, ''Ultrasonic output measurements of multiple mode diagnostic ultrasound systems,'' IEEE Trans. Ultrason. Ferroelectr. Freq. Control **35**, 220–231 (1988).
[39] J. G. Abbott, ''Rationale and derivation of MI and TI—A review,'' Ultrasound Med. Biol. **25**, 431–441 (1999).
[40] P. Gelat, R. Preston, and A. Hurrell, ''Development, validation and publication of a complete theoretical model for hydrophone/amplifier transfer characteristics,'' NPL Report No. CMAM 61, Teddington, UK, National Physical Laboratory, 2001.

Characterization of matched piezoelectric transducer bars

Boris Cugnet and Jamal Assaad[a)]
IEMN, UMR CNRS 8520, Département OAE, Université de Valenciennes et du Hainaut Cambrésis, Le Mont Houy, 59313 Valenciennes Cedex 9, France

Anne-Christine Hladky-Hennion
IEMN, UMR CNRS 8520, Département ISEN, 41 Boulevard Vauban, 59046 Lille Cedex, France

(Received 29 June 2003; accepted for publication 22 March 2004)

To aid the design of linear arrays, it is quite important to have a detailed understanding of the elementary transducer behavior. These transducer bars must be backed and matched. The aim of this work is to characterize and to optimize layers that are used to match such transducer bars. In order to show the influence of these layers, the acoustical (acoustical power, far-field directivity pattern), electrical (electrical impedance) and mechanical (displacement field) parameters of the transducer are computed using the finite element method. Numerical studies of several transducers with different ideal matching layers which satisfy the one-dimensional criterion are presented and carefully analyzed. These studies show the existence of parasitic modes in the desired operating band of the transducer, due to shear wave propagation in the matching layer. A simple choice criterion of the matching material suggesting no parasitic mode in the desired operating band of the transducer bar has been defined. This criterion is given by $W<\lambda_S/2$, where W is the width of the transducer and λ_S is the shear wavelength of the matching layer at the working frequency. Finally, experimental results of a matched transducer bar are successfully compared with numerical ones.
© *2004 Acoustical Society of America.* [DOI: 10.1121/1.1739486]

PACS numbers: 43.38.Ar, 43.40.Rj, 43.20.Tb [AJZ] Pages: 2904–2913

I. INTRODUCTION

Ultrasonic transducer arrays are widely used in imaging applications, such as medical diagnosis, nondestructive evaluation, and underwater acoustics. Designing better transducer arrays is the critical issue for improving the quality of ultrasonic imaging. For this purpose, it is necessary to obtain better fundamental understanding of the transducer behavior in order to design new and better arrays. Many issues in array transducer design—such as interelement cross coupling,[1–4] subdicing effects, baffle effect[5]—cannot be accurately studied using analytic methods—like the one-dimensional Mason model[6,7] or the transmission line model of Krimholtz, Leedom, and Matthaei[8,9]–due to the complexity of the electromechanical boundary value problem. Thus, the finite element method (FEM) is the appropriate tool to obtain more detailed information. In fact, the FEM allows one to model transducers of complex geometry and any materials. Furthermore, no simplifying assumption is made on the displacement field of the transducer and perfect radiation conditions are used.

A linear array consists of multiple parallel and identical long piezoelectric bars separated by a finite distance (interelement spacing). Epoxy is generally used to fill the array.[1,2] Usually, a backing with a high acoustic absorption coefficient is employed[10] in order to limit the number of periods in a pulse generated by ultrasonic transducers. One or more matching layers are bonded to the top of the array—between the piezoelectric material, such as ferroelectric ceramic (PZT) or piezoelectric crystal ($LiNbO_3$), and water load—in order to improve the transmission and bandwidth properties of the transducer. The use of continuous matching layer is limited by laterally propagating waves that couple energy into neighboring array elements and into the load medium.[11] The resulting interelement, cross—coupling and sidelobes are unacceptable in many array applications. An obvious solution is to dice the matching layer, penetrating fully if possible, and thus, cross-coupling is minimized; but sometimes at the expense of anomalous local modes and compromised radiation patterns.[11] Most linear arrays have one or two completely diced matching layers. In order to aid the design of high frequency transducer arrays, it is quite important to have a detailed understanding of the elementary transducer behavior.

Thus, the aims of this paper are the analysis and the optimization of matched transducer bars behavior. In this way, a two-dimensional (2D) finite element model (with the help of the ATILA code[12]) is used. In fact, the transducer bar length is quite larger than the two other dimensions; therefore, for the purpose of transducer analysis, this length can be considered as infinite and the plane strain approximation can be assumed. This 2D finite element model allows harmonic analysis of a piezoelectric transducer mounted in a rigid (or soft) baffle and radiating into water. From finite element results, acoustical, electrical, and mechanical parameters are defined in order to describe the matched transducer behavior.

In this paper, Sec. II presents analytical results provided by a one-dimensional model and for the modeling of a backed and matched transducer plate. These results allow direct comparison between transducer plate and transducer bar. Then, Sec. III gives a brief description of the 2D finite

[a)]Electronic mail: jamal.assaad@univ-valenciennes.fr

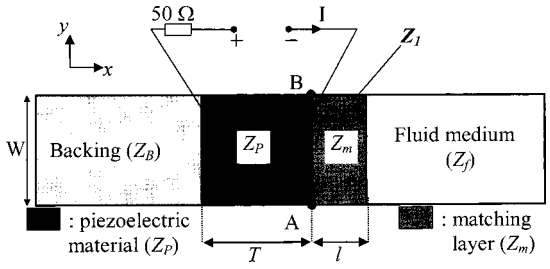

FIG. 1. In-water backed and matched transducer.

element approach and the method adopted in order to take into account electrical matching in the numerical procedure. Section IV introduces the notion of acoustical power. Finally, in Sec. V, a numerical study has been performed measuring the influence of a quarter wave matching layer, with intermediate acoustical impedance, on the transducer behavior. Two piezoelectric materials are used: PZT5H and $LiNbO_3$. This numerical study shows the existence of parasitic modes in desired operating band of the transducer, due to shear wave propagation in the matching layer. A choice criterion of the matching material is defined which can suggest no parasitic mode in the desired operating band of the transducer bar. Experimental results are provided which are in good agreement with the numerical ones.

II. ELECTRICAL IMPEDANCE AND ACOUSTICAL POWER OF A BACKED AND MATCHED TRANSDUCER PLATE (ONE-DIMENSIONAL MODEL)

In order to understand the behavior of the backed and matched transducer bar, a transducer plate is studied in this section. This allows a direct comparison between these transducers. Figure 1 shows a backed and matched transducer plate loaded with water. The fluid medium and the backing are assumed to be semi-infinite media; furthermore, the width W and the length L (in the z direction, see Fig. 1) are supposed to be much greater than the thickness T. In these conditions, the one-dimensional (1D) hypothesis can be assumed. Then using Mason's circuit, the electrical impedance (Z) and the radiated acoustical power (P_a) in the fluid medium can be analytically computed and are given by[6]

$$Z=\frac{1}{jC_0\omega}+\frac{k^2Z_P}{\pi C_0\omega f_n}\times\left[\frac{2Z_P(\cos(\pi f_n)-1)+j(Z_1+Z_B)\sin(\pi f_n)}{Z_P(Z_1+Z_B)\cos(\pi f_n)+j(Z_P^2+Z_1Z_B)\sin(\pi f_n)}\right], \tag{1}$$

$$P_a=\frac{k^2Z_P|I|^2}{\pi\omega C_0 f_n}\mathrm{Re}(Z_1)\times\left|\frac{Z_P(\cos(\pi f_n)-1)+jZ_1\sin(\pi f_n)}{Z_P(Z_B+Z_1)\cos(\pi f_n)+j(Z_P^2+Z_BZ_1)\sin(\pi f_n)}\right|^2, \tag{2}$$

where C_0 is the clamped static capacitance of the transducer, ω is the angular frequency ($\omega=2\pi f$, f being the frequency),

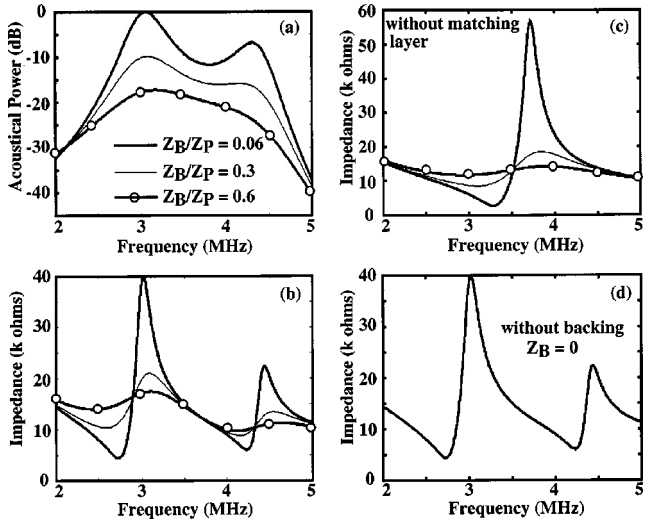

FIG. 2. Electrical impedance and acoustical power computed vs frequency (1D model) for different values of Z_B/Z_P. Electrical impedance (a) and acoustical power (b) of a backed and matched transducer plate radiating into water. (c) Electrical impedance for backed transducer. (d) Electrical impedance for matched transducer.

k is the electromechanical coupling coefficient, f_n is the normalized frequency ($f_n=f/f_0$), f_0 is the half-wavelength resonance frequency ($T=\lambda_0/2$ with $\lambda_0=V_{LP}/f_0$ and V_{LP} is the longitudinal wave speed of the piezoelectric material), and I is the entering electrical current (Fig. 1). Finally, Z_P is the real specific acoustic impedance of the piezoelectric material and Z_1 is the impedance seen at AB (Fig. 1) given by

$$Z_1=Z_m\frac{Z_f\cos\left(\frac{\omega l}{c_l}\right)+jZ_m\sin\left(\frac{\omega l}{c_l}\right)}{Z_m\cos\left(\frac{\omega l}{c_l}\right)+jZ_f\sin\left(\frac{\omega l}{c_l}\right)}, \tag{3}$$

where Z_f is the real specific acoustic impedance of the fluid medium; l, Z_m, and c_l are, respectively, the thickness, the real specific acoustic impedance, and the longitudinal wave speed in the matching layer.

A backed and matched $LiNbO_3$ plate is considered with $Z_P=34.7$ MRayls, $V_{LP}=7400$ m/s, $k^2=0.24$, $T=1$ mm, $C_0=3.5$ pF for $A=10\,\mathrm{mm}^2$, where A is the surface of the transducer. The choice of the thickness and material characteristics of the matching layer has been made with the help of the well-known 1D model: the thickness is equal to $\lambda_m/4$ at the electrical antiresonance frequency f_0 (where λ_m is the longitudinal wavelength of the matching layer, $f_0=V_{LP}/(2T)=3.7$ MHz) and the acoustical impedance Z_m is intermediate ($Z_m=\sqrt{Z_PZ_f}$). Figures 2(a) and (b) describe, respectively, the acoustical power and the electrical impedance computed [from Eqs. (1) and (2)] of a backed and matched transducer plate radiating into water. Figures 2(c) and (d) present the electrical impedance of a backed and matched transducer plate, respectively. Three different backings are considered and are represented by the ratio Z_B/Z_P. These acoustical powers are always normalized by the maximum of one of them. As is well known, Figs. 2(a) and (b) show that there

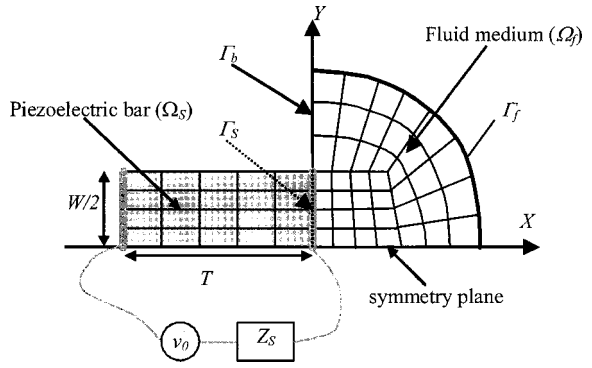

FIG. 3. Finite element mesh used to analyze the in-water radiation of a piezoelectric bar.

are two longitudinal coupled modes around the resonance frequency.[10] The presence of these two coupled modes, which contribute to increase the bandwidth of the transducer, is due to matching layer and not to the backing [see Figs. 2(c) and (d)].

The electrical impedances of the backed transducers reach a maximum at the electrical antiresonance frequency ($f_0 = 3.7$ MHz) and a minimum at the electrical resonance frequency. It is well known that when the ratio Z_B/Z_P increases, the bandwidth increases while the sensitivity decreases.[10] Consequently, the choice of acoustical impedance of backing material results in a compromise between sensitivity and bandwidth. When the backing is chosen correctly in order to absorb the outgoing wave, it cannot play a major role on the displacement field of the radiated surface (in contact with water) of the transducer. Moreover, when the transducer bar (without backing and matching layer) vibrates like a piston mode, the backed transducer bar still vibrates like a piston mode (see Fig. 9 in Ref. 13). In order to reduce the number of figures and to focus on the role of the matching layer the backing will be omitted in the following sections.

III. TWO-DIMENSIONAL FINITE ELEMENT MODEL

A. Brief description of the FEM approach

The finite element method is not detailed here. Its description can be found, for example, in Zienkiewicz's book,[14] and only the general equations are shown in this section for a 2D fluid-structure problem. The plane strain approximation is considered in the following study because the transducer length (L) is assumed to be much larger than the two other dimensions. The harmonic state is assumed and the $e^{j\omega t}$ term is implicit. Notations are defined in Fig. 3. The structure Ω_S (a piezoelectric bar of thickness T, width W, and length L) is in contact with the fluid domain Ω_f through the surface Γ_S. Ω_f is limited by a rigid baffle (Γ_b) and by a circular boundary (Γ_f) of radius (R) surrounding the fluid medium. Only one half of the domain is meshed due to symmetry. Γ_f, Γ_b, Ω_f, Γ_S, and Ω_S are divided into finite elements connected by nodes. Quadratic interpolation elements[12] are used. The physical quantities of interest are the displacement field $\mathbf{u}$, the electrical potential φ, and the pressure field p. Their nodal values are the unknowns of the problem and are, respectively, arranged in nodal vectors $\mathbf{U}$, $\mathbf{\Phi}$, and $\mathbf{P}$. Using the fact that electrical charges only appear on electrodes, assuming that "hot" electrodes are all connected to the same potential, denoted $\mathbf{\Phi}_e$, and that the reference electrodes are grounded, the resulting system of equations is[12]

$$\begin{bmatrix} [K_{uu}]-\omega^2[M] & [K^i_{u\Phi}] & K^e_{u\Phi} & -[L] \\ [K^i_{u\Phi}]^T & [K^{ii}_{\Phi\Phi}] & K^{ie}_{\Phi\Phi} & [0] \\ K^e_{u\Phi}{}^T & K^{ie}_{\Phi\Phi}{}^T & K^{ee}_{\Phi\Phi} & [0] \\ -\rho^2c^2\omega^2[L]^T & [0] & [0] & [H]-\omega^2[M_1] \end{bmatrix} \begin{bmatrix} \mathbf{U} \\ \mathbf{\Phi}_i \\ \mathbf{\Phi}_e \\ \mathbf{P} \end{bmatrix} = \begin{bmatrix} \mathbf{0} \\ \mathbf{0} \\ -\dfrac{I}{j\omega} \\ \rho c^2 \mathbf{\Psi} \end{bmatrix}, \tag{4}$$

where $\mathbf{\Phi_i}$ and $\mathbf{\Psi}$ are vectors which contain the nodal value of, respectively, the unknown potential and the normal derivative of the pressure on the external fluid domain boundary Γ_f (Fig. 3). $[K_{uu}]$, $[K_{\Phi\Phi}]$, and $[K_{u\Phi}]$ are the electroelastic stiffness matrices; $[M]$ is the consistent mass matrix; $[L]$, $[H]$, and $[M_1]$ are, respectively, the connectivity matrix that represents the coupling between the structure and the fluid, the fluid compressibility, and the consistent mass matrix. I is the current entering the structure. ρ and c are, respectively, the mass density and the sound speed of the fluid (water). In the case of elastic materials, the $[K_{\Phi\Phi}]$ and $[K_{u\Phi}]$ matrices vanish. Moreover, it is necessary to know the values of Y, ν, and ρ to compute the $[K_{uu}]$ matrix.

The third line of Eq. (4) provides the electrical impedance of the piezoelectric structure:

$$\frac{1}{Z} = \frac{-j\omega}{\mathbf{\Phi}_e}\{K^e_{u\Phi}{}^T\mathbf{U} + K^{ie}_{\Phi\Phi}{}^T\mathbf{\Phi}_i + K^{ee}_{\Phi\Phi}\mathbf{\Phi}_e\}. \tag{5}$$

Minima and maxima of this impedance correspond, respectively, to resonance and antiresonance frequencies (f_r and f_a) of successive vibration modes.[15] The resolution of the system (4) gives the nodal values of pressure field, displacement field, and electrical potential. The radiated near field of the transducer can be easily obtained using the finite element method if dipolar damping elements are attached to the mesh external circular boundary Γ_f (Ref. 16) (Fig. 3). These elements are specifically designed to absorb completely the first two components of the asymptotic expansion of the radiated field. The far-field pressure is then computed with the help of an extrapolation method.[16]

B. Electrical matching

Consider a source of impedance Z_S and a load Z_l; there is impedance matching between the source and the load if their real parts are equal and their imaginary parts are opposite, i.e., $Z_S = Z_l^*$. With electrical matching, half the total

power is dissipated in the load and the other part in the source. The role of impedance matching is to limit undesirable effects of current which can return to the source.

In order to take into account electrical matching in the numerical problem [(Eq. (4))], the potential applied on electrodes $\mathbf{\Phi_e}$ is given by

$$\mathbf{\Phi_e} = v_0 - Z_S I, \tag{6}$$

with $Z_S = Z_g + Z_a$. Generally, Z_g is equal to 50 Ω and the impedance Z_a is chosen equal to $Z_l^* - 50$ at the working frequency in order to get electrical matching. Equation (6) can be integrated to the system of Eq. (4) by eliminating the electrical current I:

$$\begin{bmatrix} [K_{uu}]-\omega^2[M] & [K^i_{u\Phi}] & K^e_{u\Phi} & -[L] \\ [K^i_{u\Phi}]^T & [K^{ii}_{\Phi\Phi}] & K^{ie}_{\Phi\Phi} & [0] \\ K^{e\ T}_{u\Phi} & K^{ie\ T}_{\Phi\Phi} & K^{ee}_{\Phi\Phi} - \dfrac{1}{j\omega Z_S} & [0] \\ -\rho^2 c^2 \omega^2 [L]^T & [0] & [0] & [H]-\omega^2[M_1] \end{bmatrix} \begin{bmatrix} \mathbf{U} \\ \mathbf{\Phi}_i \\ \mathbf{\Phi}_e \\ \mathbf{P} \end{bmatrix} = \begin{bmatrix} \mathbf{0} \\ \mathbf{0} \\ -\dfrac{v_0}{j\omega Z_S} \\ \rho c^2 \Psi \end{bmatrix}. \tag{7}$$

Then, this resulting system of equations can be solved by fixing the parameters v_0 and Z_S.

IV. ACOUSTICAL POWER

Let us consider a fluid medium Ω_f, limited by a surface Γ_f, surrounding a vibrating structure Ω_S [Fig. 4(a)]. The acoustical intensity $\vec{I}$ is defined as[17] the flow of energy through a unit area normal to the direction of propagation per unit time. This flow of instantaneous power is the product of the instantaneous pressure p by the instantaneous speed $\vec{v}$. In most cases, the time average of acoustical intensity is more significant than its instantaneous value and given by[17]

$$\vec{I}_{\text{av}} = \tfrac{1}{2}\,\text{Re}(p\vec{v}^*), \tag{8}$$

where the units of $\vec{I}_{\text{av}}$ are watts per square meter (W/m^2). In Eq. (8), p and $\vec{v}$ are complex expressions of pressure and instantaneous speed.

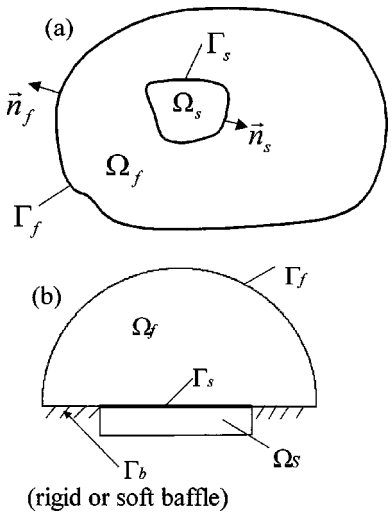

FIG. 4. (a) Schematic description of the structure and fluid domains. (b) Case of a piezoelectric structure mounted on a rigid or a soft baffle and radiating into water.

If the surface Γ_f encloses the source [Fig. 4(a)], e.g., a vibrating solid Ω_S, the average acoustical power radiated by Ω_S can be expressed as

$$P_a = \int\int_{\Gamma_f} \vec{I}_{\text{av}} \cdot \vec{n}_f \, d\Gamma, \tag{9}$$

where $\vec{n}_f$ is the unit normal vector pointing out of the volume Ω_f containing the source. The unit of P_a is watts.

If we consider the case of the radiation of a vibrating structure mounted on an infinite rigid (or soft) baffle [Fig. 4(b)], the acoustical power P_a can be expressed using Eq. (9) because Neumann ($\vec{v}=0$) or Dirichlet ($p=0$) conditions are imposed on the infinite baffle (Γ_b); in fact, the flow of energy through Γ_b is null.

A possibility to compute acoustical power transmitted by the transducer bar (Fig. 3) to the fluid medium consists in calculating the flow of energy through the surface Γ_f. In fact, if the surface Γ_f is in the far field of the source, there is a relation between pressure and particle speed:

$$p = \rho c v, \tag{10}$$

where ρ and c are, respectively, the fluid density and the sound speed equal to 1500 m/s. The 2D finite element model giving the nodal value of pressure in far field,[16] P_a, which is given by Eq. (9) is then equal to

$$P_a = \frac{1}{2\rho c} \int\int_{\Gamma_f} |p|^2 d\Gamma, \tag{11}$$

where Γ_f is in the far field of the source.

V. MODELING OF MATCHED PIEZOELECTRIC BARS

Many papers have shown how to achieve high bandwidth/efficiency using multiple matching layers, with the help of the 1D design formalism[9,18,19] determining the optimal number of discrete layers and their acoustical impedances. However, these models do not take into account the lateral waves in the matching layers. In medical arrays, these lateral modes (parasitic mode in this case) generate laterally propagating waves that increase the cross-coupling between

TABLE I. Mechanical, dielectric, and piezoelectric constants of piezoelectric materials used for the numerical study.

Parameters	PZT5H	C4-Q	$LiNbO_3$
Mass density ρ (kg/m^3)	7500	7650	4700
S_{11}^E (m^2 N^{-1})	1.65×10^{-11}	1.06×10^{-11}	0.5774×10^{-11}
S_{12}^E (m^2 N^{-1})	-4.78×10^{-12}	-3.3×10^{-12}	-0.101×10^{-11}
S_{13}^E (m^2 N^{-1})	-8.45×10^{-12}	-4.5×10^{-12}	-0.145×10^{-11}
S_{33}^E (m^2 N^{-1})	2.07×10^{-11}	1.3×10^{-11}	0.4974×10^{-11}
S_{44}^E (m^2 N^{-1})	4.35×10^{-11}	2.2×10^{-11}	1.6972×10^{-11}
S_{66}^E (m^2 N^{-1})	4.256×10^{-11}	2.8×10^{-11}	1.3578×10^{-11}
d_{15} (m V^{-1})	7.41×10^{-10}	2.8×10^{-10}	0.6788×10^{-10}
d_{31} (m V^{-1})	-2.74×10^{-10}	-1.08×10^{-10}	-0.942×10^{-12}
d_{33} (m V^{-1})	5.93×10^{-10}	2.4×10^{-10}	0.5883×10^{-11}
ϵ_{11}^S (F m^{-1})	1.4025×10^{-8}	1.01×10^{-8}	0.389×10^{-9}
ϵ_{33}^S (F m^{-1})	1.3×10^{-8}	5.91×10^{-9}	0.257×10^{-9}

neighboring elements and consequently the far-field directivity pattern is damaged. Thus, the advantage of the 2D finite element model is that it can take into account this kind of phenomenon. Moreover, it allows optimization of these layers in order to eliminate parasitic modes.

A layer whose thickness and specific acoustical impedance are, respectively, equal to $\lambda_m/4$ and $Z_m=\sqrt{Z_P Z_f}$, is named ideal. In the following, an ideal quarter wave layer is always used. These values have been obtained by considering the well-known 1D theory. Results provided by the 1D model (see Sec. II) concerning matched piezoelectric transducer plate have shown that there are two longitudinal coupled modes around the resonance frequency. It will be shown that similar results in the case of a piezoelectric bar matched by an ideal quarter wave layer can be obtained only under certain conditions (see Sec. V C). Contrary to the transducer plate (1D case), the electrical resonance frequencies for the transducer bar (2D case) do not correspond to the mechanical resonance frequencies. For this reason the acoustical power is more significant that the electrical impedance. A good discussion concerning electrical and mechanical resonance can be found in Ref. 20. The acoustical power reaches maximums at these mechanical resonance frequencies. In fact, this power is proportional to the displacement field of the radiated surface of the transducer.

A. Behavior of piezoelectric bars with a quarter wave matching layer

It is well known that for an elastic material (matching material) the longitudinal and shear wave speeds are function of the Young modulus (Y), the Poisson's ratio (ν), and the mass density (ρ) and are given by

TABLE II. Mechanical parameters of elastic materials MAT1 and MAT2.

Parameters	MAT1	MAT2
Y (Kg/m s^2)	1.59×10^{10}	9.78×10^9
$\nu(-)$	0.33	0.33
ρ (kg/m^3)	2197	3625
c_l (m/s)	3300	2000
c_S (m/s)	1650	1007

$$c_l=\sqrt{\frac{Y(1-\nu)}{\rho(1+\nu)(1-2\nu)}}, \tag{12}$$

$$c_s=\sqrt{\frac{Y}{2\rho(1+\nu)}}. \tag{13}$$

In this section, two kinds of transducer bars are considered: PZT5H ($Z_p=34.5$ MRayls, see Table I) and $LiNbO_3$ (Y1Z1w/36° cut, $Z_p=34.7$ MRayls, see Table I). For the two transducers the width to thickness ratios W/T are chosen equal to 0.5 with $T=1$ mm. Two ideal quarter wave layers described, respectively, by MAT1 and MAT2 (see Table II) will be used. Their specific acoustic impedances are equal to ($Z_m=7.25$ MRayls$\approx\sqrt{Z_P Z_f}$). Moreover, the thickness of the matching layer is calculated from

$$l=\frac{\lambda_l}{4}=\frac{c_l}{4f_r}. \tag{14}$$

It is important to note that it is possible to consider another frequency in Eq. (14). In the following, electrical resonance frequency[15] (i.e., f_r) is always chosen for the acoustical and electrical matching (see Sec. III B). It is important to note that other frequencies can be considered.

The mesh of a piezoelectric bar, with the ideal quarter wave matching layer, radiating into water is shown in Fig. 5. Only one half of the domain is meshed due to symmetry. Figure 6 presents the acoustical power, versus frequency, computed for the above-mentioned transducers matched with the MAT1 or MAT2 layer. As the backing is not considered

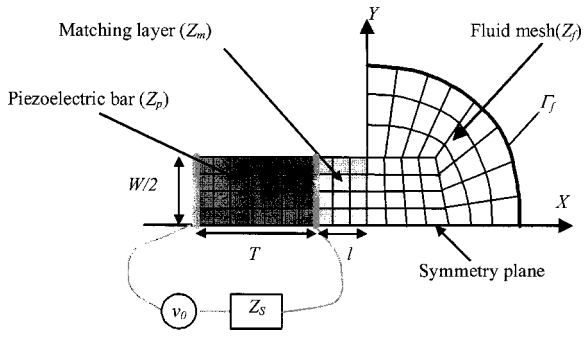

FIG. 5. Finite element mesh used to analyze the matched piezoelectric bar ($T=1$ mm, $W/T=0.5$) radiating into water.

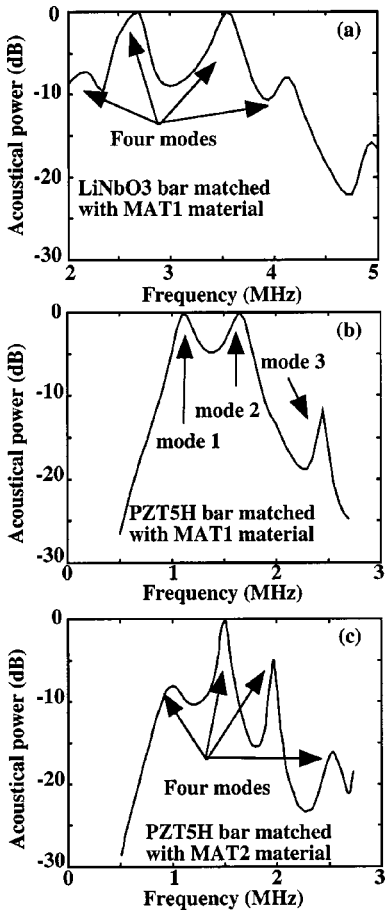

FIG. 6. Variations of acoustical power, vs frequency, computed for (a) the $LiNbO_3$ bar matched by the MAT1 quarter wave matching layer, (b) the PZT5H bar matched by the MAT1 quarter wave matching layer, (c) the PZT5H bar matched by the MAT2 quarter wave matching layer.

($Z_B=0$), this acoustical power is equal to the electrical power. It is important to note that, in all cases, one or several parasitic modes are generated. These parasitic modes exhibit lateral motion of the matching layer. The one-dimensional model cannot predict these parasitic modes because it does not take into account shear wave propagation in the matching layer. In order to get a good analysis of these different modes it is important to compute their displacement field and their far-field directivity.

For the $LiNbO_3$ transducer matched with MAT1 [Fig. 6(a)], four coupled modes appear. None of these modes is a piston mode (or thickness mode). In fact, Figs. 7(a) and (b) show, respectively, the imaginary part of the relative displacement field and far-field directivity pattern at $f=3$ MHz (second mode). As $e^{j\omega t}$ is implicit and the applied potential is retained as reference, imaginary displacement field displays the picture of the true transducer vibration at the instant $t=\tau/4$, where $\tau=2\pi/\omega$ is the period. The displacement field shows an harmonic vibration of the matching layer which generates two main lobes in the far-field directivity pattern [Fig. 7(b)]: in the axial direction ($\theta=0°$) and in the lateral direction ($\theta=90°$). For the other modes, their displacement fields show the same phenomena (i.e., harmonic vibration).

Figure 6(b) shows the acoustical power, versus frequency, computed for a PZT5H bar matched with MAT1 layer. It appears on this graph that three coupled modes exist: the first one is at 1.2 MHz, the second one is at 1.8 MHz, and the last one is at 2.5 MHz. Between 1 and 2 MHz, the transducer vibrates like a piston mode. Figures 8(a) and (b) show, respectively, the imaginary part of the relative displacement

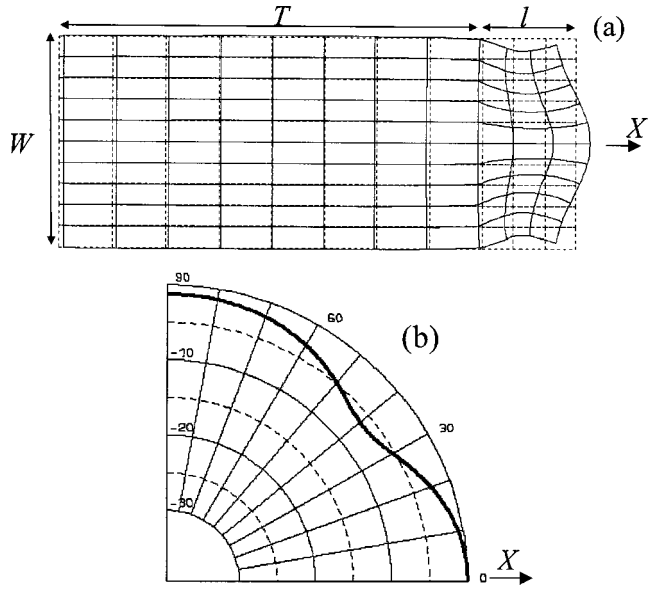

FIG. 7. Displacement field (a) and far-field directivity pattern (b) computed at the frequency $f=2.8$ MHz of a $LiNbO_3$ bar ($T=1$ mm, $W/T=0.5$ and $L=2$ cm) matched with the MAT1 quarter wave matching layer and radiating into water (2D modeling).

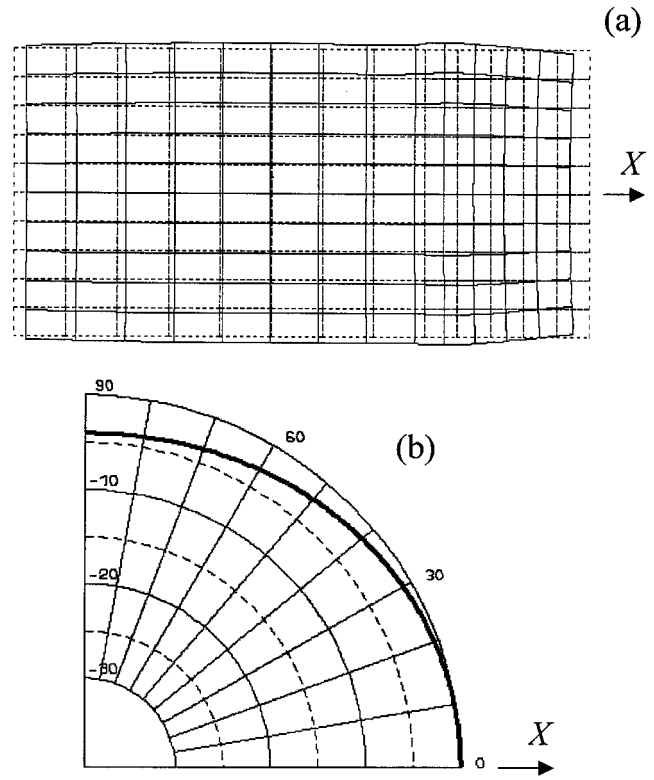

FIG. 8. Displacement field (a) and far-field directivity pattern (b) computed at the frequency $f=2$ MHz (second mode) of a PZT5H bar ($T=1$ mm, $W/T=0.5$, and $L=2$ cm) matched with the MAT1 quarter wave matching layer and radiating into water (2D modeling).

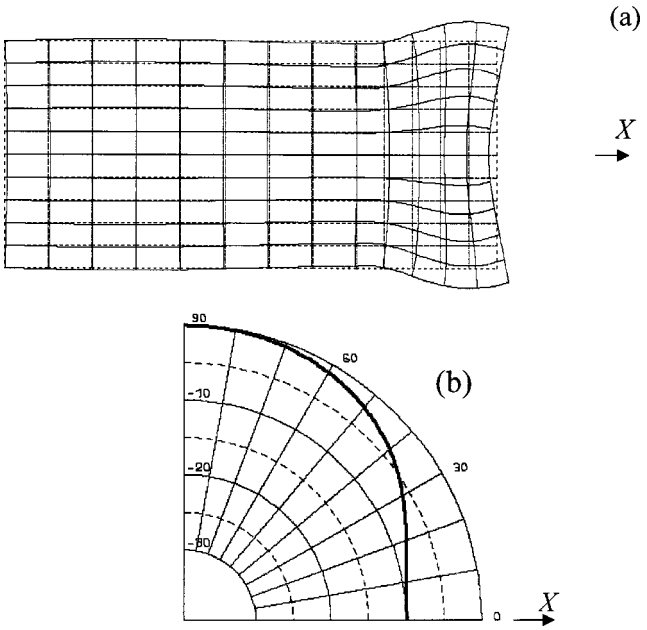

FIG. 9. Displacement field (a) and far-field directivity pattern (b) computed at the frequency $f=2.5$ MHz (third mode) of a PZT5H bar ($T=1$ mm, $W/T=0.5$, and $L=2$ cm) matched with the MAT1 quarter wave matching layer and radiating into water (2D modeling).

field and far-field directivity pattern, computed at the frequency $f=1.8$ MHz (second mode). These parameters almost perfectly characterize a thickness mode of the transducer with a far-field directivity pattern having a main lobe in the axial direction (OX). These two first coupled modes are those predicted by the one-dimensional model (see Sec. II). Figures 9(a) and (b) show, respectively, displacement field and far-field directivity pattern, computed at the frequency $f=2.5$ MHz (third mode). This vibration mode exhibits more lateral motion of the matching layer and thus the far-field directivity pattern does not characterize a piston mode. However, in this case this mode is sufficiently distant of the -3 dB band of the transducer and thus, it does not disturb the piston mode behavior of the transducer between 1 and 2 MHz.

Figure 6(c) presents the acoustical power, versus frequency, computed for a PZT5H bar matched with MAT2 layer. Four coupled modes appear in the bandwidth of the transducer. None of these modes is a piston mode (or thickness mode). In fact, their displacement fields show harmonic vibrations of the matching layer.

Results obtained by the finite element modeling of the previous three matched transducers allow us to conclude that the criteria proposed by the one-dimensional model are not enough to suggest a good matching of piezoelectric bars. In fact, the existence of parasitic modes, due to shear wave propagation, disturbs the piston mode behavior of the matched transducer. But, it is interesting to note that the characteristic of an ideal quarter wave layer (i.e., $l=\lambda_l/4$, and $Z_m=\sqrt{Z_P Z_f}$) can be obtained with different values of longitudinal and shear wave speeds [see Eqs. (12) and (13)]. Then, the next section gives numerical simulations which allows one to bring to the fore the influence of all these parameters to obtain a good criterion for the choice of matched quarter wave layers.

TABLE III. Mechanical parameters (Young modulus Y, Poisson's ratio ν, mass density ρ, longitudinal wave speed c_l, and shear wave speed c_s) of matching materials used for the numerical study. Each case defines a matching material, with its specific Y, ν, ρ, c_l, and c_S, which have an acoustical impedance of 7.25 Mrayls.

	ν			
c_l (m/s)	0.15	0.2	0.25	0.33
3300	$Y=2.26E+10$ $\rho=2197$ $c_s=2117$	$Y=2.15E+10$ $\rho=2197$ $c_s=2020$	$Y=1.99E+10$ $\rho=2197$ $c_s=1905$	$Y=1.59E+10$ $\rho=2197$ $c_s=1650$
4000	$Y=2.74E+10$ $\rho=1812$ $c_s=2564$	$Y=2.6E+10$ $\rho=1812$ $c_s=2450$	$Y=2.4E+10$ $\rho=1812$ $c_s=2301$	$Y=1.95E+10$ $\rho=1812$ $c_s=2000$
4600	$Y=3.15E+10$ $\rho=1576$ $c_s=2951$	$Y=3.0E+10$ $\rho=1576$ $c_s=2816$	$Y=2.78E+10$ $\rho=1576$ $c_s=2655$	$Y=2.25E+10$ $\rho=1576$ $c_s=2300$
5400	$Y=3.7E+10$ $\rho=1342$ $c_s=3465$	$Y=3.52E+10$ $\rho=1342$ $c_s=3305$	$Y=3.26E+10$ $\rho=1342$ $c_s=3117$	$Y=2.64E+10$ $\rho=1342$ $c_s=2700$

B. Influence of mechanical and geometrical parameters characterizing the matching layer

The mechanical parameters (Y, ν, and ρ) and the geometrical dimensions of layers can characterize them perfectly. Then the 2D finite element model is used in order to take into account the geometry and mechanical parameters of such layers. The $LiNbO_3$ transducer bar is chosen for this study. Similar results can be obtained by considering the PZT5H transducer bar.

In the following, several fictitious materials described by their mechanical parameters and shown in Table III are used in order to get ideal layers. Each case of Table III defines an ideal layer with Z_m equal to 7.25 Mrayls. The thickness of these layers is always equal to quarter wavelength [Eq. (14)]. In each case, the longitudinal and the shear wave speeds can be computed using Eqs. (12) and (13). All along the study, the thickness and the length of the piezoelectric bars are equal to 1 and 20 mm, respectively. In the following, two cases are considered.

1. First case: W/T=0.5, T=1 mm, c_l and c_S are variable

Simulations are performed in order to evaluate the influence of longitudinal wave speed on the transducer behavior; matching materials used are situated on the fourth column of Table III (Poisson's ratio $\nu=0.33$). Figures 10(a) and (d) display acoustical powers and electrical impedance computed for different values of c_l. For a value of c_l smaller than 5400 m/s, a mode appears between 4 and 5 MHz, which is a parasitic mode (shear wave propagation in the matching layer). The maximum of these powers correspond to the mechanical resonance frequencies which are not equal to the electrical resonance frequencies. We can notice that when the longitudinal wave speed increases, the parasitic mode moves away from the bandwidth of the transducer. This parasitic mode

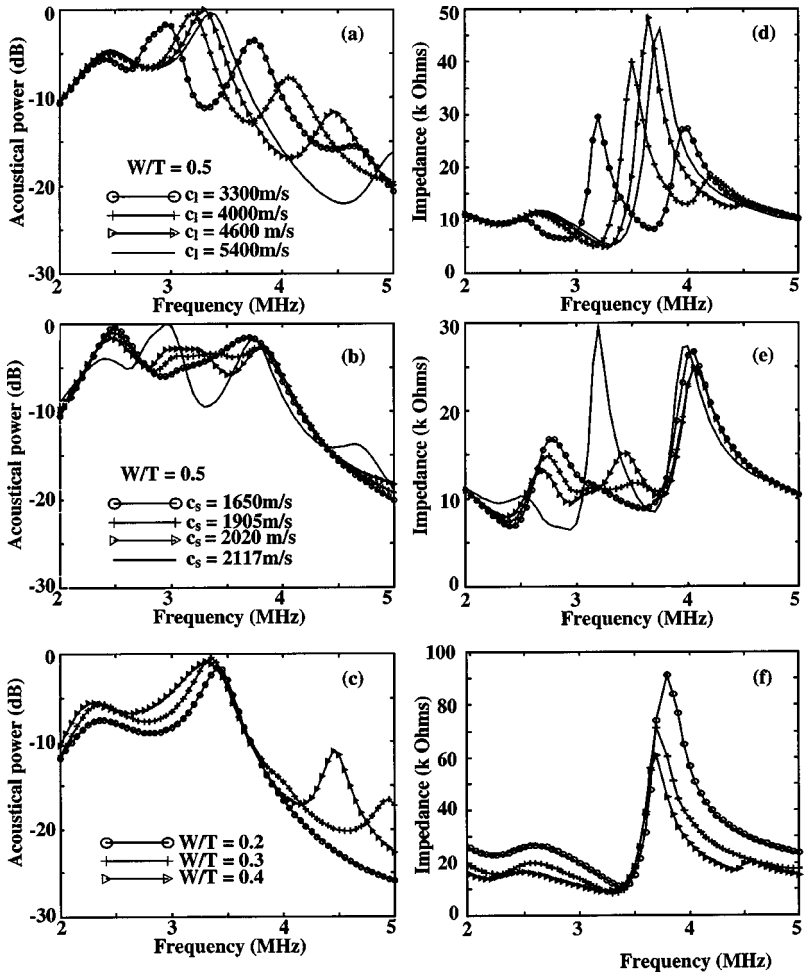

FIG. 10. Acoustical power and electrical impedance are computed vs frequency for different values of c_l, c_s and (W/T). (a) and (d) are obtained for W/T=0.5 and for different values c_l. (b) and (e) are obtained for W/T =0.5 and for different values c_s. (c) and (f) are obtained for c_l=3300 m/s (ν=0.33) and for different values of W/T.

does not appear on the graph from a value of c_l greater than or equal to 5400 m/s. In this case, we find two piston modes (already predicted by the one-dimensional theory). Moreover, when the longitudinal wave speed value is increasing, for a given ν, the shear wave speed of the matching material is increasing too (the fourth column of Table III). Another way to evaluate the influence of shear wave speed is to fix the longitudinal wave speed of matching material and to vary the Poisson's ratio ν (any line of Table III). Thus, Figs. 10(b) and (e) present acoustical powers and electrical impedances obtained by the modeling of a $LiNbO_3$ bar with a quarter wave matching layer (c_l=3300 m/s) and with a variable shear wave speed (first line of Table III). The increasing of ν (i.e., a decreasing of shear wave speed in the matching material) brings to the fore the appearance of a parasitic mode between 3 and 3.5 MHz. Thus, increasing of shear wave speed implies the suppression of parasitical modes.

2. Second case: W/T is variable, T=1 mm, c_l and c_S are fixed

In this case, the most inconvenient case (lots of parasitic modes) is considered with W/T=0.5, c_l=3300 m/s, and ν=0.33 (first line and fourth column). This case is reconsidered in order to study the influence of the width W of the matched transducer. In fact, the width of the transducer plays a major role in the appearance of parasitic modes. Figures 10(c) and (f) show the results obtained when considering four transducers of different width-to-thickness ratio ($0.2 < W/T < 0.5$). The decreasing of the ratio W/T implies the vanishing of parasitic modes. In the case of W/T=0.2, two coupled modes are obtained, already predicted by the one-dimensional theory.

C. Choice criterion of the matching material

The previous numerical studies show that it is necessary to get a choice criterion that suggests a piston mode in all the bandwidth of the transducer. By analyzing these numerical studies, a choice criterion is defined, which is function of the width of the transducer (W), the shear wave speed in the matching layer (c_S), and the resonance frequency of the piezoelectric bar (f_r). Thus, the behavior of a piezoelectric bar with an ideal quarter wave matching layer is identical to that predicted by the one-dimensional theory (no shear wave propagation in the matching layer) if W, c_s, and f_r satisfy the following relation:

$$W < \frac{c_s}{2f_r} = \frac{\lambda_S}{2}. \tag{15}$$

This criterion means that if the width of the matched transducer is smaller than half the shear wave length (λ_S) in the matching layer, then the behavior of the transducer is not disturbed by shear wave. It is important to specify that this criterion is valid only when the piezoelectric transducer bar without any matching layer vibrates (for a given frequency)

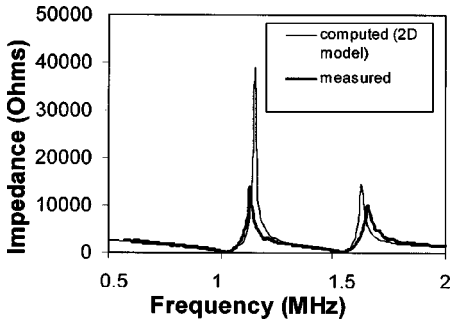

FIG. 11. Experimental and computed electrical impedance modulus of the matched transducer, as a function of frequency.

like a piston mode. For example for the above $LiNbO_3$ bars a value for W/T can be chosen smaller than 0.5 or between 1.2 and 1.7 (see Ref. 15, p. 2973). This study has been performed using $LiNbO_3$ bars, nevertheless similar results have been obtained using PZT5H bars. This criterion [Eq. (15)] can then be applicable to any piezoelectric materials.

D. Experimental results

In order to experimentally validate finite element modeling performed in this section, a matched piezoelectric bar has been manufactured by IMASONIC,[21] an ultrasonic transducer designer. The element is 25 mm long and 0.4 mm wide. The ceramic used is C4-Q (see Table I). The thickness of the piezoelectric bar is 1.4 mm, which generates an electrical antiresonance frequency of the piezoelectric bar equal to 1.5 MHz. The matching material has an acoustical impedance equal to 7.13 MRayls, a mass density $\rho=2300$ kg/m^3, a longitudinal wave speed $c_l=3100$ m/s, and a shear wave speed $c_S=1684$ m/s. The thickness of the matching layer is equal to 0.52 mm [i.e., $l=(\lambda_m/4)$]. Electrodes, situated on each face of the bar, have a thickness equal to 0.005 mm, which have been neglected. It is not simple to measure the acoustical power of the transducer. Then Fig. 11 shows the measured and the numerically computed electrical impedance curves. The measured one has been obtained using a HP 4194A network analyzer. A good agreement is observed in this graph. However, little differences observed between the two curves can be justified on the one hand by inevitable uncertainties on PZT material constants values (mechanical, dielectric, and piezoelectric constants) and, on the other hand, by the fact that losses are not taken into account in the numerical model. For this experimental sample, the width of the matched transducer checks the choice criterion defined in the previous section; thus no parasitic mode disturbs the bandwidth of the transducer. Moreover, the displacement field of this transducer has been computed for different frequencies and not given here because it looks like the displacement field as shown by Fig. 8(a). These computed displacement fields, for frequencies belonging to the desired operating band, do not contain any harmonic vibration on the radiated surface.

VI. CONCLUSION

With the help of the 2D finite element model, harmonic analysis of the matched transducer bar has been performed. Mechanical, electrical, and acoustical parameters have been defined in order to describe the transducer bar behavior. Furthermore, the analysis of numerical results of the matched transducer bar has shown the existence of parasitic modes in the desired operating band of the transducer, due to shear wave propagation in the matching layer. The presence of these modes of vibration degrades the bandwidth and the directivity of the matched transducer. Different matched transducer bars with different ideal layers have been considered and carefully analyzed. Thus a simple choice criterion of the matching material which is function of the width and shear wavelength (λ_S) of the transducer has been defined, suggesting no parasitic mode in the desired operating band of the transducer. In this optimal case, the matched transducer bar is characterized by two coupled modes that can be used in order to increase the bandwidth.

ACKNOWLEDGMENTS

We would like to thank C. Granger and F. Haine for their technical assistance.

[1] Y. Lin and K. Grosh, "Topology optimization of the kerf fillings in linear phased arrays for therapy," J. Acoust. Soc. Am. **112**, 1968–1979 (2002).
[2] J. Assaad and C. Bruneel, "Radiation from finite phased and focused linear array including interaction," J. Acoust. Soc. Am. **101**, 1859–1867 (1996).
[3] D. Certon, N. Felix, E. Lacaze, F. Teston, and F. Patat, "Investigation of cross-coupling in 1–3 piezocomposite arrays," IEEE Trans. Ultrason. Ferroelectr. Freq. Control **48**, 85–92 (2001).
[4] B. Cugnet, A.-C. Hladky, and J. Assaad, "Numerical technique to reduce cross-coupling in acoustical arrays," Ultrasonics **40**, 503–506 (2002).
[5] W. Qi and W. Cao, "Finite element study on 1-D array transducer design," IEEE Trans. Ultrason. Ferroelectr. Freq. Control **47**, 949–955 (2000).
[6] B. A. Auld, *Acoustic Fields and Waves in Solids* (Wiley, New York, 1973).
[7] W. P. Mason, *Electromechanical Transducers and Wave Filters*, 2nd ed. (Van Nostrand, Princeton, NJ, 1948).
[8] R. Krimholtz, D. Leedom, and G. Matthaei, "New equivalent circuits for elementary piezoelectric transducers," Electron. Lett. **6**, 398–399 (1970).
[9] C. S. DeSilets, J. D. Fraser, and G. S. Kino, "The design of efficient, broad-band piezoelectric transducers," IEEE Trans. Sonics Ultrason. **SU25**, 115–125 (1978).
[10] G. Kossof, "The effects of backing and matching on the performance of piezoelectric ceramic transducers," IEEE Trans. Sonics Ultrason. **SU-13**, 20–30 (1966).
[11] G. Woijcik, C. Desilets, L. Nikodym, D. Vaughan, N. Abboud, and J. Mould, "Computer modeling of diced matching layers," IEEE Ultrason. Symp., 1503–1508 (1996).
[12] ATILA is a finite element code devoted to acoustic applications, and mainly transducer design, which has been developed by the Acoustics Department at ISEN, Lille, France. See, for example, "The finite element code ATILA," in *Proceedings of the Workshop, Toulon, June 1990*, edited by B. F. Hamonic, J. C. Debus, and J.-N. Decarpigny (ISEN, Lille, France, 1990).
[13] J. Assaad, M. Ravez, and C. Bruneel, "Application of the finite-element method for modeling backed transducers," J. Acoust. Soc. Am. **100**, 3098–3103 (1996).
[14] O. C. Zienkiewicz, *The Finite Element Method*, 3rd ed. (McGraw–Hill, New York, 1977).
[15] J. Assaad, C. Bruneel, J.-N. Decarpigny, and B. Nongaillard, "Electromechanical coupling coefficients and far-field radiation patterns of lithium niobate bars (Y-cut) used in high-frequency acoustical imaging and nondestructive testing," J. Acoust. Soc. Am. **94**, 2969–2978 (1993).
[16] J. Assaad, J.-N. Decarpigny, C. Bruneel, R. Bossut, and B. Hamonic,

''Application of the finite element method to two-dimensional radiation problems,'' J. Acoust. Soc. Am. **94**, 562–573 (1993).
[17] L. E. Kinsler, A. R. Frey, A. B. Coppens, and J. V. Sanders, *Fundamentals of Acoustics*, 3rd ed. (Wiley, New York, 1982).
[18] J. H. Goll, ''The design of broad-band fluid-loaded ultrasonic transducers,'' IEEE Trans. Sonics Ultrason. **SU26**, 385–393 (1979).
[19] J. Souquet, P. Defranould, and J. Desbois, ''Design of low-loss wide-band ultrasonic transducers for noninvasive medical application,'' IEEE Trans. Sonics Ultrason. **SU26**, 75–81 (1979).
[20] O. B. Wilson, *Introduction to Theory and Design of Sonar Transducers* (Peninsula, Los Altos, CA, 1988).
[21] www.IMASONIC.com.

1-3 piezoelectric composite transducers for swept-frequency calibration of hydrophones from 100 kHz to 2 MHz

Gerald R. Harris[a)]
Food and Drug Administration, 9200 Corporate Boulevard, Rockville, Maryland 20850

Paul M. Gammell
Gammell Applied Technologies, LLC, 6139 Pleasant Cove Drive, Exmore, Virginia 23350

(Received 10 October 2003; revised 18 February 2004; accepted 24 February 2004)

Rapid calibration of hydrophones used in biomedical ultrasound is possible with swept frequency techniques such as time delay spectrometry. However, calibrations below 2 MHz largely have been neglected because of insufficient transmitting transducer bandwidth, even though important medical applications operate in this range. To address this deficiency, several transmitting transducer designs were developed and tested, and two 1-3 piezoelectric composite designs were found to have the requisite bandwidth and uniformity of response. In one the element has a plane front face and spherically concave back face (plano-concave), and in the second both faces are concave, but with different radii of curvature (biconcave). The nonuniform thickness disperses the thickness resonance, and the composite structure suppresses radial-mode resonances. Also, the composite's lower acoustic impedance provides a more efficient match to water. The piezoelectric composite transducers were found to have transmitting pressure sensitivities superior to ceramic single-element and segmented designs having similar dimensions, and their responses were significantly more uniform (<25 dB variation from 0.1–2 MHz, with <1 dB fine structure variation), likely due to decreased contributions from radial modes. [DOI: 10.1121/1.1707090]

PACS numbers: 43.38.Fx, 43.30.Yj, 43.80.Vj [AJZ] Pages: 2914–2918

I. INTRODUCTION

Medical applications of ultrasound span a wide range of frequencies, and miniature hydrophones, both piezoelectric polymer[1] and fiber-optic,[2] have evolved as the primary means for measuring the radiated fields. At the higher frequencies, techniques for hydrophone calibration have been extended beyond 50 MHz.[3] However, less attention has been devoted to the calibrations below 1–2 MHz, even though a number of current or experimental medical uses fall within the range, including extracorporeal shock wave lithotripsy,[4] high intensity focused ultrasound surgery,[5,6] bone sonometry for osteoporosis,[7] and ultrasound-mediated drug delivery.[8]

In a previous paper it was demonstrated that efficient calibration of hydrophones via the swept-frequency technique known as time delay spectrometry (TDS) can be extended to cover the important range of 100 kHz to 2 MHz.[9] However, a serious impediment to the practical implementation of TDS over this range is the lack of transducers having a transmit response that is (i) broadband and (ii) smoothly varying in both the frequency and spatial domains. This latter characteristic permits reproducible positioning of a hydrophone at the same location in the ultrasound beam, a critical requirement when calibrating hydrophones via the substitution technique, as is done with TDS.[9–12] A transmitting transducer for swept-frequency use has been described that has a well-behaved response from 250 kHz to 4 MHz, but the response drops almost 50 dB from its peak at 2 MHz to the minimum at 250 kHz.[13]

Therefore, with the goal of developing suitable transmitting transducers for this purpose, five different transducer designs were fabricated and tested, all having the common property of being disks of varying thickness to disperse the thickness resonance, a desirable property as demonstrated in Ref. 9. In the following sections the transducers are described and their performance is evaluated. It is seen that if a 1-3 piezoelectric composite transducer element is employed, then transmitting transducers having the desired characteristics are both feasible and practical.

II. METHODS

A. TDS swept-frequency system

The TDS system employed was described in Refs. 9 and 12. Briefly, a swept-frequency signal is transmitted into a water tank, and a tracking receiver distinguishes hydrophone signals with different propagation delays by their frequency offset relative to the signal being transmitted, thus eliminating spurious signals such as those reflected from the water surface or tank walls. The swept-frequency source is a Hewlett-Packard (now Agilent) 3325A ''Synthesizer/Function Generator.'' The maximum nominal output is $+23$ dBm into 50 Ω, which corresponds to an ideal equivalent output circuit comprising a voltage source with an open-circuit voltage of 6.3 V rms (17.9 V peak-to-peak) in series with a resistance of 50 Ω.

The measurements were carried out in a tank that is 35 cm deep, 35 cm wide, and 60 cm in the direction between the transmitting transducer and hydrophone. When allowance is made for the fixturing of the transducers, the maximum spac-

a)Electronic mail: gerald.harris@.fda.hhs.gov

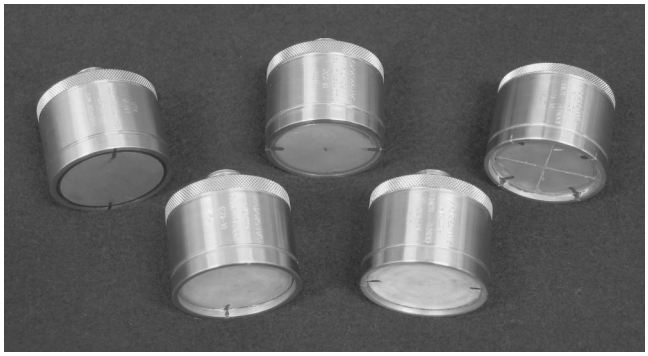

FIG. 1. Photograph of the five transmitting transducers studied. From left to right they are T1–T3 (back row) and T4–T5 (front row). See Table I for descriptions.

ing between the transmitting transducer and hydrophone was somewhat less than the 60 cm, being about 45 cm. The axial separation of the hydrophone from the transmitter can be determined to within approximately 1 mm by maximizing the TDS signal for a given time delay (TDS frequency offset).

B. Transmitting transducers

The five transducer designs studied, designated T1–T5, are shown in Fig. 1 and summarized in Table I. Because it has been demonstrated both theoretically and experimentally that a broadband transmitting response can be achieved by axially symmetric shaping of the transducer thickness,[14] T1–T4 were constructed with flat front faces and spherically concave back faces, and T5 was made spherically biconcave. T1–T3 were fabricated from a single ceramic transducer element, which for T3 was divided into four equal segments. The transducer material in T4 and T5 was a 1-3 piezoelectric composite. In all cases the thickness varied from approximately 1–2 mm in the center to 1.5 cm at the edge. Figure 2 contains a photograph of the spherically concave back face of T5.

The diameter of all transducers was 4 cm. For an ideal planar circular piston having this diameter, the last axial maximum occurs at approximately $27f$ cm, where f is the frequency in MHz. To avoid near-field variations, the measurement distance should not be much less than this value. On the other hand, the measurement distance must not be too great to avoid signal loss due to the pressure amplitude decreasing inversely with distance. Also, a practical consideration is the range of the mechanical positioning apparatus. Considering all factors, a measurement distance of 35 cm was chosen for the plano-concave transducers, which corresponds to approximately 65% of the distance to the theoretical last axial maximum at 2 MHz.

TABLE I. Description of transmitting transducers.[a]

Description	Material	Diameter (cm)	Back face ROC (cm)	Front face ROC
T1: Plano-concave, air-backed	Piezoelectric ceramic	4	2	Flat
T2: Plano-concave, damped	Piezoelectric ceramic	4	2	Flat
T3: Plano-concave, segmented and damped	Piezoelectric ceramic	4	2	Flat
T4: Plano-concave, damped	1-3 piezoelectric composite	4	2	Flat
T5: Bi-concave, damped	1-3 piezoelectric composite	4	2	20 cm

[a]T1–T5, UTX, Inc., Holmes, NY, with 1-3 piezoelectric composite elements in T4–T5 fabricated and poled by Smart Material Corp., Sarasota, FL.

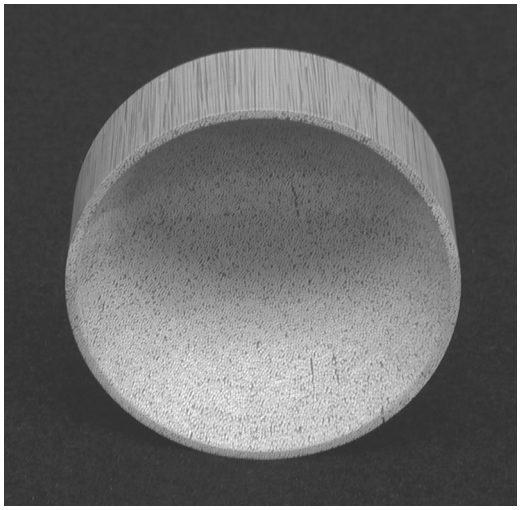

FIG. 2. Photograph of the back face of the biconcave, 1-3 piezoelectric composite transducer element (T5 in Table I).

To study the performance of the transmitting transducers, a spot-poled membrane piezoelectric polymer hydrophone having a nominal active diameter 1 mm was used. The sensitivity of this hydrophone was independently determined to be uniform to within ± 1 dB from 0.3 to 2 MHz, and by virtue of its construction its response below 0.3 MHz should be affected only by its preamplification, which had a low-frequency cutoff frequency of 30 kHz.

Measured transducer characteristics included frequency response, and beam pressure distribution and symmetry. These characteristics are important because, as mentioned earlier, in a substitution calibration procedure the ultimate accuracy depends on how well the reference and test hydrophones can be positioned at the same point in the ultrasonic field. The transmitting pressure level and related voltage response also were measured.

III. RESULTS AND DISCUSSION

A. Ceramic single-element and segmented transducers

The first transducers designed to produce a nonresonant, broadband, and smoothly varying frequency response comprised a ceramic single plano-concave transducer element that was air-backed (T1), acoustically damped (T2), and damped and segmented into four equal sectors (T3). Both damping and segmentation improved the response somewhat, as shown in Fig. 3, but all transducers were unacceptable for the desired swept-frequency calibration source because of the resonances, most likely due to lateral mode resonances and internal reflections falling within the TDS temporal window. (Note: In this and all subsequent spectral

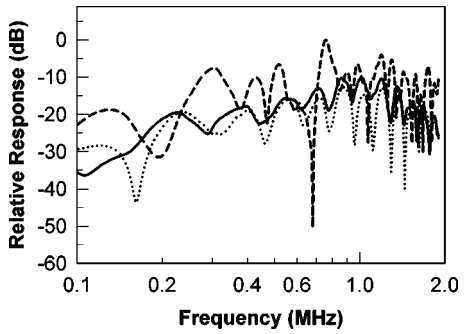

FIG. 3. Relative spectral responses of air-backed transducer T1 (dashed line), acoustically damped transducer T2 (solid line), and damped and segmented transducer T3 (dotted line), at an axial distance of 35 cm.

plots, the frequency scale is logarithmic from 0.1 to 2 MHz to emphasize the less-frequently examined response at the lower end of this range.)

B. Plano-concave, 1-3 piezoelectric composite transducer

In order to suppress the resonant behavior observed in Fig. 3, a transducer of similar geometry was constructed using a 1-3 piezoelectric composite material. The response is given in Fig. 4. Immediately obvious is the significant improvement in response uniformity, almost certainly due to the material's considerable reduction of modes other than the thickness mode. Using a 1-3 composite is known to greatly reduce the low frequency radial modes that are due to resonance from the width of the transducer.[15] Although the periodic structure of the composite lattice introduces other modes, they can be readily addressed by the proper design of the composite.[16,17] One key parameter is the periodic spacing of the ceramic elements, which should be fine enough to place the lowest of these lateral modes adequately above the thickness resonance. Typical designs place the lowest lateral mode at twice the thickness mode.

Having found a transducer design with sufficient broadband response, the beam distribution and symmetry were evaluated in a plane perpendicular to the beam axis and 35 cm from the transmitting transducer face. Figure 5 contains spectra measured at eight equally spaced points on a circle of radius 5 mm and centered on the transducer axis. For each plot in Fig. 5, the log spectrum measured on the transducer axis at 35 cm was subtracted from the response at the 5 mm

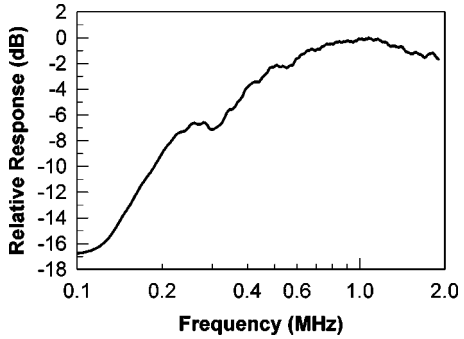

FIG. 4. Relative spectral response of the plano-concave, 1-3 piezoelectric composite transducer, T4, at an axial distance of 35 cm.

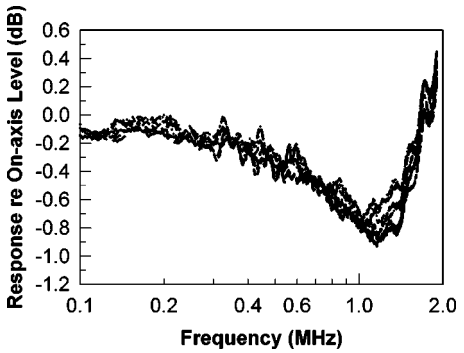

FIG. 5. Spectral responses at points in a plane 35 cm from the plano-concave, 1-3 piezoelectric composite transducer, T4. Each spectrum corresponds to a measurement made at one of eight equally spaced points on a 5 mm radius circle centered on the transducer axis relative to a measurement at a point on the transducer axis.

radial distance. The plots show the beam to be symmetric, the maximum variation at any frequency being about 0.5 dB.

To determine how accurately the hydrophone can be positioned laterally at 35 cm, spectra were recorded at six radial positions with 2 mm spacing, starting on the axis and ending 1 cm off-axis. These spectra are shown in Fig. 6. It was observed that for frequencies below about 1.4 MHz, the spectra monotonically increased to a maximum and then decreased as the hydrophone was swept through the axis, thus permitting reproducible positioning of hydrophones at a specific location in the beam. The positional sensitivity is seen to be the greatest around 1 MHz. The anomalous behavior above 1.4 MHz is reasonably attributable to near field effects at these frequencies.

While these measurements were performed at 35 cm, it is noted that an axial distance of 28 cm has been used successfully as well.[12]

C. Biconcave, 1-3 piezoelectric composite transducer

One possible improvement when using the plano-concave, 1-3 piezoelectric composite transducer would be to shorten the transmitter-to-hydrophone working distance. To that end, a similar transducer was designed, but the front face was weakly focused via spherically concave shaping with a radius of curvature of 20 cm. Measurements along the axis from 12 to 23 cm showed weak focusing. At any frequency

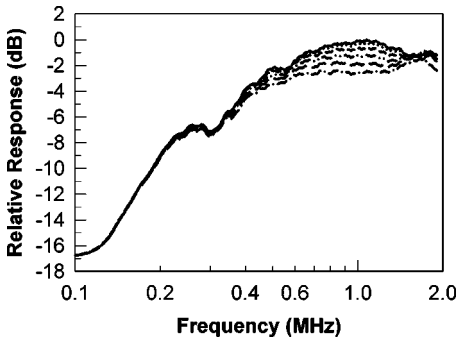

FIG. 6. Relative spectral responses at points in a plane 35 cm from the plano-concave, 1-3 piezoelectric composite transducer, T4. Measurements were made at, from top to bottom, points 0, 2, 4, 6, 8, and 10 mm from the transducer axis.

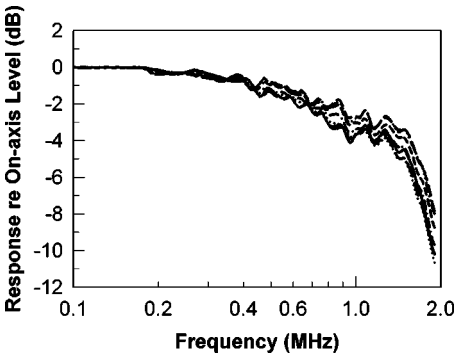

FIG. 7. Spectral responses at points in a plane 15 cm from the biconcave, 1-3 piezoelectric composite transducer, T5. Each spectrum corresponds to a measurement made at one of eight equally spaced points on a 5 mm radius circle centered on the transducer axis relative to a measurement at a point on the transducer axis.

the axial variation over the 12–18 cm range was less than 2 dB. A distance of approximately 15 cm was optimum in terms of maximizing the low frequency response.

Analogous to Figs. 5 and 6, Figs. 7 and 8 contain spectra for evaluating beam symmetry and lateral amplitude variations, respectively. Note that below about 150 kHz the plots are off-scale in Figs. 7 and 8 because, for the biconcave transducer, the dynamic range of the data slightly exceeded that of the TDS system display at the expanded sensitivity used to emphasize the small differences in these measurements.

From Fig. 7 it is seen that all spectra lie in a band whose width rises from 0 dB to ± 1.5 dB with increasing frequency. A notable feature in Fig. 8 not seen in Fig. 6 is that the spectra exhibited a distinct maximum at the higher frequencies as the hydrophone passed through the transducer axis. That is, focusing removed the near-field effects noted in Fig. 6, thus facilitating unambiguous positioning of a hydrophone at a specific on-axis location in the focused field.

A possible disadvantage in using the more tightly focused field of the biconcave transducer is that calibration errors due to spatial averaging could occur if the reference or test hydrophones are large compared to dimensions of the beam.[18] This is because in a substitution calibration it is important that there be a uniform pressure across both hydrophones' active surfaces. For hydrophones used in biomedical

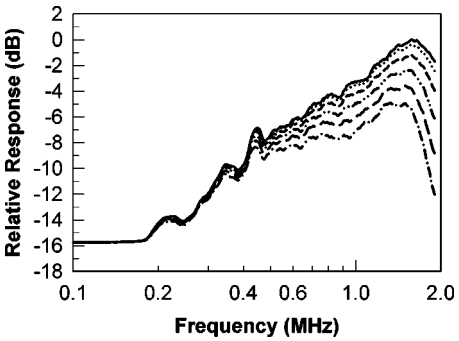

FIG. 8. Relative spectral responses at points in a plane 15 cm from the biconcave, 1-3 piezoelectric composite transducer, T5. Measurements were made at, from top to bottom, points 0, 1, 2, 3, 4, and 5 mm from the transducer axis.

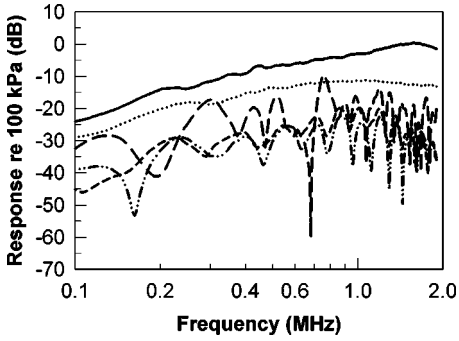

FIG. 9. Transmit peak pressure responses for the five transmitting transducers. T1–T4 were measured at 35 cm, and T5 at 15 cm. The top two plots are for T5 (solid line) and T4 (dotted line). The other three plots are as in Fig. 3. Drive level: 23 dBm. 0 dB corresponds to 100 kPa.

ultrasound, this effect is not expected to be an issue, because the effective radii typically are chosen to be less than 0.5 mm for accurate measurement of the spatial-peak pressures.

D. Transmitting pressure level and voltage response

As described in Sec. II, the maximum drive level into 50 Ω is 23 dBm. Figure 9 contains the absolute transmit pressures for the five transmitting transducers when driven at this level. These plots again illustrate the superior performance of the piezoelectric composite transducers. In terms of uniformity of response, the variation is <25 dB from 0.1 to 2 MHz, with <1 dB fine structure variation. The absolute outputs of the piezoelectric composite transducers are greater as well, with the response of the biconcave transducer exceeding that of the composite plano-concave transducer by 6–12 dB at the respective practical operating distances of 15 and 35 cm.

The actual voltages across all five transmitting transducers versus frequency at the 23 dBm drive level are listed in Table II. At this drive level the output voltage of the Hewlett-Packard 3325A varied from 18.9 to 18.6 V peak-to-peak into an open circuit and 9.5 to 9.3 V peak-to-peak into 50 Ω over the 200–1800 kHz frequency range. The transmitting voltage response (TVR) at a particular frequency can be obtained from Fig. 9 and Table II. For example, at 1 MHz the TVR for the biconcave transducer (T5) is 71 kPa peak pressure at 12.9 $V_{p\text{-}p}$, or 11.0 kPa/V (at 15 cm).

IV. CONCLUSIONS

In this study the performance of five transmitting transducers having variable thickness was evaluated, progressing from a simple air-backed ceramic transducer to a biconcave piezoelectric composite design, each approach attempting to

TABLE II. Peak-to-peak voltages across transducers T1–T5 at maximum TDS drive level.

Frequency (kHz)	T1	T2	T3	T4	T5
200	18.5	18.7	18.7	17.8	18.1
500	17.4	18.2	18.3	15.6	16.2
1000	15.7	17.0	17.2	12.4	12.9
1500	13.4	15.5	15.6	9.6	10.3
1800	12.0	14.4	14.7	8.4	9.2

overcome deficiencies or improve the usefulness of prior designs. It was found that the ceramic transducer designs, whether whole or segmented, were not suitable as calibration sources because of undesirable resonances in the response. However, transducers incorporating 1-3 piezoelectric composite material had the necessary bandwidth and uniformity of response. Advantages of the biconcave source over the plano-concave design include a greater transmitting voltage response, a shorter source-to-hydrophone working distance, and ease of hydrophone positioning. A potential disadvantage of the biconcave source is calibration errors due to spatial-averaging for larger hydrophones. The commercial availability of these piezoelectric composite transducers (see Table I) makes TDS a more viable approach for the low-frequency (<2 MHz) calibration of hydrophones used in biomedical ultrasound applications, as demonstrated in Ref. 12.

The spherical concavities used to achieve the varying transducer thickness worked well, but no attempt was made to optimize the type of curvature used, and there may be other shapes that produce an even broader response. Alternatively, it is possible that other techniques for producing uniform, broadband beams may be useful, such as the constant beamwidth transducers that have been produced by shading the transducer electrodes.[19]

No power amplifier was included in the TDS generating system, because the 23 dBm output was found to be sufficient given the high signal-to-noise level inherent in the TDS measurement scheme. However, it is likely that these transducers could be driven harder should higher pressure levels be needed for the calibration of extremely insensitive hydrophones.

Note added in proof. The mention of commercial products, their sources, or their use in conection with material reported herein is not to be construed as either an actual or implied endorsement of such products by the Food and Drug Administration.

[1] G.R. Harris, R.C. Preston, and A.S. DeReggi, ''The impact of piezoelectric PVDF on medical ultrasound exposure measurements, standards, and regulations,'' IEEE Trans. Ultrason. Ferroelectr. Freq. Control **47**, 1321–1335 (2000).

[2] J.F. Krucker, A. Eisenberg, M. Krix, R. Lotsch, and M. Pessel, ''Rigid piston approximation for computing the transfer function and angular response of a fiber-optic hydrophone,'' J. Acoust. Soc. Am. **107**, 1994–2003 (2000).

[3] V. Wilkens, ''Characterization of an optical multilayer hydrophone with constant frequency response in the range from 1 to 75 MHz,'' J. Acoust. Soc. Am. **113**, 1431–1438 (2003).

[4] M.A. Averkiou and R.O. Cleveland, ''Modeling of an electrohydraulic lithotripter with the KZK equation,'' J. Acoust. Soc. Am. **106**, 102–112 (1999).

[5] J. Sun and K. Hynynen, ''The potential of transskull ultrasound therapy and surgery using the maximum available skull surface area,'' J. Acoust. Soc. Am. **105**, 2519–2527 (1999).

[6] I.M. Hallaj, R.O. Cleveland, and K. Hynynen, ''Simulations of the thermo-acoustic lens effect during focused ultrasound surgery,'' J. Acoust. Soc. Am. **109**, 2245–2253 (2001).

[7] K.A. Wear, ''Frequency dependence of ultrasonic backscatter from human trabecular bone: Theory and experiment,'' J. Acoust. Soc. Am. **106**, 3659–3664 (1999).

[8] H. Guzman, D. Nguyen, and M. Prausnitz, ''Control of transient disruptions in cell membranes by acoustic cavitation at 500 kHz,'' J. Acoust. Soc. Am. **107**, 2814 (2000).

[9] P.M. Gammell and G.R. Harris, ''Time delay spectrometry for hydrophone calibrations below 1 MHz,'' J. Acoust. Soc. Am. **106**, L41–L46 (1999).

[10] M.E. Schafer, ''Techniques of hydrophone calibration,'' in *Ultrasonic Exposimetry*, edited by M.C. Ziskin and P.A. Lewin (CRC Press, Boca Raton, FL, 1993) Chap. 8, pp. 242–244.

[11] C. Koch, ''Amplitude and phase calibration of hydrophones by heterodyne and time-gated time-delay spectrometry,'' IEEE Trans. Ultrason. Ferroelectr. Freq. Control **50**, 344–348 (2003).

[12] G.R. Harris, P.M. Gammell, E. Radulescu, and P.A. Lewin, ''Interlaboratory evaluation of hydrophone sensitivity calibration from 0.1 MHz to 2 MHz via time delay spectrometry,'' Ultrasonics **42**, 349–353 (2004).

[13] P.A. Lewin, G. Lypacewicz, R. Bautista, and V. Devaraju, ''Sensitivity of ultrasonic hydrophones probes below 1 MHz,'' Ultrasonics **38**, 135–139 (2000).

[14] W. Sachse and N.N. Hsu, ''Ultrasonic transducers for materials testing and their characterization,'' in *Physical Acoustics*, edited by W.P. Mason and R.N. Thurston (Academic, New York, 1979), Vol. XIV, Chap. 4, pp. 304–305.

[15] E.P. Papadakis, C.G. Oakley, A.R. Selfridge, and B. Maxwell, ''Fabrication and characterization of transducers,'' in *Ultrasonic Instruments and Devices, Reference for Modern Instrumentation, Techniques, and Technology*, edited by E.P. Papadakis (Academic, San Diego, 1999), Chap. 5, pp. 519–522.

[16] D. Certon, F. Patat, F. Levassort, G. Feuillard, and B. Karlsson, ''Lateral resonances in 1–3 piezoelectric periodic composite: Modeling and experimental results,'' J. Acoust. Soc. Am. **101**, 2043–2051 (1997).

[17] X. Geng and Q.M. Zhang, ''Resonance modes and losses in 1-3 piezocomposites for ultrasonic transducer applications,'' J. Appl. Phys. **85**, 1342–1350 (1999).

[18] B. Zeqiri and A.D. Bond, ''The influence of waveform distortion on hydrophone spatial-averaging corrections—Theory and measurement,'' J. Acoust. Soc. Am. **92**, 1809–1821 (1992).

[19] K.C. Benjamin, A.L. Van Buren, S. Petrie, and J. Szelag, *A Constant Beamwidth Transducer for Ultrasonic Applications*, Proceedings of the 2000 IEEE International Ultrasonics Symposium (IEEE, New York, 2000), pp. 1013–1016.

Analysis and design of wedge transducers using the boundary element method

Guillermo Rus and Shi-Chang Wooh[a)]
NDE Lab, Department of Civil and Environmental Engineering, Massachusetts Institute of Technology, Cambridge, Massachusetts 02139

Rafael Gallego
Department of Structural Mechanics, University of Granada, Spain

(Received 14 June 2003; accepted for publication 5 December 2003)

Cones or wedges inserted between an ultrasonic transducer and a specimen enhances certain characteristics of the transducers. Such an arrangement is useful in that the transducer can be used for transmitting and receiving signals on a point (or line) source, which can eliminate the undesirable aperture effect that makes the transducer blind to waves traveling in certain directions and to those of certain frequencies. In this paper, a comprehensive numerical analysis based on a wave propagation model is carried out to study the characteristics and parameters of wedges. We study the effect of dimensions, shape and aperture on frequency response and directivity. For computational accuracy and efficiency, the boundary element method is used in the analysis. © *2004 Acoustical Society of America.* [DOI: 10.1121/1.1737738]

Pages: 2919–2927

PACS numbers: 43.38.Fx, 43.38.−p, 43.35.Yb [JGH]

I. INTRODUCTION

Ultrasonic transducers used in the non-destructive evaluation (NDE) and testing (NDT) are traditionally fabricated in circular or rectangular shapes of finite dimensions (typically 0.5 to 2.5 cm diameter). Although these transducers are easy to manufacture and they provide strong and well-directed signals, there are some disadvantages associated with their relatively large dimensions with respect to the wavelengths. The main disadvantages of a large transducer include signal distortion, the fact that certain frequency components may be cut off, and the near field effect, which are generally referred to as *aperture effects*.

The benefits of using point sources and point receivers for NDE have been addressed by Sachse.[1] One of the ways to produce point contact between the transducer and the target surface is to use a miniature or pencil-tip transducer. Lee *et al.*[2] demonstrated a technique to achieve small contact surface areas of as low as 200 to 400 μm in diameter by directly cutting a piezoelectric plate using a laser beam. Another and perhaps easier way to provide point contact is to use a cylindrical cone or a triangular wedge whose vertex or knife-edge is in contact with the surface while a normal sized transducer is mounted on the flat surface of the wedge. Note that the former (cone) produces a point contact while the latter (wedge) can be used to produce a hairline contact. The use of wedges to collimate waves and to generate point sources was first introduced by Ying in 1967.[3]

The propagation of ultrasonic waves radiating from a transducer has been studied by many investigators in an effort to understand the response of the transducer as a system. For example, Imamura[4] computed the particle velocities of the waves for circular point transducers. Kimoto and Hirose[5] studied a transmitter–receiver setup by modeling the transmitting transducer as a distributed traction and using a weight function on the displacements of the receiving transducer. They used the boundary element method (BEM) to model the pulse-echo test from a standard A-scan signal. To improve the model of the transducer, Schmerr[6] introduced the transfer function for the transducer–specimen system, which makes it possible to obtain variations of approximately 20% between the experimental and numerical signals. Marty *et al.*[7] experimented with the propagation of Lamb waves generated by point source excitation on the surface of a plate. Wooh and Zhou[8,9] and Shi and Wooh[10,11] studied the behavior of laser excited ultrasonic bulk and guided waves, respectively. A general guideline to design transducers can be found in the Nondestructive Testing Handbook.[12] Note that these are just a few examples of the many studies previously carried out.

Despite the abundance of studies in these areas and the fact that wedges have been used in practice for a long time, the response of the wedge has not been studied in great detail. To our understanding, little knowledge about the effect of mechanical coupling between the transducer and the specimen through a wedge is available. The study described in this paper is motivated by the capacity of point or hairline transducers to overcome the deleterious aperture effects of larger transducers. We report the results of a comprehensive parametric study in an effort to establish guidelines and criteria for optimum wedge design. The conclusions drawn from our numerical study allow us to predict the influences of boundary conditions and wedge geometries on the transducer–specimen coupling mechanisms.

II. TRANSDUCER DESIGN ASPECTS

A. Aperture effects

To demonstrate the aforementioned aperture effects, we take the example of a large transducer used in detecting Rayleigh waves on the surface. The response of the transducer

[a)]Send correspondence to Professor Shi-Chang Wooh, 5 Moore Cir., Bedford, Massachusetts 01730. Electronic mail: scwooh@mit.edu

TABLE I. Design criteria.

Criteria	Effect
Small contact area with specimen	Reduces the aperture effect.
Large contact area with specimen	Can transmit higher energy.
Large contact area with transducer	Can transmit higher energy.
Wedge shape	Avoids spurious eigen-modes or unexpected wave propagations (within the wedge in comparison to direct contact). Allows for feasible manufacturing processes.

can be expressed by the superposition of the wave displacements detected by the transducer as the wave propagates through the surface of contact between the transducer and the target material, that is,

$$u(t)=\frac{1}{A}\int_{\Omega}u(\mathbf{x},t)d\Omega, \tag{1}$$

where $u(t)$ is the surface displacement and Ω is the contact surface of the area A. If a one-dimensional harmonic wave of the form

$$u(x,t)=B\cos(kx-\omega t), \tag{2}$$

is considered to be detected by a circular transducer of radius a, where k is the wave number and ω is the angular frequency, then the detected signal would be expressed in the simple form

$$u(t)=\frac{2J_1(ka)}{ka}B\cos(\omega t), \tag{3}$$

whose amplitude has zero-crossing points at every root of the Bessel function $J_1(ka)$.

B. Design criteria

As explained earlier, the problem of the vanishing frequency components due to phase cancellation can be resolved by physically reducing the size of the contact area using a wedge. An optimal design can be reached by considering the effects shown in Table I. Our goals are to optimize the design based on manufacturing and operation criteria while maintaining the simplicity of signal transmission and reducing the aforementioned oscillatory effects.

III. SYSTEM RESPONSE

A. Transfer function

In order to characterize the transducer–specimen wedge system, we use the transfer function, assuming that the system is linear time-shift invariant. Transfer functions are often expressed in terms of Green's functions when averaging the measurement over the transducer's surface area.

Our objective is to analyze the performance of the wedge working as a participating component of a complete NDE measurement system. A wedge can be used either as a transmitter or receiver, or both at the same time. For this, it is arguably sufficient that we only need to study the frequency response of transducers located at two well-chosen points. We first define a number of essential components of a typical ultrasonic NDE system shown in Fig. 1. The system consists of five distinct components characterized by their respective transfer functions denoted by the symbols $h^{(IT)}$ (function generator or pulser), $h^{(TP_i)}$ (transmitting transducer), $h^{(PU)}$ (specimen), $h^{(UR)}$ (receiving transducer), and $h^{(RO)}$ (signal receiving unit). In this system, we deal with four different signal levels: $s^{(I)}$ (input signal), $s^{(O)}$ (output signal), $s^{(T)}$ (signal just emitted from the transmitting transducer), and $s^{(R)}$ (signal arrived at the receiving transducer).

The electrical and mechanical responses of a transmitting transducer are invariants that can be determined independently by choosing the wedge parameters. Thus, the transmitted signal $s^{(T)}$ is defined simply as normal stresses or tractions distributed on the area of contact between the wedge and the transducer. The function $h^{(TP)}$ relates the emitted signal and the pressure induced in the specimen at an internal point z_2 located underneath the tip of the transmitting transducer, i.e.,

$$p(z_2)=h^{(TP)}*s^{(T)}. \tag{4}$$

The function $h^{(UR)}$ relates the received signal $s^{(R)}$ and the induced displacement $u(z_1)$ at a point (z_1) located underneath the receiving wedge, i.e.,

$$s^{(R)}=h^{(UR)}*u(z_1). \tag{5}$$

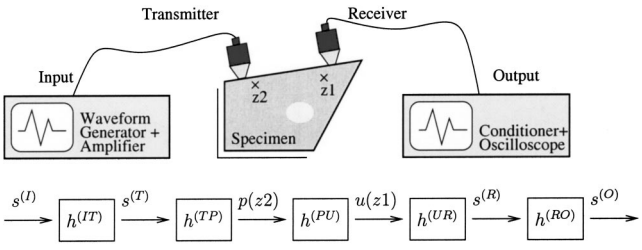

FIG. 1. Schematic of a generic NDE system.

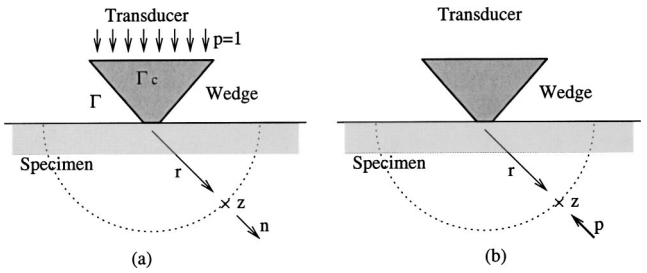

FIG. 2. Definitions of two reciprocal problems: (a) Transmitter and (b) receiver.

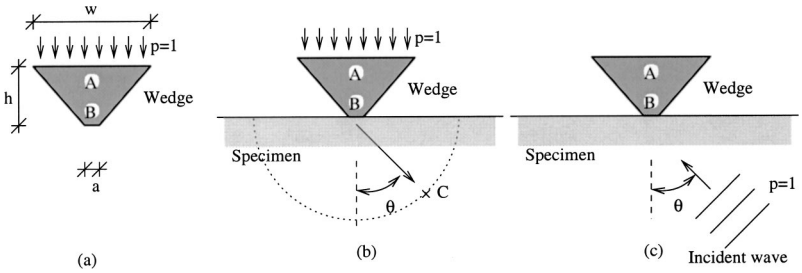

FIG. 3. Three different models used in the wedge design: Models (a), (b), and (c).

Likewise, the function $h^{(PU)}$ is the transfer function of the specimen relating u and p,

$$u(z_1)=h^{(PU)}*p(z_2), \tag{6}$$

which is also an invariant for different wedges. The transfer functions can be obtained directly in the transformed frequency domain by dividing the output signal by the input function. Similarly, $h^{(IT)}$ and $h^{(RO)}$ reflect the response of the two electrical systems of the transmitter, $s^{(T)}=h^{(IT)}*s^{(I)}$, and the receiver, $s^{(O)}=h^{(RO)}*s^{(R)}$.

The overall output of the system is the convolution of the input signal and the transfer functions of all the components in the signal path, i.e.,

$$s^{(O)}=s^{(I)}*h^{(IT)}*h^{(TP)}*h^{(PU)}*h^{(UR)}*h^{(RO)}. \tag{7}$$

Since the functions $h^{(IT)}$, $h^{(PU)}$, and $h^{(RO)}$ remain invariant through a test in regard to the wedge design, it is only necessary to study the functions $h^{(TP)}$ and $h^{(UR)}$, whose responses vary for different wedges. We use a partial model of the latter as follows.

B. Reciprocity between the transmitting and receiving subsystems

In principle, we should consider the wedges as integrated parts of the transmitting and receiving transducers. The transmitting wedge–specimen system model is shown in Fig. 2(a), in which the piezoelectric transducer is simply modeled as pressure distributed uniformly on the contact area Γ_c. Using this model, we can compute the particle displacements in the radial direction (**n**) at all the points z located on an arbitrary arc of fixed radius r. This allows us to study the directional dependency or the *directivity* of the waves propagating into the medium. To study the characteristics of the receiver assembly, a reciprocal model shown in Fig. 2(b) is considered. In this model, the particles on the arc of radius r are loaded in the **n** direction by applying pressure in the form of a Dirac delta function. Then, the output signal is calculated by integrating the normal displacements over the surface (Γ_c) of contact between the wedge and the receiving transducer.

It is sufficient to study only one of these models to analyze both cases, because the reciprocal model yields identical results. To prove this, we simply need to recall Betti's reciprocal theorem of continuum mechanics (Green's theorem) between the primary (a) and secondary (b) states, i.e.,

$$\int_\Omega b_k^b u_k^a\,d\Omega+\int_\Gamma p_k^b u_k^a\,d\Gamma=\int_\Omega b_k^a u_k^b\,d\Omega+\int_\Gamma p_k^a u_k^b\,d\Gamma, \tag{8}$$

where b_k is the body force field, u_k is the displacement field in the Ω domain, and $p_k=\sigma_{jk}n_j$ is the stress vector on the boundary Γ, respectively. If we apply the reciprocity theorem between the two states shown in Fig. 2 with the following loading and boundary conditions:

$$\text{Primary state (a)}\quad \begin{cases} b_k^a=0, \\ p_k^a=\begin{cases} (0,1), & \Gamma_c, \\ 0, & \text{elsewhere}, \end{cases} \end{cases} \tag{9}$$

$$\text{Secondary state (b)}\quad \begin{cases} b_k^b=\delta(z)n_k, \\ p_k^b=0, \end{cases} \tag{10}$$

then we get

$$n_k u_k^a(z)=\int_{\Gamma_c} u_2^b\,d\Gamma. \tag{11}$$

This means that the results of the two models are identical, and we need to study only one of the models to describe both.

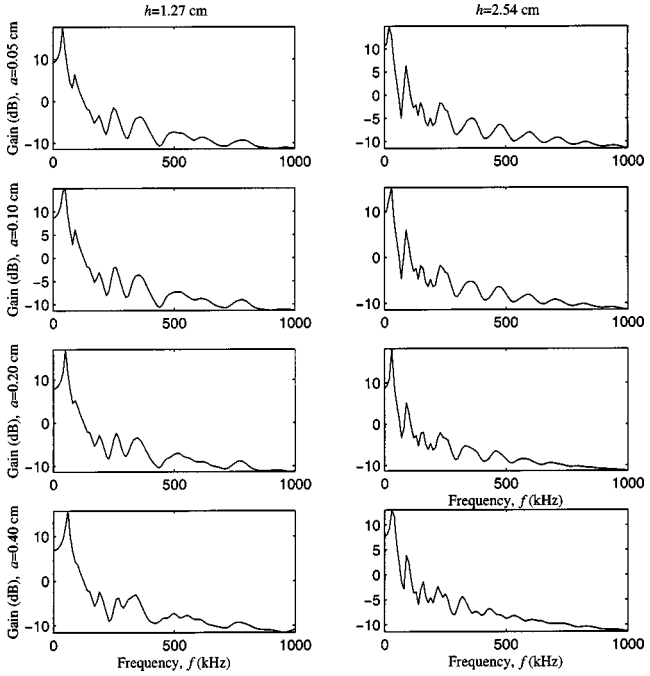

FIG. 4. Frequency response of the stocky (height=1.27 cm) and tall (height=2.54 cm) wedges with various contact areas. A wider and smoother plateau appears at high frequencies as a increases, particularly for the taller wedge.

TABLE II. Specifications of the wedge shapes considered in design.

Design	Profile	Contact area a (cm)	Height h (cm)	Focal frequency f_c (kHz)
1	Constant (no reduction of area)	2.540	0.000	0
2	Linear (narrow contact area)	0.010	1.270	489
3	Linear	0.100	1.270	489
4	Linear (wide contact area)	0.500	1.270	489
5	Linear (doubled height)	0.100	2.540	979
6	Linear (4×height)	0.100	5.080	1957
7	Linear (20×height)	0.100	25.400	9790
8	Linear (45 degrees sides)	0.100	1.220	470
9	Circular (concave: 0°–45°)	0.100	2.950	1136
10	Elliptical (vertically scaled×0.5)	0.100	1.470	566
11	Logarithmic ($y=a\log(bx)$)	0.100	1.270	489
12	Circular (convex)	0.100	1.260	485

C. Boundary element method

In studying and designing the wedge–specimen systems, we use the boundary element method (BEM) because of its clear advantages over the finite element or other discrete methods. First, the BEM does not require remeshing of the body domain at each iteration. This not only reduces the computational time but also eliminates small but important perturbations caused by changing the mesh. Second, by reducing the dimension of the problem by one, the fine meshes required by high frequency become affordable through the BEM.

We use the singular formulation of the boundary integral equation,

$$c_k^i(\mathbf{x})u_k(\mathbf{x}) + \int_\Gamma [p_k^i(\mathbf{y};\mathbf{x})u_k(\mathbf{y}) - u_k^i(\mathbf{y};\mathbf{x})p_k(\mathbf{y})]d\Gamma(\mathbf{y}) = 0.$$

This equation obviously relates the displacements u_k and the tractions p_k exclusively at the boundaries. If we use the complex presentation of fundamental harmonic solutions for p_k^i and u_k^i, then solving this equation yields fundamental harmonic solutions for a single frequency ω. In the equation, c_k^i is a geometry-dependent constant, and the integral has the sense of Cauchy's Principal Value. In implementation, we use the classical conforming discretization scheme with quadratic elements, eight-point Gauss integration after regularization and displaced collocation strategy. The implementation details are developed in Rus.[13] This equation is used for both boundary and internal points.[14,15]

IV. NUMERICAL RESULTS

The parametric design is based on three different models shown in Fig. 3. The model (a) shows an emitting transducer sitting on a standalone wedge. This model is used to study the effects of the transducer's contact areas and height. Model (b) shows the transmission of energy into the specimen through a wedge. This model is used to compute the transfer function of the combined assembly and directivity analysis. Finally, model (c) shows a signal coming from the specimen to the transducer mounted on a wedge. This model is used to demonstrate the improved reception due to the presence of the wedge. In addition, a combination of the models is used to analyze the effects of the boundary conditions.

To ensure the precision of the BEM results, the model was discretized with approximately 70 quadratic elements

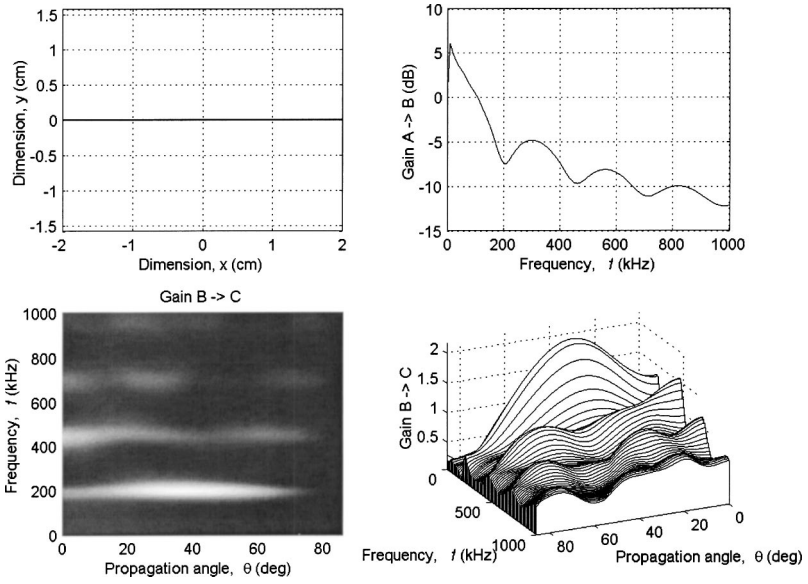

FIG. 5. Design 1. Combined frequency and directivity. Above left: wedge shape (no wedge), Above right: gain from zone *A* (transducer) to *B* (contact zone), Below: two perspectives of the gain from *B* to *C* (internal point in the specimen at every angle). Both gains should ideally be as horizontal and uniform as possible. Direct transducer–specimen contact (no wedge) gives undesirably wavy response in both frequency and directivity, as expected.

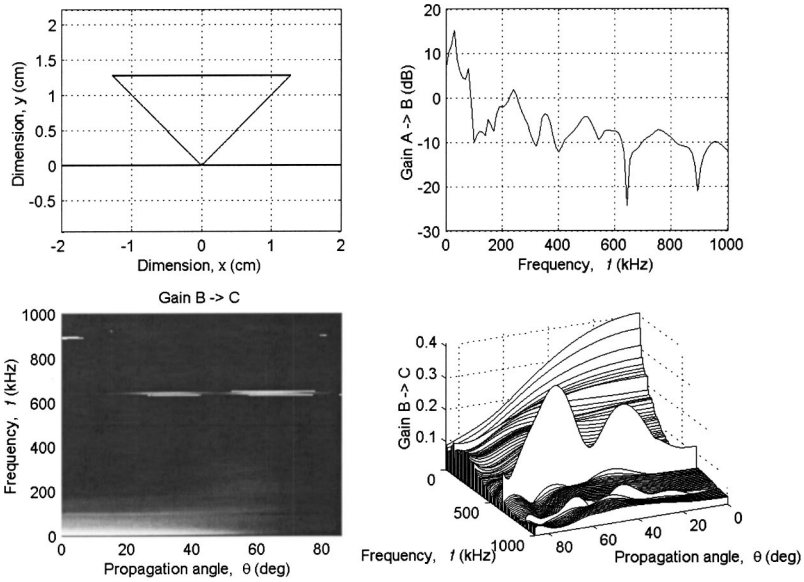

FIG. 6. Design 2. An ideally narrow contact area gives very flat directivity response in the high frequency band but with high signal attenuation. Design 3 (graphics omitted). A slightly enlarged contact area provides better results than those of Design 2.

and with a frequency sampling between 0 and 1 MHz at an increment of 10 kHz. The material used in this study is 4340 steel. The acoustical and physical properties of the material are given by its longitudinal wave speed $c_L = 5850$ m/s, transverse wave speed $c_T = 3240$ m/s and its mass density $\rho = 7220$ kg/m^3.

For the sake of convenience and without losing generality for conclusions, we only considered two-dimensional problems, in that a wedge was assumed to have an infinitely large dimension in its lateral direction. From the practical point of view, we use a fixed value of 2.54 cm (1.0 in.) for the dimension w (the area of contact between the transducer and the wedge). Then we varied the height (h) and the base contact area (a) of the transducer to study their influences on the transfer function.

A. Base contact area and height

Figure 3(a) illustrates the model of the isolated wedge with all free boundary conditions. In order to compute the transfer function of this model, we first consider a continuous monochromatic traction of unit magnitude applied on the transducer–wedge interface. Then the displacements at the bottom face (no traction) at all discrete locations are computed using the BEM, and they are integrated over the area to obtain the overall time-averaged output of the system. The ratio of the integrated displacement and the excitation function in the frequency domain yields the transfer function of the wedge.

To study the effects of the base contact area and the wedge height, we consider wedges of two slenderness ratios: stocky and tall wedges. Figure 4 shows the computed transfer functions of the stocky ($h = 1.27$ cm) and tall ($h = 2.54$ cm) wedges with various contact areas ($a = 0.05$, 0.10, 0.20, and 0.40 cm), respectively.

We should recall at this point that an ideal transfer function is represented by a uniformly flat curve for all frequencies. Since it is practically not possible to achieve this goal, we should admit that we can use only a limited range of frequencies within which the transfer function is reasonably

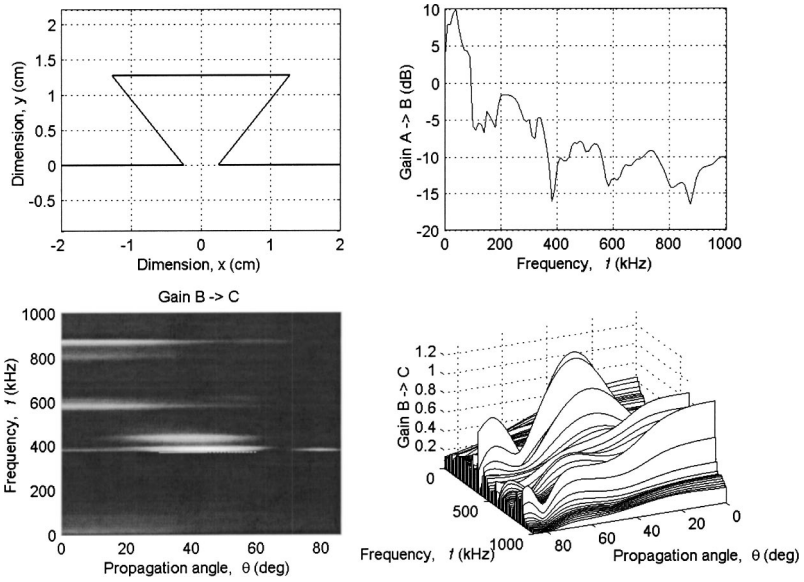

FIG. 7. Design 4. When the wedge–specimen contact area is too large, it causes undesirable aperture effects.

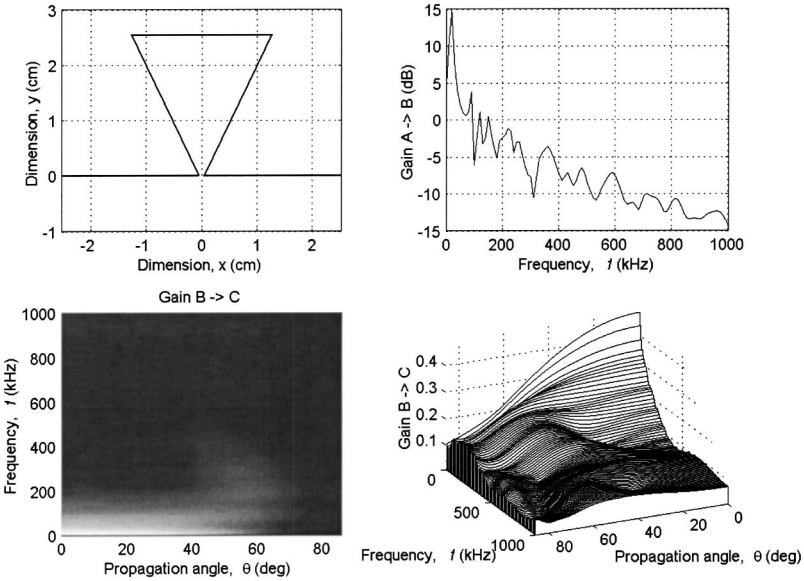

FIG. 8. Design 5. A taller linear wedge with medium contact area provides improved response in both directivity and frequency. Design 6 (graphics omitted). A taller wedge provides excellent response in terms of both frequency and directivity.

flat. Our immediate conclusion upon investigating Fig. 4 is that the base contact area a has little influence on the frequency response of the wedge. We may note that the useful frequency range in this configuration is the band above 500 kHz, where the response function is smooth and flat as compared to that in the low-frequency region. It can also be observed that increasing the base contact area extends the lower bound of the usable frequency band. This trend is particularly strong for the case $h=2.54$ cm, as shown by the extended plateau of smoother and slower slope in the response function for $a=0.40$ cm and $h=2.54$ cm.

B. Transfer functions and directivity

For proper transducer design, it is important to understand the behavior of the emitted wave field that can be characterized quantitatively by the natural focal length N and the aperture angle γ given by the relationship[12]

$$N=\frac{(0.97w)^2 f}{4c_p} \quad \text{and} \quad \sin\gamma=\frac{0.51c_p}{0.97wf}, \tag{12}$$

where c_p is the phase velocity in the specimen and f is the frequency. It can be easily shown from this relationship that the reduced source area decreases N as γ increases. As mentioned earlier, the purpose of using a wedge is to provide a quasipoint (or hairline) source. This means that we intended to generate cylindrical (for hairline sources) or spherical waves (for point sources). To validate the performance in achieving this goal, it is necessary to investigate the directional dependency of the propagating beam. In this paper, we study the directivity of the beam emitted from a transducer–wedge block using the model shown in Fig. 3(b). Directivity is obtained by computing the farfield displacements along an arc located at a fixed distance from the source (we use $w/2=1.27$ cm).

We considered thirteen different wedge shapes in our study. The most common and easiest shape is trapezoid (linear profile). In addition to this simple shape with some variations, we also considered different geometric profiles such as circular, elliptical, and logarithmic shapes. The detailed design specifications are shown in Table II and the cross-

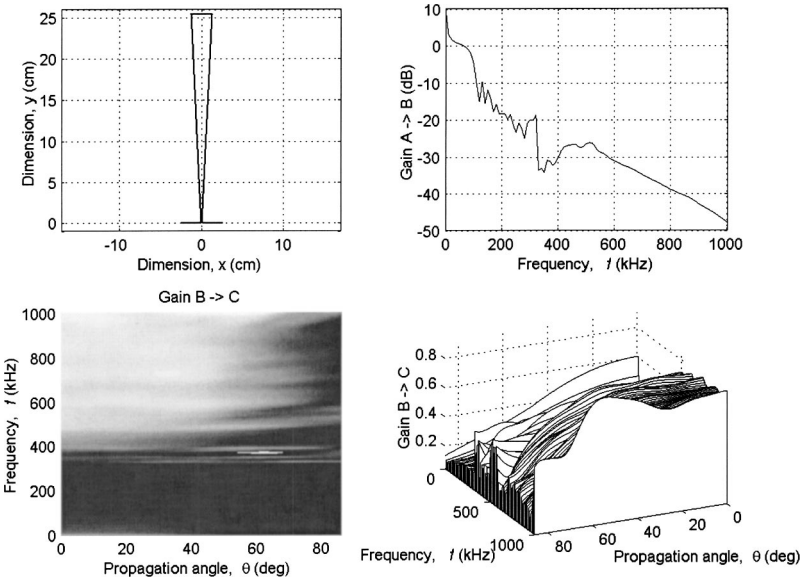

FIG. 9. Design 7. An extremely tall wedge causes instabilities due to excessive attenuation (-40 dB $A-B$) at high frequencies. Design 8 (graphics omitted). Choosing a 45° wall angle does not necessarily produce any improvement. Design 9 (graphics omitted). The frequency and directivity responses of a horn-like wedge are similar to those of Design 5, but it provides a worse gain $A-B$.—Design 10 (graphics omitted). This short horn-like design yields severe instabilities at low frequencies.

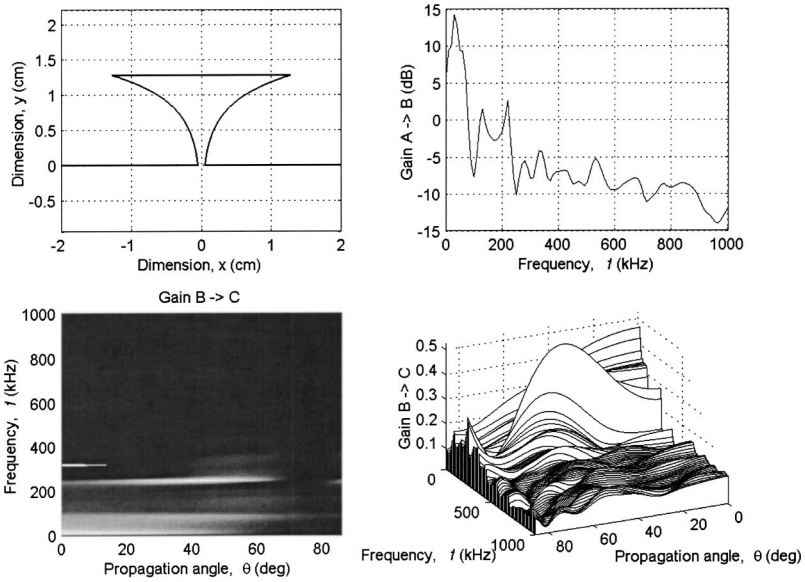

FIG. 10. Design 11. A logarithmic profile does not provide any improvement. Design 12. The performance of a half-circle design is poor.

sectionalviews of each design are illustrated in Figs. 5–10 (in the upper left hand corners of the figures). The curves in the upper right quadrants of these figures represent the frequency-dependent gain produced by the wedge itself for each design, i.e., the ratio of average displacements at the transducer–wedge interface (A) and the wedge-specimen interface (B) plotted as a function of frequency.

The plots at the bottom of Figs. 5–10 are the gains achieved while traveling from a point on B to the arc C. In other words, these figures represent the displacement at a point on C normalized by the average displacement of surface B. The gain between the points on A and C are not shown but they can easily be computed by multiplying the respective gains in paths $A-B$ and $B-C$. The gains at all the discrete points on C are computed and plotted as a function of propagation angle as well as frequency. The same results are displayed both in gray scale images (where the pixel intensity represents the gain) and perspective three-dimensional plots for a clear presentation. Remember that the goal of an ideal design is to achieve a flat platform, which provides little dependency on frequency and propagation angle. Some of the design configurations are omitted in this paper due to space limitations, but they are available by contacting authors. The following are the key observations derived from the set of figures:

Figure 5 (Design 1) shows the results for direct transducer–specimen contact, i.e., no wedge is used in this configuration. The first attempt to reduce the oscillatory performance is to insert a wedge having a very small contact area with the specimen (Design 2, Fig. 6). This certainly enhances the effective aperture angle and gives more uniform gain. But it produces excessive attenuation at some frequencies. Besides, it is difficult manufacture such a sharp wedge. As the wedge–specimen contact area is enlarged (Design 3), the response shows improvements in both frequency and directivity. However, when the area grows excessively (Design 4, Fig. 7), the performance gets worse and great instabilities occur. Up to this point, the best design is No. 3.

Now we play with the wedge height. As the wedge becomes taller (Designs 5 and 6), the directivity is improved and the response becomes smoother, but excessive attenuation at high frequencies makes tall wedges undesirable. Figure 9 (Design 7) shows an unstable response in an extreme case. No revealing relationship was found between the focal depth and the height of the wedge.

Design 8 tests a wedge with a 45° angle in an effort to reduce the effect of reflections inside the wedge, but no improvements are found and the response is very similar to that of Design 3. Horn-like shapes and other geometric variations are tested in Designs 9 to 12. They do not necessarily improve the performance. We also observe that the mechanical coupling due to the presence of the specimen affects the transfer function by attenuating the gain at some frequencies and negatively affecting its behavior. Compare the results of Fig. 4 ($a=0.10$ cm, $h=1.27$ cm) and those of Fig. 10 (Gain

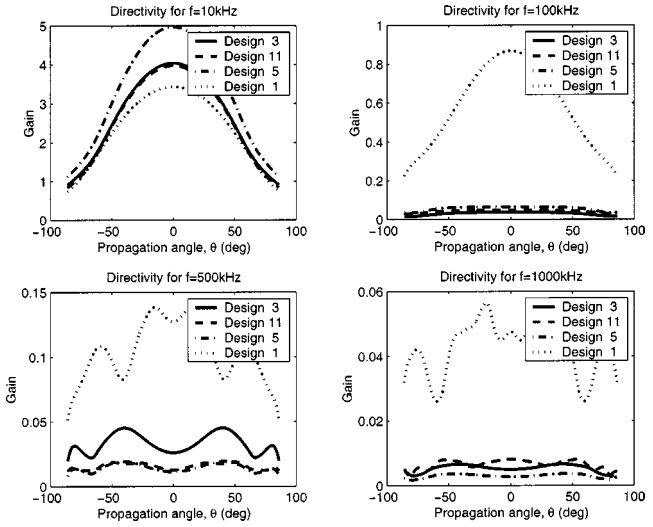

FIG. 11. Directivity plot for some frequencies and selected designs. Design 5 can be chosen as optimal, establishing a compromise between a homogeneous directivity and gain. The enhancements of this design are enlightened against the absence of the wedge (Design 1).

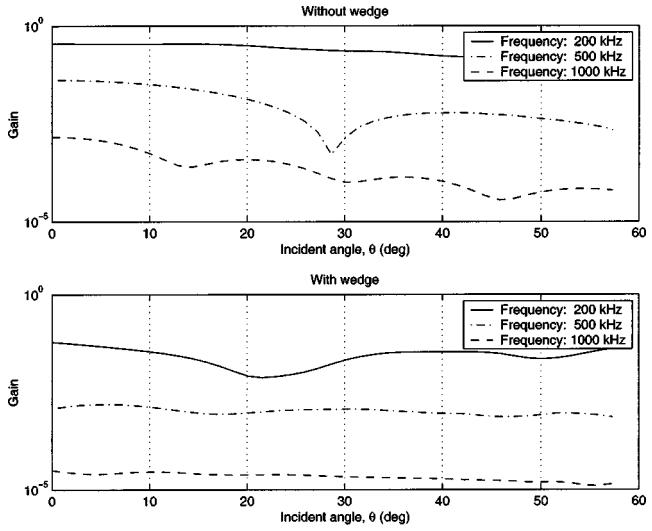

FIG. 12. Response upon inclination of incident wave. Uniformity due to the presence of the wedge is emphasized.

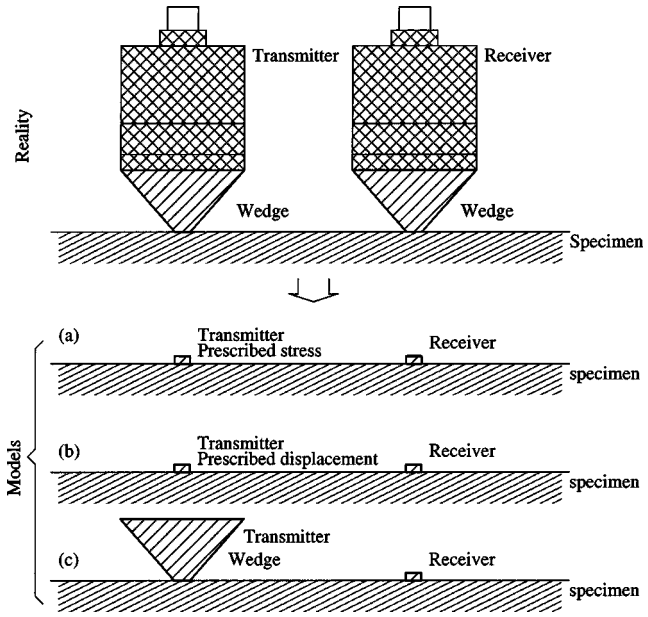

FIG. 13. Model for the study of the boundary conditions at the emitter.

$A-B$). The former takes into account the specimen whereas the latter does not.

We may conclude from these observations that a properly designed wedge can improve the directivity patterns. In order to elucidate the directivity enhancements of the best designs, we show in Fig. 11 the directivities of different designs at various frequencies.

C. Verification of the improvement

The problem of vanishing frequency components due to phase cancellation along the surface measurement can be solved by inserting a wedge. This problem is modeled numerically by considering a semiinfinite space where a plane *P*-wavefront arrives at a variable angle [see Fig. 3(c)].

Figure 12 gives the gain as a function of the incident angle. The cancellation effect is clearly observed from the gain without using the wedge (direct contact). The valleys shown in the gains at frequencies of 500 kHz and 1 MHz are the indication of the phase cancellation effect. These valleys disappear when the wedge is inserted (bottom figure) causing the responses to become more uniform.

D. Boundary conditions

The boundary conditions should take into account the coupling between the transducer and the wedge, which is equivalent to prescribing boundary conditions in terms of stresses and displacements at the transducer–wedge interface and computing the resulting stresses and displacements at the wedge–specimen interface. We can argue here that for a small contact area (point source–receiver), it is sufficient to prescribe the boundary condition at the wedge–specimen interface in terms of either tractions or displacements, which

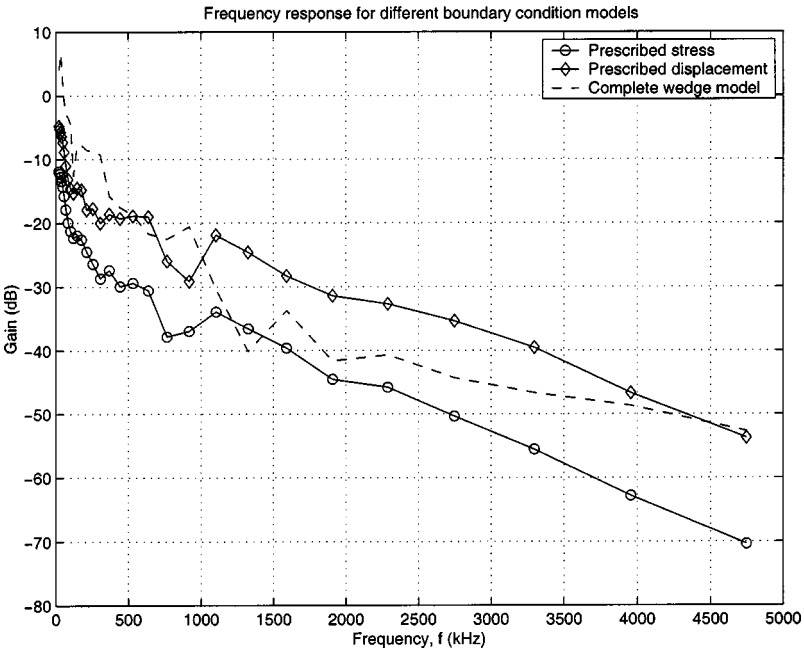

FIG. 14. A comparison of the boundary conditions at the emitter. Prescribed stress and displacements are closely related.

simplifies the modeling of a NDE system and thus reduces the computation time. To prove this, we compare the frequency response of the point source model with that of the complete model whose surface is prescribed either by displacements or by stresses.

Figure 13 shows a NDE setup where transmitting and receiving wedge transducers are placed on the surface of a half space. Figure 14 shows the frequency responses of the output signals due to uniform input. The frequency responses are computed for three different models: (a) the boundary condition of the transmitter is prescribed by uniform stresses; (b) the transmitter boundary condition is prescribed by uniform displacements; and (c) a complete wedge mode. What we can observe in Fig. 14 is that the gains for the three different modes are very similar. The only difference is their scale. This validates our argument that the three models make very little difference in analyzing a wedge-based NDE system. We may choose a simple model that significantly reduces the computation time.

V. CONCLUSIONS

From this study, we obtained conclusions and directions for the effective design of wedge transducers. We also numerically demonstrated their advantages with respect to directivity, frequency responses and computation efficiency.

We obtained a few simple but important guidelines for design, summarized as follows:

- A small contact area improves directivity.
- A higher wedge produces a uniform response for directivity and frequency, but extremely slender wedges suppress high frequency components. A wedge of medium height produces best results.
- Horn-like shapes do not necessarily improve the performance.
- The presence of a well-designed wedge significantly improves the response for the complete range of frequencies.

ACKNOWLEDGMENTS

We would like to gratefully acknowledge the Fulbright Foundation and the Ministerio de Educación Cultura y Deporte for the postdoctoral fellowship FU2002-0442 supporting this work. We would also like to acknowledge the support received by the National Science Foundation (CMS-0218648). We are grateful to Dr. Shih-Chi Liu for his support and encouragement.

[1] W. Sachse, ''Transducer considerations for point-source/point–receiver materials measurements,'' Ultrasonics **25**, 356 (1987).
[2] Y. C. Lee and S. H. Kuo, ''A new point source/point receiver acoustic transducer for surface wave measurement,'' Sens. Actuators, A **94**, 129–135 (2001).
[3] S. Ying, ''Single narrow beam ultrasonic transducer with conical and wedge shaped collimators,'' Ultrasonics **5**, 276 (1967).
[4] T. Imamura, ''Deformation of ultrasonic pulse with diffraction,'' Ultrasonics **37**, 71–78 (1999).
[5] K. Kimoto and S. Hirose, ''A numerical modeling of contact sh-wave transducers,'' in *Review of Progress in Quantitative Nondestructive Evaluation*, edited by D. O. Thompson and D. E. Chimenti (Publisher, City, 2000), Vol. 20.
[6] L. W. Schmerr, *Fundamentals of Ultrasonic Nondestructive Evaluation* (Plenum, New York, 1998).
[7] P. N. Marty, M. J. S. Lowe, and P. Cawley, ''Finite element predictions of guided ultrasonic wave fields generated by piezoelectric transducers,'' in Ref. 5.
[8] S. C. Wooh and Q. Zhou, ''Behavior of laser-induced ultrasonic waves radiated from a wet surface, Part I. Theory,'' J. Appl. Phys. **89**, 3469–3477 (2001).
[9] S. C. Wooh and Q. Zhou, ''Behavior of laser-induced ultrasonic waves radiated from a wet surface, Part II. Experimental work,'' J. Appl. Phys. **89**, 3478–3485 (2001).
[10] S. C. Wooh and Y. J. Shi, ''Synthetic phase tuning of guided waves,'' IEEE Trans. Ultrason. Ferroelectr. Freq. Control **48**, 209–223 (2001).
[11] Y. J. Shi, S. C. Wooh, and M. Orwat, ''Laser-ultrasonic generation of Lamb waves in the reaction force range,'' Ultrasonics **41**, 623–633 (2003).
[12] R. K. Miller, *Nondestructive Testing Handbook*, American Society for Nondestructive Testing, 5th ed. (Publisher, City, 1986), Vol. 5.
[13] G. Rus, ''Numerical methods for nondestructive identification of defects,'' Ph.D. thesis, Universidad de Granada, E.T.S.I. Caminos, C. y P., June 2001. Electronic mail: grus@ugr.es.
[14] J. Domínguez, *Boundary Elements in Dynamics* (Elsevier, New York, 1993).
[15] G. Rus and R. Gallego, ''Optimization algorithms for identification inverse problems with the boundary element method,'' Int. J. Eng. Anal. B.E. **26**, 315–327 (2002).

On the natural frequencies of short cylinders and the universal point. Direct determination of the shear modulus

Francisco J. Nieves[a] and Francisco Gascón
Departamento de Física Aplicada II, Universidad de Sevilla, ETS de Arquitectura, Avda. Reina Mercedes, 2, 41012 Sevilla, Spain

Ana Bayón
Departamento de Física Aplicada a los Recursos Naturales, Universidad Politécnica de Madrid, E.T.S.I. Minas, C./Ríos Rosas, 21, 28003 Madrid, Spain

(Received 17 July 2003; revised 26 February 2004; accepted 15 March 2004)

This work presents a study of the relation between the lowest nondimensional natural frequencies of a short, free cylinder vibrating in axisymmetric modes, its slenderness ratio, and its Poisson's ratio. Ritz's method applied to the study of the symmetric vibration of cylinders confirms that all curves, which show the dependence of frequency versus slenderness, pass through a point, called universal, independently of Poisson's ratio. The lowest universal frequency is 2.6036 and corresponds to a cylinder whose quotient of its length and its diameter is 0.853 22. The rules leading to the identification of the first symmetric mode are inferred from the numerical results. A cylinder with universal slenderness ratio is set into free vibration by applying an axial impact. The lowest axisymmetric natural frequencies are obtained from measurement of the axial displacement by speckle interferometry. A simple arithmetical operation permits calculation of the shear modulus from the value of the first symmetric frequency, the diameter of the cylinder, and its density. The quotient of frequencies of two similar cylinders is studied as a function of their elastic properties and diameters. © *2004 Acoustical Society of America.* [DOI: 10.1121/1.1739485]

PACS numbers: 43.40.Cw [JGM] Pages: 2928–2936

I. INTRODUCTION

The elementary theory of propagation of elastic longitudinal waves along a slender rod gives the wave velocity as $\sqrt{E/\rho}$, where E is the Young's modulus and ρ the density.[1] This elementary theory is applicable to rods whose diameter is negligible compared with the other two lengths characteristic of the phenomenon, i.e., the length of the rod and the wavelength. Longitudinal waves in a rod are then simple extensions or compressions propagated along its length, and over a cross section of the rod there will be only normal stress.

The study of the propagation of waves in cylinders, based on the classical theory of elasticity, is well known.[2] A solution of the wave equation can be obtained by the method of separation of variables applied to the propagation of waves in isotropic, linear, elastic cylinders. A plane-wave solution is assumed for the radial u, tangential v, and longitudinal w displacements

$$\begin{aligned} u &= U(r)\cos(n\theta)\exp[i(\gamma z-\omega t)],\\ v &= V(r)\sin(n\theta)\exp[i(\gamma z-\omega t)],\\ w &= W(r)\cos(n\theta)\exp[i(\gamma z-\omega t)], \end{aligned} \tag{1}$$

where r, θ, z are the cylindrical coordinates of a point, OZ is in the direction of the axis of the cylinder, n is equal to zero or an integer, $i=\sqrt{-1}$, γ is the wave number, ω is the angular frequency, and t is the time. The trigonometric factors appear because the displacements u, v, and w must be continuous as is the medium; therefore, the amplitude of displacements must be periodic with a period 2π, or 2π divided by an integer, i.e., displacements can be expressed in terms of their Fourier components in the coordinate θ.

Substitution of the assumed solution, Eqs. (1), into the wave equation, application of Hooke's law, and the boundary conditions yield the unknown functions U, V, and W. Accurate solutions for infinitely long cylinders are obtained by application of traction-free boundary condition to the cylindrical surface. This requirement leads to the condition of compatibility of a set of equations. When the determinant of the matrix of coefficients is set equal to zero, it results in the frequency equation, which relates the wave number, the frequency, and the elastic constants. Study of the spectrum shows that there are different branches for real, imaginary, or complex propagation constants.

The nondimensional frequency parameter or nondimensional frequency $\Omega=\pi f D\sqrt{\rho/G}$ is often used for economy of calculations, where $f=\omega/2\pi$ is the ordinary frequency, measured in Hz, D the diameter of the cylinder, and G the shear modulus. Shear modulus G is related to the Young's modulus and Poisson's ratio ν by $G=E/(2(1+\nu))$.

In this paper only axisymmetric vibrations are considered. When the cylinder vibrates in the axisymmetric modes, the tangential displacement v vanishes in Eq. (1), and the other two components, u and w, do not depend upon θ, i.e., $n=0$. If the identity $\Omega=\sqrt{2}\gamma D/2$ is satisfied and the Bessel function of the first kind and order one, $J_1(\gamma D/2)$, is a maximum or a minimum, it is demonstrated[3] that the compatibility conditions are satisfied. This guarantees the existence of

[a]Electronic mail: nieves@us.es

 0001-4966/2004/115(6)/2928/9/$20.00 © 2004 Acoustical Society of America

waves (frequency equation), and that shear stress identically equals zero at all points of the cylinder. From the values[4] of $\gamma D/2$ that make $J_1(\gamma D/2)$ maximum or minimum, it is found that $\Omega_u = \sqrt{2}\,\gamma D/2 = 2.6036, 7.5392, \ldots$. Thus, shear stress is zero on planes perpendicular to the axis of the cylinder for the infinite set of values of Ω_u. Each frequency is universal in the sense that it is independent of Poisson's ratio. For materials with any Poisson's ratio, all the dispersion curves in the graph Ω against wave number pass through each value of Ω_u; these values are thus called universal points.

There are no analytical solutions to the equations of motion in finite cylinders that completely satisfy the boundary conditions that normal and shear stresses must be zero at the free ends. According to Zemanek's study,[3] in a semi-infinite cylinder both stress components can be made to vanish simultaneously by assuming that a reflected wave and others with complex propagation constants are generated at the traction-free surface. The amplitude coefficients for the reflected wave and the complex modes are evaluated by setting the stresses equal to zero at a series of points along the radius of the cylinder.

A cylinder of finite length, whose nondimensional frequency Ω takes a universal value, Ω_u, is a special and simple case; then, shear stress equals zero everywhere, including at its ends. Therefore, normal stress at a free interface is canceled by only a reflected wave. Two waves having the same frequency and propagating in the positive and negative OZ direction interfere. As a result of the interference, normal stresses vanish on the planes: $z = -L/2$ and $z = L/2$, L being the length of the cylinder. For this to happen $\gamma_n L = n\pi$, i.e., $\lambda = 2L/n$, where n is an integer. The significance of this conclusion is that at these frequencies a finite length rod will be an integer number of half-wavelengths long. This condition is not verified for frequencies different from the universal values.

The interference of the two propagating waves mentioned above yields a standing wave. From the point of view of the vibration of a cylinder, the resulting phenomenon is called the normal mode and the corresponding frequency, natural frequency. When the axial displacements are symmetrical with respect to the plane $z = 0$, the mode is known as symmetric, i.e., the axial displacement is an odd function in z, whereas it is an even function in z for an antisymmetric mode.

Natural frequencies and normal modes of finite cylinders can be determined by means of numerical methods.[5,6] From Hamilton's principle applied to a system whose displacements are harmonic in time, it is concluded that the difference between the maximum kinetic and potential energies is a minimum when the cylinder is vibrating in a normal mode. A widely used methodology is the Ritz method, based on assuming approximate solutions, suitable for the system, which satisfy the boundary conditions. Convergence towards the true frequencies and mode shapes is obtained as the number of terms in the approximating expressions is increased. The work of Leissa and So[7] deserves special mention. It follows this methodology in the study of finite cylinders with different boundary conditions; the displacement functions chosen are in the form of algebraic polynomials in the cylindrical coordinates. The results provided by these authors are accurate; nondimensional frequencies are calculated for different values of the quotient of the length and diameter of the cylinder, known as aspect ratio or slenderness. The effect of Poisson's ratio upon nondimensional frequencies is also investigated for $L/D = 1$.

In a previous work,[8] the Ritz method is applied to the study of axisymmetric vibrations of cylinders with equal length and diameter in order to determine their elastic constants. The results obtained are very accurate, as confirmed by the convergence of the solutions.

In this paper, vibration of short cylinders in special cases is studied. In the analysis performed, the concept of nondimensional frequency is applied as well as the singularity of its universal value Ω_u. The Ritz method is used to determine the existing relationship between nondimensional frequency, slenderness ratio, and Poisson's ratio. Some preliminary results in relation to the universal point and the comparison of frequencies of two cylinders with universal slenderness ratio were partly presented.[9] From the study performed here, it is verified the fact that for two geometrically similar cylinders, made of the same material, frequencies are inversely proportional to diameters.[5] The existence of the universal frequency is demonstrated by the experimental results. When two cylinders have the same universal slenderness ratio, an expression relating their ordinary frequencies to their elastic properties is obtained. The lowest natural frequency for the symmetric longitudinal mode is deduced from a single experiment carried out on a cylinder of universal slenderness ratio set into axisymmetric vibration. It is demonstrated that the shear modulus of the material can be obtained from such a frequency; only simple manual calculus is required.

II. CALCULATION OF THE LOWEST NATURAL FREQUENCIES FOR THE AXISYMMETRIC MODES

When axisymmetric vibration is induced in a cylinder, the frequencies obtained in the spectrum can correspond to both symmetric and antisymmetric modes. Therefore, the correct identification of each mode is essential. In particular, interest is focused here on identification of the first symmetric mode. For this purpose, a study is carried out in order to determine natural frequencies of a free cylinder vibrating in axisymmetric modes, both symmetric and antisymmetric.

Hamilton's principle can be stated as ''the motion of a conservative system from time t_1 to time t_2 is such that the line integral of the Lagrangian has a stationary value for the correct path of the motion.'' In the present study, standing-wave solutions are sought, which can be written as

$$u = U(r,z)\sin(\omega t); \quad w = W(r,z)\sin(\omega t), \tag{2}$$

where the origin of the coordinate system is at the center of the cylinder. Hamilton's principle for harmonic motion can be expressed as the difference between the maximum kinetic and maximum potential energies is a minimum.

For convenience, r and z coordinates are nondimensionalized as: $r' = 2r/D$ and $z' = z/L$. The maximum strain energy functional for an axisymmetric mode is then given by

$$V_{\max}=2\pi GL\int_{-1/2}^{1/2}\int_{0}^{1}\left\{\frac{\nu}{1-2\nu}\left(\frac{\partial U}{\partial r'}+\frac{U}{r'}+\frac{1}{2L/D}\frac{\partial W}{\partial z'}\right)^2+\left(\frac{\partial U}{\partial r'}\right)^2+\left(\frac{U}{r'}\right)^2+\left(\frac{1}{2L/D}\frac{\partial W}{\partial z'}\right)^2+\frac{1}{2}\left(\frac{1}{2L/D}\frac{\partial U}{\partial z'}+\frac{\partial W}{\partial r'}\right)^2\right\}r'dr'dz', \tag{3}$$

and the maximum kinetic energy

$$T_{\max}=\pi\rho LR^2\omega^2\int_{-1/2}^{1/2}\int_{0}^{1}(U^2+W^2)r'dr'dz'. \tag{4}$$

The integral in Eq. (3), $I_V=V_{\max}/(2\pi GL)$, depends on parameters ν and L/D, whereas, the integral $I_T=T_{\max}/(\pi\rho LR^2\omega^2)$ in Eq. (4) is not dependent on these two parameters. As G, L, and ν are constant quantities for a given sample, the minimum of $T_{\max}-V_{\max}$ is equivalent to the minimum of $\Omega^2 I_T-2I_V$; hence, Hamilton's principle for this case is given by

$$\Omega^2 I_T-2I_V=\text{minimum}. \tag{5}$$

Since this condition for a minimum relates the quantities Ω, ν, and L/D, axisymmetric nondimensional natural frequencies depend only on Poisson's ratio and slenderness ratio, which can be expressed as

$$\Omega=\Omega(\nu,L/D). \tag{6}$$

In this work, the Ritz method is used in order to calculate axisymmetric natural frequencies of a cylinder, in the same way as it is presented by Leissa and So.[10] The basic functions chosen are products of powers of the coordinates of the points of the cylinder. Power series are formed with the basic functions multiplied by the unknown coefficients. Hence, the series used for the radial and longitudinal displacements are algebraic polynomials of the form

$$U(r',z')=\sum_{i}^{I}\sum_{j}^{J}A_{ij}r'^{i}z'^{j}\quad\text{and}$$

$$W(r',z')=\sum_{p}^{P}\sum_{q}^{Q}C_{pq}r'^{p}z'^{q}, \tag{7}$$

with $i=1,2,3,...,I$; $j=0,1,2,...,J$; $p=0,1,2,...,P$; $q=0,1,2,...,Q$; where $i=0$ is not considered in order to avoid singularities in the stresses and radial displacements in $r'=0$. In symmetric modes j only takes even values and q odd values, and in antisymmetric ones j takes odd values and q even values.

As the difference $\Omega^2 I_T-2I_V$ must be a minimum, the partial derivatives with respect to the coefficients A_{ij} and C_{pq} must vanish. Consequently

$$2\frac{\partial I_V}{\partial A_{ij}}=\Omega^2\frac{\partial I_T}{\partial A_{ij}},\qquad 2\frac{\partial I_V}{\partial C_{pq}}=\Omega^2\frac{\partial I_T}{\partial C_{pq}}. \tag{8}$$

In this set of $I(J+1)+(P+1)(Q+1)$ homogeneous equations, Ω is a function, apart from the coefficients, of the variables Poisson's ratio and slenderness ratio. The set of equations obtained will only be resolvable in A_{ij} and C_{pq} if the condition of the determinant of the coefficient matrix being zero is satisfied. Natural frequencies are determined from such a condition in terms of ν and L/D. In other words, nondimensional natural frequencies of a cylinder can be calculated if its Poisson's ratio and slenderness ratio are known.

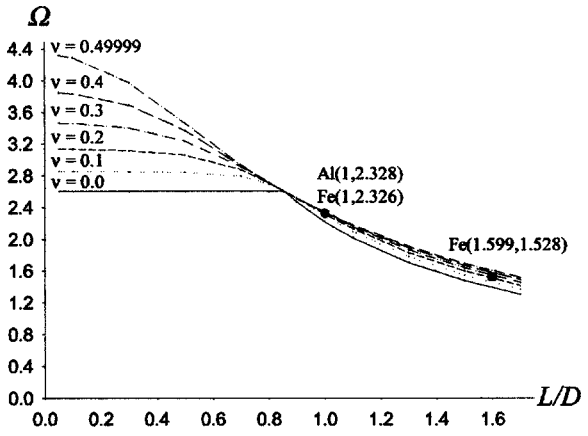

FIG. 1. Numerical results for the lowest value of nondimensional frequency $\Omega=\pi f D\sqrt{\rho/G}$ for symmetric vibration of cylinders versus slenderness ratio for several values of Poisson's ratio. All the curves pass through the universal point: $\Omega_u=2.6036$ and $(L/D)_u=0.853\,22$. The points corresponding to samples **e**, **f**, and **h** are also plotted and match the adequate curves.

III. RESULTS OF THE NUMERICAL CALCULATION

The method described in the previous section is first applied to cylinders whose slenderness ratios range from 0.05 to 1.7, made of materials with Poisson's ratio 0, 0.05,...,0.45, 0.499 99. Nondimensional frequencies Ω are obtained by setting the displacements with polynomials of the form given by Eq. (7). The upper limits I, J, P, and Q of the series are chosen for each value of L/D by following a trial with increasing values of the four indices so that the value of Ω obtained would be the minimum possible; the process is repeated until the limit of calculation of the computer is reached. In this way the Ritz method guarantees that this value of Ω is the most accurate frequency, and is an upper boundary for the exact value. The four indices reach maximum values at around 12; then, the number of unknown coefficients is about 80. For instance, the values used for $L/D=1$ and $\nu=0.3$ are $I=7$, $J=12$, $P=6$, and $Q=13$, that gives the first five frequencies 2.326 302, 3.067 140, 3.989 288, 4.896 035, and 5.592 656. These values agree precisely with those provided by Leissa and So[7] in all the comparable significant figures.

Figure 1 shows the values of the lowest nondimensional frequency Ω, for symmetric modes, calculated as a function of the slenderness ratio L/D and for materials with different Poisson's ratios. This figure shows that, independently of Poisson's ratio, all curves $\Omega-L/D$ cross through a point corresponding to the universal frequency Ω_u and to a value of L/D called the universal slenderness ratio. In order to obtain the exact values of both the universal frequency and the universal slenderness ratio by numerical calculation, the following procedure is carried out. The nondimensional symmetric

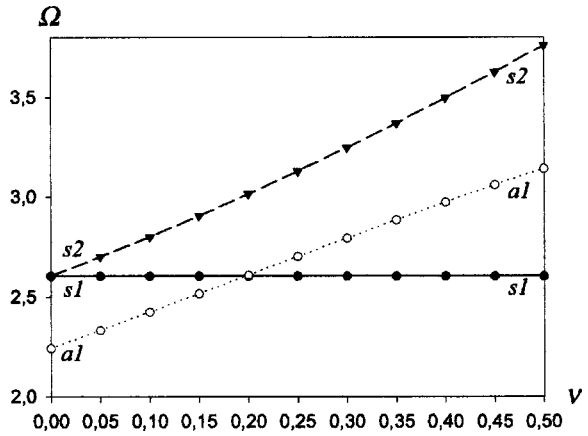

FIG. 2. Values of nondimensional frequency for the modes s_1, s_2, and a_1 as a function of Poisson's ratio for cylinders with universal slenderness ratio $(L/D)_u = 0.853\,22$. The three curves correspond to the three lowest values of Ω for any ν.

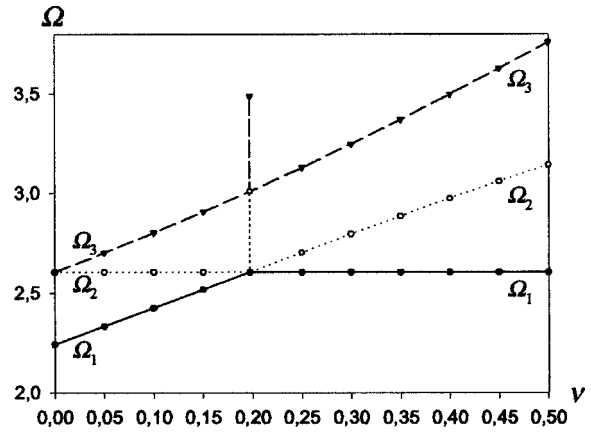

FIG. 3. Values of the nondimensional frequency Ω for axisymmetric modes and $(L/D)_u = 0.853\,22$: the first lowest value (1), the second (2), and the third (3). Note the singularity for $\nu = 0.20$.

frequencies corresponding to nine values of slenderness ratios, from 0.8 to 0.9, are calculated for different values of ν. When plotting the lowest values in the graph of Fig. 1, it is observed that the sought point must be between 0.85 (the slenderness ratio for which Ω is greater than Ω_u regardless of ν) and 0.86 (the value for which a Ω smaller than Ω_u corresponds to all ν). The average value 0.855 is thus taken. The nondimensional frequency is then calculated for this ratio and for one or more values of ν; so, it is possible to distinguish whether the value obtained is either to the right or to the left of the point to which the curves seem to tend. This iterative process leads to a slenderness ratio of $L/D = 0.853\,22$ and a value for the nondimensional frequency equal to $\Omega = 2.6036$, the result obtained for all values of ν. Therefore, this frequency is the first universal frequency. Note the good agreement of these numerical results with the analytical theoretical ones. It should be noted that the results shown in Fig. 1 refer to the first lowest frequency for the symmetric modes; however, the two sets of curves, one on the left and another on the right of the crossing point, correspond to two different mode shapes. The line $\nu = 0$ has a discontinuity of the second kind at the universal point, with a horizontal branch to the left, whereas the branch to the right seems to be a section of a hyperbola, due to these two branches corresponding to two different modes.

The Ritz method is also applied to a cylinder with universal slenderness ratio, $L/D = 0.853\,22$. Figure 2 shows the results obtained for the values of nondimensional frequency Ω for several modes against those of ν. The graph only shows the frequencies for three modes: the first symmetric mode s_1, the second s_2, and the first antisymmetric a_1. This simple representation is sufficient for the present study. Note that the mode s_1 corresponds to the straight line $\Omega_u = 2.6036$, which confirms Zemanek's[3] prediction.

Two singular facts follow from the examination of Fig. 2.

(1) There is a point of intersection of the curves corresponding to s_1 and a_1 in the neighborhood of $\nu = 0.20$. This fact is particularly important for the present study, since it shows that for values of Poisson's ratio greater than 0.20 the lowest frequency corresponds to the symmetric mode as expected for long cylinders. However, for values of ν smaller than 0.20, it is found that the lowest frequency corresponds to an antisymmetric mode, as it does for short cylinders or disks. Therefore, if Poisson's ratio for a material was known in advance, it would also be known which of the lowest detected frequencies corresponds to the symmetric mode.

In general, Poisson's ratio ν is, *a priori*, an unknown value as is, in some cases, its order of magnitude. Therefore, it is necessary to infer a practical rule that permits determination of the value of a given spectrum which corresponds to the first symmetric mode. For this reason, it is practical to draw a second graph, Fig. 3, which shows the lines for the lowest values of the frequencies Ω_1, Ω_2, and Ω_3, as a function of ν.

The definition of Ω implies that, for a given material, i.e., with G and ρ determined, the quotient of the nondimensional frequencies Ω_i/Ω_j is equal to the quotient of the ordinary frequencies f_i/f_j. This allows Fig. 4 to be drawn, which shows the quotients f_2/f_1 and f_3/f_2 as a function of ν, where f_1, f_2, and f_3 are the three lowest axisymmetric frequencies, in order of increasing size,

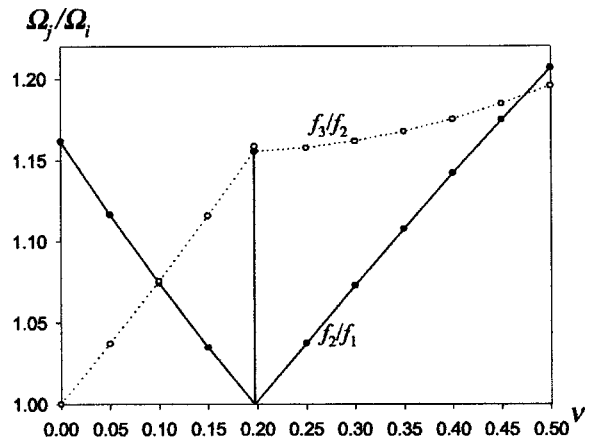

FIG. 4. Quotients f_2/f_1 and f_3/f_2 of the ordinary frequencies for $(L/D)_u = 0.853\,22$ as functions of Poisson's ratio. Such quotients show if Poisson's ratio is greater or smaller than 0.2.

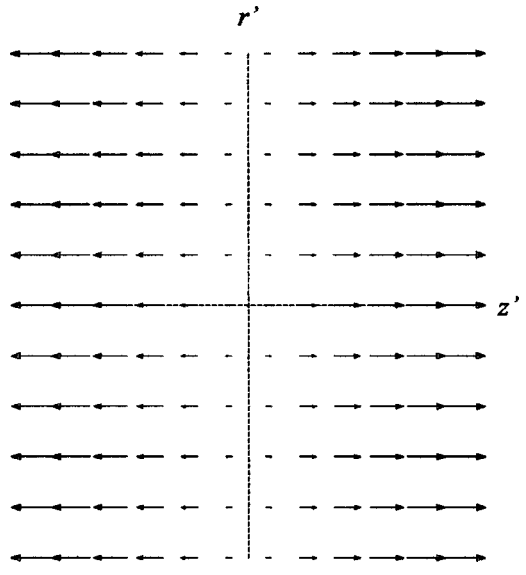

FIG. 5. Mode shape s_1 for a material with $\nu=0$ and universal slenderness ratio. The displacement of the points is entirely axial.

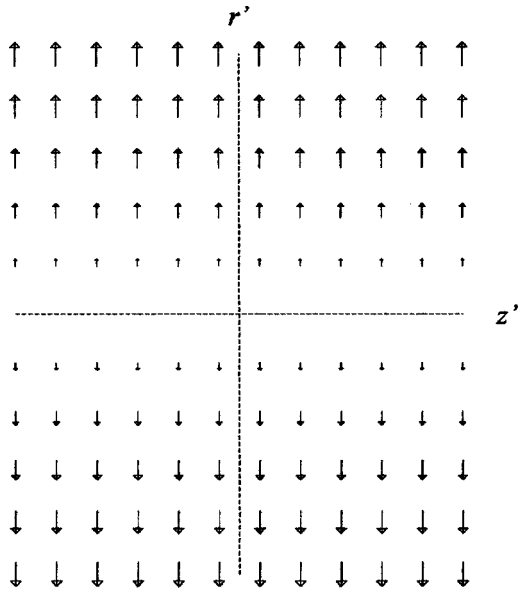

FIG. 6. Mode shape for the mode s_2 for $\nu=0$ and universal slenderness ratio. Displacements are in the radial direction. Note the great difference to the mode s_1.

detected in an experiment. Although neither of these two quotients is a single-valued function of ν, by using both quotients it is possible to easily identify which modes correspond to the three lowest experimental frequencies f_1, f_2, and f_3. So, for all quotients $f_2/f_1<1.16$, the ratio f_2/f_1 gives two possible values of ν, one being smaller and the other greater than 0.20, whereas the quotient f_3/f_2 indicates if ν is greater or smaller than 0.20. If ν is greater than 0.20, the lowest frequency f_1 corresponds to the mode s_1. But, if ν is smaller than 0.20, the lowest frequency f_1 is associated with the first antisymmetric mode a_1 and the next greatest value f_2 corresponds to the first symmetric mode s_1. In the particular case of a material with $\nu=0.20$, the frequencies corresponding to the modes s_1 and a_1 will overlap in the spectrum and f_2 will then correspond to the second symmetric mode; the quotient f_2/f_1 will be equal to 1.155 and the lowest frequency in the spectrum will correspond to s_1 (and to a_1). Therefore, it is concluded that measurement of the three lowest frequencies of the axisymmetric vibration spectrum of a cylinder with universal slenderness ratio permits the frequency corresponding to the mode s_1 to be identified.

(2) Figure 2 shows the intersection of the curves corresponding to s_1 and s_2 for $\nu=0$. This fact means that the two lowest symmetric modes have the same frequency. Since this seems contradictory, a study regarding the modes involved follows. The mode shapes are determined from the numerical calculation of the coefficients A_{ij} and C_{pq}, which in turn yield the values of U and W. Figure 5 shows the amplitude of displacements for the mode s_1 of a cylinder with slenderness ratio equal to the universal value and Poisson's ratio equal to zero: the points are on a cross section containing the axis of revolution. This figure proves that the displacement is entirely axial, as expected according to the elementary theory of longitudinal vibration of cylinders. A tensional stress is associated with such a field of displacements. Figure 6 shows the amplitudes of the displacements for the mode s_2. In this case, displacements are entirely radial. Therefore, the modes s_1 and s_2 are totally different in shape and it is not contradictory that both modes vibrate with the same frequency, for cylinders with the universal slenderness $L/D=0.853\,22$.

IV. ANALYTICAL STUDY OF THE UNIVERSAL SLENDERNESS RATIO

The universal point and the universal frequency Ω_u are complicated concepts. Since this study is focused on axisymmetric vibration of cylinders, a question arises regarding the relation of Ω_u to a more concrete property of a real cylinder. Let us show from an analytical point of view that the universal frequency is related to one quotient of the length and diameter, called the universal slenderness ratio.

In order to analytically derive the value of the universal slenderness ratio, let us consider a cylinder of arbitrary length and diameter, made of a material whose Poisson's ratio is zero. For such a material its shear modulus is $G=E(2(1+\nu))=E/2$. Let us assume that this cylinder vibrates freely in a longitudinal mode. For such a cylinder the elementary theory can be applied accurately since there is no radial expansion. Shear stress is zero at all its points, and particularly on the ends; therefore, normal stress can also be made to vanish on both ends if an incident wave is reflected with no phase shift. In the symmetric mode with the lowest frequency, the length of the rod is half of the wavelength, $L=\lambda/2$. The corresponding nondimensional frequency is given by

$$\Omega \equiv \pi f D \sqrt{\frac{\rho}{G}} = \pi \frac{1}{2L} \sqrt{\frac{E}{\rho}} D \sqrt{\frac{2\rho}{E}} = \frac{\pi}{\sqrt{2}} \frac{1}{L/D}. \qquad (9)$$

When this cylinder with $\nu=0$ is vibrating with the lowest nondimensional frequency $\Omega_u=2.6036$, its slenderness ratio

must be equal to the universal value. According to Eq. (9), this ratio is given by

$$(L/D)_u = \pi/(\sqrt{2}\,2.6036) = 0.853\,22. \tag{10}$$

As this slenderness ratio corresponds to the lowest value of Ω_u, it is the largest universal slenderness ratio. The mode related to this first universal point is symmetric.

In Sec. II it is demonstrated that nondimensional frequency Ω is, in general, a function of only L/D and ν. However, when the frequency takes the universal value, Ω does not depend on ν; consequently, Eq. (9) with $\Omega = \Omega_u$ should be satisfied for a cylinder regardless of ν. Therefore, for any cylinder the highest universal slenderness ratio is 0.853 22.

The coincidence of this analytical result with the numerical one proves the existence of the universal point, the accuracy of the numerical calculation, and the good agreement of the analytical and numerical theories.

Obviously, apart from the frequency Ω_u, a cylinder with universal slenderness ratio can vibrate with other natural frequencies.

For the second universal frequency, $\Omega_{u2} = 7.5392$, the length will be $L_{u2} = 3\lambda/2$, then $(L/D)_{u2} = 3\pi/(7.5392\sqrt{2}) = 0.883\,96$, etc.

This result can be directly obtained for a cylinder, independently of its Poisson's ratio, by relating Ω to λ and L. In effect, the identity $\Omega = \sqrt{2}\,\gamma D/2$, given in the Introduction becomes for the nth universal mode

$$\Omega_{un} = \sqrt{2}\frac{2\pi}{\lambda_{un}}\frac{D_u}{2} = \sqrt{2}\frac{\pi}{2L_{un}/(2n-1)}D_u \Rightarrow$$

$$\left(\frac{L}{D}\right)_{un} = (2n-1)\frac{\pi}{\sqrt{2}\Omega_{un}}. \tag{11}$$

The expected natural frequencies f in a cylinder with a universal slenderness ratio can then be expressed, from the definition of Ω, as

$$f_u = \frac{\Omega_u}{\pi D}\sqrt{\frac{G}{\rho}}. \tag{12}$$

Equation (12) shows that a cylinder with a universal slenderness ratio will have a natural frequency that depends on elastic constant G, but not on ν. It could be deduced from Eq. (11) that one overtone exists for $n=2$ with a frequency of three times the fundamental, for $n=3$ five times, and so on. However, this is false, since Ω_{un} in Eq. (11) also depends on n; hence, $(L/D)_{un}$ is not a linear function of n. Moreover, analyzing the dispersion curves of Ω vs $\gamma D/2$ and drawing the straight line $\Omega = \sqrt{2}\,\gamma D/2$, it is observed that this line intersects the curve corresponding to each mode of propagation at only one point; so, overtones would correspond to impossible modes of propagation. Note that the universal slenderness ratio does not depend on elastic properties of the cylinder. In other words, universal points are each characterized by their Ω_{un} and the corresponding $(L/D)_{un}$, both being independent of elastic properties of the cylinder. In this sense their universality is confirmed.

V. COMPARISON OF NATURAL FREQUENCIES OF SAMPLES

When studying natural frequencies of finite cylinders, it is concluded that, in general, nondimensional frequency Ω depends in a complicated form on Poisson's ratio and slenderness ratio. However, some conclusions can be inferred from the study of geometrically similar cylinders.

(a) Let us consider two cylinders, denoted by **a** and **b**, respectively, of the same material, of different size, but similar to each other, i.e., with the same slenderness ratio L/D. These samples are similar from the geometric point of view, that is, they have the same shape but different size. As the nondimensional frequency for a given mode only depends on Poisson's ratio and the slenderness ratio, which are equal for both cylinders, the nondimensional frequency must take the same value in both cases, obtaining

$$\Omega = \pi f_a D_a \sqrt{\rho/G} = \pi f_b D_b \sqrt{\rho/G}, \tag{13}$$

hence

$$(f_a/f_b)_t = D_b/D_a. \tag{14}$$

Therefore, in geometrically similar cylinders, of the same material, the natural frequencies for any mode are inversely proportional to their diameters.

In a first experiment, two stainless-steel Din 1.4301 cylinders are machined: one with diameter $D_a = 24.90$ mm and length $L_a = 79.90$ mm, while the other has a diameter of $D_b = 49.90$ mm and a length of $L_b = 159.90$ mm. Then, the slenderness ratios become 3.209 and 3.204, respectively, which are practically equal (relative difference 0.2%). According to the theoretical demonstration above, the quotient of frequencies must be

$$(f_a/f_b)_t = D_b/D_a = 49.90/24.90 = 2.004. \tag{15}$$

This condition will be experimentally tested, as will be described later.

(b) Let us consider two cylindrical samples, denoted by **c** and **d**, of two materials with different elastic properties: the elastic properties of one of them are ν_c and G_c, whereas those of the other are ν_d and G_d. Both samples are cut from cylinders of different diameters, so that their lengths divided by their corresponding diameters equal the universal slenderness ratio $L/D = 0.8532$. For both samples, the nondimensional frequency for the first symmetric mode is equal to the universal frequency. Therefore, according to the aforementioned definition of nondimensional frequency, it follows that

$$\pi f_c D_c \sqrt{\rho_c/G_c} = \pi f_d D_d \sqrt{\rho_d/G_d}. \tag{16}$$

Therefore, the theoretical quotients of frequencies for the first symmetric mode must be

$$(f_c/f_d)_t = D_d/D_c \sqrt{\rho_d G_c/\rho_c G_d}. \tag{17}$$

The sample used, **c**, is stainless steel with the following properties: $D_c = 49.90$ mm; $L_c/D_c = 0.85$, $\rho_c = 7884$ kg/m^3; $G_c = 76.24$ GPa. The sample **d** is commercial aluminum and its properties are: $D_d = 39.00$ mm; $L_d/D_d = 0.85$; $\rho_d = 2791$ kg/m^3; $G_d = 28.1$ GPa.

The quotient of frequencies is, according to Eq. (17)

TABLE I. Summary of the samples used in the laboratory. All properties required for the present study are shown.

Material	Sample	Diameter D (mm)	Length L (mm)	L/D	f_1 (Hz)	f_2 (Hz)	f_3 (Hz)
Steel	**a**	24.90	79.90	3.209	31 300	61 475	⋯
	b	49.90	159.90	3.204	15 550	30 510	⋯
	c	49.90	42.57	0.8532	51 725	55 325	64 150
	e	49.90	49.90	1.000	46 142	⋯	⋯
	h	50.00	79.95	1.599	30 566	⋯	⋯
Aluminum	**d**	39.00	33.27	0.85	67 275	73 300	85 950
	f	40.30	40.30	1.000	58 321	⋯	⋯
Fused quartz	**g**	47.60	40.45	0.8498	64 150	65 775	74 375

$$(f_c/f_d)_t = 0.765\,99. \tag{18}$$

This quotient will be verified by carrying out one experiment in the laboratory, as will be shown later.

(c) One cylinder is machined so that the quotient of its length and diameter is equal to the universal slenderness ratio, $L/D = 0.8532$. When such a cylinder is freely vibrating in its axisymmetric symmetric mode with the lowest frequency, this frequency is the first nondimensional universal frequency. From the definition of Ω, shear modulus can be expressed as

$$G = \frac{\pi^2 f^2 D^2 \rho}{\Omega_u^2} = \frac{\pi^2 f^2 D^2 \rho}{2.6036^2}. \tag{19}$$

This formula shows that if the first axisymmetric symmetric mode of a cylinder with universal slenderness ratio is excited and identified, as described in Sec. III, measurements of its frequency f, its diameter D, and its density ρ, lead to the value of its shear modulus G. Analogously, formulas such as Eq. (19) could be derived for other universal points with greater frequencies.

VI. EXPERIMENTAL ARRANGEMENT

Each one of the studied cylindrical samples is tested as follows. The cylinder is positioned horizontally and supported at its center on a small rubber block. A simple pendulum, consisting of a steel ball, 3.2 mm in diameter, suspended from a thread about 10 cm long, is used to apply an axial impact to the center of one of its ends. The cylinder is then left to vibrate almost freely. An optical interferometer is used as a detector of vibration at the center of the opposite end. The interferometer[11] used can detect both the normal and tangential components of displacement with a resolution of about 1 nm. For convenience, only the normal component is detected in our experiments. The beam from a He–Ne laser is split in two, each with a different frequency; one is used as a reference and the other is the incident wave at the central point of the end opposite to the impact end. The latter is scattered by the scratched surface yielding an intensity pattern, called speckle, with maxima and minima of intensity. The scattered light is collected in a direction symmetrical to the incident beam. Finally, it interferes with the reference beam at the beam mixer. The electronic demodulation circuitry produces an output proportional to the surface displacement component, which is digitized and displayed with an oscilloscope. The fast Fourier transform of the signal, FFT, provides the amplitude of the harmonics, whose maximum values correspond to the natural frequencies.

VII. EXPERIMENTAL RESULTS

The experimental results described in this section correspond to the samples listed in Table I. This table includes the main properties of the samples tested in this work.

(a) In the first series of experiments, the aforementioned stainless-steel cylinders **a** and **b** are used. They have approximately the same slenderness ratios, 3.209 and 3.204, respectively, and their quotient of frequencies, according to the theoretical demonstration, must be $f_a/f_b = 2.004$.

As it is already known that Poisson's ratio of steel is greater than 0.2, then the lowest axisymmetric frequency corresponds to $s1$. The frequencies measured in the laboratory for the first symmetric mode are 31 300 and 15 550 Hz, respectively, for samples **a** and **b**, the quotient being $f_{1,a}/f_{1,b} = 2.013$. The relative difference with the theoretical value (2.004) is 0.4%. This value is of the order of the uncertainty associated with the FFT in our experiments, with a frequency uncertainty of 25 Hz, and of the relative difference between the values of their slenderness ratios.

Greater frequencies have also been measured in the laboratory. The values obtained for the second frequencies are 61 475 and 30 510 Hz for **a** and **b**, respectively. Then, $f_{2,a}/f_{2,b} = 2.015$, a relative difference with the theoretical value (2.004) of 0.5%.

Both relative differences confirm the soundness of the theoretical approach, the quality of the experimental measurements, and the agreement between theory and practice.

(b) In a second series of experiments, two cylinders, **c** and **d**, of different materials are machined. Sample **c** is the aforementioned stainless-steel cylinder, and sample **d** is the commercial aluminum cylinder, also described in Sec. V. They both have the same slenderness ratio 0.85, approximately equal to the universal slenderness ratio.

The vibration spectrum for the steel sample is shown in Fig. 7. The results obtained for the lowest natural frequencies of the symmetric axisymmetric modes are: for the steel sample $f_{i,c} = 51\,725$, 55 325, and 64 150 Hz, and for the aluminum sample $f_{i,d} = 67\,275$, 73 300, and 85 950 Hz. Thus, the experimental quotient for the two lowest frequencies is $(f_{1,c}/f_{1,d})_e = 0.768\,86$, the sensitivity being 25 Hz.

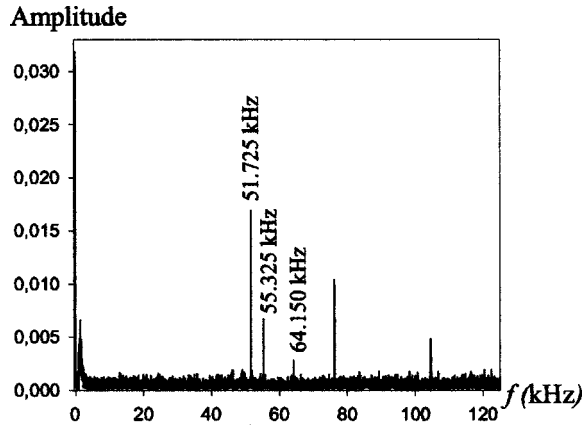

FIG. 7. Natural frequencies for the stainless-steel sample with $D_c = 49.90$ mm; $L_c/D_c = 0.85$, $\rho_c = 7884$ kg/m^3, and $G_c = 76.48$ GPa.

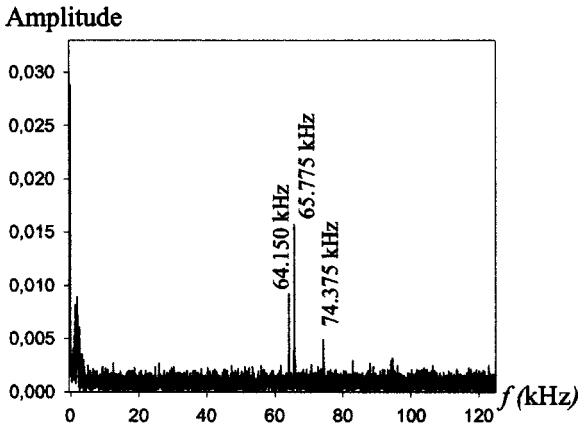

FIG. 8. Natural frequencies for the sample **g**, fused quartz with $D_g = 47.60$ mm; $L_{g/Dg} = 0.8498$, $\rho_g = 2199$ kg/m^3, and $G_g = 31.39$ GPa.

The relative difference between the theoretical quotient (0.765 99) and the experimental one is then 0.4%. This very small value demonstrates a good agreement between the theoretical and experimental results, which confirms the validity of this interpretation of the universal point and that of the experimental methods used.

(c) The values of G are calculated by means of Eq. (19) from the experimental frequencies obtained for the various cylinders. The experimental spectrum for the steel sample **c** is first analyzed. According to Fig. 7, the three lowest natural frequencies are the aforesaid values: 51 725, 55 325, and 64 150 Hz. Second, the quotient of the second and first frequencies, and that of the third and the second are calculated, obtaining 1.07 and 1.16, respectively. For these quotients Fig. 4 shows that Poisson's ratio is greater than 0.2. Consequently, the frequency 51 725 Hz corresponds to the first symmetric mode. Finally, this frequency substituted into Eq. (19) gives a shear modulus of 76.48 GPa.

Analogously, for the aluminum sample, **d**, also with the universal slenderness ratio, the natural frequencies are: 67 275, 73 300, and 85 950 Hz and the corresponding quotients become 1.09 and 1.17. From the quotient 1.17 and Fig. 4, it is deduced that Poisson's ratio is greater than 0.20. The shear modulus is then 27.9 GPa.

The last sample tested is fused quartz, denoted by **g**, whose dimensions are: $L = 40.45$ mm, $D = 47.60$ mm, then $L/D = 0.849$. The vibration spectrum is shown in Fig. 8. The values of the three lowest natural frequencies are 64 150, 65 775, and 74 375 Hz, and the aforesaid quotients become 1.02 and 1.13, respectively. From these quotients and Fig. 4, it is deduced that the material of this cylinder has a Poisson's ratio smaller than 0.2. Therefore, the second frequency, the symmetric one, should be substituted into Eq. (19), obtaining a value of $G = 31.39$ GPa.

In previous experiments a stainless-steel sample, **e**, corresponding to a cylinder $L/D = 1$, was tested in the laboratory, the shear modulus being 76.24 GPa. Similarly, an aluminum sample, **f**, with $L/D = 1$, provided a shear modulus of 28.1 GPa. In this work, the *P*-wave and *S*-wave velocities of the quartz sample are measured by the pulse–echo method; from these values and the density, the shear modulus turns out to be $G = 31.26$ GPa.

Comparing the results given in this work for the shear modulus with those described in the previous paragraph, the relative differences are 0.3%, 0.5%, and 0.4%, respectively. These very small differences show the validity of the direct method proposed for calculating the shear modulus using a cylinder with universal slenderness ratio.

The value of Poisson's ratio can also be obtained from Figs. 3 or 4. However, this is not the initial aim of our study and therefore is considered as a by-product.

(d) In order to verify the numerical calculation leading to the demonstration of the existence of the universal point, the following experimental study with three samples is carried out. The first sample, **e**, is that of stainless steel whose diameter is equal to its length, $L = D = 49.90$ mm, $m = 769.4$ g, $\nu = 0.298$, and $G = 76.24$ GPa. The first sharp peak in the spectrum of frequencies, $f_{s1} = 46\,142$ Hz, corresponds to the natural frequencies for the first axisymmetric symmetric mode. Taking into account the shear modulus of the sample and the definition of the nondimensional frequency, it is found that $\Omega = 2.326$.

The second sample used, **f**, is that of commercial aluminum with $L = D = 40.30$ mm, mass $m = 143.5$ g, and elastic properties $\nu = 0.329$ and $G = 28.1$ GPa. For this sample $f_{s1} = 58\,341$ Hz and hence $\Omega = 2.328$. The third sample, namely **h**, is made from same steel as **e**, but with $L = 79.95$ mm, $D = 50.00$ mm, and density 7900 kg/m^3. The spectrum gives a $f_{s1} = 30\,566$ Hz and then $\Omega = 1.528$.

The points $(L/D, \Omega)$ corresponding to the three samples are marked in Fig. 1. They are appropriately placed in their respective locations.

VIII. CONCLUSIONS

From the results presented in this paper it is concluded that: (1) the existence of the universal point is numerically demonstrated, where the nondimesional frequency is independent of Poisson's ratio; (2) dynamic shear modulus can be directly determined by means of a simple multiplication and a single experiment using a cylinder with universal slenderness ratio, where first frequency, diameter, and density are measured; (3) the experimental values for the nondimen-

sional frequency lie almost exactly on the curves obtained by the numerical methods; (4) both the numerical and experimental methods used are validated.

[1] L. E. Kinsler, A. R. Frey, A. B. Coppens, and J. V. Sanders, *Fundamentals of Acoustic* (Wiley, New York, 2000), pp. 68–70.

[2] T. R. Meeker and A. H. Meitzler, *Physical Acoustics* (Academic, New York, 1964), Vol. 1A, pp. 111–167.

[3] J. Zemanek, ''An experimental and theoretical investigation of elastic wave propagation in a cylinder,'' J. Acoust. Soc. Am. **51**, 265–283 (1972).

[4] C.R.C., *Standard Mathematical Tables* (The Chemical Rubber Co., Cleveland, 1967), p. 466.

[5] J. R. Hutchinson, ''Vibration of solid cylinder,'' J. Appl. Mech. **47**, 901–907 (1980).

[6] M. Senoo and T. Mishimura, ''Measurement of elastic constants of polycrystals by the resonance method in cylindrical specimen,'' Bull. JSME **27**, 2339–2346 (1984).

[7] A. W. Leissa and J. So, ''Comparisons of vibration frequencies for rods and beams from one-dimensional and three-dimensional analyses,'' J. Acoust. Soc. Am. **98**, 2122–2135 (1995).

[8] F. Nieves, F. Gascón, and A. Bayón, ''Estimation of the elastic constants of a cylinder with a length equal to its diameter,'' J. Acoust. Soc. Am. **104**, 176–180 (1995).

[9] A. Bayón, F. Gascón, and F. J. Nieves, ''Comparación de Frecuencias de Cilindros de Esbeltez Universal'' (A comparison of frequencies for universal slenderness cylinders), *XXVII Reunión Bienal de la Real Sociedad Española de Física*, Sevilla, Spain (2001).

[10] A. W. Leissa and J. So, ''Accurate vibration frequencies of circular cylinder from three-dimensional analysis,'' J. Acoust. Soc. Am. **98**, 2136–2141 (1995).

[11] J. P. Monchalin, ''Optical detection of ultrasound,'' IEEE Trans. Ultrason. Ferroelectr. Freq. Control **33**, 485–499 (1986).

Characterization of a nonrigid sphere using the backscattered fields of acoustic X waves

Maged F. Moawad and Amr M. Shaarawi[a)]
The Physics Department, The American University in Cairo, P.O. Box 2511, Cairo 11511, Egypt

Ioannis M. Besieris
The Bradley Department of Electrical and Computer Engineering, Virginia Polytechnic Institute and State University, Blacksburg, Virginia 24061

(Received 24 September 2003; revised 26 February 2004; accepted 2 March 2004)

The scattering of acoustic ultra-wideband X-wave pulses by a nonrigid sphere is simulated for purposes of material identification and characterization. Using the backscattered spectrum of the X-wave pulses, a procedure is described for estimating the radius, speed of sound, and density of the sphere. The effectiveness of the suggested technique is verified in the case that the peak of the X wave is incident on the centers of the sphere, as well as for the off-center incidence case. © *2004 Acoustical Society of America.* [DOI: 10.1121/1.1715111]

PACS numbers: 43.40.Fz, 43.20.Fn. [ANN] Pages: 2937–2946

I. INTRODUCTION

The scattering of acoustic ultra-wideband pulses from spheres has important applications in fields such as high-resolution imaging, remote sensing, material characterization, and detection of buried objects. Localized waves, one class of ultra-wideband pulses, have distinct advantages in such applications. A study along these lines has dealt with the scattering of an X wave, a specific class of localized waves, from a circular disk in free space or buried in the ground.[1] The analysis used in that investigation was based on high-frequency techniques in combination with a pulsed plane wave representation of the X-wave solution.[2] In spite of the effectiveness of the methods used in the aforementioned study, the work did not address the possibility of using the scattered signal in order to identify or characterize the scattering object. An important theoretical and experimental study of the applicability of localized waves for identification purposes was undertaken by Power, Donnelly, and MacIsaac,[3] who demonstrated the possibility of identifying the radii of various types of spheres from the spectrum of the backscattered signal; the latter arose from an incident modified power spectrum (MPS) pulse.[4] Their analysis considered acoustical scattering from nonrigid spheres. However, the underlying method was applicable only to the identification of the radii of the spheres, and could not be used to find the speed of sound or the density of the scattering material.

Our aim in this work is to investigate the possibility of using the spectrum of the backscattered acoustical X waves in order to determine the characteristic properties of the materials of the spheres. By simulating the scattered signals from different spheres, it is demonstrated that an accurate estimate of the radii of the spheres, as well as the densities and the sound speeds of their materials, can be obtained. It is important to emphasize that the different characteristic properties of the spheres are identified using different portions of the ultra-wideband spectrum of the backscattered acoustic X wave. Consequently, the ideas considered in this paper are relevant for other ultra-wideband pulses. Nevertheless, X waves have the additional advantage that their extended localization range ensures that a relatively large amount of energy reaches the scattering spheres. The plan of this work is as follows. A spectral representation of the incident X-wave is provided in Sec. II. The scattered field is deduced in Sec. III and several features of the backscattered spectrum are considered in Sec. IV. A detailed portrayal of the proposed identification scheme based on a simulation of backscattered spectra from six different materials is carried out in Sec. V. Concluding remarks are made in Sec. VI.

II. THE INCIDENT ACOUSTICAL X-WAVE PULSE

A spectral approach will be used to obtain the scattered field due to an incident acoustical X wave (AXW). Thus, it is important to be able to choose the spectral representation that is best suited to the adopted analysis. The AXW can be represented as a Fourier superposition over plane waves whose wave vectors form a conic surface,[5] as shown in Fig. 1. The series solution of a plane wave scattered from a sphere[6] can then be integrated over the Fourier spectrum of the X-wave solution in order to obtain the AXW scattered field.

To determine the AXW Fourier representation, consider the three-dimensional scalar wave equation

$$\left(\vec{\nabla}^2-\frac{1}{c^2}\frac{\partial^2}{\partial t^2}\right)p(\vec{r},t)=0 \tag{1}$$

for the pressure field; the latter can be related to a potential function $\Psi(\vec{r},t)$ as follows:

$$p(\vec{r},t)=-\rho_0\frac{\partial}{\partial t}\Psi(\vec{r},t). \tag{2}$$

The density of the surrounding medium is denoted by ρ_0. The AXW potential of the incident pulse, which is also a solution to the 3D scalar wave equation, can be represented in terms of the Fourier superposition

[a)]On leave from the Department of Engineering Physics and Mathematics, Faculty of Engineering, Cairo University, Giza 12211, Egypt.

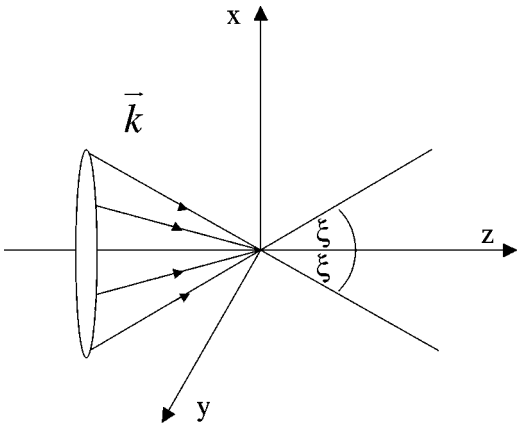

FIG. 1. Wave vectors of the normally incident X-wave lying on a conic surface having an apex angle ξ.

$$\Psi^i_{\mathrm{AXW}}(\vec{r},t)=\int_{R^3} d^3\vec{k}\int_0^\infty d(\omega/c)e^{-i\vec{k}\cdot\vec{r}} \times e^{i\omega t}\hat{\psi}(\vec{k},\omega)\,\delta(\omega-|\vec{k}|c), \tag{3a}$$

in which the AXW spectrum has the following specific form:[7]

$$\hat{\psi}(\vec{k},\omega)=ie^{-(\omega/c)a}\frac{2\pi}{c\rho_0\sin\xi}k^{q-2}\delta(\theta_k-\xi) \tag{3b}$$

in a spherical coordinate system $\vec{k}=(k,\theta_k,\phi_k)$. The fixed angle ξ is referred to as the axicon angle. One should note that the spectrum given in Eq. (3b) restricts the Fourier spectral components to plane waves propagating along directions forming a conical surface defined by the conical angle ξ. The substitution of the spectrum $\hat{\psi}(\vec{k},\omega)$ in Eq. (3a) yields

$$\Psi^i_{\mathrm{AXW}}(\vec{r},t)=\int_0^\infty dk\int_0^\pi d\theta_k\int_0^{2\pi} d\phi_k k^2\sin\theta_k\frac{i2\pi}{c\rho_0\sin\xi} \times k^{q-2}\delta(\theta_k-\xi)e^{-ka}e^{-i\vec{k}\cdot\vec{r}}e^{ikct}. \tag{4a}$$

Integrating over θ_k and ϕ_k, we obtain

$$\Psi^i_{\mathrm{AXW}}(\vec{r},t)=\frac{i4\pi^2}{c\rho_0}\int_0^\infty dk\,k^q e^{-ka}e^{-i\vec{k}\cdot\vec{r}}e^{ikct}. \tag{4b}$$

For integer values of q, the integration over k in the axisymmetric (with respect to the z axis) incident X-wave pulse, viz.,

$$\Psi^i_{\mathrm{AXW}}(\rho,z,t)=\frac{i2\pi}{c\rho_0}\frac{\partial^q}{\partial a^q} \times\{\rho^2\sin^2\xi+[a+i(z\cos\xi-ct)]^2\}^{-1/2}. \tag{5}$$

Here, ρ denotes the radial variable in cylindrical coordinates, the positive parameter a determines the width of the pulse, and q characterizes the order of the X wave. The axial and lateral widths of the AXW pulse are equal to $a/\cos\xi$ and $a/\sin\xi$, respectively.[1] The spectral bandwidth is determined by the two parameters a and q. The peak of the spectrum occurs at $\omega_{\mathrm{peak}}=qc/a$. The maximum frequency corresponding to the $1/e^4$ point is given by the expression $\omega_{\max}=(q+4)c/a$. The AXW pulse, given in Eq. (5), has a high-intensity central portion buried in an extended sparse background field. The localized central portion of the X wave has lateral and axial waists equal to $a/\sin\xi$ and $a/\cos\xi$, respectively. For an AXW pulse generated from a source having a diameter equal to D, the peak of the pulse travels without any dispersion to a distance $D/2\tan\xi$ from the source.

III. THE SCATTERED X-WAVE PULSE

Consider an AXW pulse incident on a sphere of an unknown material immersed in a fluid (e.g., water), where the center of the sphere is situated at the origin. In order to calculate the scattered AXW pulse, we shall consider the general expression for a plane wave incident in a direction specified by a propagation vector $\vec{k}=(k,\theta_k,\phi_k)$. Assuming a harmonic time dependence of the form $\exp(i\omega t)$, the spatial part of the plane-wave solution appearing in Eq. (4) is given by

$$\Phi^i(r,\phi,\theta)=e^{-i\vec{k}\cdot\vec{r}}=e^{-ikr\cos\gamma}, \tag{6}$$

where γ denotes the angle between the position vector $\vec{r}=(r,\theta,\phi)$ and the wave vector $\vec{k}=(k,\theta_k,\phi_k)$. The specific choice $\theta_k=\xi$, required in Eq. (4), results in the angle γ_k defined by the relationship $\cos\gamma_k=\cos\xi\cos\theta+\sin\xi\sin\theta\cos(\phi_k-\phi)$.

Following the standard technique for calculating the scattering of plane waves from spheres, the incident plane wave is expanded in terms of Legendre polynomials and spherical Bessel functions, viz.,[8]

$$\Phi^i(r,\theta,\phi,t)=e^{-ikr\cos\gamma_k}e^{ikct} =\sum_{n=0}^\infty(-i)^n(2n+1) \times P_n(\cos\gamma_k)j_n(kr)e^{ikct}. \tag{7}$$

The function $P_n(\cos\gamma_k)$ can be separated according to the expression

$$P_n(\cos\gamma_k)=\sum_{m=0}^n\epsilon_m\frac{(n-m)!}{(n+m)!}P_n^m(\cos\theta)P_n^m(\cos\xi) \times\cos[m(\phi_k-\phi)], \tag{8}$$

where $\epsilon_m=1$ for $m=0$ and $\epsilon_m=2$ for $m\neq 0$.

The scattered field is usually represented as a series of concentric spherical waves diverging from the scatterer by means of the mathematical expression

$$\Phi^s(r,\theta,\phi,t)=\sum_{n=0}^\infty A_nP_n(\cos\gamma_k)h_n^{(2)}(kr)e^{ikct}, \tag{9}$$

where $h_n^{(2)}$ denotes a spherical Hankel function. The field inside a nonrigid sphere can be represented as follows:

$$\Phi^{in}(r,\theta,\phi,t)=\sum_{n=0}^\infty C_nP_n(\cos\gamma_k)j_n(k_er)e^{ik_ect}. \tag{10}$$

The coefficients A_n and C_n in Eqs. (9) and (10) are determined from the appropriate boundary conditions. How-

ever, we shall only be interested in the former for evaluating the backscattered field. At the surface of a sphere of radius R, the boundary conditions are chosen such that the normal component of the fluid velocity at the surface of the sphere is the same as that of the surface proper and that the pressure on the two sides of the interface between the fluid and the sphere is a continuous function. These two conditions can be written explicitly as

$$\nu_{n1}(r=R,\theta,\phi,t)=\nu_{n2}(r=R,\theta,\phi,t),$$

$$\vec{\nu}(\vec{r},t)\equiv\vec{\nabla}\Phi(\vec{r},t), \tag{11}$$

and

$$p_1(r=R,\theta,\phi,t)=p_2(r=R,\theta,\phi,t),$$

$$p(\vec{r},t)\equiv-\rho_0\frac{\partial}{\partial t}\Phi(\vec{r},t). \tag{12}$$

Utilizing these boundary conditions, one obtains

$$A_n=-(-i)^n(2n+1)\frac{j_n'(kR)+i\alpha_n j_n(kR)}{h_n^{(2)\prime}(kR)+i\alpha_n h_n^{(2)}(kR)}, \tag{13}$$

where $\alpha_n=i(\rho_0 c/\rho_e c_e)[j_n'(k_eR)/j_n(k_eR)]$. Here, ρ_0 is the density of the medium surrounding the sphere, while ρ_e is the density of the sphere. Similarly, c and $c_e=\sqrt{B\rho_e}=\sqrt{1/(\rho_e\kappa_e)}$ are the speeds of wave propagation outside and inside the sphere, respectively. The latter is expressed in terms of the density of the sphere and the adiabatic compressibility κ_e, which, in turn, is the reciprocal of the bulk modulus B. Finally, $k=\omega/c$ and $k_e=\omega/c_e$ are the wave numbers outside and inside the sphere, respectively.

If the center of the scattering sphere lies on the axis of propagation of the AXW pulse, the problem is azimuthally symmetric; thus $m=0$ is the only surviving term and the scattered potential becomes

$$\Psi^s_{\mathrm{AXW}}(r,\theta,\phi,t)$$
$$=\frac{i4\pi^2}{c\rho_0}\int_0^\infty dk\,k^q e^{-ka}e^{ikct}\sum_{n=0}^{\infty}-(-i)^n(2n+1)$$
$$\times\frac{j_n'(kR)+i\alpha_n j_n(kR)}{h_n^{(2)\prime}(kR)+i\alpha_n h_n^{(2)}(kR)}h_n^{(2)}(kr)$$
$$\times P_n(\cos\theta)P_n(\cos\xi). \tag{14}$$

Consider, on the other hand, an AXW incident off-center on the sphere. Specifically, an AXW moving along the z direction with its axis of propagation shifted to a line parallel to the z axis and passing through the point $x=x_0$ and $y=0$. The incident AXW will be the same as given in Eq. (4a), but with x replaced by $x-x_0$. In this case, the scattered potential assumes the form

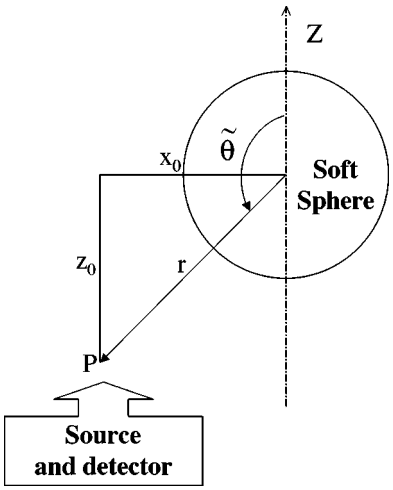

FIG. 2. Backscattered scheme due to pulse incident off center by a distance $x=-x_0$.

$$\Psi^s_{\mathrm{AXW}}(r,\theta,\phi,t)$$
$$=\frac{i4\pi^2}{c\rho_0}\int_0^\infty dk\,k^q e^{-ka}e^{ikct}\sum_{n=0}^{\infty}-(-i)^n(2n+1)$$
$$\times\frac{j_n'(kR)+i\alpha_n j_n(kR)}{h_n^{(2)\prime}(kR)+i\alpha_n h_n^{(2)}(kR)}h_n^{(2)}(kr)\sum_{m=0}^{n}(i)^m\epsilon_m$$
$$\times\frac{(n-m)!}{(n-m)!}P_n^m(\cos\tilde{\theta})P_n^m(\cos\xi)J_m(kx_0\sin\xi), \tag{15}$$

with the backscattered angle defined as $\tilde{\theta}=(\pi/2)+\cos^{-1}(x_0/r)$, as shown in Fig. 2. One should note that, in the configuration considered in Fig. 2, the detector point is placed close to the generator of the AXW. This off-axis detection position results in the two summations over m and n in Eq. (15). In addition, due to the lack of azimuthal symmetry the integration over ϕ_k yields the $J_m(kx_0\sin\xi)$ term.

IV. ANALYSIS OF THE BACKSCATTERED SPECTRUM

The scattered pressure pulse, calculated from Eq. (2), is given by

$$p^s_{\mathrm{AXW}}(r,\theta,\phi,t)$$
$$=4\pi^2\int_0^\infty dk\,k^{q+1}e^{-ka}e^{ikct}\sum_{n=0}^{\infty}-(-i)^n(2n+1)$$
$$\times\frac{j_n'(kR)+i\alpha_n j_n(kR)}{h_n^{(2)\prime}(kR)+i\alpha_n h_n^{(2)}(kR)}h_n^{(2)}(kr)P_n(\cos\theta)$$
$$\times P_n(\cos\xi) \tag{16}$$

for the on-axis incidence case, and by

TABLE I. Tabulated bulk modulus, density, and the calculated speed of sound propagation in different materials. (Ref. 10).

Material	Bulk modulus B (10^{11} N/m^2)	density ρ_e (10^3 kg/m^3)	Speed $c_e=\sqrt{B/\rho_e}$ (m/s)
Titanium	1.051	4.51	4827.40
Manganese	0.596	7.47	2824.64
Nickel	1.860	8.91	4568.96
Molybdenum	2.725	10.22	5163.66
Aluminum	0.722	2.70	5171.14
Chromium	1.901	7.19	5141.93
Copper	1.370	8.93	3916.83
Iron	1.683	7.87	4624.39
Lead	0.430	11.34	1947.28
Silver	1.007	10.50	3096.85

$$p^s_{\mathrm{AXW}}(r,\theta,\phi,t) = 4\pi^2 \int_0^\infty dk\, k^{q+1} e^{-ka} e^{ikct} \sum_{n=0}^{\infty} -(-i)^n (2n+1) \times \frac{j_n'(kR)+i\alpha_n j_n(kR)}{h_n^{(2)\prime}(kR)+i\alpha_n h_n^{(2)}(kR)} h_n^{(2)}(kr) \sum_{m=0}^{n} (i)^m \epsilon_m \times \frac{(n-m)!}{(n-m)!} P_n^m(\cos\tilde{\theta}) P_n^m(\cos\xi) J_m(kx_0 \sin\xi) \qquad (17)$$

for the off-axis incidence case.

Our aim in this section is to examine some general features of the spectra of backscattered fields from various types of spheres. In particular, we will consider the absolute spectrum, which is the square root of the sum of the squares of the real and imaginary parts of the integrand in Eq. (16) or (17). We assume that the spheres are made of materials with the properties listed in Table I. A comparison of Figs. 3(a) and 3(b) shows that spheres made of Mn and Pb have different backscattered spectra when placed in water, whereas there is a small difference when they are situated in air. Examining the expression given in Eq. (13), we notice that $\alpha_n \rightarrow 0$ if the ratio $\rho_0 c/\rho_e c_e$ is very small. For spheres placed in air, $\rho_0=1.2$ kg/m^3 and $c=350$ m/s, while for spheres in water, $\rho_0=1.0\times10^3$ kg/m^3 and $c=1500$ m/s approximately. Thus, the product $\rho_0 c$ is approximately equal to 400 for air and 1.5×10^6 for water. All the materials of Table I have $\rho_e c_e \approx (10-50)\times10^6$; therefore $\alpha_n \rightarrow 0$ for spheres placed in air. In this case, the coefficient given in Eq. (13) reduces to that of a rigid sphere. For the same spheres immersed in water α_n cannot be neglected. Since α_n depends on k_e, c_e, and ρ_e, we expect that these quantities could be extracted from the backscattered AXW spectrum. This explains the reason for Fig. 3 exhibiting different backscattered AXW spectra when the Mn and Pb spheres are immersed in water.

In Figs. 4–6, we provide the backscattered spectra for spheres made of four different materials, namely, Ti, Mn, Ni, and Mo. These spectra are calculated for radii of 30, 35, and 40 mm. From these plots, we specify three parameters: Δk_{av}, A, and $\Delta k'_{\mathrm{av}}$, which are the average spacing of the spectral dips at low frequency, the amplitude of the first peak, and the average spacing of the spectral dips over the entire spectrum,

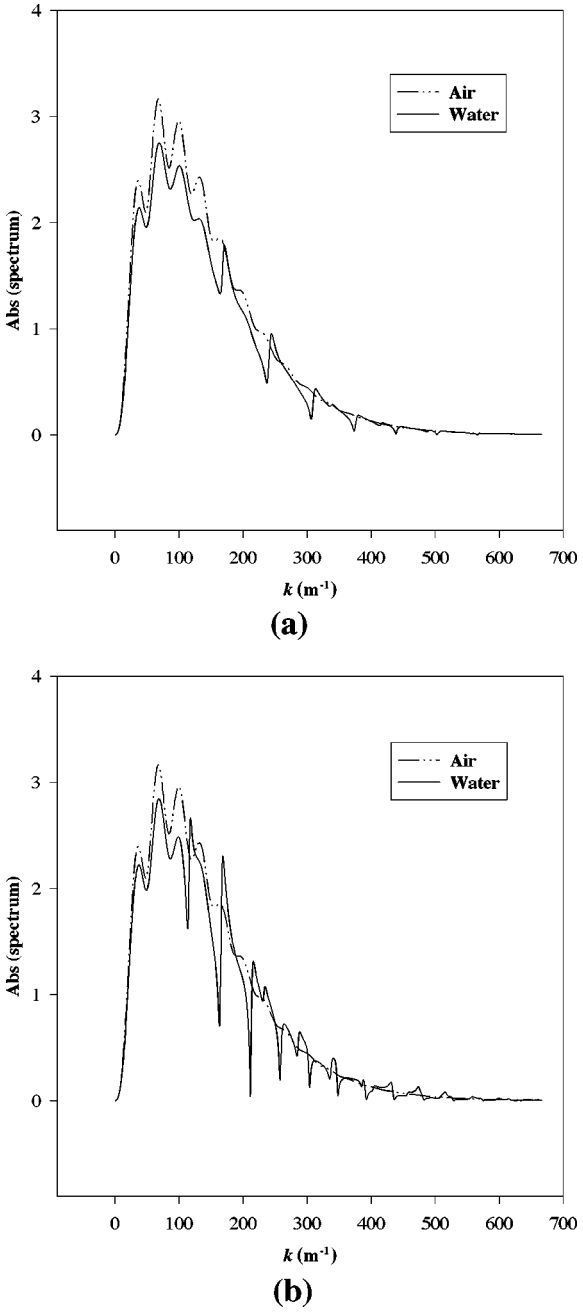

FIG. 3. Backscattered spectra by (a) Mn sphere and (b) Pb sphere having $R=35$ mm, placed in air and immersed in water, for $r=150$ mm, $a=15$ mm, and $\xi=2°$.

respectively. Figures 4–6 show that Δk_{av} varies with the radius of the scattering sphere irrespective of the material. In addition, A and $\Delta k'_{\mathrm{av}}$ change with the density of the sphere and the speed of wave propagation inside the sphere, respectively. However, it is important to note that A not only depends on the density of the material but also the radius, the observation distance, and the power of the received signal, which is proportional to the power of the source.

In Ref. 9, it has been demonstrated that more details appear in the backscattered spectrum if the radius of the sphere becomes larger, keeping the pulse width constant. In addition, as the radius of the sphere increases, the average spacing of the spectral dips becomes smaller and the ampli-

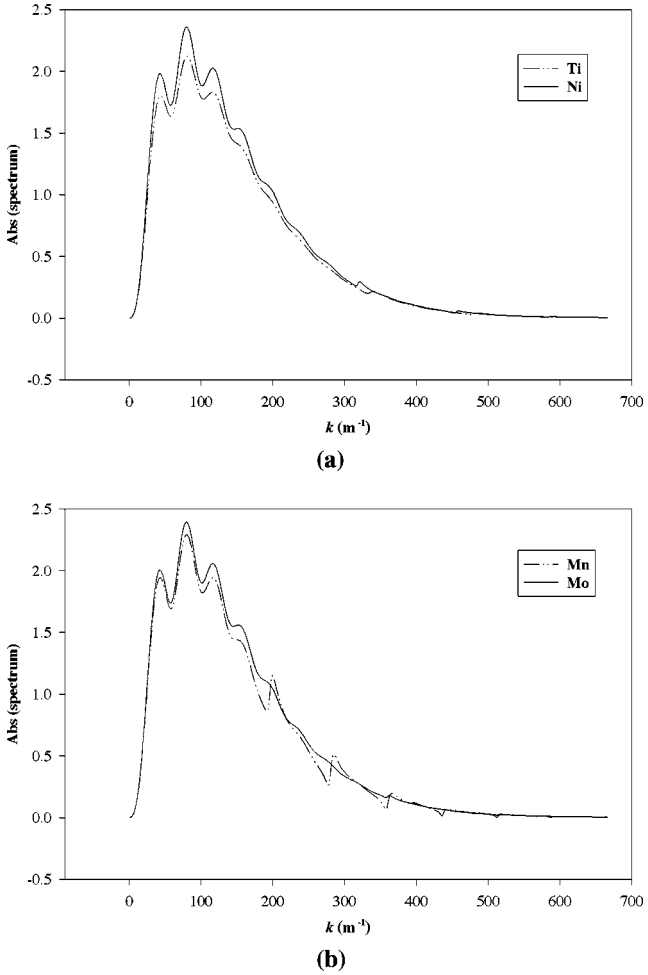

FIG. 4. Backscattered spectra of (a) Ti and Ni, (b) Mn and Mo spheres having radii $R=30$ mm, immersed in water for $r=150$ mm, $a=15$ mm, and $\xi=2°$.

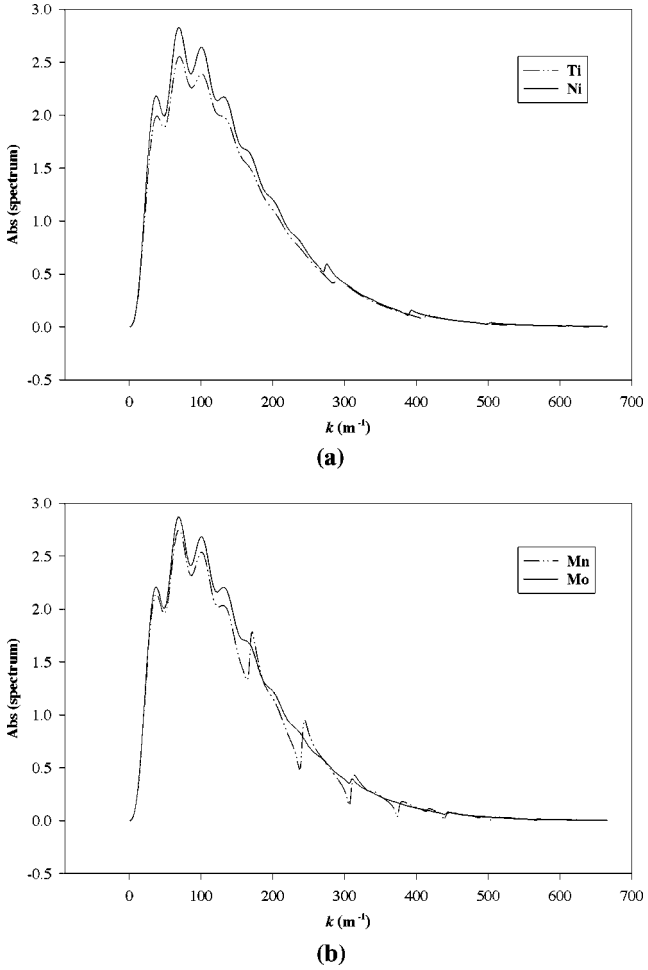

FIG. 5. Backscattered spectra of (a) Ti and Ni, (b) Mn and Mo spheres having radii $R=35$ mm, immersed in water for $r=150$ mm, $a=15$ mm, and $\xi=2°$.

tude of the spectrum becomes larger. The low-frequency portion of the backscattered spectrum (approximately up to 30 kHz) for a nonrigid sphere is similar to that of a rigid sphere. Nevertheless, in the high-frequency portion of the spectrum, one notices more pronounced dips for nonrigid spheres.[3,9] Figure 3 shows that the average spacing of the spectral dips in the low-frequency range is almost identical for Mn and Pb spheres placed in water. However, the average spacing between the dips in the high-frequency ranges are different. Using the backscattered spectra of AXW pulses resulting from spheres of different materials placed in water, we can extract information about the size of the spheres if we have a ''calibration'' curve that relates the average spacing of the spectral dips calculated from the low-frequency range and the radii of the spheres. In Fig. 7, we provide such calibration curves using the low-frequency dip separations for the four materials whose spectra are provided in Figs. 4–6; namely, Ti, Mn, Ni, and Mo. The calibration curves provided in Fig. 7 for the four materials are very close to each other. Consequently, we can choose to start with an arbitrary calibration curve that does not depend on the material. Such an arbitrary ''radius calibration'' curve is shown in Fig. 8. This curve has been created using the average spacing of the spectral dips obtained from the low-frequency range of the backscattered spectra of three different spheres having radii equal to 30, 40, and 50 mm. The spectra of the scattered fields for these radii are evaluated for $r=150\,\mathrm{mm}$, $a=15\,\mathrm{mm}$, $\rho_0=1.0\times10^3\,\mathrm{kg/m^3}$, $\rho_e=7.8\times10^3\,\mathrm{kg/m^3}$, $c=1500\,\mathrm{m/s}$, and $c_e=3000\,\mathrm{m/s}$. The points are plotted using MS Excel and a trend line is drawn, yielding the equation $R=1041.1(\Delta k_{\mathrm{av}})^{-0.937}$ for the calibration curve. In all calculations, we have used the spectra derived from Eq. (16), with the parameter values $a=15\,\mathrm{mm}$, $q=0$, and $\xi=2°$.

For scattering spheres having the same radii and situated at the same observation distance, the simulated backscattered spectra of spheres made of different materials show that each material gives a different amplitude. However, the amplitudes are not only dependent on the density of the material but also the radius of the sphere, the observation distance, and the power of the received signal. The latter is obviously proportional to the power of the source. Therefore, if we know the power of the source and the observation distance, we can relate the density of the material to the amplitude of the backscattered spectrum for spheres having different radii. In particular, we have observed that the relation between the amplitude and the density takes the form of $A\propto1/\sqrt{\rho_e}$, where A is the amplitude and ρ_e is the density of the material of the sphere. In addition, we argue that the amplitude of the first

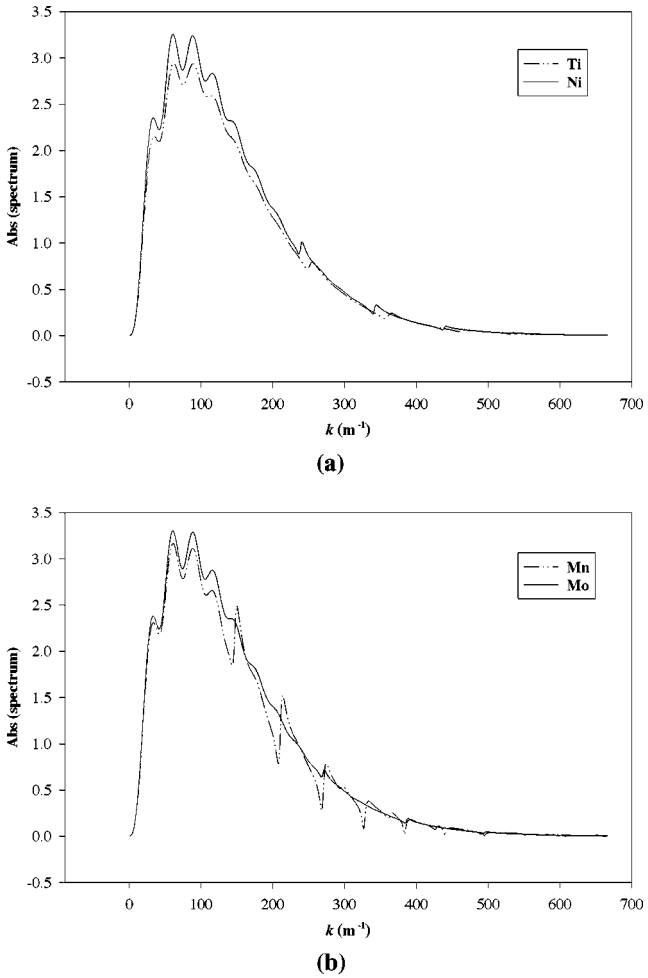

FIG. 6. Backscattered spectra of (a) Ti and Ni, (b) Mn and Mo spheres having radii $R=40$ mm, immersed in water for $r=150$ mm, $a=15$ mm, and $\xi=2°$.

peak in the spectrum yields acceptable results. Figure 9 provides calibration curves relating the amplitudes of the first peaks in the backscattered spectra of four different materials (Ti, Mn, Ni, and Mo) to their densities for radii of 30, 35, and 40 mm. The data are plotted using MS Excel and trend

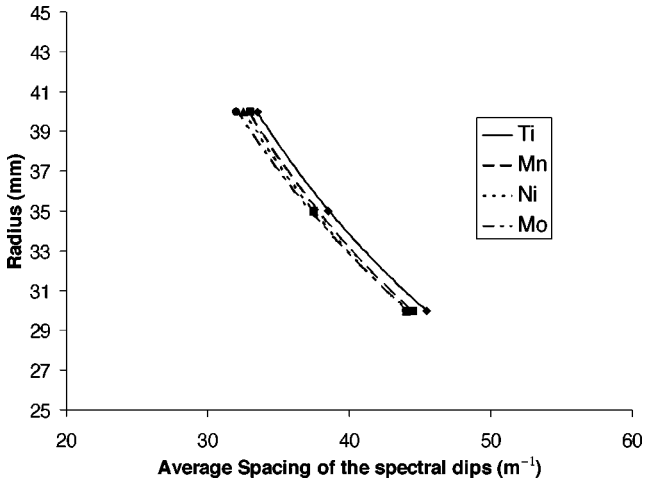

FIG. 7. Calibration curves relating the radius of the sphere to the average spacing of the spectral dips by four different materials, Ti, Mn, Ni, and Mo, immersed in water for $r=150$ mm, $a=15$ mm, and $\xi=2°$.

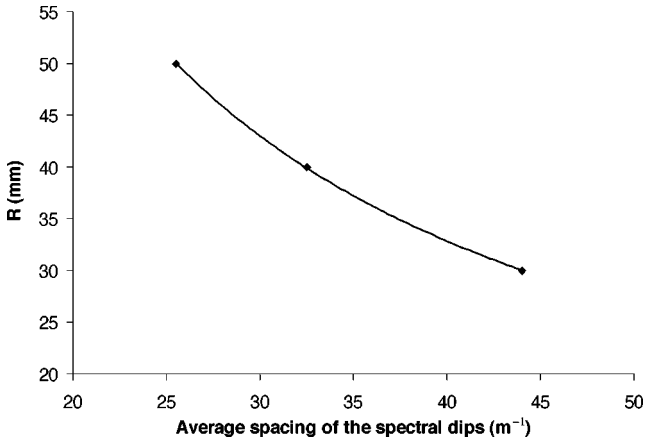

FIG. 8. Calibration curve between the radius of the sphere and average spacing of the spectral dips of the backscattered spectrum for $r=150$ mm, $\rho_0=1.0\times10^3$ kg/m^3, $c=1500$ m/s, $\rho_e=7.8\times10^3$ kg/m^3, $c_e=3000$ m/s, $a=15$ mm, and $\xi=2°$.

lines are drawn to give mathematical forms for these curves. For example, the equation of the line for $R=35$ mm, $r=150$ mm, $a=15$ mm, $\rho=1.0\times10^3$ kg/m^3, and $c_e=1500$ m/s is given by $1/\sqrt{\rho_e}=-0.0228A+0.0603$. In Fig. 10, we present typical calibration curves between density and amplitude at different observation distances. The relationship between the amplitude and observation distance, shown in Fig. 11, is the expected $A\propto 1/r$ as indicated by the trend lines of the MS Excel plot.

Although varying the speed of wave propagation inside the sphere affects the average spacing of the spectral dips in the high-frequency range, we can deduce from Fig. 7 that the speed also has a small effect on the low-frequency range because the four curves do not overlap completely. Therefore, we recommend that the average spacing of the spectral dips of the whole backscattered spectrum be calculated when doing the calibration curve for the speed of sound in the material. Figure 12 provides a typical calibration curve for the average spacing of the spectral dips of the entire spectrum with the speed of wave propagation inside the sphere

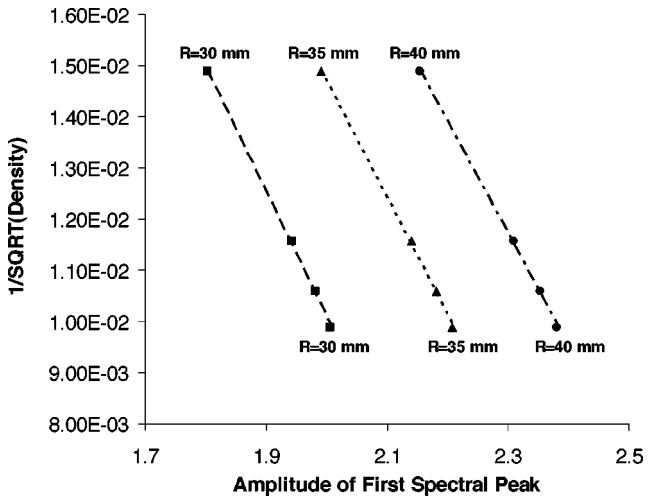

FIG. 9. Calibration curves relating the density of the material to the amplitude of the backscattered spectrum for different radii, $r=150$ mm, $\rho_0=1.0\times10^3$ kg/m^3, $c=1500$ m/s, $a=15$ mm, and $\xi=2°$.

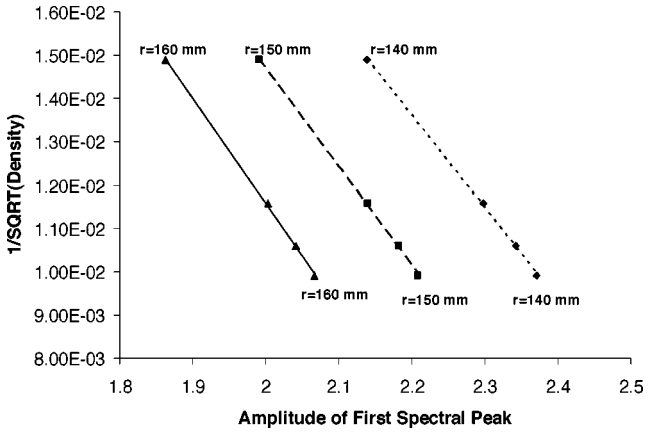

FIG. 10. Calibration curves relating the density of the material to the amplitude of the backscattered spectrum for different observation distances, $R=35$ mm, $\rho_0=1.0\times10^3$ kg/m^3, $c=1500$ m/s, $a=15$ mm, and $\xi=2°$.

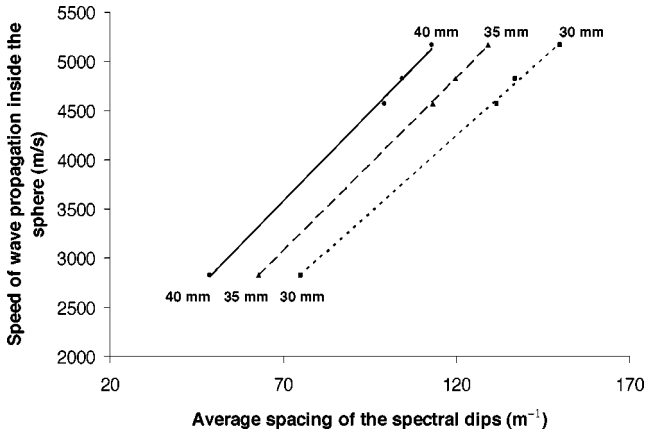

FIG. 12. Calibration curves relating the speed of wave propagation inside of the sphere to the average spacing of the spectral dips of the backscattered spectrum for different radii, $r=150$ mm, $\rho_0=1.0\times10^3$ kg/m^3, $c=1500$ m/s, $a=15$ mm, and $\xi=2°$.

for different radii. Again, we have used the backscattered spectra of Ti, Mn, Ni, and Mo with the same aforementioned pulse parameters.

V. PROPOSED IDENTIFICATION SCHEME

In the preceding section, we established calibration relations for the radius, density, and speed of wave propagation, using the backscattered spectra produced by spheres made of four different materials: Ti, Mn, Ni, and Mo. In this section, we are going to show how we can use these relations to identify the sizes and material properties of unknown spherical scatterers using their simulated backscattered spectra. Making use of the results of Sec. IV, we can outline a procedure for identifying the size and material of an unknown spherical scatterer. First, we can estimate the radius using an arbitrary ''radius calibration'' curve, which is almost material independent (cf. Figs. 7 and 8). This arbitrary calibration curve relates the average spacing of the spectral dips at low frequencies and the radius of the sphere. Using the estimated value of the radius, we choose the appropriate calibration curve between the average spectral dip spacing obtained from the entire spectrum and the speed to determine the speed of wave propagation inside the sphere. Similarly, using the estimated radius to choose the correct calibration curve relating the amplitude and density of the material, we identify the density of the scatterer.

Consider the backscattered spectra for 35-mm spheres made of the following materials: Al, Cr, Cu, Fe, Pb, and Ag

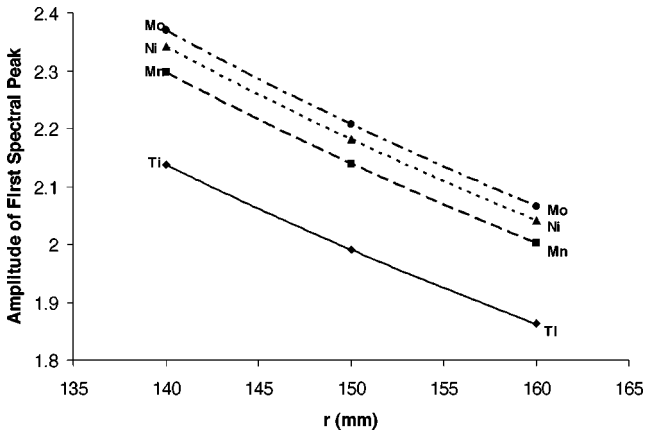

FIG. 11. Calibration curves relating the amplitude of the backscattered spectrum to the observation distance for different materials, Ti, Mn, Ni, and Mo, immersed in water for $R=35$ mm, $a=15$ mm, and $\xi=2°$.

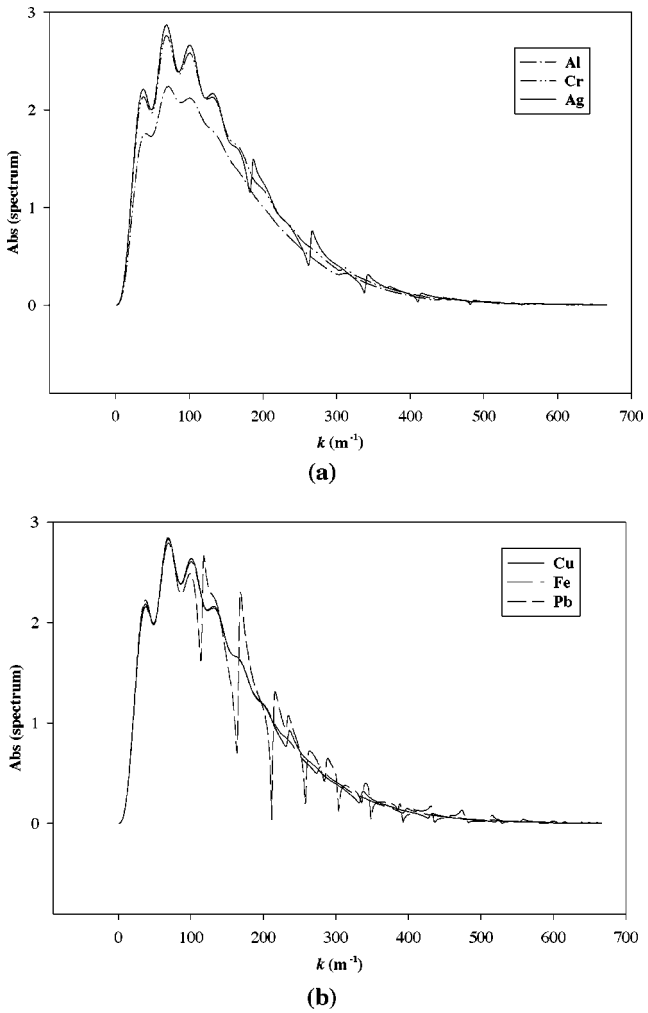

FIG. 13. Backscattered spectra for (a) Al, Cr, Ag, (b) Cu, Fe, Pb for $r=150$ mm, $\rho_0=1.0\times10^3$ kg/m^3, $c=1500$ m/s, $a=15$ mm, and $\xi=2°$.

TABLE II. The estimated and actual radii of the spheres as have been calculated from the average spacing of the spectral dips of the simulated backscattered spectra obtained for different materials due to on-center incidence, as well as for off-center incidence at distances $x_0=15$ mm and $x_0=45$ mm.

	On center			Off center					
				$x_0=15$ mm			$x_0=45$ mm		
Material	Δk_{av} (m^{-1})	Est. R (mm)	% error	Δk_{av} (m^{-1})	Est. R (mm)	% error	Δk_{av} (m^{-1})	Est. R (mm)	% error
Al	40.50	32.45	7.29	41.00	32.06	8.41	43.00	30.56	12.68
Cr	37.50	35.06	0.17	38.00	34.59	1.16	39.00	33.7	3.70
Cu	37.25	35.29	0.83	37.50	35.06	0.17	38.50	34.14	2.45
Fe	37.50	35.06	0.17	37.75	34.82	0.50	39.00	33.70	3.70
Pb	37.50	35.06	0.17	38.00	34.59	1.16	39.50	33.28	4.92
Ag	37.00	35.53	1.51	37.00	35.53	1.51	38.50	34.14	2.45

due to an AXW pulse incident on their centers. From Fig. 13, we calculate the average spacing of spectral dips at low frequencies (up to approximately 35 kHz). Using these values in the arbitrary ''radius calibration'' curve given in Fig. 8, we can estimate their radii, obtaining values that are approximately equal to 35 mm (cf. Table II). Subsequently, we obtain from the backscattered spectra the amplitudes of the first peaks and the average spacings of the spectral dips of the entire spectrum. According to the estimated radii, we use the appropriate density and speed calibration curves (cf. Figs. 9 and 12) to determine the density of the material and speed of sound propagation inside the spheres. Table II shows the estimated radii of the different materials and the percentage error. The radii are estimated for on-center and off-center incidences. For on-center incidence, the estimated radii for all the materials have accuracy levels better than 98%, except for Al, which has an accuracy level of 92% because its backscattered spectrum does not contain enough detail. In order to obtain better results for Al, we should use a smaller pulse width. This is equivalent to having a wider spectral bandwidth. However, the pulse width should not be smaller than five times the radius. For off-center incidence, the errors in the estimated radii do not vary much when $x_0=15$ mm. However, as the axis of propagation of the X wave moves out of the body of the sphere (at $x_0=45$ mm), the errors in the estimated radii start increasing, especially for Pb for which the percentage error increases to 5% and for Al it rises to 12.63%.

Table III contains estimates of the densities of the scattering spheres. It can be seen that for the on-center case, the percentage errors in estimating the densities are smaller than 6% for all materials except for Al and Ag that have approximately 12.2% and 8.2% errors, respectively. Due to the relationship $(\text{amplitude}) \propto 1/\sqrt{(\text{density})}$, the determination of the density is very sensitive to errors in the estimated radius of the sphere. Therefore, errors for 45-mm off-center incidence climb up to unacceptable values, e.g., we obtain 39% error in the estimated density of Al. Other spheres have density estimates exhibiting errors that are greater than 9%. The 15-mm off-center incidence yields acceptable estimates with errors that are smaller than 10%, except for Al. This indicates that the density values determined using this method are reliable only when the focused part of the incident pulse hits the scattering sphere. The sound speed in the material of the sphere is determined from the average dip spacings over the whole spectrum. In Table IV, we provide estimates of the sound speeds for on- and off-center incidences. For the three cases under consideration, error margins smaller than 5% are achieved except for Al that has an on-center percentage error of 6.7% and climbs up to 11.1% for the 45-mm off-incidence case. Thus, it is seen that the percentage errors in estimating the speed of wave propagation are small whether the pulse is incident on center or off center. Our discussion shows that the information extracted from the separation of dips (Δk_{av} or $\Delta k'_{av}$) is highly reliable and yields good estimates of the radii and wave speeds for the spheres. On the other hand, the accuracy by which the density is determined is highly sensi-

TABLE III. The estimated densities of the spheres for $R=35$ mm as calculated from the amplitudes of the simulated backscattered spectra obtained for different materials due to on-center incidence as well as off-center incidence by distances $x_0=15$ mm and $x_0=45$ mm.

	On center			Off center					
				$x_0=15$ mm			$x_0=45$ mm		
Material	A	Est. ρ_e (kg/m^3)	% error	A	Est. ρ_e (kg/m^3	% error	A	Est. ρ_e (kg/m^3)	% error
Al	1.7587	3.03×10^3	12.2	1.7601	3.13×10^3	16.1	1.7719	3.76×10^3	39.3
Cr	2.1334	7.36×10^3	2.3	2.1338	7.78×10^3	9.5	2.1373	9.4×10^3	9.7
Cu	2.1817	8.45×10^3	5.3	2.1819	8.98×10^3	0.6	2.1841	1.07×10^4	19.8
Fe	2.1546	8.01×10^3	1.7	2.1549	8.16×10^3	3.72	2.1579	1.03×10^4	30.9
Pb	2.2216	1.07×10^4	4.9	2.2217	1.15×10^4	1.4	2.2225	1.47×10^4	29.6
Ag	2.2120	9.64×10^3	8.2	2.2121	9.64×10^3	8.2	2.2137	1.24×10^4	18.1

TABLE IV. The estimated acoustic speeds of propagation inside the spheres for $R=35$ mm as have been calculated from the average spacing of the spectral dips of the backscattered spectra obtained for different materials due to incidence off center by a distance to on-center incidence as well as off-center incidence by distances $x_0=15$ mm and $x_0=45$ mm.

	On center			Off center					
				$x_0=15$ mm			$x_0=45$ mm		
Material	$\Delta k'_{av}$ (m^{-1})	Est. c_e (m/s)	% error	$\Delta k'_{av}$ (m^{-1})	Est. c_e (m/s)	% error	$\Delta k'_{av}$ (m^{-1})	Est. c_e (m/s)	% error
Al	128.67	4824.48	6.7	128.83	4758.39	8.0	129.33	4595.40	11.1
Cr	129.33	5162.10	0.39	129.33	5118.45	0.46	129.50	5005.17	2.66
Cu	94.62	3943.13	0.67	94.62	3939.62	0.58	94.62	3831.04	2.19
Fe	114.50	4639.71	0.33	114.67	4616.91	0.16	114.67	4488.26	2.94
Pb	40.62	2037.29	4.62	40.62	1945.39	0.1	40.62	1883.56	3.27
Ag	72.25	3139.45	1.38	72.12	3134.66	1.22	72.12	3037.62	1.91

tive to any initial inaccurate estimation of the radius of the sphere.

VI. CONCLUDING REMARKS

In this paper, we discussed the scattering of an AXW pulse by a sphere. We represented the incident AXW pulse as a spectral superposition over plane waves. Subsequently, we used the series solution of a plane wave scattered by a sphere in order to synthesize the scattered AXW pulse. The spectrum of the scattered field was shown to carry specific information regarding the size and material properties of the scattering sphere. We have undertaken a detailed study of the backscattered spectra for spheres having different radii and made out of diverse materials. Our work indicates that one can use the spectra of a few spheres of known materials and specified radii to generate a set of calibration curves. These curves can then be used to characterize unknown spherical scatterers. In particular, we can estimate the radius of the scatterer using an arbitrary calibration curve that does not depend on the material. Since the estimation of both the density and wave speed of a sphere are radius dependent, we utilize the estimated radius together with appropriate calibration curves for the density and the speed in order to identify the material. The effects of the observation distance and the power of the received signal, which is proportional to the power of the source used, must be taken into account in the process. To examine the robustness of our method, we have considered both on-center and off-center incidence.

The analysis used in this work indicates that it is advantageous to use ultra-wideband pulses for identification purposes because we can extract different pieces of information from various parts of their large spectral bandwidth. Specifically, the separation between the dips of the lower-frequency part of the spectrum is used to calculate the radius. The average spacings between the dips over the entire spectrum yield the wave speed in the material of the scatterer. The amplitude of the first peak determines the density of the material. Estimates of the radii, densities, and wave speeds of six unknown materials have been deduced using calibration curves generated for spheres made of four known materials. It has been shown that the percentage errors in our estimates are very low, except for a few exceptional cases. We have also demonstrated that the suggested procedure is robust even in the off-center incidence case, provided that the off-center distance does not exceed the radius of the sphere if the density is estimated. On the other hand, the off-center distance can be increased to approximately 40% of the observation distance if the wave speed is evaluated. Although this work has been carried out for an incident X wave, we should point out that the advocated procedure for size identification and material characterization is not restricted to X-wave pulses and can be applied to other types of ultra-wideband pulses.

Finally, we would like to point out that several theoretical studies of the scattering of electromagnetic X waves from conducting wedges and disks have been published.[11,12] In these studies, the scattered fields were evaluated by combining the pulsed plane-wave representation of X waves[1,2] with high-frequency asymptotic techniques.[11,12] Contrary to the work presented in this paper, there was no attempt to use the backscattered fields in identifying any of the attributes of the scattering objects. It is of interest to extend the identification technique introduced in this paper such that the features of scatterers having different geometries could be determined from their backscattered spectrum. Another interesting situation is to be able to acoustically identify the attributes of a scattering object when it is immersed in water or is buried underground while the source of the AXW is situated in a second medium.

[1] A. M. Attiya, "Transverse (TE) electromagnetic X-waves: Propagation, scattering, diffraction and generation problems," Ph.D. thesis, Cairo University, 2001.

[2] A. M. Attiya, E. A. El-Diwany, A. M. Shaarawi, and I. M. Besieris, "Reflection and transmission of X-waves in the presence of planarly layered media: The pulsed plane wave representation," Prog. Electromagn. Res. **30**, 191–211 (2000).

[3] D. Power, R. Donnelly, and R. MacIsaac, "Spherical scattering of superpositions of localized waves," Phys. Rev. E **48**, 1410–1417 (1993).

[4] R. W. Ziolkowski, "Localized transmission of electromagnetic energy," Phys. Rev. A **39**, 2005–2033 (1989).

[5] J. Fagerholm, A. T. Friberg, J. Huttunen, D. P. Morgan, and M. M. Salomaa, "Angular-spectrum representation of nondiffracting X waves," Phys. Rev. E **54**, 4347–4352 (1996).

[6] P. M. Morse, *Vibration and Sound* (McGraw-Hill, New York, 1948).

[7] A. M. Shaarawi, I. M. Besieris, A. M. Attiya, and E. A. El-Diwany, "Acoustic X-wave reflection and transmission at a planar interface: Spectral analysis," J. Acoust. Soc. Am. **107**, 70–86 (2000).

[8] G. B. Arfkin, *Mathematical Methods for Physicists* (Academic, San Diego, 1995).

[9] M. F. Z. Moawad, ''Scattering of ultra-wideband X-wave pulses by a sphere,'' M.Sc. thesis, American University in Cairo, Egypt, 2002.
[10] C. Kittel, *Introduction to Solid State Physics*, 7th ed. (Wiley, New York, 1996).
[11] A. M. Attiya, E. A. El-Diwany, A. M. Shaarawi, and I. M. Besieris, ''Diffraction of a transverse electric (TE) X wave by conducting objects,'' Prog. Electromagn. Res. **38**, 167–198 (2003).
[12] A. M. Attiya, E. A. El-Diwany, A. M. Shaarawi, and I. M. Besieris, ''Scattering of X-waves from a circular disk using a time domain incremental theory of diffraction,'' Prog. Electromagn. Res. **44**, 103–129 (2003).

A finite-element/boundary-element method for the modeling of piezotransducer radiation in fluids using a polynomial development of the Green's function

P. F. Edoa, S. Ballandras,[a] and M. Wilm
Laboratoire de Physique et Métrologie des Oscillateurs/CNRS UPR 3203, associé à l'Université de Franche-Comté, 32 avenue de l'Observatoire, 25044 Besançon Cedex, France

(Received 15 December 2003; accepted for publication 9 February 2004)

Ultrasound transducers are widely used in acoustic imaging applications to launch and receive pressure waves radiated and diffracted in fluids or solids. The design and optimization of these devices require the development of accurate models taking into account their actual working conditions. Particularly, much of work has been devoted to simulate ultrasound transducers radiating in semi-infinite fluids. Such developments are devoted to accurately predict the frequency bandwidth of ultrasound transducers (optimization of their axial resolution) but also their sensitivity. In the proposed work, a mixed formulation combining finite element and boundary element methods has been developed to simulate acoustic radiation of piezotransducers in fluids, using a rigorous analytical development of the 2D Green's function of the fluid. Results of the proposed calculation are compared to those provided using a more classical approach previously developed based on a numerical integration using Gauss points and weights. It is shown that the proposed approach yields efficient analysis of 2D problems with a very low sensitivity to the number of boundary elements used to simulate radiation phenomena. © *2004 Acoustical Society of America.*
[DOI: 10.1121/1.1694998]

PACS numbers: 43.40.Rj, 43.30.Jx, 43.38.Fx [ADP] Pages: 2947–2953

I. INTRODUCTION

Most of acoustic imaging probes used in biomedical applications or in nondestructive evaluation use piezoelectric transducers to transmit and detect acoustic waves radiated and diffracted in fluids or solids. The design process of such probes requires one to take into account the influence of the actual parameters of the final device, more particularly the interaction with the fluid medium. Many methods, generally based on a finite element analysis (FEA), have been developed to address this problem.[1–3] These methods consist either in meshing a part or all the acoustic medium, or in the determination of the acoustic pressure at the fluid/structure interface assuming a given radiation condition (for instance semi-infinite media).

In this latter approach, one can combine for instance the FEA with boundary element methods (BEMs). The acoustic medium is then represented by its Green's function relating the pressure to the displacement field at the boundary between the solid and the fluid. This approach is well-suited to simulate the dynamic behavior of any transducer loaded by a fluid medium using meshes smaller than those required by the first mentionned method, which is an important feature in numerical computations. Another great advantage of this approach consists in a significant gain in computation duration and asymptotic precision compared with the approach based on meshing a part of the fluid domain (this latter approach also requires infinite radiation conditions on the fluid boundaries). Furthermore, different Green's functions (of fluid or solid media) can be considered in the BEM integral formulation. In addition, an efficient treatment of the Green's function singularities can be performed, ensuring a systematic convergence of the computations.[4]

In this work, a rigorous analytical treatment of the BEM developments is proposed for ultrasound transducers radiating in fluids simulated using 2D models. It is actually well known that taking into account the singular behaviors of Green's functions used for BEM significantly helps in their accurate numerical treatment. However, the Green's function of semi-infinite fluid media, i.e., the Hankel function of zeroth order and second kind, can be nicely represented close to the origin by combining a polynomial expansion and its logarithmic behavior, allowing then explicit and exact calculations of boundary integrals of the problem. Better than only taking into account this logarithmic dependence as usually performed, the proposed approach yields a very precise approximation of the exact solution of the pressure radiation in semi-infinite fluids: the relative error between the exact Green's function and its polynomial expansion is less than 10^{-9} on the whole integration range. Furthermore, the proposed approach does not require any particular attention to the location of the integration points at the radiation boundary.

An exact integration of the convolution products with the considered polynomial approximations and Lagrange interpolation polynomials of degree 1 and 2 is performed to combine the FEA and BEM approaches. These calculations have been implemented in our FEA code, built using the Modulef package (initially developed by INRIA Rocquencourt).[5]

In the first section of the paper, the principle of FEA/

[a]Author to whom correspondence should be addressed. Electronic mail: ballandr@lpmo.edu

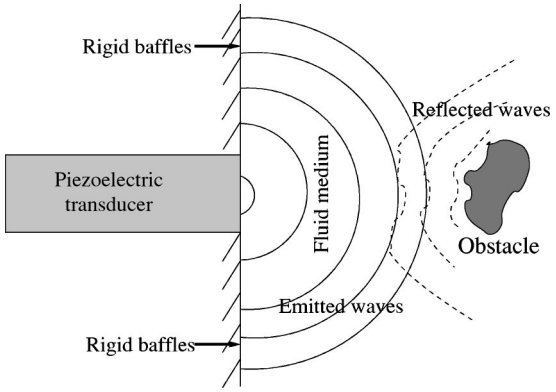

FIG. 1. Emission and reception of acoustic waves by an ultrasound transducer.

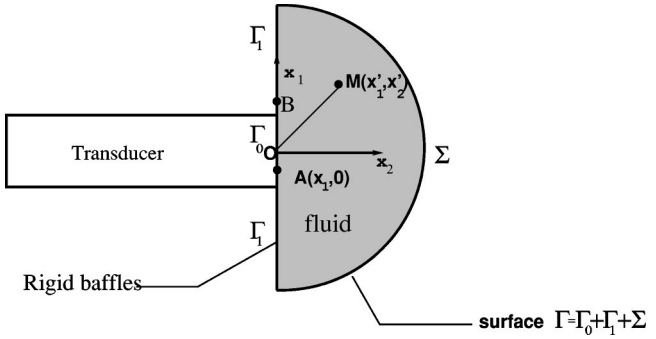

FIG. 2. Typical geometry of the considered 2D problems, definition of the context.

BEM combination is recalled. The Green's function discretization is described and the proposed method is reported. Results provided by the proposed approach are compared to those of a classical numerical integration approach based on Gauss points and weights. Finally, a validation of the proposed method is achieved by comparing the computation results of the present development with those of the unidimensional Mason model for narrow transducer elements which are known to be accurately described using this simplified approach.

II. VARIATIONAL FORMULATION OF THE PROBLEM

The description of the FEA for piezoelectric transducers can be found in many documents.[6,7] According to most of the work produced in that field, we use a standard displacement/potential formulation for the solid part of the problem.

As specified in the Introduction, we only consider two-dimensional structures. Generally, the numerical codes based on FEA allow us to simulate the behavior of piezoelectric structure vibrating in a vacuum. BEM developments are then introduced to describe a boundary condition of radiation in fluid media in the FEA.

A variational formulation is established, based on the equilibrium equations for a piezoelectric medium.[6,7] This formulation allows one to establish a Galerkine formulation written as follows:

$$\int_\Omega \rho\,\delta u_i \frac{\partial^2 u_i}{\partial t^2} + \frac{\partial \delta u_i}{\partial x_j} T_{ij} + \frac{\partial \delta \phi}{\partial x_i} D_i \, d\Omega = \int_\Omega \delta u_i f_i^\Omega d\Omega + \int_\Gamma \delta u_i T_{ij} n_j d\Gamma + \int_\Gamma \delta\phi Q d\Gamma. \quad (1)$$

In Eq. (1), the symbol δ represents the variational operator which affects the displacements u_i and the potential ϕ. ρ is the mass density of the solid, T_{ij} is the internal stress tensor and D_i the electrical displacement vector. On the right-hand side, f_i^Ω represents the volume forces (assumed null in this work) whereas $T_{ij}n_j$ and Q are respectively the surface stress and electrical charge applied or arising at the boundary of the solid. This problem can be solved assuming proper electrical boundary conditions representing the excitation of the transducer, but also mechanical boundary conditions suited to accurately represent actual working conditions of the simulated device. The simulation of piezoelectric transducers can be performed considering either a potential or a charge excitation.[6,7] Identical information are provided by both approaches. A particular interest is then devoted here to mechanical boundary conditions, and more specifically to transducer radiation in fluids.

One supposes that the boundary Γ of the domain describing the studied structures (Fig. 1) is decomposed in the following manner: $\Gamma = \Gamma_0 + \Gamma_1 + \Sigma$ (Fig. 2). Γ_0 is the part of the boundary in contact with the radiation fluid medium; Γ_1 is the adjacent boundary to Γ_0, for which rigid baffle conditions are assumed. Σ delimits the radiating half space at infinity. The boundary condition on Σ consists in outgoing waves accross the corresponding surface. In addition, the studied structures are assumed to exhibit plane radiation surfaces.

A. Surface boundary conditions

It is assumed that a perfect fluid (without shear effects) exerts a pressure on the boundary part Γ_0 of the structure. The interaction between the piezoelectric structure and the fluid medium at the interface Γ_0 implies continuity relations of mechanical stresses and displacements between the two media. Particularly, the normal displacements at Γ_0 are continuous and there is a balance between the normal surface stress and the pressure field. The relation giving the pressure field exerted by the fluid on the structure is written

$$T_{ij} n_j = -P^{\Gamma_0} n_i, \quad i = 1,2,3 \quad \text{on } \Gamma_0, \quad (2)$$

where n_j are the components of the unit normal at the boundary Γ_0. The usual Einstein rule on repeated indexes is implicitly applied.

The continuity relations are then used to describe the boundary conditions using variables that only depend on the solid (the pressure P depends on the mechanical displacements of the transducer at the radiation boundary).

According to Eq. (2), the contribution of the radiation medium is represented as a stress applied on Γ_0:

$$\int_\Gamma \delta u_i \, T_{ij} n_j \, d\Gamma = -\int_\Gamma \delta u_i P^{\Gamma_0} n_i d\Gamma. \quad (3)$$

This term which characterizes the surface boundary condition in the Galerkine formulation has to be inserted in Eq. (1). According to the hypothesis concerning the boundary $\Gamma = \Gamma_0 + \Gamma_1 + \Sigma$, one can demonstrate[8] that for the consid-

ered two-dimensional structures, the determination of the radiated acoustic field leads to the following pressure distribution:

$$P^{\Gamma_0}(B) = -\rho_f \omega^2 \int_{A\in\Gamma} G(A,B) u_i(A) n_i(A) d\Gamma, \tag{4}$$

where $G(A,B)$ is the Green's function of the fluid medium, ω is the angular frequency, ρ_f is the fluid density and $u_i(A)$ is the displacement components at each point of the interface. The notations A and B indicate two given points of the interface Γ_0. In our developments, the direction normal to this boundary is assumed along x_2.

It is well known[8] that for two-dimensional problems and under the hypothesis of the propagation of cylindrical waves in fluids, the Green's function of the semi infinite fluid media is proportional to the Hankel function of zeroth order and of second kind $H_0^{(2)}$ defined by the Bessel functions J_0 and Y_0 as follows,

$$G(A,B) = -\frac{j}{2} H_0^{(2)}(kr), \tag{5}$$

with $H_0^{(2)}(kr) = J_0(kr) + jY_0(kr)$, where k is the wave number associated to the longitudinal propagation wave and r is the distance between the points A and B (j is the unit imaginary number). Since r is always positive, G is symmetric $[G(A,B) = G(B,A)]$.

B. Discretization of the surface boundary condition

Two methods have been widely used to discretize the boundary condition given by Eq. (3) which are the collocation method[9] and the variational method.[9] In this work, the variational approach has been implemented because of its intrinsic qualities. Two processes have been developed to compute the BEM integrals, respectively consisting in a brute force numerical integration and in the analytical approach discussed in the present paper.

Whatever the chosen computation approach, one has first to insert Eq. (4) into Eq. (3) yielding the following relation,

$$\int_\Gamma \delta u_i P^{\Gamma_0} n_i d\Gamma = -\rho_f \omega^2 \int_{B\in\Gamma_0} \delta u_i(B) \int_{A\in\Gamma_0} G(A,B) \times u_j(A) n_j(A) d\Gamma\, n_i(B) d\Gamma, \tag{6}$$

where $n_1 = 0$ and $n_2 = 1$ as previously explained. The hypothesis of rigid baffles surrounding the transducer allows one to restrict the right-hand side of Eq. (6) to Γ_0.

In both approaches, the usual FEA process is applied, i.e., consisting in the transformation of continuous integrals into the sum of integrals restricted to each element of the mesh used to discretize the considered domain, and in the interpolation of the unknown displacement field u_i and the associated variationnal unknown δu_i. This yields the following expression of the surface boundary condition:

$$\int_\Gamma \delta u_i P^{\Gamma_0} n_i d\Gamma = -\rho_f \omega^2 \sum_{e=1}^{E} \int_{\Gamma_e} \langle \delta u_2^{(e)} \rangle \{p_e(x_1,x_2)\} \times \sum_{\varepsilon=1}^{E} \int_{\Gamma_\varepsilon} [G(A_\varepsilon, B_e)] \langle p_\varepsilon(x_1,x_2) \rangle \times \{u_2^{(\varepsilon)}\} d\Gamma d\Gamma, \tag{7}$$

where $[G(A_\varepsilon, B_e)]$ is a matrix representing the Green's function for the different nodal distances (A_ε, B_e), $\{p_e(x_1,x_2)\}$ represents the column vector of interpolation polynomials of the element e, and $\langle \delta u_2^{(e)} \rangle$ and $\{u_2^{(e)}\}$ are respectively the rank and column vectors of nodal variationnal unknowns and nodal displacements of the element e. E is the total number of elements of the mesh. In the present work, triangles as well as quadrangles have been considered to mesh the solid domain, and also first and second degree polynomials have been implemented. In addition, the use of the reference element technique[10] is used to ease the computation of Eq. (7). The elementary radiation matrix $[X_{(e,\varepsilon)}]$, which must be computed in the most general case for each couple of radiating elements (e,ε), is written as follows:

$$[X_{(e,\varepsilon)}] = \int_{\Gamma_e} \{p_e\} \int_{\Gamma_\varepsilon} [G(A_\varepsilon, B_e)] \langle p_\varepsilon \rangle d\Gamma d\Gamma. \tag{8}$$

The way the integrals of Eq. (8) are performed is now detailed.

1. Numerical integration

The simplest way to perform the integrals of Eq. (7) consists in applying a Gauss numerical integration procedure. In this approach, one has to compute the values of the polynomials and of the Green's function at the so-called Gauss points. The integrals of Eq. (8) change to simple summations along the number of Gauss points weighted by the Gauss coefficients w_i as follows:

$$[X_{(e,\varepsilon)}] = \sum_{i=1}^{N_{\text{Gauss}}} \sum_{j=1}^{N_{\text{Gauss}}} w_i w_j \{p_e\}_i [G(A_\varepsilon, B_e)_{i,j}] \langle p_\varepsilon \rangle_j. \tag{9}$$

Equation (9) is valid as long as A_ε and B_e do not coincide. In that case, the Green's function exhibits a singularity due to Y_0 [see Eq. (5)] which prevents the computation of the influence of the radiation of a given element with itself. In the brute force approach[9] implemented here, the integration domain of the point A_ε is divided in two sections on both sides of the point B_e. The numerical integration is normally performed for the point B_e but it is split on each abovementioned section for points A_ε. This simple trick avoids the coincidence of B_e and A_ε. The reader is not encouraged to implement this kind of procedure which is dramatically not rigourous, but it allows one to easily implement Eq. (9). Furthermore, increasing the number of Gauss points in that particular situation yields satisfying results as shown later. Whatever the quality of the treatment of the Green's function singularity is, one has to increase the number of integration points to correctly take into account the rapid variations of J_0 and of the nonsingular part of Y_0 close to a null distance

between B_e and A_ε. Practically, four integration points are considered for distinct radiating elements e and ε, but 16 integration points are used when B_e and A_ε belong to the same element.

2. Analytical calculation of the radiation matrix

In the proposed approach, the Bessel functions J_0 and Y_0 are approached according to Ref. 11 by polynomial expansions which clearly make appear the logarithmic depedence of Y_0. These approximations are given in particular, for $0 \leqslant x \leqslant 4$, by

$$J_0(x) = \sum_{l=1}^{8} \alpha_l t^{l-1} + \epsilon_0(x),$$
$$Y_0(x) = \frac{2}{\pi} \log\left(\frac{x}{2}\right) + \sum_{l=1}^{9} \beta_l t^{l-1} + \eta_0(x), \tag{10}$$

where $t=(x/4)^2$, α_l, β_l are known coefficients and $|\epsilon_0(x)| \leqslant 10^{-9}$, $|\eta_0(x)| \leqslant 4\times 10^{-10}$. See Ref. 11 for the complete expressions of $J_0(x)$ and $Y_0(x)$ for $x \geqslant 4$.

In the case of acoustic imaging transducers, the dimensions of the structures may be small (some milimeters or even less). The analysis frequencies are of the order of 1 to 10 Mhz and the wave propagation velocity is of the order of 1500 m.s^{-1}. As a consequence, we only focused our efforts on the expansions of $J_0(kr)$ and $Y_0(kr)$ for $kr \in [0,4]$. If the value of kr is greater than 4, the Gauss method of numerical integration mentioned in the previous section is accurate enough since the Green's function exhibits very smooth variations along kr. Consequently, there is no interest in applying the proposed approach for such values of kr. Furthermore, it would require much larger computation delay than the above-mentioned numerical integration procedure.

The exact integration of the coefficients of the matrix $[X_{(e,\varepsilon)}]$ is then performed. These coefficients are defined according to Eq. (8).

Using Eqs. (5) and (8), the expression of $[X_{(e,\varepsilon)}]$ can be written in the following form

$$[X_{(e,\varepsilon)}] = \tfrac{1}{2}([I_{r\,(e,\varepsilon)}] - j[I_{i\,(e,\varepsilon)}]) \tag{11}$$

with

$$[I_{r(e,\varepsilon)}] = \int_{\Gamma_e} \{p_e\} \int_{\Gamma_\varepsilon} [Y_0(kr)_{(e,\varepsilon)}] \langle p_\varepsilon \rangle d\Gamma d\Gamma,$$
$$[I_{i(e,\varepsilon)}] = \int_{\Gamma_e} \{p_e\} \int_{\Gamma_\varepsilon} [J_0(kr)_{(e,\varepsilon)}] \langle p_\varepsilon \rangle d\Gamma d\Gamma. \tag{12}$$

The analytical expressions of $[I_r]$ and $[I_i]$ have to be determined using a formal calculation software (for instance Maple) yielding very cumbersome expressions but well adapted to computer calculations. When the radiation boundaries Γ_e and Γ_ε are different (i.e., $B_e \neq A_\varepsilon$), the obtained expressions of $[I_r]$ and $[I_i]$ are regular and their evaluation is immediate. To treat the logarithmic singularity of Y_0 (i.e., $r=0$, the case where $\Gamma_e = \Gamma_\varepsilon$), only the terms of the $[I_r]$ expression that contain the expression $\log(r)$ must be carefully taken into account. It has been observed that in $[I_r]$ all these terms are multiplied by a power of r of the form r^n with $n \geqslant 1$. Using the well-known following property,

$$\text{for } n \geqslant 1,\ r^n \log(r) \to 0 \text{ when } r \to 0, \tag{13}$$

the logarithmic singularity contained in the function Y_0 is perfectly integrated in the final expression of $[I_r]$, as well as the rapid variations of J_0 and Y_0.

In both approaches, the global radiation matrix noted $[X]$ is obtained by the summation of all the elementary radiation matrices according to the standard FEA matrix assembly procedure. The obtained matrix is used to establish the expression of the surface boundary condition (the BEM part of the approach):

$$\int_\Gamma \delta u_i P^{\Gamma_0} n_i d\Gamma = \rho_f \omega^2 \langle \delta u_2 \rangle [X] \{u_2\}. \tag{14}$$

3. Symmetry properties of the radiation matrix

The particular properties of the radiation matrix are now briefly discussed. The variational formulation of the radiation problem provides a symmetrical structure of the matrix.[12] In the most general case, this matrix is complex and no other particular property can be pointed out.

However, when the distance between all the nodes of the radiation boundary is constant, the computation of $[X]$ points out a quasi-Toeplitz structure[13] of this matrix. For a Lagrange interpolation of first degree, if we exclude the two extremal boundary elements of the radiation boundary, the corresponding submatrix of the radiation matrix exhibits a Toeplitz structure. Using the Lagrange interpolation of second degree yields a Toeplitz by blocks structure of this submatrix (each block corresponds to the interaction between two radiating elements).

For instance, the radiation matrix structure is reported below considering an interpolation of first degree. In this particular case the radiation surface is composed of six nodes (five boundary elements) and the distance between two given nodes is assumed constant:

$$\begin{bmatrix} X_1 & X_2 & X_3 & X_4 & X_5 & X_6 \\ X_2 & X_0 & X_2 & X_3 & X_4 & X_5 \\ X_3 & X_2 & X_0 & X_2 & X_3 & X_4 \\ X_4 & X_3 & X_2 & X_0 & X_2 & X_3 \\ X_5 & X_4 & X_3 & X_2 & X_0 & X_2 \\ X_6 & X_5 & X_4 & X_3 & X_2 & X_1 \end{bmatrix}.$$

Quasi-toeplitz structure of a radiation matrix

This Toeplitz structure is a very interesting property that can be used to reduce the computation duration of the radiation matrices, since only six independent coefficients have to be actually calculated.

C. Final algebraic system and resolution

Classically, the analysis of the dynamic behavior of a nonloaded piezoelectric structure assuming an harmonic excitation leads to a global linear system of the following form:

$$[K - \omega^2 M] \begin{pmatrix} U \\ \Phi \end{pmatrix} = \begin{pmatrix} F \\ Q \end{pmatrix}. \tag{15}$$

TABLE I. Fundamental coefficients of the PZT ceramic.

Coefficient	Real part	Imaginary part
ρ (kg/m^3)	0.7500×10^4	0.0000
c_{11} (MPa)	0.1260×10^6	0.1260×10^4
c_{13}	0.8410×10^5	0.8410×10^3
c_{33}	0.1170×10^6	0.1170×10^4
c_{15}	0.0000	0.0000
c_{35}	0.0000	0.0000
c_{55}	0.2300×10^5	0.2300×10^3
e_{11} (mC/m^2)	0.0000	0.0000
e_{13}	0.0000	0.0000
e_{15}	0.1700×10^5	0.0000
e_{31}	-0.6500×10^4	0.0000
e_{33}	0.2330×10^5	0.0000
e_{35}	0.0000	0.0000
ε_{11} (pF/m)	-0.1504×10^5	0.1504×10^3
ε_{13}	0.0000	0.0000
ε_{33}	-0.1301×10^5	0.1301×10^3

In Eq. (15), ω designates the angular frequency, U is the assembled displacement vector, Φ is the assembled vector of the electric potential, $[M]$ is the assembled mass matrix and $[K]$ is the assembled stiffness matrix. The vectors F and Q correspond to the assembled forces and electrical charges applied to or generated by the structure.

Conformably to the developments of Sec. II B, the introduction of the surface boundary conditions via the Green's function is expressed as a new frequency dependent matrix $[X]$. The corresponding global linear system is then written as follows:

$$[K-\omega^2(M+\rho_f X(\omega))]\begin{pmatrix} U \\ \Phi \end{pmatrix}=\begin{pmatrix} F \\ Q \end{pmatrix}. \tag{16}$$

The use of appropriate solvers based on direct or iterative efficient methods is required to accurately access the solution of the problem. Particularly, the choice of this solver must be done in order to accelerate the convergence, to improve the stability of the calculations and finally to provide results with a good accuracy. In the case of piezoelectric problems, the rigidity matrix $[K]$ is not positive definite. As a consequence, a Crout factorization is used in our FEA package to solve Eq. (16). Particular attention must be paid to the numbering of the wet nodes to avoid a dramatical enlarging of the band structure of the final algebraic system. In the case that an optimal numbering cannot be achieved, the assembled algebraic system may exhibit a sparse structure. Consequently, we have added in our package the solver developed by T. A. Davis and I. S. Duff[14] to solve the global linear systems (15) and (16) to address that issues.

Results, illustrating the efficiency of the proposed method, are presented in the next section.

TABLE II. Characteristics coefficients of the heavy matching layer.

Coefficient	Real part	Imaginary part
ρ (kg/m^3)	0.4100×10^4	0.0000
λ (MPa)	0.0114×10^5	0.1714×10^4
μ (MPa)	0.3300	0.3300

TABLE III. Characteristics coefficients of the light matching layer.

Coefficient	Real part	Imaginary part
ρ (kg/m^3)	0.1150×10^4	0.0000
λ (MPa)	0.5063×10^4	0.1034×10^4
μ (MPa)	0.3300	0.3300

III. COMPARISON OF COMPUTATION RESULTS

All the theoretical developments described in the previous sections have been implemented using Lagrange interpolation polynomials of first and second degree. The developments have been performed in 2D corresponding to the case of conventional 1D acoustic probes (or 2-2 piezocomposites).

Acoustic and dielectric losses are taken into account in the numerical model under the form of complex elastic, piezoelectric and dielectric constants. Whatever the problem, the principle of the analysis consists in calculating the frequency dependent admittance of the transducer denoted Y.

Once u_i and ϕ are computed for a given value of ω, the admittance Y is determined by summing the nodal charge Q on the excited electrode and by multiplying this value by $j\omega$.

A comparison of results obtained respectively using the two developed approaches for the calculation of the radiation matrix has been performed with different 2D structures. Significant differences appeared between these results. It appears that a refinement of the mesh of the radiation boundary was necessary to get results with the brute force computation close to those obtained with the analytical treatment. The latter does not depend on the discretization of the meshed radiation boundary. On the other hand, the respective computation durations are comparable.

Results obtained with a transducer composed of a backing, a piezoelectric ceramic, a heavy matching layer and a light matching layer are now reported. In Tables I–III, the material constants are reported. The coefficients are given using conventional notations.

The transducer surrounded by rigid baffles is assumed to radiate in a semi-infinite fluid domain (water). The 2D mesh of the transducer shown in Fig. 3 and Lagrange interpolation polynomials of first degree have been used in these calculations.

We simulated the radiation of the transducer in water

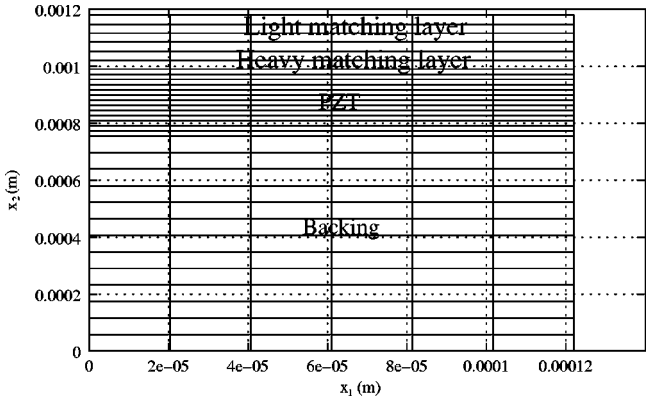

FIG. 3. A mesh of the considered 2D test-structure.

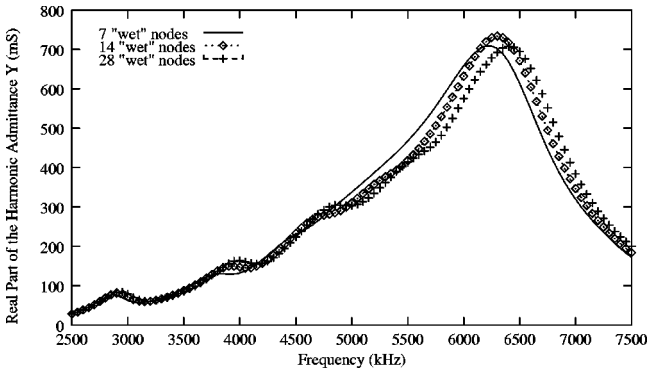

FIG. 4. Real part of the admittance obtained with the numerical integration approach using 7, 14, and 28 wet nodes.

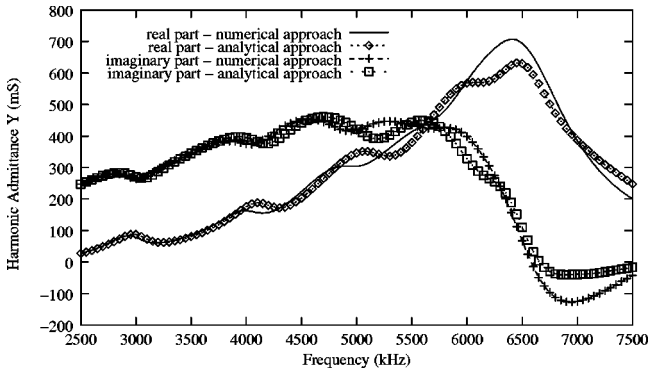

FIG. 6. Real and imaginary parts of the admittance using 28 wet nodes, best agreement between the two approaches.

respectively with 7, 14, and 28 wet nodes at the fluid/transducer interface. Figures 4 and 5 show the real part of the admittance obtained using respectively the brute force numerical integration and the analytical one for these different numbers of wet nodes.

We can observe in Fig. 4 that the results obtained with the numerical integration method is mesh dependent. In Fig. 5, the curves obtained with the analytical calculation are stable. This confirms that the proposed approach is very few dependent on the discretization of the radiation boundary, which points out the fact that the proposed approach is robust.

Finally, we noted that a judicious refinement of the mesh of the radiation boundary was necessary to get results with the brute force approach close to those obtained with the analytical one. In Fig. 6 the best agreement between the two approaches is reported. This was reached of course with 28 wet nodes. However, significant discrepancies remain between the two approaches. The analytical approach provides more details about the evolution of the admittance versus the angular frequency, whereas the brute force integration results only provide the scale order of the phenomena.

IV. VALIDATION OF THE METHOD

To validate the proposed method, a commercial acoustic probe designed and developed by Thales Microsonics (TMX) has been simulated. This probe consists in a piezoelectric ceramic, two matching layers (a heavy one and a light one) and gold electrodes. It is composed of very narrow transducer elements radiating in water. For such devices, the Mason model is known to provide accurate simulations of the admittance. Computations using this approach were provided by TMX.

A good agreement between the calculations with the Mason model and the predicted ones given by our numerical model is pointed out in Fig. 7. In particular, with our model, the estimation of the resonance frequency is very well performed and the presence of parasitic contributions to the admittance can be accurately detected.

V. CONCLUSION

An original approach based on a rigorous polynomial expansion of the Green's function in fluid medium has been proposed in this paper to model ultrasound transducer operation. The combination of this method with a finite element analysis allows one to accurately simulate the acoustic radiation of piezoelectric transducers. The developed method is operational for 2D problems whatever the discretization of the radiation surface of the considered structures.

The development of an accurate treatment of radiation conditions is a key point for the optimization of ultrasound transducers. The developed simulation tool will be used for the design of high performance 2D structures (2-2 piezocomposite based transducers) but also to provide a better understanding of unwanted contributions to the admittance of

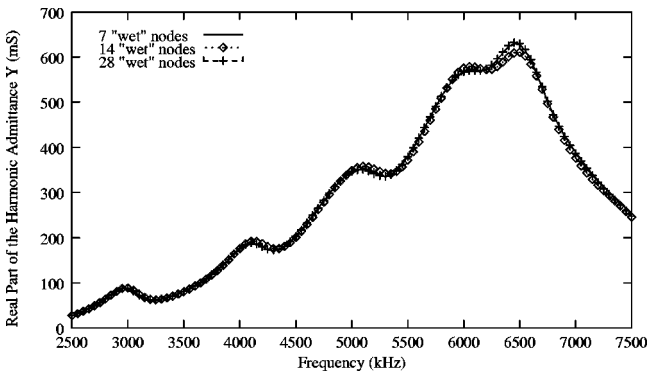

FIG. 5. Real part of the admittance obtained with the analytical calculation of the radiation matrix using 7, 14, and 28 wet nodes.

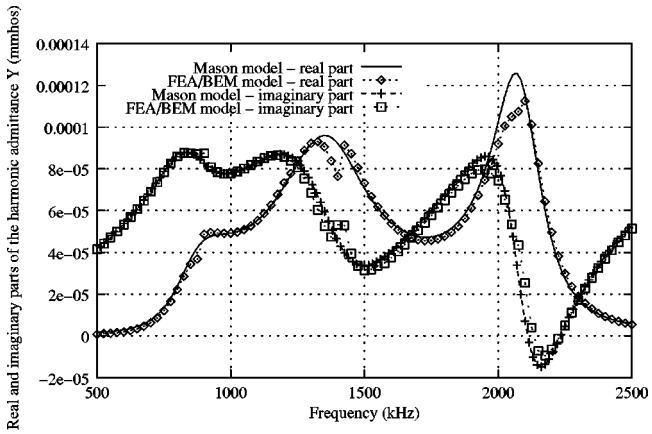

FIG. 7. Comparison between the admittances of an acoustic probe predicted by the proposed approach and using the standard Mason model.

transducers radiating in water, assumed to be caused by parasitic wave propagation at the interface fluid/solid.

The proposed approach can be transposed for 3D problems and also for other radiation media (solids, multilayers), providing a good knowledge of the Green's function and particularly of its singularities (which are well identified for 2D semi-infinite fluids).

ACKNOWLEDGMENTS

The authors would like to thank Thales Microsonics (TMX) for its support and W. Steichen and F. Lanteri for their help in the presented developments.

[1] R. Lerch, H. Landes, and H. T. Kaarmann, ''Finite element modeling of the pulse-echo behavior of ultrasound transducers,'' in *Proc. of the IEEE Ultrasonics Symposium, IEEE # 94CH3468-6* (1994), pp. 1021–1025.

[2] G. L. Wojcik, D. K. Vaughan, V. Murray, and J. Mould, ''Time-domain modeling of composite arrays for underwater imaging,'' in *Proc. of the IEEE Ultrasonics Symposium, IEEE # 94CH3468-6* (1994), pp. 1027–1032.

[3] R. McKeighen, ''Finite element simulation and modeling of 2-d arrays for 3-d ultrasonics imaging,'' IEEE Trans. Ultrason. Ferroelectr. Freq. Control **48**(5), 1395–1405 (2001).

[4] P. Ventura, J.-M. Hodé, J. Desbois, and M. Solal, ''Combined FEM and green's function analysis of periodic SAW structure, application to the calculation of reflection and scattering parameters,'' IEEE Trans. Ultrason. Ferroelectr. Freq. Control **48**(5), 1259–1274 (2001).

[5] M. Bernadou, P. L. George, A. Hassim, P. Joly, P. Laug, B. Muller, A. Perronnet, E. Saltel, D. Steer, G. Vanderborck, and M. Vidrascu, *Modulef, Une Bibliothèque Modulaire D'éléments Finis.*, INRIA, 1988.

[6] D. F. Ostergaard and T. P. Pawlak, ''Three-dimensional finite elements for analysing piezoelectric structures,'' in *Proc. of the IEEE Ultrasonics Symposium, IEEE # 86CH2375-4* (1986), pp. 639–644.

[7] R. Lerch, ''Simulation of piezoelectric devices by two and three-dimensional finite elements,'' IEEE Trans. Ultrason. Ferroelectr. Freq. Control **37**(2), 233–247 (1990).

[8] G. S. Kino, *Acoustic Waves: Devices, Imaging, and Analog Signal Processing* (Prentice–Hall, Englewood Cliffs, NJ, 1987).

[9] B. Piranda, W. Steichen, and S Ballandras, ''Comparison between different finite element/boundary formulations for modeling acoustic radiation in fluids,'' in *Proc. of the IEEE Ultrasonics Symposium* (1998), pp. 1073–1076.

[10] O. C. Zienkiewicz, *La Méthode des Elements Finis/The Finite Element Method* (McGraw-Hill, New York, 1979).

[11] S. Zhang and J. Jing, *Computation of Special Functions* (Wiley Interscience, New York, 1996).

[12] M. A. Hamdi, ''Formulation Variationnelle Par Équations Intégrales Pour Le Calcul de Champs Acoustiques Linéaires Proches et Lointains (Boundary Integral Method for the Calculation of Near and Far Acoustic Linear Fields),'' Ph.D. thesis, Université de Compiègne, France, 1982.

[13] W. H. Press, B. P. Flannery, S. A. Teukolsky, and W. T. Vetterling, *Numerical Recipes—the Art of Scientific Computing (Fortran Version)* (Cambridge U.P., Cambridge, 1989).

[14] T. A. Davis and I. S. Duff, ''An unsymmetric-pattern multifrontal method for sparse LU factorization,'' SIAM J. Matrix Anal. Appl. **18**(1), 140–158 (1994).

Active control of radiation from a piston set in a rigid sphere

Zhibin Lin[a] and Jing Lu
State Key Laboratory of Modern Acoustics and Institute of Acoustics, Nanjing University, Nanjing 210093, China

Chunhua Shen
School of Computer Science, the University of Adelaide, SA 5005, Australia

Xiaojun Qiu and Boling Xu
State Key Laboratory of Modern Acoustics and Institute of Acoustics, Nanjing University, Nanjing 210093, China

(Received 11 April 2002; revised 12 March 2004; accepted 15 March 2004)

Active control of the sound radiated from a piston set in a rigid sphere with a set of control point sources around is considered in this paper, where the scattering sound field of the control sound from the rigid sphere has been taken into account to minimize the total radiated sound power. Analytic results of the sound power are obtained and numerical simulations show that it is possible to reduce the radiation from a small piston set in a rigid sphere similar to the size of a human head up to a certain frequency. It is found that the introduction of the scattering object makes significant differences from the active control without scattering objects. This being the case, the scattering object makes the active noise control easier. To increase the global reduction of sound-power output, the optimal number and locations of the control sources and the optimal number and locations of error sensors are discussed. Finally, experiments with one control source and one error sensor around a head simulator have been carried out to verify the simulation results. © *2004 Acoustical Society of America.* [DOI: 10.1121/1.1736654]

PACS numbers: 43.50.Ki [MRS] Pages: 2954–2963

I. INTRODUCTION

Research into active control of sound has received considerable attention in the past 20 years, and is well documented in textbooks.[1–4] For active control of acoustic radiation in a free field with a number of control point monopole sources, the quadratic expression has been derived to control the field of a number of primary point monopole sources.[1] It has been demonstrated that significant reductions in power output can be achieved if control sources are placed within a distance of half wavelength of the primary source, and it was found that the size of the zone of quiet degraded as the frequency increased.[5] Some theoretical and experimental studies on the zones of quiet created by a secondary source in the diffuse sound field have been presented.[6–9] It has been shown in these papers that the average zone of quiet increases slightly as a result of the diffraction of the secondary control if it is modeled as a rigid sphere,[6,7] and if the sound pressure at a point near a reflecting surface is canceled with a remote secondary source (several wavelengths away from the cancellation point), the average zone of quiet increases with the confinement of acoustic energy produced by the reflecting surface.[8,9] More recent research on active control in a free field has been directed toward the development of near-field acoustic error sensing strategies and optimization methods for the number and locations of the control sources and error sensors.[10–13]

Although the analytic expression has already been obtained for some simple cases where both primary and control sources are point monopole[14] and the primary source is a simply supported vibrating plate mounted in an infinite rigid baffle,[11,15] few analytic expression has been derived for more practical primary sound field. This paper is concerned with the active control of free-field acoustic radiation from a piston set in a rigid sphere by using a set of point sources. One potential application is the active control of the voice of human speaking. While using a mobile phone in public, the user may not want the speech to be heard by others; here, active noise control technique may be used to improve the speech privacy by reducing the radiation of the speech power. In this paper an analytic expression will be derived for the problem with the scattering sound field of the control sound from the rigid sphere being considered. Numerical simulations and experiments will be carried out to show the feasibility of the active control of human speech up to a certain frequency. Here, the purpose of this paper is to discuss how the directionality of the sound field introduced by the rigid sphere makes the active control easier than that without scattering objects and to make full use of this phenomenon in active noise control.

An alternative way to calculate the scattering from objects in a free field is to use the equivalent source method, which is an alternative to the boundary element method, allowing the calculation of the scattering from objects in a free field with a reduced computational load compared to the boundary element method.[16–21] Sets of simple sources located inside the objects are driven to produce a normal particle velocity distribution over the surface of the objects that

[a]Electronic mail: linzhibin@nju.org.cn

 0001-4966/2004/115(6)/2954/10/$20.00 © 2004 Acoustical Society of America

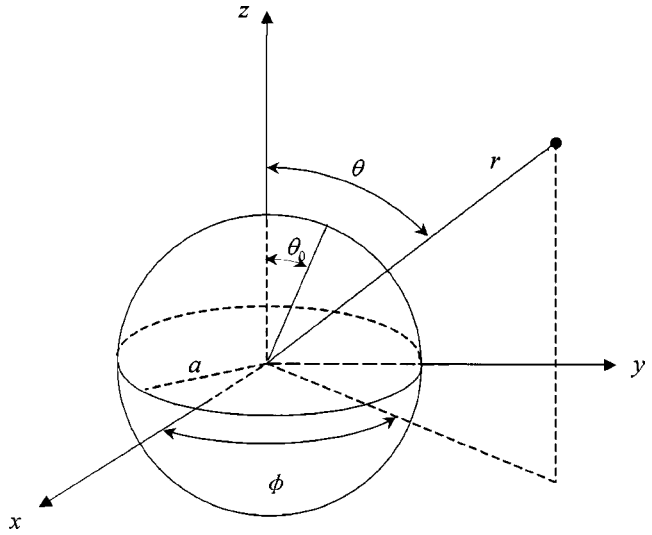

FIG. 1. Physical model description.

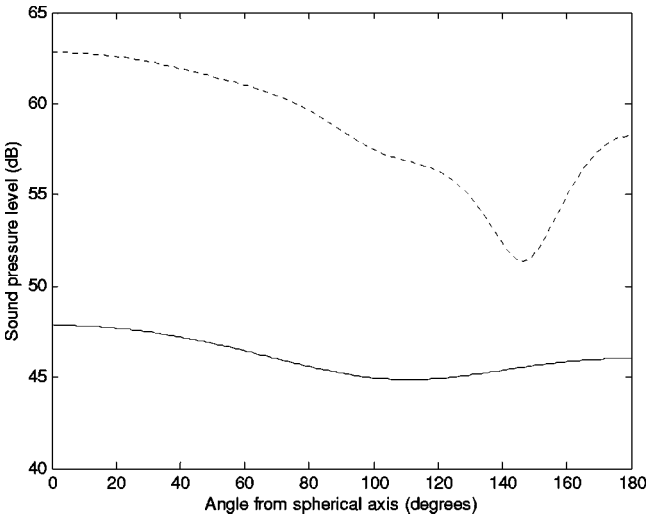

FIG. 2. Distribution in angle of sound-pressure level in the far field radiated by a piston set in a rigid sphere for 500 Hz (solid line) and 2000 Hz pure tone (dotted line).

satisfies the desired boundary condition. Then, the scattered field can be calculated from these simply equivalent sources. However, this method will not be used in this paper because it is difficult to find appropriate positions for the equivalent sources. In addition, a separate scattering problem must be solved for every control source if more than one control source is used, resulting in a large amount of computation and complexity. More recently, Nelson[22] found that for radiation from the surface of a sphere to a spherical surface in the far field, singular-value decomposition can be used to analyze the acoustics pressure at a number of field points to the strengths of a number of point sources on the surface of a body which radiates or scatters sound. Again, this method is not used here because a relatively simple analytic expression will be derived in this paper.

II. PHYSICAL MODEL

A. The primary sound field

The human head may be approximately modeled as a rigid sphere of radius a, and the mouth can be modeled as a piston of radius $a \sin\theta_0$ (shown in Fig. 1) set in the side of a rigid sphere.[23–25] The velocity amplitude of the piston is u_0. The positive harmonic time dependence of the form $e^{j\omega t}$ is implicit throughout the paper. Figure 1 shows the spherical polar coordinates used in this paper where the azimuth θ is defined as 0 deg directly in front of head (the mouth is on the z axis). As long as θ_0 is not too large, this corresponds fairly closely to the following distribution of velocity on the surface of the sphere:

$$U(\theta)=\begin{cases} u_0 & 0\leqslant\theta<\theta_0, \\ 0 & \theta_0<\theta\leqslant\pi. \end{cases} \tag{1}$$

This can be expressed in terms of a series of *Legendre functions* $P_l(x)$[25]

$$\begin{aligned} U(\theta)&=\sum_{l=0}^{\infty} U_l P_l(\cos\theta), \\ U_l&=(l+\tfrac{1}{2})\int_0^{\pi} U(\theta)P_l(\cos\theta)\sin\theta\, d\theta \\ &=\tfrac{1}{2}u_0[P_{l-1}(\cos\theta_0)-P_{l+1}(\cos\theta_0)], \end{aligned} \tag{2}$$

where for the case $l=0$, $P_{-1}(x)=1$.

The pure-tone pressure at any location $\mathbf{r}_e=(r_e,\theta_e,\phi_e)$ outside the rigid sphere source along the azimuthal coordinate can be written in terms of a sum of spherical harmonics as

$$\begin{aligned} p_p(r_e,\theta_e)&=\sum_{l=0}^{\infty} A_l P_l(\cos\theta_e)h_l(kr_e), \\ A_l&=-j\frac{\rho_0 c_0 U_l}{h_l'(ka)}, \\ h_l(x)&=j_l(x)-jn_l(x), \end{aligned} \tag{3}$$

where k is the acoustic wave number at the frequency ω of interest, $j=\sqrt{-1}$, ρ_0 is the mean air density, c_0 is the speed of sound in the air, $h_l(x)$ is the (second kind) *spherical Hankel function* of order l, $j_l(x)$ is the *spherical Bessel function* of order l, and $n_l(x)$ is the *spherical Neumann function* of order l. Note, due to the axial symmetry of the velocity distribution, the primary sound field is independent of ϕ.

Figure 2 shows the distribution in angle of sound-pressure level (re: 20 μPa) in the far field for 500- and 2000-Hz pure tones. Sharply directional pattern can be clearly observed at the higher frequency. In the calculation, the radius a is 0.0875 m,[23] u_0 is 1.0 m/s, θ_0 is 13.2 deg, and the sound-pressure level is calculated 100 m away from the center of the sphere. During the calculation the following equations were used, and the order of the summation in Eqs. (2) and (3) was 30. Up to this order, the calculated sound pressure converges.

$$P_{l+1}(x)=\frac{(2l+1)xP_l(x)-lP_{l-1}(x)}{l+1}$$

$$\text{with } P_{-1}(x)=1 \quad \text{and } P_0(x)=1,$$

$$j_{l+1}(x)=\frac{2l+1}{x}j_l(x)-j_{l-1}(x)$$

$$\text{with } j_{-1}(x)=\frac{\cos x}{x} \quad \text{and } j_0(x)=\frac{\sin x}{x},$$

$$n_{l+1}(x)=\frac{2l+1}{x}n_l(x)-n_{l-1}(x)$$

$$\text{with } n_{-1}(x)=\frac{\sin x}{x} \quad \text{and } n_0(x)=-\frac{\cos x}{x},$$

$$h_l'(x)=\frac{1}{2l+1}[lj_{l-1}(x)-(l+1)j_{l+1}(x)]$$

$$-j\frac{1}{2l+1}[ln_{l-1}(x)-(l+1)n_{l+1}(x)].$$

B. The control sound field

The sound pressure at location $\mathbf{r}_e=(r_e,\theta_e,\phi_e)$ generated by a point source located at $\mathbf{r}_c=(r_c,\theta_c,\phi_c)$ in free space without scattering objects can be expanded in terms of spherical harmonics[26]

$$p_c(\mathbf{r}_e)=\frac{j\omega\rho_0 q e^{-jkr}}{4\pi r}=k\omega\rho_0 q\sum_{l=0}^{\infty} j_l(kr_<)h_l(kr_>)$$
$$\times\sum_{m=-l}^{l} Y_{lm}^*(\theta_c,\phi_c)Y_{lm}(\theta_e,\phi_e), \tag{4}$$

where

$$Y_{lm}(\theta,\phi)=\sqrt{\frac{2l+1}{4\pi}\cdot\frac{(l-m)!}{(l+m)!}}P_l^m(\cos\theta)e^{jm\phi}, \tag{5}$$

and q is the volume velocity of the monopole source, $r=|\mathbf{r}_e-\mathbf{r}_c|$, $r_<=\min(|\mathbf{r}_e|,|\mathbf{r}_c|)$, $r_>=\max(|\mathbf{r}_e|,|\mathbf{r}_c|)$, $P_l^m(\cos\theta)$ is the associated Legendre function of degree l and order m evaluated at $\cos\theta$. Here, * denotes the complex conjugate.

The expression for the scattered wave from a sphere of radius a whose center is the polar origin can also be expanded into a spherical harmonic series as

$$p_s(\mathbf{r}_e)=\sum_{l=0}^{\infty} h_l(k|r_e|)\sum_{m=-l}^{l} A_{lm}Y_{lm}(\theta_e,\phi_e). \tag{6}$$

A_{lm} is the coefficient to be determined. After obtaining the radial velocities corresponding to the incidence wave $p_c(\mathbf{r}_e)$ and the scattering wave $p_s(\mathbf{r}_e)$ and making the combination of the total normal velocity equal to zero at $r_e=a$, the total sound field can be obtained[25,27]

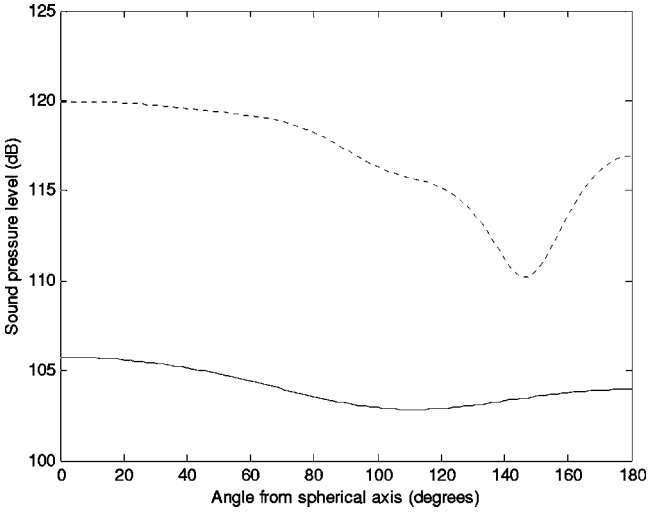

FIG. 3. Distribution in angle of total sound-pressure level in the far field of a point source scattered by a rigid sphere for 500 Hz (solid line) and 2000 Hz pure tone (dotted line).

$$p_{cs}(\mathbf{r}_e)=k\omega\rho_0 q\sum_{l=0}^{\infty}\left[j_l(kr_<)h_l(kr_>)\right.$$
$$\left.-\frac{j_l'(ka)}{h_l'(ka)}h_l(k|r_c|)h_l(k|r_e|)\right]$$
$$\times\sum_{m=-l}^{l} Y_{lm}^*(\theta_c,\phi_c)Y_{lm}(\theta_e,\phi_e)$$
$$=\frac{k\omega\rho_0 q}{4\pi}\sum_{l=0}^{\infty}(2l+1)\left[j_l(kr_<)-\frac{j_l'(ka)}{h_l'(ka)}h_l(kr_<)\right]$$
$$\times h_l(kr_>)\left\{\left(P_l(\cos\theta_c)P_l(\cos\theta_e)\right.\right.$$
$$+\sum_{m=1}^{l}2\frac{(l-m)!}{(l+m)!}P_l^m(\cos\theta_c)$$
$$\left.\left.\times P_l^m(\cos\theta_e)\cos[m(\theta_e-\theta_c)]\right\}\right. . \tag{7}$$

Figure 3 shows the distribution in angle of total sound-pressure level in the far field of a point source scattered by a rigid sphere. The volume velocity of the point source $q=1.0\,\mathrm{m}^3/\mathrm{s}$ and the location is at $\mathbf{r}_c=(0.1\,\mathrm{m},0,0)$. It can be seen that the trends of curves in Fig. 3 are quite similar to that in Fig. 2 for primary sound field, which indicates that a certain amount of global attenuation could be achieved by using a loudspeaker and a far-field error microphone. Here, the sphere acts as an obstacle and the attenuation in gain is a function of wavelength. This will be shown in the numerical simulations below.

C. Minimization of the radiation of the piston set

As the system being considered is linear, the concept of superposition is valid. Assuming that N_c point control sources with the volume velocity $\mathbf{Q}_c=[q_{c,1}\,q_{c,2,}\cdots q_{c,Nc}]^T$

are placed around the rigid sphere to cancel the primary sound field radiated by a piston set in a rigid sphere at N_e point, $\mathbf{P_p}=[p_p(\mathbf{r}_{e,1}),p_p(\mathbf{r}_{e,2}),\ldots,p_p(\mathbf{r}_{e,Ne})]^T$, outside the sphere. The value of function to minimize the influence of primary and control sources can be expressed as a quadratic function at these points

$$F=\sum_{i=1}^{N_e}|p(\mathbf{r}_{e,i})|^2=\mathrm{P}^H\mathrm{P}=\mathbf{Q}_c^H\mathbf{a}\mathbf{Q}_c+\mathbf{b}_1\mathbf{Q}_c+\mathbf{Q}_c^H\mathbf{b}_2+\mathbf{c}, \tag{8}$$

where the superscript H denotes conjugate transpose and T denotes transpose, and

$$\begin{aligned}&\mathrm{P}=\mathrm{P}_p+\mathrm{P}_{cs},\\&\mathbf{a}=\mathrm{Z}^H\mathrm{Z},\\&\mathbf{b}_1=\mathrm{P}_p^H\mathrm{Z},\quad \mathbf{b}_2=\mathrm{Z}^H\mathrm{P}_p,\\&\mathbf{c}=\mathrm{P}_p^H\mathrm{P}_p.\end{aligned} \tag{9}$$

In Eq. (9), $\mathbf{P}_{cs}=\mathbf{Z}\mathbf{Q}_c$, and $\mathbf{Z}$ is an $N_e\times N_c$ matrix in the form of

$$\mathbf{Z}=\begin{bmatrix}\mathbf{z}^T(\mathbf{r}_{e,1})\\ \mathbf{z}^T(\mathbf{r}_{e,2})\\ \vdots\\ \mathbf{z}^T(\mathbf{r}_{e,N_e})\end{bmatrix}, \tag{10}$$

where $\mathbf{z}(\mathbf{r}_{e,i})$ is an $N_c\times 1$ vector, whose mth element is the transfer function between the sound pressure at the position $\mathbf{r}_{e,i}$ and the volume velocity of the mth control source located at $\mathbf{r}_{c,m}$

$$\begin{aligned}z_m(\mathbf{r}_{e,i})=&\frac{k\omega\rho_0}{4\pi}\sum_{l=0}^{\infty}(2l+1)\\&\times\left[j_l(kr_<)-\frac{j_l'(ka)}{h_l'(ka)}h_l(kr_<)\right]h_l(kr_>)\\&\times\left\{\left(P_l(\cos\theta_{c,m})P_l(\cos\theta_{e,i})\right.\right.\\&+\sum_{m=1}^{l}2\frac{(l-m)!}{(l+m)!}P_l^m(\cos\theta_{c,m})P_l^m(\cos\theta_{e,i})\\&\left.\left.\times\cos[m(\theta_{e,i}-\theta_{c,m})]\right\},\end{aligned} \tag{11}$$

where $r_<=\min(|\mathbf{r}_{e,i}|,|\mathbf{r}_{c,m}|)$, $r_>=\max(|\mathbf{r}_{e,i}|,|\mathbf{r}_{c,m}|)$. Differentiating the above equations with respect to the control sources volume velocity $\mathbf{Q}_c$, and equating the result to zero, yields the optimum control source volume velocity as long as the matrix $\mathbf{a}$ is nonsingular

$$\mathbf{Q}_{\mathrm{copt}}=-\tfrac{1}{2}\mathbf{a}^{-1}(\mathbf{b}_1^H+\mathbf{b}_2). \tag{12}$$

The residual sound pressure at location $\mathbf{r}_e=(r_e,\theta_e,\phi_e)$ after control can be calculated by

$$\mathrm{P}(\mathbf{r}_e)=\mathrm{P}_p(\mathbf{r}_e)+\mathbf{Z}(\mathbf{r}_e)\mathbf{Q}_{\mathrm{copt}}. \tag{13}$$

If there is one single control source located at $\mathbf{r}_c=(r,0,0)$, Eq. (7) can be written as

$$\begin{aligned}p_c(\mathbf{r}_e)=&\frac{k\omega\rho_0 q}{4\pi}\sum_{l=0}^{\infty}(2l+1)\\&\times\left[j_l(kr_<)-\frac{j_l'(ka)}{h_l'(ka)}h_l(kr_<)\right]\\&\times h_l(kr_>)P_l(\cos\theta_e).\end{aligned} \tag{14}$$

By using the far-field approximation

$$h_l(x)\to\frac{1}{x}e^{-j(x-[l+1/2]\pi)}\quad\text{when } x\to\infty, \tag{15}$$

Eq. (14) becomes

$$\begin{aligned}p_c(\mathbf{r}_e)=&\frac{k\omega\rho_0 q}{4\pi}\times\frac{1}{kr_e}e^{-jkr_e}\sum_{l=0}^{\infty}j^{-l+1}(2l+1)\\&\times\left[j_l(kr_c)-\frac{j_l'(ka)}{h_l'(ka)}h_l(kr_c)\right]P_l(\cos\theta_e),\end{aligned} \tag{16}$$

and similarly Eq. (3) becomes

$$p_p(\mathbf{r}_e)=\frac{1}{kr_e}e^{-jkr_e}\sum_{l=0}^{\infty}j^{l+1}A_lP_l(\cos\theta_e). \tag{17}$$

Suitable control source strength can be selected to make the pressure at a point in the far field zero

$$\mathbf{p}(\mathbf{r}_{e0})=\mathbf{p}_p(\mathbf{r}_{e0})+\mathbf{p}_c(\mathbf{r}_{e0})=0. \tag{18}$$

Substituting Eqs. (16) and (17) into Eq. (18), the relationship between the complex control source strength q_{c0} and the primary source vibration velocity u_0 can be obtained, which ensures that zero pressure is produced in the far field at a particular angular position specified by θ_{e0}

$$q_{c0}=\frac{\lambda}{2\pi}u_0\times\frac{j\sum_{l=0}^{\infty}\dfrac{P_{l-1}(\cos\theta_0)-P_{l+1}(\cos\theta_0)}{h_l'(ka)}}{\sum_{l=0}^{\infty}(2l+1)\left[j_l(kr_c)-\dfrac{j_l'(ka)}{h_l'(ka)}h_l(kr_c)\right]}, \tag{19}$$

where λ is the wavelength of sound radiated. Then, the residual pressure field is

$$\mathbf{p}(\mathbf{r}_e)=\mathbf{p}_p(\mathbf{r}_e)+\mathbf{Z}(\mathbf{r}_e)q_{c0}. \tag{20}$$

III. NUMERICAL SIMULATIONS

A. Single control source

The candidate locations for the control sources are shown in Fig. 4. There are 10 points evenly distributed in elevation and 20 points evenly distributed in azimuth, resulting in a total of 181 candidate control locations all around the primary source. (Note when $\theta_c=0$, there is only one point despite the value of ϕ_c.) The spatial distributions of the 181 points are

$$\begin{aligned}&\theta_{ci}=i/18\times 180\ \ (\mathrm{deg}),\quad i=0,1,2,\ldots,9,\\&\phi_{ci}=i/10\times 180\ \ (\mathrm{deg}),\quad i=0,1,2,\ldots,9.\end{aligned}$$

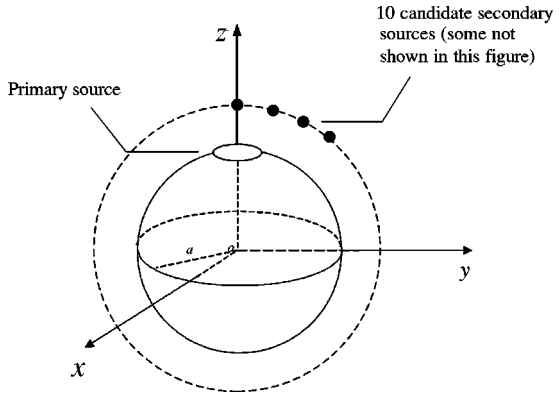

FIG. 4. The candidate control source locations for the active control.

Similarly, a total number of 201 error microphones 100 m away from the sphere center is used to evaluate the performance of control. Their spatial distributions are

$$\theta_{ei} = i/11 \times 180 \ \text{(deg)}, \quad i = 0,1,2,...,10,$$

$$\phi_{ei} = i/10 \times 180 \ \text{(deg)}, \quad i = 0,1,2,...,19.$$

The cost function used for evaluation is

$$NR(\omega) = -10 \log_{10} \frac{\sum_{i=1}^{N_e} |p(\mathbf{r}_{e,i}, \omega)|^2}{\sum_{i=1}^{N_e} |p_p(\mathbf{r}_{e,i}, \omega)|^2}, \tag{21}$$

where $p(\mathbf{r}_{e,i}, \omega)$ and $p_p(\mathbf{r}_{e,i}, \omega)$ are the residual and the primary sound pressure at the ith error microphone, ω is the angular frequency of interest, and N_e is the number of error microphones. The optimum location of the control source is determined by those that give rise to the maximum, $NR(\omega)$. Note that for the case where the effect of the rigid sphere is removed, the primary source is still the same piston set at the same location as with the rigid sphere. The way to calculate the sound field of the piston set in the free field is[25]

$$p_p(\mathbf{r}_e) = \frac{jk\rho_0 c_0 u_0 a^2}{4\pi r_e} e^{-jkr_e} \times \int_0^{\theta_0} 2\pi J_0(ka \sin\theta_p \sin\theta_e) \sin\theta_p \times e^{jka \cos\theta_p \cos\theta_e} d\theta_p, \tag{22}$$

where J_0 is the *Bessel function* of order zero. The integral above can be calculated numerically in the simulations.

Figure 5 shows NR as a function of distance between the control source and the sphere center for 500 and 2000 Hz with and without the rigid sphere. The total sound power is obtained by integrating the mean active sound intensity over a sphere in the far field, which is useful for determining the global effectiveness of the active control. For control source located at (0.1 m, 0, 0), the maximum NR is 33 dB for 500 Hz and 20 dB for 2000 Hz when the rigid sphere is present. Without the rigid sphere, the maximum NR is 22.2 dB for 500 Hz, 10.2 dB for 2000 Hz.

Figure 6 and Fig. 7 show the effects in regard to the spherical angles and it is obvious that the NR is symmetric with ϕ_c. Figure 8 shows NR curves as a function of frequency with and without the rigid sphere. From these figures, it can be seen that (1) whether the scattering rigid sphere exists or not, higher attenuation can be obtained at low frequencies; (2) The introduction of the rigid sphere changes the directionality of the sound field. And, this makes the active control easier. Thus, the noise reduction is larger when there is a rigid sphere, both at low frequencies and high frequencies.

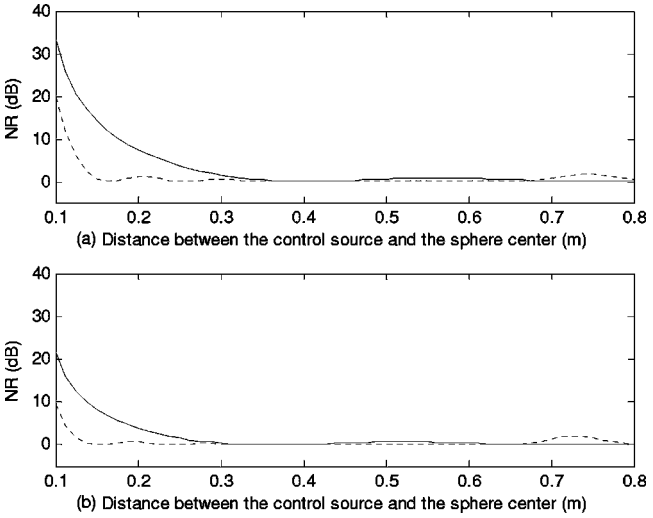

FIG. 5. NR as a function of distance between the control source (r_c, $\theta_c = 0$, $\phi_c = 0$) and the sphere center, one control source, 500 Hz (solid line) and 2000 Hz (dotted line) (a) with the rigid sphere; (b) without the rigid sphere.

Figures 9(a) and (b) show NR for a control source with a number of candidate locations outside the sphere but in equal distance of 0.0125 m from the piston center. The coordinates for the control source locations in Fig. 10(c) are

$$r_c = \{0.1, 0.0982, 0.0964, 0.0946, 0.0929, 0.0911, 0.0893, 0.0875\} \ \text{m},$$

$$\theta_c = \{0, 3.9802, 5.4588, 6.4621, 7.1835, 7.6944, 8.0263, 8.1291\} \ \text{deg}.$$

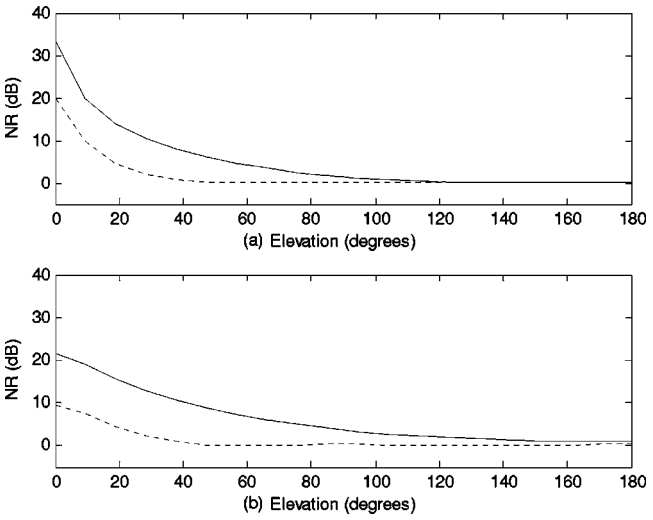

FIG. 6. NR as a function of elevation θ_c ($r_c = 0.1$ m, $\phi_c = 0$), one control source, 500 Hz (solid line) and 2000 Hz (dotted line) (a) with the rigid sphere; (b) without the rigid sphere.

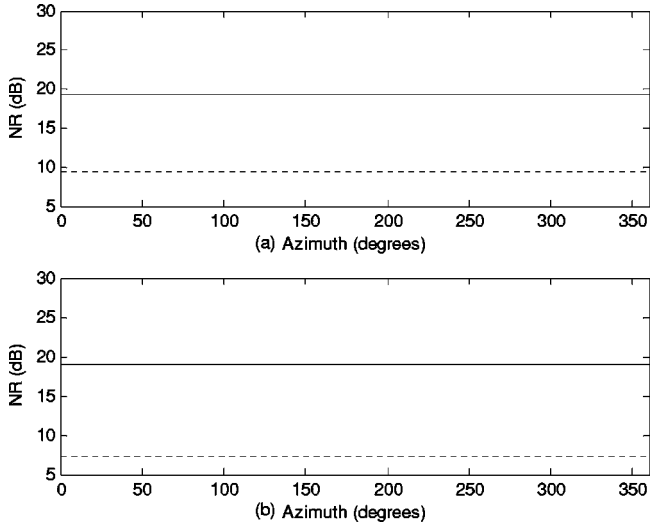

FIG. 7. *NR* as a function of azimuth ϕ_c ($r_c=0.1$ m, $\theta_c=10$ deg), one control source, 500 Hz (solid line) and 2000 Hz (dotted line) (a) with the rigid sphere; (b) without the rigid sphere.

Here, ϕ_c is set as 0 deg; however, it can be arbitrary due to its symmetry in *NR*.

It can be seen from the figures that the optimum location for a single control source with the rigid sphere is at $\mathbf{r}_{copt}=(r,0,0)$. It can also be seen from Figs. 9(a) and (b), even though the distance between the single control source and the center of the piston is identical, the *NR* for different positions can be different. This is quite different from the case where there is no rigid sphere. For the case without the rigid sphere, provided that the distances between the control sources and primary source are the same, the noise reduction should be equal. There are small variations in Fig. 9(b) for *NR* without the rigid sphere. This is because the piston is an extended source instead of a point source.

All the figures above show that it is possible to reduce the acoustics radiation from a piston set in a rigid sphere with a single control source around, and the nearer the control source is, the lower the frequency range is, and the larger the attenuation could be. This is the same as when there is no scattering object. However, it is also shown that the attenuation with the rigid sphere is usually larger than that without the rigid sphere.

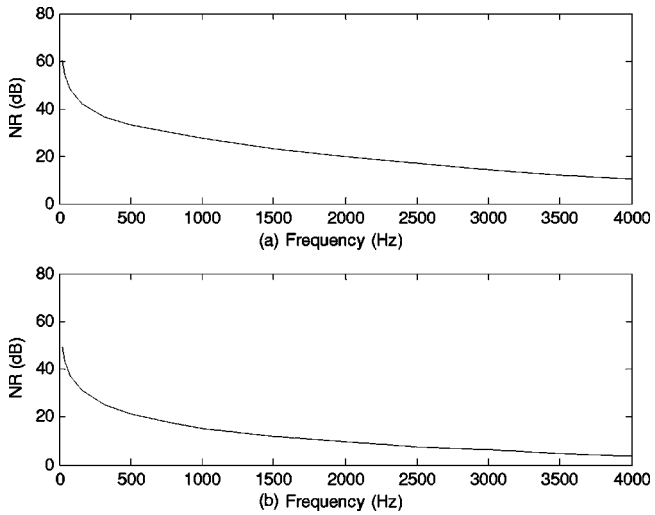

FIG. 8. *NR* as a function of frequency, one control source ($r_c=0.1$ m, $\theta_{ci}=0$, $\phi_{ci}=0$) (a) with the rigid sphere; (b) without the rigid sphere.

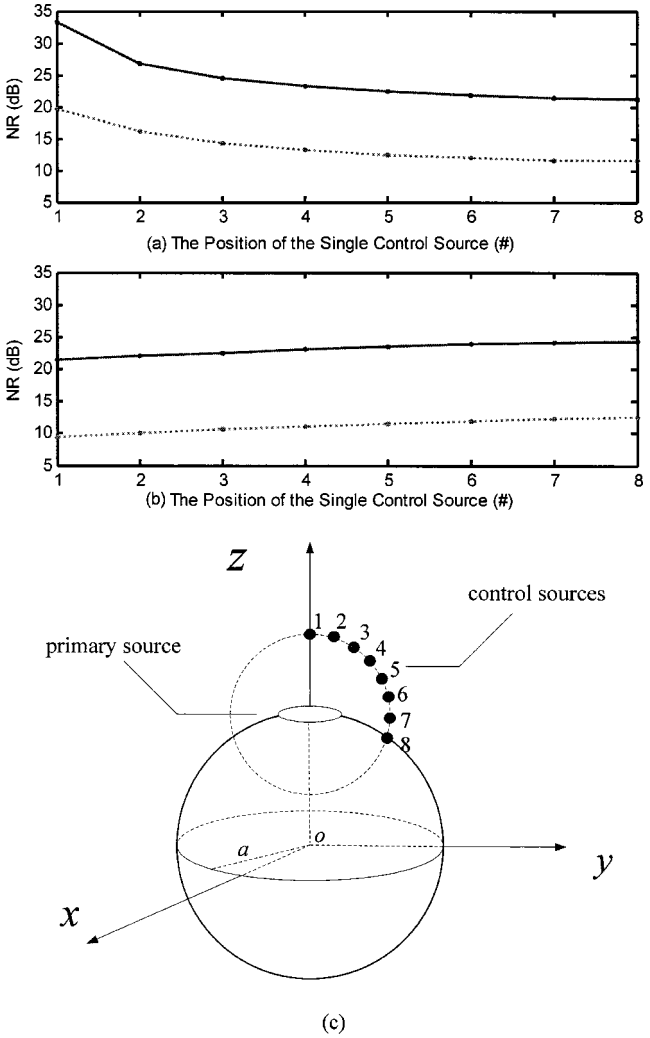

FIG. 9. *NR* for one control source with a number of candidate locations outside the sphere but in equal distance of 0.0125 m with the piston center; the solid line is for 500 Hz and the dotted line is for 2000 Hz. (a) With the rigid sphere; (b) without the rigid sphere; (c) the positions of these locations.

B. Multicontrol sources

To increase the performance of the active control, more than one control source is necessary. Under these circumstances, the location and number of the control sources should be optimized to achieve the required performance at the lowest cost. One such optimization method is the spherical harmonics expansion method.[12,13] However, this method will not be used here as it involves a huge amount of computation load for frequency up to 2000 Hz. Referring to active control of monopole primary sound using monopole sources array,[13] it has been shown that the geometrical arrangements of monopole sources array considering symmetry and directivity of control sources will produce significant reduction in power output. Therefore, this method is used in the paper for the convenience of the future practical setups. The attenuation of several practical setups considered here

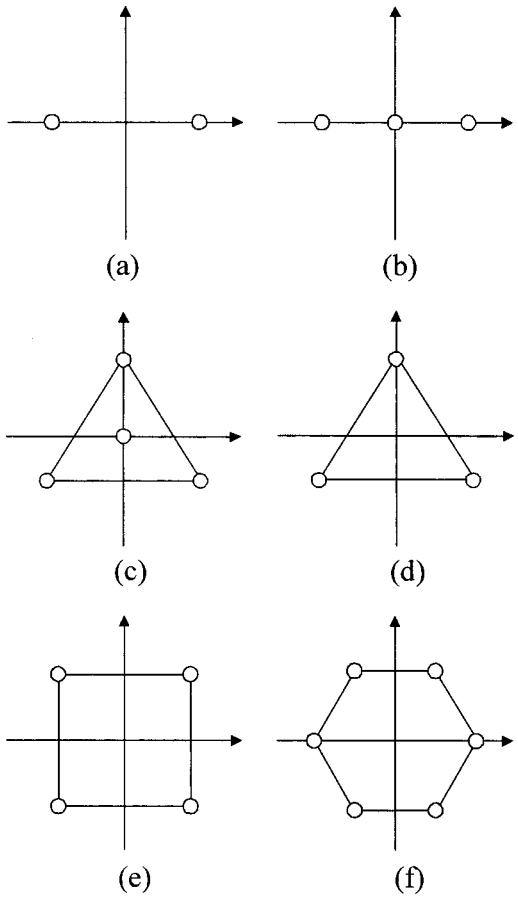

FIG. 10. Geometrical configurations (projection onto xoy plane) of the control sources, where radial coordinate r_c is kept unchanged at 0.1 m, ϕ_c are defined below for each configuration. θ_c is the variable. (a) Two control sources with $\phi_c=0$ and 180 deg. (b) Three control sources, two of them with $\phi_c=0$ and 180 deg, while the third is fixed at (0.1,0,0). (c) Four control sources, three of them with $\phi_c=90$, 210, and 330 deg, while the fourth one is fixed at (0.1,0,0). (d) Three control sources with $\phi_c=90$, 210, and 330 deg. (e) Four control sources with $\phi_c=45$, 135, 225, and 315 deg. (f) Six control sources located with $\phi_c=0$, 60, 120, 180, 240, and 300 deg.

are shown in Fig. 10, and the genetic algorithm will be used later to determine the optimum number and locations of control sources and error sensors.

Figure 10 shows the geometrical configurations (projection onto xoy plane) of two, three, four, and six control sources. For all the control sources, the radial coordinate r_c is kept unchanged at 0.1 m; ϕ_c is defined below for each configuration. θ_c is the variable, whose effects on noise reduction will be investigated below. Figure 11 shows an example of how to change θ_c for the two-source configuration of Fig. 10(a). Note, with the change of θ_c, the distance between the two secondary sources is varying; however, their distances to the sphere center remain the same. Please also note in the configurations of Figs. 10(b) and (c) that there is a fixed control source, while the other control source positions are changed with θ_c. It is obvious that in Fig. 10, the azimuth of control source has no effect on the value of cost function for each configuration due to symmetry.

Figure 12 shows the achievable maximum NR with different elevation θ_c. It should be noted that when elevation is 0 deg, NR of all the setups should be the same as the single source. NR of setups (a) (d) (e) (f) are the same while cases

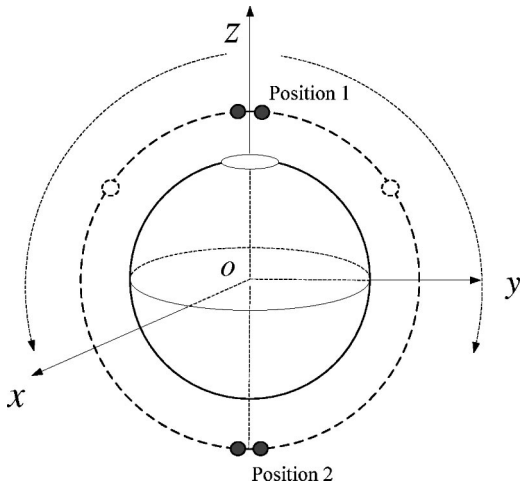

FIG. 11. Changing directions of control sources for Fig. 10(a). From position 1 to position 2, elevation of control sources varies from zero to 180 deg.

of setups (b) and (c) are different because the matrix **a** in Eq. (9) is singular when θ_c closes to zero.

It can also be found in Fig. 12 that (1) Compared with a single control source, the maximum NR does not necessarily appear at $\theta_c=0$ deg; (2) For Figs. 12(d)–(f), the attenuation does not increase significantly when the number of control sources is greater than 3; (3) For practical application, configuration (d) may be the best choice for its requirement of fewer control sources and higher maximum achievable attenuation. In some special cases, in order to achieve comparatively equal NR at all elevations around the sphere, configuration (b) or (c) is more feasible. Note here that because of the limitation of the length of the paper, robustness analysis on the position is not further performed.

Figure 13 shows the NR with different elevations using

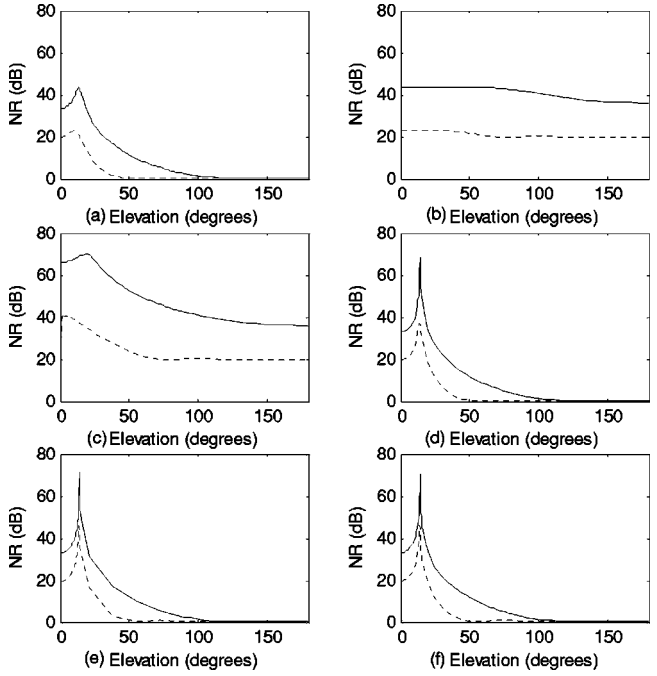

FIG. 12. NR with varying elevation for 500 Hz (solid line) and 2000 Hz (dotted line) using the setups in Fig. 10, (a)–(f) for setup (a)–(f) in Fig. 10, respectively.

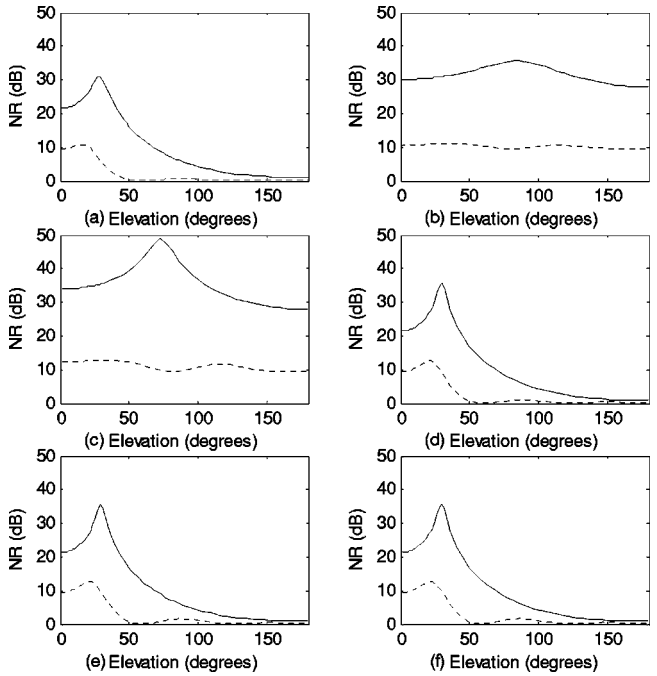

FIG. 13. *NR* with varying elevation for 500 Hz (solid line) and 2000 Hz (dotted line) using the setups in Fig. 10 without the rigid sphere, (a)–(f) in Fig. 10 for setup (a)–(f), respectively.

the setups in Fig. 10 for setups (a)–(f), respectively, without the rigid sphere. Comparing with Fig. 12, it can be seen again that noise reduction with the existence of the rigid sphere is usually larger than that without the rigid sphere, the same as in the one control source cases. The other trends are similar.

It should be noted that varying elevation angles too much in the multisource simulations will result in a large amount of computation and complexity. Thus, here only one varying elevation angle is used in these multisource simulations above.

C. Optimization of the number and location of control sources and error sensors

Although more control sources may have larger attenuation, too many control sources are not practical due to computation burden and system complexity. A genetic algorithm[13,28,29] is used to search the locations of control sources for the problem here. The efficiency of each configuration of control source is evaluated with the cost function (21). The basic genetic operations (selection, crossover, mutation) used here are linear scaling, modified random recording, simple mutation, and elitist model. The number of chromosome (population size) per generation is 150, the number of generations is 5000, the crossover probability is 0.7, and the mutation probability is 0.15. The results of the control sources optimization are shown in Table I.

From Table I it can be seen that the genetic algorithm (GA) works, however not perfectly when control sources are few. For three control sources, Fig. 12(d) got 67.4 dB for 500 Hz and 36.4 dB for 2000 Hz and for four control sources, *NR*s in Fig. 12(e) are also larger than those obtained by GA. But, for six and nine control sources, GA got the better result. For GA, although the optimized locations have been obtained among the candidate points, the actual best locations cannot be obtained as the candidate points are too sparse to include the actual best points. This is reasonable as GA is stochastic global optimization procedure for finding the global maximum (or minimum) of a multimodal function, which cannot guarantee to reach the global optimization. However, the GA optimization does show that the practical setups proposed above are near optimum for less control sources (no more than 4). In the cases above, for 6 and 9 control sources, the practical setups in Figs. 10(e) and (f) are not optimal. There must be some more complex setups to obtain better performance.

TABLE I. *NR* (dB) of GA for optimizing control source locations ($r_c = 0.1$ m).

	Frequency (Hz)	
NR (dB)	500	2000
3 control sources	51.1	30.7
4 control sources	65.5	40.2
6 control sources	91.0	51.3
9 control sources	99.4	59.7

The locations (θ_c, ϕ_c) obtained by GA for 3 control sources are (10,0), (10,144), (30,252) deg for 500 Hz (20,90), (10,198), and (20,342) deg for 2000 Hz. For 4 control sources the locations are (10,36), (30,126), (10,216), and (30,306) for 500 Hz (10,72), (30,162), (10,252), and (30,342) deg for 2000 Hz, respectively. Note that θ_c is around the range from 10 to 30 deg and ϕ_c nearly distributes with an equivalent distance among 360 deg. This matches the practical setups in Fig. 10. Compared with the practical setups in Fig. 10, this result is close to the optimum location gotten by practical setup.

For 6 and 9 control sources, the results gotten by GA are a little bit complex. They are, for 6 control sources, $\theta_c = \{20,10,30,20,20,0\}$, $\phi_c = \{72,162,162,252,342,0\}$ for 500 Hz; $\theta_c = \{20,20,70,20,20,0\}$, $\phi_c = \{36,126,162,216,306,0\}$ for 2000 Hz; For 9 control sources, $\theta_c = \{60,20,50,20,60,20,70,20,0\}$, $\phi_c = \{0,36,90,126,180,216,270,306,0\}$ for 500 Hz; $\theta_c = \{10,20,30,10,40,20,10,20,40\}$, $\phi_c = \{0,54,108,144,180,216,252,288,342\}$ for 2000 Hz.

It is interesting to note that there is a control source located at (0,0) for three of the four cases above, and their ϕ_c nearly distributes with an equivalent distance among 360 deg. It may be a direction to the optimum configuration.

When the number and locations of control sources are obtained, the next step is to decrease the number of error sensors. By using the same genetic algorithm strategy, the positions of four error microphones for configuration in Fig. 10(d) can be found. In this case, three control sources and their positions (r_c, θ_c, ϕ_c) are (0.1 m, 13.9 deg, 0 deg), (0.1 m, 13.9 deg, 120 deg), and (0.1 m, 13.9 deg, 240 deg), respectively. The number of the candidate locations is 201, which is the same as that in Sec. III A. Table II shows the results of the simulation. Note that the three control sources were optimized by minimizing the sum of the squared sound-pressure level at these four optimal error microphones. *NR* is then calculated by Eq. (21) with 201 evaluation points.

TABLE II. NR (dB) of genetic algorithm for optimizing error microphone locations ($r_e = 100$ m) for configuration (d) in Fig. 10 ($\theta_c = 13.9$ deg).

Number of error microphones	Frequency (Hz)	
	500	2000
201	67.4	36.4
4	67.1	36.3

For 500 Hz, the locations (θ_e, ϕ_e) of the optimum four error microphones are (49.1,108) deg, (32.7,216) deg, (130.9,54) deg, and (49.1,234) deg. And for 2000 Hz, they are (98.2,324) deg, (36,65.5) deg, (147.3,162) deg, and (32.7,270) deg, respectively. It can be seen that the genetic algorithm is effective here.

IV. EXPERIMENTS

Figure 14 shows the experiment setup, where a single-input–single-output system is implemented. The experiment is carried out in the anechoic chamber of Nanjing University, which has a free-field frequency above 70 Hz. Some useful results are obtained. Compared with the theoretical simulation, the achieved attenuation at high frequency in the experiment matches better than low frequency. With only one control source and one error microphone, attenuation can be achieved in nearly the whole space at low (500 Hz) and high (2000 Hz) frequencies.

The electronic controller is mainly embedded in an ADSP-21061 EZ-Kit LITE. A standard filtered-X LMS feed forward algorithm, for which the filter order is 128, was used with off-line secondary path identification. The dummy head is a real sphere, with a tiny loudspeaker inside to simulate the piston set. There is a circular mouth on the surface of the sphere. A circular short duct is set between the mouth and the loudspeaker. The experiment data are collected by a multichannel recording system, SQlabII from HeadAcoustic GmbH.

For the convenience of experiment, the control loudspeaker is 0.05 m away from the mouth of the sphere for 500 Hz, while it is 0.01 m for 2000 Hz; the error microphone is 0.4 m away from the center of the sphere. Two evaluation microphones are at 1.1 and 6.5 m away from the center of the sphere, respectively. In the experiment, the sound pressures are measured every 10 deg of angle from the spherical axis (azimuth in xoy plane).

FIG. 14. Experiment arrangement of the active control system in anechoic chamber, where #1 is the rigid sphere, #2 is the control loudspeaker, and #3 is the error microphone.

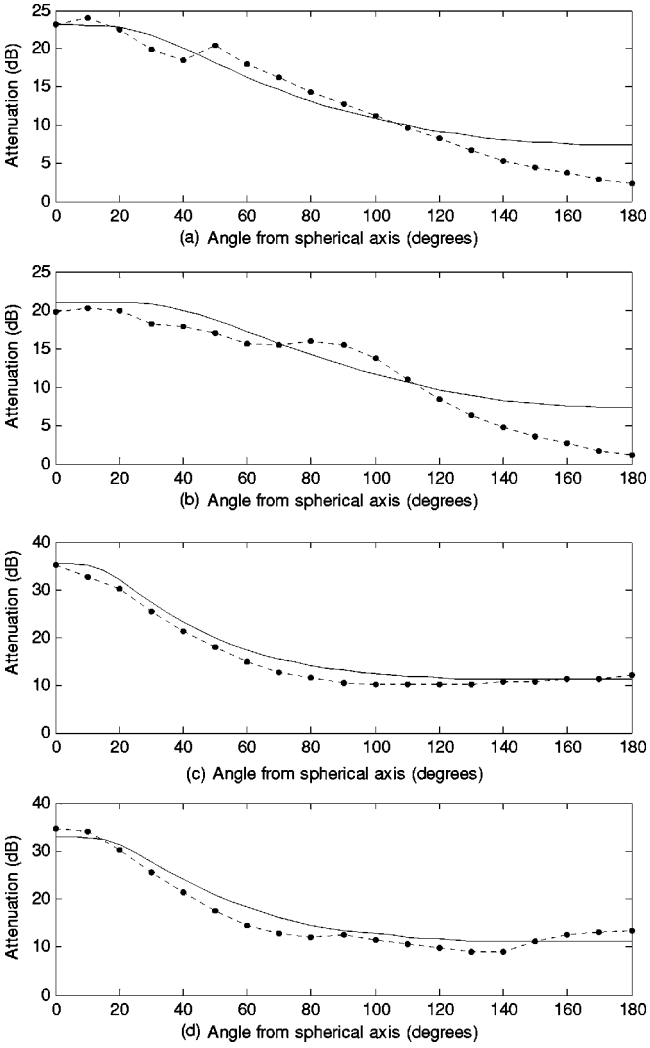

FIG. 15. Experiment attenuations compared with theoretical results (dB), experiment results (dotted line), theoretical results (solid line). (a) Near field ($r = 1.1$ m) for 500 Hz; (b) Far field ($r = 6.5$ m) for 500 Hz; (c) Near field ($r = 1.1$ m) for 2000 Hz; (d) Far field ($r = 6.5$ m) for 2000 Hz.

Figure 15 shows some results for controlling pure-tone noise at 500 and 2000 Hz. From Fig. 15 it can be seen that global sound reduction can be achieved by using only one secondary loudspeaker. Comparing the attenuations achieved in the experiment with the theoretical results, it can be seen that the system performance matches the trends of the predication and numerical simulation. The difference between the practical sound field and the theoretical sound field is very small.

In the experiment the size of the secondary loudspeaker is small (with a diameter of 3 cm), which is far less than the wavelength of 2000 Hz. It can be regarded as a point source and its scattering effect can be neglected.

The experiment results show that active control of radiation from a piston set in a rigid sphere using one secondary source can give good performance below 2000 Hz. However, this research is based on a rigid sphere instead of a ''real'' head, and surely there is some difference between the prac-

tical system and this ideal model. In the next stage we will establish a more precise model. An approach to improve the results is to model the head as an ellipsoidal surface instead of a sphere and take into account the surface acoustic impedance.

V. CONCLUSIONS

This paper investigated the global active control of free-field acoustic radiation from a piston set in a rigid sphere with a set of control point sources close to the sphere. Analytic expression has been derived, and numerical simulations and experiment results show that it is possible to control the radiation from a small piston set in a rigid sphere with the size of a human head up to 2000 Hz. A number of issues such as the number and location of the control sources, the number and location of error sensors have also been discussed.

The comparison between the performance of the active noise control system with and without the rigid sphere shows that the presence of the rigid sphere is beneficial for the active control. This is due to the scattering effect of the rigid sphere on the control acoustic field as well as the primary field. This phenomenon has also been observed in the local active control system developed by Garcia-Bonito *et al.*, although the physical phenomena and simulation conditions of their study are quite different from this paper. In their work,[8] the sound field is diffuse and the secondary source is several wavelengths away from the error point, which is close to or on the surface of a reflecting object. It seems that introducing scattering objects in an active noise control system can sometimes increase its performance; further investigation on the mechanisms is now underway so that an optimized scattering object can be designed to increase the performance of an existing active noise control system. Other future work includes considering the active control of piston sound radiation from some practical scattering objects such as ellipsoidal surface or cylinders.

ACKNOWLEDGMENTS

The authors are sincerely grateful to Professor Jie Pan (School of Mechanical Engineering, the University of Western Australia) for a careful reading of the manuscript and providing many useful comments for improvement. Also thanked are the anonymous referees for helpful suggestions which do help to improve the quality of the manuscript. This work was supported by the National Science Foundation, Nos. 60272037 and 60340420325.

[1] P. A. Nelson and S. J. Elliott, *Active Control of Sound* (Academic, New York, 1992).
[2] C. H. Hansen and S. D. Snyder, *Active Control of Noise and Vibration* (E&FN SPON, London, 1997).
[3] S. J. Elliott, *Signal Processing for Active Control* (Academic, London, 2001).
[4] S. M. Kuo and D. R. Morgan, *Active Noise Control Systems: Algorithms and DSP Implementations* (Wiley, New York, 1996).
[5] C. F. Ross, "Active control of sound," Ph.D. thesis, University of Cambridge (1980).
[6] J. Garcia-Bonito and S. J. Elliott, "Local active control of diffracted diffuse sound fields," J. Acoust. Soc. Am. **98**(2), 1017–1024 (1995).
[7] A. David and S. J. Elliott, "Numerical studies of actively generated quiet zones," Appl. Acoust. **41**, 63–79 (1994).
[8] J. Garcia-Bonito, S. J. Elliott, and M. Bonilha, "Active cancellation of pressure at a point in a pure-tone diffracted diffuse sound field," J. Sound Vib. **201**(1), 43–65 (1997).
[9] J. Garcia-Bonito and S. J. Elliott, "Active cancellation of acoustic pressure and particle velocity in the near field of a source," J. Sound Vib. **221**(1), 85–116 (1999).
[10] X. Qiu, C. H. Hansen, and X. Li, "A comparison of near-field acoustic error sensing strategies for the active control of harmonic free-field sound radiation," J. Sound Vib. **215**(1), 81–103 (1998).
[11] A. Berry, X. Qiu, and C. H. Hansen, "Near-field sensing strategies for active control of the sound radiated from a plate," J. Acoust. Soc. Am. **106**, 3394–3406 (1999).
[12] T. Martin and A. Roure, "Optimization of an active noise control system using spherical harmonic expansion of the primary field," J. Sound Vib. **201**(5), 577–593 (1997).
[13] T. Martin and A. Roure, "Active noise control of acoustic sources using spherical harmonics expansion and a genetic algorithm: Simulation and experiment," J. Sound Vib. **212**(3), 511–523 (1998).
[14] P. A. Nelson, A. R. D. Curtis, S. J. Elliott, and A. J. Bullmore, "The minimum power output of free-field point sources and the active control of sound," J. Sound Vib. **116**(3), 397–414 (1987).
[15] C. Deffayet and P. A. Nelson, "Active control of low-frequency harmonic sound radiated by a finite panel," J. Acoust. Soc. Am. **84**, 2192–2199 (1988).
[16] L. Song, G. H. Koopmann, and J. B. Fahnline, "Active control of the acoustic radiation of a vibrating structure using a superposition formulation," J. Acoust. Soc. Am. **89**(6), 2786–2792 (1991).
[17] G. H. Koopmann, L. Song, and J. B. Fahnline, "A method for computing acoustic fields based on the principle of wave superposition," J. Acoust. Soc. Am. **86**(6), 2433–2438 (1989).
[18] L. Song, G. H. Koopmann, and J. B. Fahnline, "Numerical errors associated with the method of superposition for computing acoustic fields," J. Acoust. Soc. Am. **89**(6), 2625–2633 (1991).
[19] M. E. Johnson, S. J. Elliott, K. H. Baek, and J. Garcia-Bonito, "An equivalent source technique for calculating the sound field inside an enclosure containing scattering objects," J. Acoust. Soc. Am. **104**(3), 1221–1231 (1998).
[20] R. Jeans and I. C. Mathews, "The wave superposition method as a robust technique for computing acoustic fields," J. Acoust. Soc. Am. **92**(2), 1156–1166 (1992).
[21] M. Ochmann, "The source simulation technique for acoustic radiation problems," Acoustica **81**, 512–527 (1995).
[22] P. A. Nelson and Y. Kahana, "Spherical harmonics, singular-value decomposition and the head-related transfer function," J. Sound Vib. **239**(4), 607–637 (2001).
[23] R. O. Duda, "Range dependence of the response of a spherical head model," J. Acoust. Soc. Am. **104**(5), 3048–3058 (1998).
[24] D. S. Brungart and W. M. Rabinowitz, "Auditory localization of nearby sources. I. Head-related transfer functions," J. Acoust. Soc. Am. **106**(3), 1465–1479 (1999).
[25] P. M. Morse and K. U. Ingard, *Theoretical Acoustics* (McGraw-Hill, Inc., 1968).
[26] C. Flammer, *Spherical Wave Functions* (Stanford University Press, Stanford, 1957).
[27] J. J. Bowman, T. B. A. Senior, and P. L. E. Uslenghi, *Electromagnetic and Acoustic Scattering by Simple Shapes* (North-Holland, Amsterdam, 1969).
[28] D. T. Tsahalis, S. K. Katsikas, and D. A. Manolas, "A genetic algorithm for optimal positioning of actuators in active noise control: Results from the ASANCA project," Inter-noise 93, 83–88 (1993).
[29] K. H. Beak and S. J. Elliott, "Natural algorithm for choosing source locations in active control systems," J. Sound Vib. **186**(2), 245–267 (1995).

Children's perceptions of their acoustic environment at school and at home

Julie E. Dockrell[a)]
Psychology and Human Development, Institute of Education, London University, 25 Woburn Square, London WC1H 0AA United Kingdom

Bridget Shield
School of Engineering Systems and Design, South Bank University, 103 Borough Road, London SE1 0AA United Kingdom

(Received 20 December 2002; accepted for publication 13 January 2004)

This paper describes the results of a large-scale questionnaire survey that ascertained children's perceptions of their noise environment and the relationships of the children's perceptions to objective measures of noise. Precision, specificity, and consistency of responding was established through the use of convergent measures. Two thousand and thirty-six children completed a questionnaire designed to tap (a) their ability to discriminate different classroom listening conditions; (b) the noise sources heard at home and at school; and (c) their annoyance by these noise sources. Teachers completed a questionnaire about the classroom noise sources. Children were able to discriminate between situations with varying amounts and types of noise. A hierarchy of annoying sound sources for the children was established. External L_{Amax} levels were a significant factor in reported annoyance, whereas external L_{A90} and L_{A99} levels were a significant factor in determining whether or not children hear sound sources. Objective noise measures (L_{A90} and L_{A99}) accounted for 45% of the variance in children's reporting of sounds in their school environment. The current study demonstrates that children can be sensitive judges of their noise environments and that the impact of different aspects of noise needs to be considered. Future work will need to specify the factors underlying the developmental changes and the physical and location dimensions that determine the school effects. © *2004 Acoustical Society of America.* [DOI: 10.1121/1.1652610]

PACS numbers: 43.50.Qp, 43.50.Rq [DKW] Pages: 2964–2973

I. INTRODUCTION

Primary school children are particularly vulnerable to extraneous noise sources (Shield and Dockrell, 2003), yet are likely to experience high levels of noise in classrooms (Blake and Busby, 1994). It has been shown that a child's understanding of speech in noise and reverberation does not reach an adult level until late teenage years. Before this time, the younger the child the greater the detrimental effect of noise and reverberation (Werner and Boike, 2001; Stelmachowitz *et al.*, 2000; Soli and Sullivan, 1997; Johnson, 2000) with children under about 13 years of age being particularly susceptible. Primary school children require more favorable signal-to-noise ratios than adults to achieve comparable levels of accuracy in understanding of speech (Fallon, Trehub, and Schneider, 2000; Picard and Bradley, 2001). Classrooms tend to have poor acoustics; children are subject to high levels of background noise (Berg, Blair, and Benson, 1996) and, due to long reverberation times, much speech will be distorted and not easy to understand (Airey, 1998). Moreover, younger children are more distractable than older children and adults (Gumenyuk *et al.*, 2001). This potentially exacerbates the effects of environmental noise by increasing off-task behavior (Blatchford, Edmonds, and Martin, 2003) or indiscriminate tuning out of all stimuli resulting in generalized poor attention (Stansfeld *et al.*, 2000). Research over the last 30 years has contributed to understanding of the effects of noise on children's learning and motivation (Evans and Lapore, 1993; Shield and Dockrell, 2003). Yet, little is known about children's perceptions of their school acoustic environments. This paper describes a large-scale questionnaire survey of children that was carried out to ascertain children's perceptions of their noise environment and how the children's perceptions related to objective measures of noise.

Early studies have indicated that children are exposed to high levels of noise throughout the day. Dosimeters used with children over extended periods indicate that equivalent sound-pressure levels of about 70 dB(A) are common (Roche *et al.*, 1978; Schori and McGatha, 1978, cited in Evans, 1990). More recently, noise measurements made at schools near airports (Haines *et al.*, 2001b) and near major traffic arterials have confirmed that children in these situations are exposed to high levels of environmental noise and, in some circumstances, report high levels of annoyance from the specific sound sources studied (Cohen *et al.*, 1981). Furthermore, children who live in noisier areas rate their neighborhoods as significantly more noisy (Evans *et al.*, 2001). Thus, there is increasing evidence about children's exposure to noise and some preliminary evidence that children may be able to judge their levels of noise exposure. However, there are difficulties in generalizing to school children at large from these studies. First, interpretation of the data from dosimeters with children is complex. A total day exposure will

a)Electronic mail: j.dockrell@ioe.ac.uk

 0001-4966/2004/115(6)/2964/10/$20.00 © 2004 Acoustical Society of America

not indicate what a typical school exposure is, since it will include the playground, watching TV, listening to music, and so forth. Second, the interpretation of dosimeter data from younger children is confounded by the fact that the children themselves make a lot of noise, resulting in unreliable measurements (Shield and Jeffery, 2001). Finally, it is not clear to what extent data that are collected from high noise spots created by single sound sources, such as planes or trains, will be comparable to other school contexts, where children will hear a variety of sound sources at different levels. Thus, it is important to establish children's perception of and annoyance by a range of sound sources in typical classroom environments.

The most widespread and well-documented subjective response to noise is annoyance, although there are major differences in the ways in which noise annoyance is conceptualised (Guski, Felscher-Suhr, and Schuemer, 1998). A number of studies with adults have confirmed a dose response relationship between levels of specific transportation noises and levels of annoyance reported (Fidell, Bouber, and Schultz, 1991; Miedema and Vos, 1998; Miedema and Oudshoorn, 2001). Accurate comparisons between surveys are complicated by differences in annoyance scales, noise estimation procedures, and study conditions (Fields *et al.*, 1997, 2001). Nonetheless, adult measures of noise annoyance do show reasonably high correlations with objective noise measures (0.3–0.5) with correlations for group data being higher (average=0.89) (see Job, 1988, for a discussion of these issues). Perfect correlations would never be expected since acoustic parameters are only one of a complex set of variables involved in levels of noise annoyance (Guski, Felscher-Suhr, and Schuemer, 1998). A range of other factors will impact on an individual's judgment including relative background noise levels, age, education, sex, health of the individual, and task engaged in when making the judgment (Evans and Tafalla, 1987; Job, 1988). Having reviewed the relevant literature, Job highlights the fact that attitude to noise source is ''a genuine modifying variable'' in participants' reactions to noise exposure (Jobs, 1988, p. 1000). Infrequently occurring events may play a larger role than might be expected. This may reflect the contrast between loud noise and ambient background sound. Despite the continuing interest in adults' levels of annoyance and the increasing sophistication of the interpretations of individuals' ratings, children's annoyance with noise sources appears to be an underresearched area, although there has been some work in recent years (Haines and Stansfeld, 2000; Lercher *et al.*, 2000). Data from studies of children's responses to aircraft noise indicate that the children were consistently found to be annoyed by chronic aircraft noise exposure (Evans *et al.*, 1995; Haines *et al.*, 2001a, 2001b, 2001c). In their study of the effect of high levels of aircraft noise, Haines *et al.* (2001b) have demonstrated that annoyance levels due to aircraft noise were significantly higher among children in high aircraft noise schools compared with low aircraft noise schools. This result applied to aircraft noise annoyance both at school and at home. In contrast, levels of annoyance to road traffic noise both at school and at home in the Haines *et al.* (2001b) study did not differ significantly across high- and low-noise schools. While providing initial data which indicate that children's levels of annoyance are related to specific sound sources, these data fail to capture the variety of noise sources that may impact on children in their learning environment. As yet it has not been established whether children are annoyed by general classroom noise and whether levels of annoyance are related to classroom noise levels.

Capturing an accurate reflection of annoyance and levels of annoyance is complex (Diamond and Rice, 1987; Job, 1988). The noise environment comprises more than one source of noise, so research needs to identify the range of noises that are typical for children. Not all sources of noise will be equally annoying and, as with adults, it may not be the level of the noise that is the key feature of annoyance for children (Guski, Felscher-Suhr, and Schuemer, 1998; Haines and Stansfeld, 2000; Lercher *et al.*, 2000). Different sources need to be considered individually and in combination to assess relative levels of annoyance. Measuring annoyance is premised on the fact that particular sound sources are audible. Thus, for any particular child it is necessary to establish that particular sound sources are heard before it can be determined whether they are annoying. Validity of such judgment would be enhanced if: (1) it could be shown that children can discriminate across classroom conditions in terms of teacher and peer audibility; and (2) teachers' perceptions of sound sources were similar to those of the children in their class. Thus, in addition to the children's ability to judge the presence and annoyance of a sound source, convergent evidence from teachers' ratings and children's ability to discriminate across listening conditions is required.

The present study fills a gap in the noise literature by examining children's perceptions of their noise environment across a representative sample of schools in a large urban conurbation and relates these perceptions to objective measures of noise levels in their schools. Questionnaire surveys were used to

(1) Assess children's awareness of environmental noise sources at home and at school and to consider the extent to which children are annoyed by these sources;
(2) Evaluate the extent to which the child's developmental stage impacts on perceptions of noise and relative annoyance; and
(3) Document children's ability to differentiate good and poor listening situations in classrooms.

Objective measures of noise levels were used to establish noise levels and sound sources in the children's classrooms. Research with children has often been compromised by a failure to consider the child's perspective on the variables under consideration (Dockrell *et al.*, 2000). This has often led to underestimation of children's abilities and understandings (Dockrell *et al.*, 2000) and a failure to identify the range of factors that may impact on successful school performance. To avoid these methodological failings, an important first step in evaluating children's noise environments is to gain their perceptions of the noises that they hear and the noises that annoy them. Thus, the questionnaire used in the current study was based on the results of in-depth interviews with children and their reports of the sound sources in their

environment and the classroom listening conditions that they experienced. These data were supplemented by interviews with their teachers. It was necessary to construct a questionnaire that would be understood by young children without placing too many demands on their language, memorial, or nonverbal skills (Smedslund, 1969). Pictures were used to contextualize questions, and when children were reporting whether they heard sounds or were annoyed by sounds dichotomous responses were required. To construct a valid and reliable tool two phases of pilot studies were carried out prior to the main study. The use of convergent measures of the children's awareness and reactions to noise will enhance the conclusions that can be derived from the current data set.

II. PARTICIPANTS

The sample in the main study consisted of primary schools in one area in London. The area was chosen to reflect the typical distribution of socio-economic status among London primary schools and a range of primary school environments. The borough was representative of greater London for location and for demographic qualities (subject to the exclusion of west London boroughs exposed to high levels of aircraft noise). The estimated borough adult population was 216 800, with an average household size of 2.4 and an unemployment rate of 9.4%. The average teacher–pupil ratio in the primary schools was 1:22.4 and children with special educational needs represented less than 2.4% of the primary school population. Over 50% of the population were white, with Black Afro Caribbeans representing the largest minority ethnic group (10%). The assessments of the pupils' attainments within the area fell within the normal distribution for all English Education Authorities (DfES, 1999). The two age groups identified as participants reflected the end points of infant and junior school. National tests in England provide comparative performance of reading and numeracy attainments. Thus, the study was conducted among year 2 (6- to 7-year-olds) and year 6 (10- to 11-year-old) children. Overall, the borough had, at the time of the study, 54 primary schools. The study was conducted in 43 schools. The number of the children that participated in the study was 2036. From those, 885 (43.5%) were in year 2 and 1151 (56.5%) were in year 6. The sample consisted of 1041 (51.1%) boys and 995 (48.9%) girls. The age distribution of the sample was: 6 years, 8.1%; 7 years, 35.9%; 10 years, 14.2%; 11 years, 41.8%.

Fifty-one teachers in 34 schools completed the questionnaires (12 in year 2 and 39 in year 6). Eleven were male and 40 female. Over half the sample (59%) had more than 5 years experience, with 20 percent having more than 20 years experience. For those who reported their age ($N=39$) there was a mean of 37 years (range 26–55).

III. MATERIALS

A. Questionnaire design

1. Phase 1: Child interviews

Semistructured interview methods were employed with year 2 and year 6 children and their teachers. This phase took place in one primary school in the UK. Thirty children and their teachers were interviewed. The objectives were to identify the different noise sources that children were aware of and to determine types of noise they might be exposed to and annoyed by both at school and at home. Interviews with teachers explored their perception of noise in the school environment and children's performance in noisy situations. In the interviews the research team used only the word ''sound,'' deliberately avoiding the term ''noise'' so as to reduce the possibility of bias in the responses. However, the children consistently used the words noise and sound interchangeably.

The noise sources that emerged from the analysis of the interviews via transcription were categorized as follows.

(i) Noise made by people;
(ii) Transportation noise (e.g., cars, buses, airplanes, etc.);
(iii) Entertainment noise (e.g., stereo, musical instruments, TV, etc.);
(iv) Noise from nature (e.g., trees, birds, dogs, cats, etc.); and
(v) Noise from machines (e.g., telephone, etc.).

The above information served as the basis to develop a child questionnaire and a teacher questionnaire that were used in the pilot study.

2. Phase 2: Pilot study

The questionnaires were administered to a total of 84 pupils in year 2 ($N=39$) and year 6 ($N=45$) classes and their teachers. As a result of feedback about ambiguity in certain questions, changes were made in the pupil questionnaire. A confirmatory subsample of six schools was used for the trial study. The sample consisted of 343 pupils, 164 boys (47.8%) and 179 girls (52.2%), from six year 2 classes (131 pupils, mean age 6;7) and eight year 6 classes (212 pupils, mean age 10;7). Debriefing with the participants indicated that the questionnaire was developmentally appropriate and captured the children's views. Analysis indicated that children were differentiating between home and school.

B. Pupil questionnaire—Final version

The ten-page questionnaire was divided into three sections (the questionnaire can be requested from the authors). Four versions of the questionnaire, varying the order of questions, were developed for randomization purposes. Section A examined the sound sources children were exposed to in their environment both at home and at school. In Section A children were asked for each sound: (a) whether they heard the sound source in their classroom (''hear'' questions); and (b) if they heard the sound source whether they were annoyed by it (''annoy'' questions). Questions were accompanied by a graphic representation of the noise source followed by a tick box for the children to record their responses. The same questions were repeated for hear and annoy at home. Hear and annoy questions were presented as dichotomous yes–no answers to aid completion by the younger children. Annoy questions were only completed when children reported hearing a particular noise source.

Section B examined listening situations across nine classroom activities and contexts. These situations were chosen from the pilot interviews with children and previous work (Arnold and Canning, 1999). Section B used a five-point Likert scale transformed into a smiley faces rating scale based on that of Arnold and Canning (1999). Children rated how well they hear what the teacher is saying in the eight different classroom situations and how well they hear their peers speaking in the classroom. The anchor ends of the scale were ''very well'' and ''not at all.''

The children were asked how well they could hear the teacher in the following classroom situations.

(i) when the child could not see the teacher's face;
(ii) while the teacher was moving around the classroom;
(iii) when the children were working in groups;
(iv) when there was no noise at all;
(v) when children were making noise outside the classroom;
(vi) when there was no noise from outside the classroom;
(vii) during exam conditions; and
(viii) when children were outside during physical education lessons.

Children were also asked if they could hear a classmate responding to a teacher's question.

Section C collected demographic information. Both Section A and Section B were preceded by series of trial items to familiarize the children with the demands of the questionnaire and to allow for any problems or questions raised by the children to be addressed.

A number of steps were taken to ensure the validity of the questionnaire and the reliability of the children's results. The validity was established by ensuring that the noise sources presented reflected those reported by children in the open-ended pilot interviews, the published literature, and pilot data collected in inner London locations. Differentiation between noise sources and home and school was regarded as a key indication of validity.

Children's responses to rating their ability to hear the teacher have been shown to be reliable by Arnold and Canning (1999). The hear and annoy questions were extensively piloted and shown to be understood by children of this age range and to produce high levels of agreement with interviews. In addition, following Haines and Stansfeld (2000), children were assured that there were no right or wrong answers, and the questions were read to the younger children. Four different versions of the questionnaire were used to prevent order effects, and different versions were used within each class. As indicated in the participants' section the sample was representative of inner city children. Reliability of the children's responses was further established by comparison with teacher's ratings of the same items.

C. Teacher questionnaire

To complement the children's data, a questionnaire with open-ended and closed questions was developed for the teachers to determine: (a) the environmental noise(s) teachers hear in the classroom; (b) the perceived impact that noise has on their pupils' performance; and (c) their perception of noise as related to classroom and school activities. The five-page questionnaire consisted of four parts. The sound sources included in the teacher questionnaire were identical to the ones in the children's questionnaire to allow for comparison with the children's responses.

D. Procedure

The questionnaires were administered to the year 2 and year 6 classes during the school day. At the beginning of each session, children were briefly introduced to the project. This introduction was followed by a thorough description of the questionnaire and an explanation of the way children should record their answers. Children were told that they could work at their own pace, as the questionnaire was not time limited. In addition, the administrators assured participants about confidentiality. Children were allowed and encouraged to ask questions at any time during the presentation and were assured that there were no right or wrong answers. They were told that their own views were important. Children were keen to express their opinion.

Year 6 children completed the questionnaire as a class, while year 2 children were taken in smaller groups with a maximum size of ten children. Once the task was described each question was read aloud to the children, and when the whole group was finished the next question was read aloud. The questionnaire completion time for the year 6 children was 20 min and for the year 2 pupils 35 min.

The teacher questionnaire was given to the teachers of all the classes used in the pupil survey. It took approximately 20 min to answer all the questions. The year 6 teachers completed the questionnaire at the same time as their pupils, while the year 2 teachers completed the questionnaire during break time.

IV. RESULTS

The results are presented in six sections. The first section provides objective measures of the levels of environmental noise that the children are exposed to at their schools. The second section describes the children's ability to differentiate across various listening contexts in their classrooms. The relationship between the children's scores and the objective measures of environmental noise are outlined in the next section. The subsequent section describes the noise sources heard in classrooms and homes and whether children are annoyed by these sources. The fifth section considers the relationships between children's reported hearing and annoyance levels and the objective noise measurements; the final section compares the children's and the teachers' views.

A. Exposure to environmental noise

An external noise survey of 53 schools in the area including 43 schools in the questionnaire survey was carried out (Shield and Dockrell, in press). Five-minute samples of noise were measured outside each school using a Bruel & Kjaer hand-held sound-level meter, type 2236. For security reasons measurements were made off the school premises, where possible outside the noisiest façade, at the curbside of

TABLE I. Means and standard deviations of external levels in survey area.

$L_{\text{Aeq,5 min}}$		$L_{\text{A10,5 min}}$		$L_{\text{A90,5 min}}$		$L_{\text{Amax,5 min}}$	
Mean	s.d.	Mean	s.d.	Mean	s.d.	Mean	s.d.
57.4	8.8	59.4	9.0	49.2	7.7	70.1	10.5

the nearest road. In many cases the measurement position was at approximately 4 m from the school façade. For consistency measurements at other positions were corrected to give the corresponding level 4 m from the façade.

The 5-min measurement period was chosen to be typical of the school day. For this reason rush hours, times when children were arriving at or being collected from school, and when children were outside in the school playground were avoided.

The means and standard deviations of the measured parameters $L_{\text{Aeq,5 min}}$, $L_{\text{A10,5 min}}$, $L_{\text{A90,5 min}}$, $L_{\text{Amax,5 min}}$, are shown in Table I.

In addition to noise levels, during the 5-min measurement period the noise sources heard were noted. Percentages of recorded instances of the most frequently heard external noise sources occurring during the survey are presented in Fig. 1. The most commonly occurring source of noise was road traffic, principally cars. Sirens were heard at surprisingly few schools, although they are commonly regarded as a regular feature of the London noise environment.

B. Children's ability to differentiate between listening context

Children's scores of their ability to hear the teacher (Section B of the questionnaire) in the different contexts are reported in Table II. The maximum possible rating was 5 and the minimum rating 1. As the table shows, the full scale was used by the children. These data are not normally distributed so nonparametric statistical analysis was carried out. Children's reported ability to hear the teacher varied significantly across situations ($X^2=4426, p<0.001$) with "no noise outside the classroom" and "doing a test" reported as the best listening conditions and "noise being made outside" by other children the worst. Comparisons were made between the ratings of the year 2 and year 6 children as shown in Table II. Younger children generally reported that hearing the

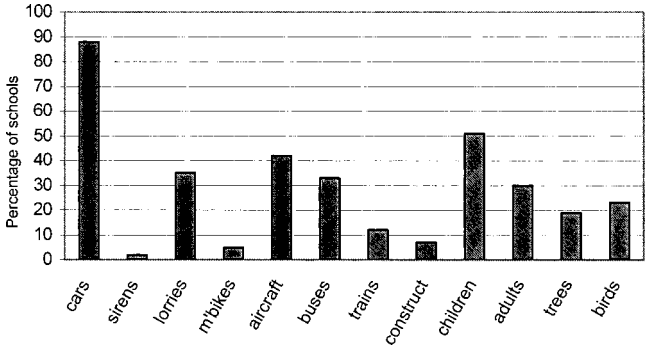

FIG. 1. Percentages of occurrences of external noise sources outside school.

teacher was significantly more difficult. There was a statistically significant difference between the two age groups in six of the nine situations assessed: when the teacher "was talking and moving" ($U=394\,579.5, p<0.001$); "no noise outside" ($U=394\,382, p<0.001$); "doing a test" ($U=355\,254.5, p<0.001$); "PE in the playground" ($U=461\,915.5, p<0.001$); "no noise at all" ($U=409\,882.5, p<0.001$); and "classmate speaking" ($U=418\,452, p<0.05$). In contrast, relative to the younger children the older children reported significantly greater difficulty when they could not "see the teacher's face" ($U=392\,595.5, p<0.001$) and when "children were making noise outside classroom" ($U=423\,164, p<0.001$). There were no group differences in reported hearing acuity when children were working in groups ($U=490\,863.5$, ns). These results indicate that primary school children are able to judge situations where they have difficulty hearing the teacher, and that younger children report relatively greater difficulty than older children. Children are thus able to discriminate between situations with varying amounts and types of noise.

C. Comparison of children's listening scores with external noise measurements

The relationships between external noise levels and children's hearing across situations was assessed by a series of correlations. There were no significant relationships between the objective external noise measures and children's reported ability to hear in eight of the nine conditions assessed. However, reported ease of hearing the teacher in the classroom in

TABLE II. Reported hearing acuity by year 2 and year 6 children in different school contexts.

Rank 1—very well 5—not at all	p	Year 2		Year 6	
		Mean	Std deviation	Mean	Std deviation
Cannot see teacher's face		1.93	0.84	2.34	1.02
Teacher talking and moving	<0.001	2.29	0.83	1.96	0.95
Working in groups		2.44	0.93	2.39	1.11
No noise outside	<0.001	1.90	0.93	1.68	1.10
Children making noise outside		2.70	1.08	3.01	1.06
Doing a test	<0.001	1.87	0.89	1.53	1.04
PE in playground	<0.001	2.79	1.05	2.62	1.09
No noise at all	<0.001	1.46	0.83	1.24	0.79
Speaking classmate	<0.05	2.47	1.00	2.15	1.00

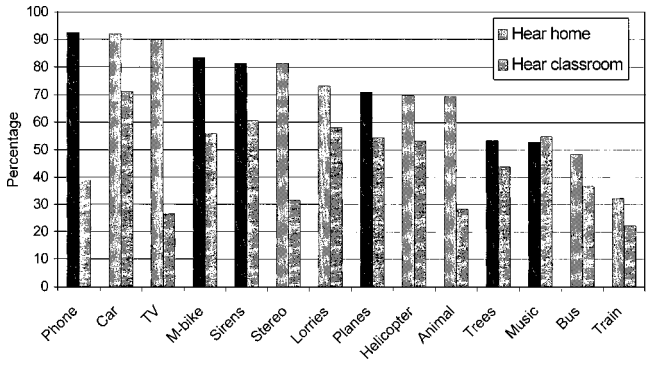

FIG. 2. Percentages of children reporting hearing the sound source at home and at school.

the ''no noise outside'' condition was related to external noise measurements. The higher the objective noise levels the less likely the children were to report being able to hear the teacher (for $L_{\mathrm{Aeq}}r=0.365$, $p<0.05$, for $L_{\mathrm{Amax}}r=0.338$, $p<0.05$, for $L_{\mathrm{A99}}r=0.330$, $p<0.05$, for $L_{\mathrm{A90}}r=0.376$, $p<0.05$, for $L_{\mathrm{A10}}r=0.345$, $p<0.05$). All aspects of the sound, ambient (L_{Aeq}), background (L_{A90}), and underlying (L_{A99}) noise levels, plus maximum levels due to individual events (L_{Amax}), were related to the children's ability to hear the teacher. These variables account for, on average, 11% of the variance in the children's responses, with L_{A90} accounting for the highest proportion of variance (14%). Thus, external school levels did affect the children's reported relative ease of hearing their teacher when other confounding noise sources such as other children in the classroom or teaching contexts were not relevant.

D. Environmental noises heard by children at home and at school

The following analyses consider children's awareness of particular forms of environmental noise at home and at school, and relative annoyance caused by different sources. Children reported hearing a wide range of environmental noise sources both at home and school. The percentages of children reporting hearing the different sources at home and at school are shown in Fig. 2. As the figure shows, different patterns emerge for reported hearing in class and at home. A mean score for hearing each sound source was computed for each class and this was compared with their class mean hearing score for hearing at home. Significant differences emerged for all home–school pairs apart from hearing music ($t=0.572$, df=50, ns) with children significantly more likely to report hearing sounds at home for animals ($t=-20.03$, df=50, $p<0.001$); phone ($t=-14.21$, df=50, $p<0.001$); bus ($t=-3.38$, df=50, $p<0.001$); TV ($t=-25.4$, df=50, $p<0.001$); motorbike ($t=-8.33$, df=50, $p<0.001$); car ($t=-6.465$, df=50, $p<0.001$); train ($t=-2.98$, df=50, $p<0.01$); trees ($t=-5.96$, df=50, $p<0.001$); helicopters ($t=-10.52$, df=50, $p<0.001$); sirens ($t=-10.18$, df=50, $p<0.001$); stereos ($t=-23.45$, df=50, $p<0.001$); planes ($t=-9.89$, df=50, $p<0.001$); trucks ($t=-5.18$, df=50, $p<0.001$). To some extent these results reflect the typical sound sources that occur in homes such as stereos and TVs. However, in addition, it is also likely to reflect a lack of precision in the question asked and the concept of ''home.'' Home could include living room, kitchen, bedroom, or garden, thus allowing much more variation in the child's interpretation of the questions, whereas the school question referred to classrooms only. Nevertheless, the fact that children discriminated between the two environments provides further evidence of the reliability of the measure.

Once the children's reporting of hearing a sound source is controlled, the annoyance levels are similar between home and school for all items. Moreover, ratings of annoyance at home and at school are highly correlated: phone ($r=0.331$,$p<0.05$); bus ($r=0.409$,$p<0.01$); TV ($r=0.445$,$p<0.001$); motorbike ($r=0.566$,$p<0.001$); car ($r=0.566$,$p<0.001$); train ($r=0.524$,$p<0.001$); trees ($r=0.676$,$p<0.001$); helicopters ($r=0.344$,$p<0.05$); sirens ($r=0.534$,$p<0.001$); stereos ($r=0.499$,$p<0.001$); planes ($r=0.646$,$p<0.001$); trucks ($r=0.421$,$p<0.001$); except for animals ($r=0.23$, ns), and music ($r=0.008$, ns). Thus, it would appear that for the children the majority of sound sources assessed in this questionnaire are annoying independent of the context in which they are heard.

Tables III and IV show year group variation in hearing and annoyance at school and school variation in hearing and annoyance.

In general, older children were more likely to report hearing a sound source when responding about classroom and home listening conditions. However, age only accounted for a small proportion of the variance, on average less than 1% of the variance. In contrast, younger children tended to report greater annoyance but again little variance was accounted for by age. Apart from trains and motorbikes the younger children were statistically significantly more likely to report being more annoyed by the external noise sources that they hear. In contrast, older children seem to be more aware of external noise sources.

Reporting of hearing and annoyance varied by school for all sound sources. To conserve space the means of the 51 schools are not presented but chi-square, significance levels, and variance accounted for by these data are presented in Table IV. There were significant differences across schools in the sound sources reported. In all cases, greater than 4% of variance was accounted for by school location and for train and phone noise school location accounted for 26% of the variance. Thus, there was a clear indication that school and class factors played a significant part in whether children were reporting the occurrence of particular types of environmental noise.

E. The relationship between objective noise measures and pupils' perceptions

The data did not allow comparison of reports of hearing individual sound sources and actual occurrences, since a maximum score of 1 occurred for the sources observed during the acoustic survey at each school. However, relative rankings of children's observations could be established and are presented in Table V. The most frequently reported sound source was given a rank of 1. As the table shows, apart from cars, which are ranked most frequently by children and observed most often, there is little agreement. Of particular

TABLE III. Percentages of children hearing a particular sound in their classroom and, having heard it, being annoyed by it.

	Heard			Annoyed		
Noise target	Year 2	Year 6	Significance	Year 2	Year 6	Significance
Animal	32.4	25.1	$X^2=13.217$	44.9	38.4	$X^2=2.534$
Phone	36.4	40.9	$X^2=4.331$[a]	41.0	41.4	$X^2=0.013$
Music	57.0	53.0	$X^2=3.919$[a]	40.4	34.8	$X^2=3.638$
Bus	35.1	37.9	$X^2=1.616$	55.9	47.5	$X^2=5.213$[a]
TV	32.3	22.2	$X^2=26.479$[b]	30.1	20.0	$X^2=7.229$[c]
Motorbike	52.1	58.8	$X^2=9.187$[c]	58.8	61.1	$X^2=0.610$
Car	67.6	73.9	$X^2=9.879$[c]	53.3	45.0	$X^2=9.778$[c]
Train	19.1	24.5	$X^2=8.474$[c]	58.2	66.1	$X^2=4.388$[a]
Trees	42.4	44.9	$X^2=1.316$	22.9	19.7	$X^2=1.376$
Helicopter	43.0	53.7	$X^2=0.098$	56.9	46.4	$X^2=11.564$[c]
Sirens	49.8	69.0	$X^2=76.908$[b]	67.6	52.0	$X^2=28.097$[b]
Stereo	27.9	34.2	$X^2=9.268$[c]	47.0	24.7	$X^2=33.812$[b]
Planes	55.5	53.5	$X^2=0.776$	47.3	34.6	$X^2=18.253$[b]
Trucks	53.4	61.9	$X^2=14.556$[b]	58.2	59.1	$X^2=0.90$

[a]Reported significance level of 0.05.
[b]Reported Significance of 0.01.
[c]Reported significance of 0.001.

significance is the high ranking of sirens by children but the low ranking from the sound source observations. These data indicate that the relationships between the observations of individual sounds and children's ratings do not correspond. However, it is possible that measured noise parameters may provide a more valid index for evaluating the children's judgments.

To establish whether children's perceptions of noise and annoyance related to the objective noise measures, it was necessary to compute a single ''hearing score'' and a single ''annoyance score'' for each school. Children's reports of hearing an environmental sound and their relative annoyance were combined to create a ''*school hearing score*'' and a ''*school annoy score*.'' Given different numbers per classroom and different base rates, these were computed as proportion scores. Three different scores were computed: ''*school hearing score*,'' which was the average of the class reporting of all 14 different sound sources; ''*school annoy score*,'' which was the average annoyance reported for the whole class, and a ''*child annoy score*,'' which was the average annoyance score for children who reported hearing a particular sound source. The scores are defined as shown in Box 1. Child annoy scores are always greater than school annoy scores since they are over a smaller base (only those children who report hearing the sound source). Overall, the mean *school hearing score* was 0.46 (range 0.31–0.59), the mean *child annoy score* 0.46 (range 0.21–0.88), and the mean *school annoy score* was 0.22 (range 0.09–0.39). While *school hearing score* was significantly associated with *school annoy score* ($r=0.615$, $p<0.01$, $n=51$), it was not related to *child annoy score* ($r=0.089$, $n=51$). Thus, the average

TABLE IV. School variation in hear and annoy data with variation accounted for (DF 42).

	Hear		Annoy	
Noise target	Significance	Variation accounted for	Significance	Variation accounted for
Animal	$X^2=153.025$[a]	8%	[b]	
Phone	$X^2=531.147$[a]	26%		
Music	$X^2=196.498$[a]	12%		
Bus	$X^2=451.864$[a]	22%		
TV	$X^2=236.398$[a]	12%		
Motorbike	$X^2=390.941$[a]	19%		
Car	$X^2=478.470$[a]	24%	$X^2=91.822$[a]	6%
Train	$X^2=534.662$[a]	26%		
Trees	$X^2=158.456$[a]	8%		
Helicopter	$X^2=113.344$[a]	6%	$X^2=80.744$[a]	7%
Sirens	$X^2=186.951$[a]	9%	$X^2=80.569$[a]	7%
Stereo	$X^2=86.880$[a]	4%		
Planes	$X^2=72.309$[c]	4%	$X^2=86.294$[a]	8%
Trucks	$X^2=233.565$[a]	12%	$X^2=59.271$[d]	5%

[a]Reported significance level of 0.001.
[b]A blank cell indicates that sig cannot be computed because greater that 5% of cells have expected frequencies less than 5
[c]Reported significance level of 0.01.
[d]Reported significance of 0.05.

BOX 1

The 'school hearing score,' 'school annoy score' and 'child annoy score' are defined as follows:

Let h_s = number of children in a school reporting hearing noise source s

a_s = number of children in a school reporting being annoyed by noise source s

n = number of children in a school who completed questionnaire

Let $H=h_1+h_2+\ldots h_{14}$

$A=a_1+a_2+\ldots a_{14}$

Then School hearing score $=H/14n$

School annoyance score $=A/14n$

Child annoyance score $=A/H$

TABLE V. Children's ranking of hearing in school by sound source and the rank of externally observed sources from most frequent (1) to least frequent (11).

Sound source	Rank of child scores	Rank of external observations
Cars	1	1
Sirens	2	11
Truck	3	3
Motorbike	4	9
Aircraft	5	2
Music	6	8
Helicopter	7	10
Trees	8	6
Bus	9	3
Birds/animals	10	5
Train	11	7

reporting of hearing sound sources was related to the overall annoyance levels expressed by a class but not individual reported annoyance levels.

School hearing score was related to L_{A99} ($r=0.52$, $p<0.01$, $n=38$), and L_{A90} ($r=0.433$, $p<0.01$, $n=38$). However, *school annoy score* was related to L_{Amax} ($r=0.326$, $p<0.05$, $n=38$), L_{Aeq} ($r=0.359$, $p<0.05$, $n=38$), and L_{A90} ($r=0.35$, $p<0.01$, $n=38$), whereas *child annoy score* was only related to L_{Amax} ($r=0.333$, $p<0.01$, $n=38$). Thus, children in classrooms where schools had higher external background noise levels reported hearing, on average, higher percentages of external sound sources. In contrast, ambient and maximum noise levels were a significant factor in reporting levels of annoyance but not levels of hearing sound sources.

Multiple regression analyses were conducted to investigate the combined and unique contribution of noise levels on both *annoy* measures and *school hearing score*. These analyses only included those noise variables that were significantly correlated with the target measure. No significant model emerged for *school annoy score*, whereas for *child annoy score* a significant model emerged ($F_{1,37}=4.485$, $p<0.05$, adjusted R square 0.086). The model accounted for little of the variance in children's responses. In contrast, a highly significant model emerged for *school hearing score* ($F_{1,37}=14.210$, $p<0.001$, adjusted R square 0.448), where objective noise measures (L_{A90} and L_{A99}) accounted for 45% of the variance in the children's responses.[1] Moreover, a stepwise regression indicated that both measurements contributed unique variance. Children who were in classes in schools with higher underlying external noise levels were reporting higher over all noise awareness.

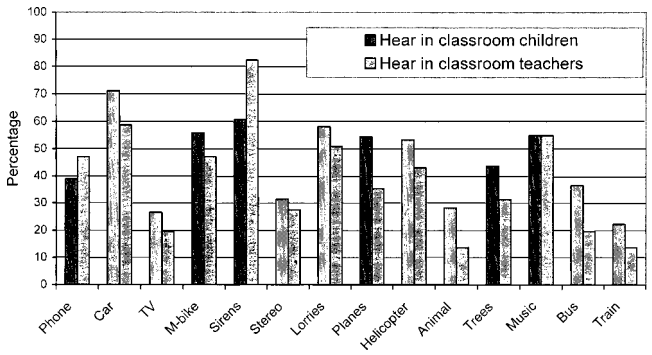

FIG. 3. Comparison of teachers' and children's reporting hearing sound sources at school.

F. The relationship between teachers' and children's reports of sound source

Figure 3 shows the percentages of both children and teachers reporting hearing various sound sources.

As shown in Fig. 3, teachers reported similar levels of hearing environmental noise sources as the pupils, but teachers reported sirens more often than the children. The correlation between children's and teachers' rankings of sound sources was very high ($r=0.945$,$p<0.001$). These data further support the reliability of the children's ratings. Since the questionnaire was completed by only one teacher in 20 schools, by two teachers in 11 schools, and by three teachers in the remaining three schools, it is not possible to calculate correlations with any of the objective noise measures and, because of high selection in the teacher sample, generalizations cannot be drawn.

V. DISCUSSION AND CONCLUSION

The current study aimed to ascertain children's perceptions of their noise environment and how the children's perceptions related to objective measures of noise. Precision, specificity, and consistency of responding were established through the use of convergent measures. The results have confirmed earlier work indicating that children in primary schools are exposed to high levels of environmental noise. In addition, the data demonstrate that external school levels influenced the children's reported relative ease of hearing their teacher when other confounding noise sources or classroom teaching contexts were not a factor. Children and teachers reported hearing similar noise sources in classrooms and children were annoyed by similar sources of noise both at home and school.

Age differences in reported audibility were noted. Older children reported greater ease of hearing in all conditions where the teacher's face was visible, but for this age group hearing was reduced relative to younger children when there was background babble from other children outside in the playground. It appears that the older children may be making greater use of the information from the teacher's face and are more distracted by speech-like interference (Shield and Dockrell, 2003). However, younger children were often placed in seating arrangements that would detract from hearing well, for example, small groups facing each other around a table. Younger children also have greater difficulties processing language and maintaining attention. These results indicate that primary school children are able to judge situations where they have difficulty hearing the teacher, and that younger children report relatively greater difficulty than older children, although the exact reasons for these developmental differences are not clear from these data.

Children reported hearing a wide range of different sound sources in their classrooms and, while there were some age differences in reporting sound sources, this vari-

able accounted for little of the variance. In contrast, a significant proportion of the variance in children's recorded sound sources was accounted for by school/classroom location. These data are likely to reflect both the school's location and the structure of the building. Moreover, children in classrooms where schools had higher objective measures of external background noise levels reported hearing, on average, higher percentages of external sound sources. This rating was related to the background noise levels measured outside their school.

In contrast to the ratings for hearing the sounds, the children's reported levels of annoyance were related to the maximum noise levels recorded outside the schools. There was a clear hierarchy of sounds that was found to be annoying, whether they were heard at home or at school. Trains, motorbikes, trucks, and sirens were rated as the most annoying, while trees were rated as the least annoying. Correlations between annoyance levels and recorded sound levels were similar to those reported in studies with adults.

The present data indicate that young children are sensitive to noises in their environment and can discriminate noise sources that annoy them. External L_{Amax} levels are a significant factor in reported annoyance, whereas external L_{A90} and L_{A99} levels are a significant factor in determining whether or not children hear sound sources. Moreover, the higher the objective external noise levels recorded for a school, the less likely the children were to report being able to hear the teacher.

Thus, the data from the current study suggest that the impact of different aspects of noise on children's perceptions and behaviors needs to be addressed. The maximum noise levels reflect sporadic episodes that the children find annoying. There is also evidence that unexpected irrelevant sounds influence the performance of adults on specific cognitive tasks (Jones *et al.*, 1999). Background noise at the levels reported outside these schools are not associated with the children's reported level of annoyance, although it is related to their awareness of noise. Nonetheless, high levels of background noise have been found to influence academic attainments.

The data from the current study support the view that children can be sensitive judges of their noise environments. Future work will need to specify the bases for developmental changes and physical and locational factors that determine the school effects.

ACKNOWLEDGMENTS

We would like to thank Rebecca Jeffery and Ioannis Tachmatzidis, who collected some of the data reported here, the schools and teachers for all their support, DOH and DETR for funding the research, David Canning for guidance on the questionnaire design, and Dr. Haines for commenting on an earlier version of this paper.

[1]To control for artificially inflating the variance accounted for by only using significantly associated measures, a second analysis was computed for *school hearing score* using all noise levels. These results were similar ($F < 7.38 = 4.7$, $p < 0.001$, adjusted R square 0.405).

Airey, S. (**1998**). ''A survey of acoustical standards in UK classrooms and their effect on pupils and teachers,'' Proc. Inst. Acoust. **20**(4), 14–21.

Arnold, P., and Canning, D. (**1999**). ''Does classroom amplification aid comprehension?'' Br. J. Audiol. **33**(3), 171–178.

Berg, F. S., Blair, J. C., and Benson, V. (**1996**). ''Classroom acoustics: The problem, impact, and solution. Speech classroom acoustics: The problem, impact, and solution,'' Speech, Lang., Hear. Serv. Schools, ASHA **27**, 16–20.

Blake, P., and Busby, S. (**1994**). ''Noise levels in New Zealand junior classrooms: Their impact on hearing and teaching,'' New Zealand Med. J. **107**, 357–358.

Blatchford, P., Edmonds, S., and Martin, C. (**2003**). ''Class size, pupil attentiveness and peer relations,'' Br. J. Educ. Psychol. **73**, 15–36.

Cohen, S., Evans, G. W., Krantz, D. S., Stokols, D., and Kelly, S. (**1981**). ''Aircraft noise and children: Longitudinal and cross-sectional evidence on adaptation to noise and the effectiveness of noise abatement,'' J. Pers Soc. Psychol. **40**(2), 331–345.

Diamond, I. D., and Rice C. G. (**1987**). ''Models of community reaction to noise from more than one source,'' in *Environmental Annoyance: Characterization, Measurement, and Control*, edited by H. S. Koelega (Elsevier Science, Amsterdam), pp. 301–312.

Dockrell, J. E., Lindsay, G., and Lewis, A. (**2000**). ''Researching children's perspective: Psychological dimension,'' in *Research in Children's Perspectives*, edited by A. Lewis and G. Lindsay (Open University Press, Buchingham), pp. 46–58.

Evans, G. W. (**1990**). ''The nonauditory effects of noise on child development.'' Proceedings of the 5th International Conference on Noise as a Public Health Problem, edited by B. Berglund, U. Berglund, J. Karlsson, and T. Lindvall, Vol. 5, pp. 425–453, Stockholm, Sweden: Swedish Council for Building Research.

Evans, G. W., and Lepore, S. J. (**1993**). ''Nonauditory effects of noise on children: A critical review,'' Child. Environ., **10**(1), 31–51.

Evans, G. W., and Tafalla, R. (**1987**). ''Measurement of environmental annoyance,'' in *Environmental Annoyance: Characterization, Measurement, and Control*, edited by H. S. Koelega (Elsevier Science, Amsterdam), pp. 11–28.

Evans, G. W., Hygge, S., and Bullinger, M. (**1995**). ''Chronic noise and psychological stress,'' Psychol. Sci. **6**, 333–338.

Evans, G. W., Lercher, P., Meis, M., Ising, H., and Kofler, W. W. (**2001**). ''Community noise exposure and stress in children,'' J. Acoust. Soc. Am. **109**(3), 1023–1027.

Fallon, M., Trehub, S., and Schneider, B. A. (**2000**). ''Children's perception of speech in noise,'' J. Acoust. Soc. Am. **108**, 3023–3029.

Fidell, A. U., Barber, D. S., and Schultz, T. J. (**1991**). ''Updating a dosage effect relationship for the prevalence of annoyance due to general transportation noise,'' J. Acoust. Soc. Am. **89**(1), 221–233.

Fields, J. M., De Jong, R. G., Brown, A. L., Flindell, I. H., Gjestland, T., Job, R. F. S., Kurra, S., Lercher, P., SchuemerKohrs, A., Vallet, M., and Yano, T. (**1997**). ''Guidelines for reporting core information from community noise reaction surveys,'' J. Sound Vib. **206**(5), 685–695.

Fields, J. M., De Jong, R. G., Gjestland, T., Flindell, I. H., Job, R. F. S., Kurra, S., Lercher, P., Vallet, M., Yano, T., Guski, R., Felscher-Suhr, U., and Schumer, R. (**2001**). ''Standardized general-purpose noise reaction questions for community noise surveys: Research and a recommendation,'' J. Sound Vib. **242**(4), 641–679.

Gumenyuk, V., Korzyukov, O., Alho, K., Escera, C., Schroger, E., Ilmoniemi, R. J., and Naatanen, R. (**2001**). ''Brain activity index of distractibility in normal school-age children,'' Neurosci. Lett. **16**(3), 147–150.

Guski, R., Felscher-Suhr, U., and Schuemer, R. (**1998**). ''The concept of noise annoyance: How international experts see it,'' J. Sound Vib. **223**(4), 513–527.

Haines, M. M., and Stansfeld, S. A. (**2000**). ''Measuring annoyance and health in child social surveys,'' Inter.Noise 2000, the 29th International Congress and Exhibition on Noise Control Engineering, 27–30 August, 2000, Nice.

Haines, M. M., Stansfeld, S. A., Brentall, S., Head, J., Berry, B., Jiggins, M., and Hygge, S. (**2001a**). ''West London Schools Study: The effects of chronic aircraft noise exposure on child health,'' Psychol. Med. **31**, 1385–1396.

Haines, M. M., Stansfeld, S. A., Job, R. F. S., Berglund, B., and Head, J. (**2001b**). ''A follow-up study of effects of chronic aircraft noise exposure on child stress responses and cognition,'' Int. J. Epidemiol. **30**, 839–845.

Haines, M. M., Stansfeld, S. A., Job, R. F. S., Berglund, B., and Head, J. (**2001c**). ''Chronic aircraft noise exposure, stress responses, mental health

and cognitive performance in school children,'' Psychol. Med. **31**(2), 265–277.
Job, R. F. S. (**1988**). ''Community response to noise: A review of factors influencing the relationship between noise exposure and reaction,'' J. Acoust. Soc. Am. **83**(3), 991–1001.
Johnson, C. E. (**2000**). ''Children's phoneme identification in reverberation and noise,'' J. Speech Lang. Hear. Res. **43**, 902–914.
Jones, D. M., Alford, D., Bridges, A., Trembley, S., and Macken, W. J. (**1999**). ''Organizational factors in selective attention: The interplay of acoustic distinctiveness and auditory streaming in the irrelevant sound effect,'' J. Exp. Psychol. Learn. Mem. Cogn. **25**, 464–473.
Lercher, P., Brauchle, G., Kofler, W., Widmann, U., and Meis, M. (**2000**). ''The assessment of noise annoyance in schoolchildren and their mothers,'' Inter.Noise 2000, the 29th International Congress and Exhibition on Noise Control Engineering, 27–30 August, 2000, Nice.
Miedema, H. M. E., and Oudshoorn, C. G. M. (**2001**). ''Annoyance from transportation noise: Relationships with exposure metrics DNL and DENL and their confidence intervals,'' Environ. Health Perspect. **104**(4), 409–416.
Miedema, H. M. E., and Vos, H. (**1998**). ''Exposure-response relationship for transportation noise,'' J. Acoust. Soc. Am. **104**(6), 3432–3445.
Picard, M., and Bradley, J. (**2001**). ''Revisiting speech interference in classroom,'' Audiology, **40**, 211–244.
Roche, A. F., Siervogel, R. M., Himes, J. H., and Johnson, D. L. (**1978**). ''Longitudinal study of hearing in children: Baseline data concerning auditory thresholds, noise exposure, and biological factors,'' J. Acoust. Soc. Am. **64**, 1593–1601.
Schori, T. R., and McGatha, E. A. (**1978**) *A real-world assessment of noise-exposure*. (Joint EPA/AF study) AMRL-TR-77-96 (Aerospace Medical Research Lab, Wright-Patterson AFB, OH).
Shield, B., and Dockrell, J. E. (**2003**). ''The effects of noise on children at school: A review,'' Build. Acoust., **10**, 97–116.
Shield, B., and Dockrell, J. E. (**2004**). ''External and internal noise surveys of London primary schools,'' J. Acoust. Soc. Am. **115**, 730–738.
Shield, B., and Jeffery, R. L. (**2001**). ''A survey of noise levels in and around primary schools in London,'' Proceedings of the 17th International Congress on Acoustics, Universita de Roma, La Sapienza, Rome, Italy.
Smedslund, J. (**1969**). ''Psychological diagnostics,'' Psychol. Bull. **71**, 237–248.
Soli, S. D., and Sullivan, J. A. (**1997**). ''Factors affecting children's speech communication in classrooms,'' J. Acoust. Soc. Am. **101**, 3070.
Stansfeld, S. A., Haines, M. M., Brentall, S., Head, J., Roberts, R., Berry, B., and Jiggins, M. (**2000**). ''West London Schools Study: Aircraft noise at school and child performance and health,'' Final report for Department of Health and DETR.
Stelmachowicz, P. G., Hoover, B. M., Lewis, D. E., Kortekaas, R. L., and Pittman, A. L. (**2000**). ''The relation between stimulus context, speech audibility and perception for normal and hearing impaired children,'' J. Speech Lang. Hear. Res. **43**, 902–914.
Werner, L., and Boike, K. (**2001**). ''Infants' sensitivity to broadband noise,'' J. Acoust. Soc. Am. **109**(5), 2103–2111.

Soft-computing base analyses of the relationship between annoyance and coping with noise and odor

Dick Botteldooren[a)]
Acoustics Group, Department of Information Technology, Ghent University, St. Pietersnieuwtraat 41, 9000 Gent, Belgium

Peter Lercher
Institute of Hygiene and Social Medicine, University of Innsbruck, Sonnenburgstrasse 16, A-6020 Innsbruck, Austria

(Received 18 June 2003; revised 18 February 2004; accepted 2 March 2004)

The majority of research on annoyance as an important impact of noise, odor, and other stressors on man, has regarded the person as a passive receptor. It was however recognized that this person is an active participant trying to alter a troubled person–environment relationship or to sustain a desirable one. Coping has to be incorporated. This is of particular importance in changing exposure situations. For large populations a lot of insight can be gained by looking at average effects only. To investigate changes in annoyance and effects of coping, the individual or small group has to be studied. Then it becomes imperative to recognize the inherent vagueness in perception and human behavior. Fortunately, tools have been developed over the past decades that allow doing this in a mathematically precise way. These tools are sometimes referred to by the common label: soft-computing, hence the title of this paper. This work revealed different styles of coping both by blind clustering and by (fuzzy) logical aggregation of different actions reported in a survey. The relationship between annoyance and the intensity of coping it generates was quantified after it was recognized that the possibility for coping is created by the presence of the stressor rather than the actual fact of coping. It was further proven that refinement of this relationship is possible if a person can be identified as a coper. This personal factor can be extracted from a known reaction to one stressor and be used for predicting coping intensity and style in another situation. The effect of coping on a perceived change in annoyance is quantified by a set of fuzzy linguistic rules. This closes the loop that is responsible for at least some of the dynamics of the response to a stressor. This work thus provides all essential building blocks for designing models for annoyance in changing environments. © *2004 Acoustical Society of America.* [DOI: 10.1121/1.1719024]

PACS numbers: 43.50.Qp, 43.50.Rq, 43.66.Lj [DKW] Pages: 2974–2985

I. INTRODUCTION

The impact of noise exposure on man has widely been studied.[1,2] Dosage effect relationships that describe the average reaction of a large group of people to noise were derived, in particular for annoyance.[3–6] It is less often recognized, however, that the receptor is an active agent trying to alter a troubled person–environment relationship or to sustain a desirable one. Any attempt to manage the specific external and internal demand of stressors which are appraised as taxing or exceeding personal resources can be labeled as coping.[7] Only a handful of researchers have included coping in the study of noise impacts.[8–11]

This paper looks in greater detail at the relationship between reported noise annoyance, which can be regarded as a mild form of expressed anger experienced when people are exposed to unwanted or intrusive sound, and more active forms of coping. It may come as a surprise to some that noise exposure is not included as a primary trigger in this study. Indeed, personal instantaneous perceived loudness and intrusiveness plays an important role in the coping process. However, as in many studies, only average (L_{dn}) façade expose could be obtained for the survey locations. Building insulation, access to quiet backyard, organization and layout of the house, temporal and spectral structure of the noise, actual day–night fluctuation, combined exposure to different sources, time spent at home, or contributions from neighbor noise cannot be taken into account accurately in a large scale study and yet they can have a significant impact on instantaneous perceived loudness and intrusiveness. Retrospective questioning regarding perceived loudness and intrusiveness in a survey is rather difficult. Annoyance, although related to loudness, is influenced by a multitude of personal and environmental factors.[12] On one hand this limits its use as an indicator for personal exposure but on the other hand it is insensitive to the above-mentioned problems related to the use of L_{dn}.

From a methodological point of view, the innovation brought about by this work rests on the recognition that noise annoyance and coping are inherently vague concepts. Models dealing with such concepts should therefore be constructed in a more soft, human-like way.[12–14] A whole arsenal of mathematical tools is available for this purpose. The analysis presented here selects and uses a few suitable ones.

The main research questions considered in this work are:

[a)]Author to whom a correspondence should be addressed; electronic mail: dick.botteldooren@intec.Ugent.be

 0001-4966/2004/115(6)/2974/12/$20.00 © 2004 Acoustical Society of America

(1) Can grouping a subset of reactions to noise lead to the identification of coping strategies or coping styles? In Sec. III soft computing techniques, in particular fuzzy clustering and self-organized maps are used to answer this question.
(2) Is annoyance a predictor for coping? Section IV addresses this question in a statistical manner for a large population and in a fuzzy, possibilistic sense for smaller groups and individuals.
(3) Do nonexposure factors influence coping intensity, coping strategy, and coping style? In Sec. V the existence of such a factor is verified by means of a comparison of coping with noise and coping with odor.
(4) Does coping have a positive or negative effect on perceived annoyance? This important question for noise management applications is considered in the final section of this paper.

II. THE DATABASE

Although the focus of this paper is on new methods to describe the soft relationships between impacts of noise exposure and their consequences, the interesting features of this new methodology will be clarified by applying them to an example database. This database is described in general in this section and relevant variables are defined to allow fast reference in subsequent sections.

The data are primarily obtained from a survey conducted in Flanders involving 3200 subjects. The general topic of the survey was the influence of odor, noise, and too much light on the living environment. The survey was presented as such to the subjects. Selection of subjects was done in two stages. In a first stage, households were randomly selected. The member of each selected household aged above 16 whom had his/her birthday coming up first was contacted by telephone, convincing the person to participate in the study. This process was repeated, making sure that the sample was representative of the demographic factors age, gender, and province. The selected subjects were then sent the questionnaire by mail. They were reminded to participate in the survey after 3 weeks by telephone if they did not send the questionnaire back promptly. Finally, 64% of the questionnaires that were sent out were received. The survey was part of the Investigation of the Environmental Living Quality performed on behalf of the Flemish Environmental Administration (AMINAL) by Deloitte&Touche and M.A.S.

The questions of relevance for this study are as follows.

(1) The general noise annoyance question that was formulated in accordance with[34] and presented a five point categorical scale to the subjects. The answer to the question will henceforth be referred to using the variable A.
(2) A similar question for annoyance by odor, variable O.
(3) A similar noise annoyance question related to particular groups of sources (e.g., road traffic, air traffic, etc.), variable A_x, where x refers to the source. O_x refers to the corresponding odor questions.
(4) A set of questions asking for the perceived change in annoyance over the past two years. A symmetrical five point categorical scale is provided, labeled "*the situation did not change*," "*annoyance increased strongly*," "*increased somewhat*," "*decreased somewhat*," "*strongly decreased*." The question was only related to noise annoyance A_d and annoyance by odor O_d, not to particular sources.
(5) Questions about "actions" taken in response to noise/odor exposure. These were yes/no questions. The "actions" inquired about were:

(a) Thought about filing a complaint C_{tc};
(b) Filed a complaint once C_{cl};
(c) Filed several complaints C_{cm};
(d) Thought about moving C_{tm};
(e) Contacted a lawyer C_{la};
(f) Joined an action group C_{ag};
(g) Talked to those responsible for the noise C_{ta};
(h) More carefully closed windows, doors, window blend, ... C_{cw};
(i) Reorganized or modified the house C_{rm}.

III. COPING

A. Short introduction to coping

Coping can briefly be defined as any attempt to manage the specific external and internal demands of stressors, which are appraised as taxing or exceeding personal resources.[7] The appraisal of the stressor comes first and the function of coping is therefore to alter a troubled person–environment relationship or to sustain a desirable one. Because the environment changes constantly the significance of these changes is reappraised and may lead to altered coping strategies. In this repeated process of appraisals and reappraisals emotions play an important role.[15] Annoyance is a mild form of anger people often experience when they are exposed to unwanted or intrusive sound which interferes with their daily life. It is of obvious importance to know which actions are triggered by the negative emotions experienced and how the actions relate to each other before we can effectively analyze the relationship between annoyance and coping under noise or odor exposure.

It has to be mentioned here that coping with such environmental stressors has been studied only on a limited scale and the few published studies show discrepant results. The few published field studies show discrepant results with regard to the effect of coping on annoyance or other indicators of health or quality of life.[11,16,17] Different concepts and methods used, different contexts, and the cross-sectional nature of these studies limit comparability.

Furthermore, differences in the effect of coping on annoyance are to be expected between noise and odors. Although both exposures fall under the umbrella of ambient stressors[18] due to their continuous background existence with varying intensity, odors are considered to be more intractable than noise—again depending on the social and environmental context of the study.[19–21] Given the inconsistency of the existing body of evidence a broad approach to the issue under study is therefore advisable.

TABLE I. Fuzzy clusters obtained by fuzzy c-means clustering using different numbers of clusters and description of the typical members of these fuzzy sets.

10 clusters	7 clusters	4 clusters	Description
cl1	√	√	C_{cw} only
cl2			C_{cw} and C_{rm} but no other action
cl3	√		C_{tc} only
cl4	√	√	C_{cw} and C_{tc} but no other action
cl5	√		C_{cw} and C_{tm} but no other action
cl6	√	√	No action at all
cl7	+/−	+/−	C_{cl} sometimes combined with C_{cw} and C_{ta}
cl8			C_{ta} and C_{cl}, C_{cm} sometimes combined with C_{cw} and C_{tm}
cl9	√		C_{ta} only
cl10			C_{tc}, C_{cw} and C_{ta}

B. Clustering coping descriptors

Grouping of response to noise exposure can be done by clustering the subjects based on their response to the nine coping related questions. Such clustering does not make use of any prior knowledge of the relationship between the actions described by these questions. The biggest pitfall associated with such blind techniques is the possibility for overfitting the data, thereby limiting the conclusions to the specific sample at hand. Two techniques are proposed for this pre-analysis task.

Fuzzy c-means clustering[22] is a direct extension of crisp k-means clustering, but allows elements to belong partly to a number of clusters. The clusters are fuzzy sets over the universe spanned by the variables. The technique alters the location of the cluster centers to minimize an objective function that contains an additional parameter that controls the degree of fuzziness in the outcome. Using the MATLAB toolbox ''fuzzy/fcm revision 1.6,'' the coping data were clustered into an increasing number of clusters. In Table I, the clusters obtained when ten clusters are initiated are described by the prominent members (having high membership values) of these fuzzy sets. Table I also indicates which clusters were already identified when only seven or four clusters are initiated.

Self-organizing maps (SOM, also referred to as Kohonen neural networks)[23] are a more subtle and highly nonlinear way to organize data, inspired by the human brain. A set of input neurons is associated with the variables representing the answers to the coping questions. Each of these nodes is connected to a two-dimensional array of neurons. An iterative procedure, the learning process, changes the weights of all connections to the neuron that responds more strongly, and its neighbors. The area of influence is gradually reduced during the process. The result is a two-dimensional mapping of all data records (subjects in the survey). Interpretation of the results is not trivial. Euclidian distance has no meaning in this map. One possibility to examine the similarity of neighbor nodes consists in computing and drawing the u-matrix. This is a matrix obtained by summing the Euclidian distances between the points in the original multidimensional space mapped to adjacent nodes. A SOM is constructed (MATLAB toolbox SOM[24]) for the coping universe.

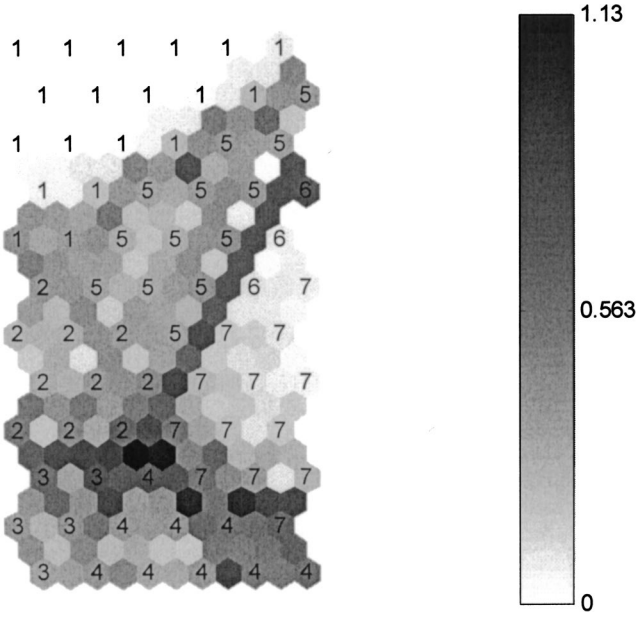

FIG. 1. U-matrix of the SOM of the coping universe.

Its u-matrix is shown in Fig. 1. Each labeled node represents a neuron and is surrounded by six cells that are shown darker if the neighbor in that direction is further away. Uniform regions are automatically labeled. By examining subjects whose coping answers are mapped to the center of a labeled area, the areas can be interpreted (Table II). From the u-matrix it is however obvious that *som3* and *som4* are on average very close and the same holds for *som2* and *som5*. The distance between this second group and *som1* is smaller than between the other clusters.

C. Social, political, and active coping

In the literature several attempts have been made to identify styles of coping. The most parsimonious classification distinguishes between problem- and emotion-oriented coping.[7] Although both coping styles are typically combined, our analysis focuses here on problem-oriented styles, which are easier to ask respondents in large field surveys, are more closely related to policy options (citizen involvement, empowerment), and have shown higher reliability scores.[17] An earlier investigation[9] also suggested that the relationship with noise annoyance is more pronounced for problem-oriented activities. It is expected that either perceived control is reached by coping and annoyance may decrease or coping failed and annoyance increases as a sign of sustained stress or activation. Studies on exposure to industrial odors have

TABLE II. Description of the areas (clusters) identified in the SOM.

Cluster	Description
som1	No action at all
som2	C_{ta} or C_{tm} and no other action
som3	C_{tc} but not C_{cw} nor C_{rm}, other actions sometimes
som4	(C_{tc} or C_{cl} or C_{cm}) and C_{cw}, other actions sometimes
som5	C_{rm} and sometimes C_{cw} but no other actions
som7	C_{cw} but not C_{rm} nor (C_{tc} or C_{cl} or C_{cm}), other actions sometimes

TABLE III. Partial truth-value associated with the aggregated coping variables for each of the coping questions.

	C_{tc}	(C_{tc}	*and not*	C_{cl}	*and not*	C_{cm})	C_{cl}	C_{cm}	(C_{cl}	*and not*	C_{cm})	C_{tm}	C_{la}	C_{ag}	C_{ta}	C_{cw}	C_{rm}	C_p	C_a	C_s
Political, C_p				0.5				0.9		0.65				0.1						
Active, C_a												0.4				0.5	0.1			
Social, C_s															1					
General, C																		0.4	0.5	0.1

revealed higher annoyance in individuals with a problem-oriented coping style, while emotional strategies seemed to reduce annoyance.[16,17] It was hypothesized that regulating the emotions may be more effective, since active coping under odor exposure is very limited. However, the effectiveness of the used emotional style (comforting versus avoidance) was inconsistent in these two major studies.

For a more focused analysis, we distinguished three substyles in this study: active coping (with an assumed direct effect on exposure level), social coping (seeking social/administrative support), and political coping (using citizen power).

The coping variables in the survey are yes/no or true/false answers, thus binary logic. To represent social, political, and active coping, partial truth will be used. The mathematical methodology (fuzzy logic) is based on extending the range of possible values from {0,1} (0=false, 1=true) to the continuum [0,1]. Table III shows the partial truth values associated with the aggregated coping variables when particular coping questions are answered affirmatively. These values are added when more than one question is answered affirmatively.

D. Discussion

From the above-noted clustering analyses, a very stable cluster of subjects that *more carefully closes windows, doors, window blend,...* but takes almost no other action, is identified. This cluster emerges in the fuzzy c-means clustering analyses and in the SOM. A second cluster of subjects *thinks about filing a complaint*. There are two subclasses in this class; a first group does not seem to combine this with other actions; a second group also copes by actually filing the complaint and by *more carefully closing windows, doors, window blend,...*. The first subclass is observed both by fuzzy c-means clustering and in the SOM, the second subclass is scattered over a few clusters if fuzzy c-means clustering is used. Another class of subjects *thinks about moving or talks to those responsible for the noise*. This group is very close to the cluster that *reorganizes or modifies their house*, sometimes combined with *closing windows*. This last cluster is also identified using fuzzy c-means clustering but only when ten clusters are used. Fuzzy clustering resulted in two clusters that contain *talking to the person responsible for the noise*. In one of those clusters several other actions are found.

In interpreting these results one should consider that there are three important causes for clustering. The action mentioned may be typical for a certain level of exposure or the subjects may react to noise in a typical personal manner. Moreover, particular actions can be better suited in response to particular causes of annoyance (e.g., road traffic noise or neighbor noise or odors).

Do these results of blind clustering correspond to the coping styles and behaviors previously defined in literature? This can be analyzed by looking at the average truth-value for social, active, and political coping in each of the classes obtained by self-organized mapping of the data of the survey in Fig. 2. In this analysis all records are categorized in exactly one class (nonfuzzy cluster), hence some noncrisp subdivisions can be expected. Nevertheless, *som2* clearly clusters social copers, *som3* clusters those mainly coping politically, and cluster *som5* and *som7* groups active copers. Those in cluster *som4* show all types of coping. A more detailed inspection revealed that this cluster groups *strongly* to *extremely* annoyed subjects which accounts for the very strong coping. This analysis shows that blind clustering indeed partly reveals coping styles.

IV. NOISE AS A PRIMARY TRIGGER FOR COPING

It is obvious that exposure to noise is a prerequisite for coping with the experienced, unwanted effects of noise. Most research on coping[8–11] includes a noise exposure (e.g., L_{dn}) variable in the analyses. In Ref. 9 it was shown that the odds ratio for several activities that fall under the larger umbrella of coping, are stronger for reported noise annoyance than for noise levels. This led us to hypothesize that reported noise annoyance might be a more accurate descriptor of the prerequisite for coping. Moreover, as explained in Sec. I, there are several reasons why the calculated L_{dn} may not be an accurate descriptor for perceived exposure and intrusiveness.

A. Average coping by a large group

Mainly for comparability with previous work, a classical analysis is performed on the survey data. The percentage of the population that is acting in response to noise as a function of reported noise annoyance is investigated for the

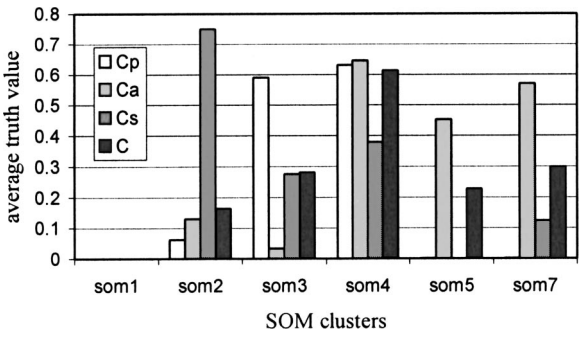

FIG. 2. Truth-value of political, active, and social coping in the clusters obtained by SOM.

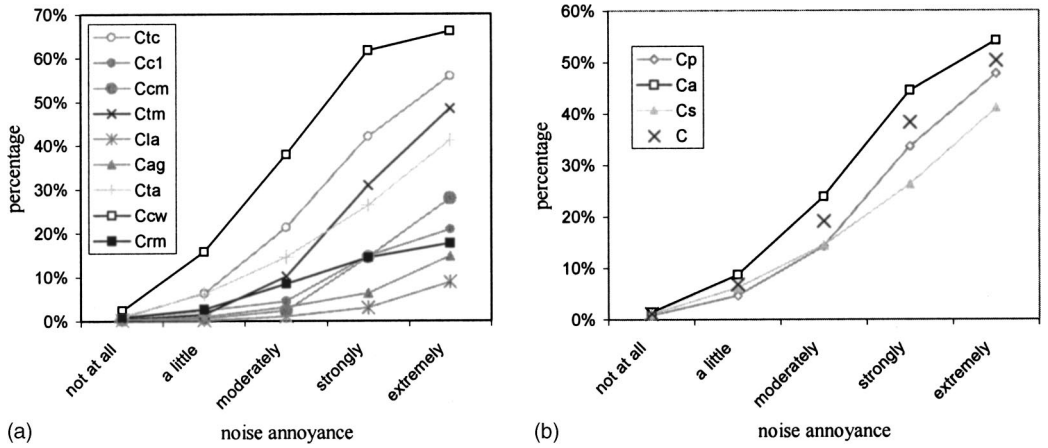

FIG. 3. Percentage of the Flemish population coping with noise as a function of reported noise annoyance category: (a) questions in the survey; (b) aggregated coping variables.

whole population of Flanders. Figure 3 shows both the percentage of the single questions and the aggregated coping styles (active, political, and social). This result is obtained by adding partial truth-values over all subjects.

B. Coping by individuals or smaller groups

Because of the inherent vagueness in the concepts involved and because not all personal, contextual, and social factors are known, it is not possible to predict coping activities for an individual or a small group in a classical crisp way. Fuzzy set theory was chosen as a concept to represent the available knowledge. The general idea here is to relate fuzzy sets defined in the antecedent space, the universe of noise annoyance U_A, to fuzzy sets defined in the consequent space, the universe of coping U_C. Since noise annoyance is already categorical, the corresponding fuzzy sets in the coping universe are derived for each annoyance category.

A fuzzy set, X, is described by a possibility distribution or membership function, $X(u)$, $\forall u \in U$. Statistical analysis of the database results in a conditional probability distribution that will be transformed into a possibility distribution using methods described in literature. Figure 4 shows a curve for noise and odor, fitted to the observed cumulative probability distributions for C under different conditions for A. For the three highest levels of annoyance, the integral of an asymmetric Gaussian distribution was fitted since it is quite commonly used for representing membership functions because of its derivability. For reported noise annoyance categories ''not at all'' and ''a little,'' an exponential distribution seemed more appropriate. Probability distributions corresponding to the fitted curves are shown in Fig. 5. With fuzzy calculus in mind, these distributions were normalized to obtain a maximum level equal to one. This is actually one of the simplest transformations from probability to possibility.[25] Geer and Klir proposed an ''information preserving transformation'' between probability and possibility.[26] They use a discrete universe for defining their distributions and obtain the ith element π_i of the possibility distribution from the probability p_i as

$$\pi_i = \left(\frac{p_i}{\sup_j(p_j)} \right)^{\alpha}, \tag{1}$$

where the exponent α is obtained by asserting that the total uncertainty must be preserved in the transformation between probability and possibility. The rationale behind this transformation is that the same underlying knowledge is to be represented in both frameworks. The exponent was calculated for each distribution given in Fig. 5, resulting in the possibility distributions shown in Fig. 6.

The possibility distributions must be interpreted as follows. As noise annoyance increases it becomes possible that individual people start coping with this burden to some extent. Without additional information on the subject, it is impossible to find out who exactly is coping and who is not.

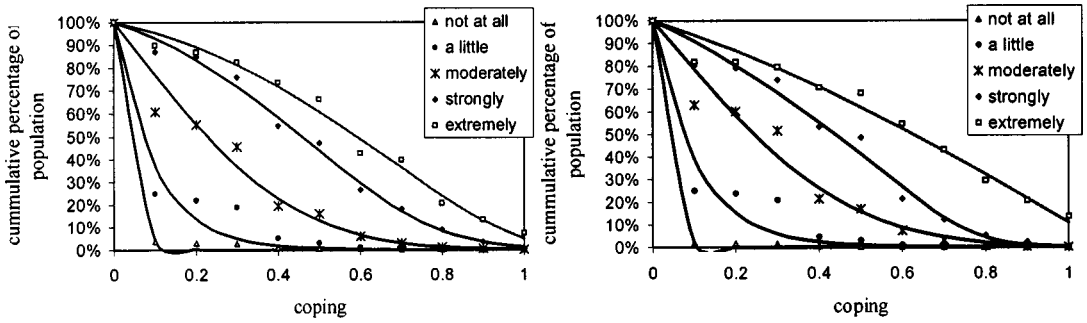

FIG. 4. Cumulative distribution of the percentage of the population reporting different intensities of coping for various levels of reported general annoyance; left: noise, right: odor.

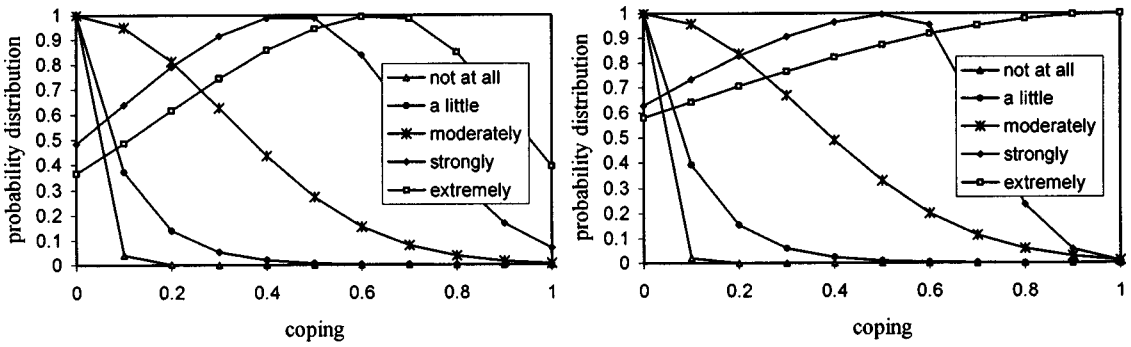

FIG. 5. Renormalized probability distributions of coping levels for different levels of reported annoyance; left: noise; right: odor.

Uncertainty (nonspecificity) increases, as the possibility distribution gets wider for higher levels of reported general noise annoyance.

It must be kept in mind that the labels used to report annoyance could also be interpreted as fuzzy sets on a universe of annoyance U_A.[27] This representation allows relating the labels to each other. The five relations between annoyance level (categorical, labels) and coping possibility distribution can be aggregated to a fuzzy rule based representation of knowledge. Here, a Mamdani approach is used. Each rule is represented as

$$\forall u \in U_A, \forall \nu \in U_C : R_i(u,\nu) = \min(A_i(u), C_i(\nu)), \qquad (2)$$

where A_i and C_i are membership functions (or possibility distributions) for the ith annoyance category and the corresponding coping possibility distribution derived earlier. All rules, R_i, relating the same universes are aggregated to

$$\forall u \in U_A, \forall \nu \in U_C : R(u,\nu) = \max_i (R_i(u,\nu)). \qquad (3)$$

Figure 7 shows this two-dimensional function R_{A-C}. The diameter of the dots represents the possibility of each combination of levels to occur together. Figure 7 is a straightforward generalization of a classical function graphically represented by a sharp line. There is no causal path on the relationship between reported general noise annoyance and coping, implied by this representation of knowledge.

C. Discussion

Particular features such as a saturation of C_{cw} and other active coping acts, and in C_a for high noise annoyance (Fig. 3) are in qualitative agreement with earlier research.[9,28,29,8] In a classical approach this fraction of the whole population showing coping behavior is interpreted as the probability for an individual to show coping behavior. For example, if it is known that a person is *strongly annoyed* (through questioning or simulation) then the probability for coping is 0.4; if annoyance is just *a little* annoyed then this percentage drops down to 0.08. The fuzzy set based view differs in two respects. First, coping is regarded as a continuous gradual variable that can take all values between *not coping at all* (the value zero) and *very strong coping* (the value one). Second, the single crisp level of coping is replaced by a possibility distribution over all levels of coping. Thus, in the above-given examples, all levels of coping are possible actions for a strongly annoyed person (Fig. 6) although the possibility for strong coping (levels close to one) is somewhat less possible. In the second example, for the person only a little annoyed the possibility distribution demonstrates that only low levels of coping have a finite possibility to be observed. The fuzzy set interpretation of the data is less precise, but does not claim any knowledge that is not available.

The dosage–effect relationship shown in Fig. 7 is rather vague, especially for the higher levels of annoyance. This vagueness has two causes; it is due to uncertainty on the one hand and to inherent vagueness in concepts on the other hand. The inherent vagueness neither in the concept noise annoyance nor in the concept coping can be removed no matter how large the amount of information regarding the subject becomes available. Strong annoyance, for example, is somewhere around 7.5 or 8 on a scale from 1 to 10 but no one can give a crisp number. The uncertainty part may eventually be removed by collecting more information on the

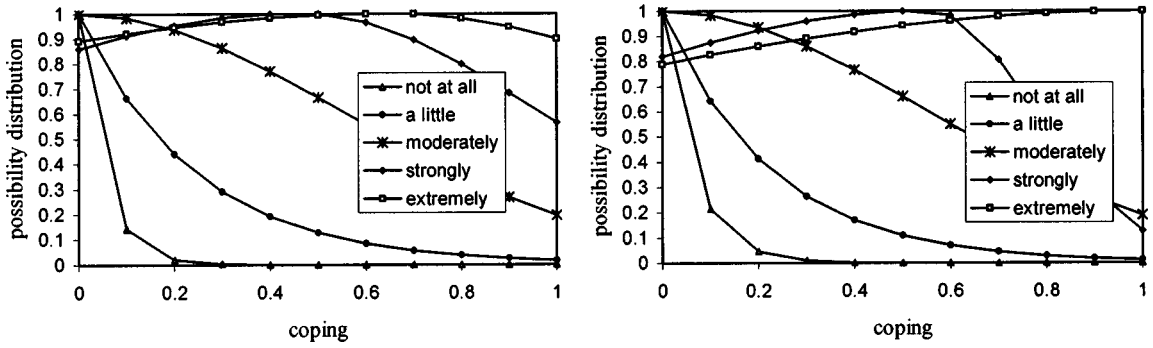

FIG. 6. Possibility distribution of coping levels for different levels of reported general annoyance; left: noise, right: odor.

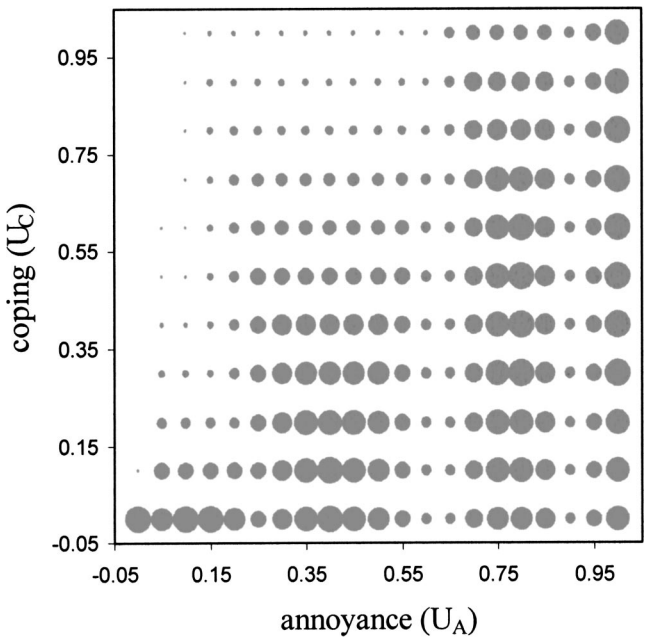

FIG. 7. Possibility distribution for the set of fuzzy rules relating general noise annoyance to coping (diameter of bubbles is proportional to possibility).

person and by constructing accurate models. In the Sec. V it will be proven that this is indeed possible.

V. FACTORS THAT COULD MODIFY COPING INTENSITY

It is reasonable to assume that the intensity of coping for a given level of noise annoyance depends on additional factors. Personal and situational factors have been shown to be the most promising candidates for research hypotheses.[10,11,31]

A. Method for average coping by a large group

In order to find out whether a stable personal factor determines the level of coping, the reaction to different stressors has to be compared. In this study, annoyance by noise and odor and coping with noise and odor are included. This allows us for the first time to test whether those people that react with strong coping efforts to noise exposure also strongly react to odor. Within the coping fuzzy sets related to *high* and *extreme* noise annoyance, the subset of subjects that actually cope with noise annoyance and those that do not are first identified. This process can be described by the following set of rules:

IF *A* is *high or extreme* AND *C* is *some* THEN *PF* is *coper*,

IF *A* is *high or extreme* AND *C* is *none* THEN *PF* is *noncoper*,

where the noise annoyance variable *A* and the aggregated coping variable *C* are used and where a new variable *PF* that could be called *personal factor* is introduced. In situations not corresponding to either of the above-mentioned rules, *PF* remains *unknown*. The reaction of these three subsets of the population to annoyance by odor can now be analyzed. The result is presented in Fig. 8.

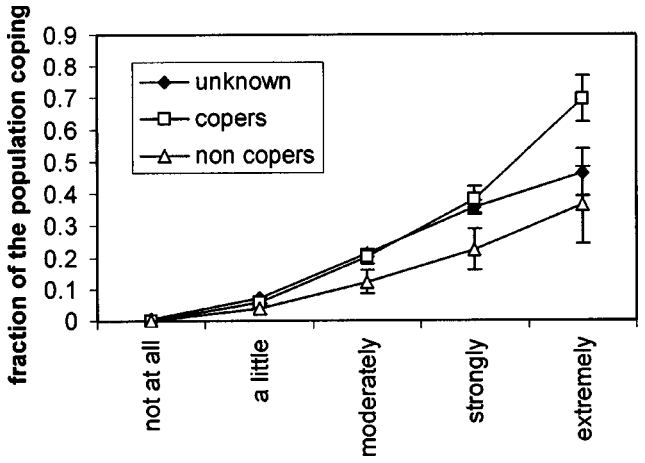

FIG. 8. Fraction of the population coping with annoyance by odor for three subsets of the population; standard error is indicated.

B. Method for coping by individuals or small groups

Let us turn back to the prediction of coping for an individual or small group. The broad possibility distributions for coping when strong or extreme noise annoyance are reported, which are shown in Fig. 6 should theoretically become sharper if information on coping habits can be introduced. Based on the identification of copers using the odor question, the fuzzy sets corresponding to *strong* annoyance are derived as explained in Sec. IV B and shown in Fig. 9.

C. Discussion

Copers, identified by their reaction to noise, on average show significantly higher coping reaction to annoyance by odor as well (Fig. 8). A similar conclusion can be drawn for the opposite relationship. Copers, identified by their reaction to odor, show significantly higher coping reaction to noise annoyance. Because less subjects are *strongly* or *extremely* annoyed by odor, the category *unknown* is much more populated and therefore the conclusion is less clear. One remark must be made. In some cases, coping with noise and odor result in the same actions (e.g., closing windows) and the sources of noise and odor may be the same (e.g., road traffic) explaining also the effect observed in Fig. 8. Therefore, caution is necessary before these results are compared with earlier results from industrial odor pollution.

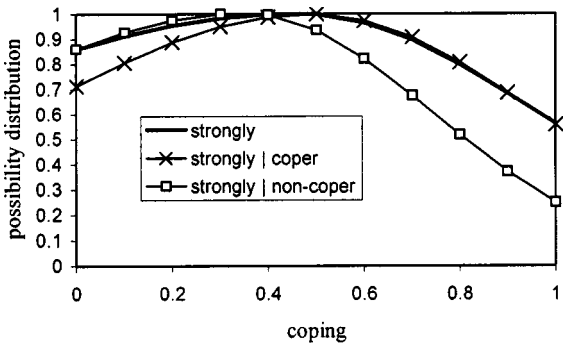

FIG. 9. Fuzzy set (possibility distribution) on the U_C corresponding to *strong* noise annoyance for a coper and a noncoper as derived from the individual's reaction to odor.

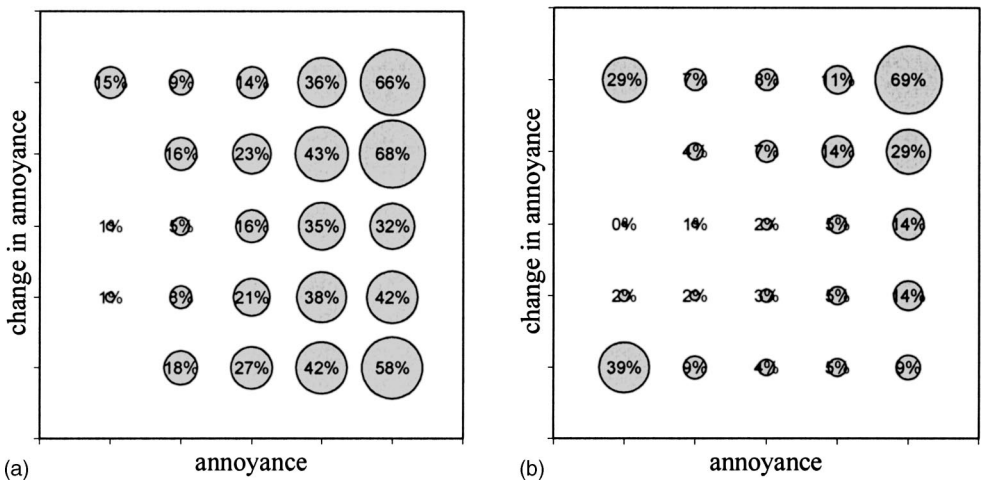

FIG. 10. Fraction of the population coping for combinations of noise annoyance categories (not at all, a little, moderately, strongly, extremely) and annoyance change (considerable increase, increase, no change, decrease, considerable decrease) (a); and 95% confidence interval (b).

This analyses relies on soft-computing techniques only for the selection of people showing some coping behavior, but this can also be done by crisp selection on the basis of individual answers to coping-related questions. Hence, we call this the classical approach. As far as we know the method used here to prove the existence of a personal factor that determines the intensity of coping is in its kind a first. Earlier studies have made direct attempts by including personality variables.

The main focus of this work is, however, on the response of an individual or small group. In Sec. IV C it was mentioned that part of the imprecision in the relationship between annoyance and coping might be removed by adding additional information regarding the individual. Knowing a person's reaction to another stressor is already more information than we can hope to gather in policy support applications, but nevertheless, the possibility distribution obtained using this knowledge (Fig. 9) is still quite vague. Further increase of precision in the description of coping may be possible by adding additional situational factors, but this result seems to indicate a large amount of intrinsic vagueness. Unfortunately the *PF coper* or *noncoper* could not be related to any of the demographic data (age, gender, type of house, education) in the database using classical or soft computing techniques due to the limited size of the database. For this reason it can only be used for modeling purposes and policy support if a reference survey for the particular small group is available.

VI. INFLUENCE OF COPING ON ANNOYANCE: FEEDBACK

Coping can influence reported noise annoyance in different ways. First, and this is the most straightforward effect that should not be neglected, coping can be effective and reduce exposure to unwanted sound. This can eventually result in lower noise annoyance. Coping was shown to reduce the potential increase of blood pressure caused by exposure to noise.[10] It is therefore not unreasonable to look for a reduction in annoyance reported by those coping with the noise. On the other hand, unsuccessful coping (that does not reduce exposure) may further increase annoyance.[9,30,11,16,17]

A noise annoyance survey represents a cross-sectional experience and does not inform about changes over time. For this reason, the survey conducted in Flanders includes a question "Thinking about your home, that is in and around your house, to what extent did annoyance by noise/odor change in the last two years? (Translated from Dutch)." A five point categorical scale (situation is unchanged, annoyance increased considerable, annoyance increased a little, annoyance decreased a little, annoyance decreased considerably) was provided for answering this question. This perceived change $A_d(O_d)$ is used in the analysis.

A. Average feedback for a large population

Noise annoyance, A, and change in annoyance, A_d, are not orthogonal and it was already illustrated that coping intensity depends strongly on annoyance. The analysis of possible effects of coping on annoyance therefore can not be performed on the change variable alone. Figure 10 shows the percentage of the population coping with noise for each combination of A and A_d categories. Since some combinations are not occurring very often in the database, confidence intervals in the corners of this chart [Fig. 10(b)] seem to be rather large.

A more detailed analysis distinguishes between coping styles. Figure 11 shows the percentage of the population reporting different categories of noise annoyance change, A_d, in each of the coping clusters obtained using SOM. These clusters emerged naturally because of different coping style and intensity. Figure 12 shows the average truth-value of coping for those reporting different categories of A_d and this for different coping styles as defined in Sec. III C.

B. Feedback at the level of an individual or a small group

To describe the influence of coping on reported change in annoyance at the level of an individual or small group, fuzzy sets and associated fuzzy rules are used. Figure 13 shows the causal relationships that have to be described in

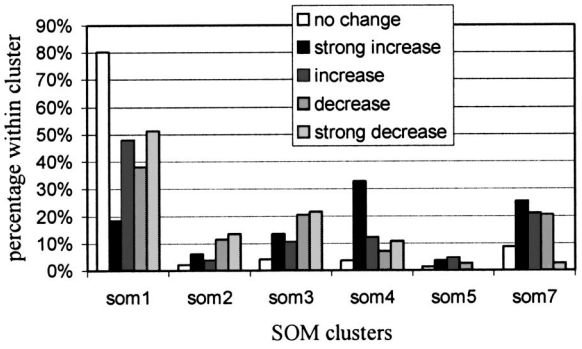

FIG. 11. Percentage of the group reporting different categories of change in noise annoyance in each coping cluster.

such a fuzzy rule based system. The relation between annoyance, A, and coping, C, has already been discussed in Sec. IV B. In much the same way a relation between A and A_d can be derived. Since no data on the meaning of the labels used to describe annoyance change are available that allow linking them to a continuous annoyance change universe U_{Ad}, fuzzy sets defined in the universes of labels U'_{Ad}={*strong increase, increase, no change, decrease, strong decrease*} and U'_A={*not at all, a little, moderately, strongly, extremely*} are used. Figure 14 shows that the possibility for a person reporting $A_d = increase$ or *strong increase* becomes larger once it is known that this person reported higher levels of annoyance.

The weak (feedback) relation between coping and resulting annoyance change can only be observed relative to the strong relations between A and C and between A and A_d. This is done by inferring knowledge on reported annoyance change from the knowledge that a person is coping with noise annoyance using the compositional rule of inference (CRI) implemented using the Mamdani approximation

$$(\forall \nu \in V)\left(B'(\nu) = \sup_{u \in U} \min(A'(u), R(u,\nu))\right), \tag{4}$$

where R represents a rule, A' is a known fuzzy set, and B' is the inferred result. More detailed information on the use of approximate reasoning based on fuzzy rule bases in the context of noise annoyance modeling can be found in Refs. 13 and 14. The CRI is applied first to obtain A from C using R_{C-A} followed by applying rule R_{A-Ad} for obtaining A_d. The resulting possibility distribution is compared (Fig. 15) to the possibility distribution obtained directly from the database by extracting the possibility distribution that would appear in a rule of the form "IF C is *some/none* THEN A_d is *change/no change*," where the label *some* refers to a minimal coping action and the fuzzy sets *change/no change* are defined by Fig. 15.

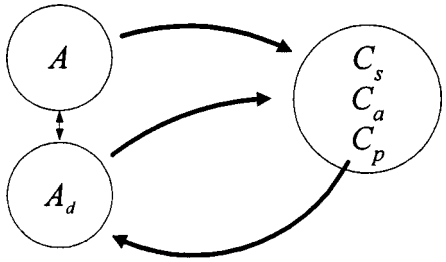

FIG. 13. Illustration of causal relations between annoyance A, coping $\{C_s, C_a, C_p\}$, and annoyance change A_d that have to be included in the fuzzy rule based system.

C. Discussion

In Sec. IV A, the higher fraction of the population that is coping with increasing level of annoyance was already demonstrated. On top of this, higher percentages of coping are also observed in changing situations. The causality between variables involved is expected to be quite different for improving and worsening situations, however.

(1) $A_d \in \{considerable\ increase, increase\}$. A first possible explanation for the higher level of coping is that the exposure to noise actually got worse and this change triggered more coping than for the part of the population where nothing changed. A second possibility is that those engaged in unsuccessful coping activities reported an increase in annoyance although exposure remained unchanged.

(2) $A_d \in \{considerable\ decrease, decrease\}$. It is extremely unlikely that a decrease in noise annoyance triggered more coping than an essentially unchanged situation. The only remaining explanation in this case is that coping results in lower reporting of noise annoyance. It is not possible to distinguish between successful coping leading to a reduction in exposure and the subjective benefit of coping.

The percentage of the population in different clusters (Fig. 11) and the average truth-value of different coping styles [Fig. 12(a)] are compatible with the hypothesis that a (*strong*) *increase* in noise annoyance triggers additional coping [and no change results in no action (*som1*)]. In particular,

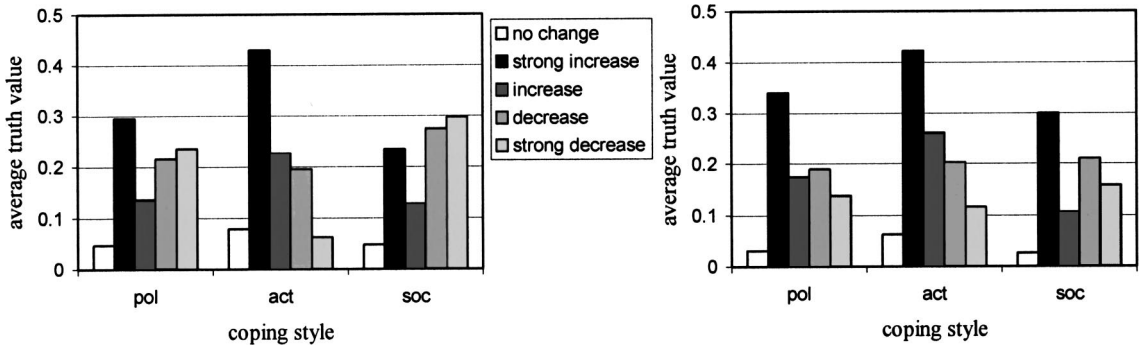

FIG. 12. Average truth-value for different coping styles for those reporting different categories of annoyance change; left: noise, right: odor.

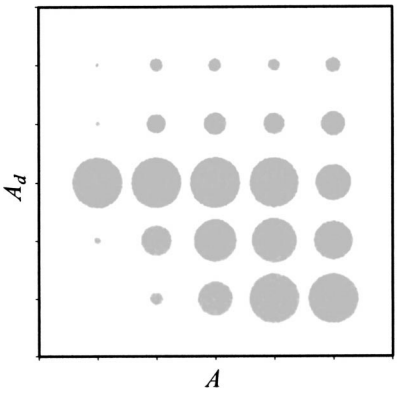

FIG. 14. Fuzzy relation, R_{A-Ad}, between annoyance categories (not at all, a little, moderately, strongly, extremely) and annoyance change categories (strong increase, increase, no change, decrease, strong decrease).

cluster *som4* that corresponds to intense coping activities of all styles is linked to this increase. Social and political coping, also well represented in clusters *som2* and *som3*, seem to be common amongst those reporting a *decrease* or strong *decrease* in noise annoyance. For the category *active coping* the relation to A_d is less obvious. This is compatible with the hypothesis that *social* and *political* coping are often successful. *Unsuccessful active* coping, on the other hand, seems to increase noise annoyance more than *social* or *political* coping. The picture for odor [Fig. 12(b)] is different. The difference between coping styles is less pronounced or even totally absent. Earlier research has shown that it is more difficult to cope with odor in a problem-oriented manner.[31,16,17] This could explain the above-mentioned observation. Furthermore, the amount of variance explained by contextual factors has been found to be smaller in odor annoyance than in noise annoyance.

The analyses of the change in annoyance of a large population due to coping given above can be called classical although some of the concepts (e.g., partial truth and clusters) from the soft-computing approach were already used. Working with averages of perceived change clearly would not give any useful insights because of the bimodal structure of this response. Using fuzzy rules for investigating possible feedback at the level of an individual (Sec. VI B) we can actually go a step further in gathering proof for the existence of a causal path between coping and decrease in noise annoyance and it is even possible to represent the available knowledge on this effect in a compact way. The proof is based on the results shown in Fig. 15. In general, the possibility distributions obtained through the annoyance path $(A|C=)$ are broader and thus less precise than those obtained directly from the data $(C=)$. This is expected since each of the two rules used to obtain annoyance change through annoyance inserts its proper uncertainty. Much more interesting is the fact that at the decrease side, information on coping does not differentiate the possibilities if the path through annoyance is followed. There is a clear increase in the possibility for reporting a decrease in annoyance if this information is extracted directly. Moreover, this possibility increases above the indirect calculation. Hence another causal path between C and A_d exists. This does not prove beyond any doubt that it is the direct path: "(C is *some*) is λ_d sufficient to conclude that A_d is *decrease* or *strong decrease*," but this path is an acceptable candidate. Also, it cannot be concluded that a similar relationship "(C is *some*) is λ_i sufficient to conclude that A_d is *increase* or *strong increase*," is not obscured in the analysis. The introduction of a sufficiency parameter λ in a fuzzy rule has been discussed in Refs. 13 and 14. With the assumption that only the direct path contributes at the decrease side of the distribution, the sufficiency parameter can be extracted from the data: $\lambda_d = 0.65$. For the increase side, a similar assumption is not possible and hence λ_i cannot be derived. The definitions for the labels *some* (coping), decrease and *strong decrease* (in noise annoyance) and the extraction of the sufficiency λ_d quantify knowledge on the effect of coping on decrease of annoyance in a compact linguistic rule.

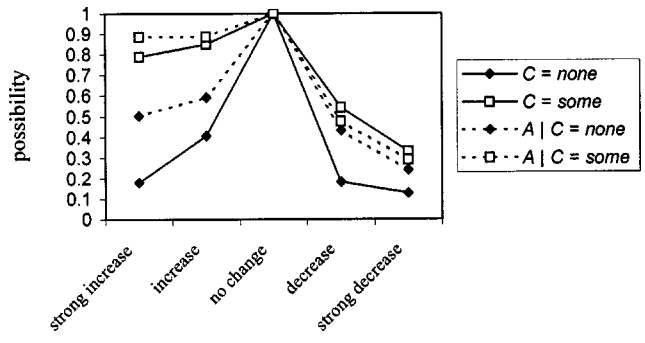

FIG. 15. Possibility distribution over U'_{Ad} corresponding to the condition *coping, C* is *none/some* and the same result derived through the relation between *C* and *annoyance, A* chained with the relation between *A* and *reported annoyance change,* A_d.

D. Closing the path from reported annoyance to reported change in annoyance

In previous sections, we have argued that a causal relationship probably exists between annoyance and coping and between coping and reported decrease in noise annoyance. Let us consider in particular the prediction for an individual or a small group. In Sec. IV B a set of fuzzy rules was extracted that allows deriving a possibility distribution for the coping variable *C*, when a level of reported noise annoyance is known. Although the nonspecificity in predicting *C* for an individual becomes quite large as noise annoyance levels increase, this variable can still be used as an input for the fuzzy rules obtained in the previous section that related coping to a reported change in annoyance. Chaining the rules using a Mamdani type inference system, results in the possibility for reporting a decrease (*decrease* or *strong decrease*) and no decrease (*no change*, *increase* or *strong increase*) in noise annoyance as a function of the category of noise annoyance before coping (Fig. 16). Reporting moderate noise annoyance seems a turning point. Above this level of annoyance it is slightly more possible that a subject reports a decrease in noise annoyance because he or she has been coping with noise. If initial annoyance is less than moderate, there will be little coping and it is evidently more possible that the subject will not report any decrease in annoyance due to coping.

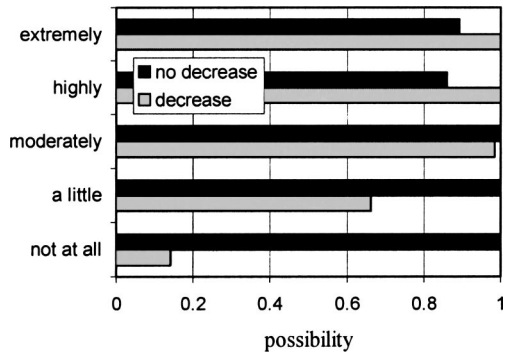

FIG. 16. Possibility for reporting a decrease in annoyance through coping for different categories of noise annoyance.

VII. CONCLUSIONS

This paper has introduced soft computing techniques for the analysis of coping with noise exposure and its interaction with annoyance. Coping was based on answers to a number of questions related to actions taken by subjects. This definition can rely on advanced clustering methods that identify related actions and activity levels. It can also be defined on the basis of expert knowledge using the concept of partial truth, a concept that is a typical product of fuzzy logic. In this case three conceptual variables C_a, C_s, and C_p: *active*, *social*, and *political* coping were introduced. The combined variables (both fuzzy and crisp) extracted on the basis of the survey data and those based on expert knowledge are sufficiently related to prove the concept.

The relationship between reported annoyance and coping was analyzed both from the classical point of view that an average effect in a larger population is the reference, and from a soft point of view that tries to analyze reactions of individuals or small groups. In the latter case, a high level of annoyance is said to generate the possibility for coping. It does not assure that actual coping occurs. By comparing coping with noise and coping with odor, the existence of a personal factor could be established that helped to identify *copers*. If information on this personal factor is available, it increases the specificity of the possibility distributions describing the knowledge on coping intensity related to higher categories of annoyance. Unfortunately, this factor could not be related to demographical data in this survey.

The strong relationship between annoyance and coping obscures possible effects (positive or negative) of coping on annoyance. Through very careful analysis of reported change in annoyance, some evidence could be found of a positive effect of coping on annoyance. The analysis does not exclude that—at the same time—there is a finite possibility that coping leads to report an increase in noise annoyance. More specifically, active coping seems to result slightly more often in reporting an increase in annoyance. A possible reason for this duality could be that coping can either be perceived as being successful or not. If perceived successful, reduced annoyance is reported, while unsuccessful coping may increase annoyance.

Fuzzy rules derived in this work can be used as part of more elaborate fuzzy rule based models for noise annoyance such as the one described in Ref. 14. In such models, the coping path is a so-called feedback mechanism in the model. It could become part of a dynamic model of the change in noise annoyance occurring after a change in exposure. Since negative and positive feedback seem possible, both a stabilizing oscillation or a strong self-stimulation can occur. The latter results in an unexpected increase of annoyance. Because, at least for small groups, the model is very fuzzy, an increase in uncertainty will be observed (higher unpredictability of the response) some time after a change in the exposure. Obviously, increasing the perceived effectiveness of coping can influence this trend.

Although there are obvious limitations by using cross-sectional population data in analyzing the process of coping with environmental stressors,[32] the broad structure of the analysis has demonstrated the wide range of options to study the complex relationship between annoyance and coping. The advantage of the soft computing techniques is especially visible when the annoyance experience of small groups is concerned, where classical approaches typically give less insight due to rapid loss in statistical power. The parallel study of coping with noise and odors is another requirement for a proper assessment of environmental impacts because coping with one stressor may impair a person's ability to cope with the other environmental stressors.

Nevertheless, to fully study the repeated feedback loops described by coping theorists we need longitudinal study designs.[33]

[1] K. D. Kryter, *The Handbook of Hearing and the Effects of Noise* (Academic, New York, 1994).
[2] *Noise and its Effects*, edited by L. Luxon and D. Prasher (Whurr, London, in press).
[3] T. J. Schultz, ''Synthesis of social surveys on noise annoyance,'' J. Acoust. Soc. Am. **64**, 377 (1978).
[4] S. Fidell, D. S. Barber, and T. J. Schultz, ''Updating a dosage-effect relationship for the prevalence of annoyance due to general transportation noise,'' J. Acoust. Soc. Am. **89**, 221–233 (1991).
[5] H. M. E. Miedema and H. Vos, ''Exposure response functions for transportation noise,'' J. Acoust. Soc. Am. **104**, 3432–3445 (1998).
[6] H. M. Miedema and C. G. Oudshoorn, ''Annoyance from transportation noise: Relationships with exposure metrics DNL and DENL and their confidence intervals,'' Environ. Health Perspect. **109**, 409–416 (2001).
[7] R. S. Lazarus and S. Folkman, *Stress, Appraisal, and Coping* (Springer, New York, 1984).
[8] J. M. Fields and F. L. Hall, ''Community effects of noise,'' in *Transportation Noise* edited by Nelson P. M. (Butterworth, London, 1986), Chap. 3.
[9] P. Lercher and W. Kofler, ''Behavioral and health responses associated with road traffic noise exposure along alpine through-traffic routes,'' Sci. Total Environ. **189/190**, 85–89 (1996).
[10] P. Lercher, ''Context and coping as moderators of potential health effects in noise-exposed persons,'' in *Biological Effects*, Advances in Noise Series. Vol. I, edited by D. Prasher and L. Luxon (Whurr, London, 1998), pp. 328–335.
[11] T. Pulles, W. Biesiot, and R. Stewart, ''Adverse effects of environmental noise on health: An interdisciplinary approach,'' in: *Noise as a Public Health Problem*, edited by B. Berglund and T. Lindvall (Swedish Council for Building Research, Stockholm, 1990), Vol. 4, pp. 337–348.
[12] D. Botteldooren, A. Verkeyn, and P. Lercher, ''Noise annoyance modeling using fuzzy rule based systems,'' Noise Health **4**, 27–44 (2002).
[13] D. Botteldooren and A. Verkeyn, ''Fuzzy models for accumulation of reported community noise annoyance from combined sources,'' J. Acoust. Soc. Am. **112**, 1496–1508 (2002).
[14] D. Botteldooren, A. Verkeyn, and P. Lercher, ''A fuzzy rule based framework for noise annoyance modeling,'' J. Acoust. Soc. Am. **114**, 1487–1498 (2003).
[15] R. S. Lazarus, *Emotion and Adaptation* (Oxford University Press, New York, 1991).

[16] P. M. Cavalini, L. G. Koeter-Kemmerling, and M. P. J. Pulles, ''Coping with odour annoyance and odour concentrations: Three field studies,'' J. Environ. Psych. **11**, 123–142 (1991).
[17] B. Steinheider and G. Winneke, ''Industrial odours as environmental stressors: Exposure-annoyance-associations and their modification by coping, age and perceived health,'' J. Environ. Psych. **13**, 353–363 (1993).
[18] J. M. Campbell, ''Ambient stressors,'' Environ. Behav. **5**, 355–380 (1983).
[19] G. W. Evans and S. V. Jacobs, ''Air pollution and human behavior,'' J. Social Issues **37**, 95–125 (1981).
[20] K. Bachrach and A. Zautra, ''Coping with a community stressor: The threat of a hazardous waste facility,'' J. Health Soc. Behav. **26**, 127–141 (1985).
[21] S. Cohen, G. W. Evans, D. Stokols, and D. S. Krantz, *Behavior, Health, and Environmental Stress* (Plenum, New York, 1986).
[22] J. C. Bezdek, *Pattern Recognition with Fuzzy Objective Function Algorithms* (Plenum, New York, 1981).
[23] T. Kohonen, ''Self-organizing maps,'' Proc. IEEE **79**, 1464–1480 (1990).
[24] E. Alhoniemi, J. Himberg, J. Parhankangas, and J. Vesanto, SOM toolbox, http://www.cis.hut.fi/projects/somtoolbox
[25] K. Yamada, ''Probability—possibility transformation based on evidence theory,'' in Proceedings of IFSA World Congress, 2001, pp. 70–75.
[26] J. F. Geer and G. J. Klir, ''A mathematical analysis of information-preserving transformations between probabilistic and possibilistic formulations of uncertainty,'' Int. J. Gen. Syst. **20**, 143–176 (1992).
[27] D. Botteldooren, A. Verkeyn, C. Cornelis, and M. De Cock, ''On the meaning of noise annoyance modifiers,'' Acta Acust. united with Acustica **88**, 239–251 (2002).
[28] J. Lambert, F. Simonet, and M. Vallet, ''Patterns of behaviour in dwellings exposed to road traffic noise,'' J. Sound Vib. **92**, 159–172 (1984).
[29] H. Meijer, P. Knipschild, and H. Salle, ''Road traffic noise annoyance in Amsterdam,'' Int. Arch. Occup. Environ. Health **56**, 285–297 (1985).
[30] P. Lercher and U. Widmann, ''Factors determining community response to road traffic noise,'' in *Noise as a Public Health Problem*, edited by M. Vallet (Institut National de Recherche sur les Transports et leur Sécurité, Nice, 1993), Vol. 2, pp. 201–204.
[31] G. Winneke and M. Neuf, ''Separating the impact of exposure and personality in annoyance response to environmental stressors, particularly odors,'' Environ. Int. **22**, 73–81 (1996).
[32] R. S. Lazarus, ''Coping theory and research: Past, present, and future,'' Mod. Nurs. Home **55**, 234–247 (1993).
[33] G. W. Evans, ''Environmental stress and health,'' in *Handbook of Health Psychology*, edited by A. Baum, T. Revenson, and J. E. Singer (Erlbaum, Mahwah, NJ, 2001), pp. 365–385.
[34] J. M. Fields, R. G. De Jong, T. Gjestland, I. H. Flindell, R. F. S. Job, S. Kurra, P. Lercher, M. Vallet, T. Yano, R. Guski, U. Felscher-Suhr, and R. Schumer, ''Standardized general-purpose noise reaction questions for community noise surveys: research and a recommendation,'' Journal of Sound and Vibration **242**(4), 641–679 (2001).

Variability of low frequency sound transmission measurements

Teresa Bravo[a] and Stephen J. Elliott
Institute of Sound and Vibration Research, University of Southampton, Southampton SO17 1BJ, United Kingdom

(Received 20 October 2003; revised 7 March 2004; accepted 18 March 2004)

In this paper we discuss the characterization of low frequency sound transmission between two rooms via a flexible panel. A fully-coupled modal model is used to investigate the individual effect of the source room and the receiving room on the measured sound reduction index, and the results are compared with the ideal case of having a free field on both sides of the panel. The effect of the source room on the measured sound reduction index at low frequencies can be reduced by using a number of suitable-driven loudspeakers close to the panel to simulate a diffuse incident field. However, the effect of the receiving room was found not to be reduced by calculating the transmitted acoustic power from a dense array of acoustic intensity measurements, instead of an array of microphones in the receiving room. © *2004 Acoustical Society of America.*
[DOI: 10.1121/1.1738452]

PACS numbers: 43.55.Rg, 43.55.Br [SFW] Pages: 2986–2997

I. INTRODUCTION

The problem of calculating the sound reduction index of flexible partitions is important in the automotive, aerospace and building acoustics industries. Low frequency sound insulation has become more important recently, due to the increasing presence of noise sources in this frequency range.[1] Consequently, there is a growing demand for appropriate methods to predict and measure the sound insulation behavior of structures over the whole frequency range.

The fundamental concepts for sound insulation were first derived for infinite walls under free field conditions on both sides.[2,3] However, the most common technique to characterize the sound insulation through partitions makes use of two finite sized reverberation rooms in a sound transmission suite.[4] An acoustic field is created by one or several loudspeakers in the source room and transmitted to the receiving room via the panel, when all flanking transmission paths are neglected. The standards for the determination of sound insulation of building elements are derived assuming that the sound fields in both rooms are perfectly diffuse,[5] i.e., with equal probability of energy flow in all directions.[6,7] The diffuse field assumption is only valid in medium and high frequency ranges, since at low frequencies the sound field in the reverberation chambers is dominated by a few normal modes.[8] As the size of the transmission suite is not completely specified in the standards, different results will be obtained from different facilities at low frequencies.

Experimental work by several laboratories has demonstrated that the sound insulation at low frequencies can experience significant variations. In the 1960's Utley[3] compared the measured transmission loss with the mass law predictions, and pointed out that low frequency discrepancies occurred because of factors related with the rooms rather than with the panel itself. He proposed the use of standardized transmission suites or ''calibrating'' facilities by measuring the transmission loss of a heavy limp panel such as lead. The same conclusions are presented by Kihlman and Nilson[9] in an inter-laboratory comparison to study the influence of the mounting conditions and the laboratory design. More recently other comparisons between different facilities have been performed[10] to determine the parameters which needed to be strictly controlled, and provide information to extend the standards in the very low frequency range.

The standardization committees have included an annex in the ISO 140-3[5] in which they propose some guidance for the measurements of sound insulation in the low frequency bands. There are recommendations to increase the distance between microphone and room boundaries and the sampling of the sound field. It is also proposed to increase the number of loudspeaker positions, the averaging time, and the use of absorbing materials to decrease the reverberation time. In spite of the new methodology proposed, some experimental results have shown very poor reproducibility of the sound reduction index in the frequency range below 250 Hz and unacceptable reproducibility below 100 Hz.[11] It has been concluded that the actual standards did not provide essential improvements of the accuracy at very low frequencies.[12]

To better understand how the finite rooms modify the free field results, analytical and numerical methods have been used to describe the insulation properties of the dividing partition and the factors that contribute to observe differences in the low frequency range of such properties. Kihlman[13] used modal analysis to study errors in sound transmission measurements. He observed that systematic deviations could occur in the low frequency range if the source and receiving room have the same dimensions and explained the discrepancies in terms of the coupling between the bending waves of the wall and the normal modes in the rooms. Similar solutions have been employed by other authors[14–18] to study the influence on the measured low frequency sound reduction index of parameters such as room dimensions, source position, reverberation time, geometry of the interface or mounting conditions. The use of numerical solutions allows the introduction of more precise measurement condi-

[a]Electronic mail: tb@isvr.soton.ac.uk

 0001-4966/2004/115(6)/2986/12/$20.00 © 2004 Acoustical Society of America

tions that are simplified in the modal approach, such as different niches and supporting frames, nonparallel walls or nonuniform absorbing materials. Several authors[19,20] have presented a comparison between the modal method, the Finite Element Method (FE) and the Boundary Element Method (BEM), obtaining similar results. Maluski and Gibbs[21] have employed the FEM to study how the configuration of two identical reverberant rooms influences the transmission loss of a partition at low frequencies. The same authors[22] have shown that the room modes normal to the panel give rise to dips in level difference, especially if these are coincident with the panel resonances. Santos and Tadeu[23] have used the BEM to assess the influence of the parallelism between the surfaces of the chambers. They concluded that the largest differences between the results for an infinite wall and those for the transmission suite at low frequencies occurred when the walls were perfectly rectangular and built with rigid materials.

The consequences of different modal coupling on each subsystem have been used by Kropp *et al.*[24] to optimize the room parameters so that the measured sound reduction index is greatest. Using the Sequential Quadratic Programming method they found that a maximum in the sound insulation is reached when the length of the receiving room is half the length of the source room for both the 63 Hz and the 125 Hz octave bands. A similar result is obtained by Maluski and Gibbs,[21] who observed that if the room volumes differ by about 40%, the predicted sound insulation could increase by at least 3 dB. Kropp *et al.*[16] recommended performing the measurements in identical rooms so that the results would represent the worst case.

Thus, although there exist a lot of experimental and theoretical work on the variability of measurements at low frequencies, the problem of reducing this variability remains unsolved. The recommendations to increase the averaging of the field can improve the situation but the validity of the results is restricted to the specific conditions of the transmission suite. To minimize the modal effects, some modifications in the measurement procedures and test facilities have been suggested. Roland[25] has proposed covering the walls facing the partition in both the source and the receiving room with absorbent material to make the excitation and the radiation more uniform. Numerical simulations were presented using the mean pressure over the whole volume in the source room and the average intensity in a cross section in the receiving room, indicating an improvement in the dispersion of the results. A similar solution has been also proposed by Fuch *et al.*[26] using special broadband resonator absorbers, and by Pedersen *et al.*[12] placing absorbing material in the receiving room only. The intensity method has also been used for low frequency sound transmission measurements, and its results compared with the traditional method by several authors.[27,28] Ideally the receiving space should be very quiet and nonreverberant, as in the case of an anechoic room. It has been pointed out[29] that it would also be very advantageous to eliminate the use of the source room, but this is not possible because direct measurements of intensity on the source side would give the sum of the incident and reflected intensities.

This paper is aimed at improving the understanding of this problem by investigating the relative importance of the source and the receiving room in the determination of the sound reduction index at low frequencies. A detailed model of the sound transmission between the two rooms is developed in terms of the modal characteristic of the uncoupled subsystems for different set-up configurations. These different configurations are used to calculate several approximations to the sound reduction index, and the results of the numerical simulations are compared. A new approach to the problem is proposed. It is based on the generation of a pressure distribution in the source room with an array of loudspeakers close to the panel, which has the same spatial correlation characteristics than a diffuse field. The feasibility of the reproduction is analyzed in terms of several error criteria, and the effects of the simulation in the receiving room are also investigated.

II. SOUND REDUCTION INDEX FORMULATION

The sound insulation characteristic of a partition is usually characterized in terms of a sound reduction index, R, expressed by[7,30]

$$R(\omega) = 10 \log_{10}\left(\frac{\Pi_{\mathrm{inc}}(\omega)}{\Pi_{\mathrm{rad}}(\omega)}\right) \quad (\mathrm{dB}), \tag{1}$$

where $\Pi_{\mathrm{inc}}(\omega)$ and $\Pi_{\mathrm{rad}}(\omega)$ are the sound power incident and radiated by the partition, respectively, at frequency ω.

The determination of these quantities depends on the particular arrangement considered. In this section, the prediction of sound transmission through partitions in different laboratory-like configurations is compared to the case when the panel is mounted on an infinite baffle with free field conditions in both sides. The formulation has been developed for a single leaf, rectangular partition. This analysis is used to help understand the relative influence on the transmission loss of the source and receiving rooms, by considering four different methods of measuring the sound reduction index:

- With the partition situated in the transmission suite.
- With the partition coupled to the source room and radiating to free field.
- With the partition coupled to the receiving room only and excited by a diffuse field.
- With the partition situated in an infinite baffle and with free field conditions in both the source and receiving sides.

A. Cavity–panel–cavity model

Before considering the calculation of the sound reduction index it is necessary to determine the response of a coupled vibro-acoustic system to exciting sources. A general arrangement comprising two rectangular enclosures coupled via a common boundary has been considered here. For structures that have a simple geometry it is possible to use analytical descriptions for the *in vacuo* modal response of the structure and the rigid enclosed space. The two uncoupled models may then be coupled via modal theory. The formula-

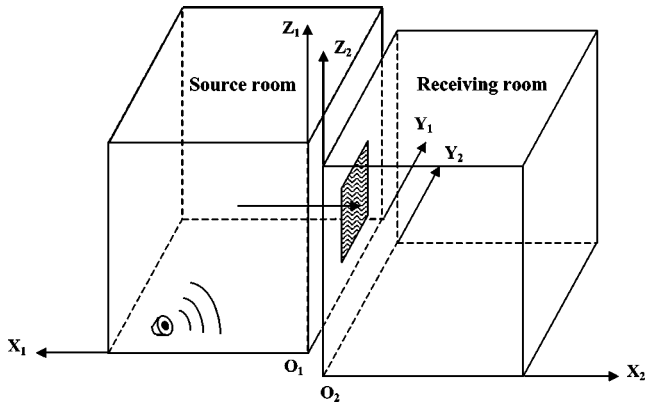

FIG. 1. Geometric arrangement of the source and receiving room connected through the partition.

tion of the response of the problem only depends on the modal properties of the subsystems involved and the nature of the excitation.

A fully-coupled system has been developed, where the pressure field in the source room is influenced by the panel motion and this is coupled with the pressure field in both the source and the receiving rooms. The approach is similar to that presented by Dowell *et al.*,[31] which has been recently summarized by Cazzolato.[32] It is assumed that there is no flanking transmission and that the panel joining the two rooms provides the only transmission path. A schematic representation of the system under study is shown in Fig. 1. The enclosures may be of different sizes, and the connecting panel may extend over some or all of the enclosure side.

The complex sound pressure at a point $\mathbf{r}$ in an enclosure of volume V and the structural velocity at a point $\mathbf{r}_p$ on a panel of surface S_p can be expressed, respectively, as a sum of modal terms of the form[33]

$$p(\mathbf{r},\omega)=\sum_{lmn=0}^{\infty} a_{lmn}^{(a)}(\omega)\psi_{lmn}(\mathbf{r}), \tag{2}$$

$$v(\mathbf{r}_p,\omega)=\sum_{qr=1}^{\infty} a_{qr}^{(p)}(\omega)\phi_{qr}(\mathbf{r}_p), \tag{3}$$

where $a_{lmn}^{(a)}(\omega)$ is the complex amplitude of the lmn acoustic pressure mode defined by the mode shape function $\psi_{lmn}(\mathbf{r})$ and the natural frequency ω_{lmn}, and $a_{qr}^{(p)}(\omega)$ is the complex amplitude of the qr structural mode defined by the mode shape function $\phi_{qr}(\mathbf{r}_p)$ and the natural frequency ω_{qr}.

After substituting (2) and (3) into the variational equations of motion for the cavity–panel–cavity system, one obtains the following coupled system for the modal amplitude in the source room, in the panel and in the receiving room, respectively:

$$a_{l_1m_1n_1}^{(1)}=\frac{\rho_0 c_0^2\omega}{V_1[2B_{l_1m_1n_1}\omega+j(\omega^2-\omega_{l_1m_1n_1}^2)]}\times\left(-\sum_{qr=1}^{\infty} a_{qr}^{(p)}G_{l_1m_1n_1,qr}^{(1)}+q_{l_1m_1n_1}^{(1)}\right), \tag{4}$$

$$a_{qr}^{(p)}=\frac{\omega}{jmS_p[\omega^2-(1+j\eta)\omega_{qr}^2]}\times\left(\sum_{l_1m_1n_1=0}^{\infty} a_{l_1m_1n_1}^{(1)}G_{l_1m_1n_1,qr}^{(1)}-\sum_{l_2m_2n_2=0}^{\infty} a_{l_2m_2n_2}^{(2)}G_{l_2m_2n_2,qr}^{(2)}\right), \tag{5}$$

$$a_{l_2m_2n_2}^{(2)}=\frac{\rho_0 c_0^2\omega}{V_2[2B_{l_2m_2n_2}\omega+j(\omega^2-\omega_{l_2m_2n_2}^2)]}\times\left(\sum_{qr=1}^{\infty} a_{qr}^{(p)}G_{l_2m_2n_2,qr}^{(2)}\right), \tag{6}$$

where ρ_0 is the fluid density, c_0 the speed of sound in the fluid, m is the surface density of the partition, B_{lmn} is the 3-dB (half power) bandwidth of the lmn acoustic mode, η is the hysteretic damping factor for the panel and $q_{l_1m_1n_1}^{(1)}$ is the generalized modal volume velocity of the sources in the first cavity. The term $G_{lmn,qr}$ is the modal coupling coefficient between the lmn acoustic mode and the qr structural mode. This term governs the coupling between the panel and the cavity and it is defined as

$$G_{lmn,qr}=\int_{S_p}\psi_{lmn}\phi_{qr}\mathrm{d}S. \tag{7}$$

The coupled system of equations can be solved for the complex modal amplitudes. The acoustic pressure in the cavities and the velocity in the panel can then be calculated using Eqs. (2) and (3), that have been used to characterize the transmission of sound between the source and the receiving rooms.

Assuming that the sound field in the two chambers is diffuse and provided that the sound is transmitted only through the dividing wall, the sound reduction index (in dB) may be evaluated from[7,30]

$$R=L_{\text{source}}-L_{\text{rec}}+10\log_{10}\left(\frac{S_p}{A_{\text{rec}}}\right), \tag{8}$$

where L_{source} is the average sound pressure level in the source room, L_{rec} is the average sound pressure level in the receiving room, S_p is the area of the dividing wall and A_{rec} is the equivalent absorption area of the receiving room, that can be determined from reverberation measurements. We can relate the mean square sound pressure average in a number of positions through the cavities to the acoustic potential energy, E_p, given by[34]

$$E_p(\omega)=\frac{1}{4\rho_0 c_0^2}\int_V |p(x,y,z;\omega)|^2\mathrm{d}V. \tag{9}$$

The acoustic pressure and structural velocities are expressed as an infinite summation of normal modes. In practice, it is necessary to truncate the series so that only a finite number of these will contribute to the response of the system. If we denote $\mathbf{a}$ the vector of complex mode amplitudes in the room, Eq. (9) can then be written as

$$E_p(\omega)=\frac{V}{4\rho_0 c_0^2}\mathbf{a}^{\mathrm{H}}\mathbf{a}. \tag{10}$$

After substituting Eq. (10) into Eq. (8) and operating, the expression for the sound reduction index of a partition between two reverberant chambers takes the final form

$$R=10\log_{10}\left(\frac{E_{p\ \mathrm{source}}}{E_{p\ \mathrm{rec}}}\frac{V_{\mathrm{rec}}}{V_{\mathrm{source}}}\right)+10\log_{10}\left(\frac{\mathrm{S}_p}{\overline{\alpha}_{\mathrm{rec}}2\cdot(s_{x\ \mathrm{rec}}+s_{y\ \mathrm{rec}}+s_{z\ \mathrm{rec}})}\right)\quad(\mathrm{dB}), \tag{11}$$

where $\overline{\alpha}_{\mathrm{rec}}$ is the average absorption coefficient of the receiving walls, assumed independent of frequency, and $s_{x\ \mathrm{rec}}$, $s_{y\ \mathrm{rec}}$ and $s_{z\ \mathrm{rec}}$ are the surface areas of the receiving room in the x, y and z directions, respectively.

B. Source room–panel model

The system now comprises the partition excited by the loudspeakers in the source room and radiating to the free field. This is an approximation to the experimental set-up employed when the reverberant receiving room is replace by an anechoic chamber.

The system of Eqs. (4)–(6) now becomes

$$a^{(1)}_{l_1m_1n_1}=\frac{\rho_0c_0^2\omega}{V_1[2B_{l_1m_1n_1}\omega+j(\omega^2-\omega^2_{l_1m_1n_1})]}\times\left(-\sum_{qr=1}^{\infty}a^{(p)}_{qr}G^{(1)}_{l_1m_1n_1,qr}+q^{(1)}_{l_1m_1n_1}\right), \tag{12}$$

$$a^{(p)}_{qr}=\frac{\omega}{jmS_p[\omega^2-(1+j\eta)\omega^2_{qr}]}\times\left(\sum_{l_1m_1n_1=0}^{\infty}a^{(1)}_{l_1m_1n_1}G^{(1)}_{l_1m_1n_1,qr}\right), \tag{13}$$

in which the influence of the receiving room has been eliminated.

For the calculation of the incident power the situation has not changed with respect to the previous section: it can be computed using the potential energy in the source room, Eq. (9), with the modal amplitudes obtained after solving the system of Eqs. (12)–(13).

The radiated power has been calculated in terms of the radiation of a number of discrete elements.[35,36] In this formulation, the partition is divided in a number of small piston sources of area s and the vector of complex linear velocities of each of these elemental sources, $\mathbf{v}$, is related to the vector of complex pressures immediately in front of each source, $\mathbf{p}$, by

$$\mathbf{p}=\mathbf{Z}\mathbf{v}, \tag{14}$$

where $\mathbf{Z}$ is a symmetric matrix of acoustic impedances. The power radiated by the array of elemental radiators is calculated as

$$\Pi_{\mathrm{rad}}=\mathbf{v}^{\mathrm{H}}\mathbf{R}\mathbf{v}. \tag{15}$$

In this expression, $\mathbf{R}$ is the matrix of radiation resistances that have the expression

$$\mathbf{R}=\frac{s}{2}\mathrm{Re}[\mathbf{Z}], \tag{16}$$

and whose elements are given by Elliott and Johnson,[35] and s is the surface of the elemental radiators, assumed to be of equal size. The vector of complex linear velocities at the positions of the elemental radiators can be written as

$$\mathbf{v}=\boldsymbol{\varphi}\mathbf{a}^{(p)}. \tag{17}$$

The elements of the matrix $\boldsymbol{\varphi}$ are the panel normal modes evaluated in the positions of the elemental radiators, and the complex modal amplitudes are the solutions of the coupled system of equations.

The sound reduction index at each frequency can then be calculated using Eq. (1).

C. Panel–receiving room model

It is also of interest to calculate the sound reduction index when the effect of the source room has been removed and the incident sound pressure on the partition corresponds to a pure diffuse field. This is approximated by the situation when calculating the sound is transmitted through vehicle walls, where cavity backed structures are encountered.

For the calculation of the power incident, a description of a diffuse pressure field is required. A proper model can be considered as an infinite number of plane waves with random phase relations, arriving uniformly from all the directions and with the propagating vector pointing toward the plate.[7,37]

The incident power over the panel is obtained through integration over a hemisphere surrounding the plate,[38,39] and takes the form

$$\Pi^{\mathrm{d}}_{\mathrm{inc}}=\int_0^{2\pi}\int_0^{\pi/2}\Pi_{\mathrm{inc}(\theta,\phi)}\sin\theta\mathrm{d}\theta\mathrm{d}\phi, \tag{18}$$

where $\Pi_{\mathrm{inc}(\theta,\phi)}$ is incident power due to one incident plane wave, given by

$$\Pi_{\mathrm{inc}(\theta,\varphi)}=\frac{|P_{\mathrm{inc}}|^2S_p}{2\rho_0c_0}\cos\theta. \tag{19}$$

The incident power on the partition is then calculated for each plane wave, defined by the angle (θ,φ) and the complex amplitude P_{inc}, to yield to the total acoustic incident power.

The model of the diffuse field used in this work corresponds to a stochastic approach described by Garcia-Bonito,[40] in which the diffuse field in the xy plane takes the form

$$p_{\mathrm{diff}}(x,y)=\sum_{K=1}^{K_{\max}}\sum_{L=1}^{L_{\max}}(a_{KL}+jb_{KL})\sin\theta_K\mathrm{e}^{jk(x\sin\theta_K\cos\phi_L+y\sin\theta_K\sin\phi_L)}. \tag{20}$$

The pressure field is due to a combination of $L_{\max}$ plane waves in the azimuthal direction (corresponding to azimuthal angles $\phi_L=2\pi L/L_{\max}$, $L=1,2,...,L_{\max}$) for each of the $\pi/K_{\max}$ vertical incident directions (corresponding to polar

angles $\theta_K = K\pi/K_{\max}$, $L = 1,2,...,K_{\max}$). The values of a_{KL} and b_{KL} are chosen from a random population with Gaussian distribution $N(0,1)$ and the multiplicative factor $\sin\theta_K$ is included to ensure that, on average, the energy associated with the incident waves is uniform from all directions. P_{inc} in Eq. (19) is then equal to $(a_{KL} + jb_{KL})$ in Eq. (20).

The integral in Eq. (18) is approximated by the sum of a sufficient number of plane waves uniformly distributed over the half space and the total response is the sum of the contribution due to each one. In this work, the double summation in Eq. (20) has been truncated in practice at $K_{\max}=8$ and $L_{\max}=32$, after checking that proper convergence was achieved in the frequency range of interest. This defines a set of 256 plane waves per sample of diffuse field, each of which is unaffected by any form of diffraction or reflection in the space where the model is applied.

The power radiated by the partition is calculated using the potential energy in the receiving room. To calculate the modal pressure amplitudes it is necessary to reformulate the theoretical description of the panel–cavity coupled configuration to account for the diffuse field excitation. The system of Eqs. (4)–(6) takes the form

$$a_{qr}^{(p)} = \frac{\omega}{jm[\omega^2 - (1+j\eta)\omega_{qr}^2]}\left(2|P_{\text{inc}}|I_q I_r - \frac{1}{S_p}\sum_{l_2 m_2 n_2 = 0}^{\infty} a_{l_2 m_2 n_2}^{(2)} G_{l_2 m_2 n_2, qr}^{(2)}\right), \tag{21}$$

$$a_{l_2 m_2 n_2}^{(2)} = \frac{\rho_0 c_0^2 \omega}{V_2[2B_{l_2 m_2 n_2}\omega + j(\omega^2 - \omega_{l_2 m_2 n_2}^2)]} \times\left(\sum_{qr=1}^{\infty} a_{qr}^{(p)} G_{l_2 m_2 n_2, qr}^{(2)}\right), \tag{22}$$

where the equation for the source room has been eliminated and the equation for the panel has been modified to include the modal terms when the panel is excited by one obliquely incident plane wave instead of being coupled with the first cavity. The factors I_q and I_r are given by Fuller *et al.*[41]

D. Free field model

In this model, a pure diffuse field is incident on the partition mounted in an infinite baffle, with free field conditions in both the source and the receiving sides.

The expressions for the calculation of the sound reduction index make use of the equations derived in the previous sections. The incident power on the panel has been approximated by integrating the contribution due to each individual plane wave, Eqs. (18)–(19).

The power radiated has been calculated using the formulation in terms of the elemental radiators, Eq. (17), in which the complex modal amplitudes when the panel is excited by an obliquely incident plane wave have the expression[41]

$$a_{qr}^{(p)} = \frac{2|P_{\text{inc}}|\omega I_q I_r}{jm[\omega^2 - (1+j\eta)\omega_{qr}^2]}. \tag{23}$$

The total radiated power is the sum over 256 incident waves. The individual results for the transmitted power due to each incident wave have been added together to calculate the total response to the diffuse field. For the calculation of the sound reduction index, Eq. (1) has been employed.

The differences obtained between this case and the previous finite sized models have been used as a measure of the influence of the modal behavior of the cavities in the sound reduction index.

III. NUMERICAL SIMULATIONS

The set of equations derived in the previous sections has been implemented in a numerical program to illustrate the influence of the modal behavior of the reverberant chambers.

The system analyzed in this work is the same than the one presented in Jo and Elliott.[42] It was motivated by an experimental investigation in a sound transmission suite located in the Institute of Sound and Vibration Research, and the same constants have been used to those measured in the physical set-up. When the numerical simulations have been repeated with a source and receiving room of different sizes and with other types of partitions, similar results are obtained.[43] The source and receiving rooms, of dimensions 2.07 m×2.52 m×2.51 m and 2.38 m×2.53 m×2.62 m, respectively, are connected via a simply supported aluminum panel of dimensions 0.69 m×0.69 m, assumed to have a thickness of 0.003 m, a Young's modulus of 70.3 GPa, a density of 2700 Kg/m^3 and a Poisson's ratio of 0.35. The partition was positioned centrally between the two rooms, as indicated in Fig. 1, with the (y,z) coordinates of the corner of the panel closest to the origin of (0.9 m, 0.91 m) for the source room, and of (0.9 m, 1.02 m) for the receiving room. This transmission suite has rather small source and receiving rooms, and would not normally be used to measure the low frequency sound reduction index, but was chosen in order to emphasize the problems with the modal responses of the source and receiving rooms. It was also hoped that the use of a near field loudspeaker array in the source room, as discussed below, would overcome at least some of these problems, and it would be possible to make accurate low frequency measurements in a significantly smaller transmission suite than was normally used.

The 3-dB bandwidth of the acoustic modes, B_{lmn} were deduced by assuming a random incidence acoustic absorption coefficient of the walls, $\overline{\alpha}$, independent of frequency.[44] The values of the acoustic absorption coefficients, $\overline{\alpha_1} = 0.11$ and $\overline{\alpha_2} = 0.08$ were chosen to be similar to those measured in the transmission suite.[42] The hysteretic loss factor of the panel, η, has been taken as 0.1. The pressure field in the source room was assumed to be generated by a loudspeaker situated in the corner opposite to the panel, at position 2 m, 0.1 m, 0.1 m, and modeled as a square piston source of dimensions 0.1 m×0.1 m.

Before using the model for the prediction of the sound reduction index in different configurations, several issues have been considered. In particular, the convergence properties of the modal model of the coupled system. Since the analysis of the coupled behavior of the system uses the *in vacuo* structural modes of the panel and the rigid walled modes for the cavities, the velocity predicted at the partition does not converge towards the exact value. The pressure field

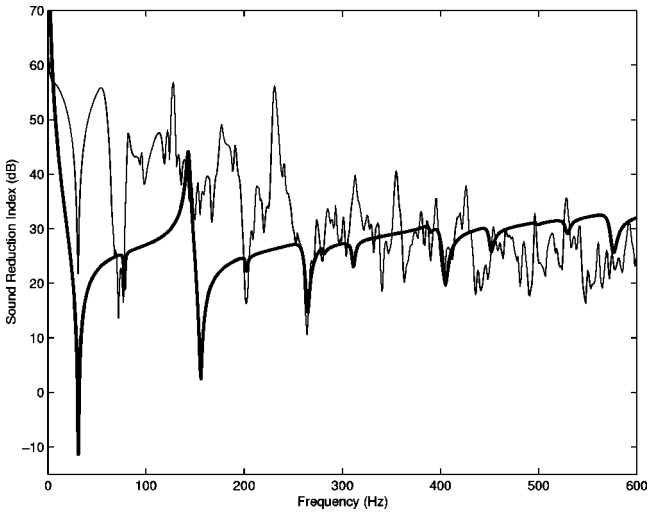

FIG. 2. Sound reduction index as a function of frequency for the aluminum partition calculated in the sound transmission suite (thin line) and mounted in an infinite baffle (thick line).

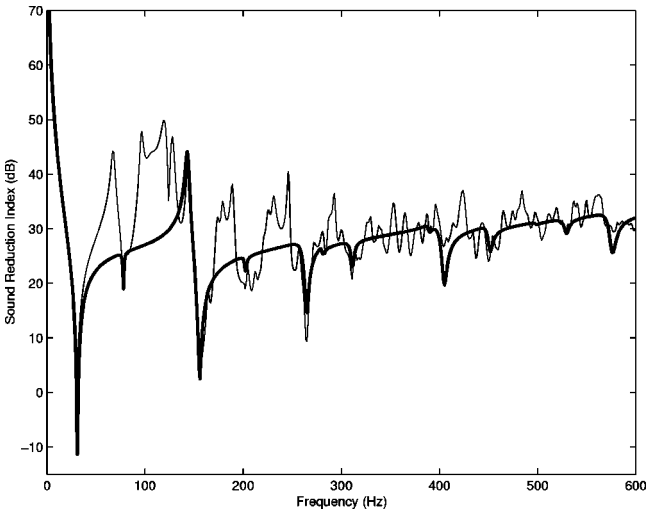

FIG. 3. Sound reduction index as a function of frequency for the aluminum partition connected to the source room only (thin line) and mounted in an infinite baffle (thick line).

is accurate in the interior of the cavity but can differ substantially in the vicinity of the vibrating surface,[43,45,46] and the effect of modal truncation could be critical for the convergence of the method. These factors have been studied as a function of the number of normal modes included in the summation. The simulation results have shown that there are no convergence problems for the source room as the pressure field is dominated by the primary source, and no substantial differences can be appreciated between accuracy of the pressure near and far from the partition. The situation is different for the receiving room. In this case, the truncated series of modal terms shows differences in the low frequency range and in close proximity to the panel. To achieve convergence, the modal superposition method must include a very high number of normal modes, making the method impractical since there is a trade-off between the calculation time and the accuracy of the solution.

The degree of coupling between the subsystems involved in the problem has also been analyzed. A weakly coupled model, where the panel motion is driven by the pressure field in the source room and only excites the receiving room, has been compared with the fully coupled system. The discrepancies are again more significant in the receiving room and they are also dependent on the number of normal modes included in the summation.

The number of modes used for this particular set-up has been 588 cavity modes for the source room, 28 structural modes for the panel and 695 cavity modes for the receiving room, which includes all the modes in the system up to 700 Hz. A fully-coupled system has been maintained in the simulations.

The differences for the sound reduction index estimated when the panel has free field conditions in the source and the receiving sides, and when a finite model has been used for its estimation are compared in Fig. 2 as a function of frequency. The sound reduction index for the plate in the free field is represented in bold. Overall, it follows the variation with frequency predicted by the mass law but also shows peaks corresponding to the normal modes of the finite sized plate. The peak corresponds to the frequencies at which the contribution to the volume velocity of the (1,1) panel mode almost cancels that due to the (3,1) mode, causing very little sound power to be radiated by the panel.

The sound reduction index for the partition in the transmission suite is also shown in Fig. 2. Two different regions can be distinguished: the low modal density zone, where the modal characteristics of the system are clearly visible, and the high modal overlap frequency range, above 300 Hz approximately. In the latter region, the curve has fewer peaks because of the increasing number of excited acoustic modes. The size of the discrepancy between the two curves, particularly below 300 Hz, implies that the results obtained in different measurement facilities must be considered carefully.

To better understand the relative influence of the source and the receiving rooms on the estimated sound reduction index, this has also been calculated for the source room–panel model, Sec. II B, and the panel–receiving room model, Sec. II C, and these are shown in comparison with the free field results in Figs. 3 and 4, respectively. It can be seen that in the low frequency range both rooms contribute to the differences in the measured transmission loss between the free field results and that in the transmission suite.

A summary of the results in this section in third octave bands is shown in Fig. 5. It is clear from these results that at very low frequencies, below 50 Hz, the modal properties of the source room alone (thin line) do not greatly affect the measured sound reduction index compared with the ideal free field results (thick line). This is because an almost uniform pressure is generated over the panel by the source room at these frequencies, which gives a good estimate of the incident power. The modal properties of the receiving room, which give results shown by the dotted line in Fig. 5, dominate the results obtained with the complete transmission suite, shown by the dashed line, because the modes of the receiving room amplify the mean square pressure in this room for a given panel excitation.

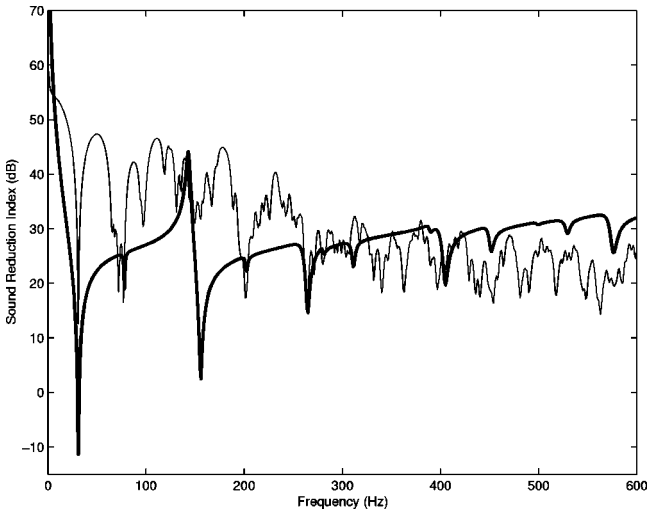

FIG. 4. Sound reduction index as a function of frequency for the aluminum partition connected to the receiving room only (thin line) and mounted in an infinite baffle (thick line).

IV. THE USE OF A NEAR FIELD ARRAY OF LOUDSPEAKERS IN THE SOURCE ROOM

The laboratory simulation of spatially correlated random pressure fields with an array of near field loudspeakers has been studied previously[47,48] for the reproduction of the wall-pressure field due to a Turbulent Boundary Layer (TBL). The initial objective was to provide a cost-effective procedure to measure the boundary layer noise transmitted through aircraft fuselage structures, but the domain of application is much broader.

Considering the problem of the lack of diffusivity of the low frequency sound pressure field in a transmission suite, a new methodology has been proposed in this work for the estimation of the sound reduction index. This new approach consists of using an array of loudspeakers driven by partially uncorrelated signals in the near field of the specimen to be evaluated and estimating the incident power by averaging the

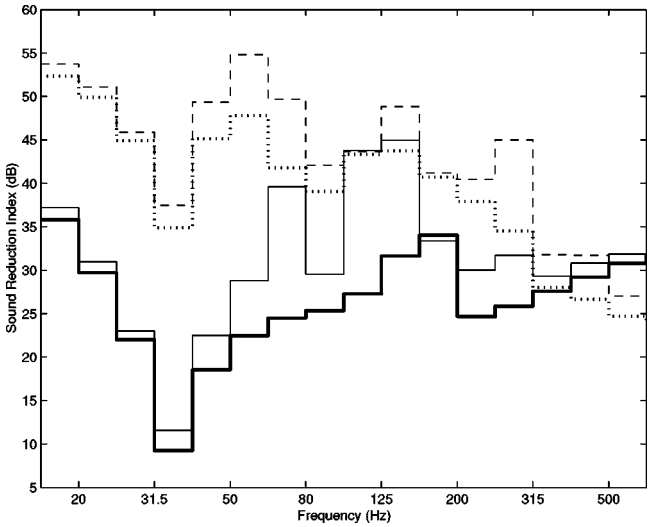

FIG. 5. Sound reduction index in third-octave bands for the aluminum partition mounted in an infinite baffle (thick line), connected to the source room only (thin line), connected to the receiving room only (dotted line) and in the sound transmission suite (dashed line).

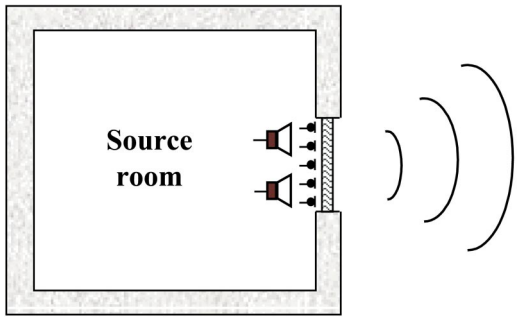

FIG. 6. Near field array of loudspeakers in the source room–panel configuration.

sound pressure level with a number of microphones situated in close proximity to the partition, as illustrated in Fig. 6.

A diffuse field can be modeled as a random process stationary both in space and time,[37] so the signal processing formulation initially developed for the reproduction of a TBL pressure field can be extended to the generation of a diffuse field for this case using the proper spatial correlation structure.

We thus consider an array of evenly spaced microphones situated over the plate on the source side. The microphone outputs provide a measure of the spatial variation of the pressure field, which ideally corresponds to that of a diffuse field, **d**. This can be assumed to be derived from a set of uncorrelated white unit variance reference signals, **x**, via a matrix of filters **D**, as illustrated in Fig. 7.

The matrix **D** can be calculated from the cross spectral matrix between the elements of the diffuse field pressures at the microphones,

$$\mathbf{S}_{dd} = \mathrm{E}[\mathbf{d}\mathbf{d}^{\mathrm{H}}], \tag{24}$$

where E denotes the expectation operator and the explicit dependence of the variables on frequency, ω, has been dropped for notational convenience. The diagonal terms of $\mathbf{S}_{dd}$ correspond to the power spectral densities of each of the microphones, which are the same in this case, and the off diagonal elements correspond to the cross spectral densities, which for two microphones A and B are assumed to be of the form[6,37]

$$\mathbf{S}_{AB}(\omega) = \mathbf{S}_{AA}(\omega)\frac{\sin k\mathbf{r}}{k\mathbf{r}}, \tag{25}$$

where $\mathbf{S}_{AA}(\omega)$ is the power spectral density at a single microphone, k is the acoustic wavenumber, ω/c_0 and $\mathbf{r}$ is the distance between the microphones A and B.

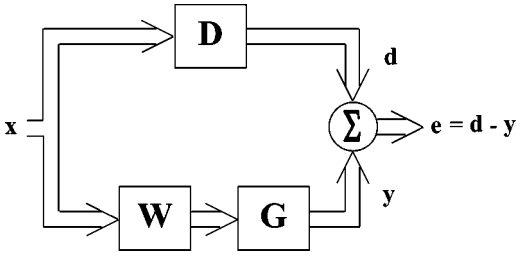

FIG. 7. Block diagram for the calculation of the least-squares control filter.

The eigenvalue/eigenvector decomposition of $\mathbf{S}_{dd}$ can be represented as

$$\mathbf{S}_{dd}=\mathbf{Q}\mathbf{\Lambda}\mathbf{Q}^{\mathrm{H}}=\mathbf{Q}\mathbf{\Lambda}^{1/2}(\mathbf{Q}\mathbf{\Lambda}^{1/2})^{\mathrm{H}}, \tag{26}$$

where $\mathbf{Q}$ is the matrix of eigenvectors and $\mathbf{\Lambda}$ is the matrix of positive real eigenvalues, whose square roots are denoted by $\mathbf{\Lambda}^{1/2}$. If $\mathbf{d}$ is generated by passing the reference signals, $\mathbf{x}$, through the filter matrix $\mathbf{D}$, then

$$\mathbf{S}_{dd}=\mathbf{D}\mathbf{S}_{xx}\mathbf{D}^{\mathrm{H}}, \tag{27}$$

but, since the reference signals are assumed to be uncorrelated and of unit amplitude, $\mathbf{S}_{xx}=\mathbf{I}$.

Thus Eq. (27) is equal to Eq. (26) if the matrix of filters is given by

$$\mathbf{D}=\mathbf{Q}\mathbf{\Lambda}^{1/2}. \tag{28}$$

The matrix of control filters, $\mathbf{W}$, is adjusted to determine the optimum input signals to an array of loudspeakers, which drive the sensor outputs, $\mathbf{y}$, to be as close as possible to those due to a diffuse field, $\mathbf{d}$.[47,49] The vector of error signals at a given frequency is thus defined to be

$$\mathbf{e}=\mathbf{d}-\mathbf{y}=(\mathbf{D}-\mathbf{G}\mathbf{W})\mathbf{x}, \tag{29}$$

where $\mathbf{G}$ is the matrix of acoustic responses between the near field loudspeakers and the near field microphones. $\mathbf{W}$ is then chosen to minimize the sum of the mean square elements of $\mathbf{e}$, which is equal to $\mathrm{Tr}(\mathbf{e}\mathbf{e}^{\mathrm{H}})$, where Tr is the trace operator.

Using the fact that the reference signals are uncorrelated, the optimal least-squares matrix of filters is given by[47,49]

$$\mathbf{W}_{\mathrm{opt}}=[\mathbf{G}^{\mathrm{H}}\mathbf{G}]^{-1}\mathbf{G}^{\mathrm{H}}\mathbf{D}=\mathbf{G}^{\dagger}\mathbf{D}, \tag{30}$$

where $\mathbf{G}^{\dagger}$ is the pseudo-inverse of $\mathbf{G}$.

Once the matrix of filters driving the loudspeakers has been optimized, the estimation of the sound reduction index in different configurations can be analyzed. In the next sections numerical results are presented in the source room–panel configuration and in the cavity–panel–cavity configuration.

A. Source room–panel configuration

In this section, an array of loudspeakers is situated in the near field of the object to be tested when this is coupled to the source room only, and with free field conditions in the receiving side. An array of twenty by twenty microphones, uniformly spaced over the length and width of the panel, has been exposed to the pressure field generated by a two by two array of secondary sources, as shown in Fig. 6, driven either by a set of uncorrelated signals or adjusted optimally according to Eq. (30).

To characterize the incident sound power in the source room using the classical method, the mean square sound pressure is averaged within the source room. Previously, we have related this quantity to the acoustical potential energy in the source room. In the new approach, the near field array of loudspeakers is aimed to produce an appropriate wall-pressure field over the surface of the panel and the measurement procedure has to be adapted accordingly.

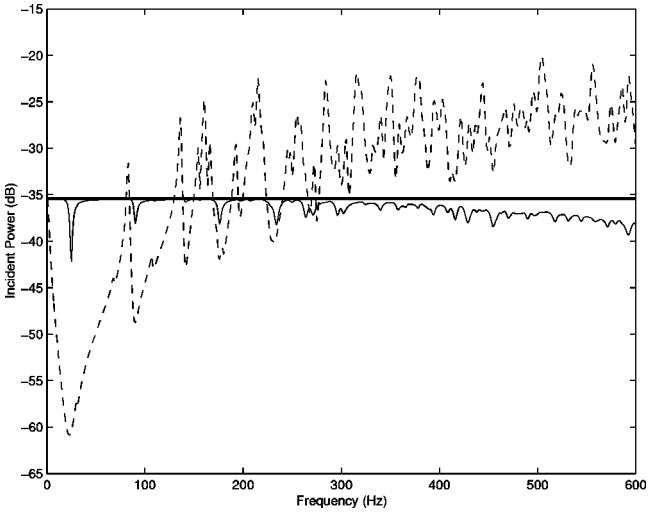

FIG. 8. Incident power for the aluminum partition in an infinite baffle under diffuse field excitation conditions (thick line), and in the source room–panel configuration obtained with four near field loudspeakers: optimized array (thin line) and uncorrelated array (dashed line).

The incident sound power has been calculated considering the mean square sound pressure averaged over the positions of the array of microphones over the partition, as

$$\Pi_{\mathrm{inc}}=\frac{s_r\mathrm{Tr}(\mathbf{y}\mathbf{y}^{\mathrm{H}})}{4\rho_0 c_0}, \tag{31}$$

where $\mathbf{y}$ is the vector of sensor outputs and s_r is the surface of the elements in the grid of microphones.

Substituting the value of the microphones signals, Eq. (31) takes the form

$$\Pi_{\mathrm{inc}}=\frac{s_r\mathrm{Tr}(\mathbf{G}\mathbf{W}\mathbf{W}^{\mathrm{H}}\mathbf{G}^{\mathrm{H}})}{4\rho_0 c_0}, \tag{32}$$

where $\mathbf{G}$ is the transfer function between the loudspeakers and the microphone positions for a cavity–panel coupled system, that can be calculated from the equations in Sec. II B and $\mathbf{W}$ is the matrix of control filters.

If the array of loudspeakers is driven by a set of uncorrelated signals $\mathbf{W}$ is a matrix with a number of ones equal to near field loudspeakers in the diagonal and all the other elements equal to zero. If the near field sources are adjusted for the reproduction of a diffuse pressure field over the surface of the partition, the expression for the incident power after the value for $\mathbf{W}_{\mathrm{opt}}$ has been substituted is given by

$$\Pi_{\mathrm{inc\ opt}}=\frac{s_r\mathrm{Tr}(\mathbf{G}\mathbf{G}^{\dagger}\mathbf{S}_{dd}\mathbf{G}^{\dagger\mathrm{H}}\mathbf{G}^{\mathrm{H}})}{4\rho_0 c_0}. \tag{33}$$

The radiated power in free field conditions has been calculated using Eqs. (15)–(17), in which the response of the panel to the uncorrelated or optimized set of loudspeakers has been calculated according to the equations for the cavity–panel coupled system, Sec. II B.

This set of equations has been implemented in a program to calculate the incident power and the radiated power, that are presented individually in Figs. 8 and 9, respectively. The results assuming a pure diffuse field in the source and receiving rooms (thick line) are compared to the case when

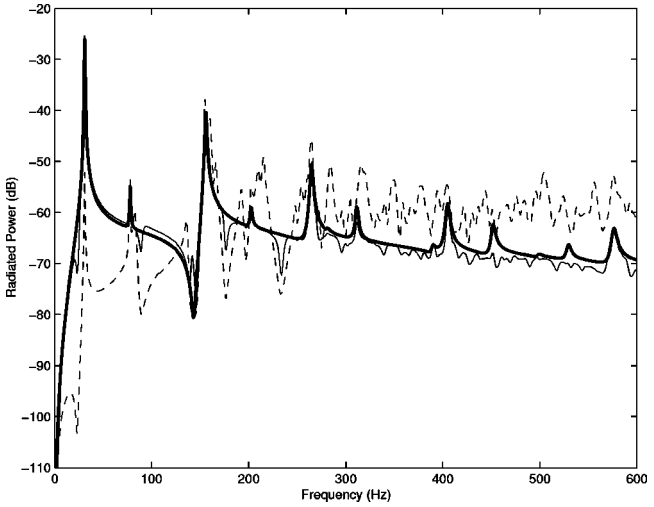

FIG. 9. Radiated power for the aluminum partition in an infinite baffle under diffuse field excitation conditions (thick line), and in the source room–panel configuration obtained with four near field loudspeakers: optimized array (thin line) and uncorrelated array (dashed line).

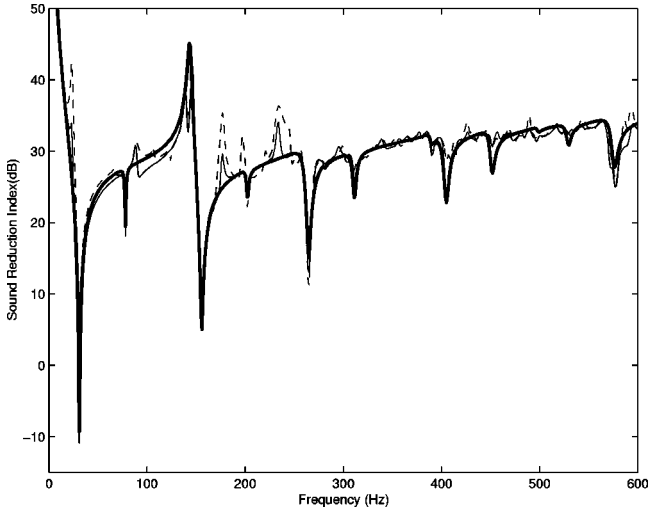

FIG. 10. Sound reduction index for the aluminum partition in an infinite baffle under diffuse field excitation conditions (thick line), and in the source room–panel configuration obtained with four near field loudspeakers: optimized array (thin line) and uncorrelated array (dashed line).

the partition is mounted in the source room and the near field array of loudspeakers is driven by uncorrelated signals (dashed line) or is optimized to reproduce a diffuse field over the surface of the panel (thin line). It can be seen that for the incident power, the optimized set of sources is able to provide a good approximation to the theoretical value in comparison with the uncorrelated array. In the latter case, the modal influence of the source room on the incident power is clearly seen. As the panel has free field conditions on the receiving side, the results obtained for the radiated power, Fig. 9, when the loudspeakers are optimized follow quite closely those obtained for a diffuse acoustic excitation. On the other hand, the graph for the set of uncorrelated signals is much more influenced by the modal coupling between the cavity and the panel, although the filtering effect due to the structure can still be seen.

The sound reduction index calculated for the three excitation models is shown in Fig. 10. Although important differences have been found in the incident and radiated power when the loudspeakers are uncorrelated or optimized, when calculating the ratio of the two quantities the discrepancies are not so evident. In the high modal overlap frequency range, the two types of excitation have an almost identical performance, which is also very close to the theoretical free field results. In the low frequency range, below 300 Hz, the optimized array provides slightly better results than the uncorrelated sources, but the improvement is not very significant.

Although the results are not presented here, it has been found that when a greater number of loudspeakers is employed, the results for the optimized array of loudspeakers get closer to the ones obtained for a diffuse field excitation, whereas the performance of the uncorrelated sources does not significantly change. In practical terms, however, four loudspeakers driven by uncorrelated random signals give a good approximation to the expected result in this case.

Figure 11 shows a direct comparison between the sound reduction index obtained for this configuration using the classical method and the new approach proposed. In the first case, four far field loudspeakers in the source room distributed according to the recommendations specified in the ISO 140-3 have been driven by a set of uncorrelated signals, and the power incident on the partition has been calculated using the potential energy of the source room. In the second case, the four near field loudspeakers have been situated close to the panel and optimized for the reproduction of a diffuse pressure field, and the power incident is taken proportional to the mean square sound pressure average on the positions of the array of microphones over the partition. The improvement in measured sound reduction index compared with the free field results is clearly seen in the low frequency regime. The near field array is able to provide an estimation of the sound reduction index that depends almost entirely on the

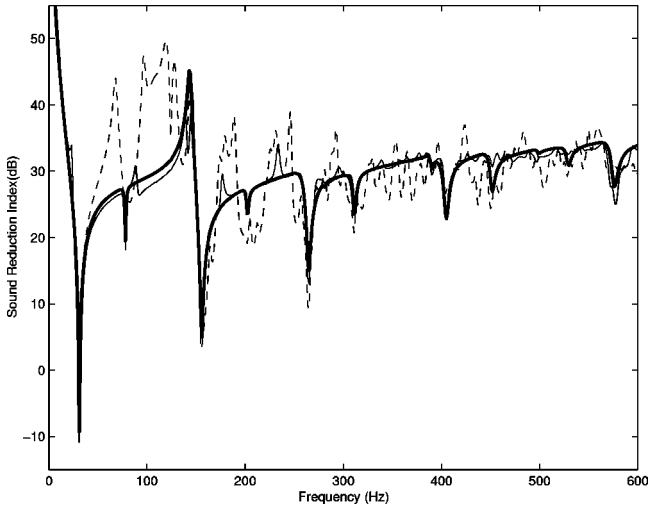

FIG. 11. Sound reduction index for the aluminum partition in an infinite baffle under diffuse field excitation conditions (thick line), and in the source room–panel configuration obtained with four near field optimized loudspeakers (thin line) and four far field uncorrelated loudspeakers (dashed line).

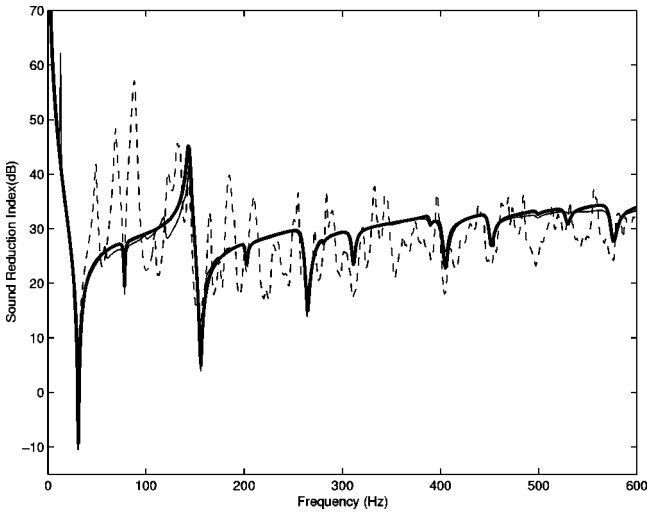

FIG. 12. Sound reduction index for the aluminum partition in an infinite baffle under diffuse field excitation conditions (thick line), and in the source room–panel configuration obtained with four near field optimized loudspeakers (thin line) and four far field uncorrelated loudspeakers (dashed line) when the dimensions of the source room have been changed to 3.07 m×3.52 m×3.51 m.

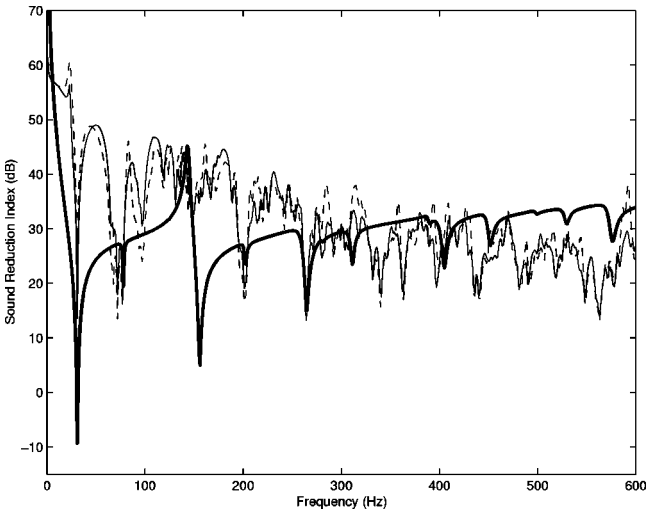

FIG. 13. Sound reduction index for the aluminum partition in an infinite baffle under diffuse field excitation conditions (thick line), and in the transmission suite using inner volume measurements in the receiving room with four near field loudspeakers: optimized array (thin line) and uncorrelated array (dashed line).

characteristics of the panel, eliminating the modal influence of the source room.

To further emphasize the advantages of this method, some numerical simulations have been carried out when the dimensions of the source room have been increased. Both the conventional and the new, near field, methodology described above have been applied for the estimation of the sound reduction index of the partition. The results are presented in Fig. 12. It can be seen that the estimation of the sound reduction index calculated with the conventional approach has changed significantly with respect to the previous case, as it depends on the modal behavior of the room, but the results of the near field method have not. Moreover, the high modal overlap region has increased with the dimensions of the cavity and the near field array of loudspeakers is thus able to provide even better results than in the previous case.

B. Cavity–panel–cavity configuration

In this section the partition is situated in the transmission suite, between the source and the receiving reverberant chambers, and the two by two array of loudspeakers and twenty by twenty microphone array are situated in the source room, in the near field of the partition.

The computation of the incident power over the panel has again been based on the outputs of the near field array of microphones, Eqs. (32) and (33), where the transfer function **G** between loudspeakers and microphones has been modified to account for the fully coupled system cavity–panel–cavity presented in Sec. II A. The power radiated in the receiving room has been calculating classically, using the potential energy over the whole cavity.

The results obtained in the numerical simulations for the incident and radiated power in the transmission suite show important differences when comparing with the cavity–panel configuration. The four near field loudspeaker array is still able to provide a good result for the incident power on the panel in the source room, with identical results for the optimized set of signals and very similar results when the loudspeakers are uncorrelated. However, the influence of the receiving room is now strong in both cases. The corresponding sound reduction index, calculated from the mean square sound pressure level averaged over the panel and using the potential energy in the receiving room, is presented in Fig. 13. The introduction of the receiving room has greatly modified the previous results, and the sound reduction index calculated using the near field array is no longer similar to the free field results, but is clearly influenced by the modal characteristics of the receiving room.

An alternative procedure for measuring the transmitted sound power in the source room has also been considered, using the sound intensity normal to the panel, determined at a dense grid of measurements on a surface covering the test opening. In this case, the acoustic power radiated is proportional to the real part of the sum of the conjugate volume velocities of each radiator, **v**, multiplied by the corresponding pressure in the receiving room, $\mathbf{p}^{(2)}$, immediately in front of each source, as

$$\Pi_{\text{trans}} = \frac{S}{2}\,\text{Re}[\mathbf{v}^{\text{H}}\mathbf{p}^{(2)}], \tag{34}$$

where the velocity of the panel and the pressure in the receiving room have been calculated from the system of equations in Sec. II A.

The results for the sound reduction index with the incident power calculated from the mean square sound pressure over the panel in the source room and the transmitted power calculated from the sound intensity in the receiving room are presented in Fig. 14. The sound reduction index measured in the transmission suite is still very different from the ideal, free field, value and is not very different from that measured using microphones in the receiving room, as shown in Fig. 13. This result has also been pointed out by Kropp *et al.*[16] when comparing experimental results obtained for the trans-

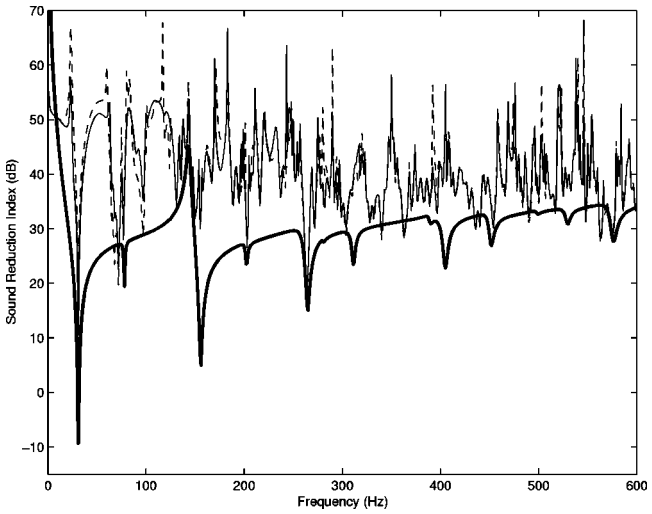

FIG. 14. Sound reduction index for the aluminum partition in an infinite baffle under diffuse field excitation conditions (thick line), and in the transmission suite using intensity surface measurements in the receiving room with four near field loudspeakers: optimized array (thin line) and uncorrelated array (dashed line).

mitted sound power with the averaged pressure level and the intensity method. The influence of the receiving room on the transmitted power could be potentially reduced by the use of moving diffusers in the receiving room, or if a larger and more anechoic receiving room was used.

V. CONCLUSIONS

This work has discussed the variability of sound reduction index measurements in the low frequency range. In practice, panels are often tested in finite sized reverberant chambers, where the acoustic field is dominated in the low frequency range by a few normal modes and does not satisfy diffuse field conditions. The use of different facilities can lead to a wide spread of results. An analytical formulation for the calculation of the sound reduction index of flexible partitions has been presented and the results compared when the panel is mounted in an infinite baffle with free field conditions on both sides and when the effects of the source and receiving room are each taken into account. The determination of the sound reduction index has been formulated using a modal approach for the cavities and the panel. A fully coupled model has been maintained in the numerical simulations. The results obtained in the transmission suite and in the free field show discrepancies of greater than 20 dB in the low frequency range.

These differences have been attributed to the modal response of the reverberation rooms for a long time, but no effective solution has been found to address this problem. The recommendations proposed in ISO 140-3, averaging the source positions and the field sampling can only improve the situation slightly. To make the measurement of the incident power more reliable at low frequencies, the use of an array of loudspeakers in the near field of the object to be tested has been proposed. The sources have been driven by a set of uncorrelated signals or have been optimized to reproduce a diffuse pressure field on the surface of the panel.

This new approach has been tested numerically. It has been shown that in the case where the panel is driven by a source room but radiating into an anechoic chamber, an array of four near field loudspeakers is able to remove the modal influence of the source room in the low frequency range. For the particular configuration analyzed here, no significant differences have been found in the sound reduction index when the loudspeakers are uncorrelated or when they have been optimally adjusted for the reproduction of a wall-pressure diffuse field over the panel. The new approach proposed is able to provide a measure of the sound reduction index that only depends on the properties of the panel itself, avoiding the modal problems presented in the classical method. The dimensions of the source room could be significantly reduced, even for low frequency testing, if such a near field array was used.

However, when the sound reduction index is determined in a transmission suite, the results are strongly influenced by the modal response of the receiving room, and are still significantly different from the free field results at low frequencies. Similar results are obtained whether the transmitted sound power is estimated from the mean-square pressure in the receiving room, or from a dense grid of intensity measurements over the panel.

Future work will be directed towards the experimental verification of the proposed technique in a real sound transmission suite. This will require *in situ* measurements of the transfer functions between the near field array of loudspeakers and microphones. The measured frequency responses can be used for numerical off-line simulations within the signal processing framework previously described and assess the accuracy of the proposed methodology. On-line sound reduction index measurements can then be performed by driving the array of loudspeakers with a set of appropriate signals. In practice, for highly absorbent thick panels, some care must be taken to avoid or account for flanking transmission paths.

ACKNOWLEDGMENT

This research has been supported through a European Marie Curie Fellowship, Contract No. HPMF-CT-2002-01618.

[1] J. Mathys, ''Low-frequency noise and acoustical standards,'' Appl. Acoust. **40**, 185–199 (1993).
[2] P. E. Sabine, ''Weight as a determining factor in sound transmission,'' J. Acoust. Soc. Am. **4**, 38–43 (1932).
[3] W. A. Utley, ''Single leaf transmission loss at low frequencies,'' J. Sound Vib. **8**, 256–261 (1968).
[4] A. C. Nilsson, ''Reduction index and boundary conditions for a wall between two rectangular rooms. Part I: Theoretical results,'' Acustica **26**, 1–18 (1972).
[5] BS EN ISO 140-3. Acoustics, Measurement of Sound Insulation in Buildings and of Buildings Elements. Part 3: Laboratory Measurements of Airborne Sound Insulation of Building Elements, 1995.
[6] F. Jacobsen, ''The diffuse sound field,'' The Acoustic Laboratory, Technical University of Denmark, Report No. 27, 1979.
[7] L. L. Beranek and I. L. Vér, *Noise and Vibration Control Engineering. Principles and Applications* (Wiley, New York, 1992).
[8] M. R. Schroeder, ''The Schroeder frequency revisited,'' J. Acoust. Soc. Am. **99**, 3240–3241 (1996).
[9] T. Kihlman and A. C. Nilson, ''The effect of some laboratory design and mounting conditions on reduction index measurements,'' J. Sound Vib. **24**, 349–364 (1972).

[10] L. Gagliardini, F. Batifo, and D. B. Pedersen, ''The use of numerical simulation to investigate measurement methods of the sound reduction index in the very low frequency range,'' *Proc. Euronoise 95*, Lyon, France, 1995, pp. 477–482.
[11] J. Roland, ''Adaptation of existing test facilities to low frequencies measurements,'' *Proceedings of Internoise 95*, Newport Beach, CA, 1995, pp. 1113–1116.
[12] D. B. Pedersen, J. Roland, G. Raabe, and W. Maysenhölder, ''Measurement of the low-frequency sound insulation of building components,'' Acust. Acta Acust. **86**, 495–505 (2000).
[13] T. Kihlman, ''Sound radiation into a rectangular room. Applications to airborne sound transmission in buildings,'' Acustica **18**, 11–20 (1967).
[14] K. A. Mulholland and R. H. Lyon, ''Sound insulation at low frequencies,'' J. Acoust. Soc. Am. **54**, 867–878 (1972).
[15] L. Gagliardini, J. Roland, and J. L. Guyader, ''The use of a functional basis to calculate acoustic transmission between rooms,'' J. Sound Vib. **143**, 457–478 (1991).
[16] W. Kropp, A. Pietrzyk, and T. Kihlman, ''On the meaning of the sound reduction index at low frequencies,'' Acta Acust. (Beijing) **2**, 379–392 (1994).
[17] A. Osipov, P. Mees, and G. Vermeir, ''Numerical simulations of airborne sound transmission at low frequencies: the influence of the room and the partition parameters,'' *Proc. of Internoise 97*, Budapest, Hungary, 1997, pp. 759–762.
[18] A. Osipov, P. Mees, and G. Vermeir, ''Low-frequency airborne sound transmission through single partitions in buildings,'' Appl. Acoust. **52**, 273–288 (1997).
[19] A. Pietrzyk and D. B. Pedersen, ''Numerical simulations of laboratory sound insulation determination experiments,'' *Proceedings of Internoise 96*, Liverpool, United Kingdom, 1996, pp. 1773–1778.
[20] V. Cutanda and A. Pietrzyk, ''Low frequency sound transmission measurements and numerical simulations: a comparative study,'' *Proceedings of Internoise 97*, Budapest, Hungary, 1997, pp. 1449–1452.
[21] P. S. Maluski and B. Gibbs, ''Application of a finite-element model to low-frequency sound insulation in dwellings,'' J. Acoust. Soc. Am. **108**, 1741–1751 (2000).
[22] P. S. Maluski and B. Gibbs, ''The inter-relation between the modal characteristics of the rooms and the separating wall in the sound insulation between dwellings at low frequencies,'' *Proceedings of Forum Acusticum*, Sevilla, Spain, 2002.
[23] P. Santos and A. Tadeu, ''A note on the acoustic insulation between two-dimensional acoustic spaces at low frequencies,'' J. Sound Vib. **261**, 185–191 (2003).
[24] W. Kropp, A. Pietrzyk, and T. Kihlman, ''Optimization of sound insulation at low frequencies,'' in Ref. 19, pp. 865–870.
[25] J. Roland, ''Adaptation of existing test facilities to low frequencies measurements,'' in Ref. 11, pp. 1113– 1116.
[26] H. V. Fuchs, X. Zha, M. Späh and M. Pommerer, ''Qualification of small freefield and reverberation rooms for low frequencies,'' *Proceedings of Euronoise 98*, 1998, pp. 657–662.
[27] R. E. Halliwell and A. C. C. Warnock, ''Sound transmission loss: comparison of conventional techniques with sound intensity techniques,'' J. Acoust. Soc. Am. **77**, 2094–2103 (1985).
[28] M. Volander and A. C. C. Warnock, ''Inter-laboratory comparisons of low frequency sound transmission: conventional and intensity methods,'' *Proceedings of Internoise 93*, Leuven, Belgium, 1993, pp. 933–936.
[29] M. J. Crocker, P. K. Raju, and B. Forssen, ''Measurement of transmission loss of panels by the direct determination of transmitted acoustic intensity,'' Noise Control Eng. J. **17**, 6–11 (1981).
[30] M. D. Egan, *Concepts in Architectural Acoustic* (McGraw-Hill, New York, 1972).
[31] E. H. Dowell, G. F. Gorman, and D. A. Smith, ''Acoustoelasticity: General theory, acoustic natural modes and forced response to sinusoidal excitation, including comparisons with experiments,'' J. Sound Vib. **52**, 519–542 (1977).
[32] B. Cazzolato, ''Sensing systems for active control of sound transmission into cavities,'' Ph.D. dissertation, The University of Adelaide, 1999.
[33] P. M. Morse, *Vibration and Sound*, 2nd ed. (McGraw-Hill, New York, 1948) (reprinted in 1981 by the Acoustical Society of America).
[34] P. A. Nelson, A. R. D. Curtis, S. J. Elliott, and A. J. Bullmore, ''The active minimization of harmonic enclosed sound fields, Part I: Theory,'' J. Sound Vib. **117**, 1–13 (1987).
[35] S. J. Elliott and M. E. Johnson, ''Radiation modes and the active control of sound power,'' J. Acoust. Soc. Am. **94**, 2194–2204 (1993).
[36] M. E. Johnson, ''Active control of sound transmission,'' Ph.D. thesis, The University of Southampton, United Kingdom, 1996.
[37] A. D. Pierce, *Acoustics, an Introduction to its Physical Principles and Applications* (McGraw Hill, New York, 1981).
[38] R. Panneton and N. Atalla, ''Numerical prediction of sound transmission through finite multiplayer systems with poroelastic materials,'' J. Acoust. Soc. Am. **100**, 346–354 (1996).
[39] F. C. Sgard, N. Atalla, and J. Nicolas, ''A numerical model for the low frequency diffuse field sound transmission loss of double-wall sound barriers with elastic porous linings,'' J. Acoust. Soc. Am. **108**, 2865–2872 (2000).
[40] J. Garcia-Bonito, ''Local active control in pure tone diffracted diffuse sound fields,'' Ph.D. thesis, The University of Southampton, United Kingdom, 1996.
[41] C. R. Fuller, S. J. Elliott and P. A. Nelson, *Active Control of Vibration* (Academic, London, 1996).
[42] C. H. Jo and S. J. Elliott, ''Active control of low-frequency sound transmission between rooms,'' J. Acoust. Soc. Am. **92**, 1461–1472 (1992).
[43] T. Bravo and S. J. Elliott, *Sound Transmission Testing at Low Frequencies*, ISVR Technical Memorandum No. 921, The University of Southampton, United Kingdom, 2003.
[44] P. A. Nelson and S. J. Elliott, *Active Control of Sound* (Academic, London, 1992).
[45] F. J. Fahy, *Sound and Structural Vibration: Radiation, Transmission and Response* (Academic, London, 1985).
[46] V. Jayachandran, S. M. Hirsch, and J. Q. Sun, ''On the numerical modelling of interior sound fields by the modal function expansion approach,'' J. Sound Vib. **210**, 243–254 (1998).
[47] S. J. Elliott, P. Gardonio, and C. Maury, ''A feasibility study for the laboratory simulation of turbulent boundary layer pressure fields,'' *Proceedings of the 7th AIAA/CEAS Aeroacoustics Conference*, AIAA 2001–2194, 2001.
[48] C. Maury, S. J. Elliott, and P. Gardonio, ''A convergence study for the laboratory simulation of random pressure fields,'' on the CD-ROM *Proceedings of the Institute of Acoustics*, University of Salford, United Kingdom, 2002.
[49] S. J. Elliott, *Signal Processing for Active Control* (Academic, London, 2000).

Estimation of ultrasound wave aberration with signals from random scatterers

Svein-Erik Måsøy[a] and Bjørn Angelsen
Department of Circulation and Imaging, Norwegian University of Science and Technology, Trondheim, Norway

Trond Varslot
Department of Mathematical Sciences, Norwegian University of Science and Technology, Trondheim, Norway

(Received 9 September 2003; revised 22 March 2004; accepted 22 March 2004)

A method for estimating waveform aberration from random scatterers in medical ultrasound imaging has been derived and its properties investigated using two-dimensional simulations. The method uses a weighted and modified cross-spectrum in order to estimate arrival time and amplitude fluctuations from received signals. The arrival time and amplitude fluctuations were used in a time delay, and a time delay and amplitude aberration correction filter, for evaluation of the retransmitted aberration corrected signal. Different types of aberration have been used in this study. First, aberration was concentrated on the plane of the transmitting/receiving array. Second, aberration was generated with a distributed aberrator. Both conditions emulated aberration from the human abdominal wall. Results show that for the concentrated aberrator, arrival time and amplitude fluctuations were estimated in close agreement with reference values. The reference values were obtained from simulations with a point source in the focal point of the array. Correction of the transmitted signal with a time delay, and a time delay and amplitude filter produced approximately equal correction as with point source estimates. For the distributed aberrator, the estimator performance degraded significantly. Arrival time and amplitude fluctuations deviated from reference values, leading to a limited correction of the retransmitted signal. © *2004 Acoustical Society of America.* [DOI: 10.1121/1.1738840]

PACS numbers: 43.58.Ry, 43.20.Fn, 43.60.Cg, 43.60.Tj, 43.80.Vj [TDM] Pages: 2998–3009

I. INTRODUCTION

Aberration in medical ultrasound imaging, mainly due to the inhomogeneities in the human body wall, enlarges the insonified scatterer region because of a defocusing of the transmitted beam.[1–6] This effect blurs the ultrasound image and reduces the physicians ability to make an accurate diagnosis.

There are two main objectives of this article.

(1) Investigate a method developed for estimating arrival time and amplitude fluctuations using signals from random scatterers.

(2) Test the estimator under two different aberration situations. First, a concentrated aberrator where all aberration is concentrated to a plane on the transmitting/receiving array. Second, a distributed aberrator with a specified thickness. Both aberration situations emulated the human abdominal wall.

Aberration correction is often based on estimating arrival time, or arrival time and amplitude fluctuations, which are used as a correction filter on transmit of the ultrasonic signal.[1,3,6–12] This method is here referred to as a time delay, or a time delay and amplitude aberration correction filter.

The time reversal mirror introduced by Fink *et al.*,[13] requires a point source in the insonified medium, which rarely is the case in an imaging situation. Liu and Waag[14] introduced a back-propagation method which propagates the signal homogeneously backward in time in order to obtain an optimal situation for estimation of a time delay screen. It is not yet sure if this method performs better for transmit correction than time delay correction estimated at the array surface.[15] In Ref. 12, it was shown that if arrival time and amplitude fluctuations in the received signals are accurately estimated, they will produce close to ideal aberration correction when used as a time delay and amplitude correction filter on transmit.

Aberration correction is a filter process which inherently assumes the aberration on receive, on a given array element, to be independent of the spatial position of the reflecting scatterer. The aberration correction filter thus assumes all aberration of the inhomogeneous medium to be concentrated in a plane on the array surface. An approximation to this situation would be for the aberration to be generated in a thin layer just in front of the array.

Assuming all aberration to be concentrated in a plane, is often denoted a concentrated aberrator or an aberrating screen in the literature. For a concentrated aberrator at the array surface this notation is not precise enough. In this article, the situation where a concentrated aberrator is situated at the array surface is denoted receive scatterer independent aberration, or simply scatterer independent aberration. The reason for this is that placing an aberrating screen some distance from the array, would not lead to a situation where

[a]Electronic mail: svein-erik.masoy@medisin.ntnu.no

 0001-4966/2004/115(6)/2998/12/$20.00 © 2004 Acoustical Society of America

aberration at a receive array element is independent on the scatterers position in space.

Scatterer independent aberration is an approximation to the more general and physical case where the aberrated receive signal, on a given array element, is expected to be dependent on the scatterers spatial position. This is because different types of aberration is generated in different parts of the human body wall, that is, over the whole thickness of the body wall.[5,16] Since body wall thickness and anatomy varies strongly between humans, this also implies that the degree to which aberration on receive will be scatterer dependent, also varies.

There exists a region of scatterers, for which the aberration (at a given array element) in a signal received from any scatterer inside this region, is practically the same. This region is termed an isoplanatic patch, a term coined in astronomy where aberration effects occur when light from stars pass through the atmosphere. By the definition of the isoplanatic patch, focusing the transmitted beam to the inside of the patch, leads to receive scatterer independent aberration even for a thick or extended aberrator. Remark that the isoplanatic patch size change with a change in the location of the array focus.

Based on the previous discussion, the results in this article show the difference of scatterer independent and scatterer dependent aberration. This information is important in understanding how these different aberration situations influence the estimation of arrival time and amplitude fluctuations.

Three simulation situations were studied to evaluate the developed estimation method for arrival time and amplitude fluctuations, and the performance of the time delay, and the time delay and amplitude aberration correction filter:

(1) Scatterer independent aberration (SIA): Simulations have been performed were all the aberration is concentrated in a plane on the transmitting/receiving array. This represents a situation were the simulated data concurs with the aberration estimation/correction method.

(2) Scatterer dependent aberration (SDA): This represents a realistic aberration situation. Now the underlying assumption for the correction method is not fulfilled, and the object is to test its validity.

(3) Scatterer dependent aberration with a corrected transmitted beam (CSDA): This is the same situation as in (2), but now the transmitted beam is corrected with a time delay and amplitude filter estimated from a point source. The motivation for this was to show that a well estimated time delay and amplitude correction filter leads to scatterer independent aberration, because the energy of the corrected retransmitted beam is focused to the inside of the isoplanatic patch.

Absorption effects and electronic/acoustic noise were not included in the simulations.

II. THEORY

A. The generalized frequency dependent screen and the time delay and amplitude correction filter

In Ref. 12, the Green's function for a heterogeneous medium was modeled in the frequency domain as

$$g_f(\mathbf{r},\mathbf{r}_s;\omega)=s(\mathbf{r},\mathbf{r}_s;\omega)g_h(\mathbf{r}-\mathbf{r}_s;\omega), \tag{1}$$

where g_f is the Green's function in the inhomogeneous medium as a function of the field coordinate $\mathbf{r}$, the source or scatterer location $\mathbf{r}_s$, and the angular frequency ω. Here g_h is the Green's function for the homogeneous medium.

Propagation in an inhomogeneous medium generates interference, which results in an aberrated signal. Interference is a frequency dependent phenomenon. The function $s(\mathbf{r},\mathbf{r}_s;\omega)$ is therefore the frequency response of a filter, that produces a distortion of the amplitude and phase of a frequency component of the wave, as it propagates through the inhomogeneous medium.

This filter is denoted the generalized frequency dependent screen, and is composed of an amplitude screen and a phase screen defined as

$$s(\mathbf{r},\mathbf{r}_s;\omega)=a_s(\mathbf{r},\mathbf{r}_s;\omega)e^{i\Theta_s(\mathbf{r},\mathbf{r}_s;\omega)}. \tag{2}$$

The generalized frequency dependent screen is dependent on the scatterers spatial position. Complex variation of the amplitude and phase with frequency of this filter, is a result of the aberration generated interference. Note that complex variation of the phase screen with frequency generates shape deformation (stretching) of the wave.

If a point impulse source is placed in the focus $\mathbf{r}_f$ of the array, it is shown in Ref. 17 (Chapter 11), that filtering the transmitted signal on each array element with the complex conjugate of the generalized frequency dependent screen, is equal to time reversal,[13] and will reproduce the diffraction limited impulse field in $\mathbf{r}_f$.

This filter, defined as

$$h(\mathbf{r}_a;\omega)=s^*(\mathbf{r}_a,\mathbf{r}_f;\omega), \tag{3}$$

where $\mathbf{r}_a$ is the array coordinate, represents an ideal diffraction limited aberration correction filter for the focal point of the array.

If the aberration is scatterer independent, the generalized frequency dependent screen is independent on the scatterer position, and

$$s(\mathbf{r}_a,\mathbf{r}_s;\omega)=s(\mathbf{r}_a,\mathbf{r}_f;\omega)\equiv s(\mathbf{r}_a,\omega), \tag{4}$$

where $s(\mathbf{r}_a,\omega)$ is denoted the generalized scatterer independent screen, or simply, the scatterer independent screen. For this case, the ideal aberration correction filter is

$$h(\mathbf{r}_a;\omega)=s^*(\mathbf{r}_a,\omega). \tag{5}$$

The scatterer independent approximation is valid inside the isoplanatic patch, and ideal aberration correction with $s^*(\mathbf{r}_a,\omega)$, will be obtained inside the patch. In Ref. 12, it was shown that correction with the complex conjugate of the generalized frequency dependent screen, produced almost ideal aberration correction (no aberration) to a level of -25 dB from the maximum value of beam profiles in the focal plane of the array, for both a weak and strong aberration situation.

In the work presented here, aberration correction was performed with a matched time delay, and a time delay and amplitude correction filter on transmit. This is an approximation of $s^*(\mathbf{r}_a,\mathbf{r}_f;\omega)$, and the aberration correction filter is now given as

$$h(\mathbf{r}_a;\omega)=e^{i\omega\tau(\mathbf{r}_a)},$$
$$h(\mathbf{r}_a;\omega)=a(\mathbf{r}_a)e^{i\omega\tau(\mathbf{r}_a)}, \tag{6}$$

where both time delays and amplitudes are assumed to be independent of frequency.

The discussion in this section shows that a time delay, or a time delay and amplitude aberration correction filter, represents a two-level approximation to aberration from an extended aberrator such as the human body wall. First, aberration is assumed to be scatterer independent $[s(\mathbf{r}_a,\mathbf{r}_f;\omega)=s(\mathbf{r}_a,\omega)]$. Second, aberration parameters (arrival time and amplitude fluctuations) are assumed to be independent of frequency.

B. Aberration estimation

The developed estimation procedure is based on estimating the generalized frequency dependent screen, $s(\mathbf{r}_a,\mathbf{r}_f,\omega)$, from back-scattered signals from a region of moving scatterers, like the heart or blood. Frequency independent arrival time and amplitude fluctuations are then determined from $s(\mathbf{r}_a,\mathbf{r}_f,\omega)$.

The method assumes scatterer independent aberration, and Eq. (4) is thus valid. The method also assumes the scatterers, used in the estimation procedure, to constitutes a statistical ensemble. Each outcome of the ensemble represents a spatial distribution of the scatterers $\nu(\mathbf{r}_s)$, where $\mathbf{r}_s$ denotes the scatterers spatial position. Averaging over the ensemble is assumed to result in a δ-correlation of the scatterer distribution given as

$$\mathrm{E}[\,\nu(\mathbf{r}_{s1})\,\nu(\mathbf{r}_{s2})\,]=\sigma_\nu^2(\mathbf{r}_{s1})\,\delta(\mathbf{r}_{s2}-\mathbf{r}_{s1}), \tag{7}$$

where $\sigma_\nu^2(\mathbf{r}_{s1})$ is the variance parameter of the distribution. This approximation is valid if the correlation length of the scatterer distribution is much smaller than the wavelength, and is normally denoted an incoherent medium.

In a practical situation it is generally difficult to perform an averaging as described above. This was solved by the use of consecutive transmit signals with the same focus and amplitude, separated in time to ensure all scatterers in the observation volume to be replaced for each transmitted signal. Each received signal can then be considered a specific realization of the ensemble.

1. Development of the estimation procedure

The far-field approximated received signal y can, in the scatterer independent aberration situation, be written in the frequency domain as[17] (p. 11.55)

$$y(\mathbf{r}_a;\omega)=s(\mathbf{r}_a,\mathbf{r}_f;\omega)f(\mathbf{r}_a;\omega)=s(\mathbf{r}_a;\omega)f(\mathbf{r}_a;\omega), \tag{8}$$

where $f(\mathbf{r}_a;\omega)$ represents the nonaberrated signal on receive. The function $f(\mathbf{r}_a;\omega)$ thus contains aberration on transmit, but not on receive.

The received signal can be written in a discrete form as

$$y_p=s_p f_p, \quad p=1,...,N, \tag{9}$$

where subscript p indicates the element number, and N the total number of elements on the array. Frequency dependency has now been dropped for notational convenience.

Assuming a Gaussian signal with zero average value, all statistical information is contained in the cross-spectrum. The cross-spectrum between element n and p on the receiving array is defined as

$$R_{np}=\mathrm{E}[y_n^* y_p], \tag{10}$$

where $\mathrm{E}[\cdot]$ denotes an expectation operator. Inserting from Eq. (9) gives

$$R_{np}=\mathrm{E}[(s_n f_n)^* s_p f_p]=s_n^* s_p F_{np}, \tag{11}$$

where $F_{np}=\mathrm{E}[f_n^* f_p]$.

In the rest of the development, the magnitude of F_{np} is assumed to be a known variable. The basis for this is discussed in the next section.

Solving for s_p gives

$$s_p=a_p e^{i\theta_p}=\frac{R_{np}}{F_{np}}\frac{e^{i\theta_n}}{a_n}, \tag{12}$$

where both s_p and s_n have been written with an amplitude and a phase. In the general case, F_{np} can have a phase due to a refraction of the transmit beam introduced by the body wall[17] (pp. 11.57–11.59). This phase is unknown and is incorporated into the phase of s_p as

$$s_p=\frac{R_{np}}{|F_{np}|}\frac{e^{i(\theta_n-\theta_{Fnp})}}{a_n}\equiv\frac{R_{np}}{|F_{np}|}\frac{e^{i\theta_n}}{a_n}=\frac{R_{np}}{|F_{np}|}\frac{1}{s_n^*}, \tag{13}$$

where $\theta_n-\theta_{Fnp}$ has been renamed θ_n for notational convenience. This has been done since θ_{Fnp} cannot be determined, and will not affect the calculation of s_p.

In a real situation the expectation R_{np} is not given, and here an estimate for R_{np} was calculated as

$$\tilde{R}_{np}=\frac{1}{K}\sum_{k=1}^{K} y_{kn}^* y_{kp}, \tag{14}$$

where K denotes the number of measurements from different realizations of the scattering region.

In Ref. 18 (p. 703) it is shown that the variance of the amplitude and phase of $\tilde{R}_{np}$ is given as

$$\mathrm{Var}[|\tilde{R}_{np}|]\sim\frac{1}{2K}|R_{np}|^2\left(1+\frac{1}{|w_{np}|^2}\right),$$
$$\mathrm{Var}[\angle\tilde{R}_{np}]\sim\frac{1}{2K}\left(\frac{1}{|w_{np}|^2}-1\right), \tag{15}$$

where the coherence w_{np} is defined as

$$w_{np}=R_{np}/\sqrt{R_{nn}R_{pp}}. \tag{16}$$

Equation (15) shows that the variance of $\tilde{R}_{np}$ is high when $|w_{np}|^2$ is low. This motivates a weighted mean estimate of s_p as

$$\tilde{s}_p=\sum_{n=1}^{N} W_{np}\frac{\tilde{R}_{np}}{|F_{np}|}\frac{1}{\tilde{s}_n^*}, \quad p=1,...,N. \tag{17}$$

Here, W_{np} is a weight defined as

$$W_{np}=|\tilde{w}_{np}|^2 \Big/ \sum_{n=1}^{N} |\tilde{w}_{np}|^2, \tag{18}$$

where $\tilde{w}_{np}$ is an estimate of w_{np} based on $\tilde{R}_{np}$.

Equation (17) is an implicit equation for $\tilde{s}_n^*$, and was solved numerically. An iterative scheme was set up as follows

$$\tilde{s}_{p,q+1}=\tilde{s}_{p,q}+\mu\left\{\tilde{s}_{p,q}-\left[\sum_{n=1}^{N} W_{np}\frac{\tilde{R}_{np}}{|F_{np}|}\frac{1}{\tilde{s}_{n,q}^*}\right]\right\}, \tag{19}$$

where q is the iteration parameter, and μ is a constant convergence parameter. After convergence of Eq. (19), the phase and amplitude estimates were defined as

$$\tilde{\theta}_p=\angle\tilde{s}_p, \quad \tilde{a}_p=|\tilde{s}_p|. \tag{20}$$

Up to this point, the estimation procedure is still dependent on frequency, and Eq. (19) can be solved independently for all frequencies in the signal. As described in Sec. II A, aberration correction was in this article performed with a frequency independent time delay, and time delay and amplitude filter [Eq. (6)]. This was done by estimating the cross-spectrum from Eq. (14), at the center angular frequency ω_0 of the transmitted signal. In addition, $\tilde{R}_{np}$ was assumed to be a smooth function around ω_0, and additional averaging around ω_0 was performed to reduce the variance in the estimate.

To obtain a pure time delay estimate, the phase estimate in Eq. (20) was assumed to be linear with the center angular frequency ω_0 of the transmitted pulse. The phase estimate $\tilde{\theta}_p$ is an absolute phase, and to obtain a relative phase estimate, the reference value for all $\tilde{\theta}_p$ was taken to be the arithmetic mean of the estimated values. The arrival time fluctuations estimate was then calculated as

$$\tau_p=\frac{1}{\omega_0}\left[\tilde{\theta}_p-\frac{1}{N}\sum_{n=1}^{N}\tilde{\theta}_n\right]. \tag{21}$$

2. Analysis of estimator

In the development of the estimator in Eq. (17), $|F_{np}|$ was assumed to be a known variable. In Ref. 17 (p. 11.55) it is shown that for an incoherent medium (δ-correlated scatterers), F_{np} can be calculated as

$$F_{np}=\sum_{l} s_l s_{l+p-n}^* o_l o_{l+p-n}^*, \quad l=1,...,N. \tag{22}$$

The function o denotes the excitation momentum amplitude of the array. Equation (22) is equivalent to the van Cittert-Zernike theorem which states that for distortionless propagation, the receive spatial covariance from an incoherent medium is the auto-covariance of the transmitted array function.[19] In this case, the array function is the product of the scatterer independent screen and the excitation momentum amplitude. Note that F_{np} is frequency dependent due to the frequency dependency of the scatterer independent screen.

The magnitude of the scatterer independent screen can be normalized to a function that varies between 0 and 1. This means that

$$|R_{np}|\leqslant|F_{np}|, \tag{23}$$

with equality if, and only if $|s|=1$. Because of the previous result, the ratio $\tilde{R}_{np}/|F_{np}|$ in Eq. (17) will be dominated by $\tilde{R}_{np}$, and little sensitive to variations in $|F_{np}|$. As a result of this, Eq. (19) was solved with the value of $|F_{np}|$ obtained from Eq. (22) with $|s|=1$ and $|o|=1$, which results in a correlation of a rectangular function with itself.

The estimate of the cross-spectrum [Eq. (14)] can be showed to be nonbiased.

$$\mathrm{E}[\tilde{R}_{np}]=\mathrm{E}\left[\frac{1}{K}\sum_{k=1}^{K} y_{kn}^* y_{kp}\right]=\frac{1}{K}\sum_{k=1}^{K} R_{np}=R_{np}. \tag{24}$$

Inserting $\tilde{a}_n=a_n$ and $\tilde{\theta}_n=\theta_n$ into Eq. (17) and calculating the expectation gives

$$\mathrm{E}[\tilde{s}_p]=\sum_{n=1}^{N} W_{np}\frac{\mathrm{E}[\tilde{R}_{np}]}{|F_{np}|}\frac{e^{i\theta_n}}{a_n}=\sum_{n=1}^{N} W_{np}\frac{R_{np}}{|F_{np}|}\frac{1}{s_n^*}$$
$$=s_p\sum_{n=1}^{N} W_{np}. \tag{25}$$

In this case the estimate is nonbiased if $\Sigma_n W_{np}=1$, which by the definition of the weights W_{np} in Eq. (18) is fulfilled.

If $\tilde{a}_n\neq a_n$ and $\tilde{\theta}_n\neq\theta_n$, it is difficult to calculate the expectation of $\tilde{s}_p$, since it requires solution of a set of implicit equations. In Ref. 12, it was shown that estimates of arrival time delay and amplitude fluctuations in the signal from a point source, provided close to optimal correction of the transmitted focused beam. This leads to the recognition that estimates of time delay and amplitude fluctuations from point sources are qualified estimates of the screen s_p, and can be used as reference values for quantifying the quality of the developed estimation procedure. This was done here.

Inserting Eq. (14) into Eq. (17) leads to

$$\tilde{s}_p=\sum_{n=1}^{N} W_{np}\frac{1}{K}\sum_{k=1}^{K} y_{kn}^* y_{kp}\frac{1}{|F_{np}|}\frac{1}{\tilde{s}_n^*}=\frac{1}{K}\sum_{k=1}^{K} y_{kp}\hat{b}_{kp}^*, \tag{26}$$

where

$$\hat{b}_{kp}=\sum_{n=1}^{N} y_{kn}\frac{W_{np}}{|F_{np}|}\frac{1}{\tilde{s}_n^*}. \tag{27}$$

The estimate $\tilde{s}_p$ can hence be viewed as a correlation of the received signal on element p with a modified beamformer output of the signal received over the whole array. The beamformer output b of a received signal is defined as

$$b=\sum_{n=1}^{N} y_n. \tag{28}$$

The modification consists of a weight term and an aberration correction term.

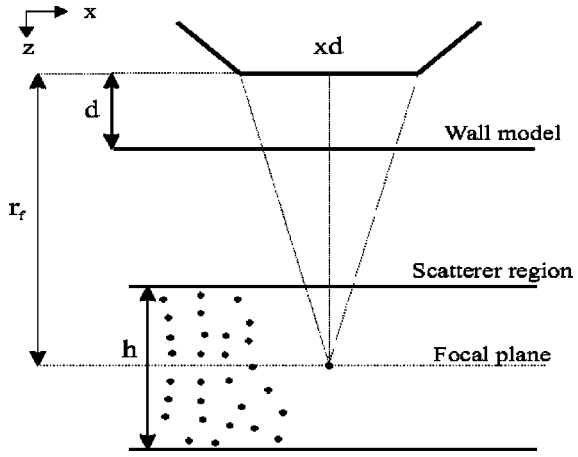

FIG. 1. Simulation setup scatterer dependent aberration.

III. METHOD

A. Modeling of aberration

To generate realistic aberration, two body wall models were created. These are the same two body wall models which were used in Ref. 12, where a weak aberrating body wall model was denoted *w*6, and a strong aberating body wall model was denoted *s*6. In this article these two body wall models are denoted the weak, and strong body wall model respectively. In Ref. 12 a thorough description of the generation of the body wall models, and their justification, is given.

B. Simulations

After creating suitable body wall models for generating aberration, 2D simulations were performed. A homogeneous angular spectrum operator, described in Ref. 12, was used to propagate the signals. All simulations were performed for 20 different realizations of the scattering region, and for both the weak and strong body wall models. The simulation setup in Fig. 1 was used in three different situations as described below.

1. Point source simulations

In order to estimate the general frequency dependent screen [Eq. (1)], and to estimate reference values for the arrival time and amplitude fluctuations, point source simulations were performed according to the setup in Fig. 1. No scattering region was now present in the setup.

A point source was simulated in the focus $\mathbf{r}_f$ of a focusing array of size *D*. The array was situated directly onto the distributed body wall models of thickness *d*. A pulse was generated at the point source and propagated homogeneously with the angular spectrum operator to the body wall models, and then through the wall models as described in Ref. 12, to the receiving array.

A point source simulation provides the ideal situation for estimation of the generalized frequency dependent screen. It was determined by filtering the received signal *y* from the point source with a Wiener-like filter h_W in the frequency domain given by the equation

$$s(\mathbf{r}_a,\mathbf{r}_f;\omega)=h_W(\mathbf{r}_a,\mathbf{r}_f;\omega)y(\mathbf{r}_a,\mathbf{r}_f;\omega), \tag{29}$$

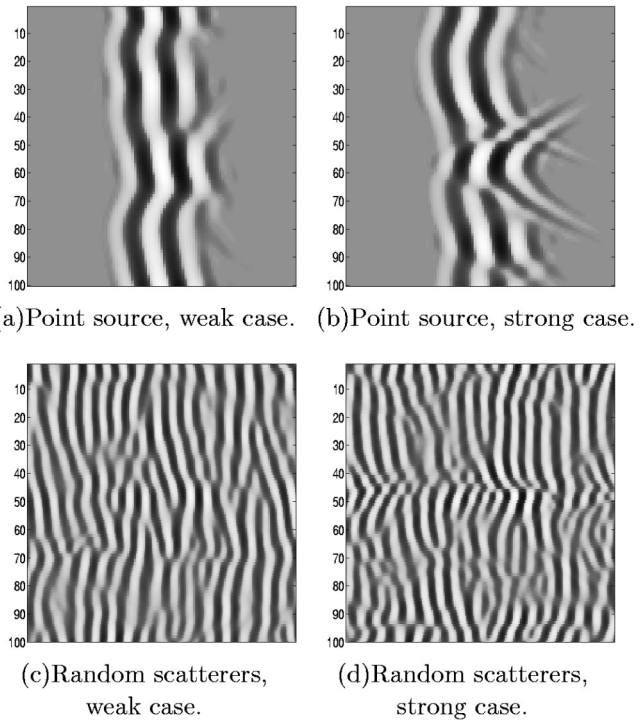

FIG. 2. Received wave forms from point sources in the focus of the array and from one realization of the random scatterers for the SDA situation. Each pane shows a temporal logarithmic gray scale picture of the wave forms at the receiving array. The dynamic range of the logarithmic scale is 40 dB. The horizontal axis represents time, and for the point source simulations it spans 2.9 μs. For the random scatterer results the time axis spans 5.7 μs. The vertical axis represents the receive array elements and spans 20 mm. The left panes shows the wave form received after propagation through the weak body wall model and the right panes shows the wave form from the strong body wall model.

where $\mathbf{r}_a$ represents the array coordinate and $\mathbf{r}_f$ the focus of the array (see Fig. 1). The transfer function for the filter was

$$h_W(\mathbf{r}_a,\mathbf{r}_f;\omega)=\frac{y_t^*(\mathbf{r}_a,\mathbf{r}_f;\omega)}{|y_t(\mathbf{r}_a,\mathbf{r}_f;\omega)|^2+\dfrac{\max(|y_t(\mathbf{r}_a,\mathbf{r}_f;\omega)|^2)}{\mathrm{SN}}}, \tag{30}$$

where y_t is the transmitted frequency dependent signal from the point source. The factor SN represents a signal-to-noise ratio parameter in the filter which was determined empirically.

2. Scatterer independent aberration simulations

In the general case, the generalized frequency dependent screen is dependent on the source position in space (in this case the focus point of the array $\mathbf{r}_f$). As explained in the introduction, scatterer independent aberration was created by concentrating all distortion of the inhomogeneous medium into a plane on the transmitting/receiving array. This is equal to assuming scatterer independent aberration as in Eq. (4).

Scatterer independent signals could then be generated without the extended aberrator in Fig. 1. These were round-trip simulations.

On transmit, the focused signal from the array was filtered with $s(\mathbf{r}_a,\mathbf{r}_f;\omega)$ as estimated in Eq. (29), to create scatterer independent aberration. The aberrated signal was

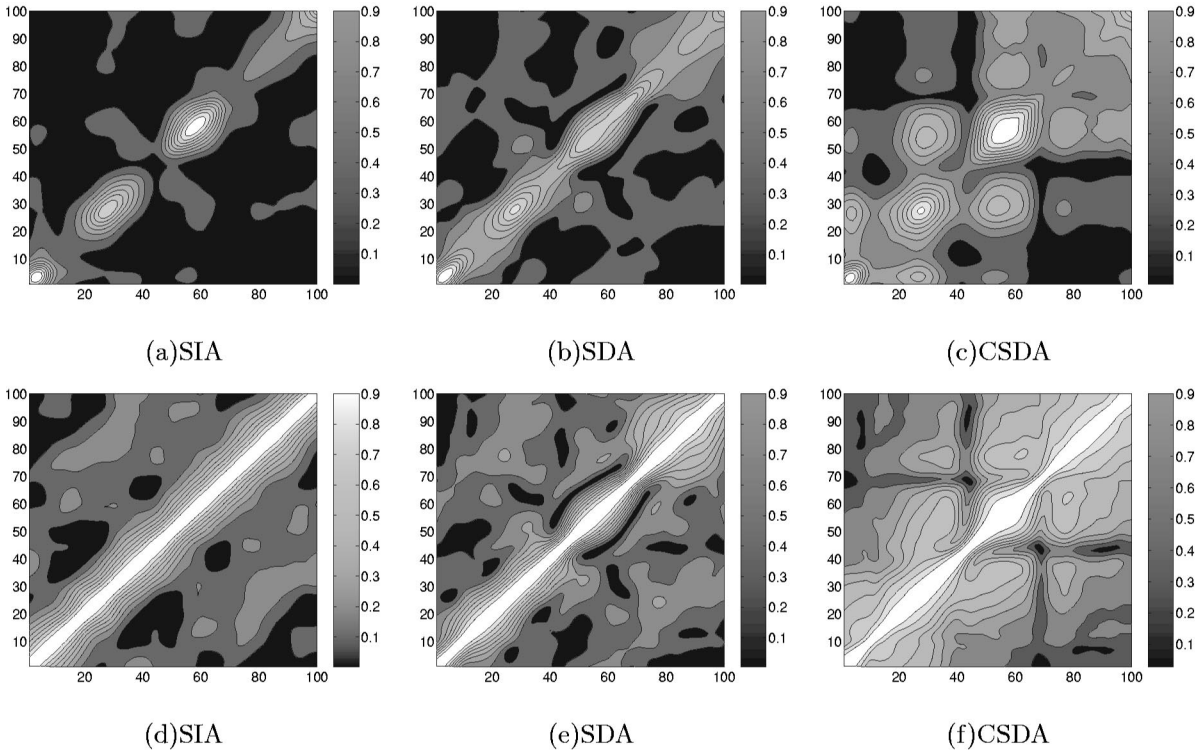

FIG. 3. Contour plots of the absolute value of the cross-spectrum and coherence between all elements on the receiving array, for the weak body wall model. The values are stacked in a matrix form. The top row shows absolute values of the cross-spectrum and the bottom row absolute values of the coherence. The cross-spectrum is normalized to the largest value in the matrix. Both the horizontal and vertical axes represent array elements. The labels explain the aberration situation. SIA: Scatterer independent aberration; SDA: Scatterer dependent aberration; and CSDA: Corrected scatterer dependent aberration.

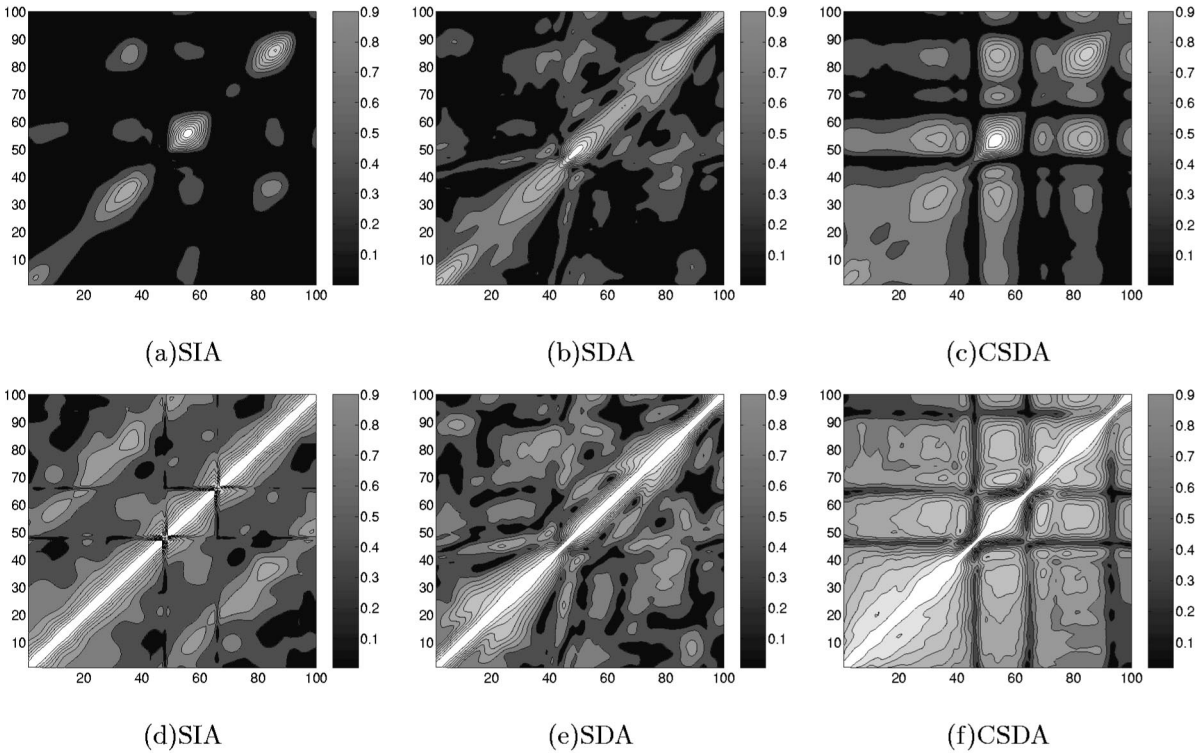

FIG. 4. Contour plots of the absolute value of the cross-spectrum and coherence between all elements on the receiving array for the strong body wall model. The values are stacked in a matrix form. The top row shows absolute values of the cross-spectrum and the bottom row absolute values of the coherence. The cross-spectrum is normalized to the largest value in the matrix. Both the horizontal and vertical axes represent array elements. Same labeling as in Fig. 3.

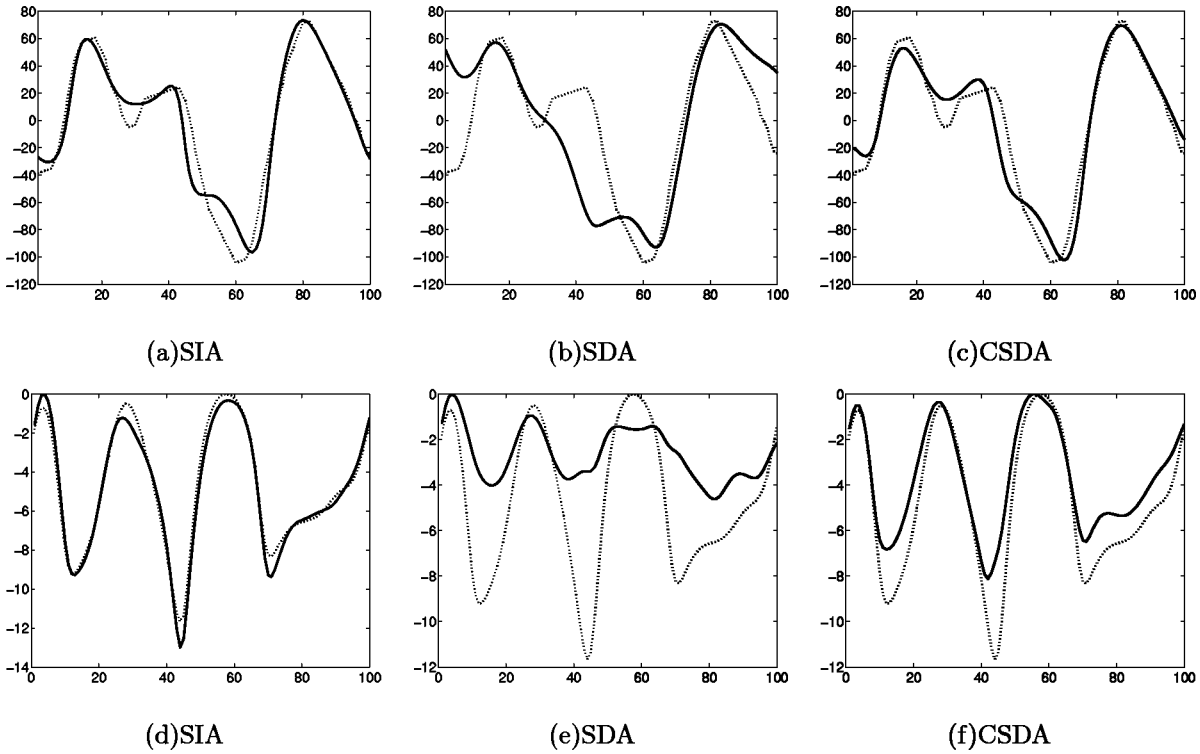

FIG. 5. Arrival time and amplitude fluctuation estimates for the weak body wall model. The top row shows arrival time fluctuations and the bottom row amplitude fluctuations. The horizontal axis in both rows represents array elements. The vertical axis for arrival time fluctuations is displayed in nanoseconds, and the vertical axis for amplitude fluctuations is in decibels. The dotted line represents estimates from point source simulations and serves as a reference. The solid line shows estimates from the random scatterer region. Same labeling as in Fig. 3.

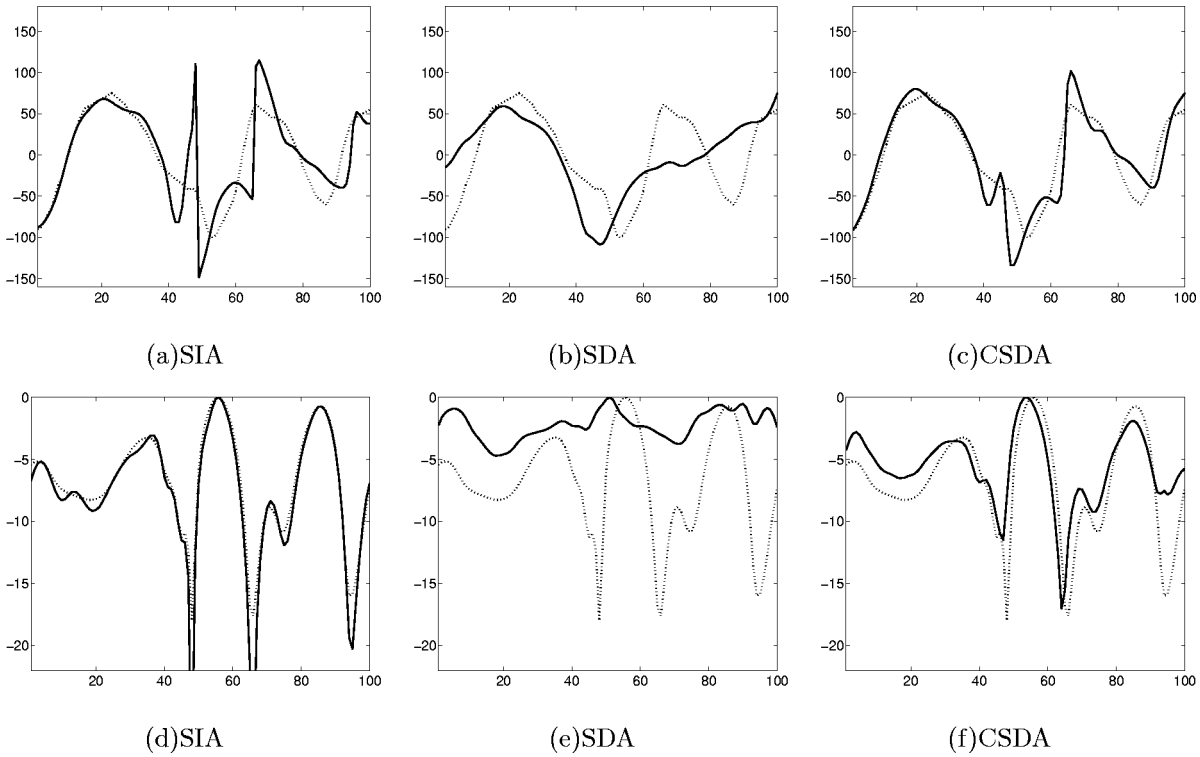

FIG. 6. Arrival time and amplitude fluctuation estimates for the strong body wall model. The top row shows arrival time fluctuations and the bottom row amplitude fluctuations. The horizontal axis in both rows represents array elements. Same notation and labeling as in Fig. 5.

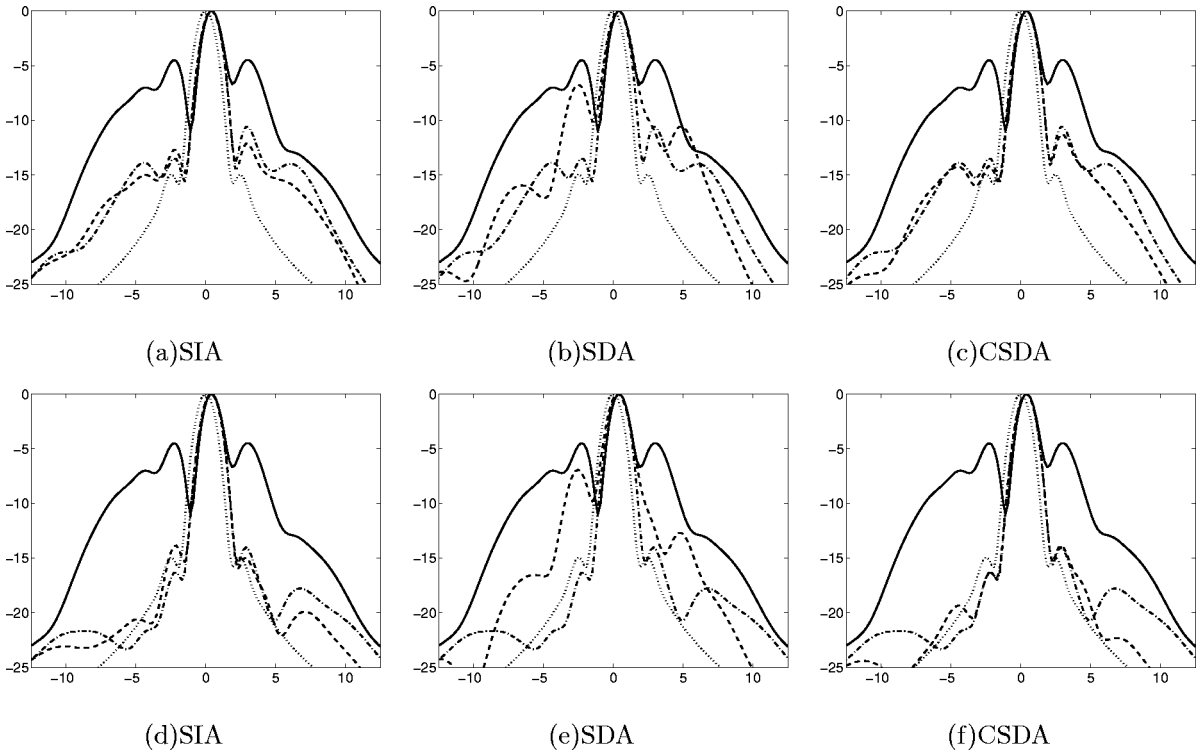

FIG. 7. Beam profiles in the focal plane for the weak body wall model. The top row shows beam profiles corrected with a time delay correction filter. The bottom row shows beam profiles corrected with a time delay and amplitude correction filter. The horizontal axis represents the focal plane (mm) and the vertical axis energy (dB). The zero point on the horizontal axis denotes the center axis of the transmitting array. The solid line represents the aberrated profile, the dashed-dotted line the profile corrected with estimates from a point source, the dashed line shows the profile corrected with estimates from the random scattering region, and the dotted line the profile with no aberration, which serves as a reference. All profiles are normalized to their maximum value. Same labeling as in Fig. 3.

propagated homogeneously to the scattering region, where it was scattered according to the Born approximation, i.e., only first order scattering was considered. The scattered signal was propagated back to the array, where it again was filtered with $s(\mathbf{r}_a,\mathbf{r}_f;\omega)$.

3. Scatterer dependent aberration simulations

Scatterer dependent aberration was created by using the distributed body wall models, as for the point source simulations. These were also round-trip simulations and the same setup was used for scatterer dependent aberration with a corrected transmitted beam.

The transmitted signal was propagated through the body wall models, and then homogeneously to the scattering region. Here it was scattered according to the Born approximation, and propagated back to the array through the body wall models.

IV. SIMULATION PARAMETERS AND DATA PROCESSING

The simulations were implemented in MATLAB, and the (FFTW) algorithm for calculation of the angular spectrum was used. The simulation area was 10.24 cm in the lateral direction (*x*-direction in Fig. 1) with a resolution of 0.2 mm. To avoid wrap-around effects from the FFT, the signal was tapered to zero over 2.54 cm at each edge, in the *x*-direction, with a raised cosine function. The tapering was performed for a sufficient number of propagation steps in order to keep the noise level from the wrap-around effects sufficiently low. The sampling frequency was 35.1 MHz providing a time window of 58.3 μs. Center frequency of the pulse was 2.5 MHz with a -6 dB bandwidth of 1.6 MHz. The pulse was filtered on transmit with a 3.7 MHz band-pass filter centered around the center frequency of the pulse. An array size of 20 mm with a pitch of 0.2 mm was chosen, giving 100 elements on the array. The focal depth of the array was set to 60 mm. Water at 37 °C was used as the propagation medium. On receive, all signals were corrected for geometric focusing for the homogeneous medium before processing of results.

To generate a realistic speckle signal, an area of 30.5 mm (time window of 20 μs), 15.25 mm to each side of the focal plane (see Fig. 1), was used as a scattering region. The scatterer density was approximately 1600 scatterers per square centimeter. The scatterers were uniformly distributed in the *x*- and *z*-direction, and had a Gaussian distributed reflection strength. Twenty different independent realizations of the scatterer region were produced.

The cross-spectrum (Sec. II B) was calculated by taking the Fourier transform of the received signal on each array element over the entire range of the scattering region. The cross-spectrum between all elements on the receiving array was then calculated according to Eq. (14), and this process was performed and averaged for the 20 generated statistically independent signals. The cross-spectrum was assumed to be a smooth function around the parameter frequency (in this case the center frequency of the signal) and was averaged over a small band of frequencies with equal weight. This

band ranged from approximately 2.4 to 2.6 MHz, which constituted 11 frequencies with the resolution used in the simulations.

Estimation of arrival time fluctuations from point source simulations was performed with a phase front tracking algorithm. In essence, the phase front tracking algorithm determined the peak of the first period of the received wave form from the point source. The tracking was then performed on each element, and the time delay between two elements was defined as the difference in time between the two peaks of the respective elements. For all arrival time fluctuations estimates presented in this article, a linear fit was subtracted in order to remove any refraction of the beam.

Arrival amplitude fluctuations across the array from point source simulations, were determined by taking the Fourier transform in time of the received signal on each element. The amplitude on each element of the array was calculated as the arithmetic mean of the amplitudes, of the now frequency dependent signal, over a band of frequencies ranging from 2–3 MHz. This band was chosen empirically.

Beam profiles in the focal plane of the array were used for visual evaluation of the effect of different aberration correction filters. All aberration corrected signals were propagated through the distributed body wall models as in Fig. 1. The profiles were calculated as the rms value in time of each spatial position.

Additional evaluation of the correction filters in the focal plane were performed by calculation of focus quality parameters. These were effective widths in the array and range direction, and calculation of a peripheral energy ratio. Details of the definition of these parameters are given in Ref. 1.

V. RESULTS

Figure 2 shows received wave forms from the point source simulations, and from one realization of the random scatterers for the SDA situation. For the point source simulations, shape distortion of the wave forms is clearly visible, and in the strong aberration case deformation of the wave form also occurs in several places. Since the wave forms are pictured with a logarithmic scale and a dynamic range of 40 dB, amplitude fluctuations do not show. For the signal from random scatterers strong decorrelation of the signals is visible.

In the expression for the variance [Eq. (15)] of the amplitude of the cross-spectrum, the absolute value of the cross-spectrum squared, and the inverse of the coherence squared enters. The variance of the phase of the cross-spectrum is given by the inverse of the coherence squared. Figure 3 displays contour plots of the absolute value of the cross-spectrum and coherence, between all elements on the receiving array for the weak body wall model. The diagonal from bottom left to top right of the cross-spectrum matrices display areas of high and low correlation in the signal due to variations in receive amplitudes. In Fig. 3(a) (SIA), such variations are clearly visible. For the SDA situation (b), cross-spectrum values are, in general, higher compared to the scatterer independent case indicating a higher variance and a poorer amplitude estimate. There is also a stretching of the high amplitude areas in the matrix, resulting in a reduced pinpointing of amplitude peaks. In the CSDA case the same variations in the cross-spectrum as in the SIA case are visible, but the width of the diagonal amplitude band is wider, indicating higher variance.

The coherence is the cross-spectrum normalized according to Eq. (16). In the SIA case, the coherence displays a diagonal band indicating high correlation along the whole of the receiving array. The width of the band (rows in the matrix) indicates how other elements of the array correlates with a specific element. For the SIA case, the width of the band is approximately constant which means that the same amount of information is used in estimation of the phase and amplitude for each element. In the SDA, the width of the band is generally narrower and varies along the diagonal resulting in increased variance of the phase estimate. Results for the CSDA situation show increased coherence along the diagonal resulting in reduced variance for the phase estimate in comparison to the SDA situation.

Figure 4 shows contour plots of the absolute value of the cross-spectrum and coherence for the strong body wall model. These results depict the same situation as for the weak body wall model. Note that the width of the coherence band for the SIA situation [Fig. 4(d)] is reduced in comparison to the weak body wall model, which shows that the correlation is reduced for the strong body wall model.

Arrival time and amplitude fluctuation estimates for the weak body wall model are presented in Fig. 5. The figure shows that estimates of arrival time fluctuations for the SIA [Fig. 5(a)], and CSDA situation [Fig. 5(c)], are approximately identical and very close to point source estimates. In the SDA case, estimates deviate from point source estimates, which is a direct result of the lowered correlation in the estimated cross-spectrum as shown in Fig. 3.

Figure 6 shows arrival time and amplitude fluctuation estimates for the strong body wall model. These results show the same trend as for the weak body wall model. In the SDA case, estimated arrival time fluctuations strongly deviates from point source estimates due to lowered correlation in the received signal. Note that for the SIA and the CSDA, discontinuities occur in the estimates. These discontinuities are due to the wave deformation clearly visible in Fig. 2(b). The wave deformation is also visible in Fig. 4, where the coherence is close to zero in the region of pulse deformation. This effect causes the variance of phase estimates to be very high, resulting in poor arrival time fluctuation estimates.

Arrival amplitude fluctuation estimates for both the weak and strong body wall models, show the same trend as estimates for arrival time fluctuations. Amplitude estimate in the SIA situation is approximately identical to point source estimates for both body wall models. Estimates for the SDA are very poor for both body walls, respectively. This is an effect of the reduced variation in the cross-spectrum as shown in Figs. 3(b) and 4(b). In the CSDA situation, estimates are not as good as point source estimates, but compared to the SDA situation they have improved substantially.

Beam profiles corrected with a time delay, and a time delay and amplitude filter for the weak body wall model, are presented in Fig. 7. The beam profiles, together with the focus quality parameter given in Table I, show the efficiency

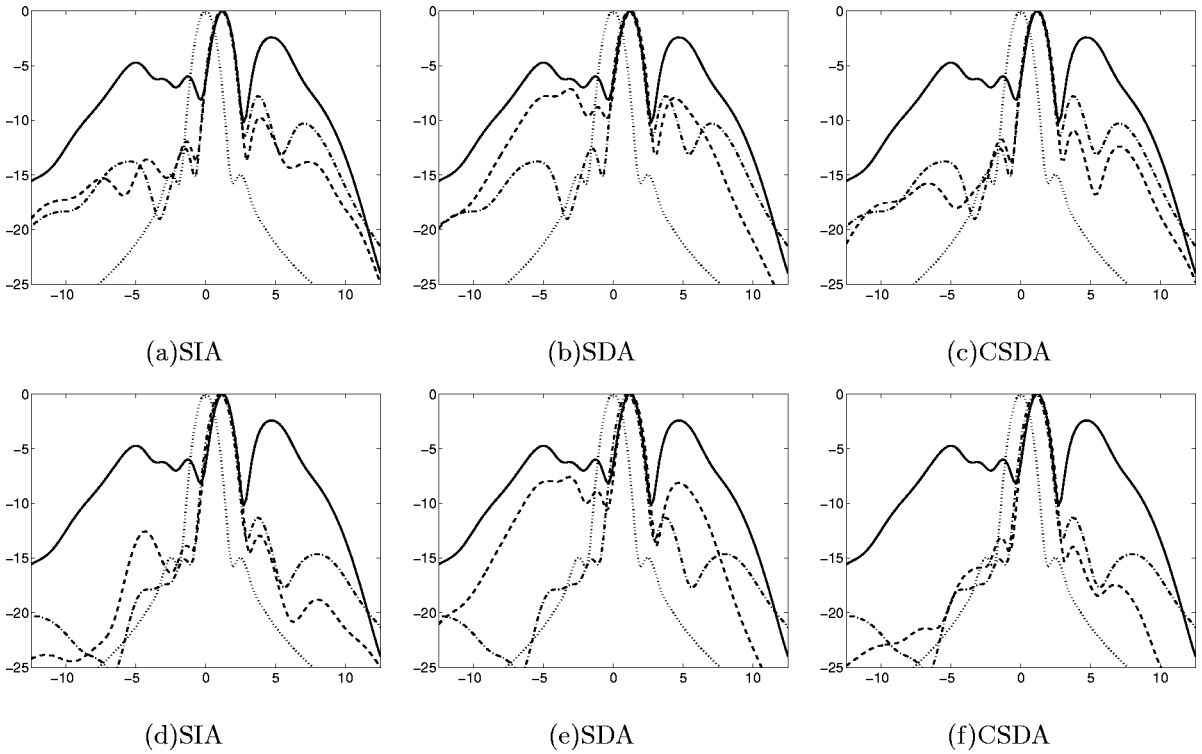

FIG. 8. Beam profiles in the focal plane for the strong body wall model. The top row shows beam profiles corrected with a time delay correction filter. The bottom row shows beam profiles corrected with a time delay and amplitude correction filter. Same notation and labeling as in Fig. 7.

of the aberration correction filter. Note that the focus quality measures in Table I cannot be directly compared to the presented beam profiles, as they are calculated in a different way. But they do portray the same effects visible in the beam profiles. It should also be stressed that focus quality measures of the aberrated beam profiles are uncertain since there is no clearly defined main lobe.

For the SIA, and CSDA situation, time delay corrected profiles are almost identical and very close to the point source corrected profile. Note that there is a slight refraction of the beam to the right of the center axis of the array. The effective widths from Table I are identical to the ideal case for these two cases, but the -10 dB peripheral energy ratio is higher due to generally higher side lobe level. In the SDA situation, estimates of arrival time fluctuations deviated from point source estimates resulting in a less focused beam profile with a relatively high side lobe level. The beam profile for the SDA situation has a turning point at approximately -10 dB, and makes the -10 dB peripheral energy ratio measure unreliable. The effective width at -10 dB is, on the other hand, very large in the array direction portraying poor correction.

Beam profiles corrected with a time delay and amplitude filter show a further reduction in side lobe level for the

TABLE I. Table of focus quality parameters. The peripheral energy ratio (PER) and all effective widths have been calculated at -10 dB level from the peak. The two column headings refers to the weak and strong aberration body wall models, respectively. The column Aberration situation indicates the aberration situation and the notation follows the notation in Fig. 3. The notation PS in this column denotes correction with estimates from the point source. The Correction column specifies the type of correction where τ denotes time delay correction filter, and τ&a time delay and amplitude correction filter. The two last rows has no value in the Correction column. The first of these rows show the ideal situation with no aberration, and the second the aberrated situation.

Weak aberrator						Strong aberrator					
Aberration situation	Correction	PER	Effective diameter (mm)	Effective width in array direction (mm)	Effective width in time direction (mm)	Aberration situation	Correction	PER	Effective diameter (mm)	Effective width in array direction (mm)	Effective width in time direction (mm)
SIA	τ	0.427	1.84	2.70	1.26	SIA	τ	0.645	1.88	2.80	1.26
SDA	τ	0.420	2.68	5.70	1.26	SDA	τ	1.060	2.34	3.70	1.47
CSDA	τ	0.418	1.84	2.70	1.26	CSDA	τ	0.554	1.88	2.80	1.26
PS	τ	0.477	1.84	2.70	1.26	PS	τ	0.763	1.88	2.80	1.26
SIA	τ&a	0.287	1.84	2.70	1.26	SIA	τ&a	0.363	1.94	3.00	1.26
SDA	τ&a	0.362	2.63	5.50	1.26	SDA	τ&a	1.080	2.03	2.80	1.47
CSDA	τ&a	0.253	1.88	2.80	1.26	CSDA	τ&a	0.315	1.91	2.90	1.30
PS	τ&a	0.300	1.84	2.70	1.26	PS	τ&a	0.439	1.91	2.90	1.26
IDEAL		0.228	1.84	2.70	1.26	IDEAL		0.228	1.84	2.70	1.26
AB		1.230	2.58	4.50	1.47	AB		1.440	3.68	6.50	2.08

SIA and CSDA situations. Note also that correction of the beam profile has improved further away from the central axis of the array. This again leads to reduced peripheral energy ratios, and for both cases they are now close to the ideal situation. For the SDA situation, amplitude estimates were very poor and do not change the corrected beam profile significantly. There is some reduction in the effective width in the array direction, and the peripheral energy ratio.

Corrected beam profiles for the strong body wall model are shown in Fig. 8. Also in this case, correction with a time delay filter for the SIA and CSDA situation improves the beam profiles. Note that refraction of the beam is stronger for this body wall model than for the weak.

Introducing amplitude correction in addition to time delay correction, improves beam profiles substantially for both these cases. This is also shown in the focus quality variables where the -10 dB peripheral energy ratio is reduced. For the SDA situation, correction with a time delay filter is very poor. Introducing amplitude correction does not change the beam profile, and there is almost no difference in the peripheral energy ratio.

VI. DISCUSSION

The aberration in the scatterer independent aberration simulations was performed by filtering the signal on transmit and receive with an estimate of the generalized frequency dependent screen [Eq. (29)]. This means that the resulting aberrated beam profiles for the SIA and SDA situation are not identical. The results of the estimated arrival time and amplitude fluctuations for these cases (Figs. 5 and 6), show that the differences are negligible.

As explained in Sec. IV, the cross-spectrum was assumed to be a smooth function around the center angular frequency, and averaged over 11 neighboring frequencies. Averaging over a number of M frequencies is equivalent to averaging in range, that is subdividing the signal in M range segments for each channel and estimating the cross-spectrum of each segment. This results in a smoothing of the frequency spectrum. The band of frequencies for averaging was chosen empirically.

The scatterers were modeled as uniformly distributed in space with a Gaussian distributed reflection strength. This constitutes an ideal set of scatterers with no interference from strong scatterers or strong scattering regions within the scattering region itself. Absorption and electronic/acoustic noise (e.g., reverberations) were not included in the simulations. In a practical situation, all of these effects would exist and probably deteriorate the estimate of the cross-spectrum. One of the purposes of this article was, on the other hand, to demonstrate the basic differences between scatterer independent aberration (which forms the general assumption for aberration correction) and scatterer dependent aberration. Thus having a receive signal as ideal as possible was in the interest of the analysis.

The range of the scatterer region was chosen to be well inside the 3 dB depth of focus of the transmitting array. The 3 dB depth of focus can be calculated as[20] (p. 1.14)

$$L_f(3\ \mathrm{dB}) \approx 7.2\lambda(FN)^2, \tag{31}$$

where λ is the wavelength of the transmitted pulse and FN the f-number defined as $FN=\mathbf{r}_f/D$ (see Fig. 1). In the simulations performed in this article, the wavelength was $\lambda=0.6$ mm and the f-number $FN=3$, which gives $L_f(3\ \mathrm{dB}) \approx 39$ mm. A scattering region of 15.25 mm in range to each side of the focal point, is thus well inside the 3 dB focal depth of the transmitting array.

The wave front tracking algorithm used to estimate arrival time fluctuations from the point source simulations is dependent on a clearly defined wave front, which is the case for a wave emanating from a single point source. The speckle signal created in this article represents the sum of signals from many point sources, and has not a clearly defined wave front. This would also be the case for tissue images in ultrasound imaging systems, and this method for arrival time estimation is only suited for ideal situations. Since the method tracks the front of the wave, it is little sensitive to wave form deformation, and for the point source simulations performed, this method proved to give very accurate estimates of arrival time fluctuations in the received wave front.

Results in this article show that for scatterer independent aberration, arrival time, and amplitude fluctuations are estimated in accordance with results obtained from point source simulations. When introducing a body wall model of thickness two centimeters, the quality of estimates of arrival time and amplitude fluctuations are significantly reduced compared to point source estimates. This is mainly due to the increased aberration interference in the signal, caused by the distributed aberrator, which results in a reduced spatial coherence (see Figs. 3 and 4).

There is some improvement in the beam profiles for the scatterer dependent aberration, especially for the weak body wall model. This leads to the notion of an iterated estimation/correction procedure. In an iteration procedure, arrival time and amplitude fluctuations could be estimated as in this article, and a corrected signal would be transmitted for the purpose of performing a new estimation of the same parameters. The process would be repeated until some convergence criterion is achieved. This is also known as adaptive imaging. The optimum convergence would be obtained when the estimates are equal to those obtained from a point source. The corrected scatterer dependent aberration situation presented in this article displays the ideal last stage of such an iteration process. The results show that if the transmitted signal is corrected with an ideal time delay and amplitude filter, aberration in the received signal is indeed scatterer independent, and arrival time fluctuations are very well estimated. Amplitude variations are not as well estimated as from the point source simulations, but this does not affect the corrected beam profiles noticeably, and the peripheral energy ratios in this case are even better than for the point source estimates (see Table I).

VII. CONCLUSIONS

An estimator for estimating arrival time and amplitude fluctuations from random signals has been developed. The method can also be used to estimate phase and amplitude

aberration for all frequency components in the received signal. It was tested on different situations of aberration, scatterer independent aberration, and scatterer dependent aberration. Results obtained with signals from random scatterers were compared with estimates from point source simulations.

For the SIA and CSDA situation, arrival time and amplitude fluctuations estimates were very close to point source estimates for both the weak and strong aberrating body wall models. Used in a time delay, and time delay and amplitude aberration correction filter, they produced equivalent correction of transmitted beam profiles as correction with point source estimates. For both the SIA and CSDA situation, a time delay and amplitude filter corrected significantly better than a time delay filter alone.

In the SDA situation, arrival time fluctuations differed significantly from point source estimates. With the strong body wall model, estimates were poor, yielding a limited correction of the beam profile. The estimator was only able to estimate arrival amplitude variations of about 4 dB for both body wall models, while for the strong body wall model, variations of up to 18 dB was estimated from the point source. The difference between a time delay, or a time delay and amplitude correction filter was negligible for the strong body wall model. This was mainly due to the poor estimates of both arrival time and amplitude variations. For the weak body wall model, correction of the beam profile was observed (there is some correction also in the strong case) and the time delay and amplitude filter corrects better than the time delay filter.

The results presented here demonstrate the difficulty of estimating and correcting ultrasound aberration with a time delay, or a time delay and amplitude aberration correction filter. This is due to the fact that aberration in general is generated over an extended part of the human body wall. Aberration correction with a time delay, or a time delay and amplitude aberration correction filter assumes all aberration to be concentrated on the transmitting/receiving array. On the other hand, the results show that if the receive aberration is scatterer independent, the developed estimation method for arrival time and amplitude fluctuations from random signals works well.

For the distributed body wall models (scatterer dependent aberration), the estimation method does not produce satisfactory results, even with 20 independent realizations of the received signals. Some correction is still obtained, and estimates could possibly be improved by iteration.

This work also demonstrates that, if correctly estimated, a time delay or a time delay and amplitude correction filter produce receive signals with aberration that is independent of the scatterers spatial position. This indicates that such a correction filter can focus the aberrated transmitted beam to the inside of the isoplanatic patch, the necessary condition for obtaining receive scatterer independent aberrated signals from randomly distributed scatterers.

ACKNOWLEDGMENTS

The work presented in this article was supported by the Medicine and Health program of the Research Council of Norway. Tonni F. Johansen and Ingmund Bjørkan developed large parts of the Born approximation scattering part of the simulation code. The authors would like to thank Professor Harald Krogstad at the Department of Mathematical Sciences, NTNU, for valuable insight into the world of stochastic processes. The reviewers are thanked for constructive comments that improved this article.

[1] D.-L. Liu and R. C. Waag, "Time-shift compensation of ultrasonic pulse focus degradation using least-mean-square error estimates of arrival time," J. Acoust. Soc. Am. **95**(1), 542–555 (1994).
[2] L. M. Hinkelman, D.-L. Liu, L. A. Metlay, and R. C. Waag, "Measurements of ultrasonic pulse arrival time and energy level variations produced by propagation through abdominal wall," J. Acoust. Soc. Am. **95**(1), 530–541 (1994).
[3] L. M. Hinkelman, D.-L. Liu, R. C. Waag, Q. Zhu, and B. D. Steinberg, "Measurement and correction of ultrasonic pulse distortion produced by the human breast," J. Acoust. Soc. Am. **97**(3), 1958–1969 (1995).
[4] L. M. Hinkelman, T. L. Szabo, and R. C. Waag, "Measurements of ultrasonic pulse distortion produced by human chest wall," J. Acoust. Soc. Am. **101**(4), 2365–2373 (1997).
[5] L. Hinkelman, T. D. Mast, L. A. Metlay, and R. C. Waag, "The effect of abdominal wall morphology on ultrasonic pulse distortion. Part I. Measurements," J. Acoust. Soc. Am. **104**(6), 3635–3649 (1998).
[6] Q. Zhu and B. Steinberg, "Deaberration of incoherent wave front distortion: An approach toward inverse filtering," IEEE Trans. Ultrason. Ferroelectr. Freq. Control **44**(3), 575–589 (1997).
[7] S. W. Flax and M. O'Donnell, "Phase-aberration correction using signals from point reflectors and diffuse scatterers: Basic principles," IEEE Trans. Ultrason. Ferroelectr. Freq. Control **35**(6), 758–767 (1998).
[8] M. O'Donnell and S. W. Flax, "Phase-aberration correction using signals from point reflectors and diffuse scatterers: Measurements," IEEE Trans. Ultrason. Ferroelectr. Freq. Control **35**(6), 768–774 (1988).
[9] L. A. Ødegaard, "Using signals scattered from diffuse inhomogeneities to correct for phase aberrations caused by a phase-screen far from the transducer," IEEE Ultrasonics Symp. Proc. **2**, 1443–1447 (1995).
[10] S. Krishnan, P.-C. Li, and M. O'Donnell, "Adaptive compensation of phase and magnitude aberrations," IEEE Trans. Ultrason. Ferroelectr. Freq. Control **43**(1), 44–55 (1996).
[11] W. E. Walker and G. E. Trahey, "Aberrator integration error in adaptive imaging," IEEE Trans. Ultrason. Ferroelectr. Freq. Control **44**(4), 780–791 (1997).
[12] S.-E. Måsøy, T. F. Johansen, and B. Angelsen, "Correction of ultrasonic wave aberration with a time delay and amplitude filter," J. Acoust. Soc. Am. **113**(4), 2009–2020 (2003).
[13] M. Fink, C. Prada, F. Wu, and D. Cassereau, "Self focusing in inhomogeneous media with 'Time Reversal' acoustic mirrors," *IEEE Ultrasonics Symposium*, 681–686 (1989).
[14] D.-L. Liu and R. C. Waag, "Correction of ultrasonic wave front distortion using backpropagation and a reference waveform method for time-shift compensation," J. Acoust. Soc. Am. **96**(2), 649–660 (1994).
[15] J. C. Lacefield, and R. C. Waag, "Evaluation of backpropagation methods for transmit focus compensation," *IEEE Ultrasonics Symposium*, **2**, 1495–1498 (2001).
[16] T. D. Mast, L. M. Hinkelman, M. J. Orr, and R. C. Waag, "The effect of abdominal wall morphology on ultrasonic pulse distortion. Part II. Simulations," J. Acoust. Soc. Am. **104**(6), 3651–3664 (1998).
[17] B. Angelsen, *Ultrasound Imaging. Waves, Signals and Signal Processing* (Trondheim, Emantec, 2000), Vol. II, http://www.ultrasoundbook.com.
[18] M. B. Priestley, *Spectral Analysis and Time Series* (Academic, New York, 1988).
[19] R. Mallart and M. Fink, "The van Cittert-Zernike theorem in pulse echo measurements," J. Acoust. Soc. Am. **90**(5), 2718–2727 (1991).
[20] B. Angelsen, *Ultrasound Imaging. Waves, Signals and Signal Processing* (Trondheim, Emantec, 2000), Vol. I, http://www.ultrasoundbook.com.

Matrix filter design for passive sonar interference suppression[a)]

Richard J. Vaccaro[b)] and Amit Chhetri[c)]
Department of Electrical and Computer Engineering, University of Rhode Island, Kingston, Rhode Island 02881

Brian F. Harrison
Naval Undersea Warfare Center, Submarine Sonar Department, Newport, Rhode Island 02841

(Received 19 June 2003; revised 23 January 2004; accepted 15 March 2004)

The performance of passive acoustic signal-processing techniques can become severely degraded when the acoustic source of interest is obscured by strong interference. The application of matrix filters to suppress interference while passing a signal of interest with minimal distortion is presented. An algorithm for single-frequency matrix filter design is developed by converting a constrained convex optimization problem into a sequence of unconstrained problems. The approach is extended to broadband data by incoherently combining the responses of matrix filters designed at frequencies across a band of interest. The responses of single-frequency and multifrequency matrix filters are shown. Examples are given which demonstrate the effectiveness of matrix filtering applied to matched-field localization of a weak source in the presence of a strong interferer and noise. These examples show the matrix filter effectively suppressing the interference, thereby enabling the localization of the weak source. Standard matched-field processing, without matrix filtering, is not effective in localizing the weak source. © *2004 Acoustical Society of America.*
[DOI: 10.1121/1.1736653]

PACS numbers: 43.60.Gk, 43.30.Wi [EJS] Pages: 3010–3020

I. INTRODUCTION

Matrix filters, provided they are properly designed, are a powerful tool for separating wanted and unwanted components in observed data. For example, it is possible to design matrix filters to suppress interference while passing a signal of interest in data collected from an array of sensors. Matrix filters are designed by defining an appropriate passband and stop band and solving a convex optimization problem. The design of matrix filters by convex optimization was proposed in Ref. 1, which includes examples of frequency-selective filters and Hilbert transform filters for short time series. In this paper we show how to design filters that are useful for suppressing surface interference for passive sonar localization.

The problem of attenuating a surface-generated directional noise field to help in localizing submerged sources was addressed by Yoo and Yang using ''matched-beam'' processing.[2] In contrast to their work, we consider the surface interference to be generated by a loud source of limited spatial extent. In other related work, Mirkin and Sibul[3] develop a maximum likelihood procedure to localize multiple acoustic sources. For the problem we consider, the algorithm of Mirkin and Sibul would proceed by localizing the loud source, eliminating its effect on the data by orthogonal projection, and finally localizing the quiet source. The orthogonal projection matrix in their algorithm is a matrix filter. However, in contrast to the filters designed in this paper, the orthogonal projection filter is not optimized for stop band attenuation and is designed to perfectly null a point source.

II. PROBLEM FORMULATION

Consider a vertical array of N sensors located at depths $z_1,\ldots,z_N$, and an acoustic source at frequency ω_n located at a depth z and a range r from the array. Under certain assumptions,[4,5] the Fourier transform of the sensor outputs, evaluated at ω_n, can be written as

$$\mathbf{d}(r,z,\omega_n)=s\boldsymbol{\Omega}(\omega_n)\boldsymbol{\alpha}(r,z,\omega_n)+\mathbf{n}, \tag{1}$$

where

$$\boldsymbol{\Omega}(\omega_n)=\begin{bmatrix}\eta_1(z_1) & \cdots & \eta_Q(z_1)\\ \vdots & & \vdots\\ \eta_1(z_N) & \cdots & \eta_Q(z_N)\end{bmatrix},$$
$$\boldsymbol{\alpha}(r,z,\omega_n)=\begin{bmatrix}\dfrac{\sqrt{2\pi}\eta_1(z)}{\sqrt{rk_1}}e^{(jk_1-\gamma_1)r}\\ \vdots\\ \dfrac{\sqrt{2\pi}\eta_Q(z)}{\sqrt{rk_Q}}e^{(jk_Q-\gamma_Q)r}\end{bmatrix}, \tag{2}$$

s is a complex scale factor, and $\mathbf{n}$ is a vector of noise samples. The functions $\eta_i(z)$, $i=1,...,Q$ are the normal modes associated with the acoustic environment; they can be calculated numerically using a program such as the one developed by Porter.[6] This program also calculates the numbers $k_1,\ldots,k_Q$ and $\gamma_1,\ldots,\gamma_Q$, which are the horizontal wave numbers and mode attenuation coefficients, respectively. In the absence of noise the data vector $\mathbf{d}$ is called a *replica*

[a)]Portions of this work were presented in ''Matrix Filters for Passive Sonar,'' Proceedings of IEEE International Conference on Acoustics, Speech, and Signal Processing, Salt Lake City, UT, May 2001.
[b)]Electronic mail: vaccaro@ele.uri.edu
[c)]Current affiliation: Dept. of Electrical Engineering, Arizona State University Main, Tempe, AZ 85287-5706.

vector and is denoted by $\mathbf{a}(r,z,\omega_n)$. In what follows, all replica vectors are normalized to unit length and the dependence on range, depth, and frequency is not shown explicitly.

A linear filtering operation on the sensor outputs can be expressed as a matrix multiplication, $\mathbf{y}=\mathbf{Md}$, where $\mathbf{M}$ is an $N\times N$ matrix of complex numbers. The purpose of a matrix filter is to attenuate unwanted components in the measured sensor data $\mathbf{d}$ while passing desired components with minimal distortion. Matrix filters are designed using a set of replica vectors defined over a region of range and depth, and stored as the columns of a matrix. The passband matrix, $\mathbf{P}$, consists of replica vectors in a given range/depth region that should ''pass'' through the filter with only a small, specified, amount of distortion. The stop band matrix, $\mathbf{S}$, consists of replica vectors that should be attenuated as much as possible by the filter. The replica vectors in $\mathbf{P}$ and $\mathbf{S}$ are calculated at grid points in range and depth and are normalized to have unit length. Replica vectors that are not in either $\mathbf{P}$ or $\mathbf{S}$ may be thought of as defining a ''don't care'' region in range and depth. Don't care regions are used to separate the pass- and stop bands so that the filter is not asked to simultaneously pass and attenuate very similar replica vectors. A typical definition of pass- and stop bands is shown in Fig. 1.

In order for matrix filtering to be effective there must be enough ''separation'' between the replica vectors in the passband and those in the stop band. This normally requires the use of a vertical array that spans the entire depth of the water, and even this is not sufficient to guarantee that there will not be ambiguities between the passband and stop band replica vectors. A more precise statement of the required separation is given in Sec. V A.

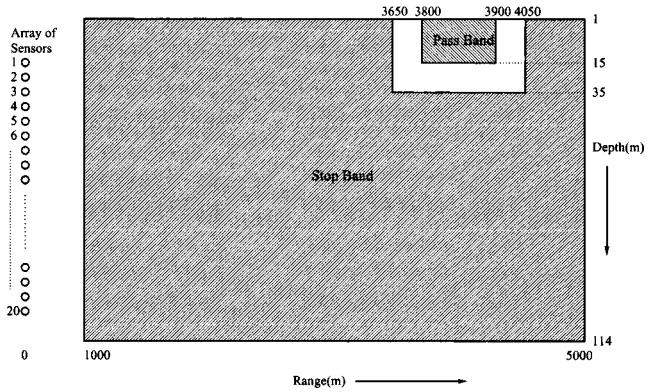

FIG. 1. Schematic diagram depicting the passband and stop band regions for a typical matrix filter.

In order to express matrix filter design as a standard optimization problem, we define a real-valued column vector $\mathbf{x}$ consisting of a concatenation of the real and imaginary parts of an $N\times N$ matrix $\mathbf{M}$. Specifically

$$\mathbf{x}=\begin{bmatrix}\mathbf{x}_1\\ \mathbf{x}_2\end{bmatrix}, \tag{3}$$

where

$$\mathbf{x}_1=[x_1\ \ x_2\ \ \cdots\ \ x_{N^2}]^T,\quad \mathbf{x}_2=[x_{N^2+1}\ \ x_{N^2+2}\ \ \cdots\ \ x_{2N^2}]^T, \tag{4}$$

and

$$\mathbf{M}(\mathbf{x})=\begin{bmatrix} x_1+jx_{N^2+1} & x_{N+1}+jx_{N^2+N+1} & \cdots & x_{N^2-N+1}+jx_{2N^2-N+1}\\ x_2+jx_{N^2+2} & x_{N+2}+jx_{N^2+N+2} & \cdots & x_{N^2-N+2}+jx_{2N^2-N+2}\\ \vdots & \vdots & \ddots & \vdots\\ x_N+jx_{N^2+N} & x_{2N}+jx_{N^2+2N} & \cdots & x_{N^2}+jx_{2N^2}\end{bmatrix}. \tag{5}$$

The design specifications for a matrix filter, $\mathbf{M}$, are given in terms of convex functions of the filter response. For example, the stop band performance is specified by the function

$$\phi(\mathbf{x})=\sum_{\mathbf{a}_i\in\mathbf{S}}\|\mathbf{Ma}_i\|^2, \tag{6}$$

which measures the total energy in the filter stop band response. The optimum matrix filter minimizes this quantity while preserving a specified level of fidelity in the passband. The filter passband fidelity is measured by the functions $f_i(\mathbf{x})$ defined as follows:

$$f_i(\mathbf{x})=\|\mathbf{Ma}_i-\mathbf{a}_i\|^2-\epsilon,\quad \mathbf{a}_i\in\mathbf{P}, \tag{7}$$

where ϵ is a user-specified constant. The matrix filter design problem may be written as the following constrained optimization problem:

$$\min_{\mathbf{x}}\ \phi(\mathbf{x})\ \text{ subject to }\ f_i(\mathbf{x})<0,\quad i=1,...,N_p, \tag{8}$$

where N_p is the number of replica vectors in the passband matrix $\mathbf{P}$. It can be shown that the objective and constraint functions in Eq. (8) are convex functions of $\mathbf{x}$.[7] Attractive features of convex optimization problems are that they can be numerically solved to a guaranteed accuracy, and there are no local minima.[8,9]

Notice in Fig. 1 that the passband of $\mathbf{M}$ is placed at shallow depths. Such a filter could be used to isolate and subtract a shallow interferer from the received data by applying the matrix filter $\mathbf{I}-\mathbf{M}$ to the data. Because the passband fidelity $f_i(\mathbf{x})<0$ is enforced for every vector in the passband, the matrix filter $\mathbf{I}-\mathbf{M}$ will provide a guaranteed amount of attenuation of $(10\log\epsilon)$ dB to any source in the passband of $\mathbf{M}$. This is true not only for a point source, but also for a distributed source contained in the passband of $\mathbf{M}$.

In order to deal with surface interference of unknown location, we use a collection of matrix filters whose passbands cover a specified region in range at shallow depths. A

statistic is introduced in Sec. V B to indicate which filter contains the interference in its passband.

A. Compressed replica vectors

Recall that a replica vector corresponding to a source at range r, depth z, and frequency ω_n can be expressed as

$$\mathbf{a}(r,z,\omega_n)=\mathbf{\Omega}(\omega_n)\boldsymbol{\alpha}(r,z,\omega_n), \tag{9}$$

normalized to unit norm, where $\mathbf{\Omega}(\omega_n)$ is a matrix of size $N\times Q$, $\mathbf{a}$ is a column vector of size $N\times 1$, and $\boldsymbol{\alpha}$ is a column vector of size $Q\times 1$. The condition for compressed replica vectors is that the number of modes is less than the number of sensors, or $Q<N$. Typically for low frequencies in our applications, N is in the range of 20 to 22 while Q is in the range of 10 to 20. Notice that the matrix $\mathbf{\Omega}(\omega_n)$ is independent of the source range and depth. It depends only on frequency and sensor depths. Thus, at a given frequency ω_n, all of the replica vectors in the passband and stop band will be in the column space of the fixed matrix, $\mathbf{\Omega}(\omega_n)$.

Let $\mathbf{\Omega}$ be a matrix whose columns are an orthonormal basis for the column space of $\mathbf{\Omega}(\omega_n)$. Then, any replica vector $\mathbf{a}_i$ can be written in terms of this basis as

$$\mathbf{a}_i=\mathbf{\Omega}\boldsymbol{\alpha}_i, \tag{10}$$

for some vector of coefficients $\boldsymbol{\alpha}_i$. Note that this coefficient vector can be written as

$$\boldsymbol{\alpha}_i=\mathbf{\Omega}^H\mathbf{a}_i, \tag{11}$$

where the superscript H is complex-conjugate (Hermitian) transpose. The vectors $\boldsymbol{\alpha}_i$ are referred to as *compressed replica vectors*. We now impose the requirement that the columns of a matrix filter $\mathbf{M}$ lie in the column space of $\mathbf{\Omega}$. This implies that filtered replica vectors will themselves be replica vectors. We impose the additional requirement that the rows of $\mathbf{M}$ lie in the row space of $\mathbf{\Omega}^H$. The reason for this requirement is that any component of the rows of $\mathbf{M}$ that is not in the row space of $\mathbf{\Omega}^H$ will be annihilated when $\mathbf{M}$ is multiplied by a replica vector. To see this, consider an arbitrary matrix $\mathbf{M}_1$, and let $\mathbf{M}$ be obtained by projecting the rows of $\mathbf{M}_1$ onto the row space of $\mathbf{\Omega}^H$; that is, $\mathbf{M}=\mathbf{M}_1\mathbf{\Omega}\mathbf{\Omega}^H$. Then

$$\mathbf{M}_1\mathbf{a}_i=\mathbf{M}_1\mathbf{\Omega}\boldsymbol{\alpha}_i=\mathbf{M}_1\mathbf{\Omega}\mathbf{\Omega}^H\mathbf{a}_i=\mathbf{M}\mathbf{a}_i, \tag{12}$$

where the second line follows from Eq. (11) and the third line follows from the definition of $\mathbf{M}$. Thus, when forming the objective or constraint functions we can work with the matrix $\mathbf{M}$, whose rows lie in the row space of $\mathbf{\Omega}^H$.

The requirements just introduced on the row and column spaces of $\mathbf{M}$ imply that there exists a $Q\times Q$ matrix $\mathbf{m}$ such that

$$\mathbf{M}=\mathbf{\Omega}\mathbf{m}\mathbf{\Omega}^H. \tag{13}$$

With this definition, we may now reformulate the terms that are summed in the objective function Eq. (6) and the passband fidelity constraint functions Eq. (7) as

$$\|\mathbf{M}\mathbf{a}_i\|^2=\|\mathbf{\Omega}\mathbf{m}\mathbf{\Omega}^H\mathbf{a}_i\|^2=\|\mathbf{\Omega}\mathbf{m}\boldsymbol{\alpha}_i\|^2=\|\mathbf{m}\boldsymbol{\alpha}_i\|^2 \quad \forall\,\boldsymbol{\alpha}_i\in\mathbf{S}_\alpha \tag{14}$$

$$\begin{aligned}\|\mathbf{M}\mathbf{a}_i-\mathbf{a}_i\|^2&=\|\mathbf{\Omega}\mathbf{m}\mathbf{\Omega}^H\mathbf{a}_i-\mathbf{a}_i\|^2\\&=\|\mathbf{\Omega}\mathbf{m}\boldsymbol{\alpha}_i-\mathbf{\Omega}\boldsymbol{\alpha}_i\|^2\\&=\|\mathbf{m}\boldsymbol{\alpha}_i-\boldsymbol{\alpha}_i\|^2 \quad \forall\,\boldsymbol{\alpha}_i\in\mathbf{P}_\alpha,\end{aligned} \tag{15}$$

Here, $\mathbf{P}_\alpha=\mathbf{\Omega}^H\mathbf{P}$ and $\mathbf{S}_\alpha=\mathbf{\Omega}^H\mathbf{S}$, where $\mathbf{P}$ is the matrix of passband replica vectors and $\mathbf{S}$ is the matrix of stop band replica vectors. We may now work with a smaller matrix $\mathbf{m}$ and use its elements as control variables for optimization. Once $\mathbf{m}$ is calculated, we may obtain $\mathbf{M}$ by using Eq. (13). The form of the objective and constraint functions in Eqs. (14) and (15) is exactly the same for the full matrix $\mathbf{M}$ and the compressed matrix $\mathbf{m}$. The only difference is that the replica vectors $\mathbf{a}_i$ are used with $\mathbf{M}$ while the compressed replica vectors $\boldsymbol{\alpha}_i$ are used with $\mathbf{m}$. An algorithm for matrix filter design is given in the next section. This algorithm is used to calculate $\mathbf{m}$ if $Q<N$, or $\mathbf{M}$ if $Q\geqslant N$.

III. MATRIX FILTER DESIGN

The matrix filter design problem, Eq. (8), is a constrained convex optimization problem. By introducing a barrier function, such a problem can be converted into a sequence of differentiable, unconstrained problems, each of which may be solved by Newton's method. This approach is described in Refs. 8 and 9, and it results in a very efficient algorithm for matrix filter design.

The standard problem Eq. (8) may be rewritten as[9]

$$\min_{\mathbf{x}}\{\phi(\mathbf{x})+I_{\text{feas}}(\mathbf{x})\}, \tag{16}$$

where $I_{\text{feas}}:\mathbf{R}^n\rightarrow\mathbf{R}$ is the (non differentiable) *indicator function* of the feasible set

$$I_{\text{feas}}(\mathbf{x})=\begin{cases}0 & f_i(\mathbf{x})\leqslant 0,\ \ i=1,...,m,\\ +\infty & \text{otherwise.}\end{cases} \tag{17}$$

Let $\hat{\psi}:\mathbf{R}^n\rightarrow\mathbf{R}$ be a continuous function that approximates the indicator function I_{feas} and has the following properties:

(1) $\hat{\psi}$ is differentiable and convex;
(2) The domain of $\hat{\psi}$ is the feasible set $\{x|f_i(\mathbf{x})<0,\ i=1,...,m\}$; and
(3) $\hat{\psi}$ grows without bound as $\mathbf{x}$ approaches the boundary of the feasible set.

Such a function $\hat{\psi}$ is called a *barrier function*. Substituting the barrier function $\hat{\psi}$ for the indicator function I_{feas}, we have the following unconstrained optimization problem:

$$\min_{\mathbf{x}}\{\phi(\mathbf{x})+\hat{\psi}(\mathbf{x})\}, \tag{18}$$

which is differentiable and convex. Note that Eq. (18) is an *approximation* to Eq. (16), while Eq. (16) is *equivalent* to the original constrained optimization problem Eq. (8). The quality of the approximation improves as $\hat{\psi}\rightarrow I_{\text{feas}}$.

A. Logarithmic barrier function

The logarithmic barrier function corresponding to a set of constraint functions $f_1(\mathbf{x}),\ldots,f_m(\mathbf{x})$ is defined as the function $\psi:\mathbf{R}^n\rightarrow\mathbf{R}$, with

$$\psi(\mathbf{x})=\begin{cases} -\sum_{i=1}^{N_p} \log(-f_i(\mathbf{x})) & f_i(\mathbf{x})<0,\ i=1,...,m \\ +\infty & \text{otherwise.} \end{cases} \tag{19}$$

It can be seen that $\psi(\mathbf{x})$ has a finite value if $f_i(\mathbf{x})<0$. However, if any $f_i(\mathbf{x})$ approaches 0, the value of $\psi(\mathbf{x})$ grows without bound, and thus $\psi(\mathbf{x})$ is a barrier function. Moreover, $\psi(\mathbf{x})$ serves as a differentiable and convex approximation to the indicator function.

The actual barrier function that is used in the unconstrained optimization problem Eq. (18) is a scaled version of the logarithmic barrier function

$$\hat{\psi}(\mathbf{x})=\frac{1}{t}\psi(\mathbf{x}), \tag{20}$$

where the scale factor is $1/t$. For any $t>0$, the function $(1/t)\psi$ is also a barrier function. The larger the value of t, the better the barrier function $(1/t)\psi$ approximates the indicator function, I_{feas}. In the limiting case of t being very large, we are essentially minimizing the objective function while satisfying the constraints, which is precisely what we need. But, we cannot begin with a large value of t because Newton's method will not converge due to numerical ill-conditioning problems.[8,9] Thus, we need to begin with a small value of t and solve a sequence of optimization problems with larger and larger values of t.

The gradient and Hessian of the logarithmic barrier function $\psi(\mathbf{x})$ are given in terms of the gradients and Hessians of the constraint functions $f_i(\mathbf{x})$ as follows:[9]

$$\begin{aligned} \nabla\psi(\mathbf{x})&=\sum_{i=1}^{N_p}\frac{-1}{f_i(\mathbf{x})}\nabla f_i(\mathbf{x}), \\ \nabla^2\psi(\mathbf{x})&=\sum_{i=1}^{N_p}\frac{1}{f_i^2(\mathbf{x})}\nabla f_i(\mathbf{x})\nabla f_i(\mathbf{x})^T+\sum_{i=1}^{N_p}\frac{-1}{f_i(\mathbf{x})}\nabla^2 f_i(\mathbf{x}). \end{aligned} \tag{21}$$

With $f_i(\mathbf{x})$ defined in Eq. (7), we use the logarithmic barrier function $\psi(\mathbf{x})$ given by (19) with gradient and Hessian given by (21). The expressions in (21) are written in terms of the gradients and Hessians of the constraint functions $f_i(\mathbf{x})$. These gradients and Hessians are derived in Ref. 7. The results are given below. The gradient can be written in terms of

$$\mathbf{z}_i=\text{conj}(\mathbf{a}_i)\otimes\mathbf{M}\mathbf{a}_i \quad \text{and} \quad \mathbf{w}_i=\text{conj}(\mathbf{a}_i)\otimes\mathbf{a}_i$$

where $\otimes$ denotes the Kronecker product. The gradient of the ith constraint function is

$$\nabla f_i(\mathbf{x})=2\begin{bmatrix}\text{real}(\mathbf{z}_i-\mathbf{w}_i)\\ \text{imag}(\mathbf{z}_i-\mathbf{w}_i)\end{bmatrix}. \tag{22}$$

The Hessian of the ith constraint function can be written in terms of

$$\mathbf{Q}_i=\text{conj}(\mathbf{a}_i)*\mathbf{a}_i^T, \tag{23}$$

and the $N\times N$ identity matrix, denoted $\mathbf{I}_N$. The superscript T is the matrix transpose. The result for the Hessian is

$$\nabla^2 f_i(\mathbf{x})=2\begin{bmatrix}\text{real}(\mathbf{Q}_i\otimes\mathbf{I}_N) & -\text{imag}(\mathbf{Q}_i\otimes\mathbf{I}_N)\\ \text{imag}(\mathbf{Q}_i\otimes\mathbf{I}_N) & \text{real}(\mathbf{Q}_i\otimes\mathbf{I}_N)\end{bmatrix}. \tag{24}$$

We also need to calculate the gradient and Hessian for $\phi(\mathbf{x})$ as they are required for Newton's method, which is discussed in Sec. III B. The gradient and Hessian for $\phi(\mathbf{x})$ may be expressed as[7]

$$\nabla\phi=2\sum_{\mathbf{a}_i\in\mathbf{S}}\begin{bmatrix}\text{real}(\mathbf{z}_i)\\ \text{imag}(\mathbf{z}_i)\end{bmatrix}, \tag{25}$$

$$\nabla^2\phi=2\sum_{\mathbf{a}_i\in\mathbf{S}}\begin{bmatrix}\text{real}(\mathbf{Q}_i\otimes\mathbf{I}_N) & -\text{imag}(\mathbf{Q}_i\otimes\mathbf{I}_N)\\ \text{imag}(\mathbf{Q}_i\otimes\mathbf{I}_N) & \text{real}(\mathbf{Q}_i\otimes\mathbf{I}_N)\end{bmatrix}. \tag{26}$$

B. Newton's method

The cost function for our problem is

$$c(\mathbf{x})=\left\{\phi(\mathbf{x})+\frac{1}{t}\psi(\mathbf{x})\right\}. \tag{27}$$

This cost function can be minimized using Newton's method. We start with an initial value of t and an initial value for the vector $\mathbf{x}$ denoted by $\mathbf{x}^{(0)}$. Newton's method constructs a quadratic approximation of the cost function at $\mathbf{x}^{(0)}$ and calculates a *Newton step* vector $\mathbf{v}$ that, when added to $\mathbf{x}^{(0)}$, results in a vector that minimizes the approximate cost function.[8,9] The Newton step is given by

$$\mathbf{v}=-[\nabla^2 c(\mathbf{x})]^{-1}\nabla c(\mathbf{x}), \tag{28}$$

where

$$\begin{aligned} \nabla c(\mathbf{x})&=\nabla\phi(\mathbf{x})+\frac{1}{t}\nabla\psi(\mathbf{x}), \\ \nabla^2 c(\mathbf{x})&=\nabla^2\phi(\mathbf{x})+\frac{1}{t}\nabla^2\psi(\mathbf{x}). \end{aligned} \tag{29}$$

Recall from Sec. II A that if the number of modes Q is less than the number of sensors N, we may use compressed replicas to design a matrix filter. In fact, we *must* use compressed replicas in this case; otherwise, it turns out that the Hessian matrix $\nabla^2 c(\mathbf{x})$ is singular and the Newton step in Eq. (28) is undefined.

In practice, the vector $\mathbf{v}$ is multiplied by a *step size* λ before being added to $\mathbf{x}$, i.e.,

$$\mathbf{x}^{(1)}=\mathbf{x}^{(0)}+\lambda\mathbf{v}^{(0)},$$

where $\mathbf{x}^{(1)}$ is the updated vector after the first iteration. We may write the general expressions for the iteration as

$$\mathbf{x}^{(k)}=\mathbf{x}^{(k-1)}+\lambda\mathbf{v}^{(k-1)}, \tag{30}$$

where $\mathbf{x}^{(k)}$ is the updated vector after k Newton iterations and $0<\lambda\leq 1$. With $\lambda=1$ the new value $\mathbf{x}^{(k)}$ in (30) may represent an infeasible set of parameters, i.e., $\psi(\mathbf{x}^{(k)})$ infinite. In this case, the value of λ is decreased until the value of the cost function evaluated at $\mathbf{x}^{(k)}$ is finite.

In order to use Newton's method for a constrained optimization problem we need a feasible initial guess for $\mathbf{x}$ (or $\mathbf{M}$), i.e., $\mathbf{x}^{(0)}$. We initialize $\mathbf{M}^{(0)}$ as an identity matrix of size $N\times N$. The identity matrix satisfies the passband constraints for any value of ϵ. The vector $\mathbf{x}^{(0)}$ may be formed from $\mathbf{M}^{(0)}$ by using Eq. (5).

TABLE I. Environmental parameters for Gulf of Mexico environment.

Parameter	Value
Water depth	114 m
Sediment sound speed	1600 m/s
Rock sound speed	1625 m/s
Sediment attenuation	0.5 dB/λ
Sediment density	1.85
Rock density	2.2

C. Maximum singular value constraint and deflation

In the optimization problem [Eq. (8)] for matrix filter design, constraints are used to achieve a desired passband fidelity. However, it turns out that the solution to Eq. (8), the optimal matrix filter, may have a maximum singular value much greater than unity.[7] Such a matrix has a large noise gain; that is, it amplifies the random component, **n**, of the data vector [see (1)]. As a result, the filtered data have a lower signal-to-noise ratio than the unfiltered data. This problem can be remedied by constraining the maximum singular value, σ_1, of the matrix filter to be less than $1+\delta$, where δ is selected by the user. Define

$$f_{N_p+1}(\mathbf{x}) = \sigma_1 - (1+\delta). \tag{31}$$

Then, the maximum singular value constraint can be written as

$$f_{N_p+1}(\mathbf{x}) < 0, \tag{32}$$

which is of the same form as the constraints in the original optimization problem, Eq. (8). The constraint Eq. (32) adds another term to the sum defining the logarithmic barrier function [see Eq. (19)]. Newton's method requires the gradient and Hessian of this new constraint function. They are derived in Ref. 7.

The derivative of the maximum singular value is defined only when the matrix has an isolated maximum singular value. However, when the constraint [Eq. (32)] is imposed, it may turn out that the optimal matrix filter has several singular values very close to the upper limit of $1+\delta$. Examples of such filters are given in the next section. In this case, the Newton algorithm will fail due to the nondifferentiability of a repeated maximum singular value. To overcome this problem, a deflation procedure is derived in Ref. 7. Whenever more than one singular value gets close to $1+\delta$, the subspace corresponding to those singular values is fixed and the optimization continues over a new, smaller set of filter parameters in the subspace corresponding to the remaining smaller singular values.

IV. MATRIX FILTER EXAMPLES

All of the examples in this section use a simulated environment that is modeled after a region in the Gulf of Mexico.[10] This is a three-layer shallow-water environment comprised of water over sediment over rock. A measured sound–velocity profile from the Gulf of Mexico was used in the simulations. The environmental parameters describing this environment are shown in Table I. The receiving array for the examples that follow is a 20-element vertical array of sensors placed every 5 meters in depth from 10 to 105 m. Replica vectors are computed on a grid of points spaced 10 m in range and 1 m in depth.

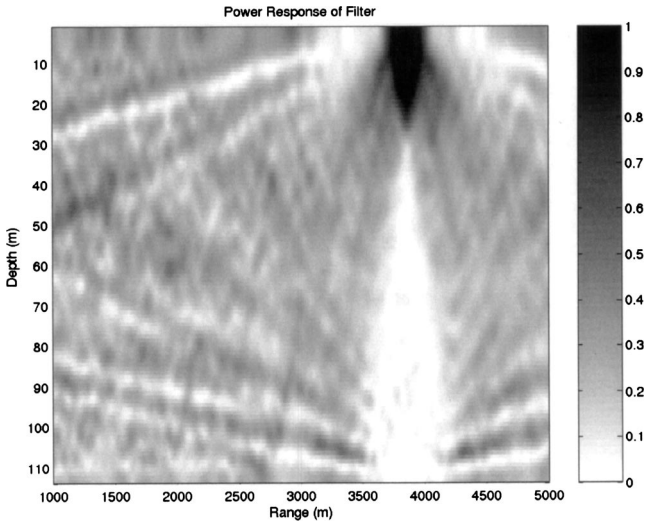

FIG. 2. Power response of a matrix filter, $F=375$ Hz.

In order to consider the response of a matrix filter, recall that the replica vectors are normalized to have unit norm. For replica vectors in the passband we know that $\mathbf{M}\mathbf{a}_i \approx \mathbf{a}_i$. The quality of the approximation is governed by the user-specified value of ϵ. Thus, the vectors $\mathbf{M}\mathbf{a}_i$ will have norm close to unity. Typically we have for the replica vectors in the passband, $0.9 \leqslant \|\mathbf{M}\mathbf{a}_i\|^2 \leqslant 1.0$. Replica vectors in the stop band are attenuated as much as possible (the total stop band energy is minimized). However, for many underwater environments, replica vectors evaluated at large differences in range and depth are not orthogonal. This limits the possible attenuation provided by the matrix filter in the stop band. Thus, typical filter response values in the stop band are $0.05 \leqslant \|\mathbf{M}\mathbf{a}_i\|^2 \leqslant 0.4$. The filter response is generated by plotting the energy $\|\mathbf{M}\mathbf{a}_i\|^2$ for all values of range and depth. Alternatively, we can plot $\|\mathbf{M}\mathbf{a}_i\|^2$ versus range for all depths.

All of the filters in the following sections were designed using ten different values of t in the cost function, Eq. (27). These values were spaced logarithmically from 1000 to 1.66×10^5 (see Ref. 9 for guidance on choosing t). For each value of t an average of five Newton steps was required to minimize the cost function.

A. A single-frequency filter

Consider the design of a matrix filter at frequency $f_1 = 375$ Hz. The passband region is 3800 to 3900 m in range and 1 to 15 m in depth. The stop band is given by the following three regions: 1000 to 5000 m in range and 34 to 114 m in depth; 1000 to 3650-m range and 1 to 34-m depth; 4050 to 5000-m range and 1 to 34-m depth. Replica vectors were calculated on a grid of points spaced every 10 m in range and 1 m in depth. The passband and stop band regions are shown in Fig. 1. The passband fidelity parameter $\epsilon=0.003$ and the maximum singular value is constrained to be less than 1.04 [i.e., $\delta=0.04$; see Eq. (31)].

The power response, $\|\mathbf{M}\mathbf{a}_i\|^2$, of this filter is shown in Figs. 2 and 3. The power in the passband is about 0.95. What

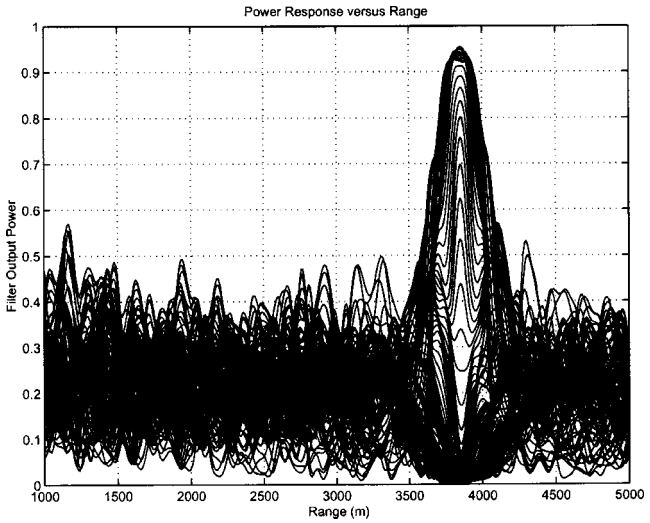

FIG. 3. Power response of a matrix filter plotted versus range for all depths, $F=375$ Hz.

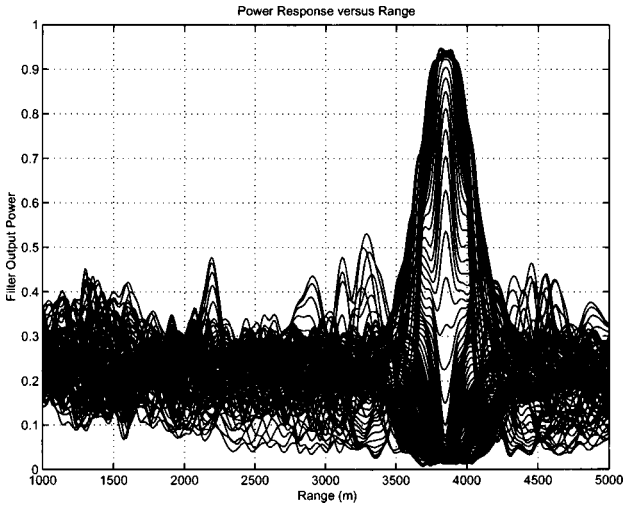

FIG. 4. Multifrequency matrix filter response, $F=[375,400,425]$.

is not shown by these figures is that the desired fidelity of $\epsilon=0.003$ is achieved at every replica vector in the passband. The power in the stop band varies between 0.01 and 0.6 with an average value of 0.21. In other words, the value of the objective function for the optimal matrix filter is $\phi=0.21$.

The five largest singular values for the optimal matrix filter are: 1.0399, 1.0398, 1.0357, 0.9610, 0.9111. Notice that the three largest singular values are all very close to the specified value of $1+\delta=1.04$. Thus, the maximum singular value constraint is active for this design and the deflation procedure was required.

If the maximum singular value constraint is not enforced in the design, the resulting optimal matrix filter has an isolated maximum singular value of 10. This filter has a large noise gain. The value of the objective function for this filter is $\phi=0.20$, which is slightly better than the ϕ value for the filter with the singular value constraint. Taking noise gain into account, however, the singular value constrained filter is preferable.

In a practical application of matrix filters, data vectors may arise from range/depth locations that do not correspond to any of the grid points used to design the filter. In order to assess the robustness with respect to grid spacing of the matrix filter designed above, the fidelity of the filter was evaluated on a dense grid of passband replica vectors, $\mathbf{P}_d$, consisting of replica vectors spaced 1 m in range and 0.25 m in depth, with the following result:

$$\max_{\mathbf{a}\in\mathbf{P}_d}\|\mathbf{M}\mathbf{a}-\mathbf{a}\|^2=0.003\,85. \tag{33}$$

At the matrix filter design points (spaced 10 m in range and 1 m in depth) the fidelity is less than the specified value of 0.003. Thus, there is some degradation in fidelity, but not enough to prevent the proposed method from working when data that are not on the design grid are used (see the example in Sec. V B).

B. A multifrequency filter

Suppose filter passband and stop band regions, passband fidelity parameter ϵ, and maximum singular value parameter δ are defined as in the previous example. These specifications may be used to design several filters at several different frequencies. For example, given a vector of frequencies $F=[f_1\,f_2\cdots f_r]$, one can design r different matrix filters $\mathbf{M}_1$, $\mathbf{M}_2,\ldots,\mathbf{M}_r$, one filter for each of the given frequencies. A broadband signal can then be processed incoherently at the r frequencies. The collection of filters $(\mathbf{M}_1,\mathbf{M}_2,\ldots,\mathbf{M}_r)$ is referred to as a *multifrequency matrix filter*. The power response of such a filter is simply the average of the power responses of the individual filters

$$\frac{1}{r}\sum_{j=1}^{r}\|\mathbf{M}_j\mathbf{a}_i(j)\|^2. \tag{34}$$

The replica vectors are indexed by i, which refers to some value of range and depth, and j, which refers to frequency.

Consider a multifrequency filter with the same specifications as in the previous example and frequency vector $F=[375\,400\,425]$ Hz. The power response of this filter is shown in Fig. 4. The sidelobes are almost all below 0.5, and the highest sidelobe is less than 0.55. Compare this with the response of the single-frequency filter shown in Fig. 3. That filter has many more sidelobes near 0.5 than the multifrequency filter. Processing several frequencies results in lower sidelobes. The number of modes at these three frequencies are 18, 19, and 20, respectively. Thus, compressed replica vectors are needed for 375 and 400 Hz.

V. INTERFERENCE SUPPRESSION AND SOURCE LOCALIZATION

Matrix filters may be employed for loud source interference suppression and, consequently, allow matched-field localization of a quiet source using a Bartlett processor.[11] Given a data vector **d** observed on the sensor array and replica vectors **a** [computed using Eq. (9)] from a range/depth search region, R, the Bartlett processor computes

$$\frac{|\mathbf{a}^H\mathbf{d}|^2}{\|\mathbf{d}\|^2}, \quad \mathbf{a}\in R. \tag{35}$$

The range and depth associated with the replica vector that produces the maximum value in the above equation is taken as the estimate of the source range and depth. The output of the Bartlett processor, displayed as a function of range and depth, is called a Bartlett surface.

Consider the numerator in Eq. (35) for the case of two sources, $\mathbf{d}=\mathbf{d}_1+\mathbf{d}_2$

$$|\mathbf{a}^H\mathbf{d}|^2=\mathbf{a}^H\mathbf{R}\mathbf{a}, \tag{36}$$

where

$$\mathbf{R}=\mathbf{d}\mathbf{d}^H=\mathbf{d}_1\mathbf{d}_1^H+2\ \ \mathrm{Real}(\mathbf{d}_1\mathbf{d}_2^H)+\mathbf{d}_2\mathbf{d}_2^H. \tag{37}$$

We make the assumption that the data vectors $\mathbf{d}_1$ and $\mathbf{d}_2$ have random phases and are uncorrelated, so that the expected value of $\mathbf{R}$ is

$$E(\mathbf{R})=\mathbf{d}_1\mathbf{d}_1^H+\mathbf{d}_2\mathbf{d}_2^H. \tag{38}$$

If the matrix $\mathbf{R}$ is formed by averaging several data snapshots, then Eq. (36) would converge to the expected value given by Eq. (38). In the examples that follow, if there are two sources, we use Eq. (36) and Eq. (38) to calculate the numerator of Eq. (35). That is, we compute the mean of the Bartlett surface for uncorrelated sources.

Assume that there is a loud source S_1 in the passband and a quiet source S_2 in the stop band of a matrix filter $\mathbf{M}$. Let $\mathbf{d}_1$ and $\mathbf{d}_2$ be the data outputs from the vertical array of sensors in response to uncorrelated sources S_1 and S_2, respectively. Suppose the observed data vector $\mathbf{d}$ consists of the sum of the two sources, $\mathbf{d}=\mathbf{d}_1+\mathbf{d}_2$. Then, applying the matrix filter $\mathbf{I}-\mathbf{M}$ to the data yields

$$(\mathbf{I}-\mathbf{M})\mathbf{d}=(\mathbf{I}-\mathbf{M})\mathbf{d}_1+(\mathbf{I}-\mathbf{M})\mathbf{d}_2\approx(\mathbf{I}-\mathbf{M})\mathbf{d}_2. \tag{39}$$

The amount of attenuation of the loud source $\mathbf{d}_1$ (i.e., the quality of the approximation in the previous equation) is determined by the passband fidelity parameter ϵ. Assuming that ϵ is small enough so that the loud source is effectively removed, the filtered data are approximately equal to $(\mathbf{I}-\mathbf{M})\mathbf{d}_2$. Thus, the process of removing the loud source has distorted the quiet source in a known way. The amount of distortion is related to the height of the sidelobes of the matrix filter. For example, if the matrix filter had *perfect* attenuation in the stop band (i.e., $\|\mathbf{M}\mathbf{d}_2\|^2=0$), then the distortion would be zero because the residual data would consist of $\mathbf{d}_2$ plus noise. In practice, we want the sidelobes to be as low as possible. Multifrequency filters may be used to keep the sidelobe power, and hence the distortion, to an acceptable level.

Processing of the filtered data must take the distortion into account. For example, in order to use a Bartlett processor to localize the quiet source after removing the loud source, Eq. (35) must be modified in the following two ways: first, the residual data vector $(\mathbf{I}-\mathbf{M})\mathbf{d}$ is used in place of $\mathbf{d}$, and second, the model replica vectors must be distorted in the same way that the quiet-source vector $\mathbf{d}_2$ is distorted. That is, $\mathbf{a}$ in Eq. (35) is replaced by $(\mathbf{I}-\mathbf{M})\mathbf{a}$, normalized to have unit length. The next two examples show that with these modifications, the Bartlett processor can localize a quiet submerged source using residual matrix filtered data.

A. Static sources

Consider the case in which the observed data vector $\mathbf{d}$ is the sum of a multifrequency loud source $\mathbf{d}_1$, a multifrequency quiet source $\mathbf{d}_2$, and a noise vector $\mathbf{n}$. The sources and noise each are composed of a collection of three frequency components

$$\mathbf{d}_1=\{\mathbf{d}_1(f_1),\mathbf{d}_1(f_2),\mathbf{d}_1(f_3)\},\quad \mathbf{d}_2=\{\mathbf{d}_2(f_1),\mathbf{d}_2(f_2),\mathbf{d}_2(f_3)\},$$
$$\mathbf{n}=\{\mathbf{n}(f_1),\mathbf{n}(f_2),\mathbf{n}(f_3)\}. \tag{40}$$

In this example $F=[f_1\,f_2\,f_3]=[375\,400\,425]$ Hz. At each frequency, the norms of the loud-source replica vectors are equal to 1 and the norms of the quiet-source replica vectors are equal to 0.2. Thus, the power of the loud source is 14 dB greater than that of the quiet source at each frequency. The noise vectors at each frequency consist of uncorrelated Gaussian random variables, one at each sensor, of variance equal to 0.001. Because the array has 20 sensors, the total noise power at each frequency is 0.02, and so the signal-to-noise ratio is 3 dB with respect to the quiet source at each frequency. The loud source is located at a range of 3850 m and a depth of 10 m, and the quiet source is located at a range of 2500 m and a depth of 40 m. The matrix filter for this example is the multifrequency filter of the previous example. Note that $\mathbf{d}_1$ is in the passband of this filter and $\mathbf{d}_2$ is in the stop band.

Figure 5 shows four Bartlett surfaces related to this problem, with each plot normalized to have a peak value of unity. This normalization gives all plots the same dynamic range, which is useful for visually comparing the peak-to-sidelobe ratios. We also report the peak values of the unnormalized Bartlett surfaces, given by Eq. (35) as well as the value of the denominator of Eq. (35). In the first figure (a) the data consist of the loud source plus noise. The value of $\|\mathbf{d}\|^2$ is 1.038. The peak of the normalized Bartlett surface is in the correct range–depth location, with an unnormalized peak value of 0.985. In the absence of noise this peak value would be unity. The actual height of the peak is related to the SNR, which is 17 dB with respect to the loud source. The highest sidelobes in this figure have a height of about 0.3 (5 dB lower than the peak) and there are sidelobes distributed throughout the surface with a height of 0.2 (7 dB below the peak). This is an indication of a good ''separation'' between the passband and stop band replica vectors for this environment. Based on our experience with other environments, the matrix filter technique will work with sidelobes 2 to 4 dB below the peak.

In the second figure (b) the data consist of the quiet source plus noise. The value of $\|\mathbf{d}\|^2$ is 0.064. The peak of the normalized Bartlett surface is at the correct range–depth location with an unnormalized peak value of 0.771. This peak height is consistent with the fact that the SNR is 3 dB with respect to the quiet source. In the third figure (c) the data consist of both the loud and quiet sources plus noise. Because the loud source is 14 dB louder than the quiet source, this figure is nearly identical to (a) and the location

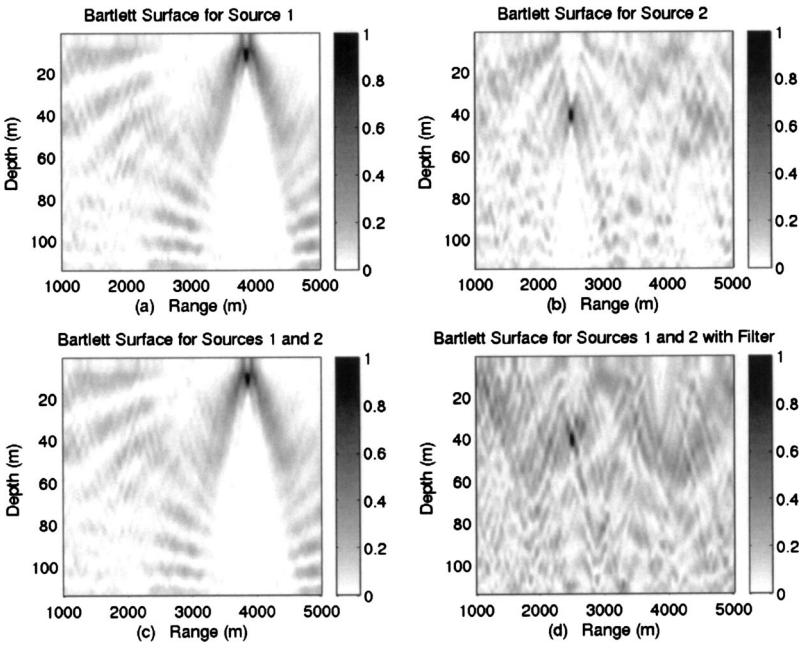

FIG. 5. Normalized Bartlett surfaces: (a) for source 1 (loud); (b) for source 2 (quiet); (c) for both sources; (d) for both sources with matrix-filtered data.

of the quiet source is not revealed in Bartlett surface (c). If the power of the quiet source had been closer to that of the loud source, say within 3 dB or less, the Bartlett surface in (c) would have shown two peaks at the locations of the two sources. From the point of view of detecting the quiet source, matrix filters would not be necessary in this case. However, when the power of the quiet source is about 7 dB or more below that of the strong source, a peak corresponding to the quiet source would not be seen in figure (c) but would be seen in figure (d).

In the fourth figure (d) the data consist of both sources plus noise. The data vector has been filtered by $\mathbf{I}-\mathbf{M}$ and the replica vectors used to form the Bartlett surface have also been filtered by $\mathbf{I}-\mathbf{M}$ and normalized. The value of $\|(\mathbf{I}-\mathbf{M})\mathbf{d}\|^2$ is 0.054. This figure is nearly identical to (b). In particular, the isolated peak clearly shows the correct location of the quiet source. The value of the unnormalized peak is 0.544.

B. Moving sources

Consider the case in which both the loud source and the quiet source are moving. We assume that the loud source is near the surface at an unknown range. A collection of multifrequency filters is designed, each with a passband of 1 to 15 m in depth and a 100-m range interval. The passband range intervals for three of these filters are

$$\mathbf{M}_1: 3800-3900 \text{ m},$$

$$\mathbf{M}_2: 3900-4000 \text{ m}, \quad \mathbf{M}_3: 4000-4100 \text{ m}. \tag{41}$$

The filter $\mathbf{M}_1$ is identical to the filter described in Sec. B. The design specifications for $\mathbf{M}_2$ and $\mathbf{M}_3$ are the same as those for $\mathbf{M}_1$ except for the passband range interval. If a collection of matrix filters is designed to cover a large range interval such as 1000 to 5000 m at shallow depths, only one of these filters will be used to suppress a loud surface interference source. The correct filter to use is the one whose passband contains the loud source. This filter may be determined by computing the ratio of energies in the matrix filtered and residual data for each of the matrix filters in the collection. This ratio, denoted by γ, is called the *filter statistic*, and is given by

$$\gamma = \frac{\|\mathbf{M}\mathbf{d}\|^2}{\|(\mathbf{I}-\mathbf{M})\mathbf{d}\|^2}, \tag{42}$$

where $\mathbf{d}$ is the data vector containing the loud and quiet sources plus noise. If the loud source is in the passband of $\mathbf{M}$ then $\|\mathbf{M}\mathbf{d}\|^2$ will be large while the energy in the residual signal, $\|(\mathbf{I}-\mathbf{M})\mathbf{d}\|^2$, will be small. Consequently the filter statistic γ will be greater than unity.

Conversely, if the loud source is in the stop band of $\mathbf{M}$ then $\|\mathbf{M}\mathbf{d}\|^2$ will be small while $\|(\mathbf{I}-\mathbf{M})\mathbf{d}\|^2$ will be large (because $\mathbf{I}-\mathbf{M}$ does not significantly attenuate the loud source). Thus, in this case, the filter statistic will be less than unity. If the filter statistic is computed for each matrix filter in the collection, then the filter producing the largest value should contain the loud source in its passband.

Consider the following scenario, illustrated in Fig. 6. A loud source at a constant depth of 12 m moves at constant velocity from range 3800 to 4100 m in 150 s. This source

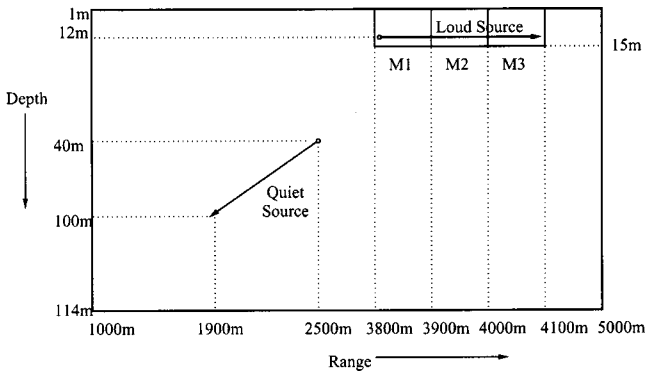

FIG. 6. Moving sources scenario with a loud surface source and a quiet submerged source.

will be in the passband of $\mathbf{M}_1$ [see Eq. (41)] for 0 to 50 s, in the passband of $\mathbf{M}_2$ for 50 to 100 s, and in the passband of $\mathbf{M}_3$ for 100 to 150 s. Simultaneously there is a quiet source moving with constant velocity from range and depth (2500,40) m to a range and depth of (1900,100) m. Data are generated at a sampling interval of 1.25 s. This causes the replica vectors for the sources to be evaluated at range grid points spaced at 2.5 m and depth grid points spaced at 0.5 m. Recall that the grid spacing used to design the matrix filters (as well as to calculate the Bartlett surfaces) is 10 m in range and 1 m in depth. The frequencies and powers of the sources and noise are the same as those in the static source example. The configuration in the static source example is identical to the first point in this moving source example.

With the sources moving along the trajectories shown in Fig. 6, the filter statistic Eq. (42) is computed every 1.25 s for all three filters; the results are shown in Fig. 7. At each point in time the filter producing the largest statistic will be used for interference suppression. As expected, the statistic for $\mathbf{M}_1$ peaks first, followed by the statistics for $\mathbf{M}_2$ and $\mathbf{M}_3$. At each sampling instant the filter producing the largest value of the filter statistic is used to form a residual data vector $(\mathbf{I}-\mathbf{M})\mathbf{d}$. A Bartlett surface is computed using this residual data vector and filtered replica vectors $(\mathbf{I}-\mathbf{M})\mathbf{a}$ (see the discussion at the beginning of Sec. V). The peak of each Bartlett surface gives the estimated range and depth of the quiet source. The Bartlett surfaces corresponding to the last point in the trajectory are shown in Fig. 8. The first three figures (a)–(c) are similar to those for the first point in the trajectory, shown in Fig. 5. In the fourth figure (d), the peaks of all of the previous Bartlett surfaces are indicated by stars superimposed on the plot. It can be seen that the trajectory of the quiet source is correctly estimated. A detailed examination of the locations of the Bartlett peaks shows that, for the 121 points along the trajectory, 106 range estimates have an error of 5 m or less, 14 have an error of 10 m or less, and one has an error of 15 m. For the 121 depth estimates, 117 have an error of 0.5 m or less and four have an error of 1 m.

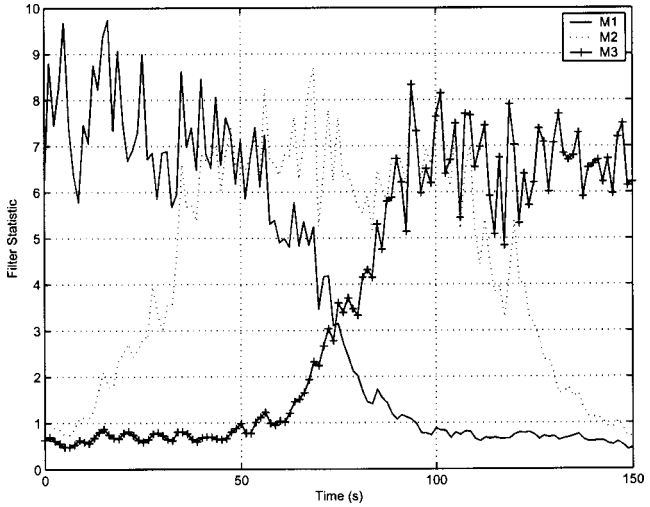

FIG. 7. Filter statistic plots for three matrix filters, $\mathbf{M}_1$, $\mathbf{M}_2$, $\mathbf{M}_3$ for the moving sources scenario.

The quality of each of the residual-data Bartlett surfaces varies only slightly along the trajectory. This quality is assessed by two ratios. The first is the peak to maximum sidelobe ratio. The maximum sidelobe is defined as the highest peak in the Bartlett surface outside a region R of ± 10 range and ± 5 depth grid points, centered at the peak. Recall that the range and depth grid points are spaced every 10 and 1 m, respectively. A second measure of quality is the peak to average background ratio. The average background is defined as the average of all the Bartlett points outside the region R. Figure 9 shows these ratios for the Bartlett surfaces formed both from the matrix filtered residual data (indicated by the word *filter*) and from data containing only the quiet source (indicated by the words *no filter*). The no-filter plots represent the ideal case in which the data contain only the quiet source and noise. We try to approximate this case with data

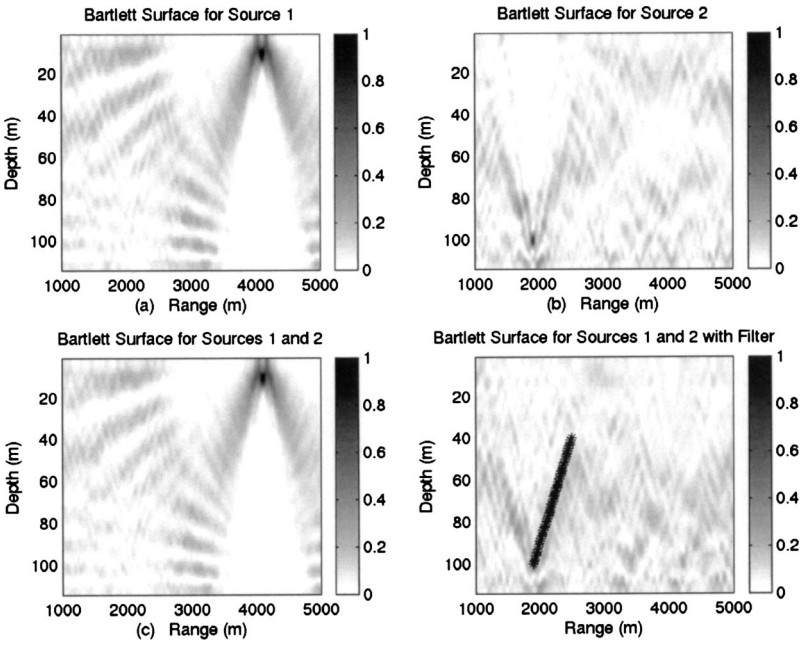

FIG. 8. Normalized Bartlett surfaces for the final point in the moving sources example. (a) For source 1 (loud); (b) for source 2 (quiet); (c) Bartlett surface for both sources; (d) Bartlett surface for both sources with matrix-filtered data. The peaks of all previous Bartlett surfaces are denoted with stars. They correctly identify the location of the quiet source.

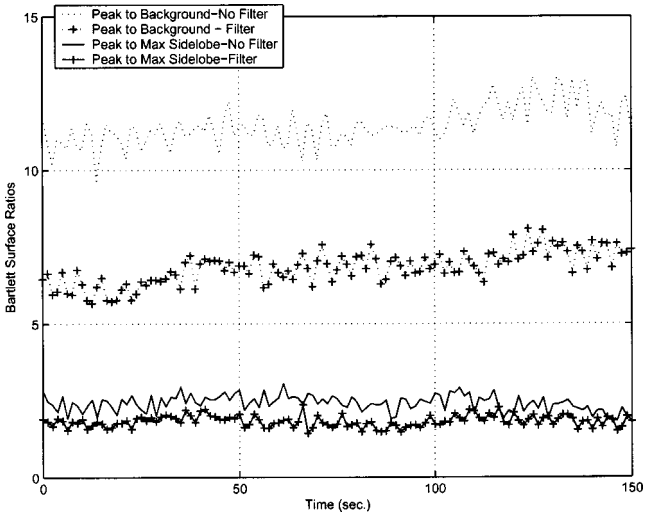

FIG. 9. Peak to maximum sidelobe and peak to average sidelobe ratios for the Bartlett surfaces at each point in the moving sources example for filtered data containing a quiet source and a loud interference, and unfiltered data containing only the quiet source.

that also contain interference by using a matrix filter to suppress the interference. Figure 9 shows that the peak to maximum sidelobe ratio varies between 1.5 and 3 along the trajectory for both the filtered and unfiltered data, with the ratio for the unfiltered data slightly higher. Using a matrix filter to suppress surface interference thus results in only a slight degradation of the peak to sidelobe ratio that would be obtained if no interference were present. Figure 9 shows that the peak to background ratio averages about 12 when no interference is present and about 7 when a matrix filter is used to suppress interference. Thus, when using a matrix filter to suppress a loud surface source, the major effect is simply an increase in the average background of the Bartlett surface.

VI. CONCLUSIONS AND ISSUES FOR FUTURE WORK

An algorithm to design matrix filters has been described. The filter specifications include the passband and stop band regions, the passband fidelity parameter, and the maximum singular value bound. The ability to design a matrix filter with a specified passband fidelity implies that the influence of a loud source in the residual data vector is attenuated by a guaranteed amount.

Given the filter specifications, a collection of matrix filters covering a large region in range and shallow depths is designed. A filter statistic, computed for each filter in the collection, is used to detect the presence of a loud source in the passband of one of the filters. This filter is then used to form the residual data vector $(\mathbf{I}-\mathbf{M})\mathbf{d}$, in which the loud source is effectively removed. A quiet source can then be localized with a Bartlett processor. The matrix filter is used to create new replica vectors $(\mathbf{I}-\mathbf{M})\mathbf{a}_i$ to use for this Bartlett processor.

It is possible to use matrix filters for tasks other than localization. For example, consider the problem of classifying a quiet, submerged source in the presence of a loud surface source. The performance of any classifier operating on the observed data would be degraded by the influence of the loud source. As described in this paper, a matrix filter could be used to obtain a residual data vector in which the loud source is attenuated and the quiet source is distorted in a known way. The classifier would have to be modified to account for this distortion just as the Bartlett processor for localization was modified in this paper. The extension of matrix filters to classification remains for future work.

The results in this paper were demonstrated in the ideal case of perfectly known environmental model and sensor locations. It is an open question how robust the method is to environmental mismatch and/or sensor location errors. It may be possible to account for these uncertainties in the following way. When forming the matrices **P** and **S** of passband and stop band replica vectors, one could generate these vectors using an ensemble of different environmental models and sensor locations. Using the resulting **P** and **S** matrices to design the matrix filters may impart some robustness at the expense of performance (e.g., stop band attenuation would be less than that of the nominal design). The issues of robustness assessment and improvement remain for future work.

Another approach to interference suppression and detection is adaptive beamforming, e.g., minimum variance distortionless response (MVDR).[12] Both the matrix filter method and adaptive beamforming attempt to reject interferer energy to improve the detection of weak sources. The matrix filtering approach uses a fixed set of filters whose design is independent of the received data. Interference suppression and detection can be accomplished with matrix filters using even a single data snapshot. The adaptive nature of the problem is dealt with by calculating the filter statistics for a bank of matrix filters to determine which filter passband contains the loud source. Adaptive beamforming, on the other hand, requires multiple snapshots to estimate the data covariance matrix, which is used to calculate a weight vector that is used to suppress the interference and detect the weak source. Comparison of the relative performance and robustness of these methods remains for future work.

ACKNOWLEDGMENTS

The authors would like to thank Brien Alkire and Professor Orlando Marino for helpful discussions. This work was supported in part by the Office of Naval Research, Dr. John Tague, ONR 321US.

[1] R. J. Vaccaro and B. F. Harrison, "Optimal Matrix-Filter Design," IEEE Trans. Signal Process. **44**, 705–709 (1996).
[2] K. Yoo and T. C. Yang, "Improved vertical array performance in shallow water with a directional noise field," J. Acoust. Soc. Am. **104**, 3326–3338 (1998).
[3] A. N. Mirkin and L. H. Sibul, "Maximum likelihood estimation of the locations of multiple sources in an acoustic waveguide," J. Acoust. Soc. Am. **95**, 877–888 (1994).
[4] H. P. Bucker, "Use of calculated sound fields and matched-field detection to locate sound sources in shallow water," J. Acoust. Soc. Am. **59**, 368–373 (1976).
[5] H. Medwin and C. S. Clay, *Fundamentals of Acoustical Oceanography* (Academic, New York, 1998).
[6] M. B. Porter, "The KRAKEN normal mode program," Tech. Rep. 6920, Naval Research Laboratory, 1992.

[7] A. Chhetri, ''Matrix Filters for Passive Sonar,'' Masters thesis, Department of Electrical and Computer Engineering, University of Rhode Island, Kingston, RI, 2002.
[8] J. Nocedal and S. J. Wright, *Numerical Optimization* (Springer, Berlin, 1999).
[9] S. P. Boyd and L. Vandenberghe, *Convex Optimization* (Cambridge University Press, Cambridge, 2004).
[10] J. Ianniello, ''A MATLAB version of the KRAKEN Normal Mode Code,'' Technical Report TM 94-1096, Naval Undersea Warfare Center, Newport, RI, October 1994.
[11] A. B. Baggeroer, W. A. Kuperman, and P. N. Mikhalevsky, ''An overview of matched field methods in ocean acoustics,'' IEEE J. Ocean. Eng. **18**, 401–424 (1993).
[12] H. L. Van Trees, *Optimum Array Processing* (Wiley, New York, 2002).

High-frequency (8–16 kHz) model-based source localization[a)]

Paul Hursky,[b)] Michael B. Porter, and Martin Siderius
Science Applications International Corporation, 10260 Campus Point Drive, San Diego, California 92121

Vincent K. McDonald
Space and Naval Warfare Systems Center, San Diego, 53560 Hull Street, San Diego, California 92152-5001

(Received 1 October 2003; revised 3 February 2004; accepted 3 February 2004)

Matched-field or model-based processing has now been widely demonstrated for improving source localization and detection in ocean waveguides. Most of the processing approaches become increasingly sensitive to fluctuations or uncertainties as the frequency increases. As a result, there has been very limited work above 1 kHz and there is a perception that above several kilohertz the technique cannot be applied. We have conducted acoustic communications experiments in a variety of shallow water sites around coastal areas of the United States. These experiments show that a clear multipath structure is readily observed even in the 8–16 kHz band. Furthermore, it is shown that model-based processing can then be exploited to localize sources at these high frequencies out to ranges of several kilometers. © *2004 Acoustical Society of America.* [DOI: 10.1121/1.1690078]

PACS numbers: 43.60.Kx, 43.30.Wi, 43.60.Uv, 43.30.Re [AIT] Pages: 3021–3032

I. INTRODUCTION

Over the last 20 years there has been a great deal of research on using or embedding acoustic models in signal processing algorithms. An example application is for vertical or horizontal line arrays in which the spatial and temporal multipath structure is used to determine the location of a source in the ocean waveguide.

The terminology for this work is not standardized. We use the term ''model-based'' processing to refer to any technique that uses a computer model of acoustic propagation in the ocean waveguide. This term encompasses:

(1) matched-field processing, which exploits the phase-amplitude structure of some small set of narrowband signals,[1–3]
(2) backpropagation or time-reversal techniques which use a computer model to propagate the field observed on the receive array and (under certain conditions) refocus it at the source location,[4–7]
(3) correlation processing, which exploits the temporal multipath structure.[8–21]

These techniques are all closely related and in some cases actually identical. However, they suggest different ways of organizing the processing and sometimes lead to different insights about how to exploit the space–time structure of the acoustic field. We will present source localization results obtained using correlation techniques. As indicated in the above mentioned citations, these techniques have been addressed in the literature at least as far back as 1971. The main thrust of this work is to extend the correlation-based techniques to significantly higher frequencies.

The motivation for working at higher frequencies includes:

(1) high spatial resolution can be achieved using small apertures,
(2) sources such as dolphins or AUVs have a signature in this band,
(3) the ambient noise background is significantly lower at high frequencies than in lower bands (where the clutter is dominated by surface shipping),
(4) understanding the propagation physics in this band will lead to insights into the performance of acoustic communications systems, and suggest better wave form and receiver designs.

Previously, source localization has been demonstrated in a midfrequency band,[22] using a 22-element vertical line array in very shallow water (<10 m) to process four tones at 2.4, 3.5, 4.6, and 5.7 kHz out to 200 m in range. In other notable work at midfrequency,[23] 15 tones in the 3–4 kHz band from an 8-element vertical line array at a range of 1.5 km were processed using an approach that also optimizes the parameters characterizing the environment, such as ocean depth, bottom properties, and sound speed profile.

The first issue that arises is that of understanding qualitatively the propagation physics in this band. Should we expect distinct echoes from the surface and bottom? A variety of phenomena might conspire to produce a diffuse smear of acoustic energy, providing little structure to be exploited by a source location estimator:

(1) surface and bottom roughness,
(2) small-scale ocean variability,
(3) source/receiver motion,
(4) near-surface bubbles.

These phenomena have been addressed in the literature,[24] although most of the studies have been devoted to single boundary interactions and/or the backscattered field, and thus

[a)]Portions of this work were presented in ''High-frequency broadband matched field processing in the 8–16 kHz band,'' Proceedings of the IEEE Oceans 2003 Marine Technology and Ocean Science Conference, San Diego, CA, 22–26 September 2003.
[b)]Electronic mail: paul.hursky@saic.com

provide little guidance as to what sort of multipath signature might be observed, or whether it exhibits a reliable enough structure to be the basis for multipath ranging. As we will show, our experiments at a variety of typical shallow water sites reveal *a clear set of surface and bottom echoes rising well above the reverberant haze*.

The second issue is whether we can predict the field accurately enough to localize a source using the echo pattern as a fingerprint of target location. Model-based source localization at high frequency either requires very accurate modeling or must be made inherently robust against model mismatch. Our results demonstrate that *source localization at high frequencies is possible out to ranges of at least several kilometers* with even a minimal receiver configuration (a single phone in Sec. II, and a pair of phones in Sec. III). However, special techniques must be applied to exploit the reliable features of the propagation.

A series of experiments, part of ONR's SignalEx program,[25] have been conducted in a variety of shallow water coastal environments to relate the performance of acoustic communications systems to different propagation and oceanographic phenomena. These experiments consisted of using a fixed receiver to record wave forms from a transmitter allowed to drift out to ranges beyond which the signal was no longer detectable (on a single hydrophone). Typically, channel probe wave forms were alternated with wave forms to test specific communication modulation and coding schemes. The probes consisted of 50 ms LFM chirps, sweeping from 8 to 16 kHz, repeated four times per second. The probe pulses have enabled the channel impulse response to be measured in a variety of acoustic waveguides. We will present the results of applying our model-based source localization (correlation-based multipath ranging) to the probe signals.

Applying a matched filter to the probe pulses (i.e., using the known LFM chirp wave form as the correlation kernel) produces measurements of the channel impulse response at the pulse repetition rate. These measurements reveal the fine-scale time variations of the individual multipath components of the channel impulse response. Using a ray-based propagation model (which tells us which eigenray interacted with the surface, for example), enables us to isolate the physical mechanisms causing these multipath fluctuations that have such a major-impact on acoustic communications, environmental inversion, and source localization. As we will show, even after stabilizing the first couple of multipath arrivals from ping to ping, the later arrivals exhibit fluctuating amplitudes and times of arrival, due to the motion of the ocean surface, water column variability, and the varying bathymetry as the transmitter drifts in range. Besides measuring the fine scale temporal structure over 10 and 30 s intervals (at the two sites which we will discuss), having the source drift out to ranges until the probe signals were no longer detectable at the receiver (typically at 6–8 km) revealed how the channel impulse response varied as a function of range.

This paper presents results using the 8–16 kHz channel probes from sites at the New England Front and off the coast of La Jolla in San Diego, CA. Section II will show data from a SignalEx test on the New England Shelf in 2000. At this site, we will present source localization results based upon matching measured and modeled impulse response functions. The impulse response is measured by applying a matched filter, using the source wave form as the correlation kernel. Obviously, in many applications, the source would not be so cooperative as to let its wave form be known. We have previously[21] demonstrated how to extend the impulse response method to auto- and cross-correlation wave forms. Section III will show data from a SignalEx test off the coast of La Jolla in San Diego in 2002. At this site, we will present results using impulse response functions, and also cross-correlation wave forms. Matching cross-correlation wave forms does not require the source signature to be known, only that it be sufficiently broadband that its cross-correlation in the time-domain produces a narrow enough pulse to resolve multipath arrivals. Comparisons will be made between measured and modeled channel impulse response functions at both sites.

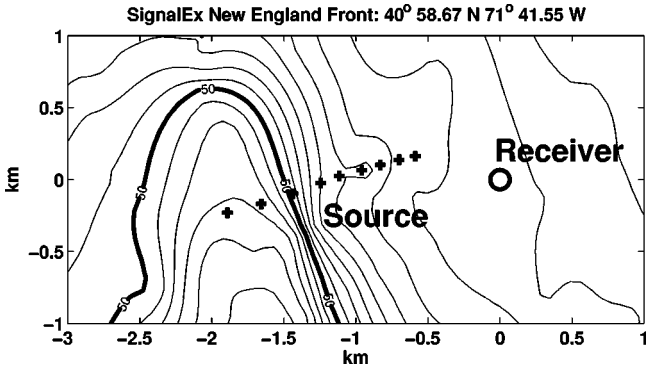

FIG. 1. SignalEx Front 2000 experiment configuration. Contour lines are spaced at 1 m intervals, with depth increasing moving west from the receiver to the heavy contour line at 50 m.

II. NEW ENGLAND SHELF RESULTS

Figure 1 shows the bathymetry on the New England Shelf where the SignalEx Front 2000 experiment was performed. The bathymetry between the receiver (indicated by the circle) and the drifting source (whose track is marked by plus marks) is mildly sloped, at least for the first several kilometers. A single radial from the receiver was used to set the bathymetry that was used to model the propagation at this site.

Figure 2 shows the measured sound speed profile and the depths of the source (29 m) and receiver (40 m). The sound speed profile is upward refracting and contains a surface duct, so there are fewer interactions with the bottom than in the La Jolla environment we will look at in Sec. III. The bottom sound speed is greater and the ocean is shallower at the New England site than in La Jolla. These effects combine to produce more multipath arrivals at the New England site than at the La Jolla site. However, the surface was rougher at the New England site, which caused the surface-interacting paths to exhibit arrival times that were not as well defined as at the La Jolla site.

All of the model-based techniques rely upon boundary interactions in the waveguide to produce multiple virtual images of the source (or receiver), which form an effective

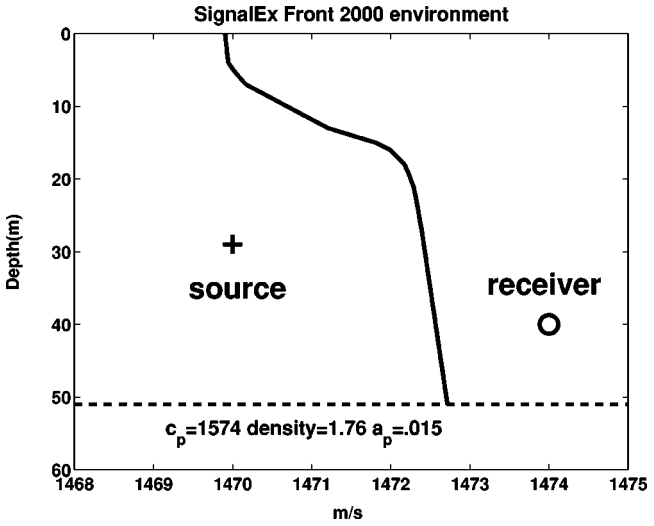

FIG. 2. SignalEx Front 2000 measured sound speed profile and presumed bottom properties, showing depths of source and receiver relative to the profile.

aperture much larger than the actual physical aperture, making it possible to estimate ranges and depths with arrays much smaller than would be needed in free space conditions.[26] As we will see, this makes source localization easier at the New England site.

Figure 3 shows two views of the wave form sequence during the SignalEx test on the New England Shelf in April of 2000. The upper plot in Fig. 3 covers 30 min, and shows different colored rectangles. The gray rectangles labeled ''P'' represent probe sequences. The rectangles labeled ''A''–''F'' represent acoustic communications test sequences. The six different test sequences are preceded by identical probe sequences. Each probe/test sequence pair occupies 5 min. The lower plot in Fig. 3 is a 10 s excerpt from the probes and shows repeating probe wave forms. Each probe interval (the ''P'' blocks) contains 40 LFM chirps. Each chirp sweeps from 8 to 16 kHz in 50 ms. The chirps are repeated every 250 ms (40 chirps in 10 s).

A. Channel impulse response measurements

The upper part of Fig. 4 shows 40 processed chirps (each row of the image is a matched filter output), from the

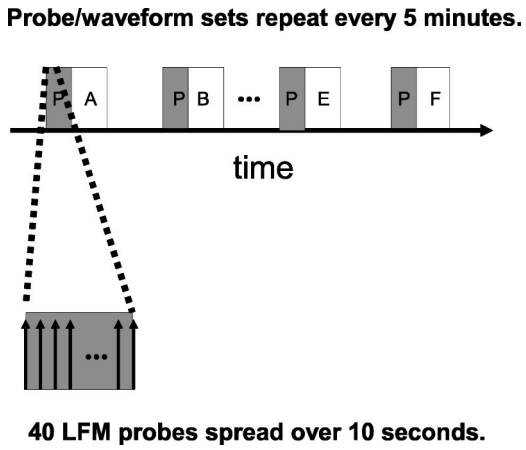

FIG. 3. Timeline of LFM probe signals (labeled P) and acoustic communications wave forms (labeled A–F) during SignalEx 2002.

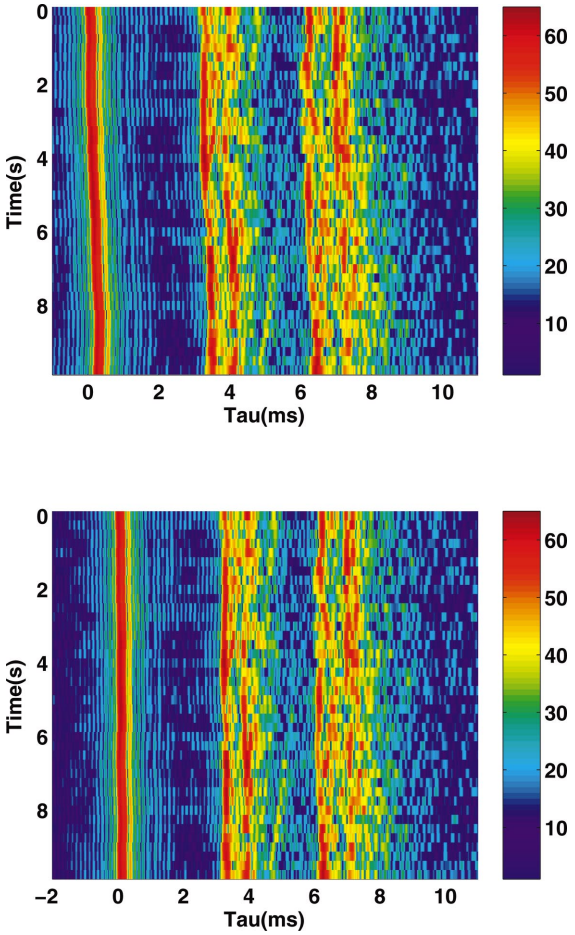

FIG. 4. The upper plot shows stacked impulse responses, aligned according to a constant Doppler correction. The lower plot shows stacked impulse responses, aligned by cross-correlating consecutive pairs of responses. Each row of these images contains the log-envelope (in decibels) of the matched filter output corresponding to a single LFM chirp. There were 40 8–16 kHz LFM chirps, each 50 ms long, transmitted every 250 ms. Only the first 10 ms of the measured channel impulse response is shown to isolate the details of the earliest arrivals (at this 500 m range, the entire impulse response lasted 50 ms).

SignalEx test on the New England Shelf, stacked one on top of the other. The rows of this image have been aligned by spacing them according to the known pulse repetition interval of 250 ms, corrected for a constant Doppler. Each row of this image contains the envelope of the matched filter output on a decibel scale, calculated using the known probe waveform as the matched filter replica.

The lower part of Fig. 4 shows the same 40 chirps, aligned by correlating each row with its predecessor. That is, each row is offset relative to the previous row so that the peak of their cross-correlation is at the zeroth lag. This method of aligning one matched filter output with respect to its predecessor is only one of many techniques we attempted, including peak picking. Using cross-correlation to align these wave forms turned out to be the most robust for this and other data sets. Because the cross-correlation is driven by the higher amplitude earlier arrivals (at least in this data set), the fluctuations are all but removed from these earlier arrivals by this process. At the same time, an alignment based on cross-correlation enables all arrivals to contribute to the alignment (and so is more robust than simply aligning on

the basis of the first peak location). However, the higher amplitude earliest arrival will clearly have the most influence. In other configurations (i.e., a different geometry, or a different propagation environment), later arrivals could very well dominate. Aligning the probes enables the structure in the later arrivals to be clearly seen, independent of the fluctuations in the early arrivals.

Although the entire impulse response has a duration of 50 ms at the range shown (500 m), we have displayed only 12 ms to isolate the first few arrivals, so that the fine structure in these arrivals can be observed. After the first arrival, two pairs of arrivals can be made out, but these later arrivals are not as stable as the first arrival, exhibiting some spread in the time of arrival and quite a bit of amplitude fading. Note that it is difficult to pick out a distinct track in any of these later arrivals. Later arrivals (not shown here) exhibited even worse fading. We speculate that this is due to the rougher surface at this site.

B. Modeling

In the previous section, Fig. 4 shows a single probes interval (10 s long, with 40 probes, each probe an LFM chirp). Rather than attempting to estimate source location from a single impulse response measurement (rarely are all the arrivals present in a single measurement, because of the amplitude fading), we averaged all 40 probe response envelopes to form a single composite impulse response estimate. Clearly, the alignment described in the previous section (based on cross-correlating consecutive impulse response measurements) is critical for this averaging to be effective. The upper part of Fig. 5 shows the result of stacking 26 such averages (roughly 2 h of the drift, out to 3 km range). Each row of the image shown in the upper part of Fig. 5 contains the average of one 10 s, 40-chirp time interval. Each of the 10 s intervals was Doppler corrected (as in the upper part of Fig. 4), aligned (chirp-to-chirp, as in the lower part of Fig. 4), and summed to form a single average impulse response function estimate. The signal-to-noise ratio (at the output of the matched filter and after averaging 40 chirps having a duty cycle of 20 percent) can be read from the upper part of Fig. 5 (the color scale is in dB). The earlier arrivals have a signal-to-noise ratio (SNR) of roughly 15 dB and the later arrivals (somewhat smeared by the averaging) have a SNR of roughly 5 dB. The averaging serves to stabilize the channel impulse response spreading and amplitude fading, but also smears out the later arrivals, whose time of arrival is not as consistent as the earliest arrival. These are the measurements that we must duplicate with a propagation model to form the source location estimate.

To reproduce the range-dependent impulse response function shown in the upper part of Fig. 5, the broadband channel impulse response function was modeled using the Bell-hop ray/beam tracing program.[27–29] This model calculates magnitudes, phases (note that envelopes are shown in the plots of modeling calculations), and times of travel of all multipath components for a particular source and receiver geometry, given a sound speed profile, geo-acoustic properties of the surface and bottom, and a potentially range-dependent bathymetry. No roughness was incorporated in the

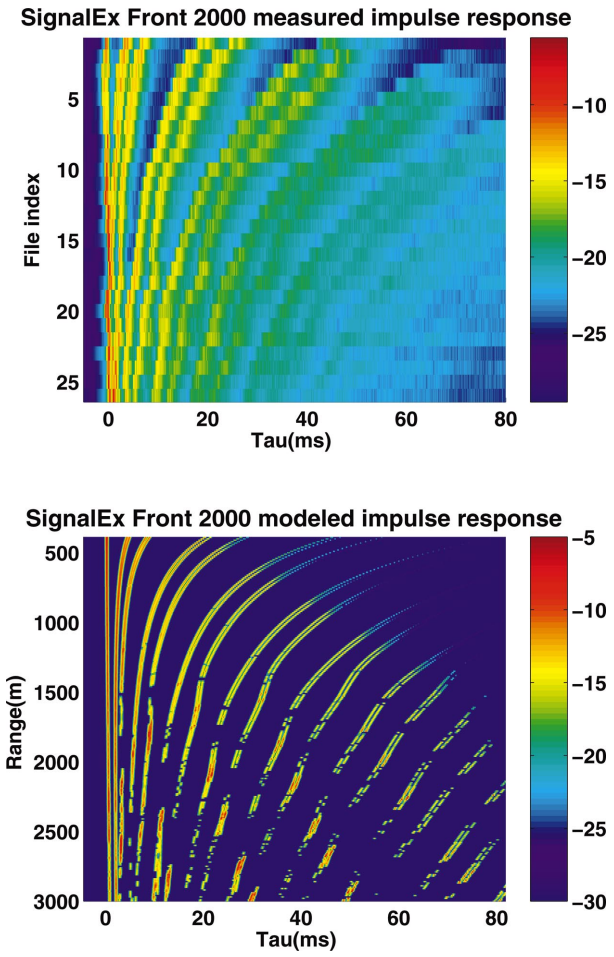

FIG. 5. Measured (upper) and modeled (lower) channel impulse response functions, as a function of range (receiver depth of 40 m and source depth of 29 m). Each scan line in the measured data is an average over 40 chirps spanning 10 s.

modeling, except for the coarse features specified by a bathymetry map. A band-limited impulse response function is synthesized from these multipath arrival parameters.

The lower part of Fig. 5 shows the multipath structure calculated by Bellhop for the experiment configuration during the New England Front SignalEx test (relative time of arrival is shown along the horizontal axis, and the ranges shown along the vertical axis are the ranges at which the data shown in Fig. 5 were measured, as calculated from GPS measurements). The agreement between the coarse features of the measured and modeled data shown in Fig. 5 is excellent, which bodes well for our model-based source localization. However, the later arrivals in the measured data, whose arrival times exhibit the fluctuations seen in the upper part of Fig. 4, have been smeared out by the averaging process, grossly underestimating the amplitudes of the later arrivals, compared to the amplitudes predicted by the model for the later arrivals in the lower part of Fig. 5. We will show how to reduce the impact of this mismatch so that source localization is possible even with significant fading.

The measured impulse response functions shown in Fig. 5 were aligned by cross-correlating consecutive rows, just as in Fig. 4 in the previous section. That is why the first arrivals do not all line up on a vertical line (the other arrivals con-

tribute and cause the alignment to move around a bit). The measured response functions are displayed using a detected early arrival to set the left edge of the first image row, and the peak cross-correlation (row to row) to set subsequent rows (as discussed earlier). The modeled results are displayed using a reduced time (range/sound speed) to set the left edge of each image row. As we will discuss in the next section, these time offsets (of one row with respect to the next, and between measured and modeled wave forms) do not impact the source location estimate.

We have used normal mode and parabolic equation models at lower frequencies to synthesize the time-domain impulse response functions (by transforming the spectrum calculated by runs of these full-wave models at each frequency), but a ray-based model provided adequate fidelity in this high frequency band, and was more convenient because it enabled direct manipulation of the time domain features of the impulse response function. Normal mode and parabolic equation models become computationally cumbersome at higher frequency.

C. Localization

As mentioned earlier, we are not introducing a novel source location estimator, but are extending correlation-based multipath ranging algorithms[8–21] to much higher frequencies, with some minor tricks to overcome difficulties peculiar to this band.

The source location metric $b(r,z)$ at source range r and depth z,

$$b(r,z)=\max_{n}\sum_{i=0}^{N-1} d_{i+n}m_i(r,z), \tag{1}$$

is calculated by cross-correlating d_{i+n}, the measured impulse response envelope, and $m_i(r,z)$, the modeled impulse response envelope, and then taking the maximum cross-correlation peak. Both d_{i+n} and m_i are wave form values, sampled at times i (or $i+n$, with n a correlation lag). The uper part of Fig. 5 shows the d_i values we will use (i corresponds to multipath time of arrival along the horizontal axis), with each row containing the impulse response function measured from a single 40-chirp interval (at a particular source range, to be estimated). The lower part of Fig. 5 shows the analogous m_i values as a function of time of arrival (along the horizontal) and source range (along the vertical). Because there is no time reference for the probe arrivals, we must match measured and modeled wave forms at all possible offsets of one with respect to the other, by cross-correlating them, as opposed to simply forming an inner product (which would have been possible, if we had a time reference). The metric used to match measured and modeled wave forms, $b(r,z)$ in Eq. (1), is taken to be the maximum value of their correlation (i.e., at whatever lag it occurs). The lag n at which this maximum value occurs does not enter into our source location estimate (because we can only measure relative times of arrival, and not the actual travel times).

Combining the multipath arrivals predicted by the ray-based model coherently, using the true spectrum, produces very short duration arrival pulses (1/bandwidth, where our chirps had a bandwidth of 8 kHz), and with complicated interference between overlapping arrivals. It is significantly more difficult to model the phases of the multipath components than the envelopes and times of arrival, even at lower frequencies.[21] Therefore, for this high frequency band, we chose to operate on the envelopes of the measured and modeled matched filter outputs, rather than the raw wave forms. Figure 5 shows envelopes (displayed using a decibel scale). Furthermore, it was very difficult to model the arrival times accurately to within the time resolution (1/8000 s) provided by our signal bandwidth of 8 kHz. In order to desensitize our modeling, we artificially reduced the bandwidth of the modeled signal (to broaden the multipath arrivals in the time domain) and combined the multiple arrivals incoherently (to avoid the increased opportunities for interference between arrivals that was a result of the reduced bandwidth).

Using the above-outlined process, a source location metric was calculated for every candidate source range r and depth z, at every time epoch for which we have measured the impulse response (as the source drifts in range). A two-dimensional ambiguity surface was produced for each time epoch, so that the overall output for the entire source drift was a three-dimensional ambiguity volume, indexed on source range, source depth, and time epoch.

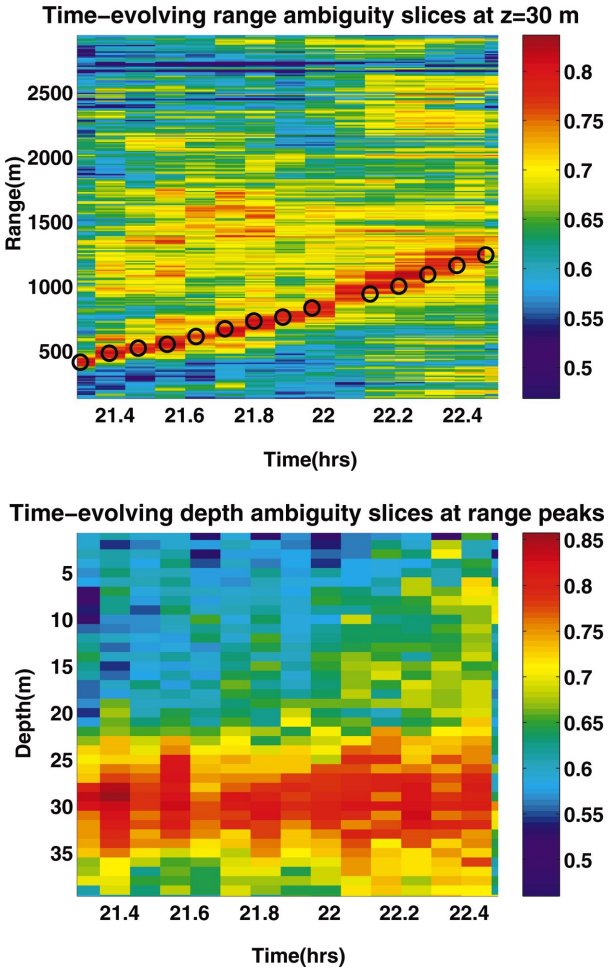

FIG. 6. Upper plot shows range track at source depth of 29 m (and receiver depth of 40 m). Black circles indicate ranges calculated from GPS measurements. Lower plot shows depth track along estimated range track.

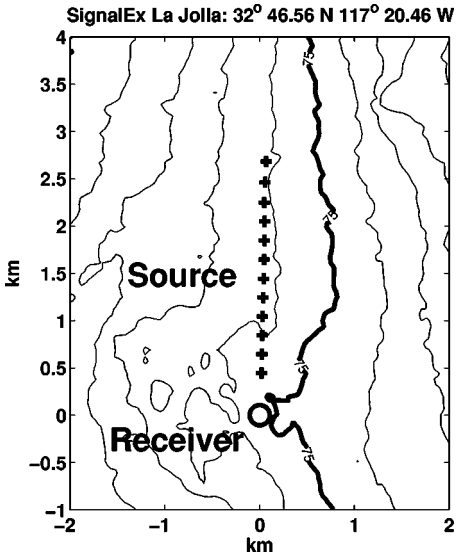

FIG. 7. SignalEx La Jolla 2002 experiment configuration. Contour lines are spaced at 5 m intervals, with depth increasing moving west. The heavy contour line indicates a depth of 75 m.

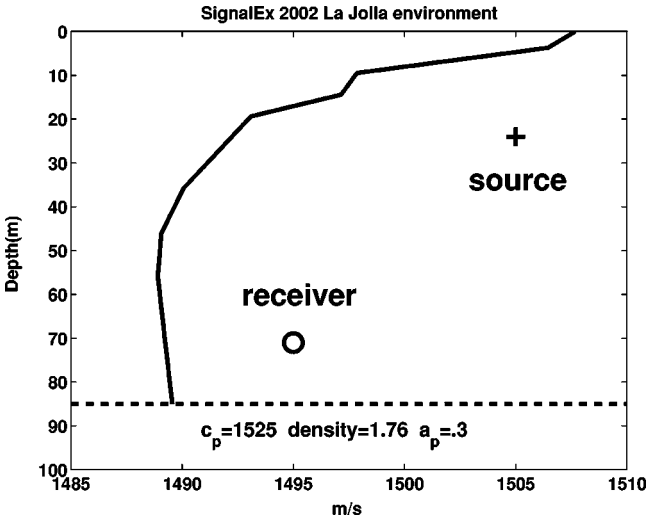

FIG. 8. SignalEx La Jolla 2002 measured sound speed profile and presumed bottom properties, showing depths of source and receiver relative to the profile.

The upper part of Fig. 6 shows the 2D slice versus range and time for the known source depth of 29 m. The circles indicate the known source range, calculated from GPS measurements at each time epoch. The range track is consistent with the GPS measurements. The lower part of Fig. 6 shows the slices versus depth that follow the source track in range. A very strong track is apparent at the known source depth of 29 m. A persistent track is apparent in both range and depth.

Note that the slice through the 3D ambiguity volume shown in Fig. 6 was selected (from among all the possible source depths) knowing the source depth. A way to independently determine the source depth from the 3D ambiguity volume would be to search for a continuous track among all depths, presuming the source depth was constant. We have scanned range-time slices (such as the one shown in Fig. 6) at all depths, and found that the most persistent track is found at the correct depth. Unfortunately, the individual 2D ambiguity surfaces in range and depth at each time epoch have so many spurious peaks that a 2D peak-picking process repeated at each time epoch does not produce a consistent track in range and depth. It is only when we seek a persistent track over many epochs that the source location reveals itself.

Despite these shortcomings, the results shown in Fig. 6 are quite surprising, given the high frequency band. Note that to get a track beyond the 500 m starting range required us to:

(1) average multiple measurements of the impulse response,
(2) operate on the envelopes of the data and the modeled wave forms (disregarding the phase),
(3) artificially increase the bandwidth of our modeled multipath arrivals to broaden them in the time domain, to reduce the sensitivity to model mismatch at these high frequencies.

III. LA JOLLA 2002 RESULTS

Figure 7 shows the bathymetry and locations of the receiver (circle) and transmitter (plus marks) at the La Jolla site, 5 km off the coast of San Diego in California. The receiver was moored to the bottom and suspended at a depth of 71 m. The transmitter was suspended at a depth of 24 m from a boat that drifted away from the receiver out to a range of roughly 7 km (only the first part of the track is shown in Fig. 7). The transmitter track follows an isobath at roughly 80 m (the heavy contour line to the right of the transmitter track is at a depth of 75 m).

Figure 8 shows the sound speed profile measured at this site and the receiver and transmitter depths relative to this profile. Note that compared with the profile at the New England site (see Fig. 2), where there is a surface duct keeping sound away from the bottom and favoring the surface, the La Jolla site has a downward refracting profile that favors interactions with the bottom. The bottom properties here, the slower compressional wave speed and greater attenuation, result in a less reflective bottom. As a result, we will see that there are fewer arrivals at the La Jolla site than at the New

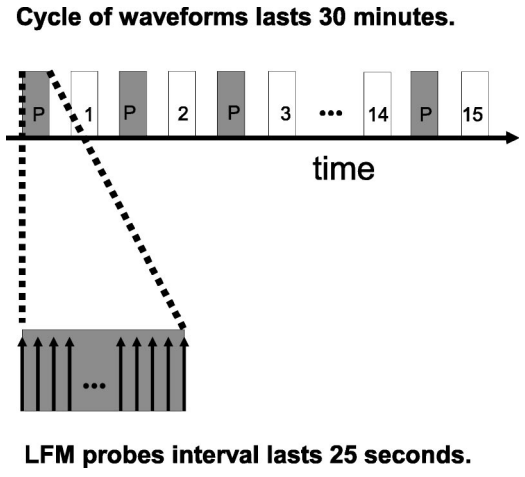

FIG. 9. Timeline of LFM probe signals (labeled P) and acoustic communications wave forms (labeled 1–15) during SignalEx 2002 in La Jolla.

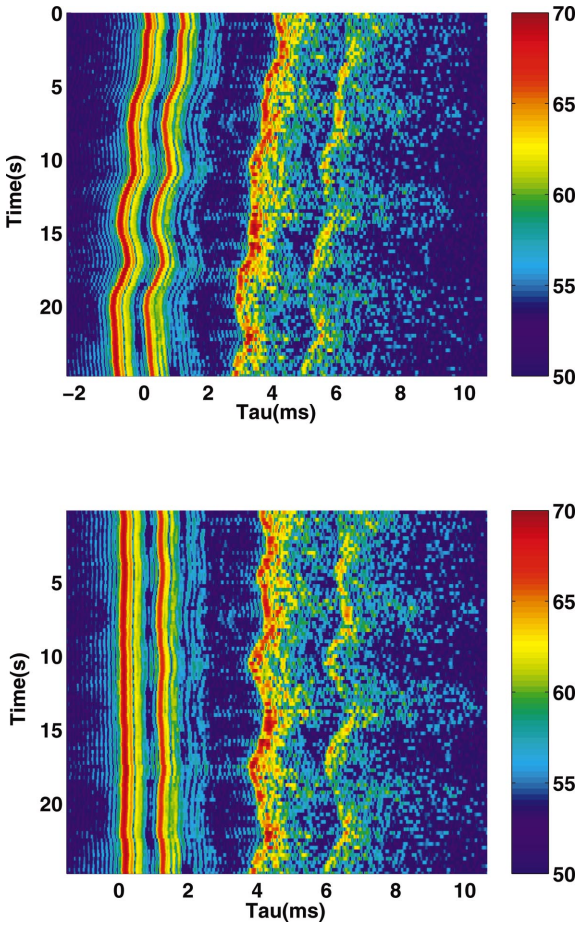

FIG. 10. The upper plot shows stacked impulse responses, aligned according to a constant Doppler correction. The lower plot shows stacked impulse responses, aligned by cross-correlating consecutive pairs of responses. Each row of these images contains the log-envelope (in decibels) of the matched filter output corresponding to a single LFM chirp. There were 100 8–16 kHz LFM chirps, each 50 ms long, transmitted every 250 ms. Only the first 10 ms of the measured channel impulse response is shown to isolate the details of the earliest arrivals (at this range, the entire impulse response lasted 60 ms).

England site. The surface was very calm, less rough than at the New England site.

Figure 9 is similar in format to Fig. 3 in Sec. II. In the 2002 SignalEx test at the La Jolla site, there were 15 acoustic communications wave forms being tested, each allotted 1 min of transmit time (the transparent boxes, labeled from 1 to 15, in the upper timeline). Each such test wave form was preceded by a probes interval (the gray boxes, labeled "P"), 1 min long, which contained 25 s of LFM chirps. Each chirp was 50 ms long, sweeping up from 8 to 16 kHz. These chirps were transmitted at a rate of 4 per s (i.e., every 250 ms). Thus, each 25 s probes interval produced 100 transmitted LFM chirps.

A. Impulse response measurements

Figure 10 is analogous to Fig. 4 in Sec. II A. The upper part of Fig. 10 shows 100 processed chirps (matched filter outputs), stacked one on top of the other, from the La Jolla 2002 site at a range of 450 m. There are significant fluctuations in all arrivals. The lower part of Fig. 10 shows the same 100 chirps, aligned by cross-correlating each row with its predecessor as described in Sec. II A. Here too, the later arrivals seem to be driven by a process that is independent of the process governing the earliest arrivals.

Note that, compared to the New England site, each arrival at the La Jolla site (in Fig. 10) is concentrated along a single well-defined track (in correlation lag time). We also see some reverberation following the third and fourth arrivals. In impulse response measurements made at the New England site (see Fig. 4), the multipath arrivals following the earliest arrival were broken up to such an extent that it was difficult to identify distinct tracks (in correlation lag time). Nevertheless, the arrivals following the first two arrivals at the La Jolla site have perhaps as much amplitude fading as those at the New England site.

Given the La Jolla configuration with the receiver close to the bottom and the source in the water column (see Fig. 8), and having modeled this configuration with a ray trace model, we can identify the first and second arrivals as direct and bottom-reflected paths, and the third and fourth arrivals as surface interacting paths. Although the fluctuations seen in the third and fourth arrivals (which appear to be strongly correlated) could be due to water column phenomena, they are probably due to the motion of the surface. The duration of the entire impulse response at this range was roughly 60 ms, but we are only showing the first 12 ms of this, so that the fine structure in the earlier arrivals can be observed. Later arrivals (not shown in this 12 ms excerpt) had similar fluctuations in (relative) arrival times and amplitudes.

B. Modeling

Figure 11 is analogous to Fig. 5 in Sec. II B. Each row in the upper part of Fig. 11 is the result of averaging the aligned matched filter outputs corresponding to 100 chirps (from a 25 s probes interval), as described in Sec. II B. The signal-to-noise ratio (at the output of the matched filter and after averaging 100 chirps having a duty cycle of 20%) can be read from Fig. 11 (the color scale is in decibels). The earlier arrivals have a SNR of roughly 15 dB and the later arrivals (somewhat smeared by the averaging) have a SNR of roughly 5 dB. These SNRs are at the output of the matched filter. The lower part of Fig. 11 shows the modeled impulse response envelopes as a function of range (the color scale is in decibels). The ranges along the vertical axis are the ranges at which the data shown in the upper part of Fig. 11 were measured, according to GPS measurements. The modeling has already been described in Sec. II B: the Bellhop ray/beam model was used along a radial (from the receiver) with a range-dependent bathymetry.

The dropouts seen along some of the later arrivals in the modeled data are due to the range-dependent bathymetry (they disappeared when a flat bottom was modeled). These were duplicated by a broadband parabolic equation calculation, run as a check on the ray tracing results. Because the measured data are the result of averaging over 25 s of drift, these dropouts are not observed in the measured data.

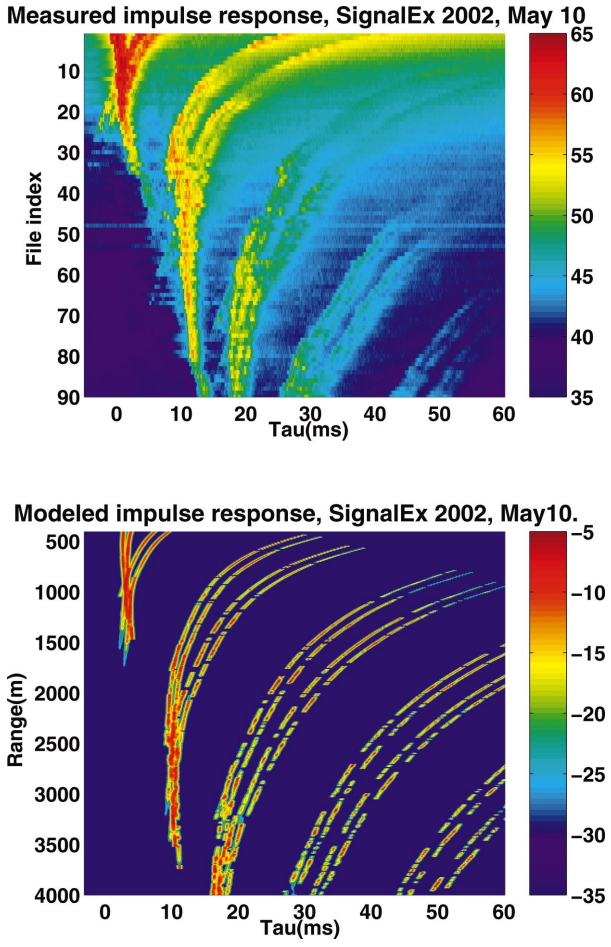

FIG. 11. Measured (upper) and modeled (lower) channel impulse response functions, as a function of range (receiver depth of 71 m and source depth of 24 m). Each scan line in the measured data is an average over 100 chirps spanning 25 s.

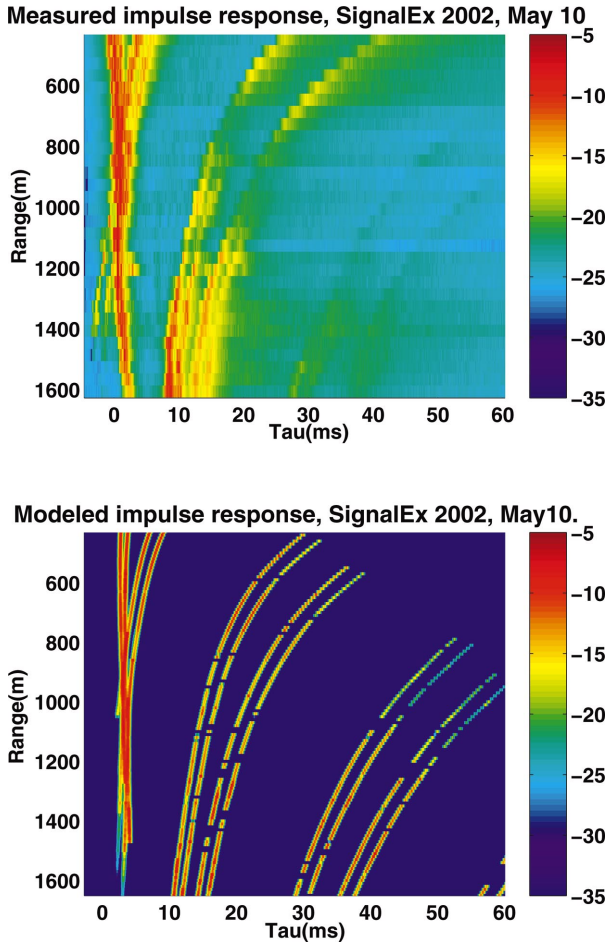

FIG. 12. Excerpts of measured (upper plot) and modeled (lower plot) impulse responses over range interval being processed.

C. Localization (source wave form known—matching matched filter outputs)

This section is analogous to Sec. II C: we present the results of matching measured and modeled impulse response functions (shown in the previous two sections) to estimate source location. However, using data from the La Jolla site, it was only possible to locate the source out to a range of 900 m using the techniques described in Sec. II C. We were able to obtain source location estimates beyond this range only after applying several transforms to the wave forms being matched. These transforms served to appropriately weight the features that served to distinguish different source ranges and depths.

When the technique presented in Sec. II C for the New England data was applied to the La Jolla data, plausible source location peaks were produced for only the first few (short) ranges. There were several reasons for this. Looking at the measured and modeled data, the mismatch in the higher amplitude earlier arrivals was dominating the information provided by the later arrivals. This was further compounded by the later arrivals being smeared out by our averaging process, due to the fluctuations in their time of travel (see Fig. 10), causing their amplitudes to be grossly overestimated by the modeling. There were also far fewer arrivals at this site (because of the downward refracting profile, a deeper ocean, and a softer bottom).

Figure 12 shows blowups of the measured and modeled data (seen in Fig. 11), showing what happens to the impulse response over ranges from 400 to 1600 m. Our initial attempt at source tracking failed at ranges around 1000 m. From 1000 to 1400 m, the pair of earliest arrivals is not predicted by the ray model. From 600 to 1200 m, the later set of arrivals (at ranges from 600 to 1100 m, between 10 and 20 ms in Fig. 12) show significant fading that is not predicted by the ray model. These differences between the measured and modeled data can be expected to cause problems for any source localization based on matching this measured and modeled data.

In previous work,[30] the log-envelope of impulse response data served to emphasize the contribution of later arrivals, which otherwise had much lower amplitudes than the earlier arrivals. Following this example, we tested several transformations of the measured and modeled impulse response wave forms to emphasize later arrivals, and as it turned out, to reduce the impact of fluctuations in the earlier arrivals.

The measured wave form was whitened using a three-pass, split-window moving average process to estimate both the mean and the standard deviation at each sample (many similar whiteners have been previously described[31]). The ini-

tial passes are used to form preliminary estimates of the mean and standard deviation (at each point in the data). These estimates are potentially biased by the presence of strong peaks. A "shearing" threshold is set based on these preliminary estimates (at a selected number of standard deviations above the mean), and any peaks exceeding this threshold are replaced by the current mean estimate (at that point). Once the peaks have been truncated, the moving average process is repeated on data that should no longer be corrupted by the presence of strong signals (an ideal noise measurement would be based on noise alone). After three passes of this process, estimated means and standard deviations have typically become reliable, and the data are whitened using estimates of its (noise) mean $\overline{x_i}$ and standard deviation σ_{xi}:

$$w_i = \frac{x_i - \overline{x_i}}{\sigma_{xi}}. \tag{2}$$

Low amplitude peaks surrounded by low power noise are transformed to values comparable to high amplitude peaks surrounded by high power noise. Since the noise typically is higher around the earlier peaks, this serves to emphasize the later arrivals and de-emphasize the earlier arrivals.

The above-described whitening process (applied to the measured data) was not appropriate for the modeled wave forms, since they are noiseless. Instead, the modeled wave form was raised to a fractional power (0.1) in order to reduce the disparity between the early and late arrival amplitudes (a transform that produces similar results to the log-envelope). In addition, the transformed modeled wave forms were forced to be zero-mean by subtracting their average value.

These somewhat *ad hoc* transforms, in addition to the steps described in Sec. II C for the New England data, resulted in the much-improved results shown in Fig. 13. The black circles in the upper plot indicate the known source ranges (as measured using GPS instruments). The lower part of Fig. 13 shows the slices versus depth intersecting the estimated ranges in the upper part of Fig. 13. In both the range and depth track plots, one-dimensional (1D) slices from a sequence of 3D volumes were stacked to form images. Because the dynamic range was not consistent across these 1D slices, each slice was rescaled to have a unit norm.

D. Localization (source wave form unknown—matching cross-correlation wave forms)

In the previous sections, the source location statistic or metric upon which the location estimate was based was calculated using the channel impulse response measured by a matched filter. These estimates presume that the source wave form is known. The more practical case occurs when we do not know the source wave form. Instead of operating on the measured impulse response, which can only be measured directly by knowing the source wave form, we operate on the auto- or cross-correlation of the impulse response function. Let $s(t)$ be the source wave form, and $S(\omega)$ its spectrum. Similarly, let $h(t)$ be the channel impulse response function, and $H(\omega)$ its spectrum. The received signal, $r(t)$, is the convolution of $s(t)$ and $h(t)$,

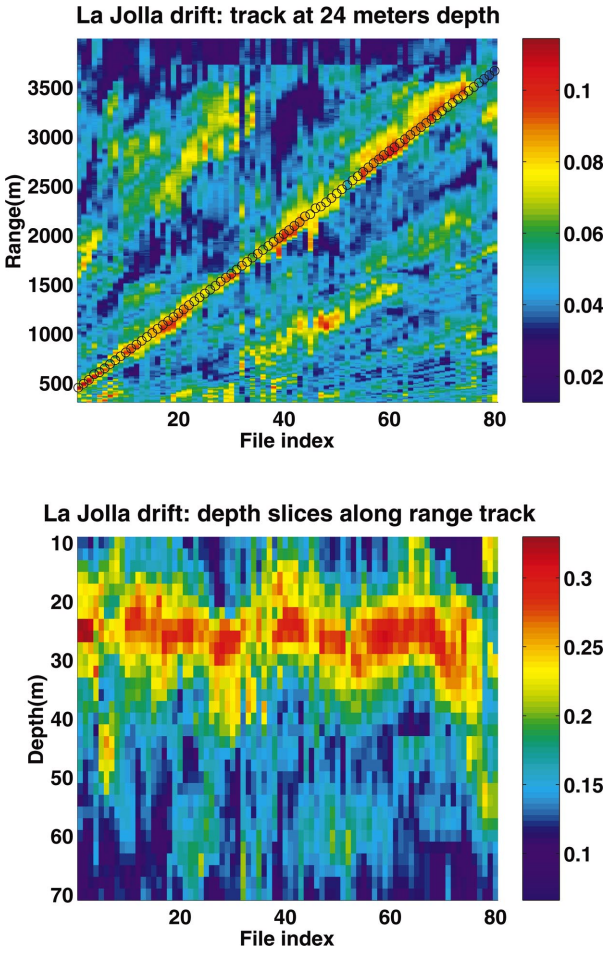

FIG. 13. Upper plot shows range track at source depth of 24 m (and receiver depth of 71 m). Black circles indicate ranges calculated from GPS measurements. Lower plot shows depth track along estimated range track.

$$r(t) = h(t) \otimes s(t),$$

where $\otimes$ is the convolution operator. Equivalently, in the frequency domain

$$R(\omega) = H(\omega) S(\omega).$$

Applying a matched filter is the same as correlating $r(t)$ with $s(t)$, which can be written in the frequency domain as

$$X(\omega) = S^*(\omega) R(\omega) = H(\omega) |S(\omega)|^2. \tag{3}$$

The superscript asterisk indicates a complex conjugate. Note that the phase of $s(t)$ no longer appears in the expression. Similarly, when we have two receiving elements, with impulse response functions $h_1(t)$ and $h_2(t)$, so that the spectra at the two receiver elements are $H_1(\omega)S(\omega)$ and $H_2(\omega)S(\omega)$, cross-correlating the two wave forms results in

$$\begin{aligned} C_{12}(\omega) &= [H_1(\omega) S(\omega)]^* [H_2(\omega) S(\omega)] \\ &= H_1^*(\omega) H_2(\omega) |S(\omega)|^2, \end{aligned} \tag{4}$$

where again the phase of the source wave form is not a factor. In Eq. (3), we recreate $H(\omega)$ using an acoustic propagation model. In Eq. (4), we use the same acoustic propagation model to recreate $H_1^*(\omega)H_2(\omega)$.

The fact that source wave form phase does not appear in the correlation wave forms means our process will work re-

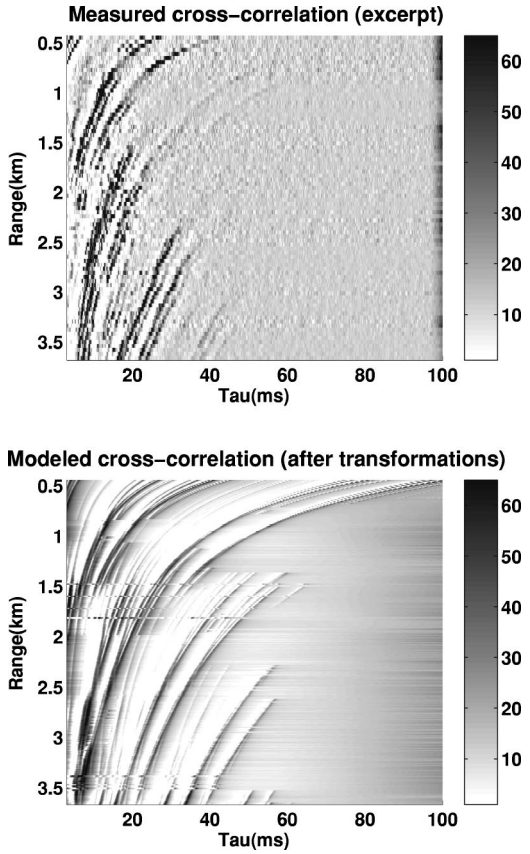

FIG. 14. Upper plot shows measured cross-correlation after whitening and excerpting. Lower plot shows the modeled cross-correlation after transformations and excerpting. An interval of 3–100 ms is shown.

gardless of whether the source wave form is a well-behaved wave form like a chirp, or whether it is closer to a completely random process. The source must have a wide enough spectrum so that its auto-correlation (the term $|S(\omega)|^2$) produces a narrow enough pulse in the time domain to resolve the multipath arrivals.

Note that using the cross-correlation envelope essentially removes the sensitivity to the center frequency—this means requirements for array element localization and source location search grid step size are set not by the high center frequency, but by the source bandwidth (which sets the pulse width in the time domain of the multipath arrivals). However, these benefits come at the cost of losing the gain otherwise available from coherently summing over frequency (if the source wave form phase is known, which for an uncooperative source is not likely anyway).

The impulse measurements do not have a time reference, so it is necessary to calculate the match at all possible relative time offsets between the measured and modeled wave forms (i.e. using a cross-correlation operation). The cross-correlation waveforms are functions of the time-difference-of-arrival only, so the measured and modeled wave forms are implicitly aligned and the match for each candidate source location is calculated using an inner product, which (in the time-domain at least) is more efficient than a cross-correlation.

The upper part of Fig. 14 shows the measured cross-correlation of two adjacent receive elements (arranged vertically and spaced 14 in. apart). The lower part of Fig. 14 shows their modeled cross-correlation. Both of these figures show wave forms after the transforms described in Sec. III C have been applied (prewhitening of the data wave form using a split-window three pass moving average process; raising the modeled wave form to the power 0.1, subtracting its mean, and re-scaling it to have unit norm).

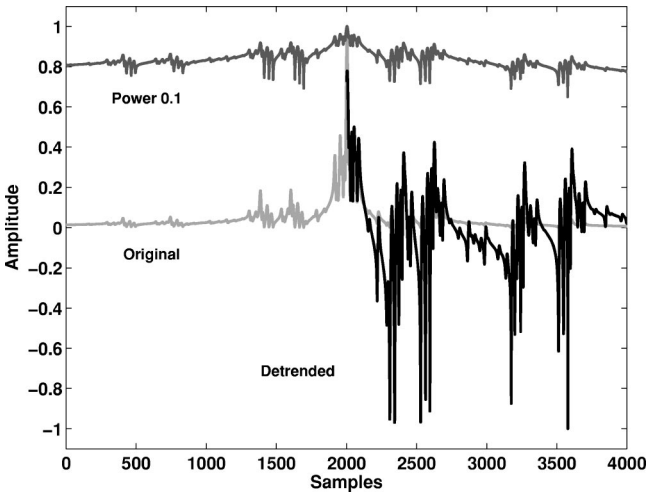

FIG. 15. This plot shows the transformations applied to the modeled cross-correlation wave forms. Shown are the original modeled wave form (light gray), this wave form raised to the power 0.1 (dark gray), and the result of subtracting the mean and rescaling so that the wave form has unit norm (black).

Figure 15 shows the effect of the transformations applied to the modeled wave form. The light gray curve is the original modeled cross-correlation wave form. The dark gray curve is the result of raising it to the power 0.1. The black curve shows the result of subtracting the overall mean and scaling the result so that it has unit norm. Only the right half of the black curve is shown—we only matched on the right half of the curve (other geometries would require matching over the entire wave form). In addition to these transformations, we omitted the first 3 ms of each correlation wave form from the source location metric calculation, because they were so unpredictable.

Figure 16 shows the range and depth tracks resulting from matching measured and modeled cross-correlations. The dynamic range is different in these two plots because the 1D slices being stacked were scaled to have unit norm.

IV. CONCLUSIONS

The most striking finding is that there seems to be a stable, exploitable impulse response of distinct and predictable multipath arrivals at these high frequencies. Although we only show results for two sites, we have seen qualitatively similar results at a number of sites where SignalEx experiments were performed.

The measured impulse response can be reproduced by standard acoustic propagation models well enough to support source localization using even a minimal receiver (we used either a single hydrophone, or a pair of hydrophones), although this was much more difficult than we have found at low frequencies.[21] At the New England site, we were able to

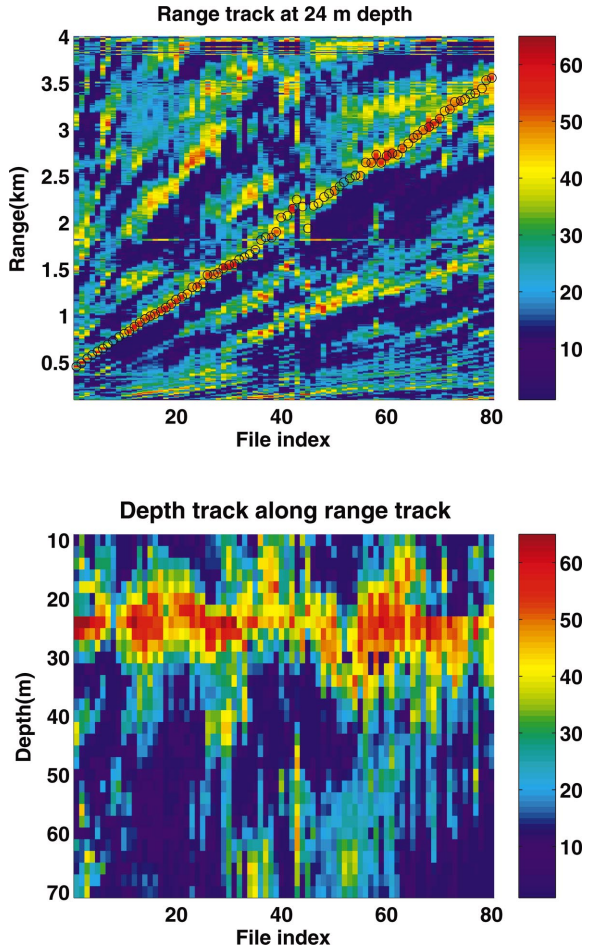

FIG. 16. Upper plot shows range track at 24 m depth. Ranges at which a depth slice is taken are indicated by black circles. The lower plot shows the depth track along the range track. The black circles over the range track show the peaks picked along the range track—these were used to set the ranges at which the slices versus depth were taken to form the depth track.

produce a persistent range and depth track out to 1.4 km, using relatively simple modeling. At the La Jolla site, where we had less multipath due to several environmental factors (downward refracting profile, softer bottom, deeper water), we had to work harder to pre-emphasize features of the impulse response function. Nevertheless, after these modifications, we were able to produce a persistent range and depth track out to 3.5 km. The additional transforms applied to the La Jolla site were not tested on the New England data.

Admittedly, using a known source wave form to measure the impulse response would not be possible with an uncooperative source, so the matched filter examples of source localization in Secs. II C and III C are perhaps academic demonstrations of feasibility only. To show that similar techniques could be applied to the more realistic problem of tracking an uncooperative source, whose wave form would not be known, in Sec. III D, we repeated the tracking at the La Jolla site using cross-correlation wave forms as data inputs (similarly to how we have done this in previous work at lower frequencies[21]). Note that only a time-domain representation could have enabled us to manipulate the relative importance of the different multipath arrivals, which produced dramatically improved localization ranges in Secs. III C and III D.

The averaging over multiple impulse response measurements proved to be a valuable preprocessing step that produced a very structured impulse response, suitable for comparison with model predictions. To reduce the sensitivity to mismatch in the times of arrival, the signal bandwidth was artifically reduced in the modeled waveforms. To obtain source location estimates beyond a kilometer in the La Jolla data, somewhat *ad hoc* transformations of the impulse response (data prewhitening and raising the modeled wave forms to a small power) were used to reduce the impact of unpredictable early arrivals and to emphasize the later arrivals, as described in Secs. III C and III D. These additional transforms were not applied to the New England data. These machinations were needed because our modeling did not incorporate phenomena that cause fluctuations in the impulse response. We speculate that incorporating better models of such phenomena would improve the source location estimates (different arrivals will behave differently, for example, depending on whether they interact with a dynamic surface, a rough bottom, or a part of the water column where the sound speed is changing). Extending our propagation models to incorporate knowledge of such ocean dynamics or its statistics is a topic for future work.

ACKNOWLEDGMENTS

This work was funded by ONR under Contract No. N00014-00-D-0115. The SignalEx experiments were funded by ONR 322OM. The tracking algorithms were developed as part of the Hydra program, supported by ONR 321SS. The propagation modeling was supported by ONR 321OA.

[1] H. P. Bucker, "Use of calculated sound fields and matched-field detection to locate sound sources in shallow water," J. Acoust. Soc. Am. **59**, 368–373 (1976).
[2] A. B. Baggeroer, W. A. Kuperman, and P. N. Mikhalevsky, "An overview of matched field methods in ocean acoustics," IEEE J. Ocean. Eng. **18**, 401–424 (1993).
[3] N. O. Booth, P. A. Baxley, J. A. Rice, P. W. Schey, W. S. Hodgkiss, G. L. D'Spain, and J. J. Murray, "Source localization with broad-band matched-field processing in shallow water," IEEE J. Ocean. Eng. **21**, 402–412 (1996).
[4] A. Parvulescu, "Signal detection in a multipath medium by M.E.S.S. processing," J. Acoust. Soc. Am. **33**, 1674 (1961).
[5] A. Parvulescu and C. S. Clay, "Reproducibility of signal transmissions in the ocean," Radio Electron. Eng. **29**, 223–228 (1965).
[6] L. Nghiem-Phu, F. D. Tappert, and S. C. Daubin, "Source localization by cw acoustic retrogration," 1985.
[7] D. R. Jackson and D. R. Dowling, "Phase conjugation in underwater acoustics," J. Acoust. Soc. Am. **89**, 171–181 (1991).
[8] R. E. Williams and H. F. Battestin, "Coherent recombination of acoustic multipathsignals propagated in the deep ocean," J. Acoust. Soc. Am. **50**, 1433–1442 (1971).
[9] W. R. Hahn, "Optimum signal processing for passive sonar range and bearing estimation," J. Acoust. Soc. Am. **58**, 201–207 (1975).
[10] N. L. Owsley and G. R. Swope, "Time delay estimation in a sensor array," IEEE Trans. Acoust., Speech, Signal Process. **ASSP-29**, 519–523 (1981).
[11] E. K. Westwood, "Broadband matched-field source localization," J. Acoust. Soc. Am. **91**, 2777–2789 (1992).
[12] M. Hamilton and P. M. Schultheiss, "Passive ranging in multipath dominant environments. I. Known multipath parameters," IEEE Trans. Signal Process. **40**, 1–12 (1992).
[13] S. M. Jesus, "Broadband matched-field processing of transient signals in

shallow water,'' J. Acoust. Soc. Am. **93**, 1841–1850 (1993).
[14] R. K. Brienzo and W. Hodgkiss, ''Broadband matched-field processing,'' J. Acoust. Soc. Am. **94**, 2821–2831 (1993).
[15] M. Hamilton and P. M. Schultheiss, ''Passive ranging in multipath dominant environments. II. Unknown multipath parameters,'' IEEE Trans. Signal Process. **41**, 1–12 (1993).
[16] Z.-H. Michalopoulou, M. B. Porter, and J. P. Ianniello, ''Broadband source localization in the Gulf of Mexico,'' J. Comput. Acoust. **4**, 361–370 (1996).
[17] Z.-H. Michalopoulou and M. B. Porter, ''Source tracking in the Hudson Canyon Experiment,'' J. Comput. Acoust. **4**, 371–383 (1996).
[18] E. K. Westwood and D. P. Knobles, ''Source track localization via multipath correlation matching,'' J. Acoust. Soc. Am. **102**, 2645–2654 (1997).
[19] J. P. Ianniello, ''Recent developments in sonar signal processing,'' IEEE Signal Process. Mag. **15**, 27–40 (1998).
[20] Z.-H. Michalopoulou, ''Matched impulse-response processing for shallow-water localization and geoacoustic inversion,'' J. Acoust. Soc. Am. **108**, 2082–2090 (2000).
[21] M. B. Porter, P. Hursky, C. O. Tiemann, and M. Stevenson, ''Model-based tracking for autonomous arrays,'' in *MTS/IEEE Oceans 2001—An Ocean Odyssey, Conference Proceedings* (IEEE Press, Honolulu, HI, 2001), pp. 786–792.
[22] W. S. Hodgkiss, W. A. Kuperman, J. J. Murray, G. L. D'Spain, and L. P. Berger, ''High frequency matched field processing,'' in *High Frequency Acoustics in Shallow Water*, edited by N. G. Pace, E. Pouliquen, O. Bergem, and A. P. Lyons (NATO SCALANT Undersea Research Centre, La Spezia, Italy, 1997), pp. 229–234.
[23] S. B. Suppappola and B. F. Harrison, ''Experimental results for matched-field processing with a small-aperture mid-frequency array,'' in *Oceans 2000 MTS/IEEE Conference and Exhibition, Conference Proceedings* (IEEE Press, 2000), Vol. 1, pp. 439–446.
[24] E. I. Thorsos, ''Report on the Office of Naval Research High-Frequency Acoustics Workshop,'' Technical Report No. APL-UW TR 9702, Applied Physics Laboratory, University of Washington, 16–18 April, 1996 (unpublished).
[25] M. B. Porter, V. K. McDonald, P. A. Baxley, and J. A. Rice, ''SignalEx: Linking environmental acoustics with the signaling schemes,'' in *MTS/IEEE OCEANS'00 Conference Proceedings of* (IEEE Press, 2000), pp. 595–600.
[26] S. Kim, G. F. Edelmann, W. A. Kuperman, W. S. Hodgkiss, H. C. Song, and T. Akal, ''Spatial resolution of time-reversal arrays in shallow water,'' J. Acoust. Soc. Am. **110**, 820–829 (2001).
[27] M. B. Porter, Acoustics Toolbox, http://oalib.saic.com/Modes/AcousticsToolbox.
[28] M. B. Porter, ''Acoustic models and sonar systems,'' IEEE J. Ocean. Eng. **OE-18**, 425–437 (1994).
[29] F. B. Jensen, W. A. Kuperman, M. B. Porter, and H. Schmidt, *Computational Ocean Acoustics* (AIP Press, Woodbury, NY, 1994).
[30] M. B. Porter, S. M. Jesus, Y. Stéphan, X. Démoulin, and E. Coelho, ''Exploiting reliable features of the ocean channel response,'' in *Shallow Water Acoustics*, edited by R. Zhang and J. Zhou (China Ocean Press, Beijing, China, 1998), pp. 77–82.
[31] W. A. Struzinski and E. D. Lowe, ''A performance comparison of four noise-background normalization schemes proposed for signal detection systems,'' J. Acoust. Soc. Am. **76**, 1738–1742 (1984).

An efficient robust sound classification algorithm for hearing aids

Peter Nordqvist[a] and Arne Leijon
Department of Speech, Music and Hearing, Drottning Kristinas v. 31, Royal Institute of Technology, SE-100 44 Stockholm, Sweden

(Received 3 April 2001; revised 4 February 2004; accepted 20 February 2004)

An efficient robust sound classification algorithm based on hidden Markov models is presented. The system would enable a hearing aid to automatically change its behavior for differing listening environments according to the user's preferences. This work attempts to distinguish between three listening environment categories: *speech in traffic noise*, *speech in babble*, and *clean speech*, regardless of the signal-to-noise ratio. The classifier uses only the modulation characteristics of the signal. The classifier ignores the absolute sound pressure level and the absolute spectrum shape, resulting in an algorithm that is robust against irrelevant acoustic variations. The measured classification hit rate was 96.7%–99.5% when the classifier was tested with sounds representing one of the three environment categories included in the classifier. False-alarm rates were 0.2%–1.7% in these tests. The algorithm is robust and efficient and consumes a small amount of instructions and memory. It is fully possible to implement the classifier in a DSP-based hearing instrument. © *2004 Acoustical Society of America.* [DOI: 10.1121/1.1710877]

PACS numbers: 43.60.Lq, 43.66.Ts [JCB] Pages: 3033–3041

I. INTRODUCTION

Hearing aids have historically been designed and prescribed mainly for only one listening environment, usually clean speech. This is a disadvantage and a compromise since the clean speech listening situation is just one among a large variety of listening situations a person is exposed to.

It has been shown that hearing aid users have different preferences for different listening environments (Elberling, 1999; Eriksson-Mangold and Ringdahl, 1993) and that there is a measurable benefit to using different amplification schemes for different listening situations (Keidser, 1995, 1996). Users appreciate taking an active part in the fitting process (Elberling, 1999). Users of a multi-programmable hearing aid prefer to use several programs in daily life (Eriksson-Mangold and Ringdahl, 1993).

This indicates the need for hearing aids that can be fitted according to user preferences for various listening environments. Several common nonlinear multi-channel hearing aids do not actually change their behavior markedly for different listening environments (Nordqvist, 2000). The most common solution today for changing the behavior of the hearing aid is that the hearing aid user manually switches between the programs by pressing a button on the hearing aid. The user takes an active role in the hearing aid behavior and controls the functionality of the hearing aid depending on the listening environment. This can be a problem for passive users or for users that are not able to press the program switch button.

The solution to the problems above is a hearing aid that can classify the current listening environments and use the preferred settings within each listening situation. The hearing aid can automatically change its behavior and have different characteristics for different listening environments according to the user's preferences, e.g., switch on noise reduction for noisy environments, have a linear characteristic when listening to music, or switch on the directional microphone in a babble environment. A hearing aid based on listening environment classification offers additional control possibilities supplementing the traditional multi-channel AGC hearing aid. It is possible to focus more on the user preferences for various listening environments during the fitting process at the clinic.

Some previous work on sound classification in hearing aids was based on instantaneous classification of envelope modulation spectra (Kates, 1995). Another system was based on envelope modulation spectra together with a neural network (Tchorz and Kollmeier, 1998). Hidden Markov models (Rabiner, 1989) have been used in a classification system to alert profoundly deaf users to acoustic alarm signals (Oberle and Kaelin, 1995).

Sound classification systems are implemented in some of the hearing aids today. They have relatively low complexity and are threshold-based classifiers or Bayesian classifiers (Duda and Hart, 1973). The tasks of these classification systems are mainly to control the noise reduction and to switch on and off the directionality feature. More complex classifiers based on, e.g., neural nets or hidden Markov models are not present in today's hearing aids.

Phonak Claro has a system called AutoSelect™. The task for the classifier is to distinguish between two listening environments, speech in noise and any other listening environment. The classifier uses four features: overall loudness level, variance of overall loudness level, the average frequency, and the variance of the average frequency. The classification decision is threshold based, e.g., all features must exceed a threshold (Büchler, 2001). Widex Diva has a classification system based on frequency distribution and amplitude distribution. The input signal is analyzed continuously

[a]Electronic mail: nordq@speech.kth.se

and percentile values are calculated. These percentile values are then compared with a set of pretrained percentile values in order to control the hearing aid (Ludvigsen, 1997). GN Resound Canta 7 has a classification system supporting the noise reduction system. The level of modulation is measured in 14 bands. Maximum modulation is achieved for clean speech. When the measured modulation is below maximum modulation the gain in the corresponding channel is reduced (Edwards *et al.*, 1998). A similar system is implemented in the Siemens Triano hearing aid (Ostendorf *et al.*, 1998). The classifier is called Speech Comfort System™ and switches automatically between predefined hearing aid settings for clean speech, speech in noise, and noise alone.

The two most important listening environments for a hearing aid user are speech in quiet and speech in noise. The speech in quiet situation has a high signal-to-noise ratio and is relatively easy to handle. Most of the early prescription methods were aimed for these situations. Speech in noise is a much more difficult environment for the hearing aid user. A different gain prescription method should be used, maybe together with other features in the hearing aid switched on/off, e.g., directional microphone or a noise suppression system. Therefore, automatic detection of noise in the listening environment can be helpful to the user. To improve hearing aid performance further, the next step is to classify various kinds of noise types. The two most common noise categories we are exposed to are probably traffic noise (in a car or outdoors in a street) and babble noise, e.g., at a party or in a restaurant. Different signal processing features in the hearing aid may be needed in these two environments.

In order to investigate the feasibility of such a more advanced classifier, three environment classes are chosen in this study. The first is *clean speech*, which is the default class for quiet listening environments or for speech in quiet listening environments. The second category is *speech in traffic*, which is the default class for noise with relatively weak and slow modulation and for speech in such noise. Finally, the third category is *speech in babble*, which is the default class for more highly modulated babblelike noise or speech in such noise. Music is probably also an important listening environment but is not included in this study.

The goal of the present work is to allow classification not only between clean speech and speech in noise, but also between speech in various types of noise. For this purpose it would not be sufficient to use level percentiles or other simple measures of envelope modulation. Different environment classes may show the same degree of modulation and differ mainly in the temporal modulation characteristics. Therefore, hidden Markov models (HMMs) were chosen to represent the sound environments. The HMM is a very general tool to describe highly variable signal patterns such as speech and noise. It is commonly used in speech recognition and speaker verification. One great advantage with the HMM is that this method allows the system to easily accumulate information over time. This is theoretically possible also using more conventional recursive estimation of modulation spectra. However, preliminary considerations indicated that the HMM approach would be computationally much less complex and, nevertheless, more general. The present study

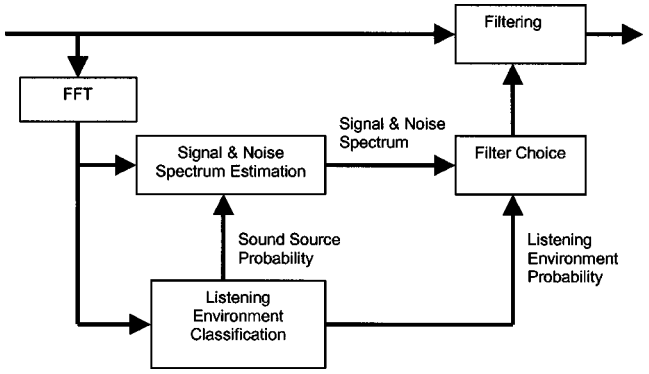

FIG. 1. Block diagram indicating a possible use of environment classification in a future hearing aid. The source models are used to estimate a signal and a noise spectrum. The output from the classifier together with the estimated signal and noise spectrum are used to select a predesigned filter or used to design a filter.

demonstrates that it is relatively easy to implement HMMs in a real-time application, even with the hardware limitations imposed by current hearing aid signal processors.

An obvious difficulty is to classify environments with a variety of signal-to-noise ratios as one single category. In principle, separate classifiers are needed for each signal-to-noise ratio. However, this would lead to a very complex system. Instead, the present approach assumes that a listening environment consists of one or two sound sources and that only one sound source dominates the input signal at a time. The sound sources used here are traffic noise, babble, and clean speech. Each sound source is modeled separately with one HMM. The pattern of transitions between these source models is then analyzed with another HMM to determine the current listening environment.

This solution is suboptimal since it does not model, e.g., speech in traffic noise at a specific signal-to-noise ratio. The advantage is a great reduction in complexity. Environments with a variety of signal-to-noise ratios can be modeled with just a few pretrained HMMs, one for each sound source. The algorithm can also estimate separate signal and noise spectra since the sound source models indicate when a sound source is active. The final signal processing in the hearing aid can then depend on user preferences for various listening environments, the current estimated signal and noise spectra, and the current listening environment. A possible block diagram for a complete generalized adaptive hearing aid is shown in Fig. 1.

The classification must be robust and insensitive to changes within one listening environment, e.g., when the user moves around. Therefore, the classifier takes very little account of the absolute sound pressure level and completely ignores the absolute spectrum shape of the input signal. These features contain information about the current listening situation but they are too sensitive to changes that can appear within a listening environment. The absolute sound pressure level depends on the distance to the sound source. The absolute spectrum shape is affected by reflecting objects, e.g., walls, cars, and other people. The present classifier uses mainly the modulation characteristics of the signal. This

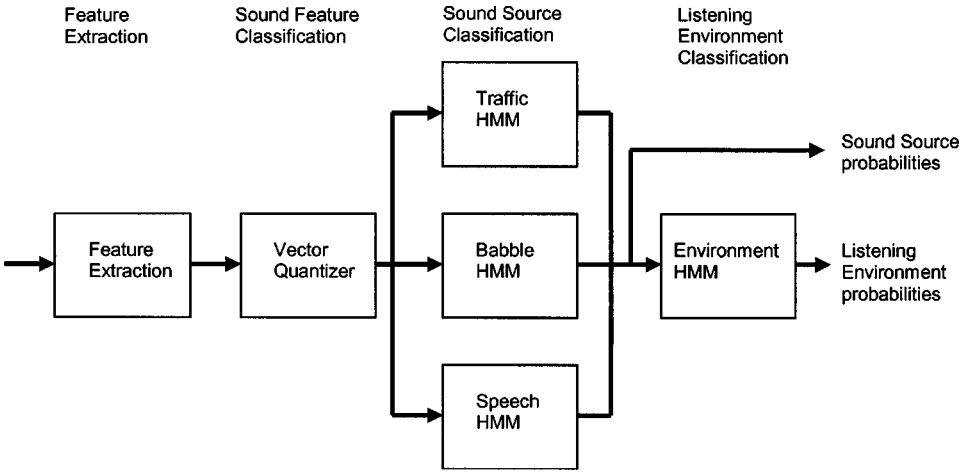

FIG. 2. Listening environment classification. The system consists of four layers: the feature extraction layer, the sound feature classification layer, the sound source classification layer, and the listening environment classification layer. The sound source classification uses three hidden Markov models (HMM), and another HMM is used in the listening environment classification.

makes it possible to distinguish between listening environments with identical long-term spectra.

This study focuses on the classification problem. The complete implementation and functionality of the hearing aid is not included. The main questions in this study are the following.

(1) Is it possible to classify listening environments with a small set of pretrained source HMMs?
(2) What is the level of performance?
(3) Is it possible to implement the algorithm in a hearing aid?

II. METHODS

A. Algorithm overview

The listening environment classification system is described in Fig. 2. The main output from the classifier, at each time instant, is a vector containing the current estimated probabilities for each environment category. Another output vector contains estimated probabilities for each sound source represented in the system. The sampling frequency in the tested system is 16 kHz and the input samples are processed blockwise with a block-length, B, of 128 points, corresponding to 8 ms. All layers in the classification system are updated for every 8-ms frame and a new decision is taken for every frame. The structure of the environment HMM does not allow rapid switching between environment categories. The classifier accumulates acoustic information rather slowly, when the input is ambiguous or when the listening environment changes. This sluggishness is desirable, as it typically takes approximately 5–10 s for the hearing-aid user to move from one listening environment to another.

1. Feature extraction

One block of samples, $\mathbf{x}(t)=\{x_n(t)\ n=0,...,B-1\}$, from the A/D-converter is the input to the feature extraction layer. The input block is multiplied with a Hamming window, w_n, and L real cepstrum parameters, $f_l(t)$, are calculated (Mammone *et al.*, 1996) as

$$f_l(t)=\frac{1}{B}\sum_{k=0}^{B-1}\left(\cos\left(\frac{2\pi lk}{B}\right)\log\left|\sum_{n=0}^{B-1}w_n x_n(t)e^{-j2\pi kn/B}\right|\right),$$
$$\text{where}\quad l=0,...,L-1. \tag{1}$$

The number of cepstrum parameters in the implementation is $L=4$. The $W=12$ latest cepstrum $\mathbf{f}(t)$ vectors are stored in a circular buffer and used to estimate the corresponding delta-cepstrum parameter, $\Delta f_l(t)$, describing the time derivatives of the cepstrum parameters. The estimation is done with a FIR filter for every new 8-ms frame as

$$\Delta f_1(t)=\sum_{\theta=0}^{W-1}\left(\frac{w-1}{2}-\theta\right)f_l(t-\theta),$$
$$\text{where}\quad l=0,...,L-1. \tag{2}$$

Both the size of the cepstrum buffer and the number of cepstrum parameters were determined through practical testing. Different combinations of these two parameters were tested and the most efficient combination, regarding memory and number of multiplications, with acceptable performance was chosen.

Only differential cepstrum parameters are used as features in the classifier. Hence, everything in the spectrum that remains constant over time is removed from the classifier input and can therefore not influence the classification results. For example, the absolute spectrum shape cannot affect the classification. The distribution of some features for various sound sources is illustrated in Fig. 3.

2. Sound feature classification

The HMMs in this work are implemented as discrete HMMs with a vector quantizer preceding the HMMs. The vector quantizer is used to convert the current feature vector into a discrete number between 1 and M.

The stream of feature vectors is sent to the sound feature classification layer that consists of a vector quantizer (VQ) with M codewords in the codebook $[\mathbf{c}^1\cdots\mathbf{c}^M]$. The feature vector $\Delta\mathbf{f}(t)=[\Delta f_0(t)\cdots\Delta f_{L-1}(t)]$ is quantized to the closest codeword in the VQ and the corresponding codeword index

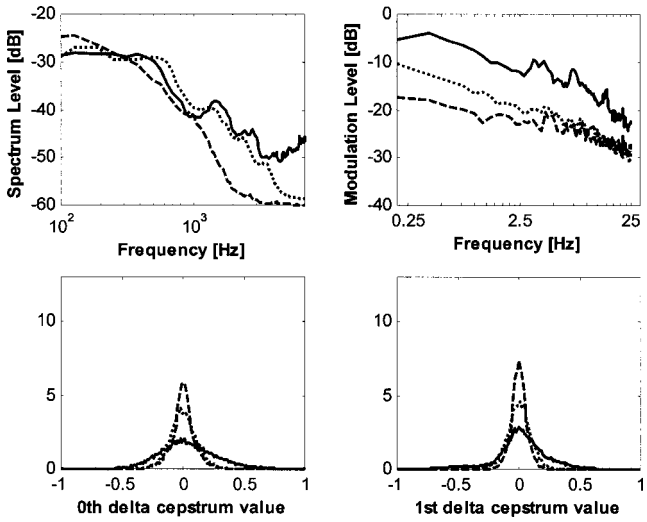

FIG. 3. The absolute spectrum shape (normalized to 0 dB) for the clean speech, traffic noise, and babble training material is illustrated in subplot 1. The modulation spectra (clean speech normalized to 0 dB and used as reference) for the clean speech, traffic noise, and babble training material are illustrated in subplot 2. Feature vector probability distributions are illustrated in subplots 3 and 4. Each subplot illustrates three probability density functions (pdf's) of the first and second delta cepstrum parameter. For all subplots, solid lines are clean speech, dotted lines are babble noise, and dashed lines are traffic noise.

$$o(t) = \arg\min_{i=1...m} \|\Delta \mathbf{f}(t) - \mathbf{c}^i\|^2 \tag{3}$$

is generated as output. The VQ is previously trained offline, using the generalized Lloyd algorithm (Linde *et al.*, 1980).

If the calculated power in the current input block corresponds to a sound pressure level less than 55 dB, the frame is categorized as a quiet frame. The signal level is estimated as the unweighted total power in the frequency range 250–7500 Hz. One codeword in the vector quantizer is allocated for quiet frames and used as output every time a quiet frame is detected. The environment that has the highest frequency of quiet frames is the clean speech situation. Hence, all listening environments that have a total sound pressure level below the quiet threshold are classified as clean speech. This is acceptable, because typical noisy environments have higher noise levels.

3. Sound source classification

This part of the classifier calculates the probabilities for each sound source category: traffic noise, babble noise, and clean speech. The sound source classification layer consists of one HMM for each included sound source. Each HMM has N internal states. The current state at time t is modeled as a stochastic variable $Q^{\text{source}}(t) \in \{1,...,N\}$. Each sound model is specified as $\lambda^{\text{source}} = \{\mathbf{A}^{\text{source}}, \mathbf{b}^{\text{source}}(\cdot)\}$ where $\mathbf{A}^{\text{source}}$ is the state transition probability matrix with elements

$$a_{ij}^{\text{source}} = \text{prob}(Q^{\text{source}}(t) = j \,|\, Q^{\text{source}}(t-1) = i) \tag{4}$$

and $\mathbf{b}^{\text{source}}(\cdot)$ is the observation probability mass function with elements

$$b_j^{\text{source}}(o(t)) = \text{prob}(o(t) \,|\, Q^{\text{source}}(t) = j). \tag{5}$$

Each HMM is trained off-line with the Baum-Welch algorithm (Rabiner, 1989) on training data from the corresponding sound source. The HMM structure is ergodic, i.e., all states within one model are connected with each other.

When the trained HMMs are included in the classifier, each source model observes the stream of codeword indices, $[o(1)\cdots o(t)]$, where $o(t) \in \{1,...,M\}$, coming from the VQ, and estimates the conditional state probability vector $\hat{\mathbf{p}}^{\text{source}}(t)$ with elements

$$\hat{p}_i^{\text{source}}(t) = \text{prob}(Q^{\text{source}}(t) = i \,|\, o(t),\ldots,o(1),\lambda^{\text{source}}). \tag{6}$$

These state probabilities are calculated with the forward algorithm (Rabiner, 1989)

$$\mathbf{p}^{\text{source}}(t) = ((\mathbf{A}^{\text{source}})^T \hat{\mathbf{p}}^{\text{source}}(t-1)) \circ \mathbf{b}^{\text{source}}(o(t)), \tag{7}$$

where $\mathbf{p}^{\text{source}}(t)$ is a non-normalized state likelihood vector with elements

$$p_i^{\text{source}}(t) = \text{prob}(Q^{\text{source}}(t) = i, o(t) \,|\, o(t-1),\ldots,o(1),\lambda^{\text{source}}), \tag{8}$$

T indicates matrix transpose, and $\circ$ denotes element-wise multiplication. The probability for the current observation given all previous observations and a source model can now be estimated as

$$\phi^{\text{source}}(t) = \text{prob}(o(t) \,|\, o(t-1),\ldots,o(1),\lambda^{\text{source}}) = \sum_{i=1}^{N} p_i^{\text{source}}(t). \tag{9}$$

Normalization is used to avoid numerical problems,

$$\hat{p}_i^{\text{source}}(t) = p_i^{\text{source}}(t) / \phi^{\text{source}}(t). \tag{10}$$

4. Listening environment classification

The sound source probabilities calculated in the previous section can be used directly to detect traffic noise, babble noise, or speech in quiet. This might be useful if the task of the classification system is to detect isolated sound sources. However, in this implementation, a listening environment is defined as a single sound source or a combination of two sound sources. For example, *speech in babble* is defined as a combination of the sound sources speech and babble. The output data from the sound source models are therefore further processed by a final hierarchical HMM in order to determine the current listening environment. The structure of this final environment HMM is illustrated in Fig. 4.

The final classifier block estimates for every frame the current probabilities for each environment category by observing the stream of sound source probability vectors from the previous block. The listening environment is represented as a discrete stochastic variable $E(t) \in \{1,...,3\}$, with outcomes coded as 1 for "*speech in traffic noise*," 2 for "*speech in babble*," and 3 for "*clean speech*." Thus, the output probability vector has three elements, one for each of these environments.

The environment model consists of five states and a transition probability matrix $\mathbf{A}^{\text{env}}$ (see Fig. 4). The current state in this HMM is modeled as a discrete stochastic variable $S(t) \in \{1,...,5\}$, with outcomes coded as 1 for "*traffic*,"

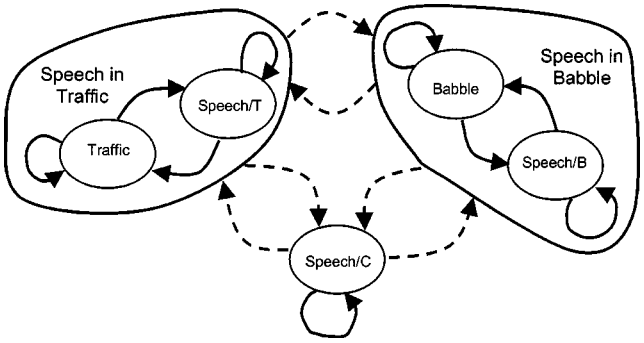

FIG. 4. State diagram for the environment hierarchical hidden Markov model containing five states representing traffic noise, speech (in traffic, "Speech/T"), babble, speech (in babble, "Speech/B"), and clean speech ("Speech/C"). Transitions between listening environments, indicated by dashed arrows, have low probability, and transitions between states within one listening environment, shown by solid arrows, have relatively high probabilities.

2 for speech (in traffic noise, "*speech/T*"), 3 for "*babble,*" 4 for speech (in babble, "*speech/B*"), and 5 for clean speech "*speech/C.*"

The *speech in traffic noise* listening environment, $E(t)=1$, has two states $S(t)=1$ and $S(t)=2$. The *speech in babble* environment, $E(t)=2$, has two states $S(t)=3$ and $S(t)=4$. The clean speech listening environment, $E(t)=3$, has only one state, $S(t)=5$. The transition probabilities between listening environments are relatively low and the transition probabilities between states within a listening environment are high. These transition probabilities were adjusted by practical experimentation to achieve the desired temporal characteristics of the classifier.

The hierarchical HMM observes the stream of vectors $[\mathbf{u}(1)\cdots\mathbf{u}(t)]$, where

$$\mathbf{u}(t)=[\phi^{\text{traffic}}(t)\phi^{\text{speech}}(t)\phi^{\text{babble}}(t)\phi^{\text{speech}}(t)\phi^{\text{speech}}(t)]^T, \tag{11}$$

contains the estimated observation probabilities for each state. The probability for being in a state given the current and all previous observations and given the hierarchical HMM,

$$\hat{p}_i^{\text{env}}=\text{prob}(S(t)=i|\mathbf{u}(t),\ldots,\mathbf{u}(1),\mathbf{A}^{\text{env}}), \tag{12}$$

is calculated with the forward algorithm (Rabiner, 1989),

$$\mathbf{p}^{\text{env}}(t)=((\mathbf{A}^{\text{env}})^T\hat{\mathbf{p}}^{\text{env}}(t-1))\circ\mathbf{u}(t), \tag{13}$$

with elements $p_i^{\text{env}}=\text{prob}(S(t)=i,\mathbf{u}(t)|\mathbf{u}(t-1),\ldots,\mathbf{u}(1),\mathbf{A}^{\text{env}})$, and, finally, with normalization,

$$\hat{\mathbf{p}}^{\text{env}}(t)=\mathbf{p}^{\text{env}}(t)/\sum p_i^{\text{env}}(t). \tag{14}$$

The probability for each listening environment, $\mathbf{p}^E(t)$, given all previous observations and given the hierarchical HMM, can now be calculated as

$$\mathbf{p}^E(t)=\begin{pmatrix}1&1&0&0&0\\0&0&1&1&0\\0&0&0&0&1\end{pmatrix}\hat{\mathbf{p}}^{\text{env}}(t). \tag{15}$$

TABLE I. Sound material used for training and evaluation. Sound examples that did not clearly belong to any of the three categories used for training are labeled "Other noise."

	Total Duration (s)	Recordings
Training material		
Clean speech	347	13
Babble noise	233	2
Traffic noise	258	11
Evaluation material		
Clean speech	883	28
Babble noise	962	23
Traffic noise	474	20
Other noise	980	28

B. Sound material for training and evaluation

Two separate databases are used, one for training and one for testing. There is no overlap between the databases. The signal spectra and modulation spectra of the training material are displayed in Fig. 3. The number of sound examples and their duration are listed in Table I. The clean speech material consisted of 10 speakers (6 male and 4 female) for training and 24 speakers for the evaluation (12 male and 12 female). One part of the clean speech material used in the training was recorded in different office rooms, one room for each speaker. The size of the office rooms varies between 3×4 m^2 and 8×8 m^2. The recording microphone was placed above the ear of the experimenter, at the microphone position for a behind-the-ear hearing aid. The distances to the speakers were normal conversation distances, 1–1.5 m. Both the experimenter and the speaker were standing up during the recordings. The reverberation time in the office rooms (measured as T60 500 Hz) were typically around 0.7 s. Another part of the clean speech material was recorded in a recording studio. The babble noise material and the traffic noise material included material recorded by the experimenter, material taken from hearing-aid demonstration CDs, and from the Internet.

C. Training

Experience has shown that a uniform initialization for the initial state distribution π and a uniform initialization for the state transition probability matrix A is a robust initialization (Rabiner, 1989). The observation probability matrix B is more sensitive to different initializations and should be initialized more carefully. A clustering method described next was used to initialize observation probability matrix B. The observation sequence from a sound source was clustered with the generalized Lloyd algorithm into N state clusters, one cluster for each state in the HMM. The vector quantizer categorizes the observation sequence into M clusters. The vector quantizer output together with the N state clustering were then used to classify each single observation in the observation sequence into one state number and one observation index. The frequency of observation indices for each state was counted and normalized and used as initialization of the observation probability matrix B. Each source HMM

was trained separately on representative recorded sound, using five iterations with the Baum–Welch update procedure (Rabiner, 1989).

As the classifier is implemented with a vector quantizer in combination with discrete HMMs, only the codewords included in the training sequences for an HMM will be assigned nonzero observation probabilities during training. Codewords that were not included in the training will have probability zero. This is not realistic but may happen because the training material is limited. Therefore, the probability distributions in the HMMs were smoothed after training. A fixed probability value was added for each observation and state, and the probability distributions were then renormalized. This makes the system more robust: Instead of trying to classify ambiguous sounds, the output remains relatively constant until more distinctive observations arrive.

D. Evaluation

The evaluation consists of five parts: (1) the hit rate and false alarm rate; (2) the dynamic behavior of the classifier when the test material shifts abruptly from one listening environment to another; (3) the classifier's performance for environments with a varied number of speakers, from 1 to 8; (4) the behavior of the classifier when the signal-to-noise ratio varies within one listening environment; and (5) the behavior of the classifier in reverberant locations.

Part (1): Examples of traffic noise, babble noise, and quiet were supplemented with other kinds of background noises in order to evaluate the performance of the classifier both for background noises similar to the training material and for background noises that are clearly different from the training material (called ''other noise types'' in Table I). A background noise and a section of speech were chosen randomly, with uniform probability, from the set of background noises and speakers. The presentation level of the speech was randomly chosen, with uniform probability, between 64 and 74 dB SPL and mixed with the noise at randomly chosen signal-to-noise ratios uniformly distributed between 0 and +5 dB. The mixed file was presented to the classifier and the output environment category with the highest probability was logged 14 s after onset. This delay was chosen to prevent transient effects. In total 47 795 tests were done, each with a duration of 14 s. The total duration of all tests was therefore about 185 h. The hit rate and false alarm rate were estimated for the listening environments speech in traffic, speech in babble, and clean speech. For the other test sounds any definition of hit rate or false alarm rate would be entirely subjective. There are 17 ''other noise types'' used in the evaluation and the classification result for these noise types is displayed simply with the number of results in each of the three classification categories.

Part (2): The dynamic behavior of the classifier was evaluated with four different test stimuli: clean speech, speech in traffic noise, speech in babble, and subway noise. The duration of each test sound was approximately 30 s. The test material for speech in traffic noise was a recorded conversation between two people standing outdoors close to a road with heavy traffic. The speech in babble was a conversation between two people in a large lunch restaurant. The clean speech material was a conversation between two people in an audiometric test booth. The subway noise was recorded on a local subway train.

Part (3): The evaluation of environments containing a varied number of speakers used four test recordings of one, two, four, and eight speakers. In this evaluation, four males and four females were used. The first test stimulus was speech from a female. The following test stimuli were a balanced mix of male and female speech.

Part (4): The evaluation of environments with varied signal-to-noise ratios used five test stimuli. Speech at 64 dB SPL was presented together with babble noise at five different signal-to-noise ratios, 0 to 15 dB with 5-dB step.

Part (5): The impact of reverberation was studied by recording clean speech in an environment with high reverberation. The focus of this test is the transition between clean speech and speech in babble. Clean speech will at some point be classified as speech in babble, when the reverberation increases in the listening environment. Speech from the person wearing the recording microphone and speech from a distant talker were recorded inside a large concrete stairwell. Hence, both speech within the reverberation radius and speech outside the reverberation radius were included. The reverberation time (T60, measured as the average of seven reverberation measurements) was 2.44 s at 500 Hz and 2.08 s at 2000 Hz. This tested listening environment can be considered as a rather extreme reverberant location, as concert halls typically have reverberation times around 2 s.

III. RESULTS

A. Classification

The number of classification results for all test environments are displayed in Table II. The listening environments are clean speech or a combination of speech and traffic noise or babble noise. The evaluation displays how well listening environments, combinations of sound sources, are classified. The hit rate and false alarm rate were estimated from these values. The hit rate for speech in traffic noise was 99.5%, i.e., test examples with traffic noise were correctly classified in 99.5% of the tests. Test examples with clean speech or speech in babble noise were classified as speech in traffic noise in 0.2% of the tests, i.e., the false alarm rate was 0.2%. For speech in babble noise the hit rate was 96.7% and the false alarm rate was 1.7%. For clean speech the hit rate was 99.5% and the false alarm rate 0.3%. For the other test sounds any definition of hit rate or false alarm rate would be entirely subjective. The classification result for these noise types are therefore only listed in Table II.

The second part of the evaluation showed the dynamic behavior of the classifier when the test sound shifted abruptly (Fig. 5). The classifier output shifted from one environment category to another within 5–10 s after the stimulus changes, except for clean speech to another listening environment which took about 2–3 s.

The third part of the evaluation showed the behavior of the classifier for environments with a varied number of speakers (Fig. 6). The test signals with one or two speakers were classified as clean speech, and the four- and eight-

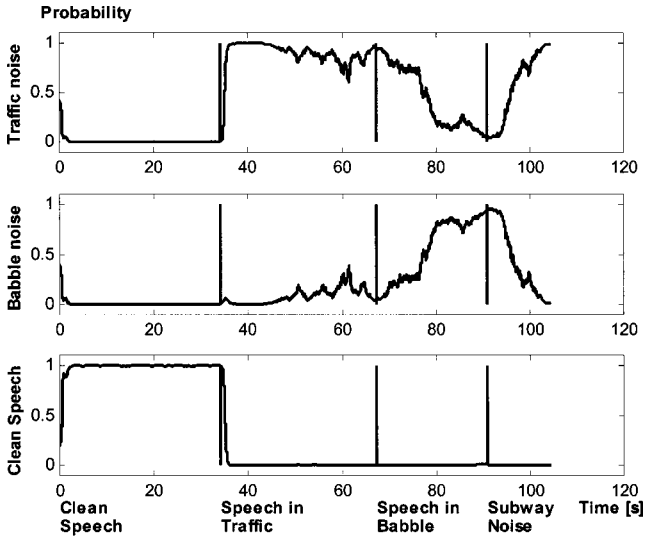

FIG. 5. Listening environment classification results as a function of time, with suddenly changing test sounds. The curve in each panel, one for each of the three environment categories, indicates the classifier's output signal as a function of time. The concatenated test materials from four listening environments are represented on the horizontal time axis. The thin vertical lines show the actual times when there was a shift between test materials.

speaker signals were classified as speech in babble.

The fourth part of the evaluation showed the effect of the signal-to-noise ratio (Fig. 7). For signal-to-noise ratios in the interval between 0 and +5 dB, the test signal, speech at 64 dB SPL, was classified as speech in babble. Test signals with signal-to-noise ratios at +10 dB or greater were classified as clean speech.

The fifth part of the evaluation examined the impact of reverberation. Speech from the hearing aid wearer (within the reverberation radius) was clearly classified as clean speech. Speech from a distance speaker (outside the reverberation radius) was classified as babble.

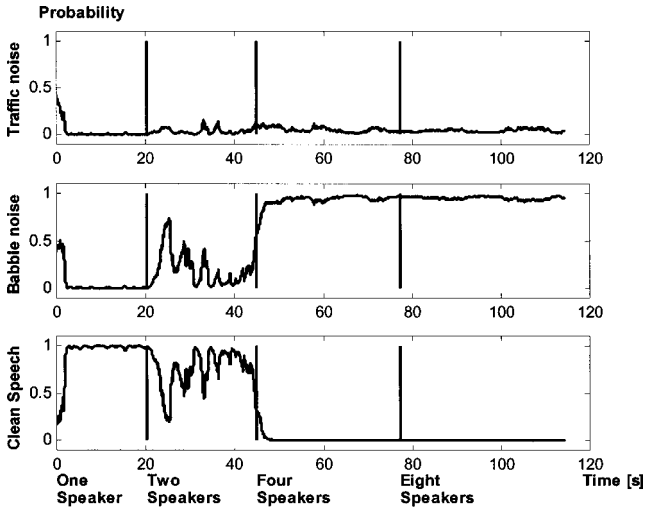

FIG. 6. Listening environment classification results for test sounds with an increasing number of speakers. The curve in each panel, one for each of the three environment categories, indicates the classifier's output signal as a function of time. The concatenated test material from a recording with an increasing number of speakers is represented on the horizontal time axis. The vertical lines show the actual times when there was a sudden change in the number of speakers.

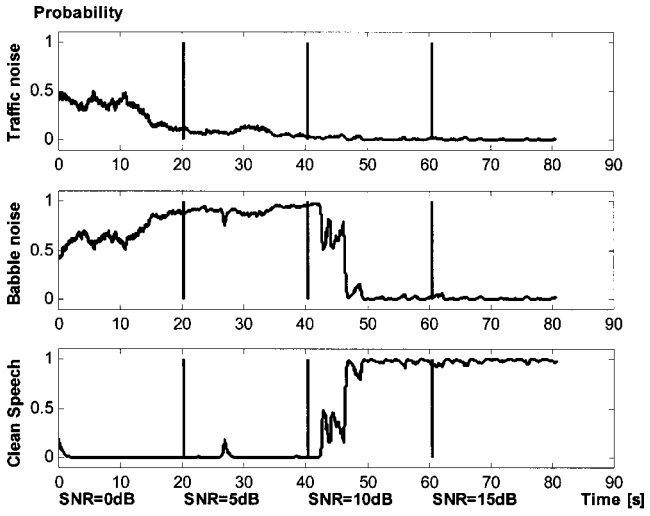

FIG. 7. Listening environment classification results for a variety of signal-to-noise ratios. The curve in each panel, one for each of the three environment categories, indicates the classifier's output signal as a function of time. The concatenated test material from speech in babble at 64 dB SPL (250–7500 Hz) with ascending signal-to-noise ratio from left to right is represented on the horizontal time axis. The vertical lines show the actual times when there was a sudden change in signal-to-noise ratios.

B. Computational complexity

The current configuration uses four delta-cepstrum coefficients in the feature extraction. The vector quantizer contains 16 codewords and the three source HMMs have four internal states each. The buffer with cepstrum coefficients used to estimate delta-cepstrum coefficients is 100 ms long. The estimated computational load and memory consumption in a Motorola 56k architecture or similar is less than 0.1 million instructions per second (MIPS) and less than 700 words. This MIPS estimate also includes an extra 50% overhead since a realistic implementation may often require some overhead. This estimation includes only the classification algorithm and shows the amount of extra resources that is needed when the algorithm is implemented in a DSP based hearing aid. Modern DSP-based hearing instruments fulfill these requirements.

IV. DISCUSSION

The results from the evaluation are promising but the results must of course be interpreted with some caution. In this implementation a quiet threshold was used, currently set to 55 dB SPL (250–7500 Hz). This threshold actually determines at what level an environment is categorized as quiet. Such a threshold is reasonable since there are several categories of low-level signals each with its own characteristics, and there is no need to distinguish between them. Without this threshold, all low-level sounds would be classified as either traffic noise or babble noise with this implementation of the classifier. This will happen since the classifier uses only differential features and ignores the absolute sound pressure level and absolute spectrum shape.

The classifier has two noise models, one trained for traffic noise and one for babble noise. Traffic noise has a relatively low modulation and babble has a higher modulation (see Fig. 3). This is important to remember when interpreting

TABLE II. Classification results. The input stimuli are speech mixed with a variety of background noises. The presentation level of the speech was randomly chosen, with uniform probability, between 64 and 74 dB SPL (250–7500 Hz) and mixed with a background noise at randomly chosen signal-to-noise ratios uniformly distributed between 0 and +5 dB. Background noises represented in the classifier, speech in traffic, speech in babble, and clean speech, and other background noises that are not represented in the classifier are used. Each test stimulus is 14 s long and the evaluation contains a total of 47 795 stimuli representing 185 h of sound.

	Classification result		
Test sound	Speech in traffic noise	Speech in babble noise	Clean speech
Speech in traffic noise	14 114	539	0
Speech in babble noise	64	14 485	3
Clean speech	0	0	14 668
Speech in rain noise	1365	24	0
Speech in applause noise	1357	0	0
Speech in jet engine noise	1304	0	0
Speech in leaves noise	1303	0	0
Speech in ocean waves noise	1271	48	90
Speech in subway noise	1205	183	18
Speech in wind noise	1178	104	5
Speech in industry noise	822	543	0
Speech in dryer machine noise	716	587	0
Speech in thunder noise	702	632	21
Speech in office noise	684	612	14
Speech in high frequency noise	669	564	67
Speech in instrumental classical music	549	397	387
Speech in basketball arena noise	103	769	476
Speech in super market noise	83	1219	0
Speech in shower noise	5	1327	0
Speech in laughter	0	559	723

the results from the evaluation. Some traffic noise sounds, e.g., from an accelerating truck, may temporarily be classified as babble noise due to the higher modulation in the sound.

The HMMs in this work are implemented as discrete models with a vector quantizer preceding the HMMs. The vector quantizer is used to convert each feature vector into a discrete number between 1 and M. The observation probability distribution for each state in the HMM is therefore estimated with a probability mass function instead of a probability density function. The quantization error introduced in the vector quantizer has an impact on the accuracy of the classifier. The difference in average error rate between discrete HMMs and continuous HMMs has been found to be on the order of 3.5% in recognition of spoken digits (Rabiner, 1989). The use of a vector quantizer together with a discrete HMM is computationally much less demanding compared to a continuous HMM. This advantage is important for implementations in digital hearing aids, although the continuous HMM has slightly better performance.

Two different algorithms are often used when calculating probabilities in the HMM framework, the Viterbi algorithm, or the forward algorithm. The forward algorithm calculates the probability of observed data for all possible state sequences and the Viterbi algorithm calculates the probability only for the best state sequence. The Viterbi algorithm is normally used in speech recognition where the task is to search for the best sequence of phonemes among all possible sequences. In this application where the goal is to estimate the total probability of a given observation sequence, regardless of the HMM state sequence, the forward algorithm is more suitable.

The major advantage with the present system is that it can model several listening environments at different signal-to-noise ratios with only a few small sound source models. The classification is robust with respect to level and spectrum variations, as these features are not used in the classification. It is easy to add or remove sound sources or to change the definition of a listening environment. This makes the system flexible and easy to update.

The ability to model many different signal-to-noise ratios has been achieved by assuming that only one sound source is active at a time. This is a known limitation, as several sound sources are often active at the same time. The theoretically more correct solution would be to model each listening environment at several signal-to-noise ratios. However, this approach would require a very large number of models. The reduction in complexity is important when the algorithm is implemented in hearing instruments.

The stimuli with instrumental music were classified either as speech in traffic or speech in babble with approximately equal probability (see Table II). The present algorithm was not designed to handle environments with music. Music was included in the evaluation only to show the behavior of the classifier when sounds not included in the training material are used as test stimuli. Additional source models or additional features may be included in order to correctly classify instrumental music.

The really significant advance with this algorithm over previously published results is that we clearly show that the

algorithm can be implemented in a DSP-based hearing instrument with respect to processing speed and memory limitations. We also show that the algorithm is robust and insensitive to long-term changes in absolute sound pressure levels and absolute spectrum changes. This has been discussed very little in previous work, although it is important when the classifier is used in a hearing aid and exposed to situations in daily life.

V. CONCLUSION

This study has shown that it is possible to robustly classify the listening environments speech in traffic noise, speech in babble, and clean speech, at a variety of signal-to-noise ratios with only a small set of pretrained source HMMs.

The measured classification hit rate was 96.7%–99.5% when the classifier was tested with sounds representing one of the three environment categories included in the classifier. False-alarm rates were 0.2%–1.7% in these tests.

For other types of test environments that did not clearly belong to any of the classifier's three predefined categories, the results seemed to be determined mainly by the degree of modulation in the test noise. Sound examples with high modulation tended to be classified as speech in babble, and sounds with less modulation were more often classified as speech in traffic noise. Clean speech from distance speakers in extreme acoustic locations with long reverberation times (T60 2.44 s at 500 Hz) are misclassified as speech in babble.

The estimated computational load and memory consumption clearly show that the algorithm can be implemented in a hearing aid.

ACKNOWLEDGMENT

This work has been sponsored by GN ReSound.

Büchler, M. (**2001**). ''Usefulness and acceptance of automatic program selection in hearing instruments,'' Phonak Focus **27**, 1–10.

Duda, R. O., and Hart, P. E. (**1973**). *Pattern Classification and Scene Analysis* (Wiley-Interscience, New York).

Edwards, B., Hou, Z., Struck, C. J., and Dharan, P. (**1998**). ''Signal-processing algorithms for a new software-based, digital hearing device,'' Hearing J. **51**, 44–52.

Elberling, C. (**1999**). ''Loudness scaling revisited,'' J. Am. Acad. Audiol **10**, 248–260.

Eriksson-Mangold, M., and Ringdahl, A. (**1993**). ''Mätning av upplevd funktionsnedsättning och handikapp med Göteborgsprofilen,'' Audionytt **20**(1-2), 10–15.

Kates, J. M. (**1995**). ''On the feasibility of using neural nets to derive hearing-aid prescriptive procedures,'' J. Acoust. Soc. Am. **98**, 172–180.

Keidser, G. (**1995**). ''The relationships between listening conditions and alternative amplification schemes for multiple memory hearing aids,'' Ear Hear. **16**, 575–586.

Keidser, G. (**1996**). ''Selecting different amplification for different listening conditions,'' J. Am. Acad. Audiol **7**, 92–104.

Linde, Y., Buzo, A., and Gray, R. M. (**1980**). ''An algorithm for vector quantizer design,'' IEEE Trans. Commun. **COM-28**, 84–95.

Ludvigsen, C. (**1997**). Patent No. European Patent EP0732036.

Mammone, R. J., Zhang, X., and Ramachandran, R. P. (**1996**). ''Robust speaker recognition: A feature-based approach,'' IEEE Signal Process. Mag. **13**, 58–71.

Nordqvist, P. (**2000**). ''The behavior of non-linear (WDRC) hearing instruments under realistic simulated listening conditions,'' QPSR **2-3/2000**, 65–68.

Oberle, S., and Kaelin, A. (**1995**). ''Recognition of acoustical alarm signals for the profoundly deaf using hidden Markov models,'' presented at the IEEE International Symposium on Circuits and Systems, Hong Kong.

Ostendorf, M., Hohmann, V., and Kollmeier, B. (**1998**). ''Klassifikation von akustischen Signalen basierend auf der Analyse von Modulationsspektren zur Anwendung in digitalen Hörgeräten,'' presented at the DAGA'98.

Rabiner, L. R. (**1989**). ''A tutorial on hidden Markov models and selected applications in speech recognition,'' Proc. IEEE **77**, 257–286.

Tchorz, J., and Kollmeier, B. (**1998**). ''Using amplitude modulation information for sound classification,'' presented at the Psychophysics, Physiology, and Models of Hearing, Oldenburg.

Time-reversal imaging with multiple signal classification considering multiple scattering between the targets

Fred K. Gruber[a)]
Department of Industrial Engineering and Management Systems, University of Central Florida, Orlando, Florida 32816 and Department of Electrical Engineering, Technological University of Panama, Apartado 6-2894, Panama City, Panama

Edwin A. Marengo
Department of Electrical and Computer Engineering, Northeastern University, Boston, Massachusetts 02115 and Department of Electrical Engineering, Technological University of Panama, Apartado 6-2894, Panama City, Panama

Anthony J. Devaney
Department of Electrical and Computer Engineering, Northeastern University, Boston, Massachusetts 02115

(Received 29 October 2003; revised 23 February 2004; accepted 13 March 2004)

The time-reversal imaging with multiple signal classification method for the location of point targets developed within the framework of the Born approximation in Lehman and Devaney [''Transmission mode time-reversal super-resolution imaging,'' J. Acoust. Soc. Am. **113**, 2742–2753 (2003)] is generalized to incorporate multiple scattering between the targets. It is shown how the same method can be used in the location of point targets even if there is multiple scattering between them. On the other hand, both the conventional images and the calculated values of the target scattering amplitudes are scattering model-dependent. © *2004 Acoustical Society of America.*
[DOI: 10.1121/1.1738451]

PACS numbers: 43.60.Pt, 43.35.Zc [JCB] Pages: 3042–3047

I. INTRODUCTION

Time-reversal (TR) methods have been of interest for a number of years, with applications ranging from medicine, to communications, to radar, and to imaging in general.[1–6] A particular TR technique that has received much attention is a TR imaging with multiple signal classification (MUSIC) method for the location of point targets (whose size is much smaller than the wavelength) established first for coincident arrays,[7] and elaborated further in a recent generalization to noncoincident arrays and nonreciprocal media[8] and a recent super-resolution analysis based on real data.[9] This TR imaging with MUSIC method blends the original TR focusing[10,11] with signal subspace methods, in particular, with the MUSIC estimation technique. In its basic form the method is designed to deduce the location of point targets embedded in a known background medium from knowledge of the measured multistatic response matrix K of an acoustic or electromagnetic transceiver array actively interrogating the targets. It provides a powerful approach for locating targets in both homogeneous and heterogeneous backgrounds, especially in cases of closely spaced targets and/or very sparse transceiver arrays. However, these developments are based on the (distorted wave) Born approximation. The present letter addresses the corresponding generalization if there is nonnegligible multiple scattering between the targets.

[a)]Electronic mail: fgruber@mail.ucf.edu

II. GENERALIZATION INCLUDING MULTIPLE SCATTERING BETWEEN THE TARGETS

We consider an array of N time-harmonic transceivers located at the space points $\mathbf{R}_j$, for $j=1,2,\ldots,N$. Each transceiver can radiate into a reciprocal propagating medium in which are embedded $M<N$ point targets having unknown positions $\mathbf{X}_m$ and unknown target scattering amplitudes τ_m, for $m=1,2,\ldots,M$. For simplicity, we model the field radiated by the jth transceiver as the scalar field $G(\mathbf{r},\mathbf{R}_j)e_j$ where $G(\mathbf{r},\mathbf{r}')$ is the Green function of the propagating medium (in principle, the ''medium'' can include the transceivers themselves so inter-transceiver coupling can be built in this Green function) and e_j is the excitation applied to the transceiver.

A. Review of the TR imaging with MUSIC method

Under the Born approximation the TR imaging with MUSIC method is based on the fact that, for fewer targets than transceivers, the space $\mathcal{C}^N$ of voltage vectors applied to the N-transceiver array can be decomposed into the direct sum $\mathcal{C}^N=\mathcal{S}\oplus\mathcal{N}$, where the signal subspace $\mathcal{S}$ is orthogonal to the noise subspace $\mathcal{N}$, where $\mathcal{S}$ is spanned by the principal eigenvectors μ_i of the TR matrix $T=K^\dagger K$ (where † denotes the adjoint) having nonzero eigenvalues (if there are $M<N$ targets then there are at most M such eigenvalues indexed from 1 to M) whereas $\mathcal{N}$ is spanned by the eigenvectors μ_i of T having zero eigenvalues (if there are $M<N$ targets then there are at least $N-M$ such eigenvalues indexed from $M+1$ to N). The key result is that the TR matrix T is essentially a projection operator onto the space spanned by the complex conjugates g_m^* of the Green function vectors defined

 0001-4966/2004/115(6)/3042/6/$20.00 © 2004 Acoustical Society of America

as $g_m=[G(\mathbf{R}_1,\mathbf{X}_m),G(\mathbf{R}_2,\mathbf{X}_m),\ldots,G(\mathbf{R}_N,\mathbf{X}_m)]^t$ where t denotes the transpose, so that in general the principal eigenvectors of T are linear combinations of the g_m^*'s. It follows from this and the orthogonality of the signal and noise subspaces that the target locations must correspond to the poles in the MUSIC pseudospectrum

$$D(\mathbf{X}_p)=\frac{1}{\sum_{i=M+1}^{N}|\langle\mu_i^*|g_p\rangle|^2}, \tag{1}$$

where for all $i=M+1,M+2,\ldots,N$ the inner product $\langle\mu_i^*|g_p\rangle\equiv\mu_i^t g_p=0$ whenever $\mathbf{X}_p$ is the actual location of one of the targets.

B. Our main results

Essentially, what we show next is that not only for the Born-approximated model but also for the more general case when there is multiple scattering between the targets the TR matrix T is a projection operator onto the space spanned by the complex conjugates g_m^* of the Green function vectors g_m so that in general the principal eigenvectors of T are linear combinations of the g_m^*'s. It follows that the same TR imaging with MUSIC method described in connection with Eq. (1) can be used in the location of point targets even if there is multiple scattering between them. On the other hand, both the conventional TR images,[10,11] corresponding to back-propagations of the principal eigenvectors, and the calculated values of the target scattering amplitudes are scattering model-dependent.

C. Formulation

The exact scattered field $\psi_j^{(s)}(\mathbf{r})$ at position $\mathbf{r}$ due to the excitation of the jth transceiver alone can be expressed as the Newman series

$$\begin{aligned}\psi_j^{(s)}(\mathbf{r})=&\sum_{m=1}^{M}G(\mathbf{r},\mathbf{X}_m)\tau_m G(\mathbf{X}_m,\mathbf{R}_j)e_j\\&+\sum_{m=1}^{M}\sum_{m'=1}^{M}G(\mathbf{r},\mathbf{X}_m)\tau_m G(\mathbf{X}_m,\mathbf{X}_{m'})\\&\times\tau_{m'}G(\mathbf{X}_{m'},\mathbf{R}_j)(1-\delta_{m,m'})e_j\\&+\sum_{m=1}^{M}\sum_{m'=1}^{M}\sum_{m''=1}^{M}G(\mathbf{r},\mathbf{X}_m)\tau_m G(\mathbf{X}_m,\mathbf{X}_{m'})\\&\times\tau_{m'}G(\mathbf{X}_{m'},\mathbf{X}_{m''})\tau_{m''}G(\mathbf{X}_{m''},\mathbf{R}_j)\\&\times(1-\delta_{m,m'})(1-\delta_{m',m''})e_j+\cdots,\end{aligned} \tag{2}$$

where $\delta_{.,.}$ denotes the Kronecker delta. The first sum in Eq. (2) corresponds to the Born-approximated case, the second sum corresponds to the second-order scattering contribution, and so on.

The multistatic response matrix K, whose entry $K_{l,j}$ is defined as the value of the scattered field detected at the lth transceiver (in receive mode) due to the unit excitation at the jth transceiver (in transmit mode), can be shown from Eq. (2) to be given by (see also Borcea *et al.*[12])

$$K=\sum_{m=1}^{M}g_m\tau_m\Lambda_m^t, \tag{3}$$

where

$$\begin{aligned}\Lambda_m^t=&g_m^t+\sum_{m'=1}^{M}G(\mathbf{X}_m,\mathbf{X}_{m'})\tau_{m'}(1-\delta_{m,m'})g_{m'}^t\\&+\sum_{m'=1}^{M}\sum_{m''=1}^{M}G(\mathbf{X}_m,\mathbf{X}_{m'})\tau_{m'}G(\mathbf{X}_{m'},\mathbf{X}_{m''})\tau_{m''}(1\\&-\delta_{m,m'})(1-\delta_{m',m''})g_{m''}^t+\cdots\end{aligned} \tag{4}$$

(the approximation $\Lambda_m^t\simeq g_m^t$ yields the multistatic response matrix in the Born-approximated model). It follows from Eq. (3) that the TR matrix $T=K^\dagger K=K^*K$, where the second equality follows from reciprocity, can be expressed as

$$T=\sum_{m=1}^{M}\sum_{m_0=1}^{M}g_m^*\tau_m^*\langle\Lambda_m|g_{m_0}\rangle\tau_{m_0}\Lambda_{m_0}^t. \tag{5}$$

Put in this form, the TR matrix T is identified to be under the most general multiple scattering conditions a projection operator onto the space spanned by the complex conjugates g_m^* of the Green function vectors g_m so that in general the principal eigenvectors of T are linear combinations of the g_m^*'s, with the music pseudospectrum $D(\mathbf{X}_p)$ in Eq. (1) having poles at the locations of the targets, as desired. We illustrate this generalization next for a few canonical examples based on the free space Green function in two-dimensional space.

D. TR imaging with MUSIC in the second-order scattering case

In the following computer illustrations we consider the second-order scattering approximation of the preceding general theory. Our main goal is to show that despite the presence of non-negligible second-order scattering the TR imaging with MUSIC method works well in predicting the target locations. We will introduce a normalized quantity, to be referred to as "the second-order scattering contribution factor," and defined as $\eta=|\mathrm{Tr}[(K_{2\mathrm{nd}}-K_{\mathrm{Born}})^*(K_{2\mathrm{nd}}-K_{\mathrm{Born}})]|/\mathrm{Tr}(T_{\mathrm{Born}})$, where Tr denotes the trace, K_{Born} and T_{Born} are the multistatic response matrix and the TR matrix, respectively, assuming the Born approximation, and $K_{2\mathrm{nd}}$ is the multistatic response matrix for a more general second-order scattering model, as a way to quantify the global effect of the second-order scattering contribution relative to that of the first-order scattering term alone as seen by the array in receive mode. This factor measures the deviation of the data matrix (K), as determined by the energy norm or inner product metric, relative to the purely Born-approximated vector, due to the second-order scattering contribution.

Figures 1 and 2 show plots in gray color map of the MUSIC pseudospectra under a second-order scattering model for a number of transceiver and target configurations. Next to each MUSIC pseudospectrum plot we have provided another plot showing the corresponding simulation geometry where the transceiver locations are indicated with triangles while the target locations are indicated with asterisks. All dimensions are relative to the wavelength λ (which equals

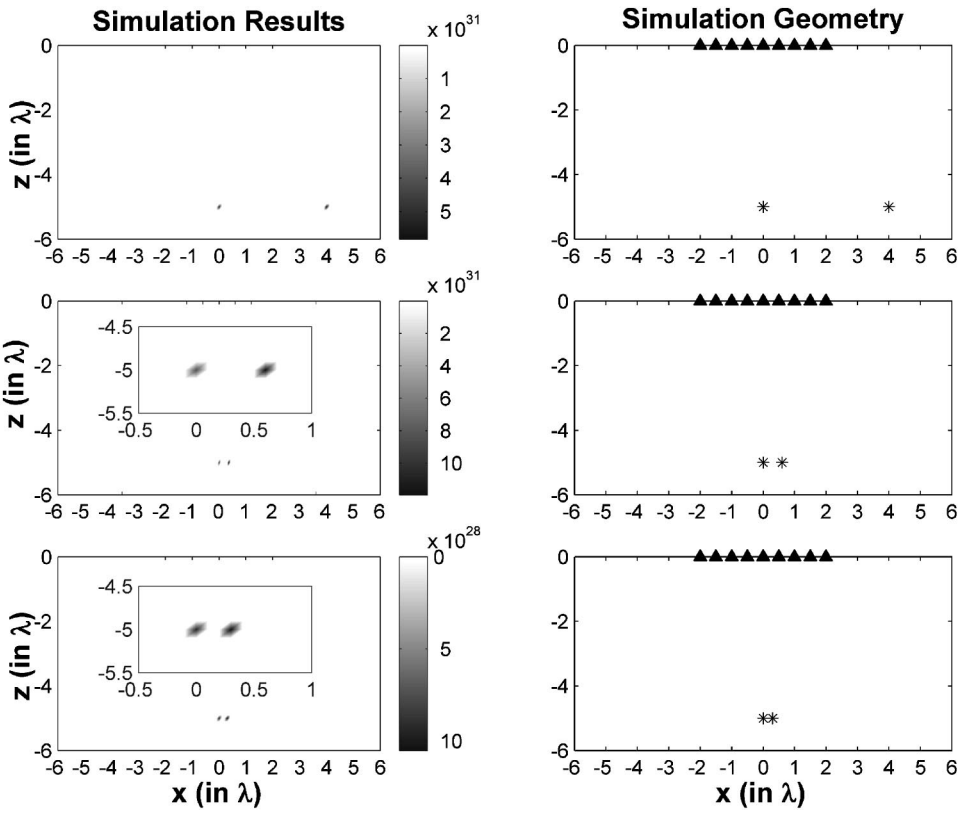

FIG. 1. Reconstructed image with an inverse gray color map for the second-order scattering simulation pseudospectrum for a two target configuration. Three target separations are shown: 4λ (top), 0.6λ (middle), and 0.3λ (bottom). A linear scale was used for the horizontal and vertical axes.

1), and all targets have unit scattering amplitude. The plot in Fig. 1 illustrates the super-resolution capabilities of the technique[9] since even for a target separation as small as 0.3λ the target locations remain sharply resolved [the method was found to work for yet smaller target separations, in particular, 0.1λ (results not shown)]. For the 0.6λ and 4λ target separation cases the second-order contribution factor is not very strong ($\eta = 0.17$ and $\eta = 0.03$, respectively). However, for the 0.3λ and 0.1λ target separation cases, the second-order contribution factor is $\eta = 0.33$ and $\eta = 0.89$, respectively.

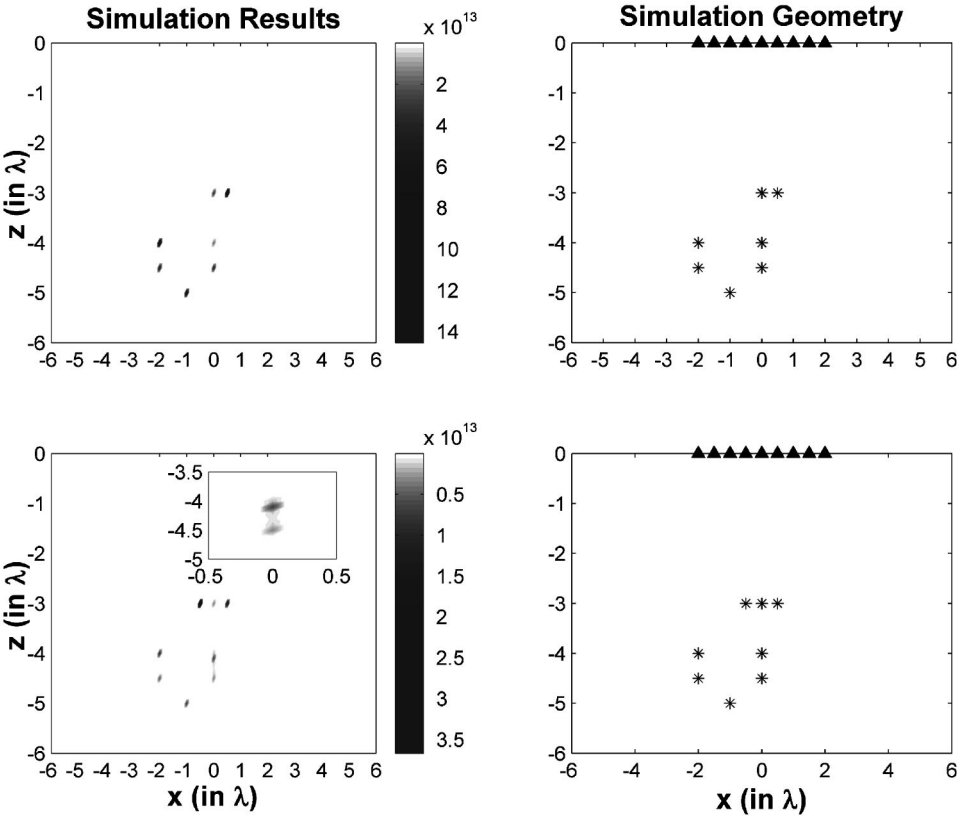

FIG. 2. Reconstructed image with an inverse gray color map for the second-order scattering simulation pseudospectrum for 7 and 8 targets in a *J* conformation. A linear scale was used for the horizontal and vertical axes.

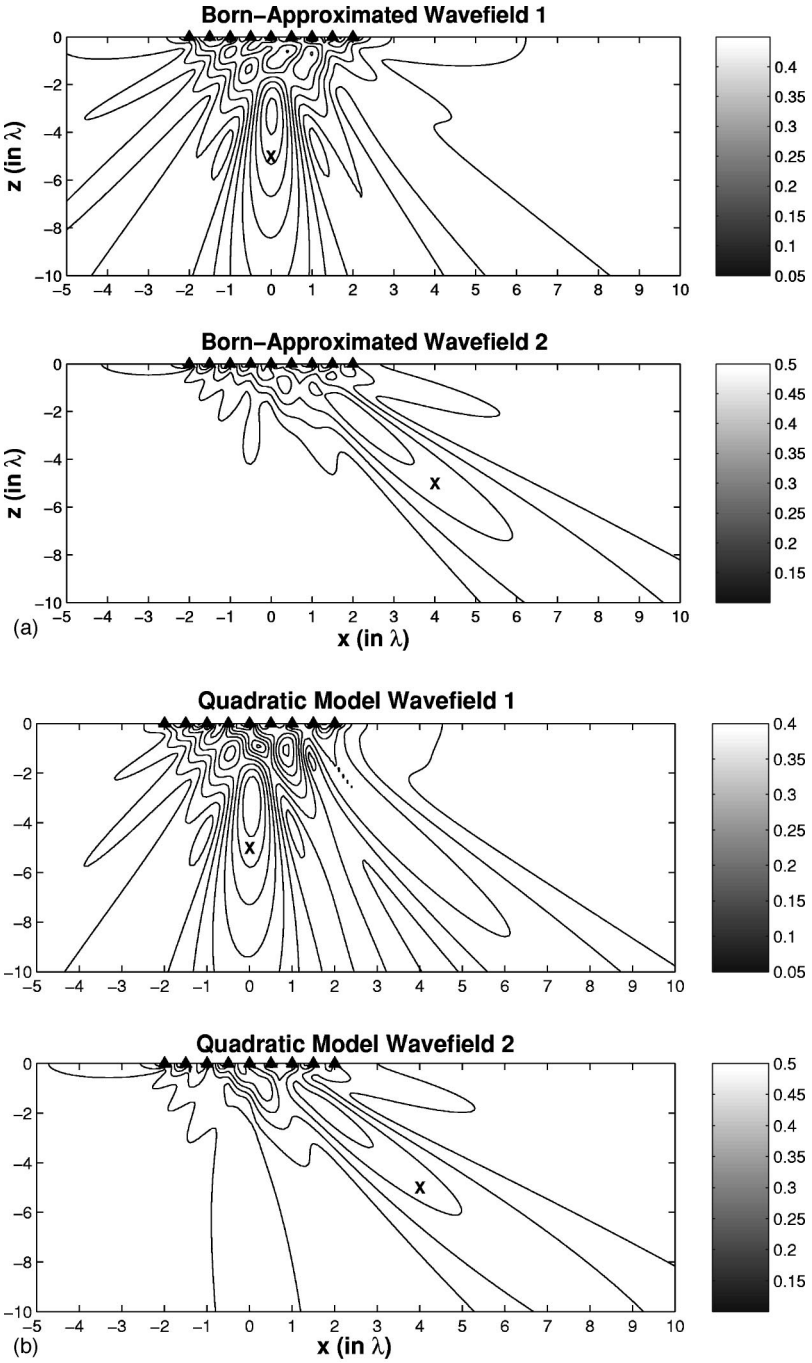

FIG. 3. (a) Conventional, backpropagated images of the two principal eigenvectors corresponding to the 4λ target separation geometry in Fig. 1. Results for the Born-approximated model. A linear scale was used for the horizontal and vertical axes. (b) Corresponding results for the second order scattering model.

This means that in the 0.3λ target separation configuration the amount of additional signal due to the presence of second-order scattering is of the order of the Born-approximated signal alone as perceived by the array in receive mode. In the 0.1λ target separation case the presence of second-order scattering is even more dominant. Yet the TR imaging with MUSIC was found to succeed in determining the target locations. More complicated seven and eight target configurations forming a J and having significant second-order scattering contribution factors of $\eta=0.31$ and $\eta=0.30$, respectively, are considered in Fig. 2. The method works well in predicting the target locations but for the eight target case the prediction for one of the target locations, in particular, the one at the plot coordinates $(0,-4\lambda)$, has a slight error which we attribute to computational sensitivity under reduced noise subspace conditions (in this extreme case when $M=8$ and $N=9$ the noise subspace has a single eigenvector).

E. Time-reversed images: Born-approximated versus second-order scattering cases

The field radiated by the array due to excitation with an arbitrary voltage vector is $\psi(\mathbf{r})=\Sigma_{j=1}^{N} G(\mathbf{r},\mathbf{R}_j)e_j$. In the original TR focusing one obtains backpropagated images $\psi(\mathbf{r})$ of the targets by replacing the arbitrary input voltage vectors in this expression with the principal eigenvectors of the TR matrix. If there is no second-order scattering between the targets then the principal eigenvectors are precisely the complex conjugates of the Green function vectors and each

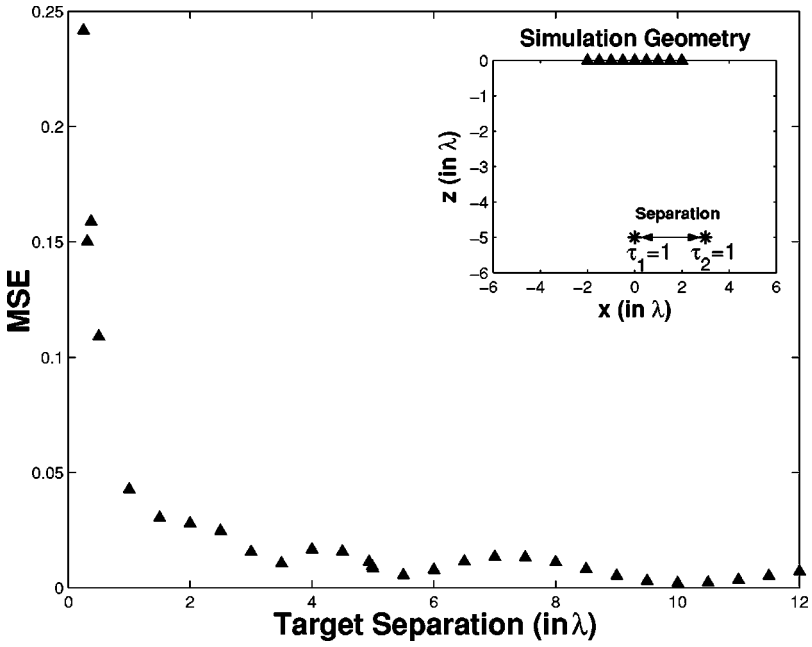

FIG. 4. MSE in scattering amplitude estimation, incurred if one uses the Born-approximated model instead of the more exact second-order scattering model, as a function of target separation for the general two target configuration used in Fig. 1.

one of them is associated with (focuses on) a particular target. Consequently, as shown in Fig. 3(a), corresponding to the 4λ target separation case in Fig. 1, in the Born-approximated case each ''eigenimage'' focuses on a particular, corresponding target (in the plots we have superimposed an *X* in the location of the corresponding target). On the other hand, if there is second-order scattering between the targets, then the principal eigenvectors become linear combinations of the complex conjugates of the Green function vectors so that each eigenimage focuses in general on more than one target (this is somehow similar to the results in Ref. 11 for non-well-resolved targets). Figure 3(b) illustrates this effect for the second-order scattering case where each eigenimage is seen to focus on *both* targets.

F. Target scattering amplitudes: Born-approximated versus second-order scattering cases

In the general case including multiple scattering considered here, once the target locations are determined from the poles in the MUSIC pseudospectrum one can compute the unknown target scattering amplitudes by substituting the values of these locations in Eq. (3) and solving the resulting system of equations. In general, such computed values will depend on the scattering model employed, being more exact for a more exact scattering model. To illustrate this let us assume that in reality the response obeys a second-order scattering model. If we try to determine the scattering amplitudes considering a Born-approximated model then we will have model-induced errors. Figure 4 shows, again for the geometry in Fig. 1, the mean square error (MSE) in the estimation of the scattering amplitudes (as measured relative to the more exact second-order scattering model) as a function of target separation. The errors are significant (relative to the value $\tau_1=\tau_2=1$) for targets in close proximity, as expected (second-order scattering becomes then more prevalent).

III. CONCLUSION

In this letter we showed that the TR imaging with MUSIC method can be used to locate point targets not only in the usual framework of the Born approximation but also in more general nonlinear scattering frameworks where there is multiple scattering between the targets. This finding is important toward practical implementations of the TR technique facing multiple scattering effects. The super-resolution results of a previous paper[9] can now be better characterized theoretically in the multiple scattering regime. They were also corroborated numerically for second-order scattering (see Fig. 1). The method was found to work well even for a large number of targets relative to the number of transceivers (see Fig. 2) although slight numerical challenges may arise as the number of targets approaches the number of transceivers (see the zooming part of Fig. 2). We showed how both the conventional, backpropagated images of the principal eigenvectors and the predicted values of the target scattering amplitudes are scattering model-dependent (see Figs. 3 and 4). In this the effect of scattering model is significant, particularly for targets in close proximity, as expected (see Fig. 4).

ACKNOWLEDGMENT

This work was supported in part by the United States Air Force Office of Scientific Research under Grant No. F49620-02-1-0309.

[1] M. Fink, D. Cassereau, A. Derode, C. Prada, P. Roux, M. Tanter, J. L. Thomas, and F. Wu, ''Time-reversed acoustics,'' Rep. Prog. Phys. **63**, 1933–1995 (2000).
[2] G. Montaldo, P. Roux, A. Derode, C. Negreira, and M. Fink, ''Generation of very high pressure pulses with 1-bit time reversal in a solid waveguide,'' J. Acoust. Soc. Am. **110**, 2849–2857 (2001).
[3] J. S. Kim and K. C. Shin, ''Multiple focusing with adaptive time-reversal mirror,'' J. Acoust. Soc. Am. **115**, 600–606 (2004).
[4] A. Derode, A. Tourin, J. de Rosny, M. Tanter, S. Yon, and M. Fink,

''Taking advantage of multiple scattering to communicate with time-reversal antennas,'' Phys. Rev. Lett. **90**, 014301 (2003).
[5] D. M. Fromm, C. F. Gaumond, J. F. Lingevitch, R. C. Gauss, and R. Menis, ''Detection in shallow water using broadband-DORT,'' J. Acoust. Soc. Am. **114**, 2399 (2003).
[6] L. Carin, H. Liu, T. Yoder, L. Couchman, B. Houston, and J. Bucaro, ''Wideband time-reversal imaging of an elastic target in an acoustic waveguide,'' J. Acoust. Soc. Am. **115**, 259–268 (2004).
[7] H. Lev-Ari and A. J. Devaney, ''The time-reversal technique re-interpreted: Subspace-based signal processing for multi-static target location,'' IEEE Sensor Array and Multichannel Signal Processing Workshop, Cambridge, MA, 2000, pp. 509–513.
[8] S. K. Lehman and A. J. Devaney, ''Transmission mode time-reversal super-resolution imaging,'' J. Acoust. Soc. Am. **113**, 2742–2753 (2003).
[9] C. Prada and J. L. Thomas, ''Experimental subwavelength localization of scatterers by decomposition of the time reversal operator interpreted as a covariance matrix,'' J. Acoust. Soc. Am. **114**, 235–243 (2003).
[10] C. Prada, J. L. Thomas, and M. Fink, ''The iterative time reversal process: Analysis of the convergence,'' J. Acoust. Soc. Am. **97**, 62–71 (1995).
[11] C. Prada, S. Manneville, D. Spoliansky, and M. Fink, ''Decomposition of the time reversal operator: Detection and selective focusing on two scatterers,'' J. Acoust. Soc. Am. **99**, 2067–2076 (1996).
[12] L. Borcea, G. Papanicolaou, C. Tsogka, and J. Berryman, ''Imaging and time reversal in random media,'' Inverse Probl. **18**, 1247–1279 (2002).

Microseismic source deconvolution: Wiener filter versus minimax, Fourier versus wavelets, and linear versus nonlinear

Jianye Ching,[a] Albert C. To, and Steven D. Glaser[b]
Department of Civil and Environmental Engineering, University of California at Berkeley, Berkeley, California 94720

(Received 3 August 2002; revised 13 February 2004; accepted 13 February 2004)

Deconvolution is commonly performed on microseismic signals to determine the time history of a dislocation source, usually modeled as combinations of forces or couples. This paper presents a new deconvolution method that uses a nonlinear thresholding estimator, which is based on the minimax framework and operates in the wavelet domain. Experiments were performed on a steel plate using artificially generated microseismic signals, which were recorded by high-fidelity displacement sensors at various locations. The source functions were deconvolved from the recorded signals by Wiener filters and the new method. Results were compared and show that the new method outperforms the other methods in terms of reducing noise while keeping the sharp features of the source functions. Other advantages of the nonlinear thresholding estimator include (1) its performance is close to that of a minimax estimator, (2) it is nonlinear and takes advantage of sparse representations under wavelet bases, and (3) its computation is faster than the fast Fourier transform.
© *2004 Acoustical Society of America.* [DOI: 10.1121/1.1705658]

PACS numbers: 43.60.Pt, 43.40.Le, 43.60.Bf [JCB] Pages: 3048–3058

I. INTRODUCTION

Microseismic (MS) signals carry important information about the dislocation mechanisms within the solid that contains the source. It is of great interest to infer the characteristics of the dislocation source using the recorded MS signals, and a common way of achieving this is to deconvolve the recorded MS signals by the corresponding Green's functions. The result of the deconvolution is an estimate of the MS source function, e.g., the slip time history of the dislocation source. Using the estimated source function, it is possible to infer the dislocation mechanisms of the crack that generates the MS energy. This technique has been routinely implemented by geophysicists to invert seismic source functions using seismograms (e.g., Stump and Johnson, 1977) and by researchers in nondestructive testing (e.g., Michaels *et al.*, 1981) and fracture mechanics (e.g., Scruby *et al.*, 1985; Kim and Sachse, 1986) to determine the fracture mechanisms of cracks in solids.

A standard way of performing deconvolution is to implement time-invariant Wiener filters (e.g., Oldenburg, 1981; Bertero, 1989; Chung and Liu, 1998), which are Wiener filters with stationary assumptions. The time-invariant Wiener filters are linear estimators operating in the Fourier domain. It is intuitive to implement such time-invariant Wiener filters because (1) sinusoidal functions are eigenfunctions of convolution operators, therefore it is convenient and efficient to represent the operators in the Fourier domain. (2) Because of (1), the Fourier coefficients of stationary random processes over different frequencies are uncorrelated, and this simplifies the analyses if the MS source function is also stationary. (3) They are computationally convenient since there is only a linear inverse problem to solve, and the fast Fourier transform can be calculated rapidly.

However, time-invariant Wiener filters may perform poorly if the assumed stationary properties are not appropriate. Also, Wiener filters reject the use of a nonlinear estimator, and the Fourier basis does not necessarily provide sparse representations for MS signals and MS source functions. Last, to implement Wiener filters usually requires the knowledge of the noise power spectrum, which is another parameter to be determined.

In this paper, we introduce the nonlinear thresholding estimator (NTE) developed by Donoho and Johnstone (1992) and Johnstone and Silverman (1997). The estimator provides the following advantages: (1) It does not assume a stationary source function. Instead, the estimator is based on the minimax concept (Bickel and Doksum, 1977) from decision theory. We argue that a minimax estimator is more suitable for a deconvolution problem than time-invariant Wiener filters. (2) The NTE does not require the knowledge of the noise power spectrum. (3) The resulting algorithm is faster than the fast Fourier transform. (4) The NTE is close to a minimax estimator for a large class of functions, which no linear estimators can achieve. (5) The NTE uses sparse representations of wavelet bases, and it is particularly suitable for estimating MS source functions (MS source functions are transient and are therefore sparse under wavelet bases).

The NTE has been introduced and applied to deconvolution problems by Masuda *et al.* (1999) for synthetic data. In this paper, we apply the NTE to experimental data and discuss the following concepts that were not presented in Masuda *et al.* (1999) but are crucial to deconvolution problems: (1) the importance of sparse representations of MS signals and MS source functions, (2) the advantage of using a nonlinear filter for transient MS source functions, and (3) the advantage of a minimax estimator over Wiener filters.

[a]Electronic mail: jyching@caltech.edu
[b]Electronic mail: glaser@ce.berkeley.edu

 0001-4966/2004/115(6)/3048/11/$20.00 © 2004 Acoustical Society of America

We first define the problem of MS source deconvolution in Sec. II. Then in Sec. III, we introduce Wiener filters and time-invariant Wiener filters. In Sec. IV, we introduce the minimax framework and the NTE, and some important properties of the NTE are discussed. Section V states the key considerations regarding how to choose the estimator for deconvolution problems. Section VI presents two case studies, from which we compare the performances of four different deconvolution strategies. Sections VII and VIII contain discussions and conclusions.

II. DEFINITION OF THE PROBLEM

The MS deconvolution problem is defined as follows. Assume G is a known Green's function characterizing the host from the MS source to the sensor, $z(t)$ is stationary Gaussian random process (noise) at time t, and T is the total number of discrete data points. Given a noisy MS sensor signal $\{d(t): t=1,2,...,T\}$, where

$$d(t)=\int G(t-\tau)f(\tau)d\tau+z(t), \quad t=1,2,...,T, \tag{1}$$

our goal is to estimate the unknown MS source function f. We assume d, f, and z in the equation are all continuous-time functions in $\mathbf{L}^2$ ($\mathbf{L}^2$ is the function space that contains all functions with finite $\mathbf{L}^2$ norms). We discuss two estimators of f, Wiener filters and minimax estimator, and show that the minimax framework can lead to nonlinear estimators based on thresholding rules.

III. WIENER FILTER ESTIMATE OF AN UNKNOWN SOURCE FUNCTION

To begin with the discussions for Wiener filters (Haykin, 1991; Clarkson, 1993), let the estimated f, denoted by $\hat{f}$, be generated by passing the data d through a general linear filter h (not necessarily time-invariant):

$$\hat{f}(t)=\int_{-\infty}^{\infty} h(t,\tau)\cdot d(\tau)\cdot d\tau, \tag{2}$$

where $h(t,\tau)$ is the impulse response of the linear filter. The optimal linear filter h that minimizes the risk (also known as mean-square error)

$$E_Z(\|\hat{f}-f\|_2^2), \tag{3}$$

where $E_Z(\cdot)$ denotes expectation with respect to the probability density function (PDF) of z, and $\|\hat{f}-f\|_2^2 \equiv \int(\hat{f}(t)-f(t))^2\,dt$ is the squares of the $\mathbf{L}^2$ norm of g, is a (time-varying) Wiener filter. A Wiener filter can be found by solving the following Wiener–Hopf equation:

$$\int_{-\infty}^{\infty} R_d(\xi-t,\tau)\cdot h(t,\tau)\cdot d\tau=R_{df}(\xi-t,t) \quad \forall \xi,t, \tag{4}$$

where $R_d(t,\tau)$ is the auto-correlation function between $d(t)$ and $d(\tau)$; $R_{df}(t,\tau)$ is the cross-correlation function between $d(t)$ and $f(\tau)$.

In practice, a time-invariant Wiener filter is often used, which requires the assumption that both f and d are weakly stationary processes. Under this assumption, Eq. (4) becomes

$$\int_{-\infty}^{\infty} R_d(\xi-\tau)\cdot h(\tau)\cdot d\tau=R_{df}(\xi) \quad \forall \xi, \tag{5}$$

where $R_d(\xi)$ and $R_{fd}(\xi)$ are the auto-correlation function of d and the cross-correlation function between f and d, respectively, with lag ξ; h is now a time-invariant filter, and $h(\tau)$ is its impulse response. With the assumption that f and z in Eq. (1) are uncorrelated, Eq. (5) can be written in the frequency (Fourier) domain as

$$(|G(\omega)|^2\cdot|F(\omega)|^2+P_Z(\omega))\cdot H(\omega)=G(\omega)^*\cdot|F(\omega)|^2, \tag{6}$$

where $G(\omega)$ is the Fourier transform of the Green's function G; $H(\omega)$ and $F(\omega)$ are the Fourier transforms of h and f; G^* denotes the complex conjugate of G; and $P_Z(\omega)$ is the power spectrum of z. It follows that

$$H(\omega)=\frac{G(\omega)^*}{|G(\omega)|^2+P_Z(\omega)/|F(\omega)|^2}. \tag{7}$$

In principle, $|F(\omega)|^2$ is not completely known *a priori*, so a key step in designing a Wiener filter is to choose a reasonable $|F(\omega)|^2$. Different choices of $|F(\omega)|^2$ lead to different designs of Wiener filters. For instance, Oldenburg (1981) chooses $|F(\omega)|^2=1/\tan\theta$, where θ is a resolution factor that varies from 0 to 2π; Bertero (1989) chooses $|F(\omega)|^2=\mu\cdot|D(\omega)|^2/P_Z(\omega)$, where μ is usually chosen as the average power of the noise spectrum; Chung and Liu (1998) choose $|F(\omega)|^2=|D(\omega)|^2/|G(\omega)|^2$. All of these algorithms lead to low-pass filters, i.e., estimators with time-invariant moving-average windows.

IV. MINIMAX ESTIMATE OF AN UNKNOWN SOURCE FUNCTION

A. Minimax rule

Under the minimax framework, it is assumed that f is smooth in a certain sense, i.e., f is within some known function set $\mathbf{H}$. For instance, if f is a solution of some second-order differential equation, f is within $\mathbf{H}=\mathbf{C}^2$, the function space of twice differentiable functions. Formally, the minimax estimate of f over $\mathbf{H}$ is the one that ''minimizes'' the ''maximum'' risk over $\mathbf{H}$. In other words,

$$\begin{aligned}\hat{f}_H^M(d)&=\arg\inf_{\hat{f}(\cdot)} R^M(\hat{f}(d),H)\\&=\arg\inf_{\hat{f}(\cdot)}\left[\sup_{f\in H} R(\hat{f}(d),f)\right]\\&=\arg\inf_{\hat{f}(\cdot)}\left[\sup_{f\in H} E_Z\left\|\hat{f}(d)-f\right\|_2^2\right],\end{aligned} \tag{8}$$

where $\hat{f}_H^M(\cdot)$ denotes the minimax estimator, which is an operator mapping $d\in\mathbf{L}^2$ to another function in $\mathbf{L}^2$, and $R^M(\hat{f}(d),H)$ denotes the maximum risk over the function set $\mathbf{H}$. That is, the minimax estimator $\hat{f}_H^M(\cdot)$ is the operator $\hat{f}(\cdot)$ that minimizes the maximum risk $R^M(\hat{f}(d),H)$. The minimized risk is called the minimax risk, i.e.,

$$R^{Min\ max}(d,H)=\inf_{\hat{f}(\cdot)} R^M(\hat{f}(d),H). \tag{9}$$

It can be seen from Eqs. (8) and (9) that

$$E_Z\|\hat{f}_H^M(d)-f\|_2^2=R(\hat{f}_H^M(d),f)<R^{Min\ max}(d,H) \quad \forall f\in H, \tag{10}$$

where the definition of $R(\hat{f}(d),f)$ is identical to the one in Eq. (3). That is, the resulting risk $R(\hat{f}_H^M(d),f)$ for every f in $\mathbf{H}$ is guaranteed to be less than the fixed number $R^{Min\ max}(d,H)$, which is minimized in the minimax framework. In the case that $\mathbf{H}$ is sufficiently large, the minimax framework allows us to find an estimate of f without applying strong subjective constraints to f, e.g., the stationary properties assumed by time-invariant Wiener filters.

Unfortunately, even for the simple deconvolution problem, the minimax estimator cannot be found for any arbitrary $\mathbf{H}$. Nevertheless, Donoho and Johnstone (1994) showed that it is possible to construct estimators, the so-called nonlinear thresholding estimators, which have maximum risks that are close to the minimax risk [Eq. (9)] over all Besov function classes (Triebel, 1983), i.e.,

$$\sup_{f\in B_{p,q}^s} R(\hat{f}^{NTE}(d),f)\sim R^{Min\ max}(d,B_{p,q}^s), \tag{11}$$

where $\hat{f}^{NTE}(\cdot)$ is the NTE estimator; $B_{p,q}^s$ is a Besov function space defined as follows:

$$B_{p,q}^s=\left\{ f:\left(\int \left(\frac{w_{r,p}(f;h)}{h^s}\right)^q \frac{dh}{h}\right)^{1/q}<\infty\right\},$$

$$w_{r,p}(f;h)=\left\| \sum_{k=0}^{r} \binom{r}{k}(-1)^k f(t+kh)\right\|_{L^p}. \tag{12}$$

Since the NTEs operate under wavelet bases, we discuss wavelet bases in the next section.

B. Wavelet bases and sparse representations

Traditionally, deconvolution problems are usually manipulated in the Fourier domain, e.g., a low-pass filter is a linear estimator operating in the Fourier domain. However, the Fourier basis can seldom provide a sparse representation for f unless f is a periodic function. In this section, we introduce wavelet bases, which are more suitable to represent transient functions. In MS signal analysis, wavelets have been applied to material classification (Qi, 2000) and fracture mode classification and determination of phase and group velocities (Takemoto *et al.*, 2000).

A wavelet basis (Daubechies, 1992; Meyer, 1992; Mallat, 1998) is an orthonormal basis that decomposes the $\mathbf{L}^2$ function space into a series of function spaces containing functions with different degrees of oscillations:

$$L^2=\bigoplus_{j=-\infty}^{\infty} W_j, \tag{13}$$

where $\oplus$ is the direct sum of linear spaces. W_j with a small j contains functions with slow oscillations; W_j with a large j contains functions with rapid oscillations. Wavelet basis functions include father wavelets $\{\varphi_{m,k}:k=1,2,...,2^m\}$, which span $V_m=\oplus_{j=-\infty}^{m-1}W_j$, and mother wavelets $\{\psi_{j,k}:k=1,2,...,2^j\}$, which span W_j (Mallat, 1998). We denote the wavelet coefficients of a function $\xi\in\mathbf{L}^2$ by $\alpha_{m,k}(\xi)=\langle\varphi_{m,k},\xi\rangle$ and $\beta_{j,k}(\xi)=\langle\psi_{j,k},\xi\rangle$, where $\langle g,h\rangle$ is the inner product between function g and h. For a sampled function of sample size $T=2^J$, the decomposition of f is

$$f=\sum_{k=1}^{2^m}\alpha_{m,k}(f)\cdot\varphi_{m,k}+\sum_{j=m}^{J-1}\sum_{k=1}^{2^j}\beta_{j,k}(f)\cdot\psi_{j,k}. \tag{14}$$

An appealing feature of a wavelet basis is that many useful functions have sparse representations under wavelet bases. The sparseness is due to the following two facts: (1) with a careful selection of mother wavelets, the functions can be made orthogonal to polynomials less than a certain degree (Mallat, 1998), and (2) mother wavelets have compact support (or nearly compact support) regions. Consequently, transient signals which are usually piecewise smooth functions are sparse in the wavelet domain since many wavelet coefficients $\beta_{j,k}$ in the smooth regions that are close to polynomials are close to zeros. In addition, a nonsmooth function whose region of support does not intersect with the support region of a mother wavelet is orthogonal to that mother wavelet; hence, a small support region also helps supply sparseness.

C. Nonlinear thresholding estimators

Equation (1) can be rewritten using an operator form as the following equation:

$$d(t)=(G\cdot f)(t)+z(t), \quad t=1,2,...,T, \tag{15}$$

where $(G\cdot)$ denotes the corresponding convolution operator. Then the following equation is equivalent to Eq. (15):

$$(G^{-1}\cdot d)(t)=f(t)+(G^{-1}\cdot z)(t), \quad t=1,2,...,T, \tag{16}$$

where G^{-1} denotes the inverse operation of G. The philosophy of the NTE is to compare the magnitudes of $G^{-1}\cdot d$ and $G^{-1}\cdot z$ under a wavelet basis. If the wavelet coefficient $\beta_{j,k}(G^{-1}\cdot d)$ is much larger than $\beta_{j,k}(G^{-1}\cdot z)$, $\beta_{j,k}(G^{-1}\cdot d)$ is considered to contain a significant amount of information about f and is therefore kept; otherwise, $\beta_{j,k}(G^{-1}\cdot d)$ is discarded and set to zero. Formally, the two NTEs proposed by Johnstone and Silverman (1997), called hard and soft thresholding estimators, are described by the following algorithms:

(1) Compute $y=G^{-1}\cdot d$ (or pseudo-inverse if G^{-1} does not exist) and find $\alpha(y)_{m,k}$ and $\beta(y)_{j,k}$.

(2) Find the estimate of the standard deviation of $\beta_{j,k}(G^{-1}\cdot z)$ for scale j, denoted by $\hat{\sigma}_j$, by the median value of $\{|\beta_{j,k}(y)|:k=1,...,2^j\}$ divided by 0.6745 (Donoho and Johnstone, 1992) and compute the level-dependent thresholding level $\lambda_j=\hat{\sigma}_j\sqrt{2\log(T)}$.

Discussion: Due to the fact that f is sparse under wavelet bases, the set $\{|\beta_{j,k}(f)|:k=1,...,2^j\}$ contains mostly numbers that are close to zero. Therefore, most of the numbers contained in the set $\{|\beta_{j,k}(y)|:k=1,...,2^j\}$ are close to those in the set $\{|\beta_{j,k}(G^{-1}z)|:k=1,...,2^j\}$. Consequently, the median value of $\{|\beta_{j,k}(y)|:k=1,...,2^j\}$ should be close to $\{|\beta_{j,k}(G^{-1}z)|:k=1,...,2^j\}$.

Also, since mother wavelets are almost eigenfunctions for many convolution operators (Meyer, 1992), so the stationary Gaussian noise $G^{-1}\cdot z$ becomes almost independent under wavelet bases. Therefore, the median value of $\{|\beta_{j,k}(G^{-1}z)|:k=1,...,2^j\}$ divided by 0.6745 is a plausible estimate of its standard deviation. The constant $\sqrt{2\log(T)}$ is chosen because $\beta_{j,k}(G^{-1}z)$ can be greater than λ_j with only an insignificant probability.

(3) Threshold $\beta_{j,k}(y)$ uses the hard thresholding, i.e.,

$$\tilde{\beta}_{j,k}(y)=\begin{cases}\beta_{j,k}(y) & |\beta_{j,k}(y)|>\lambda_j,\\ 0 \quad \text{otherwise,}\end{cases} \qquad \forall j,k, \tag{17}$$

or uses the soft thresholding, i.e.,

$$\tilde{\beta}_{j,k}(y)=\begin{cases}(|\beta_{j,k}(y)|-\lambda_j)\operatorname{sgn}(\beta_{j,k}(y)) & |\beta_{j,k}(y)|>\lambda_j,\\ 0 \quad \text{otherwise,}\end{cases} \qquad \forall j,k. \tag{18}$$

(4) Find the NTE of f, denoted by $\hat{f}^{NTE}$, by the inverse wavelet transform

$$\hat{f}^{NTE}=\sum_{k=1}^{2^m}\alpha_{m,k}(y)\phi_{m,k}+\sum_{j=m}^{J-1}\sum_{k=1}^{2^j}\tilde{\beta}_{j,k}(y)\varphi_{j,k}. \tag{19}$$

Equations (17) and (18) indicate that the NTEs depend on the data d in nonlinear ways. The thresholding estimator described above does not require any knowledge about the power spectrum of the noise z: all we need to do is to estimate $\hat{\sigma}_j$ for each scale. The thresholding estimate $\hat{f}^{NTE}$ is nearly minimax over every Besov function space, while no linear estimator can be nearly-minimax over every Besov function space (Johnstone and Silverman, 1997). This uniform near-minimaxity over all the Besov spaces has the following advantage: although in principle we need to know which Besov space [i.e., the values of p, q, and s in Eq. (11)] that f belongs to before we implement the NTEs, in practice we can ignore this step because it is very unlikely that f does not belong to any of the Besov function classes.

V. KEY CONSIDERATIONS

We have introduced Wiener filters and NTEs in the last few sections. We now summarize the key considerations regarding the original deconvolution problem:

A. Wiener filters versus minimax

Which framework should we choose, Wiener filters or minimax? For designing a time-invariant Wiener filter, assigning a reasonable $|F(\omega)|^2$ [Eq. (7)] is crucial. Unfortunately, for the deconvolution problem it is usually difficult to gain knowledge about $|F(\omega)|^2$ *a priori*. Also time-invariant Wiener filters assume that f is stationary; however, it is hardly the case that the MS source function is stationary. MS source functions are usually transient, hence nonstationary.

On the other hand, the minimax framework does not assume f to be stationary. Also, under the minimax framework, it is guaranteed that the resulting risk $R(\hat{f}_H^M(d),f)$ is smaller than $R^{Min\ max}(d,H)$ for every f in $\mathbf{H}$ [see Eq. (10)]. We have seen that the NTEs perform close to a minimax estimator over any Besov function class; this makes the NTEs even more attractive.

B. Linear versus nonlinear

In general, nonlinear estimators can be assumed superior to linear ones since linear estimators are special cases of nonlinear ones. Another way of justifying the superiority is through the following example. Consider the following function estimation problem:

$$d(t)=f(t)+e(t), \quad t=1,2,...,T, \tag{20}$$

where e is a white Gaussian process. The goal is to estimate f based on the data $\{d(t):t=1,2,...,T\}$. Now let us restrict ourselves with a keep-or-kill estimator in the Fourier domain: the estimation procedure is to first compute the Fourier coefficients of d, keep $K(\ll T)$ Fourier coefficients of d and set others to zeros, and the estimate of f is computed as the inverse Fourier transform of the manipulated Fourier coefficients of d.

Clearly, the best strategy is to keep the K largest Fourier coefficients if the goal is to minimize the estimation risk $R(\hat{f}(d),f)$, and this strategy corresponds to a nonlinear estimator since the decision of keeping or killing any coefficient depends on the Fourier amplitude of d. A linear estimator prohibits the dependence of the estimator on the data, so the corresponding K Fourier coefficients have to be prechosen. Therefore, all linear estimators perform worse than the best nonlinear estimator unless the prechosen K coefficients coincide with the K largest coefficients.

Wiener filters are linear estimators while the NTEs are nonlinear. In fact, the NTEs behave similarly as the best nonlinear estimator mentioned in the last paragraph: the NTEs tend to keep wavelet coefficients with large amplitudes and kill those with small amplitudes.

C. Fourier versus wavelets

Which orthonormal basis should we choose, Fourier or wavelets? A transient signal f is usually sparse in the wavelet domain. However, f is usually not sparse under the Fourier domain unless f is periodic or stationary. Therefore, the wavelet domain is usually a better platform for function estimation than the Fourier domain for transient f since in the wavelet domain, it is easier to distinguish the patterns of the signal f and the noise z (z is never sparse under any orthonormal basis). MS source functions are usually transient, i.e., nonperiodic and nonstationary, and so are not sparse in the Fourier domain, but are sparse under the wavelet domain. Time-invariant Wiener filters operate in the Fourier domain while the NTEs operate in the wavelet domain.

VI. CASE STUDIES

A. Experimental setup and data processing

In order to demonstrate the utility of our proposed method, several experiments are conducted on a 600 $\times$600$\times$50 mm steel plate (see Fig. 1). Artificial sources are used to generate MS signals, which are recorded by wide-

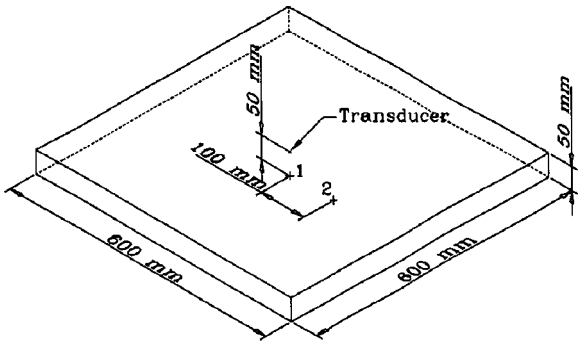

FIG. 1. The geometry of the steel plate (in mm). The location of the sensor is indicated, and numbers 1 and 2 in the figure indicate the two locations where the artificial sources were applied.

band, high-fidelity displacement sensors (Glaser *et al.*, 1998). Using the sensor signals, our goal is to estimate the time histories of the artificial MS source functions. Three classical artificial vertical force sources (Breckenridge *et al.*, 1990) are applied on the surface of the steel plate. They are (1) the fracture of a glass capillary of 0.4-mm diameter (called the capillary break), (2) the fracture of a pencil lead of 0.3-mm diameter (called the pencil lead break), and (3) the impact of a 3.16-mm-diam stainless steel ball dropped vertically (called the ball drop). Figure 2 shows the highly accurate source time functions of a 0.4-mm capillary break, a 0.3-mm pencil lead break and a 3.175-mm-diam steel ball drop obtained by deconvolution from signals measured by capacitive sensors (Breckenridge *et al.*, 1990). All these sources are well documented and can be reproduced easily and consistently.

The capillary break is generated by loading a rod vertically on a glass capillary placed flat on the plate until the capillary shatters suddenly. Immediately before the capillary breaks, the plate is displaced locally by the vertical force exerted by the rod through the capillary. Once the capillary breaks, the surface displacement recovers suddenly. This sudden rebound generates a steplike function that has a short rise time [Fig. 2(a)]. The pencil lead break is generated by loading vertically the tip of a mechanical lead pencil that is held at some angle relative to the plate until the lead tip breaks. The mechanism of the pencil lead break is similar to that of the capillary break except that when the lead tip breaks, the fracture energy displaces the broken lead tip further into the plate before the local displacement on the plate rebounds. Therefore, the source function of the pencil lead break has a distinct ''dip'' at the wavefront before the rebound occurs with a steplike function as shown in Fig. 2(b). The ball drop source is the most reproducible and has a bell-shaped source function [Fig. 2(c)].

Because of the wideband steplike source function, the capillary break signal is used to derive the empirical Green's function from which the pencil lead break and the ball drop sources are calculated. In the calculation, the rise time of the capillary break is neglected and its source signal is treated as a perfect step function. Therefore, the numerical derivative (the central difference method) of the capillary break signal is treated as a perfect impulse response and is used as the empirical Green's function. The technique has been performed by Michaels *et al.* (1981), who have shown excellent results.

A Glaser-type broadband piezoelectric sensor (Glaser *et al.*, 1998) (bandwidth 12 kHz to 1 MHz) is placed at the center of the upper side of the steel plate (see Fig. 1). The sources are applied at two different surface locations of the steel plate (see Fig. 1): location 1 (epicentral through plate), on the bottom side of the plate directly below the sensor, and location 2 (off-epicentral through plate), on the bottom side

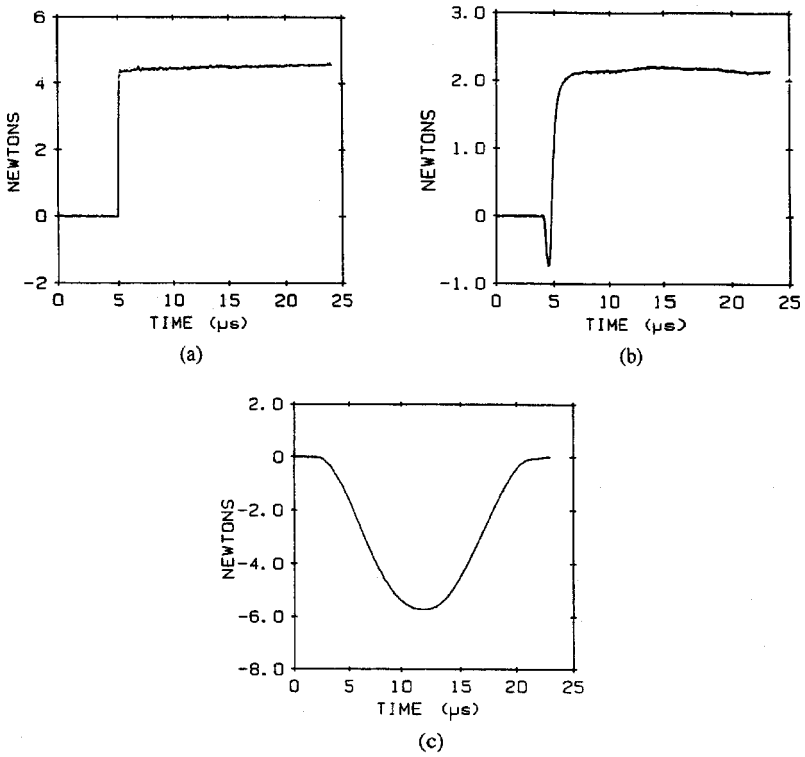

FIG. 2. (a) The glass capillary break source function; (b) The pencil lead break source function; (c) The ball drop source function; (from Breckenridge *et al.*, 1990).

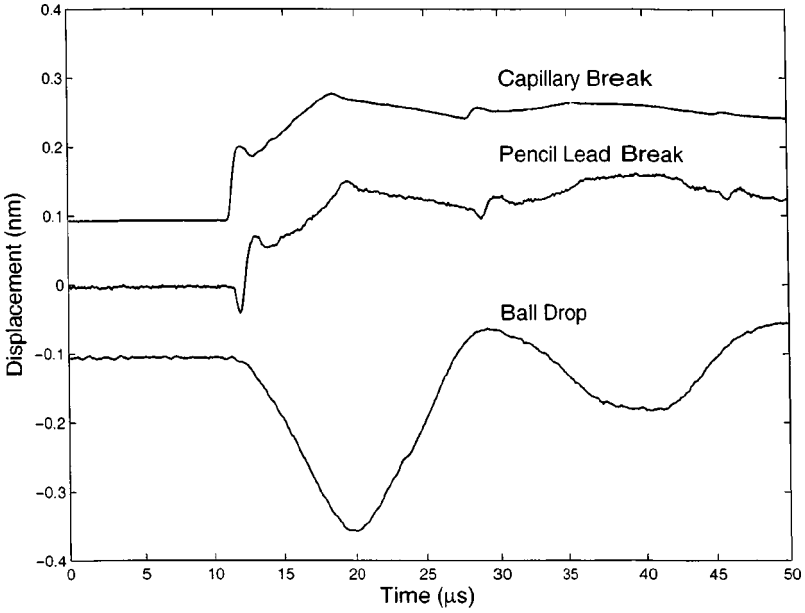

FIG. 3. Sensor signals for the three artificial sources applied at location 1. The pencil lead break and ball drop signals are added with white Gaussian noise of constant amplitude.

at a horizontal distance of 100 mm from the sensor. The transient responses (MS signals) are digitally sampled at a 0.1-μs interval with 14-bit resolution.

Given the recorded MS signals and the Green's functions, i.e., d and G in Eq. (1), we adapt four deconvolution methods to estimate the unknown MS source functions—f in Eq. (1). The four methods are (1) the nonlinear hard thresholding estimator, (2) the maximum likelihood estimator, i.e., the direct deconvolution estimate $G^{-1}d$, which maximizes the likelihood function, and two time-invariant Wiener filters, (3) Eq. (7) with $|F(\omega)|^2=|D(\omega)|^2/|G(\omega)|^2$, and (4) Eq. (7) with $|F(\omega)|^2=\text{avg}(|D(\omega)|^2)/|G(\omega)|^2$, where $|D(\omega)|^2$ is the power spectrum of the data estimated by the smoothed periodogram of the data (Marple and Lawrence, 1987). Both Wiener filters are intuitive because one expects the prior PDF of the unknown source function to be close to that of the data. These two Wiener filters also coincide with the deconvolution filters used by Chung and Liu (1998) and Oldenburg (1981), respectively. The nonlinear hard thresholding estimator is implemented using the procedure presented in Sec. VIII with the Daubechies wavelet (Mallat, 1998) of order 12.

As discussed before, the numerical derivative of the capillary break signal is used as the empirical Green's function at each source location (locations 1 and 2 in Fig. 1), and the pencil lead break and the ball drop source functions are estimated for each location. Artificial white Gaussian noise of constant variance is added to the recorded pencil lead break and ball drop signals to study the effects of noise (noise was not added to the capillary break signals since they were used as empirical Green's functions). The amplitude of the artificial Gaussian noise is much larger than usual experimental noise, so the noise power spectrum, which is needed for the two Wiener filters, can be computed *a priori*. Note that the noise power spectrum is not necessary for the NTE and the maximum likelihood estimator.

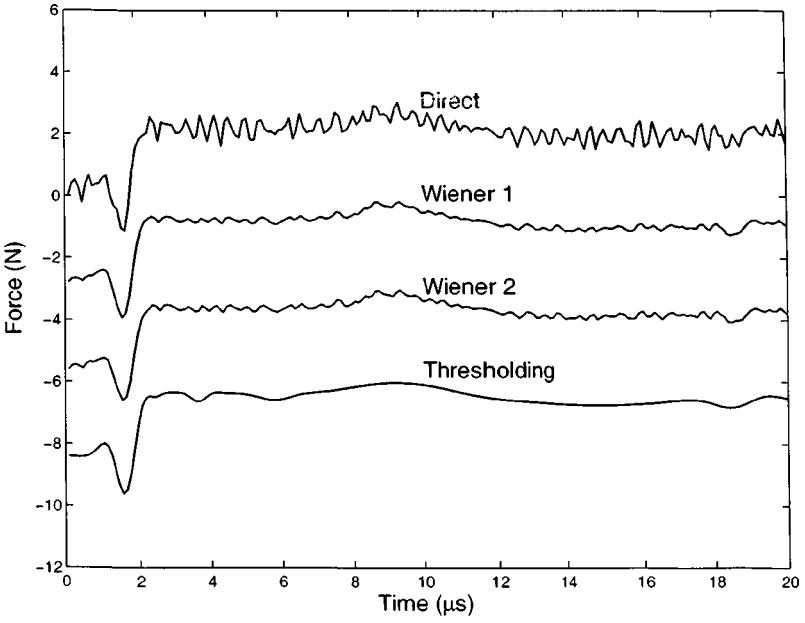

FIG. 4. The estimated pencil lead source functions using the four deconvolution methods (location 1).

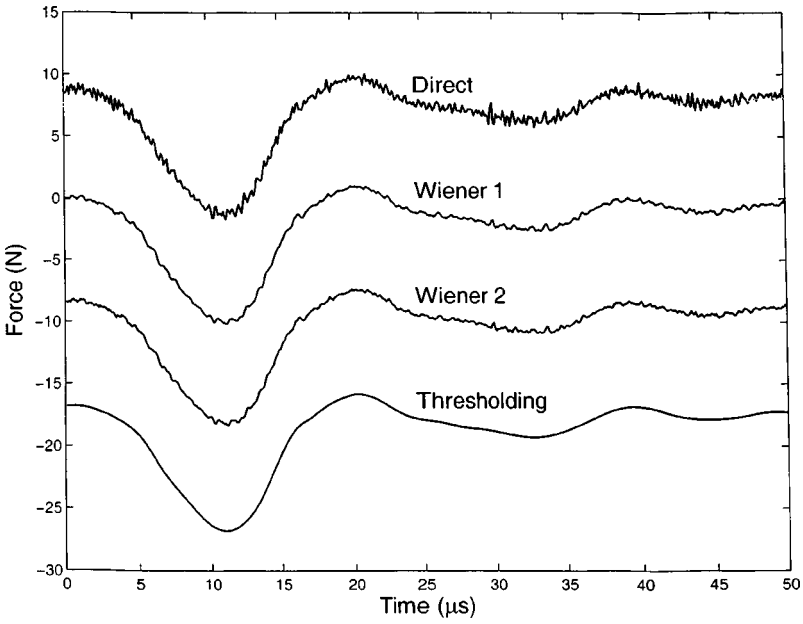

FIG. 5. The estimated ball drop source functions using the four deconvolution methods (location 1).

B. Analysis of results at location 1

The sensor signals for the three artificial sources applied at location 1 (epicentral) are shown in Fig. 3. Gaussian noise of 5% signal power is added to the pencil lead break and ball drop signals to simulate noisy experimental conditions. The numerical derivative of the capillary break signal is taken as the empirical Green's function. Given the empirical Green's function, the pencil lead and ball drop source functions are estimated using the four deconvolution methods. (The estimated pencil lead and ball drop source functions are shown in Figs. 9 and 10, respectively.) The four estimates are similar except that the direct deconvolution estimate is more noisy. Note that the four estimators preserve the sharp downward jump at the beginning of the pencil lead break source function.

All the waveforms of our estimated source time functions (Figs. 4 and 5) compare favorably to those estimated by Breckenridge *et al.* (1990) shown in Figs. 2(b) and 2(c). Table I summarizes the rise times and peak forces of our estimated source time functions and those of Breckenridge *et al.* (1990). The values of the rise time and peak force of the pencil lead break source time functions are very similar. For the ball drop, the rise time and peak force for various estimates (Table I) are different because the diameter of the ball and the height of the drop are different among the estimates. In general, the larger the diameter of the ball and the higher the ball is dropped, the longer the rise time and the larger the peak force. Nonetheless, the waveforms of the ball drop estimates are very similar.

The sources applied at location 1 generate sensor signals of large amplitudes, so the signal-to-noise ratios are high. Therefore, the direct deconvolution estimates are not dramatically noisy, and the two Wiener filters and the NTE can only improve the results with limited degrees by filtering out the high-frequency noise from the direct deconvolution estimates. It is also found that the two Wiener filters and the NTE perform similarly in the location 1 cases.

Some measure of goodness of fit can be obtained by convolving each of the four estimated source functions with the empirical Green's function. These fits should be close to the actual recorded pencil lead or ball drop signals. The fits by the four estimators together with the recorded signals are shown in Figs. 6 and 7 for pencil lead and ball drop sources, respectively. The direct deconvolution estimate always give excellent fits since the estimate is simply $G^{-1}d$ and must return d when convolved with the Green's function. However, this perfect fit is not desirable since the direct deconvolution estimate does not only fit the signal but also the noise. The other three estimates all tend to fit the signals instead of the noise. But notice that the fits of the second Wiener filter estimates cannot adapt the sharp features of the signals. The fits of the first Wiener filter estimates can adapt those sharp features, but the estimates themselves are more noisy. Compared to the other estimates, the nonlinear thresholding estimates are noise-free while being able to adapt the sharp features of the signals.

TABLE I. Summary of properties of source time functions.

Sources	Rise time (μs)	Peak force (N)
Pencil lead break 0.3 mm (from Breckenridge *et al.*, 1990)	2.50	2.05
Pencil lead break 0.3 mm (at location 1 based on the new method)	2.15	1.84
Pencil lead break 0.3 mm (at location 2 based on the new method)	2.31	2.22
Ball drop (diameter 3.18 mm and drop height 2.6 mm) (from Breckenridge *et al.*, 1990)	9.50	5.72
Ball drop (diameter 3.16 mm and drop height 5.1 mm) (at location 1 based on the new method)	10.30	10.05
Ball drop (diameter 3.16 mm and drop height 3.9 mm) (at location 2 based on the new method)	9.00	8.68

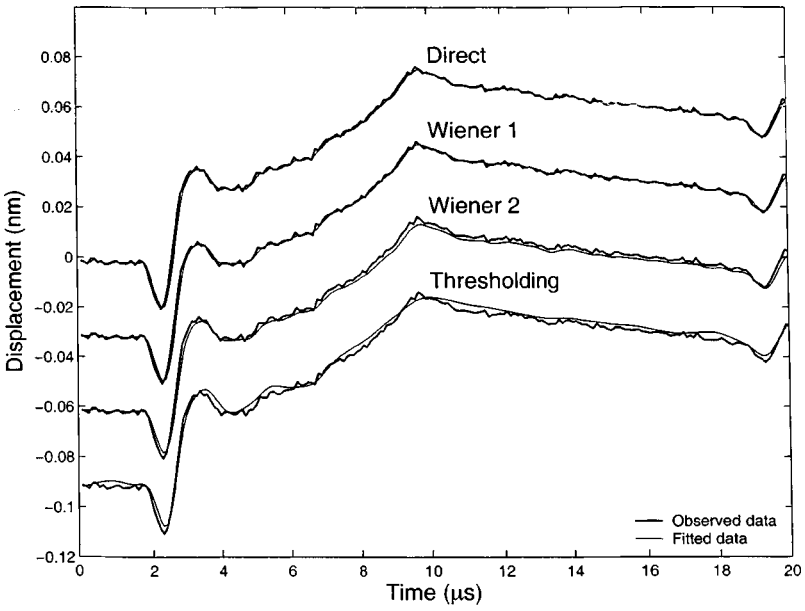

FIG. 6. The fits of the four estimates for the pencil lead break data (location 1). The recorded pencil lead break signal added with Gaussian noise is plotted as heavy lines.

C. Analysis of results at location 2

The sensor signals for the three artificial sources applied at location 2 (off-epicentral) are shown in Fig. 8. Gaussian noise of the same amplitude as the epicentral case is added to the pencil lead break and ball drop signals to simulate noisy experimental conditions. Since the off-epicentral signals are weaker, the corresponding signal-to-noise ratios are lower (the Gaussian noise is roughly 10% of the signal power). The numerical derivative of the capillary break signal is again taken as the empirical Green's function. The estimated pencil lead and ball drop source functions using the four deconvolution methods are shown in Figs. 9 and 10. Note that the direct deconvolution estimator is quite noisy because of the low signal-to-noise ratios, and the two Wiener filters and the NTE significantly improve the results by removing the high-frequency noise from the direct deconvolution estimates. Also note that the estimated source functions are not as sharp as those for location 1, and the Wiener filters and NTE tend to suppress sharp features of their estimates as they eliminate noise.

There is a clear difference between the two Wiener filters in Figs. 9 and 10: the first Wiener filter results in sharper estimates than the second one does, also the amplitudes of the first Wiener filter estimate are larger than those of the second one. On the other hand, the estimated ball drop source function of the first Wiener filter contains more high-frequency oscillations than that of the second one. This phenomenon is due to the bias-variance tradeoff: the first Wiener filter is less biased while its variance is larger, but the converse is true for the second one. Since the Wiener filters are linear, the second Wiener filter reduces the noise level by smoothing its estimates uniformly over time. However, this time-invariant smoothing strategy tends to shrink the overall amplitudes of the estimates as well, not just the noise ampli-

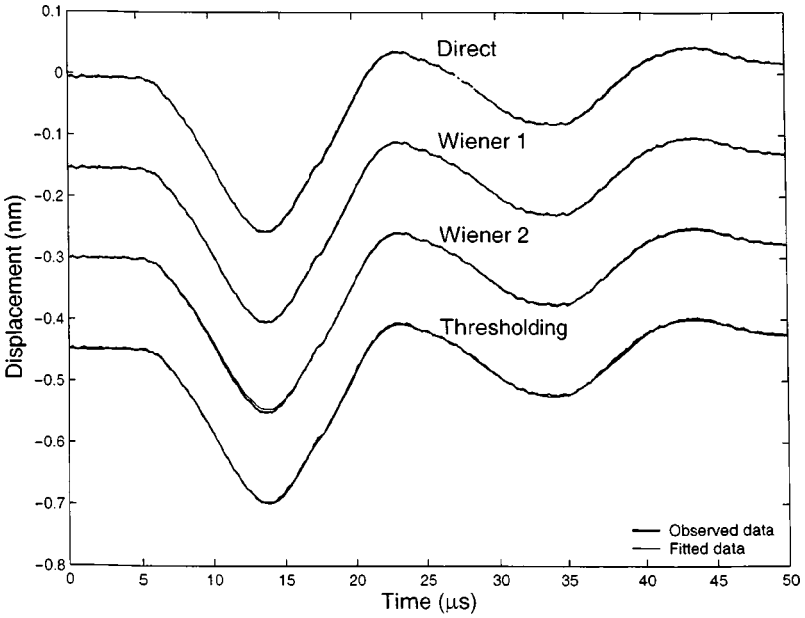

FIG. 7. The fits of the four estimates for the ball drop data (location 1). The recorded ball drop signal added with Gaussian noise is plotted as heavy lines.

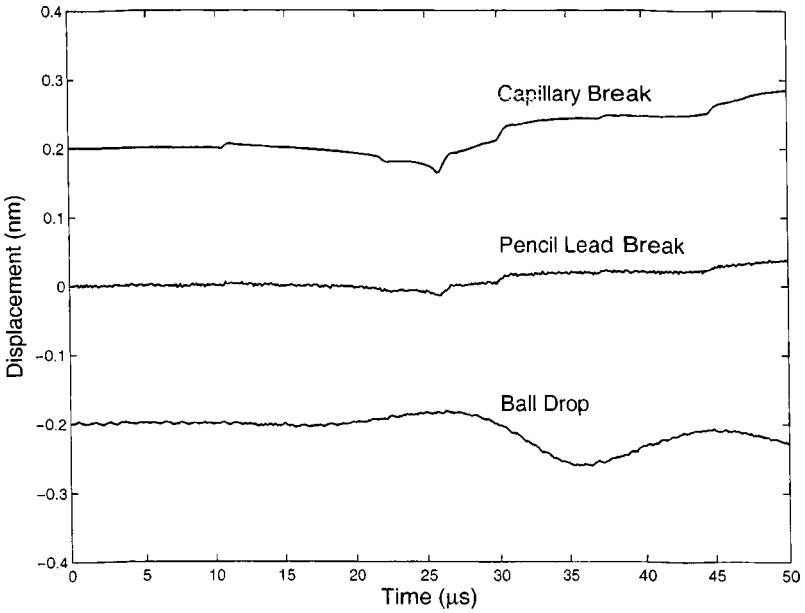

FIG. 8. Sensor signals for the three artificial sources applied at location 2. The pencil lead break and ball drop signals are added with white Gaussian noise of constant amplitude.

tude. Moreover, if the unknown function f is highly nonstationary, this linear time-invariant smoothing strategy can result in large bias. Both pencil lead break and ball drop source functions can be considered highly nonstationary. Therefore, large bias is found in the second Wiener filter for both the pencil lead break and ball drop source functions. This bias-variance tradeoff is not significant for the cases of location 1 since the signal-to-noise ratios are high.

On the other hand, the NTE simultaneously eliminates noise and preserves the amplitudes and sharp changes of the estimates. Note that the NTE also preserves the downward jump at the beginning of the pencil lead break source function, while the jump is smoothed out by the second Wiener filter. As discussed previously, this excellent performance is due to the implementation of the minimax framework of the NTE, the nonlinearity of the NTE, and sparse representations of transient functions under wavelet bases.

Similar to those at location 1, the waveforms of our estimated pencil lead break and ball drop source time functions at location 2 compare favorably with those obtained by Breckenridge *et al.* (1990) (Fig. 2). The rise times and peak forces of the sources at location 2 are summarized in Table I and are similar to those obtained at location 1. The fits by the four estimators together with the recorded signals are shown in Figs. 11 and 12 for pencil lead and ball drop sources, respectively. They are all close to the recorded signals.

VII. DISCUSSION

Our results show that the NTE outperforms the two time-invariant Wiener filters in the experimental case studies. The success of the NTE is because wavelet bases provide sparse representations for the transient MS source functions, the estimator is nonlinear, and it is based on the minimax

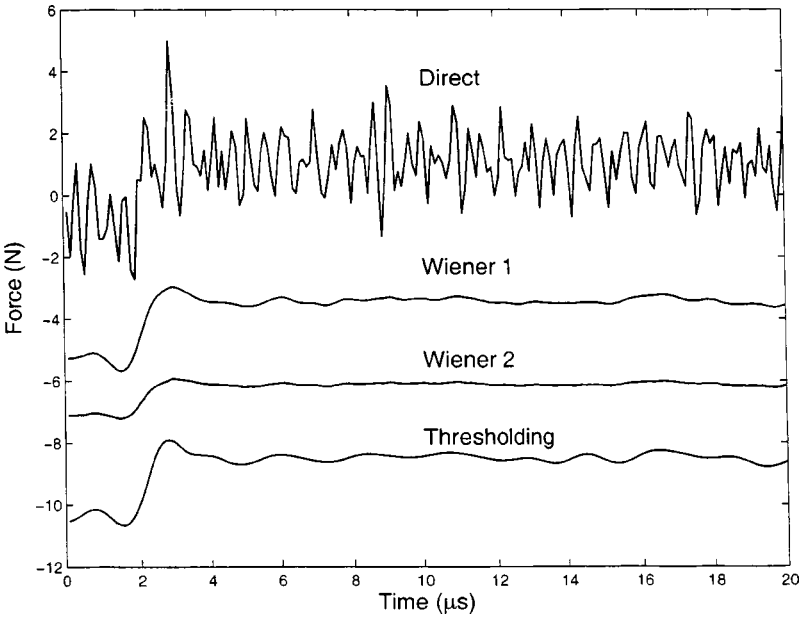

FIG. 9. The estimated pencil lead source functions using the four deconvolution methods (location 2).

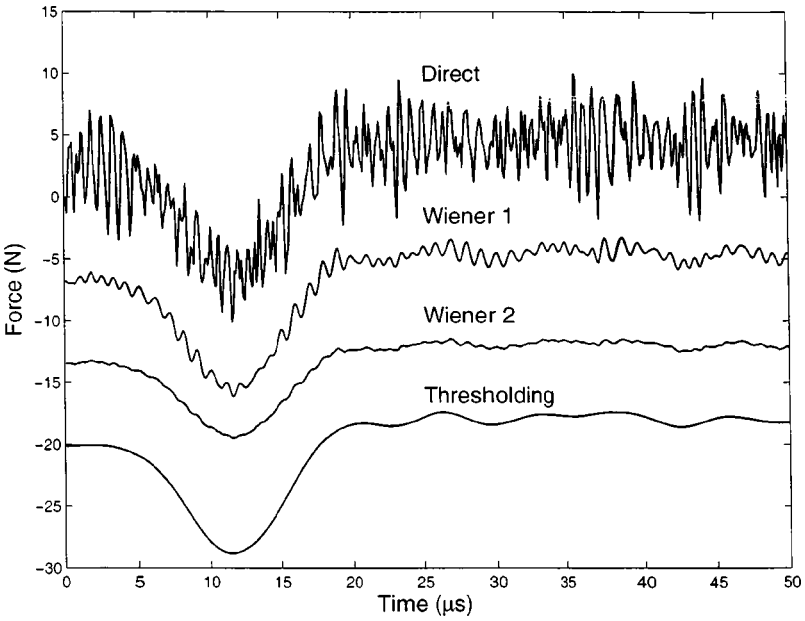

FIG. 10. The estimated ball drop source functions using the four deconvolution methods (location 2).

framework. On the other hand, Wiener filters perform worse probably because the assumed stationary properties are not appropriate for MS source functions.

Some previous research has found that it is possible to finely tune a time-invariant Wiener filter to get better estimation results, e.g., Oldenburg (1981) developed a time-invariant Wiener filter with a fine-tuning parameter θ. The second Wiener filter used in the case studies is actually a special case of the Wiener filter having θ equals 45°. It is possible to adjust θ to get a better estimate than our second Wiener filter estimate, but this leads to an *ad hoc* parameter fitting procedure while it still excludes the use of a nonlinear estimator. In contrast, the NTE does not have such a free parameter.

VIII. CONCLUSIONS

Two types of estimators, Wiener filters and minimax estimators, for microseismic deconvolution problems are described and discussed. Time-invariant Wiener filters are linear filters operating in the Fourier domain. These estimators assume stationary properties for the unknown microseismic source function. They are usually not optimal for deconvolution problems due to the following reasons: (1) microseismic source functions are usually transient and nonstationary, hence the assumed stationary properties are not appropriate. (2) Microseismic source functions do not necessarily have sparse representations under the Fourier basis. (3) Linear estimators are usually not the best estimators to use.

A nonlinear thresholding estimator is presented in this paper, which operates in the wavelet domain. This estimator is usually more suitable than Wiener filters for deconvolution problems because (1) wavelet bases provide sparse representations transient microseismic source functions, (2) the estimator is nearly minimax over all Besov function classes; therefore, in practice, prior information about the microseis-

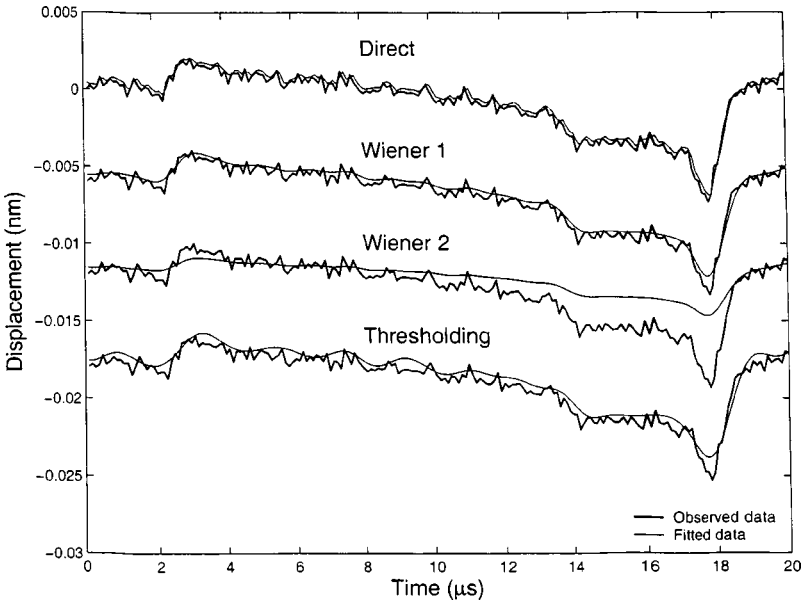

FIG. 11. The fits of the four estimates for the pencil lead break data (location 2). The recorded pencil lead break signal added with Gaussian noise is plotted as heavy lines.

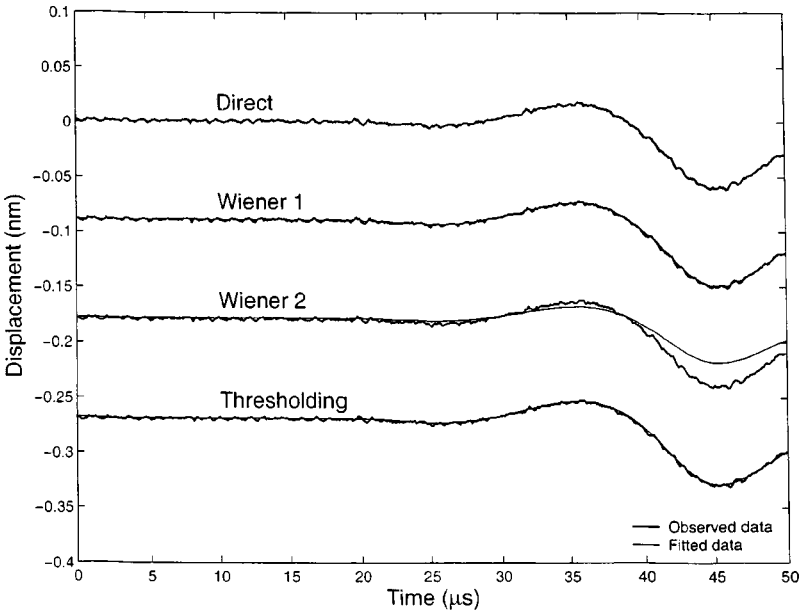

FIG. 12. The fits of the four estimates for the ball drop data (location 2). The recorded ball drop signal added with Gaussian noise is plotted as heavy lines.

mic source function is not needed, and (3) the estimator is nonlinear.

Two time-invariant Wiener filters and the nonlinear thresholding estimator are compared using several case studies of experimental microseismic data. From the results of the case studies, we conclude that the nonlinear thresholding estimator outperforms the Wiener filters. The nonlinear thresholding estimator is able to achieve two goals simultaneously: (1) effectively remove estimation noise and (2) preserve the sharp features in the source functions. The two Wiener filters fail to achieve the two goals simultaneously in some of the case studies.

ACKNOWLEDGMENTS

We would like to acknowledge the valuable discussions and opinions from Dr. Jenher Jeng for the wavelet theory and the concepts of nonparametric statistics. We also would like to acknowledge the valuable opinions and comments from the reviewers.

Bertero, M. (**1989**). ''Linear inverse and ill-posed problems,'' in *Advances in Electronics and Electron Physics*, edited by P. W. Hawkes (Academic, New York), pp. 1–120.

Bickel, P. J., and Doksum, K. A. (**1977**). *Mathematical Statistics: Basic Ideas and Selected Topics* (Holden-Day, San Francisco).

Breckenridge, F. R., Proctor, T. M., Hsu, N. N., Fick, S. E., and Eitzen, D. G. (**1990**). ''Transient sources for acoustic emission work,'' in *Progress in Acoustic Emission, V, Proc. 10th International Acoustic Emission Symposium*, edited by K. Yamagushi, H. Takakashi, and H. Niitsuma (Japanese Society for Non-Destructive Inspection, Tokyo), pp. 20–37.

Chung, C., and Liu, Q. H. (**1998**). ''Inversion of source-time functions using borehole array sonic waveforms,'' J. Acoust. Soc. Am. **103**, 3163–3168.

Clarkson, P. M. (**1993**). *Optimal and Adaptive Signal Processing* (CRC, Boca Raton, FL).

Daubechies, I. (**1992**). *Ten Lectures on Wavelets* (SIAM, Philadelphia).

Donoho, D. L., and Johnstone, I. M. (**1992**). ''Minimax estimation via wavelet shrinkage,'' Technical Report, Department of Statistics, Stanford University.

Donoho, D. L., and Johnstone, I. M. (**1994**). ''Ideal spatial adaptation by wavelet shrinkage,'' Biometrika **81**, 425–455.

Glaser, S. D., Weiss, G., and Johnson, L. R. (**1998**). ''Body waves recorded inside an elastic half space by an embedded, wideband velocity sensor,'' J. Acoust. Soc. Am. **104**, 1404–1412.

Haykin, S. (**1991**). *Adaptive Filter Theory*, 2nd ed. (Prentice-Hall, Englewood Cliffs, NJ).

Johnstone, I. M., and Silverman, B. W. (**1997**). ''Wavelet threshold estimators for data with correlated noise,'' J. R. Stat. Soc. Ser. B. Methodol. **59**, 319–351.

Kim, K. Y., and Sachse, W. (**1986**). ''Characteristics of a microseismic source from a thermal crack in glass,'' Int. J. Fract. **31**, 211–231.

Mallat, S. G. (**1998**). *A Wavelet Tour of Signal Processing* (Academic, San Diego).

Marple, S. L., and Lawrence, S. (**1987**). *Digital Spectral Analysis with Applications* (Prentice-Hall, Englewood Cliffs, NJ).

Masuda, A., Yamamoto, S., and Sone, A. (**1999**). ''Deconvolution of time series using wavelet transform (Introduction of wavelet packets with soft-thresholding and generation of optimized wavelets),'' JSME Int. J., Ser. C **42**, 188–194.

Meyer, Y. (**1992**). *Wavelets and Operators* (Cambridge U.P., London).

Michaels, J. E., Michaels, T. E., and Sachse, W. (**1981**). ''Applications of deconvolution to microseismic signal analysis,'' Mater. Eval. **39**, 1032–1036.

Oldenburg, O. W. (**1981**). ''A comprehensive solution to the linear deconvolution problem,'' Geophys. J. R. Astron. Soc. **65**, 331–357.

Qi, G. (**2000**). ''Wavelet-based AE characterization of composite materials,'' NDT&E Int. **33**, 133–144.

Scruby, C. B., Baldwin, G. R., and Stacey, K. A. (**1985**). ''Characterisation of fatigue crack extension by quantitative microseismic,'' Int. J. Fract. **28**, 201–222.

Stump, B. W., and Johnson, L. R. (**1977**). ''The determination of source properties by the linear inversion of seismograms,'' Bull. Seismol. Soc. Am. **67**, 1489–1502.

Takemoto, M., Nishino, H., and Ono, K. (**2000**). ''Wavelet transform: applications to AE signal analysis,'' in *Acoustic Emission—beyond the millennium*, edited by T. Kishi, M. Ohtsu, and S. Yuyama (Elsevier, New York), pp. 35–56.

Triebel, H. (**1983**). *Theory of Function Spaces* (Birkhäuser Verlag, Boston).

Zukas, J., Nicholas, T., Swift, H., Greszczuk, L., and Curran, D. (**1982**). *Impact Dynamics* (Wiley, New York).

Viscoacoustic wave form inversion of transmission data for velocity and attenuation

Toshiki Watanabe[a)]
Department of Earth Resources Engineering, Kyoto University, Yoshida-hon-machi, Sakyo-ku, Kyoto 606-8501, Japan

Kurt T. Nihei, Seiji Nakagawa, and Larry R. Myer
Earth Sciences Division, Lawrence Berkeley National Laboratory, 1 Cyclotron Road, Berkeley, California 94720

(Received 13 February 2004; accepted for publication 20 February 2004)

This study investigates the performance of a frequency domain viscoacoustic full wave form nonlinear inversion to obtain high resolution images of velocity and attenuation. An efficient frequency domain implementation is applied that consists of performing a series of single frequency inversions sweeping from low to high frequency. A cascaded inversion was adopted in which the real part of the velocity is first imaged using the phase information, then the quality factor (Q) is imaged using the amplitude information. Tests with synthetic data indicate that our approach yielded better images than the simultaneous determination of the real and imaginary parts of the complex velocity. The method is applied to laboratory data obtained in a water tank with suspended acrylic bars. Broadband 200 kHz data are obtained for a crosshole configuration with a computer-controlled scanning system and piezofilm source and detector. The velocity image produced by the full wave form inversion is compared to a curved ray travel time tomography velocity image, and was observed to possess higher resolution and more precise locations of the acrylic bars. The Q image shows a lower resolution than the velocity image, but recovers the correct Q for acrylic. This method can be applied for geophysical applications targeted to soil, unconsolidated rocks, and marine sediments and also nondestructive evaluation and medical applications. © *2004 Acoustical Society of America.* [DOI: 10.1121/1.1710878]

PACS numbers: 43.60.Rw, 43.60.Pt, 43.20.Hq [JCB] Pages: 3059–3067

I. INTRODUCTION

A number of studies[1–5] have demonstrated that compressional wave attenuation can be significant in porous materials such as marine sediments, clay-rich rocks, and partially saturated granular rocks. Because this attenuation is directly related to the imaginary part of the bulk modulus, it provides additional information about the material.

In geophysical applications, imaging viscoacoustic properties have proven to be useful for monitoring and evaluating soil conditions and fluid flow for environmental use.[6,7] Ray-based travel time tomography is widely used for imaging acoustic velocities of the subsurface.[8] It is relatively robust and provides an image within a modest computation time. Attenuation tomography by use of amplitude,[9] spectral decay,[10] frequency shift,[11] and pulse broadening[12] has also been studied to obtain attenuation (Q^{-1}) images. However, the resolution of ray-based tomography is limited to the Fresnel zone scale.[13] Furthermore, it does not utilize additional information that may be contained in scattered, reflected, and guided waves.

The quest for higher resolution imaging techniques has resulted in a growing interest in wave form inversion. Acoustic wave form inversion[14–17] is a process for obtaining the acoustic properties of materials such as the bulk modulus, density, and attenuation, from the recoded wave field using nonlinear least-squares inversion. It can image acoustic properties with subwavelength resolution. Wave form inversion can be implemented both in the time domain[14,15] and in the frequency domain.[16,17] Although these two approaches are mathematically equivalent, each has its own advantages and disadvantages. The time domain method is straightforward and easy to implement using an explicit time-domain acoustic finite-difference modeling code. The frequency domain method typically uses an implicit acoustic modeling code that requires the solution of a large sparse matrix. The primary benefit of performing wave form inversion in the frequency domain is that once the matrix is inverted, it can be used to compute the wave field for multiple sources. In addition, an efficient implementation can be achieved by performing a series of single-frequency inversions.

In the frequency domain approach for viscoacoustic imaging, intrinsic attenuation can be easily incorporated using a complex velocity or bulk modulus, allowing both the velocity and attenuation[18–20] to be imaged. Although the modeling-based approach is computationally intensive, it has a capability for proper evaluation of the velocity and attenuation in the presence of heterogeneities that may give rise to scattering, focusing, and multipathing.

Song *et al.*[18] first applied the full wave form inversion to viscoacoustic problems. They employed the simultaneous reconstruction of the complex velocity in which the real and

[a)]Present address: Research Center for Seismology, Volcanology, and Disaster Mitigation, Nagoya University, Furo-cho, Chikusa-ku Nagoya 464-8602, Japan; electronic mail: watanabe@seis.nagoya-u.ac.jp

imaginary parts of velocity are reconstructed simultaneously. However, they stated that the reconstruction of the imaginary part is of considerably worse quality than the real part. Keers *et al.*[21] used a different approach, expanding the asymptotic ray theory to viscoacoustic problems and showed that the ray paths are not affected by the attenuation (Q^{-1}) if Q is not too small. Tests to separate the attenuation caused by velocity heterogeneities from the amplitude data for attenuation tomography were conducted.[12] Those achievements lead to the idea of cascading the inversion into two consecutive inversions. The velocity structure (the real part of the complex velocity) is imaged first, then, the attenuation structure (the imaginary part of the complex velocity) is imaged.

This study investigates the performance of frequency domain nonlinear wave form inversion for imaging the velocity and attenuation. The method is applied to synthetic and laboratory cross-hole data obtained in a water tank with a two-axes computer-controlled scanning system and a piezofilm source and detector.

This study focuses on cross-hole measurement because in geophysical imaging, sources and receivers can be positioned close to target structures, allowing higher frequencies to be used. Furthermore, cross-hole measurements avoid the effects of heterogeneous, attenuative surface layers that typically lower the bandwidth and signal to noise ratio of seismic data. The proposed method, however, can be applied to any source-receiver configuration including single-hole measurement and surface reflection measurement. Although we primarily focus our discussion on geophysical application, such as shallow soil structures, unconsolidated rocks, and marine sediments,[5,6] the proposed method should also work for nondestructive evaluation of soft and attenuative materials and medical applications.

II. INVERSION THEORY

A. Forward modeling

Posing the monochromatic acoustic wave equation in frequency domain with a finite-difference manner yields the following matrix equation:

$$\mathbf{Fp} = -\mathbf{s}, \tag{1}$$

where $\mathbf{F} = (\partial^2/\partial x^2, \partial^2/\partial z^2, -\omega^2/c^2)$ denotes the differential operator matrix which is dependent on the angular frequency ω and the velocity c only under the condition of constant density. $\mathbf{p}$ is the pressure field and $\mathbf{s}$ is the source term. $\mathbf{F}$ is a sparse symmetric banded matrix with size $n_x n_z \times n_x n_z$ where n_x and n_z are the number of grid points in x and z directions. We adopt a nine-point rotated difference template[22] because the template improves accuracy without increasing the bandwidth, thereby keeping the total memory comparable to the second-order finite difference template. Using this differencing scheme, the elements of $\mathbf{F}$ are stored in a matrix of $(2n_x+3)\times n_x n_z$. Equation (1) is solved using LU decomposition.[16,19] Since $\mathbf{F}$ is independent of the source, once the matrix is decomposed, it can be used to solve Eq. (1) for different source terms, $\mathbf{s}$.

B. Introducing intrinsic attenuation

The intrinsic loss in a general viscoacoustic media can be incorporated using a complex bulk modulus.[23] The quality factor Q is defined as;

$$Q = \frac{\mathrm{Re}(M_c)}{\mathrm{Im}(M_c)}, \tag{2}$$

where M_c is the complex bulk modulus, Re( ) and Im( ) represent the real and imaginary operators, respectively. In general viscoacoustic media, M_c is frequency dependent.

In this study, we assumed a nondispersive, constant Q model (i.e., the quality factor (Q) is independent of the frequency within the frequency range being considered). Q is defined as

$$Q = \frac{c_r}{2c_i}, \tag{3}$$

where c_r and c_i ($c_i > 0$) denote the real and imaginary parts of the velocity, respectively. Equation (3) is valid for relatively large Q ($Q > 10$). It also provides a good approximation for other constant Q and near-constant Q theories[24,25] over a limited frequency range.

C. Inversion basics

Acoustic wave form inversion described here is a modeling-based iterative least-squares inversion[14] in the frequency domain.[16,17] Starting with an initial velocity model, the velocity model is updated so that the differences between the calculated complex spectra $P_{\mathrm{cal}}(x,\omega)$ and the observed complex spectra $P_{\mathrm{obs}}(x,\omega)$ shown below are minimized in a least squares (l_2) sense

$$S = \frac{1}{2}\sum_s \sum_r \int \delta P(x,\omega)^2 d\omega, \tag{4}$$

where the two sums are over the source (s) and receiver (r) locations. δP is the residual spectra defined as

$$\delta P(x,\omega) = P_{\mathrm{obs}}(x,\omega) - P_{\mathrm{cal}}(x,\omega). \tag{5}$$

The velocity is updated using the steepest descent method expressed as

$$c_{k+1}(x) = c_k(x) - \alpha_k \gamma_k(x), \tag{6}$$

where α is the step length, $\gamma(x)$ is the gradient vector, and k denotes the iteration. $\gamma(x)$ is calculated from the correlation of a forward-propagated wave field $P(x,\omega)_{\mathrm{forward}}$ and a backward-propagated residual wave field $P'(x,\omega)_{\mathrm{backward}}$ as[26]

$$\gamma(x) = \frac{1}{c(x)^3}\sum_s \int \omega^2 P(x,\omega)_{\mathrm{forward}} P'(x,\omega)_{\mathrm{backward}} d\omega, \tag{7}$$

$$P'(x,\omega)_{\mathrm{backward}} = \sum_r G(x,\omega;x_r)\,\delta P^*(x,\omega), \tag{8}$$

where $G(x,\omega;x_r)$ is the Green's function describing propagation from the receiver location x_r to a location x in the medium, $*$ denotes the complex conjugate which is equivalent to time-reversal in the time domain.

The calculation time for the inversion is proportional to the number of discrete frequency components used in the inversion since $\gamma(x)$ is an integral over frequency. For an efficient calculation, we used a single frequency in each iteration step.

A basic problem of the frequency domain method is the ''cycle skip'' or ''phase wrapping'' that results from the 2π uncertainty in determining the phase. The phase error between the observed wave forms and the calculated wave forms from the current velocity model should be smaller than π to avoid this effect. This requires that the starting velocity model should be close enough to the true velocity model with respect to the frequency (wavelength) of the wave being used for the inversion. A robust implementation can be achieved by performing a series of single-frequency inversions sweeping from low to high frequencies.[27] It should be noted that the single frequency inversion acts as a spatial wave number filter for the structure. Therefore, by starting from low frequencies, the low wave number (rough) structures are first reconstructed. This allows us to use higher frequencies. Finally, the detailed structures are reconstructed using high frequencies.

D. Cascaded inversion

Theoretically, the velocity and Q can be imaged either simultaneously or consecutively. Previous experience with simultaneous inversion,[18,19] however, has indicated that it can be an unstable process that tends to yield inaccurate images, especially Q images, as stated in Song *et al.*[18] Liao and McMechan[19] successfully imaged the Q structure using the simultaneous approach. Their paper, however, does not addresses this question in detail. The problem of the simultaneous approach is that the velocity and Q are coupled since

$$Q=\frac{\mathrm{Im}(M_c)}{\mathrm{Re}(M_c)}, \quad c=[(\mathrm{Re}(M_c)+i\,\mathrm{Im}(M_c))/\rho]^{1/2}. \tag{9}$$

Some numerical studies indicate that the normalized sensitivities obey

$$c_r\frac{\partial P}{\partial c_r}>c_i\frac{\partial P}{\partial c_i} \tag{10}$$

for typical ranges of the complex c contrasts. This establishes that the velocity (the real part of the velocity) is the controlling parameter, therefore the velocity c_r needs to be obtained accurately before the less sensitive parameter Q can be inverted for.

We have found through synthetic tests that a reliable Q image can be obtained with the following ''cascaded'' inversion scheme.

(1) The real part of the complex velocity is calculated from the phase information of the wave form data (stage I). The following normalized residual is used instead of Eq. (5) in order to suppress the amplitude information.

$$\delta p_{\mathrm{norm}}=P_{\mathrm{obs}}(x,\omega)-\frac{|P_{\mathrm{obs}}(x,\omega)|}{|P_{\mathrm{cal}}(x,\omega)|}P_{\mathrm{cal}}(x,\omega). \tag{11}$$

This may result in some loss of accuracy in the velocity because the viscous effect on the phase is ignored. Although the effect is usually small, we can employ an approximate Q model to compensate it.

(2) Next, the imaginary part of the velocity is inverted from the wave form data by fixing the real-valued velocities computed in the first step (stage II). The real velocities can be updated to compensate the viscous effect on the phase that is ignored in the stage-I inversion.

(3) Finally, the quality factor (Q) is derived from the real and imaginary parts of the velocity using Eq. (3).

The inversion approach can decouple the effect of the real and imaginary parts of the velocity on the gradient vector. In addition, providing an accurate velocity structure when starting the Q inversion leads the Q inversion to a successful convergence with stability because the amplitude is a function of the velocity structure (scattering, focusing, and multipathing) as well as the Q distribution. A similar approach was conducted by Hicks and Pratt.[20] They started a high wave number velocity and Q inversion in a simultaneous manner after obtaining the low wave number velocity structure using the low wave number velocity inversion.

This approach improves the accuracy of the imaginary part of the velocity, resulting in a stable inversion process for the viscoacoustic properties (Q).

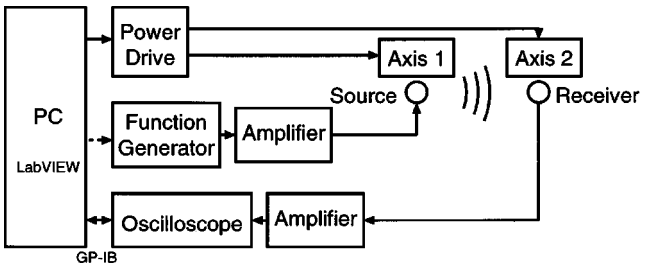

FIG. 1. Schematic of the experimental acoustic imaging system composed of the scanning system and the acoustic equipment.

III. LABORATORY EXPERIMENT

A water tank experiment was conducted with a computer-controlled scanning system and piezofilm source and detector. Ultrasonic 200 kHz data were obtained for a cross-hole configuration with suspended acrylic bars as the target.

Figure 1 illustrates a schematic diagram of the laboratory experiment composed of a scanning system and the acoustic measuring system. The PC controls the motion control and data acquisition instruments for the experiments as follows:

(1) Initializes the motion controller, GPIB (general purpose interface bus) device, and the digital oscilloscope.
(2) Obtains parameters needed for the experimental setups via GUI (graphical user interface).
(3) Drives the stepping motors and moves the stages to an expected position.
(4) Communicates with the oscilloscope via GPIB, triggers data acquisition and obtains digitized wave data after averaging.
(5) Displays the wave form and stores the data to a file.

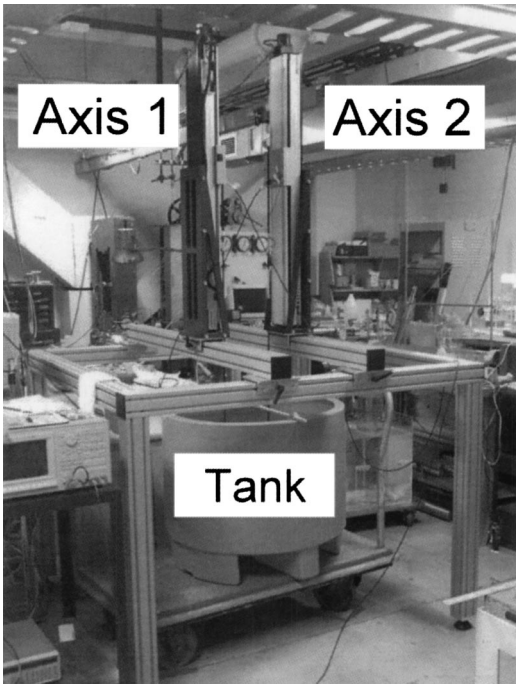

FIG. 2. Two-axes computer-controlled scanning system.

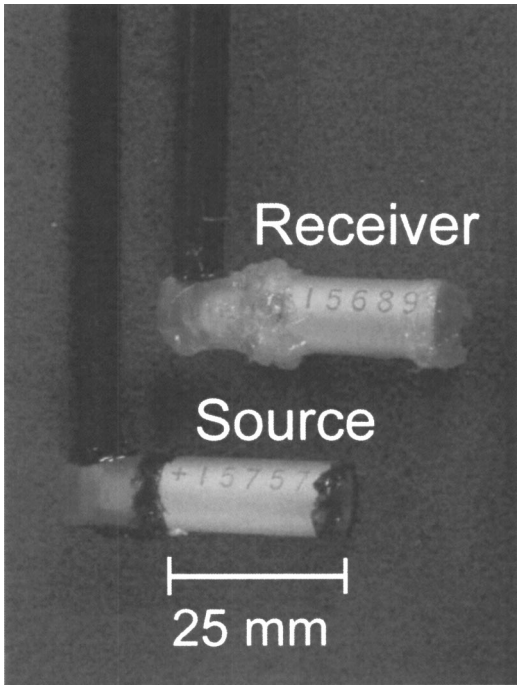

FIG. 3. Cylindrical piezofilm source and receiver used in the laboratory experiment. The sensors are attached to fiberglass rods.

Figure 2 shows the two-axes computer-controlled scanning system. The frame is made of high-stiffness aluminum. The size of the frame is $1.5\,\mathrm{m}\,(W)\times 1.5\,\mathrm{m}\,(D)\times 1.0\,\mathrm{m}\,(H)$. The scanning length along the z axes is approximately 0.9 m. The scanning stage is driven by vertical screws with submillimeter positioning accuracy and can be used for repeated measurements such as time-lapse experiments.

Figure 3 shows the cylindrical piezofilm elements [ϕ(diameter)$=$11 mm, L (length)$=$25 mm, d (thickness)$=$1 mm] used as the source and the receiver for the laboratory experiment. The elements were bonded to fiberglass rods and placed so that their axes are perpendicular to a common vertical plane. The source piezofilm element is excited below its natural resonance by an amplified pulse that is generated by an arbitrary wave form generator. A Ricker wavelet with a center frequency of 100 kHz was used for the experiment. A miniature junction field effect transistor impedance matching circuit was installed in the receiver piezofilm cylinder to minimize signal losses between the piezofilm element and the shielded cable.

The radiation pattern of the source and the directional sensitivity of the receiver were measured by moving the receiver around the source with fixed distance. Figure 4(a) shows the radiation pattern (directional sensitivity) of the source (receiver) in a vertical section that is perpendicular to the sensor axis. As this section coincides with the measurement plane, this plot shows that the source acts as a nondirectional point source. The narrow focused azimuthal sensitivity shown in Fig. 4(b) indicates that most of the energy propagates along the plane of measurement.

Figure 5 illustrates the experimental model and the source-receiver configuration. Sixteen sources were used with a spacing of 17.2 mm. Thirty-one receivers were used with a spacing of 8.6 mm. Three acrylic bars were suspended in a water tank as high-velocity, attenuative anomalies. The density, $\rho=1.18\times 10^3\,\mathrm{kg/m^3}$, the acoustic wave velocity, $c=2300\,\mathrm{m/s}$, and the Q value, $Q=30$, were measured in separate experiments. The diameter of the top, center, and bottom bars are 12.7, 50.8, and 25.4 mm (1/2, 2, and 1 in.), respectively. The diameter of each of the three bars was chosen so that they are smaller than, larger than and comparable to the wavelength of the waves.

Figure 6 shows a wave form obtained by the experiment for the fifth source from the bottom, indicated by an arrow in Fig. 5. Effects of the bars, such as time shifts in the wave arrivals, amplitude variations, and scattered waves, are clearly visible in the wave forms. The downward propagating, large amplitude waves arriving after 0.3 ms are the reflections from the water surface. Figure 7 shows synthetic

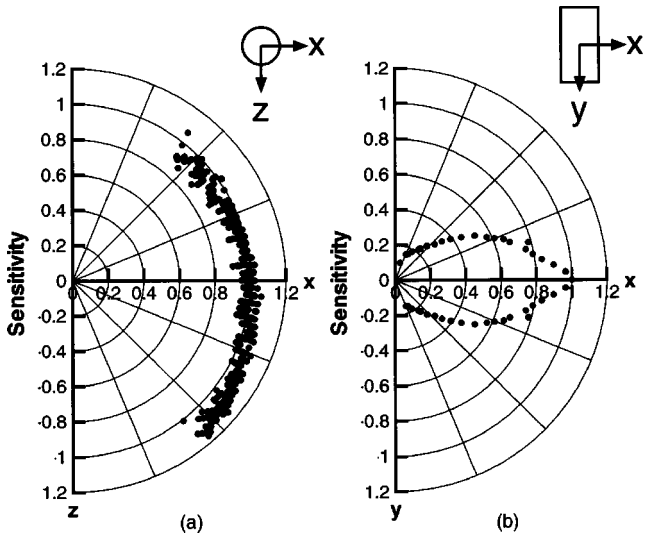

FIG. 4. Radiation pattern (directional sensitivity) of the piezofilm source (receiver): (a) in the $x-z$ vertical plane, (b) in the $x-y$ horizontal plane.

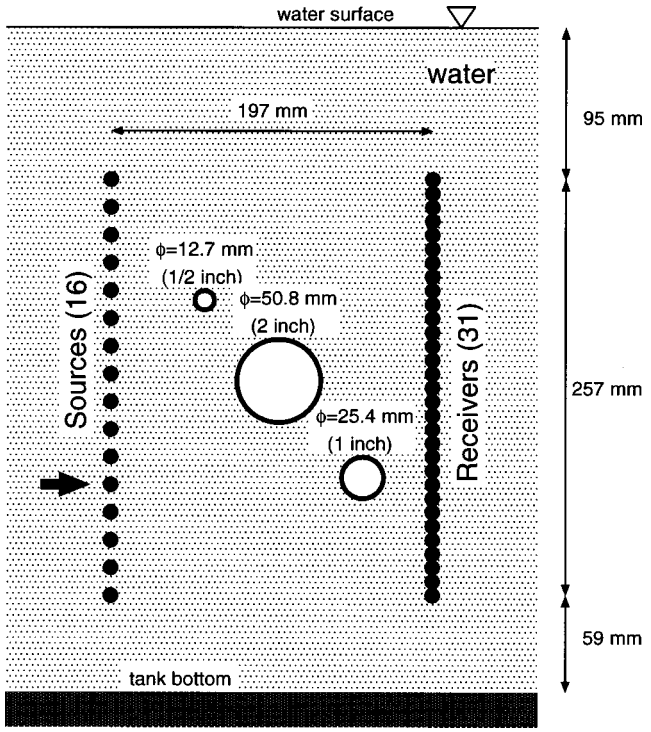

FIG. 5. Experimental model and the source-receiver configuration. The open circles indicate the location and the size of the acrylic bars. The closed circles indicate the location of the sources and the receivers.

wave forms generated using a numerical model of the water tank experiment. The physical properties are given in Table I. The overall features of these wave forms are quite similar, except that the synthetic data lack reflections from the bottom of the tank. It should be noted that P–S–P converted waves transmitted through the bars are not contained in the acoustic synthetic wave forms.

IV. INVERSION ANALYSIS

A. Travel time tomography

Travel time were obtained from the first arrival of wave forms picked manually. Figure 8 shows the velocity image obtained by travel time tomography using SIRT (simultaneous iterative reconstruction technique) with curved ray-tracing after 19 iterations. Here, the area was divided into

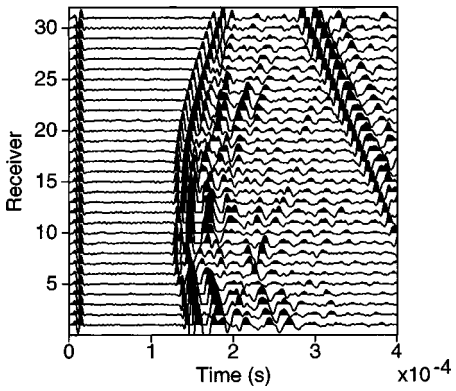

FIG. 6. Observed wave forms for the source location indicated by the arrow in Fig. 5.

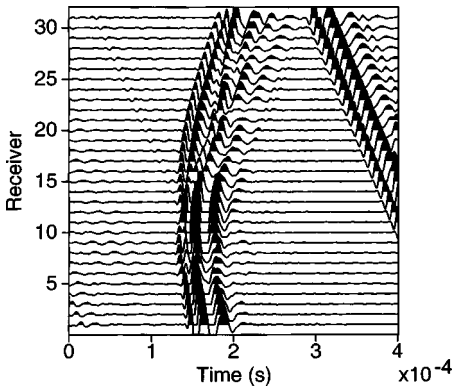

FIG. 7. Synthetic wave forms for the source location indicated by the arrow in Fig. 5. The waves preceding the direct wave arrivals are the wraparounds generated by frequency-domain finite-difference method.

$23\times31=713$ cells of size $\Delta x=\Delta z=8.6$ mm. The open circles in the figure show the locations and dimensions of the three acrylic bars. Two high-velocity anomalies were detected. However, neither the locations nor the dimensions are correct, and the smallest anomaly is not imaged. The velocity image shows an artifact pattern typical for a cross-hole configuration, including low-velocity artifacts at the upper and lower areas of the high-velocity target and smearing in the horizontal direction.

The resolution of the travel time tomography[13] is approximated by the Fresnel zone given by $\sqrt{\lambda L}$, where λ is the wavelength and L is the propagation distance. In our experiment, $\sqrt{\lambda L}$ is approximately 5 cm (using $c=1500$ m/s, $f=100$ kHz, and $L=0.2$ m), which is comparable to the size of the largest anomaly. This theoretical resolution limit is supported by the low resolution velocity image obtained from the travel time tomography.

B. Wave form inversion

The analysis area was divided into $112\times183=20496$ grid cells whose spacing $\Delta x=\Delta z$ is 2.15 mm. The same cells are used for both the forward modeling and the inversion. The model parameters were updated only within a 99×119 region encompassed with the sources and the receivers. The model parameters outside the area were fixed during the inversion.

The initial velocity model is the velocity distribution obtained from the travel time tomography shown in Fig. 8. The initial Q model had a homogeneous high-Q distribution ($Q=200$).

Figure 9 shows the frequency component used at each iteration step. For efficiency, a single frequency was used at each iteration step. The inversion was made robust by performing a series of single frequency inversions sweeping from low to high frequencies.[27] The same frequency sweep-

TABLE I. Physical properties of materials used to generate synthetic data.

	Velocity (m/s)	Q value
Acrylic resin	2300	30
Water	1500	∞
Air	350	∞

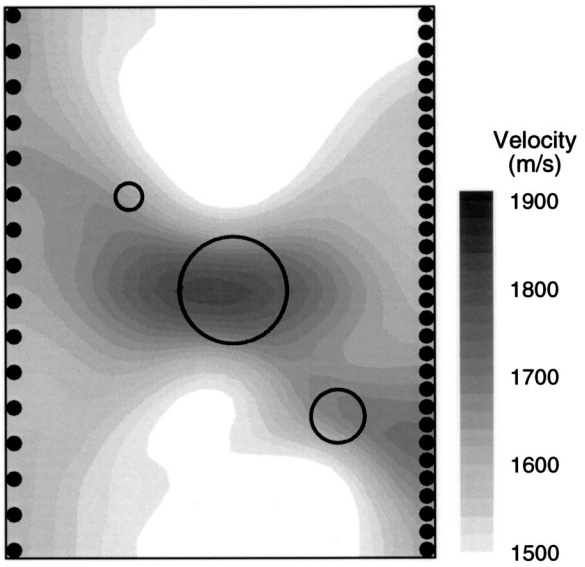

FIG. 8. The velocity image obtained using travel time tomography after 19 iterations of SIRT with curved ray-tracing.

ing schedule is used for both the real-velocity inversion (stage-I inversion) and the imaginary velocity inversion (stage-II inversion) in the cascaded inversion.

To stabilize the inversion, smoothing and restriction were implemented. Since the inversion of the real part of velocity is stable, we applied a weak smoothing to the updated velocity image using a weighted moving average with 3×3 templates in each iteration. Strong smoothing and regularization were required to stabilize the inversion of the imaginary velocity. At each iteration, a variable sized, cosine shaped moving average filter, $\cos(2\pi/\lambda r)$ was applied to the updates of the imaginary velocity. Here, λ is a wavelength corresponding to the frequency being used for the current iteration, and r is the distance from the cell being smoothed. The maximum imaginary velocity update is restricted to 10% of the current velocity image, and is restricted so that the Q derived from the updated imaginary velocity is limited to lie between 20 and 200.

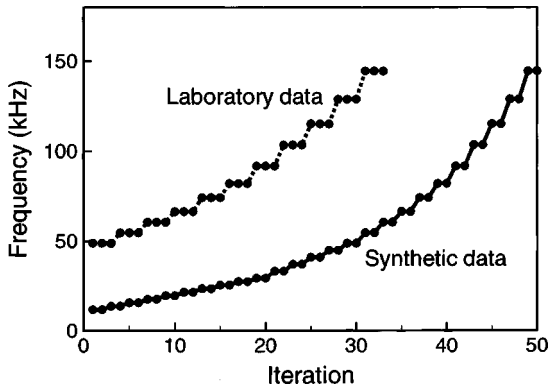

FIG. 9. The frequency used for each iteration. A series of single-frequency inversions is iterated while sweeping from low to high frequencies. Higher frequencies were used in the laboratory data because of noise contamination in the lower frequency range ($<$50 kHz).

C. Inversion of synthetic data

Figure 10 shows the result of the cascaded inversion for the synthetic data. In the real component velocity image, all three anomalies are imaged clearly at their correct locations with almost their correct sizes. The velocities of the anomalies, however, are lower than those given in the model. In the Q image, the anomalies are detected clearly as low-Q anomalies. The Q image is slightly less accurate than the velocity image. Figure 11 compares the synthetic wave forms generated for the true model (the data), the initial velocity model, and the model obtained from the inversion. The source position is the same as that of the wave forms shown in Fig. 7. As previously mentioned, the cycle skip, the 2π uncertainty in determining the phase, is a major problem of the frequency domain method. Comparison of the wave forms in the time domain demonstrates that no cycle skip between the arrivals of these wave forms of (a) and (d) is observed. That indicates that our approach in selecting frequencies in the inversion (sweeping from low to high frequency) is suitable for inverting the phase information to obtain the real component velocity image. The amplitude of the residual wave forms significantly decreases after the inversion.

Figure 12 shows the result of the simultaneous inversion

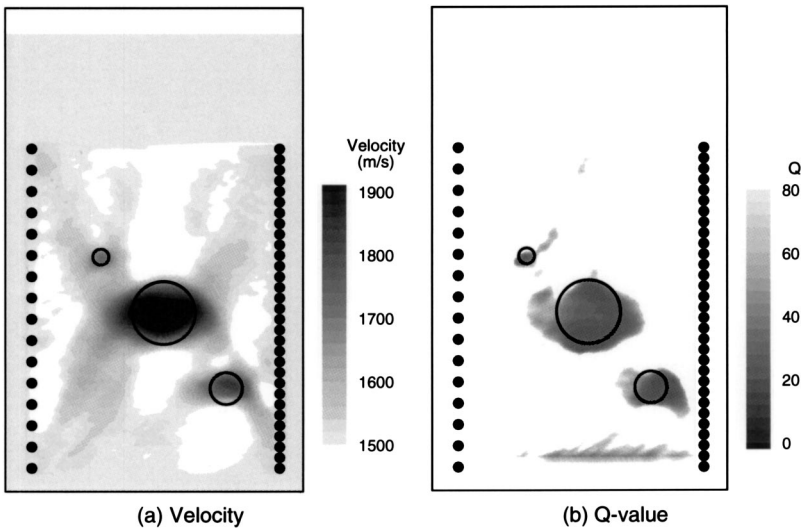

FIG. 10. The result of inversion of the synthetic data using cascaded approach. (a) Real part of the velocity and (b) Q value.

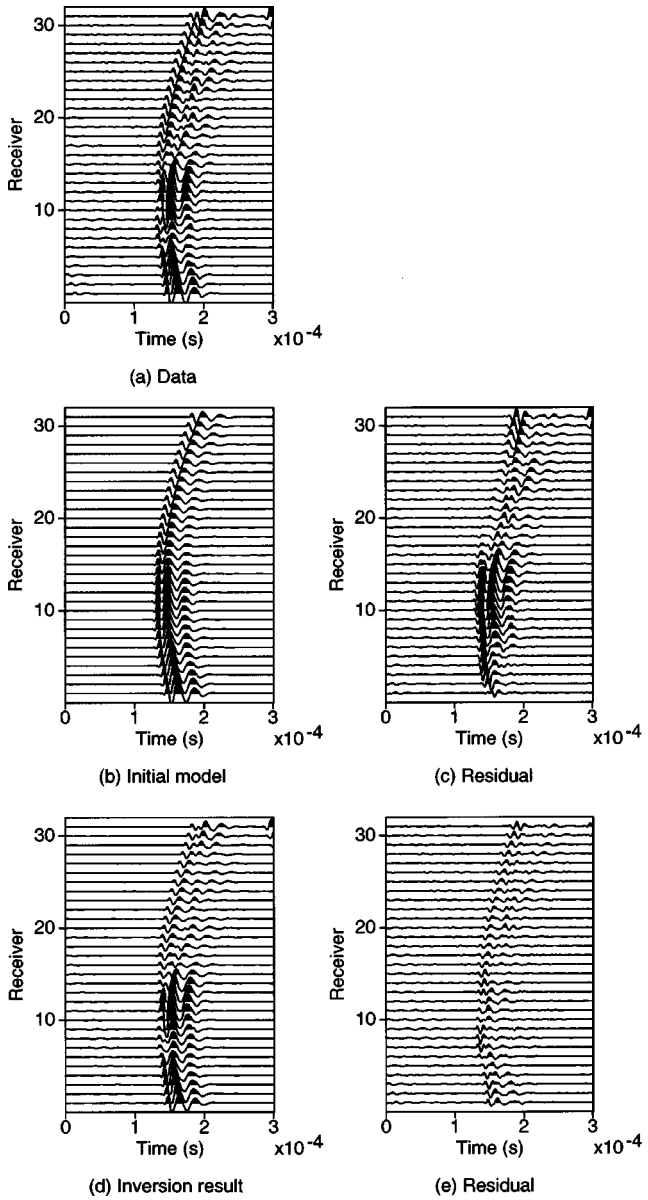

FIG. 11. Wave forms with respect to (a) the synthetic data, (b) the initial model, (c) the initial residual, (d) the final model obtained from the inversion, and (e) the final residual for the source location indicated by the arrow in Fig. 5.

for the same synthetic data after 34 iterations. Although we kept all parameters (choice of frequency, smoothing and restrictions) the same except the inversion procedure, the iterative inversion diverged and generated erroneous images after 35th iterations. As the inversion stopped before the high frequencies are used, the velocity image has lower resolution compared to the velocity image shown in Fig. 10. Although some attenuative areas imaged correspond to the low-Q anomalies, the Q image contains many artifacts in the background. The comparison clearly demonstrates that the cascaded inversion generates much better Q image than the simultaneous inversion.

D. Inversion of laboratory data

Preprocessing of laboratory data consisted of a 10–200 kHz bandpass filter, and muting of the water surface reflections. A 100 ms time window was applied starting at the first arrivals. The mute and windowing did not affect the result of the real component velocity image much. However, the imaginary component velocity result was improved, leading to an improved final Q image.

The source wave form was measured using a reference model with no velocity or attenuation anomalies. Therefore this includes the source and receiver characteristics and energy loss during propagation in the water tank. Even though careful compensation and estimation for the initial amplitude were taken, some ambiguity in the source amplitude still remains. Therefore, by providing different initial amplitudes, the result that provides the best fit at the dominant frequency was chosen. The initial models for the velocity and Q are the same as those of the synthetic data analysis. In the laboratory data analysis, frequencies below 50 kHz were omitted because of noise contamination which typically degraded the quality of the image of the imaginary velocity.

Figure 13 shows the result of the cascaded inversion of the laboratory data. In the real velocity image, all three bars are imaged clearly with a slightly larger size than the actual size of the bars. Note that the smallest bar, which is smaller than the wavelength, is imaged. The Q image has lower resolution and includes artifacts, although it shows the presence of attenuative anomalies.

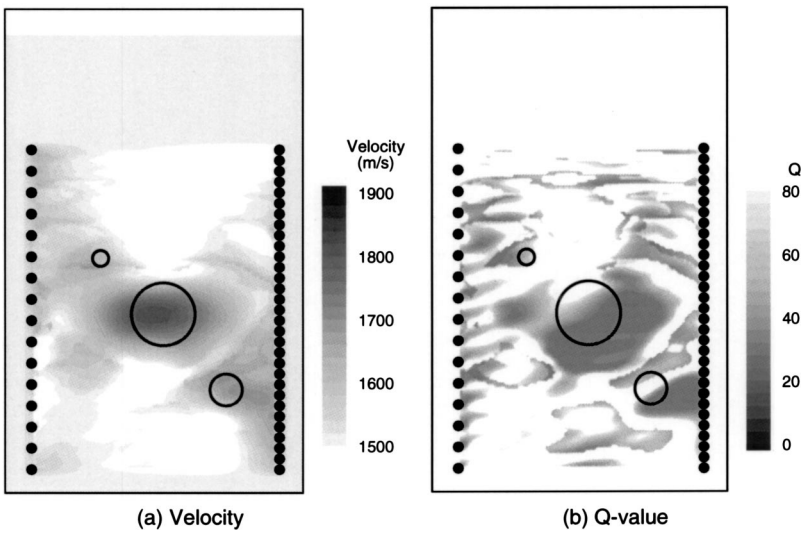

FIG. 12. The result of inversion of the synthetic data using simultaneous approach. (a) Real part of the velocity and (b) Q value.

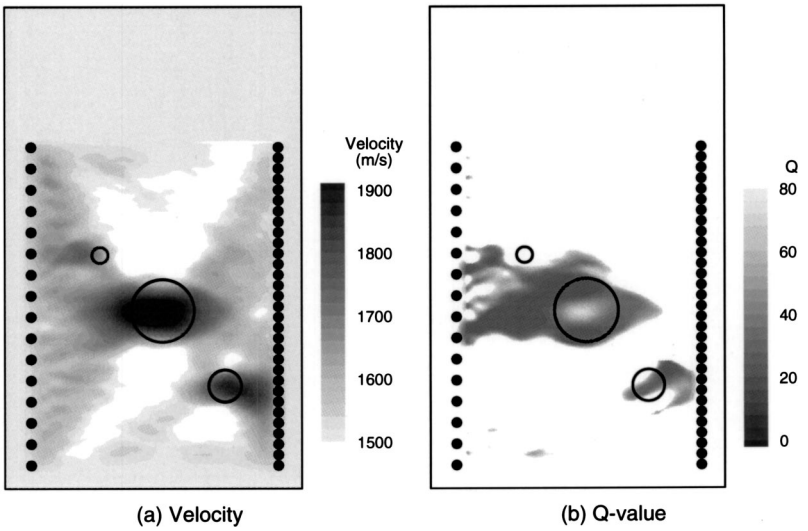

FIG. 13. The result of the cascaded inversion of the laboratory data. (a) Real part of the velocity and (b) Q value.

Figure 14 compares the wave forms of the observed data and the synthetic wave forms generated from the final inversion model. No cycle skip between the arrivals of these wave forms is observed. The primary difference between these wave forms are the decrease in amplitude at the upper receivers of the final wave form. This is caused by the attenuative artifacts in the middle part of the Q image shown in Fig. 13(b). The density contrast between the water and the solid material and S-wave conversion in the solid material cause an energy loss. Ignoring these effects in the inversion results in generating the attenuative artifact.

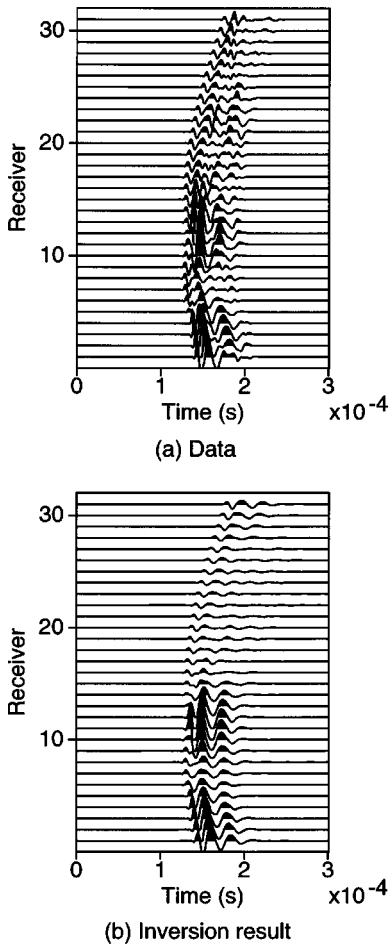

FIG. 14. Comparison of the wave forms of the laboratory data and the synthetic data for the model obtained from the inversion for the source location indicated by the arrow in Fig. 5.

V. CONCLUSIONS

The performance of viscoacoustic full wave form inversion of laboratory data was examined for a cross-hole configuration using a two-axes computer-controlled scanning system. The result of this study indicates that the wave form inversion technique yields a higher resolution velocity image compared to travel time tomography. The result also indicates that both the velocity and Q can be imaged using the viscoacoustic wave form inversion technique. We found that the ''cascaded'' inversion scheme yielded a reliable Q image. Also, we found that regularization improved the stability of the inversion process. The Q image, however, has lower resolution than the velocity image. The proposed method can be applied to delineate the physical properties of saturated and unsaturated soil and unconsolidated rocks. And it should also work for nondestructive evaluation of soft and attenuative materials and medical application.

ACKNOWLEDGMENTS

T.W. would like to thank the Ministry of Education, Culture, Sports, Science and Technology of Japan for the financial support that enabled his stay in LBNL. He also thanks Y. Ashida and T. Matsuoka of Kyoto University for their support, S. Uesaka of SONY Corp. for providing the prototype inversion code. The authors are grateful to R. G. Pratt of Queen's University for his encouraging suggestions on this study and his comments on the manuscript. The work was supported by the Director, Office of Energy Research, Office of Basic Sciences, U.S. Department of Energy under Contract No. DE-ACO3-765700098.

[1] R. D. Stoll and G. M. Bryan, ''Wave attenuation in saturated sediments,'' J. Acoust. Soc. Am. **47**, 1440–1447 (1970).
[2] M. N. Toksöz, D. H. Johnston, and A. Timur, ''Attenuation of seismic waves in dry and saturated rocks I. Laboratory measurements,'' Geophysics **44**, 681–690 (1979).

[3] T. Cadoret, G. Mavko, and B. Zinszner, ''Fluid distribution effect on sonic attenuation in partially saturated limestones,'' Geophysics **63**, 154–160 (1998).
[4] Z. Liu, J. W. Rector, K. T. Nihei, L. Tomutsa, L. R. Myer, and S. Nakagawa, ''Extensional wave attenuation and velocity in partially-saturated sand in the sonic frequency range,'' The 38th U.S. Rock Mechanics Symposium, 2001.
[5] A. Turgut and T. Yamamoto, ''Measurements of acoustic wave velocities and attenuation in marine sediments,'' J. Acoust. Soc. Am. **87**, 2376–2383 (1990).
[6] T. Yamamoto, ''Velocity variabilities and other physical properties of marine sediments measured by crosswell acoustic tomography,'' J. Acoust. Soc. Am. **98**, 2235–2248 (1995).
[7] J. T. Geller, M. B. Kowalsky, P. K. Seifert, and K. T. Nihei, ''Acoustic detection of immiscible liquids in sand,'' Geophys. Res. Lett. **27**, 417–420 (2000).
[8] J. Wong, N. Bregman, G. West, and P. Hurley, ''Cross-hole seismic scanning and tomography,'' Leading Edge **6**, 36–41 (1987).
[9] N. D. Bregman, C. H. Chapman, and R. C. Bailey, ''Travel time and amplitude analysis in seismic tomography,'' J. Geophys. Res., B **94**, 7577–7587 (1989).
[10] R. W. Ward and C.-H. Young, ''Mapping seismic attenuation within geothermal systems using teleseisms with application to the Geysers-Clear Lake region,'' J. Geophys. Res. B **85**, 5227–5236 (1980).
[11] Y. Quan and J. M. Harris, ''Seismic attenuation tomography using the frequency shift method,'' Geophysics **62**, 895–905 (1997).
[12] T. Watanabe and K. Sassa, ''Seismic attenuation tomography and its application to rock mass evaluation,'' Int. J. Rock Mech. Min. Sci. **33**, 467–477 (1996).
[13] P. R. Williamson and M. H. Worthington, ''Resolution limits in ray tomography due to wave behavior: Numerical experiments,'' Geophysics **58**, 727–735 (1993).
[14] A. Tarantola, ''Inversion of seismic reflection data in the acoustic approximation,'' Geophysics **49**, 1259–1266 (1984).
[15] C. Zhou, W. Cai, Y. Luo, G. T. Schuster, and S. Hassanzadeh, ''Acoustic wave-equation traveltime and waveform inversion of crosshole seismic data,'' Geophysics **60**, 765–773 (1995).
[16] R. G. Pratt and M. H. Worthington, ''Inverse theory applied to multi-source cross-hole tomography. I. Acoustic wave-equation method,'' Geophys. Prospect. **38**, 287–310 (1990).
[17] R. G. Pratt, ''Seismic wave form inversion in the frequency domain. I. Theory and verification in a physical scale model,'' Geophysics **64**, 888–901 (1998).
[18] Z.-M. Song, P. R. Williamson, and R. G. Pratt, ''Frequency-domain acoustic-wave modeling and inversion of crosshole data. II. Inversion method, synthetic experiments and real-data results,'' Geophysics **60**, 796–809 (1995).
[19] Q. Liao and G. A. McMechan, ''Multifrequency viscoacoustic modeling and inversion,'' Geophysics **61**, 1371–1378 (1996).
[20] G. J. Hicks and R. G. Pratt, ''Reflection waveform inversion using local descent methods: Estimating attenuation and velocity over a gas-sand deposit,'' Geophysics **66**, 598–612 (2001).
[21] H. Keers, D. W. Vasco, and L. R. Johnson, ''Viscoacoustic crosswell imaging using asymptotic wave forms,'' Geophysics **66**, 861–870 (2001).
[22] C.-H. Jo, C. Shin, and J.-H. Suh, ''An optimal 9-point, finite-difference, frequency-space, 2-D scalar wave extrapolator,'' Geophysics **61**, 529–537 (1996).
[23] R. M. Christensen, *Theory of Viscoelasticity: An Introduction* (Academic, New York, 1982).
[24] E. Kjartansson, ''Constant *Q*-wave propagation and attenuation,'' J. Geophys. Res. B **84**, 4737–4747 (1979).
[25] W. I. Futterman, ''Dispersive body wave,'' J. Geophys. Res. **67**, 5279–5291 (1962).
[26] R. G. Pratt, C. Shin, and G. J. Hicks, ''Gauss-Newton and full Newton methods in fequency-space seismic wave form inversion,'' Geophys. J. Int. **133**, 341–362 (1998).
[27] T. Watanabe, S. Uesaka, T. Matsuoka, and Y. Ashida, ''Frequency domain acoustic wave form inversion,'' EOS, Transactions, AGU 2000 Fall Meeting, S21B-09 (2000).

Eigenfunction analysis of stochastic backscatter for characterization of acoustic aberration in medical ultrasound imaging

Trond Varslot[a] and Harald Krogstad
Department of Mathematical Sciences, Norwegian University of Science and Technology, 7491 Trondheim, Norway

Eirik Mo and Bjørn A. Angelsen
Department of Circulation and Imaging, Norwegian University of Science and Technology, 7491 Trondheim, Norway

(Received 3 September 2003; revised 20 February 2004; accepted 11 March 2004)

Presented here is a characterization of aberration in medical ultrasound imaging. The characterization is optimal in the sense of maximizing the expected energy in a modified beamformer output of the received acoustic backscatter. Aberration correction based on this characterization takes the form of an aberration correction filter. The situation considered is frequently found in applications when imaging organs through a body wall: aberration is introduced in a layer close to the transducer, and acoustic backscatter from a scattering region behind the body wall is measured at the transducer surface. The scattering region consists of scatterers randomly distributed with very short correlation length compared to the acoustic wavelength of the transmit pulse. The scatterer distribution is therefore assumed to be δ correlated. This paper shows how maximizing the expected energy in a modified beamformer output signal naturally leads to eigenfunctions of a Fredholm integral operator, where the associated kernel function is a spatial correlation function of the received stochastic signal. Aberration characterization and aberration correction are presented for simulated data constructed to mimic aberration introduced by the abdominal wall. The results compare well with what is obtainable using data from a simulated point source. © *2004 Acoustical Society of America.* [DOI: 10.1121/1.1736274]

PACS numbers: 43.60.Tj, 43.60.Cg, 43.20.Bi [JJM] Pages: 3068–3076

I. INTRODUCTION

An ultrasound image is formed as a map of the intensity of the reflected sound pulse from different spatial locations. By focusing the transmitted sound pulse at a specific location, the intensity of the transmitted field is highest around the focal point. The reflected signal then largely originates from this region. A limitation is therefore imposed on the image resolution by the size of the focal zone. The smallest obtainable size is limited by diffraction.

In medical ultrasound imaging, the transmitted pulse typically travels through the body wall before arriving at the intended focal point. The body wall consists of a heterogeneous configuration of muscular, fatty, and connective tissue. The result of propagation through a medium with variable speed of sound is degradation of the initial geometric focus beam by a widening of the focal zone. The transmitted pulse is then said to be *aberrated*. Experimental studies[1–5] and simulations[6,7] show that this aberration can significantly reduce the image resolution.

Several different approaches have been suggested to reduce the effect of the aberration. These are mostly based on either a time-reversal mirror[8] or a time delay filter.[9] To use the time-reversal mirror, a well-defined point scatterer is needed in order to focus the signal at a point. This limits its applicability in clinical situations. Time delay (and amplitude) filters rely on the ability to estimate filter coefficients. When the received signal is from a single, known point reflector, this is mostly a trivial task; time delay and amplitude fluctuations may be observed directly in the signal.[10] For scattering from a stochastic medium, the filter must be estimated from the stochastic properties of the received signal. If the scattering medium is δ correlated, the resulting received signal is approximately a Gaussian process.[11] By considering scattering from a limited depth interval, the process may be assumed to be stationary and have zero mean. Since all information about a Gaussian process may be expressed in terms of its mean and its covariance function, it is reasonable to base a characterization of the aberration on the covariance function. Various algorithms for doing this are available.[12]

This paper considers the characterization of aberration based on measurements of acoustic backscatter from a stochastic distribution of scatterers, as depicted in Fig. 1. The aberration is introduced in a layer close to the transducer and is, therefore, modeled using an infinitesimal aberrating layer on the transducer surface. This layer is called a *generalized frequency dependent screen*[10,11] or simply a *generalized screen*. The received signal is scattering from a region with δ correlated scatterers around the focal point. This situation is found in medical imaging applications, e.g., when imaging organs like liver and spleen.

It has been shown that transmitting an eigenfunction of the scattering operator will result in focusing the energy

[a]Electronic mail: varslot@math.ntnu.no

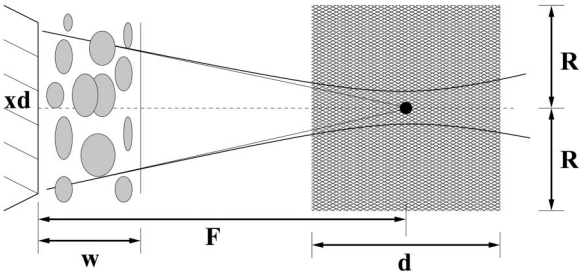

FIG. 1. Situation of interest. The presented simulation results use a focal depth F of 6 cm, body wall thickness w of 2 cm, and scattering region extending 1.5 cm to either side of the focal point ($d=3$ cm).

within the support of a deterministic scattering object.[13] The eigenfunctions associated with high eigenvalues will focus on regions with high scattering intensity. In the case of deterministic, well-separated point scatterers, each with a unique scattering intensity, an eigenfunction of the scattering operator corresponds to a diffraction-limited focusing on one of the scatterers.[13] The corresponding eigenvalue will, in this case, reflect the intensity of the respective point scatterer. Furthermore, it has been shown that under these circumstances, an iterative application of the time-reversal mirror will converge to a diffraction limited focusing on the point scatterer with strongest intensity.[14]

This paper shows how a similar analysis may be performed on stochastic backscatter signals. The main difference from previous work done in Refs. 13 and 14 is that the focal region does not contain any distinguished scatterers. However, the initially transmitted aberrated pulse will have higher amplitude in certain regions, partly due to the geometric focusing and partly due to the aberration. The aberration correction method presented is shown to focus on regions where the initially transmitted pulse has high amplitude. The location of the focal point is, therefore, determined by the aberration. The size of the focal region, however, will be close to that of an unaberrated, diffraction limited transmit beam.

The starting point for the aberration characterization is the intuitive notion of adjusting the receive signal so that, on average, it is as coherent as possible. This leads to a characterization of the aberration consistent with the generalized screen model.

The paper is organized in the following way. A short review of first-order scattering is given in Sec. II A. Then a model for the stochastic signal received at the transducer is discussed in Sec. II B. A formulation for maximizing the energy in the received signal is developed in Sec. II B 1. The connection between this energy formulation and aberration characterization is discussed in Sec. II B 2. The simulated data are described in Sec. III. Results are presented in Sec. IV. Discussion and concluding remarks are given in Secs. V and VI, respectively.

II. THEORY

A. First-order scattering

The theory of first-order scattering is thoroughly covered in the literature,[11,15] and is briefly included here for completeness and to set the notation.

Lagrangian coordinates are particularly well suited for a description of the propagation of an ultrasonic pulse as seen in medical ultrasound imaging.[16] For simplicity, both nonlinear and dissipative terms have been neglected. Conservation of mass, conservation of inertia, and a compressibility relation produce a linear wave equation for the Lagrangian pressure,[17]

$$\mathrm{div}\left(\frac{1}{\rho}\nabla p\right)-\kappa\frac{\partial^2 p}{\partial t^2}=0.$$

Here, $\rho(r)$ and $\kappa(r)$ are the material density and compressibility at equilibrium, i.e., they are not time dependent. Following Ref. 18, introduction of an adjusted pressure $\tilde{p}=p/\sqrt{\rho}$ simplifies the following:

$$\nabla^2\tilde{p}-\frac{1}{c^2}\frac{\partial^2\tilde{p}}{\partial t^2}=\Phi\tilde{p}, \tag{1}$$

where $\Phi=\sqrt{\rho}\nabla^2(1/\sqrt{\rho})$. In the following, the adjusted pressure will be denoted p.

In soft tissue, e.g., muscle, fat, and blood, the density and compressibility ranges from 950 to 1070 kg/m^3 and 350 to 500×10^{-12} Pa^{-1} respectively.[16] It is therefore appropriate to express the material parameters ρ and κ as

$$\rho(r)=\rho_0+\gamma\rho_1(r),$$

$$\kappa(r)=\kappa_0+\gamma\kappa_1(r),$$

where ρ_0 and κ_0 are constant background values, and ρ_1 and κ_1 represent deviation from these background values with a small nondimensional factor γ. A reasonable value for γ in this case is 0.1. This suggests looking for a perturbation solution[19] of Eq. (1) of the form

$$p(r,t)=p_0(r,t)+\gamma p_1(r,t)+O(\gamma^2).$$

Let $c_1(r)$ be given from

$$\frac{1}{c^2}=\frac{1}{c_0^2}-\gamma\frac{2c_1}{c_0^3},$$

where $1/c_0^2=\rho_0\kappa_0$. Using this definition $c(r)=c_0+\gamma c_1(r)+O(\gamma^2)$. Note also that Φ will be $O(\gamma)$. Let therefore $\Phi(r)=\gamma\Phi_1(r)$. Using these definitions, Eq. (1) may be written as

$$\nabla^2 p-\frac{1}{c_0^2}\frac{\partial^2 p}{\partial t^2}=\gamma\left(-2\frac{c_1}{c_0^3}\frac{\partial^2 p}{\partial t^2}+\Phi_1 p\right) \tag{2}$$

to first order in γ. A perturbation solution is found from

$$\nabla^2 p_0-\frac{1}{c_0^2}\frac{\partial^2 p_0}{\partial t^2}=0,$$

$$\nabla^2 p_1-\frac{1}{c_0^2}\frac{\partial^2 p_1}{\partial t^2}=-2\frac{c_1}{c_0^3}\frac{\partial^2 p_0}{\partial t^2}+\Phi_1 p_0.$$

Now p_0 is the solution of the wave equation in a homogeneous medium, and p_1 represents a first-order correction term introduced by the inhomogeneities, i.e., first-order scattering. When transmitting an initial pulse from the transducer, and receiving the acoustic backscatter from an inho-

mogeneous medium, the backscatter will be approximately p_1. This is known as the *Born approximation* of the scattered signal.

In the frequency domain, the problem will be formulated as

$$\nabla^2\hat{p}_0+\left(\frac{\omega}{c_0}\right)^2\hat{p}_0=0,$$

$$\nabla^2\hat{p}_1+\left(\frac{\omega}{c_0}\right)^2\hat{p}_1=\Psi\hat{p}_0.$$

Here

$$\Psi(r,\omega)=2\,\frac{c_1(r)}{c_0}\left(\frac{\omega}{c_0}\right)^2+\Phi_1(r). \tag{3}$$

Thus, p_1 on the transducer is found from p_0 by means of the appropriate Green's function[20] g,

$$\hat{p}_1(\xi,\omega)=\int g(\xi-r,\omega)\Psi(r,\omega)\hat{p}_0(r,\omega)dr. \tag{4}$$

Calculations presented in this paper are obtained using the Green's function for the Helmholtz equation in $\mathbb{R}^3$,

$$g(r,\omega)=\frac{e^{-i\omega|r|/c_0}}{4\pi|r|}.$$

Throughout this paper, r denotes a coordinate in the scattering region, and ξ is a coordinate on the transducer surface.

B. Modeling of the received scattered signal

The situation studied here is one where all aberration takes place in a region close to the transducer, while all measured scattering emerges from a region close to the focal point. This is a situation typical for medical ultrasound imaging. The body wall, consisting of a heterogeneous mixture of fat, muscle, and connective tissue, produces considerable distortion of the propagating pulse, while the organs inside the body have very little impact to this effect.[11]

Instead of dealing with ρ_1, κ_1, and c_1 directly, let Ψ be an appropriate scattering distribution. For simplicity, $\Psi(r,\omega)$ is assumed to be a spatial point process for each frequency ω, such that the "covariance function" R_Ψ is proportional to the Dirac δ function,

$$R_\Psi(r_2-r_1,\omega)=\mathrm{E}[\Psi(r_1,\omega)\overline{\Psi(r_2,\omega)}]=\begin{cases}\sigma_\omega^2\delta(|r_2-r_1|), & r_1,r_2\in\Omega\\ 0 & \text{otherwise}\end{cases}.$$

Here $\mathrm{E}[\cdot]$ is the expectation operator, σ_ω^2 is the intensity of the point process[21] at frequency ω, and Ω is the scattering region.

A common assumption is that the aberration introduced by the body wall is the same for all locations within the focal zone. This is valid as long as the focal zone is narrow enough, i.e., located within what is referred to as the isoplanatic patch or region.[11] Using this assumption, propagation through the body wall may be modeled by propagating through a homogeneous medium and then applying a filter. The received signal $\hat{p}_r$ is thus obtained from the scattered signal $\hat{p}_1$ as

$$\hat{p}_r(\xi,\omega)=s(\xi,\omega)\hat{p}_1(\xi,\omega).$$

The function s, which accounts for the aberration, is denoted *generalized screen*. The time-reversal argument implies that transmitting a pulse $\hat{p}(\xi,\omega)$ through the aberrating layer, the beam pattern in the focal zone will be as if the pulse $s(\xi,\omega)\hat{p}(\xi,\omega)$ was transmitted through a homogeneous medium.

As the aberration is mainly introduced by tissue structures in the body wall, it does not change over the time scale of the imaging process. Therefore, keeping the body wall fixed relative to the transducer, scattering from within a given isoplanatic region will have undergone the same aberration. The function $s(\xi)$ is therefore the same for all realizations.

In the rest of this paper, all computations will be performed in the temporal frequency domain, unless otherwise stated. Explicit dependence of ω in quantities like pressure pulses, screens, and scatterer distributions is therefore omitted. Hence, the field $\hat{p}_0(r)$, for a transmitted pulse $\hat{p}$, geometrically focused at r_f, is given as

$$\hat{p}_0(r)=\hat{p}\int_T L(\xi)\,\frac{e^{-i(\omega/c_0)(|r-\xi|+|r_f-\xi|-|r_f|)}}{4\pi|r-\xi|}\,d\xi,$$

where $L(\xi)=s(\xi)l(\xi)$, and $l(\xi)$ is the apodization function used on transmit. Here T indicates that integration is done over the transducer surface.

Applying the Fraunhofer approximation, valid for large f numbers, the transmitted field is given by

$$\hat{p}_0(r)=\hat{p}\,\frac{e^{-i\omega|r|/c_0}}{4\pi|r|}\hat{L}\left(\frac{\omega}{c_0}e_r\right), \tag{5}$$

where $e_r=r/|r|$ and $\hat{L}$ denotes the spatial Fourier transform of L obtained when L is extended by zero outside the transducer aperture. The pressure in the far field is, therefore, approximately a spherical wave modified by the Fourier transform of the product of the screen and the transducer apodization.

The scattered pressure field p_1 at a coordinate ξ on the transducer is now calculated using Eq. (4) as

$$\hat{p}_1(\xi)=\int_\Omega\frac{e^{i\omega|\xi-r|/c_0}}{4\pi|\xi-r|}\Psi(r)\hat{p}_0(r)dr. \tag{6}$$

The Fraunhofer approximation then gives the received signal at the transducer surface as

$$\hat{p}_r(\xi)=s(\xi)\,\frac{e^{i\omega|\xi-r_f|/c_0}}{4\pi|r_f|}\times\int_\Omega\exp\left(i\,\frac{\omega}{c_0}\,\frac{\xi\cdot r}{|r_f|}\right)\Psi(r)\hat{p}_0(r)dr.$$

The term $\exp i\omega|\xi-r_f|/c_0/4\pi|r_f|$ represents geometric curvature of this signal, and is customarily removed before further processing. The measured signal is thus defined as

$$\hat{p}_m(\xi) = s(\xi) \int_\Omega \exp\left(i \frac{\omega}{c_0} \frac{\xi \cdot r}{|r_f|} \right) \Psi(r) \hat{p}_0(r) dr.$$

The corresponding (spatial) covariance function for a frequency ω is given as

$$\begin{aligned} R_{\hat{p}_m}(\xi_1, \xi_2) &= E[\hat{p}_m(\xi_1) \overline{\hat{p}_m(\xi_2)}] \\ &= s(\xi_1) \overline{s(\xi_2)} \sigma^2 \int_\Omega \exp\left(i \frac{\omega}{c_0} \frac{(\xi_1 - \xi_2) \cdot r}{|r_f|} \right) \\ &\quad \times |\hat{p}_0(r)|^2 dr. \end{aligned} \tag{7}$$

Here use has been made of the fact that the scatterer distribution is δ correlated. Strictly speaking, it is the time-dependent received signal at each transducer element which is a zero-mean Gaussian stochastic process. Thus, Eq. (7) is really the cross spectrum between the received signal at coordinates ξ_1 and ξ_2 as a function of ω. However, for the purpose of this paper, it is more convenient to consider the cross spectrum as a function of ξ_1 and ξ_2 for a fixed frequency ω. This is therefore denoted the covariance function for the received signal at frequency ω.

1. Eigenfunction formulation for random signals

Let $\hat{p}_m(\xi)$ be the measured signal at location ξ on the transducer surface. This is now assumed to be a second-order random field (as a function of space for each frequency). Let x be a complex L^2 function with norm 1, and define the stochastic linear functional $\mathcal{L}_x$ as

$$\mathcal{L}_x \hat{p}_m = \langle \hat{p}_m, x \rangle = \int_T \hat{p}_m(\xi) \overline{x(\xi)} d\xi,$$

where T indicates integration over the transducer aperture. Then

$$\begin{aligned} \|\mathcal{L}_x \hat{p}_m\|^2 &\equiv \mathrm{E}[\mathcal{L}_x \hat{p}_m \overline{\mathcal{L}_x \hat{p}_m}] \\ &= \int_{T^2} \overline{x(\xi_1)} x(\xi_2) \mathrm{E}[\hat{p}_m(\xi_1) \overline{\hat{p}_m(\xi_2)}] d\xi_1 \, d\xi_2 \\ &= \int_{T^2} \overline{x(\xi_1)} x(\xi_2) R_{\hat{p}_m}(\xi_1, \xi_2) d\xi_1 \, d\xi_2. \end{aligned}$$

Physically, $\mathcal{L}_x \hat{p}_m$ may be interpreted as a *modified beamformer output signal*. The quantity $\|\mathcal{L}_x \hat{p}_m\|^2$ is the variance of the signal, i.e., the expected energy of the modified beamformer output.

Define the positive semidefinite linear operator A as

$$Ax(\xi) = \int_T R_{\hat{p}_m}(\xi, \xi_2) x(\xi_2) d\xi_2. \tag{8}$$

Now

$$\|\mathcal{L}_x \hat{p}_m\|^2 = E[|\mathcal{L}_x \hat{p}_m|^2] = \langle Ax, x \rangle.$$

The operator A is Hermitian and compact with kernel function $R_{\hat{p}_m}$. Therefore, all eigenvalues are real and nonnegative, eigenfunctions belonging to distinct eigenvalues are orthogonal and there exists a largest eigenvalue.[22] It follows that the expected energy of the modified beamformer output signal is maximized when x is an eigenfunction of A associated with the largest eigenvalue.

The eigenvalues and their corresponding eigenfunctions may be ordered according to the magnitude of the eigenvalues. The eigenfunction associated with the largest eigenvalue, denoted λ_1, is then referred to as x_1 and so on.

2. Focusing properties

In order to investigate further the properties of the eigenfunctions of the operator A defined in Eq. (8), consider

$$\langle Ax, x \rangle = \int_{T^2} R_{\hat{p}_m}(\xi_1, \xi_2) x(\xi_2) \overline{x(\xi_1)} d\xi_2 \, d\xi_1.$$

Using $R_{\hat{p}_m}$ from Eq. (7) and defining $\alpha(r)$ to be

$$\alpha(r) = \int_T s(\xi) \overline{x(\xi)} \exp\left(i \frac{\omega}{c_0} \frac{\xi \cdot r}{|r_f|} \right) d\xi, \tag{9}$$

this may be expressed as

$$\langle Ax, x \rangle = \sigma^2 \int_\Omega |\hat{p}_0(r)|^2 |\alpha(r)|^2 dr. \tag{10}$$

Furthermore, transmitting the pulse $\overline{x(\xi)} \hat{p}$, geometrically focused at r_f, will have the far-field approximation

$$\hat{p}_{\mathrm{cor}}(r) = \hat{p} \frac{e^{-i\omega|r|/c_0}}{4\pi|r|} \alpha(r). \tag{11}$$

This expression assumes that no apodization is used on transmit for the corrected pulse, i.e., $l(\xi) = 1$ when compared to Eq. (5). Thus, correcting the transmitted pulse using the eigenfunction x_1 as an aberration correction filter, will focus the transmitted energy according to the initially transmitted field $\hat{p}_0$, in order to maximize Eq. (10). Note that there is a separate eigenvalue problem to be solved for each frequency.

Consider first the extreme case when $|\hat{p}_0(r)| = 1$, i.e., the transmitted field insonifies the whole scattering region with equal intensity. Assume also that the scattering region is cylindrical with height d and radius R (see Fig. 1). Noting that $\alpha(r)$ is independent of the distance from the transducer along the focal axis, then

$$\begin{aligned} \langle Ax, x \rangle &= \sigma^2 \int_\Omega |\alpha(r)|^2 \, dr \\ &= \sigma^2 \int_{T^2} s(\xi_1) \overline{s(\xi_2)} x(\xi_2) \overline{x(\xi_2)} \Lambda \, d\xi_1 \, d\xi_2, \end{aligned}$$

where

$$\Lambda = dR \frac{\mathrm{J}_1(R\omega|\xi_1 - \xi_2|/c_0|r_f|)}{\omega|\xi_1 - \xi_2|/c_0|r_f|},$$

and J_1 is the Bessel function of first kind. In the current situation $\omega/c_0|r_f| \sim 10^5$. As a consequence of this, $\Lambda \sim \delta(|\xi_1 - \xi_2|)$. The largest possible value $\langle Ax, x \rangle$ is therefore obtained if $|x|^2$ is proportional to $|s|^2$. The amplitude of the eigenfunction x_1 thus matches that of s. A shift of the corrected focus will not influence the eigenvalue, as long as the focus is kept within the scattering region. The phase is therefore not determined.

In the other extreme case, when $p_0(r)=\delta(|r-r_f|)$ is the Dirac δ function, then

$$\langle Ax,x\rangle=\sigma^2|\alpha(r_f)|^2=\sigma^2\left|\int_T s(\xi)\overline{x(\xi)}d\xi\right|^2.$$

The maximum for this expression is obtained if x is proportional to s. Thus, the eigenfunction x_1 will be proportional to the screen.

In the general case, which lies somewhere between these two extremes, it is difficult to find a direct relationship between the screen x_1 and s. Let $1/|r|$ be approximated by $1/|r_f|$ in the region where $\hat{p}_0(r)$ is significantly different from zero, i.e., the region which contributes to the integral in Eq. (10). Combining Eqs. (10) and (11) yields

$$\langle Ax,x\rangle\left(\frac{|\hat{p}|}{4\pi|r_f|}\right)^2=\sigma^2\int_\Omega|\hat{p}_0(r)|^2|\hat{p}_{\mathrm{cor}}(r)|^2\,dr.$$

The intensity of the transmit signal using x_1 as a correction filter will, therefore, be focused into areas where the intensity of $p_0(r)$ was high.

It is worth noting that there is an upper bound for the largest eigenvalue since

$$\left(\frac{|\hat{p}|}{4\pi|r_f|}\right)^2\langle Ax,x\rangle\leqslant\sigma^2\|\hat{p}_0\|_4^2\|\hat{p}_{\mathrm{cor}}\|_4^2. \tag{12}$$

Furthermore,

$$\|\hat{p}_{\mathrm{cor}}\|_4^4\sim\int_{T^4}\beta(\xi_1)\overline{\beta(\xi_2)}\beta(\xi_3)\overline{\beta(\xi_4)}\Lambda\times d\xi_1\,d\xi_2\,d\xi_3\,d\xi_4, \tag{13}$$

where

$$\beta(\xi)=s(\xi)\overline{x(\xi)},$$

$$\Lambda=dR\frac{\mathrm{J}_1(R\omega|\xi_1-\xi_2+\xi_3-\xi_4|/c_0|r_f|)}{(\omega|\xi_1-\xi_2-\xi_3+\xi_4|/c_0|r_f|)}.$$

Again, since $\Lambda\sim\delta(|\xi_1-\xi_2+\xi_3-\xi_4|)$,

$$\|\hat{p}_{\mathrm{cor}}\|_4^4\sim\int_{T^3}\beta(\xi_1)\overline{\beta(\xi_2)}\beta(\xi_3)\overline{\beta(\xi_1-\xi_2+\xi_3)}\times d\xi_1\,d\xi_2\,d\xi_3.$$

Maximum for $\|\hat{p}_{\mathrm{cor}}\|_4^2$ is attained when the phase of β is zero, i.e., the phase of x is equal to that of s. Inequality (12) is, however, an equality if $|\hat{p}_{\mathrm{cor}}(r)|$ is proportional to $|\hat{p}_0(r)|$. An iterative correction process is therefore suggested, where the eigenfunction associated with the largest eigenvalue is used to transmit a corrected pulse. The scattering of this corrected transmit pulse has a correlation function which then is used to find a new eigenfunction. By repeating this process, no further improvement is possible only if inequality (12) is satisfied as an equality, and $\|\hat{p}_{\mathrm{cor}}\|_4^2$ attains its maximum.

A net prism effect of the body wall manifests itself as a shift of the actual focal point from the intended location of r_f to the location r_0 (see Fig. 2). However, due to reciprocity, scattering from r_0 will appear as if emerging from r_f, when observed at the transducer.[11] Therefore, scattering from a uniform distribution of scattering will always appear to emerge from a location around r_f. A consequence of this is that observations of the screen s based on such random scattering data do not contain information about the shift from r_f to r_0, i.e., what is observed is not $s(\xi)$ but a different screen $\tilde{s}(\xi)$. The phase of $\tilde{s}(\xi)$ does not contain a linear component as a function of ξ,

$$\int_T\arg\{\tilde{s}(\xi)\}\xi\,d\xi=\int_T\arg\left\{s(\xi)\exp\left(-i\frac{\omega}{c_0}\frac{r_0\cdot\xi}{|r_f|}\right)\right\}\xi\,d\xi=0.$$

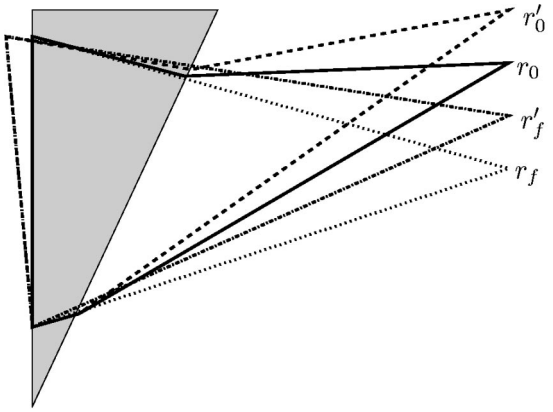

FIG. 2. The actual focal point is shifted from the intended location r_f to r_0 by a net prism effect in the body wall. Thus, steering the beam toward r_f' will in reality steer the beam toward r_0'.

Now, using $\tilde{s}(\xi)$ as a correction filter, but adding a steering angle to the transmit beam in order to move the focus from r_f to r_f', will in fact move the focus of the transmit beam from r_0 to r_0', where $r_f'-r_f=r_0'-r_0$,

$$\tilde{s}(\xi)\exp\left(i\frac{\omega}{c_0}\frac{(r_f'-r_f)\cdot\xi}{|r_f|}\right)=s(\xi)\exp\left(i\frac{\omega}{c_0}\frac{(r_f'-r_f-r_0)\cdot\xi}{|r_f|}\right).$$

Therefore, a linear term (as a function of ξ) in the phase of the correction filter is related to a shift of the focal point away from r_0. As there is no way to identify a shift from r_0 to r_f based on the available random scattering data, no distinction will be made here between s and $\tilde{s}$.

Thus far, most of the calculations have been performed assuming everything is within an isoplanatic region. The idea of maximizing the expected energy of the received signal makes physical sense without this assumption. Intuitively, maximizing the energy will align the aberrated wave front, thus countering the aberration experienced in the receive signal. Furthermore, studies have concluded that the isoplanatic assumption is justified in practical situations of interest.[23]

III. METHOD

The simulated ultrasound measurements were created using ABERSIM, a simulation package with routines for simulating forward propagation of an acoustic wave field[24] and aberration of the ultrasonic pulse.[10] In this study, only linear effects without absorption were studied. All simulations were conducted in two dimensions (2D). This does not alter the fundamental results, as a similar theory may be developed

using the 2D Green's function for the Helmholtz equation instead of the three-dimensional Green's function as done here.

A transmit pulse with center frequency of 2.5 MHz and a geometric focal point at a depth of 6.0 cm was transmitted from a 2.0-cm-wide transducer. The *f* number of the simulations is therefore approximately 3.0. Aberration was introduced in a 2.0-cm-thick aberrating layer close to the transducer. The acoustic scattering was produced by a $d=3.0$-cm-thick scattering region. The scattering region extended symmetrically about the focal plane; between ranges 4.5 and 7.5 cm from the transducer. The width of the scattering region was $R=5$ cm to either side of r_f (see Fig. 1). It consisted of a spatially uniform distribution of point scatterers, approximately 1600 scatterers per square centimeter. Each point scatterer was independently assigned a scattering intensity from a Gaussian distribution. In accordance with Eq. (3), the scattering was simulated as proportional to ω^2.

Uncorrelated realizations of the backscatter signal were obtained by replacing the set of point scatterers from one simulation to the next. In order to estimate the required spatial correlation functions, 20 uncorrelated realizations of the acoustic backscatter were used.

Two different aberrators were utilized in this study; a weak aberrator, and a strong aberrator. A detailed description of them is given by Måsøy *et al.*,[10] where they are referred to as w6 and s6, respectively. The weak aberrator produced arrival time fluctuations with a rms value of 49.8 ns and a correlation length of 6.4 mm. The corresponding energy level fluctuations had a rms value of 3.1 dB with a 3.6 mm correlation length. The strong aberrator produced arrival time fluctuations with a rms value of 53.7 ns and a correlation length of 5.8 mm. The corresponding energy level fluctuations had a rms value of 4.1 dB with 1.4 mm correlation length. These aberrators were created to produce aberration exhibiting similar characteristics to that of published measurements. Måsøy showed that almost ideal aberration correction was obtained for both aberrators using a time delay and amplitude correction filter. This filter was obtained by identifying the wave front from a known point source, and is an approximation of the screen *s* by making the phase a linear function of frequency.

The fact that a point source correction filter was found to work well, motivates the use of this as a reference in the current study. However, in order for this to be comparable to a correction filter based random scattering, the point source was placed in the real focal point of the transmit beam r_0, and not in the intended focal point r_f (see the discussion at the end of Sec. II B 2). It further motivates looking for a time delay and amplitude correction filter only, instead of solving the eigenvalue problems for each frequency and performing aberration correction using a general filter.

IV. RESULTS

In the following, eigenvalues and their corresponding eigenfunctions are ordered according to the magnitude of the eigenvalues. The eigenfunction associated with the largest eigenvalue is then referred to as the first eigenfunction, and so on.

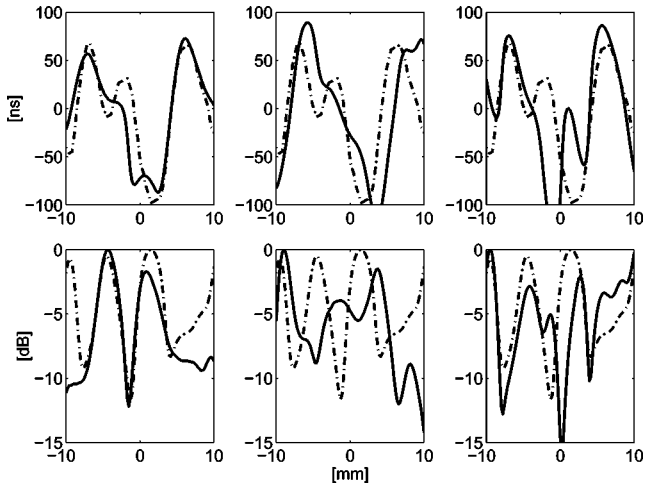

FIG. 3. Characterizations of the aberration. The transmit pulse had three distinct, diffraction limited focal points (not aberrated). The acoustic backscatter was aberrated by the weak aberrator. Time delay and amplitude characterization was obtained from the covariance function estimated at the center frequency (solid line) and compared to a reference obtained from point source simulations (dash-dot line). Top: time delays estimated from the first, second, and third eigenfunctions (left to right). Bottom: amplitude fluctuations estimated from the first, second, and third eigenfunctions (left to right). Relative magnitude of the eigenvalues were: 1, 0.8, and 0.5. A linear term corresponding to a steering of $-1.4°$, $-16.5°$, and 4.9° (left to right) was removed from the time delays before presentation.

A transmit pulse was created being the sum of three pulses u_1, u_2, and u_3. These pulses had focal points r_f, 0.4 mm to the left of r_f, and 0.4 mm to the right of r_f, respectively. No aberration was used for the transmitted beam, thus p_0 consisted of three diffraction-limited lobes with different peak values. Aberration was introduced using the weak aberrator for the scattered signal. The three first eigenfunctions were then used to compute time delay and amplitude characterizations of the aberration. The time delay and amplitude screens were used to correct the transmit signal. Figure 3 shows the result with relative transmit amplitudes 1.0, 0.75, and 0.5 for u_1, u_2, and u_3, respectively. Time delay and amplitude estimates from the first eigenfunction are very similar to the reference, although an additional apodization is included in the estimate. The corresponding corrected beam profiles are shown in Fig. 4. It is evident that each eigenfunction focuses on a location with high initial transmit amplitude. The strength of these maxima is associated with the respective eigenvalue.

A transmit pulse with a single focal point r_f was then transmitted through the weak aberrator, producing an aberrated beam profile. Figure 5 displays the results using the first eigenfunction for correction. Again, in agreement with Eq. (10), using the first eigenfunction focuses the transmit signal onto maxima for the amplitude of the initial transmit signal.

Figures 6 and 7 display the estimation and correction results using a transmit pulse with a single focal point and the strong aberrator on both transmit and receive. In this case, the first eigenfunction does a good job of gathering the beam in a narrow focus, but causes a shifted focal point. However, using the second eigenfunction recovers the correct focal point. Note that the linear term in the phase is

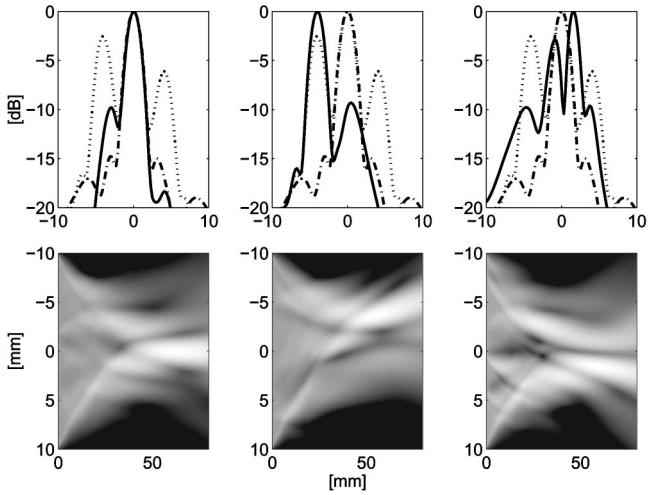

FIG. 4. Corrected beam profiles. The amplitude and delay screen characterization of the weak aberrator, presented in Fig. 3, was used to transmit a corrected signal through the aberrator. Top: beam profiles in the focal plane. Bottom: corrected beam profiles as a function of depth. The corrected profile (solid line) is plotted with the initial transmit pulse beam profile (dotted line), and the ideally corrected transmit pulse (dash-dot line).

larger for the first eigenfunction than for the second eigenfunction.

In accordance with the theory, these simulations show that eigenfunctions associated with a reasonably large eigenvalue have focusing properties. Furthermore, the linear contribution to the eigenfunction phase is related to a shift of the focal point relative to the focal point of a transmit beam with ideal correction.

In order to improve the tightness of the focus while minimizing the shift of the focal point caused by the aberration correction, a modification of the iterative approach would be to choose among the eigenfunctions associated with reasonably large eigenvalues, the one with the smallest

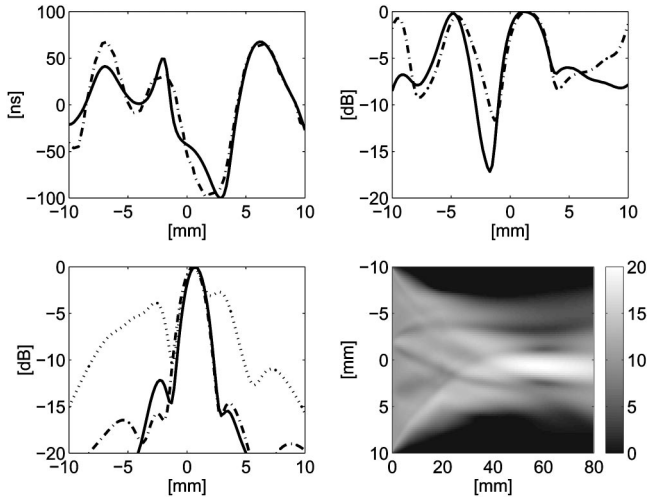

FIG. 5. Aberration correction for the weak aberrator. An aberrated transmit pulse with a single focal point was scattered, and again aberrated. Results are shown for aberration characterization from the first eigenfunction. Top left: estimated time delay (solid line), reference (dash-dot line). Top right: estimated amplitude (solid line), reference (dash-dot line). Bottom left: beam profiles in the focal plane, corrected using estimate (solid line), aberrated (dotted line), corrected using reference (dash-dot line).

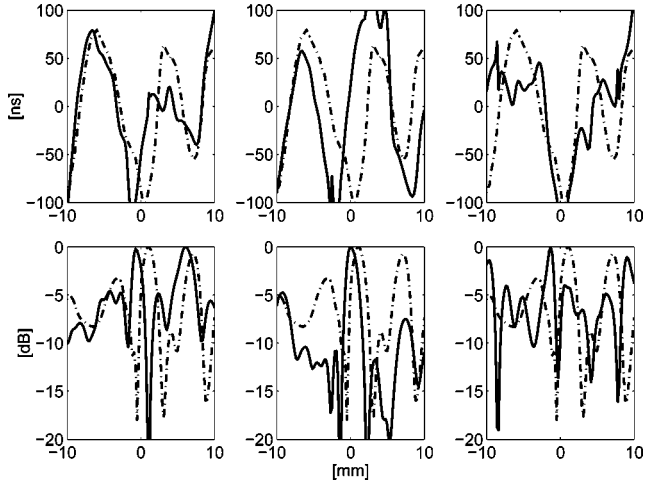

FIG. 6. Characterizations of the aberration. The transmit pulse with a single focal point was aberrated both on transmit and receive using the strong aberrator. The panel layout is the same as in Fig. 3. Relative magnitude of the eigenvalues were: 1, 0.7, and 0.4. A linear slope of 7.9°, 5.8°, and 5.9° (left to right) was removed from the time delays before presentation.

linear contribution to the phase. Iteration should be repeated until one eigenvalue is dominant.

Figure 8 shows how consistently choosing the eigenfunction associated with a large eigenvalue but with the smallest linear term in the screen phase will result in improved focusing.

V. DISCUSSION

The beam profiles obtained from corrected transmit pulses in Fig. 4 show that the first two eigenfunctions will focus the transmit pulse at maxima for the initial transmit pulse. The corresponding eigenvalues are 1.0 and 0.8, respectively. Therefore they will both result in a reasonable focusing, but at different locations. The third eigenfunction is associated with a smaller eigenvalue (0.5), and hence does not produce the same degree of focusing when used as an aberration correction filter. The same trend is also apparent in Fig. 7 for the strong aberration. However, the corrected pulse here shows a more marked split into two relatively large lobes. This is due to the severe aberration also having two more or less equal lobes.

When comparing the estimated time delays and amplitudes to their respective references, there is relatively good agreement for the first eigenfunction in the simulations using the weak aberrator and for the second eigenfunction in the simulations using the strong aberrator. The amplitude of the eigenfunction does, however, include an additional apodization compared to the reference. Apodization is commonly used to reduce the sidelobe levels at the expense of broadening the main lobe. In the presence of aberration, however, apodization may well produce increased aberration instead of reduced sidelobe levels. As the eigenfunction will produce a corrected transmit pulse which focuses the energy according to Eq. (10), the appropriate apodization will be part of the eigenfunction itself. No additional apodization is therefore necessary, and may indeed alter the transmit pulse sufficiently for the eigenfunction not to be a good correction filter.

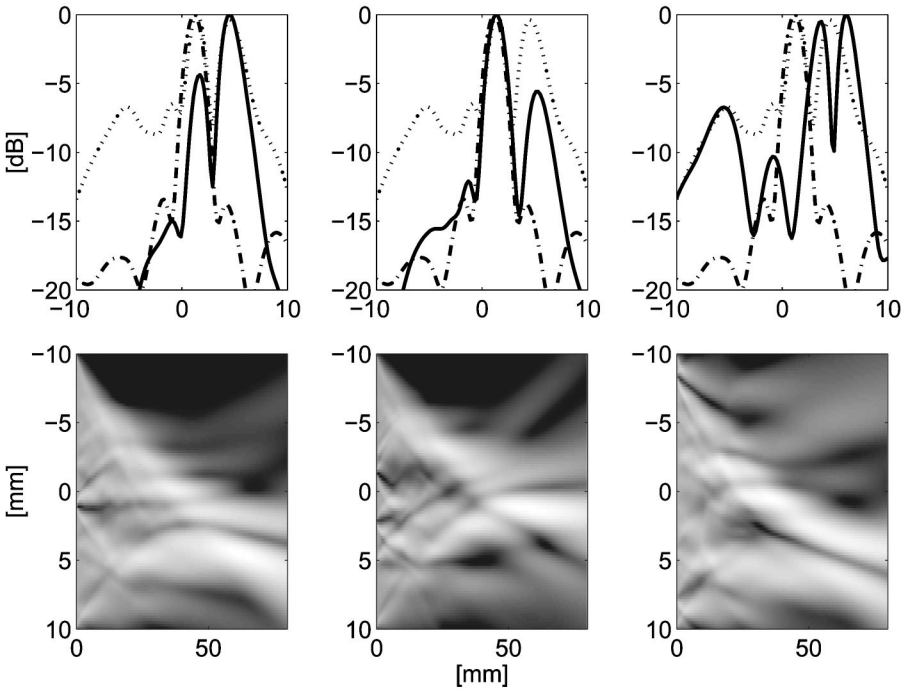

FIG. 7. Corrected beam profiles. The characterization of the strong aberrator, presented in Fig. 6, was used to transmit a corrected transmit signal through the aberrator. Panel layout is the same as in Fig. 4.

For the strong aberrator, the first eigenfunction produces a corrected beam profile with a maximum which does not coincide with the maximum of the reference. The second eigenfunction does recover the correct maximum. The eigenfunction which produces a shifted focus also has a linear term in the phase, corresponding to a larger steering angle. However, even the second eigenfunction has a significant linear term, although it is smaller than for the first eigenfunction. This is due to the fact that asymmetric sidelobes will contribute to an effective shift of the center of mass for the beam profile. It is tempting, although not necessarily correct to assume that removing the linear slope observed in the phase estimate will recover the correct focal point. Again this is because the filter has been constructed to focus transmit energy according to a specific criterion. Altering the filter may invalidate these properties. That being said, when the steering angle is small, the isoplanatic assumption justifies removing the slope.

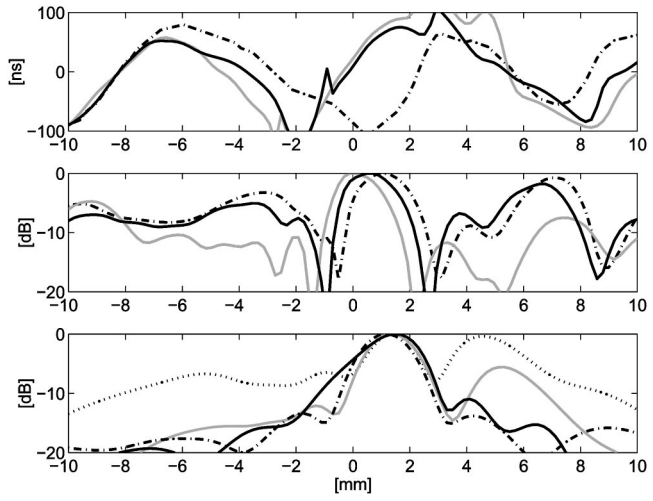

FIG. 8. Iterative characterization of aberration from the strong aberrator. Top: initial delay estimate (solid light gray line), iterated delay estimate (solid black line) compared to reference (dash-dot line). Middle: initial amplitude estimate (solid light gray line), iterated amplitude estimate (solid black line) compared to reference (dash-dot line). Bottom: aberrated beam profile (dotted line), beam profile from first correction (solid light gray line), beam profile for second correction (solid black line), beam profile for correction with reference.

Subsequent eigenfunctions will have corresponding eigenvalues which are smaller, and do not concentrate the beam to the same extent when used for aberration correction. They are, therefore, not as compelling for focusing purposes. In addition, the linear phase will be highly influenced by asymmetric sidelobes, making it difficult to predict their actual focal point.

Using the argument about the linear component of the eigenfunction phase, an eigenfunction with minimal linear term of the phase will concentrate the corrected pulse around the same location as the initial pulse. It will, therefore, not add significantly to the translation of the focal point. However, the focusing will be weaker for smaller eigenvalues. As a result a trade-off will have to be made, depending on if a narrow focus is desired or if a correctly located focus is more important. An iterative procedure will improve the focus. This is demonstrated in Fig. 8.

The aberration correction technique presented here is based on an energy maximization, and hence will focus the signal according to Eq. (10). The focusing properties are therefore preserved even for strong aberration.

The focus of this paper has been to show how eigenfunctions may be applied as aberration correction filters in order to improve the transmit focus for ultrasound imaging. It is obvious, however, that aberration correction also needs to be applied on the receive signal in order to form a good image. By construction, using the eigenfunction associated with the largest eigenvalue will produce the highest expected energy in the beamformer output of any aberration correction filters for the given receive signal. As the image is formed

from the envelope of this beamformer output, the filter therefore maximizes what has been referred to as *speckle brightness*.[25] Zhao and Trahey[26] have suggested using speckle brightness as an image quality factor. Using this measure, the eigenfunction will not only produce an improved transmit focus, but also result in an optimal ultrasound image, when applied for aberration correction on the received signal.

VI. CONCLUSION

Theoretical considerations of the far-field scattering pattern suggest that eigenfunctions associated with large eigenvalues of a Fredholm integral operator possess the desired focusing properties when used as an aberration correction filter. The kernel function of this operator is the covariance function of the received stochastic backscatter. In the limiting case, where the transmitted pulse is reflected from only the focal point, the operator will have only one nonzero eigenvalue, and the corresponding eigenfunction will coincide with the generalized screen model for the aberration. This is analogous to the focusing properties of eigenfunctions investigated in Refs. 13 and 14.

Scattering simulations have been presented to illustrate this property. The degree of aberration correction obtained depends on the size of the corresponding eigenvalue relative to the others.

A linear term in the phase of the eigenfunction indicates that the focal point of the corrected pulse will be shifted relative to the initially transmitted pulse. This will therefore contribute to a shift of the corrected focal point away from the intended focal point. Allowing the use of eigenfunctions with a lower eigenvalue makes it possible to reduce this movement by selecting an eigenfunction with a small linear term. This comes at the expense of the focus quality of the corrected transmit pulse. An iterative approach where the eigenfunction with smallest linear term is used in each step, will recover the lost degree of focusing, and thus give an optimal focus recovery.

ACKNOWLEDGMENTS

This work was financed, in part, by a grant from the Norwegian Research Council, and partly by the Norwegian University of Science and Technology.

[1] M. O'Donnell and S. W. Flax, "Phase-aberration correction using signals from point reflectors and diffuse scatterers: Measurements," IEEE Trans. Ultrason. Ferroelectr. Freq. Control **35**, 768–774 (1988).
[2] U. Haberkorn, G. Layer, V. Rudat, I. Zuna, A. Lorenz, and G. van Kaick, "Ultrasound image properties influenced by abdominal wall thickness and composition," J. Clin. Ultrasound **21**, 423–429 (1993).
[3] L. Hinkelman, D.-L. Liu, L. A. Metlay, and R. C. Waag, "Measurements of ultrasonic pulse arrival time and energy level variations produced by propagation through abdominal wall," J. Acoust. Soc. Am. **95**, 530–541 (1994).
[4] L. Hinkelman, T. D. Mast, L. Metlay, and R. C. Waag, "The effect of abdominal wall morphology on ultrasonic pulse distortion. I. Measurements," J. Acoust. Soc. Am. **104**, 3635–3649 (1998).
[5] G. E. Trahey, P. D. Freiburger, L. F. Nock, and D. C. Sullivan, "In-vivo measurements of ultrasonic beam distortion in the breast," Ultrason. Imaging **13**, 71–90 (1991).
[6] T. D. Mast, L. Hinkelman, M. O. V. Sparrow, and R. C. Waag, "Simulation of ultrasonic pulse propagation through the abdominal wall," J. Acoust. Soc. Am. **102**, 1177–1190 (1997).
[7] T. D. Mast, L. Hinkelman, M. Orr, and R. C. Waag, "The effect of abdominal wall morphology on ultrasonic pulse distortion. II. Simulations," J. Acoust. Soc. Am. **104**, 3651–3664 (1998).
[8] M. Fink, "Time reversal of ultrasonic fields. I. Basic prinsiples," IEEE Trans. Ultrason. Ferroelectr. Freq. Control **39**, 555–567 (1992).
[9] S. W. Flax and M. O'Donnell, "Phase-aberration correction using signals from point reflectors and diffuse scatterers: Basic prinsiples," IEEE Trans. Ultrason. Ferroelectr. Freq. Control **35**, 758–767 (1988).
[10] S. E. Måsøy, T. F. Johansen, and B. Angelsen, "Correction of ultrasonic wave aberration with a time delay and amplitude filter," J. Acoust. Soc. Am. **113**, 2009–2020 (2003).
[11] B. A. Angelsen, *Ultrasound Imaging. Waves, Signals and Signal Processing* (Trondheim, Norway, Emantec, 2000), Vol. 2, http://www.ultrasoundbook.com
[12] G. C. Ng, S. S. Worrell, P. D. Freiburger, and G. E. Trahey, "A comparative evaluation of several algorithms for phase aberration correction," IEEE Trans. Ultrason. Ferroelectr. Freq. Control **41**, 631–643 (1994).
[13] T. D. Mast, A. I. Nachman, and R. C. Waag, "Focusing and imaging using eigenfunctions of the scattering operator," J. Acoust. Soc. Am. **102**, 715–725 (1997).
[14] C. Prada, J. L. Thomas, and M. Fink, "The iterative time reversal process," J. Acoust. Soc. Am. **97**, 62–71 (1995).
[15] M. F. Hamilton and D. T. Blackstock, *Nonlinear Acoustics* (Academic, San Diego, 1997).
[16] B. A. Angelsen, in Ref. 11, Vol. 1.
[17] G. Taraldsen, "Derivation of a generalized westervelt equation for nonlinear medical ultrasound," J. Acoust. Soc. Am. **109**, 1329–1333 (2001).
[18] T. D. Mast, L. Sourian, D.-L. Liu, M. Tabei, A. Nachman, and R. C. Waag, "A *k*-space method for large-scale models of wave propagation in tissue," IEEE Trans. Ultrason. Ferroelectr. Freq. Control **48**, 341–354 (2001).
[19] L. A. Segel, *Mathematics Applied to Continuum Mechanics* (Dover, New York, 1987).
[20] R. McOwen, *Partial Differential Equations* (Prentice–Hall, Englewood Cliffs, NJ, 1996).
[21] D. L. Snyder, *Random Point Processes* (New York, Wiley, 1975).
[22] E. Kreyszig, *Introductory Functional Analysis* (Wiley, New York, 1989).
[23] D. L. Liu and R. C. Waag, "Estimation and correction of ultrasonic wavefront distortion using pulse-echo data received in a two-dimensional aperture," IEEE Trans. Ultrason. Ferroelectr. Freq. Control **45**, 473–489 (1988).
[24] T. Varslot, G. Taraldsen, T. Johansen, and B. Angelsen, "Computer simulation of forward wave propagation in non-linear, heterogeneous, absorbing tissue," in *2001 IEEE Ultrasonics Symposium Proceedings*, 2001 (unpublished), pp. 1193–1196.
[25] G. E. Trahey and S. W. Smith, "Properties of acoustical speckle patterns in the presence of phase aberration. I. First order statistics," Ultrason. Imaging **6**, 12–28 (1988).
[26] D. Zhao and G. E. Trahey, "A statistical analysis of phase aberration correction using image quality facros in coherent imaging systems," IEEE Trans. Med. Imaging **11**, 446–452 (1992).

Siamang gibbons exceed the saccular threshold: Intensity of the song of *Hylobates syndactylus*

Neil P. McAngus Todd[a] and Bjorn Merker
Department of Psychology, University of Manchester, Oxford Road, Manchester, M13 9PL, United Kingdom and Department of Psychology, Uppsala University, Box 1225, SE-75142 Uppsala, Sweden

(Received 17 November 2003; revised 26 February 2004; accepted 6 March 2004)

Measurements are reported of the intensity of the siamang gibbon loud call obtained from the vocal bouts of three family groups at Twycross Zoo, UK. Across 25 samples the maximum intensity ranged from 95 to 113 dB SPL (linear frequency-weighting and fast time-weighting) and exhibited three frequency modes of 250–315 Hz, 630–800 Hz and 1.2–1.6 kHz. The lowest frequency mode, which may correspond to the ''boom'' sound produced by resonance of the siamang inflated vocal sac, had a mean maximum intensity of 99 dB SPL. These values, which are in excess of the saccular acoustic threshold of about 90 dB at 300 Hz for air conducted sound, suggest that primate loud calls recruit a primitive mode of acoustic sensitivity furnished by the sacculus. Thus reproductive vocal behavior of primates may be influenced by a primitive acoustical reward pathway inherited from a common ancestor with anamniotes. In humans such a pathway could explain the compulsion for exposure to loud music. © *2004 Acoustical Society of America.* [DOI: 10.1121/1.1736273]

PACS numbers: 43.64.Bt, 43.64.Tk, 43.80.Ka [WA] Pages: 3077–3080

I. INTRODUCTION

In anamniotes the otoliths, and sacculus in particular, are important auditory structures, but in reptiles, birds and mammals their role has been assumed to be purely vestibular (Lewis *et al.*, 1985). An accumulating body of evidence suggests, however, that the sacculus of the inner ear has conserved an acoustic sensitivity throughout vertebrate phylogeny. For example, auditory sensitivity has been demonstrated in fish (Popper *et al.*, 1982), amphibians (Moffat and Capranica, 1976), reptiles (Lewis *et al.*, 1985), birds (Wit *et al.*, 1984) and, among mammals, in guinea-pigs (Murofushi and Curthoys, 1997), cats (McCue and Guinnan, 1995) and squirrel monkeys (Young *et al.*, 1977). The acoustically responsive fibers have irregular spontaneous discharge rates, associated with type I hair-cells, a best stimulus frequency between about 200 and 1000 Hz, and a rate threshold of about 90 dB SPL.

In humans evidence for otolithic acoustic sensitivity has been largely based on vestibular evoked myogenic potentials (VEMPs). VEMPs are produced by tonic modulation of muscles of the vestibulocollic reflex system, and may be readily evoked by acoustic stimulation (Colebatch *et al.*, 1994). In response to air-conducted (AC) clicks or tone-bursts the VEMP threshold is about 90 dBA and for tone-bursts the VEMP exhibits a tuning property with a maximum at about 300 Hz (Todd *et al.*, 2000). VEMPs also show evidence of adaptation characteristic of normal sensory processing (Todd and Cody, 2002). Recently it has been shown that for bone conducted (BC) sound the VEMP threshold, at about 30 dB above the acoustical sensation level, is considerably lower than for AC sound (Welgamola *et al.*, 2003; Todd *et al.*, 2003) with a tuning somewhat below that of the AC tuning, i.e., less than 300 Hz. The vestibulocollic basis of the VEMP has been supported by extensive single unit recordings from the vestibulo-spinal tract of various mammals, including cats and primates (Uchino *et al.*, 1997).

A question remains, however, regarding the function that might be served by a retained acoustic sensitivity of the otoliths in amniotes. One possibility is that the sacculus mediates positive affective responses to loud, low-frequency sounds via a central pathway to reward centers in the brain (Todd, 2001). Such a positive affect or reward response would be essential for vocal courtship displays to be effective. In the case of anamniotes reproductive vocal behavior involves neural pathways proceeding via a relay in the second isthmal nucleus, also associated with the secondary visceral and gustatory nuclei, to the hypothalamus and limbic structures (McCormick, 1992). In amniotes the homologue of the second isthmal nucleus is thought to be the parabrachial nucleus (Dubbeldam, 1998; ten Donkelar, 1998a, b), which also acts as a sensory relay to diencephalic structures mediating affective responses, including responses to visceral and gustatory inputs via the solitary tract. Recent physiological work has shown that there are strong vestibular projections to the parabrachial region (Balaban *et al.*, 2002), which means that in principle an acoustic saccular-parabrachial pathway is available as a candidate mechanism for mediating acoustic reward in mammals including primates. The existence of a specific saccular-parabrachial projection in humans is also supported by recent data on otolith-ocular projections which suggest that the sacculus shares a projection with the anterior canal to the contra-lateral oculomotor nucleus via the Y group nucleus and brachium conjunctivum (Todd *et al.*, 2004).

In order to further substantiate the acoustic reward hypothesis it is necessary to show that the physical parameters of mammalian reproductive vocal behavior meet the thresh-

[a]Correspondence address: MARCS Auditory Laboratories, Building 24, Bankstown Campus, University of Western Sydney, NSW 1797, Australia.

TABLE I. Intensity measures of siamang loud call.

L_{LFMax} (dB)		L_{LpkMax} (dB)		L_{Leq} (dB)		Mode1 (dB)		Duration (s)		Group
Mean	SD	Mean	SD	Mean	SD	Mean	SD	Mean	SD	
99.9	3.8	111.2	5.1	89.6	3.2	95.2	4.6	64	18.0	I ($n=8$)
108.3	3.9	120.3	2.8	94.0	2.5	105.3	6.6	111	69	II ($n=8$)
102.8	3.2	113.6	3.4	93.8	3.2	97.8	2.2	54	38	III ($n=9$)
103.6	4.9	115.0	5.3	92.4	3.5	99.4	6.2	75	51	all ($n=25$)

old and sensitivity conditions for saccular activation. The gibbons, as highly vocal primates whose loud calls play a role in territorial (Marshall and Marshall, 1976; Mitani, 1985) and reproductive behavior (Geissmann, 1999; see also Cowlishaw, 1992), are ideal subjects for this purpose. The siamang, *Hylobates syndactylus*, is the largest of the gibbon species. Its inflatable throat sac is an anatomical specialization exclusively used for song, during which the inflated sac balloons to proportions that match or exceed those of the animal's head. Its possible functions presumably include that of serving as a resonator for low-frequency components of its ''boom'' phrases during song (Tembrock, 1974; Haimoff, 1984; Hewitt *et al.*, 2002). Though the loudness of the song bouts of siamangs and other gibbons has often been remarked upon, no empirical documentation of the loudness level achieved by any gibbon species is available in the literature. In view of the relevance of this issue to the question of saccular acoustic function in mammals, the aim of the present study was to measure the physical intensity of siamang loud calls.

II. METHOD

Intensity measurements were made of vocal bouts from three siamang family groups at Twycross Zoo consisting of two bonded pairs and a larger family group of five. The animals were housed in a central ''walk-through'' one story indoor facility, from both sides of which six adjacent large wire-mesh outdoor cages, measuring 12.8 m in depth by 5.0 m in height, extended on each side. All recorded singing took place in the outdoor cages, with only wire mesh between animals and recording equipment. Since no major sound-reflective structures surrounded the recording site, the recordings were essentially free-field.

Three intensity parameters and a measure of spectral distribution were assessed by means of a B&K 2260 Investigator using a B&K 4189 free-field microphone. All measurements were taken from the cage perimeter fence 1.8 m directly in front of the cages. An animal clinging to the wire mesh directly in front of the microphone was thus at 1.8 m from the microphone, as happened in the case of the loudest recorded sound level. Typically, however, animals were at a greater and variable distance from the microphone during call bouts, which invariably are accompanied by locomotor activity in which calling animals constantly change position and orientation. Since only lower bounds on sound intensity are needed for the comparison with saccular thresholds, the obtained estimates were deemed adequate to the purpose. Eight or nine samples were taken from each of the three groups, resulting in 25 samples in total. The time duration of each sample varied considerably, depending on the specific vocal activity within a bout. The bouts lasted between 11 and 16 min.

III. RESULTS

The results of the measurements are shown in Table I. Three intensity parameters are indicated, all of which use a linear frequency-weighting: (a) L_{LFMax} the maximum value of fast time-weighted sound pressure level (SPL), a standard measure for decibel meters, (b) L_{LpkMax} the maximum value of peak intensity level and (c) L_{Leq} the equivalent continuous level. Also indicated is the L_{LFMax} value for the $\frac{1}{3}$ octave band containing the first mode (250–315 Hz) in the spectral distribution which corresponds to the boom sound, which includes resonance of the inflated siamang vocal throat sac (Haimoff, 1984). The other two modes (not indicated) correspond to the fundamental and second harmonic of the bark and female great call components of siamang song bouts. Booms and barks were the most frequent call elements in the bouts. They were performed in all parts of the song cycle, and were produced by both males and females, while so called great call elements were produced by females alone, in good agreement with previous descriptions (Haimoff, 1984; Geissmann, 1999, 2000).

IV. DISCUSSION

Ideally, a determination of the acoustic power of the gibbon or any animal would require an accurate and continuous estimate of the distance between the microphone and the vocal apparatus. Since the conditions under which gibbons emit their loud calls include obligatory locomotor displays, this would be difficult to obtain. However, given that for our purposes only lower bound estimates are required for comparison with saccular thresholds, the considerable variability in the intensity measures, contingent on variations in the distance and orientation of individual animals, can safely be disregarded, since the L_{LF} measure indicates that the entire range of 95–113 dB over all samples was above the saccular threshold. The highest value in the range was obtained from the male of group II vocalizing directly in front of the microphone at 1.8 m. During the duet the members of a pair may be in very close proximity to one another, often less than 1 m (Haimoff, 1981), and so it is reasonable to infer that the intensity experienced by an individual animal may easily equal or exceed that of our measured values and therefore exceed the saccular acoustic threshold.

The energy was concentrated in three frequency bands with modes at 250–315 Hz, 630–800 Hz and 1.2–1.6 kHz.

The lowest of these, which may correspond to the vocal sac resonance, was generally the dominant of the three with a mean intensity of 99 ± 6.2 dB. It is also very close to the region of maximum sensitivity of the sacculus for humans, but the other two modes also fall within the range of sensitivity exhibited by a range of animals. This frequency distribution taken together with the intensity measures indicates that it is very likely that saccular receptors are being acoustically activated during siamang song bouts. Further, given the proximity of the vocal sac to the skull, it is highly likely that otolithic receptors are being additionally activated via BC transmission, particularly since there may be a close matching of resonance properties of the vocal sac and the sacculus itself.

Gibbon loud calls are generally assumed to serve a dual function: as territorial advertisement to neighboring families and to maintain the pair bond. It is clear that high intensity calls are needed for the first function, to effectively broadcast over typical rainforest distances separating family groups, but it is by no means obvious why they should be required for the pair-bonding function. Partners tend to maintain physical proximity, and this is particularly true of the song bout, which is a joint vocal and behavioral display which repeatedly brings male and female into close physical proximity during the cyclical unfolding of the duet (Haimoff, 1981). It has been suggested that the loud dueting bout serves to broadcast specifically the presence of a *pair* on a territory to its extraterritorial conspecifics (Cowlishaw, 1992), but our intensity measurements allow us to add an additional basic function. As we have shown, siamang loud calls, within the interindividual distances obtaining during a pair duet, easily exceed the saccular thresholds of the dueting partners. This means that the ancient reward pathways driven by otolithic acoustic sensitivity should be activated by the vocal intensity of a siamang duet.

In anamniotes the acoustic reward pathway is specifically engaged in the vocal courtship displays of reproductive behavior (Pitcher, 1986; McCormick, 1992). It would accordingly appear to supply an ideal mechanism for introducing hedonic reward into vocal courtship of other classes of vertebrate, including primates and specifically the pair duet of siamangs and other gibbons. We therefore propose this as a basic and hitherto overlooked function of the loud calls of dueting primates, namely the stimulation of central motive states driven by an ancient system of acoustic reward conserved from a common ancestor with anamniotes. While extant species of vocal anamniotes, particularly teleost fish and anuran amphibians, are highly derived from the common ancestor with primates and have evolved radically different mechanisms for sound production, the otolithic mechanism of sound detection and the neuroanatomy of the central reward pathway have remained remarkably constant.

The essential neuroanatomical homologies of primitive acoustical reward pathways, i.e., not including input from the cochlea, were reviewed in the Introduction and extend to a system of central projections that includes the hypothalamus, prepotic and ventral tegmental areas and amygdala (Neary, 1988; McCormick, 1992). In the case of mammals the parabrachial area also projects to several cortical targets associated with reward and affective behavior including orbitofrontal, retro-olfactory and infralimbic cortex (Voogd *et al.*, 1998). A primitive acoustical reward pathway is almost certainly present in primates, as there are proven vestibular projections to the parabrachial area (Balaban *et al.*, 2002) and saccular projections through the brachium conjuctivum via the Y nucleus. Our results would suggest that it is acoustically functional in animals with vocal resources comparable to those of the siamang.

For humans a primitive acoustic reward pathway may account for the conspicuous use of loud percussive music to accompany human dancing (Todd and Cody, 2000), arguably an important part of human reproductive behavior (Todd, 2001). In this respect the gibbon is an interesting model as it is the nearest hominoid relative which shares features of a monogomous mating system with humans (Geissmann, 2000), and there is an association between loud dueting and monogamy in primates (Haimoff, 1986). While evolution has produced in all classes of vertebrate a great diversity of vocal courtship displays, loud synchronous chorusing employing amplitude summation of multiple voices may have played a special role in human evolution (Merker, 2000). With subsequent brain expansion and culture, humans would have supplemented such behavior by instruments for the generation of loud music, such as drums, which are cross-culturally ubiquitous. An apparently paradoxical aspect of the human use of loud music is why such intense sounds, which may reach harmful levels (Dibble, 1995), are not found to be aversive. The answer to this, we suggest, is to be found in the existence of a specific reward mechanism of the kind we propose, as this mechanism is also consistent with the considerable individual differences in affective responsivity to loud music (Todd, 2001; Gerra *et al.*, 1998) whereby some individuals do in fact find such sounds aversive. These individual differences can be explained in terms of inherited variations in brain dopamine activity, which is thought to be the neural substrate for variation in the trait of impulsive sensation seeking (Depue and Collins, 1999). However, more direct evidence is required to demonstrate its existence beyond doubt. One source of such evidence would be psychoneuropharmacological (Gerra *et al.*, 1998) as the above parabrachial projections involve all monaminergic transmitters, but most strongly adrenergic, noradrenergic and dompaminergic systems (Voogd *et al.*, 1998). Such an approach brings within reach noninvasive techniques for investigating responsivity of human saccular-reward pathways to acoustic stimulation.

ACKNOWLEDGMENTS

We are grateful to Twycross Zoo for permission to make the gibbon recordings and to staff members of Twycross Zoo for their assistance. We dedicate this paper to the memory of the late Maria Ujhelyi.

Balaban, C. D., McGee, D. M., Zhou, J., and Scudder, C. A. (**2002**). ''Response of primate caudal parabrachial nucleus neurons to whole body rotation,'' J. Neurophysiol. **88**, 3175–3193.

Colebatch, J. G., Halmagyi, G. M., and Skuse, N. F. (**1994**). ''Myogenic potentials generated by a click-evoked vestibulocollic reflex,'' J. Neurol., Neurosurg. Psychiatry **57**, 190–197.

Cowlishaw, G. (**1992**). ''Song function in gibbons,'' Behaviour **121**, 131–153.
Depue, R. A., and Collins, P. F. (**1999**). ''Neurobiology of the structure of personality: Dopamine, facilitation of incentive motivation and extraversion,'' Behav. Brain Sci. **22**, 491–517.
Dibble, K. (**1995**). ''Hearing loss and music,'' J. Audio Eng. Soc. **43(4)**, 251–266.
Dubbeldam, J. L. (**1998**). ''Birds,'' in *The Central Nervous System of Vertebrates, Vol. 3*, edited by R. Niewenhuys, H. J. Donkelaar, and C. Nicholson (Springer, Berlin), pp. 1525–1636.
Geissmann, T. (**1999**). ''Duet songs of the siamang, Hylobates syndactylus: II. Testing the pair-bonding hypothesis during a partner exchange,'' Behaviour **136**, 1005–1039.
Geissmann, T. (**2000**). ''Gibbon song and human music from an evolutionary perspective,'' in *The Origins of Music* edited by N. L. Wallim, B. Merker, and S. Brown (MIT, Cambridge, MA), pp. 103–123.
Gerra, A., Zaimovic, D., Franchini, M., Palladino, G., Giucastro, N., Reali, D., Maestri, R., Caccavari, R., Delsignore, R., and Brambilla, F. (**1998**). ''Neuroendocrine responses of healthy volunteers to ''techno-music:'' relationships with personality traits and emotional state,'' Int. J. Psychophysiol **28**, 99–111.
Haimoff, E. H. (**1981**). ''Video analysis of siamang (*Hylobates syndactylus*) songs,'' Behaviour **76**, 128–151.
Haimoff, E. H. (**1984**). ''Acoustic and organizational features of gibbon songs,'' in *The Lesser Apes: Evolution and Behavioural Biology*, edited by H. Preuschoft, D. J. Chivers, W. Y. Brockleman, and N. Creel (Edinburgh U.P., Edinburgh,), pp. 333–353.
Haimoff, E. H. (**1986**). ''Convergence in the duetting of monogamous Old World primates,'' J. Hum. Evol. **15**, 51–59.
Hewitt, G., MacLarnon, A., and Jones, K. (**2002**). ''The functions of laryngeal air sacs in primates: A new hypothesis,'' Folia Primatologica **73**, 70–94.''
Lewis, E. R., Leverenz, E., and Bialek, W. (**1985**). *The Vertebrate Inner Ear* (CRC, Boca Raton).
Marshall, J., and Marshall, F. (**1976**). ''Gibbons and their territorial songs,'' Science **193**, 235–237.
McCormick, C. A. (**1992**). ''Evolution of central auditory pathways in anamniotes,'' in *The Evolutionary Biology of Hearing*, edited by D. B. Webster, R. R. Fay, and A. N. Popper (Springer-Verlag, New York), pp. 323–350.
McCue, M., and Guinan, J. (**1995**). ''Spontaneous activity and frequency selectivity of acoustically responsive vestibular afferents in the cat,'' J. Neurophysiol. **74**(4), 1563–1572.
Merker, B. (**2000**). ''Synchronous chorusing and human origins,'' in *The Origins of Music*, edited by N. L. Wallin, B. Merker, and S. Brown (MIT, Cambridge, MA), pp. 315–327.
Murofushi, T., and Curthoys, I. S. (**1997**). ''A physiological and anatomical study of click-sensitive primary vestibular neurons in guinea pigs,'' Acta Otolaryngol. (Stockh) **117**, 66–72.
Mitani, J. C. (**1985**). ''Gibbon song duets and intergroup spacing,'' Behaviour **92**, 59–96.
Moffat, A., and Capranica, R. (**1976**). ''Auditory sensitivity of the sacculus in the American toad (*Bufo americanus*),'' J. Comp. Physiol. **105**, 1.
Neary, T. J. (**1988**). ''Forebrain auditory pathways in Ranid frogs,'' in *The Evolution of the Amphibian Auditory System*, edited by B. Fritzch, M. J. Ryan, W. Wilcynski, T. E. Hetherington, and W. Wilkowiak (Wiley, New York), pp. 233–352.
Pitcher, T. J. (**1986**). *Behavior of Teleost Fish* (Chapman and Hall, London).
Popper, A., Platt, C., and Saidal, W. (**1982**). ''Acoustic functions in the fish ear,'' Trends Neurosci. **August**, 276–280.
Tembrock, G. (**1974**). ''Sound production in *Hylobates and Symphalangus*,'' in *Gibbon* and *Siamang*, Vol. 3 edited by D. M. Rumbaugh (Karger: Basel), pp. 176–205.
ten Donkelaar, H. J. (**1998a**). ''Anurans,'' in *The Central Nervous System of Vertebrates, Vol 2*, edited by R. Niewenhuys, H. J. Donkelaar, and C. Nicholson (Springer, Berlin), pp. 1151–1314.
ten Donkelaar, H. J. (**1998b**). ''Reptiles,'' in *The Central Nervous System of Vertebrates, Vol. 2*, edited by R. Niewenhuys, H. J. Donkelaar, and C. Nicholson (Springer, Berlin), pp. 1315–1524.
Todd, N. P. McAngus (**2001**). ''Evidence for a behavioral significance of saccular acoustic sensitivity in humans,'' J. Acoust. Soc. Am. **110**, 380–390.
Todd, N. P., McAngus, and Cody, F. W. (**2000**). ''Vestibular responses to loud dance music: a physiological basis for the 'rock 'n' roll threshold?' '' J. Acoust. Soc. Am. **107**, 496–500.
Todd, N. P. McAngus, and Cody, F. W. (**2002**). ''Adaptation in saccular acoustical responses,'' Int. J. Audiol. **41**, 236.
Todd, N. P. McAngus, Cody, F. W. J., and Banks, J. R. (**2000**). ''A saccular origin of frequency tuning in myogenic vestibular evoked potentials?: implications for human responses to loud sounds,'' Hear. Res. **141**, 180–188.
Todd, N. P. McAngus, Rosengren, S. M., and Colebatch, J. C. (**2003**). ''A short latency vestibular evoked potential (VsEP) produced by bone-conducted acoustic stimulation,'' J. Acoust. Soc. Am. **114**, 3264–3272.
Todd, N. P. McAngus, Rosengren, S. M., and Colebatch, J. C. (**2004**). ''Vestibular evoked ocular responses to air- (AC) and bone-conducted (BC) acoustic stimulation II: A neuroanatomical and physiological interpretation of AC ocular vestibular evoked myogenic potentials (OVEMPs),'' J. Vestibular Res. 14.
Uchino, Y., Sato, H., Sasaki, M., Imagawa, M., Ikegemi, H., Isu, N., and Graf, W. (**1997**). ''Sacculo-collic reflex arcs in cats,'' J. Neurophysiol. **77**, 3003–3012.
Voogd, J., Niewenhuys, R., van Dongen, P. A. M., and ten Donkelaar, H. J. (**1988**). ''Mammals,'' in *The Central Nervous System of Vertebrates, Vol. 3*, edited by R. Niewenhuys, H. J. Donkelaar, and C. Nicholson (Springer, Berlin), pp. 1637–2098.
Welgampola, M. S., Rosengren, S. M., Halmagyi, G. M., and Colebatch, J. C. (**2003**). ''Vestibular activation by bone-conducted sound,'' J. Neurol. Neurosurg. Psychiatry **74**, 771–778.''
Wit, H., Bleeker, J., and Mulder, H. (**1984**). ''Response of pigeon vestibular nerve fibres to sound and vibration with audio frequencies,'' J. Acoust. Soc. Am. **75**, 202–208.
Young, E., Fernandez, C., and Goldberg, J. (**1977**). ''Responses of squirrel monkey vestibular neurons to audio-frequency sound and head vibration,'' Acta Oto-Laryngol. **84**, 352–360.

Similarity in loudness and distortion product otoacoustic emission input/output functions: Implications for an objective hearing aid adjustment

Jörg Müller and Thomas Janssen[a)]
Hals-Nasen-Ohrenklinik, Technische Universität München, Ismaningerstraße 22, D-81675 Munich, Germany

(Received 15 December 2003; revised 5 March 2004; accepted 13 March 2004)

The aim of the present study was to compare distortion product otoacoustic emissions (DPOAEs) to loudness with regard to the potentiality of DPOAEs to determine characteristic quantities of the cochlear-impaired ear and to derive objective hearing aid parameters. Recently, Neely *et al.* [J. Acoust. Soc. Am. **114**, 1499–1507 (2003)] compared DPOAE input/output functions to the Fletcher and Munson [J. Acoust. Soc. Am. **5**, 82–108 (1933)] loudness function finding a close resemblance in the slope characteristics of both measures. The present study extended their work by performing both loudness and DPOAE measurements in the same subject sample, and by developing a method for the estimation of gain needed to compensate for loss of cochlear sensitivity and compression. DPOAEs and loudness exhibited similar behavior when plotted on a logarithmic scale and slope increased with increasing hearing loss, confirming the findings of Neely *et al.* To compensate for undesired nonpathological impacts on the magnitude of DPOAE level, normalization of DPOAE data was implemented. A close resemblance between gain functions based on loudness and normalized DPOAE data was achieved. These findings suggest that DPOAEs are able to quantify the loss of cochlear sensitivity and compression and thus might provide parameters for a noncooperative hearing aid adjustment. © *2004 Acoustical Society of America.*
[DOI: 10.1121/1.1736292]

PACS numbers: 43.64.Jb, 43.64.Yp, 43.66.Cb [BLM] Pages: 3081–3091

I. INTRODUCTION

In normal-hearing ears, the auditory system behaves nonlinearly. From animal data it is known that the mechanical response of the basilar-membrane (BM) is compressive in order to extend the dynamic range of sound (Rhode, 1971; Johnstone *et al.*, 1986; Ruggero *et al.*, 1997). At low stimulus levels close to threshold, the response grows approximately linearly and becomes compressive at moderate to high levels. The compressive sound processing is basically due to the nonlinear level-dependent amplification of BM displacement executed by the outer hair cell (OHC) system (Dallos, 1992). The OHC system is known to be vulnerable to different influences, such as intense sound exposure (Zhang and Zwislocki, 1995) or salicylate overdose (Russell and Schauz, 1995). OHC dysfunction is accompanied by threshold elevation and loss of compression. There is also evidence that the human auditory system behaves comparably. Nonlinear behavior of the human cochlea can be observed in both objective and subjective measurements.

An objective and noninvasive measurement procedure giving evidence of the nonlinear cochlear function in humans is the recording of distortion product otoacoustic emission (DPOAE) input/output (I/O) functions. DPOAEs are sound emissions apparently produced by the OHC system (Brownell, 1990) in response to a two-tone stimulation. DPOAE I/O functions show compressive behavior for normal-hearing subjects and gradually increasing linear behavior as hearing loss increases (Janssen *et al.*, 1998; Kummer *et al.*, 1998; Neely *et al.*, 2003). These observations suggest that DPOAEs could be a reliable measure to diagnose dysfunctions of sound processing on the OHC level and to quantify the resulting loss of sensitivity and compression.

Psychoacoustic experiments, including measurements based on behavioral masking data (Oxenham and Plack, 1997), loudness matching procedures (Steinberg and Gardner, 1937; Schlauch *et al.*, 1998; Moore *et al.*, 1999), and absolute loudness measurements (Hellman and Meiselman, 1990, 1993; Launer, 1995) also support the thesis of nonlinear cochlear behavior in normal-hearing ears and linearized behavior in ears with OHC dysfunction. All these studies show that loudness behavior bears a good resemblance to BM characteristics, exhibiting compressive loudness functions for normal-hearing subjects and steeper, less compressive loudness functions for hearing-impaired subjects (recruitment). Consequently, the BM action and thus the influence of the OHC system seems to affect the form of the loudness function (Yates *et al.*, 1990), even if there might be other more complex influences in the eventual loudness encoding process (Relkin and Doucet, 1997; Moore and Glasberg, 2004).

Altogether, both DPOAEs and loudness are supposed to be influenced by BM displacement and thus by the OHC function and therefore provide an insight into cochlear sound processing in humans. However, any inner hair cell damage or dysfunctions on the neural level that have an influence on loudness sensation can not be recognized with DPOAEs. On account of this, it seems to be reasonable to compare objective DPOAE with subjective loudness measurements in order

[a)]Author to whom correspondence should be addressed. Electronic mail: t.janssen@lrz.tum.de

to examine the possibility of using DPOAE I/O functions as a means of estimating loudness in ears with a hearing loss related to OHC damage. Since loudness estimates are used among other measurements for hearing aid fitting, DPOAEs would then offer the potentiality of basic hearing aid adjustment especially for non-cooperative patients such as children or mentally retarded people for whom subjective measurements are not practicable.

Neely *et al.* (2003) already showed that there is some correlation between DPOAEs and loudness. They compared the Fletcher and Munson (1933) loudness function with DPOAE growth functions both plotted on a logarithmic scale, basically focusing on an absolute comparison of compression in normal-hearing subjects. This study showed that both the Fletcher and Munson loudness function and the averaged DPOAE I/O data in normal-hearing subjects could be described by similar log functions resulting in equal compression. They concluded that this suggests that the same source of nonlinearity determines the growth of both I/O functions. Also DPOAE I/O functions of hearing-impaired subjects were recorded to show that the slope of DPOAE growth functions gradually increased with advancing hearing loss. However, interindividual variability was reported to be quite high. Consequently, the authors stated that individual predictions of loudness might be difficult.

The present study extended the work of Neely *et al.* (2003) by measuring and comparing both loudness and DPOAE I/O functions in the same subject sample. This includes (*i*) the application of a uniform measurement system and sound probe for loudness and DPOAE measurements, (*ii*) the measurement of loudness and DPOAE I/O functions in normal-hearing and hearing-impaired subjects, (*iii*) the application of categorical loudness scaling (CLS) (Pascoe, 1978; Heller, 1985; Allen *et al.*, 1990; Hohmann and Kollmeier, 1995; Kollmeier, 1997; Madsen, 2000; Brand and Hohmann, 2002) for loudness measurements, and (*iv*) relative comparisons between data of normal-hearing and hearing-impaired subjects.

The main purpose of the present study was to examine the correlation between DPOAE and loudness in normal-hearing and hearing-impaired subjects and hence to investigate the practicability of using DPOAE I/O functions as a means of fundamental hearing aid adjustment.

II. METHODS

A. Subjects

Ten subjects with normal hearing and nine patients suffering from moderate hearing loss participated in the present study. Data was collected only from one ear per subject. The normal-hearing subjects (seven male, three female) were aged between 25 and 30 years. Measurements were conducted at 2, 3, 3.5 and 4 kHz. According to clinical audiometry their hearing loss was 15 dB HL or lower in the examined frequency range. Hearing loss at 3.5 kHz was derived from interpolation between 3 and 4 kHz since it is not an audiometer frequency. The patients (six male, three female) were aged between 14 and 67 years and were examined at at least one of the test frequencies used with normal-hearing subjects, depending on the possibility to get suitable DPOAE I/O functions. Hearing losses ranged from 20 to 45 dB HL, exclusively regarding the hearing loss at the individual frequencies which were used in the measurement procedure on each subject. Hearing loss was presumably due to cochlear defect considering clinical history, tympanometry, and auditory brainstem response measurements, which excluded middle ear and retrocochlear disorders.

B. Stimulus generation

DPOAE and categorical loudness scaling (CLS) measurements were conducted with the same hardware and sound probe (Etymotic Research ER-10C) based on a commercial DPOAE measurement system (Starkey DP2000), using custom-made software. For CLS measurements, an additional customized amplifier was used to generate high-level sine signals of up to 100 dB SPL. Signal levels were adjusted according to a modified constant voltage calibration strategy since the commonly used in-the-ear-calibration was expected to result in enormous variances in sound pressure level due to standing wave problems (Siegel, 1994; Whitehead *et al.*, 1995, Neely and Gorga, 1998). For the applied calibration strategy the frequency transfer function of the ear probe loudspeaker was recorded in an ear simulator (Brüel & Kjær Type 4157). The distance between the ER-10C ear tip and the microphone of the B & K ear simulator amounted to 25 mm. This transfer function was then used as a reference curve. To account for the individual ear canal volume the reference curve was shifted corresponding to the difference to the individual transfer function at 1 kHz. This frequency was chosen because resonance effects in the ear canal are smallest at low frequencies. This strategy is also not free of errors, but is expected to cause less calibration errors in the test frequency range than in-the-ear-calibration (Whitehead *et al.*, 1995).

C. DPOAE measurement procedure

DPOAEs were elicited in response to a stimulation with two primary tones. Their frequency ratio was $f_2/f_1=1.2$ for all test conditions. The primary tone levels L_1 and L_2 were set according to the equation $L_1=0.4\,L_2+39$ dB (Janssen *et al.*, 1995; Kummer *et al.*, 2000). This level setting was used to account for the nonlinear interaction of the two primaries at the DPOAE generation site at the f_2 place. The assumption of the f_2 place as main DPOAE generation site is supported by the fact that DPOAE iso-suppression tuning curves have their characteristic frequencies at f_2 when using $L_1=0.4\,L_2+39$ dB (Kummer *et al.*, 1995; Gorga *et al.*, 2003b). L_2 was set to a maximum of 65 dB SPL and was decreased in 5-dB steps to a minimum of 20 dB SPL. The averaging time for recording DPOAEs was set to 4 s. DPOAEs were accepted as valid for a signal-to-noise ratio exceeding 6 dB. If a DPOAE value failed to fulfill this criterion, the measurement of this point in the DPOAE I/O function was repeated up to three times. Each measurement of a complete DPOAE I/O function for a specific frequency was repeated twice (for three patients with qualitatively good DPOAE I/O functions the measurement was just conducted

once) in order to get both general information about repeatability and to increase certainty in the decision to erase outliers or inconsistent data.

Outliers were defined as (i) data that were at least 10 dB above the adjoining lower and upper DPOAE levels or (ii) data that occurred below L_2 levels at which no valid data could have been measured. Inconsistent data were defined either as (i) data that led to a local negative slope of the DPOAE I/O function in the upper L_2 region or (ii) data that resulted in a relative local increase of slope in the lower L_2 region and which often ran parallel to the course of the noise floor. All in all, in the normal-hearing group 46 values (5.8%) and in the hearing-impaired group 40 values (17.4%) were excluded from further analysis.

D. CLS measurement procedure

In general, a problem which arises in studying loudness of sounds is that loudness is a subjective quantity, and as such can not be directly related to the physical magnitude of sound pressure level. There are different methods of achieving loudness evaluations in humans, including absolute magnitude estimation (Stevens, 1957), relative magnitude estimation (Hellman and Zwislocki, 1961), relative loudness production (Geiger and Firestone, 1933; Zwicker, 1958), and categorical loudness scaling (CLS) (Pascoe, 1978; Heller, 1985; Allen *et al.*, 1990; Hohmann and Kollmeier, 1995; Kollmeier, 1997; Madsen, 2000; Brand and Hohmann, 2002). The last one was finally chosen for this study, since it is a method that is relatively simple and thus easy to understand for inexperienced subjects. Furthermore, the CLS is applied in clinical examinations as a tool for hearing aid adjustment.

For the categorical loudness scaling (CLS), sine tone signals with a frequency at f_2 were used in order to assure best possible comparability to DPOAE measurements. Before the actual subjective estimation process was started, the individual maximal tolerable level was determined in a premeasurement phase to ensure that the subject was not exposed to levels that would cause any painful sensation. The lowest level was always set to 0 dB SPL. For the actual CLS measurement procedure all stimulus levels from 0 dB SPL in steps of 5 dB to maximal 100 dB SPL were presented three times in random order. The length of the stimulus was 1 s. Frequencies were tested successively. The response scale consisted of 11 response alternatives, partly titled with common language expressions for loudness. Five categories were labeled ''very quiet,'' ''quiet,'' ''medium volume,'' ''loud,'' and ''very loud.'' Between two adjoining verbal categories there was always one unnamed response alternative to enlarge the number of possible choices. Additionally, the limiting response alternatives were titled ''inaudible'' and ''extremely loud.'' All category buttons were presented on screen as horizontal pushbuttons with increasing width from ''inaudible'' to ''extremely loud'' (Hohmann and Kollmeier, 1995). For numeral representation loudness categories were associated with numbers from 0 (''inaudible'') to 50 (''extremely loud'') in steps of 5 and were labeled with the dimension categorical unit (CU) (Kollmeier, 1997). Moreover, a ''repeat'' button was available to replay the last signal. The subjects were instructed to use this button only if necessary and to evaluate the presented signals as spontaneously as possible on the given scale, pressing the category button which best agreed with the elicited loudness sensation. Moreover, all subjects were asked to evaluate loudness perception as far as possible independently of the previously offered signals, merely considering absolute loudness sensation.

Data were analyzed and outliers removed. Outliers were defined as (i) data that were at a certain stimulus level at least three categories away from the median at that level and at least two categories above/below the maximal/minimal categorical value at the adjoining upper/lower stimulus level and (ii) data that were categorized as audible even if there were exclusively ''inaudible'' estimates at at least two higher stimulus levels. Altogether, in the normal-hearing group six values (0.2%) and in the group of hearing-impaired subjects seven values (0.8%) were discarded.

III. RESULTS

A. Normative data

Discrete DPOAE and categorical loudness scaling (CLS) data of all ten normal-hearing subjects were averaged separately for each frequency to obtain normative I/O functions. These functions were then used for comparisons to single frequency-specific I/O functions of hearing-impaired subjects. For both DPOAE and CLS data averaging was done throughout for each input level.

1. DPOAE

Figure 1(a) shows average DPOAE sound pressure levels as a function of L_2 for each test frequency (2, 3, 3.5, 4 kHz) for the normal-hearing group. All I/O functions, independent of test frequency, had a similar compressive shape [compression ($=1$/slope) for extrapolated I/O functions at $L_2=65$ dB SPL for 2 kHz: 5.5 dB/dB, 3 kHz: 5.6 dB/dB, 3.5 kHz: 6.1 dB/dB, and 4 kHz: 5.9 dB/dB, mean across all frequencies: 5.8 dB/dB] and were mainly different in respect to absolute DPOAE levels. It is important to note that the shift ΔL_{dp} of a DPOAE I/O function presented in a logarithmic scale [Fig. 1(a)] is, as shown in Eq. (1), equivalent to a multiplication with a factor k of the DPOAE I/O function plotted in a linear scale [Fig. 1(c)]:

$$\log(p_{dp}\cdot k)=\log(p_{dp})+\log(k)=L_{dp}+\Delta L_{dp},$$
$$\Delta L_{dp}=\log(k). \tag{1}$$

Thus, the slope of the DPOAE I/O function in a linear plot is highly contingent on the magnitude of the DPOAEs in a logarithmic plot. Since influences on DPOAE magnitude other than OHC damage, e.g., ear canal length, middle ear impedance, individual cochlear conditions, or calibration errors, can not be excluded, DPOAE data were normalized. Normalization was executed by setting the maximum value of a DPOAE I/O function, which was located at the maximal stimulus level ($L_2=65$ dB SPL), to a defined value, e.g., to the maximal DPOAE level of one of the DPOAE I/O functions used for relative comparison. The result of this procedure applied to the DPOAE I/O functions from Fig. 1(a) is shown in Fig. 1(b). Please note that all DPOAE I/O functions

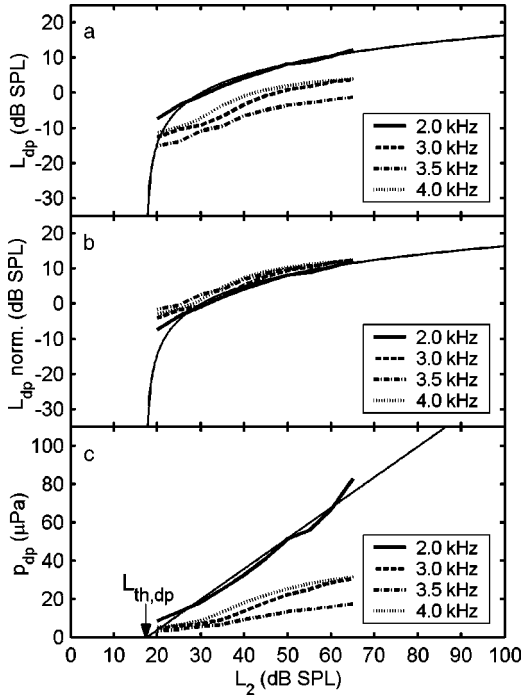

FIG. 1. DPOAE I/O functions for 2, 3, 3.5, and 4 kHz for the normal-hearing group. Panel (a) shows DPOAE data in logarithmic scale, panel (b) normalized DPOAE data in logarithmic scale, and panel (c) DPOAE data in linear scale. $L_{th,dp}$ in panel (c) shows the DPOAE threshold level, which serves as an estimate for hearing threshold. In each panel bold lines represent discrete DPOAE data, the single thin line exemplifies the linear DPOAE data extrapolation for 2 kHz.

in logarithmic scale still have the same shape and thus the same compression as in Fig. 1(a), but now coincide at $L_2 = 65$ dB SPL.

Moreover, linear extrapolation lines were fitted to the discrete mean DPOAE data given in sound pressure p_{dp}. This linear fitting procedure was established as a means of objective hearing threshold estimation by Boege and Janssen (2002) and was confirmed and improved by further studies (Gorga *et al.*, 2003a; Oswald and Janssen, 2003). These studies showed that for most DPOAE I/O functions a linear fit is an adequate approximation of DPOAE behavior, presupposed DPOAEs are elicited with an optimal parameter setting (Janssen *et al.*, 1995; Kummer *et al.*, 2000). Examples of extrapolation curves are shown for the 2-kHz test frequency in logarithmic [Figs. 1(a) and (b)] as well as in linear [Fig. 1(c)] DPOAE scale. The estimated DPOAE threshold level $L_{th,dp}$ was defined as the stimulus level L_2 at which the linear extrapolation equals $p_{dp} = 0$ Pa [Fig. 1(c)] or at which the linear extrapolation curve transformed into logarithmic presentation equals $L_{dp} = -\infty$ [compare Figs. 1(a) and (b)]. It is important to note that the hearing threshold estimation is independent of normalization, since a multiplication with a constant factor k [see Eq. (1)] results in a rotation of the linearly scaled DPOAE I/O function around the rotation point at $p_{dp} = 0$ Pa, which remains zero when multiplied with any factor.

The standard deviation of the DPOAE level L_{dp} (not shown) across all individual mean DPOAE I/O functions (interindividual repeatability) of the normal-hearing group was on an average 6.4 dB but amounted dependent on frequency

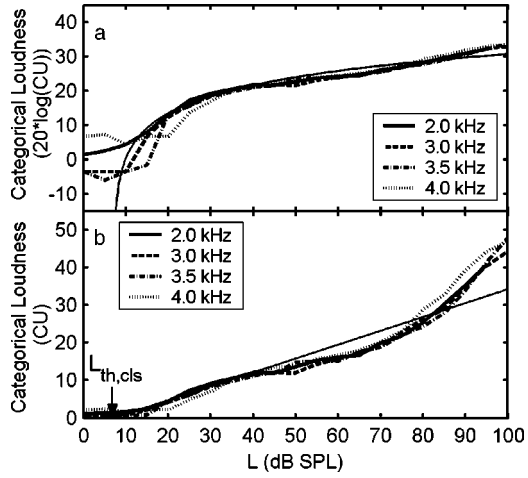

FIG. 2. CLS I/O functions for 2, 3, 3.5, and 4 kHz for the normal-hearing group. Panel (a) shows CLS data in logarithmic scale, panel (b) CLS data in linear scale. $L_{th,cls}$ in panel (b) shows the CLS threshold level, which serves as an estimate for hearing threshold. In each panel bold lines represent discrete CLS data, the single thin line exemplifies the linear CLS data extrapolation for 2 kHz.

and level to more than 10 dB. In contrast, the average difference of DPOAE level between two successive measurement runs in one subject (intraindividual repeatability) was only 0.8 dB. The compression at $L = 65$ dB SPL of the individually extrapolated DPOAE I/O function of each normal-hearing subject plotted in a logarithmic scale ranged between 3.9 and 8.9 dB/dB (mean: 5.9 dB/dB, standard deviation: 1.2 dB/dB).

2. CLS

Figure 2 shows CLS data averaged across the normal-hearing subjects. Categorical loudness is plotted as a function of the stimulus level L in the commonly used linear (categorical loudness in CU) [Fig. 2(b)] and in logarithmic scale [categorical loudness in $20 \cdot \log(\mathrm{CU})$] [Fig. 2(a)]. The unusual logarithmic plot was chosen to better visualize the similar behavior of loudness functions in comparison to DPOAE I/O functions plotted in logarithmic scale. All CLS I/O functions, independent of frequency, had in logarithmic presentation a similar compressive shape (compression for extrapolated I/O functions at $L = 65$ dB SPL for 2 kHz: 6.7 dB/dB, 3 kHz: 6.3 dB/dB, 3.5 kHz: 6.2 dB/dB, and 4kHz: 6.2 dB/dB, mean across all frequencies: 6.3 dB/dB) and approximately equal absolute loudness values.

Linear extrapolation lines were fitted to the average CLS values given in a linear scale. There would also have been other strategies for extrapolating CLS data (e.g., two extrapolation lines for different level sections or polynomial of second order), but linear extrapolation was chosen to provide best possible comparability to linear DPOAE I/O function extrapolation. For the calculation of linear extrapolation lines, mean values equal zero were excluded in order to avoid the flattening of extrapolation lines dependent on the number of levels which were exclusively rated ''inaudible.'' An example of linear extrapolation is shown for the 2-kHz test frequency for categorical loudness in linear scale [Fig. 2(b)] and transferred to logarithmic scale [Fig. 2(a)]. The

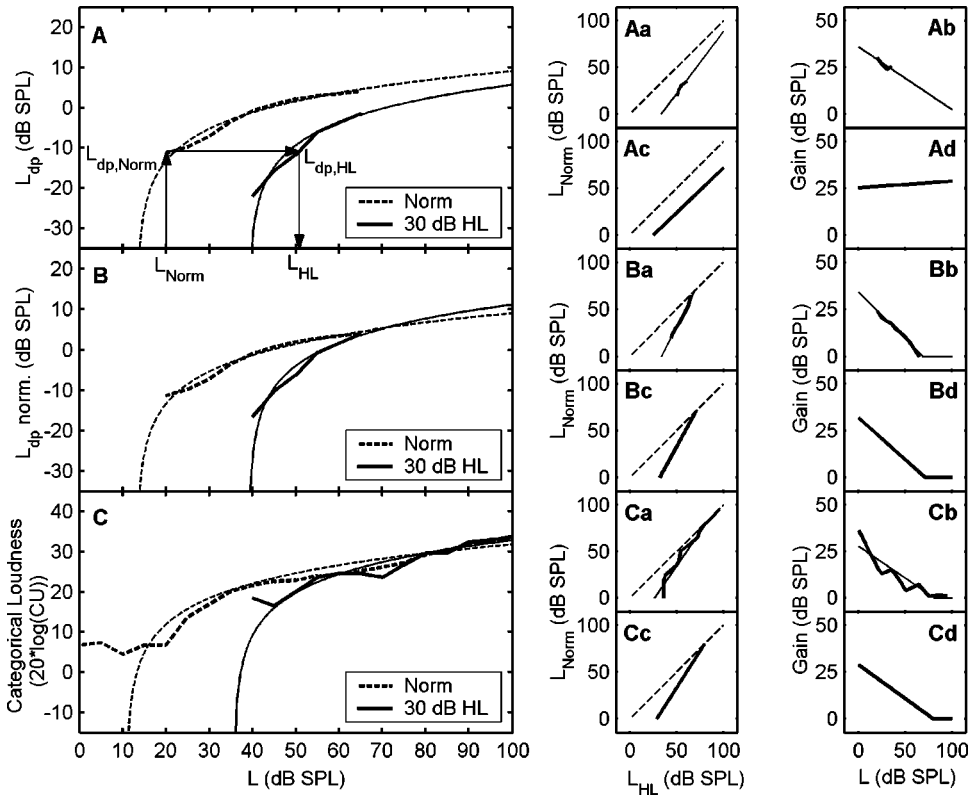

FIG. 3. Data of case example P1 with a hearing loss of 30 dB HL at 4 kHz is shown in comparison to normative data. Panel (A) shows DPOAE, panel (B) normalized DPOAE, and panel (C) CLS data on a logarithmic scale. Bold lines represent discrete, thin lines extrapolated data. Panels (Aa), (Ba), and (Ca) show discrete values of L_{Norm} plotted above L_{HL} (relative growth function) for the respective discrete measuring data (bold solid lines) and extrapolations of the discrete relative growth functions (thin solid lines). Panels (Ac), (Bc), and (Cc) show relative growth functions for the respective extrapolated measuring data (bold solid lines). The thin dashed lines represent the respective normative function $L_{Norm}=L_{HL}$. Panels (Ab), (Bb), and (Cb) show gain functions for the respective discrete measuring data (bold solid lines) and extrapolations of the discrete gain functions (thin solid lines). Panels (Ad), (Bd), and (Cd) show gain functions for the respective extrapolated measuring data.

estimated CLS threshold level $L_{th,cls}$ was defined analogously to the DPOAE approach as the stimulus level L at which the extrapolation line equals 0 CU [Fig. 2(b)] or at which the linear extrapolation transformed into logarithmic presentation equals a logarithmic categorical loudness value of $-\infty$ [compare Fig. 2(a)].

Standard deviations of categorical loudness in a linear plot (not shown) across individual mean CLS I/O functions (interindividual repeatability) were calculated for the normal-hearing group. On an average across all levels it amounted to 3.0 CU and was thus lower than one category step. In contrast, the average difference between the maximal and minimal categorical loudness value at a certain level for three repetitive measurements in one subject (intraindividual repeatability) amounted to 4.2 CU. The compression at $L=65$ dB SPL of the individually extrapolated CLS I/O functions of each normal-hearing subject plotted in a logarithmic scale ranged between 3.6 and 8.1 dB/dB (mean: 6.0 dB/dB, standard deviation: 0.9 dB/dB).

When comparing extrapolations of normative CLS and DPOAE data presented on a logarithmic scale, a close correspondance was apparent, even if the exemplarily presented threshold estimates at the test frequency of 2 kHz differed about 10 dB [compare the intersection points with the stimulus level axis $L_{th,dp}$ in Fig. 1(c) for DPOAE and $L_{th,cls}$ in Fig. 2(b) for CLS]. On average across all test frequencies, the threshold level estimates $L_{th,dp}$ and $L_{th,cls}$ of the normative functions differed about 5 dB (not shown are the differences $L_{th,dp}-L_{th,cls}$ at 3 kHz: 6 dB, 3.5 kHz: 1 dB, and 4 kHz: 2 dB). Moreover, the compression values of the extrapolated normative CLS and DPOAE I/O functions were quantitatively very similar to each other and differed on average only 0.5 dB/dB. Regarding individual DPOAE and CLS I/O functions of each normal-hearing subject, compression was for both measures in a similar range with an average difference between DPOAE and CLS compression of only 0.2 dB/dB but with a standard deviation of 1.6 dB/dB.

B. Hearing loss case examples

1. Comparison of DPOAE and CLS data

Two hearing loss case examples and their respective DPOAE [Figs. 3(A) and 4(A)], normalized DPOAE [Figs. 3(B) and 4(B)] and CLS [Figs. 3(C) and 4(C)] data are presented in comparison to normative data (compare Figs. 1 and 2). Patient P1 was afflicted with a hearing loss of 30 dB HL at 4 kHz [Figs. 3(A)–(C)], while patient P2 suffered from a hearing loss of 45 dB HL at 3 kHz [Fig. 4(A)–(C)]. Bold lines in the figures symbolize discrete, thin lines extrapolated data.

DPOAE I/O functions were for both hearing-impaired subjects (solid lines) in comparison to normative data (dashed lines) less compressive, consequently steeper and also lower in respect to absolute DPOAE levels [Figs. 3(A) and 4(A)]. The described effects were more distinct in patient P2, reflecting the higher hearing loss for this patient. The compression of the extrapolated I/O functions at $L_2=65$ dB SPL amounted to 3.0 dB/dB (P1), respectively 2.2 dB/dB (P2), whereas the absolute difference in DPOAE level at $L_2=65$ dB SPL in comparison to the respective normative I/O function amounted to 5.5 dB (P1), respectively 7.2 dB (P2). Normalization of DPOAE I/O functions was executed to compensate for these deviations [Figs. 3(B) and 4(B)]. The estimated hearing thresholds $L_{th,dp}$ due to linear extrapolation of DPOAE data were for the hearing-impaired subjects 39 dB SPL (P1) and 46 dB SPL (P2). Presupposed

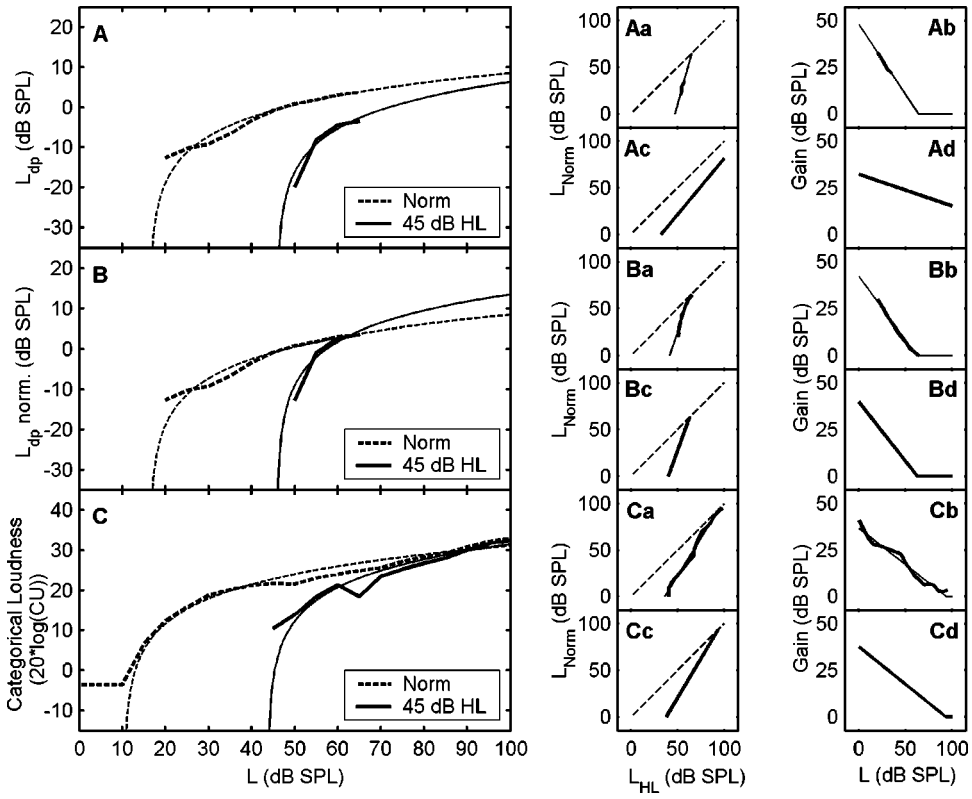

FIG. 4. Data of case example P2 with a hearing loss of 45 dB HL at 3 kHz is shown in comparison to normative data. For the meaning of each panel see the descriptions in Fig. 3.

that in the regarded frequency range dB SPL is approximately equal to dB HL, the DPOAE threshold level estimates were with a difference of 9 dB (P1) and 1 dB (P2), especially for patient P2 very close to the respective audiogram hearing threshold.

CLS I/O functions for both hearing-impaired subjects were less compressive than the normative functions [Figs. 3(C) and 4(C)]. As for DPOAE data, the effects were more distinct in the case of example P2. The compression of the extrapolated I/O functions at $L=65$ dB SPL amounted to 3.4 dB/dB (P1) and 2.4 dB/dB (P2). The discrete CLS values for the hearing-impaired patients above about $L=55$ dB SPL (P1), respectively $L=90$ dB SPL (P2), were of similar magnitude as for the average normal-hearing subject. The estimated hearing thresholds $L_{th,cls}$ due to linear extrapolation of CLS data were for the hearing-impaired subjects 36 dB SPL (P1) and 44 dB SPL (P2). Once again making use of the assumption that in the studied frequency range dB SPL is very close to dB HL, the CLS threshold level estimates exhibited a good resemblance to the respective audiogram hearing thresholds with a difference of 6 dB (P1) and -1 dB (P2).

All in all, for both patients DPOAE and CLS behavior were qualitatively similar. Both DPOAE and CLS data for both patients showed a steeper, less compressive course of the I/O functions in comparison to normative data. For DPOAE and CLS data this effect was more distinct in patient P2 with the greater hearing loss. For both hearing-impaired subjects, compression and hearing threshold estimates were similar when obtained by extrapolated CLS and DPOAE I/O functions. Compression differences between extrapolated CLS and DPOAE I/O functions at $L_2=65$ dB SPL were with 0.4 dB/dB (P1) and 0.2 dB/dB (P2) quite low and estimated threshold level differences $L_{th,dp}-L_{th,cls}$ amounted to only 3 dB (P1) and 2 dB (P2).

2. Estimation of gain for compensating loss of sensitivity and compression

The normal-hearing and the hearing-impaired subjects were compared relatively to each other for both DPOAE and CLS data. The chosen procedure for comparison was derived from a strategy used by Steinberg and Gardner (1937).

The basic steps in the procedure of comparison are illustrated for discrete DPOAE data in Fig. 3(A). The approach for CLS and extrapolated data is analogous to this. For each stimulus level, designated as L_{Norm}, the respective corresponding DPOAE level of the normal-hearing group $L_{dp,Norm}$ was compared to the DPOAE level data of the hearing-impaired subject in order to find the stimulus level, designated as L_{HL}, that was required to elicit the same DPOAE level $L_{dp,HL}$ $(=L_{dp,Norm})$ in the hearing-impaired subject. For comparing discrete data, linear interpolation was used, because discrete numerical DPOAE and CLS values were usually not identical for the normal-hearing group and the hearing-impaired subject. So, in most cases no exact matches would have been found without interpolation. Moreover, if there was no unequivocal decision due to several possible matches in the data of the hearing-impaired subject (this situation occurred if data were not monotonically increasing), the corresponding L_{Norm} value was skipped. All valid data are displayed in a graph with L_{Norm} plotted above L_{HL} [Fig. 3(Aa)]. Both discrete values (bold solid line) and the extrapolation line calculated on the basis of these discrete values (thin solid line) are shown. These functions, which are in the following referred to as relative growth functions, vi-

sualize the relative growth behavior of the I/O function of the hearing-impaired subject in comparison to the normative I/O function, which is in this plot displayed by the function $L_{Norm}=L_{HL}$ (dashed line). The deviation $L_{HL}-L_{Norm}$, which represents the level-dependent gain for hearing aid adjustment, was calculated for each L_{Norm} and is plotted as a function of L $(=L_{Norm})$ in Fig. 3(Ab). Gain representation is displayed for discrete values (bold line) and for the extrapolation line computed on the basis of the discrete gain values (thin line). Figures 3(Ac) and 3(Ad) show relative growth and gain functions for extrapolated DPOAE data. Moreover, L_{HL} values, which failed the criterion $L_{HL}(L_{Norm})\geqslant L_{Norm}$ and would thus have led to negative gain values, were set to $L_{HL}=L_{Norm}$ [compare, e.g., Fig. 3(Bb)] since level-dependent attenuation seemed not to be reasonable for hearing-aid adjustment.

For both case examples, relative growth and gain functions are plotted on the right-hand side of Figs. 3 and 4. In the following, further examinations are restricted to the presentation of the resulting gain functions [respective panels (b) and (d)], since they shall constitute the basis for hearing-aid adjustment. CLS gain functions [Figs. 3(Cb), 3(Cd), 4(Cb), 4(Cd)] were considered as particular reference for comparisons between CLS and DPOAE gain functions. At first glance, one can observe for both case examples that most of the gain functions had a similar shape. However, gain functions calculated on the basis of extrapolated non-normalized DPOAE data [Figs. 3(Ad) and 4(Ad)] resulted in an exceedingly deviant behavior and made up a poor fit for CLS gain estimation. For both case examples best resemblance was achieved when comparing extrapolated CLS data [Figs. 3(Cd) and 4(Cd)] with extrapolated normalized DPOAE data [Figs. 3(Bd) and 4(Bd)]. The resulting gain differences $\text{gain}_{CLS}(L)-\text{gain}_{normDP}(L)$ at $L=0$ dB SPL were for both hearing-impaired subjects quite small and amounted to -3 dB (P1) and -2 dB (P2). However, the level at which gain became zero was especially in case example P2 for normalized DPOAE gain estimation far apart from CLS gain estimation. The level difference amounted to 3 dB (P1) and 9 dB (P2). Consequently, comparisons of CLS and normalized DPOAE gain estimations resulted in a maximum gain difference of 3 dB (P1) and 11 dB (P2).

Altogether, it is important to notice that gain estimations based on DPOAE measurements were highly influenced by the magnitude of the DPOAE levels and thus by the deviation between normative and hearing loss data. For both case examples normalization of DPOAE data resulted in an improvement of gain estimations compared to gain functions based on non-normalized DPOAE data, especially when extrapolated data were used.

C. Comparison of DPOAE and CLS I/O and gain functions for pooled data

Data of all nine hearing-impaired subjects were included in a joint comparison between DPOAE and CLS data. DPOAE and CLS I/O functions and their respective compressions and estimated threshold levels were compared to each other for each hearing-impaired subject. The difference between the estimated threshold levels $L_{th,dp}-L_{th,cls}$ amounted on average to 4 dB (standard deviation: 6 dB). The difference between the estimated thresholds and the audiometric thresholds (given in dB HL, which is supposed to be approximately equal to dB SPL in the studied frequency range) were for the estimated DPOAE threshold levels on average 8 dB (standard deviation: 7 dB) and for the estimated CLS threshold levels 5 dB (standard deviation: 8 dB). The average compression amounted to 3.0 dB/dB (DPOAE) and 3.5 dB/dB (CLS) and thus resulted in a mean difference in compression between CLS and DPOAE I/O functions, which amounted to 0.5 dB/dB (standard deviation: 0.7 dB/dB).

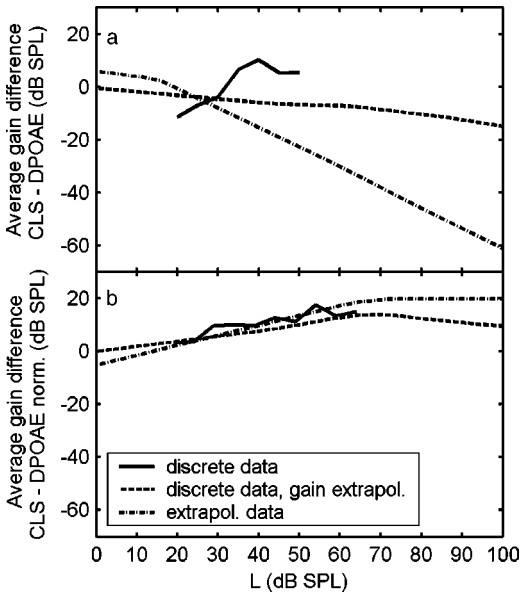

FIG. 5. Average difference of level-dependent gain between CLS and DPOAE [panel (a)] resp. normalized DPOAE [panel (b)] across all frequencies and all hearing-impaired subjects. In each panel solid lines represent gain differences calculated on the basis of discrete measuring data, dashed lines represent gain differences calculated on the basis of extrapolated discrete gain functions, and dash-dotted lines represent gain differences calculated on the basis of extrapolated measuring data.

Comparing DPOAE and CLS gain functions, each of the 14 single-frequency data sets of the nine hearing-impaired subjects was compared to the respective normative function. This procedure was in each case done for non-normalized DPOAE, normalized DPOAE, and CLS data. The difference between the gain functions based on CLS and non-normalized DPOAE [Fig. 5(a)] or normalized DPOAE [Fig. 5(b)] was calculated and averaged for all test frequencies and across all 14 gain difference functions of all hearing-impaired subjects. Using extrapolated I/O functions, average gain differences were calculated and plotted in steps of 5 dB between 0 and 100 dB SPL.

First of all, gain differences between CLS and non-normalized DPOAE [Fig. 5(a)] are described. Examining discrete CLS and DPOAE data (solid line), it must be mentioned that just a small fraction of all existing data was available for averaging. The higher the stimulus level, the fewer points that were available. Data at levels above $L=55$ dB SPL were excluded, since there were two or fewer points left for statistical analysis. Average gain differences ranged from -11 dB at $L=20$ dB SPL to 10 dB at $L=40$ dB SPL with an

average standard deviation (not shown) of 12 dB. Mean gain differences in extrapolated gain functions calculated on the basis of discrete DPOAE and CLS data (dashed line) were 0 dB at $L=0$ dB SPL and -15 dB at $L=100$ dB SPL. The average standard deviation across all levels amounted to 29 dB. Especially for extrapolated data (dash-dotted line), mean gain differences were extremely high, ranging from 6 dB at $L=0$ dB SPL to a maximum of -62 dB at $L=100$ dB SPL, and were furthermore accompanied by enormous standard deviations with a mean across all levels of 59 dB.

When looking at the gain differences between CLS and normalized DPOAE [Fig. 5(b)], it is striking that the discrepancies, especially for extrapolated data, were considerably lower. Further, the mean as well as the standard deviation (not shown) of the gain difference were in a rather similar range of magnitude for discrete and extrapolated data. To begin with, discrete data results (solid line) are described. Maximal average gain difference between CLS and normalized DPOAE amounted to 17 dB at $L=55$ dB SPL, while minimal gain difference was 3 dB at $L=20$ dB SPL. The average standard deviation across all levels amounted to 13 dB. Extrapolated gain values computed on the basis of discrete data (dashed line) achieved best results with regard to gain difference and its variability. Average gain differences ranged from 0 dB at $L=0$ dB SPL to 14 dB at $L=70$ dB SPL. Between $L=0$ and 70 dB SPL gain differences increased continuously and then decreased above $L=70$ dB SPL. Standard deviations were quite constant at 9 dB. A similar behavior occurred examining gain difference functions computed on the basis of extrapolated CLS and normalized DPOAE data (dash-dotted line). Gain differences ranged on average from -5 dB at $L=0$ dB SPL to 20 dB at $L=100$ dB SPL (standard deviation: 11 dB). Thus, in comparison to normalized DPOAE data CLS data resulted on average in shallower gain functions with a gain of zero at higher stimulus levels. For normalized DPOAE data gain became zero at levels around $L=65$ dB SPL due to the implemented normalization strategy, which forced discrete DPOAE levels of the normative and hearing loss I/O function to be equal at this stimulus level.

Consequently, using discrete data, the absolute difference in gain estimation was fairly similar between non-normalized and normalized DPOAE data. For extrapolated I/O functions, normalized DPOAE data resulted in better estimations of gain than non-normalized DPOAE data compared to the reference CLS gain functions. Especially for extrapolated functions standard deviations were much lower using normalized DPOAE data. Altogether, discrete normalized DPOAE data and extrapolated gain functions yielded the best performance when compared to CLS data.

IV. DISCUSSION

The main aim of our study was to compare DPOAEs to loudness estimations with regard to the potentiality of DPOAEs to determine characteristic quantities of the impaired ear and to derive objective hearing aid fitting parameters. In the present study, the work of Neely *et al.* (2003), which focused on an absolute comparison between DPOAEs and the Fletcher and Munson (1933) loudness data, was extended by measuring DPOAEs and loudness with the same measurement system, the same subject sample, and by developing a method for the estimation of level-dependent gain, which should serve as a fitting parameter in dynamic compression hearing aids for compensating loss of cochlear sensitivity and compression.

DPOAEs, an objective quantity, and loudness, a subjective quantity, were found to be closely related to each other. Both loudness and DPOAE I/O functions exhibited similar behavior when plotted on a logarithmic scale. This is manifested in similar threshold level estimates (the average difference between DPOAE and CLS threshold level estimates was 5 dB for the normal-hearing group and 4 dB for the individual hearing-impaired subjects) and compression (the average difference between DPOAE and CLS compression at $L_2=65$ dB SPL was 0.5 dB/dB for both the normal-hearing group and for the individual hearing-impaired subjects). The slope of loudness and DPOAE I/O functions increased with increasing hearing loss (compression decreased on average for both DPOAE and CLS I/O functions by 2.8 dB/dB for hearing-impaired subjects in comparison to the normal-hearing group; compare also case examples in Figs. 3 and 4) and is therefore suggested to reflect loss of cochlear sensitivity and compression. This confirms the results of Neely *et al.* (2003) and suggests both DPOAE and loudness growth may be determined by the same source of nonlinearity. Since DPOAEs directly reflect cochlear compression, loudness seems to be essentially formed by peripheral sound processing mechanisms. However, it remains questionable if there is a direct relationship between DPOAE and loudness, i.e., if loudness is exclusively due to cochlear sound processing or if it is additionally affected by retrocochlear mechanisms.

The similarity of DPOAE and CLS threshold estimates and compression was furthermore consistently manifested in the small difference of the calculated gain functions (Fig. 5). However, small differences and low standard deviations were only achieved if the calculation of gain was based on normalized DPOAE data. The close relationship between the gain functions derived from DPOAE and loudness measurements [compare Fig. 3(Bb) and 3(Bd), 4(Bb) and 4(Bd)] suggests DPOAEs may permit objective assessment of recruitment and hence may provide parameters for an input-level-dependent compensation of the cochlear defect of hearing loss ears. Since extrapolated gain functions based on discrete normalized DPOAE data yielded the most accurate gain estimation (gain differences ranged from 0 to 14 dB SPL with an average standard deviation of 9 dB) we recommend to apply this strategy for the derivation of basic parameters for the adjustment of dynamic compression hearing aids.

However, there were some fundamental problems when comparing loudness and DPOAE data, that is, (i) the comparison of quantities with different units, (ii) the influence of calibration errors, (iii) the interindividual reproducability, and (iv) the question of how to execute DPOAE normalization. Some proposals are given for the solution of these problems.

Absolute comparisons between two different quantities are subject to the selected numerical representation (e.g.,

loudness categories could be associated with any sequence of numbers) and the chosen style of graphic representation (e.g., linear or logarithmic plot). Therefore, a relative comparison strategy, which was deduced from Steinberg and Gardner (1937) and which is independent of the scaling of the measured data, was applied in our study to examine deviations in DPOAE and CLS I/O functions between normal-hearing and hearing-impaired subjects. Nevertheless, a comparison between DPOAE and loudness is difficult since both measures are totally different with respect to the nature of the measure (DPOAEs are a physiological and loudness is a psychophysical measure) and the kind of stimulation (two-tone versus single-tone stimulation).

The relevant magnitude for the generation of DPOAEs and for the generation of loudness is the actual sound pressure level at the eardrum. In general, calibration errors yield a deviance of unknown quantity between actual and nominal sound pressure levels. The magnitude of the deviation varies, particularly with individual influencing factors such as ear canal length and middle ear impedance. The calibration error at f_2 occurs uniformly in DPOAE and CLS measurements, but deteriorates interindividual comparability of I/O functions. Moreover, it is important to notice that for DPOAE measurements, calibration errors may occur with different magnitude at the two primary tone frequencies f_1 and f_2. If the calibration errors at the two primary tone frequencies result in a deviation of the two primary tone stimulus levels from an optimal stimulus paradigm, this usually results in an additional stimulus-level-dependent decrease of DPOAE level and thus may cause a change in the shape and thus the compression of the DPOAE I/O function (Kummer *et al.*, 2000). It should be emphasized that an additional source of error in the compression estimate may result from the deviation between the individual optimal stimulus paradigm and the applied constant stimulus paradigm. This is in accordance with the observations of Neely *et al.* (2003), who found the compression of DPOAE I/O functions plotted on a logarithmic scale to be variable (compression at $L_2=65$ dB SPL ranged from 1.8 to 7.6) among normal-hearing subjects, suggesting that this effect might occur at least partly due to calibration errors. The same effect, though a little less distinct, was existent in our measured CLS and DPOAE I/O functions of normal-hearing subjects, which showed a similar variance in compression at $L_2=65$ dB SPL and ranged between 3.9 and 8.9 (DPOAE) and between 3.6 and 8.1 (CLS) for normal-hearing subjects. However, the standard deviation of compression was only 1.2 for DPOAE and 0.9 for CLS. We believe this variance in compression, which detoriorates the individual quality of gain estimations, is mainly due to calibration errors.

Calibration errors, which vary considerably among subjects, are supposed to have an undesired impact on the magnitude of DPOAE and CLS data and hence on the resultant interindividual variance. Moreover, the ear canal length and the middle ear transfer function are supposed to directly influence the propagation of DPOAEs through the middle ear and outer ear canal and may cause an individually differing attenuation of DPOAE amplitude, which may bring about increased interindividual deviations in DPOAE level. The interindividual deviance of CLS data (average standard deviation: 3.0 CU) is within the reproducibility of a single person (average difference: 4.2 CU). In contrast, the deviation of DPOAE level was substantial across normal-hearing subjects (average standard deviation: 6.4 dB). The deviation should be lower, proceeding on the assumption that the single influencing factor is OHC damage, which should hardly be existent in the tested normal-hearing subjects. In comparison, DPOAE levels were quite constant for successive measurements within a single subject (average difference: 0.8 dB), suggesting that the DPOAE amplitude hardly varies within a short period of time when measured with an unaltered ear probe position. Therefore, it is likely that the absolute variance of DPOAE level is not only dependent on OHC dysfunction, but also on other side effects, which can be of external (ear canal length, middle ear impedance, calibration error) or intracochlear origin. We believe that the external components are more influential on the DPOAE amplitude and thus obstructive to relative comparisons of different DPOAE I/O functions. The fact that there is a high variability in DPOAE magnitude, but only a small variability in loudness across frequency [compare Figs. 1(a) and 2(a)], may disprove cochlear effects because intracochlear variability is supposed to influence both DPOAEs and loudness. It is assumed that calibration errors and the ear canal resonance are influencing DPOAE more than loudness measurements because the DPOAE amplitude is highly sensitive to slight deviations from the individual optimal primary tone level setting, which occurs due to standing waves especially around 3 kHz. Also, the ear canal resonance influences the backward sound propagation of the DPOAE to the microphone and hence results in a frequency-dependent attenuation of DPOAE amplitude. To compensate for the undesired effects, a normalization strategy was implemented.

The applied normalization procedure with an equalization of DPOAE levels at a constant stimulus level of $L_2=65$ dB SPL [see Fig. 1(b), 3(B), and 4(B)] was chosen, because $L_2=65$ dB SPL was the highest stimulus level at which DPOAEs can be measured without getting distorted signals due to microphone clipping effects. Other stimulus levels could have been chosen for normalization by using extrapolations, but since there was no *a priori* evidence for any optimal solution, $L_2=65$ dB SPL was arbitrarily selected. It is interesting to note that results of DPOAE gain functions could have been further improved by executing an individual DPOAE shift, making use of knowledge about behavior of individual CLS data. Using this strategy, gain differences between DPOAE- and CLS-based computation amounted to a maximum of just about 2 dB (not shown in results). However, this approach is not reasonable if the main aim is to develop a method for objective hearing-aid adjustment on the exclusive basis of DPOAEs. Thus, one of the most prominent and influencing factors was the difference in absolute magnitude of DPOAE I/O functions. This problem is directly linked to the question to what extent the amplitude differences result from OHC dysfunction and from nonpathological impacts. Therefore, further improvements in DPOAE measuring techniques and especially in the quality

of calibration are necessary to minimize the influence of undesired side effects.

We are aware of the fact that the proposed hearing aid adjustment strategy is only a small step on the way to a non-cooperative adjustment. The limiting factor for the application of the proposed strategy in clinical practice is that with the available commercial DPOAE measurement systems it is just possible to elicit DPOAEs free of artefacts at stimulus levels of up to 65 dB SPL. Thus, DPOAEs are currently only useful in detecting loss in sensitivity and compression in hearing-impaired subjects with hearing losses of up to 50 dB HL and hence predictions of level-dependent gain are only possible for impaired ears of that category. However, there is a way out of this dilemma through the development of sound probes that are able to measure DPOAEs with low technical distortions at primary tone levels exceeding 65 dB SPL. Therefore, sound probe manufacturers are asked to provide such systems. As long as such systems are not available one can follow the strategy of Dorn *et al.* (2001) to measure DPOAEs over the widest range possible without running the risk of misinterpreting system distortions for biological distortions. Using this strategy, Dorn *et al.* were able to record DPOAE I/O functions for an extended primary tone level range, with an L_2 of up to 95 dB SPL. With the possibility to measure DPOAEs at higher stimulus levels, our proposed strategy for providing objective hearing aid adjustment parameters (i.e., the gain for compensating loss of sensitivity and compression of the impaired ear) should be successful in patients with cochlear hearing losses higher than 50 dB HL.

V. CONCLUSIONS

The main intention of this study was to establish a general new approach for the development of an objective hearing-aid adjustment procedure for non-cooperative patients. I/O and gain functions based on CLS and DPOAE data suggest that DPOAE data is qualitatively and quantitatively related to categorical loudness estimations in humans. Further studies are needed to enhance the proposed objective hearing-aid adjustment strategy. It is necessary to improve hardware abilities in order to make such a DPOAE-based strategy applicable for patients with major hearing losses. The behavior of DPOAE I/O functions at high-level stimuli must be further examined and compared to loudness functions. Additionally, it is necessary to improve sound probe calibration and to develop strategies to detect undesired side effects in order to improve the applied DPOAE normalization strategy.

ACKNOWLEDGMENTS

This work was supported by the Deutsche Forschungsgemeinschaft (Ja 597/6).

Allen, J. B., Hall, J. L., and Jeng, P. S. (**1990**). ''Loudness growth in $\frac{1}{2}$-octave bands (LGOB)—A procedure for the assessment of loudness,'' J. Acoust. Soc. Am. **88**, 745–753.

Boege, P., and Janssen, T. (**2002**). ''Pure-tone threshold estimation from extrapolated distortion product otoacoustic emission I/O-functions in normal and cochlear hearing loss ears,'' J. Acoust. Soc. Am. **111**, 1810–1818.

Brand, T., and Hohmann, V. (**2002**). ''An adaptive procedure for categorical loudness scaling,'' J. Acoust. Soc. Am. **112**, 1597–1604.

Brownell, W. E. (**1990**). ''Outer hair cell electromotility and otoacoustic emissions,'' Ear Hear. **11**, 82–92.

Dallos, P. (**1992**). ''The active cochlea,'' J. Neurosci. **12**, 4575–4585.

Dorn, P. A., Konrad-Martin, D., Neely, S. T., Keefe, D. H., Cyr, E., and Gorga, M. P. (**2001**). ''Distortion product otoacoustic emission input/output functions in normal-hearing and hearing-impaired human ears,'' J. Acoust. Soc. Am. **110**, 3119–3131.

Fletcher, H., and Munson, W. A. (**1933**). ''Loudness, its definition, measurement and calculation,'' J. Acoust. Soc. Am. **5**, 82–108.

Geiger, P. A., and Firestone, F. A. (**1933**). ''The estimation of fractional loudness,'' J. Acoust. Soc. Am. **5**, 25–30.

Gorga, M. P., Neely, S. T., Dorn, P. A., and Hoover, B. M. (**2003a**). ''Further efforts to predict pure-tone thresholds from distortion product otoacoustic emission input/output functions,'' J. Acoust. Soc. Am. **113**, 3275–3284.

Gorga, M. P., Neely, S. T., Dierking, D. M., Dorn, P. A., Hoover, B. M., and Fitzpatrick, D. F. (**2003b**). ''Distortion product otoacoustic emission suppression tuning curves in normal-hearing and hearing-impaired human ears,'' J. Acoust. Soc. Am. **114**, 263–278.

Heller, O. (**1985**). ''Hörfeldaudiometrie mit dem Verfahren der Kategorienunterteilung (KU),'' Psychologische Beiträge **27**, 478–493 (in German).

Hellman, R. P., and Meiselman, C. H. (**1990**). ''Loudness relations for individuals and groups in normal and impaired hearing,'' J. Acoust. Soc. Am. **88**, 2596–2606.

Hellman, R. P., and Meiselman, C. H. (**1993**). ''Rate of loudness growth for pure tones in normal and impaired hearing,'' J. Acoust. Soc. Am. **93**, 966–975.

Hellman, R. P., and Zwislocki, J. J. (**1961**). ''Some factors affecting the estimation of loudness,'' J. Acoust. Soc. Am. **33**, 687–694.

Hohmann, V., and Kollmeier, B. (**1995**). ''Weiterentwicklung und klinischer Einsatz der Hörfeldskalierung,'' Audiologische Akustik **34**, 48–59 (in German).

Janssen, T., Kummer, P., and Arnold, W. (**1995**). ''Wachstumsverhalten der Distorsionproduktemissionen bei kochleären Hörstörungen,'' Otorhinolaryngol. NOVA **5**, 34–46 (in German).

Janssen, T., Kummer, P., and Arnold, W. (**1998**). ''Growth behavior of the $2f_1-f_2$ distortion product otoacoustic emission in tinnitus,'' J. Acoust. Soc. Am. **103**, 3418–3430.

Johnstone, B. M., Patuzzi, R., and Yates, G. (**1986**). ''Basilar membrane measurements and the travelling wave,'' Hear. Res. **22**, 147–153.

Kollmeier, B. (**1997**). *Hörflächenskalierung—Grundlagen und Anwendung der kategorialen Lautheitsskalierung für Hördiagnostik und Hörgeräte-Versorgung*, (Median, Heidelberg, Germany) (in German).

Kummer, P., Janssen, T., and Arnold, W. (**1995**). ''Suppression tuning characteristics of the $2f_1-f_2$ distortion-product otoacoustic emissions in humans,'' J. Acoust. Soc. Am. **98**, 197–210.

Kummer, P., Janssen, T., and Arnold, W. (**1998**). ''The level and growth behavior of the $2f1-f2$ distortion product otoacoustic emission and its relationship to auditory sensitivity in normal hearing and cochlear hearing loss,'' J. Acoust. Soc. Am. **103**, 3431–3444.

Kummer, P., Janssen, T., Hulin, P., and Arnold, W. (**2000**). ''Optimal $L1-L2$ primary tone level separation remains independent of test frequency in humans,'' Hear. Res. **146**, 47–56.

Launer, S. (**1995**). ''Loudness perception in listeners with sensorineural hearing loss,'' Ph.D. Thesis, Oldenburg, Germany.

Madsen (**2000**). *Aurical Reference Guide*, Copenhagen, Denmark, Chap. 3.6, pp. 66–91.

Moore, B. C., and Glasberg, B. R. (**2004**). ''A revised model of loudness perception applied to cochlear hearing loss,'' Hear. Res. **188**, 70–88.

Moore, B. C. J., Glasberg, B. R., and Vickers, D. A. (**1999**). ''Further evaluation of a model of loudness perception applied to cochlear hearing loss,'' J. Acoust. Soc. Am. **106**, 898–907.

Neely, S. T., and Gorga, M. P. (**1998**). ''Comparison between intensity and pressure as measures of sound level in the ear canal,'' J. Acoust. Soc. Am. **104**, 2925–2934.

Neely, S. T., Gorga, M. P., and Dorn, P. A. (**2003**). ''Cochlear compression estimates from measurements of distortion-product otoacoustic emissions,'' J. Acoust. Soc. Am. **114**, 1499–1507.

Oswald, J. A., and Janssen, T. (**2003**). ''Weighted DPOAE Input/Output-functions: A tool for automatic assessment of hearing loss in clinical application,'' Z. Med. Phys. **13**, 93–98.

Oxenham, A. J., and Plack, C. J. (**1997**). ''A behavioral measure of basilar-

membrane nonlinearity in listeners with normal and impaired hearing,'' J. Acoust. Soc. Am. **101**, 3666–3675.
Pascoe, D. P. (**1978**). ''An approach to hearing aid selection,'' Hear. Instrum. **29**, 12–16.
Relkin, E. M., and Doucet, J. R. (**1997**). ''Is loudness simply proportional to the auditory nerve spike count?'' J. Acoust. Soc. Am. **101**, 2735–2740.
Rhode, W. S. (**1971**). ''Observations of the vibration of the basilar membrane in squirrel monkeys using the Mössbauer technique,'' J. Acoust. Soc. Am. **49**, 1218–1231.
Ruggero, M. A., Rich, N. C., Recio, A., Narayan, S., and Robles, L. (**1997**). ''Basilar-membrane responses to tones at the base of the chinchilla cochlea,'' J. Acoust. Soc. Am. **101**, 2151–2163.
Russell, I., and Schauz, C. (**1995**). ''Salicylate ototoxity: Effects on the stiffness and electromotility of outer hair cells isolated from the guinea pig cochlea,'' Aud. Neurosci. **1**, 309–319.
Schlauch, R. S., DiGiovanni, J. J., and Ries, D. T. (**1998**). ''Basilar membrane nonlinearity and loudness,'' J. Acoust. Soc. Am. **103**, 2010–2020.
Siegel, J. H. (**1994**). ''Ear-canal standing waves and high-frequency sound calibration using otoacoustic emission probes,'' J. Acoust. Soc. Am. **95**, 2589–2597.
Steinberg, J. C., and Gardner, M. B. (**1937**). ''The dependence of hearing impairment on sound intensity,'' J. Acoust. Soc. Am. **9**, 11–23.
Stevens, S. S. (**1957**). ''On the psychophysical law,'' Psychol. Rev. **64**, 153–181.
Whitehead, M. L., Stagner, B. B., Lonsbury-Martin, B. L., and Martin, G. K. (**1995**). ''Effects of ear-canal standing waves on measurements of distortion-product otoacoustic emissions,'' J. Acoust. Soc. Am. **98**, 3200–3214.
Yates, G. K., Winter, I. M., and Robertson, D. (**1990**). ''Basilar membrane nonlinearity determines auditory nerve rate-intensity functions and cochlear dynamic range,'' Hear. Res. **45**, 203–219.
Zhang, M., and Zwislocki, J. J. (**1995**). ''OHC response recruitment and its correlation with loudness recruitment,'' Hear. Res. **85**, 1–10.
Zwicker, E. (**1958**). ''Über psychologische und methodische Grundlagen der Lautheit,'' Acustica **1**, 237–258 (in German).

Development of auditory sensitivity in budgerigars (*Melopsittacus undulatus*)

Elizabeth F. Brittan-Powell[a] and Robert J. Dooling
Department of Psychology, University of Maryland, College Park, Maryland 20742

(Received 24 January 2003; revised 6 March 2004; accepted 15 March 2004)

Auditory feedback influences the development of vocalizations in songbirds and parrots; however, little is known about the development of hearing in these birds. The auditory brainstem response was used to track the development of auditory sensitivity in budgerigars from hatch to 6 weeks of age. Responses were first obtained from 1-week-old at high stimulation levels at frequencies at or below 2 kHz, showing that budgerigars do not hear well at hatch. Over the next week, thresholds improved markedly, and responses were obtained for almost all test frequencies throughout the range of hearing by 14 days. By 3 weeks posthatch, birds' best sensitivity shifted from 2 to 2.86 kHz, and the shape of the auditory brainstem response (ABR) audiogram became similar to that of adult budgerigars. About a week before leaving the nest, ABR audiograms of young budgerigars are very similar to those of adult birds. These data complement what is known about vocal development in budgerigars and show that hearing is fully developed by the time that vocal learning begins.
© *2004 Acoustical Society of America.* [DOI: 10.1121/1.1739479]

PACS numbers: 43.64.Ri, 43.64.Tk [WWA] Pages: 3092–3102

I. INTRODUCTION

The auditory brainstem response (ABR) has been an effective tool for studying the development of auditory sensitivity in a wide variety of mammals. ABRs recorded from altricial mammals show elevated thresholds, prolonged latencies, and diminished amplitudes early in development (e.g., Boettcher *et al.*, 1993a, 1993b; Burkard and Voigt, 1989; Burkard *et al.*, 1996b; Jewett and Romano, 1972; Mair *et al.*, 1978; McFadden *et al.*, 1996; Mills *et al.*, 1990; Walsh *et al.*, 1986a,b,c). Developmental ABR studies in precocial birds show the same general trends (Dmitrieva and Gottlieb, 1992, 1994; Saunders *et al.*, 1973, 1974), but there are no ABR studies relating hearing, latency, and amplitude development in altricial birds.

Although there are some similarities in hearing development across vertebrate classes, there can also be large differences in maturational state at birth and in the rate of postnatal maturation with regard to hearing, especially across precocial and altricial species. For precocial birds, like chickens and ducks, auditory sensitivity begins to develop while the animal is still in the egg and is adult-like at low to mid frequencies at hatching (Dmitrieva and Gottlieb, 1992; Saunders *et al.*, 1973, 1974). On the other hand, altricial birds, such as songbirds and parrots, are probably more comparable to altricial mammals than precocial birds in terms of mode of hearing maturation (see Aleksandrov and Dmitrieva, 1992).

The budgerigar (*Melopsittacus undulatus*), a small Australian parrot, is one of the most widely studied altricial parrots and has been the focus of many studies of hearing and vocalizations (see reviews in Dooling *et al.*, 2000; Farabaugh and Dooling, 1996). Budgerigars are open-ended vocal learners who rely on hearing for learning and maintaining their vocal repertoire. Isolation, or other unusual acoustic and social rearing conditions, has little effect on the budgerigars' long-term ability to produce and imitate species-specific vocalizations (Brittan-Powell *et al.*, 1997). Deafening, on the other hand, causes major disruptions in vocal production (Dooling *et al.*, 1987; Heaton and Brauth, 1999; Heaton *et al.*, 1999). A study of auditory development in this species may set the stage for more refined questions of the role of hearing in vocal learning in this species.

ABR responses to both clicks and tone-burst stimuli in adult budgerigars can be recorded from the scalp and provide a reliable measure of hearing sensitivity in these birds (Brittan-Powell *et al.*, 2002). Little is known about the development of the middle ear, the sensory epithelium with hair cells and accessory structures, or the innervation of the auditory system in budgerigars, and nothing is known about when these structures are mature enough to support synchronous neural activity necessary for the emergence of auditory brainstem responses. Here, we address development of hearing in nestling budgerigars by recording ABRs to determine both the onset and development of hearing sensitivity. In two experiments, we measured ABRs elicited by clicks and tone-burst stimuli in nestling budgerigars. Experiment 1 tracked the maturation of hearing thresholds and other ABR details as a function of age, intensity, and frequency. Experiment 2 examined the effects of increased presentation rate on ABR wave latency and amplitude as a function of development.

II. METHODS

Nestling budgerigars served as subjects in these experiments. The birds were reared in standard wooden nest boxes attached to small wire cages (37.5×30×37.5 cm) and housed in an avian vivarium at the University of Maryland. Over the course of the experiment, there were approximately 70–80 birds housed in the animal colony with all birds tested raised under similar acoustic conditions. Nestlings were

[a]Electronic mail: bbrittanpowell@psyc.umd.edu

taken from their nests 5–10 min prior to testing and returned to their nests once they recovered from anesthesia. No supplemental care was given by the experimenters.

All birds used in this study were sedated with either an intramuscular injection (for fledglings and older nestlings) or a subcutaneous injection (younger nestlings) of ketamine (25–50 mg/kg) and diazepam (2 mg/kg) prior to electrode placement. Older animals remained relatively motionless for up to 75 min, whereas younger animals metabolized the anesthetic typically within 30 min. Animals were given up to two supplementary injections, as needed. Body temperature was maintained at 41±0.5 °C for older animals and 35–38 ±0.5 °C for younger animals by placing the bird on a heating pad with a thermistor probe placed under the wing (temperature control unit; Frederick Haer and Co., model 40-90-2 and 40-90-5, Bowdoinham, ME).

The procedure for recording ABRs in budgerigars has been described earlier (Brittan-Powell *et al.*, 2002). The bird was positioned so that the speaker (KEF SP 3235, model 60S, frequency range 100 Hz to 20 kHz, KEF Electronics of America, Inc., Holliston, MA) was 30 cm from the bird's right ear (90° azimuth relative to the bird's beak; 0° elevation relative to the bird's right ear). Standard platinum alloy, subdermal needle electrodes (Grass F-E2; West Warwick, RI) were placed just under the skin in the conventional electrode array: high at the vertex (noninverting), directly behind the right ear canal (the ear ipsilateral to the speaker, inverting), and directly behind the left ear canal (the ear contralateral to stimulation, common). The stimulus presentation, ABR acquisition, equipment control, and data management were coordinated using a Tucker-Davis Technologies (TDT, Gainesville, FL) modular rack-mount system controlled by an optical cable-linked 350-MHz Pentium PC containing a TDT AP2 digital signal process board and running TDT BIOSIG software. Sound stimuli were generated using TDT SIGGEN software and fed through a DA1 digital–analog converter, a PA4 programmable attenuator, and a power amplifier (HB6) which directly drove the speaker. The electrodes were connected to the TDT HS4 Headstage which amplified and digitized the signal before being relayed over fiberoptic cables to the TDT DB4 digital biological amplifier. This amplifier also allowed additional filtering and gain to be added. A TDT TG6 timing generator synchronized the A/D and D/A conversion.

Stimulus intensities were calibrated in the free field by placing the $\frac{1}{2}$-in. microphone of a sound-level meter (System 824; Larson Davis, Inc. Provo. UT) at the approximate position of the bird's right ear. Continuous tones, with the same peak-to-peak amplitude as the subsequently used tone bursts, were generated using the TDT BIOSIG program and measured using the fast-weighting A scale on the sound-level meter (dB SPL). To determine the intensity of the click, we used the peak equivalent SPL of the click. This was determined using an oscilloscope and noting the peak-to-peak voltage of the click. A test tone, e.g., a 1000-Hz tone, was played and adjusted until the peak-to-peak voltage was the same as it was for the click. The SPL required to match the amplitude of the click, as indicated by the sound-level meter, was the peak equivalent SPL (dB pSPL) of the click stimulus.

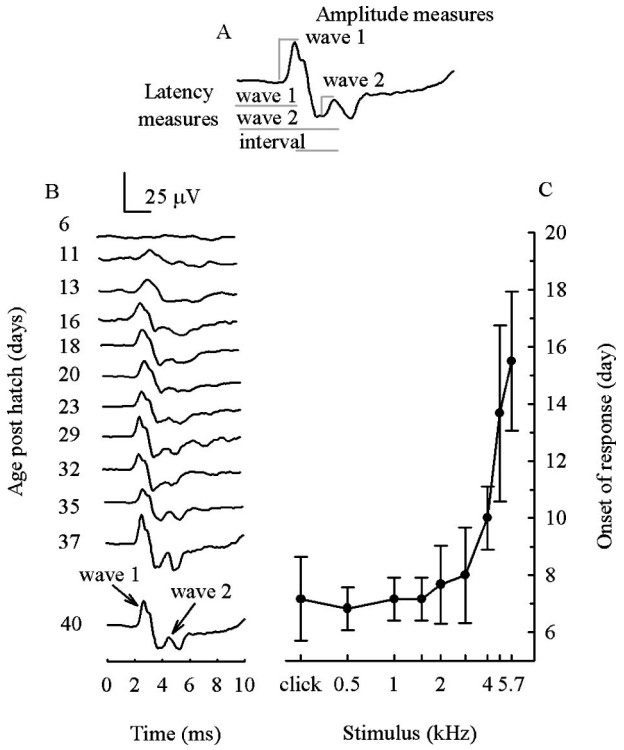

FIG. 1. (A) Schematic showing how latency and amplitude measurements were taken for waves 1 and 2. (B) Typical ABR waveforms in response to the click (85 dB pSPL) for a single nestling. For this bird, wave 1 can be discerned by day 11 and followed as it decreases in latency and increases in amplitude. By 16 days of age, wave 2 can be seen. From day 37–40, there is little change in the waveform. (C) Average age of onset of a response as a function of stimulus frequency. Responses to low and middle frequencies appear first, with high-frequency responses appearing at later ages. The bars are s.d.

For all experiments, only the first two wave components of the ABR waveform, designated by sequential Arabic numerals, were described by their amplitude and latency characteristics [Fig. 1(A); see also, Brittan-Powell *et al.*, 2002)]. Positive evoked potential peaks were identified manually by cursor control and associated latencies and amplitudes were automatically stored by the computer. Latencies to wave 1 and wave 2 were corrected for conduction delays between the sound source and the entrance of the ear canal of the animal (0.88 ms). The latency of the interwave interval (referred to as 1–2 interval) was calculated as the difference in latency from the peak of wave 1 to the peak of wave 2. ABR wave amplitudes were measured using baseline-to-peak for wave 1 and peak-to-peak (preceding trough) amplitude for wave 2.

III. EXPERIMENT 1: THE DEVELOPMENT OF AUDITORY SENSITIVITY

A. Subjects

Four of the six birds used in this experiment originated from three different broods produced by the same parents over a span of 6 months. The other two birds were brood mates. Where feasible, ABRs were recorded every 2–3 days during the first 2 weeks posthatching and every 3–5 days

during the last 4 weeks of the study. The day of hatch is denoted as day 0. Each individual bird was recorded a minimum of 13 times, from approximately day 5 until 1 week postfledging (about day 43).

B. Stimuli

The sound stimulation protocol is the same as used in Brittan-Powell *et al.* (2002). Briefly, subjects were presented with multiple intensity stimulus trains that varied in frequency and intensity. Each train consisted of nine single clicks or frequency tone bursts that increased in intensity (5–10-dB steps, depending on age) and were presented at a rate of 4/s. The rectangular-pulse broadband clicks were 0.1 ms in duration, with a 25-ms interstimulus interval (ISI). Each individual tone burst was 5 ms in duration (1-ms rise/fall $\cos^2$) with a 20-ms ISI. The tone bursts used were 0.5, 1, 1.5, 2, 2.86, 4, 4.8, and 5.7 kHz, with the highest stimulus intensity employed being 95–100 dB SPL. High-intensity tone bursts were played through the speaker and sampled at 40 kHz into the A/D module of the TDT rack. Spectra of these tone bursts were generated using 1024-pt fast Fourier transform (FFT). Spectral analysis showed all second and third harmonics were at least 30 dB down from the peak of the frequency of interest, except for the first harmonic of the 0.5-kHz stimulus, which was 18 dB down.

Each ABR was sampled at 20 kHz for 235 ms following onset of the stimulus train. This allows for 25-ms recording time for each stimulus. Five hundred averages for each polarity/phase were added together to cancel the cochlear microphonic. The biological signal was amplified ($\times$100 K) and notch filtered at 60 Hz with the DB4 during collection. The signal was bandpass filtered below 0.03 kHz and above 3 kHz after collection using the BIOSIG program.

C. Analysis

ABR waveforms produced in response to high intensities were examined visually to determine which peaks would be used to measure latencies, amplitudes, and thresholds. A response was expected between 1 ms after the onset of the stimulus (travel time from the speaker to the ear) and 15 ms because the response latency tends to be longer in younger animals and also increases at low SPLs in all animals. Using this time window, the wave components were described by their latency and amplitude characteristics.

Response onset was defined as the earliest age at which ABR waves met the following criteria: (1) the response showed at least one positive deflection within the latency range described above [see Fig. 1(B), day 11 for example)] and (2) the response was replicable on successive trials (onset of response criteria was modified from Walsh *et al.*, 1986a).

ABR threshold was defined as the intensity 2.5 dB (one-half step in intensity) below the lowest stimulus level at which a response could be visually detected on the trace, regardless of wave (see, for example, Boettcher *et al.*, 1993a). On a few occasions, a response could still be detected at the lowest intensity presented. In all of these cases, the peak amplitudes of the responses to the series of higher intensity stimuli showed decreasing response amplitudes that indicated that the next intensity step would not evoke a visible response. In these cases, threshold was defined as 2.5 dB below the lowest intensity presented.

All data for the different response variables (e.g., threshold, latency, amplitude) were excluded from the analysis if only one of the six nestlings for that age met the criteria defined above. In other words, at least two birds are represented in every averaged data point and at least two birds for the given time point met the above defined criteria when individual data were used. Individual data were used for all statistical tests. For averaged plots, responses for the nestlings were averaged across 3-day periods (e.g., 4–6-days posthatching), except for the last time period that consisted of a 4-day period (days 40–43). In all figures, the median age of the time period is shown on the abscissa. The dependent variables examined were threshold, latency, and amplitude.

All ABR data collected from the nestling budgerigars were analyzed in a manner similar to that collected from adult budgerigars under the same conditions (as reported in Brittan-Powell *et al.*, 2002).

D. Results

1. Onset

Example ABR waveforms in response to an 85-dB pSPL click are shown for an individual nestling from 6–40 days of age [Fig. 1(B)]. The ABR waveforms from the youngest birds possessed at least one long-duration positive wave which was low in amplitude (<2 μV) and had a prolonged latency (about 4–5 ms). This was the case for all responses, regardless of frequency. This positive-going deflection corresponded to wave 1 of the adult budgerigar ABR waveform. As the animal aged, wave latencies decreased and wave amplitudes increased. The overall waveform was adult-like by 5 weeks of age.

ABR responses could first be evoked by low frequencies and then to increasingly higher frequencies [Fig. 1(C)]. By the end of the first week, responses were typically obtained to frequencies up to 2.86 kHz, and by the end of the second week, the bandwidth of frequencies extended up to 4.8 kHz. Responses could be elicited at all test frequencies by the bird's third week posthatch.

2. Threshold

Figure 2 shows thresholds over time. These data were fitted with exponential decay functions $y=a+be^{-cx}$, where a was the asymptote of the curve, b was the intercept, and c represented the curvature (see Walsh *et al.*, 1986a) (see Table I for parameters). Since a represented an asymptote in threshold improvement, this value most closely corresponded to adult levels of sensitivity as measured by the ABR. When b was large, the values declined along a steep trajectory. The reciprocal of c provided the time constant of the function. In general, frequencies up to and including 4 kHz showed rapid decreases in threshold that stabilized by day 30. Thresholds

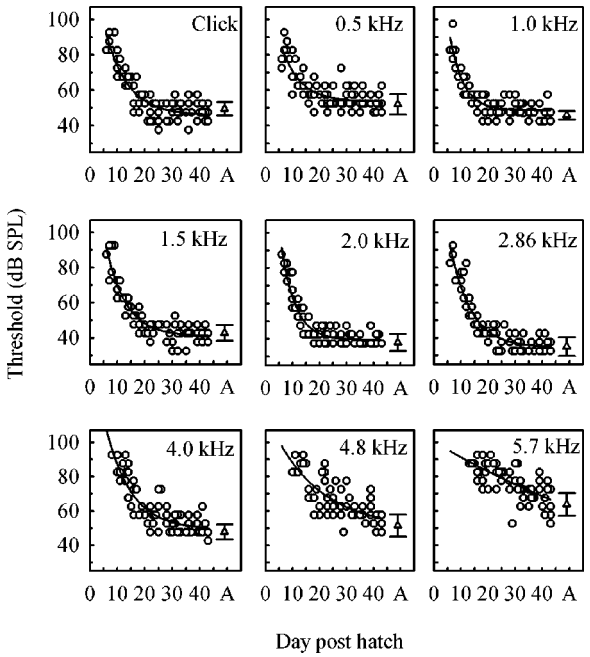

FIG. 2. Exponential decay functions are shown for the individual nestling threshold data (open circles), with parameters presented in Table I. In general, nestlings attain adult thresholds (A=average thresholds for adult with open triangles with s.d. bars; adult data from Brittan-Powell *et al.*, 2002) for most frequencies by 17–20 days of age. Overall, the data were represented well by exponential decay functions except for 5.7 kHz, where the decay was linear ($y=-0.74x+99.3$).

were more variable at the higher frequencies but still showed decreases as the animal aged. Overall, the exponential decay functions fit the data well ($r^2>0.75$; Table I) for the click as well as frequencies between 1–4 kHz.

To determine the ages where nestlings' thresholds differed from the adult budgerigars, one-way ANOVAs were performed on the individual data for each frequency. As expected, there was a significant decrease in threshold at all frequencies as the birds aged (see Table II). *Post hoc* t-tests (Tukey-Kramer HSD) revealed the ages where nestling thresholds differed from the adult thresholds. By 16–18 days of age, ABR thresholds for the click and 0.5, 1.0, 1.5, and 2.0 kHz for nestlings were no longer significantly different from adult thresholds. Thresholds for 2.86 and 4.0 kHz were adult-like by the end of the third week of life, whereas thresholds for 5.7 kHz did not reach adult levels until approximately 1 month of age.

TABLE II. ANOVA results for when nestlings' thresholds differed from adult thresholds.

Stimulus	df	F	P
Click	13, 62	33.32	0.0001
0.5	13, 63	14.65	0.0001
1.0	13, 62	19.30	0.0001
1.5	13, 62	41.05	0.0001
2.0	13, 61	41.42	0.0001
2.86	13, 60	46.70	0.0001
4.0	11, 57	21.03	0.0001
4.8	11, 50	12.60	0.0001
5.7	10, 49	7.09	0.0001

Threshold changed significantly as a function of frequency at different developmental time periods [$F(63,198)=0.0845$, $p=0.002$; see Fig. 3]. The ABR audiogram for the earliest ages (e.g., end of the first week) was relatively flat between 0.5 and 2.86 kHz and showed poor sensitivity across frequency. By 14 days, the thresholds improved between 20–40 dB for frequencies below 4 kHz. The smallest improvement in threshold was for 5.7 kHz (20-dB improvement from day 14–42). At approximately 20 days, there was a shift in the frequency of best hearing from 2 to 2.86 kHz. Even though the audiograms for birds 1 month and older were not significantly different from that of adults [$F(35,95)=0.396$, $p=0.911$], nestlings' absolute sensitivity above 2.86 kHz remained 15 dB higher than adult values until around the time of fledging.

As a check on the validity of the visual detection level definition of threshold, a second threshold estimate was also used. Here, threshold was defined as the lowest stimulus intensity corresponding to a response amplitude of 0.5 μV (at least 1 s.d. above the mean noise level). A one-way multivariate analysis of variance (MANOVA) showed no significant differences between the threshold estimates [$F(1,104)=0.969$, $p=0.07$].

3. Latency and amplitude

Latency decreased and amplitude increased with increasing intensity level for all peaks in the ABR waveform. There were also age-dependent effects. As the animal aged, peak latencies to wave 1 and 2 decreased (Fig. 4) and peak amplitude increased (Fig. 5). Peak latencies were the longest during the first 2 weeks posthatch. Latencies for wave 1 de-

TABLE I. Decaying exponential parameters for threshold ($y=a+be^{-cx}$).

Frequency	Asymptote (a)	Y-intercept (b)	Curvature (c)	Time constant ($1/c$)	$r2$
Click	45.75	95.16	0.122	8.2	0.81
0.5	53.50	72.26	0.142	7.0	0.66
1	48.56	137.38	0.200	5.0	0.80
1.5	40.90	115.44	0.138	7.3	0.85
2	39.38	162.51	0.189	5.3	0.88
2.86	34.51	127.49	0.131	7.6	0.88
4	48.88	112.27	0.108	9.26	0.76
4.8	49.36	67.70	0.056	17.86	0.58
5.7	−3.76	104.04	0.009	111.00	0.45

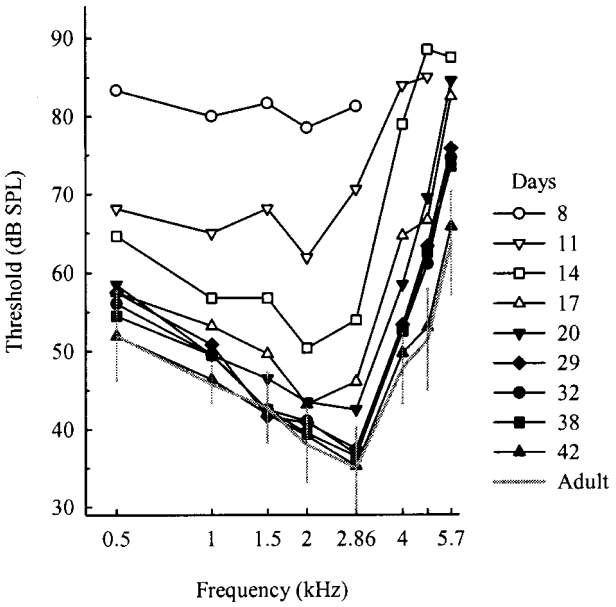

FIG. 3. Average ABR audiograms over development for six nestlings. The solid gray line represents the adult average±s.d. (Brittan-Powell *et al.*, 2002). There is a considerable change in threshold from 8–17 days, after which thresholds improve more slowly, with lower frequency thresholds becoming adult-like first, followed by middle and higher frequencies.

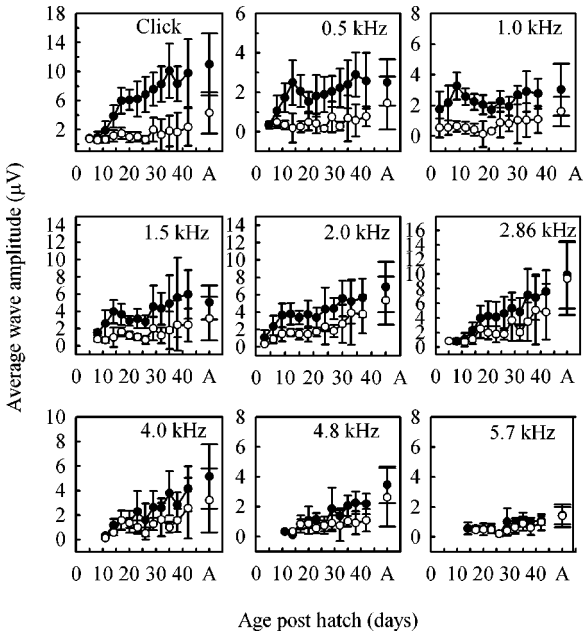

FIG. 5. Average t.s.d. peak amplitudes for wave 1 (closed circles) and wave 2 (open circles) plotted as function of age for a constant intensity level of 85 dB SPL. Amplitude for both wave 1 and wave 2 increases as the animal ages, but the growth of wave 2 amplitude occurs at a later age. *A*=adult average±s.d. (Brittan-Powell *et al.*, 2002) with symbols being the same as for the nestlings (e.g., closed circles=wave 1).

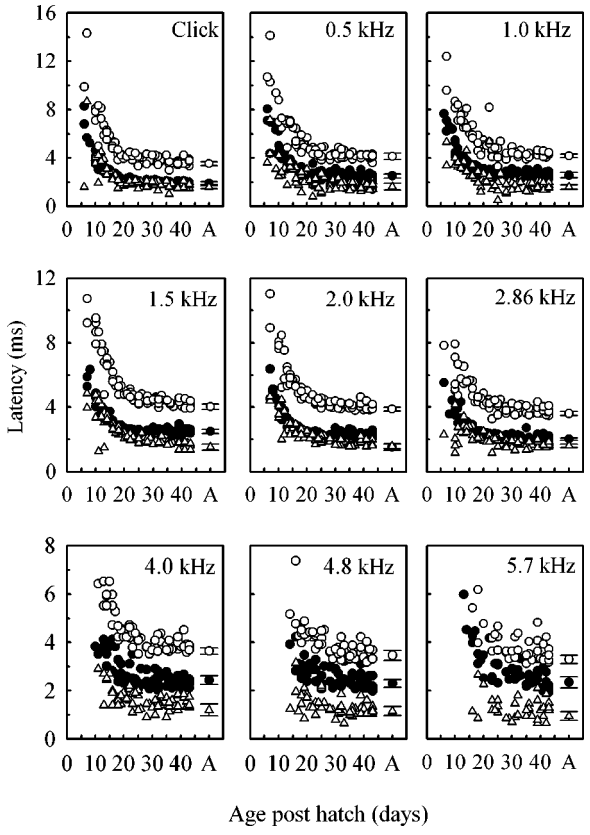

FIG. 4. Latencies to the peaks of wave 1 (closed circles), wave 2 (open circles), and the 1–2 interval (open triangles) plotted as function of age for a constant intensity level of 85 dB SPL. Latency decreases as a function of increasing age, but the 1–2 interval remains fairly consistent throughout development. *A*=adult average±s.d. (Brittan-Powell *et al.*, 2002) with symbols being the same as for the nestlings (e.g., closed circles=wave 1).

creased from 4–12 ms to the adult average of 2–3 ms by the end of week 3. Similar decreases were seen for wave 2 latencies. Exponential decay functions fit to the data shown in Fig. 4 (see Table III for parameters) revealed that the overall rate of latency decay was high for all frequencies (as indicated by large *b* term) and that wave 1 matured faster than wave 2, except at 4 kHz (as indicated by smaller time constants). Lower frequencies showed more change in latency than higher frequencies perhaps because responses to lower frequencies were first recorded 7–10 days earlier than responses for higher frequencies. Increasing the intensity level presented to the nestlings at high frequencies may have resulted in similar latency changes at higher frequencies. Even so, latencies and intervals between the peaks were typically within 1 s.d. of the adult values by one month of age for all frequencies (see Fig. 4).

Peak amplitude of wave 1 in young animals ranged from 1 to 8–18 μV for the frequencies within the birds' best range of hearing. Wave 2 amplitudes were always low (below 2 μV) in the early weeks and rarely exceeded 4–6 μV. Figure 5 shows the average peak amplitudes of wave 1 and 2 as a function of age. Linear regressions fit to the individual data showed r^2 that ranged between 0.03–0.51 for wave 1 and 0.04–0.25 for wave 2. Amplitudes increased for all waves with age but by varying degrees. Wave 1 peak amplitudes showed nearly linear increases for the click and 1.5–4 kHz. Compared to the increases seen in wave 1, amplitudes for wave 2 showed little amplitude growth until approximately 1 month of age, especially for low (0.5–1.5 kHz) and high frequencies (4.8–5.7 kHz). Again, the high-frequency data may be accounted for by the lack of a definable response before 15 days posthatch.

TABLE III. Decaying exponential parameters for latency ($y=a+be^{-cx}$).

Frequency	Wave	Asymptote (a)	Y-intercept (b)	Curvature (c)	Time constant ($1/c$)	r^2
Click	1	1.98	20.20	0.22	4.6	0.96
	2	3.59	23.60	0.17	5.9	0.86
	1–2 interval	1.58	7.30	0.12	8.3	0.53
0.5	1	2.30	14.44	0.17	5.9	0.85
	2	4.10	21.97	0.17	5.9	0.88
	1–2 interval	1.64	7.48	0.14	7.1	0.60
1	1	2.63	18.23	0.21	4.8	0.94
	2	4.19	19.13	0.15	6.7	0.85
	1–2 interval	1.47	6.32	0.10	10	0.59
1.5	1	2.46	13.45	0.19	5.3	0.91
	2	4.14	16.94	0.14	7.1	0.87
	1–2 interval	1.59	6.31	0.11	9.1	0.73
2	1	2.26	14.09	0.21	4.8	0.92
	2	4.02	19.85	0.17	5.9	0.91
	1–2 interval	1.71	7.05	0.13	7.7	0.81
2.86	1	2.06	9.17	0.16	6.3	0.86
	2	3.66	8.91	0.12	8.3	0.80
	1–2 interval	1.25	1.81	0.04	25.0	0.34
4	1	2.24	7.16	0.12	8.3	0.54
	2	3.79	18.10	0.16	6.3	0.79
	1–2 interval	1.48	16.75	0.23	4.4	0.42
4.8	1	2.41	20.18	0.19	5.3	0.42
	2	3.47	13.39	0.13	7.7	0.57
	1–2 interval	1.11	2.90	0.09	11.1	0.21
5.7	1	2.49	35.12	0.19	5.3	0.74
	2	3.57	27.04	0.16	6.3	0.48
	1–2 interval	1.18	4.53	0.14	7.1	0.07

IV. EXPERIMENT 2: EFFECTS OF CLICK REPETITION RATE ON ABR LATENCY AND AMPLITUDE IN DEVELOPING BUDGERIGARS

A. Introduction

The effects of increasing presentation rate on ABRs have been well studied in both developing and mature animals. Generally, ABRs can be elicited to stimulus presentation rates as high as 100 clicks/s in the mature auditory system but not in the immature auditory system of the same animal (Jewett and Romano, 1972). In adult humans and other mammals, reduced ABR amplitudes and increased ABR latencies in response to high presentation rates may be a function of neural fatigue and adaptation (e.g., Burkard and Voigt, 1989; Donaldson and Rubel, 1990; Hall, 1992; Jewett and Romano, 1972). Other studies have shown that increasing the stimulus presentation rate produces greater latency and amplitude changes in young animals as compared to older animals (e.g., Burkard and Voigt, 1989; Burkard *et al.*, 1996a,b; Donaldson and Rubel, 1990; Mair *et al.*, 1979; Shipley *et al.*, 1980). The working hypothesis is that adaptation associated with reduced synaptic transmission (e.g., decreased axon diameter, incomplete myelination, and neurotransmitter reuptake) may be the neurophysiological basis for the interaction between age, rate, and ABR latency and amplitude (Burkard *et al.*, 1996a,b; Hecox, 1975).

As far as we know, a developmental ABR rate study has only been measured in one bird, the chick (Saunders *et al.*, 1973). In the chick, and probably other precocial birds, the relation between stimulus rate and ABR latency and amplitude is almost adult-like at hatch. Such a pattern of development is different from altricial mammals, which do not show adult-like responses to temporal properties of the stimulus at birth. This experiment examined responses to changes in the temporal patterns of the click in five developing budgerigars. All equipment and recording procedures were the same as in experiment 1, except where noted.

B. Stimuli

Short-duration (0.1 ms), broadband clicks were presented at 100 dB pSPL for each of five rates: 5, 10, 30, 60, and 90 per second (Hz). Each ABR represents the average response of 1000 stimulus presentations (500 averages for each polarity), sampled at 20 kHz for 10 ms following onset of the stimulus. As with experiment 1, the biological signal was amplified ($\times$100 K) and notch filtered at 60 Hz during collection. The signal was bandpass filtered below 0.03 and above 3 kHz after collection.

C. Analysis

As described earlier, latency and amplitude measures were calculated for waves 1 and 2 for all repetition rates.

D. Results

Responses from animals less than 2 weeks of age were poorly developed. The waveform had only one positive-going wave that was relatively low in amplitude (below 3 μV) and had a latency which exceeded 4 ms. As the animals

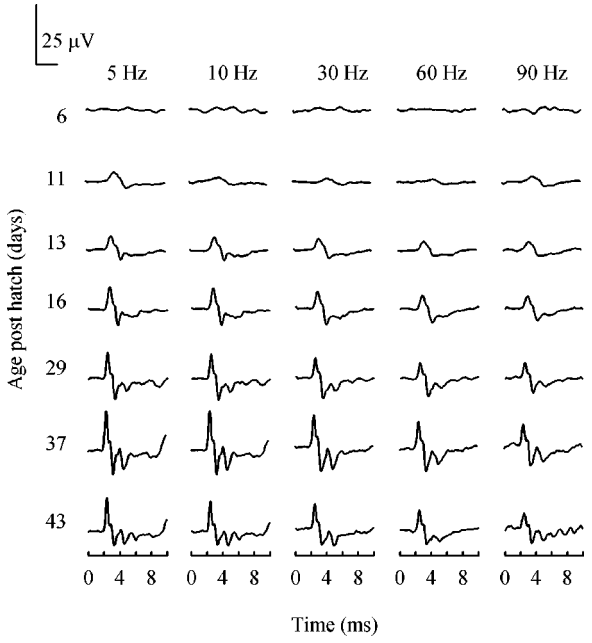

FIG. 6. ABR waveforms for each presentation rate through development for an individual bird. By 11 days of age, peaks in the waveform are visible. As the bird aged, latency increased and amplitude decreased as a function of increased presentation rate.

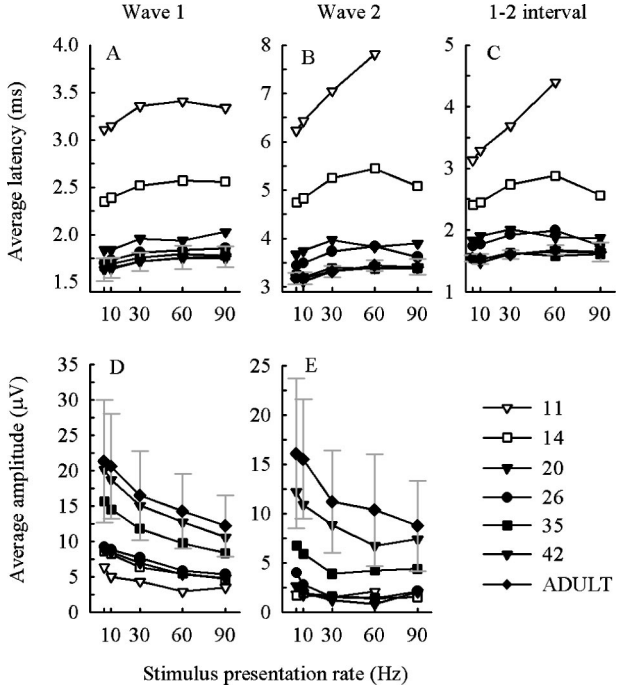

FIG. 7. (Top row) Average latency to the peaks of wave 1 (A), wave 2 (B), and the 1–2 interval (C) plotted as a function of presentation rate. Latency decreases as a function of age for all presentation rates and is more affected in the younger animals (<15 days old) than in the older animals. (Bottom row) Average amplitude for wave 1 (D) and 2 (E) plotted as a function of presentation rate. Amplitude increases as the birds' age but decreases for most ages as a function of increasing presentation rate. Adult measures are averages±s.d. (Brittan-Powell *et al.*, 2002).

aged, the waveform increased in sharpness for almost all presentation rates, and all peaks decreased in latency and increased in amplitude (Fig. 6). Typically, a second and possibly a third wave could be identified at later ages.

The youngest animals had the longest latencies and showed the largest changes in latency with increasing presentation rate [open symbols in Figs. 7(a)–(c)]. However, as the animals aged, peak latency decreased for wave 1 when click rate increased from 5 to 90 Hz. For example, shifts decreased, on average, from 0.21 ms at 14 days to 0.12 ms at 42 days. The adult latency change for this same increase in presentation rate was 0.13 ms—similar to the 42-day-old fledglings. This same type of change was seen in shifts for wave 2 peak latencies. For young animals, shifts were 0.33 ms at 14 days and decreased to 0.18 by 42 days of age. Adults showed a latency shift of 0.24 ms for wave 2. The interval between wave 1–2 decreased from 0.15 ms at 14 days of age to 0.06 ms at 42 days; adult birds showed a 0.10-ms shift. In general, latency decreased sharply in the first 2 weeks after hatching. After this age, even though latency shifts were variable, latency shifts exhibited by budgerigars in response to increasing presentation rate were adult-like by about 1 month of age, regardless of presentation rate.

Overall, absolute amplitudes for both wave 1 and 2 increased with age but decreased with increased rate [Figs. 7(d)–(e)]. Responses from older animals had the highest amplitudes, regardless of presentation rate. Between 10–15 days of age, there was a doubling of amplitude for wave 1. Over development, the peak amplitude of wave 1 increased 10–15 μV, and it was within 1 s.d. of adult values by 5 weeks of age. In contrast, the peak amplitude of wave 2 was slower to increase and was still well below adult amplitudes by this age. However, by the sixth week posthatch, nestlings' responses to increases in presentation rate were within 1 s.d. of adult amplitude values for wave 2 as well. The coefficient of variation showed that wave 1 amplitudes were always less variable than wave 2 amplitudes.

V. DISCUSSION

A. Onset of hearing

At high stimulus levels, responses to frequencies up to 2.86 kHz could be consistently evoked by 10 days posthatch, and by 14 days, ABRs could be evoked to almost all test frequencies. An additional nestling budgerigar was presented with tones of intensity levels of at least 110 dB SPL at all frequencies. For this one animal, synchronous responses to 4.8 and 5.7 kHz were elicited at slightly earlier ages (11 and 14 days, respectively), but it is hard to imagine that stimulation by these high intensity levels is biologically relevant to the bird. For example, the parents can produce vocalizations in excess of 100 dB SPL, but they rarely vocalize at such levels within the nest. Also, during the first 7 to 10 days of life, the birds' own vocalizations can barely be heard within 0.2 m of nest box, but after this age, the birds' begging calls could be heard over 6 m away (Stamps *et al.*, 1985).

B. Changes in threshold with development

It is a general property of vertebrates with elongated cochleae that the first auditory responses occur to low frequencies, despite the morphological developmental gradient

of the cochlea from the base (high) to the apex (low frequencies) (see the review in Harris and Dallos, 1984; Manley, 1996; Rubel and Parks, 1988). Like other animals, ABRs in budgerigars follow a similar developmental course—responses are first obtained at low frequencies and then at progressively higher ones. The rates of threshold maturation can differ considerably among animals. Some mammals, such as guinea pigs (Dum, 1984) and humans (see the review in Werner and Marean, 1996), are born with functioning auditory systems, exhibit adult-like thresholds, at most or all frequencies, and are considered precocial with respect to hearing. Other mammals, such as the gerbil (McFadden *et al.*, 1996) or cat (Walsh *et al.*, 1986a), are considered deaf at birth and are thus altricial with respect to hearing. These mammals also show different rates of maturation. For example, threshold development is frequency dependent in cats, with thresholds at high frequencies reaching adult level before low frequencies (Walsh *et al.*, 1986a). Gerbils, however, show faster maturation at the middle frequencies, with low and high frequencies developing at similar but slower rates (McFadden *et al.*, 1996).

Development of high-frequency sensitivity before low-frequency sensitivity in altricial mammals correlates well with the development of the basoapical maturation of the cochlea. Birds, on the other hand, show a different pattern of ABR threshold maturation. Precocial birds show adult-like thresholds to low and middle frequencies by the time of hatching, with sensitivity to higher frequencies continuing to improve after this time (Saunders *et al.*, 1973). Altricial birds, such as the barn owl (Köppl and Nickel, 2001) and the budgerigar (current study), show developmental patterns similar to precocial birds (low to high frequency), except that the maturation occurs after hatching. Like mammals, the basilar papilla of birds develops from the base to the apex (Saunders *et al.*, 1973); however, unlike mammals (but see, for example, Arjmand *et al.*, 1988; Romand, 1987), the physiological threshold development progresses from low to high frequencies such that higher frequency thresholds are the last to become adult-like in birds.

Some mammals show a period early in development where thresholds improve but the ABR audiogram remains relatively flat (McFadden *et al.*, 1996; Walsh *et al.*, 1986a). After this initial period, thresholds across the frequency range improve rapidly. Precocial birds do not show a flat frequency-threshold curve early in development. Young chicks (D12–13 of incubation) exhibit poor sensitivity across frequency but threshold improvement is not equivalent across frequencies. Rather, the audiogram takes on the U-shape appearance by D14–15 (Saunders *et al.*, 1973). This is also true for ducks (Dmitrieva and Gottlieb, 1992). Pied-flycatchers, on the other hand, do show flat frequency-thresholds curves for the first few days after hatching, but respond only to frequencies between 0.3 and 1 kHz. In young budgerigars, the initial audibility curve is relatively flat and thresholds are high (see Fig. 3), but there is rapid improvement from that time on, with 2 kHz becoming the most sensitive frequency by the end of the second week.

In more well-studied animals, the rapid improvement in threshold and the increase in frequency bandwidth to which the animals respond is correlated with fluid from the middle ear being resorbed and the improvement of middle-ear function as shown in cats (Walsh *et al.*, 1986a), gerbils (McFadden *et al.*, 1996), and chickens (Saunders *et al.*, 1973). In budgerigars, the external ear canal is open by day 10. The opening of the canal is coincident with a dramatic improvement of threshold between 11–17 days of age and an increase in bandwidth of effective frequencies by this time. It is possible that the increase in sensitivity and bandwidth during this phase in budgerigars is partially due to external and middle-ear maturation.

C. Changes in ABR latency and amplitude over development

Latency decreased and amplitude increased with increasing age. Evaluation of latency maturation based on exponential decay functions showed that latencies to wave 1 matured first, followed closely by latencies to wave 2. Wave amplitudes matured slightly later than wave latencies, but this may be a function of variability between subjects. The coefficients of variation in amplitude across development were always greater ($>20\%$) than the coefficients for latency across development ($<20\%$). Wave 1 and wave 2 also showed differences in amplitude growth. For the most part, wave 1 increased in an almost linear fashion, but wave 2 showed little growth across most frequencies until late in development. These results suggest that wave 2 amplitude may still be increasing well after the bird leaves the nest.

As with all species studied to date, increasing intensity level results in shorter response latencies and larger response amplitudes at all ages tested. Even as the animal grows and distances within the papilla and along the VIIIth nerve increase, the latencies to waves 1 and 2 as well as the 1–2 interval show consistent decreases. Explanations offered for these decreases in latency include increasing axon diameter, myelination, and synaptic efficiency which lead to decreases in the time course of action potential generation (e.g., Walsh *et al.*, 1986b). Similarly, increases in amplitude may be due to increased fiber diameter and myelination, resulting in increased neural synchrony (e.g., Walsh *et al.*, 1986c). Nothing is known about whether similar physical changes occur in developing budgerigars. However, the present results, showing that latencies to wave 2 reached adult levels at a slightly later age, do suggest that brainstem development may lag peripheral development in budgerigars, as it does in cats (Walsh *et al.*, 1986b).

Overall, thresholds and latencies tended to stabilize (reach adult levels) at approximately the same age for budgerigars. Response amplitudes, on the other hand, increased in a nonlinear fashion during development for both wave 1 and wave 2. For the highest frequencies (4.8 and 5.7 kHz), amplitudes changed only slightly over the developmental period studied, with birds also exhibiting the highest thresholds at those frequencies. Even though ABR thresholds and latencies stabilize in budgerigars by about 3–4 weeks of age, amplitude did not reach adult values until about 6 weeks of age.

In chickens and kittens, improved mechanical transmission in the external and middle ear is hypothesized to con-

tribute to decreases in ABR latency (Katayama, 1985; Walsh *et al.*, 1986b). In kittens, increased fiber diameter and myelination may also be involved in the continued improvement of latency and amplitude measurements (Walsh *et al.*, 1986b,c). In barn owls, decreasing latencies elicited by click stimuli between P21–23 coincide with the maturation of the endbulbs of Held (Kubke and Carr, 2000)—the innervation between the auditory nerve and cochlear nucleus magnocellularis (NM). Further ABR changes in barn owls are attributed to continuing myelination. Also, synaptic transmission between the auditory nerve and cochlear nuclei is mediated by excitatory amino acids, like glutamate (see the review in Kubke and Carr, 2000), and adult patterns of glutamate expression are attained between P14 and P21. Temporal patterns become adult-like in the barn owl ABR at this same time. On the basis of these data, it seems likely that changes in latency and amplitude in the budgerigar (seen by day 20–26) may be due to increased synaptic transmission between the auditory nerve and the cochlear nuclei, and increased myelination and nerve-fiber diameters as well as the increased transmission function of the middle ear.

D. Effects of click repetition rate on latency and amplitude in developing budgerigars

Temporal aspects of stimulus delivery have a more pronounced effect on younger budgerigars than older budgerigars, as has been found in mammals and chicks (e.g., Burkard and Voigt, 1989; Burkard *et al.*, 1996a; Saunders *et al.*, 1973). Latency to individual waves of the budgerigar ABR increased with increasing rate, even while latency decreased as a function of increasing age. In nestling budgerigars, higher rates of stimulus presentation resulted not only in longer latencies, but showed greater effects in younger animals. The interval between waves was greater at younger ages, suggesting that young budgerigars, like mammals, show greater adaptation which was cumulative across synapses (Burkard *et al.*, 1996a; Donaldson and Rubel, 1990; Jewett and Romano, 1972; Lasky, 1997; Mair *et al.*, 1979; Salamy *et al.*, 1978; Shipley *et al.*, 1980).

Peak-to-peak ABR amplitude increased with age, but ABR amplitude in budgerigar ABR waveforms decreased with increasing rate. This is similar to what was seen in the adult budgerigar data (Brittan-Powell *et al.*, 2002), as well as data shown in mammals, such as gerbils (Burkard and Voigt, 1989; Donaldson and Rubel, 1990), kittens (Burkard *et al.*, 1996a; Mair *et al.*, 1979; Shipley *et al.*, 1980), and human infants (Lasky, 1997; Salamy *et al.*, 1979). In sum, these data suggest that younger budgerigars show greater neural adaptation than older budgerigars, resulting in a greater reduction in ABR amplitudes at higher stimulus rates.

E. Hearing and vocal development

Vocal learning in songbirds has been suggested as a model of vocal development in humans. Studies of ABR development in human infants show that by 6 months of age, hearing thresholds have reached adult values (see the review in Werner and Marean, 1996). This is about the time that the first signs of babbling in infants occur, suggesting that hearing is necessary for this stage of vocal production to occur at this age. The inability to hear one's own voice delays or discourages babbling—deaf infants do not begin this stage until 10–11 months of age (Oller and Eilers, 1988). Thus, normal vocal development in human infants depends on the ability of the baby to hear adult models and feedback from its own vocalizations by 5–10 months of age.

In birds, the first stage of song learning is totally dependent on hearing. Studies of the sensitive period of song learning show that birds tutored with song before P10–13 never produce the tutored song (see the review in Catchpole and Slater, 1995). This parallels developmental studies of hearing in songbirds showing that hearing in altricial birds is not fully developed at hatching but continues to improve even into the nestling period (Aleksandrov and Dmitrieva, 1992; Khayutin, 1985).

The budgerigar is an open-ended learner (i.e., it retains the ability learn vocalizations throughout adulthood), but the sensory and sensory motor phases of vocal learning have yet to be precisely determined. Through studies of budgerigar contact call development (Brittan-Powell *et al.*, 1997; Hall *et al.*, 1997; Heaton and Brauth, 1999), we know that these birds require auditory feedback in order to produce species-specific vocalizations. Deafening birds between 9–11 days of age has a profound effect on the bird's vocal behavior (Heaton and Brauth, 1999) but does not affect all calls equally. Food-begging calls from these birds progressed from high-frequency vocalizations (stage I—stages refer to Brittan-Powell *et al.*, 1997) to the harsh noisy calls observed at later ages (stage II). The birds, however, never produced patterned food-begging calls exhibited by normally hearing birds at 4 weeks of age (stage III) (Heaton and Brauth, 1999). These findings suggest that auditory feedback is important for the transition from stage II to stage III vocalizations.

The present results show that budgerigars hear little, if at all, at hatch. By day 10, the bird's outer ear canals are open and hearing thresholds improved rapidly, primarily at frequencies below 4 kHz. This represents somewhat of a mismatch since the vocalizations of young birds have a peak frequency of 4 kHz or higher. It is unlikely, then, that vocalizations produced before 11 days of age depend on hearing—a conclusion paralleled by what has been found in songbird tutoring studies.

Between days 12 to 28, however, there are dramatic changes going on in both vocal production and hearing development. From 13–27 days, the peak frequency of the nestlings' calls drops to between 3–3.5 kHz, but bandwidth and duration of calls increase. At the same time, the frequency range of hearing increases to include all frequencies tested and sensitivity in the 2–4-kHz range increases by 30–35 dB. It is also during this time that deafening can essentially derail further vocal development. Taken together, these data suggest that stage II may be the start of the sensitive period for auditory feedback in the budgerigar.

By the fourth week of life, the birds' auditory thresholds are near adult levels of sensitivity. During this same time (28–34 days of age), many of the acoustic characteristics of budgerigar vocalizations are stabilizing (e.g., peak frequency

by 1 month and bandwidth and duration of calls at or around fledging). By 1-week postfledging, adult contact calls (a variant of their food-begging call) are readily elicited from the birds (Brittan-Powell *et al.*, 1997). Therefore, adult levels of hearing are reached about a week before of the appearance of the budgerigars' first adult sound (the contact call), but budgerigar vocal development continues beyond the production of the first contact call. Budgerigars show their first signs of vocal mimicry at about 4 weeks postfledging (Brittan-Powell *et al.*, 1997), which is over 2–3 weeks after hearing thresholds are adult-like. Thus, the ''sensitive phase'' for vocal learning in this species, as in songbirds and human infants, continues well after hearing thresholds reach adult levels.

VI. CONCLUSIONS

This study tracked the development of auditory sensitivity in nestling budgerigars through the auditory brainstem response. We can conclude that in general, changes in the ABR of nestling budgerigars due to changes in intensity, frequency, and repetition rate were comparable to what has been found in other vertebrates, both precocial and altricial. As with all animals tested to date, latency decreases, amplitude increases, and the ABR waveform becomes more complex as the animal ages.

Auditory feedback influences the development of vocalizations in budgerigars, and other vocal learning birds, but until now, little was known about hearing in these birds. This study extends the findings of threshold development in altricial birds to include budgerigars. It shows that budgerigars probably cannot hear at hatching and that auditory sensitivity develops, as in other altricial birds, well into the nestling period (Aleksandrov and Dmitrieva, 1992; Köppl and Nickel, 2001). When combined with what is known about budgerigar vocal development, the present results provide a developmental timetable for future studies pertaining to the anatomical development of the auditory system in the budgerigar as well as direct testing of hearing deprivation at ages where both hearing and vocal ability are now known.

ACKNOWLEDGMENTS

The authors would like to thank C. Carr, O. Gleich, F. Kubke, C. Köppl, D. Higgs, K. Poling, A. Lauer, and M. Dent, as well as two anonymous reviewers, for comments on earlier drafts. This work was supported in part by training grant DC00046 from the National Institute of Deafness and Communicative Disorders of the National Institutes of Health to E.F.B.P. and National Institutes of Health Grant DC00198 to R.J.D. The work described here was in partial fulfillment of the requirement of a doctor of philosophy to E.F.B.P. (University of Maryland, College Park, 2002).

Aleksandrov, L. I., and Dmitrieva, L. P. (**1992**). ''Development of auditory sensitivity of altricial birds: Absolute thresholds of the generation of evoked potentials,'' Neurosci. Behav. Physiol. **22**, 132–137.

Arjmand, E., Harris, D., and Dallos, P. (**1988**). ''Developmental changes in frequency mapping of the gerbil cochlea: Comparison of two cochlear locations,'' Hear. Res. **32**, 93–96.

Boettcher, F. A., Mills, J. H., and Norton, B. L. (**1993a**). ''Age-related changes in auditory evoked potentials of gerbils. I. Response amplitudes,'' Hear. Res. **71**, 137–145.

Boettcher, F. A., Mills, J. H., Norton, B. L., and Schmiedt, R. A. (**1993b**). ''Age-related changes in auditory evoked potentials of gerbils. II. Response latencies,'' Hear. Res. **71**, 145–156.

Brittan-Powell, E. F., Dooling, R. J., and Farabaugh, S. M. (**1997**). ''Vocal development in budgerigars (*Melopsittacus undulatus*): Contact calls,'' J. Comp. Psychol. **111**, 226–241.

Brittan-Powell, E. F., Dooling, R. J., and Gleich, O. (**2002**). ''Auditory brainstem responses (ABR) in adult budgerigars (*Melopsittacus undulatus*),'' J. Acoust. Soc. Am. **112**, 999–1008.

Burkard, R., and Voigt, H. F. (**1989**). ''Stimulus dependencies of the gerbil brainstem auditory-evoked response (BAER). I. Effects of click level, rate, and polarity,'' J. Acoust. Soc. Am. **85**, 2514–2525.

Burkard, R., McGee, J., and Walsh, E. J. (**1996a**). ''Effects of stimulus rate on feline brainstem auditory evoked response during development. I. Peak latencies,'' J. Acoust. Soc. Am. **100**, 978–990.

Burkard, R., McGee, J., and Walsh, E. J. (**1996b**). ''Effects of stimulus rate on feline brainstem auditory evoked response during development. II. Peak amplitudes,'' J. Acoust. Soc. Am. **100**, 991–1002.

Catchpole, C. K., and Slater, P. J. B. (1995). *Bird Song: Biological Themes and Variations* (Cambridge University Press, Cambridge, Great Britain).

Dmitrieva, L. P., and Gottlieb, G. (**1992**). ''Development of brainstem auditory pathway in mallard duck embryos and hatchlings,'' J. Comp. Physiol. **171**, 665–671.

Dmitrieva, L. P., and Gottlieb, G. (**1994**). ''Influence of auditory experience on the development of brainstem auditory-evoked potentials in Mallard duck embryos and hatchlings,'' Behav. Neural Biol. **61**, 19–28.

Donaldson, G. S., and Rubel, E. W. (**1990**). ''Effects of stimulus repetition rate on ABR threshold, amplitude, and latency in neonatal and adult Mongolian gerbils,'' Electroencephalogr. Clin. Neurophysiol. **77**, 458–470.

Dooling, R. J., Gephart, B. F., Price, P. H., McHale, C., and Brauth, S. E. (**1987**). ''Effects of deafening on the contact calls of the budgerigar (*Melopsittacus undulatus*),'' Anim. Behav. **35**, 1264–1266.

Dooling, R. J., Lohr, B., and Dent, M. L. (**2000**). ''Hearing in birds and reptiles,'' in *Comparative Hearing: Birds and Reptiles*, edited by R. J. Dooling, A. N. Popper, and R. R. Fay (Springer, New York), pp. 308–359.

Dum, N. (**1984**). ''Postnatal development of the auditory evoked brainstem potentials in the guinea pig,'' Acta Oto-Laryngol. **97**, 63–68.

Farabaugh, S., and Dooling, R. J. (**1996**). ''Acoustic communication in parrots: Laboratory and field studies of budgerigars, *Melopsittacus undulatus*,'' in *Ecology and Evolution of Acoustic Communication in Birds*, edited by D. E. Kroodsma and E. H. Miller (Cornell University Press, Ithaca, NY), pp. 97–118.

Hall, J. (**1992**). *Handbook of Auditory Evoked Responses* (Allyn and Bacon, Boston).

Hall, W. S., Cookson, K. K., Heaton, J. T., Roberts, T., Shea, S., and Brauth, S. E. (**1997**). ''Audio-vocal learning in budgerigars,'' Proc. New York Acad. Sci. **807**, 352–367.

Harris, D. M., and Dallos, P. (**1984**). ''Ontogenetic changes in frequency mapping of the mammalian ear,'' Science **225**, 741–743.

Heaton, J. T., and Brauth, S. E. (**1999**). ''Effects of deafening on the development of nestling and juvenile vocalizations in budgerigars (*Melopsittacus undulatus*),'' J. Comp. Psychol. **113**, 314–320.

Heaton, J. T., Dooling, R. J., and Farabaugh, S. M. (**1999**). ''Effects of deafening on the calls and warble song of adult budgerigars (*Melopsittacus undulatus*),'' J. Acoust. Soc. Am. **105**, 2010–2019.

Hecox, K. (**1975**). ''Electrophysiological correlates of human auditory development,'' in *Infant Perception: From Sensation to Cognition*, edited by L. B. Cohen and P. Salapatek (Academic, New York), pp. 151–192.

Jewett, D., and Romano, M. (**1972**). ''Neonatal development of the auditory system: Potentials averaged from the scalp of rat and cat,'' Brain Res. **36**, 101–115.

Katayama, A. (**1985**). ''Postnatal development of auditory function in the chicken revealed by auditory brainstem responses (ABRs),'' Electroencephalogr. Clin. Neurophysiol. **62**, 388–398.

Khayutin, S. N. (**1985**). ''Sensory factors in the behavioral ontogeny of altricial birds,'' Adv. Stud. Behav. **15**, 105–152.

Köppl, C., and Nickel, R. (**2001**). *Maturation of Evoked Cochlear Potentials in the Barn Owl* (6th International Congress of the Society for Neuroethology, University of Bonn, Germany).

Kubke, M. F., and Carr, C. E. (**2000**). ''Development of the auditory brainstem of birds: Comparison between barn owls and chickens,'' Hear. Res. **147**, 1–20.

Lasky, R. E. (**1997**). ''Rate and adaptation effects on the auditory evoked

brainstem response in human newborns and adults,'' Hear. Res. **111**, 165–176.
Mair, I. W., Elverland, H. H., and Laukli, E. (**1978**). ''Development of early auditory-evoked responses in the cat,'' Audiology **17**, 469–488.
Mair, I. W. S., Elverland, H. H., and Laukli, E. (**1979**). ''Early auditory-evoked responses in the cat: Rate effects,'' Audiology **18**, 265–278.
Manley, G. A. (**1996**). ''Ontogeny of frequency mapping in the peripheral auditory system of birds and mammals: A critical review,'' Aud. Neurosci. **3**, 199–214.
McFadden, S. L., Walsh, E. J., and McGee, J. (**1996**). ''Onset and development of auditory brainstem responses in the Mongolian gerbil (*Meriones unguiculatus*),'' Hear. Res. **100**, 68–79.
Mills, J. J., Schmiedt, R. A., and Kulish, L. F. (**1990**). ''Age-related changes in auditory potentials of Mongolian gerbil,'' Hear. Res. **46**, 210–210.
Oller, D. K., and Eilers, R. E. (**1988**). ''The role of audition in infant babbling,'' Child Dev. **59**, 441–449.
Romand, R. (**1987**). ''Tonotopic evolution during development,'' Hear. Res. **28**, 117–123.
Rubel, E. W., and Parks, T. N. (**1988**). ''Organization and development of the avian brain-stem auditory system,'' in *Brain Function*, edited by G. M. Edelman, W. Einar Gall, and W. Maxwell Cowan (Wiley, New York), pp. 3–92.
Salamy, A., McKean, C., Pettett, G., and Mendelson, T. (**1978**). ''Auditory brainstem recovery process from birth to adulthood,'' Psychophysiology **15**, 214–220.
Salamy, A., Birtley Fenn, C., and Bronshvag, M. (**1979**). ''Ontogenesis of human brainstem evoked potential amplitude,'' Dev. Psychobiol. **12**, 519–526.
Saunders, J. C., Coles, R. B., and Gates, G. R. (**1973**). ''The development of auditory evoked responses in the cochlea and cochlear nuclei of the chick,'' Brain Res. **63**, 59–74.
Saunders, J. C. (**1974**). ''The development of auditory evoked responses in the chick embryo,'' Estratto da Minerva Otorinolaringlogica **24**, 221–229.
Saunders, J. C., Gates, G. R., and Coles, R. B. (**1974**). ''Brainstem evoked responses as an index of hearing thresholds in one-day-chicks and ducklings,'' J. Comp. Physiol. Psychol. **86**, 426–431.
Shipley, C., Buchwald, J. S., Norman, R., and Guthrie, D. (**1980**). ''Brainstem auditory evoked response development in the kitten,'' Brain Res. **182**, 313–326.
Stamps, J., Clark, A., Arrowood, P., and Kus, B. (**1985**). ''Parent offspring conflict in budgerigars,'' Behaviour **94**, 1–40.
Walsh, E. J., McGee, J., and Javel, E. (**1986a**). ''Development of auditory-evoked potentials in the cat. I. Onset of response and development of sensitivity,'' J. Acoust. Soc. Am. **79**, 712–724.
Walsh, E. J., McGee, J., and Javel, E. (**1986b**). ''Development of auditory-evoked potentials in the cat. II. Wave latencies,'' J. Acoust. Soc. Am. **79**, 725–744.
Walsh, E. J., McGee, J., and Javel, E. (**1986c**). ''Development of auditory-evoked potentials in the cat. III. Wave amplitudes,'' J. Acoust. Soc. Am. **79**, 745–754.
Werner, L. A., and Marean, G. C. (**1996**). *Human Auditory Development* (Westview, Boulder, CO).

Testing the concept of softness imperception: Loudness near threshold for hearing-impaired ears

Brian C. J. Moore[a)]
Department of Experimental Psychology, University of Cambridge, Downing Street, Cambridge CB2 3EB, United Kingdom

(Received 19 November 2003; revised 19 March 2004; accepted 22 March 2004)

Buus and Florentine [J. Assoc. Res. Otolaryngol. **3**, 120–139 (2002)] have proposed that loudness recruitment in cases of cochlear hearing loss is caused partly by an abnormally large loudness at absolute threshold. This has been called ''softness imperception.'' To evaluate this idea, loudness-matching functions were obtained using tones at very low sensation levels. For subjects with asymmetrical hearing loss, matches were obtained for a single frequency across ears. For subjects with sloping hearing loss, matches were obtained between tones at two frequencies, one where the absolute threshold was nearly normal and one where there was a moderate hearing loss. Loudness matching was possible for sensation levels (SLs) as low as 2 dB. When the fixed tone was presented at a *very* low SL in an ear (or at a frequency) where there was hearing impairment, it was matched by a tone with approximately the same SL in an ear (or at a frequency) where hearing was normal (e.g., 2 dB SL matched 2 dB SL). This relationship held for SLs up to 4–10 dB, depending on the subject. These results are not consistent with the concept of softness imperception. © *2004 Acoustical Society of America.* [DOI: 10.1121/1.1738839]

PACS numbers: 43.66.Cb, 43.66.Sr [NFV] Pages: 3103–3111

I. INTRODUCTION

People with cochlear hearing loss often experience a perceptual effect called loudness recruitment (Fowler, 1936; Steinberg and Gardner, 1937; Hood, 1972). The effect can be characterized in the following way: the absolute threshold is higher than normal, but at high sound levels, the loudness is almost the same for an impaired ear and a normal ear. Loudness recruitment is most easily measured in subjects with one normal ear and one impaired ear (Miskolczy-Fodor, 1960; Hood, 1972; Moore and Glasberg, 1997). Typically, a tone of a given frequency is presented alternately to the two ears. The tone is fixed in level in one ear, and the subject is asked to adjust the level in the other ear until the tones in the two ears sound equal in loudness. This is repeated for a series of levels of the fixed tone, which may be presented either to the normal ear, the impaired ear, or (preferably) both. For levels close to absolute threshold, the level (in dB SPL) required for equal loudness in the two ears is much greater in the impaired than in the normal ear, but the difference in level decreases with increasing overall level. It is as if the loudness in the impaired ear ''catches up'' with that in the normal ear at high sound levels.

The traditional view of loudness recruitment is that it is an abnormally rapid growth in loudness level once the sound level exceeds the (elevated) absolute threshold (Allen and Jeng, 1990; Moore, 1995; 1998). However, recently, Buus and Florentine (2002) proposed that loudness recruitment is caused at least partly by an abnormally large loudness *at* absolute threshold. They argued that, above threshold, loudness grows only a little more rapidly than normal in an impaired ear. Buus and Florentine developed this proposal on the basis of an experiment in which hearing-impaired subjects were asked to compare the loudness of single tones with that of complex tones containing four or ten sinusoidal components (all tones were presented to one ear of each subject). The data were used to construct loudness-matching functions. It was assumed that, if the components in the complex tones were widely spaced, the loudness of each complex corresponded to the sum of the loudness of the individual components. For example, a four-tone complex composed of equally loud components should sound four times as loud as any single component. More generally, the level difference between equally loud pure tones and *n*-tone complexes should indicate the increase in level necessary to produce an *n*-fold increase in loudness.

Buus and Florentine inferred from their results that, close to the absolute threshold, the rate of growth of loudness is similar for impaired and normal ears. This is consistent with previous data obtained using loudness scaling (Hellman and Zwislocki, 1964) and other methods (Hellman, 1997). From this finding, and on the basis of a model, Buus and Florentine argued further that the loudness at threshold is greater for impaired than for normal ears. Hellman and coworkers (Hellman, 1994; 1997; Hellman and Meiselman, 1990) have also suggested that the loudness at threshold is greater for hearing-impaired than for normally hearing ears, although this suggestion is largely based on extrapolation of data obtained using loudness scaling techniques, such as magnitude estimation and magnitude production. Since loudness grows very rapidly with increasing sound level for levels close to absolute threshold (for both normal and impaired ears), it is difficult to determine from such data the precise value of the loudness at absolute threshold.

According to Buus and Florentine (2002), when a sound is at or only just above its absolute threshold in an impaired

a)Electronic mail: bcjm@cam.ac.uk

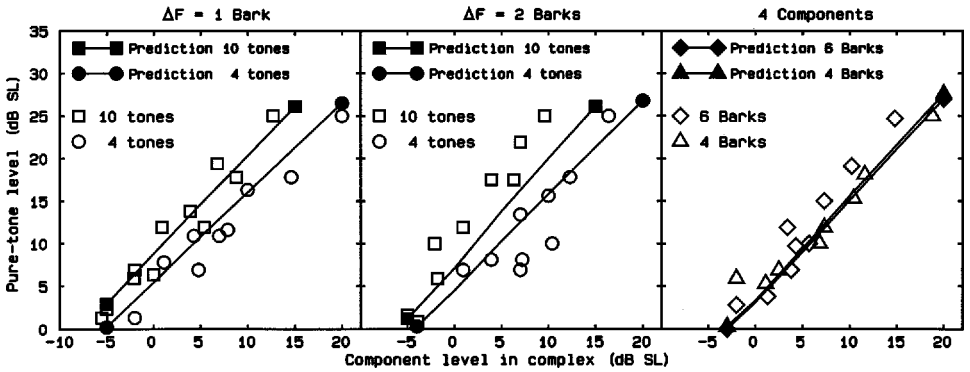

FIG. 1. The open symbols show data from Buus and Florentine (2002), for loudness matches between multicomponent complexes and a single 1600-Hz sinusoid, for their listener ''L1.'' The default parameter values of the model were assumed. The sensation level (SL) of the single tone is plotted as a function of the SL per component of the complex. The key for each panel shows the spacing of the components in Barks and the number of components in each complex. Lines show predictions of the model of Moore and Glasberg (2004).

ear, it already sounds louder than normal. In other words, the impaired ear never hears really soft sounds. This has been called ''softness imperception'' (Florentine *et al.*, 2004). However, the finding that, near threshold, loudness grows at a similar rate in impaired and normal ears does not necessarily imply that the loudness at threshold is greater in an impaired ear. Moore and Glasberg (2004) have described a loudness model which is partly based on the assumption that the loudness at threshold is *equal* for normal and impaired ears. This model, which is described in more detail later, correctly predicts that, near threshold, loudness grows at a similar rate in impaired and normal ears. However, at levels more than a few decibels above threshold, the loudness grows more rapidly than normal in an impaired ear, and this accounts for the loudness recruitment effect. The model presented by Moore and Glasberg can provide a good fit to published loudness-matching functions obtained for subjects with unilateral hearing loss. Furthermore, it gives a good fit to the data of Buus and Florentine (2002), described earlier, which involved loudness comparisons of single tones and multi-tone complexes for hearing-impaired subjects. An example of the fit to their data is given in Fig. 1, which is taken from Moore and Glasberg (2004).

There are few data that allow a direct evaluation of the concept of softness imperception, since loudness-matching and loudness-scaling functions have typically not been obtained for stimuli at very low SLs. Hellman and Zwislocki (1964) presented a re-analysis of loudness-matching data from Miskolczy-Fodor (1960), apparently based on individual data (which were not presented by Miskolczy-Fodor), but the lowest SL used appears to be around 5 dB in the impaired ears. Experiments based on magnitude estimation or cross-modality matching (Hellman, 1994) have not used SLs below 4 dB, and, as noted earlier, it is difficult to use such data to determine the exact loudness in the vicinity of threshold, due to the steepness of the loudness-growth function.

The present experiment was intended to provide a more direct test of the concept of softness imperception, using loudness matching rather than magnitude estimation or magnitude production. According to the model described by Buus and Florentine (2002), if loudness-matching functions are obtained between a normal ear and an impaired ear, then, close to threshold, the SL at equal loudness should be higher in the normal ear than in the impaired ear. For example, for a tone frequency where the impaired ear has a 70 dB hearing loss, a tone at 2 dB SL in the impaired ear should be matched by a tone at 12–14 dB SL in the normal ear; see Fig. 4 in Buus and Florentine (2002). The present experiment tested this prediction by obtaining loudness matches across ears at very low SLs for two subjects with highly asymmetric hearing loss. Additional evidence was obtained using two subjects with sloping hearing loss, for whom loudness matches were obtained between a tone at a frequency where hearing was near-normal, and a tone at a frequency where there was a significant hearing loss.

II. METHOD

A. Subjects

Four subjects were tested. The audiograms of the test ears for all four subjects are shown in Fig. 2; these were measured using a GSI16 audiometer and TDH50 earphones, with a 1 or 2 dB final step size. For all subjects, the hearing losses were diagnosed as sensorineural (probably cochlear) in origin, based on the absence of an air-bone gap and normal results for impedance audiometry. No subject showed any evidence for dead regions (regions of the cochlea where there are no functioning inner hair cells and/or neurons) over the frequency range 500–4000 Hz, as assessed using the TEN test (Moore *et al.*, 2000; Moore, 2001) or the newer TEN(HL) test (Moore *et al.*, 2004).

Subject S1, aged 57, had an asymmetric sloping hearing loss of unknown origin. He did not use hearing aids. For him, loudness matches were obtained between a 1-kHz tone in the right ear (absolute threshold 17 dB SPL) and a 6-kHz tone in the left ear (absolute threshold 74.5 dB SPL). Subject S2, aged 33, had a symmetric hearing loss with normal hearing up to 0.5 kHz and a 50–60 dB loss above that; the loss was congenital. She used bilateral multichannel fast-acting compression hearing aids. She was tested using the left ear only; loudness matches were obtained between a 0.5-kHz tone (absolute threshold 15 dB SPL) and a 2-kHz tone (absolute threshold 70 dB SPL). Subject S3, aged 43, had an

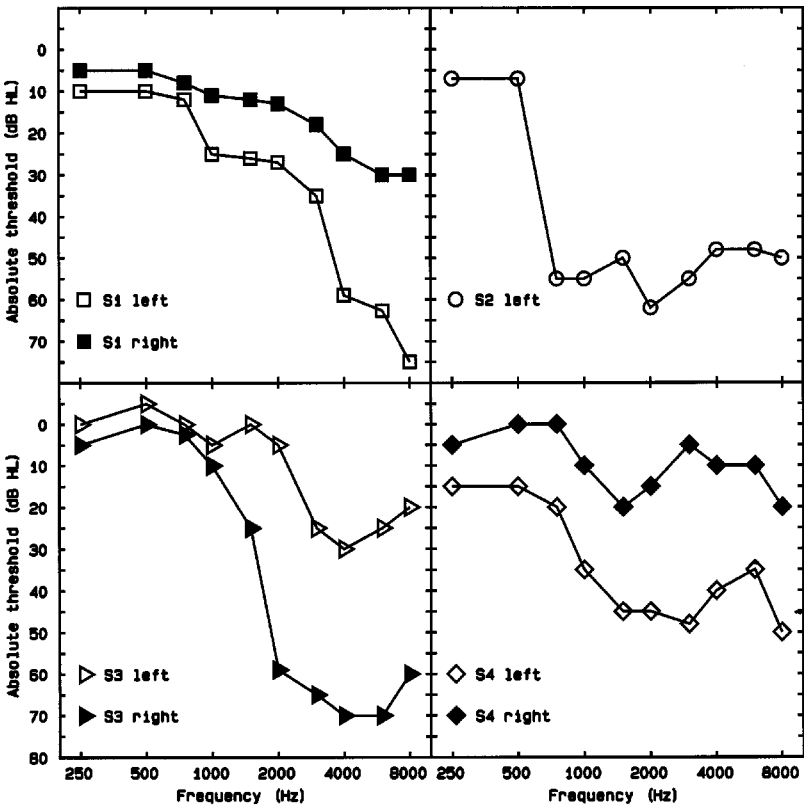

FIG. 2. Audiograms (air-conduction thresholds) of the test ears of the hearing-impaired subjects, in dB HL, obtained using manual audiometry.

asymmetric high-frequency loss probably caused by rifle shooting. He did not use hearing aids. Loudness matches were obtained across ears for a frequency of 2500 Hz; the absolute threshold for this frequency was 27 dB SPL in the left ear and 71 dB SPL in the right ear. Subject S4, aged 34, had an asymmetric high-frequency loss of unknown origin. She used a two-channel hearing aid with little compression in the low-frequency channel and slow-acting compression in the high-frequency channel, in the left ear only. Loudness matches were obtained across ears for a frequency of 3000 Hz; the absolute threshold for this frequency was 63 dB SPL in the left ear and 21 dB SPL in the right ear. No subject wore hearing aids during the testing.

Subjects were trained until their performance appeared to be stable and consistent. This typically took two 2 h sessions. Subjects were paid for their participation, except for S1, who was the author.

B. Measurement of absolute thresholds

Absolute thresholds at the test frequencies were measured using an adaptive three-interval forced-choice task with a ''3-down 1-up'' method; this tracks the 79.4% correct point on the psychometric function (Levitt, 1971). The signal duration was 500 ms, including 20 ms rise/fall ramps shaped with a raised-cosine function. The three intervals in which the signal might occur were indicated by lights on the response box; the intervals were separated by 500 ms. The signal was presented in one of the intervals, selected at random. Subjects indicated the interval thought to contain the signal using a three-button response box; the buttons were positioned below the three lights. Feedback was provided after each trial by lighting the light for the correct interval. The initial step size was 5 dB, and this was reduced to 2 dB after four reversals. Twelve reversals were obtained and threshold was defined as the mean of the signal levels at the last eight reversals.

At least twelve threshold estimates were obtained for each subject and each test frequency/ear. Usually, six estimates were obtained during the first test session, and two or three estimates were obtained in each subsequent test session. There was no evidence for systematic changes in absolute threshold across sessions. The standard deviation (s.d.) of the estimates for a given ear and frequency ranged from 1.0 to 3.8 dB (mean s.d.=2.0 dB). The corresponding standard error (SE) of the estimates was always 1 dB or less.

C. Loudness-matching procedure

The two tones to be matched (denoted A and B) were presented in a regular alternating sequence. The duration of each tone was 500 ms, including 20 ms rise/fall ramps shaped with a raised-cosine function. This is the same duration as used to measure absolute thresholds. There was a 500-ms interval between A and B and an 800-ms interval between B and A. Each stimulus was accompanied by a light on the response box. Subjects were asked to press the button under the light associated with the louder tone. For example, if tone B was initially louder, they had to press the button under the light that was on when tone B was presented (the right button). They were told that this would have the effect either of making B softer, or of making A louder. The level of the variable tone was changed only between presentations, and not within a presentation. If no button was pressed, the level of the variable stimulus stayed the same. A change from pressing the left button to changing the right button, or vice

versa, was termed a ''turnaround.'' The step size for the change in level was 3 dB until two turnarounds had occurred and was 1 dB thereafter. Subjects were instructed to ''bracket'' the point of equal loudness several times, by making the variable stimulus clearly louder than the fixed stimulus and then clearly softer, before using the buttons to make the stimuli equal in loudness. When subjects were satisfied with a loudness match, they indicated this by pressing a third button, and the level of the variable stimulus at this point was taken as the matching level. This button press was not accepted until two turnarounds had occurred. For the majority of runs (>90%), four to six turnarounds were made before the third button was pressed.

The variable stimulus was equally often the A tone and the B tone. Also, the tone presented to the impaired ear (or at the frequency where hearing was impaired) was equally often the A tone and the B tone. Matches were made equally often with the level fixed in the better ear (or at the frequency where the absolute threshold was lower) and with the level fixed in the worse ear (or at the frequency where the absolute threshold was higher). The starting level of the variable stimulus was randomly chosen from within a certain starting range. The center of this range was chosen, on the basis of pilot data obtained during the initial training sessions, so as to be as close as possible to the final matching level. This was done to reduce bias effects (Gabriel *et al.*, 1997). When the mean matching level differed by more than 4 dB from the center of the starting range, the data were discarded, and new matches were obtained with a revised range of starting levels. The range of starting levels was ±5 dB when the level of the fixed tone was more than 10 dB above absolute threshold, i.e., more than 10 dB sensation level (SL). The range was reduced to ±3 dB for SLs of the fixed tone between 6 and 10 dB, and to ±2 dB for SLs of the fixed tone below 6 dB. The range was reduced in this way to avoid the variable stimulus being inaudible at the start of a run. At least six matches were obtained for each level of the fixed tone. The range of levels of the fixed tone was chosen individually for each subject.

During training, loudness matches were first made with the fixed stimuli at moderate levels (10–20 dB SL for the impaired ear/frequency and 10–40 dB SL for the better ear/frequency). Once subjects gave consistent matches for this range of starting levels, matches were obtained for progressively lower SLs and then for progressively higher SLs. The matches at higher levels were obtained to confirm that the subjects did have loudness recruitment.

D. Equipment

The sinusoidal signals (one for each frequency and/or each ear) were digitally generated using two separate digital-to-analog converters (DACs) of a Tucker-Davies Technologies (TDT) System II, controlled by a PC. The sampling rate was 50 kHz. The outputs of the DACs were each filtered using a Kemo VBF8/04 filter set to lowpass at 8 kHz (slope=90 dB/oct). The signals were individually attenuated by TDT PA4 programmable attenuators. For subject S2 they were then mixed. For the other subjects, they were kept separate. Stimuli were then passed to a headphone buffer (TDT HB6) and to Sennheiser HD580 earphones. Sound levels are specified as estimated SPLs at the eardrum, based on measurements with a KEMAR manikin (Burkhard and Sachs, 1975), using the average of results for the ''large'' and ''small'' ears. Subjects were tested in a double-walled sound-attenuating chamber.

The ''cross-talk'' of the Sennheiser HD580 earphones was measured using an Etymōtic Research ER7C probe microphone. The microphone was used to measure the sound level close to the eardrum in one ear when a sound was delivered to the earphone on the opposite ear. The results indicated that the inter-aural attenuation was greater than 50 dB over the frequency range of interest. The difference in absolute threshold for the two ears of the subjects in the present experiments did not exceed 44 dB at any test frequency. Thus, the SL of the tone presented to the impaired ear was always at least 6 dB greater than the SL resulting from ''cross-talk'' in the normal (or better) ear. Given that the subjects experienced loudness recruitment in the impaired ear, this means that the loudness contribution from the impaired ear would always have been markedly above the loudness contribution from the normal ear. Consistent with this, subjects S1, S3, and S4 (who made loudness matches across ears) reported that, in the loudness-matching task, they always heard tones alternating between the two ears.

III. RESULTS

Three subjects were able to make loudness matches for SLs of the fixed stimulus as low as 2 dB. One subject (S3) did not feel able to make matches at 2 dB SL, but he was able to make matches with the fixed stimulus at 4 dB SL in both the better and poorer ear. The ability to make loudness matches at very low SLs was certainly helped by the presentation of the stimuli in a regular repeating sequence, accompanied by lights. The variability of the loudness matches was actually slightly smaller for very low SLs than for medium to high SLs. This is consistent with the idea that the rate of change of loudness with sound level is greater for levels close to absolute threshold than for higher levels, for both normally hearing and hearing-impaired subjects (Hellman and Zwislocki, 1964; 1968; Moore *et al.*, 1997; Moore and Glasberg, 2004).

The results for S1 are shown in Fig. 3. The left panel shows loudness matches plotted in terms of the SL of the tones, and the right panel shows the same data plotted in terms of the SPL of the tones (the solid line will be described later). The dashed line in the left panel shows where the matches would lie if stimuli with equal SLs were equally loud. According to the idea of softness imperception, the matches should not converge on the dashed line at low SLs, but should reach an asymptotic value 10–12 dB above the dashed line for a hearing loss like that of S1; see Fig. 4 of Buus and Florentine (2002). In fact, the matches *do* converge on the line, for SLs below about 6 dB. The fact that the low-SL matches lie on the diagonal line is consistent with the idea that, close to absolute threshold, the rate of growth of loudness with increasing level is similar for a frequency where hearing is impaired and a frequency where hearing is normal. However, the results do not support the idea that, at

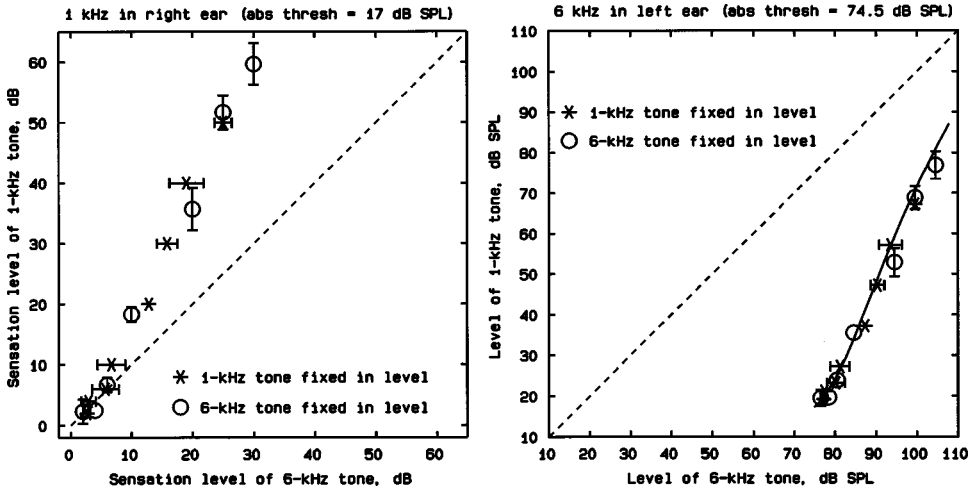

FIG. 3. Loudness-matching results for S1. Matches were made between a 1-kHz tone in the right ear and a 6-kHz tone in the left ear. Asterisks show matches with the 1-kHz tone fixed in level and open circles show matches with the 6-kHz tone fixed in level. In the left panel, levels are expressed in dB SL. In the right panel, levels are expressed in dB SPL. The solid line shows predictions of the loudness model of Moore and Glasberg (2004). Error bars show ±1 standard deviation across at least six matches. Error bars are omitted when they would be smaller than the symbol used to plot the point.

very low SLs, a tone sounds louder at a frequency where hearing is impaired than at a frequency where hearing is normal.

For SLs above 6 dB, the matches lie consistently above the diagonal line. When plotted in terms of SPL (right panel), the matches become closer to the diagonal line at higher sound levels. These findings confirm that loudness recruitment was present; the loudness grew more rapidly at the frequency where hearing was impaired than at the frequency where hearing was normal, once the SL exceeded 6 dB.

The results for S2 are shown in Fig. 4. The format is the same as for Fig. 3. Again, for very low SLs the matches converge on the diagonal line, indicating that equal SLs lead to equal loudness. However, for S2 this occurs only for SLs of 4 dB and below. The loudness-matching function for this subject is very steep. For example, a 2-kHz tone at about 15 dB SL is matched by a 0.5-kHz tone at about 60 dB SL. This remarkably steep function probably results mainly from two factors. For the 2-kHz tone, the rate of growth of loudness with increasing sound level was probably more rapid than normal, corresponding to the loudness-recruitment effect. However, for the 0.5-kHz tone, the rate of growth of loudness with increasing sound level may have been much lower than normal, as the hearing loss increased markedly for frequencies above 0.5-kHz (see Fig. 2). The rapid increase in absolute threshold above 0.5 kHz may have led to a reduced contribution of loudness from the high-frequency side of the excitation pattern (Hellman, 1994; 1997).

Results for S3 are shown in Fig. 5. Recall that, for this subject, loudness matches were obtained across ears using a frequency of 2.5 kHz. The matches shown in the left panel converge on the diagonal line for SLs of 10 dB and below. Thus, compared to S1 and S2, S3 has a relatively extended range of levels over which equal SLs lead to equal loudness. Again, there is no evidence to support the concept of softness imperception. For high SPLs (right panel), the matches converge on the diagonal line, indicating near-complete loudness recruitment.

Results for S4 are shown in Fig. 6. Recall that, for this subject, loudness matches were obtained across ears using a frequency of 3 kHz. The results resemble those of the other subjects, except that the loudness-matching function has a relatively shallow slope (but a slope that is clearly greater than one). The loudness matches for SLs of 6 dB or less (left panel) lie very close to, but 1–2 dB above the diagonal line.

In summary, when the fixed tone was presented at a very low SL to an ear and/or at a frequency where there was a hearing loss, it was matched by a tone at a frequency where hearing was normal with approximately the same SL (e.g., 2 dB matched 2 dB). This implies that the fixed tone sounded very soft when it was at a very low SL, which is not consistent with the concept of softness imperception. At moderate

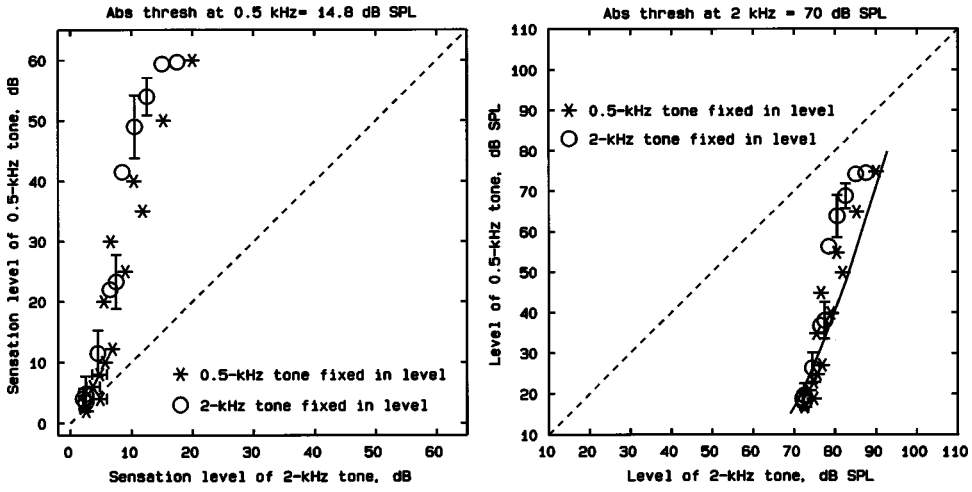

FIG. 4. As in Fig. 3, but for S2. Matches were made between 0.5- and 2-kHz tones, both in the left ear.

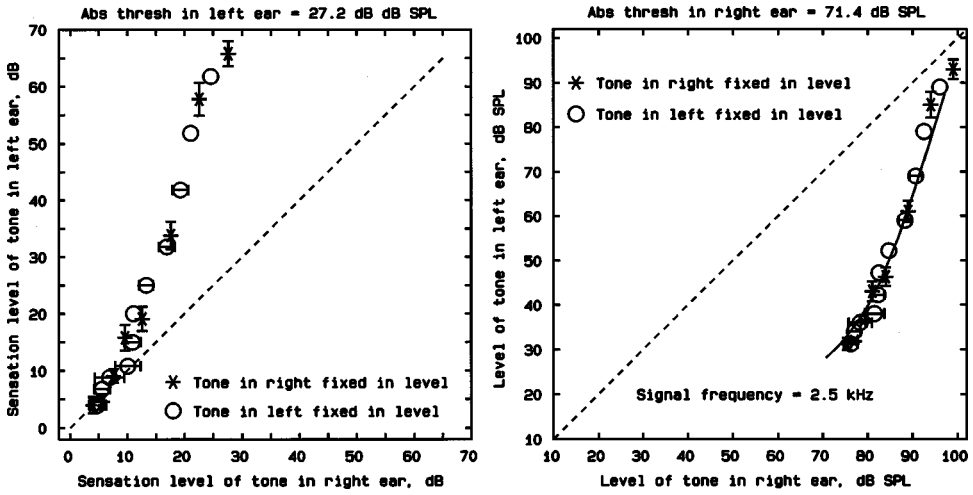

FIG. 5. As in Fig. 3, but for S3. Matches were made for a 2.5-kHz tone presented alternately to the left and right ears.

SLs, the data were consistent with the traditional account of loudness recruitment. The data support the following characterization of loudness recruitment:

(1) Very close to absolute threshold, equal SLs led to equal loudness in an impaired ear and a normal ear. This is consistent with the idea that, at threshold, the loudness is the same in an impaired ear and a normal ear.
(2) Very close to absolute threshold, the rate of growth of loudness is similar in impaired ears and normal ears. This occurs for SLs in the impaired ear up to 4–10 dB, depending on the subject.
(3) For SLs above 4–10 dB in an impaired ear, the rate of growth of loudness with increasing level is greater than normal; this is the main basis of the loudness-recruitment effect.

IV. DISCUSSION

A. Compatibility with earlier data

The loudness-matching functions obtained here show an initial low-SL portion with a slope close to 1 (although this portion is hardly apparent for S2), and then a steeper portion. This is consistent with earlier data obtained using loudness matching, magnitude estimation, and cross-modality matching (Hellman and Zwislocki, 1964; Hellman, 1997). The results also show that, at very low SLs, equal SLs in an impaired and a normal ear lead to equal loudness. This is not consistent with the concept of softness imperception.

Florentine *et al.* (2004) have presented reaction-time data which they argue to support the concept of softness imperception. Their arguments are based on the assumption that reaction time is directly related to loudness (Chocholle, 1940; Scharf, 1978). They measured reaction times as a function of SL using subjects with sloping hearing loss. For each subject, reaction times were compared for a frequency where hearing was near-normal and a frequency where hearing was impaired. For low SLs, including 0 dB (i.e., for stimuli at absolute threshold), reaction times were shorter for the frequency where hearing was impaired than for the frequency where hearing was near-normal. This was argued to support the concept of softness imperception.

There are a number of problems in interpreting the results of Florentine *et al.* First, for five subjects out of six, the reaction times for the frequency where hearing was impaired remained below those for the frequency where hearing was near-normal, even when the stimuli were well above absolute threshold. In some cases (e.g., their subjects HI-4 and HI-5), the reaction times were shorter for the frequency where hearing was impaired even when the comparison was made at equal, high SPLs. If reaction time were a direct indicator of loudness, this would imply ''over-recruitment,'' i.e., at the same high SPL, the tone would sound louder at the fre-

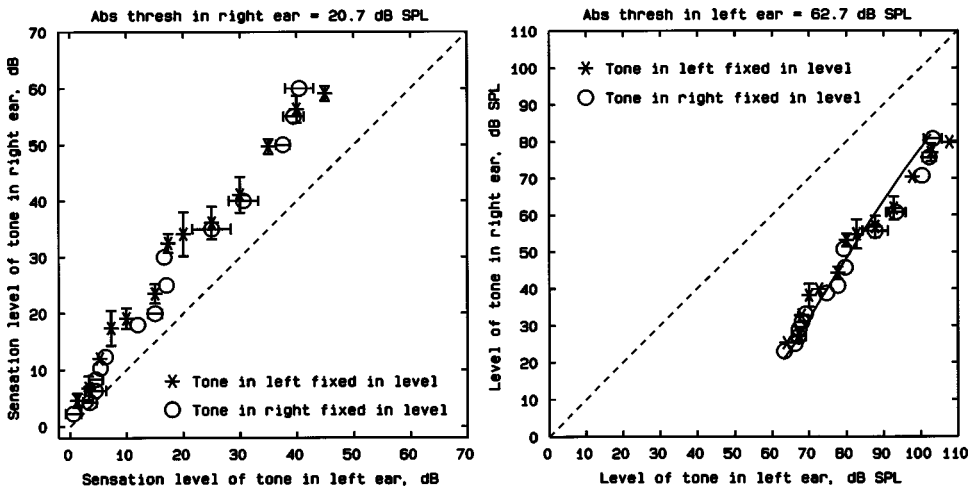

FIG. 6. As in Fig. 3, but for S4. Matches were made for a 3-kHz tone presented alternately to the left and right ears.

quency where hearing was impaired than at the frequency where hearing was near-normal. This seems unlikely to be the case.

A second problem is connected with how false positives and misses were treated for stimuli at very low SLs. This is a complex issue, and the reader is referred to the discussion following the paper of Florentine *et al.* (2004) for details. In any case, the interpretation of the reaction time data of Florentine *et al.* is not clear cut; I would argue that their data do not provide clear support for the concept of softness imperception. The loudness-matching data presented in this paper provide a more direct indication of loudness perception, and show clearly that, for SLs very close to threshold, equal SLs lead to equal loudness in an impaired and a normal ear. It is of course possible that some hearing-impaired subjects do experience softness imperception. Tests with a greater number of subjects would be needed to assess this possibility. However, the present data suggest that softness imperception is likely to be the exception rather than the rule.

Moore *et al.* (1996) presented data using amplitude-modulated tones that are consistent with the notion that loudness recruitment reflects a more rapid than normal rate of growth of loudness for SLs above 4–10 dB. They tested subjects with unilateral hearing loss. Subjects were required to match the perceived modulation depth (the amount of perceived fluctuation) of amplitude-modulated tones presented alternately to the two ears at levels well above absolute threshold. At the point of perceived equality, the modulation depth was greater in the normal ear than in the impaired ear. This is consistent with the idea that loudness recruitment effectively magnifies the perceived modulation depth of amplitude modulated sounds that are well above threshold. Other data consistent with this view have been presented by Glasberg and Moore (1992) and by Moore *et al.* (2001).

The concept that loudness recruitment reflects a more rapid than normal rate of loudness growth above about 4 dB SL is also consistent with the data of Hellman and Meiselman (1990). They calculated the slopes of loudness-growth functions for levels above 4 dB SL and found that slope values for 100 listeners with cochlear hearing loss were greater than slope values for 51 listeners with normal hearing.

B. Modeling and interpreting the data

Moore and Glasberg (1997) described a model of loudness perception applicable to cases of cochlear hearing loss. A problem with the model is that it predicts zero loudness for a sound at absolute threshold. This is not correct, as the threshold is defined statistically, for example as the level of a sound which is detected 75% of the time in a two-alternative forced-choice task. Since the sound is detected on some trials, it must, on average, have a finite loudness (Hellman and Zwislocki, 1961; 1963; 1964; 1968; Zwislocki, 1965; Hellman, 1997; Buus *et al.*, 1998). A second problem with the model is that it predicts that the rate of growth of loudness at levels near absolute threshold should be markedly greater for an ear with cochlear hearing loss than for a normal ear. The present data, and the data cited earlier, indicate that this is not the case.

Recently, Moore and Glasberg (2004) presented a revised loudness model that was intended to overcome these problems. The revised model is based on the idea that a sound at absolute threshold has a small but finite loudness; this loudness is assumed to be constant regardless of frequency and spectral content and is also assumed to be the same in a hearing-impaired and a normal ear. It is assumed that a hearing loss can be partitioned into two parts, caused by loss of function of outer hair cells (OHCs) and inner hair cells (IHCs) and/or neurons, respectively. The hearing loss produced by these is denoted HL_{OHC} and HL_{IHC}, respectively. It is assumed that, at each frequency, $HL_{OHC} + HL_{IHC} = HL_{TOTAL}$, where HL_{TOTAL} is the overall hearing loss in dB HL. When applied to impaired hearing, the model requires specification of the absolute thresholds of the ear under consideration in dB HL at the standard audiometric frequencies (which are empirically measured), and specification of the values of HL_{OHC} at these frequencies, which have to be estimated in some way (Moore *et al.*, 1999). When there is no independent estimate of the values of HL_{OHC}, default values are assumed in the model. The model also requires specification of the frequency limits of any dead region that might be present.

I consider next how well the revised model accounts for the loudness-matching data shown in Figs. 3–6. As some of the hearing losses varied markedly between the ''standard'' audiometric frequencies, the absolute thresholds in dB HL were specified not only at octave-spaced frequencies from 0.125 to 8 kHz, but also at the intervening frequencies, namely 0.75, 1.5, 3, and 6 kHz. Where necessary, the hearing loss at the test frequency (or frequencies) for a given ear was adjusted by a few decibels (typically less than 3) so that the predicted absolute threshold, specified in dB SPL at the eardrum, corresponded as closely as possible to the obtained threshold (as measured using the three-alternative forced-choice task).

The loudness-matching functions were predicted by determining the input sound level required for each ear at each test frequency to obtain a series of fixed loudness levels, from 2 phons up to about 50 phons. The resulting predictions are shown by the solid lines in the right panels of Figs. 3–6. For S1 (Fig. 3), the predictions were obtained using the default values of HL_{OHC}. The predicted function fits the data very well, including the obtained decrease in slope at levels close to threshold. For S2 (Fig. 4), the predictions were obtained using the maximum values of HL_{OHC} allowed by the model. The fit is reasonable, although the predicted function is not quite as steep as the obtained function. For S3 (Fig. 5), the predictions were obtained using the default values of HL_{OHC}. The predicted function fits the data very well, including the obtained decrease in slope at levels close to threshold. For subject S4 (Fig. 6) the predictions were obtained assuming that almost all of the hearing loss was due to loss of IHC and/or neural function; the values of HL_{OHC} were set to 1 dB at all frequencies, much lower than the default values. This made it possible to predict the rather shallow loudness-matching function.

In summary, the revised loudness model was able to give reasonably good fits to the data. It correctly predicted

the slightly shallower slopes of the functions for levels close to absolute threshold. In two cases (S1 and S3), the fits were obtained using the default values of HL_{OHC} specified in the model. For S2, the values of HL_{OHC} were set to the maximum possible values, and for S4 they were set close to the minimum possible values.

It is noteworthy that the two subjects for whom relatively extreme parameter values were used, and for whom the fits were poorest, both wore hearing aids (S2 bilaterally and S4 in the left ear only). Loudness perception appears to be influenced by hearing aid use (Robinson and Gatehouse, 1995; Olsen *et al.,* 1999; Marriage *et al.,* 2004). For example, Olsen *et al.* (1999) showed that, for hearing losses of 50–75 dB, the mean level rated as ''loud'' by long-term full-time users of hearing aids was 4.5 dB above the mean level rated as ''loud'' by nonusers. Marriage *et al.* (2004) showed that the gain preferred by new users of hearing aids was about 3 dB less than the gain preferred by long-term users. The revised loudness model of Moore and Glasberg (2004) does not take into account effects of long-term learning or ''acclimatization'' on loudness perception.

It is possible that the very steep loudness matching-function for S2 (Fig. 4) was partly caused by the fact that S2 was used to fast-acting compression at high frequencies (her hearing aid processed frequencies of 500 Hz and below almost linearly). Recall that S2 made loudness matches across frequency within the left ear. When she was tested without her aids, small changes in level at high frequencies may have led to relatively large changes in loudness, because she was used to hearing only small changes in level at high frequencies. In contrast, subject S4, who made loudness matches across ears at 3 kHz, wore a single hearing aid in the left ear which incorporated slow-acting compression at high frequencies. Such compression does not affect rapid amplitude fluctuations (Stone and Moore, 1992), so she would have been used to hearing the ''normal'' rapid fluctuations in level associated with speech and other sounds, and would have been used to hearing brief high-level sounds. This may have led to a reduced perception of loudness for high-level sounds in the aided ear and contributed to the relatively shallow loudness-matching function shown in Fig. 6.

V. CONCLUSIONS

The results show that, for levels very close to absolute threshold, a given SL leads to approximately the same loudness for an ear with a hearing impairment at the test frequency and an ear with normal hearing at the test frequency. This finding is not consistent with the concept of softness imperception. Very close to absolute threshold, the rate of growth of loudness is similar in impaired ears and normal ears, a finding in accord with other data (Hellman and Zwislocki, 1964; Hellman, 1997; Buus and Florentine, 2002). This occurs for SLs in the impaired ear up to 4–10 dB, depending on the subject. For SLs above 4–10 dB in an impaired ear, the rate of growth of loudness with increasing level is greater than normal; this is the main basis of the loudness-recruitment effect.

ACKNOWLEDGMENTS

This work was supported by the MRC (UK). I thank Thomas Stainsby for assistance in gathering the data, Tom Baer for programming, and Brian Glasberg for assistance with modeling. I also thank Brian Glasberg, Hedwig Gockel, Virginia Richards, Neal Viemeister, Mary Florentine and two anonymous reviewers for helpful comments on an earlier version of this paper.

Allen, J. B., and Jeng, P. S. (**1990**). ''Loudness growth in 1/2-octave bands (LGOB); a procedure for the assessment of loudness,'' J. Acoust. Soc. Am. **88**, 745–753.

Burkhard, M. D., and Sachs, R. M. (**1975**). ''Anthropometric manikin for acoustic research,'' J. Acoust. Soc. Am. **58**, 214–222.

Buus, S., and Florentine, M. (**2002**). ''Growth of loudness in listeners with cochlear hearing losses: Recruitment reconsidered,'' J. Assoc. Res. Otolaryngol. **3**, 120–139.

Buus, S., Müsch, H., and Florentine, M. (**1998**). ''On loudness at threshold,'' J. Acoust. Soc. Am. **104**, 399–410.

Chocholle, R. (**1940**). ''Variation des temps de réaction auditifs en fonction de l'intensité à diverse fréquences (Variation of auditory reaction time with intensity for various frequencies),'' L'Ann. Psychol. **41**, 65–124.

Florentine, M., Buus, S., and Rosenberg, M. (**2004**). ''Reaction-time data support the existence of Softness Imperception in cochlear hearing loss,'' in *Auditory Signal Processing: Physiology, Psychoacoustics and Models*, edited by D. Pressnitzer, A. de Cheveigné, S. McAdams, and L. Collet (Springer, New York).

Fowler, E. P. (**1936**). ''A method for the early detection of otosclerosis,'' Arch. Otolaryngol. **24**, 731–741.

Gabriel, B., Kollmeier, B., and Mellert, V. (**1997**). ''Influence of individual listener, measurement room and choice of test-tone levels on the shape of equal-loudness level contours,'' Acust. Acta Acust. **83**, 670–683.

Glasberg, B. R., and Moore, B. C. J. (**1992**). ''Effects of envelope fluctuations on gap detection,'' Hear. Res. **64**, 81–92.

Hellman, R. P. (**1994**). ''Relation between the growth of loudness and high-frequency excitation,'' J. Acoust. Soc. Am. **96**, 2655–2663.

Hellman, R. P. (**1997**). ''Growth of loudness in sensorineural impairment: Experimental results and modeling implications,'' in *Modeling Sensorineural Hearing Loss*, edited by W. Jesteadt (Erlbaum, Mahwah, NJ).

Hellman, R. P., and Meiselman, C. H. (**1990**). ''Loudness relations for individuals and groups in normal and impaired hearing,'' J. Acoust. Soc. Am. **88**, 2596–2606.

Hellman, R. P., and Zwislocki, J. J. (**1961**). ''Some factors affecting the estimation of loudness,'' J. Acoust. Soc. Am. **35**, 687–694.

Hellman, R. P., and Zwislocki, J. J. (**1963**). ''Monaural loudness summation at 1000 cps and interaural summation,'' J. Acoust. Soc. Am. **35**, 856–865.

Hellman, R. P., and Zwislocki, J. J. (**1964**). ''Loudness function of a 1000-cps tone in the presence of a masking noise,'' J. Acoust. Soc. Am. **36**, 1618–1627.

Hellman, R. P., and Zwislocki, J. J. (**1968**). ''Loudness determination at low sound frequencies,'' J. Acoust. Soc. Am. **43**, 60–64.

Hood, J. D. (**1972**). ''Fundamentals of identification of sensorineural hearing loss,'' Sound **6**, 21–26.

Levitt, H. (**1971**). ''Transformed up-down methods in psychoacoustics,'' J. Acoust. Soc. Am. **49**, 467–477.

Marriage, J. E., Moore, B. C. J., and Alcántara, J. I. (**2004**). ''Comparison of three procedures for initial fitting of compression hearing aids. III. Inexperienced versus experienced users,'' Int. J. Audiol. (in press).

Miskolczy-Fodor, F. (**1960**). ''Relation between loudness and duration of tonal pulses. III. Response in cases of abnormal loudness function,'' J. Acoust. Soc. Am. **32**, 486–492.

Moore, B. C. J. (**1995**). *Perceptual Consequences of Cochlear Damage* (Oxford University Press, Oxford).

Moore, B. C. J. (**1998**). *Cochlear Hearing Loss* (Whurr, London).

Moore, B. C. J. (**2001**). ''Dead regions in the cochlea: Diagnosis, perceptual consequences, and implications for the fitting of hearing aids,'' Trends Amplif. **5**, 1–34.

Moore, B. C. J., and Glasberg, B. R. (**1997**). ''A model of loudness perception applied to cochlear hearing loss,'' Aud. Neurosci. **3**, 289–311.

Moore, B. C. J., and Glasberg, B. R. (**2004**). ''A revised model of loudness perception applied to cochlear hearing loss,'' Hear. Res. **188**, 70–88.

Moore, B. C. J., Glasberg, B. R., Alcántara, J. I., Launer, S., and Kuehnel, V. (**2001**). ''Effects of slow and fast-acting compression on the detection of gaps in narrow bands of noise,'' Br. J. Audiol. **35**, 365–374.
Moore, B. C. J., Glasberg, B. R., and Baer, T. (**1997**). ''A model for the prediction of thresholds, loudness and partial loudness,'' J. Audio Eng. Soc. **45**, 224–240.
Moore, B. C. J., Glasberg, B. R., and Stone, M. A. (**2004**). ''A new version of the TEN test with calibrations in dB HL,'' Ear Hear. (submitted).
Moore, B. C. J., Huss, M., Vickers, D. A., Glasberg, B. R., and Alcántara, J. I. (**2000**). ''A test for the diagnosis of dead regions in the cochlea,'' Br. J. Audiol. **34**, 205–224.
Moore, B. C. J., Vickers, D. A., Plack, C. J., and Oxenham, A. J. (**1999**). ''Inter-relationship between different psychoacoustic measures assumed to be related to the cochlear active mechanism,'' J. Acoust. Soc. Am. **106**, 2761–2778.
Moore, B. C. J., Wojtczak, M., and Vickers, D. A. (**1996**). ''Effect of loudness recruitment on the perception of amplitude modulation,'' J. Acoust. Soc. Am. **100**, 481–489.
Olsen, S. O., Rasmussen, A. N., Nielsen, L. H., and Borgkvist, B. V. (**1999**). ''Loudness perception is influenced by long-term hearing aid use,'' Audiology **38**, 202–205.
Robinson, K., and Gatehouse, S. (**1995**). ''Changes in intensity discrimination following monaural long-term use of a hearing aid,'' J. Acoust. Soc. Am. **97**, 1183–1190.
Scharf, B. (**1978**). ''Loudness,'' in *Handbook of Perception, Volume IV. Hearing*, edited by E. C. Carterette and M. P. Friedman (Academic, New York).
Steinberg, J. C., and Gardner, M. B. (**1937**). ''The dependency of hearing impairment on sound intensity,'' J. Acoust. Soc. Am. **9**, 11–23.
Stone, M. A., and Moore, B. C. J. (**1992**). ''Syllabic compression: Effective compression ratios for signals modulated at different rates,'' Br. J. Audiol. **26**, 351–361.
Zwislocki, J. J. (**1965**). ''Analysis of some auditory characteristics,'' in *Handbook of Mathematical Psychology*, edited by R. D. Luce, R. R. Bush, and E. Galanter (Wiley, New York), Vol III.

The temporal growth and decay of the auditory motion aftereffect

Michael F. Neelon[a] and Rick L. Jenison
Department of Psychology, 1202 W. Johnson St., University of Wisconsin, Madison, Wisconsin 53706

(Received 26 September 2003; revised 21 January 2004; accepted 26 January 2004)

The present work investigated the temporal tuning of the auditory motion aftereffect (aMAE) by measuring the time course of adaptation and recovery to auditory motion exposure. On every trial, listeners were first exposed to a broadband, horizontally moving sound source for either 1 or 5 seconds, then presented moving test stimuli after delays of 0, $\frac{2}{3}$, or $1\frac{2}{3}$ seconds. All stimuli were synthesized from head related transfer functions recorded for each participant. One second of motion exposure (i.e., a single pass of the moving source) produced clearly measurable aMAEs which generally decayed monotonically after adaptation ended, while five seconds exposure produced stronger aftereffects that remained largely unattenuated across test delays. These differences may imply two components to the aMAE: a short time-constant motion illusion and a longer time-constant response bias. Finally, aftereffects were produced only by adaptor movement toward but not away from listener midline. This aftereffect asymmetry may also be a consequence of brief adaptation times and reflect initial neural response to auditory motion in primate auditory cortex. © *2004 Acoustical Society of America.* [DOI: 10.1121/1.1687834]

PACS numbers: 43.66.Ed, 43.66.Mk, 43.64.Qp [RD] Pages: 3112–3123

I. INTRODUCTION

A. Spatial and frequency tuning of the aMAE

A sound source repeatedly traversing horizontal auditory space may produce an auditory motion aftereffect (aMAE) in listeners in which sensitivity to subtly moving test stimuli shifts in the direction opposite of that presented during adaptation. Several basic attributes of the aMAE have been specified over the course of several recent experiments, most notably its tuning in the spatial and frequency domains (Grantham, 1998; Dong *et al.*, 2000). The general findings have been that the aftereffect is localized to both the spatial and spectral region of adaptation.

However, one component of the aMAE that has not been investigated in detail is its growth and decay as a function of adaptation duration. In the present work we attempt to measure these temporal aspects of the auditory motion aftereffect. Regarding the spatial tuning of the aMAE, Dong *et al.* (2000) adapted listeners for two minutes to broadband and filtered noise stimuli emanating from a speaker attached to a moving robotic arm. They found that aMAE magnitude was greatest when the test region spatially coincided with the region of adaptation and declined fairly linearly with a broad space constant as testing moved outside this region. For spatially coincident adaptation and test regions, however, the magnitude of the aMAE appeared to be largely equivalent for adaptor motion trajectories up to $\pm 35°$ around the frontal midline.

In the frequency domain, it has been known for some time that the aMAE is stronger for broadband than for pure tone adaptors (Grantham, 1989). The recent studies by Grantham (1998) and Dong *et al.* (2000) further showed that aMAEs can be created using low-, band-, and high-pass adaptors, though they often appear stronger for lowpass stimuli relative to other bandwidths. These effects of the bandwidth appear consistent with the ideas that (1) a stimulus with a broader frequency spectrum should adapt a larger area of units across tonotopic maps found at multiple physiological stages throughout the auditory system (Palmer and Summerfield, 2002); and (2) units at spatially-sensitive (and potentially motion-sensitive) stages beyond AI show a greater response to spectrally rich stimuli (Clarey *et al.*, 1992; Rauschecker *et al.*, 1995; Wessinger *et al.*, 2001). The impact of lower-frequency stimuli may further reflect the dominance of interaural time-difference cues in the horizontal motion trajectories used by these studies (Wightman and Kistler, 1992; Macpherson and Middlebrooks, 2002; Neelon and Jenison, 2003).

B. Temporal tuning of the aMAE

Judgments of visual motion can show prolonged and unexpected temporal effects to adaptation such as storage and residual effects that may last on the order of hours (Mather *et al.*, 1998). In contrast, the time course of the auditory motion aftereffect has not been well specified. Two studies have measured the duration of spatial auditory aftereffects, but only after prolonged periods of adaptation. Ehrenstein (1994) charted the recovery of adaptation to pure tones independently changing in either interaural time or level difference (ITD, ILD), and, while not finding motion aftereffects *per se*, reported a displacement aftereffect in which subjects' settings of the interaural midline had been shifted after adaptation. Plots of the mean results showed that while the displacement aftereffects initially declined in

[a]Corresponding author. Electronic mail: mfneelon@wisc.edu. Current address: 619 Waisman Center, 1500 Highland Ave., Madison, Wisconsin 53705.

 0001-4966/2004/115(6)/3112/12/$20.00 © 2004 Acoustical Society of America

magnitude very quickly after the adaptor ceased, some bias was still present up to 30 seconds later. Aftereffects to dynamic ILD adaptation appeared to last even longer with effects lingering up to two minutes after adaptation. This difference in recovery between motion produced by ITD and ILD cues may have some physiological support (Sanes *et al.*, 1998).

In a more recent study, Dong *et al.* (1999) explored the duration of the aMAE after 10 minutes of adaptation to a 1-octave lowpass noise source emanating from a speaker attached to a horizontally moving robotic arm. Their results also show that the aMAE is largest immediately after adaptation, and declines exponentially to near zero after approximately 10 minutes. Ehrenstein's data must be interpreted with caution since, as noted above, motion aftereffects are more reliably produced with free-field, wideband stimuli rather than pure tones (Grantham, 1998; Dong *et al.*, 2000), possibly making his findings of a qualitatively different nature. Despite the results of both of these studies, Grantham (Grantham and Wightman, 1979; Grantham, 1989; 1998) has stated that the lifespan of auditory motion aftereffects is very brief, perhaps only lasting for a few seconds after adaptation ends. Given that aftereffects produced by different types of visual motion may show different time courses (Mather *et al.*, 1998), it is possible that these conflicting statements are a result of measuring aMAEs with different stimuli and procedures which may have produced adaptation effects on different time scales (Malone *et al.*, 2002). Grantham has further suggested there are in fact two components to the aMAE: a short time-constant motion illusion (i.e., a true motion aftereffect), and a longer time-constant motion desensitization in the direction of adaptation (i.e., response bias). It is possible that the recovery from motion adaptation charted by Ehrenstein and Dong, *et al.* mostly reflects the latter effects.

C. Contrast explanations of aftereffects

Exploring these temporal issues may help determine whether the aMAE truly arises from the adaptation of auditory motion selective cells, or is instead related to the briefer contrast effect a moving stimulus may have on a neuron's subsequent response properties. The latter result would argue against the necessity of dedicated motion detectors to explain phenomena like the aMAE. McAlpine and his colleagues have in fact proposed such a contrast model to explain apparent motion selectivity in the guinea pig inferior colliculus (IC) (McAlpine *et al.*, 2000; Ingham *et al.*, 2001). Several physiological studies have claimed that auditory cells in the mammalian brainstem and cortex can exhibit motion direction selectivity (Ahissar *et al.*, 1992; Spitzer and Semple, 1993; Jiang *et al.*, 2000; Jenison *et al.*, 2001; Malone *et al.*, 2002). This conclusion is often based on the finding that the receptive fields of many cells are skewed by auditory motion such that they exhibit greater responsiveness to a sound source passing through the field in one but not the opposite direction (Spitzer and Semple, 1998; Wilson and O'Neill, 1998; Malone *et al.*, 2002). Though these latter studies found virtually no neurons that are only responsive to moving sources rather than stationary sources, such skewed responses might be viewed as a neural basis for signaling direction of sound source movement.

McAlpine and colleagues (McAlpine *et al.*, 2000; Ingham *et al.*, 2001) have argued that this change in the receptive field shape may be due to the history of source movement through the response area rather than a specialized reaction to a particular motion vector. The authors exposed IC cells to dichotic pure tones whose interaural phase differences (IPD) were oscillated to simulate back-and-forth interaural movement. They found that the change in the receptive field shape was caused by a cell's adaptation to the interaural locus of the dynamic stimulus passing through its IPD receptive field. Direction selectivity appeared because the cell responded strongly to the initial movement of the phase into its receptive field and more weakly when the phase change suddenly reversed direction and exited the receptive field. Adaptation to the initial stimulation was reported to have time constants no greater than 500 ms for the majority of the recorded cells. This implied that the skewed response should disappear if enough time was allowed to pass before the reversal of the stimulus movement (e.g., >500 ms). Indeed, the authors showed that this skewed response, and as a consequence the apparent motion selectivity, could be attenuated when the cell was given such time to recover from its initial response to the dynamic IPD stimulus. A biologically-inspired computational model of binaural processing has also made use of a similar time constant to properly reproduce the neural response to dynamic IPD stimuli (Cai *et al.*, 1998).

A comparable debate between contrast effects and the selective adaptation of specialized feature detectors also appeared in the speech perception literature in the 1970s. At the time, speech perception was thought to be mediated by specialized detectors which could be experimentally adapted by the repeated presentation of their corresponding phonemic features. Diehl *et al.* (1985), however, showed that many of these effects could be created after a single presentation of the ''adapting'' phoneme and thus argued that it was the contrastive context of the adaptor and test pairing that created the shift rather than the fatiguing of dedicated phonemic feature detectors. In an interesting parallel to McAlpine and colleagues' study, Diehl, *et al.* also showed that inserting pauses between each repetition of the stimulus during the adaptation period altered the resulting judgments of the subsequent test stimuli. The relevance to the current work is that the aMAE has always been considered analogous in nature to the vMAE and hence assumed to arise from the adaptation of direction-selective cells by prolonged, continuous motion exposure. Both the early behavioral results of Diehl, *et al.*, and the recent neurophysiological findings of McAlpine, *et al.*, question whether the aMAE must be created in this manner and call for a more detailed psychophysical investigation into the growth of and recovery from auditory motion adaptation.

D. Time course of aMAE may specify physiological sources

The brief duration of the adaptation used by McAlpine and colleagues to explain apparent motion direction selectiv-

ity in the IC implies short-lived aMAEs. However, a more recent physiological investigation (Malone *et al.*, 2002) provides evidence that the adaptation of cortical cells to auditory motion may operate on multiple time scales, from tens of milliseconds to several seconds. Also using pure tones varying in IPD, Malone *et al.* found many units in primary auditory cortex of awake rhesus monkeys that appeared to be direction selective for simulated azimuthal motion within ecological ranges. This sensitivity manifested itself in two ways: as greater responses to moving versus stationary stimuli across the same IPDs, and as dramatic shifts in azimuthal tuning toward the origin of motion (see also Wilson and O'Neill, 1998). In the majority of these units, the receptive field shift resulted in greater activation for a single direction of motion (within ecologically plausible IPDs), suggesting a basis for encoding auditory motion direction.

However, these shifts diminished after even a few seconds of exposure to the moving stimulus, and azimuthal receptive field shapes approached those of the cells' responses to static IPD stimuli. That is, brief exposure to auditory motion may have reduced the potential ability of such cells to code for motion direction. This change due to adaptation could provide a physiological foundation for the desensitization component of the auditory motion aftereffect (Grantham, 1998). These researchers also reported that unadapted units showed post-inhibitory rebound when movement ended and the stimulus remained in a static position (see Sanes *et al.*, 1998, for a similar effect in IC). Such a rebound in activity could also be taken as a signal for the presence of motion in the opposite direction and has been cited as another potential basis of the motion aftereffect in vision (Niedeggen and Wist, 1998). These results provide important evidence that the effects of adaptation to auditory motion may evolve over several seconds time, rather than milliseconds, and have multiple physiological loci, including primary auditory cortex.

E. The present experiment

The preceding discussion has established that many details remain unknown regarding the time course of the auditory motion aftereffect. Further, two possible physiological locations in the brainstem and cortex (e.g., inferior colliculus vs auditory cortices) have been identified as potential sources for the aMAE; however, their adaptation to auditory motion may exhibit different temporal responses. In order to better characterize the time course of the auditory motion aftereffect and hence its possible physiological contributors, several combinations of timing parameters are explored in the following experiment. The typical aMAE paradigm initially presents a moving sound repeatedly for an extended period of adaptation, followed by a series of brief test probes and shorter re-adaptation periods. In the current experiment, the initial prolonged adaptation period is skipped and listeners instead hear sequences of either one or five seconds of initial motion adaptation, followed by probe stimuli presented after different time delays. Regarding the chosen adaptor durations, it is possible that the aMAE may emerge after one second of motion adaptation (e.g., a single pass of a one second duration moving adaptor), as was discovered by Diehl *et al.* (1985). In this case, the aMAE for one second of adaptation should be as strong as for five seconds; alternatively, the longer adaptation period may create a significantly larger bias in judgments of subsequent moving test stimuli, suggesting a more linear growth of the aftereffect with the amount of motion exposure. Finally, it is possible both 1 and 5 seconds of adaptation may not be enough to fully realize the motion aftereffect. These exposure durations are chosen mainly to ease general listener fatigue by limiting experimental sessions to reasonable durations. Results will determine whether these adaptation durations are reasonable.

At the same time, the experiment also varies how quickly the test stimulus is presented after adaptor cessation, using delays of 0, $\frac{2}{3}$, or $1\frac{2}{3}$ seconds. This range spans the different adaptation time courses reported in McAlpine *et al.* (2000) and Malone *et al.* (2002). Finally, test stimuli are also pseudo-randomly presented over the course of a single experimental block (see below) such that an equal number of test stimulus parameters are presented across each third of the block. This allows for measuring the possible growth of the aMAE over the course of multiple re-adaptation periods which occur during testing blocks.

II. METHODS

A. Subjects

5 females and 3 males (age range: 21–30 yrs.) served as subjects. All 8 were experienced in auditory motion aftereffect experiments but were naïve to the purposes of this particular study. Five of the subjects had also participated in a pilot version of this experiment. All had clinically normal hearing as assessed by an audiogram and were paid for their participation.

B. Stimuli

1. Synthesis of auditory motion

The pinnae, head and shoulders impose spectral and timing changes on an incident sound at the two ears which can be characterized by a pair of filters known as head-related transfer functions (HRTFs). Different source positions result in different filter pairs, and thus HRTFs carry information about spatial location. One method for synthesizing auditory motion under headphones is to interpolate across HRTFs recorded for an individual listener at particular spatial locations (Wightman and Kistler, 1999; Jacobsen *et al.*, 2001; Carlile and Best, 2002). This process mimics the change at a listener's ears that occurs when a real sound source changes spatial position in the environment. The headphone presentation of a stimulus convolved with these interpolated filters should then result in the perceptual experience of an externalized sound moving smoothly across space.

In an anechoic chamber, HRTFs for both ears were recorded for each listener using Sennheiser capsule microphones (KE4-211-2) in blocked meatus placement (Møller *et al.*, 1995). Filters were measured with a roughly 75 dB SPL, 100 k sampled wideband periodic chirp stimulus presented from loudspeakers at 541 source positions (10-degree azimuth intervals from 180 to −170 degrees and 10-degree

elevation intervals from 90 to −60 degrees relative to the horizontal plane). The effects of the presentation headphones (Beyer Dynamic DT 990) were also measured at the listener's ears at this time in order to compensate for their effect on stimulus presentation during experimentation. Following measurement, all HRTFs were downsampled to 50 k.

Minimum-phase versions of the time domain counterpart to the recorded HRTFs, the head-related impulse responses (HRIRs), were used in the interpolation process (Kistler and Wightman, 1992). This process removed the phase component while retaining the amplitude spectrum of the HRIR, thus allowing for an accurate spatial interpolation of the impulse responses across time samples while easing independent parametrization of ITD. For each listener and each ear, left and right minimum-phase HRIRs were piecewise cubic Hermite interpolated across the range of motion for each moving stimulus at a resolution fine enough to produce smooth apparent movement (see below for details). Interaural time delays were estimated from the peak of the cross-correlation between the left and right HRIRs for each recorded spatial location. An equal resolution was also interpolated for the timing delays between the two ears, which were then applied to the two signal channels. Recombining the interpolated delays and minimum-phase HRIRs resulted in two signals which mimicked the natural changes in spatial cues (ITD, ILD, monaural spectral cues) that occur at the two ears to a sound source when it moves around a listener. These signals were then convolved with inverse filters of the presentation headphones to cancel out their nonspatial filtering effects during stimulus delivery.

2. Moving adaptors

Adaptors were 1-second Gaussian noise samples convolved with interpolated HRIRs as described above for each listener to simulate leftward and rightward motion between 0 and ±30 degrees azimuth (0 degrees elevation). Adaptors were thus simulated to move in both directions in both frontal hemifields, where negative/positive signs indicate azimuths left/right of listener midline, respectively. Given the predominant responsiveness of IC and cortical neurons to contralaterally located sound stimuli (Ahissar *et al.*, 1992; Brugge *et al.*, 1996; Clarey *et al.*, 1992; Spizter and Semple, 1998; McAlpine *et al.*, 2000; Malone *et al.*, 2002; Middlebrooks *et al.*, 2002), stimuli did not cross midline in order to limit the recovery of such physiological structures from adaptation, which could occur if sounds were allowed to move through ipsilateral space. Figure 1 provides a depiction of the adaptor trajectories. 1200 filters were interpolated for the 30-degree trajectories which resulted in spatial motion resolution of approximately 0.025 degrees. This resolution was fine enough to create smooth apparent motion according to both previous studies using auditory motion synthesized in a similar manner (Wightman and Kistler, 1999; Carlile and Best, 2002) and listeners' comments in this experiment. At the end of generation, all stimuli (adaptors and test probes) were down-sampled from 50 k to 40 k Hz in order to conserve computer memory space, normalized to an approximately 66 dB(A) sound pressure level (SPL), and then 10 ms cosine-windowed to eliminate onset/offset transients

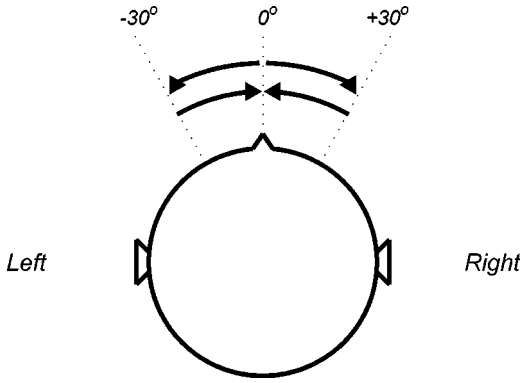

FIG. 1. Depiction of adaptor motion trajectories used in the present experiment.

3. Test stimuli (probes)

Test stimuli were also 1-second Gaussian noise samples convolved with interpolated individualized HRIRs to simulate auditory motion as described earlier. Test stimuli began at either ±20 degrees (sign indicates hemifield) and moved ±10, ±6 or ±2 degrees from the starting point, where the negative/positive sign here indicates movement leftward/rightward of the starting position, respectively. This range of test stimuli motion was chosen to encompass endpoints spanning reported minimum audible movement angles of approximately 3 degrees (Grantham, 1995), and has been successfully used before in auditory motion aftereffect studies (Grantham, 1998; Dong *et al.*, 1999). Spatial resolution of interpolated HRIRs was the same as used for the moving adaptors.

4. Experimental stimuli combined with delays

To ensure the proper timing of experimental stimuli, each trial presented a single auditory stimulus formed from the desired number of adaptors (i.e., adaptation duration), the desired test stimulus, and the desired experimental delay inserted between them. This was achieved by adding to either a single or 5 concatenated adaptors one of the 6 possible test stimuli (±10, ±6, ±2 degrees) from the same hemifield, with zero-padded buffers inserted in between to create silent delays of 0, $\frac{2}{3}$ and $1\frac{2}{3}$ seconds. No delays were inserted between repetitions of the moving adaptor in the 5-second condition beyond the 10ms rise/fall cosine windows. Nine replications of each combination of adaptor, delay, and test movement level were created off-line and presented to the listener during a single experimental block, totaling 162 stimuli. Listeners' ''left/right'' responses to these nine test exemplars formed the basis of the psychometric functions used to asses the effects of auditory motion adaptation.

C. Procedure

Subjects sat in front of a computer which controlled all instruction and stimulus presentation and recorded all re-

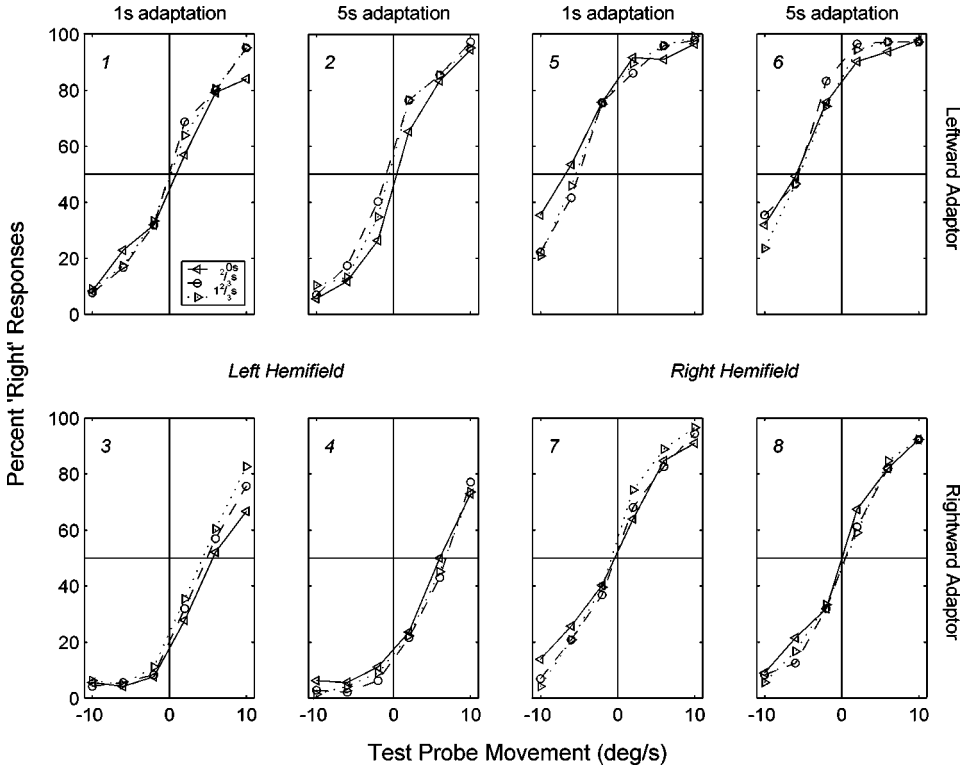

FIG. 2. Results averaged across 8 subjects for each hemifield (*left* = subplots *1–4*; *right* = subplots *5–8*), adaptor duration (*columns*), adaptor direction (*rows*), and test delay (*solid left arrows* = 0 s; *dashed circles* = $\frac{2}{3}$ s; *dotted right arrows* = $1\frac{2}{3}$ s) in terms of percent "right" responses as a function of the test probe movement.

sponses via the keyboard. On a single trial, subjects were presented with 1 s or 5 s of motion adaptation (i.e., exposed to 1 or 5 adaptors in a row), a delay of either 0, $\frac{2}{3}$ and $1\frac{2}{3}$ seconds, and then a 1 s test stimulus. After this combined stimulus had finished, two boxes, each 14×12 cm, appeared side-by-side in the middle of the screen bearing the labels *rightward* ("*p*") and *leftward* ("*q*"). Subjects were required to respond whether the test stimulus had moved rightward or leftward by pressing a "*p*" or "*q*," respectively, on the keyboard. To cue listeners as to which part of the combined stimulus they should respond, the two response boxes were not displayed during stimulus presentation while instead a 4×25 cm box was shown in the upper part of the screen. The color of this box was red during the adaptation and delay period of each stimulus presentation, indicating the subject was only to listen during this time; at the end of the delay period, the box color changed to green to indicate the start of the target test stimulus to which the subject had to respond. At least one second passed after a response and before the next trial began, though the actual delay of the next stimulus could be greater depending upon the speed of response. No feedback was provided for responses to the test stimuli.

Subjects performed in 2 repetitions of the 8 possible experimental blocks representing each combination of the two hemifields (left, right), two adaptor durations (1 s, 5 s), and two adaptor motion directions (leftward, rightward). A single block presented sounds for only one hemifield, one adaptor duration, and one adaptor motion direction, in order to properly create a well-localized aftereffect (i.e., presenting opposite adaptor directions during the same block should theoretically cancel out adaptation effects and thus fail to produce an aftereffect). Individual blocks lasted either approximately 10–12 or 21–23 minutes, depending on adaptor duration.

After completing a block, subjects were required to wait at least 5 minutes before beginning the next block, to allow them time to recover from the previous adaptation effects. Stimuli in the same hemifield were never presented in two successive blocks; otherwise, the presentation order of adaptor duration and direction was random. Subjects normally did not complete more than 3 blocks per session (i.e., per day) and entire testing lasted several weeks for each listener.

III. RESULTS AND DISCUSSION

A. Effect of adaptor hemifield and motion direction on the aMAE

In the following analyses, data were averaged across all 8 listeners, across the two repetitions of each experimental block for each listener, and across the 9 repetitions of each test stimulus movement level within a single block. The eight numbered subplots in Fig. 2 present the mean results of the experiment for each combination of hemifield (*left* = subplots *1–4*; *right* = subplots *5–8*), adaptor duration (*columns*), and adaptor direction (*rows*) in terms of percent "right" responses as a function of the test probe movement level. Line types represent different delays of the test probe presentation (*solid* = 0 s; *dashed* = $\frac{2}{3}$ s; *dotted* = $1\frac{2}{3}$ s).

In theory, aftereffects should be seen as an increase (decrease) in percent "right" responses after exposure to leftward (rightward) moving adaptors. This increase (decrease) should result in a shift of the mean (50% point) of the "right" psychometric function leftward (rightward) from the zero degree point indicating no directional response bias. The most immediate impression from Fig. 2 is that such

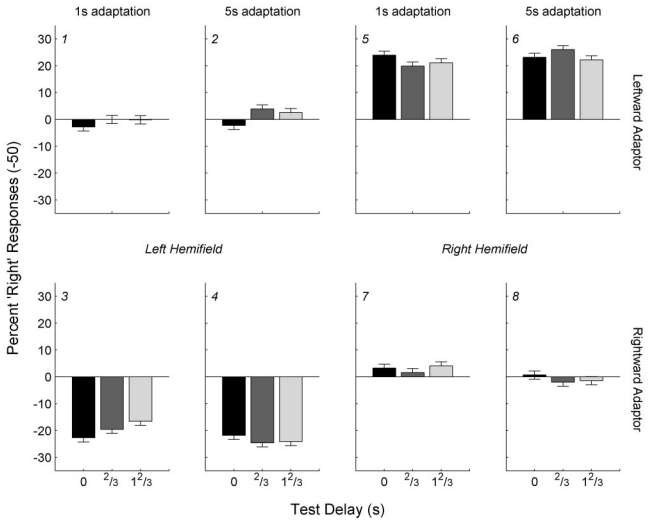

FIG. 3. Mean results presented as percent ''right'' responses after averaging across the test probe movement level, with an estimate of the pooled standard error. Test delays are presented along the abscissa (*shading*). Columns and rows are otherwise the same as for Fig. 2.

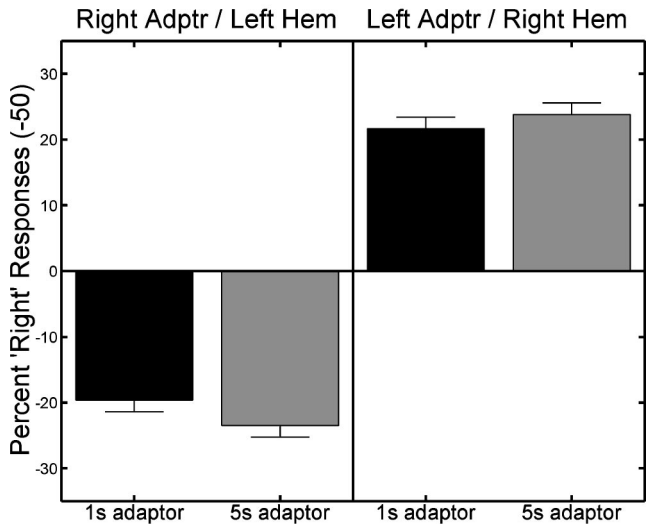

FIG. 4. Effect of 1 vs 5 seconds of motion adaptation, with an estimate of the pooled standard error. Data are presented as percent ''right'' responses averaged across all levels of test motion and delays for the two adaptor directions and hemifields.

aftereffect shifts away from 0 degrees are apparent for only four of the 8 experimental conditions: for rightward adaptation in the left hemifield (subplots *3*, *4*) and leftward adaptation in the right hemifield (subplots *5*, *6*). This result is supported by a significant 3-way interaction in the omnibus 5-factor within-subject ANOVA testing for hemifield, adaptor direction, and test probe movement level [$F(5,35) = 7.31$; Greenhouse–Geisser corrected $p < 0.005$]. No other interactions of equivalent or higher order were significant.

Another view of this result is presented in Fig. 3 which graphs percent ''right'' responses after averaging across test probe movement level. In this view, the lack of an aftereffect should result in average percent ''right'' responses of 50% (i.e., unbiased responses to test motion on average), while leftward (rightward) adaptation should result in mean aftereffect biases greater (less) than 50%. To better view potential aftereffect shifts, 50 is subtracted from all results before presentation. Error bars represent an estimate of the pooled standard error. The hemifield × adaptor direction × test motion interaction is quite evident in this depiction of the data.

The pattern of results in Figs. 2 and 3 can be described generally as follows: strong aftereffects occur only for adaptor movement *toward* the midline, while no aftereffects appear for adaptor movement *away* from midline, regardless of the hemifield of auditory presentation. Though this result was unexpected given previous reports of aMAE uniformity across ±35 degrees of the frontal midline (Dong *et al.*, 2000), it may be explainable in light of recent physiological studies into the cortical neural effects of exposure to auditory motion. These explanations are postponed for now and discussed more thoroughly at the end of this section.

Remaining analyses further investigate this significant 3-way interaction by examining in more detail only those conditions which produced clear aftereffects. Specifically, 4 of the 8 conditions tested in this experiment (subplots *3*, *4*, *5*, and *6* of Fig. 2) produced aftereffect shifts whose intersections significantly deviated from the unbiased 50% point. Therefore only data from rightward adaptors in the left hemifield and leftward adaptors in the right hemifield are further considered unless otherwise noted.

B. Effects of adaptor duration on the aMAE

1. Effect of 5 vs 1 second of motion adaptation

This experiment was designed to investigate two fundamental issues regarding the auditory motion aftereffect: the effect of adaptor duration on the resulting aMAE, and the decay of the aftereffect after adaptation ends. One question raised by the first issue is whether the amount of aftereffect shift differs after 5 seconds versus 1 second of adaptation. For the data from rightward adaptation in the left hemifield and leftward adaptation in the right hemifield, the adaptor direction x duration interaction is significant [$F(1,7) = 5.66$; Greenhouse–Geisser corrected $p < 0.05$] and is presented in Fig. 4.

This significant interaction contrast is clearly due to the differences in adaptor movement direction between the two hemifields, rather than due to the adaptor durations. Hence, another method for analyzing these data is to equalize the aftereffect shifts across hemifield/direction; that is, to measure their magnitudes due to adaptor motion toward the midline regardless of the hemifield. This would then allow aftereffect shifts for the same adaptor duration to be combined across the two adaptor hemifields/directions without their opposing directions canceling out, and thus increase the statistical power of the comparison between 1 and 5 s adaptation.

To equalize aftereffect shifts, the percent ''right'' responses for rightward adaptation in the left hemifield are converted for each listener to their corresponding shift if the adaptor had been moving leftward instead. Specifically, a reflection in the psychometric scatter is made about the zero test probe velocity point on the abscissa, and then complemented about the ordinate axis.[1] Data from rightward adaptation in the left hemifield were converted for all listeners in this manner and then analyzed with data for leftward adaptation in the right hemifield. A 4-factor

TABLE I. AMAE magnitudes resulting from 1 second of adaptation.

	Rightward motion in left hem			Leftward motion in right hem		
	0 s delay	$\frac{2}{3}$ s delay	$1\frac{2}{3}$ s delay	0 s delay	$\frac{2}{3}$ s delay	$1\frac{2}{3}$ s delay
Listener 1	6.32°/s	7.05	7.98	−5.42	−6.73	−5.85
2	2.57	1.97	0.53	−4.95	−4.01	−3.50
3	0.74	4.08	1.95	0.89	1.63	−1.00
4	5.05	3.26	1.82	−9.01	−5.00	−3.62
5	12.99	11.21	10.02	−12.27	−8.96	−9.11
6	12.37	4.47	6.19	−44.41	−7.26	−10.23
7	3.82	2.80	1.88	−4.27	−3.56	−4.98
8	14.69	8.50	6.38	−10.93	−8.43	−8.56

ANOVA (hemifield/direction × adaptor duration × test delay × test motion)^2 on these results revealed a significant main effect of adaptor duration [$F(1,7)=5.66$; Greenhouse–Geisser corrected $p<0.05$]. Hence, when aftereffects are equalized for an adaptor direction, 5 seconds of adaptation does produce a slightly greater aMAE shift than does 1-second adaptation (mean of 5 s adaptation = 73.63% equalized ''right'' responses; mean of 1 s adaptation = 70.62% equalized ''right'' responses).

2. AMAE magnitude for 1-second adaptation

The previous result indicates that aftereffect strength is a positive function of adaptor duration. However, the small percentage difference between the two durations (as measured in the average equalized percent ''right'' responses) suggests at first glance that the aMAE grows compressively with adaptor duration, with most of the effect arising after a single pass of a moving adaptor. This raises the question of how the aftereffect magnitude created from exposure to a single moving source compares to those generated in previously published studies after much longer adaptation periods.

The aMAE magnitude provides a single summary measure of the strength of the aftereffect in terms other than percent ''right'' responses. Two published measures of the aMAE magnitude are (1) the percentage area difference between the psychometric functions created by moving and stationary adaptors (Grantham, 1998); and (2) the bias parameter estimated from functions fitted to the psychometric curves (Neelon and Jenison, 2003). The later technique expresses the aMAE magnitude as the speed of a hypothetical moving test sound which should appear stationary to the listener after adaptation. For example, Dong *et al.* (2000) adapted listeners to broadband noise moving in a horizontal arc between ±15° for a period of 2 minutes. Using probit analysis (Finney, 1971) to estimate the point at which listeners should respond to a moving test stimulus leftward or rightward equally often, the authors reported for four listeners an average aMAE magnitude of near 3 deg/sec created by an adaptor speed of 20 deg/sec.

For comparison with the results of Dong *et al.*, magnitudes for our listeners were estimated from the bias parameters of logistic fits to the psychometric functions. This function is described by

$$f(x)=100\times 1/(1+e^{-(X-a)/b}), \quad (1)$$

where a and b are free parameters minimized to best fit the observed data, and X is the vector of test stimuli motion values (±10, 6, and 2 d/s). a represents the test stimulus which should appear stationary after adaptation (i.e., the 50% performance point, or the overall bias in listeners' responses) and is used as a summary measure of the magnitude of the motion aftereffect for each listener. If a motion aftereffect is present, then adaptation to leftward motion should produce negative aMAE magnitudes; that is, a slightly leftward moving test stimulus should appear stationary after adaptation (vice versa for rightward adaptor motion).

Bias terms were estimated for 1 s second adaptation at the 3 test delays for rightward motion in the left hemifield and leftward motion in the right hemifield (i.e., the quadrants in which aftereffects were present) for all data over the relevant blocks. These values are presented in Table I.

To calculate the grand average aMAE magnitude across all listeners and all irrelevant experimental conditions, these terms were first averaged across test delays (the subcolumns in Table I). The resulting values were then averaged again for each listener across the adaptor direction/hemifield (supercolumns in Table I) by reversing the sign of the aMAE magnitudes for leftward motion in the right hemifield. This process combined results across the two directions while preserving individual differences in degree and sign of the magnitudes (Neelon and Jenison, 2003). The end result was a single estimate of the aMAE magnitude for each listener for 1 s adaptation, averaged across hemifield, direction, and test delay. Averaged once more across all 8 listeners (rows in Table I), the grand mean aMAE magnitude produced by 1 second of motion adaptation in this study was 6.63 deg/sec (4.52 deg/sec standard deviation).

It is impressive that the grand average aMAE magnitude for 1 second of adaptation in this experiment is almost twice as large as that reported in Dong *et al.* (2000) for 2 minutes of adaptation to a real moving source. There are at least two explanations for this larger magnitude rather than concluding 1 second of motion adaptation is equivalent to 120 seconds. First is the slightly faster adaptor speed used in this experiment compared to that used by Dong *et al.* (30 deg/sec vs. 20 deg/sec, respectively). However, they also found that aMAE magnitudes increased as a negatively accelerating function of adaptor speed, suggesting that the aMAE magnitude reported here should not be 100% larger for an adaptor only 50% faster. This raises a second, perhaps more likely explanation

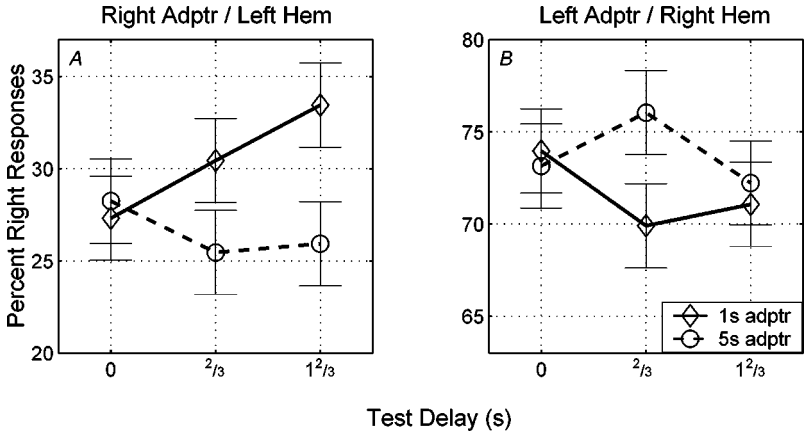

FIG. 5. Percent "right" responses as a function of adaptor duration (*line type*) and test delay (*abscissa*) for rightward adaptation in the left hemifield (*a*) and leftward adaptation in the right hemifield (*b*), averaged across test stimuli movement, with an estimate of the pooled standard error.

for this difference: that adaptation builds up over the entire course of the 10 minute long block for the 1-second adaptor duration to create the observed motion aftereffects. This question is addressed in more detail later.

It is also apparent from Table I that there were large individual differences in the data reported here. This may be one consequence of the briefer adaptation durations used here, or it may also stem from the limited number of test probe movement values. Nonetheless, it seems that for many listeners a single pass of a moving sound is enough to create dramatic biases in subsequent auditory motion judgments, which suggests a very quick onset of the modulating effect of preceding motion on subsequent motion perception. This rapid modulating effect appears to be consistent with findings in the physiological literature that only a brief exposure to auditory motion is necessary to dramatically alter the receptive fields of brainstem and cortical auditory neurons, and by extension, the possible perception of auditory motion (Spizter and Semple, 1998; McAlpine *et al.*, 2000; Malone *et al.*, 2002).

C. Effect of test delay on aMAE

The second fundamental question this experiment investigated was whether the measured strength of the auditory motion aftereffect would change as the presentation of the test stimulus was progressively delayed after cessation of the moving adaptor. As discussed in the Introduction, there are data showing that IC neurons may exhibit auditory motion direction selectivity only for very brief durations (500 ms or less) (McAlpine *et al.*, 2000): if the units are given time beyond this amount to recover from their initial response to sounds moving into their receptive fields, skewed responses for particular motion directions disappear. These data suggest that potential aMAEs would be strongest immediately after exposure to auditory motion, and should decay if measured more than 500 ms after exposure.

On the other hand, psychophysical experiments have shown that the effects of adaptation after minutes-long exposure to auditory motion may themselves last on the order of minutes or longer (Ehrenstein, 1994; Dong *et al.*, 1999). These behavioral results are complemented by recent physiological data showing that the neural adaptation to dynamic auditory stimuli may grow over time and last longer than 500 ms (Sanes *et al.*, 1998; Malone *et al.*, 2002). The current experiment was designed to explore these issues by delaying the presentation of the test stimulus by 0, $\frac{2}{3}$, or $1\frac{2}{3}$ seconds after the adaptation ended.

Analysis once again focuses only on those adaptor hemifield/direction combinations that produced reliable aftereffects. Figure 5 graphs percent "right" responses as a function of the adaptor duration (symbol) by the test delay (x-axis), averaged across test stimuli movement, for rightward adaptors in the left hemifield (A) and leftward adaptors in the right hemifield (B). The interaction (hemifield/direction$\times$adaptor duration$\times$test delay) presented in this figure is significant [$F(2,14)=4.49$; Greenhouse–Geisser corrected $p<0.05$]. A partial interaction analysis on the data in Fig. 6(a) reveals a significant effect of adaptor duration$\times$delay [$F(2,14)=4.68$; Greenhouse–Geisser corrected $p<0.05$]. Post-hoc analyses (Tukey's HSD) showed that performance at $\frac{2}{3}$ and $1\frac{2}{3}$ s test delays for the 5 s adaptor differ significantly from the $1\frac{2}{3}$ s test delay for the 1 s adaptor ($p<0.014$; $p<0.022$, respectively). Further, for the 1 s adaptor by itself, the difference in performance between the 0 and $1\frac{2}{3}$ s test delays is marginally significant ($p<0.074$).

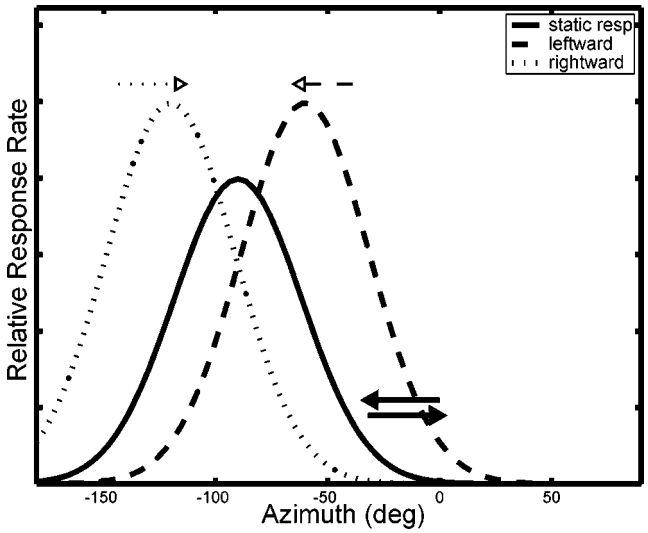

FIG. 6. Idealized response of a cortical auditory motion-sensitive neuron to static and moving sound sources (*line type*) (based upon Malone *et al.*, 2002). Solid arrows depict adaptor movement in the left hemifield from the present experiment.

The partial interaction of the data from leftward adaptor motion in the right hemifield [Fig. 6(b)], however, shows the difference between 1 s and 5 s adaptors across the test delays to be only marginally significant [$F(2,14)=3.16$; Huynh–Feldt corrected $p<0.75$]. Though the pattern of results appears to be similar to the left hemifield results for 0 and $\frac{2}{3}$ s test delays, there is little difference in the aftereffect for the two durations at the $1\frac{2}{3}$ s test delay.

As was done for the effects of adaptor duration in the previous section, the results of the two adaptor hemifields/directions were equalized to examine the overall effects of test delay. A 3-factor ANOVA on these equalized percent ''right'' responses confirms the significant interaction between adaptor duration and test delay [$F(2,14)=4.5$; Greenhouse–Geisser corrected $p<0.05$]. A post-hoc test (Tukey's HSD) reveals that the result for the 5 s adaptor measured at a $\frac{2}{3}$ s test delay, across the hemifield/direction, is significantly different from those for the 1 s adaptor at $\frac{2}{3}$ and $1\frac{2}{3}$ s test delays ($p<0.04$ and $p<0.013$, respectively).

This analysis of the effects of delaying the presentation of the test stimulus has produced the following results. For 1 second of auditory motion exposure, the aMAE is strongest immediately after exposure ends and declines significantly over a period of almost 2 seconds. The trend of this result initially appears to correspond with the McAlpine *et al.* (2000) finding that motion direction selectivity, and by extension a possible source of the aMAE, arises from very brief neural adaptation to auditory motion.

However, for 5 seconds of auditory motion exposure, the aMAE appears to be equally strong up to approximately 2 seconds after adaptation ends. This increasing duration of the aMAE with increasing amounts of adaptation may reflect a general trend that culminates with the prolonged aMAE that has been reported after several minutes of motion adaptation (Ehrenstein, 1994; Dong *et al.*, 1999). This result is not predicted by models of auditory motion selectivity emerging in the brainstem as a result of only brief adaptation (McAlpine *et al.*, 2000), and may therefore reflect the effects of motion adaptation across longer timescales and over greater physiological regions.

Again, it must be kept in mind that any failure to find even larger differences in the aMAE between 1 versus 5 seconds of adaptation may be the result of viewing the data over entire block lengths. The total motion exposure in the two adaptor durations over the course of an entire block may be much more similar than that caused by 1 versus 5 seconds of adaptation in isolation. This possible effect of block length is explored in the next section.

D. Effects of first versus last third of blocks

As noted earlier, experimental blocks lasted between 10–12 minutes on average for 1-second adaptor durations, and between 21–23 minutes for 5-second adaptor durations. Listeners were thus exposed to substantial amounts of auditory motion by the end of any single experimental block regardless of the number of moving stimuli heard on each individual trial. This raises the possibility that the lack of more obvious differences between 1 and 5 seconds adaptor durations is due to the overall adaptation incurred over an entire block.

This issue had been expected during the design of this experiment and hence the presentation of the 6 test motion levels (± 10, ± 6, ± 2 degrees) and the three test delays (0 s, $\frac{2}{3}$ s, $1\frac{2}{3}$ s) were balanced so that equal numbers of each combination were presented in three sections across the length of a single experimental block. Specifically, three exemplars of each combination of test motion and delay were presented in the first, second, and third sections of a block (within each section, however, the presentation order of the stimuli was otherwise random). This provided the opportunity to compare effects of interest after approximately 3–4 (7–8) minutes of overall motion exposure to 1-(5-)second adaptation (i.e., first third of blocks) versus effects near the end of experimental blocks. Though it is clear that the first third of a block for the 5-second adaptor is still longer than the first third for the 1-second adaptor, these sections were compared directly at this point for ease of analysis.

1. Effect of adaptor duration for first vs last 3rd of block data

Analysis once again focuses only on those adaptor hemifield/direction combinations that produced reliable aftereffects. Data from the first third of the experimental blocks that induced aftereffects were analyzed in the 4-factor partial interaction ANOVA used in the previous sections. As was found for data over entire experimental blocks (Sec. III B I), the adaptor hemifield/direction$\times$duration interaction over the first 3rd of experimental blocks is significant, though its effect is considerably larger [$F(1,7)=21.58$; Greenhouse–Geisser corrected $p<0.01$]. When the data are equalized across the hemifield/direction, the differences between the adaptor durations in percent equalized ''right'' responses are indeed slightly greater than was previously found for the data over the entire experiment (mean of 5 s adaptation $=74.83\%$ equalized ''right'' responses; mean of 1 s adaptation$=69.16\%$ equalized ''right'' responses).

This effect of adaptor duration disappears, however, by the end of experimental blocks: the hemifield/direction x duration interaction is no longer significant [$F(1,7)=0.002$; $p>0.95$] and the equalized difference between the two adaptor durations has all but vanished (a mean of 5 s adaptation $=72.69\%$ equalized ''right'' responses; mean of 1 s adaptation$=72.57\%$ equalized ''right'' responses). This difference in the effect of adaptor duration between the first and last third of experimental blocks confirms what was hypothesized previously: the aftereffect created by 5 seconds adaptation is initially reliably stronger than that created from 1 second adaptation; however, the repeated presentation of moving adaptors over the course of an entire experiment eventually adapts listeners an equal amount, regardless of the adaptor duration on individual trials.

2. Effect of test delay for first vs last 3rd of block data

The same ANOVAs described above indicate no significant effects of delays for either the first or last 3rd of block data at the $p<0.05$ criterion level. However, for both time periods, the interaction between adaptor duration and test delay is marginally significant ($p<0.08$). This suggests that differences in the temporal decay of the aftereffect, as measured by the effect of test delay, may only emerge for the different adaptor durations after prolonged exposure to auditory motion (e.g., over an entire experimental block). It appears that the following conclusions may be drawn considering the results presented in sections $C1$ and $C2$: auditory motion aftereffects become stronger and last longer as subjects become more adapted to auditory motion over the course of an experimental session, regardless of the duration of sound motion on individual trials.

E. Asymmetrical aMAE.

An attempt is made here to explain the asymmetrical aMAE seen in Figs. 2 and 3 using recent data on neural response in mammalian primary auditory cortex (AI) to simulated auditory motion (Ahissar *et al.*, 1992; Wilson and O'Neill, 1998; Ingham *et al.*, 2001; Malone *et al.*, 2002). These data show that the majority of neurons respond to auditory motion in the contralateral hemifield and, further, that many shift their receptive field response profiles toward the direction of source motion. For nonhuman mammals, maximal responses to static source position appear to occur at lateral azimuths near the acoustic axis (Brugge *et al.*, 1996; Malone *et al.*, 2002). Hence, for source motion near midline (such as used in this study), these units should respond more strongly to movement away from rather than toward midline, and consequently lead to greater aftereffect shifts toward the midline.

Figure 6 presents an idealized depiction of these response changes (*line type*) for units hypothetically recorded from right auditory cortex with maximal response to sources near −90° azimuth (illustrations are based upon data from Malone *et al.*, 2002). As can be seen, a source starting at the midline and moving leftward (upper black arrow) should evoke a much stronger neural response than a sound starting at −30 degrees and moving rightward (lower black arrow). It is this response asymmetry between source motion into and out of laterally centered receptive fields that may have lead researchers to find a majority of neurons ''preferring'' contralateral rather than ipsilateral sound source motion (Ahissar *et al.*, 1992; Stumpf *et al.*, 1992; Malone *et al.*, 2002). This asymmetry may arise from common response adaptation as described in leaky integrate-and-fire neural models (Gerstner & Kistler, 2002), for example, rather than reflect a specialized reaction to sound motion direction. More relevant to the purposes of this work, this response asymmetry for motion near the midline could provide the basis for the asymmetrical aftereffects found in this experiment.

The difficulty with this portrayal of neural response to auditory motion is that, at first glance, it appears to predict an opposite aftereffect asymmetry to the one reported here. Specifically, for units with the best response near −90° azimuth, the response to leftward motion in the left hemifield (i.e., away from midline) should evoke the greatest response in motion sensitive neurons and hence result in the greatest adaptation; in contrast, rightward motion should produce little activation and likewise little adaptation. This would imply the creation of strong rightward aftereffects (i.e., bias shifts toward the midline) for leftward motion adaptation and no leftward aftereffects for rightward adaptation. But the aMAE asymmetry reported here showed just the opposite pattern: for motion in the left hemifield, strong aftereffects appeared for rightward (toward midline) but not for leftward adaptor motion.

One possible explanation for this mismatch would be if maximal azimuthal responses in the human auditory cortex occurs nearer to 0° rather than at the acoustic axis. In this circumstance, motion toward the midline would create a strong increase in neural response, which should result in observable aftereffects away from the midline (and *vice versa* for ipsilaterally directed adaptation). Though data in nonhuman mammals indicate that maximal spatial responses fall at more lateral azimuths (Brugge *et al.*, 1996; Malone *et al.*, 2002), the distribution of receptive field maxima for humans remains empirically unknown. This explanation of the aMAE asymmetry must await confirmation by future data on the spatial response properties of neurons in human AI.

It should be noted that the asymmetrical aMAE seen here has not been reported in previous studies investigating the spatial extent of the auditory motion aftereffect (Grantham, 1998; Dong *et al.*, 2000). One source of this discrepancy is most certainly the briefer adaptation times used here versus those used in previous experiments. However, an asymmetrical aMAE based on the adaptor direction may be more robust to adaptation duration than implied by a superficial comparison of the cited aMAE studies. Grantham (1998) measured aftereffects after 30 seconds adaptation to pass-band noise moving toward and away from the midline in a single hemifield, though he did not test statistically for any differences of the adaptor direction on aMAE magnitude. Nonetheless, a plot of his results (Fig. 13, 1998) suggests that movement toward the midline may have produced larger aftereffects than movement away from midline.

Dong *et al.* (2000) tested adaptation regions constrained to single hemifields using only a rightward moving, 2-minute adaptor. If their results were to parallel those found here, then aMAE shifts would be seen only for adaptors in the left hemifield (i.e., movement toward the midline). However, plots of their data do not show significant differences in aMAE magnitudes for rightward motion in the two hemifields. The differences in the aMAE asymmetry between these three experiments (including this one) thus appears to be a function of the increasing adaptation periods used: a significant aMAE asymmetry after 1–5 seconds of adaptation (reported here), a slight aMAE asymmetry after 30 seconds of adaptation (suggested in Grantham, 1998), and no apparent aMAE asymmetry after 120 seconds of adaptation (Dong *et al.*, 2000). It is also possible that these differences may reflect different adaptive processes: the depicted recep-

tive field shifts underlie a true motion illusion with very short time constants of growth and decay, while bi-directional aMAEs arise from other, longer lasting response changes.

Nonetheless, the imbalanced aMAEs found here and suggested in Grantham's plots after 30 seconds of adaptation, may signify a real, robust difference in neural response to sound motion toward versus away from the midline. The fact that asymmetrical responses to sound motion have also been found in mammalian AI (Jenison *et al.*, 2001) suggests a possible cortical component to the auditory motion aftereffect. It remains to be determined whether extra-auditory cortical areas also contribute to the aMAE, as has been demonstrated for visual motion aftereffects (Culham *et al.*, 2000; Van Wezel and Britten, 2002).

IV. CONCLUSIONS

This study investigated the temporal growth and decay of the auditory motion aftereffect (aMAE) by manipulating how much motion listeners were exposed to during adaptation (1 versus 5 seconds) and how quickly test stimuli were presented following this exposure (0, $\frac{2}{3}$, and $1\frac{2}{3}$ seconds delay). Regarding the effects of adaptor duration, 1 second of exposure to auditory motion (i.e., a single pass of a moving sound source) produced strong biases in response to the motion direction of subsequent test stimuli. This result is taken as evidence of the rapid growth of the aMAE, and is consistent with findings in the physiological literature that only brief exposure to auditory motion is necessary to dramatically affect the receptive fields of brainstem and cortical auditory neurons and, by extension, the possible perception of auditory motion (Spitzer and Semple, 1998; McAlpine *et al.*, 2000; Malone *et al.*, 2002).

However, 5 seconds of exposure to auditory motion generally produced stronger aMAEs. The apparently small increase in the magnitude of the aMAE for 5 seconds relative to 1 second of motion adaptation may also indicate that a substantial amount of adaptation builds up after an entire experimental session of motion exposure (e.g., lasting at least 10 minutes or more), regardless of adaptor duration on individual trials. This hypothesis was further supported by analyses showing that the differences in aMAE for the two adaptor durations were greatest in the initial third of an experimental block (over the course of the first 4–7 minutes), and decreased by its end.

Concerning timing of the test stimulus presentation, the aMAE was strongest immediately after adaptation ceased for 1 second of motion exposure on each trial, and decayed significantly by $1\frac{2}{3}$ seconds. However, for 5 seconds of motion exposure on each trial, the aMAE appeared as strong after $1\frac{2}{3}$ seconds as it was immediately after adaptation ends. This argues that greater amounts of motion adaptation result in longer lasting motion aftereffects (Dong *et al.*, 1999). The stronger and longer lasting aMAEs for longer exposure to auditory motion further suggest that models of motion selectivity in inferior colliculus relying on very brief forms of adaptation [e.g., <500 ms (Cai *et al.*, 1998; McAlpine *et al.*, 2000)] may not be able to completely account for all aspects of the auditory motion aftereffect. These differences between 1 and 5 seconds of adaptation may also imply two components to the aMAE: a short time-constant motion illusion (i.e., a true motion aftereffect), and a longer time-constant motion desensitization in the direction of adaptation (i.e., response bias) (Grantham, 1998).

Finally, one of the most dramatic findings of this experiment was also one of the least expected: aftereffects arising from both adaptor durations were produced only by stimuli moving toward but not away from the midline (that is, aftereffects were only seen as shifts away from the midline). This result is not congruent with previous studies reporting equivalently strong bi-directional aftereffects for adaptation regions across ± 35 deg of the midline (Dong *et al.*, 2000).

Ultimately, it is possible that the auditory motion aftereffect arises from both the long- and short-term adaptation of cells at multiple brainstem and cortical sites. One caveat that must be kept in mind when trying to explain the behavioral results seen here using neurophysiological data is that many of the aforementioned physiological studies measured neural responses using tonal stimuli varying only in phase differences (Spitzer and Semple, 1993; 1998; McAlpine *et al.*, 2000; Malone *et al.*, 2002). The experiment reported here used virtual auditory motion stimuli which incorporated all natural auditory spatial cues (ITD, ILD, monaural spectral cues). Given the convergent projections from the superior olive to the inferior colliculus and beyond, as well as the myriad cortico-cortical and cortico-collicular loops in the auditory system (Winer *et al.*, 1998; Kaas *et al.*, 1999; Thompson and Schofield, 2000), the presentation of stimuli rich in spatial cues could produce quite dramatic responses to auditory motion across the entire auditory system. A complete explanation of the aMAE must await more detailed information on how the human auditory system responds to and encodes sound motion.

ACKNOWLEDGMENTS

The authors are grateful to Doris Kistler and Fred Wightman for their generous assistance in recording and preparing the HRTFs used in this experiment, and to the commitment of the listeners who participated in this work. This work was supported in part by the Vilas Trust and NIH DC03554.

[1]As an example, if a listener reported a $+2$ deg/sec test stimulus was moving rightward 20% of the time after rightward adaptation (i.e., a typical leftward aMAE), then the corresponding result for hypothetical leftward adaptation should be that a -2 deg/sec test stimulus would be labeled as moving rightward 80% of the time (i.e., a rightward aMAE).

[2]Even though adaptor hemifields/directions have been equalized in this analysis, there still may be differences in the aMAE between these two conditions.

Ahissar, M., Ahissar, E., Bergman, H., and Vaadia, E. (**1992**). "Activity of single neurons and interactions between adjacent neurons in the monkey auditory cortex," J. Neurophysiol. **67**, 203–215.

Brugge, J. F., Reale, R. A., and Hind, J. E. (**1996**). "The structure of spatial receptive fields of neurons in primary auditory cortex of the cat," J. Neurosci. **16**, 4420–4437.

Cai, H., Carney, L. H., and Colburn, H. S. (**1998**). "A model for binaural response properties of inferior colliculus neurons. II. A model with inter-

aural time difference-sensitive excitatory and inhibitory inputs and an adaptation mechanism,'' J. Acoust. Soc. Am. **103**, 494–506.
Carlile, S., and Best, V. (**2002**). ''Discrimination of sound source velocity in human listeners,'' J. Acoust. Soc. Am. **111**, 1026–1035.
Clarey, J. C., Barone, P., and Imig, T. J. (**1992**). ''Physiology of thalamus and cortex,'' in *The Mammalian Auditory Pathway: Neurophysiology*, edited by A. N. Popper and R. R. Fay (Springer-Verlag, New York, NY), pp. 232–334.
Culham, J. C., Verstraten, F. A. J., Ashida, H., and Cavanaugh, P. (**2000**). ''Independent aftereffects of attention and motion,'' Neuron **28**, 607–615.
Diehl, R. L., Kluender, K. R., and Parker, E. M. (**1985**). ''Are selective adaptation and contrast effects really distinct?,'' J. Exp. Psych. Human Percep. Perform. **11**, 209–220.
Dong, C. J., Swindale, N. V., and Cynader, M. S. (**1999**). ''A contingent aftereffect in the auditory system,'' Nat. Neurosci. **2**, 863–865.
Dong, C. J., Swindale, N. V., Zakarauskas, P., Hayward, V., and Cynader, M. S. (**2000**). ''The auditory motion aftereffect: Its tuning and specificity in the spatial and frequency domains,'' Percept. Psychophys. **62**, 1099–1111.
Ehrenstein, W. H. (**1994**). ''Auditory aftereffects following simulated motion produced by varying interaural intensity or time,'' Perception **23**, 1249–1255.
Finney, D. J. (**1971**). *Probit Analysis* (Cambridge University Press, Cambridge).
Gerstner, W., and Kistler, W. M. (**2002**). *Spiking Neuron Models* (Cambridge University Press, Cambridge).
Grantham, D. W., and Wightman, F. L. (**1979**). ''Auditory motion aftereffects,'' Percept. Psychophys. **26**, 403–408.
Grantham, D. W. (**1989**). ''Motion aftereffects with horizontally moving sound sources in the free field,'' Percept. Psychophys. **45**, 129–136.
Grantham, D. W., (**1995**). *Spatial hearing and related phenomena*, in Hearing. (Academic Press, N.Y.), pp. 297–345.
Grantham, D. W. (**1998**). ''Auditory motion aftereffects in the horizontal plane: The effects of spectral region, spatial sector and spatial richness,'' Acta Acust. (Beijing) **84**, 337–347.
Ingham, N. J., Hart, H. C., and McAlpine, D. year. ''Spatial receptive fields of inferior colliculus neurons to auditory apparent motion in free field,'' J. Neurophysiol. **85**, 23–33.
Jacobsen, G., Poganiatz, I., and Nelken, I. (**2001**). ''Synthesizing spatially complex sound in virtual space: an accurate offline algorithm,'' J. Neurosci. Methods **106**, 29–38.
Jenison, R. L., Schnupp, J. W. H., Reale, R. A., and Brugge, J. F. (**2001**). ''Auditory space-time dynamics revealed by spherical white noise analysis,'' J. Neurosci. **21**, 4408–4415.
Jiang, H., Lepore, F., Poirier, P., and Guillemot, J-P. (**2000**). ''Responses of cells to stationary and moving sound stimuli in the anterior ectosylvian cortex ofcats,'' Hear. Res. **139**, 69–85.
Kaas, J. H., Hackett, T. A., and Tramo, M. J. (**1999**). ''Auditory processing in primate cerebral cortex,'' Curr. Opin. Neurobiol. **9**, 164–170.
Kistler, D. J., and Wightman, F. L. (**1992**). ''A model of head-related transfer functions based on principal components analysis and minimum-phase reconstruction,'' J. Acoust. Soc. Am. **91**, 1637–1647.
Macpherson, E. A., and Middlebrooks, J. C. (**2002**). ''Listener weighting of cues for lateral angle: the duplex theory of sound localization re revisited,'' J. Acoust. Soc. Am. **111**, 2219–2236.
Malone, B. J., Scott, B. H., and Semple, M. N. (**2002**). ''Context-dependent adaptive coding of interaural phase disparity in the auditory cortex of awake macaques,'' J. Neurosci. **22**, 4625–4638.
Mather, G., Verstraten, F., Anstis, S. (**1998**). *The Motion Aftereffect* (MIT, Cambridge, Massachusetts).
McAlpine, D., Jiang, D., Shackleton, T. M., and Palmer, A. R. (**2000**). ''Responses of neurons in the inferior colliculus to dynamic interaural phase cues: evidence for a mechanism of binaural adaptation,'' J. Neurophysiol. **83**, 1356–1365.
Middlebrooks, J. C., Xu, L, Furukawa, S., Mickey, B. J., (**2002**). *Location signaling by cortical neurons.* In Integrative Functions in the Mammalian Auditory Pathway, edited by D. Oerlel, R. R. Fay, and A. N. Popper (Handbook in Auditory Research (Springer Verlag, New York).
Møller, H., Sørensen, M. F., Hammershøi, D., and Jensen, C. B. (**1995**). ''Head-related transfer functions of human subjects,'' J. Audio Eng. Soc. **43**, 300–321.
Neelon, M. F., and Jenison, R. L. (**2003**). ''The effect of trajectory on the auditory motion aftereffect,'' Hear. Res. **180**, 57–66.
Niedeggen, M., and Wist, E. R. (**1998**). ''The physiologic substrate of motion aftereffects,'' in *The Motion Aftereffect*, edited by G. Mather, F. Verstraten, and S. Anstis (MIT Press, Cambridge, MA), pp. 125–156.
Palmer, A. R., and Summerfield, A. Q. (**2002**). ''Microelectrode and neuroimaging studies of central auditory function,'' Br. Med. Bull. **63**, 95–105.
Rauschecker, J. P., Tian, B., and Hauser, M. (**1995**). ''Processing of complex sounds in the macaque nonprimary auditory cortex,'' Science **268**, 111–114.
Sanes, D. H., Malone, B. J., and Semple, M. N. (**1998**). ''Role of synaptic inhibition in processing of dynamic binaural level stimuli,'' J. Neurosci. **18**, 794–803.
Spitzer, M. W., and Semple, M. N. (**1993**). ''Responses of inferior colliculus neurons to time-varying interaural phase disparity: Effects of shifting the locus of virtual motion,'' J. Neurophysiol. **69**, 1245–1263.
Spitzer, M. W., and Semple, M. N. (**1998**). ''Transformation of binaural response properties in the ascending auditory pathway: influence of time-varying interaural phase disparity,'' J. Neurophysiol. **80**, 3062–3076.
Stumpf, E., Toronchuk, J. M., and Cynader, M. S. (**1992**). ''Neurons in cat primary auditory cortex sensitive to correlates of auditory motion in three-dimensional space,'' Exp. Brain Res. **88**, 158–168.
Thompson, A. M., and Schofield, B. R. (**2000**). ''Afferent projections of the superior olivary complex,'' Microsc. Res. Tech. **51**, 330–354.
Van Wezel, R. J. A., and Britten, K. H. (**2002**). ''Motion adaptation in area MT,'' J. Neurophysiol. **88**, 3469–3476.
Wessinger, C. M., VanMeter, J., Tian, B., Lare, J. Van, Pekar, J., and Rauschecker, J. P. (**2001**). ''Hierarchical organization of the human auditory cortex revealed by functional magnetic resonance imaging,'' J Cogn. Neurosci. **13**, 1–7.
Wightman, F. L., and Kistler, D. J. (**1992**). ''The dominant role of low-frequency interaural time differences in sound localization,'' J. Acoust. Soc. Am. **91**, 1648–1661.
Wightman, F. L., and Kistler, D. J. (**1999**). ''Resolution of front-back ambiguity in spatial hearing by listener and source movement,'' J. Acoust. Soc. Am. **105**, 2841–2853.
Winer, J. A., Larue, D. T., Diehl, J. J., and Hefti, B. J. (**1998**). ''Auditory cortical projections to the cat inferior colliculus,'' J. Comp. Neurol. **400**, 147–174.
Wilson, W. W., and O'Neill, W. E. (**1998**). ''Auditory motion induces directionally dependent receptive field shifts in inferior colliculus neurons,'' J. Neurophysiol. **79**, 2040–2062.

Contrasting monaural and interaural spectral cues for human sound localization

Craig Jin[a)]
Department of Electrical and Information Engineering, The University of Sydney, New South Wales 2006, Australia

Anna Corderoy
Department of Physiology, The University of Sydney, New South Wales 2006, Australia

Simon Carlile
Department of Physiology, and Institute for Biomedical Research, The University of Sydney, New South Wales 2006, Australia

André van Schaik
Department of Electrical and Information Engineering, The University of Sydney, New South Wales 2006, Australia

(Received 11 December 2001; revised 9 March 2004; accepted 9 March 2004)

A human psychoacoustical experiment is described that investigates the role of the monaural and interaural spectral cues in human sound localization. In particular, it focuses on the relative contribution of the monaural versus the interaural spectral cues towards resolving directions within a cone of confusion (i.e., directions with similar interaural time and level difference cues) in the auditory localization process. Broadband stimuli were presented in virtual space from 76 roughly equidistant locations around the listener. In the experimental conditions, a ''false'' flat spectrum was presented at the left eardrum. The sound spectrum at the right eardrum was then adjusted so that either the true right monaural spectrum or the true interaural spectrum was preserved. In both cases, the overall interaural time difference and overall interaural level difference were maintained at their natural values. With these virtual sound stimuli, the sound localization performance of four human subjects was examined. The localization performance results indicate that neither the preserved interaural spectral difference cue nor the preserved right monaural spectral cue was sufficient to maintain accurate elevation judgments in the presence of a flat monaural spectrum at the left eardrum. An explanation for the localization results is given in terms of the relative spectral information available for resolving directions within a cone of confusion. © *2004 Acoustical Society of America.* [DOI: 10.1121/1.1736649]

PACS numbers: 43.66.Qp, 43.66.Ba, 43.66.Pn [LRB] Pages: 3124–3141

I. INTRODUCTION

The interaural time and level difference cues extracted by the auditory system are spatially ambiguous in elevation angle as a consequence of the rather symmetrical arrangement of the ears on either side of the head. This spatial ambiguity is referred to as the cone of confusion (Wallach, 1939), and can be resolved using spectral cues associated with the acoustic filtering of the external auditory periphery. The external ears filter sound differently depending on the direction of the sound source relative to the ears. However, exploiting these cues for localization implies that the spectrum of the sound source is known, at least in part, *prior* to the acoustic filtering of the external auditory periphery. Of course, the spectrum of the sound source cannot be known *a priori*. The question of how the auditory system disambiguates the ear-filtered spectrum from the spectrum of the source remains unanswered. Nevertheless, the auditory localization system demonstrates a remarkable capacity for localizing transient, broadband sounds with random and widely varying sound spectra (see Macpherson and Middlebrooks, 2003; Wightman and Kistler, 1997).

The dependence of human auditory localization on the monaural versus the interaural spectral cues has been the focus of copious research with interesting, but also conflicting results (e.g., Butler, 1969a,b; Duda, 1997; Gardner, 1973; Hebrank, 1976; Hebrank and Wright, 1974; Janko *et al.*, 1997; Macpherson and Middlebrooks, 2003; Searle *et al.*, 1975; Wightman and Kistler, 1997, 1999). Numerous psychophysical methods have attempted to reduce the significance of the interaural time difference (ITD) and interaural level difference[1] (ILD) cue in order to focus on the spectral cues. Such methods involve: (1) restricting sound locations to the midsagittal plane and listening binaurally or blocking one ear so that monaural and binaural sound localization can be compared (Butler, 1969a; Gardner, 1973; Hebrank and Wright, 1974); (2) using headphones to present diotic sound stimuli with correct spectral cues for only one ear (Searle *et al.*, 1975); (3) using spectrally irregular sounds (Macpherson and Middlebrooks, 2002; Wightman and Kistler, 1997); (4) filling in the pinna cavities of the ear and thus unilaterally

a)Electronic mail: craig@ee.usyd.edu.au

 0001-4966/2004/115(6)/3124/18/$20.00 © 2004 Acoustical Society of America

or bilaterally degrading the spectral cues (Gardner, 1973). The primary novelty of the work presented here is the use of virtual auditory space so that the binaural difference cues (overall ITD and overall ILD) can be preserved and the monaural spectral cues disrupted. In addition, we present a new information-theoretic analysis of the spectral cues that clarifies the relative importance of the monaural and interaural spectral cues.

II. METHODS

A. Listeners and localization paradigm

Four subjects (3 male, 1 female) participated in the localization experiments. Three of the subjects were authors of the paper and one subject was naive as to the purpose of the experiment. Each participant was an unpaid volunteer with normal hearing (as verified by an audiometric examination). All of the subjects were experienced listeners and had participated in previous localization experiments within the laboratory. The sound localization experiments were conducted in an anechoic chamber using a head-pointing localization paradigm that has been described in detail previously (Carlile *et al.*, 1997). The sound stimuli were presented in virtual auditory space using the ER-2 insert earphones (Etymotic Research) that are designed to produce an approximately flat frequency response, within 3 dB, at the human eardrum over the frequency range 300 Hz to 10 kHz. The subject's head position was continuously monitored using an electromagnetic sensor system in which the receiver was attached to a headband worn by the subject. Prior to the VAS localization tests, the four subjects were first trained in the free-field acoustic environment to accurately use head pointing to indicate the location of a broadband sound source. A single localization trial consisted of the following steps.

(1) The subject stood on a platform in the darkened anechoic chamber and oriented himself/herself with the calibrated start position of (0,0), indicated by LED light feedback.
(2) The subject pressed a push button indicating his/her readiness, after which the sound stimulus was played over the earphones.
(3) The subject turned and pointed his/her head in the perceived direction of the sound source.
(4) The subject pressed the push button to indicate his/her completion of the head-pointing task, after which the response direction as measured by the electromagnetic sensor system was logged by the controlling computer.

B. Measuring directional transfer functions

The pressure transformation from a location in space to the listener's eardrum is referred to as the head-related transfer function (HRTF). There is a different HRTF for each ear and each direction in space. A set of HRTFs was recorded for each of the four subjects who participated in the VAS localization experiments. Recordings were carried out in a triple-walled anechoic sound chamber. Inside the chamber was a height-adjustable platform used to position the subject so that his/her head was in the center of the room. There was also a robotic arm inside the chamber configured as a double-hoop system that could revolve about the subject. The robotic arm was able to position a loudspeaker accurately (within a fraction of 1 deg) at points on an imaginary surface of a sphere 1 meter in radius and centered about the subject's head. The HRTF measurements were made for both ears simultaneously using a ''blocked ear'' recording technique with a small Sennheiser electret microphone (KE4-211-2) placed in each ear (Møller *et al.*, 1995). For each subject, 393 HRTF measurements were made at locations evenly distributed around the subject's head. In order to improve the signal-to-noise ratio, digitally constructed Golay codes with a 1024 length were used as the recording stimulus. The response of the microphone was bandpass filtered from 200 Hz to 16 kHz, digitized at 80 kHz, and averaged over 16 repetitions of the stimulus. The standard processing technique for Golay sequences was then used to derive the impulse responses (see Zhou *et al.*, 1992). The transfer function of the external ear was obtained by deconvolving the response of the microphone in the free field from the response recorded at the entrance to the blocked ear (see Mehrgardt and Mellert, 1977; Pralong and Carlile, 1994; Wightman and Kistler, 1989). The free-field calibration of the recording system was recorded without the subject in the anechoic chamber and at the position corresponding to the center of the subject's head.

The directional transfer functions (DTFs) were derived from the HRTFs as described in Middlebrooks and Green (1990). First, the average log-magnitude spectrum was calculated across all 393 positions to provide an estimate of the location-independent transfer function. The location-independent transfer function was then deconvolved from the HRTFs to obtain the DTFs. The virtual-space sound stimuli were constructed by convolving the stimuli with the measured DTFs. The sound stimuli were presented to the subjects using the ER-2 earphones. The ear-canal resonance, although not present in the blocked ear recording, is not reintroduced by the earphones and was not compensated for when synthesizing virtual noise stimuli using the DTFs. The reasons for ignoring this detail are that: (1) accurate localization of broadband noise stimuli is empirically obtained without simulating the ear-canal resonance (see Carlile *et al.*, 1997, for details), and (2) the ear-canal resonance generally occurs between 3 and 4 kHz and does not play a significant role with respect to the high-frequency (>5 kHz) spectral cues of the outer ear (see Blauert, 1997), which are the primary focus of this work. To assess the quality of the DTF measurements and the virtual-space sound stimuli, the subjects' VAS localization performance was compared with their free-field performance (data presented in Sec. V A). We refer to this step as empirical validation of the DTF filters and have found that most subjects can accurately localize sounds filtered with DTF filters.

C. The VAS stimuli

Four different sound conditions were used in the VAS localization experiments. These sound conditions differed by the manipulations applied to the frequency magnitude spectrum of the subjects' DTF filters. Specifically, as discussed below, there were two control conditions (A and B), a ver-

idical interaural (VI) condition, and a veridical right (VR) condition. For each condition in which the DTF magnitude spectra were modified, minimum-phase filter approximations were used to generate new FIR filters. When using the minimum-phase filters, the relative phase delay (ITD) between the original left and right filters was analytically determined by filtering a low-pass (4-kHz cutoff) noise stimulus with the filters and then calculating the delay corresponding to the peak of the cross correlation between the signals. This relative phase delay was then modeled by applying an appropriate all-pass delay to the minimum-phase filters. Kulkarni *et al.* (1999) have recently observed that there can be an intrinsic phase delay between the filters for the left and right ears that should be taken into account when creating the all-pass delay. This phase correction was not applied in this work when generating the all-pass delay. However, we empirically demonstrate control-level localization performance (control B sound condition, see below) for the minimum-phase DTF filters, so the intrinsic phase delay errors are presumably small.

The noise stimuli consisted of Gaussian noise (300 to 14 000 Hz, 150-ms duration with 10-ms raised-cosine onset and offset ramps) that was regenerated for each localization trial. In the control A sound condition, the virtual noise stimuli were digitally filtered with the subjects' original DTF filters for the left and right ear. In the control B sound condition, the virtual noise stimuli were filtered using a minimum-phase approximation of the subject's DTF filters with an all-pass delay applied to model the ITD as described above. In the two test sound conditions, the magnitude of the frequency spectrum of the DTF filter for the left ear was made spectrally flat between 300 and 14 000 Hz for all target locations. This resulted in sound stimuli with a flat frequency spectrum being presented to the left eardrum regardless of the direction of the virtual source. The sound-pressure level of the noise stimuli at the left ear was then adjusted so that averaged across frequency it was equal to that of the corresponding control stimulus for that ear and location [Fig. 1(a)]. After setting the filter for the left ear, the magnitude of the frequency spectrum of the right ear's filter was determined. In the VI sound condition, an effort was made to preserve the interaural spectral difference (ISD) cue by spectrally shaping the filter for the right ear. In the VR sound condition, the original and spectrally correct right-ear DTF filter was used, resulting in an incorrect ISD cue.

In order to clarify the description of the sound conditions, the spectra of example sound stimuli for the location (−40°,0°) are shown in Fig. 1. Consider first the left monaural spectra. The spectrum for the control sound stimulus shows a broad peak around 5 kHz, a notch around 8 kHz (indicated by an arrow), and another broad peak between 12 and 14 kHz. In contrast, the magnitude spectrum of the left sound stimulus for both the VI and VR sound conditions has been flattened and is at roughly the same level across frequency. The levels of the spectra for the VI and VR sound stimuli have been set at the linear average level across frequency corresponding to the control sound stimulus. Note that this results in varying level changes across frequency, so that, for example, at 5 kHz the test sound stimuli are roughly

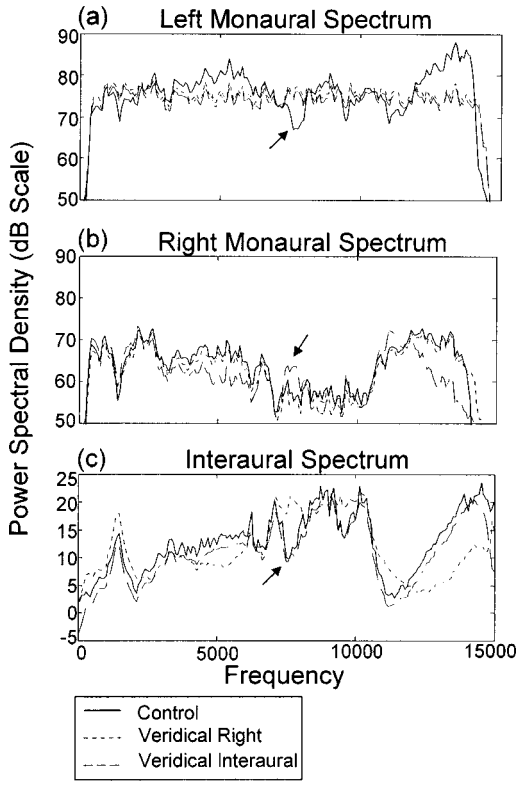

FIG. 1. Spectra corresponding to the three sound conditions for the location (−40°,0°) are contrasted in each plot. The plots show in top-down order: the spectra corresponding to the left ear, the right ear, and the interaural difference spectra.

6 dB *lower* than the control stimulus, while at 7 kHz they are approximately 8 dB *higher*. Consider next the right monaural spectra. In this case, the control sound stimulus and the VR sound stimulus have a similar spectral shape. The spectrum of the VI sound stimulus, on the other hand, has level changes across frequency that correspond to the *opposite or negative* of the level changes in the left ear. These level changes preserve the interaural spectral differences. This is shown in Fig. 1(c), where the shape of the interaural spectra for the control and VI conditions are well matched. For example, the interaural spectral notch at 7 kHz (indicated by the arrow) is preserved for the VI sound condition, but removed for the VR sound condition.

The crux of the method for this experiment, then, was how to shape the frequency spectrum of the right ear's DTF filter in order to preserve the ISD cue for a specified target location *despite* the flat sound spectrum present at the left eardrum. To accomplish this task, we made the simplifying approximation (justified below) that a sound's cochlear excitation pattern can be estimated by a smoothed version of the logarithm of the magnitude of the sound's frequency spectrum. The logarithm was applied to approximate the cochlear compression of the signal, and a moving average was applied to improve the spectral inversion process, which involves dividing one spectrum by another. With this approximation, the ISD excitation pattern was calculated as the difference between the smoothed magnitudes of the left and right sound spectrums on a logarithmic (or decibel) scale. If the ISD

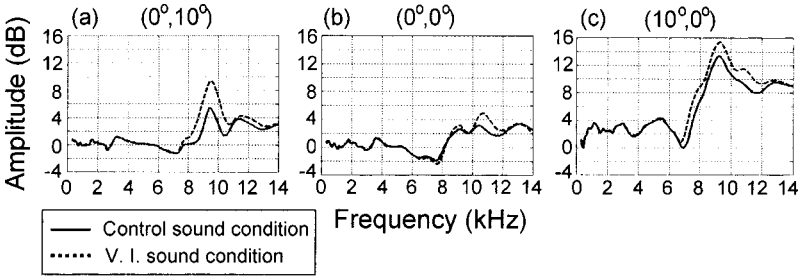

FIG. 2. The ISD excitation pattern for the VI sound condition is compared with that for the control sound condition at three neighboring locations (in degrees of azimuth and elevation): (a) (0°,10°); (b) (0°,0°); (c) (10°,0°). Although there is a consistent difference of a few dB at the high frequencies between the control and VI sound condition, the change at the high frequencies between neighboring positions on the sphere is much greater.

excitation pattern is defined as the left excitation pattern minus the right excitation pattern, e.g.,

$$\mathrm{ISD}_{\mathrm{e.p.}} = \mathrm{Left}_{\mathrm{e.p.}} - \mathrm{Right}_{\mathrm{e.p.}},$$

then the sound excitation pattern required at the right eardrum is simply the left excitation pattern minus the ISD excitation pattern

$$\mathrm{Right}_{\mathrm{e.p.}} = \mathrm{Left}_{\mathrm{e.p.}} - \mathrm{ISD}_{\mathrm{e.p.}}.$$

A detailed list of the methodological steps used to generate the stimuli for the VI sound condition is given in Appendix A.

The validity of the sound stimuli derived using the above spectral manipulations was checked using the Glasberg and Moore cochlear excitation pattern model (see Appendix B for a description of the model). After the sound stimuli for the VI condition were generated for a particular target direction, its ISD excitation pattern was calculated using the Glasberg and Moore model. If the approximations made above were reasonable, then this ISD excitation pattern should be similar to the ISD excitation pattern calculated for the control sound condition for a source at the same location. A graphical comparison of the differences between the ISD excitation patterns for the control sound condition and the VI sound condition is shown in Fig. 2. The graphs show that although the approximations made were not perfect, the ISD excitation patterns were very similar given the amount of spectral variation associated with adjacent spatial locations. That is to say, the spectral variation between the ISD excitation patterns for the control and VI sound conditions was much less than the spectral variation between the ISD excitation patterns for adjacent locations. It is also evident that larger errors were made at the higher frequencies. In order to quantify these results, the mean-square difference across frequency between the corresponding ISD excitation patterns of the VI sound condition and the control sound condition was calculated (i.e., the error in the VI excitation patterns was calculated for each frequency, squared, and then averaged across frequency). A similar analysis was also applied to the spectral difference between the ISD excitation patterns for neighboring spatial locations separated by 10° of spherical angle in the control sound condition. The mean-square errors described above were calculated and averaged over the full database of DTF filters. It was found that the spectral difference errors associated with the VI sound condition were approximately 60 percent smaller than the spectral difference associated with the ISD excitation patterns of neighboring locations separated by 10° of spherical angle. This suggests that the approximations used to generate the sound stimuli for the VI sound condition were reasonable, at least for the task in question.

D. Testing procedure

For each sound condition, the four subjects performed five repeat localization tests at each of 76 test locations evenly distributed around the sphere within ±40° of elevation. The same 76 test locations were used for each sound condition. In order to ensure that the listeners were not biased by an unbalanced attraction of localization responses to a particular region of space, the sound stimuli for the two test conditions (VI and VR) were randomly interleaved with the control sound stimuli, from the control A sound condition (see Sec. II C). The randomization was performed such that the three stimulus types were evenly balanced across three sound lists. Each sound list contained 76 interleaved sounds that were identified with a random sequence of the 76 test locations. A different random sequence of locations was used for every trial, with the constraint imposed that across the three sound lists each stimulus type would be presented from each of the 76 test locations once. Because the sequence of locations was randomized for every trial, it would be virtually impossible for a listener to anticipate the location of a sound source. The localization tests for the control B sound condition were performed separately in five repeat localization trials containing a random sequence of the 76 test locations.

As this experiment involved stimuli that were not natural, it should be made clear that none of the subjects reported a break in their perceptual spatialization of the sound stimuli. Subjects did at times report ''spatial broadness and blurring,'' but none of the subjects observed multiple images or ''in-the-head'' listening or lateralization of the sound stimuli. The subjects were instructed to point their nose in the direction of the sound source, with no explicit instructions given regarding spatially broad sound images. Also, when performance on early control blocks was compared with later control blocks, no learning effects were observed in these subjects.

III. GRAPHICAL PRESENTATION OF LOCALIZATION DATA

Scatter plots have been used to display the localization data for the test sound conditions because there were many large localization errors and these plots render a relatively ''clean'' picture of the data. In addition, spherical and circular statistics provided a convenient means for analyzing the sound localization data visually as well as numerically. Be-

cause a complete description of these graphical methods is rather lengthy, a detailed presentation has been reserved for Appendix C and only a brief presentation is provided here. With respect to describing the statistics and the localization data, it is important to note that we use the lateral–polar angle coordinate system, where the lateral angle indicates the angle of incidence with respect to the midsagittal plane and the polar angle indicates the angle around the interaural axis. The method of spherical statistics is well suited to the task of describing the global distribution of the localization responses for all spatial directions about the subject. The spherical correlation coefficient, mean spherical angle error, and front–back error rates were statistical quantities used to describe the data. Circular statistics, in contrast to spherical statistics, is well suited to describing the distribution of the polar angle component of the localization responses. In this context, the correspondence between the response and target polar angles was analyzed visually using plots that are referred to here as circular hair plots. The utility of these plots over scatter plots is that the clustering of polar angle responses to one direction, as might be expected because a flat spectrum stimuli was continuously presented to the left ear, becomes much more readily apparent. Also, the von Mises distribution was used to model the polar angle data and a nonparametric homogeneity test know as the WWM test was used to statistically compare two different polar angle data distributions.

IV. MUTUAL INFORMATION AND THE CONE OF CONFUSION

Information theory was used to theoretically compare the amount of information contained within the monaural and interaural spectral cues. The analysis was aimed at differentiating which spectral cue provides more information for resolving directions within a cone of confusion. To this end, the average mutual information between spectral cue and location was examined for 32 different cones of confusion spaced every 5 deg in lateral angle from $-80°$ to 80°. Importantly, the mutual information was calculated based on cochlear excitation patterns corresponding to stimulus spectra and is a theoretical quantity that is later compared with observed performance data. A detailed presentation of the mutual information analysis is provided in Appendix D.

V. RESULTS

A. Psychophysical validation of the fidelity of VAS

The validity of each subject's measured acoustic transfer functions was assessed by comparing his/her free-field sound localization performance with his/her VAS localization performance in a set of validation localization trials. As with all of the localization experiments, the subjects performed 5 repeat localizations for 76 test locations. Note that the validation localization data are separate and in addition to the control localization data obtained in the main experiment. Localization performance for all subjects was evaluated both visually and statistically using the methods of spherical statistics (Appendix C 2). The localization data indicated that accurate localization performance was obtained in VAS as well as in the free field (see Table I). Although there was a definite increase in the percentage of front–back errors for Subjects A and D in the VAS as compared to the free-field condition, this increase is small compared to the increase obtained in the test conditions of the main experiment. In addition, an increase in front–back errors is a common occurrence with most VAS presentations (see Carlile *et al.*, 1997). Since conclusions are only drawn from comparisons between test and control conditions, the statistical data for the validation localization trials indicate that the DTF filters properly rendered the acoustic filtering of the subjects' external auditory periphery.

TABLE I. A comparison of free-field and VAS localization performance.

		Spherical correlation coefficient	Mean spherical angle error	Percentage front–backs
Subject A	Free-field	0.92	11	0.2
	VAS	0.88	13	5.3
Subject B	Free-field	0.90	13	2.0
	VAS	0.92	12	1.8
Subject C	Free-field	0.93	10	1.3
	VAS	0.91	13	2.4
Subject D	Free-field	0.91	13	1.8
	VAS	0.89	13	6.0

B. Control localization performance

The subjects' localization performance in the two control sound conditions was measured and compared with their corresponding localization in the VAS validation trials. The purpose of the comparisons was to check that the performance effects of interleaving the sounds (control A) and using a minimum-phase filter approximation (control B) were relatively small compared with the performance effects seen across the two test sound conditions. A statistical summary of the localization performance results for both control sound conditions is given in Table II. In the control A sound condition the mean spherical correlation coefficient across all subjects was 0.90, which was indicative of accurate localization performance similar to that obtained in the VAS validation trials. In the control B sound condition, the subjects also demonstrated accurate localization performance, with a mean spherical correlation coefficient across all subjects of 0.89 and the lowest spherical correlation coefficient being 0.85. The average spherical angle error for each subject in both of

TABLE II. Summary localization statistics for the two control conditions.

		Spherical correlation coefficient	Mean spherical angle error	Percentage front–backs
Subject A	Control A	0.91	12	0.7
	Control B	0.85	14	1.6
Subject B	Control A	0.89	13	2.3
	Control B	0.92	11	0.5
Subject C	Control A	0.88	17	5.3
	Control B	0.89	16	4.2
Subject D	Control A	0.90	13	1.3
	Control B	0.88	15	10

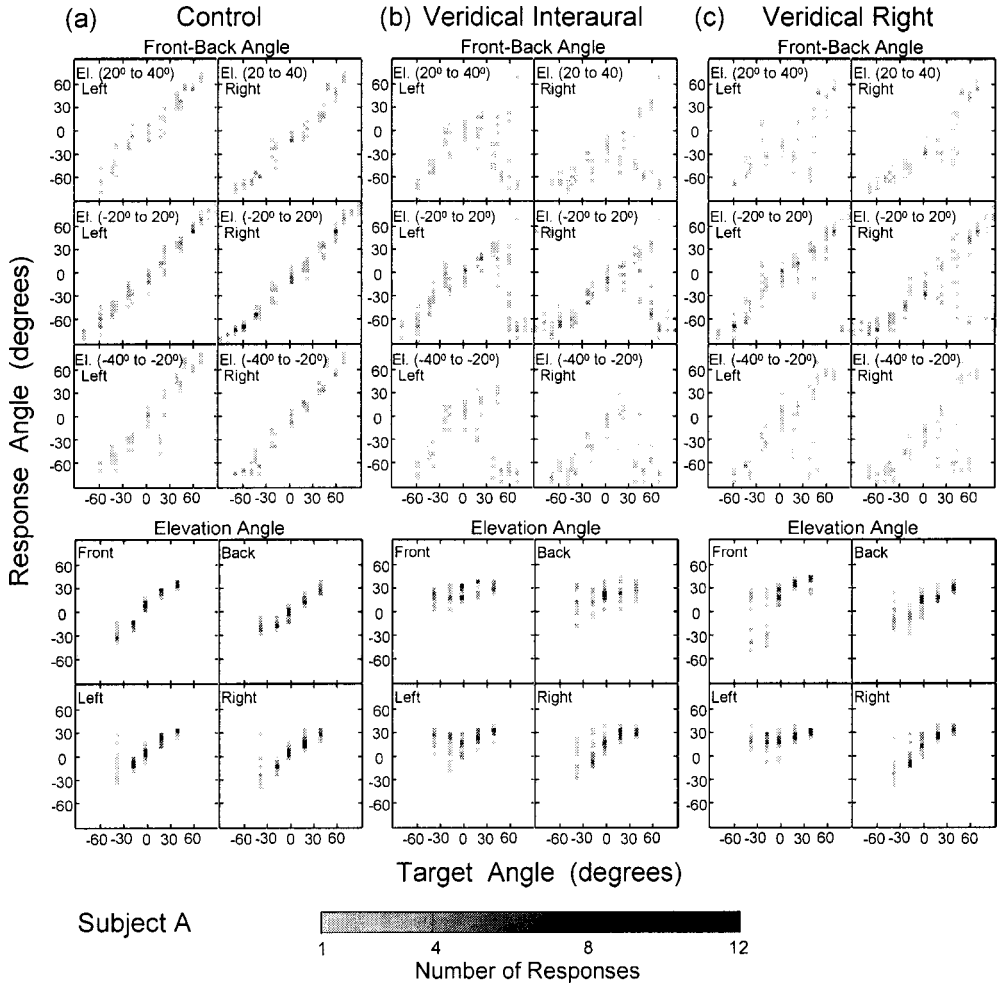

FIG. 3. A scatter plot of the front–back angles and the elevation angles associated with the localization performance data of Subject A are shown for the three sound conditions: (a) control; (b) veridical interaural; and (c) veridical right. The target angle is indicated by the horizontal axis and the response angle is indicated by the vertical axis. The number of responses falling in each 5 by 5-deg square in the plane was indicated by a gray-scale color value, with the darker colors indicating a greater number of responses. The data have been divided into groups based on spatial regions to make it more accessible. See the text for further details.

the control sound conditions was approximately 15° and the rate of front–back confusions was less than 6 percent, except for Subject D in the control B sound condition, for whom the rate of front–back errors was 10 percent. Visual inspection of the localization data (see Figs. 3–6) for each subject also indicated accurate localization performance. Finally, it should be noted that the variations described here are *much* smaller than those seen in the two test sound conditions (described in Sec. V C below).

C. Localization performance in the two test sound conditions

All subjects demonstrated a substantial degradation in their localization performance for the veridical interaural (VI) and veridical right (VR) test sound conditions, as compared to the control sound condition. In order to provide a suitable reference with which to compare the localization results in the two test sound conditions, the data for all subjects in the control B sound condition are shown along side the localization data for the test sound conditions in Figs. 3–6, which show scatter plots (see Appendix C 1) of the front–back angle and the elevation angle. The control B sound condition is used as *the* control sound condition. In the scatter plots, the target angle is indicated by the horizontal axis and the response angle is indicated by the vertical axis. The plane spanning the target and response angles was divided into square sections with a side length of 5 deg. The number of responses in each square was indicated by a gray-scale color value, with the darker colors indicating a greater number of responses.

The localization data for the VI and VR sound conditions clearly indicate that the subjects' localization performance was disrupted by the flat monaural sound spectrum presented to the left eardrum *despite* the preserved interaural sound spectrum or preserved right monaural sound spectrum. The data show an increase in front–back confusions, elevation errors, and an increased mean spherical angle error as compared to the control localization data (compare Tables III and II). Nonetheless, the data do not show a complete absence of spatial discrimination in the left hemisphere of space (as would be expected for monaural VAS sound localization by naturally binaural listeners, e.g., see Wightman and Kistler, 1997). A distinguishing characteristic of the localization data is that the probability of responses to the front

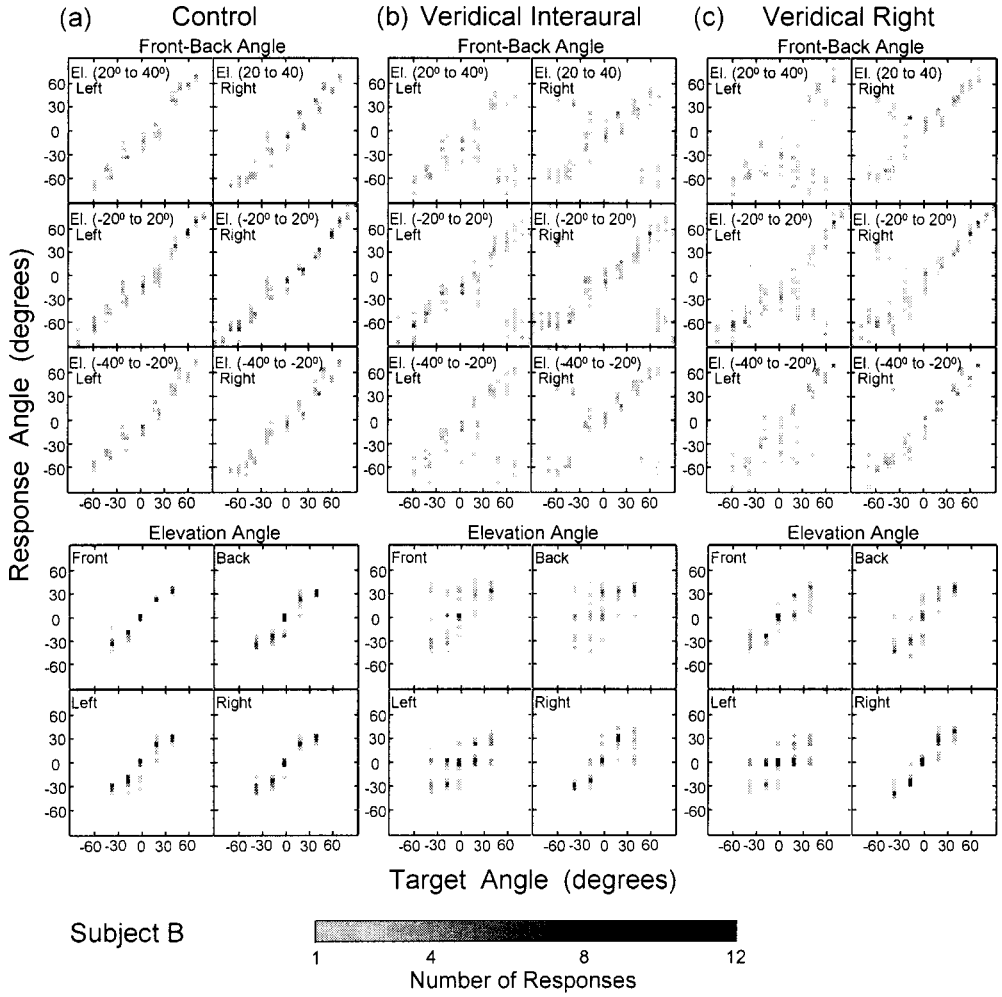

FIG. 4. A scatter plot of the front–back angles and the elevation angles associated with the localization performance data of Subject B are shown for the three sound conditions: (a) control; (b) veridical interaural; and (c) veridical right. See the text for further details.

hemisphere is somewhat reduced in the VI sound condition compared to the VR sound condition (see Table III and Figs. 3–6). Because of the bilateral symmetry of the human external auditory periphery, a flat sound spectrum at the left eardrum in the VI sound condition entails a relatively flat sound spectrum at the right eardrum for target directions on and close to the midsagittal plane. For the VR sound condition, on the other hand, the sharp spectral features associated with the acoustic filtering of the external auditory periphery in the front hemisphere of space were preserved in the sound spectrum at the right eardrum. Therefore, the reduced number of localization responses to the front hemisphere of space in the VI sound condition, as compared with the VR sound condition, suggests that the monaural spectral features may be playing an important role in human auditory localization with respect to the accurate localization of sounds to the front hemisphere of space.

It is clear that the flat sound spectra that were present at the left eardrum for all test stimuli disrupted auditory localization performance and that the cue information in the VI and VR conditions was unable to support control level localization. This raises the issue of whether the flat sound spectrum at the left ear was causing localization responses to be clustered toward a specific region of space. This question, which cannot be answered easily from the scatter plots, is the focus of the next section.

D. Analysis of the lateral and polar angles

In order to better characterize the subjects' mislocalizations and the possible clustering of responses as a result of the flat sound spectra presented to the left eardrum in the two test sound conditions, the localization data were analyzed in terms of the lateral–polar angle coordinate system. The analyses indicate that the mislocalizations largely preserved the lateral angle component of the target direction, but not the polar angle component. In other words, the subjects' ability to resolve the virtual source direction within the cone of confusion was disrupted.

1. Lateral angle analysis

There is a strong correlation between the lateral angle of the response direction and the lateral angle of the target direction. This correlation is an important feature of the localization performance data that was constant across all of the subjects and all of the sound conditions. The average magnitude of the lateral angle error across all of the performance data was approximately 10°, with a standard deviation of about 10°. The lateral angle data were analyzed visually us-

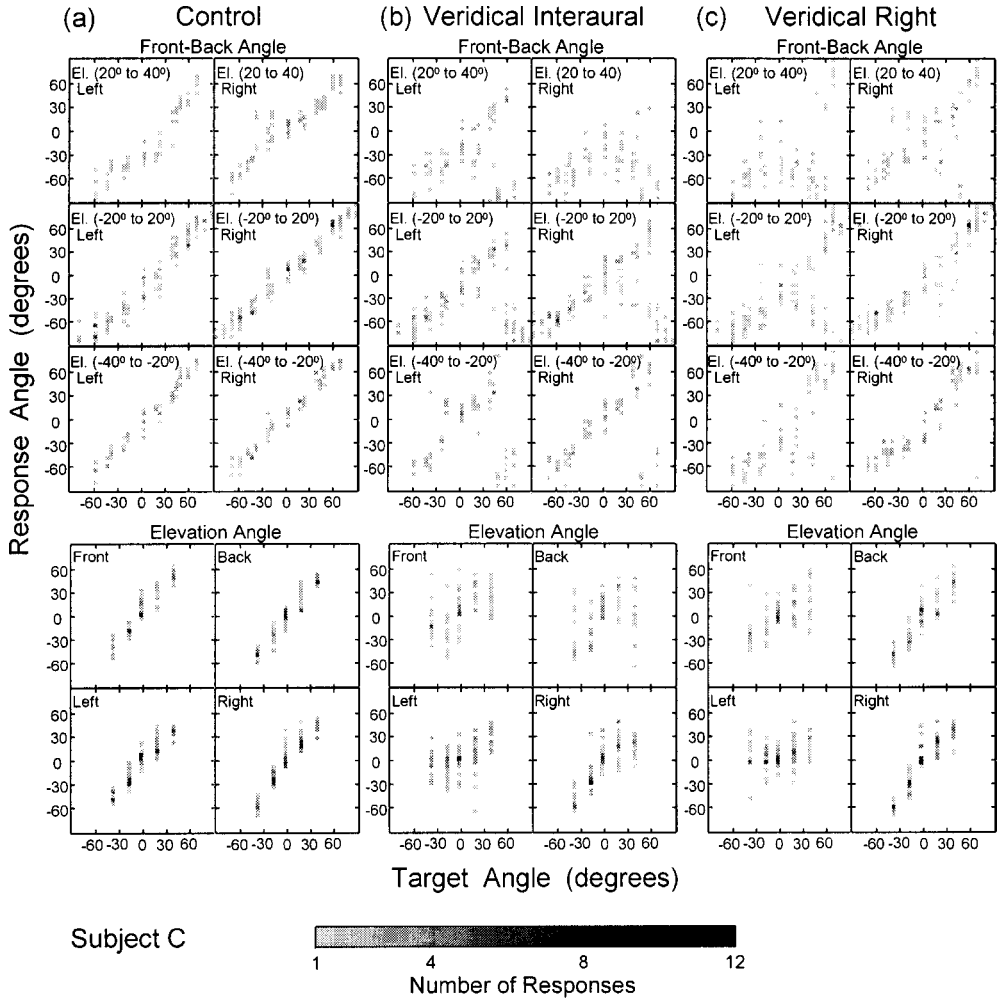

FIG. 5. A scatter plot of the front–back angles and the elevation angles associated with the localization performance data of Subject C are shown for the three sound conditions: (a) control; (b) veridical interaural; and (c) veridical right. See the text for further details.

ing a scatter plot for each subject and each sound condition. As the data were visually similar across all of the subjects, the data were pooled across all of the subjects (shown in Fig. 7). The lateral angle data were modeled using linear regression. In all three sound conditions, the lateral angle of the target location is a good predictor of the lateral angle of the response location.[2] Despite the ''unnatural'' and modified sound spectra, the interaural time and level difference cues preserved accurate perception of the target direction's lateral angle.

2. Polar angle analysis

The accuracy of the subjects' response directions within the cone of confusion was analyzed by collapsing the localization data across lateral angles and examining the polar angle component of the subjects' response directions. The polar angle data for the control B sound condition is shown in Fig. 8 using a separate circular hair plot (see Sec. III and Appendix C 3) for locations in the left hemisphere (azimuthal angles: $-140°$ to $-40°$), in the right hemisphere (azimuthal angles: 40° to 140°), and in the front and back hemispheres near the midline (azimuthal angles: $-50°$ to 50°, 130° to 180°, and $-130°$ to $-180°$). For each circular hair plot, a circle was drawn representing the cone of confusion. The target polar angles were then indicated by the location of small dots on the circle. For a given target direction, the response polar angle was indicated by a short line segment that was connected to the small dot and drawn such that it pointed in the direction of the response polar angle. So, for example, front–back errors correspond to a dot on the circle connected to a horizontal line, and up–down errors correspond to a dot on the circle connected to a vertical line. For the control B sound condition, the hair lines were approximately tangent to the circle, indicating quite accurate localization performance. For each circular hair plot, a von Mises distribution was fit to all of the response polar angle data within the plot, and the concentration parameter, κ, of the fit is shown underneath the plot. The concentration parameter, κ, is a metric of the degree of clustering of the responses within the plot. In the case that $\kappa > 0.65$, an arrow is drawn on the plot to indicate the mean circular direction across all of the response polar angle directions.

The polar angle data distributions for the VI and VR sound conditions are shown in Figs. 9 and 10, respectively. Comparisons of these two figures show that for the two test sound conditions, the circular hair plots corresponding to the same subject and the same hemisphere of space are remarkably similar. That is to say, the circular hair plots show a

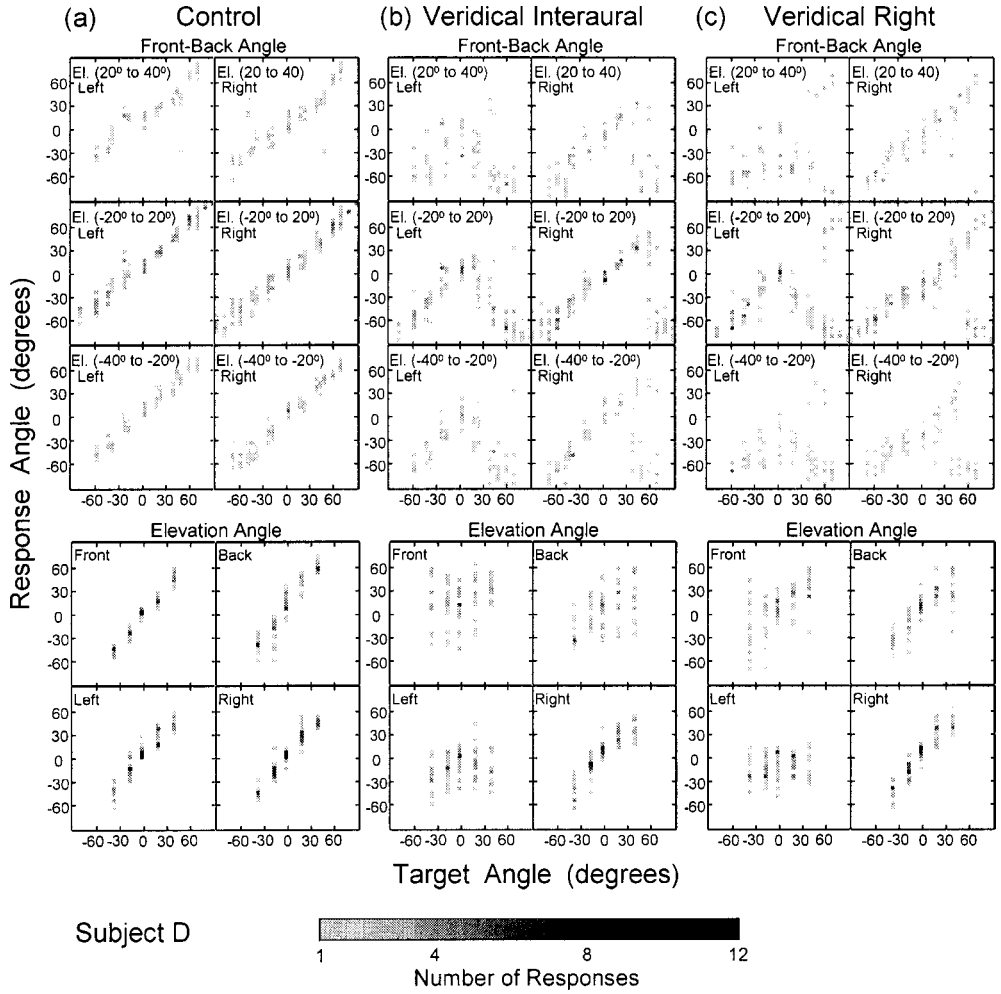

FIG. 6. A scatter plot of the front–back angles and the elevation angles associated with the localization performance data of Subject D are shown for the three sound conditions: (a) control; (b) veridical interaural; and (c) veridical right. See the text for further details.

clustering of response directions in the left hemisphere of space, numerous front–back errors, and a mild clustering of response directions in the right hemisphere of space. The most salient characteristic of these data is the tendency for many responses to sources in the left hemisphere of space to cluster to a polar angle that was relatively constant for each subject, but that varied across subjects. This observation indicates that it is likely that the subjects' response directions in the left hemisphere of space were partially driven by the flat sound spectrum that was presented to the left eardrum, despite the fact that the interaural spectral cue was preserved in the VI sound condition and the right monaural spectral cue was preserved in the VR sound condition. In addition, the clustering of the response directions in the left hemisphere of space, as indicated by κ, was greater for all subjects in the VR sound condition compared to the VI sound condition. The significance of the increased clustering of response directions in the VR condition compared to the VI condition was statistically tested using the WMM test (see Appendix C 3) and was significant for all subjects, excepting Subject A (see Table IV). The reduced clustering of responses in the left hemisphere of space for the VI sound condition compared to the VR sound condition is consistent with a reduction in the mean value of the magnitude of the polar angle error as shown in Table V.

TABLE III. Summary localization statistics for the two test conditions. VI and VR refer to veridical interaural and veridical right, respectively.

		Spherical correlation coefficient	Mean spherical angle error	Percentage front–backs
Subject A	VI	0.08	50	33
	VR	0.34	35	21
Subject B	VI	0.35	34	18
	VR	0.64	24	13
Subject C	VI	0.26	33	24
	VR	0.45	33	18
Subject D	VI	0.09	46	30
	VR	0.20	42	29

A difference between the VI sound condition and the VR sound condition is also seen for the response directions near the median plane. In this region of space, the clustering of the responses directions, as indicated by κ, was greater for all subjects in the VI sound condition compared to the VR sound condition. The significance of the increased clustering of response directions in the VI condition compared to the VR condition was statistically tested using the WMM test and was significant for all subjects, excepting Subject D (see

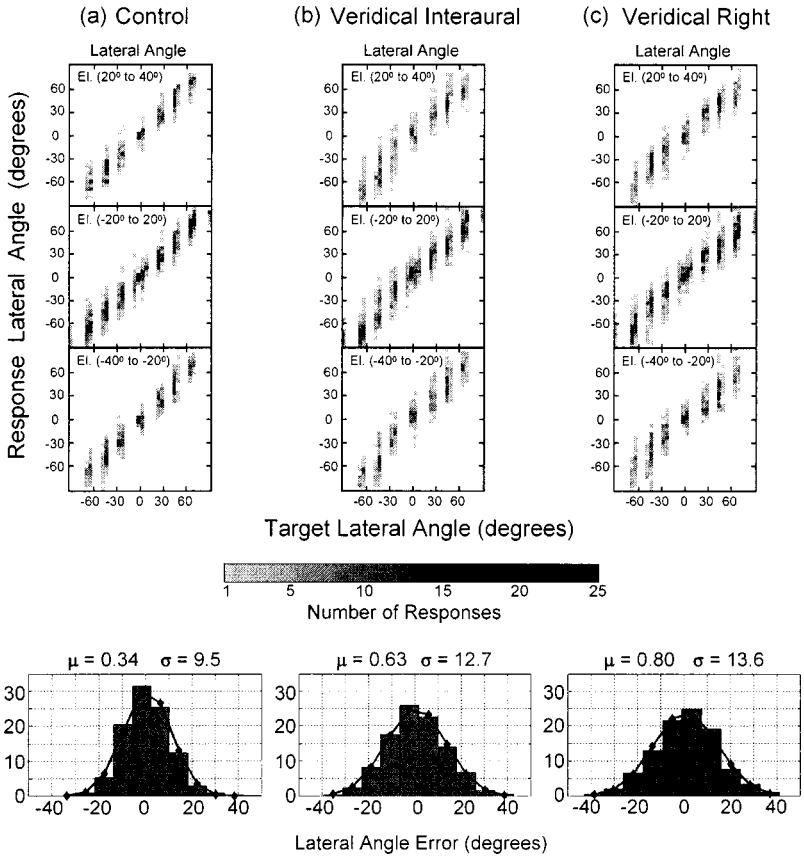

FIG. 7. The lateral angle component of the localization performance data was pooled across all subjects and is shown using a scatter plot for the three sound conditions: (a) control; (b) veridical interaural; and (c) veridical right. The lateral angle error was Gaussian distributed and the distribution for each sound condition is shown below the scatter plots (μ is the mean and σ is the standard deviation.) See Fig. 3 for further details concerning the scatter plots.

Table IV). The reduced clustering of responses in the median plane region of space for the VR condition compared to the VI condition is consistent with a reduction in the mean value of the magnitude of the polar angle error as shown in Table V.

With regard to the polar angle data distributions in the right hemisphere of space, there were no statistically significant differences between the two sound conditions for all subjects, excepting Subject D (see Table IV). In addition, there is no consistent trend across subjects in the mean value of the magnitude of the polar angle error for the right hemisphere of space (see Table V).

Relative to previous experiments, the polar angle data shown here have been collected across a wide range of directions in space and demonstrate that neither the veridical interaural spectrum nor the veridical right monaural spectrum preserves control levels of localization performance in the face of conflicting monaural spectral cues. Circular statistics indicate that the differences between the VI and VR condition are not significant for 3 of the 4 subjects for the right hemisphere of space, but are significant for 3 of the 4 subjects for the left hemisphere of space and also for the region of space near the median plane. For the left hemisphere of space, the localization responses are slightly less clustered and more accurate for the VI condition compared to the VR condition. The opposite is true for the median plane region of space, where the localization responses are slightly less clustered and more accurate for the VR condition compared to the VI condition.

E. Comparison of mutual information for the spectral cues

The information available for the discrimination of locations within a cone of confusion can be analyzed quantitatively using mutual information as discussed in Sec. IV (see Appendix D for details). More precisely, the mutual information between spectral cue and location provides a quantitative measure of the degree of spatial discrimination conferred by the spectral cue. The mutual information varies depending on the spectral cue and the cone of confusion as shown in Fig. 11. In Fig. 11, the mutual information associated with the left, right, and interaural spectral cues is shown for 32 different cones of confusion varying in lateral angle by 5° between −80° and 80° for all 4 subjects who participated in the localization experiments. What is shown is that depending upon the lateral angle, different spectral cues provide more or less information and are therefore more or less reliable. For example, for all 4 subjects the monaural spectra provide more information than the interaural spectra (with respect to resolving locations within a cone of confusion) for lateral angles within 20° of the median plane. As one moves more laterally toward one side or the other, the information provided by the interaural spectral cue increases and can, in some cases, even exceed the information provided by the monaural spectral cues. The fact that the mutual information between the ISD cue and locations within the cone of confusion is smaller for the midsagittal plane (i.e., 0° lateral angle) than for any other lateral angle is a reasonable finding in view of the fact that if one assumes that the subject has a bilaterally symmetric body (mainly, head and ears), then the

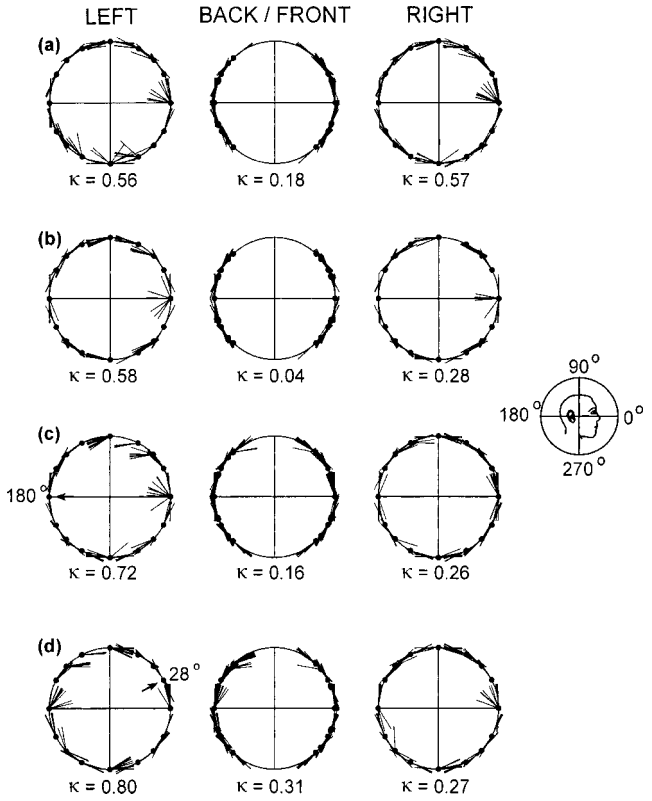

FIG. 8. The polar angle component of the localization performance data is shown for all subjects in the control sound condition using circular hair plots. The four subjects (Subjects A–D) are identified by the letters of the alphabet (a)–(d), respectively. Each row corresponds to one subject. Each column shows polar angle data that have been collapsed across a region of space, as indicated by the column headings, based on the target direction of the sound source. The target polar angle is indicated by the angular position of a solid black dot on the perimeter of the circle. The response polar angle matching that target angle is indicated by a short line segment that is connected to the black dot and points in the direction of the response polar angle. Thus, the response polar angle can be determined by extending the short line segment until it intersects the circle. The angular position of the point of intersection along on the circle gives the response polar angle. The orientation of the circle with respect to the listener is the same in all cases and is indicated by a compass outline in the right margin of the figure. See the text for further details.

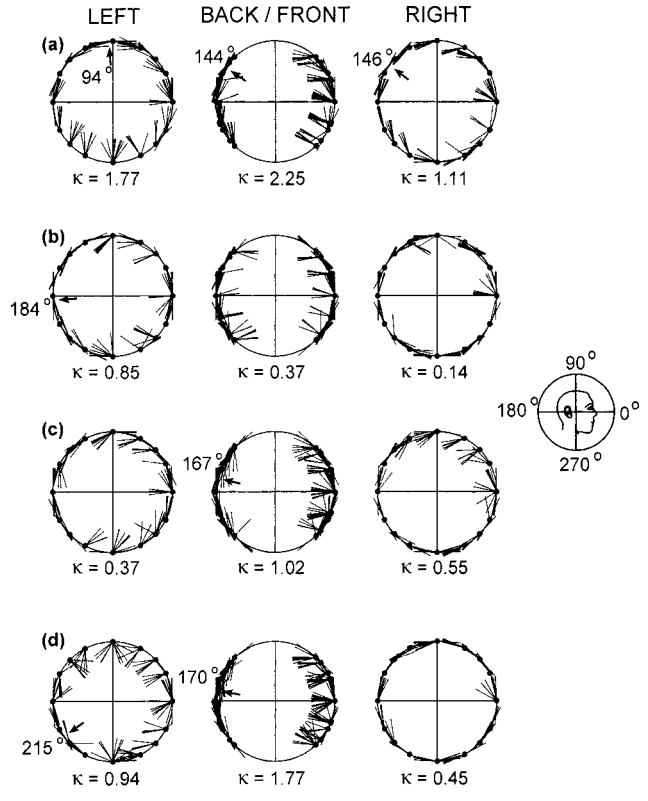

FIG. 9. The polar angle component of the localization performance data for the VI sound condition is shown for all subjects using circular hair plots. See Fig. 8 for further details describing the circular hair plots.

ISD cue would not vary at all along the midsagittal plane. However, people are not perfectly bilaterally symmetric and Duda (1997) has shown that estimates of sound elevation can be extracted computationally from the ISD cue even along the midsagittal plane (see also Carlile and Pralong, 1994). Figure 11 also shows that for all subjects the near ear generally carries more information than the far ear, although substantial intersubject variations exist.

VI. DISCUSSION

The psychoacoustic experiment presented here investigates the ability of the auditory localization system to use the ISD cue (i.e., the pattern of interaural intensity differences across frequency) and monaural spectral cues to resolve directions within a cone of confusion. In other words, we have focused on the accuracy of polar angle localization as opposed to azimuth angle localization. Compared to many of the very early experiments, the target locations are not restricted to the midsagittal plane or the frontal hemisphere of

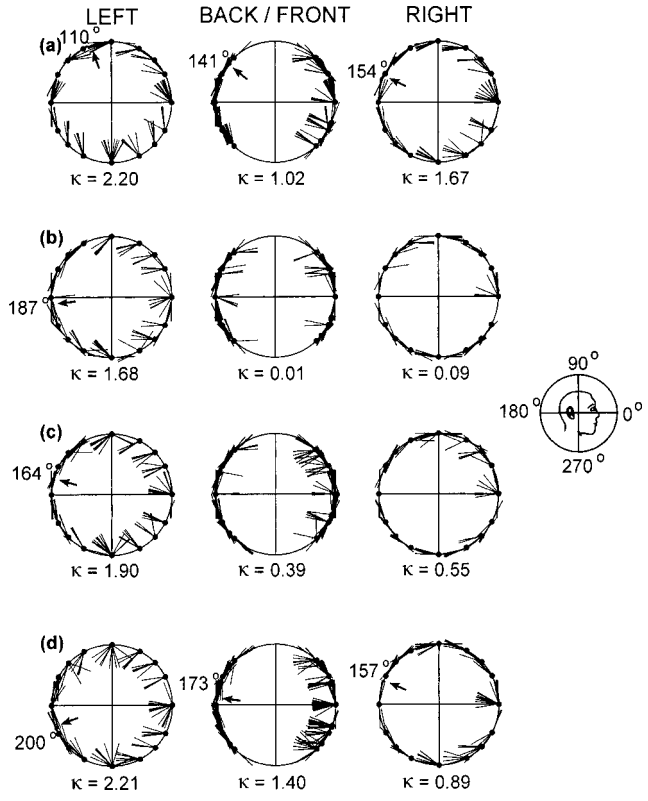

FIG. 10. The polar angle component of the localization performance data for the VR sound condition is shown for all subjects using circular hair plots. See Fig. 8 for further details describing the circular hair plots.

TABLE IV. Comparison of the localization performance between the VI and VR sound conditions in the left and right hemispheres of space and also in the region of space near the median plane.

	Left hemisphere VI and VR			Right hemisphere VI and VR			Median plane region VI and VR		
	W	df	P	W	df	P	W	df	P
Subject A	3.18	2	0.20	2.1	2	0.36	37.3	2	<0.001
Subject B	21.4	2	<0.001	0.2	2	0.90	17.8	2	<0.001
Subject C	33.8	2	<0.001	0.72	2	0.70	16.0	2	<0.001
Subject D	26.3	2	<0.001	8.9	2	0.01	1.7	2	0.43

TABLE V. Comparison of the mean value of the magnitude of the polar angle error, in degrees, between the VI and VR sound conditions in the left and right hemispheres of space and also in the region of space near the median plane.

	Left hemisphere		Right hemisphere		Median plane region	
	VI	VR	VI	VR	VI	VR
Subject A	63	66	42	51	77	43
Subject B	47	65	21	15	48	23
Subject C	53	79	35	30	57	37
Subject D	80	89	21	33	74	61

space (as in, e.g., Butler, 1969a,b; Fisher and Freedman, 1968; Gardner, 1973; Hebrank and Wright, 1974; Searle *et al.*, 1975) and conclusions are not drawn from comparisons between monaural and binaural listening conditions (as in, e.g., Butler, 1969a,b; Fisher and Freedman, 1968). In addition, this experiment preserves the natural overall ITD cue and overall ILD cue, while investigating the ISD cue and the monaural spectral cues, similar to several recent experiments, e.g., Searle *et al.* (1975), Humanski and Butler (1988), Hofman and Opstal (2003), Morimoto (2001). Unlike the previous experiments, however, this experiment includes a sound condition in which the veridical ISD cue is presented in the presence of conflicting monaural spectral cues. The experimental data (VI condition) presented here indicate that preservation of the ISD cue does not lead to accurate localization in the face of conflicting monaural spectral cues. In other words, the ISD cue is not such a powerful cue that it can overcome the conflicting monaural spectral information. In addition, the data (VR condition) also indicate that in the absence of a veridical ISD cue, veridical spectral information within only one ear does not lead to accurate localization, especially within the contralateral hemisphere of space.

Early on, it was argued (e.g., Butler, 1969a,b; Fisher and Freedman, 1968) that because the binaural listening condition improved auditory localization performance as compared with monaural listening, the ISD cue was playing an important role. Our results indicate, however, that the ISD cue is not so important as to overcome conflicting monaural spectral information. For example, the flat spectrum presented to the left eardrum led to substantial clustering of the localization data in the left hemisphere of space in the VI condition (Fig. 9). In the early experiments mentioned above, the monaural listening conditions in naturally binaural listeners present an unnatural ILD and ITD cue. Therefore, it is unclear as to whether the binaural localization performance was improved by the presence of an ISD cue or alternatively that the monaural localization performance was hindered by an unnatural ITD and ILD cue. Furthermore, more recent sound localization experiments in virtual auditory space show that naturally binaural listeners *cannot* localize sounds monaurally[3] (Wightman and Kistler, 1997). Wightman and Kistler (1997) have suggested that the ''plug and mufl'' methods of past free-field monaural experiments did not provide adequate attenuation and that sound localization at low intensity levels is difficult to evaluate.

A number of recent studies examine the role of spectral cues in human sound localization (e.g., Hofman and Opstal, 2003; Humanski and Butler, 1988; Kulkarni and Colburn, 1998; Langendijk and Bronkhorst, 2002; Morimoto, 2001; Searle *et al.*, 1976; Shinn-Cunningham *et al.*, 2000). Of these, we focus on those which have the most direct relevance to the data presented here. Searle *et al.* (1976) developed a signal detection localization model based on the localization data from 42 published experiments between 1969 and 1976. They conclude that the ''results suggest the existence of an interaural pinna cue which is stronger than the individual monaural pinna cue.'' Their model uses the lateral–polar angle coordinate system and calculates the weighted sum of four different localization cues in order to predict a source position. These four cues consist of: (1) a single lateral angle cue that combines the three cues of interaural time delay, interaural head shadow, and monaural head shadow; (2) an interaural pinna cue; (3) a monaural pinna

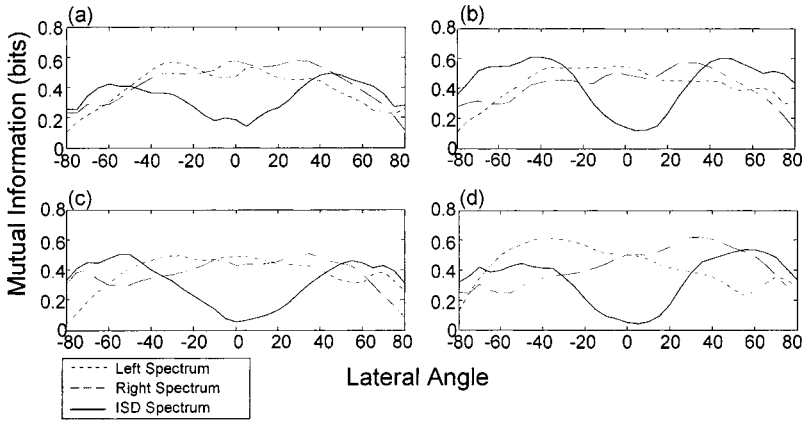

FIG. 11. The average mutual information for the left and right monaural spectral cue and the interaural spectral cue is shown for Subjects A–D (a–d, respectively).

cue; and (4) a shoulder-bounce cue. The weights for these cues are the reciprocal of their estimated variance (in degrees squared) which were determined from the average angle errors given in the localization data. Searle *et al.* (1976) point out, however, that the cumulative localization data were insufficient to reliably separate the polar angle variance from the lateral angle variance. Therefore, they determined only a single weight for the monaural (weight 0.0017) versus interaural pinna cues (weight 0.0045). Based on the data presented here, we suggest that the lateral angle variations contribute principally to the results obtained by Searle *et al.* (1976) and that a veridical ISD cue cannot overcome conflicting monaural spectra with respect to resolving directions within the cone of confusion.

Experimental results comparing the relative importance of the near and far ear to the perception of the vertical or elevation angle have been described by Humanski and Butler (1988), Morimoto (2001), and Hofman and Opstal (2003). In these studies, the ISD cue is not directly compared with the monaural spectral cues, but rather the relative significance of the monaural spectral cues obtained from the near and far ear is obtained from behavioral data obtained following manipulation of the pinna structure. In these experiments, ear molds were used to distort the spectral cues at either one or both ears. The general conclusion is that there is a smooth change in the relative importance of the near and far ear as a function of the sound's lateral angle, with the near ear playing the more important role. The data presented here are in accordance with the observation that the near ear generally seems to play an important role in resolving directions within a cone of confusion. For example, when the spectra presented to the near (left) ear were falsely flat and the spectra presented to the far (right) ear were veridical, the polar angle data for the left hemisphere were strongly clustered (Figs. 9 and 10, left column). Also, when the spectra for the near (right) ear were veridical and the spectra for the far (left) ear were falsely flat, the polar angle data for the right hemisphere were much less clustered and more accurate (Figs. 9 and 10, right column). Hofman and Opstal (2003) have suggested further that the azimuth angle is being used by the auditory system to somehow weight the relative importance of the spectral cues from the near and far ear. However, it may be that an ear mold that essentially fills the cavity of the outer ear disrupts the spectral information from the near ear more than for the far ear as a smooth function of lateral angle. In other words, the effect of the ear molds used in the above experiments is *not* independent for each lateral angle.

With regard to the relative importance of the ISD cue versus the monaural spectral cues for resolving directions within a cone of confusion, considering the information available to the auditory system is likely to be important. As a first step in this direction, Fig. 11 compares the theoretical mutual information between the spectral cues and locations within the cone of confusion as a function of lateral angle. What is shown is that within 20° of the midline, the monaural spectral cues carry more information for resolving directions within a cone of confusion than the ISD cue, but as one moves more laterally there is a substantial increase in the information associated with the ISD cue. In this context, it is interesting that the behavioral results indicate that the polar angle data for the left hemisphere of space are slightly more accurate for the VI condition compared to the VR condition, and that this result was statistically significant for 3 of 4 subjects (see Sec. V D 2). Similarly, it is interesting that for the region of space near the median plane, the behavioral results indicate that the polar angle data are slightly more accurate for the VR condition compared to the VI condition, and that this result was also statistically significant for 3 of 4 subjects (Sec. V D 2). These results indicate that with respect to localization in the left hemisphere of space, the auditory localization system seems to be extracting more information from the ISD cue than from the monaural spectral cue for the far (right) ear, and that within the region of space near the median plane, the auditory localization system seems to be extracting more information from the right monaural spectral cue than from the ISD cue. These observations are consistent with the fact that the mutual information analysis shows that, for lateral locations, the ISD cue can carry more information than the monaural spectral cue for the far ear (see Fig. 11) and that near the median plane, the monaural spectral cues carry more information than the ISD cue. The difficulty with the above interpretation is that the mutual information analysis also shows that, in some cases and for lateral locations, the ISD cue carries more information than even the monaural spectral cue for the near ear. Clearly, one would *not* want to argue that, in the left hemisphere of space, the monaural spectrum from the near ear is less significant than the ISD cue. The data certainly show that the flat spectrum at the left ear strongly influenced the response directions in the left hemisphere of space. Obviously then, our understanding is incomplete, but perhaps the resolution to this difficulty is related to the fact that the mutual information analysis does not take into account sound level or signal-to-noise ratio, and that the signal-to-noise ratio at the near ear is certainly greater than that at the far ear. In addition, the mutual information analysis does not consider variations in the spectra of the source. Given these limitations, one should not overinterpret the mutual information analysis.

An important reason for seriously considering the ISD cue as a localization cue for resolving locations within a cone of confusion is its robustness to spectral irregularities in the source spectrum (see Hebrank, 1976; Hebrank and Wright, 1974; Searle *et al.*, 1975). This should allow separation of the spectral filtering of the external auditory periphery from the source spectrum. Indeed, Searle *et al.* (1975) demonstrated that the ISD cue or ''binaural pinna disparity cue'' gives an advantage in the presence of spectral irregularities. Auditory localization performance was tested at only five restricted directions in the midsagittal plane (0°,45°,90°,135°, 180°) and localization performance in the binaural listening condition was much better than in a diotic listening condition where the spectra presented to the two ears were identical. Furthermore, when the spectrum of the sound source was scrambled by ± 5 dB in 1/3-octave bands, the binaural listening condition demonstrated even greater advantage, consistent with the idea that the ISD cue is robust to spectral irregularities. A serious criticism of the above methodology is that the diotic listening condition disrupted

the monaural spectral cue to one ear as much as it supposedly removed the ISD cue. By presenting the same sound to both ears, *both* the ISD cue and one monaural spectral cue were disrupted, and it is difficult to clearly argue that one is more important than the other. It would be interesting to repeat the VAS localization experiment presented here with spectrally scrambled stimuli as in Searle *et al.* (1975).

VII. CONCLUSIONS

The differential contribution of the monaural and interaural spectral cues have been examined from a psychoacoustical and mutual information viewpoint. Techniques of virtual auditory space were used to present a flat spectrum sound to the left eardrum. The sound spectrum at the right eardrum was then adjusted so that either the true right monaural spectrum (VR condition) or the true interaural spectrum (VI condition) was preserved, while maintaining both the overall ITD cue and overall ILD cue at their natural values. To the extent that the signal manipulations were able to preserve the auditory system's internal representation of the ISD information in the VI condition, the psychoacoustical evidence indicates that the ISD cue cannot preserve accurate localization performance in the face of conflicting monaural spectral cues. Also, in the absence of a veridical ISD cue, veridical spectral information within one ear (the right ear in the VR condition) does not lead to accurate localization. Using an information analytic approach, it was shown that the amount of spectral information available for resolving the cone of confusion varies with lateral angle. The experimental data and analytical results are consistent with the view that the auditory localization system can extract information from both the monaural spectral cues and ISD cue for resolving locations within a cone of confusion.

ACKNOWLEDGMENTS

The authors would like to thank Barbara Shinn-Cunningham, Steve Colburn, an anonymous reviewer, and the editor Leslie Bernstein for their valuable comments. This research was supported by the Dora Lush Biomedical Postgraduate Scholarship and the Australian Research Council.

APPENDIX A: GENERATING STIMULI FOR THE VI SOUND CONDITION

(1) The logarithms of the magnitude of the frequency spectrum (referred to as the log-magnitude spectrum) for the true left and true right DTF filters representing a specific target direction were calculated.
(2) A moving average spanning approximately 200 Hz was applied to the log-magnitude frequency spectra.
(3) The ISD spectrum was estimated as the left smoothed log-magnitude frequency spectrum minus the right smoothed log-magnitude frequency spectrum.
(4) A ''false'' spectrally flat log-magnitude frequency spectrum was generated for the left ear.
(5) The level of the spectrally flat log-magnitude frequency spectrum for the left ear was set equal to the mean level across frequency of the original, unsmoothed log-magnitude frequency spectrum for the left ear.
(6) The log-magnitude frequency spectrum for the right ear was then calculated as the left ear's new spectrally flat log-magnitude spectrum minus the calculated ISD spectrum.
(7) New minimum-phase FIR filters were generated from the calculated left and right log-magnitude frequency spectra.
(8) The correct relative phase delay (ITD) between the left and right filters was set by adding an all-pass delay.
(9) The sound stimulus for each ear was created by filtering the noise stimuli with the new filters.

APPENDIX B: EXCITATION PATTERN MODEL

The basic premise of excitation pattern models is that the pattern of auditory-nerve excitation as a function of frequency can be represented by the output of a bank of overlapping bandpass filters whose filter shapes broaden with increasing level (e.g., Baker *et al.*, 1998; Glasberg and Moore, 1990; Lutfi and Patterson, 1982; Moore and Glasberg, 1987; Moore *et al.*, 1997; Patterson, 1976; Patterson and Moore, 1986). Estimates of the ISD cue for a given direction in space were derived using the subject's DTFs and an updated version of the Glasberg and Moore excitation pattern model (Moore *et al.*, 1997). This model was essentially composed of a set of modified rounded-exponential auditory filters. These filters were logarithmically spaced on the frequency axis with a total of 200 filters between 300 Hz and 14 kHz. The cochlea's compressive nonlinearity was modeled mathematically using a logarithmic function. Thus, the logarithm of the output energy of a given filter indicated the amount of neural activity in that particular cochlear channel.

The computer program for the model was written using the MATLAB software package and calibrated according to the psychophysical sound conditions used in the laboratory. The calibration was accomplished by measuring the sound-pressure level of a 1-kHz tone at the maximum amplitude of the sound system (comprised of TDT system II hardware and ER-2 earphones) and incorporating this value (75 dB SPL) as a stored parameter in the model. A Zwislocki coupler and Brüel & Kjær 4192 pressure microphone were used for the sound-level measurements.

After calibration of the model, three basic steps were used to calculate the interaural spectrum: (1) a broadband Gaussian noise was filtered with the subject's left and right ear DTF filters corresponding to a specified location in space; (2) the directional sounds for both ears were then further processed using the excitation pattern model described above to produce directional excitation patterns (DEPs); (3) the linear spectral difference between the left and right auditory-nerve excitation patterns was then taken as the computational representation of the interaural spectrum.

APPENDIX C: GRAPHICAL AND STATISTICAL METHODS FOR LOCALIZATION DATA

1. Scatter plots of localization data

Scatter plots have been used to display the localization data for the test sound conditions (see Fig. 3). These plots are

similar in style to the ''triple pole'' scatter plots described by Kistler and Wightman (1992). In order to create these plots, the azimuth component of the localization responses was decomposed into two angles: (i) the left–right angle formed by the response location vector and the midsagittal plane (negative angles towards the left and positive angles towards the right); (ii) the front–back angle formed by the response location vector and the vertical plane containing the interaural axis (negative angles towards the back, positive angles towards the front). The elevation component of the response directions is described by the elevation angle which is equivalent to the up–down angle described by Kistler and Wightman, 1992. In the scatter plots, the target angle is indicated by the horizontal axis and the response angle is indicated by the vertical axis. The plane spanning the target and response angles was divided into square sections with a side length of 5 deg. The number of responses in each square was indicated by a gray-scale color value, with the darker colors indicating a greater number of responses. The front–back angle data have been separated into two groups depending upon whether the target direction lies in the left or right hemispheres of space. This division highlights the hemispheric differences that may be attributable to the different sound stimuli presented to the left and right ears in the different sound conditions. In addition, the front–back angle data have been sorted into three groups depending on the elevation of the target direction. The elevation angle component of the localization data is shown for the four hemispheres of space: front, back, left, and right.

2. Spherical statistics

Statistical summary of localization performance is specified in terms of spherical correlation coefficient, front–back error rates, and mean spherical angle error. The front–back errors were defined as the localization responses in which the perceived location, relative to the target location, crossed the vertical plane through the interaural axis which separates the anterior and posterior hemispheres of space. However, target locations within 5° of lateral angle with respect to the vertical plane containing the interaural axis were excluded from the front–back error analysis. The correlation between two sets of spherical data (*viz.*, the target directions of sound stimuli and the directions of human localization responses to those sound stimuli) can be calculated using the spherical correlation coefficient (see p.232 of Fisher *et al.*, 1993a). The spherical correlation coefficient ranges from -1 for complete negative correlation to $+1$ for complete positive correlation. Assuming that the direction cosines (i.e., the Cartesian coordinates) of the unit length vectors for N target directions are specified by an $N\times 3$ matrix, $\mathbf{X}$, and that the corresponding matrix of direction cosines for the unit length vectors of N response directions is specified by $\mathbf{Y}$, the spherical correlation coefficient, ρ, is calculated as

$$\rho = \frac{\det(\mathbf{X}^T\mathbf{Y})}{[\det(\mathbf{X}^T\mathbf{X})\det(\mathbf{Y}^T\mathbf{Y})]^{1/2}}.$$

3. Circular statistics

The correspondence between the response and target polar angles was analyzed visually using plots that are referred to here as circular hair plots. The utility of these plots over scatter plots is that the clustering of polar angle responses to one direction, as might be expected because a flat spectrum stimuli was continuously presented to the left ear, becomes much more readily apparent. For example, for the VR condition and Subject A, contrast the elevation data for the right hemisphere of space in Fig. 3(c) with the polar angle data for the right hemisphere in Fig. 10(a). The degree of clustering is clear in Fig. 10(a), but not in Fig. 3(c). In order to create these plots, for each subject, the localization data were divided into overlapping groups based on the azimuthal angle of the target direction. The groups were centered at -90, 90, 0, 180 deg of azimuth, and all target directions within a 50-deg span of the center azimuth in both the clockwise and anticlockwise directions were included in each group. In other words, the data were collapsed over lateral angle for the midline and the left and right hemispheres of space. The polar angle component of the localization data was then displayed in three separate circular hair plots: (i) one for the left hemisphere of space (the group centered at $-90°$ and spanning $-140°$ to $40°$); (ii) one for the right hemisphere of space (the group centered at $90°$ and spanning $40°$ to $140°$); and (iii) one for both the front hemisphere of space (the group centered at $0°$ and spanning $-50°$ to $50°$) and back hemisphere of space (the group centered at $180°$ and spanning $130°$ to $180°$ and $-130°$ to $-180°$). For each circular hair plot, a circle was drawn representing the cone of confusion. The target polar angles were then indicated by the location of small dots on the circle. For a given target direction, the response polar angle was indicated by a short line segment that was connected to the small dot and drawn such that it pointed in the direction of the response polar angle. That is to say, if the short line segment was extended until it intersected the circle, the intersection point would be the location of the response polar angle. For example, a front–back error would be represented by a dot on the circle connected to a horizontal line pointing inwards (toward the other half of the circle), and an up–down error would be represented by a dot connected to a vertical line. If the response polar angle matches the target polar angle, the short line becomes tangent to the circle. The tangent lines are not so noticeable and by contrast thereby emphasize the localization errors. For targets with multiple identical responses, the lines were overlaid on top of each other.

The distribution of the polar angle of the response directions across all target polar angles shown in the circular hair plot was then modeled using a von Mises distribution, $VM(\mu,\kappa,\theta)$, which is commonly used to model unimodal circular data distributions (see Fisher, 1993b). The von Mises probability density function for θ, the sample angle, is given by

$$VM(\mu,\kappa,\theta) = \frac{1}{2\pi I_0(\kappa)}\exp[\kappa\cos(\theta-\mu)],$$

where

$$I_0(\kappa)=\frac{1}{2\pi}\int_0^{2\pi}\exp[\kappa\cos(\phi-\mu)]d\phi$$

is the modified Bessel function of order 0, μ represents the mean direction, and κ, the concentration parameter, is inversely related to the ''spread'' in the distribution and therefore provides a measure of the data clustering. In the case that the κ of the response polar angle distribution was greater than the arbitrary, but reasonable, cutoff of 0.65, an arrow was drawn on the plot to indicate the mean circular direction of the polar angle data distribution.

In addition, a nonparametric homogeneity test known as the Wheeler–Watson–Mardia (WWM) statistical test (see Fisher 1993b) was used to measure the similarity of two different polar angle data distributions. The first step in this test is to pool the data across the two sample groups and then calculate the ''circular ranks'' of the pooled data. The circular ranks of the data can be calculated as follows. The pooled data are first treated as linear data and arranged in ascending order according to their direction. The linear rank, *r*, of each data point is calculated as its position in the ordered arrangement, with a rank of 1 indicating the smallest value. The circular rank, γ, of each data point is then defined as

$$\gamma=\frac{2\pi r}{N},$$

where *N* is the total number of data points in the pooled data. In other words, the circular rank maps the linearly ranked data around a circle so that each data point represents a direction on the unit circle. Now, let γ_{ij} represent the circular rank of the *j*th data point in the *i*th sample group within the pooled data. For each sample group, labeled by *i*, the quantities, C_i and S_i are defined as

$$C_i=\sum_{j=1}^{n_i}\cos\gamma_{ij},\quad S_i=\sum_{j=1}^{n_i}\sin\gamma_{ij},$$

where n_i is the number of data points in the *i*th sample group. The test statistic, *W*, is then given as

$$W=2\sum_{i=1}^{2}\frac{(C_i^2+S_i^2)}{n_i},$$

and is proportional to the sum of the squared magnitude of the vector sum of the directions for each sample group. If the two sample groups are similar, then the circular rank interleaves and rather evenly distributes the data points for each sample group around the circle so that vector sum of the directions for each sample group is a short vector and *W* is small. On the other hand, if the two sample groups are very different, then the circular rank will cluster the data points for each sample group on one half of the circle and the vector sum of the directions for each sample group is now a longer vector and *W* is larger. Statistical significance at the $100(1-\alpha)\%$ level is determined by comparing *W* with the upper $100(1-\alpha)\%$ point of the χ^2_{2M-2} distribution.

APPENDIX D: MUTUAL INFORMATION ANALYSIS OF SPECTRAL CUES

The average mutual information between spectral cue and location was examined for 32 different cones of confusion spaced every 5 deg in lateral angle from −80° to 80°. For each lateral angle, 88 positions were chosen evenly distributed around the cone of confusion, i.e., 88 polar angles were chosen. For each of the 88 polar angles, there exists a corresponding left and right monaural spectral cue as well as an interaural spectral difference cue. Given one of these spectral cues for one of the 88 positions as an input, one can ask how probable is it that any of the 88 positions would actually be chosen as the source position by some sound localization algorithm. In other words, one pairs a spectral cue with a position on the cone of confusion and asks how probable is the given combination of spectral cue and position. Intuitively, the probability of a response at a given location, L_i, is related to the spectral similarity between the spectral cue, S_i, associated with the chosen position and the given spectral cue, S_j. In other words, the conditional probability $p(L_i|S_j)$ is based, in theory, on the degree of spectral similarity between the DEP spectra (calculated as described in the Appendix B) corresponding to locations L_i and L_j, and would therefore be inversely proportional to the spectral variance between the two spectra. Thus, the conditional probability $p(L_i|S_j)$ was taken as proportional to the reciprocal of the spectral variance across frequency between the spectral cues S_i and S_j. The spectral variance between S_i and S_j was calculated as described in Middlebrooks (1999). For each frequency bin, the difference in dB between the two spectra was determined and the variance of these values calculated. The variance of these values (in dB^2) represents the spectral variance. In this way, a constant dB offset across frequency between the spectra does not change the value of the spectral variance. In order to ensure that the spectral variance was never zero (i.e., an infinite conditional probability), a small constant offset (approximately 20% of the mean spectral variance across all pairs of spectra) was added to all spectral variance calculations representing noise in the system.

Within information theory, it is well-known that all of the properties of a discrete communication channel are completely determined by the joint probability matrix specifying the joint probabilities for a given pairing of transmitted and received letters (e.g., Reza, 1961). In this case, the machinery of information theory can be employed by considering the pairing as not between letters of the alphabet, but between a given spectral cue and a given position on the cone of confusion. It then follows that one can calculate (e.g., see Reza, 1961) the average of the mutual information, $I(L;S)$, for the pairing of a given type of spectral cue with locations within the cone of confusion

$$I(L;S)=\sum_{j=1}^{88}\sum_{i=1}^{88}p(L_i,S_j)\log_2\left(\frac{p(L_i|S_j)}{p(L_i)}\right),\qquad\text{(D1)}$$

where $L=\{L_i|i\leqslant 88\}$ represents the set of 88 locations within the cone of confusion, $S=\{S_j|j\leqslant 88\}$ represents the set of 88 spectral cues corresponding to the 88 locations,

$p(L_i, S_j)$ represents the joint probability for the pairing of L_i and S_j, $p(L_i|S_j)$ represents the conditional probability for L_i given S_j, and $p(L_i)$ represents the marginal probability for L_i. For the purposes of calculation, it is convenient to use the rules of probability to re-express the above formula as

$$I(L;S) = \sum_{j=1}^{88} \sum_{i=1}^{88} p(L_i|S_j) p(S_j) \log_2 \left(\frac{p(L_i|S_j)}{\sum_{k=1}^{88} p(L_i|S_k) p(S_k)} \right), \tag{D2}$$

where $p(S_j)$ represents the marginal probability for S_j. The advantage of the second equation is that the mutual information is expressed in terms of only two quantities, $p(L_i|S_j)$ and $p(S_j)$, which can be readily determined. The determination of $p(L_i|S_j)$ has already been described above. With regard to $p(S_j)$, it is reasonable to assume that the source positions in the localization experiment were randomly chosen so that each S_j is equally likely, i.e., $p(S_j) = 1/88$. All probabilities were normalized appropriately to be within 0 and 1.

[1]The ILD cue is used here to refer to an interaural intensity difference calculated as a single value averaged across frequency, while the interaural spectral difference (ISD) cue is used to refer to a spectral intensity pattern representative of the intensity differences in and across each frequency band.

[2]The distribution of the lateral angle error for the pooled data was modeled using the normal distribution and the goodness-of-fit tested. The statistical results showed that the null hypothesis that the data possess a normal distribution could not be rejected for all three sound conditions. Figure 7 shows that the variance of the lateral angle data was greater for the two test sound conditions than for the control sound condition.

[3]It has been shown that some chronically monaural listeners can use the monaural spectral cues for auditory localization in the absence of the interaural cues (see Slattery and Middlebrooks, 1994).

Baker, R. J., Rosen, S., and Darling, A. M. (**1998**). ''An efficient characterisation of human auditory filtering across level and frequency that is also physiologically reasonable,'' in *Psychophysical and Physiological Advances in Hearing*, edited by A. R. Palmer, A. Rees, and A. Q. Summerfield (Whurr, London), pp. 81–88.

Blauert, J. (**1997**). *Spatial Hearing: The Psychophysics of Human Sound Localization* (The MIT Press, Cambridge, MA).

Butler, R. A. (**1969a**). ''Monaural and binaural localization of noise bursts vertically in the median sagittal plane,'' J. Aud Res. **3**, 230–235.

Butler, R. A. (**1969b**). ''On the relative usefulness of monaural and binaural cues in locating sound in space,'' Psychonomic Sci. **17**(4), 245–246.

Carlile, S., Leong, P., and Hyams, S. (**1997**). ''The nature and distribution of errors in the localization of sounds by humans,'' Hear. Res. **114**, 179–196.

Carlile, S., and Pralong, D. (**1994**). ''The location-dependent nature of perceptually salient features of the human head-related transfer function,'' J. Acoust. Soc. Am. **95**(6), 3445–3459.

Duda, R. O. (**1997**). ''Elevation dependence of the interaural transfer function,'' in *Binaural and Spatial Hearing in Real and Virtual Environments*, edited by R. H. Gilkey and T. R. Anderson (Erlbaum, Mahwah, NJ), Chap. 3, pp. 49–75.

Fisher, H. G., and Freedman, S. J. (**1968**). ''The role of the pinna in auditory localization,'' J. Aud Res. **8**, 15–26.

Fisher, N. I, Lewis, T., and Embleton, B. J. J. (**1993a**). *Statistical Analysis of Spherical Data* (Cambridge University Press, Cambridge) (Revised edition).

Fisher, N. I. (**1993b**). *Statistical Analysis of Circular Data* (Cambridge University Press, Cambridge).

Gardner, M. (**1973**). ''Some monaural and binaural facets of median plane localization,'' J. Acoust. Soc. Am. **54**(6), 1489–1495.

Glasberg, B., and Moore, B. (**1990**). ''Derivation of auditory filter shapes from notched-noise data,'' Hear. Res. **47**(1–2), 103–138.

Hebrank, J. (**1976**). ''Pinna disparity processing: A case of mistaken identity?'' J. Acoust. Soc. Am. **59**, 220–229.

Hebrank, J., and Wright, D. (**1974**). ''Are the two ears necessary for localization of sound sources on the median plane?'' J. Acoust. Soc. Am. **56**(3), 935–938.

Hofman, P. M., and Opstal, J. A. V. (**2003**). ''Binaural weighting of pinna cues in human sound localization,'' Exp. Brain Res. **148**, 458–470.

Humanski, R. A., and Butler, R. A. (**1988**). ''The contribution of the near and far ear toward localization of sound in the sagittal plane,'' J. Acoust. Soc. Am. **83**(6), 2300–2310.

Janko, J. A., Anderson, T. R., and Gilkey, R. H. (**1997**). ''Using neural networks to evaluate the viability of monaural and interaural cues for sound localization,'' in *Binaural and Spatial Hearing in Real and Virtual Environments*, edited by R. H. Gilkey and T. R. Anderson (Erlbaum Mahwah, NJ), Chap. 26, pp. 557–570.

Kistler, D., and Wightman, F. (**1992**). ''A model of head-related transfer functions based on principal components analysis and minimum-phase reconstruction,'' J. Acoust. Soc. Am. **91**(3), 1637–1647.

Kulkarni, A., and Colburn, H. S. (**1998**). ''Role of spectral detail in sound-source localization,'' Nature (London) **396**(6713), 747–749.

Kulkarni, A., Isabelle, S. K., and Colburn, H. S. (**1999**). ''Sensitivity of human subjects to head-related transfer function phase spectra,'' J. Acoust. Soc. Am. **105**(5), 2821–2840.

Langendijk, E. H. A., and Bronkhorst, A. W. (**2002**). ''Contribution of spectral cues to human sound localization,'' J. Acoust. Soc. Am. **112**(4), 1583–1596.

Lutfi, R. A., and Patterson, R. D. (**1982**). ''Combination bands and the measurement of the auditory filter,'' J. Acoust. Soc. Am. **71**, 421–423.

Macpherson, E. A., and Middlebrooks, J. C. (**2002**). ''Listener weighting of cues for lateral angle: The duplex theory of sound localization revisited,'' J. Acoust. Soc. Am. **111**(5), 2219–2236.

Macpherson, E. A., and Middlebrooks, J. C. (**2003**). ''Vertical-plane sound localization probed with ripple-spectrum noise,'' J. Acoust. Soc. Am. **114**(1), 430–445.

Mehrgardt, S., and Mellert, V. (**1977**). ''Transformation characteristics of the external human ear,'' J. Acoust. Soc. Am. **61**(6), 1567–1576.

Middlebrooks, J. C. (**1999**). ''Virtual localization improved by scaling nonindividualized external-ear transfer functions in frequency,'' J. Acoust. Soc. Am. **106**(3), 1493–1510.

Middlebrooks, J., and Green, D. (**1990**). ''Directional dependence of interaural envelope delays,'' J. Acoust. Soc. Am. **87**(5), 2149–2162.

Møller, H., Sørensen, M. F., Hammershøi, D., and Jensen, C. B. (**1995**). ''Head-related transfer functions of human subjects,'' J. Audio Eng. Soc. **43**(5), 300–321.

Moore, B. C. J., and Glasberg, B. R. (**1987**). ''Formulae describing frequency selectivity as a function of frequency and level, and their use in calculating exitation patterns,'' Hear. Res. **28**, 209–225.

Moore, B. C. J., Glasberg, B. R., and Baer, T. (**1997**). ''A model for the prediction of thresholds, loudness, and partial loudness,'' J. Audio Eng. Soc. **45**(4), 224–240.

Morimoto, M. (**2001**). ''The contribution of two ears to the perception of vertical angle in sagittal planes,'' J. Acoust. Soc. Am. **109**, 1596–1603.

Patterson, R. D. (**1976**). ''Auditory filter shapes derived with noise stimuli,'' J. Acoust. Soc. Am. **59**(3), 640–654.

Patterson, R. D., and Moore, B. C. J. (**1986**). ''Auditory filters and excitation patterns as representations of frequency resolution,'' in *Frequency Selectivity in Hearing*, edited by B. C. J. Moore (Academic, London), pp. 123–177.

Pralong, D., and Carlile, S. (**1994**). ''Measuring the human head-related transfer functions: A novel method for the construction and calibration of a miniature 'in-ear' recording system,'' J. Acoust. Soc. Am. **95**(6), 3435–3444.

Reza, F. M. (**1961**). *An Introduction to Information Analysis* (McGraw-Hill, New York).

Searle, C., Braida, L., Cuddy, D., and Davis, M. (**1975**). ''Binaural pinna disparity: Another auditory localization cue,'' J. Acoust. Soc. Am. **57**(2), 448–455.

Searle, C., Braida, L., Davis, M., and Colburn, H. S. (**1976**). ''Model for auditory localization,'' J. Acoust. Soc. Am. **60**(5), 1164–1175.

Shinn-Cunningham, B. G., Santarelli, S., and Kopco, N. (**2000**). ''Tori of confusion: Binaural localization cue for sources within reach of a listener,'' J. Acoust. Soc. Am. **107**(3), 1627–1636.

Slattery, W. H., and Middlebrooks, J. C. (**1994**). ''Monaural sound localization: Acute versus chronic unilateral impairment,'' Hear. Res. **75**, 38–46.

Wallach, H. (**1939**). ''On sound localization,'' J. Acoust. Soc. Am. **10**, 270–274.

Wightman, F. L., and Kistler, D. J. (**1989**). ''Headphone simulation of free field listening II. Psychophysical validation,'' J. Acoust. Soc. Am. **85**(2), 868–878.
Wightman, F. L., and Kistler, D. J. (**1997**). ''Monaural sound localization revisited,'' J. Acoust. Soc. Am. **101**, 1050–1063.
Wightman, F. L., and Kistler, D. J. (**1999**). ''Sound localization with unilaterally degraded spectral cues,'' J. Acoust. Soc. Am. **105**(2), 1162.
Zhou, B., Green, D., and Middlebrooks, J. (**1992**). ''Characterization of external ear impulse responses using Golay codes,'' J. Acoust. Soc. Am. **92**, (Pt. 1), 1169–1171.

Localization dominance in the median-sagittal plane: Effect of stimulus duration

Roberto M. Dizon and Ruth Y. Litovsky[a)]
Hearing Research Center, Boston University, Boston, Massachusetts 02215

(Received 19 June 2003; accepted for publication 22 March 2004)

Localization dominance is an aspect of the precedence effect (PE) in which the leading source dominates the perceived location of a simulated echo (lagging source). It is known to be robust in the horizontal/azimuthal dimension, where binaural cues dominate localization. However, little is known about localization dominance in conditions that minimize binaural cues, and most models of precedence treat the phenomena as ''belonging'' to the binaural system. Here, localization dominance in the median-sagittal plane was studied where binaural cues are greatly reduced, and monaural spectral/level cues are thought to be the primary cues used for localization. Lead–lag pairs of noise bursts were presented from locations spaced in 15° increments in the frontal, median-sagittal plane, with a 2-ms delay in their onsets, for source durations of 1, 10, 25, and 50-ms. Intermixed with these trials were single-speaker trials, in which lead and lag were summed and presented from one speaker. Listeners identified the speaker that was nearest to the perceived source location. With single-speaker stimuli, localization improves as signal duration is increased. Furthermore, evidence of elevation compression was found with a dependence on duration. With lead–lag pairs, localization dominance occurs in the median plane, and becomes more robust with increased signal duration. These results suggest that accurate localization of a co-located lead–lag pair is necessary for localization dominance to occur when the lag is spatially separated from the lead. © *2004 Acoustical Society of America.* [DOI: 10.1121/1.1738687]

PACS numbers: 43.66.Qp, 43.66.Rq, 43.66.Pn [AK] Pages: 3142–3155

I. INTRODUCTION

Sounds generated in reverberant rooms produce multiple reflections that arrive from hard surfaces such as walls, and that contribute to the spatial character of the sound. However, they have a surprisingly small effect on source localization when the source contains a well-defined onset (Hartmann, 1983). This phenomenon has commonly been referred to as the ''precedence effect'' (PE) (Wallach *et al.*, 1949; Zurek, 1980) or ''law of the first wavefront'' (Blauert, 1997; Litovsky *et al.*, 1999). The PE has gained interest since it is thought that the auditory system may perform specialized processing to achieve this performance. The PE has been described as resulting from a temporary reduction in sensitivity to localization information contained in reverberation following the onset of a source. As such, in a simple paradigm whereby a source (lead) and single echo (lag) occur, perceived location of the lead–lag pair is dominated by the localization information associated with the leading stimulus. For click stimuli, this dominance is most robust when the lagging stimulus occurs within a few ms of the lead.

The PE and related phenomena have been a topic of interest for over half a century (for review see Litovsky *et al.*, 1999), although most of what is known relates to temporal characterization of the phenomena, rather than spatial variables, including the locations of the source and simulated reflections. Furthermore, experiments have typically utilized or simulated stimuli that occur in the azimuthal plane, where changes in source locations are associated with clearly defined and often perceptible differences in binaural cues such as interaural differences in time and level. Cue manipulation in the azimuthal dimension has been preferred since interaural cues map precisely to azimuthal locations. In addition, they are easily generated, as well as replicated and presented in a realistic manner to subjects. An additional benefit of presenting sounds in the azimuthal dimension is that results can be compared with what is known about neurophysiological activity in the auditory pathway in a relatively straightforward manner (Yin, 1994; Fitzpatrick *et al.*, 1995; Litovsky *et al.*, 1997a; Litovsky and Yin, 1998a,b). Finally, models of the PE that can successfully predict performance rely on interaural cues that are available in the azimuthal dimension (e.g., Lindemann, 1986; Shinn-Cunningham *et al.*, 1993; Hartung and Trahiotis, 2001; Tollin, 1998).

In contrast, the processes involved in determining the location of sound sources occurring in the median-sagittal plane are more poorly understood and little is known about the PE in the median plane. This problem is especially interesting because localization in the median-sagittal plane is mediated primarily by spectral filtering by the pinnae, head and torso of stimuli reaching the ears from various elevations (Searle *et al.*, 1975; Gardner and Gardner, 1973; Butler, 1969; Hebrank and Wright, 1974; Middlebrooks and Green, 1991). While it has been shown that binaural cues cannot be ruled out as contributing to median plane localization (e.g., Middlebrooks, 1992; Hofman and Van Opstal, 2003), a significant amount of evidence suggests that monaural spectral cues may be primary. To date, little is known about the PE in the median plane and the extent to which directional infor-

[a)]Present address: University of Wisconsin, 1500 Highland Avenue, Madison, WI 53705; electronic mail: Litovsky@waisman.wisc.edu.

mation in reflections can be outweighed by information contained in the source when spectral cues are the primary cue for localization.

One study reported that fusion echo thresholds measured in the median sagittal plane are similar to those found in the azimuthal plane (Rakerd *et al.*, 2002). Two studies have attempted to measure dominance of the leading source in localization for stimuli in the median-sagittal plane. In a brief report, Blauert (1971) suggested that the leading stimulus dominates localization for inter-stimulus intervals of 550 μs, but not for smaller delays (within the summing localization range). Litovsky *et al.* (1997a) found dominance by the lead location for delays up to 5-ms (within the range of the PE), with diminished dominance at longer delays. In both studies however, source locations were limited to front, back, and overhead, where localization of single source sounds is difficult to interpret, both due to front–back errors and to the fact that sounds presented overhead are very poorly localized. There are also physiological data which suggest that the strength of echo suppression in the responses of single neurons in the inferior colliculus is highly similar in the azimuthal and median planes (Litovsky *et al.*, 1997a; Litovsky and Yin, 1998a). Although that does not predict the relative strength of localization dominance in the two planes, it provides further evidence for the existence of precedence phenomena in the median plane. Our hypothesis, that well-localized sounds should produce localization dominance regardless of which directional cues are being utilized, could not be affirmed by previous work.

In the present study, we selected six locations, all in the frontal hemifield on the median-sagittal plane, where single-source noise bursts were well localized by all subjects. Lead and lag stimuli were presented from various combinations of these locations, and the effect of source duration was also explored. Using these parameters we tested the hypotheses that localization dominance is robust in the median-sagittal plane, providing that a co-located lead and lag stimulus produces a well-localized image.

II. METHODS

A. Subjects

Four subjects (two male, two female) between the ages of 18 and 24 participated in the experiments. Each had some prior experience in sound localization experiments. However, all subjects were naive as to the nature of the stimuli and the goals of the experiment. Each was given at least an hour of practice with feedback to become familiar with the experimental setup and paradigm before the start of the experiment. Subjects were also given 10 min of practice with feedback prior to each session. All subjects had normal hearing as verified by a standard audiometric threshold exam.

B. Apparatus

The experiments were performed in an anechoic chamber. The subject was seated with his or her head at the center of a circular arc approximately 2.4 m in diameter mounted vertically and positioned such that it was aligned with the subject's median-sagittal plane. Six speakers composed of a single 6.35 cm driver in a sealed enclosure ($7.9\,\mathrm{cm}\,H \times 7.6\,\mathrm{cm}\,W \times 12\,\mathrm{cm}\,D$) were mounted at 15° increments between −30° and 45°. The speakers produced a flat response from 300 Hz to 15 kHz. Variations in frequency response among the speakers were minimal and not compensated for. The speakers were visible to the subjects and were labeled 1 through 6 as shown in the Fig. 1.

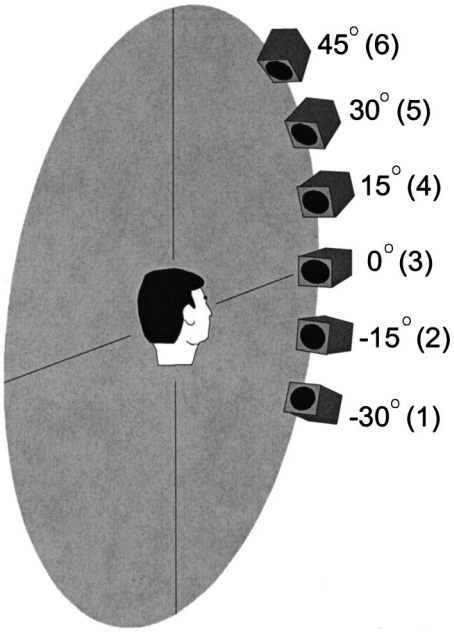

FIG. 1. Speakers are placed on a circular ring 2.4 m in diameter in the positions shown. The subject is seated with his/her head in the center of this ring.

The subject's head was constrained by a headrest mounted on the rear of the seat (Whitmeyer Biomechanix Soft-2S). The headrest has adjustable padded supports on the back of the head and under the jaws that provide support but which are not constrictive, while also being minimally acoustically obtrusive. The subjects were also told to keep their head still during stimulus presentation. They were however free to look at the speakers, which were all within the subject's visual field.

Hardware including Tucker Davis Technologies (TDT) System II hardware (AP2,DD1,PM1) in conjunction with a PC host, was responsible for stimulus computation and generation, control of the multiplexer for speaker switching, communication with the response terminal, and used as the user interface for the experimenter. The direct sound and simulated reflection signals from the D/A converter (sampling rate 50 kHz) were amplified by a Crown D-75 amplifier which was calibrated for equal gain to both channels. The amplified signals were directed to the appropriate speaker(s) with a multiplexer (TDT PM1).

C. Stimuli

Measurements were made on single-speaker and precedence (localization dominance) trials. On each trial, stimuli were comprised of a train of four identical broadband noise bursts, whose onsets were spaced 250-ms apart, as shown in Fig. 2. Noise bandwidth was effectively limited only by the

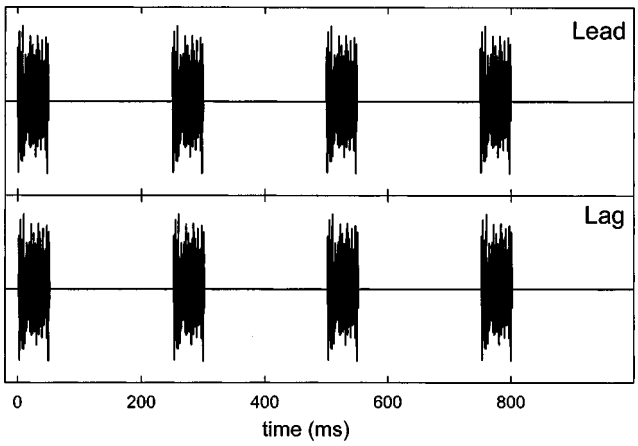

FIG. 2. Plot of sample lead and lag stimuli for the precedence conditions. This example includes 50-ms bursts, hence the 2-ms delay might be difficult to discern on this scale. All bursts within each train are identical, as are the lead and lag bursts. Lead and lag stimuli differ only in the onset delay of the lag.

speaker drivers, which are flat to 15 kHz. A different sample of noise was used for every trial. Onset and offset ramps were not applied, resulting in abrupt onsets and offsets since the broadband bursts were presented at full bandwidth by the playback system. On precedence trials, two trains were presented from separate speakers; lead and lag noise bursts were always identical to one another except for the 2-ms onset delay in the lag. Noise burst durations were 1, 10, 25, and 50-ms. Since the lead–lag delay was always 2-ms, the lead and lag bursts overlapped in time for durations of 10, 25, and 50-ms but not for the 1-ms duration. For the single-speaker trials, the lead and lag stimuli were digitally summed prior to presentation from the single speaker. The lag is included in the single-speaker trials so that differences between single-speaker and PE performance can be attributed to lag location specifically, as opposed to both the presence and the location of the lag. It is important to note that the spectral comb filtering created by the addition of the delayed repetition would occur for the single-speaker trials as well as the precedence trials.

Presentation levels were chosen for each subject individually. Detection thresholds were first established for the 1-ms stimulus presented from speaker 3 (directly in front). Subsequent presentations of 1-ms bursts were presented at 40 dB above this level, while the amplitudes of the longer duration signals were digitally attenuated by the square root of their durations to provide some degree of loudness compensation.

For the precedence paradigm trials, three pairs of speaker positions were used. These were position pairs 1 and 5, 2 and 5, and 2 and 6, using the position numbering convention shown in Fig. 1. These pairs contain angular separations of 60° (1-5 and 2-6), or 45° (2-5). These wide separations were chosen based on pilot data (Dizon *et al.*, 1997), which suggested that separations as wide as these were necessary to observe the influence of the PE, given the decrease in localization precision for the PE stimuli in that study. The three position pairs, along with their alternate order equivalents, result in six combinations of lead and lag positions. These, combined with all six single-speaker trials (lead and lag from the same speaker), result in twelve possible position types. Each position type was presented at each of the four durations 30 times, for a total of 1440 trials per subject. Trials were mixed randomly and presented in blocks of 100 (with one block of 40). Hence, single-speaker localization was measured within the same blocks as the precedence trials.

D. Testing protocol

Responses were made using a small handheld response terminal (QSI Qterm II). The subject's task was to identify a speaker that was nearest to the perceived location of the auditory image. If the stimulus appeared to emanate from more than one speaker or from a location other than one of the six possible locations, instructions were to choose the one speaker that appeared to be most salient and to contain the majority of the sound image. No feedback was provided during the experimental runs. However, subjects were trained on the single-speaker condition, and given feedback during a 1 h training session before the experiments begun, as well as for 10 min at the beginning of each session.

The forced choice protocol was chosen based on the results of an earlier median plane study (Dizon *et al.*, 1997) in which a more unconstrained response method produced a high inter-subject variability in the mapping of their perceptions onto the response choices. In that study, subjects were permitted to choose either one or two locations, depending on which one better described their percept. One subject chose two locations almost exclusively, while another chose two locations only twice out of 1500 trials. Given the variability in the data, the poor evidence of localization dominance for the nonfused judgments, and the informal comments regarding the vagueness of the stimuli, it was decided that a simple and constrained response method would best uncover a bias toward the leading stimulus. Finally, the identification paradigm was selected in an attempt to maximize any effects of localization dominance, bearing in mind the fact that identification paradigms are easier for subjects than unconstrained localization paradigms. One of the motivations for this study (see Sec. I) was to extend an earlier report by Litovsky *et al.* (1997a) in which an identification paradigm was used with only three source positions, including directly overhead.

III. SINGLE-SPEAKER RESULTS AND DISCUSSION

A. Results

Single-speaker results are shown in Fig. 3. Each row comprises data from one subject and results for the four durations are organized according to columns. These data correspond to trials in which both the lead and the lag emanated from the same speaker. Data are presented as confusion matrices, where the *x*-axis corresponds to the actual speaker number and the *y*-axis corresponds to the subject's response. The area of each closed circle is proportional to the number of responses for each condition.

Perfect source identification performance would correspond to subject responses exclusively consistent with the

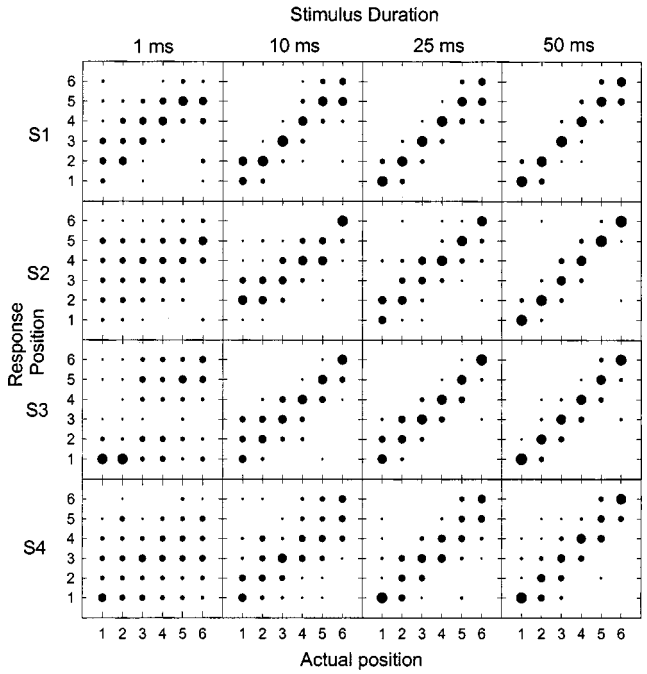

FIG. 3. Results for the single-speaker trials. Each row comprises data from one subject and results for the four durations are organized according to columns. The *x*-axis labels correspond to the actual speaker number and the *y*-axis labels correspond to the subject's response. The area of each closed circle is proportional to the number of responses for each condition.

source speaker, which would appear as maximal response frequencies along the positive diagonal in each panel. Comparing single-speaker performance across durations for each subject reveals that identification accuracy improves as burst duration is increased. Specifically, there is only a weak trend toward the diagonal in the responses for the 1-ms duration, with variation in the trend between individual subjects, while there is a strong trend toward responses near the diagonal for the 50-ms duration case for each subject.

Precision of responses improves as burst duration is increased, which can be seen by qualitatively comparing the ''spread'' in the responses across the speaker positions for each burst duration. The response distributions for the 50-ms case are much more tightly clustered than those in the 1-ms cases. Also noticeable is the inter-subject variability, which is most evident in the 1-ms duration data. Subjects 1 and 3 appear to be able to extract some directional information at this duration, while subjects 2 and 4 are less able to do so. These data were exposed to a number of statistical analyses to allow more quantitative descriptions of trends in the data.

The response mean $M[k]$ was computed for each subject as the mean of that subject's responses when speaker k was presented, and is given by

$$M[k]=\frac{1}{N}\sum_{n=1}^{N} r_{n,k},$$

where $r_{n,k}$=response to trial n when speaker k was presented (if the subject responded ''4'' when speaker 2 was presented for the 25th time, then $r_{25,2}=4$). N=the number of presentations at each speaker (30).

The response standard deviation $\sigma[k]$ for each subject is the standard deviation from the mean response $M[k]$ expressed in degrees,

$$\sigma[k]=\sqrt{\frac{A^2}{N}\sum_{n=1}^{N}(r_{n,k}-M[k])^2}.$$

where A=the speaker spacing in degrees (15°).

The rms error $E[k]$ for each subject is the standard deviation from the actual speaker number k expressed in degrees, as given by

$$E[k]=\sqrt{\frac{A^2}{N}\sum_{n=1}^{N}(r_{n,k}-k)^2}.$$

Additionally, an average of each of these statistics over the four subjects was computed, which are denoted as $\langle M[k]\rangle$, $\langle \sigma[k]\rangle$, and $\langle E[k]\rangle$.

These across-subject averages are shown in Fig. 4. In each panel, data for each burst duration are shown and differentiated from each other with symbols as indicated in the legend. Also within each panel, a sub-panel is shown which represents the standard deviation of that statistic averaged over the four subjects for each duration. A ''chance'' statistic is also shown within each panel using a dashed line, and is computed from a hypothetical response distribution representing chance performance, in which responses to the 30 trials for each source speaker position are distributed evenly over the six possible responses.

Considering the response mean $\langle M[k]\rangle$ in Fig. 4(a), the slopes of these mean curves start out shallow for the shortest duration, and approach a slope of 1 as duration is increased. Perfect performance would correspond to a slope of 1, while chance performance is indicated with the dashed horizontal line, and is simply a mean of the angles of the six speakers. Based on $\langle M[k]\rangle$ alone, there appears to be a compression of perceived elevation that is more pronounced as burst duration is shortened. However, without considering the other statistics, such as the standard deviation, it is difficult to make a claim of a perceived compression of elevation.

The standard deviation $\langle \sigma[k]\rangle$ is shown in Fig. 4(b), and represents the deviation from the mean $M[k]$, for individual subjects at each duration. $\langle \sigma[k]\rangle$ gets smaller as duration is increased, with the largest jump in $\langle \sigma[k]\rangle$ between 1 and 10-ms. In addition, $\langle \sigma[k]\rangle$ is of similar magnitude across the six positions for each of the durations. All values of $\langle \sigma[k]\rangle$ are less than the chance statistic, which is fixed at 27.5°. Based on $\langle \sigma[k]\rangle$, localization precision improves as burst duration is increased. This is evident qualitatively in the raw response distributions shown in Fig. 3.

The rms error $\langle E[k]\rangle$ is shown in Fig. 4(c). Similar to $\langle \sigma[k]\rangle$, $\langle E[k]\rangle$ decreases as duration is increased. However, unlike $\langle \sigma[k]\rangle$, $\langle E[k]\rangle$ increases toward either edge of the set of responses for the 1-ms case, and also somewhat for the 10-ms case, while $\langle \sigma[k]\rangle$ remained approximately constant with k relative to the response set. Since $\langle E[k]\rangle$ is referenced to the actual speaker presented, this statistic is a reflection of the compression in $\langle M[k]\rangle$, which is more pronounced for the shorter durations.

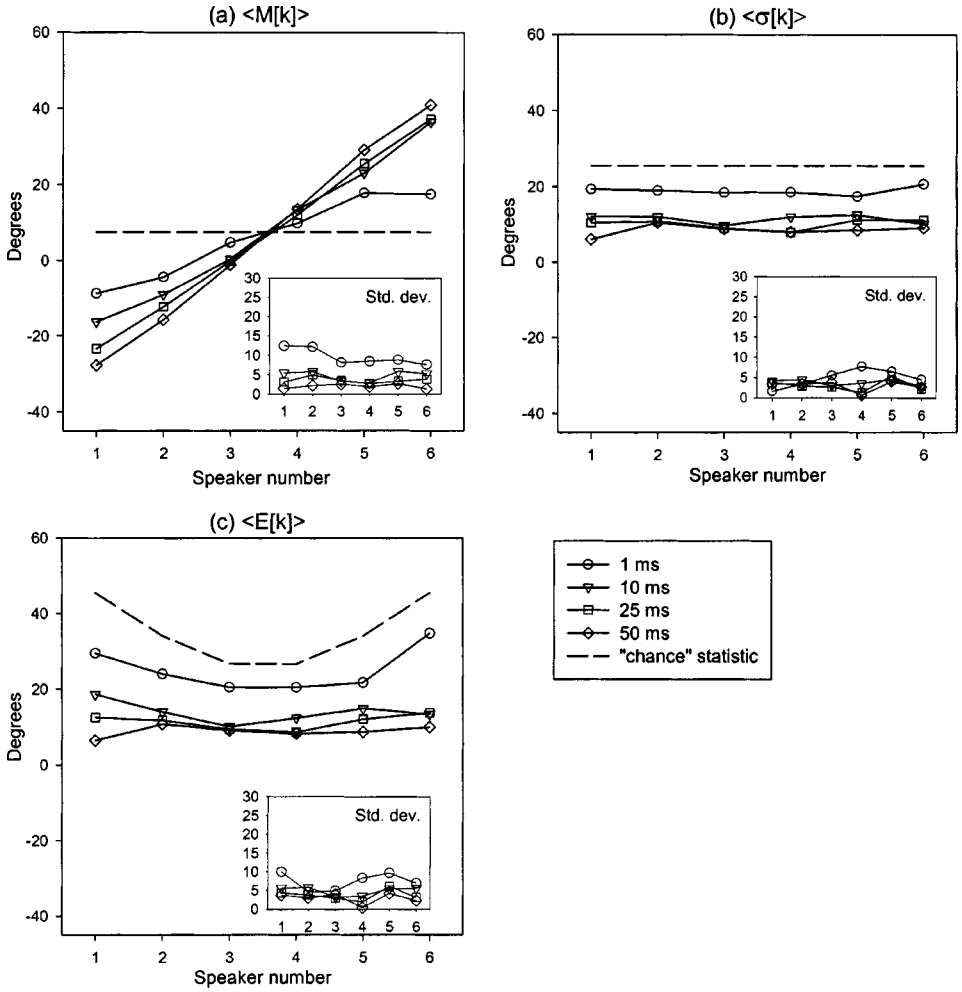

FIG. 4. (a) Mean response in degrees $M[k]$, (b) standard deviations $\langle\sigma[k]\rangle$, and (c) rms error $\langle E[k]\rangle$ for the single-speaker condition plotted against actual speaker number for each of the four durations as indicated in the legend. Each data point represents a mean of the statistic over the four subjects. The standard deviations about each mean are plotted in the inset of each panel. The dashed line represents the statistic for chance performance.

These statistics, as well as the raw data, suggest that localization of overlapping lead and lag bursts of noise in the median plane is more difficult for burst durations less than approximately 10-ms. The statistics further suggest that this increased difficulty is manifested as a decrease in precision and an apparent compression of perceived elevation as well.

B. Discussion

The most notable features in the above-presented single-speaker data are the influence of stimulus duration on source location identification and the compression that characterizes performance for shorter durations. Preliminary experiments (Dizon *et al.*, 1997) indicated that clicks were difficult to localize precisely, while 100-ms noise bursts were well localized. Hence, the present study focused on stimuli with intermediate durations. Evidence of duration-dependent compression in median-plane localization has been reported previously in the literature.

Hofman and Van Opstal (1998) studied median plane localization for stimuli with identical long term spectra, but with varying short term spectra. The intent was to characterize the temporal course of spectral estimation, and also to investigate the ability of subjects to benefit from ''multiple looks'' of a short-time spectrum. The authors fitted an ''elevation gain'' to their data, corresponding to the slope of the best fit line to the scatter plot data of response elevation versus actual elevation. Elevation gains indicated a high degree of compression at the shortest durations (3-ms) with increasing gains with longer duration, stabilizing near unity at approximately 80 ms.

Linear regression statistics were calculated on our single-speaker data to permit direct comparison with Hofman and Van Opstal's statistics. Table I lists the correlation coefficient ρ, the elevation gain g, the y-intercept b in degrees, as well as the rms δ of the differences between each data point and the fitted line. The statistics indicate that the correlations are too low for the 1-ms duration for the computed slopes to be meaningful. However, the correlations for 10, 25, and 50-ms are significant. The elevation gains for these durations climb steadily for each subject, indicating less elevation compression as duration is increased from 10-ms ($0.63<g<0.82$) to 50-ms ($0.91<g<0.95$). Hofman and Van Opstal's gains, measured for durations between 3 and 80 ms, are quite similar both qualitatively and quantitatively [Table II in Hofman and Van Opstal (1998)].

Macpherson and Middlebrooks (2000) also found elevation compression for short 3-ms bursts that was not evident with the longer 100-ms bursts. However, this result was found to be dependent on presentation level, such that higher level ($\sim$50–60 dB SL) stimuli produced significant elevation compression while lower level stimuli did not. The stimuli used in the present study were presented at 40 dB SL only,

TABLE I. Linear regression statistics for the single-speaker data for each subject. Included are the correlation coefficient ρ, the elevation gain g, the y-intercept b in degrees, as well as the rms δ of the differences between each data point and the fitted line.

Subject	Dur (ms)	Corr ρ	Gain g	Offset b (deg)	δ (deg)
S1	1	0.32	0.42	8.58	16
	10	0.82	0.82	0.28	9.8
	25	0.88	0.87	−1.45	8.2
	50	0.92	0.95	−0.39	7.4
S2	1	0.30	0.64	−3.2	25
	10	0.75	0.75	2.4	11
	25	0.86	0.85	1.3	8.6
	50	0.89	0.95	−1.5	8.4
S3	1	0.09	0.24	11	18
	10	0.67	0.64	6.4	11
	25	0.73	0.75	4.1	12
	50	0.89	0.95	1.1	8.7
S4	1	0.09	0.25	−3.1	20
	10	0.49	0.63	1.6	16
	25	0.70	0.79	−2.3	13
	50	0.80	0.91	−1.2	12

which is a level for which the data of Macpherson and Middlebrooks did not show significant compression.

Interestingly, neither Hofman and Van Opstal nor Macpherson and Middlebrooks found any dependence of localization precision on duration, even for a duration of 3-ms, the shortest duration used in either study. In our study, we find a slight increase in variability between 10 and 50-ms (δ in Table I), with a much larger increase in variability for a duration of 1-ms.

The difference in performance for the shortest duration in our study compared with either of the referenced studies may relate to the shorter duration (1-ms as compared to 3-ms), but may also relate to the comb filtering present in our study that was not present in either of the referenced studies. One might expect the comb filtering to influence localization performance due to the additional notches in the high frequency spectrum. However, the comb filtering did not appear to degrade performance for the three longer durations. The elevation gains and the response variability at these durations are quite similar to those found by Hofman and Van Opstal. Perhaps the 1-ms duration combined with the comb filtering was sufficient to degrade performance.

Regarding the compression at the three longer durations, two possible sources for the compression in the elevation responses can be considered: spectral variability in the noise bursts, and edge effects resulting from the response paradigm. Since localization in the median plane is assumed to depend on elevation dependent spectral filtering by the pinnae, it follows that good localization performance is contingent on the subject's ability to acquire an accurate and clean estimate of this spectral filtering (Wightman and Kistler, 1997). Stimuli such as clicks or Gaussian noise are well suited for use in median plane localization experiments due to the smoothness of their magnitude spectra. However, the perceived smooth spectra of Gaussian noise results from peripheral filtering of the finely spaced peaks and notches in the spectra of noise samples of sufficient length. For shorter samples, peaks and notches may persist beyond peripheral filtering due to their wider spacing, and thus may compete with the spectral features that are the primary cues for median plane localization.

In a hypothesized model of performance, Hofman and Van Opstal suggested that the compression observed in their studies could have been due to subjects relying on an initial ''default'' estimate of elevation when there is an absence of sufficient spectral information to generate a more accurate judgment. In their study, the subject responded with saccadic eye movements, where the saccade always originated from a location directly in front of the listener. In our study, the subject's head was constrained to face directly in front, which is near the center of the speaker array. It is thus possible that in our experiment, subjects were biased toward the center of the distribution when localization was difficult.

Although previous work suggests that elevation compression is not unexpected in these experiments, it is possible that ''edge effects,'' which refer to the influence of the limited spatial range of response choices available to the listener in this identification task, may contribute to the apparent compression in our study. The two studies discussed above (Hoffman and Van Opstal, 1998; MacPherson and Middlebrooks, 2000) used analog response methods which were effectively unconstrained at the edges.

If we assume here that a listener who localized a stimulus at a position outside the range of responses would choose the speaker nearest the perceived elevation, which would simply be the speaker at the appropriate edge of the response range, we would expect the standard deviation $\sigma[k]$ and the rms error $E[k]$ error to decrease toward the edge speakers since the spatial variance in the responses is rectified by the limited response range. In the data, $\sigma[k]$ is relatively constant across the speaker positions while $E[k]$ grows toward the edge speakers. Thus, the error statistics are not consistent with the hypothesis that the elevation compression is due solely to edge effects. We also note that Hofman and Van Opstal (1998) as well as Macpherson and Middlebrooks (2000) observed compression in elevation using paradigms where edge effects were likely not a factor.

In summary, the most notable features in the data described in the present study are the apparent compression in perceived elevation as well as the increased spatial variance in the responses, especially for the 1-ms duration. It was suggested that the compression may have been partly due to the stimuli themselves (duration dependent spectral variability) or to the response paradigm (edge effects).

IV. PRECEDENCE RESULTS AND DISCUSSION

A. Results

The single-speaker results provide a measure of baseline localization performance of stimuli at the six speaker locations for the four durations chosen. The results with precedence pairs can be compared directly with the single-speaker results as a means of investigating whether and how the location of the lagging noise burst influenced localization. In Fig. 5, results for the PE trials for subject S1 are shown using

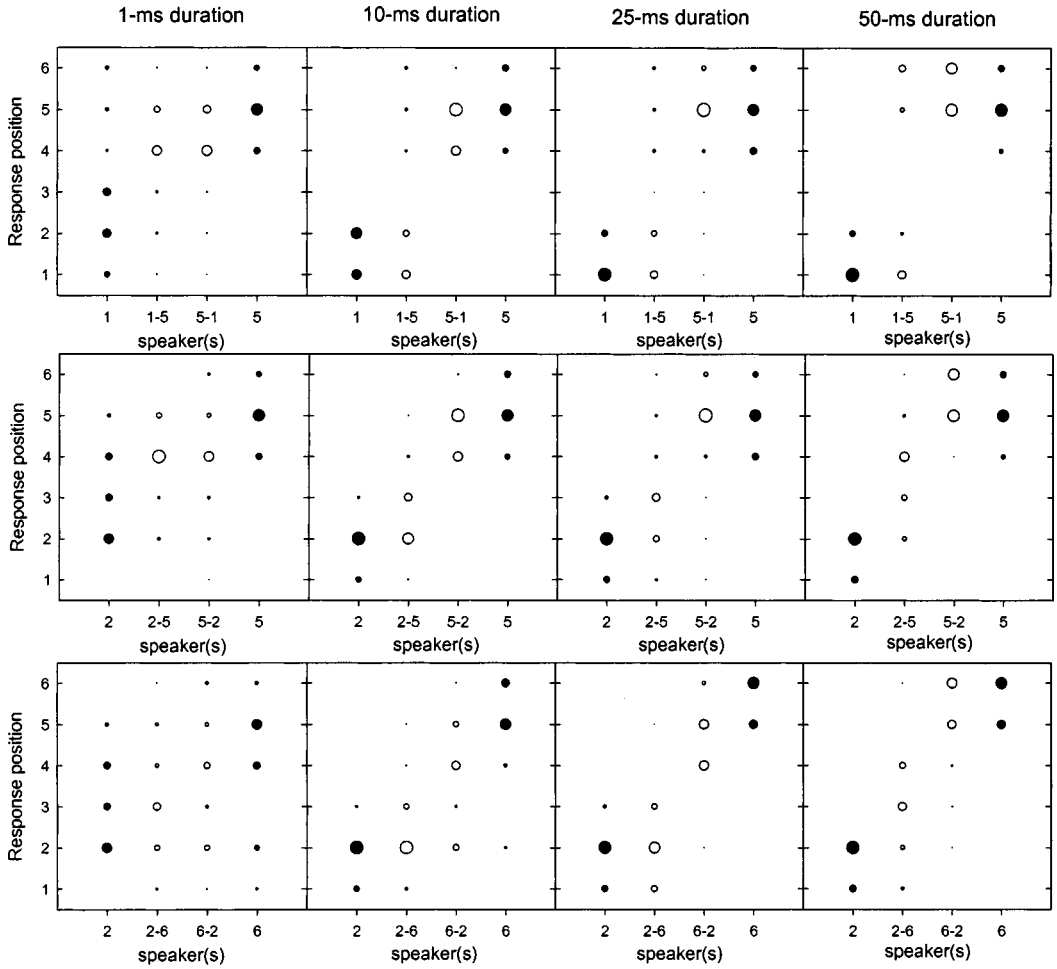

FIG. 5. Raw precedence data for subject S1. Each panel shows response distributions for a position pair and its swapped-speaker counterpart (open symbols), flanked by the single-speaker distributions for each of the speakers in the position pair (closed symbols). Each of the three rows contains data for the same position pair, while the four columns indicate the duration. As in Fig. 3, the area of the bubbles is proportional to the number of responses.

bubble plots similar to those used for the single-speaker data in Fig. 3. Each panel in Fig. 5 shows PE data for a single lead–lag combination, its swapped-pair counterpart, as well as the matching single-speaker results for the lead and lag positions. By comparing the perceived location on single-speaker trials (closed symbols) with that of the PE trials (open symbols) in which either the leading or lagging sources matched the single-speaker position, the extent of PE can be effectively visualized. If the PE is operating, then the distribution of perceived locations on PE trials should be similar to that of the single speaker condition matching the lead. It is important to consider the single-speaker data when viewing the PE data, since a certain amount of the variability and bias in performance should be common to the single-speaker and PE conditions. Certainly, one would not expect performance in the PE trials to be any better than that seen in the single-speaker trials.

In Fig. 5, each row of panels contains data for one lead–lag pair combination, one panel for each of the four durations. The three rows correspond to the three lead–lag pairs chosen (1-5, 2-5, and 2-6), as described in Sec. II. Figures 6–8 show the same data for subjects S2, S3, and S4, respectively.

Considering the data in Figs. 5–8, it should be evident qualitatively that while the localization dominance is not complete, in most conditions there is a clear bias in responses toward the speaker position corresponding to the leading speaker of each PE pair. However, this bias toward the leading speaker is in all cases not as strong as it is for the single-speaker response distribution for the leading speaker. It can be concluded from this difference in bias shifts that localization dominance is not complete, since absolute localization dominance predicts that the precedence stimuli would be localized identically with their single-speaker counterparts corresponding to the leading speaker location. In addition, subjects appear to be able to localize the single-speaker stimuli more precisely, with the exception of the 1-ms duration, where performance is generally poor for both single-speaker and precedence stimuli. Thus, it appears that the presence of the spatially separated lagging stimulus influences the variance in the responses for the combined lead–lag stimulus as well.

The influence of the lag on the shape of the response distributions is often not consistent across subjects for the same position and duration. For instance, for the 50-ms duration, position pair 1-5 response distribution for subject S1 (Fig. 5) is bimodal, while that of the other three subjects are not. For subject S3 (Fig. 7) at a duration of 50-ms, the re-

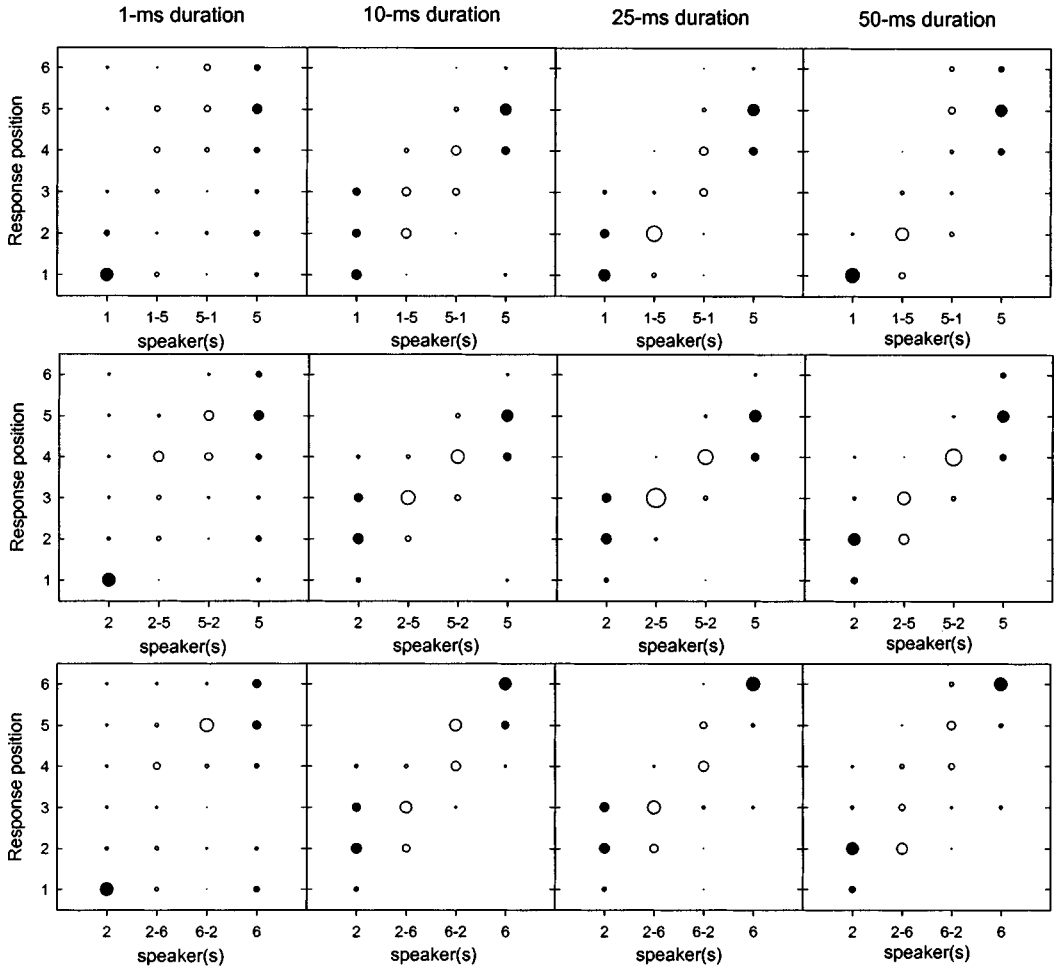

FIG. 6. Same as Fig. 5 but for subject S2.

sponse distribution for position pair 6-2 is clustered very close to position 6, while the response distribution for the swapped-speaker counterpart (2-6) is spread fairly evenly over the whole distribution range. The other three subjects did not exhibit this pattern of performance. Additionally, for the same subject and duration, the response distributions across the three position pairs can differ as well (consider subject S1 at the 50-ms duration).

As a comparison of localization precision between the single-speaker and PE trials, Fig. 9 shows the standard deviations of the response distributions for both single-speaker and PE trials as a function of duration. For each data point, data are averaged over all positions for the single-speaker data, and over all lead–lag pairs for the PE data. Precision appears to be better for the single-speaker trials than for the PE trials at the longer-duration stimuli, as evidenced by the higher standard deviations for the PE trials. Note also that while precision generally improves for single-speaker trials as duration is increased, there is little evidence of an influence of duration on precision for the PE trials, other than an increase in precision in S2's data going from 1 to 10-ms.

The extent of localization dominance in a paired setup can be quantified using a descriptive statistic (accounting for both localization dominance and discrimination suppression) proposed by Shinn-Cunningham (1993) for headphone data and validated for free-field data by Litovsky and Macmillan (1994). A single metric c is calculated, which is bounded between 0 and 1 and represents the extent of leading source localization dominance. It is calculated using the following formula:

$$c=(\alpha_p-\tau_2)/(\tau_1-\tau_2),$$

where α_p is the judged position (or ITD), and τ_1 and τ_2 are the lead and lag positions, respectively. The metric c will equal 1.0 for localization judgments at the leading position, 0.5 for judgments consistent with an equal contribution of lead and lag, and 0.0 for judgements at the lagging position. We extend this model to the median-sagittal plane by using the elevation of the lead and lag speaker positions in degrees for τ_1 and τ_2, and the elevation of the judgment in degrees for α_p.

A c value was computed for every trial at each lead–lag pair. The means are plotted in Fig. 10, with one subject's data in each panel. A thickened horizontal dashed line marking the point at which c equals 0.5 demarcates the boundary between lead dominance and lag dominance in localization. Data for all six of the lead–lag pairs are plotted in a group above the appropriate duration indicated on the x axis. The symbols indicate the lead–lag pair as indicated in the legend, and the error bars represent the standard deviation of c across the 30 trials.

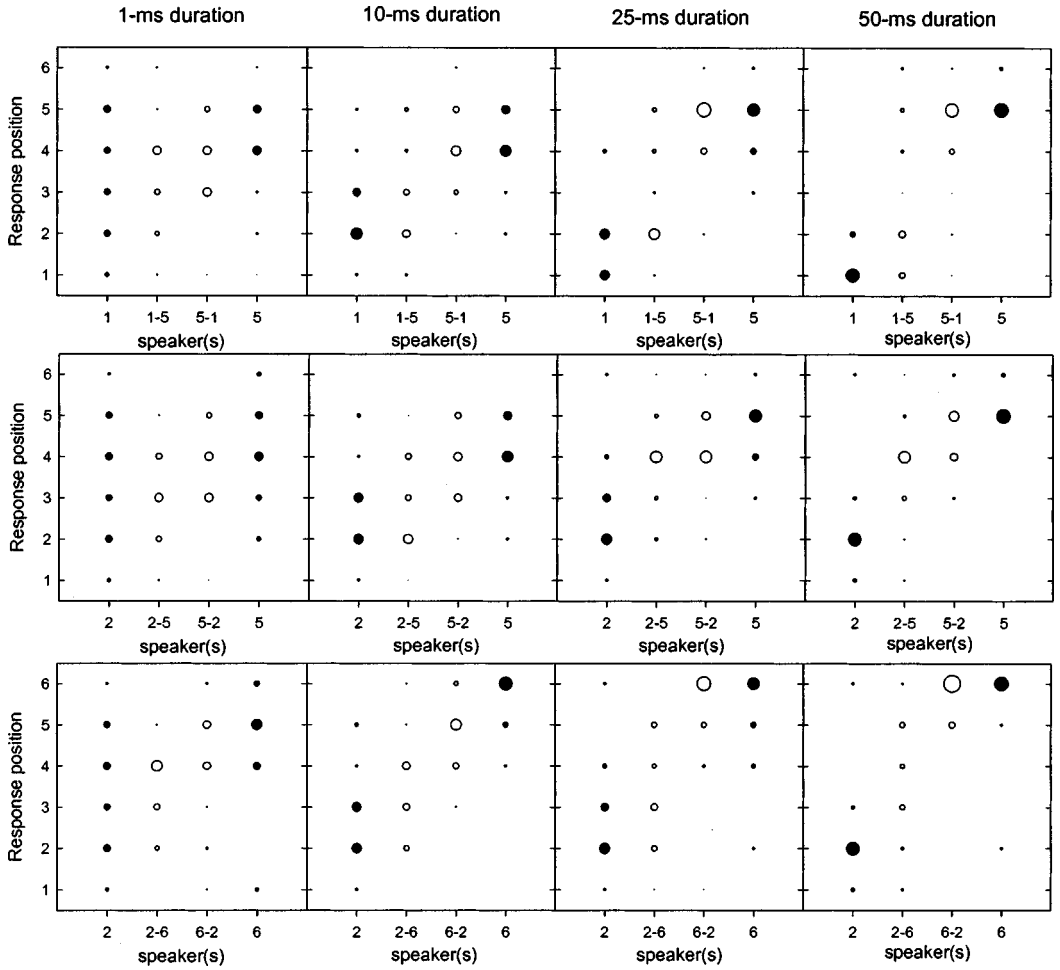

FIG. 7. Same as Fig. 5 but for subject S3.

A majority of the mean values of *c* are above 0.5, with a few close to 1. Note that it is possible for *c* to be above 1 or below 0 if the judgment is not within the range between the lead and lag positions. The standard deviations are quite high, indicating that subjects were not consistent across trials, and frequently localized nearer to the lagging stimulus. These observations on the mean and standard deviations are qualitatively consistent with the scatter plots in Figs. 5–8, which showed response distributions with a lot of spread but generally skewed toward the lead, especially at the longer durations.

Also interesting in Fig. 10 is the variation in *c* over the lead–lag pairs. For example, S3's data at 25 and 50-ms indicate higher *c* values when the lead is at high elevations (the open symbols) as compared to when the lead is low. This may indicate individual bias toward the higher elevations in this paradigm. Conversely, S4's data indicate the opposite, with lower elevations having higher *c* values.

The low means (near 0.5 to 0.7, rather than 1.0) and high variance in the *c* values highlights the fact that the PE is not as strong in the median plane as it is in the free-field azimuthal plane or when ITDs are used over headphones. In the study by Shinn-Cunningham *et al.* (1993) in which *c* values were computed for their own data as well as other studies on precedence using ITDs, *c* values typically reached close to unity (generally above 0.8) for delays near 2 ms. Similarly, Litovsky and Shinn-Cunningham (2001) reported average *c* values of 0.9–1.0 for localization dominance with ITDs at delays of 1 and 2-ms. In free field, Stecker and Hafter (2002) used a similar observer weighting method to estimate localization dominance for lead–lag click pairs, and reported values between 0.7 and 0.8 for delays of 1 to 3-ms.

A note of caution to observing the *c* values alone is that a high *c* value does not necessarily imply localization dominance in our analyses, since a high *c* value (>0.5) for a lead–lag pair combined with a low *c* value (<0.5) for the swapped pair counterpart can indicate a *positional dominance*, signifying a dominance of one elevation over another independent of which contained the leading stimulus. To see why this is the case, recall that when *c* equals zero, the subject localizes toward the lag. If *c* equals one for a lead–lag pair and zero for the swapped pair, then the subject localized both pairs at the same position. Thus, to more effectively gauge the strength of localization dominance, we must look at statistics that compare the response distribution of a lead–lag pair with that of its swapped-pair counterpart.

The following discussion focuses on statistical analyses comparing the responses to presentations of a lead–lag pair with those of its swapped-speaker counterpart. If localization dominance is not effective, then an appropriate statistical test should indicate that the two distributions are not statistically different. The two distributions could have any of the follow-

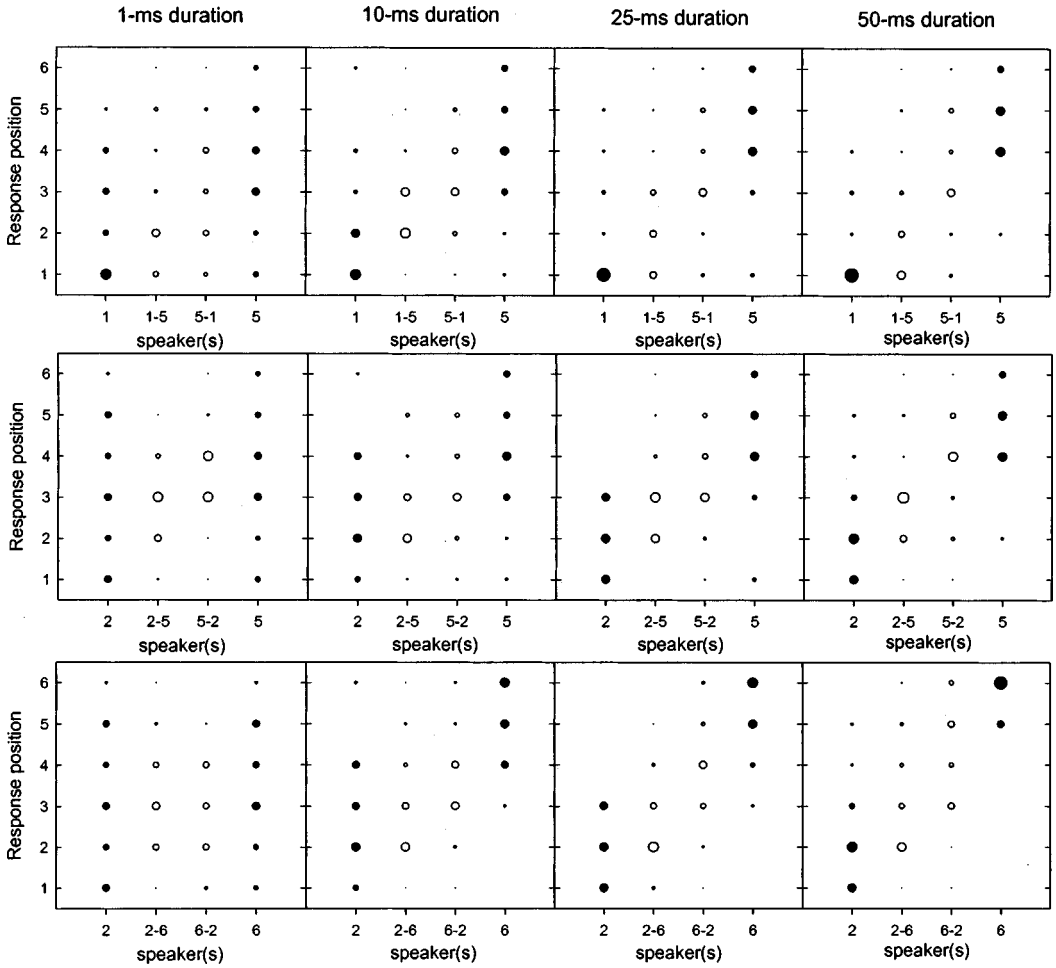

FIG. 8. Same as Fig. 5 but for subject S4.

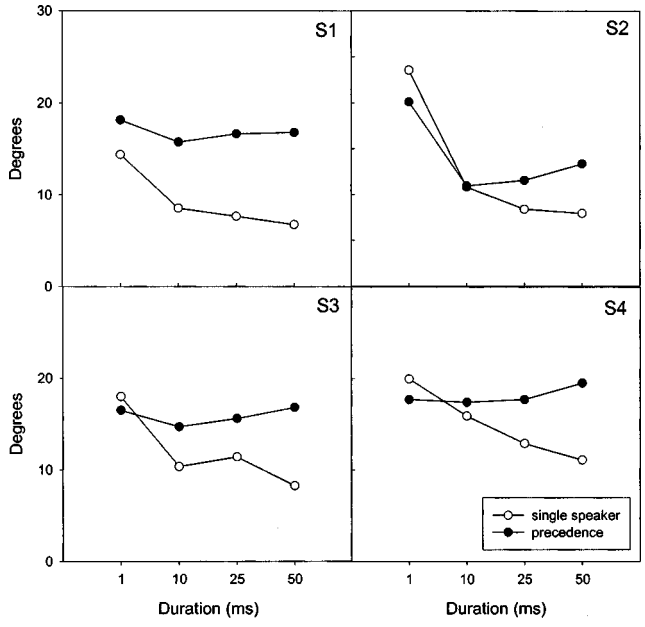

FIG. 9. Standard deviations of the responses for each subject in units of degrees. Each point represents the mean of the individual standard deviations across all positions (for the single-speaker trials) or position pairs (for the precedence trials). Closed symbols represent the precedence trials, open symbols the single-speaker trials.

ing configurations: (1) near one of the two locations, reflecting biased judgments, (2) bimodally distributed in the event that the lead and lag were both heard/localized, or (3) at a location between the lead and lag, in the event that both sounds contributed equally to localization.

A t-test was performed on the response distribution for a given lead–lag pair with that of its swapped-speaker counterpart. For example, for the combinations of 1-5 and 5-1 (stimuli at $-30°$ and $+30°$), a strong PE would produce distributions that were near location 1 for the 1-5 case and near location 5 for the 5-1 case. The generalized t-statistic for two distributions A and B is given by

$$t_{2N-2}=\frac{M_A-M_B}{\hat{\sigma}_{A,B}},$$

where $\hat{\sigma}_{A,B}$ is a pooled variance given by

$$\hat{\sigma}_{A,B}=\sqrt{\frac{\sigma_A^2+\sigma_B^2}{N}},$$

and where M_A, M_B, σ_A, and σ_B are the mean and standard deviations of the response distributions A and B.

We denote the mean of the distribution for a lead–lag pair as $M[k_1;k_2]$, where k_1 denotes the lead speaker number and k_2 the lag. $M[k_1,k_2]$ is given by

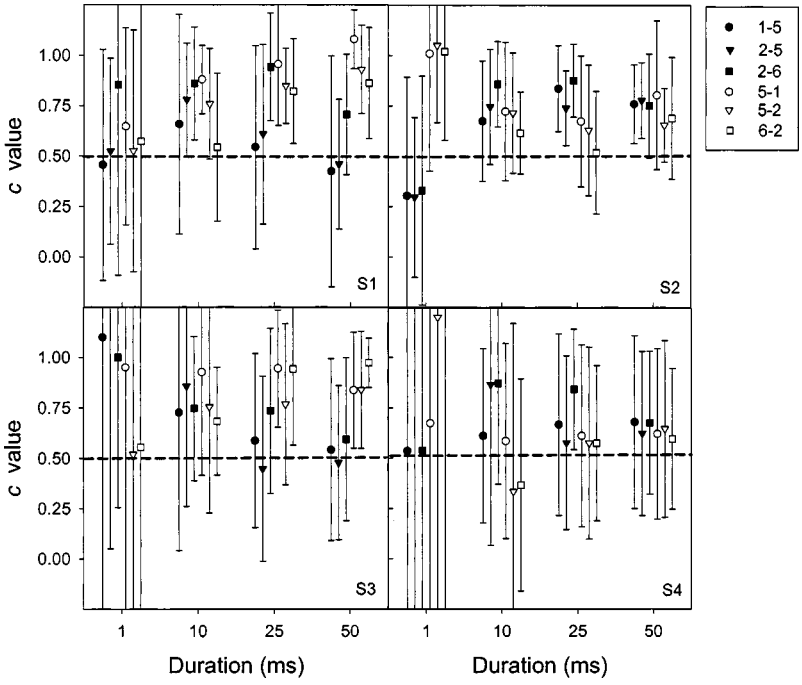

FIG. 10. c values computed as indicated in the text. Data represent the mean c value across the 30 trials at each position-pair and duration for each subject. Position pair is indicated by symbols defined in the legend. The error bars represent the standard deviation of the c across those 30 trials. Data are shown grouped above the duration indicated on the x axis, and are shifted laterally for clarity.

$$M[k_1,k_2]=\frac{A}{N}\sum_{n=1}^{N} r_{n,k_1,k_2},$$

where $r_{n,k1,k2}$=response to trial n when the leading sound was presented from speaker k_1 and the lagging sound was presented from speaker k_2. Similarly, $\sigma[k_1;k_2,k_2;k_1]$ denotes the pooled variance for the two swapped-pair distributions, and is given by

$$\hat{\sigma}[k_1;k_2,k_2;k_1]=\sqrt{\frac{\sigma^2[k_1;k_2]+\sigma^2[k_2;k_1]}{N}},$$

where

$$\sigma[k_1,k_2]=\sqrt{\frac{A^2}{N}\sum_{n=1}^{N}(r_{n,k_1,k_2}-M[k_1,k_2])^2}.$$

The t-statistic for the swapped-pair test is given by

$$t_{2N-2}=\frac{M[k_1;k_2]-M[k_2;k_1]}{\hat{\sigma}[k_1;k_2,k_2;k_1]}.$$

Note that this formulation of the t-statistic presumes that $M[k_1;k_2]>M[k_2;k_1]$ for the statistic to be positive. This requires the mean of each distribution to be biased toward the leading side *relative to the other mean*—a requirement that is consistent with localization dominance. This requirement held for all but one of the 48 statistics computed.

It is useful to compare the swapped-pair t-statistic with the "single–single" statistic, which is a t-test comparing the distributions of responses to each position presented in isolation. These distributions are available from the single-speaker trials. If localization dominance was complete, the leading source completely dominates the lag, so we would expect the statistic from the swapped pair comparison to be identical to the single–single statistic.

The t-statistic for the single–single test is given by

$$t_{2N-2}=\frac{M[k_1]-M[k_2]}{\hat{\sigma}[k_2,k_1]},$$

where $\sigma[k_1,k_2]$ is a pooled variance given by

$$\hat{\sigma}[k_2,k_1]=\sqrt{\frac{\sigma^2[k_2]+\sigma^2[k_1]}{N}}.$$

Figure 11 shows the t-statistic for the swapped-pair test on the y axis plotted against burst duration on the x axis for all four subjects (one in each panel). In each panel, the statistics for each of the three lead–lag pairs (open symbols) are

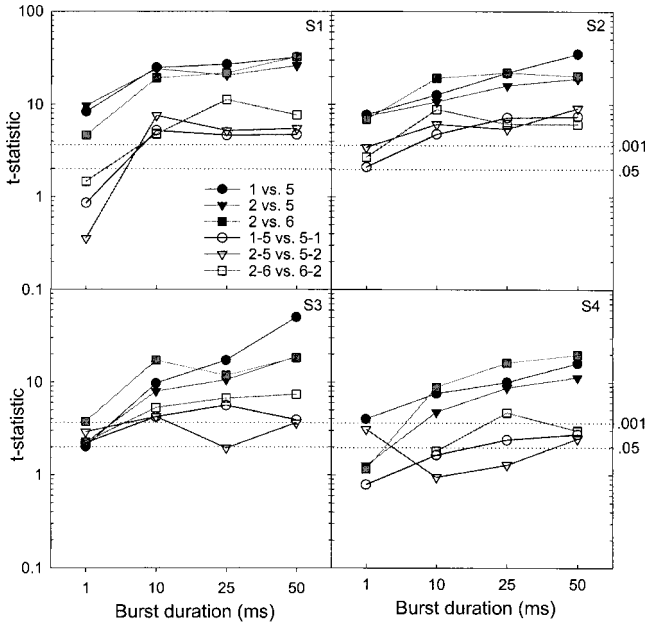

FIG. 11. t-statistics for both the precedence data (open symbols) and the single-speaker data (closed symbols). Symbols indicate position or position pair as shown in the legend. t-statistics for the 0.05 and 0.001 levels are shown as dashed lines.

shown along with those for the single–single comparison (closed symbols). Dashed horizontal lines are shown representing t-statistic values significant to the 0.05 and 0.001 levels. One value is not shown (S4, square symbol at 1-ms) since the means for the two distributions were biased toward the lag rather than the lead. The standard deviations of the response distributions were frequently very high for this stimulus, particularly for subject S4.

The single–single statistics are consistently higher than those for the swapped pairs. This indicates that either the mean shifts are larger for the single–single case, or the variance is smaller. It is notable, however, that the swapped-pair statistics are still highly significant. It is not surprising that the single–single statistics are high given the accuracy and precision of localization of the single-speaker stimuli (Fig. 3). However, the high significance of the swapped pair statistics is not as obvious from a qualitative view of the raw data in Figs. 5–8. The statistical results also suggest some dependence on duration, since the 1-ms statistics are lower for almost all cases. From 10 to 50-ms there is no clear trend in the swapped-pair statistics. It is likely that the higher variability in the responses to these stimuli makes any trends difficult to observe. There is also some inter-subject variation, with subjects S1 and S2 having generally higher statistics overall.

Overall, these analyses indicate that there is a statistically significant temporal order effect favoring the leading stimulus. Recall that this result was not obvious from the *c* values, which consider the distributions in isolation, rather than relative to each distribution's swapped speaker counterpart. Specifically, this means that the response distribution for a lead–lag pair is biased toward the leading stimulus relative to the distribution for its swapped-speaker counterpart. The distributions themselves may be both biased toward one position or another, they may differ in width, or one or both may have bimodal qualities. The raw data in Figs. 5–8 indicate that many of these cases occur. The t-statistics only indicate that the temporal order influences judgments in a manner consistent with localization dominance.

B. Discussion

This study was designed to find evidence for localization dominance in the median-sagittal plane. The two studies cited in Sec. I (Blauert, 1971 and Litovsky *et al.*, 1997a) indicated that certain aspects of precedence exist in the median-sagittal plane, but neither used as fine an elevation spacing as that used in the present study, nor did those studies investigate the influence of duration. The results of the present study are significant in that they are free of front/back confusions (as a result of the positions chosen). Also, they are compared to the single-speaker conditions, allowing the effects of precedence to be separated from localization phenomena related to the comb filtering. This comparison establishes a link between the single-speaker performance and PE performance. Specifically, if a stimulus comprised of a lag co-located with the lead cannot be localized accurately, then one cannot expect to find localization dominance when the lag is at a different location.

The reasons for the poor performance at 1-ms for both the single-speaker and precedence trials could include spectral variability in the short samples of noise, and also the comb filtering imparted by the presence of the lag. As noted in the Single Speaker Discussion (Sec III B), one might have expected the comb filtering to degrade localization for all durations, yet only the 1-ms duration performance is significantly degraded. Perhaps in the 1-ms case, both factors were responsible. The poor single-speaker performance at 1-ms leads logically to the weak evidence of localization dominance at this duration. Specifically, localization dominance of a leading source over a lagging source at a different location is not expected, given that the same stimulus but with the lag co-located with the lead could not be localized precisely.

The choice of positions enabled a better characterization of localization dominance in the median plane than had been shown in the literature. In the present study, both the lead and lag positions are localized accurately, yet the combination produces localization dominance. In the prior median plane studies, there was evidence that a strongly localizable location (front) dominated a weakly localizable location (above) (Litovsky *et al.*, 1997a). This ''positional dominance'' makes it difficult to observe the influence of localization dominance.

The use of longer duration noise bursts in the present study was shown to improve both the accuracy and the precision of single-speaker localization. This performance improvement was helpful for demonstrating statistically significant effects of localization dominance that may not be obvious with shorter duration stimuli. Overall, the results reaffirmed that localization dominance is effective in median plane localization. The results also indicate that the effect is weaker in the median plane as compared to its strength as reported in the azimuthal plane in other studies (e.g., Shinn-Cunningham *et al.*, 1993). Accompanying the present results are considerable inter-subject variability and evidence of positional dependence (variance in performance across position combinations), neither of which are typically as influential in azimuthally based PE experiments (e.g., Litovsky and Shinn-Cunningham, 2001; Saberi and Antonio, 2003).

The reason for weak localization dominance in the median plane is not entirely clear. Echo suppression (measure of whether the lag is heard as a separate sound) appears to be similar in strength in the azimuthal and median-sagittal planes, as measured with single-neuron responses (Litovsky *et al.*, 1997a; Litovsky and Yin, 1998a) or psychophysically (Litovsky *et al.*, 1997b; Rakerd *et al.*, 2000). Hence, it is difficult to argue that auditory mechanisms underlying suppression of echoes are generally weaker in the median plane. However, there is another aspect of the PE, discrimination suppression, which appears to be different in azimuth and elevation. Listeners' ability to discriminate small shifts in the vertical position of the lag is not compromised at any delays, but discrimination of small shifts in the azimuthal position is delay-dependent, being quite poor at brief delays and improving as delays are increased (Litovsky *et al.*, 1997b). Taken together, previous work along with findings from the present study suggest that, while at brief delays the lag may

not be subjectively audible, directional properties of the lead do not dominate (take precedence) over those of the lag as strongly in the median plane as they do in azimuth. Weaker dominance of directional cues might be due to the fact that in the median plane there is poorer spatial resolution for source locations than in azimuth. That is, the strength of localization dominance may be a by-product of localization accuracy in each plane.

Computational models of precedence in the azimuthal plane would be difficult to adapt to median plane data. Modeling of elevation localization for single sources is itself not well understood. Computations based on the actual received spectra using the subject's HRTFs as well as the actual noise samples may provide some insight into performance. However, if long term statistics are used, these are likely to bear little fruit in predicting precedence since long-term spectra (assuming that all operations are linear) will be the same if the leading and lagging positions are switched, whereas psychophysical performance clearly depends on which position is leading. More complex models incorporating peripheral nonlinearities (Hartung and Trahiotis, 2001), onset-driven suppression (Lindemann, 1986), or spectral weighting of interaural differences (Tollin, 1998) have shown some success in describing many aspects of azimuthally based precedence. To describe median plane precedence, all of these models would need to be modified to produce an elevation judgment, and may also require sensitivity to spectral profiles. On the other hand, if pinna disparity cues provide a usable cue to median plane localization (e.g., Middlebrooks, 1992; Hofman and Van Opstal, 2003), perhaps interaural difference models of precedence could predict median plane localization dominance as well.

V. CONCLUSIONS

The experiments presented here studied localization dominance in the median-sagittal plane. Localization of single sources in the median plane is mediated primarily by spectral cues, and localization performance in this plane is characterized by front–back confusions as well as high variability when compared to azimuthal localization. The single-speaker data provided a baseline measure of performance in the task using speaker positions in the frontal portion of the median-sagittal plane as a function of burst durations. These data indicated that stimulus duration has a big effect on the single-speaker localization, with longer durations leading to greater precision and less elevation compression. The precedence data were characterized by higher variability in the response distributions, but with a statistically significant bias toward the leading speaker for the longer burst duration conditions. Thus, the *c* values reported here, when compared with those of Shinn-Cunningham *et al.* (1993) are consistent with there being weaker localization dominance in the median-sagittal plane than in the azimuthal plane, not unlike the differences observed by Litovsky *et al.* (1997a).

Considering the precedence effect in general, the existence of localization dominance in the median plane indicates that it is a general phenomenon that applies to paired stimuli in (at least) a two-dimensional space, rather than being confined to the azimuthal dimension only. If one presumes that the phenomenon serves as a means of suppressing reflections, then it should not be surprising that it is a general spatial effect.

ACKNOWLEDGMENTS

The authors are extremely grateful to Dr. H. S. Colburn for numerous helpful discussions of the data and comments on previous versions of the manuscript, and to Gerald Ng for help and participation in earlier versions of these studies. This work was supported by NIH-NIDCD Grant Nos. R01-DC003083 and R01-00100. Portions of the data were presented at the 133rd and 139th Meetings of the Acoustical Society of America.

Blauert, J. (**1971**). ''Localization and the law of the first wavefront in the median plane,'' J. Acoust. Soc. Am. **50**, 466–470.

Blauert, J. (**1997**). *Spatial Hearing: The Psychophysics of Human Sound Localization*, Revised ed. (MIT, Cambridge, MA).

Butler, R. A. (**1969**). ''Monaural and binaural localization of noise bursts vertically in the median sagittal plane,'' J. Aud Res. **3**, 230–235.

Dizon, R., Litovsky, R. Y., and Colburn, H. S. (**1997**). ''Positional dependence on localization dominance in the median-sagittal plane,'' J. Acoust. Soc. Am. **101**, S3106.

Fitzpatrick, D. C., Kuwada, S., Batra, R., and Trahiotis, C. (**1995**). ''Neural responses to simple, simulated echoes in the auditory brainstem of the unanesthetized rabbit,'' J. Neurophysiol. **74**, 2469–2486.

Gardner, M. B., and Gardner, R. S. (**1973**). ''Problem of localization in the median plane: Effect of pinnae cavity occlusion,'' J. Acoust. Soc. Am. **53**, 400–408.

Hartmann, W. M. (**1983**). ''Localization of sound in rooms,'' J. Acoust. Soc. Am. **74**, 1380–1391.

Hartung, K., and Trahiotis, C. (**2001**). ''Peripheral auditory processing and investigations of the 'precedence effect' which utilize successive transient stimuli,'' J. Acoust. Soc. Am. **110**, 1505–1513.

Hebrank, J., and Wright, D. (**1974**). ''Spectral cues used in the localization of sound sources on the median plane,'' J. Acoust. Soc. Am. **56**, 1829–1834.

Hofman, P. M., and Van Opstal, A. J. (**1998**). ''Spectro-temporal factors in two-dimensional human sound localization,'' J. Acoust. Soc. Am. **103**, 2634–2648.

Hofman, P. M., and Van Opstal, A. J. (**2003**). ''Binaural weighting of pinna cues in human sound localization,'' Exp. Brain Res. **148**, 458–470.

Lindemann, W. (**1986**). ''Extension of a binaural cross-correlation model by contralateral inhibition. II. The law of the first wavefront,'' J. Acoust. Soc. Am. **80**, 1623–1630.

Litovsky, R. Y., Colburn, H. S., Yost, W. A., and Guzman, S. (**1999**). ''The precedence effect,'' J. Acoust. Soc. Am. **106**, 1633–1654.

Litovsky, R. Y., Hawley, M. L., Dizon, R., and Colburn, H. S. (**1997b**). ''Measurements of precedence phenomena in binaural and monaural conditions,'' J. Acoust. Soc. Am. **101**, S3083.

Litovsky, R., and Macmillan, N. (**1994**). ''Minimum auditory angle for clicks with simulated echoes: Effects of azimuth and standard,'' J. Acoust. Soc. Am. **96**, 752–758.

Litovsky, R. Y., and Yin, T. C. T. (**1998a**). ''Physiological studies of the precedence effect in the inferior colliculus of the cat. I. Correlates of psychophysics,'' J. Neurophysiol. **80**, 1285–1301.

Litovsky, R. Y., and Yin, T. C. T. (**1998b**). ''Physiological studies of the precedence effect in the inferior colliculus of the cat. II. Neural Mechanisms,'' J. Neurophysiol. **80**, 1302–1316.

Litovsky, R. Y., Yin, T. C. T., Rakerd, B., and Hartmann, W. M. (**1997a**). ''Psychophysical and physiological evidence for a precedence effect in the median sagittal plane,'' J. Neurophys. Rapid Communication **77**, 2223–2226.

Litovsky, R. Y. and Shinn-Cunningham, B. G. (**2001**). ''Investigation of the relationship among three common measures of precedence: fusion, localization dominance, and discrimination suppression,'' J. Acoust. Soc. Am. **109**, 346–358.

Macpherson, E. A., and Middlebrooks, J. C. (**2000**). ''Localization of brief

sounds: Effects of level and background noise,'' J. Acoust. Soc. Am. **108**, 1834–1849.
Middlebrooks, J. C. (**1992**). ''Narrow-band sound localization related to external ear acoustics,'' J. Acoust. Soc. Am. **92**, 2607–2607.
Middlebrooks, J. C., and Green, D. M. (**1991**). ''Sound localization by human listeners,'' Annu. Rev. Psychol. **42**, 135–159.
Rakerd, B., Hartman, W. M., and Hsu, J. (**2000**). ''Echo suppression in the horizontal and median sagittal planes,'' J. Acoust. Soc. Am. **107**, 1061–1064.
Saberi, K. and Antonio, J. V. (**2003**). ''Precedence-effect thresholds for a population of untrained listeners as a function of stimulus intensity and interclick interval,'' J. Acoust. Soc. Am. **114**, 420–429.
Searle, C. L., Braida, L. D., Cuddy, D. R., and Davis, M. F. (**1975**). ''Binaural pinna disparity: Another auditory localization cue,'' J. Acoust. Soc. Am. **57**, 448–455.
Shinn-Cunningham, B. G., Zurek, P. M., and Durlach, N. I. (**1993**). ''Adjustment and discrimination measurements of the precedence effect,'' J. Acoust. Soc. Am. **93**, 2923–2932.
Stecker, G. C. and Hafter, E. R. (**2002**). ''Temporal weighting in sound localization,'' J. Acoust. Soc. Am. **112**, 1046–1057.
Tollin, D. J. (**1998**). ''Computational model of the lateralisation of clicks and their echoes,'' in ''Proceedings of the NATO Advanced Study Institute on Computational Hearing,'' edited by S. Greenberg and M. Slaney, I-Lucca, Italy, 1–12 July, 1998, pp. 77–82.
Wallach, H., Newman, E. B., and Rosenzweig, M. R. (**1949**). ''The precedence effect in sound localization,'' Am. J. Psychol. **LXII**, 315–336.
Wightman, F. L., and Kistler, D. J. (1997). ''Factors affecting the relative salience of sound localization cues,'' in *Binaural and Spatial Hearing in Real and Virtual Environments*, edited by R. H. Gilkey and T. R. Anderson (Earlbaum, Mahwah, NJ).
Yin, T. C. T. (**1994**). ''Physiological correlates of the precedence effect and summing localization in the inferior colliculus of the cat,'' J. Neurosci. **14**, 5170–5186.
Zurek, P. M. (**1980**). ''The precedence effect and its possible role in the avoidance of interaural ambiguities,'' J. Acoust. Soc. Am. **67**, 952–964.

Sensitivity to interaural intensitive disparities: Listeners' use of potential cues

Leslie R. Bernstein[a)]
Departments of Neuroscience and Surgery (Otolaryngology), University of Connecticut Health Center, Farmington, Connecticut 06030

(Received 24 July 2003; accepted for publication 8 March 2004)

Thresholds for interaural intensitive disparities (IIDs) for a 500-Hz tone were measured in several stimulus conditions including those in which the use of intracranial position as a cue was effectively eliminated by roving the *interaural temporal disparity* of the stimuli. Removing position as a cue resulted in substantial degradation of sensitivity to IID. The overall patterning of the data suggests that threshold-IIDs measured in standard binaural paradigms that yield fused intracranial images reflect the use of changes in intracranial position. That is, comparisons among the data suggest that listeners' judgments depend upon binaural spatial cues and not on comparisons of the concomitant monaural increments and decrements in level, per se, that inevitably result from the imposition of IIDs. © *2004 Acoustical Society of America.* [DOI: 10.1121/1.1719025]

PACS numbers: 43.66.Pn, 43.66.Ba [AK] Pages: 3156–3160

I. INTRODUCTION

Much of what is known about how and how well human listeners process interaural temporal disparities (ITDs) and interaural intensitive disparities (IIDs) has been gleaned from investigations in which the sounds have been presented via earphones (for reviews, see Durlach and Colburn, 1978 and Hafter and Trahiotis, 1997). If identical stimuli are presented to each ear in this fashion, the perception is of a single fused ''auditory image'' that is perceived to be located within the head (i.e., *intracranially*) and near midline. The introduction of ITDs or IIDs can result in the intracranial position of the sound being perceived as displaced, or *lateralized*, toward the ear at which the physical waveform either leads in time or is more intense.

The focus of this report is on the resolution of IIDs. A number of investigators have measured listeners' sensitivities to changes in IID as a function of several parameters of the stimuli including center frequency, bandwidth, interaural coherence, baseline overall level, baseline ITD, and/or baseline IID (e.g., Domnitz, 1973; Domnitz and Colburn, 1977; Hafter *et al.* 1977; Grantham and Ahlstrom, 1982; Nuetzel, 1982; Grantham, 1984; Yost and Dye, 1988).

Despite these efforts, it remains unclear whether and to what degree listeners' threshold-IIDs reflect their use of a binaural spatial cue, i.e., changes in the lateral position of intracranial images or, instead, reflect their use of strictly monaural cues. This is so because the imposition of an IID, besides potentially changing lateral position, necessarily produces a change of intensity at one or both ears. This results in there being at least three potential manners by which listeners could resolve IIDs. One way would be to attend to changes in the intracranial position of the acoustic image, a binaural cue referred to here as the *position cue*. A second way would be to attend to changes in intensity (increments or decrements) that occur in one or both ears. That is, the listeners could attend to changes in intensity occurring at *one ear* or to changes in intensity occurring at *each ear*, considered as independent channels. Depending upon the method used to produce the IID, an increment may be presented at one ear, a decrement may be presented at one ear, or there may be a combination of increments and decrements at the ears. All of these types of monaural cues are referred to here as *single-ear cues*. It should be noted that if an IID is imposed via symmetric (up in one ear and down at the other) changes in level across the ears, then another potential cue, a change in binaural loudness, is rendered ineffective for IIDs$\leq$about 10 dB (Keene, 1972; Domnitz and Colburn, 1977).

In an attempt to limit the confounding use of single-ear cues, some investigators have followed Leshowitz *et al.* (1974) and measured threshold-IIDs while ''roving'' the overall level of the stimuli. Given a sufficiently large range over which the intensities of the stimuli are roved, one can partition the measured threshold-IIDs into two regions: those that are so large that performance could be attributable to monaural changes in intensity and those that are so small that the monaural changes available are insufficient to explain performance (e.g., Nuetzel, 1982; Grantham, 1984; Hartmann and Constan, 2002).

While roving the levels of the stimuli can allow one to preclude the use of single-ear cues as the basis for threshold-IIDs, the listener could still solve the task by yet a third strategy. Logically, the listener could solve the task by somehow comparing *independent* measures of the level of the stimuli that are simultaneously present at each ear. This potential cue is referred to here as the *monaural difference cue*. For the purposes of this report, it is important to note that both the monaural difference cues and the single-ear cues could, logically, be used to solve the IID-task in the absence of any fused binaural image and in the absence of any informative changes in lateral position.

Taking all of the above into consideration, when threshold-IIDs are measured in the absence of roving overall

a)Electronic mail: les@neuron.uchc.edu

 0001-4966/2004/115(6)/3156/5/$20.00 © 2004 Acoustical Society of America

level, the listener would have available the position cue, the single-ear cue(s), and the monaural difference cue. Roving overall level can eliminate the use of the single-ear cue(s), but would leave available both the position cue and the monaural difference cue. The purpose of this study was to measure threshold-IIDs in several stimulus conditions including those in which the position cue was effectively eliminated by roving the *ITD* of the stimuli. It will be seen that removing the position cue produced substantial degradation of sensitivity to IID. That result, taken together with other comparisons among the data, suggests that threshold-IIDs, as typically measured, do, indeed, reflect the use of the binaurally based position cue, and not the use of single-ear cue(s) and/or the monaural difference cue.

II. EXPERIMENT

A. Procedure

Two monaural conditions and four binaural conditions were employed. In the monaural conditions, the listeners' task was to detect an increment in the intensity of a 500-Hz tone. Thresholds were measured separately for the left and right ears. In the binaural conditions, the listener's task was to detect the presence of an IID imposed on a 500-Hz tone. The IID was always produced by altering the level of the tone across the ears symmetrically (up in the left ear and down at the right) by IID/2. Imposing the IID in this manner precluded the use of binaural changes in loudness as cues to the presence of the IID (e.g., Keene, 1972; Domnitz and Colburn, 1977).

In the ''No Rove,'' binaural condition, neither the overall level nor the ITD was roved. Thus, based on the discussion in the previous section, three types of cues were available to the listener: single-ear, position, and monaural difference.

In the ''Level Rove'' binaural condition, the overall level of the 500-Hz tone at both ears was chosen randomly, on each presentation, within and across trials, from a range of 10 dB (1.0 dB steps). Roving the overall level in this manner effectively eliminated the single-ear cues, leaving the position and monaural difference cues as potential bases on which to detect the IID.

In the ''ITD Rove'' binaural condition, the ITD of the 500-Hz tone was chosen randomly, on each presentation, within and across trials, from a range of ± 400 μs (5-μs steps). Roving the ITD in this manner effectively eliminated the position cue, leaving the single-ear and monaural difference cues as potential bases on which to detect the IID.

Finally, in the ''ITD/Level Rove'' condition, both overall level and ITD were roved on each and every presentation in the manners described above. This effectively eliminated both the single-ear and position cues, leaving the monaural difference cue as a potential basis on which to solve the task.

For all conditions, 500-Hz tones were presented for 300 ms (including 20-ms $\cos^2$ rise-decay ramps). The tones were generated digitally with a sampling rate of 20 kHz (TDT array processor). Subsequent to digital-to-analog conversion (TDT Power-DAC), the stimuli were low-pass filtered at 8.5 kHz (TDT FLT2) and presented via TDH-39 earphones to listeners seated in single-walled, IAC booths. The overall level of the tones (prior to the imposition of an increment, IID, or rove) was 70 dB SPL.

Thresholds were determined using a two-cue, two-alternative, temporal forced choice adaptive task (see Bernstein and Trahiotis, 1982). Each trial consisted of a warning interval (500 ms) and four 300-ms observation intervals separated by 400 ms. Each interval was marked visually on a computer monitor. Correct-answer feedback, which was based on the interval containing the increment (monaural conditions) or the interval containing the nonzero IID (binaural conditions), was provided for approximately 400 ms following the listener's response. The stimuli in the first and fourth intervals served as ''cues.'' For the monaural conditions, the cues were 500-Hz tones presented at the ''standard'' level of 70 dB SPL. For the binaural conditions, the cues were 500-Hz tones presented with an IID of 0 dB. The ''signal'' to be detected (an increase of level in the monaural conditions, an IID in the binaural conditions) was presented either in the second or the third interval with equal *a priori* probability. The nonsignal interval, like the first and fourth ''cueing'' intervals contained an IID of 0 dB. When roving conditions were employed, the rove was applied independently and in the same manner to all four intervals. The size of the signal was varied adaptively in order to estimate 71% correct (Levitt, 1971). The step sizes within the adaptive track depended upon the size of the signal. Prior to the second reversal, if the size of the signal was $\geqslant$3 dB, then the step size was 1.0 dB; if the size of the signal was between 1 and 3 dB, then the step size was 0.5 dB; if the size of the signal was $<$1 dB, then the step size was 0.2 dB. Following the second reversal, the step sizes were reduced to 0.5, 0.2, and 0.1 dB, respectively. A run was terminated after 12 reversals and ''threshold'' was defined as the mean value of the signal (an increase of level in the monaural conditions, an IID in the binaural conditions) across the last ten reversals.

Five normal-hearing young-adults served as listeners. For each listener, three consecutive thresholds were first obtained in the left-ear and then in the right-ear monaural conditions. Then, three thresholds were obtained from each listener, sequentially, in the No Rove, Level Rove, and ITD Rove conditions. The ordering of conditions was then reversed and three more thresholds were obtained for each listener. This process was repeated until each listener's performance became asymptotic. Typically, this required measuring about 12 thresholds per listener per condition. Thresholds in the ITD/Level Rove condition were measured subsequent to those in the other conditions because the need for them became apparent as this report was being prepared.

The adaptive tracks corresponding to the final two sets of three thresholds for each combination of listener and condition were examined. Any set of three thresholds that contained an adaptive track with a standard deviation larger than 0.75 dB was discarded and new sets of three thresholds were measured until all the standard deviations for all three adaptive tracks were $\leqslant$ 0.75 dB. Such ''re-runs'' proved to be necessary for only the ITD Rove and ITD/Level Rove conditions. The final estimate of threshold for each combination

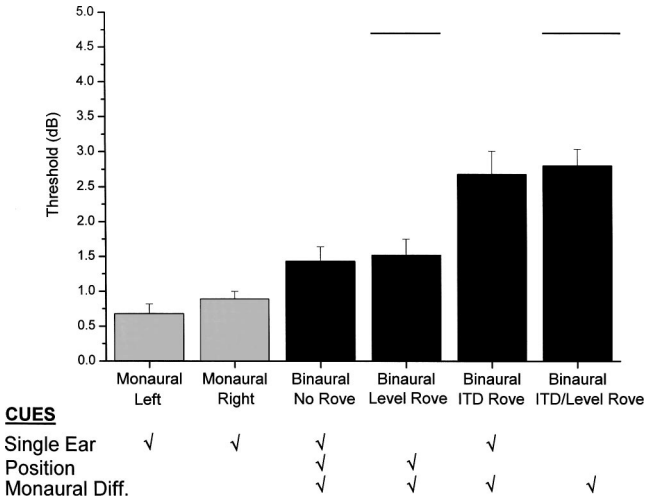

FIG. 1. Mean thresholds, in dB, computed across the five listeners in the six experimental conditions. Error bars indicate the standard error of the mean. Thresholds for the two monaural conditions (leftmost pair of bars) represent the increase in level at threshold ($10\log(I+\Delta I)-10\log I$). Thresholds for the binaural conditions (remaining four bars) represent IIDs ($10\log(I+\Delta I/2)-10\log(I-\Delta I/2)$). The horizontal line plotted above the fourth and sixth bars from the left represents the IID that would have to be imposed in order for an ideal observer to achieve 71% correct if decisions were based solely on the increment in level available at one ear. The types of cues available (i.e., position, single-ear, monaural difference) to the listener in each of the six stimulus conditions are indicated below the abscissa by check marks.

of listener and condition was computed as the average of the last six accepted measurements.

B. Results and discussion

Because the patterning of the data was highly similar across the five listeners, the mean thresholds are representative and only they are displayed in Fig. 1. The error bars indicate the standard error of the mean computed across the five estimates of threshold, one being provided by each listener. The thresholds for the two monaural conditions (leftmost pair of bars) are plotted as the difference in decibels between the level required to detect the increment and the level of the standard (i.e., $10\log(I+\Delta I)-10\log I$). The remaining four bars represent the threshold-IIDs obtained in the binaural conditions. They represent the difference in decibels between the level at the left ear and the level at the right ear (i.e., $10\log(I+\Delta I/2)-10\log(I-\Delta I/2)$). The horizontal line plotted above the fourth and sixth bars from the left represents the IID that would have to be imposed in order for an ideal observer to achieve 71% correct if the decisions were based solely on the increment in level available at one ear (e.g., Green, 1988; Hartmann and Constan, 2002). The types of cues available (i.e., position, single-ear, monaural difference) to the listener in each of the six stimulus conditions are indicated below the abscissa by checkmarks.

Beginning with the two monaural conditions (left-most pair of bars), the mean thresholds obtained were essentially identical, being 0.7 dB for the left ear and 0.9 dB for the right ear. The mean threshold-IID obtained in the binaural condition with no rove was 1.4 dB. As indicated in the figure, this is the only condition in which all three types of cues were available. This threshold-IID of 1.4 dB was produced by imposing an increment and a decrement of 0.7 dB in the left and right ears, respectively. Therefore in the binaural No Rove condition, there was a sufficient increment in level at the left ear to support threshold performance. Note that thresholds in these three ''baseline'' conditions are consistent with those obtained in earlier studies (e.g., Hafter *et al.*, 1977; Jesteadt and Wier, 1977; Grantham, 1984; Bernstein *et al.*, 1998).

Roving the levels of the stimuli in the binaural Level Rove condition (fourth bar from the left) resulted in a threshold-IID of 1.5 dB, a value essentially unchanged from that obtained in the binaural No Rove condition (third bar from the left). This outcome indicates that performance in the binaural No Rove condition was *not* based on a single-ear cue. If listeners had relied solely on the single-ear cue, then roving the overall level of the stimuli by ± 5 dB would have degraded performance and led to a threshold-IID of at least 4.7 dB, as indicated by the solid line above the bar representing threshold in the binaural Level Rove condition. As described earlier, that is the value that would have to be imposed in order for the listener to achieve threshold performance if the decisions were based solely on the increment in level available at one ear. Alternatively, if performance were based on an optimal combination of single-ear cues and if sensitivity to increments and decrements were equal, then, following Jesteadt and Wier (1977), one would expect a threshold-IID 3.7 dB. Neither of these outcomes occurred. Therefore, it seems reasonable to infer that single-ear cue(s) did not mediate performance in the binaural No Rove task.

On the other hand, roving the ITD, the manipulation of principal interest in this experiment because it can render ineffective the position cue, led to a threshold-IID of 2.7 dB (fifth bar from the left). Assuming an ITD/IID ''trading ratio'' at 500 Hz of between 20 and 40 μs/dB (see Table I of Trahiotis and Kappauf, 1978), then one can compute the IID necessary to overcome the randomly occurring changes in intracranial position produced by the ± 400 μs rove of ITD. The assumption of a particular trading ratio, taken together with the optimal processing scheme described earlier, leads to the conclusion that listeners would require an IID between 4.7 and 9.4 dB in order to reach threshold. Clearly, the *measured* threshold-IID of 2.7 dB would not produce a sufficient change in lateral position to overcome the effects of roving the ITD.

The crucial observation is that, when ITD is roved, so that the *position cue* is rendered ineffective, threshold-IIDs become much larger than those obtained in the binaural No Rove condition and much larger than those obtained in the binaural condition in which the overall level was roved. These findings suggest that the position cue *is* a primary determiner of threshold-IID in both the No Rove and Level Rove conditions and that the monaural difference cue, which was available in all three binaural conditions discussed so far, *is not* a primary determiner of threshold-IID. If it were, then threshold-IIDs measured with roving ITDs would be expected to be as small as those measured in the No Rove and Level Rove conditions. This is so because the monaural

difference cue relies only on a comparison of the average level computed at each ear. As discussed explicitly by Hartmann and Constan (2002), who measured threshold-IIDs with diotic, interaurally phase-reversed, and interaurally uncorrelated noises, such measurements of level at each ear would be made independently of the measurements at the other ear and would not stem from, and would not be affected by, the imposition of an ITD.

Finally, it is important to evaluate the potential use of single-ear cues in the ITD Rove condition. Those cues, like the monaural difference cue, would be unaffected by roving the ITD. Were the listeners able to make use of single-ear cues (i.e., increments or decrements occurring at one ear), their threshold-IIDs in the ITD Rove condition would be expected to be about 1.4 dB, a value commensurate with the threshold increment of 0.7 dB that was measured in the monaural stimulus conditions. Instead, the threshold-IID measured in the ITD Rove condition was 2.7 dB. This means that, at threshold, there were increments and decrements of 1.35 dB in the left and right ears, respectively. Those increments are essentially twice the 0.7 dB increments (decrements) in level required in the monaural stimulus condition. Therefore, it appears that even when it would be advantageous for the listener to use the single-ear cue, as in the roving ITD stimulus condition, listeners either cannot use single-ear cues or do so in a manner that yields substantially elevated threshold-IIDs. On the other hand, as indicated in the figure, the listeners could have solved the task by using the monaural difference cue. That possibility was explored by investigating one more stimulus condition.

After the main experiment was completed, threshold-IIDs were obtained while roving *both* ITD and overall level. This was done to determine how well listeners could perform the task when both the position cue and the single-ear cue were rendered ineffective, leaving the monaural difference cue as a potential mediator of performance. The right-most bar indicates that threshold-IIDs in this condition were 2.8 dB, essentially identical to those measured in the ITD Rove condition, an outcome consistent with the use of the monaural difference cue in both ITD Rove and the additional ITD/Level Rove conditions.

It is also possible that listeners may have, at least in part, based their decisions on a binaural spatial cue in the ITD Rove and ITD/Level Rove conditions. Specifically, listeners may have utilized changes in the perceived width/diffuseness of intracranial images produced by incongruent combinations of ITDs and IIDs often produced in those two stimulus conditions (see Domnitz, 1973, p. 1550 and Gaik, 1993). The potential use of such a cue in those two stimulus conditions is supported by the listeners' statements that they felt that they could determine which interval contained the IID by choosing the one containing the ''wider'' intracranial image. At this time, the use of such cues is presented as conjecture because independent control and measurement of perceived width/diffuseness was well beyond the scope of this investigation.

III. GENERAL DISCUSSION AND CONCLUSIONS

Threshold-IIDs were measured in several stimulus conditions including those in which the use of lateral position as a cue was effectively eliminated by roving the ITD of the stimuli. Removing lateral position as a cue resulted in substantial degradations of sensitivity to IID. That result, taken together with other comparisons among the data, suggests that threshold-IIDs, as typically measured in standard binaural paradigms (in which ITD is not roved), do, indeed, reflect the use of changes in the intracranial position of fused, binaural auditory images. In such paradigms, it appears that neither the monaural increments and decrements in level nor the monaural difference cues that are concomitant with the imposition of an IID are utilized.

This is not to say that single-ear cues and/or monaural difference cues are only utilized or utilizable when ITD is roved while measuring threshold-IIDs. For example, at the 103rd meeting of the Acoustical Society of America, Nuetzel (1982) reported that threshold-IIDs were fairly constant, independent of whether the ''standard'' stimuli presented to the two ears were interaurally correlated noises (i.e., diotic), interaurally uncorrelated noises, diotic tones, interaurally phase-reversed tones, or tones differing interaurally in frequency by over half an octave. Similar results were reported at the same meeting by Grantham and Ahlstrom (1982), who employed interaurally correlated and uncorrelated narrowband and wideband noises. More recently, Hartmann and Constan (2002) measured threshold-IIDs with interaurally uncorrelated noises and obtained data consistent with the earlier two studies.

In summary, the experiments and analyses reported here suggest that when threshold-IIDs are measured in standard binaural paradigms with stimuli that produce fused, auditory images, listeners' judgments appear to be based upon changes in the position of intracranial images and not on changes in single-ear cues or monaural difference cues. This appears to be so even under conditions for which it would be advantageous for listeners to attend to single-ear cues. For stimuli that do not foster fused, acoustic images and for which position cues are unavailable or impoverished, listeners may rely upon single-ear and/or monaural difference cues.

ACKNOWLEDGMENTS

The author wishes to thank Dr. Constantine Trahiotis for many valuable insights, points of view, and suggestions shared during extended discussions during the preparation of the manuscript. Dr. Tom Buell and Miles Paterson provided several valuable comments on an earlier draft of the manuscript. The author also thanks Dr. Armin Kohlrausch and Dr. Wes Grantham and two anonymous reviewers for their helpful comments. This research was supported by research Grant Nos. NIH DC-04073 and DC-04147 from the National Institute on Deafness and Other Communication Disorders, National Institutes of Health.

Bernstein, L. R., and Trahiotis, C. (**1982**). ''Detection of interaural delay in high frequency noise,'' J. Acoust. Soc. Am. **71**, 147–152.

Bernstein, L. R., Trahiotis, C., and Hyde, E. L. (**1998**). ''Inter-individual differences in binaural detection of low-frequency or high-frequency tonal signals masked by narrow-band or broadband noise,'' J. Acoust. Soc. Am. **103**, 2069–2078.
Domnitz, R. (**1973**). ''The interaural time JND as a simultaneous function of interaural time and interaural amplitude,'' J. Acoust. Soc. Am. **53**, 1549–1552.
Domnitz, R. H., and Colburn, H. S. (**1977**). ''Lateral position and interaural discrimination,'' J. Acoust. Soc. Am. **61**, 1586–1598.
Durlach, N. I. and Colburn, H. S. (**1978**). ''Binaural phenomena,'' in *Hearing*, Handbook of Perception, Vol. IV, edited by E. C. Carterette and M. P. Friedman (Academic, New York).
Gaik, W. (**1993**). ''Combined evaluation of interaural time and intensity differences: Psychoacoustic results and computer modeling,'' J. Acoust. Soc. Am. **94**, 98–110.
Grantham, D. W. (**1984**). ''Interaural intensity discrimination: Insensitivity at 1000 Hz,'' J. Acoust. Soc. Am. **75**, 1191–1194.
Grantham, D. W., and Ahlstrom, J. B. (**1982**). ''Interaural intensity discrimination of noise as a function of center frequency, duration, and interaural correlation,'' J. Acoust. Soc. Am. Suppl. 1 **71**, S86.
Green, D. M. (**1988**). *Profile Analysis* (Oxford University Press, New York).
Hafter, E. R., Dye, R. H., Nuetzel, J. M., and Aronow, H. (**1977**). ''Difference thresholds for interaural intensity,'' J. Acoust. Soc. Am. **61**, 829–834.
Hafter, E. R., and Trahiotis, C. (**1997**). ''Functions of the binaural system,'' in *Encyclopedia of Acoustics*, edited by M. Crocker (Wiley, New York), Vol. I.
Hartmann, W. M., and Constan, Z. A. (**2002**). ''Interaural level differences and the level-meter model,'' J. Acoust. Soc. Am. **112**, 1037–1045.
Jesteadt, W., and Wier, C. A. (**1977**). ''Comparison of monaural and binaural discrimination of intensity and frequency,'' J. Acoust. Soc. Am. **61**, 1599–1603.
Keene, K. (**1972**). ''Preservation of constant loudness with interaural amplitude asymmetry,'' J. Acoust. Soc. Am. **52**, 1193–1196.
Leshowitz, B., Zurek, P., and Ricard, G. (**1974**). ''Measurement of the interaural amplitude threshold for a 500-Hz tone,'' J. Acoust. Soc. Am. Suppl. 1 **56**, S56.
Levitt, H. (**1971**). ''Transformed up-down methods in psychoacoustics,'' J. Acoust. Soc. Am. **49**, 467–477.
Nuetzel, J. M. (**1982**). ''Sensitivity to interaural intensity differences in tones and noises as measured with a roving level procedure,'' J. Acoust. Soc. Am. Suppl. 1 **71**, S47.
Trahiotis, C., and Kappauf, W. E. (**1978**). ''Regression interpretation of differences in time-intensity trading ratios obtained in studies of laterality using the method of adjustment,'' J. Acoust. Soc. Am. **64**, 1041–1047.
Yost, W. A., and Dye, R. H. (**1988**). ''Discrimination of interaural differences of level as a function of frequency,'' J. Acoust. Soc. Am. **83**, 1846–1851.

Measurements of vocal fold tissue viscoelasticity: Approaching the male phonatory frequency range[a)]

Roger W. Chan[b)]
Department of Otolaryngology–Head and Neck Surgery and Graduate Program in Biomedical Engineering, University of Texas Southwestern Medical Center, Dallas, Texas 75390-9035

(Received 31 December 2003; revised 5 March 2004; accepted 8 March 2004)

Viscoelastic shear properties of human vocal fold tissues have been reported previously. However, data have only been obtained at very low frequencies ($\leqslant$15 Hz). This necessitates data extrapolation to the frequency range of phonation based on constitutive modeling and time-temperature superposition. This study attempted to obtain empirical measurements at higher frequencies with the use of a controlled strain torsional rheometer, with a design of directly controlling input strain that introduced significantly smaller system inertial errors compared to controlled stress rheometry. Linear viscoelastic shear properties of the vocal fold mucosa (cover) from 17 canine larynges were quantified at frequencies of up to 50 Hz. Consistent with previous data, results showed that the elastic shear modulus (G'), viscous shear modulus (G''), and damping ratio (ζ) of the vocal fold mucosa were relatively constant across 0.016–50 Hz, whereas the dynamic viscosity (η') decreased monotonically with frequency. Constitutive characterization of the empirical data by a quasilinear viscoelastic model and a statistical network model demonstrated trends of viscoelastic behavior at higher frequencies generally following those observed at lower frequencies. These findings supported the use of controlled strain rheometry for future investigations of the viscoelasticity of vocal fold tissues and phonosurgical biomaterials at phonatory frequencies. © *2004 Acoustical Society of America.* [DOI: 10.1121/1.1736272]

PACS numbers: 43.70.Aj, 43.70.Bk, 43.35.Mr [AL] Pages: 3161–3170

I. INTRODUCTION

It has been shown that the biomechanical properties of vocal fold tissues, particularly their elastic and viscous shear properties, are important data for a wide range of applications, including the computer modeling of vocal fold vibration, the quantification of phonation onset or threshold conditions, and the prediction of clinical voice outcomes for phonosurgical implantable biomaterials (Alipour *et al.*, 2000; Berry, 2001; Chan and Titze, 1999; Chan *et al.*, 2001). In our previous studies, a rotational or torsional rheometer (Bohlin CS-50, Bohlin Instruments, Inc., East Brunswick, NJ) was used to measure the viscoelastic shear properties of the vocal fold mucosa, specifically the human vocal cover (i.e., the superficial layer of the lamina propria extracellular matrix) (Chan, 1998; Chan and Titze, 1999). However, valid rheometric data were obtained at relatively low frequency (up to only 15 Hz), an order of magnitude below the typical physiological frequency range of voice production, which is usually around 125 to 175 Hz for men and around 200 to 250 Hz for women (Titze, 1994).

Although the low-frequency viscoelastic shear data obtained previously could be extrapolated to physiological frequencies of phonation based on constitutive modeling approaches (Chan and Titze, 2000) as well as the principle of time-temperature superposition (Chan, 2001), the applicability of these modeling and extrapolation approaches to the description of vocal fold tissues has to be corroborated by empirical data obtained at higher frequency, preferably in the physiological range of phonation.

The limitation of the previous data to a low-frequency range was at least partially due to the fact that they were obtained with oscillatory shear rheometry on the basis of prescribing and controlling an input stress and measuring the output strain, i.e., *controlled stress rheometry*. In the controlled stress torsional rheometer system used in our previous studies (Bohlin CS-50 with a parallel-plate geometry), a test sample was subjected to a precise sinusoidal torque (controlled stress) introduced by a drag cup motor rotating the upper plate while the lower plate remained stationary (Fig. 1). The deformation of the test sample resulting from the small-amplitude oscillatory torque input was detected as the sinusoidal angular velocity or displacement of the upper plate by a sensitive optical transducer assembly attached to the shaft of the upper plate (Chan and Titze, 1999, p. 2012). Unfortunately, there existed a major source of measurement errors with such controlled stress rheometry design that limited the valid frequency range of the measurements. Due to the moment of inertia of the upper plate and shaft assembly (including the actuator or motor shaft and coil, part of the air bearing, as well as the optical transducer disk), the system introduced significant inertial errors into the transduction and measurements of the oscillation of the upper plate, particularly at higher frequencies and for test samples of low viscosities. Specifically, the angular displacement of the oscillating upper plate lagged behind the actual sinusoidal deformation of the test sample, introducing response delays due to the instrument system inertia or *inertial time delays*. In a thorough analysis of system inertial errors in controlled

[a)]Portions of this work were presented in the 142nd Meeting of the Acoustical Society of America, Fort Lauderdale, Florida, 3–7 December 2001.
[b)]Electronic mail: roger.chan@utsouthwestern.edu

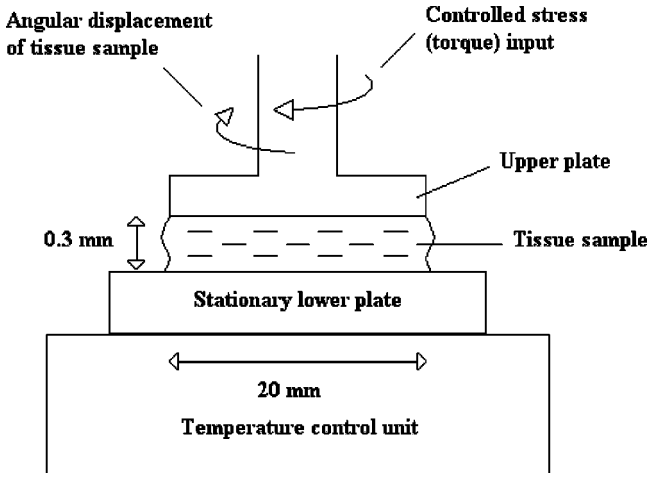

FIG. 1. Schematic of the torsional controlled stress rheometer setup used in Chan and Titze (1999), with a parallel plate geometry (cross-sectional view not to scale).

stress rheometers, Krieger (1990) showed that such response delays on the order of 1.0 s are typical for test samples with viscosities less than 0.1 Pa·s. These inertial errors ultimately limit the usefulness of controlled stress rheometry for quantifying the frequency-dependent tissue viscoelasticity of the vocal fold cover, which has been shown to demonstrate a shear thinning behavior, with its dynamic viscosity decreasing monotonically with frequency and dropping below 0.1 Pa.s at 15 Hz (Chan and Titze, 1999). Under this premise, this paper attempted to explore the use of a rheometer system with an alternative and improved rheometric design, namely by prescribing and controlling an input strain and measuring the output stress, i.e., *controlled strain rheometry*. This methodology significantly reduced the response time delays associated with the system inertia of the instrument, allowing for the measurement of empirical viscoelastic data of vocal fold tissues at a frequency up to around 50 Hz in the present study, more than three times higher than the previously achievable limit of 15 Hz, and approaching the lower limit of the physiological fundamental frequency range for male speakers. The empirical data obtained were also characterized theoretically by two previously used constitutive models, namely the quasilinear viscoelastic model and the statistical network model (Chan and Titze, 2000), in order to facilitate comparison between the present and previous data, and to better understand the applicability of these models to the description of vocal fold tissue constitutive response. Such theoretical constitutive modeling would enhance the parametric and microstructural descriptions of the tissue behavior under small-strain (small-amplitude) oscillatory shear deformation, which is key to the study of mucosal wave mechanics and its interaction with the glottal airflow.

II. METHOD

A. Controlled strain rheometer

A rheometric fluid spectrometer (Model RFS-III) (Rheometric Scientific, Piscataway, NJ) was used for the empirical measurements. It was a state-of-the-art controlled strain torsional rheometer system for characterizing the rheological and mechanical properties of fluids and gel-like semi-solid materials, including biological soft tissues and biomaterials. The RFS-III is based on the principle of controlled strain rheometry, and it is a truly controlled strain rheometer. Some controlled stress rheometers in the market, including the Bohlin CS-50 used in our previous study (Chan and Titze, 1999), allow the user to switch to pseudo-controlled strain operations by imposing a stress (torque) that would maintain a prescribed level of deformation based on an electronic negative-feedback control loop (typically with an ''automatic strain'' mode), yet they are not truly controlled strain designs because the torque motor and the angular velocity transducer are still attached to the same rotating structure for many of these rheometers, typically the upper plate assembly (Fig. 1). Such designs tend to introduce significant inertial time delays into the measurements and limit the effective frequency range for obtaining valid dynamic viscoelastic data, especially for test samples with low viscosity or low elastic modulus where inertia of the sample also becomes a concern, in addition to the errors introduced by system inertia of the instrument. Vocal fold tissues and phonosurgical biomaterials are primarily low-modulus samples, hence the effects of both sample inertia and instrument system inertia have to be taken into account.

B. Effect of sample inertia

As discussed in our previous study (Chan and Titze, 1999, p. 2013), inertial forces arising from a sample under oscillatory shear in a parallel-plate geometry with one plate moving and another plate fixed can be neglected if the so-called ''gap loading limit'' applies (Ferry, 1980):

$$h \ll \sqrt{\frac{2\pi\eta}{\rho f}}, \tag{1}$$

where h is the gap size between the parallel plates, η is viscosity of the test sample, ρ is density of the sample, and f is oscillation frequency. According to Ferry (1980) and Schrag (1977), the gap loading condition refers to the limiting situation where the sample sheared between the two plates is so thin (i.e., the gap size so small) that the planar shear wave developing and propagating away from the moving plate is immediately reflected to create a strain field in the sample that is uniformly in phase with the driving plate. Practically, it is not easy to achieve this limiting condition because a complex standing shear wave could be created in the strain field instead to introduce significant magnitude and phase deviations from the target deformation prescribed for the sample. According to Eq. (1), the gap loading condition may no longer apply when one or more of these conditions occur: increasing the sample thickness (the gap size), increasing the oscillation frequency, or decreasing the sample viscosity. In a thorough analysis of the deviation of spatial velocity gradient profiles from the gap loading limit, Schrag (1977) showed that the ratio of shear wavelength (λ_s) to gap width (h) dictates whether the gap loading condition is applicable or not. The shear wavelength λ_s can be determined based on Eq. (10) in Schrag (1977):

$$\Delta = \omega \sqrt{\frac{\rho}{|G^*|}} \cos\frac{\delta}{2}, \tag{2}$$

where Δ is a phase factor of the complex shear wave propagation coefficient [as β in Schrag (1977)], ω is angular frequency, $|G^*|$ is magnitude of the complex shear modulus G^*, and δ is the phase shift between stress and strain. By definition, $\Delta = 2\pi/\lambda_s$, hence

$$\lambda_s = \sqrt{\frac{|G^*|}{\rho}} \Big/ f\cos\frac{\delta}{2}. \tag{3}$$

Schrag (1977) showed that the ratio λ_s/h should be 40 or larger for the gap size to be sufficiently smaller than the shear wavelength such that the gap loading condition would apply and the inertia of the sample becomes negligible. From Eq. (3), it can be seen that decreasing the modulus magnitude of the sample, increasing the oscillation frequency, or increasing the phase shift (or damping ratio of the sample, $\tan\delta$) would all reduce the ratio λ_s/h, as would increasing the gap size h, obviously. In our previous study of the human vocal fold cover using the Bohlin CS-50 rheometer (Chan and Titze, 1999), the gap size h was 0.3 mm, thus the shear wavelength λ_s had to be at or larger than 12 mm for a ratio of $\lambda_s/h \geq 40$. At a frequency of 15 Hz, with the assumption of $\rho \approx 1100$ kg/m^3 and observation of $\delta \approx 0.1$ rad, in order to have $\lambda_s \geq 12$ mm, $|G^*|$ had to be equal to or larger than 35.55 Pa at 15 Hz [Eq. (3)]. This calculation shows that the gap loading limit could be safely achieved with valid viscoelastic measurements up to 15 Hz only for those tissue specimens with a high enough elastic modulus ($|G^*| \geq 35.55$ Pa). A careful inspection of the original $|G^*|$ data not reported in Chan and Titze (1999) (only the elastic shear modulus G' was reported) revealed that all of the male vocal fold specimens fulfilled this criterion but only the stiffest female specimen (71-year-old female) had a complex shear modulus magnitude higher than 35.55 Pa.

C. Effect of instrument system inertia

For an estimation of the inertial effects arising from the rotating part of the rheometer, the response time delays due to instrument system inertia in controlled stress rheometry can be quantified by a retardation time constant β according to Krieger (1990):

$$\beta = \frac{KI}{\eta}, \tag{4}$$

where I is the moment of inertia of the rotating part of the rheometer, and K is an instrument constant dictated by the specific rotational geometry. For a circular parallel plate geometry,

$$K = \frac{2h}{\pi r^4}, \tag{5}$$

where r is radius of the rotating upper plate. For the Bohlin CS-50 rheometer used in Chan and Titze (1999) (Fig. 1), the gap size h was 0.3 mm (0.0003 m) and the upper plate radius r was 10 mm (0.01 m), hence $K = 19\,098.59\ \text{m}^{-3}$. The mass moment of inertia I of the upper plate and shaft assembly

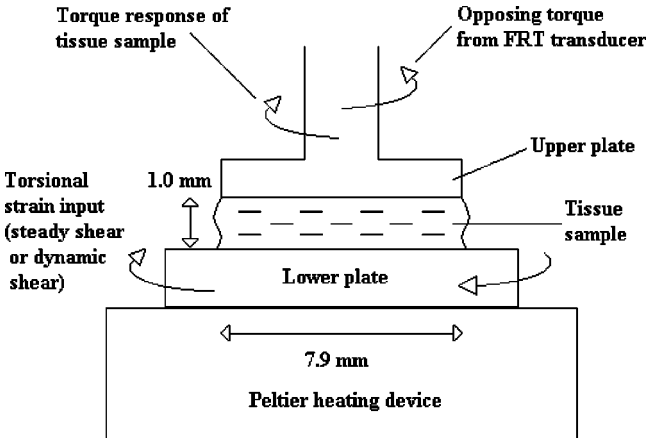

FIG. 2. Schematic of the torsional controlled strain rheometer in the present study, with a parallel plate geometry (cross-sectional view not to scale).

was 1.322×10^{-5} kg·m^2 according to the Bohlin manufacturer, including that of the motor and transducer assembly (1.3×10^{-5} kg·m^2) and that of the 20-mm stainless steel upper plate (2.2×10^{-7} kg·m^2). Based on Eq. (4), and assuming a test sample viscosity of 0.1 Pa·s, the retardation time β due to system inertia of the controlled stress rheometer (inertia of the rotating upper plate and shaft assembly) was around 2.52 s. Inertial time delays of such magnitudes introduced apparent time-dependent artifacts into the rheometric measurements, such as phase errors in the system response, and limited the valid frequency range of the viscoelastic data that can be obtained.

D. Controlled strain rheometry

Unlike in controlled stress rheometry, a test sample in the controlled strain torsional rheometer (RFS-III) in the present study was subjected to a precise sinusoidal deformation (controlled shear strain) from the lower plate, and the shear stress (torque) that developed in the sample as a result of the induced deformation was detected by a sensitive torque transducer attached to the upper plate (Fig. 2). Torsional shear (twist) of the sample was realized by an actuator (motor) attached to the lower plate, while the resulting torque of the sample was transduced by a ''force rebalance torque'' (FRT) transducer attached to the upper plate. The unique feature of the present controlled strain design was that the upper plate is highly noncompliant, i.e., it is kept almost stationary by an imposed torque in the opposite direction that attempts to precisely counter-balance the torque output generated by the sample deformation. This FRT torque balancing mechanism is mediated by a negative-feedback control circuitry as the sample is twisted by the oscillating lower plate (Fig. 2). When this balancing mechanism for torque and the feedback control of strain are tuned optimally, such a design can minimize errors introduced by inertial time delays since the oscillation amplitude of the rotating structure (upper plate assembly) would become almost zero and would thus have a much smaller effective moment of inertia. For the present testing geometry using an upper plate with a diameter of 7.90 mm, the mass moment of inertia of the upper plate assembly (including the FRT trans-

ducer) was minimal (around 31.0 $g \cdot cm^2$), leading to response delays of less than 100 ms, which are typical for controlled strain rheometers (Krieger, 1990). This was much smaller than the estimated response delays of around 2.52 s for the controlled stress rheometer (Bohlin CS-50) used previously, partly because of the controlled strain design with FRT torque balancing mechanism, and also because of a smaller nominal moment of inertia of the upper plate assembly (31.0 $g \cdot cm^2$ or $3.1 \times 10^{-6}\, kg \cdot m^2$ versus $1.322 \times 10^{-5}\, kg \cdot m^2$ for the Bohlin CS-50). This difference in inertial response delays resulted in significantly smaller phase errors in computation of the viscoelastic functions, namely the complex shear modulus G^*, yielding a wider effective frequency range.

The RFS-III system we used was equipped with an actuator (motor) with a dynamic strain amplitude (γ_0) range of 0.005–500 mrad (milli-radians) and an angular deflection resolution of 0.001 mrad, and an FRT transducer with a torque range of 0.000 39–100 mNm and a resolution of 0.0001 mNm. These sensitivities and resolutions were at state-of-the-art precision levels for controlled strain rheometers at the time of the empirical experiments (2001–2002), but were lower than those of the most advanced controlled stress rheometers available in the market. Nonetheless, dynamic rheological measurements of vocal fold tissue samples up to a frequency of 316 rad/s, or approximately 50 Hz, could be achieved. This frequency range was limited by errors in maintaining optimal tuning of the FRT torque balancing mechanism and the feedback control of strain, and also by inertia of the sample (deviations from the gap loading limit). It is anticipated that ongoing improvements in system design, precision, and corrections for inertial errors will further extend the effective frequency range of valid viscoelastic measurements to reach the typical physiological range of phonation, up to 100–200 Hz.

E. Vocal fold tissue specimens

Vocal fold tissue specimens were harvested from 17 dogs, following experiments that led to painless euthanasia of the animals. No animals were sacrificed specifically for the present study. The animal use protocol was approved by the Institutional Animal Care and Use Committee of the University of Wisconsin—Madison, in accordance with the PHS Policy on Humane Care and Use of Laboratory Animals, the NIH *Guide for the Care and Use of Laboratory Animals*, and the Animal Welfare Act (7 U.S.C. et seq.). All specimens were obtained from healthy male Beagles of 1.5–2 years old with an average weight of 12.52 kg (standard deviation $=1.45$ kg). An otolaryngologist and a speech pathologist examined all of the animals and there was no evidence of any head and neck abnormalities or laryngeal pathologies observed. Tissue scarring was mechanically induced in one of the vocal folds in some of the dogs as part of a separate study, but the specimens procured for the present study were obtained from the contralateral normal vocal folds in those cases.

For each excised canine larynx, the cover or mucosa (lamina propria plus the epithelium) of one vocal fold was carefully isolated from its thyroarytenoid muscle as there is no vocal ligament in the canine larynx. Specimens were excised and dissected immediately postmortem, quickly frozen with liquid nitrogen, and stored at $-80\,^{\circ}C$. Biomechanical data obtained from postmortem and frozen tissues were believed to be representative of the tissues *in vivo*, as a previous study showed that postmortem changes up to 24 h and frozen storage up to 1 month following quick freezing with liquid nitrogen did not significantly alter the viscoelastic shear properties of the canine vocal fold mucosa (Chan and Titze, 2003). All specimens were shipped overnight while frozen in dry ice to the author's laboratory at Purdue University, where empirical measurement of tissue viscoelasticity was conducted. Prior to the rheometric measurements, the specimens were thawed quickly in an incubator at $37\,^{\circ}C$ and mounted on the rheometer, such that the epithelium was in complete contact with the upper plate and the inferior surface (or cut surface) of the lamina propria was in complete contact with the lower plate. The epithelium remained attached to the lamina propria in the specimen throughout tissue dissection and testing, serving as a natural boundary of attachment between the specimen and the rheometer.

F. Experimental measurements of tissue viscoelasticity

A parallel-plate torsional geometry was used in the rheometer, where the dissected vocal fold mucosa specimen was sandwiched between a 7.9-mm upper plate and a 55-mm lower plate, with a 1.0-mm gap (Fig. 2). With this sample geometry, the sample volume required to completely fill the gap between the plates was around 0.05 cm^3, close to the typical volume of a canine vocal fold cover specimen. The specimen was incubated in 0.9% saline solution to prevent water loss and maintain a constant osmotic level throughout the experiments. All measurements were made at a temperature of $37\,^{\circ}C$, maintained by the lower plate coupled to a solid-state Peltier heating device capable of rapid temperature changes ($30\,^{\circ}C$/min).

For controlled strain rheometry involving the parallel-plate torsional geometry in the RFS-III rheometer (Fig. 2), average strain and stress quantities can be derived from the torsional twist applied and the torque developed in the tissue sample, respectively. A twist angle ϕ (in radians) was applied to the tissue sample via the lower plate, resulting in a shear strain γ given by

$$\gamma = \frac{R}{H}\phi, \tag{6}$$

where R is radius of the upper plate (3.95 mm) and H is the gap size between the two plates (1.0 mm). The torque T developed in the sample was measured by the FRT transducer in the RFS-III in nonstandard cgs units [g·cm]. An average shear stress τ in standard units (Pascals) can be derived from the torque T measured at the upper plate:

$$\tau = \frac{200\,g}{\pi R^3}T, \tag{7}$$

where g is gravitational acceleration in cgs units (980.665 cm/s^2), and $R = 0.395$ cm. Based on the measured shear stress and strain and the phase difference (δ) between τ and

γ, linear viscoelastic functions of the tissue sample were computed by the software of the RFS-III system according to the theory of linear viscoelasticity (Chan and Titze, 1999; Ferry, 1980; Fung, 1993). Specifically, components of the complex shear modulus G^*, i.e., the real part, elastic shear modulus (G'), and the imaginary part, viscous shear modulus (G''), as well as the dynamic viscosity (η') and the damping ratio (ζ) of the tissue sample were obtained under a variety of linear small-amplitude oscillatory shear conditions, with oscillation frequency (angular frequency ω) and the amplitude of shear strain (γ_0) being the independent variables. Details of the mathematics of oscillatory shear deformation and the derivations of these viscoelastic functions can be found in Chan and Titze (1999).

In order to ensure that the rheometer was accurately calibrated and to provide an estimate of the magnitude of experimental error associated with the oscillatory shear tests of the rheometer, the elastic shear modulus (G') and viscous shear modulus (G'') of a silicone putty (polydimethylsiloxane) sample were measured as a function of frequency (ω), i.e., under dynamic frequency sweep. The silicone putty sample was provided by the manufacturer as a rheological standard for calibration of the rheometer and had precisely known viscoelastic properties under standard conditions. The test was performed with a standardized 25-mm parallel-plate torsional geometry, a strain amplitude (γ_0) of 0.25 rad, and a standard temperature of 25 °C.

Next, a dynamic strain sweep test was conducted on a tissue specimen from one dog in order to estimate the linear viscoelastic limit of the vocal fold mucosa. Oscillatory shear deformation was applied to the specimen across a range of shear strain amplitude ($\gamma_0 = 0.0001 - 0.5$ rad), and the complex shear modulus (G^*) of the specimen was quantified according to the theory of linear viscoelasticity. This was an important test prior to measurements of the linear viscoelastic properties because rheometric measurements in the nonlinear region would violate the assumption of a linear constitutive equation and invalidate the viscoelastic measurements.

The primary experimental protocol consisted of dynamic frequency sweep tests performed on all of the vocal fold mucosa specimens. Linear small-amplitude oscillatory shear conditions were applied on the tissue specimens, with the strain amplitude γ_0 set at a level within the linear region of viscoelasticity, which was identified by the dynamic strain sweep test described above. Measurements of the linear viscoelastic shear properties of the specimens were made in an angular frequency range of $\omega = 0.1 - 316.23$ rad/s (corresponding to a range of 0.016–50.33 Hz), in upward frequency sweeps. No tests were done in downward frequency sweeps because no significant differences have been observed between upward and downward sweeps (Chan, 1998). No preconditioning or repeated testing of the tissue specimens was done, because previous results showed that preconditioning did not appear to significantly change the viscoelastic shear properties of vocal fold tissues (Chan and Titze, 1999).

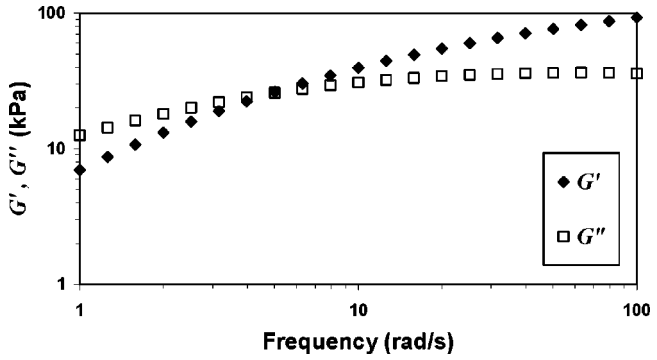

FIG. 3. Elastic shear modulus (G') and viscous shear modulus (G'') of a rheological standard material (polydimethylsiloxane) measured as a function of frequency (ω) (shear strain amplitude $\gamma_0 = 0.25$ rad, temperature = 25 °C).

G. Constitutive characterization of linear viscoelastic properties

The viscoelastic shear properties of the vocal fold mucosa measured empirically were also described by two constitutive models of viscoelasticity previously used for characterizing vocal fold tissues, namely the quasilinear viscoelastic model (Fung, 1993) and the statistical network model (Zhu *et al.*, 1991). Chan and Titze (2000) showed that both models were capable of predicting the viscoelastic behavior of the human vocal fold cover under small-amplitude oscillatory shear deformation reasonably well, but it was not entirely clear which of the two models was superior in the predictability of the viscoelastic shear properties at higher frequencies (the extrapolated frequencies in particular), because empirical data was only available at frequencies up to 15 Hz at the time for validating the models. In order to better understand the applicability of these models to the description of vocal fold tissue constitutive response, particularly at high frequencies, the present empirical data were fitted to theoretical output of the two models based on adjustments of specific model parameter values, using a procedure similar to that described in Chan and Titze (2000).

III. RESULTS AND DISCUSSION

Viscoelastic measurements of the rheological standard material (polydimethylsiloxane silicone putty) under standard test conditions are shown in Fig. 3. The data for the dynamic frequency sweep test consisted of the elastic shear modulus (G') and the viscous shear modulus (G'') of the sample plotted as a function of frequency on a log-log scale (the standard for rheological data display). The dynamic shear moduli curves conformed closely to the standard shapes or slope changes, and the cross-over point between G' and G'' occurred at $\omega = 5.0119$ rad/s and G' (or $G'') = 26.0195$ kPa. These data were within 5% of the known values of the rheological standard material, as provided by the manufacturer. The findings suggested that the rheometer was accurately calibrated and it was estimated that the repeatability or magnitude of experimental error of the RFS-III system was around 5% within the 1–100 rad/s frequency range.

Figure 4 shows the results of a dynamic strain sweep test on a canine vocal fold mucosa specimen, performed in order

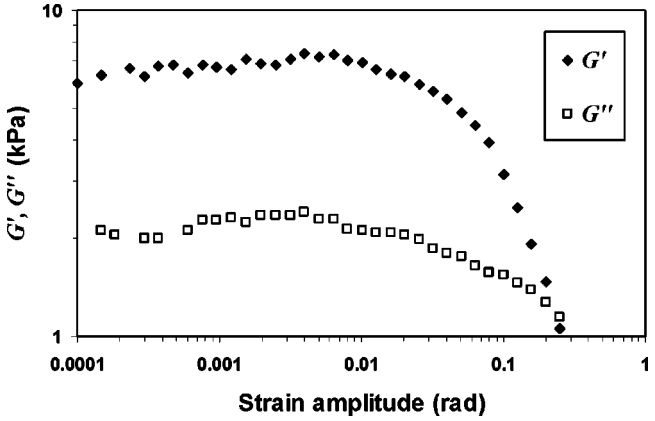

FIG. 4. Elastic shear modulus (G') and viscous shear modulus (G'') of a specimen of canine vocal fold mucosa as a function of shear strain amplitude (γ_0) (frequency ω=100 rad/s, temperature=37 °C).

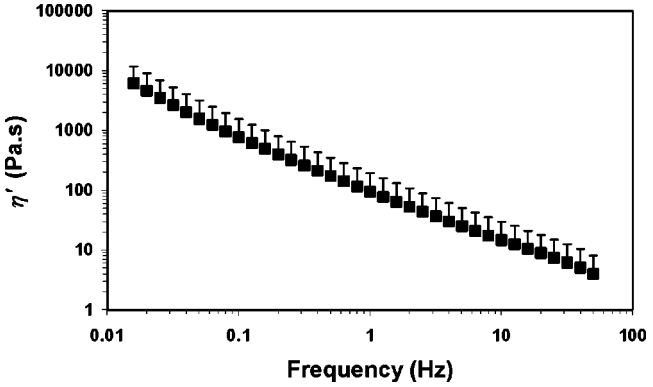

FIG. 6. Dynamic viscosity (η') of canine vocal fold mucosa as a function of frequency. Means and standard deviations (upper error bars) of 17 specimens are shown.

to estimate the small-strain linear region of viscoelasticity. G' and G'' of the tissue specimen were measured as a function of strain amplitude (γ_0) at ω=100 rad/s and at 37 °C. Results showed that small-amplitude oscillation of the specimen was linear in the region with $\gamma_0 \leqslant 0.01$ rad, where G' and G'' remained roughly constant as γ_0 increased. As γ_0 further increased beyond around 0.01 rad, G' and G'' began to decrease with γ_0, indicating a dependence of the phase difference δ on γ_0, which was representative of stress-strain nonlinearity and would violate the assumption of a linear constitutive equation underlying the derivations of the viscoelastic functions. Hence, viscoelastic measurements of all specimens were performed under dynamic frequency sweep tests with the strain amplitude γ_0 set at 0.01 rad, where the linearity assumption was valid and the viscoelastic data obtained can be assured to be in the meaningful linear regime (Ferry, 1980; Fung, 1993).

The results of dynamic frequency sweep tests performed on the canine vocal fold mucosa specimens are shown in Figs. 5–7. Figure 5 shows the viscoelastic functions G' and G'' of the vocal fold mucosa measured as a function of frequency in the linear viscoelastic region ($\gamma_0 = 0.01$ rad) at 37 °C. With the use of the controlled strain RFS-III system, the effective frequency range of viscoelastic measurement was 0.016–50.33 Hz. The data showed that both the elastic and viscous shear moduli of the canine vocal fold mucosa increased slowly with frequency, similar to that observed previously for the canine and the human vocal fold cover (Chan and Titze, 1999, 2003). It is clear that the storage component G' always remained larger than the loss component G'', indicating relatively low energy loss in the tissue during oscillatory shear deformation, a behavior that can be characterized as ''viscoelastic solid'' (Ferry, 1980). The data at higher frequencies previously unattainable (at 15–50 Hz) generally followed the trends established at the lower frequencies, without sudden changes in the slope of the curves. This was a significant finding because it provided general support to the use of data extrapolation approaches for the prediction of tissue viscoelastic behavior at frequencies beyond the reach of experiments, whether the extrapolation involves constitutive characterization or alternative approaches (like time–temperature superposition). Indeed, it has been shown that both constitutive characterization and time-temperature superposition tend to predict trends of viscoelastic shear properties that would follow those empirically observed at lower frequencies, rather than drastically deviate from them (Chan, 2001; Chan and Titze, 2000).

Figure 6 shows the dynamic viscosity (η') of the canine vocal fold mucosa as a function of frequency. Similar to the results of previous experiments, η' decreased monotonically with frequency or the rate of deformation, a ''shear thinning''

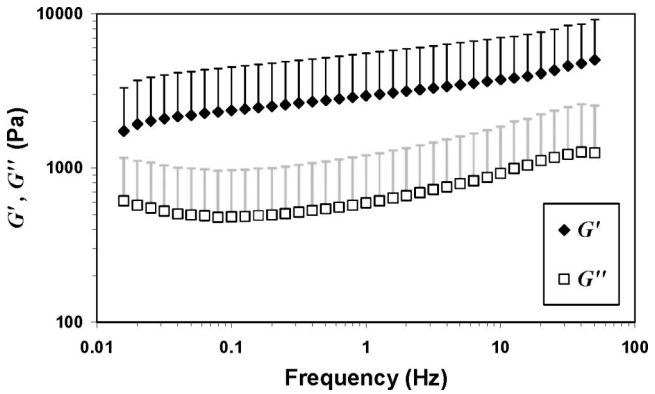

FIG. 5. Elastic shear modulus (G') and viscous shear modulus (G'') of canine vocal fold mucosa as a function of frequency. Means and standard deviations (upper error bars) of 17 specimens are shown.

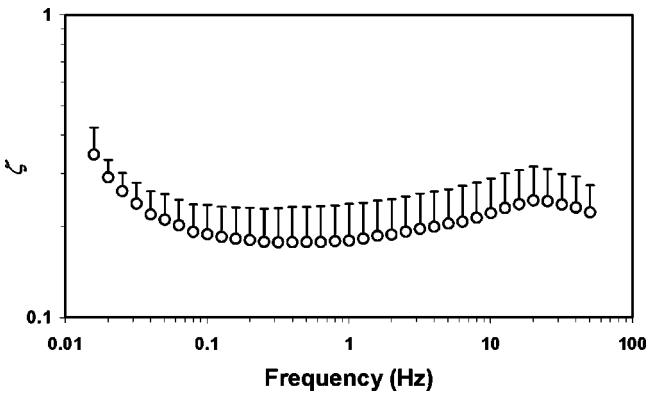

FIG. 7. Damping ratio (ζ) of canine vocal fold mucosa as a function of frequency. Means and standard deviations (upper error bars) of 17 specimens are shown.

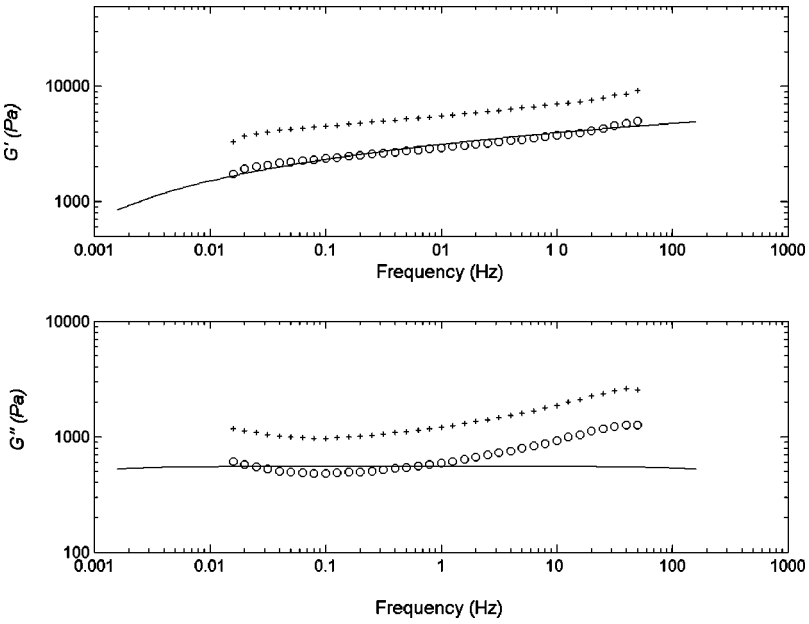

FIG. 8. Constitutive characterization of elastic shear modulus G' (upper panel) and viscous shear modulus G'' (lower panel) of canine vocal fold mucosa based on the quasilinear viscoelastic model (best fit line with "O"=mean data and "+"=standard deviations).

effect that has been observed repeatedly and was predicted by both of the constitutive models. It has been proposed that this effect is important for phonation to be possible at high frequency, as viscous energy loss keeps decreasing with frequency at the same time as tensile tissue stiffness increases with frequency (Chan and Titze, 2000). The data obtained at higher frequencies (15–50 Hz) seemed to provide support to the continuation of this shear-thinning effect into phonatory frequencies, which would help to explain the sustaining of vocal fold oscillation during high-pitched vocalizations such as singing.

The damping ratio (ζ) of the canine vocal fold mucosa was found to be not as much a relatively flat function of frequency as was observed in previous human data (Chan and Titze, 1999), and it was particularly evident that ζ increased slowly with frequency between a frequency range of around 1–20 Hz, with a local peak developing at about 20 Hz (Fig. 7). However, the numerical values of ζ were actually within a relatively small range of 0.1–0.3, quite similar to the range previously observed for the human vocal fold cover (0.1–0.5). These damping ratio values suggested that small-amplitude oscillation of the vocal fold would be underdamped (when $\zeta<1.0$) for the frequency range observed, explaining why phonation may be energetically feasible for both canine and human.

The empirical viscoelastic data were characterized constitutively based on the quasilinear viscoelastic model and the statistical network model. Theoretical predictions based on specific parameter values of the two models were optimized and curve-fitted to the average empirical data shown in Figs. 5–7. The curve fitting was performed using a procedure similar to that described in Chan and Titze (2000), and it was implemented in the software package MATLAB for the present study. The parameters of the quasilinear viscoelastic model included the constant "parameter c," and the limits of a continuous relaxation spectrum τ_1 and τ_2, whereas for the statistical network model there were four independent model parameters η_0 (zero shear-rate viscosity), η_∞ (infinite shear-rate viscosity), λ_0 (maximum relaxation time of the statistical network), and s_0 (maximum number of segment complexity that defines the range of chain segments under shear in the network), and one dependent parameter α (a function of η_0, η_∞, and s_0).

In order to assess the agreement or "goodness of fit" between the empirical data and the theoretical predictions based on the two models, a correlation coefficient r_c was calculated for each of the viscoelastic functions as follows (the subscript "c" stands for constitutive modeling):

$$r_c = \sqrt{1-\frac{\Sigma_i (y_i-\hat{y}_i)^2}{\Sigma_i (y_i-\overline{y})^2}}, \tag{8}$$

where y_i were the empirical data values, $\hat{y}_i$ were the predictions based on constitutive modeling, and $\overline{y}$ was the average of the empirical values. The "best fits" were found by fine-tuning the model parameters individually until the sum of the correlation coefficients r_c for the four viscoelastic functions (G', G'', η', and ζ) was maximized.

For descriptions based on the quasilinear viscoelastic model, the best fit was obtained with the parameter values $c=10$, $\tau_1=0.0001$ s, $\tau_2=1000$ s, and a scaling factor of 5750, which was introduced to scale the theoretical predictions to approximate the higher stiffness and viscosity of the canine vocal fold mucosa compared to human values. The numerical values of the correlation coefficient r_c as estimates of the goodness of fit of curve-fitting between the empirical data and the theoretical predictions were $r_c=0.972\,070$ for G', 0.00 for G'', 0.995 523 for η', and 0.00 for ζ. The model was capable of describing the changes of G' and η' with frequency reasonably well (Figs. 8 and 9), as indicated by the large values of r_c. However, the correlation coefficients were zeroes for G'' and ζ. As shown in Fig. 8, it is clear that the quasilinear viscoelastic model could only predict the viscous shear modulus G'' as a flat function of frequency, but not the gradual increase of G'' with frequency between 1 to 50 Hz. For the damping ratio ζ, the model could only predict

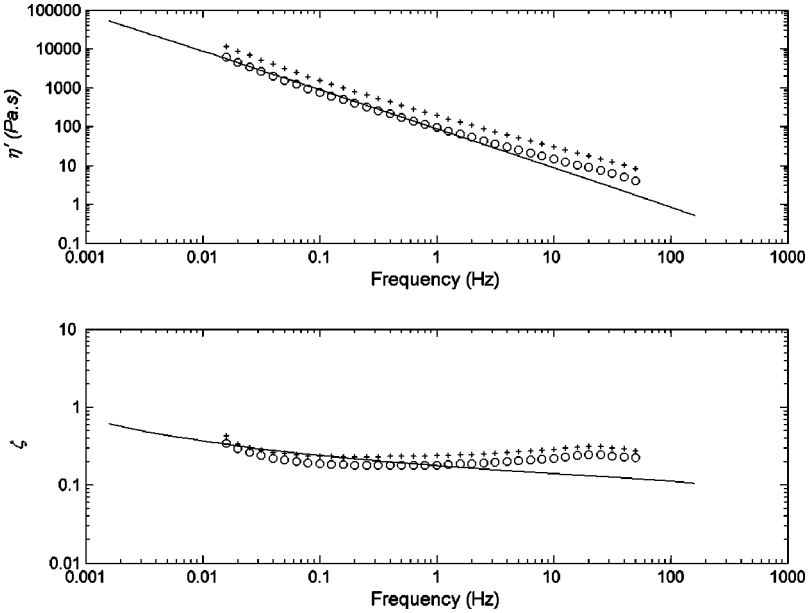

FIG. 9. Constitutive characterization of dynamic viscosity η' (upper panel) and damping ratio ζ (lower panel) of canine vocal fold mucosa based on the quasilinear viscoelastic model (best fit line with "O"=mean data and "+"=standard deviations).

a gradually decreasing function of frequency instead of the observed relatively flat function with gradual changes of the slope. In particular, deviations between the data and the predictions were the most evident between 10 and 50 Hz, surrounding the observed local peak of ζ at around 20 Hz (Fig. 9). The quasilinear viscoelastic model did not seem to be very capable of following the trends of the observed tissue viscoelastic behavior, particularly at the relatively high frequencies (15–50 Hz).

For the statistical network model, the best fit was achieved with the independent model parameters $\eta_0 = 4.10 \times 10^9$ Pa·s, $\eta_\infty = 0.025$ Pa·s, $\lambda_0 = 1.10 \times 10^8$ s, $s_0 = 34$, and with the dependent parameter $\alpha = 8.26318$. The goodness-of-fit statistical estimate was $r_c = 0.980\,111$ for G', 0.845 992 for G'', 0.930 199 for η', and 0.218 948 for ζ. Unlike the quasilinear viscoelastic model, it is clear from Figs. 10 and 11 that the statistical network model was capable of closely describing most of the changes of G', G'', η', and ζ with frequency, as supported by the high correlation coefficients for three of the four viscoelastic functions (G', G'', η'). For the description of ζ, it is actually evident that the graphical curve fit was quite good (Fig. 11), despite a low correlation coefficient value. This was related to the fact that the best-fit line for ζ was almost a completely flat function of frequency, as the computation of r_c based on Eq. (8) was not meaningful for situations of near-zero correlation.

In summary, results of the present study indicated that viscoelastic shear properties of the canine vocal fold mucosa obtained at frequencies up to 50 Hz seemed to generally follow the data trends established at lower frequencies. This was observed empirically as well as being confirmed by the results of constitutive characterization, especially with the statistical network model. Obviously, only canine tissues were used for the present investigation, so implications of these data for human phonation are limited. However, the

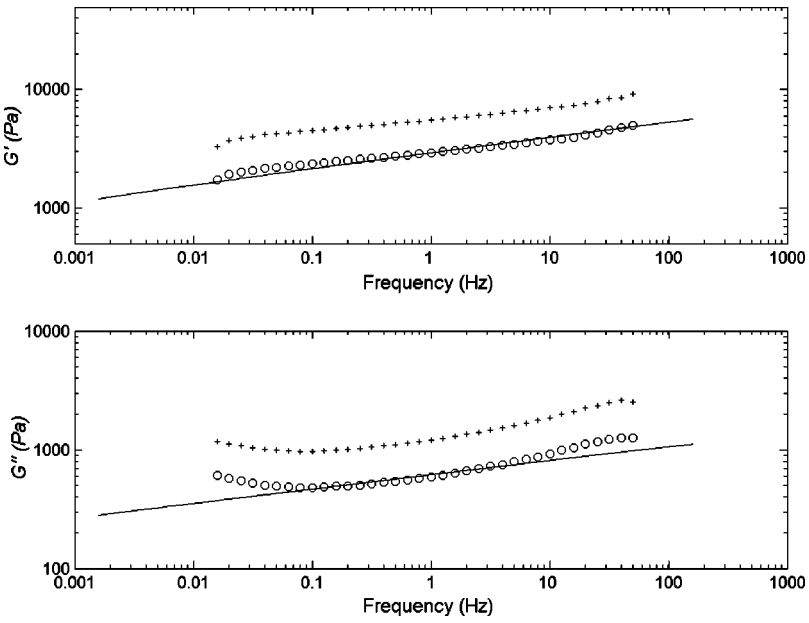

FIG. 10. Constitutive characterization of elastic shear modulus G' (upper panel) and viscous shear modulus G'' (lower panel) of canine vocal fold mucosa based on the statistical network model (best fit line with "O"=mean data and "+"=standard deviations).

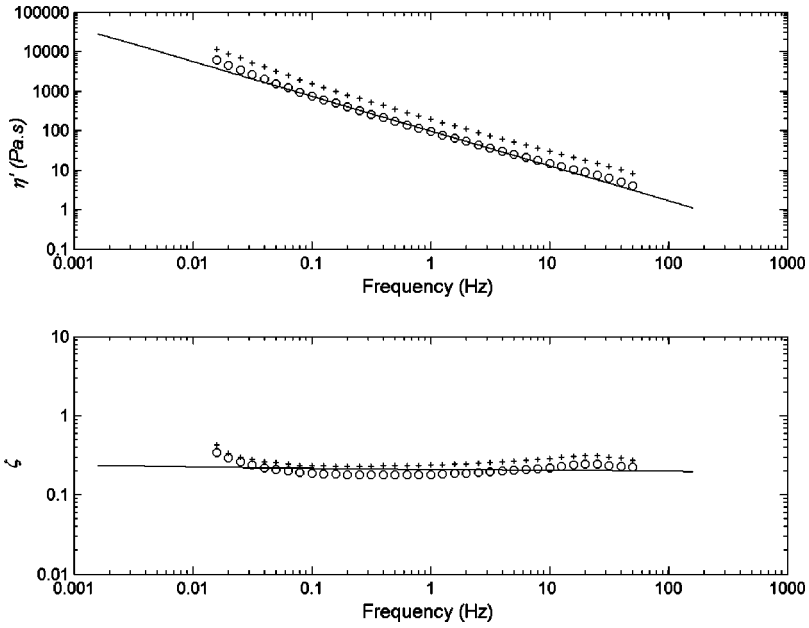

FIG. 11. Constitutive characterization of dynamic viscosity η' (upper panel) and damping ratio ζ (lower panel) of canine vocal fold mucosa based on the statistical network model (best fit line with "O"=mean data and "+"=standard deviations).

present study has demonstrated the potential of using controlled strain rheometry for the empirical viscoelastic measurements of vocal fold tissues at higher frequencies, which would involve experiments with human tissues in the next step.

IV. CONCLUSION

System inertia-related response delays have been a major source of measurement errors for controlled stress rheometers in the viscoelastic measurements of low-modulus and low-viscosity materials at high frequencies. A controlled strain torsional rheometer with significantly smaller inertial time delays due to instrument system inertia was used to quantify the linear viscoelastic shear properties of the canine vocal fold mucosa as a function of frequency ranging from 0.016 to 50 Hz. The upper frequency limit was more than three times higher than that achieved previously with a controlled stress rheometer (Chan and Titze, 1999), and it approached the physiological fundamental frequency range of male voice production. The empirically measured elastic shear modulus (G'), viscous shear modulus (G''), dynamic viscosity (η'), and damping ratio (ζ) of the vocal fold tissue specimens demonstrated trends of tissue elastic and viscous behaviors similar to those reported previously, and these trends were generally corroborated by theoretical descriptions of tissue constitutive response based on the statistical network model. These findings supported the methodology of controlled strain rheometry for further investigations of the viscoelasticity of vocal fold tissues. More effort is needed to quantify the roles of sample inertia and instrument system inertia in controlled strain rheometry, and their relative contributions to measurement errors. Future studies should also involve viscoelastic measurements of the human vocal fold cover and implantable biomaterials at frequencies of phonation.

ACKNOWLEDGMENTS

This work was supported by NIH Grant No. 7 R01 DC006101-02 from the National Institute on Deafness and Other Communication Disorders. Empirical rheological data were collected in a vocal fold physiology and biomechanics laboratory at Purdue University, with support from new faculty start-up funds provided by Purdue University. The author also thanks Diane Bless, Bernard Rousseau, and Troy Scheidt of the University of Wisconsin—Madison for their courtesy in procuring canine laryngeal tissues, and Min Fu of UT Southwestern Medical Center for her assistance in computational constitutive modeling using MATLAB.

Alipour, F., Berry, D. A., and Titze, I. R. (**2000**). "A finite element model of vocal fold vibration," J. Acoust. Soc. Am. **108**, 3003–3012.

Berry, D. A. (**2001**). "Mechanisms of modal and nonmodal phonation," J. Phonetics **29**, 431–450.

Chan, R. W. (**1998**). "Shear properties of vocal fold mucosal tissues and their effect on vocal fold oscillation," Ph.D. dissertation, The University of Iowa, Iowa City, Iowa.

Chan, R. W. (**2001**). "Estimation of viscoelastic shear properties of vocal fold tissues based on time-temperature superposition," J. Acoust. Soc. Am. **110**, 1548–1561.

Chan, R. W., and Titze, I. R. (**1999**). "Viscoelastic shear properties of human vocal fold mucosa: Measurement methodology and empirical results," J. Acoust. Soc. Am. **106**, 2008–2021.

Chan, R. W., and Titze, I. R. (**2000**). "Viscoelastic shear properties of human vocal fold mucosa: Theoretical characterization based on constitutive modeling," J. Acoust. Soc. Am. **107**, 565–580.

Chan, R. W., and Titze, I. R. (**2003**). "Effect of post-mortem changes and freezing on the viscoelastic properties of vocal fold tissues," Ann. Biomed. Eng. **31**, 482–491.

Chan, R. W., Gray, S. D., and Titze, I. R. (**2001**). "The importance of hyaluronic acid in vocal fold biomechanics," Otolaryngol.-Head Neck Surg. **124**, 607–614.

Ferry, J. D. (**1980**). *Viscoelastic Properties of Polymers*, 3rd eds. (Wiley, New York).

Fung, Y. C. (**1993**). *Biomechanics. Mechanical properties of living tissues*, 2nd ed. (Springer-Verlag, New York), pp. 23–65, 242–320.

Krieger, I. M. (**1990**). ''Bingham Award Lecture—1989. The role of instrument inertia in controlled-stress rheometers,'' J. Rheol. **34**, 471–483.
Schrag, J. L. (**1977**). ''Deviation of velocity gradient profiles from the 'gap loading' and 'surface loading' limits in dynamic simple shear experiments,'' Trans. Soc. Rheol. **21**, 399–413.
Titze, I. R. (**1994**). *Principles of Voice Production* (Prentice-Hall, Englewood Cliffs, NJ).
Zhu, W. B., Lai, W. M., and Mow, V. C. (**1991**). ''The density and strength of proteoglycan–proteoglycan interaction sites in concentrated solutions,'' J. Biomech. **24**, 1007–1018.

Listener sensitivity to individual talker differences in voice-onset-time

J. Sean Allen and Joanne L. Miller[a)]
Department of Psychology, Northeastern University, Boston, Massachusetts 02115

(Received 24 July 2003; revised 30 January 2004; accepted 2 February 2004)

Recent findings in the domains of word and talker recognition reveal that listeners use previous experience with an individual talker's voice to facilitate subsequent perceptual processing of that talker's speech. These findings raise the possibility that listeners are sensitive to talker-specific acoustic-phonetic properties. The present study tested this possibility directly by examining listeners' sensitivity to talker differences in the voice-onset-time (VOT) associated with a word-initial voiceless stop consonant. Listeners were trained on the speech of two talkers. Speech synthesis was used to manipulate the VOTs of these talkers so that one had short VOTs and the other had long VOTs (counterbalanced across listeners). The results of two experiments using a paired-comparison task revealed that, when presented with a short- versus long-VOT variant of a given talker's speech, listeners could select the variant consistent with their experience of that talker's speech during training. This was true when listeners were tested on the same word heard during training and when they were tested on a different word spoken by the same talker, indicating that listeners generalized talker-specific VOT information to a novel word. Such sensitivity to talker-specific acoustic-phonetic properties may subserve at least in part listeners' capacity to benefit from talker-specific experience. © *2004 Acoustical Society of America.*
[DOI: 10.1121/1.1701898]

PACS numbers: 43.71.Bp, 43.71.Es [RLD] Pages: 3171–3183

I. INTRODUCTION

Listeners successfully understand the speech produced by many different talkers. Under normal conditions they appear to do so effortlessly, despite the presence of a high degree of variability across talkers in the acoustic properties of their speech, including those properties that specify particular phonetic segments (i.e., consonants and vowels) that make up the words of the language (Allen *et al.*, 2003; Hillenbrand *et al.*, 1995; Newman *et al.*, 2001; Peterson and Barney, 1952). Traditional approaches have typically assumed that during the course of phonetic processing such individual talker variation is eliminated, or ''normalized'' (e.g., Ladefoged and Broadbent, 1957; Miller, 1989). Thus, it has generally been assumed that talker-specific information is discarded from the speech signal for the purposes of recognizing phonetic segments (see Lachs *et al.*, 2003).

However, a growing number of studies have provided converging evidence that linguistically relevant talker-specific information is not in fact discarded by the perceptual system but is instead retained in memory (see Goldinger, 1998, for a review). It may be that individual talker differences, rather than being a perceptual problem that must be eliminated through a normalization mechanism, are instead stored as useful information to be exploited during speech processing (see Johnson and Mullennix, 1997; Nygaard and Pisoni, 1995). Memory for talker-specific acoustic-phonetic information would allow listeners to customize for each experienced talker the mapping from acoustic form to phonetic categories, thus permitting better perceptual performance as more experience is gained with the speech of particular talkers.

One line of research in particular strongly supports the notion that listeners bring talker-specific information to bear during speech processing. Several studies of word recognition have shown that familiarity with a particular talker's voice improves word recognition performance, suggesting that listeners can learn individual talkers' characteristic implementations of phonetic segments and are thus better able to perform the mapping from acoustic form to phonetic categories (Bradlow and Pisoni, 1999; Goldinger, 1996; Nygaard *et al.*, 1994; Nygaard and Pisoni, 1998; Sheffert and Fowler, 1995). For example, Nygaard *et al.* (1994) trained listeners over a period of 9 days to recognize the voices of ten different talkers, and on the 10th day tested their ability to recognize novel words in noise. Listeners who heard words spoken by familiar talkers (the ten talkers on whose voices they had been trained) performed better in the word recognition task than did listeners who heard words spoken by unfamiliar talkers (ten new talkers). This study showed that, at least with extensive exposure, listeners were able to benefit from talker-specific experience. Other evidence suggests that considerably less exposure might be required for listeners to benefit from talker-specific experience: In a large study of word intelligibility, Bradlow and Pisoni (1999) found that, holding talker identity constant for a given listener over the course of a single experimental session, word recognition performance improved from the first portion of the session to the final portion of the session, after listeners had accumulated experience with the speech of the talker over the course of the experiment.

Evidence from another domain, that of talker recogni-

a)Electronic mail: j.miller@neu.edu

tion, also supports the notion that listeners are sensitive to individual talker differences in linguistically relevant acoustic properties, and to phonetically relevant acoustic properties in particular. Traditionally, talker recognition has been thought to be mediated by acoustic properties distinct from the acoustic properties involved with phonetic perception (Abercrombie, 1967). These nonphonetic acoustic properties have commonly been referred to as indexical acoustic properties. Because individual talkers differ systematically in indexical properties, listeners can use these properties as one source of information to identify talkers from their voices (see Bricker and Pruzansky, 1976). Recent experiments (Fellowes *et al.*, 1997; Remez *et al.*, 1997; Sheffert *et al.*, 2002) suggest that phonetic properties can provide another source of information that listeners can use to identify talkers. In fact, these experiments indicate that phonetic properties alone—in the absence of indexical properties—are sufficient for talker recognition. In these experiments, sine wave synthesis (Remez *et al.*, 1981) was used to create replicas of sentences produced by ten different talkers. The sine wave replicas preserved the time-varying formant structure of the speech signal by using sine waves of the same central frequencies as the first three formants. Thus, critical phonetically relevant information was preserved while other information, including indexical information, was eliminated. Even with such drastically impoverished stimuli, Remez *et al.* (1997) showed that listeners could successfully recognize most of the talkers by matching the sine wave replicas to the corresponding natural samples of the talkers' voices. Other listeners who were highly familiar with the voices of the ten talkers from everyday interactions were able to recognize most of the talkers even without reference to a natural sample, that is, by relying solely on long-term memory of talker-specific voice information. Though it is not known specifically what acoustic properties of the sine wave replicas underlie listeners' performance in these experiments, follow-up analyses carried out by Fellowes *et al.* (1997) suggest that listeners' response patterns were not based on any simple, gross spectral or temporal acoustic properties (e.g., central spectral tendency, overall duration), but instead that listeners relied on some more complex, detailed acoustic properties derived from the time-varying sine wave patterns that mimicked the formant structure of the speech. Thus, the most plausible explanation of these findings is that listeners were sensitive to individual talker differences in phonetically relevant acoustic properties and identified talkers' voices on the basis of these individual differences.

These results from studies of talker recognition provide converging evidence that listeners are sensitive to individual talker differences in linguistically relevant acoustic properties. Together with the studies of word recognition reviewed above, a strong case can be made that listeners retain talker-specific linguistic information and use such information to inform perception. However, we do not yet know specifically what acoustic properties underlie listeners' ability to benefit from talker-specific experience, and we do not yet know for any given phonetically relevant acoustic property whether listeners can track that property in a talker-specific manner. The goal of the current study was to test directly whether listeners are indeed capable of tracking individual talker differences in a particular phonetic property.

The property tested was voice-onset-time, or VOT, an acoustic property defined as the interval from the onset of the burst associated with a stop consonant to the onset of periodic energy associated with a following vowel. VOT robustly specifies voicing in English stop consonants, with voiced stop consonants (/b d g/) having relatively short VOT values and voiceless stop consonants (/p t k/) having relatively long VOT values (Lisker and Abramson, 1964). This property was selected for test for two main reasons. First, the VOT used to specify voiceless stop consonants is known to differ systematically from talker to talker, even when differences among talkers in speaking rate are controlled (Allen *et al.*, 2003). Second, listeners are known to be sensitive to fine-grained variation in VOT, even within a given phonetic category (e.g., Carney *et al.*, 1977; Miller and Volaitis, 1989). VOT was therefore deemed a good candidate as a property that listeners might track in a talker-specific manner.[1]

The two experiments reported below addressed this issue using a training/test paradigm. Listeners were exposed during training to the speech of two different talkers producing isolated words beginning with /d/ or /t/. Critically, the VOT of the /t/ tokens was manipulated, so that one talker had relatively short VOTs and the other talker had relatively long VOTs; which talker served as the short-VOT talker versus the long-VOT talker was counterbalanced across listeners. At test, listeners were presented with two variants of a word from a given talker, differing only in VOT, and were asked to choose which of the two variants sounded more like the talker, based on their experience with that talker's speech during training.

The experiments consisted of two sessions. In the first session, listeners were tested on the same /t/-initial word heard during training in order to determine whether they would demonstrate a sensitivity to individual talker differences in VOT. In the second session, listeners were tested on a /t/-initial word different from that heard during training in order to test whether they would generalize talker-specific experience to novel words. This generalization test in the second session was included to assess the specificity of what listeners had learned about the speech of the two talkers based on the limited exposure in training. The previous studies of word recognition reviewed above (e.g., Nygaard *et al.*, 1994) found that listeners benefited from talker-specific experience even when tested on novel words, that is, words spoken by a given talker that were not heard previously by listeners in the experiment. This suggests that listeners are capable of generalizing what they learn from a sample of a given talker's speech, applying that experience to facilitate the recognition of new words spoken by the talker. The generalization tests in the current experiments tested whether listeners would generalize talker-specific VOT experience from a single experienced word beginning with /t/ (repeated many times during training) to a different word beginning with /t/ presented at test.

Experiments 1 and 2 differ from one another only in which stimuli served as the familiar versus novel word. In

experiment 1, listeners were trained on the word *town* (and its voiced counterpart *down*) and generalization was tested on the word *time*; in experiment 2, listeners were trained on the word *time* (and its voiced counterpart *dime*) and generalization was tested on the word *town*. The predictions for the two experiments are the same. If listeners are sensitive to individual talker differences in VOT, then their training experience should predict their responses at test. That is, during the first session listeners should more often choose the short- or long-VOT variant for a given talker consistent with whether they heard that talker produce short or long VOTs during training. Further, if listeners can generalize talker-specific VOT information to a novel word, then the same should be true for the generalization test in the second session.

II. EXPERIMENT 1

In each of two sessions, there were two primary phases, a training phase and a test phase. (These two phases alternated with one another during a given session, as described in the Procedure subsection.) During the training phase of both sessions, subjects were exposed to the speech of two female talkers fictitiously labeled ''Annie'' and ''Laura.'' Half of the subjects heard Annie producing *town* with relatively long VOTs and Laura producing *town* with relatively short VOTs (the A-LONG/L-SHORT training group); the other half of the subjects heard Annie producing *town* with short VOTs and Laura producing *town* with long VOTs (the A-SHORT/L-LONG training group). These *town* tokens from the two talkers were intermixed with *down* tokens from the two talkers in randomly ordered lists. (The VOT of the *down* tokens was not manipulated, given that the VOTs of voiced stop consonants vary only minimally; see, e.g., Volaitis and Miller, 1992.) The subjects' task during training was to identify both the talker (Annie versus Laura) and the initial consonant of the word (/d/ versus /t/) on each trial.

The test phase was the same for both training groups. During the test phase of the first session, the subjects were presented, on a given trial, with two tokens of *town* produced by one of the talkers, a short-VOT variant and a long-VOT variant. The test phase of the second session was the same, except that on a given trial short- and long-VOT variants of a novel word, *time*, were presented. The subjects' task during both sessions was to select, on each trial, which variant sounded more like the talker, based on their experience listening to that talker during training. The critical question was whether the choices of the two groups of subjects would differ, in line with their training experience.

A. Method

1. Subjects

Twenty subjects participated in the experiment. All were native speakers of English, aged 18 to 45 years, with no reported speech or hearing disorders. Subjects were either paid or received course credit for their participation. Any subject who did not consistently discriminate between the two talkers' voices used in the study was replaced with a new subject (see Sec. II B); three subjects were replaced for this reason.

2. Stimulus preparation

The stimuli consisted of two sets, a *down/town* set and a *dime/time* set, described below. Stimuli from the *down/town* set were used as training stimuli in this experiment and as test stimuli for the first session. Stimuli from the *dime/time* set were used to test generalization during the second session of this experiment and were used further in experiment 2.

a. Down/town stimuli. The preparation of the *down/town* stimuli involved nine steps. The final product of these nine steps was a set of stimuli consisting of synthesized versions of these words, based on the speech of two female talkers. Critically, multiple variants of each talker's *town* were synthesized such that they differed from one another in VOT. As described below, separate stimulus sets were created for use during training and during test. Several training stimulus sets and several test stimulus sets were created; these training and test stimulus sets were presented in alternation with one another over the course of the experiment (see the Procedure subsection).

Step (1). Acquisition of matched down tokens from two talkers. Several female native speakers of American English produced 20 tokens of the word *down*, along with many other monosyllabic words beginning with voiced and voiceless stop consonants. Their speech was recorded onto digital audiotape (Aiwa HHB 1 PRO DAT recorder, AKG C 460B microphone) in a sound-attenuated room and was transferred to a Pentium PC at a sampling rate of 20 kHz, using the CSL system (Kay Elemetrics Corp.). Each *down* token was isolated using the CSL waveform display, and the VOT and overall word duration of each were measured. VOT was measured from the burst onset to the onset of high-amplitude periodic energy associated with the vowel. Overall word duration was measured from the burst onset to the offset of low-amplitude periodic energy associated with the nasal consonant. Two talkers whose overall word durations were roughly comparable were selected to serve as talkers for the main study. (These talkers were unfamiliar to listeners in the experiment; listeners were screened to ensure that this was the case.) One of the two talkers was designated ''Annie,'' and the other talker was designated ''Laura.'' One *down* token from each of the talkers was selected such that the two selected tokens were approximately matched on both VOT and on overall word duration. For Annie, the selected *down* token had a VOT of 13 ms and an overall word duration of 533 ms. For Laura, the selected *down* token had a VOT of 9 ms and an overall word duration of 528 ms. In order that these two tokens be exactly matched in overall duration, both tokens were truncated to 527 ms in duration by deleting from the end of the nasal. These two tokens were then equated for root-mean-square (rms) amplitude.

Step (2). Creation of synthesized versions of the two matched down tokens. Using the ASL system (Kay Elemetrics Corp.), a pitch-synchronous LPC analysis was performed on the waveforms of the two matched *down* tokens, using the autocorrelation method with a filter order of 16. The results of this analysis were listed in a numeric table where information on peak amplitude, fundamental frequency ($F0$), and formant frequencies and bandwidths was available frame by frame. The analyzed data (with the residual excitation) were

used to create synthesized versions of the two tokens.

*Step (3). Creation of two down-town-*town series based on the two synthesized down tokens*. Two series of stimuli, one for each of the talkers, were created by systematically changing parameters on a frame-by-frame basis and synthesizing new stimuli using the modified parameters. The first token in each series used the originally extracted parameters of the *down* tokens (see the previous step). The next step in the series was created by changing three parameters in the first voiced frame. Specifically, the excitation parameter was changed from the residual to a noise source, the $F0$ parameter was changed to 0, and the peak amplitude parameter was scaled down by multiplying the original peak amplitude of the frame by a scaling factor of 0.15. The rest of the stimuli in each series were created by repeating this procedure for progressively increasing numbers of voiced frames. Each series consisted of 50 items in all, ranging in VOT from 13 to 249 ms for Annie's series and 9 to 246 ms for Laura's series. The step size of these series corresponded to the duration of each successive pitch period of the vowel (roughly 5 ms). Perceptually, the initial consonant in each series ranged from a clear /d/ at short VOT values, through a clear /t/ at intermediate VOT values, to a breathy exaggerated version of /t/ (labeled*/t/ for notational purposes) at long VOT values. As a result of this procedure, syllable duration (527 ms) was constant across all tokens in the series (see Allen and Miller, 1999).

Step (4). Perceptual testing of the series. Two preliminary experiments were conducted for each of the two *down-town-*town* series in order to ensure that the stimuli were perceived as expected and to provide criteria for stimulus selection for the main experiment. Eight different subjects participated in each of the preliminary experiments. In each experiment, approximately half of the steps from a given series, spread across the series, were presented to subjects in random order with each stimulus presented numerous times throughout the experiment. One experiment was a forced-choice phonetic identification experiment, in which subjects decided for each stimulus whether the initial consonant was /d/ or /t/. The results showed that, as expected, stimuli with relatively short VOT values were identified as /d/, and stimuli with relatively long VOT values were identified as /t/, with a small area of ambiguity around 45 ms for both series. The other experiment was a goodness-rating experiment, in which subjects rated each stimulus based on how good of a /t/ it was, using a 7-point scale with 7 being the best. As expected from previous work using this paradigm (see, e.g., Miller and Volaitis, 1989), the results showed that stimuli with relatively short VOT values were given low ratings, with ratings systematically increasing as VOT increased—peaking at roughly 85 to 100 ms—and then systematically decreasing as VOT continued to increase.

Step (5). Selection of stimuli from the series to be presented during training. Several tokens were selected from the two series to serve as training stimuli in the main experiment. The VOT values of these stimuli are given in Table I. These stimuli were selected from the two series as follows: (1) First, a *voiced* token (i.e., one perceived as *down*) was selected from each series—from Annie's series the first token in the series (with VOT=13 ms) was selected, and from Laura's series the second token in the series (with VOT=15 ms) was selected. These voiced tokens were presented during training to both training groups. (2) Next, two *short-VOT voiceless* tokens (perceived as *town*) were selected from each series. The two selected tokens were two steps apart (roughly 10 ms) in their respective series. The purpose of this separation was to simulate naturally occurring within-talker variability in VOT. These tokens were selected so as to have as short a VOT as possible while still being identified consistently as *town* (80% or higher identification as /t/ by all subjects in the preliminary phonetic identification experiment) and, further, so that across series the short-VOT stimuli would be well matched both in terms of absolute VOT and in the mean goodness rating received in the preliminary goodness-rating experiment. The short-VOT voiceless tokens for Annie's series were presented during training to the A-SHORT/L-LONG training group, and the short-VOT voiceless tokens for Laura's series were presented to the A-LONG/L-SHORT training group. (3) Finally, two *long-VOT voiceless* tokens (also perceived as *town*) were selected from each series. Like the selected short-VOT voiceless tokens, the long-VOT voiceless tokens were two steps apart in their respective series. These tokens were selected so as to have as long a VOT as possible without being perceived as very poor exemplars of /t/ (mean rating of 3.5 or higher on the 7-point scale in the preliminary goodness-rating experiment) and, further, so that across series the long-VOT stimuli would be well matched both in terms of absolute VOT and in the mean goodness rating received in the preliminary goodness-rating experiment. The long-VOT voiceless tokens for Annie's series were presented during training to the A-LONG/L-SHORT training group, and the long-VOT voiceless tokens for Laura's series were presented to the A-SHORT/L-LONG training group. The goal in selecting the

TABLE I. VOT values, in milliseconds, of the *down/town* training and test stimuli.

Training stimuli—A-LONG/L-SHORT group			
	"*down*"	"*town*"	
Test voice		Variant 1	Variant 2
Annie	13	172	182
Laura	15	78	87

Training stimuli—A-SHORT/L-LONG group			
	"*down*"	"*town*"	
Test voice		Variant 1	Variant 2
Annie	13	76	86
Laura	15	175	186

Test stimuli (both groups)		
	"*town*"	
Test voice	Short-VOT	Long-VOT
Annie	81	177
Laura	82	180

short- and long-VOT stimuli in this manner was to create as large a discrepancy in VOT as possible between them in order to maximize the chances that subjects would succeed in discriminating the difference in VOT in the main experiment.[2]

Step (6). Selection of stimuli from the series to be presented at test. Both training groups received the same test stimuli. The VOT values of these stimuli are given in Table I. A short-VOT stimulus and a long-VOT stimulus were selected for each talker. Recall from step 5 that for each talker the two short-VOT stimuli and the two long-VOT stimuli used in training were selected so that they were two steps apart in the *down-town-*town* series. The intervening step in each case served as a test stimulus. That is, for each series, the step between the two short-VOT training stimuli served as the short-VOT test stimulus, and the step between the two long-VOT training stimuli served as the long-VOT test stimulus. As a result of this method of selection, during the test phase of the experiment subjects never heard a stimulus identical to that heard during the training phase; the subject's task during test, then, was to determine which of the two presented variants was more similar to the training stimuli (see the Procedure subsection).

Step (7). Elimination of possible amplitude-based confound. As a consequence of the way the *down-town-*town* series were constructed, stimuli early in the series (toward the *down* endpoint) were higher in overall amplitude than were stimuli late in the series (toward the **town* endpoint). This occurs because, as more successive voiced frames are converted to voiceless frames, those converted frames are necessarily lower in amplitude (see step 3) and thus the overall amplitude of the syllable decreased slightly with each successive step in the series. As a result, the short-VOT test and training stimuli were higher in overall amplitude than were the long-VOT test and training stimuli. Though subtle (approximately 2-dB difference), this was a concern in the present experiment because subjects might identify the two talkers during the training phase in terms of amplitude, one talker (the short-VOT talker) whose *town* utterances were relatively high in overall amplitude and one (the long-VOT talker) whose utterances were relatively low in amplitude, and then in the test phase respond on the basis of overall amplitude. This could give rise to misleading results, in that subjects may perform well on the task due to a sensitivity to overall amplitude rather than a sensitivity to VOT. To rule out this possibility, the relationship between VOT and overall amplitude in these stimuli was decoupled, as follows. Three amplitude levels were used—high, medium, and low—which corresponded at presentation to 75, 73, and 71 dB SPL, respectively. This pattern of amplitudes corresponded roughly to the pattern of rms amplitudes observed among the unmodified stimuli selected from each *down-town-*town* series—that is, *down* was roughly 2 dB more intense than the short-VOT *town* stimuli, which were in turn roughly 2 dB more intense than the long-VOT *town* stimuli. Each *training* stimulus was presented at all three levels (75, 73, and 71 dB SPL) corresponding to the range of levels among the unmodified stimuli (*down*, short-VOT *town*, and long-VOT *town* training stimuli). Each *test* stimulus was presented at two levels (73 and 71 dB SPL) corresponding to the range of levels among the unmodified stimuli (short-VOT *town* and long-VOT *town* test stimuli). As described in the next step, the stimuli presented at different levels were ordered randomly during the main experiment, with the result that overall amplitude varied randomly from trial to trial, both in training and in test. This eliminated the possibility that subjects could rely on overall amplitude to make their judgments in the experiment.

Step (8). Construction of training stimulus sets. A training stimulus set consisted of the high-, medium-, and low-amplitude versions of each training stimulus. As described in step 5, for the A-LONG/L-SHORT training group, the training stimuli consisted of Annie's *down* and two long-VOT *town* stimuli, and Laura's *down* and two short-VOT *town* stimuli. For the A-SHORT/L-LONG training group, the training stimuli consisted of Annie's *down* and two short-VOT *town* stimuli, and Laura's *down* and two long-VOT *town* stimuli. In addition, an extra *down* token for each talker was included among the training stimuli so the number of voiced- and voiceless-initial stimuli would be balanced in each training set. These stimuli were then placed in random order into a list for presentation. Two such lists concatenated together constituted a complete training set. A training set thus consisted of 48 items (4 stimuli$\times$2 talkers$\times$3 amplitude levels$\times$2 randomized lists). Ten such training sets were constructed for each of the training groups, to be presented to the subjects interspersed with the test stimulus sets. In addition, a familiarization training set was constructed for each of the training groups. The familiarization set consisted of 24 items (4 stimuli$\times$2 talkers$\times$3 amplitude levels) in random order, to be presented during the familiarization phase of the experiment (see the Procedure subsection).

Step (9). Construction of test stimulus sets. A test stimulus set consisted of eight pairs of a given talker's test stimuli. Each pair consisted of the short-VOT test stimulus and the long-VOT test stimulus of a given talker, as described in step 6. Each of these stimuli was presented at each of two amplitude levels, as described in step 7. The order in which the short- and long-VOT variants were heard on a given trial was counterbalanced across trials. This resulted in eight pairings which were placed in random order to make a test set. Four such test sets were created for each talker, to be presented to the subjects interspersed with the training stimulus sets. In addition, a practice test set was constructed for each talker. A practice test set consisted of four pairs of test stimuli (not all amplitude variations appeared in practice) in random order, to be presented during the practice phase of the experiment (see the Procedure subsection).

b. Dime/time stimuli. The *dime/time* stimuli were prepared according to the same steps that were used to prepare the *down/town* stimuli. Except where noted below, the details of these steps are the same as described for *down/town* in the previous section.

Step (1). Acquisition of matched dime tokens from two talkers. One *dime* token was selected from each of the talkers' naturally produced utterances, recorded during the initial recording session. For Annie, the selected *dime* token had a VOT of 13 ms and an overall word duration of 526 ms. For

Laura, the selected *dime* token had a VOT of 12 ms and an overall word duration of 545 ms. In order that these two tokens be exactly matched in overall duration, both tokens were truncated to 516 ms in duration by deleting from the end of the nasal. A descending cosine ramp was applied over the final 20 ms of Laura's *dime* token in order to simulate a realistic amplitude contour for the truncated syllable; no such ramp was required for Annie's *dime* token. These two tokens were equated for rms amplitude.

Step (2). Creation of synthesized versions of the two matched dime tokens. See step 2 of previous section.

*Step (3). Creation of two dime-time-*time series based on the two synthesized dime tokens*. The *dime-time-*time* series were created in the same manner as the *down-town-*town* series, except that for Laura's speech the first and second frames to be edited were multiplied by a scaling factor of 0.8 and 0.6, respectively, instead of 0.15. The resulting series consisted of 50 items each, ranging in VOT from 13 ms to 277 ms for Annie's series and 12 ms to 245 ms for Laura's series.

Step (4). Perceptual testing of the series. As with the *down-town-*town* series, the two *dime-time-*time* series were subjected to perceptual evaluation in a preliminary phonetic identification experiment and a preliminary goodness-rating experiment, each with eight different subjects. The identification experiment showed that the series were perceived as expected; stimuli with relatively short VOT values were identified as /d/ and stimuli with relatively long VOT values were identified as /t/, with a small area of ambiguity around 40 ms for both series. The goodness-rating experiment showed the expected response function; stimuli with relatively short VOT values were given low ratings, with ratings systematically increasing as VOT increased—peaking at roughly 70 to 85 ms—and then systematically decreasing as VOT continued to increase.

Step (5). Selection of stimuli from the series to be presented during training. Table II lists the VOT values of the selected training stimuli. The first token in each series (VOT=13 ms for Annie; VOT=12 ms for Laura) served as the *voiced* token during training. The *short-VOT voiceless* tokens and the *long-VOT voiceless* tokens were selected for the two training groups using the same criteria described in step 5 of the previous section. Note that, as a result of this method of stimulus selection, the selected *time* training stimuli (as well as the *time* test stimuli; see the next step) were not precisely matched in VOT with the corresponding *town* stimuli, but had somewhat shorter VOTs than the corresponding *town* stimuli. Note also that these *dime/time* training stimuli are described here for purposes of explication but were not in fact used in the present experiment because this experiment does not involve training with *dime/time*. Experiment 2 makes use of these stimuli.

Step (6). Selection of stimuli from the series to be presented at test. Table II lists the VOT values of the selected test stimuli, selected according to the same criteria described in step 6 of the previous section.

Steps (7), (8), and (9). Elimination of possible amplitude-based confound, Construction of training stimulus sets, and *Construction of test stimulus sets,* respectively. These steps were identical to those described in the previous section.

TABLE II. VOT values, in milliseconds, of the *dime/time* training and test stimuli.

Training stimuli—A-LONG/L-SHORT group			
	"*dime*"	"*time*"	
Test voice		Variant 1	Variant 2
Annie	13	159	169
Laura	12	68	77

Training stimuli—A-SHORT/L-LONG group			
	"*dime*"	"*time*"	
Test voice		Variant 1	Variant 2
Annie	13	66	75
Laura	12	157	166

Test stimuli (both groups)		
	"*time*"	
Test voice	Short-VOT	Long-VOT
Annie	71	164
Laura	72	161

3. Procedure—Session 1

Half of the subjects were assigned to the A-LONG/L-SHORT training group and half to the A-SHORT/L-LONG training group. They were seated in front of a response key pad and computer monitor in a sound-attenuated booth. In two sessions, subjects participated alternately in training and test phases of the experiment, as described below.

a. Training. During training, subjects were presented with the *down* and *town* training stimuli. Subjects in the A-LONG/L-SHORT training group heard Annie's *town* with long VOT values and Laura's *town* with short VOT values, whereas subjects in the A-SHORT/L-LONG training group heard Annie's *town* with short VOT values and Laura's *town* with long VOT values (see Table I). As described above, the training stimuli for each group were organized into randomized sets of 48 trials each, and one randomized set of 24 trials for use during familiarization.

Familiarization took place at the beginning of the first session, before the first training phase. A familiarization trial consisted of the auditory presentation of the word followed by a visual display indicating the name of the talker on that trial (either "Annie" or "Laura"). This visual display appeared 1750 ms after offset of the auditory stimulus and remained on the computer screen for 1500 ms. After a pause of 2000 ms, the next trial began. The subjects' task during familiarization was to attend to the stimuli and learn to recognize the two voices. No responses were collected.

There were nine training phases in the first session, which alternated with the test phases, as described below. During a given training phase, subjects were presented with the stimuli from one of the nine training stimulus sets; the order in which subjects heard the nine training sets over the

experimental session was determined randomly for each subject. The subjects' task during training was to simultaneously identify the talker and the initial consonant on each trial in a forced-choice paradigm (the phonetic identification task was included to ensure that these listeners perceived the short-VOT stimuli as voiceless under these experimental conditions). Four response buttons on the key pad were labeled ''Annie D,'' ''Annie T,'' ''Laura D,'' and ''Laura T.'' Feedback was provided on each trial in the form of a visual display reading ''YES'' and the name of the talker when the subject correctly identified the talker, or ''NO'' and the name of the talker when the subject incorrectly identified the talker. This visual feedback appeared 750 ms after the keypress response (or after 5 s passed with no response; on such trials the feedback consisted only of the talker's name) and remained on the computer screen for 1500 ms. No feedback was provided for the phonetic decision. After a pause of 2000 ms, the next trial began.

b. Test. During test, subjects were presented with the *town* test stimuli. As described above, the test stimuli were placed in pairs into eight randomized sets, four sets containing Annie's speech and four sets containing Laura's speech. Each set contained eight pairs, with each pair consisting of the short-VOT variant of *town* and the long-VOT variant of *town*. In addition, two randomized sets, one for each talker, were constructed for use during the practice test phase; these practice sets contained four test pairs each.

During the practice test phase, the two practice sets were presented in sequence; the order in which the two practice sets were presented was counterbalanced across subjects. The purpose of this phase was to introduce the subjects to the paired-comparison task to be used during the test phase. At the beginning of each practice test, the name of the talker for that practice set was briefly displayed on the screen, thus explicitly informing subjects of the identity of the talker under test. Subjects were given instructions explaining that on each trial they would hear two variants of the word *town* spoken by that talker. Their task was to decide which of the two variants sounded more like the talker, based on their experience listening to the talker during the initial training phase. Two response buttons on the key pad were labeled ''1'' and ''2,'' and subjects were instructed to press the first button if they thought the first variant sounded more like the talker and the second button if they thought the second variant sounded more like the talker. The interstimulus interval between the two variants of *town* was 750 ms. No feedback was provided on this task. After each response there was a pause of 2000 ms before the next trial began (the next trial began after 5 s if there was no response).

There were eight test phases in the experiment (four for each talker), which alternated with the training phases. During a given test phase, subjects were presented with the stimuli from one of the eight test stimulus sets; the order in which subjects heard the eight test sets over the experimental session was determined randomly for each subject, with the constraint that no more than three of a given talker's test sets occurred consecutively. At the beginning of each test phase, the name of the talker for that test set was displayed briefly on the screen, thus explicitly informing subjects of the identity of the talker under test. The task during the test phases was identical to that used in the practice test phase.

c. Alternation between training and test. The experiment was designed so that subjects alternated between training and test phases over the course of an experimental session. The relatively brief test phases (8 trials in length) were intermixed with the longer training phases (48 trials in length) in this way in order to minimize interference of test experience on talker-specific memory. The concern was that, during test, exposure to the two alternatives on a given trial—a ''correct'' alternative (where the VOT corresponded to what the subject heard during training) and an ''incorrect'' alternative (where the VOT did not correspond to what the subject heard during training)—would interfere with a subject's memory for VOT information. Specifically, exposure to the incorrect variant might lead subjects to modify their mental representations of the talker's VOT, despite receiving instructions to base their decisions during test only on experience gained during training. Because of this concern, the number of test trials was kept to a minimum, interspersed among a larger number of training trials. The delay between the last trial of a training set and the first trial of the following test set was roughly 20 s. Subjects were given a short break after completing the third and sixth test sets.

As a result of this design, the sequence of phases in the first session was as follows: (1) familiarization phase; (2) training phase; (3) practice test phase; (4) training phase; (5) test phase; (6) further alternation between training phases and test phases until all eight test phases had been completed. There was a total of 432 training trials in nine training sets (the tenth training set was not used during the first session), and across all eight test sets, there was a total of 32 test trials for Annie's voice and 32 test trials for Laura's voice. Upon completion of the first session, subjects were told that they would be hearing the same two talkers' voices on the following day, and were instructed to try and remember what their voices sounded like.

4. Procedure—Session 2

The second session was always carried out on the day following the first session. In the second session, subjects first participated in a short review of the previous session, to reacquaint them with the stimuli and procedure. The review consisted of a training phase using the *down* and *town* stimuli, followed by a test phase using the *town* stimuli for one of the two talkers, followed by a second training phase (again using the *down* and *town* stimuli), followed by a second test phase (again using the *town* stimuli) for the other talker. Which of the talkers subjects heard first in the review was counterbalanced across subjects, and which of the training and test stimulus sets was presented was determined randomly for each subject.

After completing the short review, subjects were told that the remainder of the experiment would alternate between training and test phases as during the first session, with one difference: During the test phases, subjects would hear two variants of the word *time* instead of *town*. Their task during the test was to decide which of the two variants sounded more like the talker, based on their experience with

the talker saying *town* during the training phases. The training phases remained unchanged; subjects would still hear *down* and *town* during training. Subjects then participated in a practice test phase using the *time* test stimuli. Following practice, subjects alternately participated in training and test phases until all eight test sets and the remaining nine training sets had been completed. The order in which subjects heard the test sets was determined randomly (with the constraint that no more than three of a given talker's test sets occurred consecutively), as was the order in which they heard the training sets. Across all ten training sets, there was a total of 480 training trials, and across all eight test sets (excluding the review portion), there was a total of 32 test trials for Annie's voice and 32 test trials for Laura's voice.

TABLE III. Mean results from the test phases of the two experiments, in terms of the percent of trials on which subjects chose the long-VOT variant for each the two test voices in each of the two sessions. Mean results are shown separately for the A-LONG/L-SHORT training group and the A-SHORT/L-LONG training group, with standard errors of the mean in parentheses.

		Test voice: Annie		Test voice: Laura	
Experiment	Session	A-LONG/ L-SHORT	A-SHORT/ L-LONG	A-LONG/ L-SHORT	A-SHORT/ L-LONG
Experiment 1	1	87 (4.4)	11 (6.3)	33 (9.8)	82 (6.2)
	2	82 (5.4)	10 (5.7)	37 (12.1)	90 (5.5)
Experiment 2	1	78 (7.8)	20 (7.5)	29 (9.0)	70 (8.1)
	2	87 (6.9)	49 (14.1)	20 (9.4)	60 (11.9)

B. Results and discussion

1. Training

On the forced-choice talker and phonetic identification task used during training, accuracy was assessed separately in terms of percent-correct talker identification and percent-correct phonetic identification during each session. Correct talker identification was defined for a given trial as an ''Annie D'' or ''Annie T'' response when Annie was the talker and as a ''Laura D'' or ''Laura T'' response when Laura was the talker. Correct phonetic identification was defined for a given trial as an ''Annie D'' or ''Laura D'' response when the word was *down* and as an ''Annie T'' or ''Laura T'' response when the word was *town*. Trials on which subjects did not respond were discarded from the analyses (these trials accounted for 0.1% of the total trials across the two sessions for the 20 subjects included in the study). Mean percent-correct talker identification and mean percent-correct phonetic identification were calculated for each subject, across all training sets of a given session.[3] Good performance on distinguishing the talkers' voices in the first session was taken as a prerequisite for inclusion in the study. If on any given stimulus (across all amplitude levels) a subject performed at less than 90% correct on talker identification, that subject was excluded from the study. Three subjects were replaced for this reason.

For the 20 subjects included in the study, performance on the training task was near ceiling, with mean percent-correct talker and phonetic identification at 97% or better for both the A-LONG/L-SHORT training group and the A-SHORT/L-LONG training group in both sessions 1 and 2. Thus, the two talkers' voices were easily distinguished by these listeners, and the VOT manipulation was effective in creating a robust voicing distinction for both voices.

2. Test

On the paired-comparison task used during test, performance was analyzed separately for each session (and excluding the review portion of the second session). Each response was categorized as either a short-VOT response or a long-VOT response based on the listener's choice on that trial. Trials on which listeners did not respond were discarded from the analyses; these trials accounted for 0.8% of the total trials during the first session and 0.2% of the total trials during the second session. For a given subject, performance across all four test sets for a given test voice was quantified as the percent of trials on which the subject made short-VOT responses and the percent of trials on which the subject made long-VOT responses.[4] Note that because percent short-VOT responses and percent long-VOT responses must sum to 100, these two measures are redundant with one another. As a result, only one of the measures, percent long-VOT responses, was arbitrarily selected for analysis. Results for the paired-comparison task (in terms of percent long-VOT responses) are presented numerically in Table III and graphically in Fig. 1. The upper half of Fig. 1 shows results from the first session, and the lower half shows results from the second session. In each case, the left panel compares responses for the two training groups when the test voice was Annie's, and the right panel compares responses for the two training groups when the test voice was Laura's.

An analysis of variance (ANOVA) was conducted on the percent long-VOT data with the factors of training group (between-subjects), test voice (within-subjects), and session (within-subjects). The critical prediction was the presence of an interaction between training group and test voice, with responses patterning according to each group's training experience. We tested for such a pattern using two sets of planned contrasts. The first set involves considering each test voice separately (i.e., considering the left and right panels in Fig. 1 separately). For these between-group contrasts we used the t distribution with $df=18$, $\alpha=0.05$. If subjects' training predicts their responses at test, then when the test voice was Annie's, the A-LONG/L-SHORT training group should choose the long-VOT variant significantly more often than does the A-SHORT/L-LONG training group; and when the test voice was Laura's, the A-LONG/L-SHORT training group should choose the long-VOT variant significantly less often than does the A-SHORT/L-LONG training group. The second set of planned contrasts involves considering each training group separately (i.e., comparing across the left and right panels in Fig. 1). For these within-group contrasts we used the t distribution with $df=9$, $\alpha=0.05$. If listeners in a given training group respond differently to the two test voices depending on their training experience, then the A-LONG/L-SHORT training group should choose the long-VOT variant significantly more often for Annie's voice than for Laura's voice, and the A-SHORT/L-LONG training

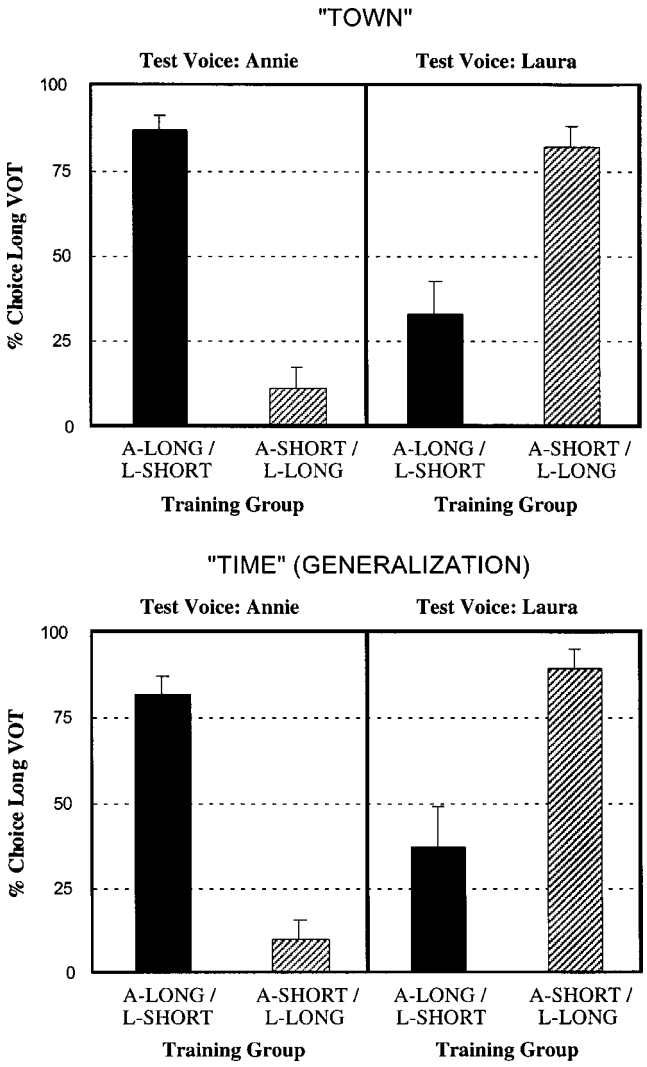

FIG. 1. Mean results from the test phases of experiment 1, in terms of the percent of trials on which subjects chose the long-VOT variant in the paired-comparison task. The top half of the figure shows the results from the first session and the bottom half shows the results from the second session. The left panels show the results when the test voice was Annie's, and the right panels show the results when the test voice was Laura's. Responses for the A-LONG/L-SHORT training group are indicated by the solid bars, and responses for the A-SHORT/L-LONG training group are indicated by the scored bars. The error bars show the standard error of the mean.

group should choose the long-VOT variant significantly less often for Annie's voice than for Laura's voice. Finally, if listeners generalized talker-specific VOT information to the novel word, the overall pattern just described should occur in both sessions. Moreover, if such generalization is complete (i.e., performance on the novel word does not differ from that on the familiar word), then there should be no main effect of session in the ANOVA and no interactions involving session. (The presence of any other main effects are incidental to the purpose of the study.)

The ANOVA indicated no main effect of test voice [$F(1,18)=2.8$, $p>0.10$], the presence of a main effect of training group [$F(1,18)=4.3$, $p=0.05$], and an interaction between test voice and training group [$F(1,18)=63.6$, $p<0.001$]. There was no main effect of session and no interactions involving session [$p>0.10$ in all cases]. The first set of planned contrasts confirmed that the data patterned as predicted, in both sessions. For Annie's voice (see the left panels of Fig. 1), the A-LONG/L-SHORT training group chose the long-VOT variant significantly more often than did the A-SHORT/L-LONG training group, whereas for Laura's voice (see the right panels of Fig. 1), the A-LONG/L-SHORT training group chose the long-VOT variant significantly less often than did the A-SHORT/L-LONG training group. The second set of planned contrasts also confirmed the predicted pattern, in both sessions. The A-LONG/L-SHORT training group chose the long-VOT variant significantly more often for Annie's voice than for Laura's voice, and the A-SHORT/L-LONG training group chose the long-VOT variant significantly less often for Annie's voice than for Laura's voice. Taken together, these results indicate that the different training received by the two groups had a significant impact on their responses for the two test voices. Moreover, this was true both in the first session when listeners were tested on the same word heard during training and in the second session when listeners were tested on a novel word.

The results discussed thus far indicate that listeners can retain talker-specific VOT. However, they do not necessarily indicate that listeners retain such information automatically. It may be that the within-category VOT manipulation at test encouraged subjects to place special attention on this dimension during training and, without this special attention to within-category VOT, subjects would not have retained talker-specific VOT for the /t/-initial stimuli. Initial evidence that this was not the case can be found in the results from the practice test phase from the first session. Recall that the practice test phase occurred prior to any of the test phases and therefore the practice responses reflect a relatively pristine measure of what subjects retained in memory about the speech of Annie and Laura during training; at this point in the experiment, no special importance has been assigned to the individual talker differences in VOT of the /t/-initial stimuli. Thus, if the practice responses show the same general pattern as the responses from the test phases of the experiment, then this provides evidence that subjects retained talker-specific VOT information automatically without special attention to within-category VOT variation. The practice data were analyzed in the same manner as the test data. For each subject, the mean long-VOT responses for Annie's speech and the mean long-VOT responses for Laura's speech were calculated (each based on four responses from each subject), and an ANOVA with the factors of test voice and training group was carried out on the data. The results revealed no main effect of test voice [$F(1,18)=2.1$, $p>0.10$], no main effect of training group [$F(1,18)=2.3$, $p>0.10$], and an interaction between test voice and training group [$F(1,18)=31.7$, $p<0.001$]. The same sets of planned contrasts were performed on these data as were performed on the main data, and they revealed the same pattern of results. The data from the practice test phase thus provide at least initial evidence that subjects automatically retained talker-specific VOT information in memory even when attention was not specifically directed to the individual talker differences in VOT.

Taken together, the results of experiment 1 indicate that

listeners retain talker-specific information about VOT, and that they can generalize this information to novel words. To gain further evidence with this paradigm and to replicate these results under slightly different stimulus conditions, experiment 2 was run.

III. EXPERIMENT 2

Experiment 2 was identical to experiment 1, except that the roles of the *down/town* and *dime/time* stimuli were reversed; during the first session, subjects were trained on *dime* and *time* and tested on *time*, and during the second session, they continued to be trained on *dime* and *time* but (following a brief review) were tested on the novel word *town*. It was expected that the results of this experiment would replicate those of experiment 1.

A. Method

1. Subjects

Twenty new subjects participated in the main experiment. All subjects were native speakers of English, aged 18 to 45 years, with no reported speech or hearing disorders. Subjects were either paid or received course credit for their participation. As per the same criteria used in experiment 1, any subject who did not consistently discriminate between the two talkers' voices used in the study was replaced with a new subject; two subjects were replaced for this reason.

2. Stimuli and procedure

The same stimuli and procedures described for experiment 1 were also used in experiment 2, with the following differences in configuration. First, the *dime* and *time* training stimuli (instead of *down* and *town*) were presented during training in the two sessions. Second, during session 1, the *time* test stimuli were presented at test (instead of *town*), and during session 2, the *town* test stimuli were presented at test (instead of *time*).

B. Results and discussion

1. Training

Performance on the training task was assessed as in experiment 1. Two subjects were replaced because they failed to consistently discriminate between the two talkers' voices during the first session, using the same criteria as in experiment 1. Trials on which subjects did not respond were discarded from the analyses (these trials accounted for 0.2% of the total trials across the two sessions for the 20 subjects included in the study). For the subjects included in the study, performance on the talker and phonetic identification task was near ceiling for both the A-LONG/L-SHORT training group and the A-SHORT/L-LONG training group, with mean percent-correct talker and phonetic identification at 96% or better for both groups for both sessions. This closely replicates the training results from experiment 1.

2. Test

Performance on the paired-comparison task was analyzed as in experiment 1. Trials on which subjects did not respond were discarded from the analyses; these trials accounted for 0.8% of the total trials during the first session and 0.5% of the total trials during the second session.

Results for the paired-comparison task are shown in Table III and Fig. 2. The upper half of the figure shows results from the first session, and the lower half shows results from the second session. In each case, the left panel compares responses for the two training groups when the test voice was Annie's, and the right panel compares responses for the two training groups when the test voice was Laura's. An ANOVA comparable to that used in experiment 1 indicated no main effect of test voice [$F(1,18)=2.4$, $p=0.14$] or training group [$F(1,18)<1$], and an interaction between test voice and training group [$F(1,18)=25.3$, $p<0.001$]. Although there was no main effect of session [$F(1,18)<1$], there was a session by test voice interaction [$F(1,18)=15.8$, $p<0.001$]; no other interactions were significant [$p>0.10$ in all cases]. The session by test voice interaction indicated that the effect of test voice changed from the first session to the second session, suggesting that perfect generalization did not occur. In order to further investigate the nature of these results, separate ANOVAs were conducted on the data from the first session and the data from the second session. These ANOVAs included a test voice factor and a training group factor.

The ANOVA on the data from the first session revealed no main effect of test voice [$F(1,18)<1$] and no main effect of training group [$F(1,18)=1.6$, $p=0.23$], but a strong interaction between test voice and training group [$F(1,18)=28.9$, $p<0.001$]. Two sets of planned contrasts were conducted, as for the first experiment. Both confirmed that the data patterned as predicted. First, for Annie's voice, the A-LONG/L-SHORT training group chose the long-VOT variant significantly more often than did the A-SHORT/L-LONG training group, whereas for Laura's voice, the A-LONG/L-SHORT training group chose the long-VOT variant significantly less often than did the A-SHORT/L-LONG training group. Second, the A-LONG/L-SHORT training group chose the long-VOT variant significantly more often for Annie's voice than for Laura's voice, and the A-SHORT/L-LONG training group chose the long-VOT variant significantly less often for Annie's voice than for Laura's voice. Thus, the findings from the first session replicated the findings from the first session in experiment 1.

However, unlike in experiment 1, the pattern of data in second session did not mirror that from the first session. The ANOVA for the second session revealed the presence of a main effect of test voice [$F(1,18)=8.0$, $p=0.01$], no main effect of training group [$F(1,18)<1$], and an interaction between test voice and training group [$F(1,18)=16.2$, $p<0.001$]. The first set of planned contrasts did confirm that for Annie's voice, the A-LONG/L-SHORT training group chose the long-VOT variant significantly more often than did the A-SHORT/L-LONG training group, whereas for Laura's voice, the A-LONG/L-SHORT training group chose the long-VOT variant significantly less often than did the A-SHORT/L-LONG training group. However, the second set of planned contrasts showed a pattern of performance that was different from that in the first session. Although listeners in the A-LONG/L-SHORT training group chose the long-

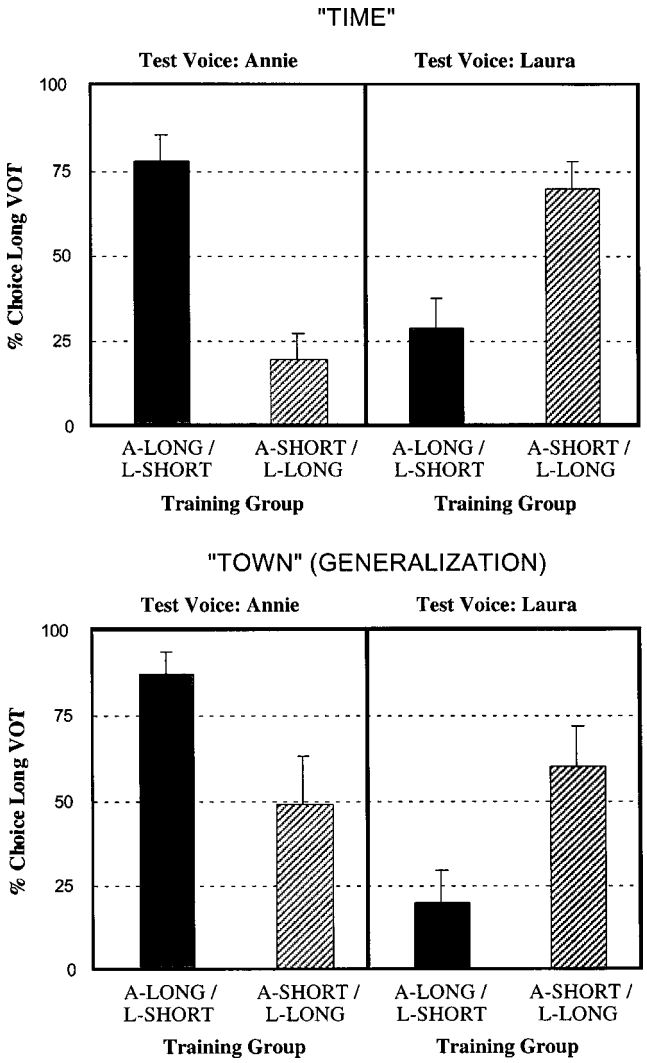

FIG. 2. Mean results from the test phases of experiment 2, in terms of the percent of trials on which subjects chose the long-VOT variant in the paired-comparison task. The top half of the figure shows the results from the first session and the bottom half shows the results from the second session. The left panels show the results when the test voice was Annie's, and the right panels show the results when the test voice was Laura's. Responses for the A-LONG/L-SHORT training group are indicated by the solid bars, and responses for the A-SHORT/L-LONG training group are indicated by the scored bars. The error bars show the standard error of the mean.

VOT variant significantly more often for Annie's voice than for Laura's voice, listeners in the A-SHORT/L-LONG training group did not respond differently to the two voices [$p > 0.10$]. This pattern of results suggests that one of the subject groups, the A-LONG/L-SHORT training group, generalized to the novel word but the other group, the A-SHORT/L-LONG training group, did not.

As in experiment 1, the practice test data from the first session were also analyzed in order to assess whether subjects automatically retained talker-specific VOT information prior to any special emphasis being placed on within-category VOT variation. An ANOVA on the practice data revealed the presence of a main effect of test voice [$F(1,18)=8.9$, $p<0.01$], a main effect of training group [$F(1,18)=5.7$, $p<0.05$], and an interaction between test voice and training group [$F(1,18)=33.8$, $p<0.001$]. The two sets of planned contrasts confirmed that the data patterned as did the main results for session 1. Thus, as in experiment 1, the practice test data from the first session indicated that subjects retained talker-specific VOT information even when no special attention was focused on within-category VOT variation.

The results from the first session of experiment 2 indicate that listeners retained talker-specific VOT information, as was found in the first experiment. However, the generalization results from the second session were less clear than those in experiment 1. Strong evidence of generalization was present for one but not both groups. This mixed result was surprising, given that both groups of listeners heard stimuli which were similar in all respects except VOT. Considering experiments 1 and 2 together, three groups out of four showed clear evidence of generalization, but this group did not.

To follow up on this aberrant finding, we ran ten new listeners in the A-SHORT/L-LONG group. For the first session, the results for the new listeners were similar to those for the original A-SHORT/L-LONG group; mean percent long-VOT responses for Annie's voice was 13% (compared to 20%), and for Laura's voice it was 68% (compared to 70%). However, the generalization results from the second session were quite different for the new subjects for one of the test voices. Specifically, mean percent long-VOT responses for Annie's voice in the second session was 9% (compared to 49%); for Laura's voice mean percent long-VOT responses remained at 60%. The data from the new A-SHORT/L-LONG group were combined with those of the A-LONG/L-SHORT group from the main experiment and a new ANOVA was calculated. The results indicated no main effect of test voice [$F(1,18)<1$], a main effect of training group [$F(1,18)=8.1$, $p=0.01$], and an interaction between test voice and training group [$F(1,18)=38.1$, $p<0.001$]. There was no main effect of session and no interactions involving session ($p>0.10$ in all cases except for the session by test voice interaction, where $p=0.08$). The two sets of planned contrasts confirmed that the data patterned as in experiment 1. During both sessions, for Annie's voice, the A-LONG/L-SHORT training group chose the long-VOT variant significantly more often than did the A-SHORT/L-LONG training group, whereas for Laura's voice, the A-LONG/L-SHORT training group chose the long-VOT variant significantly less often than did the A-SHORT/L-LONG training group. Moreover, within each training group, listeners responded differently to the two test voices during both sessions. The A-LONG/L-SHORT training group chose the long-VOT variant significantly more often for Annie's voice than for Laura's voice, and (unlike in the main experiment) the A-SHORT/L-LONG training group chose the long-VOT variant significantly less often for Annie's voice than for Laura's voice. These results indicate that listeners were sensitive to talker-specific VOT and that they successfully generalized to the novel word. This suggests that the lack of clear evidence for generalization for the A-SHORT/L-LONG group in the main experiment may have been spurious.

IV. GENERAL DISCUSSION

The present study tested whether listeners can retain talker-specific information about the phonetically relevant acoustic property of VOT. Subjects were exposed during a training task to the speech of two talkers producing words beginning with /d/ or /t/. Critically, the VOT of the word beginning with /t/ was manipulated across the two talkers so that subjects heard one talker with a short VOT and the other talker with a long VOT; which talker served as the short-VOT talker versus the long-VOT talker was counterbalanced across subjects. Interleaved with this training on the two voices, subjects were periodically tested to determine whether VOT was retained in a talker-specific manner. The test consisted of pairs of stimulus items, each consisting of a short-VOT variant and a long-VOT variant of a /t/-initial word produced by a given talker. In the first session, subjects were tested on the same word heard during training, and in the second session, subjects were tested on a novel word. The subjects' task was to select which of the two variants sounded more like the talker, based on their experience listening to the speech of that talker during training. The results showed that talker-specific experience during training predicted listeners' responses at test, so that whether listeners chose the short- or long-VOT variant more often for a given talker during test depended on whether they heard that talker produce short or long VOTs during training. This was true when subjects were tested on the familiar word and, in all but one group, it was true when subjects were tested on the novel word.

Thus, listeners were able to track individual talker differences in a phonetically relevant acoustic property. These findings have implications for the kind of exposure that is required for listeners to benefit from talker-specific experience. Because listeners can generalize talker-specific phonetic information across words, it may be that exposure to only a few different words is sufficient for a listener to learn a talker's implementation of a given phonetically relevant acoustic property. Once this talker-specific mapping from acoustic form to phonetic category is learned for a given phonetic segment (e.g., /t/), it can inform subsequent phonetic processing of novel words containing that segment, facilitating word recognition (e.g., Nygaard *et al.*, 1994). And, though the present experiments were not designed to test the amount of exposure required for a listener to learn a talker's mapping for a particular property, the results from the first of the test phases in each of the experiments (i.e., the practice test phases) indicated that listeners were sensitive to a talker-specific phonetic property after even a relatively small amount of training; listeners' responses in these cases were of the same general pattern as in the subsequent tests. Thus, talker-specific phonetic information can be quickly learned.

Other evidence indicates that such information can be long remembered. Goldinger (1996) found that the benefit of talker-specific experience extended over relatively long periods of time; subjects listening to familiar versus unfamiliar talkers were better able to recognize the identity of spoken words after a delay of a week. This suggests that talker-specific phonetic properties are stored in a stable long-term memory (though explicit memory for these properties, as tapped by the overt paired-comparison task used in the current study, may fade more quickly; see Goldinger, 1996). Thus, listeners display a sensitivity to individual talker differences in phonetic properties that is impressive in how quickly it can be learned and in how long it can be remembered.

The current study demonstrated that listeners are sensitive to individual talker differences in one phonetically relevant acoustic property, VOT. Of course, it will be important to test whether listeners are sensitive to individual talker differences in other phonetically relevant properties as well. And, with respect to the property of VOT, several other relevant questions remain to be answered. For example, the current study showed that listeners generalize talker-specific VOT to novel words beginning with the same consonant as heard during training, but it will also be of interest to test whether listeners will generalize to novel words beginning with other voiceless consonants as well. For example, if a talker is heard saying *time* with a long VOT, will listeners also expect that talker to produce *coal* with a long VOT?

A further remaining question concerns the role of speaking rate. In the current study, speaking rate, as reflected by overall word duration, was held constant within and across talkers for a given word and was very similar across words. However, speaking rate can vary considerably within a talker's speech and individual talkers can vary considerably from one another in their typical speaking rates (Allen *et al.*, 2003; Miller *et al.*, 1984). Moreover, VOT varies strongly as a function of speaking rate (Allen *et al.*, 2003; Miller *et al.*, 1986; Summerfield, 1975; Volaitis and Miller, 1992). Listeners are known to be sensitive to changes in speaking rate, such that VOT is mapped onto phonetic categories in a rate-dependent manner; as speaking rate slows down, the perceptual category boundary between voiced and voiceless stop consonants shifts toward longer VOTs (Summerfield, 1981), and the best exemplars of the voiceless category also shift toward longer VOTs (Miller and Volaitis, 1989). Given that VOT is processed in a rate-dependent manner, it may well be that listeners track talker-specific VOT in a rate-dependent manner as well. Thus, it would be expected that listeners would generalize talker-specific VOT information from a talker's speech at one speaking rate to a different speaking rate.

The present findings demonstrate that listeners can learn talker-specific phonetic information and that such information is stored in such a way that it can be generalized to novel words. Listeners may use this talker-specific memory to facilitate subsequent phonetic processing of familiar talkers' speech. Any complete model of speech perception must account for this listener sensitivity to individual talker differences in phonetic properties.

ACKNOWLEDGMENTS

This research was conducted as part of a doctoral dissertation at Northeastern University by the first author under the direction of the second author. We thank committee members Larry Brancazio, Neal Pearlmutter, and Adam Reeves for their advice throughout the course of this project, and Michèle Mondini for her critical reading of an earlier version

of the manuscript. This work was supported by NIH Grant DC00130 from the National Institute on Deafness and Other Communication Disorders.

[1]Of course, we do not mean to imply that VOT is the only acoustic-phonetic property that listeners track in a talker-specific manner or that VOT holds any privileged status in this regard. Indeed, the sine wave speech studies reviewed above (e.g., Remez *et al.*, 1997) suggest that VOT, which is absent from sine wave speech, need not be present in the signal for listeners to benefit from talker-specific experience. Rather, VOT is likely one among a host of acoustic-phonetic dimensions along which individual talkers differ and which listeners might therefore exploit.

[2]As a consequence of this method of stimulus selection, the short-VOT stimuli were better exemplars of /t/ than were the long-VOT stimuli, based on the ratings from the preliminary goodness-rating experiment. Ideally, the short- and long-VOT stimuli would have been matched in goodness while still being substantially separated in VOT. However, given the constraint that short-VOT stimuli in the experiment should not be confusable with voiced tokens, it was necessary to extend the choice of long-VOT stimuli toward more extreme values in order to achieve a substantial separation in VOT between the short- and long-VOT conditions. (Though the long-VOT stimuli have quite long VOT values, these values are not beyond the range of VOTs that can occur with isolated word productions.) Note that because the short- and long-VOT stimuli differed in perceived goodness, it is conceivable that during training listeners might associate one talker (the short-VOT talker) with ''better'' voiceless exemplars and the other talker (the long-VOT talker) with ''poorer'' voiceless exemplars, and then use this difference in goodness, rather than differences in VOT *per se*, as the basis for discrimination at test. However, because the within-category goodness differences are themselves based on differences in VOT, such discrimination would still indicate that listeners are sensitive to individual talker differences in VOT.

[3]No trends were apparent in the data across the nine training sets. It was not the case, for example, that subjects' performance tended to improve or decline systematically over the course of the experiment. Thus, all training sets were averaged together to assess each subject's overall performance during training.

[4]No trends were apparent in the data across the individual test sets. It was not the case, for example, that subjects' performance tended to improve or decline systematically over the course of the experiment. Thus, all test sets were averaged together to assess each subject's overall performance during tests.

Abercrombie, D. (**1967**). *Elements of General Phonetics* (Aldine, Chicago, IL).

Allen, J. S., and Miller, J. L. (**1999**). ''Effects of syllable-initial voicing and speaking rate on the temporal characteristics of monosyllabic words,'' J. Acoust. Soc. Am. **106**, 2031–2039.

Allen, J. S., Miller, J. L., and DeSteno, D. (**2003**). ''Individual talker differences in voice-onset-time,'' J. Acoust. Soc. Am. **113**, 544–552.

Bradlow, A. R., and Pisoni, D. B. (**1999**). ''Recognition of spoken words by native and non-native listeners: Talker-, listener-, and item-related factors,'' J. Acoust. Soc. Am. **106**, 2074–2085.

Bricker, P. D., and Pruzansky, S. (**1976**). ''Speaker recognition,'' in *Contemporary Issues in Experimental Phonetics*, edited by N. J. Lass (Academic, New York), pp. 295–326.

Carney, A. E., Widin, G. P., and Viemeister, N. F. (**1977**). ''Noncategorical perception of stop consonants differing in VOT,'' J. Acoust. Soc. Am. **62**, 961–970.

Fellowes, J. M., Remez, R. E., and Rubin, P. E. (**1997**). ''Perceiving the sex and identity of a talker without natural vocal timbre,'' Percept. Psychophys. **59**, 839–849.

Goldinger, S. D. (**1996**). ''Words and voices: Episodic traces in spoken word identification and recognition memory,'' J. Exp. Psychol. Learn. Mem. Cogn. **22**, 1166–1183.

Goldinger, S. D. (**1998**). ''Echoes of echoes? An episodic theory of lexical access,'' Psychol. Rev. **105**, 251–279.

Hillenbrand, J., Getty, L. A., Clark, M. J., and Wheeler, K. (**1995**). ''Acoustic characteristics of American English vowels,'' J. Acoust. Soc. Am. **97**, 3099–3111.

Johnson, K., and Mullennix, J. W. (Eds.) (**1997**). *Talker Variability in Speech Processing* (Academic, San Diego, CA).

Lachs, L., McMichael, K., and Pisoni, D. B. (**2003**). ''Speech perception and implicit memory: Evidence for detailed episodic encoding of phonetic events,'' in *Rethinking Implicit Memory*, edited by J. Bowers and C. Marsolek (Oxford University Press, Oxford), pp. 215–235.

Ladefoged, P., and Broadbent, D. E. (**1957**). ''Information conveyed by vowels,'' J. Acoust. Soc. Am. **29**, 98–104.

Lisker, L., and Abramson, A. S. (**1964**). ''A cross-language study of voicing in initial stops: Acoustical measurements,'' Word **20**, 384–422.

Miller, J. D. (**1989**). ''Auditory-perceptual interpretation of the vowel,'' J. Acoust. Soc. Am. **85**, 2114–2134.

Miller, J. L., Green, K. P., and Reeves, A. (**1986**). ''Speaking rate and segments: A look at the relation between speech production and speech perception for the voicing contrast,'' Phonetica **43**, 106–115.

Miller, J. L., Grosjean, F., and Lomanto, C. (**1984**). ''Articulation rate and its variability in spontaneous speech: A reanalysis and some implications,'' Phonetica **41**, 215–225.

Miller, J. L., and Volaitis, L. E. (**1989**). ''Effect of speaking rate on the perceptual structure of a phonetic category,'' Percept. Psychophys. **46**, 505–512.

Newman, R. S., Clouse, S. A., and Burnham, J. L. (**2001**). ''The perceptual consequences of within-talker variability in fricative production,'' J. Acoust. Soc. Am. **109**, 1181–1196.

Nygaard, L. C., and Pisoni, D. B. (**1995**). ''Speech perception: New directions in research and theory,'' in *Speech, Language, and Communication*, edited by J. L. Miller and P. D. Eimas (Academic, San Diego, CA), pp. 63–96.

Nygaard, L. C., and Pisoni, D. B. (**1998**). ''Talker-specific learning in speech perception,'' Percept. Psychophys. **60**, 355–376.

Nygaard, L. C., Sommers, M. S., and Pisoni, D. B. (**1994**). ''Speech perception as a talker-contingent process,'' Psychol. Sci. **5**, 42–46.

Peterson, G. E., and Barney, H. L. (**1952**). ''Control methods used in a study of vowels,'' J. Acoust. Soc. Am. **24**, 175–184.

Remez, R. E., Fellowes, J. M., and Rubin, P. E. (**1997**). ''Talker identification based on phonetic information,'' J. Exp. Psychol. Hum. Percept. Perform. **23**, 651–666.

Remez, R. E., Rubin, P. E., Pisoni, D. B., and Carrell, T. D. (**1981**). ''Speech perception without traditional speech cues,'' Science **212**, 947–950.

Sheffert, S. M., and Fowler, C. A. (**1995**). ''The effects of voice and visible speaker change on memory for spoken words,'' J. Mem. Lang. **34**, 665–685.

Sheffert, S. M., Pisoni, D. B., Fellowes, J. M., and Remez, R. E. (**2002**). ''Learning to recognize talkers from natural, sine wave, and reversed speech samples,'' J. Exp. Psychol. Hum. Percept. Perform. **28**, 1447–1469.

Summerfield, Q. (**1975**). ''Aerodynamics versus mechanics in the control of voicing onset in consonant–vowel syllables,'' in Speech Perception Report (No. 4). Belfast, Northern Ireland: Department of Psychology, The Queen's University of Belfast.

Summerfield, Q. (**1981**). ''Articulatory rate and perceptual constancy in phonetic perception,'' J. Exp. Psychol. Hum. Percept. Perform. **7**, 1074–1095.

Volaitis, L. E., and Miller, J. L. (**1992**). ''Phonetic prototypes: Influence of place of articulation and speaking rate on the internal structure of voicing categories,'' J. Acoust. Soc. Am. **92**, 723–735.

Adult–child differences in acoustic cue weighting are influenced by segmental context: Children are not always perceptually biased toward transitions

Catherine Mayo[a] and Alice Turk
Theoretical & Applied Linguistics, University of Edinburgh, Adam Ferguson Building, 40 George Square, Edinburgh, EH8 9LL, United Kingdom

(Received 18 November 2003; revised 16 March 2004; accepted 21 March 2004)

It has been proposed that young children may have a perceptual preference for transitional cues [Nittrouer, S. (**2002**). J. Acoust. Soc. Am. **112**, 711–719]. According to this proposal, this preference can manifest itself either as heavier weighting of transitional cues by children than by adults, or as heavier weighting of transitional cues than of other, more static, cues by children. This study tested this hypothesis by examining adults' and children's cue weighting for the contrasts /saɪ/-/ʃaɪ/, /de/-/be/, /ta/-/da/, and /ti/-/di/. Children were found to weight transitions more heavily than did adults for the fricative contrast /saɪ/-/ʃaɪ/, and were found to weight transitional cues more heavily than nontransitional cues for the voice-onset-time contrast /ta/-/da/. However, these two patterns of cue weighting were not found to hold for the contrasts /de/-/be/ and /ti/-/di/. Consistent with several studies in the literature, results suggest that children do not always show a bias towards vowel–formant transitions, but that cue weighting can differ according to segmental context, and possibly the physical distinctiveness of available acoustic cues. © *2004 Acoustical Society of America.* [DOI: 10.1121/1.1738838]

PACS numbers: 43.71.Ft [RLD] Pages: 3184–3194

I. INTRODUCTION

It is well established that listeners do not pay equal attention to all acoustic information available to them in the speech stream. Instead, when perceiving speech, listeners give some acoustic cues more attention than others (Dorman *et al.*, 1977; Ohde and Haley, 1997; Walley and Carrell, 1983; Wardrip-Fruin, 1982, 1985; Whalen, 1991). These patterns of acoustic cue weighting appear to change developmentally: Children have been found to show different cue weighting strategies from adults. Nittrouer and colleagues, for example, have found that in identifying fricative contrasts (e.g., /su/-/ʃu/) based on frequency of frication noise and vowel-onset formant transition cues, young children give more attention or weight to the formant transitions than do older children and adults (Nittrouer and Studdert-Kennedy, 1987). Other researchers have also found differences between children and adults in their relative weighting of acoustic cues (Krause, 1982; Lacerda, 1992; Mayo *et al.*, 2003; Morrongiello *et al.*, 1984; Ohde and Haley, 1997; Parnell and Amerman, 1978; Watson, 1997; Wardrip-Fruin and Peach, 1984).

Nittrouer and colleagues (Nittrouer, 1993; Nittrouer and Miller, 1997) have suggested that these differences in cue weighting between adults and children are not random, but are related to developmental changes in the way in which listeners process speech. This hypothesis, called the Developmental Weighting Shift (DWS) theory, is based on the premise that children start out processing speech globally, in terms of large units such as syllables or monosyllabic words. With development, it is proposed, processing becomes more analytical, such that adults parse speech in terms of smaller units (e.g., Jusczyk and Derrah, 1987; Menn, 1971; Studdert-Kennedy, 1987, although note that contrasting views exist, see, e.g., Dollaghan, 1994; Gerken *et al.*, 1995). The DWS proposes that this change in processing impacts on speech perception development, and that it does so in terms of the acoustic cues that listeners attend to or weight most heavily. That is, children and adults show different patterns of acoustic cue weighting because they process speech in terms of different sized units.

Nittrouer has gone on to suggest that the acoustic correlates of more global speech perception could be syllable-internal formant transitions, because these cues are ''perceptually salient and delimit signal portions corresponding to syllables'' (Nittrouer *et al.*, 2000, p. 268). In other words, children, as more global perceivers, should be perceptually biased toward making heavier use of vowel-formant transitional cues. How this bias is manifested is not entirely straightforward. Initially, based on the results of the /s-vowel/-/ʃ-vowel/ study noted earlier, it was proposed that children give more weight to transitional cues than do adults. This was indeed found to be the case for a number of other /s-vowel/-/ʃ-vowel/ studies (Nittrouer, 1992; Nittrouer and Miller, 1997; Mayo *et al.*, 2003; Watson, 1997), but a later study of /f-vowel/-/θ-vowel/ perception (Nittrouer, 2002) showed no significant difference between adults and children in their weighting of transitional cues. This /f-vowel/-/θ-vowel/ study did show, though, that for this contrast children (and adults) gave more weight to transitional cues than to the other available cue, frequency of frication noise. In light of this, Nittrouer (2002) suggested that for those contrasts in which nontransitional cues are particularly uninformative to both adults and children (such as in /f/-/θ/, see, e.g., Harris,

[a]Electronic mail: catherin@ling.ed.ac.uk

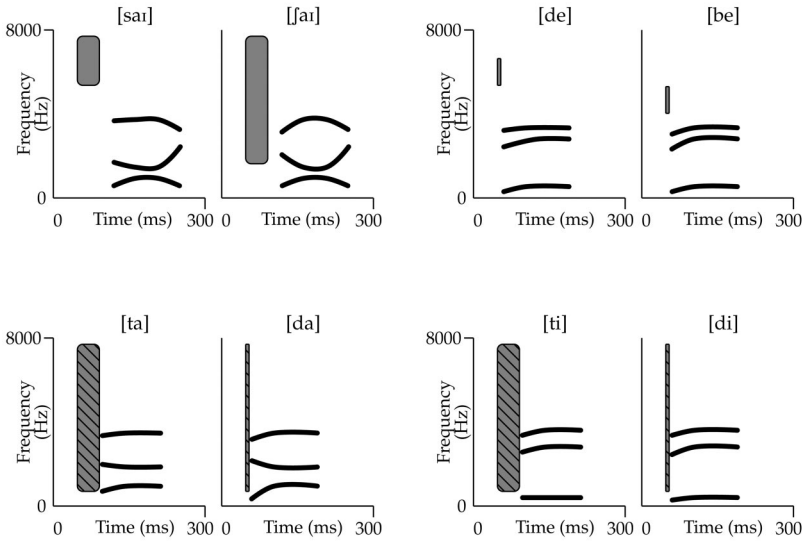

FIG. 1. Stylized spectrograms of prototypical tokens of the contrasts used in this study. The gray boxes represent frication noise (/saɪ/-/ʃaɪ/), stop burst (/de/-/be/), and burst+aspiration (/ta/-/da/,/ti/-/di/). The black lines represent vowel formants (F1,F2,F3).

1958) children's preference for transitional information could operate acoustically, leading children to weight transitional cues more heavily than other acoustic cues to the same contrast. In summary, according to this theory, children should weight transitions either (i) more heavily than do adults (what we will call the *developmental transitional bias hypothesis*), or (ii) more heavily than they weight other acoustic cues (what we will call the *acoustic transitional bias hypothesis*). Furthermore, there should not exist a contrast for which children are *not* biased in one of these two ways toward vowel-formant transitional cues.

Evidence for the two aspects of this theory is equivocal. Supporting the developmental transitional bias hypothesis, studies have shown that children are more influenced by transitional cues than are adults in determining voicing in final stops (Krause, 1982; Wardrip-Fruin and Peach, 1984), in identifying place of articulation of some initial stops (particularly /g/, Ohde *et al.*, 1996; Ohde and Haley, 1997), and in determining voicing for some initial stops (/biz/-/piz/ with long VOT, and /bat/-/pat/ with both long and short VOT, Howell *et al.*, 1992). However, children appear to be less influenced by transitions than older listeners for some VOT contrasts (/got/-/kot/, Simon and Fourcin, 1978, /biz/-/piz/ with short VOT, Howell *et al.*, 1992), and for identifying vowels (Malech and Ohde, 2003; Sussman, 2001). Furthermore, while the acoustic transitional bias hypothesis would predict that in these latter cases children should give more weight to transitional than to nontransitional cues, this does not appear to be the case: In the same studies, children gave *less* weight to transitional than to nontransitional cues. Children were found to give more weight to vowel duration (Ohde *et al.*, 1996; Ohde and Haley, 1997) or to steady-state formant frequencies (Sussman, 2001) than to formant transitions when identifying vowel contrasts. In identifying voicing in initial stops, children have been consistently found to weight VOT more heavily than vowel-onset transitions (Simon and Fourcin, 1978; Howell *et al.*, 1992).

It appears from these studies that children may not always attend more closely to transitional cues. The studies suggest that adult–child differences in cue weighting may change both with the segmental context of the contrast, and with the acoustic characteristics of the cues available to signal the contrast. Based on evidence such as this, a number of researchers have suggested alternatives to the DWS, most notably an account based on general auditory processing differences between adults and children (e.g., Elliott *et al.*, 1981; Elliott and Busse, 1984; Eisenberg *et al.*, 2000; Sussman, 1993, 2001). This type of explanation generally proposes that because children have less well developed auditory systems than do adults, they will have trouble processing acoustic cues that are not physically distinct. However, there are problems with dismissing the two transitional bias hypotheses based only on evidence from the above-noted studies. In particular, the variety of different methods and stimulus types (natural, modified-natural, or synthetic speech) used across these studies makes direct comparisons between the results complicated at best.

It therefore remains unclear to what extent the transitional bias hypothesis holds for different segmental contexts if experimental conditions remain constant. Our goal, therefore, was to examine cue weighting strategies across multiple contrasts using the same methodology for each. Two different place of articulation contrasts were used in the study: The fricative contrast /saɪ/-/ʃaɪ/, and the stop burst contrast /de/-/be/. Two voice-onset time (VOT) contrasts were chosen, due to the contradictory evidence found previously for VOT: /ta/-/da/ and /ti/-/di/.[1] Figure 1 shows stylized spectrograms of all four contrasts. For each contrast, we tested adults' and children's weighting of (i) a vowel-onset formant transition cue, and (ii) one of the following nontransitional cues: Frequency of frication noise for /saɪ/-/ʃaɪ/, frequency of stop burst for /de/-/be/, and duration of VOT for /ta/-/da/ and /ti/-/di/.

Two types of analysis were carried out on the results. First, adults' and children's cue weighting strategies were compared for each of the different contrasts. This allowed for an examination of the possible role of segmental context in adult–child cue weighting differences. This also enabled us to determine the scope of children's possible transitional bias as it relates to adults' cue weighting patterns. Second, for a set of contrasts which did not support the developmental transitional bias hypothesis, logistic regression was em-

ployed to compare the weight given to transitional cues and the weight given to nontransitional cues. This allowed us to test the acoustic version of the transitional bias hypothesis.

It should be noted that varying contrasts also means varying the physical distinctiveness of the available transitional and nontransitional acoustic cues in those contrasts. For example, in the contrast /su/-/ʃu/, the difference in F2 frequency at vowel onset is relatively larger (more distinct) than the difference in F2 frequency at vowel onset in the contrast /si/-/ʃi/. Nittrouer (1992) has shown that this type of difference in physical distinctiveness impacts on listeners' perception for /s-vowel/-/ʃ-vowel/ contrasts. Both adults and children were found to weight transitional cues less when perceiving /si/-/ʃi/ than when perceiving /su/-/ʃu/ (although note that children were consistent in weighting transitional cues more heavily than adults for both contrasts). This suggests that the transitions in the /si/-/ʃi/ contrast provided less useful information overall. Similar differences in physical distinctiveness, and thus presumably in informativeness, should be expected for the transitional cues manipulated in this study. Additionally, the nontransitional cues used in the current study (frication noise, stop burst, voice onset time) are also likely to differ in their perceptual informativeness, although quantifying the difference in informativeness between three different types of cue is more complex than comparing the informativeness of two different sets of one type of cue. Therefore, while this is not the focus of the current study, the fact that informativeness often co-varies with segmental context will need to be borne in mind when analyzing the results.

II. METHOD

A. Participants

For the /saɪ/-/ʃaɪ/ contrast, 10 adults (age range of 20–35 years, average age 26 years) out of 15 adults tested,[2] 8 seven-year-olds (age range 7;3–7;10 [year;month], average age 7;6) out of 15 seven-year-olds tested, 6 five-year-olds (age range 5;1–5;10, average age 5;4) out of 10 five-year-olds tested, and 9 three- to four-year-olds (age range 3;7–4;9, average age 4;3) out of 11 three- to four-year-olds tested met the testing criterion (described below).

For the /de/-/be/ contrast, 7 out of 7 adults tested (age range 21–33 years, average age 26 years) met the testing criterion, but only 2 seven-year-olds (both 7;5) out of 10 seven-year-olds tested, 2 five-year-olds (5;5 and 5;7) out of 7 five-year-olds tested, and 1 three- to four-year-old (4;0) out of 8 three- to four-year-olds tested met the criterion.

For the /ta/-/da/ contrast, 8 out of 8 adults tested (age range 21–49 years, average age 33 years), 10 seven-year-olds (age range 7;0–7;11, average age 7;7) out of 11 seven-year-olds tested, 9 five-year-olds (age range 5;1–5;8, average age 5;5) out of 10 five-year-olds tested and 12 three- to four-year-olds (age range 3;0–4;11, average age 4;0) out of 18 three- to four-year-olds tested met the testing criterion.

For the /ti/-/di/ contrast, 8 out of 8 adults tested (age range 21–49 years, average age 33 years), 10 seven-year-olds (age range 7;0–7;11, average age 7;7) out of 11 seven-year-olds tested, 9 five-year-olds (age range 5;1–5;8, average age 5;5) out of 10 five-year-olds tested and 9 three- to four-year-olds (age range 3;7–4;11, average age 4;1) out of 18 three- to four-year-olds tested met the testing criterion.

All of the five- and seven-year-olds were in full-time primary education (first and third year) in Edinburgh (Scotland). The three- to four-year-old children were selected from independent and school-associated nursery (pre-school) classes. All of the children were monolingual native speakers of Scottish Standard English (SSE), and all performed appropriately for their age on standardized tests of reading (Schonell Graded Word Reading Test, Schonell and Goodacre, 1971) and receptive vocabulary (BPVS, Dunn *et al.*, 1997). Parental questionnaires determined that all of the children and their siblings were free from speech/language disorders, hearing deficits and histories of chronic otitis media (defined as more than three ear infections between birth and 3;0, and/or the implantation of myringotomy tubes, see Nittrouer, 1996). No child was tested if he or she was suffering from, or had suffered from at any point in the weeks preceding the test session, any upper respiratory infection.

All adults were monolingual native speakers of English living in Edinburgh (average duration of time in Scotland: 12 years). All of the adults reported themselves as being free from speech/language disorders, hearing deficits, and histories of chronic otitis media. Again, no adult was tested if he or she was suffering from, or had suffered from at any point in the weeks preceding the test session, any upper respiratory infection.

B. Stimuli

The contrasts used in this study were /saɪ/-/ʃaɪ/, /de/-/be/, /ta/-/da/ and /ti/-/di/.[3] Continua of synthetic speech sounds were created for each contrast. The end points of the synthetic continua were copy-synthesized versions of the above-noted syllables based on detailed acoustic analysis of natural tokens spoken by a male native speaker of SSE (aged 39 years, with normal speech, language and hearing). The stimuli were created using SENSYN (Sensimetrics Org.), a cascade/parallel formant synthesizer based on Klatt (1980).

In order to make direct comparisons between the results of this study and those of Nittrouer and colleagues, the design of the stimuli followed the modified trading relations paradigm used by Nittrouer in most of her studies of /s/-/ʃ/ contrasts (e.g., Nittrouer and Studdert-Kennedy, 1987; Nittrouer, 1992). In this paradigm, two continua of speech sounds are created in which (at least) two acoustic cues are manipulated. One of the two cues is varied *along* both continua. The two continua are therefore identical in terms of this cue. The other cue is varied *across* the two continua. The two continua therefore differ in terms of this cue. In most of Nittrouer and colleagues' studies of cue weighting for /s/-/ʃ/ contrasts (see, e.g., Nittrouer, 1992), the two cues manipulated were frequency of frication noise, and vowel-onset formant transitions. The frication pole varied along both continua from a frequency appropriate for /s/ to one appropriate for /ʃ/. The vowel-onset formant transitions varied across the two continua: One continuum had transitions that were appropriate for a preceding /s/, the other continuum had transitions that were appropriate for a preceding /ʃ/ (see Fig. 2).

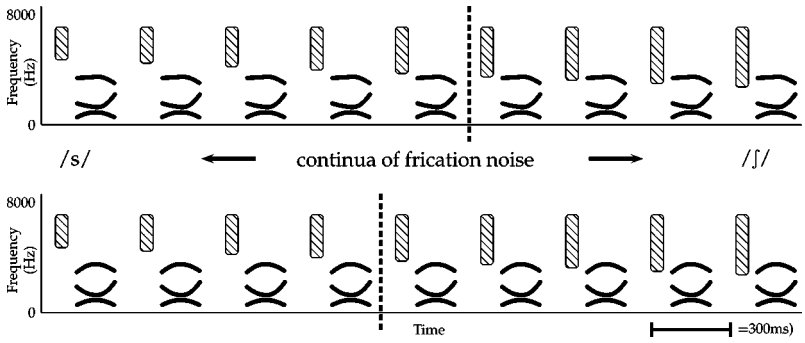

FIG. 2. Stylized spectrograms of two /saɪ/-/ʃaɪ/ continua. The top continuum has /s/-transition vowels, the bottom continuum has /ʃ/-transition vowels. The dashed lines represent hypothetical category boundaries for a listener whose perception is influenced by the transitions.

This type of design allows for an investigation of the perceptual effect of the two cues. A listener who is not influenced by the cue that changes across the continua (e.g., the transitional cue in the /s/-/ʃ/ example above) will perceive the two continua as the same. In contrast, a listener who *is* influenced by the cue that changes across the continua will perceive the two continua differently (see the category boundaries marked in Fig. 2).

The current study followed the general design of those carried out by Nittrouer and colleagues by manipulating one nontransitional cue and one transitional cue for each contrast. The nontransitional cues were: Frequency of frication noise for /saɪ/-/ʃaɪ/, frequency of stop burst for /de/-/be/, and duration of VOT for /ta/-/da/ and /ti/-/di/. The transitional cues were the frequency and time-varying properties of vowel-onset formant transitions in two conditions: (i) appropriate for having followed the first consonant in the contrast, or (ii) appropriate for having followed the second consonant in the contrast. As these transitional cues were closely modeled on natural speech they had gradually changing formant frequencies rather than the straight line transitional slopes typical of some synthetic stylisations. Two 9-point continua were created for every contrast, in which the nontransitional cue varied along both continua and the transitional cue varied across the two continua. Following Nittrouer (1992), five different repetitions of the same vowel were synthesized for each transition condition. This was done to enhance the naturalness of the synthetic speech by capturing a small amount of within-speaker variability. Subsequent examination of the results showed no obvious influence of any one vowel token on listeners' responses. Each of these vowels was combined with the 9 continuum values, resulting in 90 stimuli per contrast. In the following are details of the parameters manipulated for each contrast.

1. /saɪ/-/ʃaɪ/

Nine different single-pole frication noises were synthesized, ranging from 3100 Hz (most /ʃ/-like) to 5800 Hz (most /s/-like). Two sets of /aɪ/ vowels were created, one with onset frequencies appropriate for a preceding /s/ and one with onset frequencies appropriate for a preceding /ʃ/. The average /ʃ/-transition formant onset frequencies were F1: 435 Hz, F2: 1574 Hz, F3: 2400 Hz; the average /s/-transition formant onset frequencies were F1: 537 Hz, F2: 1536 Hz, F3: 2551 Hz. The average vowel target values for the /a/ portion of the diphthong for all 10 synthetic vowels were F1: 762 Hz, F2: 1184 Hz, F3: 2784 Hz. The vowel target values for the /ɪ/ portion of the diphthong for all 10 synthetic vowels were F1: 448 Hz, F2: 1958 Hz, F3: 2419 Hz (see Appendix A for all values used for synthetic stimuli).

The total duration of each syllable was 540 ms, with 155 ms of frication noise and 385 ms of vowel. The average duration of vowel formant transitions as measured from vowel onset to vowel steady state was 60 ms for /s/-transition stimuli and 80 ms for /ʃ/-transition stimuli.[4] F0 for each complete syllable began at 140 Hz at onset of voicing, rose to 150 Hz 110 ms after onset of voicing, and fell to 90 Hz at vowel offset.

2. /de/-/be/

Nine different complex bursts were synthesized. The spectral shape of the bursts was modeled by means of three spectral peaks, one of which was designed to model a cavity at the front of the mouth.[5] The amplitude of these bursts ranged from 54 dB at 5550 Hz, 36 dB at 2700 Hz, and 20 dB at front cavity peak (most /d/-like) to 6 dB at 4500 Hz, 0 dB at 2100 Hz, and 50 dB at front cavity peak (most /b/-like). Two sets of /e/ vowels were created, one with onset frequencies appropriate for having followed /d/ and one with onset frequencies appropriate for having followed /b/. The average /d/-transition formant onset frequencies were F1: 220 Hz, F2: 1809 Hz, F3: 2446 Hz; the average /b/-transition formant onset frequencies were F1: 257 Hz, F2: 1694 Hz, F3: 2247 Hz. The average vowel target values for all 10 synthetic vowels were F1: 428 Hz, F2: 2116 Hz, F3: 2539 Hz.

The total duration of each syllable was 400 ms, with 15 ms of burst, and 385 ms of vowel. The average duration of vowel formant transitions as measured from vowel onset to vowel steady state was 100 ms for /d/-transition stimuli and 110 ms for /b/-transition stimuli. F0 for each complete syllable began at 140 Hz at onset of voicing, rose to 150 Hz 110 ms after onset of voicing, and fell to 90 Hz at vowel offset.

3. /ta/-/da/

Nine different VOT values were synthesized, varying in 5 ms steps from 40 ms (most /t/-like) to 0 ms (most /d/-like). Two sets of /a/ vowels were created, one with onset frequencies appropriate for having followed /t/ and one with onset frequencies appropriate for having followed /d/. The average /ta/-transition formant onset frequencies were F1: 537 Hz, F2: 1536 Hz, F3: 2551 Hz; the average /da/-transition formant onset frequencies were F1: 261 Hz, F2: 1642 Hz, F3:

2472 Hz. The average vowel target values for all 10 synthetic vowels were F1: 711 Hz, F2: 1433 Hz, F3: 2665 Hz.

The total duration of each syllable ranged from 315 ms for the shortest VOT to 355 ms for the longest VOT, with 315 ms of vowel. The average duration of vowel formant transitions as measured from vowel onset to vowel steady state was 55 ms for /t/-transition stimuli and 85 ms for /d/-transition stimuli. F0 for each complete syllable began at 124 Hz at onset of voicing, rose to 130 Hz 90 ms after onset of voicing, and fell to 60 Hz at vowel offset.

4. /ti/-/di/

The VOT values used for the /ti/-/di/ contrast were the same as those used for the /ta/-/da/ contrast. These varied in 5 ms steps from 40 ms (most /t/-like) to 0 ms (most /d/-like). Two sets of /i/ vowels were created, one with onset frequencies appropriate for having followed /t/ and one with onset frequencies appropriate for having followed /d/. The average /ti/-transition formant onset frequencies were F1: 311 Hz, F2: 1924 Hz, F3: 2599 Hz; the average /di/-transition formant onset frequencies were F1: 221 Hz, F2: 1893 Hz, F3: 2569 Hz. The average vowel target values for all ten synthetic vowels were F1: 309 Hz, F2: 2183 Hz, F3: 2819 Hz.

The total duration of each syllable ranged from 315 ms for the shortest VOT to 355 ms for the longest VOT, with 315 ms of vowel. The average duration of vowel formant transitions as measured from vowel onset to vowel steady state was 110 ms for /t/-transition stimuli and 105 ms for /d/-transition stimuli. F0 for each complete syllable began at 124 Hz at onset of voicing, rose to 130 Hz 90 ms after onset of voicing, and fell to 60 Hz at vowel offset.

C. General procedure

With the exception of the subjects who heard the VOT contrasts, each subject was asked to listen to only one set of contrasts; those subjects who heard the VOT contrasts listened to both the /ta/-/da/ and the /ti/-/di/ contrasts. All subjects were tested individually in a quiet room. The stimuli were presented over headphones (Sennheiser HD 490, frequency response 17–22000 Hz) via a CD player. Volume was set at a comfortable listening level. Each subject was asked to indicate that the level was both comfortable and audible (for the child subjects, the signal was split to two headphones and the chosen listening level was monitored by the experimenter); very few adjustments to the level were made by the subjects. No adjustments to listening level were made within the presentation of a single contrast. Testing for the child subjects took place over two or three days. Testing for the adult subjects took place on one day, with a short break half-way through testing.

All subjects were introduced to the target words for their contrast. The child subjects were also familiarized with pictures that corresponded to each word in their contrast (see Appendix B for a description of the pictures used in the study). During testing, the children indicated which word they had heard by saying the word aloud, and by placing a counter on the relevant picture. Before testing, the children were given an opportunity to practice responding to natural productions of the target words. This ensured that the children were able to identify the targets in natural speech, and that they clearly associated each picture with the relevant target. The children received feedback throughout this practice, and did not proceed to the pretest with synthetic stimuli until they had, unprompted, correctly identified a complete set of 10 randomly presented natural stimuli (5 of each CV syllable).

A pretest was administered to both child and adult subjects to ensure that they understood the task. This test consisted of the congruent end points of the continua, that is, the end point values of the nontransitional cue followed by the congruent vowel-formant transitions for each nontransitional cue condition. For example, the congruent end points for the /ta/-/da/ contrast were the 40 ms VOT plus vowels with /t/-transitions (the most /ta/-like stimuli) and the 0 ms VOT plus vowels with /d/-transitions (the most /da/-like stimuli). There were 10 stimuli in the pretest (5 per congruent end point), presented in random order. No feedback was given during this pretest.

For each contrast, five different random orders of the 90 stimuli were created. During the main test, the five-year-old, seven-year-old, and adult subjects heard a complete set of 90 stimuli twice, in two different random orders, resulting in 180 responses per subject and 10 responses per transition type for each point on the continuum. The three- to four-year-old subjects heard a complete set of 90 stimuli only once, resulting in 5 responses per transition type for each point on the continuum for this group. Although this smaller number of presentations may have lead to noisier data than if 10 responses per transition type had been collected, it was only practical to test a smaller number of responses for this age group because of limitations on the children's attention span. Subsequent examination of the data showed that the results from the three- to four-year-olds were not qualitatively different from those of the other child subjects. Each randomization was split into blocks of 10 stimuli for presentation. The interstimulus interval for presentation to the adult subjects was 3 s, with an interblock interval of 10 s. Following Walley and Carrell (1983), the interstimulus interval was not fixed for presentation to the children. Instead, the presentation was paused briefly after every stimulus, allowing the children sufficient time to respond.[6] At the end of each block, the children were allowed to choose a small prize.

Here, as in the literature (see Nittrouer, 1992), only those listeners who responded correctly to 80% of the congruent continuum end points presented within the test proper were included in quantitative analysis. The purpose of this was to eliminate listeners whose responses were random or inconsistent.

III. ANALYSIS 1: ADULT VERSUS CHILD WEIGHTING OF TRANSITIONS

Each contrast engendered two sets of responses, one for each transition condition. The responses for the /saɪ/-/ʃaɪ/, /ta/-/da/ and /ti/-/di/ contrasts were normalized using a probit

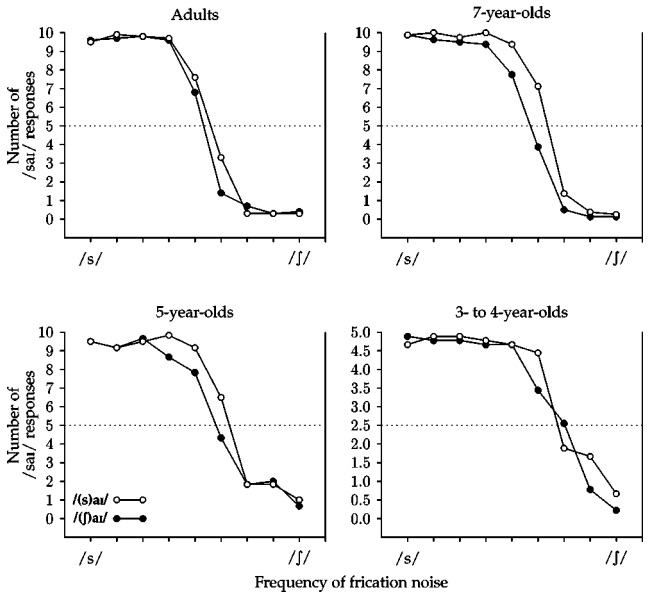

FIG. 3. Adults' and children's responses to /saɪ/-transition stimuli (open circles) and /ʃaɪ/-transition stimuli (closed circles). Responses are presented in terms of /saɪ/-responses as a function of frequency of frication noise ranging from most /s/-like (5800 Hz) to most /ʃ/-like (3100 Hz). The dotted lines indicate the 50% /saɪ/ response point. The *y*-axis range for the three- to four-year-olds is half that of the other subjects because this group heard half as many repetitions per point on the continuum.

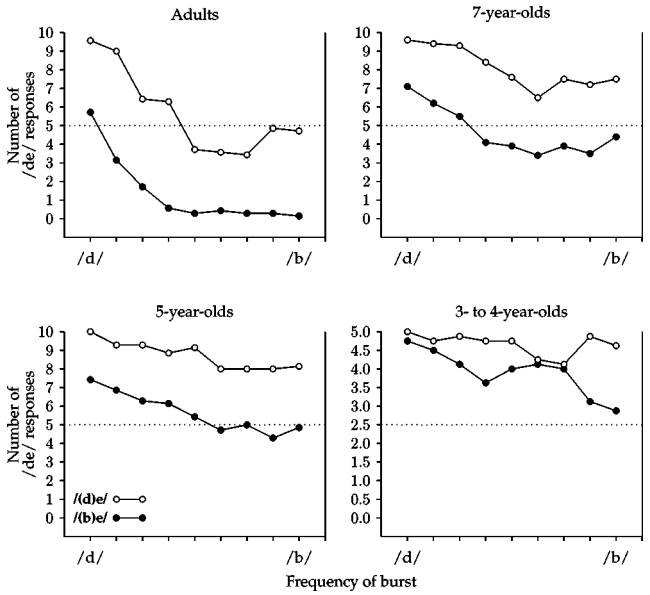

FIG. 4. Adults' and children's responses to /de/-transition stimuli (open circles) and /be/-transition stimuli (closed circles). Responses are presented in terms of /de/-responses as a function of frequency of complex stop burst ranging from most /d/-like to most /b/-like (see the text for details of frequency range). The dotted lines indicate the 50% /de/ response point. See Fig. 3 for more details.

transformation. This transform extracts rate-of-change information from data appropriately modeled with an S-shaped curve and yields estimates of the slope and the mean of the curve (Cohen and Cohen, 1983). The slope corresponds to the degree of categoriality of the responses and the mean corresponds to the point on the continuum at which the responses reach 50% (i.e., 50% /s/ or /ʃ/ responses). The degree of separation of the two response curves was calculated by taking the difference of the two means (e.g., the mean of the continuum with /s/-transitions and the mean of the continuum with /ʃ/-transitions). This gives a measure of the extent to which listeners' responses were influenced by the change in transitional information across continua.

As noted above, only five children met the testing criterion for the /de/-/be/ contrast. The responses to these contrasts were therefore not analyzed quantitatively.

A. Results

1. /saɪ/-/ʃaɪ/

The results for the /saɪ/-/ʃaɪ/ contrast are shown in Fig. 3. The listeners' responses are generally consistent with the results found previously by Nittrouer and colleagues and others for /s/-/ʃ/ contrasts: The children in the current study showed greater influence of transitional cues than adults. That is, children as a group showed a significantly greater separation of response curves than did adults in response to a change in transitional information [$F(1,31)=5.50$, $p=0.026$]. There was also a significant difference between adults and children for placement of category boundary along the frication continuum for the /saɪ/-transition response curves [$F(1,31)=10.53$, $p=0.003$] and for the /ʃaɪ/-transition response curves [$F(1,31)=6.03$, $p=0.020$]. Although Nittrouer reported differences in slope between adults and children (Nittrouer and Studdert-Kennedy, 1987; Nittrouer, 1992), which she has taken to reflect a difference between the two groups in reliance on frication noise (i.e., the cue that changes along the two continua), we did not find any significant difference between adults and children for the slope of either the /s/-transition or the /ʃ/-transition response curves. Nittrouer and colleagues also found significant differences between children of different ages for both separation and slope of response curves. However, no significant effect of age amongst the children was found for these two factors in this study.

2. /de/-/be/

Figure 4 shows the results for the /de/-/be/ contrast. Only five children met the testing criterion for this contrast. Despite this, the perceptual behavior of all of the children tested on this contrast appeared to be relatively nonrandom both along and across the continua. That is, there seemed to be a principled relationship between responses to consecutive points on each continuum, and differences between responses to points on each continuum were comparable at successive points. Therefore, for illustrative purposes, the responses of *all* subjects, including those that did not meet the testing criterion, are shown here.

Adults' response curves were both widely separated and slightly sloping, indicating that they relied on both transitional and nontransitional (stop burst) cues in making their responses. In contrast, children's response curves showed much less consistent separation and little identifiable slope;

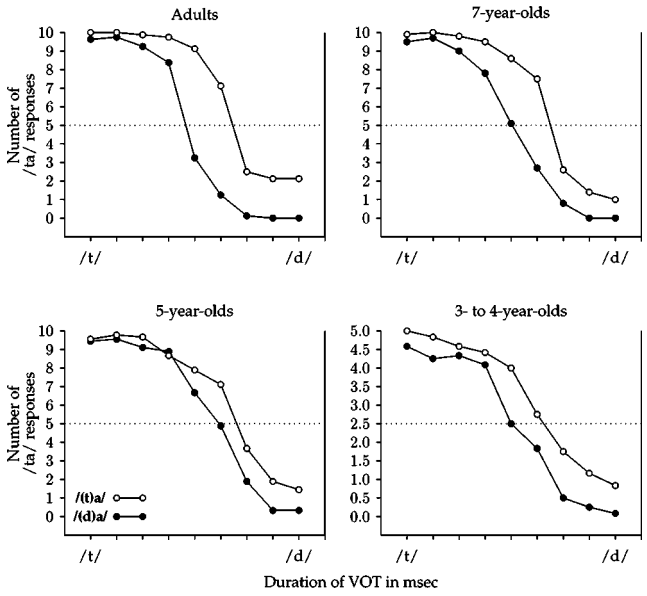

FIG. 5. Adults' and children's responses to /ta/-transition stimuli (open circles) and /da/-transition stimuli (closed circles). Responses are presented in terms of /ta/-responses as a function of VOT ranging from most /t/-like (40 ms) to most /d/-like (0 ms). The dotted lines indicate the 50% /ta/ response point. See Fig. 3 for more details.

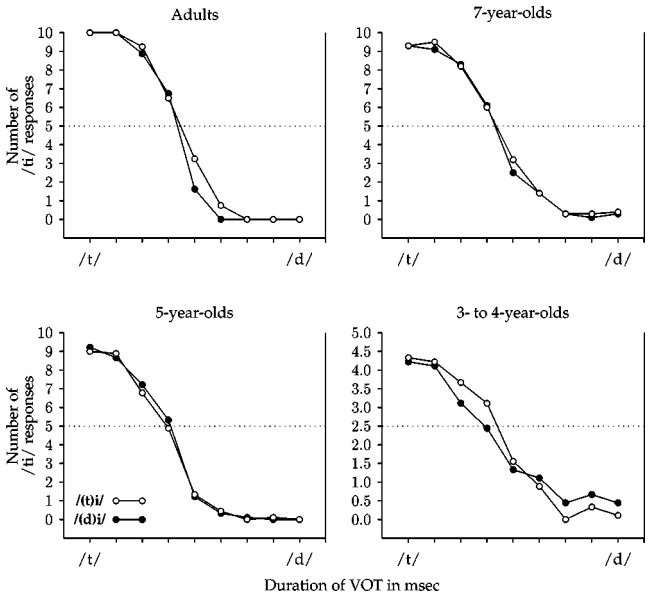

FIG. 6. Adults' and children's responses to /ti/-transition stimuli (open circles) and /di/-transition stimuli (closed circles). Responses are presented in terms of /ti/-responses as a function of VOT ranging from most /t/-like (40 ms) to most /d/-like (0 ms). The dotted lines indicate the 50% /ti/ response point. See Fig. 3 for more details.

in fact, many three- to four-year-olds appeared not to be able to consistently identify any of the /de/-/be/ stimuli as different at all. This, in addition to the fact that so few children met the testing criterion of 80% correct identification of congruent end points, suggests that children were unable to reliably make use of either the transitional or the nontransitional cues to identify this contrast.

B. /ta/-/da/ and /ti/-/di/

Figures 5 and 6 show the results for the /ta/-/da/ and /ti/-/di/ contrasts. The results appear to be qualitatively different from those seen for /saɪ/-/ʃaɪ/. Children do not appear to pay more attention to transitional information than adults in their identification of /ta/-/da/ or /ti/-/di/. For the /ti/-/di/ contrast, children give the same weight as adults to transitional cues. This is indicated by the fact that there is no significant difference between children as a group and adults in separation of response curves for this contrast. For the /ta/-/da/ contrast, children give less weight than adults to transitional cues. This is reflected in the fact that children as a group show a significantly smaller separation of response curves due to a change in transitional information than do adults [$F(1,37)=5.89$, $p=0.02$]. Children of different ages did not differ significantly from each other for this dimension for any of the three contrasts. There was no significant difference between adults and children for placement of category boundary along the VOT continuum for /ta/-transition response curves, /da/-transition response curves, /ti/-transition response curves, or /di/-transition response curves.

C. Discussion

As noted earlier, adults' and children's responses to the /saɪ/-/ʃaɪ/ contrast are consistent with previous /s/-/ʃ/ studies, as well as with the proposal that children give more weight to transitional cues than do adults. However, the findings that children and adults are equally influenced by transitions for /ti/-/di/, and that children show less influence of transitional cues than adults for /ta/-/da/ appear to contradict the developmental transitional bias hypothesis. In fact, the results from all three contrasts taken together suggest that, rather than being consistently more biased than adults toward transitions, the extent to which children make use of transitional information as compared to adults changes with segmental context.

However, there is an alternative explanation for these VOT results, which makes reference to the qualitative difference between transitions following /t/ and /d/ and those following /s/ and /ʃ/. For low or back vowels following /s/ and /ʃ/, formants differ in both direction and extent. That is, F2 transitions following /s/ are greater in extent than F2 transitions following /ʃ/ and F3 transitions following /s/ are relatively flat, while F3 transitions following /ʃ/ are rising. For vowels following /t/ and /d/, the formant transitions move in the same direction, but not to the same extent: Voiced transitions following /t/ are much less extensive than those following /d/, due to the presence of voiceless aspiration. This means that the voiced transition of a vowel following /t/ looks like a frequency-truncated version of a vowel following /d/ (for example, the frequency of F2 at the voiced onset of /ta/ is lower than the frequency of F2 at the voiced onset of /da/, see Fig. 1). One could therefore interpret the results of the two current VOT experiments as meaning that children are so much more sensitive to transitional information than adults that they are prepared to accept even ''frequency-truncated'' /d/-transitions (i.e., /t/-transitions) as indicating a /d/, and thus need only a short silence duration to persuade them that what they have heard is indeed /d/. This behavior would result in a smaller separation of response curves for

children than for adults. This proposal was put forward by Nittrouer (1992) to explain results of a study of ''say-stay'' perception, and is consistent with the claim that children are more perceptually sensitive to transitions than adults.

There is, however, evidence against this interpretation. First, as noted earlier, a truncation explanation requires a smaller separation of response curves for children than for adults. While this is true for the /ta/-/da/ contrast, for the /ti/-/di/ contrast there was no significant difference between adults and children for separation of the /ti/ and /di/ response curves. Also, in order for a truncation explanation to be correct, the category boundaries for all of the subjects should be the same for the unambiguous, ''untruncated'' /d/-transition stimuli, but there should be a difference between children and adults for the ambiguous, ''truncated'' /t/-transition stimuli: If children require less silence to hear these as voiced, they should place their boundaries closer to the 0 ms end of the VOT continuum than do the adults (Nittrouer, 1992). However, as noted earlier, although the difference in separation of response curves between adults and children was significant for /ta/-/da/, suggesting that the (nonsignificant) shift for each type of boundary was comparable in magnitude, there was no significant effect of age on the placement of either the /ta/-transition response curves or the /da/-transition response curves. There was also no significant difference between adults and children for the placement of either the /ti/-transition response curves or the /di/-transition response curves.

Further evidence against this interpretation of the current VOT results comes from studies of fricative contrast perception. The results for the /ta/-/da/ contrast showed greater separation of response curves for adults as compared to children. If this pattern is due to the fact that /t/-transitions are simply ''frequency-truncated'' versions of /d/-transitions then the same pattern of results should be seen for all contrasts in which the transitional information in one syllable is a ''frequency-truncated'' version of the other, no matter what the segmental context. However, this is not what is found. In the /su/-/ʃu/ contrasts that have been shown to engender cue weighting differences in children and adults, F2 following /s/ is a ''frequency-truncated'' version of F2 following /ʃ/, in the sense that the onset frequency of F2 following /s/ is lower than the onset frequency of F2 following /ʃ/. Therefore, if F3 is neutralized in both of the syllables, the resulting /su/-/ʃu/ contrast will be cued by the same type of relationship between transitions as found in the /ta/-/da/ contrast above. According to the truncation view, children should accept more of these neutral-F3-/su/ stimuli as ''truncated'' versions of /ʃu/. They should therefore show a smaller separation of response curves than adults in perception of this contrast.

Nittrouer and Miller (1997) have tested children's and adults' cue weighting of a /su/-/ʃu/ contrast in which F3 was neutralized. However, the results of that study showed that, unlike for the /ta/-/da/ contrast, young children (4 years) showed *greater* separation of response curves than older children (7 years) and both groups of children showed *greater* separation than adults. This is in keeping with studies of /s/-/ʃ/ contrasts in which F3 was not neutral. It would therefore appear that cue weighting differences between adults and children for /ta/-/da/ are not due to /t/-transitions being ''frequency-truncated'' versions of /d/-transitions.

TABLE I. Results of logistic regression for /ta/-/da/ and /ti/-/di/.

		Children[a]	Adults[a]
/ta/-/da/	VOT	0.3944	0.2878
	Transitions	3.4064	14.1490
/ti/-/di/	VOT	0.4123	0.1409
	Transitions	Not significant	1.6334, $p=0.0282$

[a]Regression is reported in terms of exp(B), $d.f.=1$. Values are significant at $p<0.001$ unless otherwise indicated.

To summarize, the pattern of responses seen for /ta/-/da/ and /ti/-/di/ cannot be explained by the developmental transitional bias hypothesis, that is, that children are more biased toward transitional information than are adults. However, it is possible that both sets of results can be explained by the acoustic transitional bias hypothesis, that is, that children are more biased toward transitional than toward nontransitional cues. Analysis 2 will examine this possibility.

The results for the /de/-/be/ contrast should be touched on here. The fact that very few children were able to meet the testing criterion for this contrast suggests a possible inability in the children to make use of either of the available cues (stop burst or vowel formant transitions). This in itself contradicts both the developmental and acoustic transitional bias hypotheses which state that children should always be more biased toward—and thus presumably able to use—transitional cues. These results are consistent with the view that the acoustic distinctiveness or salience of cues plays a role in adult–child cue weighting differences (e.g., Sussman, 2001).

IV. ANALYSIS 2: RELATIVE WEIGHT GIVEN BY CHILDREN TO NONTRANSITIONAL CUES

A. Results and Discussion

The responses to the two VOT contrasts, /ta/-/da/ and /ti/-/di/, were subjected to logistic regression. This type of analysis is used when the dependent variable (the listeners' response) has two possible values (e.g., the responses for each stimulus in the /ta/-/da/ contrast could be either /ta/ or /da/). It is used here to determine the amount of variance in the responses that can be explained by each of the two acoustic cues varied in each contrast, and to rank the importance of the two cues for each group of listeners: The higher the value of exp(B), the higher the relative importance of the cue.

Results and discussion. The results of the logistic regression analysis can be found in Table I. For the /ta/-/da/ contrast, transitions play a greater role than the nontransitional VOT cue for both adults and children. Therefore, although the responses to the /ta/-/da/ contrast cannot be explained by the claim that children always give more weight to transitional cues than do adults, they *can* be explained by the claim that children start out more biased toward transitions than other cues, and gradually give less or more weight (in this case, more) to these cues as the children develop percep-

tually. Interestingly, it was suggested earlier that the acoustic transitional bias hypothesis might only be required in order to account for perception of contrasts in which nontransitional cues are known to be uninformative to adults. This is not, however, the case for /ta/-/da/: The nontransitional VOT cue in this contrast is known to be very informative to adult listeners in the perception of voicing in CV syllables (Lisker and Abramson, 1970).

For the /ti/-/di/ contrast, on the other hand, transitions play a smaller role in perception than does the nontransitional VOT cue for children. In fact, the influence of transitional information on children's responses is so small that it is nonsignificant (it remains significant for adult listeners). This means that the responses to the /ti/-/di/ contrast cannot be explained by either the original claim of the developmental transitional bias hypothesis that children give more weight to transitional cues than do adults, or the claim of the acoustic transitional bias hypothesis that children start out more biased toward transitions than other cues.

These results show that the acoustic transitional bias hypothesis does not appear to account for all situations in which children give less or the same weight to transitional cues as adults. This in turn means that the general premise of the transitional bias theory—that children are more biased (in some way) toward vowel-formant transitional cues—cannot account for all adult–child differences in acoustic cue weighting.

V. GENERAL DISCUSSION AND CONCLUSIONS

The aims of this study were (a) to test the two nonexclusive versions of the transitional bias theory, and (b) to determine to what extent cue weighting patterns displayed by adults and children are affected by segmental context.

The Developmental Weighting Shift (DWS) theory states that differences between adults and children in the way in which they process speech—children being more ''global'' and adults being more ''analytical'' in their processing—lead to differences in perceptual cue weighting strategies between the two groups. While the results of the current study neither support nor refute this claim, the perceptual behavior observed in this study is problematic for existing interpretations of the *way* in which changes in processing might impact on speech perception. To date, Nittrouer and colleagues' tests of the DWS theory have been based on the assertion that the acoustic correlate of more global, or ''child-like'' speech perception is vowel formant transitions (the transitional bias hypothesis). However, the current study has shown that if children do use a more global mode of speech perception, it must be triggered by something other than, or in addition to, formant transitions. While children do appear to be more ''transitional'' for some contrasts, they are not consistently biased toward transitions. The first version of the transitional bias hypothesis proposes that children should weight vowel-formant transitions more heavily than should adults. The results of the current study show that, as found by Nittrouer and colleagues, children do weight vowel-onset formant transitions more heavily than do adults for fricative contrasts such as /saɪ/-/ʃaɪ/. However, children were found to give less weight than adults to transitions for the /ta/-/da/ contrast, and the same weight as adults for the /ti/-/di/ contrast. Additionally, children, but not adults, appear to have difficulty making use of transitional cues at all for the contrast /de/-/be/. The second version of the transitional bias hypothesis proposes that, where children are found not to weight transitions more than do adults, children should weight transitional cues more heavily than they weight other acoustic cues to the same contrast. However, it appears that while this may be the case for some contrasts, it is not true for all of them. While children do indeed weight vowel-formant transitions more heavily than nontransitional acoustic cues for /ta/-/da/, they weight transitions *less* heavily than nontransitional cues for /ti/-/di/. Therefore, contrary to Nittrouer's transitional bias theory, children are not always biased toward transitions, either in comparison to adults or in relation to the weight that they give to nontransitional cues.

The results of previous studies showed different types of adult–child cue weighting differences, some consistent with Nittrouer's transitional bias theory (e.g., Krause, 1982; Wardrip-Fruin and Peach, 1984), and others contradicting the theory (e.g., Howell *et al.*, 1992; Sussman, 2001). It was not clear, however, whether these contradictory results were due to variation in the segmental context being tested, or to differences in the methods used for testing. The results of the current study suggest that even when methods are held constant, the observed types of adult–child cue weighting differences are likely to change depending on the segmental context being tested. Given this variation in perceptual behavior, it is not immediately clear what the underlying cause of adult–child cue weighting differences might be. The results from the /de/-/be/ contrast suggest a possible explanation. For this contrast, children appeared to have difficulty making use of the available acoustic cues. As noted earlier, poor auditory skills in children as compared to adults has been proposed as an alternative account for adult–child differences in cue weighting (e.g., Sussman, 2001). In particular, children's incomplete auditory development is said to cause them to have difficulty in making use of less acoustically distinctive cues. It does appear from the results of the /de/-/be/ contrast that there may be certain weaker cues that young children cannot use in some circumstances. However, a recent study has shown that this difference in ability to make use of less physically distinct cues cannot explain all adult–child differences in acoustic cue weighting (see Mayo and Turk, submitted). Therefore, while this and earlier studies show clear differences between adults and children in the way in which the two groups make use of acoustic cues, we are left without a satisfactory explanation for these developmental differences.

ACKNOWLEDGMENTS

This work was supported by a grant from the Wellcome Trust. The authors would like to thank Jocelynne Watson for comments on an earlier version of this paper.

APPENDIX A: VALUES FOR SYNTHETIC CV STIMULI

Vowel-formant onset and target values for synthetic /saɪ/ stimuli.

Stimulus No.	F1 onset	F1 target (/a/)	F2 onset	F2 target (/a/)	F3 onset	F3 target (/a/)
1	465	788	1444	1170	2626	2817
2	428	781	1423	1195	2620	2809
3	433	751	1464	1197	2535	2777
4	397	771	1433	1204	2518	2771
5	376	764	1408	1189	2585	2779

Vowel-formant onset and target values for synthetic /ʃaɪ/ stimuli.

Stimulus No.	F1 onset	F1 target (/a/)	F2 onset	F2 target (/a/)	F3 onset	F3 target (/a/)
1	469	796	1566	1183	2427	2799
2	489	734	1510	1172	2409	2795
3	449	761	1621	1183	2402	2775
4	411	723	1597	1185	2446	2770
5	358	753	1578	1159	2319	2750

Vowel-formant onset and target values for synthetic /de/ stimuli.

Stimulus No.	F1 onset	F1 target	F2 onset	F2 target	F3 onset	F3 target
1	219	425	1806	2096	2477	2554
2	231	436	1810	2116	2491	2542
3	221	416	1821	2093	2419	2536
4	221	443	1814	2109	2401	2544
5	206	426	1796	2112	2442	2520

Vowel-formant onset and target values for synthetic /be/ stimuli.

Stimulus No.	F1 onset	F1 target	F2 onset	F2 target	F3 onset	F3 target
1	249	420	1694	2100	2259	2535
2	247	429	1771	2114	2293	2540
3	271	427	1631	2094	2213	2524
4	247	429	1680	2117	2254	2540
5	273	429	1693	2104	2214	2553

Vowel-formant onset and target values for synthetic /ta/ stimuli.

Stimulus No.	F1 onset	F1 target	F2 onset	F2 target	F3 onset	F3 target
1	528	709	1530	1433	2560	2685
2	526	715	1524	1416	2536	2662
3	555	702	1555	1416	2513	2638
4	531	707	1541	1443	2577	2697
5	544	716	1528	1435	2564	2713

Vowel-formant onset and target values for synthetic /da/ stimuli.

Stimulus No.	F1 onset	F1 target	F2 onset	F2 target	F3 onset	F3 target
1	261	716	1631	1423	2498	2653
2	291	705	1629	1443	2490	2675
3	271	708	1667	1434	2442	2662
4	243	721	1643	1461	2496	2630
5	238	712	1639	1421	2433	2631

Vowel-formant onset and target values for synthetic /ti/ stimuli.

Stimulus No.	F1 onset	F1 target	F2 onset	F2 target	F3 onset	F3 target
1	324	324	1948	2192	2571	2831
2	306	306	1861	2171	2584	2752
3	316	316	1943	2184	2606	2832
4	300	300	1918	2153	2623	2831
5	310	310	1951	2197	2610	2856

Vowel-formant onset and target values for synthetic /di/ stimuli.

Stimulus No.	F1 onset	F1 target	F2 onset	F2 target	F3 onset	F3 target
1	225	305	1857	2202	2560	2799
2	210	302	1904	2206	2574	2837
3	199	305	1923	2189	2573	2825
4	238	305	1870	2149	2534	2812
5	235	314	1911	2186	2605	2815

APPENDIX B: PICTURES USED TO ELICIT CHILD RESPONSES

CV syllable	Picture
/saɪ/	A boy called ''Si''
/ʃaɪ/	A shy boy hiding behind a tree
/de/	A street scene with the sun coming up (''day'')
/be/	A typical Scottish bay
/ta/	A girl receiving a present (''ta'' is British English slang for ''thank you'')
/da/	A father (''da'' short for ''dada'')
/ti/	A teapot and teacup (''tea'')
/di/	A girl called ''Dee''

[1]The vowel in the /ta/-/da/ contrast, as well as the initial vowel in the diphthong in the /saɪ/-/ʃaɪ/ contrast is the Scottish low front vowel, best approximated by the IPA symbol /a/.

[2]The rejection rate for adults for this contrast may reflect the quality of the synthetic speech stimuli used for this contrast. These stimuli were judged by the two experimenters to appropriately model natural tokens of /saɪ/ and /ʃaɪ/; however, it is possible that these stimuli were more difficult to identify than others used in this and previous studies. There are, however, no data on adult rejection rate available from Nittrouer and colleagues' studies of /s-vowel/-/ʃ-vowel/ perception with which to compare these results.

[3]The data for the /de/-/be/, /ta/-/da/ and /ti/-/di/ contrasts are also featured in Mayo and Turk (submitted), where they are analyzed for a different purpose.

[4]The duration of the vowel formant transitions for all of the synthetic stimuli reflects both the steep and more gradual slope components of a natural transition.

[5]The frication excited bypass path in Sensyn's Klatt synthesiser (Sensimetrics Org.); no frequency value is given for this parameter.

[6]In general, pauses were minimal—sufficiently long for the child subject to respond aurally and by placing a marker on the correct picture. Longer pauses were taken as indicating that the child was tiring, and in this case testing was discontinued until a later time (usually only the case for the three- to four-year-old subjects).

Cohen, J., and Cohen, P. (**1983**). *Applied Multiple Regression/Correlation Analysis for the Behavioral Sciences*, 2nd ed. (LEA, Hillsdale, NJ).

Dollaghan, C. A. (**1994**). ''Children's phonological neighbourhoods—half empty or half full?'' J. Child Lang **21**, 257–271.

Dorman, M. F., Studdert-Kennedy, M., and Raphael, L. J. (**1977**). ''Stop-

consonant recognition: Release bursts and formant transitions as functionally equivalent, context-dependent cues,'' Percept. Psychophys. **22**, 109–122.
Dunn, L. M., Dunn, L. M., Whetton, C., and Burley, J. (**1997**). *British Picture Vocabulary Test*, 2nd ed. (NFER-NELSON, Berkshire, UK).
Eisenberg, L. S., Shannon, R. V., Schaefer Martinez, A., Wygonski, J., and Boothroyd, A. (**2000**). ''Speech recognition with reduced spectral cues as a function of age,'' J. Acoust. Soc. Am. **107**, 2704–2710.
Elliott, L. L., and Busse, L. A. (**1984**). ''Syllable identification by children and adults for two task conditions,'' J. Acoust. Soc. Am. **77**, 1258–1260.
Elliott, L. L., Longinotti, C., Meyer, D., Raz, I., and Zucker, K. (**1981**). ''Developmental differences in identifying and discriminating CV syllables,'' J. Acoust. Soc. Am. **78**, 669–677.
Gerken, L., Murphy, W. D., and Aslin, R. N. (**1995**). ''3-year-olds and 4-year-olds perceptual confusions for spoken words,'' Percept. Psychophys. **57**, 475–486.
Harris, K. S. (**1958**). ''Cues for the discrimination of American English fricatives in spoken syllables,'' Lang Speech **1**, 1–7.
Howell, P., Rosen, S., Lang, H., and Sackin, S. (**1992**). ''The role of F1 transitions in the perception of voicing in initial plosives,'' in *Speech, Hearing and Language: Work in Progress* (University College, London).
Jusczyk, P. W., and Derrah, C. (**1987**). ''Representation of speech sounds by young infants,'' Dev. Psychol. **23**, 648–654.
Klatt, D. (**1980**). ''Software for a cascade/parallel formant synthesizer,'' J. Acoust. Soc. Am. **67**, 971–995.
Krause, S. E. (**1982**). ''Vowel duration as a perceptual cue to postvocalic consonant voicing in young children and adults,'' J. Acoust. Soc. Am. **71**, 990–995.
Lacerda, F. (**1992**). ''Young infants' discrimination of confusable speech signals,'' in *The Auditory Processing of Speech: From Sounds to Words*, edited by M. E. H. Schouten (Mouton de Gruyter, Berlin), pp. 229–238.
Lisker, L., and Abramson, A. (**1970**). ''The voicing dimension; some experiments in comparative phonetics,'' in *Proceedings of the Sixth International Congress of Phonetic Sciences, Prague, 1967* (Academia, Prague), pp. 563–567.
Malech, S. R., and Ohde, R. N. (**2003**). ''Cue weighting of static and dynamic vowel properties in children versus adults,'' J. Acoust. Soc. Am. **113**, 2257(A).
Mayo, C., Scobbie, J. M., Hewlett, N., and Waters, D. (**2003**). ''The influence of phonemic awareness development on acoustic cue weighting in children's speech perception,'' J. Speech Lang. Hear. Res. **46**, 1184–1196.
Mayo, C., and Turk, A. (submitted). ''The influence of cue magnitude on acoustic cue weighting in children's and adults' speech perception.''
Menn, L. (**1971**). ''Phonotactic rules in beginning speech,'' Lingua **26**, 225–241.
Morrongiello, B. A., Robson, R. C., Best, C. T., and Clifton, R. K. (**1984**). ''Trading relations in the perception of speech by five-year-old children,'' J. Exp. Child Psychol. **37**, 231–250.
Nittrouer, S. (**1992**). ''Age-related differences in perceptual effects of formant transitions within syllables and across syllable boundaries,'' J. Phonetics **20**, 351–382.
Nittrouer, S. (**1993**). ''The emergence of mature gestural patterns is not uniform—Evidence from an acoustic study,'' J. Speech Hear. Res. **36**, 959–972.
Nittrouer, S. (**1996**). ''The relation between speech perception and phonemic awareness: Evidence from low-SES children and children with chronic OM,'' J. Speech Hear. Res. **39**, 1059–1070.
Nittrouer, S. (**2002**). ''Learning to perceive speech: How fricative perception changes, and how it stays the same,'' J. Acoust. Soc. Am. **112**, 711–719.
Nittrouer, S., and Miller, M. E. (**1997**). ''Predicting developmental shifts in perceptual weighting schemes,'' J. Acoust. Soc. Am. **101**, 2253–2266.
Nittrouer, S., Miller, M. E., Crowther, C. S., and Manhart, M. J. (**2000**). ''The effect of segmental order on fricative labeling by children and adults,'' Percept. Psychophys. **62**, 266–284.
Nittrouer, S., and Studdert-Kennedy, M. (**1987**). ''The role of coarticulatory effects in the perception of fricatives by children and adults,'' J. Speech Hear. Res. **30**, 319–329.
Ohde, R. N., and Haley, K. L. (**1997**). ''Stop-consonant and vowel perception in 3- and 4-year-old children,'' J. Acoust. Soc. Am. **102**, 3711–3722.
Ohde, R. N., Haley, K. L., and McMahon, C. W. (**1996**). ''A developmental study of vowel perception from brief synthetic consonant-vowel syllables,'' J. Acoust. Soc. Am. **100**, 3813–3824.
Parnell, M. M., and Amerman, J. D. (**1978**). ''Maturational influences on perception of coarticulatory effects,'' J. Speech Hear. Res. **21**, 682–701.
Schonell, F., and Goodacre, E. (**1971**). *The Psychology and Teaching of Reading* (Oliver and Boyd, London).
Sensimetrics Org. (n.d.). ''SenSyn: Speech Synthesizer Package,'' Cambridge, MA.
Simon, C., and Fourcin, A. J. (**1978**). ''Cross-language study of speech pattern learning,'' J. Acoust. Soc. Am. **63**, 925–935.
Studdert-Kennedy, M. (**1987**). ''The phoneme as a perceptuomotor structure,'' in *Language Perception and Production: Relationships Between Listening, Speaking, Reading and Writing*, edited by A. Allport, D. G. MacKay, W. Prinz, and E. Scheerer (Academic, London), pp. 67–84.
Sussman, J. E. (**1993**). ''Auditory processing in children's speech perception: Results of selective adaptation and discrimination tasks,'' J. Speech Hear. Res. **36**, 380–395.
Sussman, J. E. (**2001**). ''Vowel perception by adults and children with normal language and specific language impairment: Based on steady states or transitions,'' J. Acoust. Soc. Am. **109**, 1173–1180.
Walley, A. C., and Carrell, T. D. (**1983**). ''Onset spectra and formant transitions in the adult's and child's perception of place of articulation in stop consonants,'' J. Acoust. Soc. Am. **73**, 1011–1022.
Wardrip-Fruin, C. (**1982**). ''On the status of temporal cues to phonetic categories: Preceding vowel duration as a cue to voicing in final stop consonants,'' J. Acoust. Soc. Am. **71**, 187–195.
Wardrip-Fruin, C. (**1985**). ''The effect of signal degredation on the status of cues to voicing in utterance-final stop consonants,'' J. Acoust. Soc. Am. **77**, 1907–1912.
Wardrip-Fruin, C., and Peach, S. (**1984**). ''Developmental aspects of the perception of acoustic cues in determining the voicing feature of final stop consonants,'' Lang Speech **27**, 367–379.
Watson, J. (**1997**). ''Sibilant-vowel coarticulation in the perception of speech by children with phonological disorder,'' Ph.D. thesis, Queen Margaret College, Edinburgh.
Whalen, D. H. (**1991**). ''Perception of the English /s/-/ʃ/ distinction relies on fricative noises and transitions, not brief spectral slices,'' J. Acoust. Soc. Am. **90**, 1776–1784.

Rational approximations of viscous losses in vocal tract acoustic modeling[a)]

Reiner Wilhelms-Tricarico[b)] and Richard S. McGowan[c)]
CReSS LLC, Lexington, Massachusetts 01007

(Received 17 July 2003; revised 12 March 2004; accepted 22 March 2004)

The modeling of viscous losses in acoustic wave transmission through tubes by a boundary layer approximation is valid if the thickness of the boundary layer is small compared to the hydraulic radius. A method was found to describe the viscous losses that extends the frequency range of the model to very low frequencies and very thin tubes. For higher frequencies, this method includes asymptotically the spectral effects of the boundary layer approximation. The method provides a simplification for the rational approximation of the spectral effects of viscous losses. © *2004 Acoustical Society of America.* [DOI: 10.1121/1.1738686]

PACS numbers: 43.72.Ja, 43.75.Ef, 43.75.Np [LLT] Pages: 3195–3201

I. INTRODUCTION

Our immediate goal is to realize relatively accurate approximations of viscous effects in digital filter designs that can be used to simulate one-dimensional wave propagation in tubes, such as the vocal tract or certain musical instruments. This paper deals with the following prerequisite for digital simulation: Viscous losses depend on transcendental functions of frequency that must be approximated using rational functions, i.e., ratios of polynomials.

II. VISCOUS LOSS

A. Boundary layer approximation

Following Lighthill (Ref. 1, pp. 128–136), we consider fluid flow in a region $z>0$ above a wall at $z=0$, with a small spatially uniform pressure gradient $p_x=\partial p_e/\partial x$ only in the x direction that oscillates at a circular frequency ω. The resulting equilibrium of forces is

$$\rho\frac{\partial u}{\partial t}=-p_x+\mu\frac{\partial^2 u}{\partial z^2} \quad \text{or} \quad -i\omega\rho u+\mu\frac{\partial^2 u}{\partial z^2}=p_x. \tag{1}$$

In the frequency representation, the flow u varies as $\exp(i\omega t)$. A solution to this equation, satisfying the boundary condition $u(z,\omega)=0$ for $z=0$ and at the same time the condition of being finite for $z\to\infty$, is the following:

$$u(z,\omega)=-\frac{p_x}{i\omega\rho}\left[1-\exp\left(-\sqrt{\frac{i\omega\rho}{\mu}}z\right)\right]. \tag{2}$$

For $z\to\infty$ the particle velocity, $u(z,\omega)$, reduces to the flow without rotation that would have been obtained if the viscosity was neglected: $u_0=-p_x/(i\omega\rho)$. This equation is approximately correct for axial acoustic flow in a duct with sufficiently large cross-sectional area A_0. That is, for a given frequency ω the value of z at which the exponential in the equation becomes nearly zero should be small compared to the hydraulic radius $R=\sqrt{A_0/\pi}$. This is the boundary layer approximation. To obtain the rate of the volume flow U in tube of cross-sectional area A_0, the flow field needs to be integrated over the tract's cross-sectional area:

$$U(\omega)=-\frac{p_x}{i\omega\rho}\left[A_0-\int_{A_0}\frac{p_x}{i\omega\rho}\exp\left(-\sqrt{\frac{i\omega\rho}{\mu}}z\right)dA\right]. \tag{3}$$

If the boundary layer is thin compared to the hydraulic radius, the integration of the exponential can be carried out from the boundary wall to infinity, and multiplied by the circumference of the tract. The result is

$$U(s)=-p_x(s)\frac{A_0}{\rho}\frac{1}{s}\left[1-\frac{S_0}{A_0}\sqrt{\frac{\nu}{s}}\right], \tag{4}$$

where now s replaces $i\omega$ as the generalized frequency variable, so that $U(s)$ represents the Laplace transform of the volume velocity, and $\nu=\mu/\rho=0.168\ \text{cm}^2/\text{s}$ is the kinematic viscosity in air at 37 °C. This boundary layer approximation breaks down at low frequencies and/or small cross-sectional areas. For these situations the imposed pressure gradient is largely balanced by viscous stress over most of the cross-sectional area. Two distinct duct shapes are considered in the following: the rectangular duct and cylindrical duct.

B. Symmetric flow in a flat rectangular duct

In a shallow duct that has an area $A_0=2Rb$, with $b\gg R$, and where R is half the height and b is the cross length of the duct, it is reasonable to assume that the flow is maximal near the geometrical center of the duct, as shown in Fig. 1.

Let z be a variable that parametrizes the rectangular duct cross section as follows: z is zero at the center plane and becomes equal to R at one of the walls. Assuming that the flow is symmetric, the following constraints hold: $u(R)=0$ as before, and $u'(0)=0$, and the unique solution to Eq. (1) is

$$u(r,s)=-\frac{1}{s\rho}p_x\left(1-\frac{\cosh(z\sqrt{s/\nu})}{\cosh(R\sqrt{s/\nu})}\right), \tag{5}$$

[a)]A preliminary version was presented at the 145th Meeting of the Acoustical Society of America as poster 5aSC22, titled "Padé approximations for boundary-layer losses in articulatory synthesis."
[b)]Electronic mail: rewt@cressllc.net
[c)]Electronic mail: rsmcgowan@cressllc.net

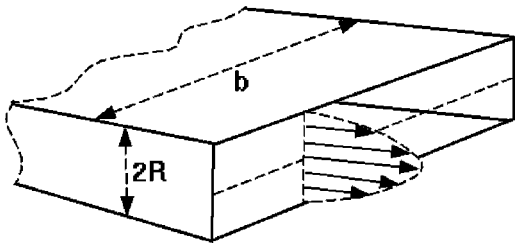

FIG. 1. Expected symmetrical flow through a narrow rectangular duct.

again replacing $i\omega$ by s. For sufficiently high frequencies or large cross sections of the duct, the cosh-flow profile looks very much like that of the boundary layer approximation, Eq. (2), but for low frequencies or small R they differ considerably (Fig. 2).

C. Flow in a cylindrical duct

The other extreme case is that of a small cylindrical cross section. Written in cylindrical coordinates with the assumption of circular symmetry the momentum conservation equation, Eq. (1) from above, becomes

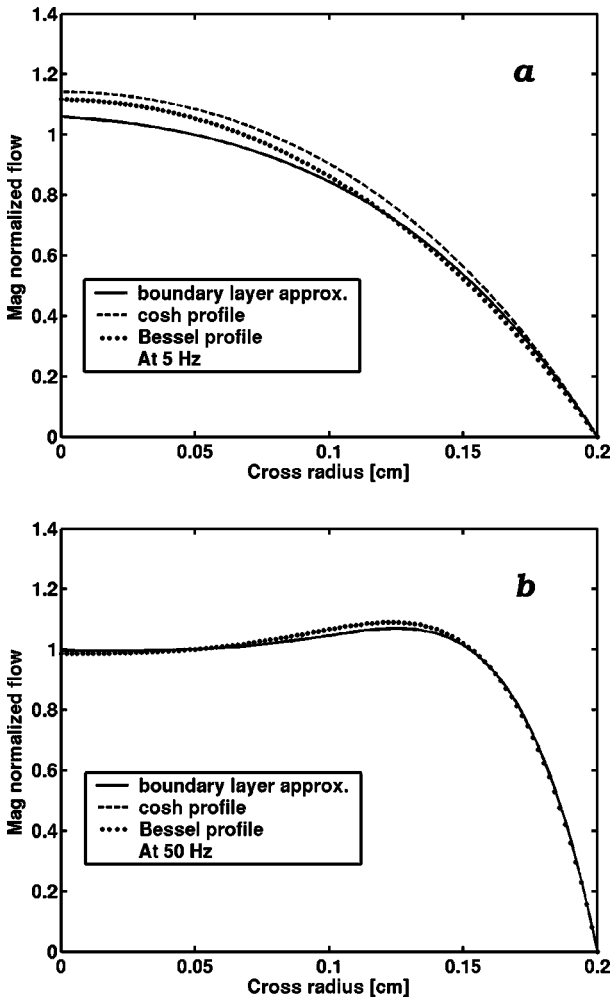

FIG. 2. The three flow profiles for the in-the-boundary layer for 5 Hz (a) and 50 Hz (b). The wall is to the right in each case, where the flow is zero. In the computation, the term $-p_x/(\rho s)$ in $u(r,s)$ was dropped for normalization.

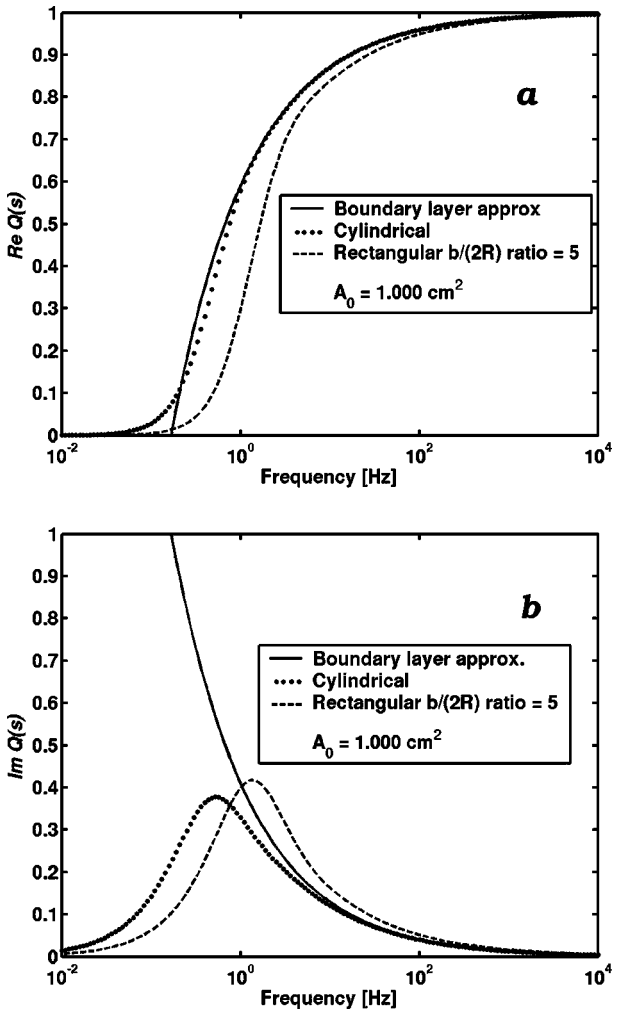

FIG. 3. Real (a) and imaginary part (b) of the damping factor function $Q(s)$.

$$-s\rho u+\mu\left(\frac{\partial^2 u}{\partial r^2}+\frac{1}{r}\frac{\partial u}{\partial r}\right)=p_x\,. \tag{6}$$

In this case, r is a parameter that is zero at the center of the duct and becomes R at the walls. Changing the variable to $z=r\sqrt{s/\nu}$, this equation can be transformed into a modified Bessel equation of zeroth order (see Ref. 2, p. 374, 9.6.1). Using only solutions that have no singularity at zero, and taking the nonslip condition $u(R)=0$ into account, the solution becomes

$$u(r,s)=-\frac{1}{s\rho}p_x\left(1-\frac{I_0(r\sqrt{s/\nu})}{I_0(R\sqrt{s/\nu})}\right). \tag{7}$$

Here $I_0(x)$ represents the modified (or hyperbolic) Bessel function of the first kind of zeroth order. Again, for sufficiently high frequencies, or large cross sections, this solution looks like the other two, as is seen in Fig. 2.

D. Volume velocities

Volume velocities are obtained by integrating the axial particle velocity over the cross-sectional area of the duct. In the case of the rectangular channel (see Fig. 1), ignoring the effects at the wall of the small sides, the result is

$$U_R(s) = -p_x(s)\frac{A_0}{s\rho}\left(1 - \frac{\tanh(R\sqrt{s/\nu})}{R\sqrt{s/\nu}}\right), \tag{8}$$

where the change of variables $R = A_0/(2b)$ was used to eliminate b.

For the case of a cylindrical duct, the flow given by Eq. (7) is integrated over a disk, with $RS_0/A_0 = 2$. This and the fact that $\int_0^y I_0(x)\,dx = yI_1(y)$, where $I_1(y)$ represents the first-order modified Bessel function of the first kind, can be used to obtain

$$U_C(s) = -p_x(s)\frac{A_0}{s\rho}\left(1 - 2\frac{I_1(R\sqrt{s/\nu})}{R\sqrt{(s/\nu)}I_0(R\sqrt{s/\nu})}\right). \tag{9}$$

All three expressions for volume velocity (4), (8), and (9) are of the form $U(s) = -p_x(s)(A_0/s\rho)Q(s)$ where $Q(s)$ is a frequency-dependent damping factor. The following three versions of $Q(s)$ are shown in Fig. 3:

$$Q(s) = \begin{cases} 1 - \dfrac{2}{R\sqrt{s/\nu}} & \text{(10a)} \\ 1 - \dfrac{\tanh(R\sqrt{s/\nu})}{R\sqrt{s/\nu}} & \text{(10b)} \\ 1 - 2\dfrac{I_1(R\sqrt{s/\nu})}{R\sqrt{(s/\nu)}I_0(R\sqrt{s/\nu})} & \text{(10c)} \end{cases}$$

[Eq. (10a) boundary layer approximation, Eq. (10b) rectangular duct, Eq. (10c) cylindrical duct]. As can also be seen in Fig. 3, the third form of $Q(s)$ [Eq. (10c), dotted graph] including the Bessel functions approaches the first form [Eq. (10a), solid graph] and according to Eq. (4), already for relatively low frequencies (the frequency scales are logarithmic to emphasize the difference between the curves for low frequencies). For the rectangular case [Eq. (10b), dashed graph in Fig. 3] the ratio of 5 between sides was used. The curves are located more to the right for higher values of the ratio and to the left for lower value, while the maximal similarity (but not identity) between cases (b) and (c) can be found for a ratio of about 2.

III. EFFECTS ON VOCAL TRACT TRANSFER FUNCTION

For a tube with a time-constant cross-sectional area $A(x)$, the Laplace transform, $p(x,s)$, of the pressure, and $U(x,s)$ of the volume velocity obey the following differential equations (see also Ref. 3):

$$\begin{aligned} \frac{d}{dx}p(x,s) &= -s\frac{\rho}{A(x)}U(x,s), \\ \frac{d}{dx}U(x,s) &= -s\frac{A(x)}{\rho c^2}p(x,s). \end{aligned} \tag{11}$$

This system can be written in matrix form while including $Q(s)$, which now is written as $Q(x,s)$ in order to represent its dependence upon the cross-sectional area at x via the hydraulic radius R [see Eq. (10)]:

$$\begin{aligned} \frac{d}{dx}\begin{pmatrix} p(x,s) \\ U(x,s) \end{pmatrix} &= L(x,s)\begin{pmatrix} p(x,s) \\ U(x,s) \end{pmatrix} \\ &= \begin{pmatrix} 0 & -s\dfrac{\rho}{A(x)}\dfrac{1}{Q(x,s)} \\ -s\dfrac{A(x)}{\rho c^2} & 0 \end{pmatrix} \\ &\quad \times \begin{pmatrix} p(x,s) \\ U(x,s) \end{pmatrix}. \end{aligned} \tag{12}$$

By calculating the matrix exponent of $\Delta x L(x,s)$, shown above, a propagation matrix for a constant area tube segment of length Δx is obtained. It transforms variables at one end of a segment with constant properties of length Δx to the variables on the other end,

$$\begin{pmatrix} p(x+\Delta x,s) \\ U(x+\Delta x,s) \end{pmatrix} = \begin{pmatrix} \cosh(\phi(x,s)) & -\dfrac{1}{Y(x,s)}\sinh(\phi(x,s)) \\ -Y(x,s)\sinh(\phi(x,s)) & \cosh(\phi(x,s)) \end{pmatrix} \begin{pmatrix} p(x,s) \\ U(x,s) \end{pmatrix}, \tag{13}$$

using the following functions, evaluated at point x:

$$\text{propagation phase:} \quad s\frac{\Delta x}{c} \rightarrow \phi(x,s) = \frac{\Delta x}{c}\frac{s}{\sqrt{Q(x,s)}}, \tag{14}$$

$$\text{admittance:} \quad \frac{A(x)}{\rho c} \rightarrow Y(x,s) = \frac{A(x)}{\rho c}\sqrt{Q(x,s)}. \tag{15}$$

The transfer function of, for example, a vocal tract can then be obtained by multiplying the partial chain matrices, while accounting for the radiation impedance. To be able to compare the effects of viscous losses for different geometries, we make the assumption that a piece of tube is terminated with a simplified radiation impedance, which is obtained as a low order frequency approximation of radiation load of a piston set in an infinite plane baffle (see, for example, Ref. 3). The radiation impedance is

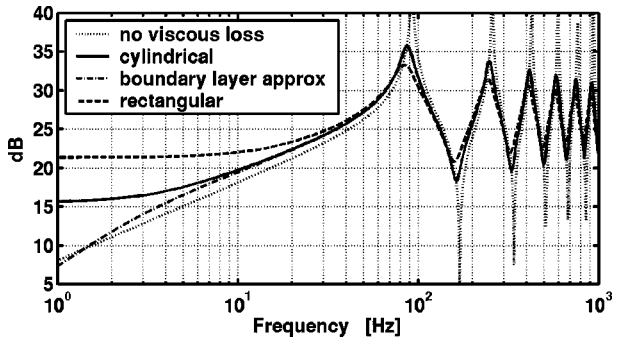

FIG. 4. Input impedance of a thin exponential tube of 100 cm length, modeled by 25 constant segments of equal length. The area starts from 0.1 cm^2 and ends at 0.1492 cm^2. The radiation impedance is calculated from the final segment's area. The curve with the highest peaks (dots) is input impedance with no viscous loss, the other curves are obtained by taking the viscous loss into account using three different models. The curve for the rectangular cross sections is calculated for a length ratio of 1:8.

$$Z_{\mathrm{rad}}(s)=\frac{\rho c}{\pi a^2}\,\frac{(8a/3\pi c)s}{1+(3\pi a/16c)s}$$

where a is the piston radius. (16)

As commonly done, we denote the elements of the duct's propagation matrix as $\left(\begin{smallmatrix}A & B\\ C & D\end{smallmatrix}\right)$, which can be obtained by multiplying the individual propagation matrices of all segments together. Its determinant is equal to 1 since it is obtained as product of matrices of the type shown in Eq. (13). The volume velocity transfer function, $H(s)$, defined here as the ratio of volume flow at the radiating end of the tube divided by volume flow across the beginning, and the input impedance $Z_{\mathrm{in}}(s)$, are

$$H(s)=\frac{1}{A-CZ_{\mathrm{rad}}}\quad\text{and}\quad Z_{\mathrm{in}}(s)=\frac{DZ_{\mathrm{rad}}-B}{A-CZ_{\mathrm{rad}}}. \tag{17}$$

Figure 4 shows the input impedance for a very thin exponential horn that has either circular cross sections or rectangular cross sections. In both cases, the cross-sectional areas vary from 0.1 to 0.1492 cm^2 exponentially; in the cylindrical case the hydraulic radius R varies from 0.1784 to 0.2179 cm, and R varies from 0.0559 to 0.0683 cm in the rectangular case (where the ratio of long to short side was set to 8). For such small cross sections and hydraulic radii we expect a strong effect of the viscous losses and differences among the three different situations. In order to separate the effects of viscous losses from the effects of losses by radiation, the same radiation impedance, namely that of a circular piston, is used in all cases. It can be seen that the two curves for the cylindrical tube, one resulting from the boundary layer approximation, using the square-root of s in $Q(s)$, and the other using modified Bessel functions, are very nearly the same for frequencies as low as 50 Hz.

IV. RATIONAL APPROXIMATION AND DIGITAL FILTERS

The three expressions for $Q(s)$ can be used to obtain an analytical description of the volume velocity over frequency, while a digital filter implementation to simulate vocal tract acoustics requires rational expressions. The three representations of $Q(s)$ that have been considered here involve a square root of frequency law for the boundary layer approximation, hyperbolic functions, or hyperbolic Bessel functions. These result in nearly the same influence on the transfer function. However, the rational approximations of the latter two functions are more easily obtained than for the square root-of-frequency dependence. This is because $\sqrt{x}$ possesses an essential singularity at zero, while the two other functions have only isolated singularities.

For the case of the function $[\tanh(x)]/\sqrt{x}$, a straightforward method of implementation as a filter can be based on the infinite product representation of the $\sinh x$ and $\cosh x$: The function $\sinh x$ has zeros at 0 and at $\pm ik\pi$, $k=1,...,\infty$, and $\cosh x$ has zeros at $\pm i(2k-1)\pi$, $k=1,...,\infty$. Since the zero of $\sinh x$ at zero is eliminated by $1/x$,

$$\frac{\tanh x}{x}=\frac{\sinh x}{x\cosh x}$$

$$=\prod_{k=1}^{\infty}\frac{1+x^2/k^2\pi^2}{1+4x^2/(2k-1)^2\pi^2},\quad\text{therefore:}$$

$$\frac{\tanh\sqrt{x}}{\sqrt{x}}=\prod_{k=1}^{\infty}\frac{1+x/k^2\pi^2}{1+4x/(2k-1)^2\pi^2}. \tag{18}$$

A digital filter can then be obtained by truncating the product at some finite N and replacing the Laplace variable s by a bilinear transform,

$$s\rightarrow 2f_s\frac{1-z^{-1}}{1+z^{-1}}\quad\text{whereby } f_s \text{ is the sampling frequency.} \tag{19}$$

The resulting approximation of $Q(s)$ of Eq. (10b) is a series of stable bilinear filters with poles at

$$\frac{4\alpha-(2k-1)^2\pi^2}{4\alpha+(2k-1)^2\pi^2}\quad\text{with}\quad\alpha=\frac{R^2}{\nu}\cdot 2f_s:$$

$$Q(s)\rightarrow 1-\prod_{k=1}^{N}\left(\frac{2k-1}{k}\right)^2\frac{(\alpha+k^2\pi^2)-(\alpha-k^2\pi^2)z^{-1}}{(4\alpha+(2k-1)^2\pi^2)-(4\alpha-(2k-1)^2\pi^2)z^{-1}}. \tag{20}$$

It should be noted that all poles of the resulting digital filter lie within the unit circle. Figure 5 shows a comparison of magnitude of the exact function $Q(s)$ for a case of a rectangular duct with two approximations by five and ten product terms.

The convergence of the product type of approximation is

somewhat slow. Better methods are based on Padé approximations or continued fraction expansions (see Ref. 4). In short, the $[L/M]$ Padé approximation of a function $f(s)$ is a rational function with numerator degree L and denominator degree M which best represents a $M+L+1$-degree series approximation (e.g., Taylor or MacLaurin) of the function. (Working implementations of this method can be found in Maple or in the Mathematica software which was used in this work.) The rational approximation of the function $Q(s)$ by Padé approximants has strong advantages over Taylor or MacLaurin series approximation because of a considerably wider range of close approximation. The representation in digital filters is obtained in two steps: (a) approximation of the trancendental functions by rational function in the generalized frequency, or s, domain; (b) mapping of the resulting rational functions into digital filters by means of the bilinear transform.

Rational approximants for the functions $Q(s)$ are then found based on, for example, a [4/6] Padé approximation:

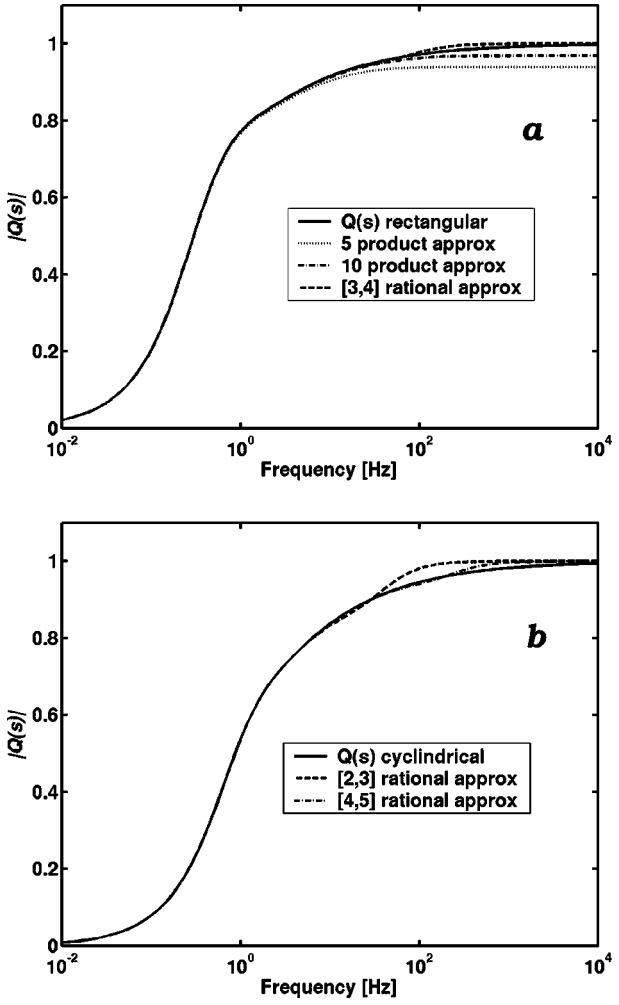

FIG. 5. Magnitudes of the function $Q(s)$ and its approximations. (a) The case of a rectangular cross section. The [3, 4] rational approximation (uppermost dashed curve) is based on the [6/8] Padé approximation of $\tanh(x)/x$. (b) Circular cross section. The [2, 3] and [4, 5] rational approximations result from [4/6] and [8/10] Padé approximations of $I_1(x)/xI_0(x)$.

$$\frac{\tanh(R\sqrt{s/\nu})}{R\sqrt{s/\nu}} \approx \frac{1+\frac{4}{33}x+\frac{1}{495}x^2}{1+\frac{5}{11}x+\frac{2}{99}x^2+\frac{1}{10\,395}x^3} \quad \text{with } x=\frac{R^2}{\nu}s. \tag{21}$$

Similarly,

$$\frac{I_1(R\sqrt{s/\nu})}{R\sqrt{s/\nu}\,I_0(R\sqrt{s/\nu})} \approx \frac{1}{2}\frac{1+\frac{1}{12}x+\frac{1}{960}x^2}{1+\frac{5}{24}x+\frac{1}{160}x^2+\frac{1}{46080}x^3} \quad \text{with } x=\frac{R^2}{\nu}s. \tag{22}$$

Note that both functions being approximated are even functions, and, thus, only even powers of their arguments appear in the Padé approximation.

It is also possible to use the continued fraction expansion (CFE) of the above expressions (Ref. 4, pp. 175–177). The following CFEs, if truncated as shown, are equivalent to the [4/6] Padé approximants:

$$\frac{\tanh\sqrt{x}}{\sqrt{x}} = \cfrac{1}{1+\cfrac{x}{3+\cfrac{x}{5+\cfrac{x}{7+\cfrac{x}{9+\cfrac{x}{11+\ldots}}}}}} \tag{23}$$

and

$$\frac{I_1(\sqrt{x})}{\sqrt{x}I_0(\sqrt{x})} = \cfrac{1}{2+\cfrac{x}{4+\cfrac{x}{6+\cfrac{x}{8+\cfrac{x}{10+\cfrac{x}{12+\ldots}}}}}}\,. \tag{24}$$

The CFE for tanh, from which Eq. (23) is obtained, can be found in Ref. 2 (p. 75, 4.3.94). To obtain Eq. (24), the continued fraction expansion of $J_1(x)/J_0(x)$ given in Ref. 4 was transformed to obtain the above CFE for the expression with the modified Bessel functions. Since these CFEs are valid also for $x=0$, the essential singularity at 0 caused by the square root in the boundary layer approximation is not present in these approximations.

A simple transformation of the expressions (23) and (24), obtained by dividing every other fraction of the CFE by x, yields an electrical network whose input impedance is equal to the approximated functions above. This electrical network structure is shown in Fig. 6.

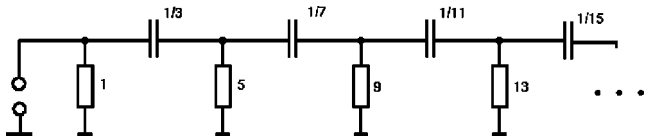

FIG. 6. The input impedance of the electrical network shown here approximates $\tanh\sqrt{s}/\sqrt{s}$ [see Eq. (23)], since the CFE of this function can be rewritten as $\cfrac{1}{1+\cfrac{1}{3/s+\cfrac{1}{5+\cfrac{1}{7/s+\cfrac{1}{9+\cfrac{1}{11/s+\cfrac{1}{13+\cdots}}}}}}}$

V. SKETCH OF A DIGITAL IMPLEMENTATION

The implementation of a digital simulation of wave guide acoustics in the time domain is accomplished by forwards and backwards traveling waves, sampled at a sampling time interval that is proportional to tube segment length. While in the lossless Kelly–Lochbaum model (Ref. 5) the traveling waves in each segment are represented by simple delay elements, for frequency-dependent viscous loss these are replaced by more general digital filters.

The transformation from pressure and volume flow representation to forward and backward traveling waves is given by

$$\begin{pmatrix} V^+ \\ V^- \end{pmatrix} = R(x)\begin{pmatrix} p \\ U \end{pmatrix} = \begin{pmatrix} 1 & \dfrac{c\rho}{A(x)} \\ 1 & -\dfrac{c\rho}{A(x)} \end{pmatrix}\begin{pmatrix} p \\ U \end{pmatrix}. \tag{25}$$

Using the above transformation from left and right, the ABCD matrix of a segment is transformed into a transmission matrix that relates forward and backward traveling waves at the beginning and end of a segment of length Δx [for brevity $Q(x,s)$ is written as Q]:

$$G(x,s) = \begin{pmatrix} \cosh\left(\dfrac{\Delta x}{c}\dfrac{s}{\sqrt{Q}}\right) - \dfrac{1+Q}{2\sqrt{Q}}\sinh\left(\dfrac{\Delta x}{c}\dfrac{s}{\sqrt{Q}}\right) & -\dfrac{Q-1}{2\sqrt{Q}}\sinh\left(\dfrac{\Delta x}{c}\dfrac{s}{\sqrt{Q}}\right) \\ \dfrac{Q-1}{2\sqrt{Q}}\sinh\left(\dfrac{\Delta x}{c}\dfrac{s}{\sqrt{Q}}\right) & \cosh\left(\dfrac{\Delta x}{c}\dfrac{s}{\sqrt{Q}}\right) + \dfrac{1+Q}{2\sqrt{Q}}\sinh\left(\dfrac{\Delta x}{c}\dfrac{s}{\sqrt{Q}}\right) \end{pmatrix} \tag{26}$$

Since sinh is an odd function and cosh is an even function of its argument, the square root, $\sqrt{Q(s,x)}$, never appears or can be canceled in rational approximations of the above expressions. For example, using the [5/5] Padé of sinh, the following rational approximation is obtained:

$$\frac{1+Q}{2\sqrt{Q}}\sinh\left(\frac{\Delta x}{c}\frac{s}{\sqrt{Q}}\right) \approx \frac{1+Q}{2}\,\frac{s\left(\Delta x/c + \frac{53}{396}(\Delta x/c)^3 s^2/Q + \frac{551}{166320}(\Delta x/c)^5 s^4/Q^2\right)}{1 - \frac{13}{396}(\Delta x/c)^2 s^2/Q + \frac{5}{11088}(\Delta x/c)^4 s^4/Q^2}. \tag{27}$$

Similar expressions containing rational functions with powers of s and $Q(x,s)$ are obtained for the other components of $G(x,s)$.

The transformation into digital filters then requires the implementation of a rational approximation and bilinear transformation of the filter $s/Q(s,x)$, and powers of this filter are obtained by cascading the same filter structure. The analog filter with transfer function $s/Q(s,x)$ is a differentiator (multiplication by s) followed by one of the two CFEs [Eqs. (23) or (24)] in a feedback loop.

The absolute value of the input impedance of the two passive electrical networks (see Fig. 6) is limited from above by 1. Therefore, an analog system with these networks in the feedback loop must be stable. In fact, it can be shown by induction that for all truncated CFEs of this form, all except one pole of the approximated filter $s/Q(s,x)$ are on the negative real axis and one pole is at $s=0$. The bilinear transform (19) renders directly the rational functions in the approximation of $G(x,s)$ into digital filters. Note that the coefficients $\Delta x/c$ are cancelled if the sampling frequency is chosen as $f_s = c/\Delta x$.

The structure of a digital filter corresponding to the analog filter $s/Q(s,x)$ is a lattice structure that can be derived by replacing the variable s by the bilinear transform and by using Euler's recursion (see Ref. 4, p. 125) for the evaluation of continued fractions. The bilinear transformation preserves the stability property. The resulting structure has one delay-free path which can be eliminated by generalizing a method that was shown for a special class of filters in Ref. 6. The practical implementation and verification of these digital filters is currently a work in progress.

ACKNOWLEDGMENT

This work was supported by Grant No. NIDCD-01247 to CReSS LLC.

[1] J. Lighthill, *Waves in Fluids* (Cambridge U. P., Cambridge, 1978).
[2] M. Abramowitz and I. A. Stegun (eds.), *Handbook of Mathematical Functions* (Dover, New York, 1965), SCI QA3.U58 No. 55, 1965.
[3] M. R. Portnoff, ''A Quasi-One-Dimensional Digital Simulation for the Time-Varying Vocal Tract,'' Master thesis, MIT, 1973.
[4] G. A. Baker, Jr. and P. Graves-Morris, *Padé Approximants*, 2nd ed. (Cambridge U. P., Cambridge, 1996).
[5] J. L. Kelly, Jr. and C. Lochbaum, ''Speech synthesis,'' *in Proceedings of the Stockholm Speech Communications Seminar* (RIT, Stockholm, Sweden, 1962).
[6] A. Härmä, ''Implementation of frequency-warped recursive filters,'' Signal Process. **80**, 543–548 (2000).

A continuous-wave ultrasound system for displacement amplitude and phase measurement[a)]

James J. Finneran[b)] and Mardi C. Hastings[c)]
The Ohio State University, Department of Mechanical Engineering, 206 W. 18th Avenue, Columbus, Ohio 43210

(Received 9 October 2003; revised 6 March 2004; accepted 19 March 2004)

A noninvasive, continuous-wave ultrasonic technique was developed to measure the displacement amplitude and phase of mechanical structures. The measurement system was based on a method developed by Rogers and Hastings [''Noninvasive vibration measurement system and method for measuring amplitude of vibration of tissue in an object being investigated,'' U.S. Patent No. 4,819,643 (1989)] and expanded to include phase measurement. A low-frequency sound source was used to generate harmonic vibrations in a target of interest. The target was simultaneously insonified by a low-power, continuous-wave ultrasonic source. Reflected ultrasound was phase modulated by the target motion and detected with a separate ultrasonic transducer. The target displacement amplitude was obtained directly from the received ultrasound frequency spectrum by comparing the carrier and sideband amplitudes. Phase information was obtained by demodulating the received signal using a double-balanced mixer and low-pass filter. A theoretical model for the ultrasonic receiver field is also presented. This model coupled existing models for focused piston radiators and for pulse–echo ultrasonic fields. Experimental measurements of the resulting receiver fields compared favorably with theoretical predictions. © *2004 Acoustical Society of America.*
[DOI: 10.1121/1.1739481]

PACS numbers: 43.80.Ev, 43.80.Jz [FD] Pages: 3202–3209

I. INTRODUCTION

Displacement measurement is a fundamental technique used to characterize biomechanical structures. Displacement measurements are often made to obtain information about the structure and/or function of tissues. For example, the function of the mammalian middle-ear ossicles was revealed, in part, from direct measurements of ossicular motion in cadavers (e.g., von Békésy, 1960). Displacement measurements may also be used to estimate the material properties of tissues or to discriminate normal from abnormal system functions. For example, changes in the vibration characteristics of materials and structures can be used to find defects or other structural anomalies.

Ultrasonic devices are widely used for displacement measurements because they allow noninvasive, subcutaneous operation. These systems rely on frequency or phase shifts that occur when the transmitted ultrasound is reflected from a moving target. Doppler ultrasound techniques are often used to image biological tissues, inspect mechanical structures for defects, estimate elastic constants, and to measure fluid flow velocity. Several related Doppler ultrasound methods have been used to detect hard tumors or lesions surrounded by relatively soft tissues. These methods, collectively referred to as elasticity imaging, include compression or strain imaging, transient elastography, and vibration sonoelastography (Taylor *et al.*, 2000). In strain imaging, a quasistatic compression is applied and precompression and postcompression echo signals are compared to calculate the strain map in the tissue (Ophir *et al.*, 1991; O'Donnell *et al.*, 1994). Transient elastography uses low-frequency transient vibration to generate tissue displacements which are then measured using pulse–echo ultrasound (Catheline *et al.*, 1999). Vibration sonoelastography uses real-time Doppler ultrasound to image the vibration pattern resulting from low-frequency (less than 1 kHz) shear waves propagated through tissue (Krouskop *et al.*, 1987; Lerner *et al.*, 1998; Yamakoshi *et al.*, 1990; Taylor *et al.*, 2000). Low-frequency shear waves are produced using an electromechanical shaker or audio speaker. Doppler ultrasound methods are used to measure vibration amplitudes in a region of interest and construct a gray-scale image to display vibration amplitudes (Taylor *et al.*, 2000).

Continuous-wave ultrasound has also been used to measure the motion of biological tissues undergoing acoustically induced vibrations (e.g., Cox and Rogers, 1987; Rogers and Hastings, 1989). The system developed by Rogers and Hastings (1989) has been referred to as the noninvasive vibration amplitude measurement system (NIVAMS). Like vibration sonoelasticity, the NIVAMS relies upon an external source (a loudspeaker) to generate harmonic displacements in the tissue of interest; however, the NIVAMS is not an imaging method and does not require a commercial ultrasonic scanner. The NIVAMS was designed to measure the displacement amplitude of a particular structure, rather than generate an image of the vibration pattern of a general region. The strengths of the NIVAMS technique are the potentially fine

[a)]Portions of these data were presented in ''A noninvasive ultrasonic technique for measuring the dynamic properties of biological tissues,'' at the 132nd Meeting of the Acoustical Society of America, Honolulu, HI.

[b)]Author to whom correspondence should be addressed, at U.S. Navy Marine Mammal Program, Space and Naval Warfare Systems Center, San Diego, Code 2351, 53560 Hull St., San Diego, CA 92152.

[c)]Present address: Office of Naval Research, Marine Mammal S&T Program, BCT-1, Code 341, 800 North Quincy St., Arlington, VA 22217-5660.

 © 2004 Acoustical Society of America

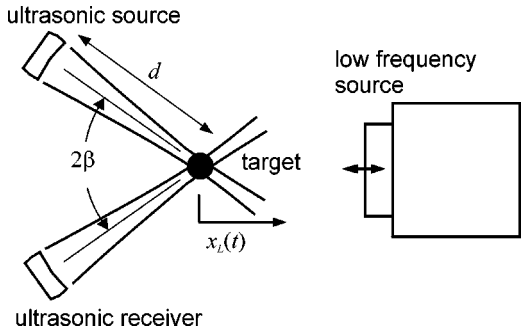

FIG. 1. Measurement system configuration: The low-frequency source induces motion $x_L(t)$ in the structure being investigated (the target). Continuous-wave ultrasound from the ultrasonic source is reflected (or scattered) by the target and received by a separate ultrasonic receiver. The target motion $x_L(t)$ causes the received ultrasound to be phase modulated.

spatial resolution (e.g., −3-dB sample volume dimensions of 0.3×3 mm), small displacement threshold (e.g., 2.5 nm) (Cox and Rogers, 1987), and noninvasive, noncontact target excitation, which makes it particularly well-suited for *in vivo* measurements.

The NIVAMS has been used to measure the displacement amplitude as a function of frequency for the peripheral auditory organs in teleost fish (e.g., Cox and Rogers, 1987), human and porcine lungs (Lewis *et al.*, 1994; Martin *et al.*, 2000), and corneas of enucleated bovine eye globes (Schroeder and Hastings, 1994). These data have been used to estimate resonant frequencies of structures under investigation (Martin *et al.*, 2000), estimate corneal stiffness (Schroeder and Hastings, 1994), and to help identify the functional relationships between peripheral auditory organs in fish (Lewis *et al.*, 1994; Cox and Rogers, 1987).

Although the NIVAMS was able to measure displacement amplitudes of small structures with high resolution, in its original form the NIVAMS was unable to extract the displacement phase angle. Phase information is particularly important when attempting to identify resonant frequencies, estimate viscoelastic properties, and determine relationships between the motions of different structures. This paper describes a modified version of NIVAMS that allows measurement of the phase as well as the amplitude of the displacement. The operating principles of the device, including both the amplitude and phase measurement techniques, are presented. A method for predicting the spatial resolution of the measurement system is also described. Experimental measurements of the system performance and sample volume size are compared to theoretical predictions.

II. MEASUREMENT PRINCIPLES

Figure 1 shows the main components of the measurement system: a low-frequency sound source used to excite the structure under test (the "target"), an ultrasonic source, and an ultrasonic receiver. When insonified by the low-frequency source, the target vibrates with a displacement $x_L(t)=X_L\cos(\omega_L t-\phi_L)$, where X_L and ϕ_L are the target displacement amplitude and phase, respectively, ω_L is the frequency of the low-frequency source, and t is time. The ultrasonic source generates continuous waves at the ultrasonic (carrier) frequency ω_H. Ultrasound reflected from the target is detected by the receiver. The source and receiver are separated by an angle 2β. If the ultrasonic receiver is uniformly sensitive to pressure, the receiver output voltage, $e_r(t)$, is

$$e_r(t)=K_e R P_i \cos(\omega_H t-\phi_r), \tag{1}$$

where K_e is a constant, R is the pressure reflection coefficient magnitude, P_i is the ultrasonic pressure amplitude incident on the target, and ϕ_r is the phase of the received ultrasound (relative to the phase of the transmitted ultrasound).

The received phase ϕ_r is the product of the ultrasonic wave number and the source–target–receiver path length, plus the pressure reflection coefficient phase. For a stationary target $\phi_r=2k_H d+\phi_R$, where k_H is the ultrasonic wave number ($k_H=\omega_H/c$, where c is the sound speed), d is the distance to the target from both the source and the receiver, and ϕ_R is the pressure reflection coefficient phase. If the target is moving, the received phase is time dependent and the received ultrasound is phase modulated. For small target motions, the measurement system is only sensitive to displacement in the direction of the transducer bisector. For harmonic motions of the form $x_L(t)$, the receiver output is

$$e_r(t)=K_e R P_i \cos[\omega_H t-2k_H d-2k_H X_L\cos\beta \times\cos(\omega_L t-\phi_L)-\phi_R]. \tag{2}$$

The measurement system objective is to extract the target displacement amplitude X_L and phase ϕ_L from the received ultrasonic signal. The displacement amplitude may be obtained from the received signal using a high-frequency spectrum analyzer. Phase measurement is more complicated because ω_L is typically a small fraction of ω_H and the amplitudes associated with acoustic vibrations are small. The specific techniques used to measure the amplitude and phase are discussed next.

A. Amplitude measurement

The technique for amplitude measurement has been described previously (Cox and Rogers, 1987; Rogers and Hastings, 1989), and is only briefly summarized here. If $k_H X_L$ is small and the phase term $(-2k_H d-\phi_R)$ is neglected, Eq. (2) may be written

$$e_r(t)=K_e R P_i\{\cos(\omega_H t)+k_H X_L\cos\beta\sin[(\omega_H+\omega_L)t-\phi_L]+k_H X_L\cos\beta\sin[(\omega_H-\omega_L)t+\phi_L]\}. \tag{3}$$

Equation (3) shows that the low-frequency vibration introduces sidebands into the received frequency spectrum. The sidebands are located at $\omega_H\pm\omega_L$, and each has an amplitude of $k_H X_L\cos\beta$ relative to the high-frequency carrier amplitude. The amplitude of the low-frequency vibration, X_L, may be determined from $k_H X_L\cos\beta=E_s/E_c$, where E_c is the carrier amplitude and E_s is the sideband amplitude.

Figure 2 shows the frequency spectrum of 90-kHz ultrasound reflected from an enucleated bovine cornea simultaneously insonified by a 650-Hz source (Schroeder and Hastings, 1994). This measurement was conducted in air. The spectrum was measured using an HP 35665A digital signal analyzer with a frequency resolution of 8 Hz. The spectrum is dominated by the carrier at $\omega_H=90$ kHz. Sidebands are

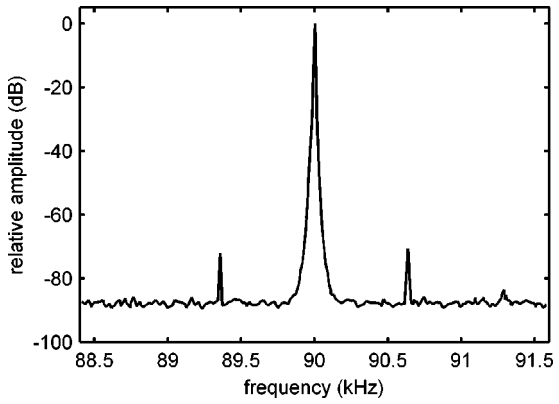

FIG. 2. Frequency spectrum of received ultrasound (90 kHz) reflected from an enucleated bovine cornea excited by a 650-Hz source. The target motion produces sidebands located at 90 kHz±650 Hz. This trace was obtained from a digital signal analyzer with a frequency resolution of 8 Hz.

also visible at $\omega_H \pm \omega_L$, or 90±0.65 kHz. For this example, E_s/E_c is approximately -70 dB, $\beta \approx 30°$, and $X_L \approx 220$ nm.

B. Phase measurement

Since the low-frequency source operates at only a small fraction of the ultrasonic source frequency, phase measurement requires demodulating the receiver output. The goal of the demodulation is to shift the carrier and sidebands from being centered about ω_H to being centered about zero. This moves the sideband formerly occurring at $(\omega_H + \omega_L)$ to ω_L, where it may be examined with relatively low-frequency instrumentation.

Many demodulation techniques rely on the principle of frequency mixing. When two periodic signals are mixed or multiplied, the resulting signal has components at the sum and difference frequencies of the inputs. Low-pass filtering removes the components at and above the sum frequency, leaving the difference term only. For this study, phase demodulation was achieved using a phase detector (Mini-Circuits model ZRPD-1) consisting of a double-balanced mixer and low-pass filter. The phase detector output is $e_\phi(t) = -K_\phi \cos(\phi_1 - \phi_2)$, where ϕ_1 and ϕ_2 are the phase angles of the detector inputs and K_ϕ is the phase detector maximum dc output (Scientific Components, 1992). If the ultrasonic carrier and receiver signals are the phase detector inputs, the detector output is

$$e_\phi(t) = -K_\phi \cos[2k_H d + 2k_H X_L \cos\beta \times \cos(\omega_L t - \phi_L) + \phi_R]. \quad (4)$$

If $k_H X_L$ is small, the phase detector output may be expanded to

$$e_\phi(t) = -K_\phi \cos(2k_H d + \phi_R) + K_\phi \sin(2k_H d + \phi_R) \times 2k_H X_L \cos\beta \cos(\omega_L t - \phi_L), \quad (5)$$

which is of the form

$$e_\phi(t) = C_1 + C_2 \cos(\omega_L t - \phi_L), \quad (6)$$

where C_1 and C_2 are constants. The phase ϕ_L is obtained by measuring the phase of $e_\phi(t)$; however, potential complications are introduced by the phase of the target reflection coefficient and any low-frequency target motion (e.g., caused by respiration or low-frequency cardiac output). These complications are described in detail next.

For a rigid target, $\phi_R = 0$ and Eq. (5) reduces to

$$e_\phi(t) = -K_\phi \cos(2k_H d) + K_\phi \sin(2k_H d) 2k_H X_L \cos\beta \times \cos(\omega_L t - \phi_L). \quad (7)$$

If the target consists of a pressure-release surface, $\phi_R = \pi$ and Eq. (5) reduces to

$$e_\phi(t) = K_\phi \cos(2k_H d) + K_\phi \sin(2k_H d) 2k_H X_L \cos\beta \times \cos(\omega_L t - \phi_L \pm \pi). \quad (8)$$

The measured phase of a pressure-release surface must therefore be corrected by $\pm\pi$. The phase of rigid structures does not require correction.

Examination of Eq. (5) reveals a potentially more serious error than that described above. Although $2k_H d$ is nominally a constant, small, uncontrollable target motions or a slow drift in carrier frequency may cause it to vary. Because of the large magnitude of k_H at ultrasonic frequencies, small changes in d may result in sizable variations in $2k_H d$. If a change in $2k_H d$ causes $\sin(2k_H d)$ to switch sign, then the measured phase will be shifted by $\pm\pi$. The values of ω_H and d influence the chance of $\pm\pi$ phase shifts occurring. The worst situation would be if $k_H d = n\pi$, where n is an integer. In this case $\sin(2k_H d)$ approaches zero and any deviation is likely to cause a sign change. To minimize the occurrence of these phase shifts, the carrier frequency can be adjusted to make $2k_H d = (2n-1)\pi/2$, where n is an integer. This is accomplished by monitoring the dc component of the phase detector output, e_{dc}, and adjusting ω_H to drive e_{dc} to zero. From Eqs. (7) and (8), $e_{dc} = \pm K_\phi \cos(2k_H d)$. If $e_{dc} = 0$ then $\sin(2k_H d) = \pm 1$, where small changes in $k_H d$ will be less likely to cause $\pm\pi$ phase shifts than if $\sin(2k_H d) = 0$. The adjustment to ω_H is performed according to the following rule: If $|e_{dc}| > 0$, decrease ω_H; if $|e_{dc}| < 0$, increase ω_H.

The adjustment to ω_H has the added benefit of making the phase measurement insensitive to the target reflection coefficient phase. If $\phi_R = 0$, then $e_{dc} = -K_\phi \cos(2k_H d)$ and the adjustment moves $2k_H d$ towards $\pi/2$, where $\sin(2k_H d) = +1$. This is illustrated in Fig. 3(a). If $\phi_R = \pi$, then $e_{dc} = +K_\phi \cos(2k_H d)$ and the adjustment moves $2k_H d$ towards $3\pi/2$, where $\sin(2k_H d) = -1$ [Fig. 3(b)]. Therefore, regardless of the reflection coefficient phase, proper adjustment of ω_H simplifies Eq. (5) to

$$e_\phi(t) = K_\phi 2k_H X_L \cos\beta \cos(\omega_L t - \phi_L), \quad (9)$$

and no phase correction is necessary.

Although Eq. (6) implies that the phase detector output may also be used to measure the target amplitude, this is impractical for *in vivo* measurements, because $\sin(2k_H d)$ is not absolutely known. For phase measurement, precise knowledge of $\sin(2k_H d)$ is not required—only that it will not change sign.

III. MEASUREMENT VERIFICATION AND ACCURACY

The measurement process was verified by using the ultrasonic system to measure the amplitude and phase of an

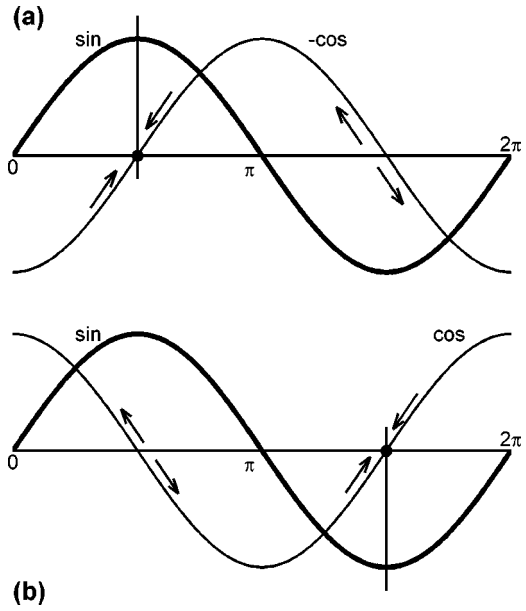

FIG. 3. Carrier frequency adjustment for (a) $\phi_R=0$ and (b) $\phi_R=\pi$. The carrier frequency was adjusted to make $\sin(2k_Hd)=\pm1$, where small changes in k_Hd would be less likely to cause $\pm\pi$ phase shifts than if $\sin(2k_Hd)=0$. This was accomplished by adjusting the dc component of the phase detector output, $\pm K_\phi\cos(2k_Hd)$, to zero. The adjustment to ω_H was performed according to the following rule: If $|K_\phi\cos(2k_Hd)|>0$, decrease ω_H; if $|K_\phi\cos(2k_Hd)|<0$, increase ω_H.

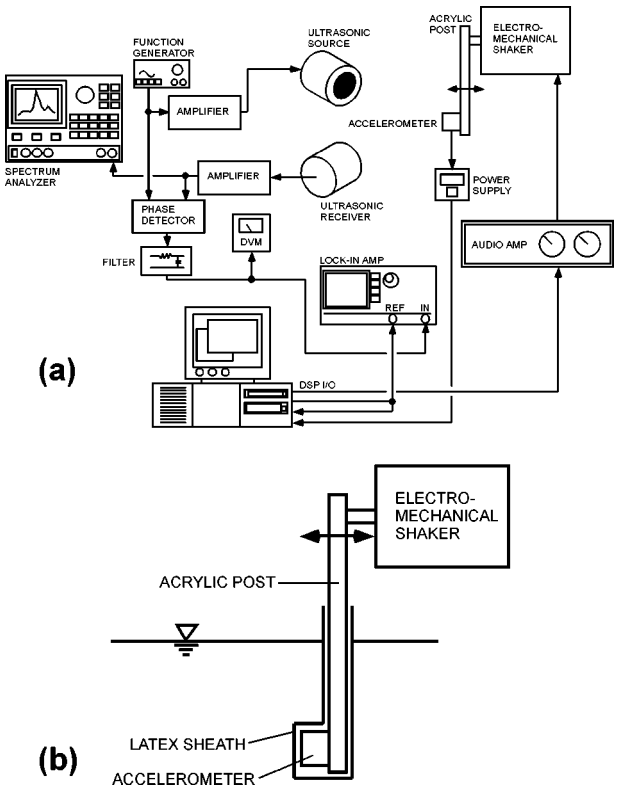

FIG. 4. (a) Experimental setup used to evaluate the ultrasonic measurement system. The amplitude and phase of an acrylic post driven by an electromechanical shaker were measured by an accelerometer and the ultrasonic system. (b) Detail of the shaker, acrylic post, and accelerometer.

acrylic post excited by an electromechanical shaker. Figure 4(a) shows the experimental setup. The displacement amplitude and phase measured with the ultrasonic system were compared to the ''actual'' amplitude and phase, obtained from a calibrated accelerometer (PCB model 352B22), which was also mounted to the acrylic post. Figure 4(b) shows the details of the shaker and accelerometer mountings. The shaker was placed above the waterline, with only a portion of the acrylic post and the accelerometer located underwater. A thin latex sheath was used to cover and seal the region of the post located underwater. To insure that the ultrasonic system and accelerometer were both sensing the same motion, the ultrasonic transducers were focused on the accelerometer housing, rather than the post. The orientation was such that the directions of positive displacement were identical for each measurement device.

The high-frequency carrier, supplied by an HP 33120A function generator operating near 15 MHz, was split into two signals: one was used to drive the ultrasonic source, the other was used as the reference signal in the phase detector. The ultrasonic receiver output was amplified and split into two signals: one input to the phase detector and the other input to an HP 3585B spectrum analyzer. The spectrum analyzer was used to measure the displacement amplitude from the ultrasonic system. The phase detector output was low-pass filtered and input to a Stanford Research Systems SR 850 lock-in amplifier, which was used to measure the displacement phase.

The shaker was driven with a pure tone generated from one output of a National Instruments DSP 2200 board; the second DSP 2200 output generated a pure tone at the same frequency for the reference inputs to the lock-in amp and one input channel of the DSP board. The accelerometer output was connected through a power supply/signal conditioner (PCB model 482A16) to the second input channel of the DSP board, which was used to digitize the accelerometer output. The arrangement allowed the phase angles measured from both the ultrasonic system and the accelerometer to share a common reference. The measurement process was controlled by a 486 DX2/66 personal computer (PC) with an HP 82335 IEEE-488 interface.

To assess the performance of the amplitude measurement scheme, the voltage amplitude input to the shaker was varied in discrete steps as the ultrasonic system and accelerometer measured the resulting motion amplitude. To assess the performance of the phase measurement system, the shaker input voltage phase was varied with respect to the phase reference signal as the ultrasonic system and accelerometer measured the resulting motion phase. These tests were repeated for a number of frequencies.

Figure 5(a) shows the measured displacement amplitude vs the actual displacement amplitude at 1 kHz. The symbols represent the experimental data. The solid line is a least-squares linear fit to the data with a slope of 1.0 and $R^2=0.997$. The displacement amplitude obtained with the ultrasonic measurement system agrees extremely well with that measured by the accelerometer. Figure 5(b) shows the measured displacement phase vs the actual displacement phase at 1 kHz. The symbols are the experimental data and the solid line is a least-squares linear fit to the data. For the data of Fig. 5(b), the slope is 1.0 and $R^2=0.9999$, which indicates

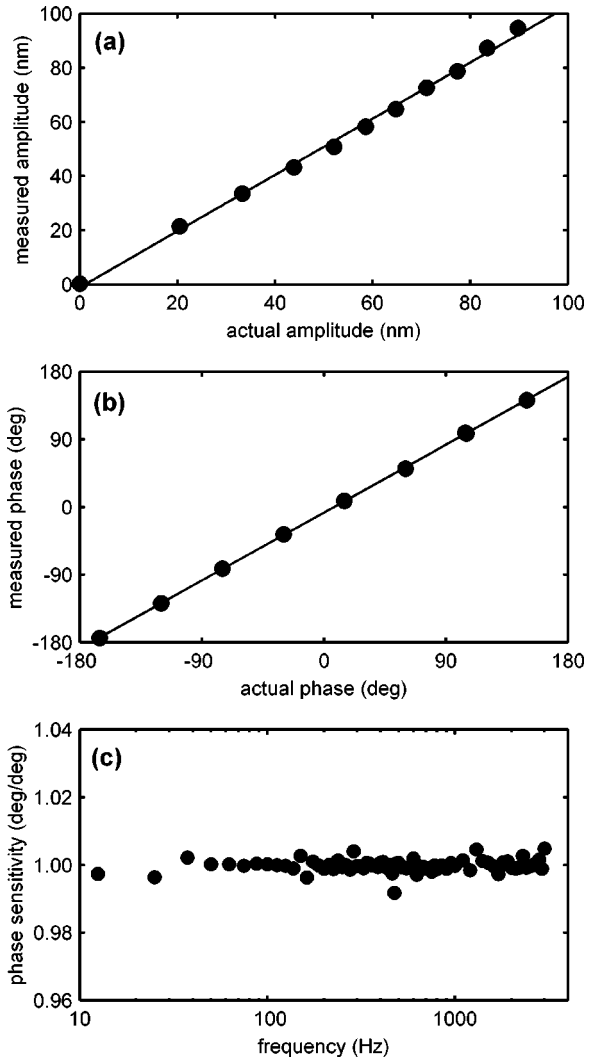

FIG. 5. (a) Displacement and (b) phase calibration curves for the ultrasonic system at 1 kHz. These plots compare the amplitude and phase, respectively, measured by the ultrasonic system with those measured by the accelerometer. (c) Phase sensitivity as a function of frequency.

that the displacement phase obtained with the ultrasonic system agrees with that measured with the accelerometer. Plots such as Fig. 5(b) were constructed for frequencies between 12.5 and 3000 Hz. Figure 5(c) shows the slopes of these plots, which represent the measurement system phase sensitivity as a function of frequency. Phase sensitivity is 1.0 deg/deg over the frequency range tested.

Data analogous to those of Figs. 5(a) and (b) were also used to estimate the accuracy of the amplitude and phase measurement schemes. Table I summarizes the results. The accuracy estimates are based on the $\pm 3s$ limits, where s is the standard deviation of the measured data (Doebelin, 1983). Because the HP 3585B analyzer utilizes a logarithmic amplitude scale, the amplitude resolution is a percentage of the displacement amplitude; i.e., at any particular displacement amplitude, a 1.2% change is necessary to produce a detectable change in the measurement system output.

TABLE I. Accuracy, resolution, and threshold estimates for the amplitude and phase measurement systems.

	Amplitude measurement	Phase measurement
Accuracy (±3-s limits)	±4.2 nm	±3.0 deg
Resolution	1.2%	<1 deg
Threshold	1.5 nm	<1 deg

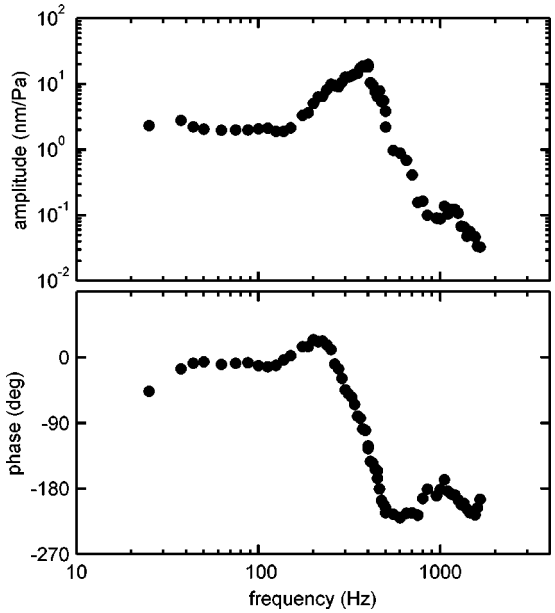

FIG. 6. Frequency response of a 20-mm-diameter balloon submerged in water and insonified by an underwater sound source. Upper: Displacement amplitude divided by $\rho c\sqrt{\epsilon/\rho}$, where ϵ is the (low-frequency) acoustic energy density at the balloon location, ρ is the medium density, and c is the medium sound speed. Lower: phase angle relative to the pressure phase.

Figure 6 shows the frequency response of a small balloon submerged in water and insonified by an underwater sound projector (NRL J13 or J9, depending on the frequency). The balloon target allowed further validation of the measurement technique because it approximates a spherical air bubble, a target whose resonant frequency can be theoretically estimated. The balloon diameter was approximately 20 mm. The measured displacement amplitude was normalized by dividing by $\rho c\sqrt{\epsilon/\rho}$, where ϵ is the (low-frequency) acoustic energy density at the balloon location and ρ is the medium density (in this case, water). The phase reference was the acoustic pressure phase at the target location. Positive displacement was defined as away from the ultrasonic system (see Fig. 1), which in this case corresponds to inward radial motion. The data were smoothed using a 5-point moving average. The data fit the expected second-order mechanical system behavior well (Doebelin, 1972). The amplitude and phase data suggest a resonant frequency near 370 Hz for the balloon tested. At low frequencies the acoustic pressure and balloon displacement were in phase; above resonance they were 180° out of phase. The theoretical resonant frequency of a spherical air bubble with the same volume as the balloon is approximately 330 Hz (Minnaert, 1933). Deviation from the theoretical behavior may have been caused by the nonuniform balloon wall thickness, nonspherical shape, viscoelasticity of the balloon wall, and the method by which the balloon was suspended.

Figure 7 shows the *in vivo* frequency response of the posterior swimbladder in a 10-cm-long goldfish. These data

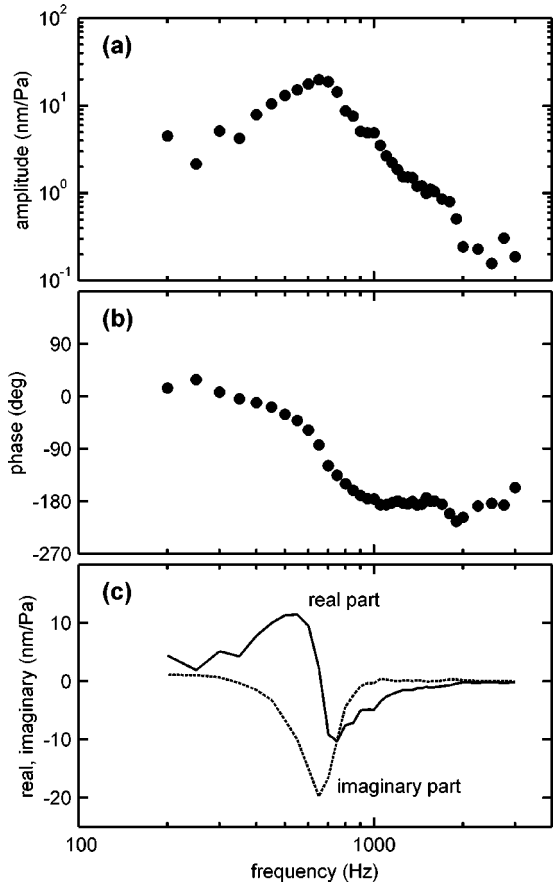

FIG. 7. Frequency response of the posterior swimbladder (with anterior bladder deflated) measured *in vivo* for a 10-cm-long goldfish (Finneran and Hastings, 2000). (a) Displacement amplitude normalized by dividing by $\rho c\sqrt{\epsilon/\rho}$; (b) Phase angle relative to the pressure phase; (c) Real and imaginary parts of the normalized displacement.

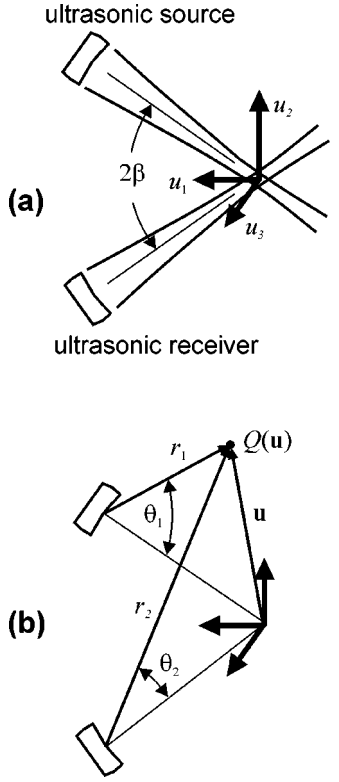

FIG. 8. Coordinate systems used to calculate the ultrasonic system spatial resolution.

were used by Finneran and Hastings (2000) to estimate tissue properties for a mathematical model of the goldfish peripheral auditory system. Figures 7(a) and (b) show the displacement amplitude and phase angle. These data are analogous to Fig. 6: the amplitude is normalized by dividing by $\rho c\sqrt{\epsilon/\rho}$ and the phase reference is the acoustic pressure phase at the target. Positive displacement corresponded to inward radial motion. Figure 7(c) shows the real and imaginary parts of the normalized displacement. Resonant frequencies are often estimated from frequency response data as the frequency at which the real part crosses zero or the imaginary part reaches a minimum. The swimbladder resonant frequency estimated from Fig. 7 is approximately 650 Hz.

IV. SPATIAL RESOLUTION

The spatial resolution of the ultrasonic measurement system is dictated by the size of the sample volume, which may be envisioned as the three-dimensional volume enclosed within the intersection of the beams of the ultrasonic source and receiver transducers (Baker and Yates, 1973).

A. Theory

The ultrasonic measurement system features two focused ultrasonic transducers, arranged so that their axes intersect at their focal points, as shown in Figs. 1 and 8(a). The transducer axes lie within the u_1-u_2 plane. The observation point Q at $\mathbf{u}=(u_1,u_2,u_3)$, is referenced to the ultrasonic source by coordinates (r_1,θ_1), and to the ultrasonic receiver by coordinates (r_2,θ_2), as shown in Fig. 8(b).

The pressure incident on an infinitesimal target located at point $\mathbf{u}$, $p_i(\mathbf{u})$, is

$$p_i(\mathbf{u})=p(r_1,\theta_1). \tag{10}$$

The average pressure over the surface of a target with projected area A_T located at point $\mathbf{u}$ is the integral of Eq. (10) over the area of the target, divided by the target area

$$p_i(\mathbf{u})=\frac{1}{A_T}\int_T\int p(r_1,\theta_1)dT, \tag{11}$$

or, in terms of the normalized pressure $\zeta(r,\theta)=p(r,\theta)/\rho c v_s$

$$p_i(\mathbf{u})=\frac{\rho c v_s}{A_T}\int_T\int \zeta(r_1,\theta_1)dT, \tag{12}$$

where v_s is the normal component of the source surface velocity, ρ is the medium density, and c is the medium sound speed.

If the target is a small, rigid reflector, and the incident ultrasound is locally plane, then the target will act as a spherical source with velocity $v_T=-p_i(\mathbf{u})/\rho c$, or

$$v_T=\frac{-v_s}{A_T}\int_T\int \zeta(r_1,\theta_1)dT. \tag{13}$$

If reciprocity is assumed to hold, then the output voltage amplitude from a reversible transducer receiving sound emitted from **u** is proportional to the pressure amplitude at **u** resulting from transmission of the same waves by the reversible transducer acting as a source (Weight and Hayman, 1978). The output voltage $e_r(\mathbf{u})$ from the ultrasonic receiver caused by a target located at **u** is then

$$e_r(\mathbf{u}) = K_e \rho c v_T \zeta(r_2, \theta_2), \tag{14}$$

where K_e is a constant. Substituting Eq. (13) into Eq. (14) gives

$$e_r(\mathbf{u}) = -K_e \rho c \frac{v_s}{A_T} \zeta(r_2, \theta_2) \int\int_T \zeta(r_1, \theta_1) dT. \tag{15}$$

The normalized receiver output, $E_r(\mathbf{u}) = e_r(\mathbf{u})/\rho c v_s$, is

$$E_r(\mathbf{u}) = K \zeta(r_2, \theta_2) \int\int_T \zeta(r_1, \theta_1) dT, \tag{16}$$

where K is a constant. The theoretical spatial resolution of the system was obtained by solving Eq. (16) in a point-by-point fashion. The normalized pressures $\zeta(r_1, \theta_1)$ and $\zeta(r_2, \theta_2)$ were obtained from a numerical solution of the Rayleigh integral for a spherically concave piston source (Chen *et al.*, 1993).

Equation (16) was solved for a 6.35-mm-diameter source and receiver focused at 19 mm and operated at 15 MHz. The angle 2β was 60°. The target was assumed to be circular with a diameter of 0.2 mm. The results are presented in Figs. 9(a)–(c) as contour plots of the normalized receiver output in dB *re*: the maximum amplitude. The −3-, −6-, −10-, −20-, and −30-dB contours are displayed. Sample volume sizes, defined by the −3-dB contours, were estimated to be 0.44, 0.25, and 0.22 mm for the u_1, u_2, and u_3 directions, respectively.

B. Experiment

Theoretical predictions for the spatial resolutions were verified by performing experimental measurements using a configuration similar to Fig. 4(a). The ultrasonic source and receiver were 6.35-mm-diameter immersion transducers focused at 19 mm (Panametrics V317-SU F0.75). Each transducer had a resonance at approximately 20 MHz with a −6-dB frequency bandwidth of 12.2 MHz. The source and receiver were both mounted to steel posts (Krautkramer Branson model ST-015) and immersed in water. The source post was attached to a manual positioning system that allowed motion in the u_2 direction and rotation about the vertical. The receiver was attached to a manual positioning system that allowed linear motion along the three coordinate axes and rotation about the vertical. The source was driven directly using an HP 33120A function generator operating at 15 MHz. The receiver output passed directly into an HP 3585B spectrum analyzer, which was connected to a 486 DX2/66 PC via an HP 82335 IEEE-488 interface board.

The target was a 0.2-mm-diameter brass wire aligned so that the its front face was parallel to the u_2–u_3 plane and its length was parallel to the u_1 axis. The target was mounted on a steel post and immersed in fresh water. The target post was attached to a motorized positioning system (Aerotech ATS-100 series) that allowed motion along the three coordinate axes. The PC controlled the positioning system via an Aerotech Unidex 500 motion control board. As the target was moved point-by-point through a 2×2-mm grid of locations in each of the u_1–u_2, u_1–u_3, and u_2–u_3 planes, the receiver amplitude was recorded from the HP 3585B.

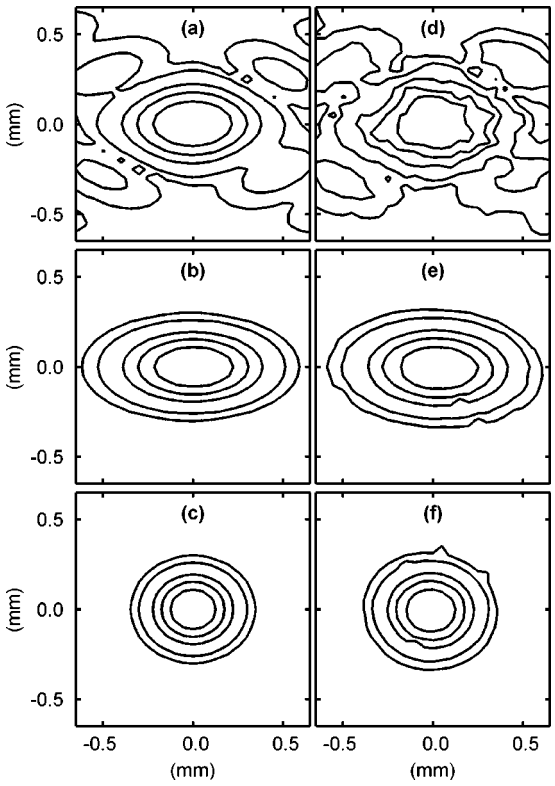

FIG. 9. (a)–(c) Theoretical and (d)–(f) experimental contour plots of the source–receiver fields for the measurement system operating at 15 MHz, with 6.35-mm-diameter transducers focused at 19 mm. (a), (d) u_1–u_2 plane; (b), (e) u_1–u_3 plane; (c), (f) u_2–u_3 plane. Contours are −3, −6, −10, −20, and −30 dB *re*: the maximum amplitude.

Figures 9(d)–(f) show the experimental contour plots for the receiver field of the ultrasonic measurement system operated at 15 MHz with $2\beta = 60°$. The data are presented in dB *re*: the maximum receiver amplitude in each plane; the −3-, −6-, −10-, −20-, and −30-dB contours are shown. The experimental contours agree very well with the theoretical results of Figs. 9(a)–(c); R^2 values are 0.964, 0.981, and 0.979 for the u_1–u_2, u_1–u_3, and u_2–u_3 planes, respectively. Sample volume dimensions (−3 dB) were 0.42, 0.27, and 0.23 mm for the u_1, u_2, and u_3 directions, respectively.

The measurement described above was repeated with $2\beta = 50°$ and 70°. The sample volume dimensions were then estimated from the −3-dB contour lines in each plane and compared to the theoretical predictions based on Eq. (16). Figure 10 illustrates the variation of each sample volume dimension with the bisected angle. The symbols are the experimental data; the lines are the theoretical predictions. This plot shows that the size of the sample volume in the u_3 direction is independent of the angle; it depends only on the ultrasonic source and receiver dimensions. The length in the u_2 direction is also nearly independent of bisected angle.

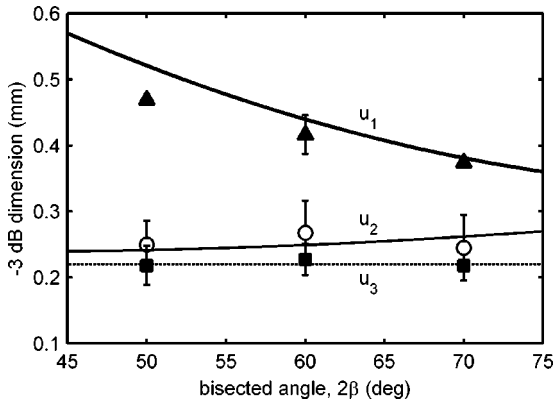

FIG. 10. Sample volume dimensions (−3 dB) plotted versus transducer bisected angle 2β for the u_1, u_2, and u_3 sample volume dimensions.

Only in the u_1 direction (along the bisector) is the change with angle significant. As the angle increases, the sample volume depth decreases. Therefore, to reduce the sample volume depth, the bisected angle should be increased.

V. CONCLUSIONS

The NIVAMS developed by Rogers and Hastings (1989) was modified to include phase angle measurement. The phase measurement was obtained by demodulating the received ultrasound using a double-balanced mixer and low-pass filter. Modifications to the phase angle measurement scheme were necessary because of small, uncontrollable target motions and the unknown phase of the target pressure reflection coefficient. The modified procedure adjusted the ultrasonic frequency to drive the dc component of the phase detector output to zero. The resulting device had amplitude and phase accuracies of ± 4.2 nm and $\pm 3°$, respectively.

The ultrasonic sample volume size was predicted using a mathematical model for the source–receiver field. Experimental measurements of the sample volume contours and dimensions agreed well with the theoretical predictions. Sample volume dimensions for a system operating at 15 MHz with a 60° angle between transducers were approximately $0.4\times0.3\times0.2$ mm.

ACKNOWLEDGMENT

This work was supported by the Office of Naval Research Grant No. N00014-94-1-0337.

Baker, D. W., and Yates, W. G. (**1973**). "Technique for studying the sample volume of ultrasonic Doppler devices," Med. Biol. Eng. **11**, 766–770.

Catheline, S., Wu, F., and Fink, M. (**1999**). "A solution to diffraction biases in sonoelasticity: The acoustic impulse technique," J. Acoust. Soc. Am. **105**, 2941–2950.

Chen, X., Schwarz, K. Q., and Parker, K. J. (**1993**). "Radiation pattern of a focused transducer: A numerically convergent solution," J. Acoust. Soc. Am. **94**, 2979–2991.

Cox, M., and Rogers, P. H. (**1987**). "Automated noninvasive motion measurement of auditory organs in fish using ultrasound," J. Vib. Acoustics, Stress, Rel. Des. **109**, 55–59.

Doebelin, E. O. (**1972**). *System Dynamics: Modeling and Response* (Ohio State University Press, Columbus, OH).

Doebelin, E. O. (**1983**). *Measurement Systems: Application and Design* (McGraw-Hill, New York).

Finneran, J. J., and Hastings, M. C. (**2000**). "A mathematical analysis of the peripheral auditory system mechanics in the goldfish (*Carassius auratus*)," J. Acoust. Soc. Am. **108**, 1308–1321.

Krouskop, T. A., Doughtery, D. R., and Levinson, S. F. (**1987**). "A pulsed Doppler ultrasonics system for making noninvasive measurements of the mechanical properties of soft tissues," J. Rehab. Res. Biol. **14**, 1–8.

Lerner, R. M., Parker, K. J., Holen, J., Gramiak, R., and Waag, R. C. (**1998**). "Sono-elasticity: Medical elasticity images derived from ultrasound signals in mechanically vibrated targets," Acoustical Imaging Vol. 19, Proc. 16th Int. Symp. (Plenum, New York), pp. 317–327.

Lewis, T. N., Martin, J. S., and Rogers, P. H. (**1994**). "Measurement of the vibrational response of porcine lungs to low-frequency underwater sound," J. Acoust. Soc. Am. **95**, 2830(A).

Martin, J. S., Rogers, P. H., Cudahy, E. A., and Hanson, E. L. (**2000**). "Low-frequency response of the submerged human lung," J. Acoust. Soc. Am. **107**, 2813(A).

Minnaert, M. (**1933**). "On musical air bubbles and the sounds of running water," Philos. Mag. Ser. 7 **16**, 235–248.

O'Donnell, M., Skovorada, A. R., Shapo, B. M., and Emalianov, S. Y. (**1994**). "Internal displacement and strain imaging using ultrasonic speckle tracking," IEEE Trans. Ultrason. Ferroelectr. Freq. Control **41**, 314–325.

Ophir, J., Cespedes, I., Ponnekanti, H., Yazdi, Y., and Li, X. (**1991**). "Elastography: A quantitative method for imaging the elasticity of biological tissues," Ultrason. Imaging **13**, 111–134.

Rogers, P. H., and Hastings, M. C. (**1989**). "Noninvasive vibration measurement system and method for measuring amplitude of vibration of tissue in an object being investigated," U.S. Patent No. 4,819,643.

Schroeder, L. E., and Hastings, M. C. (**1994**). "An ultrasonic system for measurement of the dynamic response of biological tissue," Proceedings of the 1994 International Mechanical Engineering Congress and Exhibition, 94-WA/NCA-5.

Scientific Components (**1992**). *RF/IF Designer's Handbook* (Mini-Circuits, Brooklyn, NY).

Taylor, L. S., Porter, B. C., Rubens, D. J., and Parker, K. J. (**2000**). "Three-dimensional sonoelastography:principles and practices," Phys. Med. Biol. **45**, 1477–1494.

von Békésy, G. (1960). *Experiments in Hearing* (AIP, New York).

Weight, J. P., and Hayman, A. J. (**1978**). "Observations of the propagation of very short ultrasonic pulses and their reflection by small targets," J. Acoust. Soc. Am. **63**, 396–404.

Yamakoshi, Y., Sato, J., and Sato, T. (**1990**). "Ultrasonic imaging of internal vibration of soft tissue under forced vibration," IEEE Trans. Ultrason. Ferroelectr. Freq. Control **37**, 45–53.

Feasibility of bone assessment with leaky Lamb waves in bone phantoms and a bovine tibia

K. I. Lee and Suk Wang Yoon[a)]
Acoustics Research Laboratory and BK21 Physics Research Division, Department of Physics, SungKyunKwan University, Suwon 440-746, Republic of Korea

(Received 16 September 2003; revised 17 February 2004; accepted 23 February 2004)

In this study, the effect of cortical thickness variation on the propagation of leaky Lamb waves is investigated by using an axial transmission technique commonly used to characterize long bones. Three Lucite™ plates with thicknesses of 1, 3, and 5 mm as bone phantoms and one bovine tibia with a cortical thickness of 2 mm were used at various low frequencies. Experimental measurements in bone phantoms show that the peak frequency and amplitude of excited Lamb modes strongly depend on the thickness of the Lucite plate. In the bovine tibia, the S0 and A0 Lamb modes are consistently observed in the frequency-thickness region from 0.2 to 1.0 MHz mm, and can be effectively launched at a frequency of 200 kHz, suggesting 200 kHz to be the optimal signal frequency for *in vivo* clinical applications. It can be also seen that both modes are affected by the frequency-thickness product, but the effect is greater for the A0 mode. Hence, the A0 Lamb mode seems more sensitive to cortical thickness change due to aging and osteoporosis. This study suggests that the use of leaky Lamb waves is feasible for ultrasonic bone assessment. © *2004 Acoustical Society of America.* [DOI: 10.1121/1.1707086]

PACS numbers: 43.80.Ev, 43.80.Jz, 43.80.Qf [FD] Pages: 3210–3217

I. INTRODUCTION

Continuing improvements have been made since the introduction of the first clinical quantitative ultrasound (QUS) devices using through-transmission techniques, either by enhancing hardware performance or by optimizing analysis algorithms. Although QUS is being used increasingly to predict the risk of osteoporotic fractures and to monitor treatment progress, one limitation until now has been that very few skeletal sites were accessible. In recent years, ultrasonic measurement along the axial direction of long bones has attracted the attention of a number of researchers.[1–10] Axial transmission techniques currently use a pair of transducers to measure the ultrasound velocity through a fixed distance of the cortical layer of the bone along its long axis. In contrast to through-transmission techniques, which require placing a transducer on each side of the bone, axial transmission techniques can be easily applied to a number of skeletal sites, including the radius, finger phalanges, tibia, and hand metacarpal because of its easy transducer setup.

Two commercial QUS devices using axial transmission techniques have been developed to measure various nonheel anatomical sites such as the Soundscan 2000 (Myriad Ultrasound Systems Ltd., Rehovot, Israel) and the Sunlight Omnisense (Sunlight Medical Corp., Rehovot, Israel).[11] These systems mainly measure the ultrasound velocity along the anteromedial cortical border of the mid-tibia and the wrist, thereby taking advantage of a site that is easily accessible in most individuals. The ultrasound velocity obtained this way is claimed to reflect the whole bone strength (failure load), a property that is related to bone size, mass distribution, cortical thickness, internal architecture, density, and elastic properties of the bone.[12] Furthermore, excellent correlation between tibial speed of sound (SOS) and material properties of the tibial cortex has been shown.[5] On the other hand, the tibial SOS shows only a modest correlation with the failure load of the femoral neck as compared with dual energy x-ray absorptiometry.[13]

The dependence on cortical thickness of ultrasound velocity is predicted by the theory of wave propagation in linearly elastic, homogeneous, solid materials.[6,7] Simulation of fluid–solid interface and experimental validation of the lateral wave were reported by Camus *et al.*[6] on test materials of known acoustic properties and on human cortical bones. Recently, the relationship between ultrasound velocity and cortical thickness in bone plates has been studied by Bossy *et al.*[7] using two-dimensional numerical simulations of 1 MHz ultrasound propagation. Theoretical analysis of the field reflected from a fluid–solid interface for an incident spherical wave predicts the existence of a lateral wave propagating along the sample surface at a velocity close to the longitudinal velocity, in addition to the ordinary reflected wave and vibration modes.

Ultrasonic guided waves are well known to be suitable for characterizing thin plates and layered media.[14,15] A Lamb wave is a form of elastic perturbation that can propagate in a solid plate with free boundaries. This type of wave was first described in theory by Lamb[16] in 1917, even if he never attempted to produce a Lamb wave. The use of Lamb waves is very attractive in ultrasonic bone assessment since they can propagate throughout the cortical thickness of long bones, which means that the entire thickness of the bone can be interrogated. In the case of immersion techniques, Lamb waves leak out from a plate as they propagate; such waves are called leaky Lamb waves. A leaky Lamb wave technique uses specific modes of guided waves that are generated and

a)Electronic mail: swyoon@skku.ac.kr

 0001-4966/2004/115(6)/3210/8/$20.00 © 2004 Acoustical Society of America

detected through the mode-converted waves in the medium surrounding the plate.

Diaphyseal cortical bone has a shape of irregular tubular layer with thicknesses of typically 3–8 mm in the human tibia. Acoustic properties of soft tissue overlying the bone are very close to those of water so that leaky Lamb waves can be produced along the cortical layer, which arise from the reflection and mode conversion of longitudinal and shear waves at the boundaries of the layer, provided the ultrasonic wavelength is larger than the cortical thickness. Earlier studies[1,2] indicate that guided waves can be measured by the low-frequency ultrasonic method in human cortical bones. In recent studies, guided waves were measured *in vitro* on bone specimens[8] and *in vivo* in human.[9,10] Lefebvre *et al.*[8] confirmed that guided waves could be excited at 100 kHz in two bovine femur and one tibia and could be used to estimate thickness and elastic properties. Nicholson *et al.*[9] performed similar work in acrylic plates, and also described *in vivo* tibial measurements of the lowest order antisymmetrical (A0) Lamb mode in human subjects. Lamb wave theory and numerical simulations of wave propagation were used to gain insights into the expected behavior of guided waves in bone. Experimental measurements were performed at a frequency of about 200 kHz with a series of acrylic plates with thicknesses ranging from 2 to 24 mm as bone mimicking phantoms. They confirmed the presence of a second slower wave whose behavior was consistent with the A0 mode, and also suggested the A0 mode to be a more sensitive indicator of osteoporosis from a pilot study of healthy and osteoporotic subjects.[9]

In this study, the effect of cortical thickness variation on the propagation of leaky Lamb waves is investigated by using an axial transmission technique since the cortical thickness changes with aging and osteoporosis, which has been shown to be a risk factor for fracture. The main purpose of the present study is to identify the leaky Lamb mode and the signal frequency that are most effective in bone assessment. To this purpose, three Lucite™ plates with thicknesses of 1, 3, and 5 mm as bone phantoms and one bovine tibia with a cortical thickness of 2 mm were used at various low frequencies.

II. MATERIALS AND METHODS

A. Bone phantoms and bovine tibia

Three Lucite plates with thicknesses of 1, 3, and 5 mm were used as bone phantoms. Lucite was selected as a preliminary test phantom for cortical bone since it can be easily manipulated, has well-known material properties, and has been used as a bone mimic in previous studies.[9,17] The thicknesses were chosen to imitate thickness variation in skeletal sites such as radius, tibia, femur, metacarpal, and phalanx in simplified and general manner since, due to the anatomical variation of the cortical thickness, all thickness values can be found in each type of bone at different locations.[17–20] They were submerged in a water tank to simulate the surrounding soft tissue since the ultrasound velocity in water is close to that in soft tissue. The velocities of the longitudinal and the shear bulk waves propagating in this material were measured

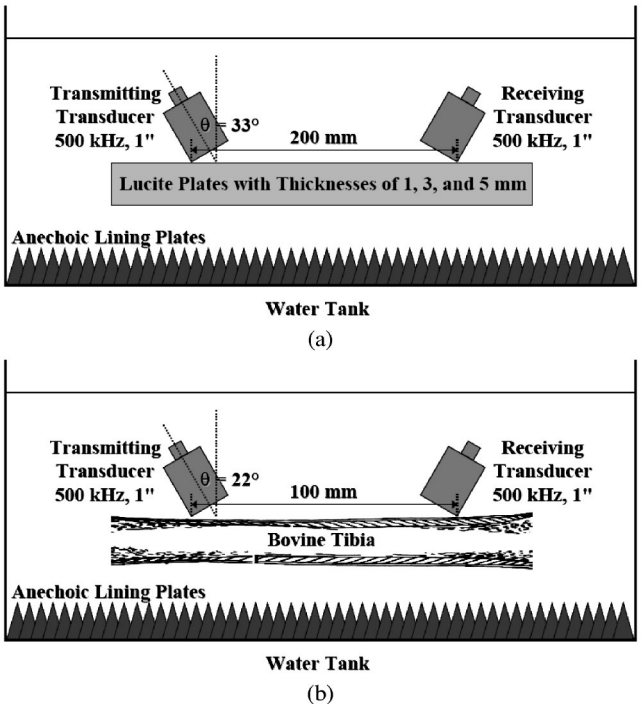

FIG. 1. Schematic diagrams of the experimental setup for ultrasonic measurements with leaky Lamb waves for (a) Lucite plates and (b) a bovine tibia.

with a conventional ultrasonic technique. The longitudinal bulk wave velocity was measured as 2743 m/s, and the shear bulk wave velocity as 1427 m/s. They were used as input data to calculate the dispersion curves for a Lucite plate.

The tibia specimen used in this study was taken from one piece of a bovine tibia. The proximal ends of the tibia were removed by using a rotary electric saw to make a hollow tube-shaped tibia without any soft tissue and marrow. The specimen was defatted by boiling for 1 h in water. Cortical thickness of the tibia specimen was measured using calipers. The least irregularly shaped area of the tibia at which thickness was relatively well defined was chosen for ultrasonic measurements. Typical longitudinal and shear bulk wave velocities in the cortical part of the femur found in the literature are 4000 and 1800 m/s along the axial direction, respectively.[21] They were used as input data to calculate the dispersion curves for a cortical bone plate.

B. Ultrasonic measurements

The schematic diagrams of the experimental setup for ultrasonic measurements with leaky Lamb waves are shown in Fig. 1. Ultrasonic measurements were performed in a water tank maintained at room temperature between 18 and 2 °C. In an attempt to make the tank less reverberant, anechoic lining plates were installed at the bottom of the tank. Conventional wideband ultrasonic immersion transducers with a center frequency of 500 kHz (Panametrics V301, 1.0 in. diameter) were used in all the experiments. A pair of transducers as a transmitter and a receiver was placed at angles of $\theta = 33°$ and 22° to the specimen interface for Lucite plates and a bovine tibia, respectively, which are the longitudinal critical angles of incidence from water to the

specimens. Individual Lamb waves were selectively excited by applying the coincidence principle.[22] The incidence angle θ that is required for the excitation of the desired mode was determined from Snell's law, $\theta = \sin^{-1}(c_w/c_l)$, where c_w is the phase velocity of a longitudinal bulk wave incident on the surface of the plate and c_l is the phase velocity of the leaky Lamb wave to be excited. The transmitter was driven with a function generator (HP 3314A). The received signals, amplified by a preamplifier (SRS SR560), were analyzed with a 500 MHz digital storage oscilloscope (LeCroy LT322). The appropriate transmitter–receiver spacing was determined by taking into account the acceptable signal loss for the voltage sensitivity of the data acquisition system. A spongy block with a thickness of 30 mm was placed between transmitter and receiver in order to exclude the direct wave that travels in water directly from transmitter to receiver and the wave specularly reflected at the water–specimen interface. The spongy block is not shown in Fig. 1.

C. Frequency selection

The most important procedure in exciting an appropriate leaky Lamb wave is to select an appropriate driving frequency. This procedure commences by finding the Lamb solution for the wave equation and plotting the dispersion curves for each section to be monitored.[14] Figure 2 shows the phase velocity dispersion curves as functions of the frequency-thickness product (MHz mm) for a free Lucite plate and a free cortical bone plate. These curves were calculated using a longitudinal velocity of 2743 m/s and a shear velocity of 1427 m/s for a Lucite plate, and a longitudinal velocity of 4000 m/s and a shear velocity of 1800 m/s for a cortical bone plate. The resulting dispersion curves provide a range of potential wave velocities for the antisymmetric and the symmetric modes driven at different frequency-thickness products.

As can be observed in Fig. 2, above a certain frequency-thickness product value, more than two orders of each mode exist. For a given thickness, ideally one would like to choose the least dispersive driving frequency for the leaky Lamb wave being generated, which generally exists where the slope of the phase velocity curve is equal to zero. At lower frequencies, fewer Lamb modes are excited so that the response signal is more distinguishable and the velocity is lower. At these frequencies, however, the dispersion curves have steep slopes and are very sensitive to small variations in the frequency, making it difficult to predict the time of flight. At higher frequencies, when more modes are present, the slope tends to flatten out with the consequence of a shorter wave pulse. The selected optimal frequencies are based on slopes and locations on the dispersion curves and on experimentation using a function generator to excite the maximum response amplitude for a range of driving frequencies.

III. RESULTS

A. Bone phantoms: 1-, 3-, and 5-mm-thick Lucite plates

There are two sets of results obtained from feasibility tests to apply leaky Lamb waves in bone assessment. The first set of tests was performed to identify the thickness dependence of the propagation of leaky Lamb waves in bone phantoms. Figure 3 shows the response of a 500 kHz tone burst with five cycles in the 1-, 3-, and 5-mm-thick Lucite plates. The response of a 500 kHz tone burst in a 1-mm-thick Lucite plate is shown in Fig. 3(a) and gives a center frequency thickness of 0.5 MHz mm. In the response of the time-domain signal, it is not possible to identify the excited modes, though some evidence of the S0 mode is seen in the frequency spectrum below 300 kHz.

Figure 3(b) shows the response of a 500 kHz tone burst in a 3-mm-thick Lucite plate. The excitation gives a center frequency thickness of 1.5 MHz mm. As the frequency spectrum shows, the maximum amplitude of the response is at 500 kHz, which corresponds to the center frequency of the input tone burst. The shape of the time-domain signal indicates the presence of leaky Lamb waves with different group velocities since the wave packets are well separated. The first arriving wave packet was identified as the S1 mode by measuring the time of flight of the leading edge of the signal, and the second one as the A1 mode. These modes correspond to

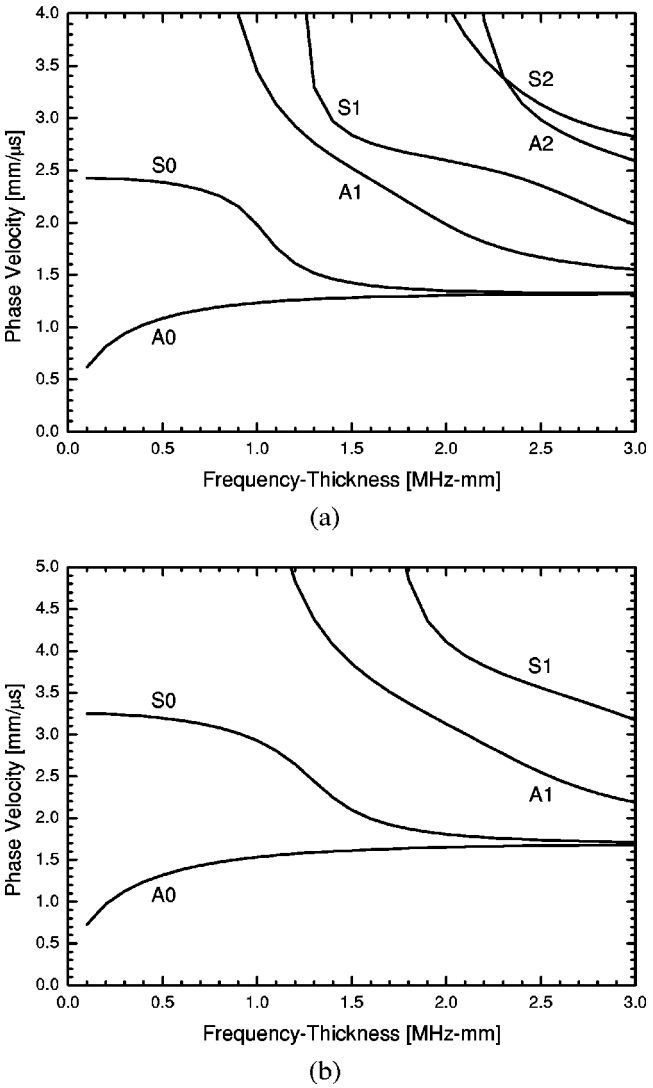

FIG. 2. Phase velocity dispersion curves as functions of the frequency-thickness product (MHz mm) for (a) a free Lucite plate and (b) a free cortical bone plate.

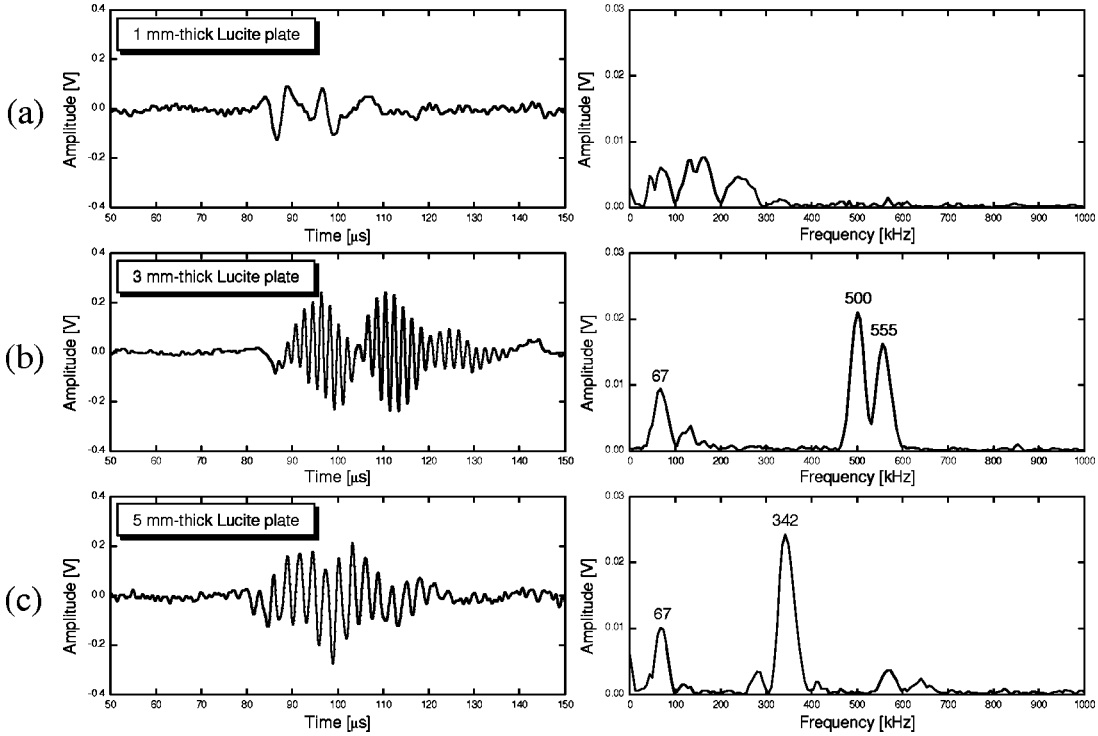

FIG. 3. Time-domain signal and frequency spectrum of the measured response for a 500 kHz tone burst in the (a) 1-, (b) 3-, and (c) 5-mm-thick Lucite plates.

peak frequencies of 555 and 500 kHz, respectively. The peak frequency of 67 kHz in the frequency spectrum corresponds to the S0 mode.

The response of a 500 kHz tone burst in a 5-mm-thick Lucite plate is shown in Fig. 3(c) and gives a center frequency thickness of 2.5 MHz mm. The signals shown in the time domain are dominated by the S1 mode. The shape of the response indicates the presence of leaky Lamb waves with similar group velocities since the wave packets have not been separated. The frequency spectrum obtained from the time-domain signal shows the maximum peak frequency at 342 kHz, which corresponds to the S1 mode. In addition, there is a peak frequency at 67 kHz that corresponds to the S0 mode.

B. Bovine tibia: 2-mm-thick cortical bone plate

The second set of tests was designed to identify the leaky Lamb mode and the signal frequency that are most effective in bone assessment. Experimental measurements were performed in a 2-mm-thick cortical bone plate of the mid-tibia because of its long, straight, and smooth surface. The transmitting and receiving transducers at oblique incidence were placed on the mid-tibial plane parallel to the long axis of the bone. Five-cycle tone bursts with the center frequencies of 100, 200, and 500 kHz were used. The center frequencies of the excitation tone bursts were based on experimentation using a function generator to excite the maximum response amplitude for a range of driving frequencies.

The response of a 100 kHz tone burst is shown in Fig. 4(a). This excitation gives a center frequency thickness of 0.2 MHz mm in a 2-mm-thick cortical bone plate. In this frequency-thickness region, only the A0 and S0 modes can propagate along the bone plate, as shown in the dispersion curves of Fig. 2(b). In the frequency spectrum, the amplitude reaches a maximum at 104 kHz, which corresponds to the S0 mode identified from a measurement of its group velocity using the time-of-flight method. Its group velocity was determined as 3210 m/s.

Figure 4(b) shows the response of a 200 kHz tone burst. The excitation gives a center frequency thickness of 0.4 MHz mm. The response of the time-domain signal is similar to that of the 350 kHz tone burst in the 5-mm-thick plate. The shape of the response wave packet indicates that very little dispersion is present over the frequency-thickness interval of the input signal. The wave packet was identified as the S0 mode and its group velocity was determined as 3197 m/s. In the frequency spectrum, the amplitude reaches a maximum at 204 kHz, which corresponds to the S0 mode though some evidence of the A0 mode is seen at 250 kHz. The observed amplitude of the A0 mode is significantly less than its true value because the coincidence angle of 22° is not appropriate for the excitation of the A0 mode in the frequency-thickness region of 0.4 MHz mm, so it was inefficiently received by the transducer oriented at 22°. The A0 mode is therefore partially decoupled by the orientation of the receiving transducer.

The response of a 500 kHz tone burst is shown in Fig. 4(c) and gives a center frequency thickness of 1.0 MHz mm. The time-domain signal indicates the presence of leaky Lamb waves with similar group velocities since the wave packets are not separated. Therefore, it is not possible to measure the group velocities of the modes in the time domain unless the propagation distance between transmitter and receiver is increased considerably so that the modes can be separated. The frequency spectrum shows the maximum

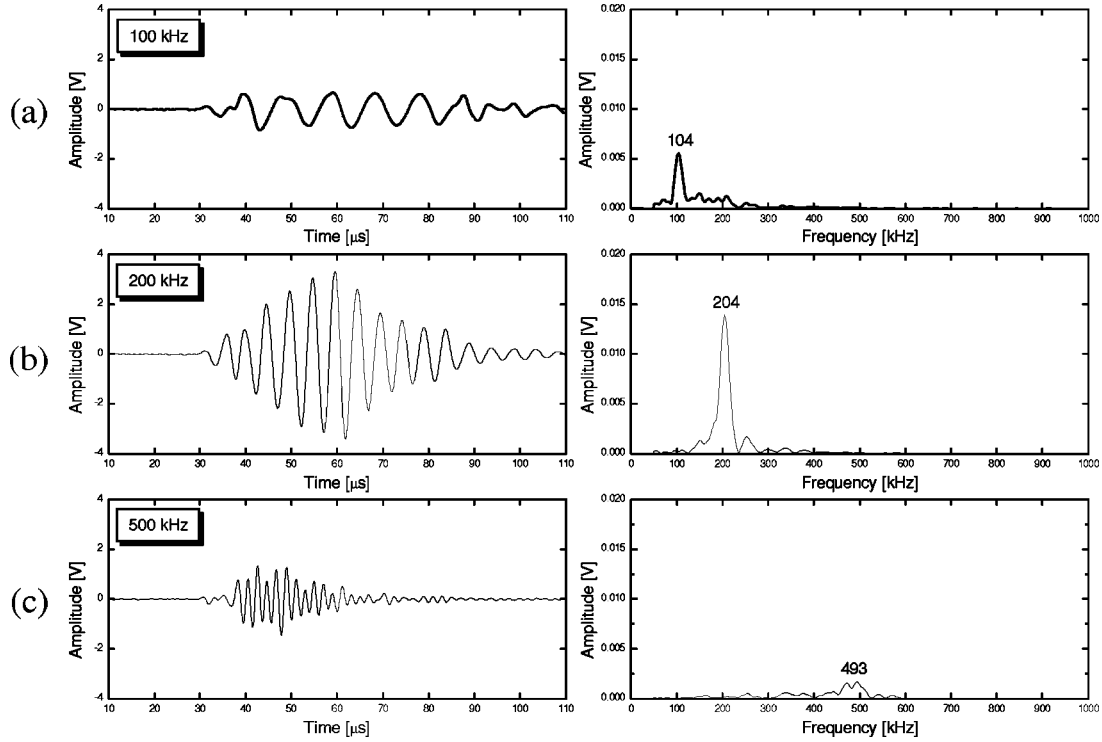

FIG. 4. Time-domain signal and frequency spectrum of the measured response for (a) 100, (b) 200, and (c) 500 kHz tone bursts in a 2-mm-thick cortical bone plate.

peak frequency at 493 kHz which corresponds to the S0 mode.

C. Phase velocity dispersion curves in a cortical bone plate

In order to determine the phase velocity of leaky Lamb waves in a cortical bone plate, the transmitter–receiver distance was increased from 100 to 110 mm in 2 mm steps. The transmitter was excited by an one-cycle tone burst. The excitation frequencies were then varied from 100 to 500 kHz in 50 kHz steps, which gave the center frequency-thickness values from 0.2 to 1.0 MHz mm in a 2-mm-thick cortical bone plate. The S0 and A0 Lamb modes were consistently observed in this frequency-thickness region. Figure 5 shows the time-domain signal of the response for a 200 kHz tone burst at transmitter–receiver distances of 100 and 110 mm. The first arriving signal was identified as the S0 mode by measuring the time of flight of the leading edge of the signal, and the second one as the A0 mode. The phase velocities of the S0 and A0 modes were determined as 3196 and 1486 m/s, respectively. The S0 mode seems to interfere with the wave reflected from the bottom of the bone plate. Both the direct wave from transmitter to receiver and the wave specularly reflected at the water–bone plate interface were excluded by placing the spongy block between transmitter and receiver. Moving the receiving transducer in the direction of increasing the transmitter–receiver distance, the excited modes were more separated in the time domain. However, their amplitudes decreased significantly with increasing transmitter–receiver distance.

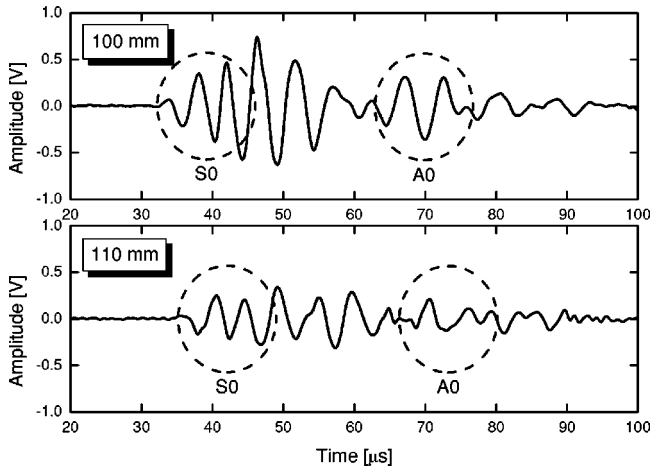

FIG. 5. Time-domain signal of the response for a 200 kHz tone burst at transmitter–receiver distances of 100 and 110 mm.

Figure 6 shows the experimental and theoretical phase velocity dispersion curves as functions of the frequency-thickness product (MHz mm) in a 2-mm-thick cortical bone plate. The solid and dotted lines correspond to the theoretical phase velocities of the S0 and A0 modes. The longitudinal and shear velocities assumed for a cortical bone plate in calculating the theoretical phase velocities are the same as in Fig. 2(b). The squares and circles correspond to the experimental phase velocities obtained from the time-of-flight method described in the previous paragraph. The experimental phase velocity of the A0 mode at 0.2 MHz mm is not presented in Fig. 6 since it was not possible to identify the A0 mode in the response of the 100 kHz tone burst due to an interference between the S0 mode and the A0 mode. The experimental phase velocities of the S0 mode are in good agreement with its theoretical curve. On the other hand, the

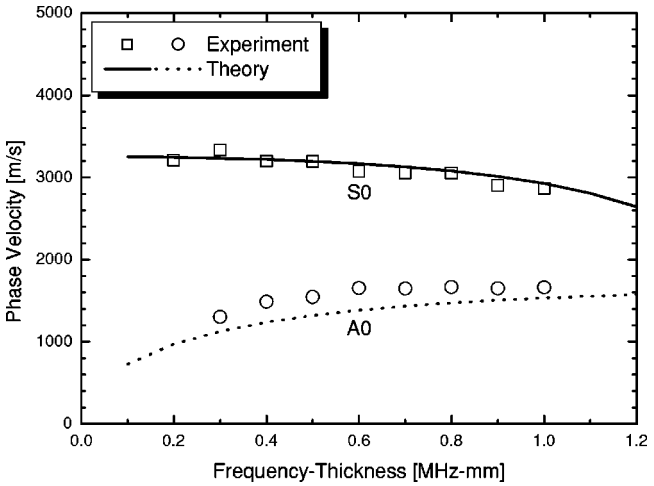

FIG. 6. Experimental and theoretical phase velocity dispersion curves as functions of the frequency-thickness product (MHz mm) in a 2-mm-thick cortical bone plate.

experimental phase velocities of the A0 mode are somewhat higher than predicted values. The trends of both modes clearly correspond to predictions from theory. It should be noted here that both modes are affected by the frequency-thickness product, but the effect is greater for the A0 mode from their normalized experimental phase velocities in Fig. 7. Hence, in the frequency-thickness region from 0.2 to 1.0 MHz mm where only the lowest Lamb modes can propagate, the A0 Lamb mode seems more sensitive to cortical thickness change due to aging and osteoporosis.

IV. DISCUSSION

In this study, we have shown that the peak frequencies and the amplitudes of excited Lamb modes in three Lucite plates with thicknesses of 1, 3, and 5 mm as bone phantoms strongly depend on plate thickness. As can be observed in Fig. 3, the peak frequency of the S1 mode is shifted from 342 to 555 kHz when the thickness of the plate is varied from 5 to 3 mm. It can be also seen that the excited Lamb modes are dominated by the S1 mode in the 5-mm-thick Lucite plate while they are more influenced by the A1 mode in the 3-mm-thick Lucite plate. These results show that the propagation of leaky Lamb waves is strongly affected by the plate thickness.

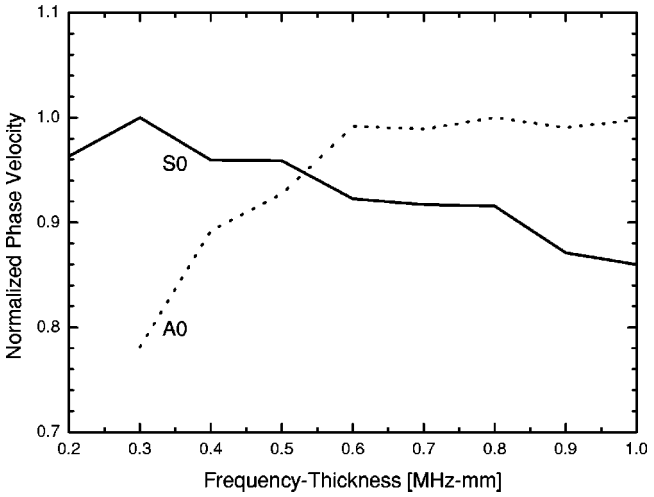

FIG. 7. Normalized experimental phase velocity as functions of the frequency-thickness product (MHz mm) in a 2-mm-thick cortical bone plate.

Lucite was selected as a preliminary test phantom for cortical bone since it can be easily manipulated, has well-known material properties, and has been used as a bone mimic in previous studies.[9,17] The shear velocity in Lucite of 1427 m/s is lower than the longitudinal velocity in water or soft tissue of about 1500 m/s whereas the shear velocity in cortical bone of about 1800 m/s is larger than 1500 m/s. This prevents the A0 Lamb mode from radiating from a Lucite plate immersed in water, and therefore precludes its measurement with a leaky Lamb wave technique.[9] This may be the reason why the A0 mode could not be observed during measurements on Lucite plates while it could be observed on the cortical bone specimen. Hence, Lucite may not be an appropriate bone phantom for the purpose of the current study to identify the leaky Lamb mode and the signal frequency that are most effective in bone assessment.

The Soundscan 2000 (Myriad Ultrasound Systems Ltd., Rehovot, Israel) is the first clinical instrument designed to measure longitudinal transmission of an ultrasonic pulse along the cortical layer of the mid-tibia. The mid-tibia has been chosen because of its long, straight, and smooth surface. This device measures the transit time of a 250 kHz pulse along a defined 50 mm distance. The velocity values of typically 3600 m/s obtained with Soundscan 2000 in axial measurements on whole bones tend to be lower than the values for the longitudinal bulk velocity in cortical bone specimens.[23–26] These values are similar to those of the S0 Lamb mode measured in this study (2865–3331 m/s). This indicates that the Soundscan 2000 may employ an S0 Lamb mode along the cortex rather than a pure longitudinal bulk wave. Our results also show that a pure S0 mode can be effectively launched at a frequency of 200 kHz in a 2-mm-thick cortical bone plate, suggesting 200 kHz to be the optimal signal frequency of the S0 Lamb mode for *in vivo* clinical applications.

Nicholson *et al.*[9] performed experimental measurements in acrylic plates using a prototype axial pulse transmission device at a frequency of about 200 kHz, and measured the velocities of two distinct propagating waves. In thick plates, the velocity of the first arriving wave, which was consistent with a lateral wave,[6,7] was close to the longitudinal velocity, but decreased with decreasing thickness toward that of the S0 Lamb mode. The velocity of the second slower wave, which behaved as predicted for the A0 Lamb mode, was close to the Rayleigh velocity in thick plates, with velocity decreasing strongly with decreasing thickness in excellent agreement with the predictions for the A0 mode. A pilot study also suggested the A0 Lamb mode to be a more sensitive indicator of osteoporosis.[9] Our study has shown that the S0 and A0 Lamb modes can be observed consistently from 0.2 to 1.0 MHz mm in the cortical bone plate. Both modes were affected by the frequency-thickness product, but the effect was greater for the A0 mode. These *in vitro* results from the bovine tibia are consistent with recent *in vivo*

studies[9,10] and therefore validate the presence of the A0 mode in cortical bone.

One novel approach in the current work is the use of fluid coupling at oblique incidence rather than direct contact with the bone. Previous studies[9,10] have relied on direct contact at normal incidence with a relatively small contact area, and this is problematic in terms of *in vivo* measurements, which have to be made through overlying soft tissue. Under these conditions, the transducers are effectively omnidirectional and may excite all the possible waves that may propagate in axial transmission, since energy is propagated and received in all directions. There is therefore sufficient energy radiating axially to produce detectable Lamb waves in the cortex, but a major component of the incident wave will be perpendicular to the long axis, potentially exciting transverse waves. The approach of the present study has potential advantages compared to direct contact. Practically, our results are applicable to a clinical device by tilting the transducers relative to the surface of the bone. This new QUS approach with an axial transmission technique may point to a new way of characterizing bone status and fragility.

For *in vivo* clinical measurements of the Lamb mode velocities, one important factor is the presence of overlying soft tissue which may cause errors. In this *in vitro* study, a spongy block was placed between transmitter and receiver in order to exclude undesired signals such as the direct wave that travels in water directly from transmitter to receiver and the wave specularly reflected at the water–specimen interface. However, *in vivo* the velocity in soft tissue of about 1500 m/s is similar to that of the A0 Lamb mode measured in this study (1301–1665 m/s) so that these undesired signals propagating through soft tissue only can be expected to make the interpretation of received signals difficult and lead to signal-to-noise problems. There should be further studies on the role of the overlying soft tissue in order to minimize errors in the velocity measurements.

Future studies will be required to address some important limitations of the present study. A major limitation lies in the fact that only one bovine tibia *in vitro* was investigated for the S0 and A0 Lamb modes at various frequencies. The experimental phase velocity dispersion curves as functions of the frequency-thickness product could be determined by varying the excitation frequency in a 2-mm-thick cortical bone plate. Future *in vivo* studies with a large number of human subjects are needed. Another limitation involves the modeling of an irregular hollow tube-shaped tibia by a plate. However, the tibia can be approximated to a plate with constant thickness since the least irregularly shaped area of the tibia at which thickness was relatively well defined was chosen for ultrasonic measurements. Previous studies[7,9,17,27] suggest that the dependence on cortical thickness of ultrasound velocity of leaky Lamb waves appears to be similar for a plate and a tube. The axial Lamb-like modes in a cylindrical tube are also similar in behavior to those in a plate provided the wall thickness is small compared to the tube diameter.[28] Nevertheless, further work by using tubular bone phantoms of various thicknesses is required to validate the current approach. Further work should also include the influence of heterogeneity, anisotropy, and irregularity on the propagation of leaky Lamb waves.

V. CONCLUSIONS

We have shown that both antisymmetric and symmetric leaky Lamb waves can be excited and detected successfully in bone phantoms and a bovine tibia by using an axial transmission technique. Experimental measurements in bone phantoms show that the peak frequency and amplitude of excited Lamb modes strongly depend on the thickness of the Lucite plate. In the bovine tibia, the S0 and A0 Lamb modes are consistently observed in the frequency-thickness region from 0.2 to 1.0 MHz mm, and can be effectively launched at a frequency of 200 kHz, suggesting 200 kHz to be the optimal signal frequency for *in vivo* clinical applications. It can be also seen that both modes are affected by the frequency-thickness product, but the effect is greater for the A0 mode. Hence, the A0 Lamb mode seems more sensitive to cortical thickness change due to aging and osteoporosis. This study suggests that the use of leaky Lamb waves is feasible for ultrasonic bone assessment.

ACKNOWLEDGMENTS

This work was supported by the Underwater Acoustics Research Center (UA-33) and the BK21 Program of the Ministry of Education in Korea.

[1] E. Jansons, A. Tatarinov, V. Dzenis, and A. Kregers, ''Constructional peculiarities of the human tibia defined by references to ultrasound measurement data,'' Biomaterials **5**, 221–226 (1984).
[2] A. Tatarinov, V. Dzenis, and E. Jansons, ''Role of compact bone tissue thickness in the investigation of tubular bones by ultrasonic exponential concentrators,'' Mech. Compos. Mater. **21**, 342–357 (1985).
[3] A. J. Foldes, A. Rimon, D. D. Keinan, and M. M. Popovtzer, ''Quantitative ultrasound of the tibia: A novel approach for assessment of bone status,'' Bone (N.Y.) **17**, 363–367 (1995).
[4] G. Lowet and G. Van der Perre, ''Ultrasound velocity measurement in long bones: Measurement method and simulation of ultrasound wave propagation,'' J. Biomech. **29**, 1255–1262 (1996).
[5] S. C. Lee, B. S. Coan, and M. L. Bouxsein, ''Tibial ultrasound velocity measured *in situ* predicts the material properties of tibial cortical bone,'' Bone (N.Y.) **21**, 119–125 (1997).
[6] E. Camus, M. Talmant, G. Berger, and P. Laugier, ''Analysis of the axial transmission technique for the assessment of skeletal status,'' J. Acoust. Soc. Am. **108**, 3058–3065 (2000).
[7] E. Bossy, M. Talmant, and P. Laugier, ''Effect of bone cortical thickness on velocity measurements using ultrasonic axial transmission: A 2D simulation study,'' J. Acoust. Soc. Am. **112**, 297–307 (2002).
[8] F. Lefebvre, Y. Deblock, P. Campistron, D. Ahite, and J. J. Fabre, ''Development of a new ultrasonic technique for bone and biomaterials *in vitro* characterization,'' J. Biomed. Mater. Res. **63**, 441–446 (2002).
[9] P. H. Nicholson, P. Moilanen, T. Karkkainen, J. Timonen, and S. Cheng, ''Guided ultrasonic waves in long bones: modelling, experiment and *in vivo* application,'' Physiol. Meas. **23**, 755–768 (2002).
[10] P. Moilanen, P. H. Nicholson, T. Karkkainen, Q. Wang, J. Timonen, and S. Cheng, ''Assessment of the tibia using ultrasonic guided waves in pubertal girls,'' Osteoporosis Int. **14**, 1020–1027 (2003).
[11] C. F. Njeh, D. Hans, T. Fuerst, C. C. Gluer, and H. K. Genant, *Quantitative Ultrasound: Assessment of Osteoporosis and Bone Status* (Dunitz, London, 1999).
[12] R. B. Martin, ''Determinants of the mechanical properties of bones,'' J. Biomech. **24**, 79–88 (1991).
[13] M. L. Bouxsein, B. S. Coan, and S. C. Lee, ''Prediction of the strength of the elderly proximal femur by bone mineral density and quantitative ultrasound measurements of the heel and tibia,'' Bone (N.Y.) **25**, 49–54 (1999).

[14] I. A. Viktorov, *Rayleigh and Lamb Waves, Physical Theory and Applications* (Plenum, New York, 1967).
[15] A. H. Nayfeh, *Wave Propagation in Layered Anisotropic Media with Applications to Composites* (Elsevier, Amsterdam, 1995).
[16] H. Lamb, ''On waves in an elastic plate,'' Proc. R. Soc. London, Ser. A **93**, 293–312 (1917).
[17] C. Njeh, D. Hans, C. Wu, E. Kantorovich, M. Sister, T. Fuerst, and H. K. Genant, ''An *in vitro* investigation of the dependence on sample thickness of the speed of sound along the specimen,'' J. Med. Eng. Phys. **21**, 651–659 (1999).
[18] H. Sievanen, S. Cheng, S. Ollikainen, and K. Uusi–Rasi, ''Ultrasound velocity and cortical bone characteristics *in vivo*,'' Osteoporosis Int. **12**, 399–405 (2001).
[19] S. Prevrhal, T. Fuerst, B. Fan, C. Njeh, D. Hans, M. Uffmann, S. Srivastav, and H. K. Genant, ''Quantitative ultrasound of the tibia depends on both cortical density and thickness,'' Osteoporosis Int. **12**, 28–34 (2001).
[20] K. A. Wear, ''Autocorrelation and cepstral methods for measurement of tibial cortical thickness,'' IEEE Trans. Ultrason. Ferroelectr. Freq. Control **50**, 655–660 (2003).
[21] S. S. Mehta and P. P. Antich, ''Measurement of shear-wave velocity byultrasound critical-angle reflectometry (ucr),'' Ultrasound Med. Biol. **23**, 1123–1126 (1997).
[22] D. C. Worlton, ''Ultrasonic testing with Lamb waves,'' Nondestr. Test. (Chicago) **15**, 218–222 (1957).
[23] J. Saulgozis, I. Pontaga, G. Lowet, and G. Van der Perre, ''The effect of fracture and fracture fixation on ultrasonic velocity and attenuation,'' Physiol. Meas **17**, 201–211 (1996).
[24] J. L. Cunningham, J. N. Fordham, T. A. Hewitt, and C. A. Speed, ''Ultrasound velocity and attenuation at different skeletal sites compared with bone mineral density measured using dual x-ray absorptiometry,'' Br. J. Radiol. **69**, 25–32 (1996).
[25] S. Lees, P. F. Clearly, and E. F. Gariepy, ''Distribution of sonic plesiovelocity in a compact bone sample,'' J. Acoust. Soc. Am. **66**, 641–647 (1979).
[26] R. Lakes, H. S. Yoon, and J. L. Katz, ''Ultrasonic wave propagation and attenuation in wet bone,'' J. Biomed. Eng. **8**, 143–148 (1986).
[27] R. Barkmann, E. Kantorovich, C. Singal, D. Hans, H. K. Genant, M. Heller, and C. C. Gluer, ''A new method for quantitative ultrasound measurements at multiple skeletal sites,'' J. Clin. Densitom. **3**, 1–7 (2000).
[28] K. F. Graff, *Wave Motion in Elastic Solids* (Dover, New York, 1991).

The interaction of outgoing echolocation pulses and echoes in the false killer whale's auditory system: Evoked-potential study

Alexander Ya. Supin[a)]
Institute of Ecology and Evolution of the Russian Academy of Sciences, 33 Leninsky Prospect, 119071 Moscow, Russia

Paul E. Nachtigall,[b)] Whitlow W. L. Au,[c)] and Marlee Breese
Marine Mammal Research Program, Hawaii Institute of Marine Biology, University of Hawaii, Kaneohe, Hawaii 96744-1106

(Received 27 October 2003; revised 25 February 2004; accepted 26 February 2004)

Brain auditory evoked potentials (AEP) associated with echolocation were recorded in a false killer whale *Pseudorca crassidens* trained to accept suction-cup EEG electrodes and to detect targets by echolocation. AEP collection was triggered by echolocation pulses transmitted by the animal. The target was a hollow aluminum cylinder of strength of −22 dB at a distance from 1 to 8 m. Each AEP record was obtained by averaging more than 1000 individual records. All the records contained two AEP sets: the first one of a constant latency and a second one with a delay proportional to the distance. The timing of these two AEP sets was interpreted as responses to the transmitted echolocation pulse and echo, respectively. The echo-related AEP, although slightly smaller, was comparable to the outgoing click-related AEP in amplitude, even though at a target distance as far as 8 m the echo intensity was as low as −64 dB relative to the transmitted pulse in front of the head. The amplitude of the echo-related AEP was almost independent of distance, even though variation of target distance from 1 to 8 m influenced the echo intensity by as much as 36 dB. © *2004 Acoustical Society of America.* [DOI: 10.1121/1.1707088]

PACS numbers: 43.80.Lb [FD] Pages: 3218–3225

I. INTRODUCTION

Although a few decades have passed since echolocation was discovered in toothed whales and dolphins, many mechanisms of the sonar of odontocetes remain unexplored. One of the unsolved problems is the interaction between the transmitted acoustic pulse and returning echo in the dolphin's auditory system. When an animal echolocates, it hears not only the echo but also its own outgoing acoustic pulse. When a target is small and distant, the echo is many times weaker than the outgoing pulse. So, the echolocating animal must hear a weak echo signal shortly after the intense outgoing sound. Due to high sound velocity in water, the delay between the transmitted and echo sounds may be very short, down to a few milliseconds. Normally, in these conditions, one would expect a strong forward masking of the echo but successful performance of the sonar of odontocetes indicates that this sort of masking is absent.

Some mechanisms serving to avoid or diminish the forward-masking effects in the odontocete's auditory system are already known. In particular, to be able to distinguish the outgoing clicks from the echo, their auditory system has a very high temporal resolution as demonstrated by a variety of psychophysical (Au, 1993; Nachtigall *et al.*, 2000; Helweg *et al.*, 2003) and physiological (evoked response) data (Supin and Popov, 1995b; Dolphin *et al.*, 1995; Popov and Supin, 1997; Supin *et al.*, 2001). Nevertheless, in passive acoustic stimulation experiments, when two acoustic pulses were presented with the first pulse of a much higher intensity than the second one, deep suppression of the second evoked response was observed during a few, to a few tens, of milliseconds (Popov and Supin, 1990; Supin and Popov, 1995a; Popov *et al.*, 2001). But, it is not known yet whether similar masking takes place during natural echolocation. Nothing is currently known about how loudly a dolphin hears its outgoing echolocation click and the corresponding echo, and how much outgoing clicks mask the echoes at various click intensities, target strengths, and distances.

We approached the problem by recording the brain auditory evoked potentials (AEP) during natural echolocation in dolphins. AEPs show whether or not the brain responds to a sound; thus, recording AEPs during echolocation shows whether or not the brain responds to both the emitted click and the echo sound. An attempt to record AEP in dolphins made by Bullock and Ridgway (1972) with the use of implanted electrodes has shown that voluntary click emission by a dolphin as well as external stimulation (''artificial echo'') resulted in AEPs. However, quantitative investigation of outgoing pulse-related and echo-related AEPs was not achievable. A recent pilot study in a false killer whale (Supin *et al.*, 2003) has shown that this task is feasible with the use of noninvasive recording technique: during echolocation, a set of AEPs was recorded containing responses to both the outgoing sound pulse and the echo. In the present study, we investigated how AEPs to the outgoing click and echo de-

[a)]Electronic mail: alex_supin@sevin.ru
[b)]Electronic mail: nachtiga@hawaii.edu
[c)]Electronic mail: wau@hawaii.edu

 0001-4966/2004/115(6)/3218/8/$20.00 © 2004 Acoustical Society of America

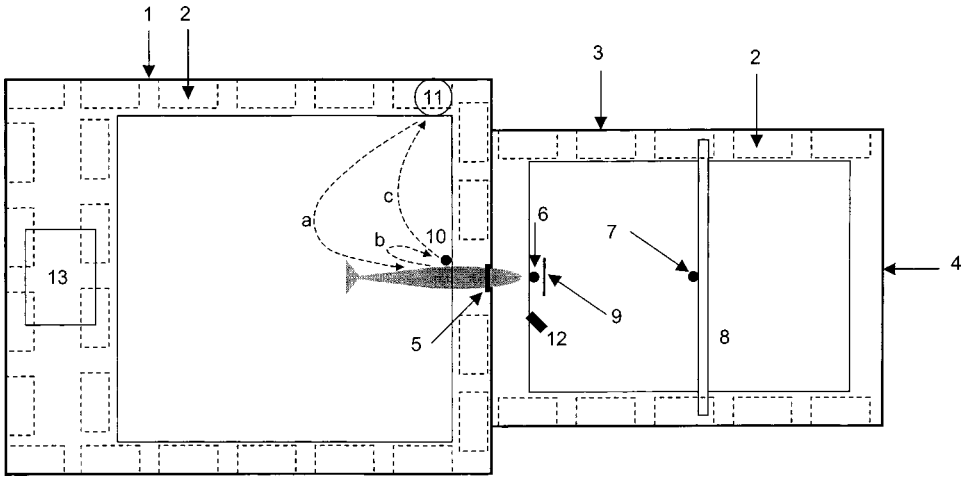

FIG. 1. Experimental facilities and design (top view). Explanation of pos. 1 to 13 and a to c—in the text.

pend on the distance to a target. Variation of the distance results in simultaneous variation of the transmitted-to-echo level ratio and echo delay; thus, we hoped to find how the forward-masking effect, if it exists, depends on combinations of these two parameters.

II. MATERIALS AND METHODS

A. Subject and experimental conditions

The experiments were carried out in facilities of the Hawaii Institute of Marine Biology, Marine Mammal Research Program. The subject was a false killer whale *Pseudorca crassidens*, an approximately 20-year-old female kept in a wire-net enclosure in Kaneohe Bay, Hawaii. The animal was trained to accept soft latex suction cups containing human EEG electrodes for evoked-potential recording and to ensonify and recognize targets by echolocation and to report the target's presence or absence using a go/no-go reporting paradigm.

Experimental facilities were designed as follows (Fig. 1). The experimental enclosure was constructed of a floating pen frame (1) 8×10 m in size, supported by floats (2) and bearing an enclosing net. This enclosure (the animal section) linked to a target section—another floating frame (3) 6×8 m in size which served only to mount targets and did not bear net. The supporting floats were only under the side parts of the target-section frame, so the front part (4) of this section (3) was free of any sound-reflecting objects in water. In the net divider separating these two sections, there was an opening bounded by a hoop (5), 55 cm in diameter, that served as a hoop station for the animal. In front of the hoop, a B&K 8103 hydrophone (6) was mounted to record sounds emitted by the animal during its positioning in the hoop station. A target (7) was mounted on a beam (8) fastened above the water surface across the target-section frame. The beam could be fixed at various distances from the animal. The target was hung from a thin monofilament line and could be pulled up out of water and lowered down into water. The hoop station (5), the hydrophone (6), and the lowered target (7) were in a longitudinal straight line at a depth of 80 cm. Behind the hydrophone (6) there was a movable baffle (9). When pulled up, this baffle screened the target section from the animal positioned in the hoop station; when lowered down, it opened the space in front of the animal. Near the hoop station, a response ball (10) was mounted above the water surface serving as a target-present indicator response. The trainer kept a position (11) to give instructions to the animal and to reward it for correct responses. Positioning of the animal in the station hoop was monitored through an underwater video camera (12). The electronic equipment and the operator were housed in an instrument enclosure (13).

B. Experimental procedure

Each session included both target-present and target-absent trials, assuring that the animal was indeed echolocating the target. The experimental procedure was as follows.

(i) Each session began with the trainer attaching suction-cup electrodes for AEP recording (see below for detail). (ii) The animal was sent to a hoop station (trace *a* in Fig. 1); the animal swam into the hoop in such a position that the hoop was at the level of the pectoral fins. During the animal positioning, the baffle [(9) in Fig. 1] was in the raised position that screened the target from the animal. The target was either lowered into the water (target-present trial) or removed from the water (target-absent trial) in advance. (iii). When the animal took the proper position in the hoop station, the baffle was lowered, thus allowing the animal to inspect the space by echolocation. The animal immediately emitted a train of echolocating clicks, as a rule 20 to 50 clicks in a train. (iv) When the target was presented, the animal was required to signal its detection by leaving the hoop and touching a signal ball (trace *b* in Fig. 1), then coming to the trainer for the fish reward (trace *c*). In no-target trials, the animal was required to wait until it was signaled to leave the hoop (trace *b* was absent) and come for the fish reward (trace *c*).

Each session consisted of 30 trials, 20 target-present and 10 target-absent, randomly alternated. In target-present trials, the AEP-acquisition system (see below) was turned on as soon as the baffle was lowered down, and it was kept on until the end of the echolocation click train. Thus, AEPs triggered by echolocation clicks were collected. In target-absent trials, AEPs were not collected because the animal emitted only a few clicks to make its decision; therefore, it was not possible to collect satisfactory AEP records. The purpose of target-

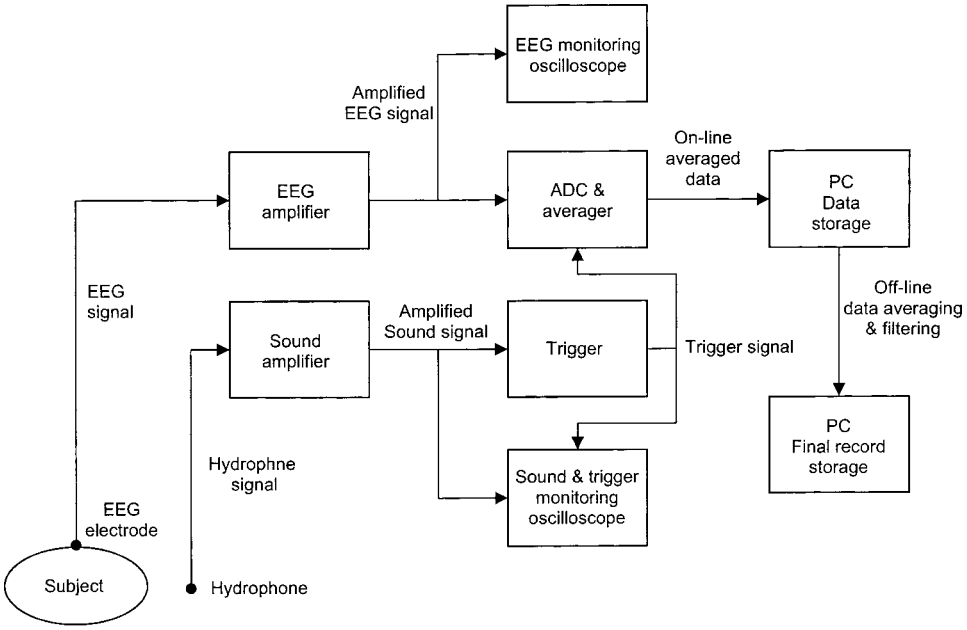

FIG. 2. Data acquisition equipment diagram. Explanation of all positions in the text.

absent trials was primarily to maintain correct echolocation activity reporting target presence or absence.

C. Equipment and AEP recording technique

To record AEP evoked by outgoing locating clicks and echoes, equipment was designed as shown in Fig. 2. Brain potentials were picked up from the *subject* (see the designations in Fig. 2) by *EEG electrodes* which were gold-plated disks 10 mm in diameter mounted within latex suction cups 60 mm in diameter. A drop of EEG gel under the disk served for lower impedance. The suction cups served both to fix the electrodes at the body surface and to insulate the near-electrode area from surrounding electric-conductive sea water. The active electrode was fixed at the dorsal head surface, at the midline, 5–7 cm behind the blowhole. This position was shown to be the best to record a kind of AEP, namely the auditory brainstem responses (ABR) in a number of dolphin species (Supin *et al.*, 2001). The other (reference) electrode was fixed at the animal's back. Brain potentials were led by shielded cables to a balanced *EEG amplifier* and amplified by 5×10^4 within a frequency range from 200 to 5000 Hz. The amplified signal was monitored by an *EEG monitoring oscilloscope* Tektronix TDS-2001 and entered an analog-to-digital converter (*ADC*) and coherent-averaging unit (*averager*) integrated in a custom-made ADC-averaging instrument. The latter served to extract low-amplitude AEPs from the background noise.

A distinctive feature of the evoked-response acquisition in the present study was that to extract a response from noise, the coherent averaging was triggered not by external stimuli controlled by the experimenter, but by sound clicks emitted by the animal. For that, sounds were picked up by a B&K 8103 *hydrophone* positioned in front of the animal's head. The hydrophone signal was amplified by 40 dB by a custom-made *sound amplifier* (frequency band 1–200 kHz). The amplified sound pulses were monitored by a digital-storage oscilloscope (*sound and trigger monitoring oscilloscope*) and entered a *trigger* device (integrated with the sound amplifier in a custom-made instrument) that produced at its output a standard pulse each time when a sound pulse appeared at its input. These standard triggering pulses served to trigger the evoked-response averager; the triggering pulses were monitored at the same oscilloscope as the sound pulses. After each click, a 15- to 17.5-ms-long temporal window of evoked-potential recording was picked up; all the individual records within the trial were averaged. The on-line averaged AEP records were stored in PC memory (*PC data storage*).

The number of on-line averaged individual records was not constant; it varied from trial to trial depending on the number of triggering clicks picked up. As a rule, the number of picked-up clicks (from 10 to 30) was not sufficient to achieve good extraction of AEPs from noise. Therefore, to obtain AEP records of good signal-to-noise ratio, all records obtained under similar conditions (one and the same distance to the target) were then averaged off-line. The off-line averaging was performed taking into account the number of individual records averaged in each on-line records, that is, the ordinates of the final record were computed as

$$y(t)=\frac{\Sigma\, y_i(t)n_i}{\Sigma\, n_i},$$

where $y(t)$ is the ordinate of the final record at an instant t, $y_i(t)$ is the ordinate of the ith on-line averaged record, and n_i is the number of individual records averaged on-line. The final AEP record was stored in PC memory (*PC final record storage*).

D. Target characteristics

The target was a hollow aluminum cylinder with an outer diameter of 38 mm and 25.5-mm inner diameter, 180 mm long, axis vertical. To obtain its frequency response and target strength, the target was ensonified by short pulses produced by excitation of a 60-mm spherical piezoceramic transducer with 10-μs rectangular pulses. Both the emitted

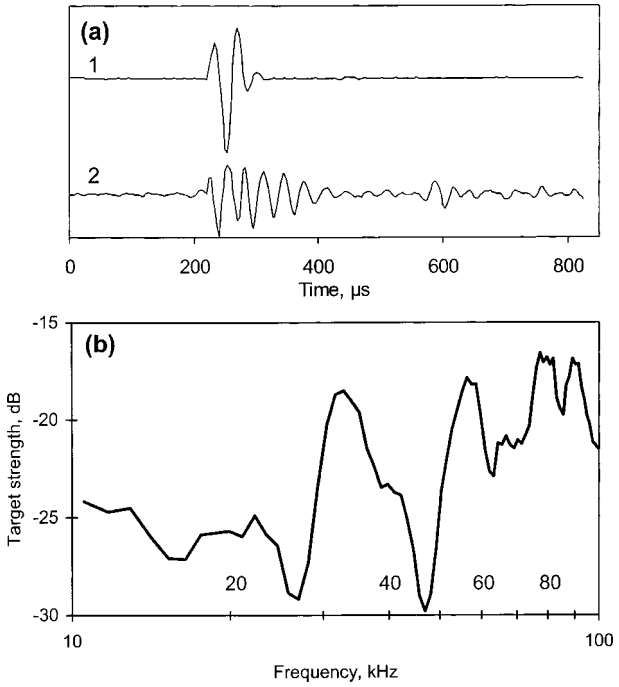

FIG. 3. Target frequency response. (a) 1—ensonifying pulse recorded near the target, 2—the echo recorded at a distance of 1 m from the target. In (2) gain is 15 dB higher than in (1). (b) The target frequency response obtained by subtraction of Fourier spectrum of ensonifying pulse from that of the echo.

pulse and echo [Fig. 3(a)] were recorded by a B&K 8103 hydrophone. The transducer and target were 1 m apart, and the receiving hydrophone was in the midpoint between them, that is 0.5 m from both the transducer and target. The picked-up emitted pulse and echo were digitized at a sampling rate of 300 kHz, and Fourier transformed. The target frequency response was computed by subtraction of the emitted-pulse dB spectrum (normalized to the level near the target) from the target-response dB spectrum (normalized to its level at a distance of 1 m from the target). The obtained frequency response of the target is shown in Fig. 3(b). The overall target strength TS was calculated as

$$\mathrm{TS} = I_t - I_e + 20\log(d_{tr}) - 20\log(d_{er}/d_{et}), \tag{1}$$

where I_t is the target echo intensity, I_e is the emitted pulse intensity (both in dB measure), d_{tr} is the target–receiver distance, d_{er} is the emitter–receiver distance, and d_{et} is the emitter–target distance. When $d_{tr} = d_{er} = 0.5\,\mathrm{m}$, Eq. (1) reduces to

$$\mathrm{TS} = I_t - I_e\,. \tag{2}$$

Evaluation of I_t and I_e both by peak-to-peak amplitudes of pulses presented in Fig. 3(a) and by integration of their spectra resulted in overall target strength of -22 dB; however, Fig. 3 shows that at certain highlight frequencies the target strength increased up to -17 dB.

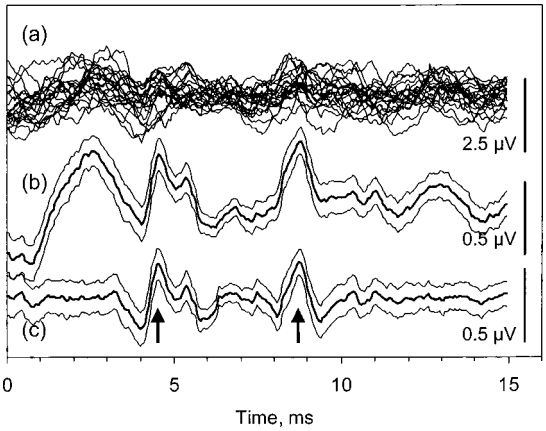

FIG. 4. Steps of echolocation-related AEP acquisition at a target distance of 3 m. (a) Overlapped on-line averaged records. (b) Off-line averaged record before digital filtering. (c) Off-line averaged record after high-pass digital filtering. In (b) and (c), solid line—mean (averaged) values; thin lines depict the standard error region. Arrows mark two AEP sets. Note different calibration for (a) and for (b) and (c). Active electrode negativity upward.

III. RESULTS AND DISCUSSION

A. Stages of ABR collection and ABR characteristics

Successive stages of collection of echolocation-related AEP are demonstrated in Fig. 4. In this experiment, the target was at a distance of 3 m from the reference point. Figure 4(a) presents superimposed 22 on-line averaged traces, each recorded in one trial. These data were collected during three experimental sessions, each containing 20 target-present trials, that is, 60 trials in total. However, trials strongly contaminated by artifacts of more than 1 μV peak-to-peak amplitude were rejected, so only 22 records were selected as presented in Fig. 4(a). Their averaging resulted in a final record presented in Fig. 4(b). The final record contained two clearly visible responses, one with the negative peak at 4.6 ms and the other at 8.8 ms after the triggering instant.

In spite of averaging of more than a thousand individual records in total, the obtained record in Fig. 4(b) was still markedly contaminated by slow-wave artifacts. In particular, the record began with a slow wave with no latency, obviously beginning *before* triggering the record. We suppose this slow wave was produced by some muscle activity associated with sound production. Late slow waves may be also associated in a certain (yet unknown) way with some movements accompanying echolocation activity. To reject these artifacts, high-pass digital filtering was used. We found that artifacts can be filtered out with a high-pass filter with a cutoff frequency of 400 Hz at the -3-dB level. The result of filtering is presented in Fig. 4(c). It revealed two definite responses in the record; their negative peaks were at 4.55 and 8.85 ms. The amplitude of the responses, although rather low (less than 0.5 μV), well exceeded the background noise amplitude.

To be assured that the high-pass filtering did not markedly distort the AEP waveform and amplitude, we examined how such filtering influenced the standard AEP provoked in the same subject by short, artificial sound clicks. This AEP is shown in Fig. 5(a) as recorded before (1) and after (2) the same high-pass filtering that was used to extract

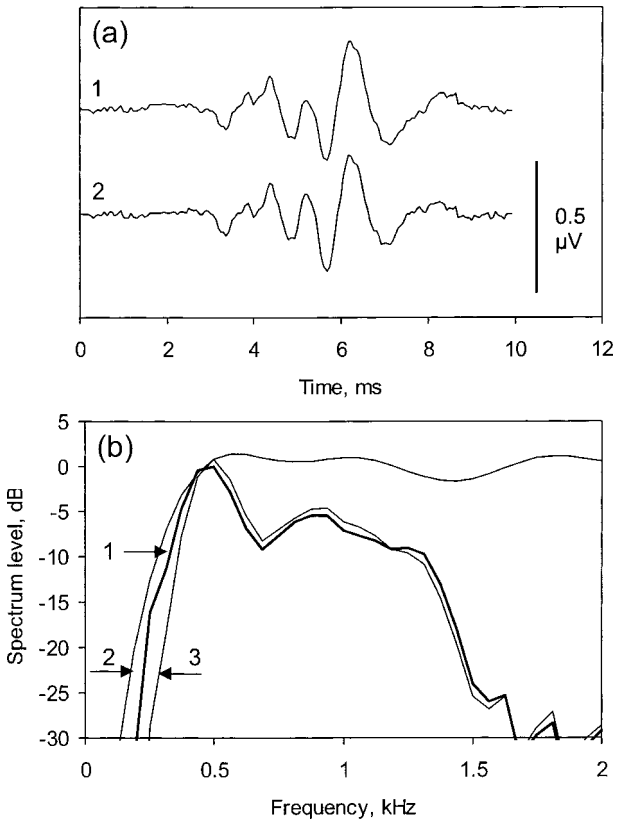

FIG. 5. Influence of high-pass digital filtering on the waveform and frequency spectrum of a standard ABR. (a) Time-domain presentation, 1—waveform before, 2—after digital filtering. (b) Frequency-domain presentation, 1 (solid line)—ABR spectrum before digital filtering, 2—filter form, 3—ABR spectrum after digital filtering.

echolocation-related responses; Fig. 5(b) shows the spectra of these records together with the filter frequency response. This AEP had qualitatively the same waveform as a typical auditory brainstem response (ABR) described in several other dolphin species (Supin *et al.*, 2001). Its amplitude was less than 0.5 μV, which is comparable with the amplitude of echolocation-related AEP. Presentations in both time (a) and frequency (b) domains show that high-pass filtering slightly changed the ABR waveform without appreciable change in its amplitude. We considered this degree of distortion as negligible.

B. AEP at various distances to the target

The final AEP records obtained at various distances to the target are presented in Fig. 6. A common feature of all of the records was the presence of two AEP sets. The first one consisted of several alternative positive and negative waves; the latency of this AEP complex was one and the same in all records, independent of the target position: the onset latency of 3.6–3.7 ms, the first positive peak at 4.1 ms, the next negative peak at 4.6 ms, etc. (all latencies are from the start of the record, i.e., from the instant of picking up the emitted locating pulse). The second AEP complex was of somewhat simpler waveform (mostly positive–negative–positive) and its latency directly depended on the distance to the target: the longer the distance, the longer the latency.

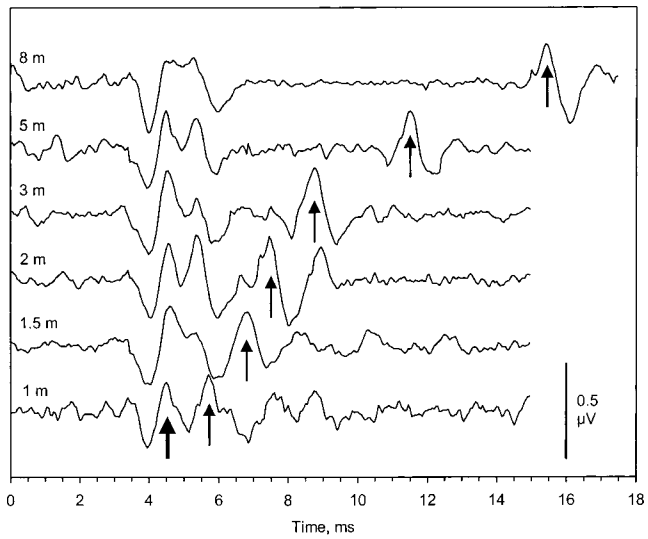

FIG. 6. Echolocation-related AEP at different target distances. The distance (1 to 8 m) is indicated near the records. Bold arrow marks the outgoing pulse-related AEP; thin arrows mark echo-related AEPs. Active electrode negativity upward.

These features of the two AEP complexes suggested that they were responses to the outgoing click and to the echo, respectively. To confirm this interpretation, we plotted the delay between two AEP complexes as a function of the distance to the target. The delay was measured as the time separation between the major negative peak of the first AEP complex (marked by the bold arrow in Fig. 6) and the negative peak of the second complex (marked by other arrows). The plot (Fig. 7) showed that all experimental points, except the only one at 1-m distance, fell exactly on a straight line. The slope of the regression line within a range of 1.5 to 8 m was 1.33 ± 0.01 ms/m. This ratio exactly corresponded to the two-way echo-delay dependence on distance that should be at a sound velocity of 1500 m/s. Thus, the second AEP complex can be interpreted as a response to the echo from the target. As to the point at 1-m distance, its deviation does not contradict this interpretation, since at this short delay the AEP waveform was distorted because of superimposition of the two AEP complexes; a result of this distortion may be a shift of the peak latency.

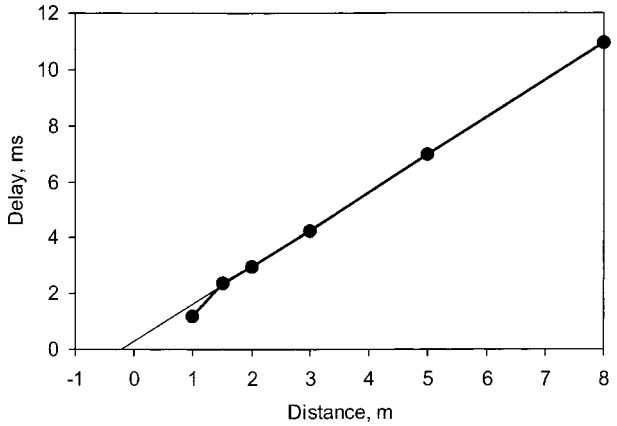

FIG. 7. Echo-related AEP delay relative to the outgoing pulse-related AEP as a function of target distance. Solid line with dots—experimental data, thin line—regression line (for a range of 1.5–8 m) extrapolated to zero delay.

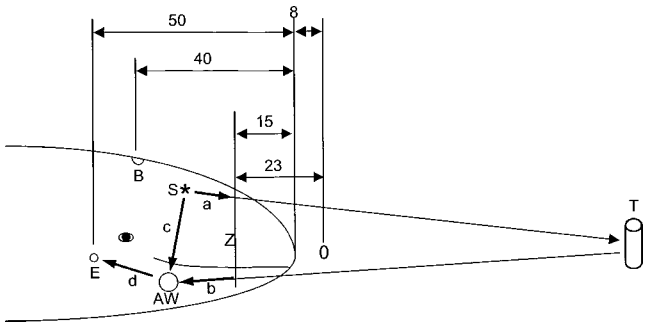

FIG. 8. Main dimensions of the animal's head and positions of key points. 0—zero point of the target distance scale, E—ear, B—blowhole, AW—lower-jaw acoustic window, Z—zero-delay level, S (marked by asterisk)—assumed position of the sound source, T—target. Arrows show supposed distance from the sound source to the zero-delay level (a), from this level to the acoustic window (b), from the sound source to the acoustic window (c), and from the acoustic window to the ear (d).

The straight regression line approximating experimental points in Fig. 7 (except the point at 1-m distance) reached the zero delay at a point of −0.23 m of the target–distance scale. Video monitoring of the animal's position in the hoop station showed that the zero point of the target–distance scale was 7–8 cm in front of the head tip (point 0 in Fig. 8); thus, the zero-delay distance (Z) is approximately 15 cm behind the head tip, that is, within the melon. The time of sound travel from the sound source to this plane (arrow *a* in Fig. 8) and back (arrow *b*) to a sound receiver (e.g., the acoustic window at the lower jaw, AW) must be equal to the time of transmitted sound travel from the sound source to the same receiver (arrow *c*; of course, actually the transmission way may not be as straight as shown in the diagram). Supposing that the sound source (S) is located in between of the blowhole and melon (Cranford *et al.*, 1996; Cranford, 2000), this agrees with the found position of the zero-delay point. This provides additional evidence that the two AEP complexes are evoked by direct spread from the sound source to the ears and by the echo, respectively.

Therefore, we designate these two AEP complexes as the outgoing click-related and echo-related AEP, respectively.

With this interpretation of the recorded AEPs, at least two of their features may be considered as remarkable.

(i) The echo-related AEP, although slightly less, was nevertheless comparable to the outgoing click-related AEP in amplitude.

(ii) The amplitude of the echo-related AEP was almost independent of distance, at least within the tested distance range from 1 to 8 m. Although there were some small differences between the records in the waveform and amplitude of echo-related AEPs, this difference was not systematic and looked more like random variation rather than a trend indicating dependence on distance.

IV. GENERAL DISCUSSION

A. The nature of the echolocation-related AEP

The position of recording electrodes used in the present study was appropriate to pick up a kind of AEP known as the auditory brainstem response (ABR). It was done since, among a variety of AEP types described previously in dolphins (Supin *et al.*, 2001), ABRs are the easiest to record noninvasively from the head surface. They are very consistent and have a rather high amplitude. Short sound clicks similar to the echolocation sounds of dolphins are appropriate stimuli to provoke ABRs.

Therefore, there are good reasons to believe that recorded echolocation-related AEPs, both outgoing pulse-related and echo-related, are ABRs. With corrections for the expected acoustical delays of 0.67 ms/m, their onset latency may be assessed as about 3.5 ms. This is the same latency as that of typical ABR (again, with correction for the acoustic delay) recorded with standard extrinsic auditory stimulation (Fig. 5). Echolocation-related AEP consisted of waves of the same order of duration (less than 1 ms) as the standard ABR in odontocetes, in particular in the false killer whale.

Nevertheless, the overall waveform of echolocation-related AEPs differed to a certain extent from the waveform of standard ABRs (compare Figs. 4 and 5). To a greater extent it was characteristic of the echo-related AEP: they were of simpler waveform that the standard ABRs. This difference may be explained, on the one hand, by lower intensity of echoes as compared to the used extrinsic stimuli. On the other hand, the waveform of echo-related AEPs may be smoothed because of small variations of the echo delays from trial to trial due to some inconstancy of the animal position and other factors influencing the echo delay. Regardless of the cause, among all the AEP types described in dolphins, ABRs feature the largest similarity to the echolocation-related AEPs described herein.

B. Comparison of outgoing pulse-related and echo-related AEP amplitudes

The data presented above have shown that the echo-related AEP, although slightly less, was nevertheless comparable to that of the outgoing click-related AEP in amplitude. This feature seems remarkable for the following reasons. Let us compare the intensity of the echo with intensity of the outgoing click right in front of the animal's head, say at an arbitrarily taken point at a distance of 0.5 m from the sound source. Being expressed in dB measure, this difference δI is

$$\delta I = 20\log(0.5/d) + \mathrm{TS} + 20\log(1/d),$$

where d is the distance to the target and TS is the target strength. With $d = 8$ m and TS $= -22$ dB, $\delta I = -64$ dB. With this huge difference in intensities, one might expect a large difference in amplitudes of the outgoing click-related and echo-related responses, in particular, because of deep masking of the echo-related response by the preceding strong outgoing sound pulse. However, this was not the case.

The absence of deep masking of the echo-related response can at least partially be explained by the high temporal resolution of the dolphin's auditory system, which was noted above. The integration time, or equivalent rectangular duration of the temporal transfer function in the dolphin's auditory system, was estimated as around 300 μs in both

psychophysical (Moore *et al.*, 1984; Au *et al.*, 1988; Au, 1990; Dubrovskiy, 1990) and evoked-potential (Supin and Popov, 1995a, b; Popov and Supin, 1997) measurements. During conditions of double-click stimulation (which may be considered as a model of an outgoing click and echo), complete recovery of the second response from masking by the first click required a time longer than 300 μs because of a rather long ''tail'' of the integration transfer function. Nevertheless, the recovery time is short enough: ABR to the second click of the pair recovered from masking during a few hundred μs to a few ms (Popov and Supin, 1990; Supin and Popov, 1995b). Even when intensities of two clicks in a pair differed by as much as 60 dB, the recovery appeared as soon as 20 ms after the strong preceding click (Popov and Supin, 1990). This high temporal resolution helps the animal to perceive a weak echo shortly after the outgoing sound pulse.

On the other hand, there is a reason to assume that the dolphin hears the outgoing click with significant muffling. Indeed, double-click experiments have shown that at a difference of 40 dB between the two clicks, the second ABR recovered at a delay of about 10 ms; at a difference of 60 dB and a delay of 10 ms, the second ABR was suppressed almost completely (Popov and Supin, 1990). In the echolocation experiments presented here, the echo response was released from masking at approximately the same delay (11 ms at the target distance of 8 m) when the emitted click *outside and near the head* exceeded the echo by as much as by 64 dB. Therefore, it is quite probable that the emitted sound reached the dolphin's ears at a much lower intensity than it was outside the head. If so, the dolphin's head is bound to contain some structures which provide lower sound power inside the head as compared to outside the head. First, the role of the skull and melon as concentrators of transmitted sounds in front of the head should be mentioned (Au, 1993) along with the presence of sound-muffling structures inside the head; in particular, air-filled peribullar and pterygoid sinuses may play this role. It may be noted that investigations of binaural hearing in dolphins (Popov and Supin, 1992; Supin and Popov, 1993) have shown interaural intensity difference as large as 20 dB; it means that some head tissues are capable of shadowing sound spread across the head as deeply as up to 20 dB. Maybe the same or similar structures shadow the dolphin's ears from its sound-emitting organs.

C. Independence of echo-related AEP amplitude of the distance to the target

As shown above, the amplitude of the echo-related AEP was almost independent of distance, at least within the tested distance range (up to 8 m). Taking into consideration that the echo intensity decreases as much as by 36 dB when the distance to the target changes from 1 to 8 m, this phenomenon is of special interest.

An explanation of this phenomenon may be suggested as follows. It has been shown (Popov and Supin, 1990; Supin *et al.*, 2001) that ABR recovery in double-click stimulation experiments has a remarkable feature: when the intensity difference between two clicks increased, the recovery time increased also (which is not surprising by itself), and the rate of this increase approached 10 times per 40-dB intensity-difference increase. Note that when the distance to a small target varies, the ratio between the echo delay and echo intensity is all the same: 40 dB per 10-times distance (and delay) change. This coincidence allowed the suggestion that a dolphin may perceive echoes almost invariant of the distance to a target. Indeed, when the distance, for example, increases, the echo intensity decreases, but the echo-response releases from masking in a greater extent due to a longer delay. These two processes may compensate one another because of similar intensity-to-distance and recovery-to-delay ratios. The data presented herein have confirmed this prediction by direct echolocation experiments.

ACKNOWLEDGMENTS

The study was supported by the Office of Naval Research, Award N0014-98-1-687 from Robert Gisiner (USA) and the Russian Ministry of Science and Technology, Award NSh.2152.2003.4 (Russia). Funding is gratefully acknowledged.

Au, W. W. L. (**1990**). ''Target detection in noise by echolocating dolphins,'' in *Sensory Abilities of Cetaceans. Laboratory and Field Evidence*, edited by J. A. Thomas and R. A. Kastelein (Plenum, New York), pp. 203–216.

Au, W. W. L. (**1993**). *The Sonar of Dolphins* (Springer, New York).

Au, W. W. L., Moore, P. W. B., and Pawloski, D. A. (**1988**). ''Detection of complex echoes in noise by an echolocating dolphin,'' J. Acoust. Soc. Am. **83**, 662–668.

Bullock, T. H., and Ridgway, S. H. (**1972**). ''Evoked potentials in the central auditory system of alert porpoises to their own and artificial sounds,'' J. Neurobiol. **3**, 79–99.

Cranford, T. W. (**2000**). ''In search of impulse sound sources in odontocetes,'' in *Hearing by Whales and Dolphins*, edited by W. W. L. Au, A. N. Popper, and R. F. Fay (Springer, New York), pp. 109–155.

Cranford, T. W., Amundin, M., and Norris, K. S. (**1996**). ''Functional morphology and homology in the odontocete nasal complex: Implications for sound generation,'' J. Morphol. **228**, 223–285.

Dolphin, W. F., Au, W. W. L., and Nachtigall, P. (**1995**). ''Modulation transfer function to low-frequency carriers in three species of cetaceans,'' J. Comp. Physiol., A **177**, 235–245.

Dubrovskiy, N. A. (**1990**). ''On the two auditory systems in dolphins,'' in *Sensory Abilities of Cetaceans. Laboratory and Field Evidence*, edited by J. A. Thomas and R. A. Kastelein (Plenum, New York), pp. 233–254.

Helweg, D. A., Moore, P. W. B., Dankewicz, L. A., Zafran, J. M., and Brill, R. L. (**2003**). ''Discrimination of complex synthetic echoes by an echolocating bottlenose dolphin,'' J. Acoust. Soc. Am. **113**, 1138–1144.

Moore, P. W. B., Hall, R. W., Friedl, W. A., and Nachtigall, P. E. (**1984**). ''The critical interval in dolphin echolocation: What is it?,'' J. Acoust. Soc. Am. **76**, 314–317.

Nachtigall, P. E., Lemonds, D. W., and Roitblat, H. L. (**2000**). ''Psychoacoustic Studies of Whale and Dolphin Hearing,'' in *Hearing By Whales*, edited by W. W. L. Au, A. N. Popper, and R. J. Fay (Springer, New York), pp. 330–364.

Popov, V. V., and Supin, A. Ya. (**1990**). ''Auditory brain stem responses in characterization of dolphin hearing,'' J. Comp. Physiol., A **166**, 385–393.

Popov, V. V., and Supin, A. Ya. (**1992**). ''Electrophysiological study of the interaural intensity difference and interaural time-delay in dolphins,'' in *Marine Mammal Sensory Systems*, edited by J. A. Thomas, R. A. Kastelein, and A. Ya. Supin (Plenum, New York), pp. 257–267.

Popov, V. V., and Supin, A. Ya. (**1997**). ''Detection of temporal gaps in noise in dolphins: Evoked-potential study,'' J. Acoust. Soc. Am. **102**, 1169–1176.

Popov, V. V., Supin, A. Ya., and Klishin, V. O. (**2001**). ''ABR recovery in the dolphin as revealed by double sound pulses of different frequencies,'' J. Acoust. Soc. Am. **110**, 2227–2233.

Supin, A. Ya., Nachtigall, P. E., Pawloski, J., and Au, W. W. L. (**2003**). ''Evoked potential recording during echolocation in a false killer whale *Pseudorca crassidens*,'' J. Acoust. Soc. Am. **113**, 2408–2411.
Supin, A. Ya., and Popov, V. V. (**1993**). ''Direction-dependent spectral sensitivity and interaural spectral difference in a dolphin: Evoked potential study,'' J. Acoust. Soc. Am. **93**, 3490–3495.
Supin, A. Ya., and Popov, V. V. (**1995a**). ''Envelope-following response and modulation transfer function in the dolphin's auditory system,'' Hear. Res. **92**, 38–46.
Supin, A. Ya., and Popov, V. V. (**1995b**). ''Temporal resolution in the dolphin's auditory system revealed by double-click evoked potential study,'' J. Acoust. Soc. Am. **97**, 2586–2593.
Supin, A. Ya., Popov, V. V., and Mass, A. M. (**2001**). *The Sensory Physiology of Aquatic Mammals* (Kluwer, Boston).

Defining optimal axial and lateral resolution for estimating scatterer properties from volumes using ultrasound backscatter

Michael L. Oelze[a] and William D. O'Brien, Jr.
Bioacoustics Research Laboratory, Department of Electrical and Computer Engineering, University of Illinois, 405 North Mathews, Urbana, Illinois 61801

(Received 25 June 2003; revised 6 March 2004; accepted 19 March 2004)

The rf signals used to construct conventional ultrasound B-mode images contain frequency-dependent information that can be examined through the backscattered power spectrum. Typically, the backscattered power spectrum is calculated from a region of interest (ROI) within some larger volume. The dimensions of the ROI are defined axially by the spatial length corresponding to the time gate and laterally by the number of scan lines included in the ROI. Averaging the backscattered power spectra from several independent scan lines can reduce the presence of noise caused by electronics and by the random scatterer spacings, but also decreases the lateral resolution of the interrogation region. Furthermore, larger axial gate lengths can be used to reduce the effects of noise and improve the precision and accuracy of scatterer property estimates but also decreases the axial resolution. A trade-off exists between the size of the ROI (the number of scan lines used, the separation distance between each scan line, the axial gate length) and the accuracy and precision of scatterer property estimates. A series of simulations and measurements from physical phantoms were employed to examine these trade-offs. The simulations and phantom measurements indicated the optimal lateral and axial sizes of the ROI, where estimate accuracy and precision were better than 10% and 5%, respectively, occurred at 4 to 5 beamwidths laterally and 15 to 20 spatial pulse lengths axially. © *2004 Acoustical Society of America.*
[DOI: 10.1121/1.1739484]

PACS numbers: 43.80.Qf, 43.80.Vj [FD] Pages: 3226–3234

I. INTRODUCTION

A conventional B-mode image is made up of several parallel or consecutively spaced axial rf time signals. Each rf time signal is a series of echoes backscattered from structures in the interrogated medium. In a conventional B-mode image, the frequency-dependent information in an rf time signal is not utilized. Instead, conventional B-mode images of tissues using ultrasound are made by generating a gray-scale image using the envelope-detected rf signal backscattered from the tissues.

The frequency-dependent information in an rf time signal may be related to the tissue microstructure (structures less than the ultrasound wavelength).[1–13] Parametrizing the frequency-dependent information of backscattered signals from tissues allows the characterization and differentiation of tissues. Several researchers have used quantitative ultrasound (QUS) or parameter information about the shape of the spectrum of scattered ultrasound to classify tissue microstructure and identify disease.[2,9,11–16] Other researchers have been able to estimate the size, shape, and internal make-up of scatterers in tissues from models.[3,5–7,9–11,16]

Scattering from tissues is often modeled using the Born approximation (weak scattering with no multiple scattering).[17] Regions of interest (ROIs) are chosen from interrogated volumes, and the spectral properties of the rf signal corresponding to the ROIs are quantified and related to models of tissue scattering. Tissue scattering often represents a stochastic process that gives rise to incoherent and coherent spectra.[17–19] The incoherent spectrum includes information about the size, shape, density, and mechanical properties of the scatterers.[19] If a model accurately describes the incoherent spectrum, then estimates of scatterer properties can be made. The coherent part of the spectrum is also a function of the individual scatterer properties but is strongly dependent on the spatial variation of the scatterers.[19] If the scatterers are not randomly spaced in the volume, than resonance peaks would appear in the coherent spectrum corresponding to the spacings of the scatterers.[20] For random scattering, the coherent spectrum appears as noise (called spatial variation noise).

The spatial variation noise can adversely affect the ability to estimate the shape and magnitude of the incoherent spectrum.[21] The spatial variation noise can be reduced by two means. If the gated length of the corresponding rf time signal is sufficiently long, the spatial variation noise is reduced.[18] Second, to reduce the influence of the spatial variation noise, the backscattered spectra from several independent rt time samples (denoted herein as A-lines) are spatially averaged.[5,6,17,18,21] If the interrogated scattering volume is homogeneous (uniform distribution of random, nearly identical scatterers), then samples throughout the volume can be measured and averaged.

If the interrogated volume has regions with different scattering statistics, smaller ROIs within the interrogated volume are needed to distinguish and characterize the different regions within the interrogated volume. Smaller ROIs are chosen within the interrogated volume to resolve changing

[a]Electronic mail: oelze@brl.uiuc.edu

 0001-4966/2004/115(6)/3226/9/$20.00 © 2004 Acoustical Society of America

structure within the interrogated volume (assuming that the scatterers are much smaller than the sizes of the ROIs). The ROIs are assumed to have relative uniform scattering within the interrogated volume composed of possible nonuniform scattering.

The smaller the ROIs, the better the approximation that structure within an individual ROI is uniform. However, as the ROI becomes smaller, the number of independent samples that can be measured decreases and the length of the gate decreases. The volume interrogated by a single scan line depends on the beamwidth of the transducer and the gated length along the transducer axis.

Several studies have examined the effects of the axial gate length and windowing function on the ability to make scatterer property estimates. One study indicated that when the gated length was not large (five times the wavelength at the center frequency) the measured backscattered power spectrum did not fit the theoretical power spectrum well.[22] As the size of the gated length increased, the measured backscattered power spectrum fit the theoretical power spectrum better. Further, a better fit to the theoretical power spectrum was revealed at a gate length of 12.5 times the wavelength at the center frequency when a Hanning window was used over a rectangular window. Other studies indicated that if the length of the axial gate was larger than the pulse length, the contribution of the spatial variation noise was reduced.[18,23] As the axial gate length was reduced to the length of the pulse, it was noted that truncation errors occurred and that the length of the pulse needed to be incorporated into spectral estimates.[24] Attempts were made with limited success to correct for the small gate truncation errors using a deconvolution method.[25]

In another study, axial resolution for ROIs was optimized at a length of 10 times the wavelength of interrogation.[15] In that study, a line was fit to the backscattered power spectrum versus gated axial length using a Hanning window. The 10-wavelength ROI was chosen at the point where the slope estimates from the best-fit line first converged. The study examined the accuracy of slope estimates versus axial length but did not consider the precision in making estimates versus axial length. A similar study examined the precision limits of estimating the frequency dependence of the backscattered power spectrum versus gate length.[26] The study showed that as the gate length increased the precision of estimates improved. Further, the study did not take into account the effects of the lateral ROI size on the accuracy and precision of estimates.

The lateral ROI length and the A-line separation are other important considerations to the accuracy and precision of estimates. A rule of thumb has been that the averaged backscattered spectrum should consist of a number of A-lines sampled at a half beamwidth apart.[21,27] Some researchers have suggested spatially averaging 25 A-lines for sufficient sampling and noise reduction, while others have suggested 5–10 A-lines.[17,18] The half beamwidth center-to-center distance between A-lines is conjectured to give nearly independent samples and further reduce spatial variation noise.[21] However, no definitive rules for determining the optimal lateral ROI length and A-line center-to-center distance have been indicated.

One study examined the precision and accuracy of spectral estimation with both axial and lateral ROI size.[28] The study compared theoretical predictions of precision with experimental measurements. The study indicated that longer axial and lateral lengths gave better precision and accuracy. However, in order to determine the size of an ROI yielding a particular accuracy and precision, both the axial and lateral ROI lengths must be examined at the same time.

In the study reported herein, a technique is developed to quantify the spatial variation noise and its decrease after spatially averaging. The axial and lateral ROI length (assuming that the scatterers are much smaller than the ROI size) for making scatterer property estimates are examined to determine the optimal ROI resolution. Further, the A-line center-to-center distance is examined to determine the optimal A-line separation distance for estimating scattering properties from weakly scattering volumes. Section II describes the theory behind backscattering from weakly scattering volumes and quantification of spatial variation noise. Section III details the simulation construction and physical phantom measurements with randomly spaced glass beads. Section IV presents the results of the simulations and phantom measurements for reducing the spatial variation noise and optimizing ROI resolution. The final section (Sec. V) gives some conclusions about the study.

II. THEORY

Consider a signal of the form, $g_L(t)$, representing a backscattered time sequence from a gated length, L, in a scattering medium. The function, $g_L(t)$, is the convolution of an impulse response $h(t)$ that incorporates the electromechanical characteristics of the transducer and diffraction, and a scattering function, $r_L(t)$, from randomly spaced, nearly identical particles[20,27]

$$g_L(t) = h(t) * r_L(t). \tag{1}$$

The Fourier transform of the signal is given by

$$G_L(f) = H(f) R_L(f). \tag{2}$$

The scattering function can be written as

$$r_L(t) = s(t + 2d_1/c) + s(t + 2d_2/c) + \cdots + s(t + 2d_N/c), \tag{3}$$

where c is the speed of sound in the medium, d_i represents the individual scatterer spacings, $s(t)$ is the scattering function for a single scatterer, and N represents the number of scatterers in the interrogated volume. The interrogated volume is determined by the length of the gate, L, and the cross-sectional area of the ensonifying beam. The Fourier transform of $r_L(t)$ is given by

$$R_L(f) = S(f)[e^{-i2\pi f(2d_1/c)} + e^{-i2\pi f(2d_2/c)} + \cdots + e^{-i2\pi f(2d_N/c)}], \tag{4}$$

where $S(f)$ is the scattering spectrum. The scattering spectrum depends on the shape and the mechanical properties of the scattering particles. The backscattered power spectrum is

the magnitude squared of Eq. (2), and is given by

$$W(f)=|G_L(f)|^2=|H(f)|^2|S(f)|^2|e^{-i2\pi f(2d_1/c)} + e^{-i2\pi f(2d_2/c)}+\cdots e^{-i2\pi f(2d_N/c)}|^2. \quad (5)$$

The backscattered power spectrum can be separated into the coherent and incoherent spectra by simplifying Eq. (5)

$$W(f)=|H(f)|^2|S(f)|^2 \times\left\{\sum_{n=1}^{N} 1+\sum_{n\neq m=1}^{N} e^{-i2\pi(f/c)(d_n-d_m)}\right\}, \quad (6)$$

where the first term on the right is the incoherent spectrum and the second term is the coherent spectrum. Rearranging terms yields

$$W(f)=|H(f)|^2|S(f)|^2\left\{N+2 \times\sum_{m>n=1}^{N}\left[\frac{e^{i2\pi(f/c)(d_n-d_m)}+e^{-i2\pi(f/c)(d_n-d_m)}}{2}\right]\right\},$$

or

$$W(f)=|H(f)|^2|S(f)|^2\left\{N+2\sum_{m>n=1}^{N}\cos(k\delta_{nm})\right\}, \quad (7)$$

where $k=2\pi f/c$, $\delta_{nm}=d_n-d_m$, and the number of terms in the coherent spectrum is $[N(N-1)]/2$. For random scattering, the form of $N|S(f)|^2$ can be estimated by assuming that the incoherent spectrum is the backscattered power spectrum, while the coherent spectrum acts as noise (spatial variation noise) that reduces the accuracy and precision of the estimation technique.

If the scatterers are randomly distributed within the interrogated volume, estimates of the scatterer properties are obtained by modeling the scatterers and fitting the model to the incoherent portion of the backscattered power spectrum. Assuming the model correctly describes the scattering, the spatial variation noise reduces the accuracy and precision of the scattering property estimates. Because the spatial variation noise depends on the random spacing of the scatterers in the interrogated volume, spatially averaging the backscattered power spectra from several different, nonoverlapping interrogated volumes can reduce the spatial variation noise. When samples from nonoverlapping, interrogated volumes are averaged, the variance in some estimated parameter, $\hat{x}$, is reduced by the number of averaged samples as[21,29]

$$\mathrm{var}(\overline{\hat{x}})=\frac{\mathrm{var}(\hat{x})}{N_s}, \quad (8)$$

where N_s is the number of averaged samples and $\overline{\hat{x}}$ represents the estimate from the averaged samples.

In making backscatter measurements using ultrasound, ROIs are selected from the interrogated volume. The ROIs are constructed from gating the different A-lines that are separated by some predetermined distance. Typically, the ultrasound source/receiver scans, or is steered, laterally across the scattering medium with individual A-lines separated by a predetermined distance related to the beamwidth. A rule of thumb has been that the A-lines be separated by a half beamwidth because it was conjectured that separating by that distance gave sufficiently independent measurements for spatial variation noise reduction.[21,30] Though the half-beamwidth separation does not give truly independent samples, a further reduction of spatial variation noise can be achieved over full-beamwidth sample separation for a particular lateral ROI length.[21] The number of samples in a particular lateral ROI length is doubled for half-beamwidth separation over full-beamwidth separation. Furthermore, the larger the lateral ROI length the greater the reduction of spatial variation noise because more independent samples would then be averaged. The distance of the separated A-lines and the number of A-lines determine the lateral resolution of an ROI.

The effects of the A-line center-to-center distance and number of samples averaged can be determined by quantifying the spatial variation noise for the backscattered power spectrum. The spatial variation noise spectrum (dB) is found by dividing the averaged measured power spectrum by the impulse response and the scattering function for the medium, $N|H(f)|^2|S(f)|^2$, giving

$$W_{svn}(f)=\left|10\log_{10}\frac{\frac{1}{N_{\mathrm{avg}}}\sum_{i=1}^{N_{\mathrm{avg}}}W_i(f)}{N|H(f)|^2|S(f)|^2}\right|, \quad (9)$$

where N_{avg} is the number of measured power spectra from different A-lines that are averaged. The spatial variation noise can be quantified by taking the average of the spatial variation noise spectrum over the analysis bandwidth

$$\langle W_{svn}\rangle=\frac{1}{B}\sum_{i=1}^{B}W_{svn}(f_i), \quad (10)$$

where B is the number of samples in the bandwidth.

If two consecutive A-lines are separated by a small distance relative to the beamwidth, the spatial variation noise spectra of the two A-lines will be highly correlated. If two A-lines are compared that correspond to completely nonoverlapping scattering volumes, the correlation between the spatial variation spectra should be close to zero. The averaging of the spatial variation noise spectra of any two different A-lines from a statistically homogeneous region will result in a decrease in the overall spatial variation noise and a subsequent decrease in $\langle W_{svn}\rangle$ over the analysis bandwidth. The relative decrease in spatial variation noise was defined according to

$$\langle W_{svn}\rangle_{\mathrm{rel}}=\frac{\frac{1}{B}\sum_{j=1}^{B}\left|10\log_{10}\frac{\frac{1}{N_{\mathrm{avg}}}\sum_{i=1}^{N_{\mathrm{avg}}}W_i(f_j)}{N|H(f_j)|^2|S(f_j)|^2}\right|}{\frac{1}{B}\sum_{j=1}^{B}\left|10\log_{10}\frac{W(f_j)}{N|H(f_j)|^2|S(f_j)|^2}\right|}, \quad (11)$$

where the numerator is $\langle W_{svn}\rangle$ for N_{avg} power spectra from different A-lines and the denominator is $\langle W_{svn}\rangle$ for a single A-line. Equation (11) compares the spatial variation noise from averaging the spatial variation spectra from several A-lines to a single A-line.

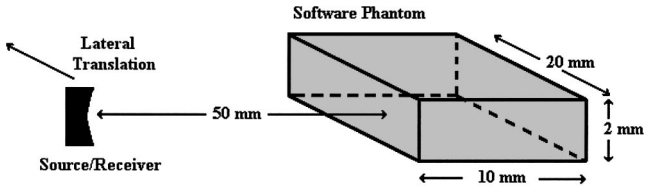

FIG. 1. Diagram of the simulated phantom with orientation and placement of the simulated source/receiver.

III. SIMULATION AND EXPERIMENTAL METHODS

The center-to-center spacing between A-lines, the number of A-lines, and the gated axial length are key factors to determining the level of spatial variation noise. There exists a trade-off between the lateral and axial length (resolution of the ROI) and the amount of spatial variation noise reduced by averaging a number of A-lines. In order to examine the trade-off between lateral and axial resolution and noise reduction, simulations from software phantoms and measurements from physical phantoms were made.

The software phantoms were constructed by first choosing a number density for each phantom of 64 mm^{-3}. A scattering volume (Fig. 1) was selected for each phantom and a number of point scatterers, number density times the phantom volume, were randomly placed in the volume. The software phantoms were assumed to be acoustically lossless. The source had a center frequency of 10 MHz and a -6-dB pulse/echo bandwidth of 5 MHz. A waveform (Fig. 2) was propagated from the source into the scattering volume at normal incidence. The source produced a Gaussian beam (laterally) with a -6-dB beamwidth of 0.6 mm. The source was weakly focused and all estimates were made within the depth of focus. Two other waveforms with beamwidths of 0.3 and 0.9 mm were simulated to evaluate whether the beamwidth was the limiting factor in lateral resolution. Each A-line was then constructed with individual point (Rayleigh) scatterers in the corresponding beam field, spherically scattering the incident pulse with the amplitude of the incident pulse and summing each scattered echo signal back at the source. Individual A-lines were constructed by translating the simulated source/receiver laterally across the length of the phantom with a step size of 25 μm.

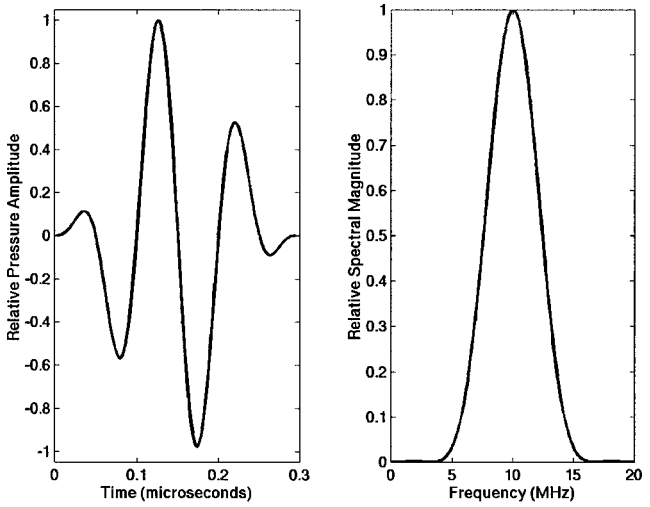

FIG. 2. Time pulse (left) and the magnitude of the frequency spectrum (right) of the simulated excitation pulse.

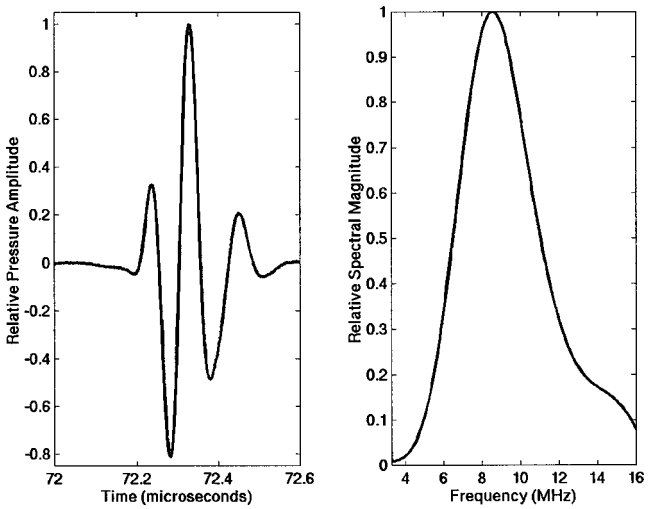

FIG. 3. Time pulse (left) and the magnitude of the frequency spectrum (right) from ultrasound reflected from a Plexiglas® reflector located at the focus of the transducer used in the physical phantom measurements.

Individual A-lines were gated using a Hanning window centered at a depth corresponding to 5 mm inside the phantom (the middle of the phantom). The backscattered power spectrum was found by taking the magnitude squared of the Fourier transform of the gated signal. The spatial variation noise in the coherent part of the backscattered spectrum was calculated from Eq. (9) with $|H(f)|^2$ equal to the power spectrum of the excitation pulse, $|S(f)|^2$ equal to the power spectrum of the point scatterers (f^4 dependence), and N equal to the number density of scatterers times the ensonified volume (cross-sectional beamwidth area times the gated length).

Measurements from two physical phantoms were made with a single-element weakly focused transducer (f number of 4) that had a center frequency of 10 MHz. The -6-dB pulse/echo bandwidth of the transducer was 6.5 MHz and the -6-dB pulse/echo beamwidth at the focus was measured to be 670 μm using the wire method.[31] Figure 3 displays an example of the incident pulse reflected from a Plexiglas® plate centered at the focus. The pulse reflected from the Plexiglas® was used as a reference pulse.[5,6,17]

In a measurement, the transducer was placed parallel to the face of the phantom so that the ultrasound would propagate normal to the surface. Both phantoms were filled with randomly placed glass beads with diameters ranging from 45 to 53 μm.[32] Phantoms A and B had measured attenuations of approximately 0.5 and 0.65 dB/MHz/cm over the range of 5–12 MHz, respectively. The number density of phantom A was close to half that of phantom B. The phantoms were scanned laterally 2 cm in length along their surface with a step size of 25 μm between each scan line (A-line). For each A-line, the backscattered signal was temporally averaged for 300 realizations to reduce any electronic noise associated with the measurement.

Individual A-lines were gated using a Hanning window of variable lengths with the edge at a depth corresponding to 2 mm inside the phantom. The backscattered power spectrum

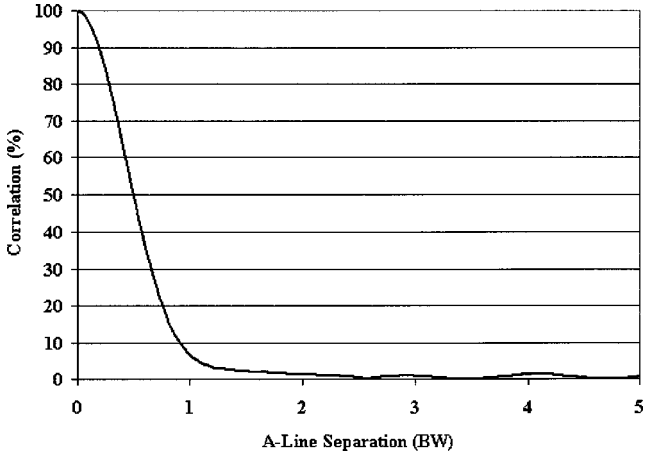

FIG. 4. Percent correlation of the spatial variation noise spectra from A-lines separated by varying distances (simulations). The line represents the average of 40 samples.

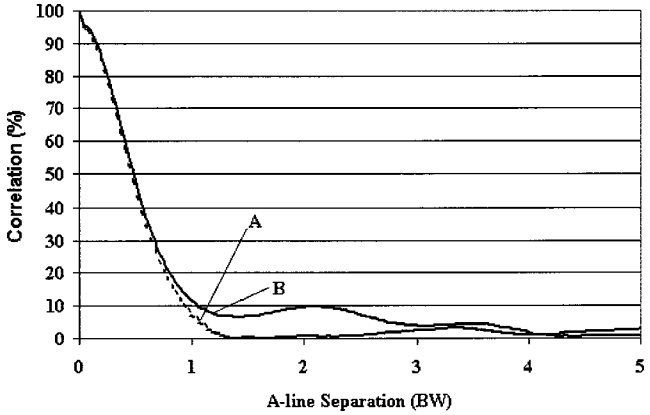

FIG. 5. Percent correlation of the spatial variation noise spectra from A-lines separated by varying distances from the physical phantoms. Each plotted line represents the average of 40 samples. Correlation lines were plotted for the two phantoms, ---, phantom A; ———, phantom B.

was found by taking the magnitude squared of the Fourier transform of the gated signal. The backscattered power spectrum was then multiplied by a frequency-dependent attenuation-compensation function.[27] The spatial variation noise spectra from the phantom measurements were calculated from Eq. (9). $|H(f)|^2$ was given by the power spectrum of the reference pulse, $|S(f)|^2$ was determined by the theory of Faran[33] for glass beads of diameter 49 μm, and N was found from the acoustic concentration determined using the MASD method.[5]

IV. SIMULATION AND EXPERIMENTAL RESULTS

The percent correlation at zero lag between the spatial variation noise spectra of two A-lines versus the A-line separation distance was determined for both the simulated phantoms and the physical phantoms according to

$$C(\%) = \frac{\Sigma_{i=1}^{B} W^*_{svn_1}(f_i) W_{svn_2}(f_i)}{\Sigma_{i=1}^{B} |W_{svn_1}(f_i)|^2} \times 100\%, \tag{12}$$

where B represents the number of sampled points in the analysis bandwidth and the two lines are represented by the subscripts 1 and 2, respectively. The center-to-center distance was normalized by dividing by the −6-dB beamwidth of the source/receiver. Figure 4 shows the percent correlation between the spatial variation noise spectra of two A-lines versus the center-to-center distance (in beamwidths, BW) for the simulated phantoms. The correlation steadily decreased as the center-to-center distance increased until the A-line center-to-center distance was about 1 beamwidth. The correlation at about 1 beamwidth began to level off to near zero. The reason for the correlation decreasing and then leveling off at a separation of near 1 beamwidth is that the compared A-lines represented nearly independent scattering volumes.

Similarly, Fig. 5 shows the percent correlation between the spatial variation noise spectra of two A-lines versus the A-line separation distance for the physical phantom measurements. In the phantom measurements, the correlation did not reach its minimum value until after the A-line separation distance exceeded the −6-dB pulse/echo beamwidth. Similar to the simulation phantoms, the correlation appeared to level off after the A-line separation distance exceeded 1 beamwidth.

The next set of measurements evaluated the decrease in $\langle W_{svn} \rangle_{\text{rel}}$ due to lateral length of the ROI. Typically, an ROI is chosen within the interrogated volume and the ROI is made up of several gated A-lines. The smaller the A-line separation distance, the more A-lines are included in a ROI. Furthermore, the larger the lateral length of the ROI, the more independent A-line samples that are included in the ROI and the greater decrease in $\langle W_{svn} \rangle_{\text{rel}}$.

Figures 6 and 7 show the decrease of $\langle W_{svn} \rangle_{\text{rel}}$ in the simulated phantoms and the physical phantoms, respectively, versus the lateral ROI length for several A-line separation distances. In both figures, $\langle W_{svn} \rangle_{\text{rel}}$ decreased with increased lateral ROI length and appeared to level off at a lateral ROI size of 15 to 20 BW for the phantom measurements. To compare the decrease in $\langle W_{svn} \rangle_{\text{rel}}$ versus lateral ROI distance for both simulated and physical phantoms, the distance at which $\langle W_{svn} \rangle_{\text{rel}}$ decreased to 1/e of its value for a single, unaveraged A-line sample was used. For the case of the simulated phantom, the 1/e decrease of $\langle W_{svn} \rangle_{rel}$ occurred at a lateral ROI size of around 5 BW and the 1/e value for the

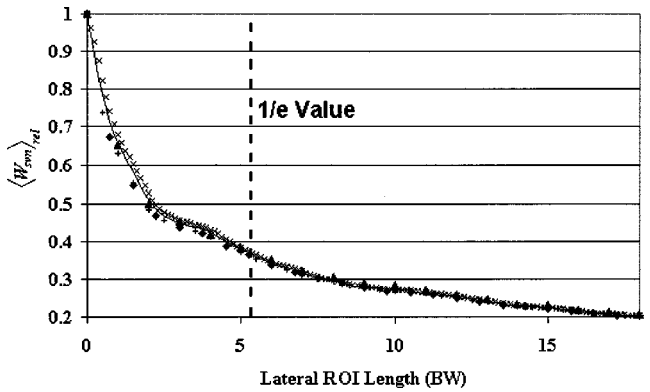

FIG. 6. $\langle W_{svn} \rangle_{\text{rel}}$ determined from the simulated phantoms over the frequency bandwidth 6–14 MHz relative to $\langle W_{svn} \rangle_{\text{rel}}$ for a single A-line. The number of averaged A-lines depends on the lateral ROI length and the A-line separation distances, ———, 0.125 BW; ×, 0.25 BW; +, 0.50 BW; ◆, 0.75 BW; ▲, 1.0 BW.

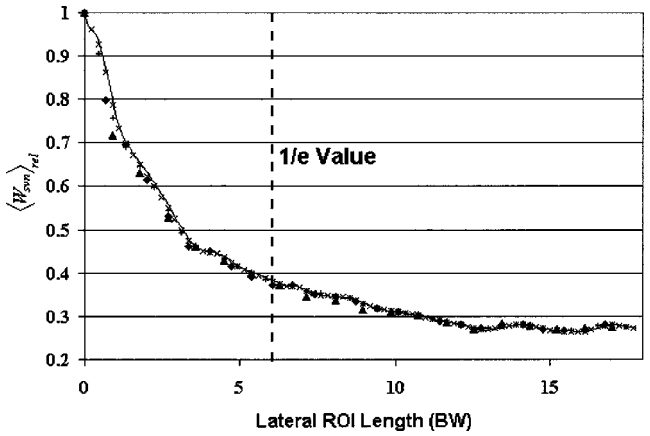

FIG. 7. $\langle W_{svn}\rangle_{\text{rel}}$ measured from the physical phantoms over the frequency bandwidth 6–14 MHz relative to $\langle W_{svn}\rangle_{\text{rel}}$ for a single A-line. The number of averaged A-lines depends on the lateral ROI length and the A-line separation distances, ———, 0.125 BW; ×, 0.25 BW; +, 0.50 BW; ♦, 0.75 BW; ▲, 1.0 BW.

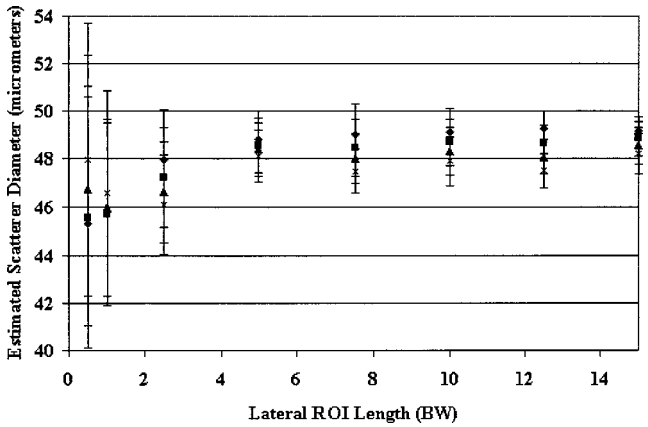

FIG. 8. Estimates of the average scatterer size of glass beads. The error bars represent the standard deviation of six measurements from phantom A and six measurements from phantom B with ROIs of the same size and same depth in the phantoms.

physical phantom measurements occurred at around 6 BW. In the simulations and the physical phantom measurements, the A-line separation distance did not appear give additional decreases in $\langle W_{svn}\rangle_{\text{rel}}$.

Figures 6 and 7 indicated that the most important factor to reducing spatial variation noise was not the A-line separation distance but rather the lateral length of the ROI. Averaging the backscattered spectra from any two different A-lines, whether they are from independent samples or not, will decrease the spatial variation noise. The lateral ROI length was the most important factor in spatial variation noise reduction; however, using A-lines with smaller separation distances means that you have a greater sampling over the lateral ROI length. Furthermore, any electronic noise in the backscattered spectrum will have little correlation from one A-line to the next, no matter the separation distance. The advantage to averaging the backscattered power spectra from many A-lines, because the A-lines separation distance is small, is that the electronic noise is reduced more than averaging the backscattered power spectra from just a few A-lines. In at least one study, improvement in scatterer property estimates was indicated by choosing smaller A-line separation distances.[34]

Figure 8 reveals the importance of the lateral ROI length for decreasing the spatial variation noise. The average size of the scatterers in the phantoms was estimated from the backscattered power spectrum using the MASD estimation technique and the theory of Faran.[5,33] The backscattered power spectrum was measured by selecting ROIs in the physical phantoms with axial lengths of 4 mm and varying the lateral ROI lengths. The analysis bandwidth used for the estimates was from 5–12 MHz. The analysis bandwidth corresponded to a ka range of 0.5 to 1.2, which has been measured to be the optimal range for estimating glass bead sizes.[6]

Estimates of glass bead sizes indicated that both accuracy and precision were affected by the lateral ROI length and not significantly by the A-line separation distance. The estimates of average glass bead size converged as the lateral ROI length approached 5 BW (Fig. 8). Furthermore, the error bars indicate that the precision of the estimates increased as the lateral ROI length increased up to a lateral ROI length of 5 BW. Beyond a lateral ROI length of 5 BW, no significant gains were made in accuracy and precision of the estimates.

Measurements of the spatial variation noise with source/receivers having different beamwidths indicated the optimal lateral ROI length in terms of BW was independent of the width of the beam. $\langle W_{svn}\rangle_{\text{rel}}$ was calculated at an A-line separation of 0.25 BW with beams of lateral length of 0.3, 0.6, and 0.9 mm. Figure 9 shows the relative spatial variation noise decrease in $\langle W_{svn}\rangle_{\text{rel}}$ as the lateral ROI length increased. The 1/e decrease in the spatial variation noise occurred in each measurement at a lateral ROI length of approximately 5 BW. The measurements indicate the optimal lateral ROI resolution is independent of the beamwidth of the source/receiver.

The decrease in $\langle W_{svn}\rangle_{\text{rel}}$ was also examined versus the axial gate length. Figure 10 shows a plot of the axial length in pulse lengths (PLs) versus the 1/e lateral ROI distance (BW) at which $\langle W_{svn}\rangle_{\text{rel}}$ decreased to 1/e of the maximum

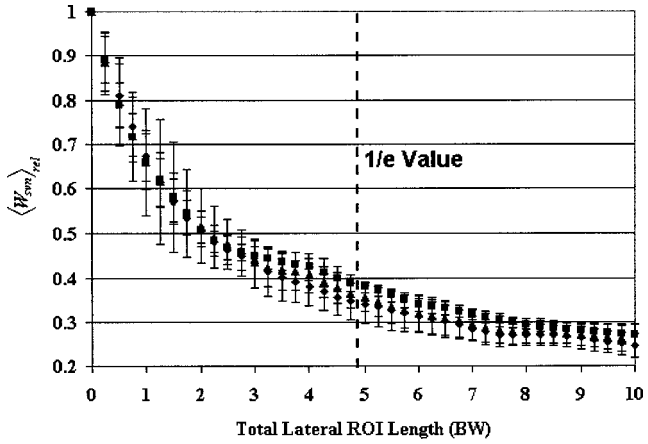

FIG. 9. $\langle W_{svn}\rangle_{\text{rel}}$ measured from the physical phantoms over the frequency bandwidth 6–14 MHz relative to $\langle W_{svn}\rangle_{\text{rel}}$ for a single A-line versus the lateral ROI length. The measurements were made with simulated source/receivers having beamwidths defined as, ♦, 0.3 mm; ■, 0.6 mm; ▲, 0.9 mm with A-line separation of 0.25 BW. The error bars represent the standard deviation about the mean of six independent measurements.

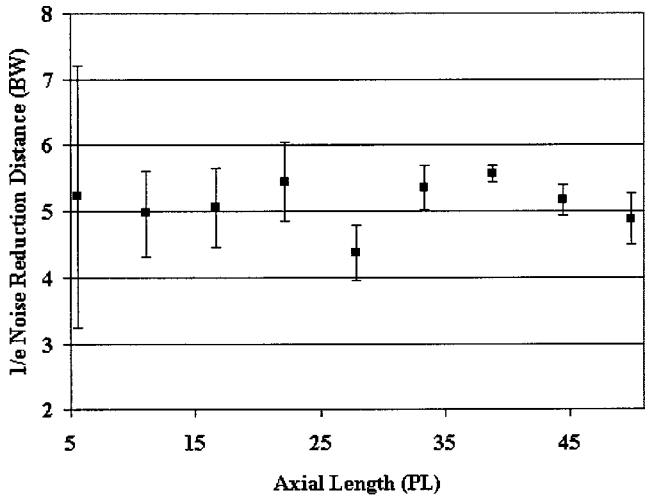

FIG. 10. The lateral ROI length where $\langle W_{svn} \rangle_{\text{rel}}$ reduces by 1/e of the value relative to $\langle W_{svn} \rangle_{\text{rel}}$ for a single A-line versus the axial gate length. The error bars represent the standard deviation of four simulated phantoms.

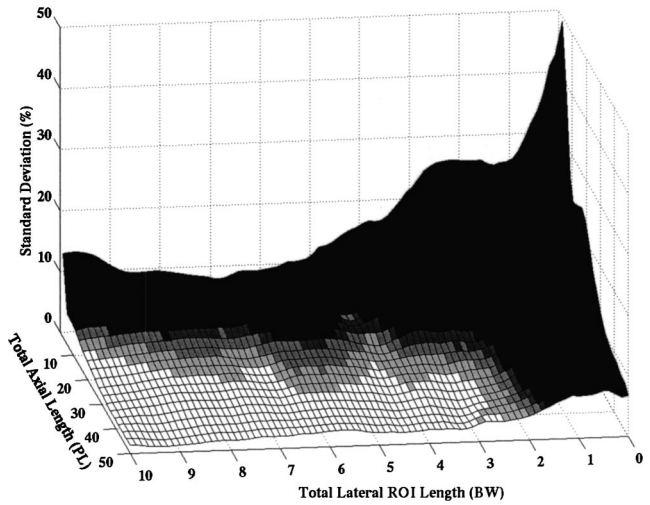

FIG. 12. Standard deviation of estimates of frequency dependence of backscattered power spectrum from randomly placed point scatterers as a percent of actual value versus axial and lateral ROI length.

value. The axial gate length did not appear to effect the average lateral ROI distance at which $\langle W_{svn} \rangle_{\text{rel}}$ was decreased to 1/e of the initial value. The dominant factor in decreasing $\langle W_{svn} \rangle_{\text{rel}}$ was the lateral ROI length. However, at smaller gate lengths the standard deviation for estimating the 1/e decrease in $\langle W_{svn} \rangle_{\text{rel}}$ was much greater. The axial gate length will affect the ability to make accurate and precise estimates. The spatial variation noise explains the effects of the lateral ROI length on the accuracy and precision of scatterer property estimates, but may not be the best measure for determining the optimal axial length for an ROI. Other effects than the spatial variation noise contribute to the loss of accuracy and precision at smaller axial gate lengths.[25]

The next simulation examined the accuracy and precision of parametrizing the frequency dependence of the backscattered power spectrum versus different lateral and axial ROI lengths affected. Point scatterers have frequency dependence to the fourth power for backscatter. Figures 11 and 12, respectively, show the accuracy and precision of estimating the frequency dependence of point scatterers versus different sizes of ROIs. The best accuracy and precision of estimates were obtained when the axial gate length and lateral ROI length were the largest. However, if smaller ROIs are desired to improve resolution and to increase the likelihood that the ROI contains uniform scattering statistics, then smaller ROIs that still retain good accuracy and precision of estimates should be chosen. For example, if the smallest possible ROI is desired while still retaining within 5% accuracy and precision, an ROI of 15 PLs times 5 BWs would fit.

The importance of the axial and lateral length of an ROI to the accuracy and precision of estimates can be seen from the phantom measurements (Figs. 13 and 14, respectively). The average size of the scatterers in the phantoms was estimated from the backscattered power spectrum using the MASD estimation technique and the theory of Faran.[5,33] The backscattered power spectrum was measured by selecting ROIs in the physical phantoms with variable axial and lateral

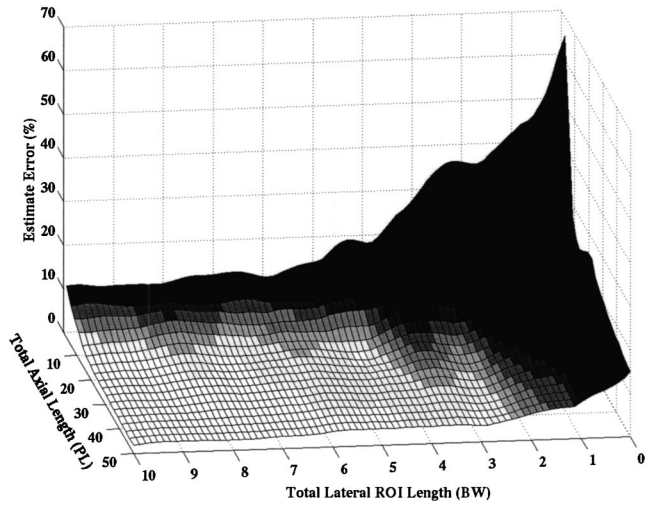

FIG. 11. Percent error between estimates of frequency dependence of backscattered power spectrum from randomly placed point scatterers and actual value (f^4) for point scatterers versus axial and lateral ROI length.

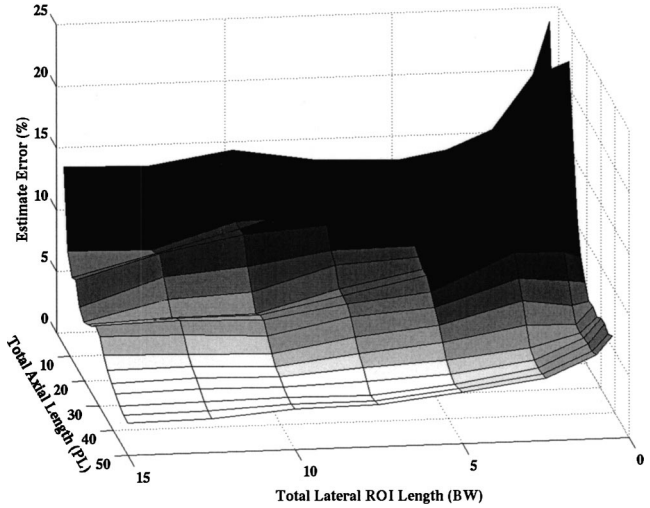

FIG. 13. Percent error between estimates of glass bead size from the backscattered power spectrum and actual values versus axial and lateral ROI length.

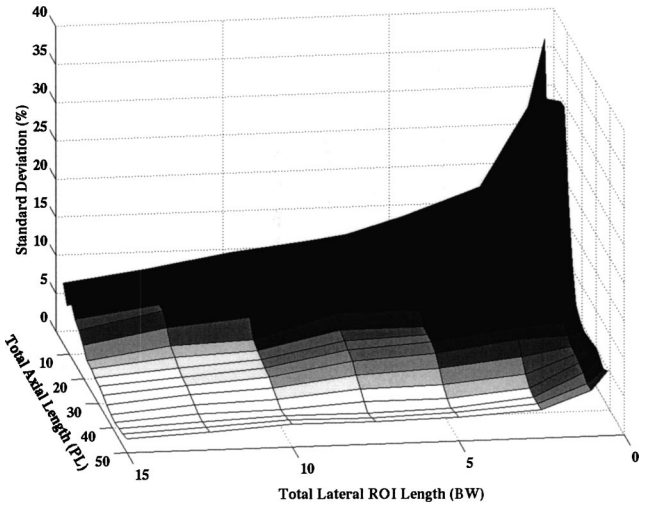

FIG. 14. Standard deviation of glass bead size estimates from the backscattered power spectrum as a percent of actual value versus axial and lateral ROI length.

ROI lengths. The analysis bandwidth used for the estimates was from 5–12 MHz.

Estimates of glass bead sizes indicated that the lateral and axial ROI length affected both accuracy and precision. Small axial gate lengths led to the largest inaccuracies in the estimate of scatterer size (Fig. 13). Errors of less than 10% occurred with axial gate lengths equal to or larger than 12 PLs and lateral ROI lengths of 5 BW. Smaller lateral lengths can be used with equivalent errors by using larger axial gate lengths. The precision of the estimates improved as the ROI area increased (Fig. 14). The standard deviation of less than 5% occurred when the ROI had an axial length of around 15–20 PLs and a lateral length of 5 BWs.

In order to obtain accurate and precise estimates, it must be noted that the number of samples within the lateral ROI length must be large enough. The importance of obtaining enough samples in the lateral ROI length was indicated from the 1-beamwidth separation data (Figs. 6 and 7). At the 5 BW, lateral ROI length line, 6 A-lines at the 1-full-beamwidth separation distance were sampled. The data point at the zero lateral ROI length value could be thought of as sampling one independent sample over a lateral ROI length of 5 BW. The data point at the lateral ROI length of 1 beamwidth could be thought of as sampling two independent samples over a lateral ROI length of 5 BW. The same goes for each data point up to the lateral ROI length of 5 BW (six independent samples). The data indicate that to get the best accuracy at the lateral ROI length of 5 BW there must minimally be an A-line separation of 1 beamwidth, with 6 being the total number of samples. The A-line separation distance can be as small as desired but the upper bound should be at most 1 beamwidth.

V. DISCUSSION

When making estimates of scatterer properties from the backscattered spectra of weakly scattering volumes, the sizes of ROIs selected are important to obtaining good estimates. In tissues it is especially important to minimize the ROI size because of possible variations throughout a larger volume. ROIs are chosen within the interrogated volume under the assumption that within the individual ROIs, the scattering properties are statistically uniform while in the larger volume, variation in the scattering properties may exist. Smaller ROIs allow for regions with different scattering statistics to be resolved in the overall volume. However, if the ROIs are too small, the accuracy and precision of scattering estimates suffer.

Optimizing the resolution (ROI size) with regards to the accuracy and precision of spectral estimates is important to tissue characterization. Typically, the rule of thumb has been that backscattered spectra should be averaged from A-lines separated by a distance of a half beamwidth. The more A-lines (longer lateral ROI length) the better the spectral characterization. Further, longer gate lengths were revealed to produce better estimates.

Results from simulation and physical phantom experiments indicated that the separation distance of the A-lines was not as important a factor in determining the accuracy and precision of scattering estimates as the lateral ROI length. However, when optimizing for ROI size, the separation distance of A-lines in the ROI should be at most 1 beamwidth. Choosing A-line separation distances smaller than 1 beamwidth can reduce the electronic noise further.

The key factor in reducing spatial variation noise and improving the accuracy and precision of scattering estimates was the overall axial and lateral lengths of the ROI. The simulations and phantom measurements indicated the optimal lateral and axial length, where estimate accuracy was consistently within 10% and precision within 5% of actual values, occurred at 4 to 5 beamwidths and 15 to 20 pulse lengths, respectively. Optimally, the results of the simulation and phantom experiments showed that the total lateral length of an ROI should be 5 BW. The total lateral length of 5 BW represents the length where the spatial variation noise was reduced by 1/e through averaging of the backscattered spectra from the individual A-lines. Furthermore, the lateral length size of 5 BW represented the length where the best accuracy and precision of glass bead estimates from the physical phantoms were reached. There was minimal advantage to increasing the ROI size beyond 4 to 5 beamwidths laterally and 15–20 pulse lengths axially. Increasing the size of the ROI gave some improvement in accuracy and precision, but such gains may be offset by tissue inhomogeneity. Similar accuracy and precision could be achieved by increasing either the axial length and decreasing the lateral length, or vice versa. The A-line separation distance should be less than or equal to 1 beamwidth, with smaller A-lines separation distances typically giving further reductions in electronic noise.

ACKNOWLEDGMENTS

Supported by NIH CA 079179 and NIH F32 CA96419 to M.L.O.

[1] D. Nicholas, ''Evaluation of backscattering coefficients for excised human tissues: Results, interpretation, and associated measurements,'' Ultrasound Med. Biol. **8**, 17–28 (1982).

[2] E. J. Feleppa, F. L. Lizzi, D. J. Coleman, and M. M. Yaremko, ''Diagnostic spectrum analysis in ophthalmology: A physical perspective,'' Ultrasound Med. Biol. **12**, 623–631 (1986).
[3] F. L. Lizzi, M. Ostromogilsky, E. J. Feleppa, M. C. Rorke, and M. M. Yaremko, ''Relationship of ultrasonic spectral parameters to features of tissue microstructure,'' IEEE Trans. Ultrason. Ferroelectr. Freq. Control **33**, 319–329 (1986).
[4] D. K. Nassiri and C. R. Hill, ''The use of angular scattering measurements to estimate structural parameters of human and animal tissues,'' J. Acoust. Soc. Am. **87**, 179–192 (1990).
[5] M. F. Insana, R. F. Wagner, D. G. Brown, and T. J. Hall, ''Describing small-scale structure in random media using pulse–echo ultrasound,'' J. Acoust. Soc. Am. **87**, 179–192 (1990).
[6] M. F. Insana and T. J. Hall, ''Parametric ultrasound imaging from backscatter coefficient measurements: Image formation and interpretation,'' Ultrason. Imaging **12**, 245–267 (1990).
[7] M. F. Insana, J. G. Wood, and T. J. Hall, ''Identifying acoustic scattering sources in normal renal parenchyma from the anisotropy in acoustic properties,'' Ultrasound Med. Biol. **18**, 587–599 (1992).
[8] K. K. Shung and G. A. Thieme, *Ultrasonic Scattering in Biological Tissues* (CRC Press, Boca Raton, 1993).
[9] M. F. Insana, T. J. Hall, J. G. Wood, and Z.-Y. Yan, ''Renal ultrasound using parametric imaging techniques to detect changes in microstructure and function,'' Invest. Radiol. **28**, 720–725 (1993).
[10] M. F. Insana, ''Modeling acoustic backscatter from kidney microstructure using an anisotropic correlation function,'' J. Acoust. Soc. Am. **97**, 649–655 (1995).
[11] T. J. Hall, M. F. Insana, L. A. Harrison, and G. G. Cox, ''Ultrasonic measurement of glomerular diameters in normal adult humans,'' Ultrasound Med. Biol. **22**, 987–997 (1996).
[12] E. J. Feleppa, T. Liu, A. Kalisz, M. C. Shao, N. Fleshner, and V. Reuter, ''Ultrasonic spectral-parameter imaging of the prostate,'' Int. J. Imaging Syst. Technol. **8**, 11–25 (1997).
[13] F. L. Lizzi, M. Astor, T. Liu, C. Deng, D. J. Coleman, and R. H. Silverman, ''Ultrasonic spectrum analysis for tissue assays and therapy evaluation,'' Int. J. Imaging Syst. Technol. **8**, 3–10 (1997).
[14] R. M. Golub, R. E. Parsons, B. Sigel, E. J. Feleppa, J. Justin, H. A. Zaren, M. Rorke, J. Sokil-Melgar, and H. Kimitsuki, ''Differentiation of breast tumors by ultrasonic tissue characterization,'' J. Ultrasound Med. **12**, 601–608 (1993).
[15] K. A. Topp, J. F. Zachary, and W. D. O'Brien, Jr., ''Quantifying B-mode images of *in vivo* rat mammary tumor with frequency dependence of backscatter,'' J. Ultrasound Med. **20**, 605–612 (2001).
[16] M. L. Oelze, J. F. Zachary, and W. D. O'Brien, Jr., ''Parametric imaging of rat mammary tumors *in vivo* for the purposes of tissue characterization,'' J. Ultrasound Med. **21**, 1201–1210 (2002).
[17] F. L. Lizzi, M. Greenbaum, E. J. Feleppa, M. Elbaum, and D. J. Coleman, ''Theoretical framework for spectrum analysis in ultrasonic tissue characterization,'' J. Acoust. Soc. Am. **73**, 1366–1373 (1983).
[18] E. L. Madsen, M. F. Insana, and J. A. Zagzebski, ''Method of data reduction for accurate determination of acoustic backscatter coefficients,'' J. Acoust. Soc. Am. **76**, 913–923 (1984).
[19] J. F. Chen, E. L. Madsen, and J. A. Zagzebski, ''A method for determination of frequency-dependent effective number density,'' J. Acoust. Soc. Am. **95**, 77–85 (1994).
[20] K. A. Wear, R. F. Wagner, M. F. Insana, and T. J. Hall, ''Application of autoregressive spectral analysis to cepstral estimation of mean scatterer spacing,'' IEEE Trans. Ultrason. Ferroelectr. Freq. Control **40**, 50–58 (1993).
[21] R. Kuc, ''Bounds on estimating the acoustic attenuation of small tissue regions from reflected ultrasound,'' Proc. IEEE **73**, 1159–1168 (1985).
[22] J. F. Chen, J. A. Zagzebski, and E. L. Madsen, ''Tests of backscatter coefficient measurement using broadband pulses,'' IEEE Trans. Ultrason. Ferroelectr. Freq. Control **40**, 603–607 (1993).
[23] M. F. Insana, E. L. Madsen, T. J. Hall, and J. A. Zagzebski, ''Tests of the accuracy of a data reduction method for determination of acoustic backscatter coefficients,'' J. Acoust. Soc. Am. **79**, 1230–1236 (1986).
[24] M. Ueda and Y. Ozawa, ''Spectral analysis of echoes for backscattering coefficient measurement,'' J. Acoust. Soc. Am. **77**, 38–47 (1985).
[25] M. Akita and M. Ueda, ''The effect of windowing on spectral estimation of echoes scattered by a random medium,'' J. Acoust. Soc. Am. **83**, 1243–1248 (1988).
[26] K. A. Wear, ''Fundamental precision limitations for measurements of frequency dependence of backscatter: Applications in tissue-mimicking phantoms and trabecular bone,'' J. Acoust. Soc. Am. **110**, 3275–3283 (2001).
[27] M. L. Oelze and W. D. O'Brien, Jr., ''Frequency-dependent attenuation-compensation functions for ultrasonic signals backscattered from random media,'' J. Acoust. Soc. Am. **111**, 2308–2319 (2002).
[28] H. J. Huisman and J. M. Thijssen, ''Precision and accuracy of acoustospectrographic parameters,'' Ultrasound Med. Biol. **22**, 855–871 (1996).
[29] A. Oppenheim and R. Schafer, *Digital Signal Processing* (Prentice Hall, Englewood Cliffs, NJ, 1975).
[30] F. Padilla, F. Peyrin, and P. Laugier, ''Prediction of backscatter coefficient in trabecular bones using a numerical model of three-dimensional microstructure,'' J. Acoust. Soc. Am. **113**, 1122–1129 (2003).
[31] K. Raum and W. D. O'Brien, Jr., ''Pulse–echo field distribution measurement technique for high-frequency ultrasound sources,'' IEEE Trans. Ultrason. Ferroelectr. Freq. Control **44**, 810–815 (1997).
[32] E. L. Madsen, F. Dong, G. R. Frank, B. S. Garra, K. A. Wear, T. Wilson, J. A. Zagzebski, H. L. Miller, K. Shung, S. H. Wang, E. J. Feleppa, T. Liu, W. D. O'Brien, Jr., K. A. Topp, N. T. Sanghvi, A. V. Zaitsev, T. J. Hall, J. B. Fowlkes, O. D. Kripfgans, and J. G. Miller, ''Interlaboratory comparison of ultrasonic backscatter, attenuation, and speed measurements,'' J. Ultrasound Med. **18**, 615–631 (1999).
[33] J. J. Faran, Jr., ''Sound scattering by solid cylinders and spheres,'' J. Acoust. Soc. Am. **23**, 405–418 (1951).
[34] M. E. Anderson, M. S. C. Coo, and G. E. Trahey, ''*In vivo* breast tissue backscatter measurements with 7.5- and 10-MHz transducers,'' Ultrasound Med. Biol. **27**, 75–81 (2001).

Forced linear oscillations of microbubbles in blood capillaries

E. Sassaroli[a] and K. Hynynen
Department of Radiology, Brigham and Women's Hospital, Harvard Medical School, Boston, Massachusetts 02115

(Received 15 October 2003; revised 16 March 2004; accepted 19 March 2004)

A theoretical investigation of the forced linear oscillations of a gas microbubble in a blood capillary, whose radius is comparable in size to the bubble radius is presented. The natural frequency of oscillation, the thermal and viscous damping coefficients, the amplitude resonance, the energy resonance, as well as the average energy absorbed by the system, bubble plus vessel, have been computed for different kinds of gas microbubbles, containing air, octafluropropane, and perflurobutane as a function of the bubble radius and applied frequency. It has been found that the bubble behavior is isothermal at low frequencies and for small bubbles and between isothermal and adiabatic for larger bubbles and higher frequencies, with the viscous damping dominating over the thermal damping. Furthermore, the width of the energy resonance is strongly dependent on the bubble size and the natural frequency of oscillation is affected by the presence of the vessel wall and position of the bubble in the vessel. Therefore, the presence of the blood vessel affects the way in which the bubble absorbs energy from the ultrasonic field. The motivation of this study lies in the possibility of using gas microbubbles as an aid to therapeutic focused ultrasound treatments. © *2004 Acoustical Society of America.* [DOI: 10.1121/1.1738456]

PACS numbers: 43.80.Sh, 43.35.Pt, 43.20.Ks [FD] Pages: 3235–3243

I. INTRODUCTION

Cavitation microbubble production and behavior in liquids under ultrasound exposure have been studied for several decades.[1–3] In recent years, there has been an increased interest in investigating the bio-effects of acoustic cavitation for potential applications to therapeutic focused ultrasound. Ultrasound contrast agents, which are stabilized gas bodies of a few microns in diameter can serve as an ultrasound cavitation nuclei when destabilized by the ultrasonic interaction.[4]

Microscopic hemorrhage in gas-rich organs such as lungs and intestine have been attributed to cavitation-related effects.[5–8] Cavitation has been reported to occur *in vivo* in other mammalian tissues as well, yielding diverse thresholds in different tissues.[9–19] Ultrasound-mediated delivery into cells have been demonstrated *in vitro* by uptake of extracellular fluid, drugs and DNA.[20–28] The combination of ultrasound with microbubble contrast agents seem to be more effective than ultrasound alone in inducing bio-effects *in vitro* as well as *in vivo*.[4,6,29–36]

To these various experimental studies of acoustic cavitation in biological systems do not correspond as many theoretical and numerical investigations. This is certainly due to the limited ability at the present time, of mathematical models and computer simulations to explain experimental data of complex processes, such as acoustic cavitation in living things. In relation to bubble dynamics for example, the oscillations of a cavitation bubble in an ultrasonic field are usually discussed in terms of the Gilmore equation[3] or Keller–Miksis equation,[37] which are strictly valid when the bubble is in an unbounded liquid, i.e., when the liquid is in a container whose size is much larger than the bubble size. These equations have been used in some situations of interest in medical applications of ultrasound (see, for example, Refs. 38–40), giving very useful insights, however in fine blood capillaries where the bubble size is comparable to capillary radius the effect of the boundary proximity may become significant, as it is demonstrated in this study. As a first approach in understanding a highly complex phenomenon such as gas bubble behavior in the microvasculature, we will concentrate on the linear oscillations of a microbubble confined in a fine capillary. Not only the linear response is easier to treat, but it provides some useful information into the bubble behavior in general. For example, it is well known that in unbounded liquids the natural frequency of oscillation affects the way in which bubbles absorb energy from the ultrasonic field. When a bubble is sonicated at its resonance frequency it intercepts and reradiates more acoustic power than one would expect from its cross-section area. Furthermore, when a bubble undergoes noninertial cavitation in response to an ultrasonic field, if its natural frequency is larger or equal to the applied frequency, the bubble oscillates with a period close to the ultrasonic period. Bubbles having their resonance frequencies smaller then the applied frequency, pulsate with a period roughly equal to the natural period of the bubble. Moreover, after a bubble undergoes an inertial collapse, it oscillates unsteadily roughly at its resonance frequency, giving the rise to characteristic ''afterbounces.'' The continuous part of the noise spectrum, emitted by bubbles experiencing inertial cavitation, is attributed to these unsteady oscillations of the bubbles (afterbounces) at their natural frequencies of oscillations. Therefore the determination of the natural frequencies of oscillations of microbubbles in the microvasculature is a first necessary step in

[a]Author to whom correspondence should be addressed. Electronic mail: esassaro@bwh.harvard.edu

order to develop a tractable and realistic theory on the subject.

Therapeutic applications of focused ultrasound in medicine are under development and include among other things minimally invasive thermal ablation of tumors,[41] drug and gene delivery.[42] The possible role of cavitation in these therapeutic applications needs to be investigated. This work is designed to provide some useful insights into the mechanisms of energy absorption of a cavitation bubble in fine capillary vessels as an aid for therapeutical focused ultrasound treatments. The paper is organized as follows: In Sec. I the theoretical model is discussed. After a brief introduction to the rheology and anatomy of capillary blood vessels of interest here, we will describe our mathematical model which consists of two forced coupled harmonic oscillators, which can be solved analytically. In the linear regime the natural frequency of oscillation, the damping coefficient (thermal plus viscous), and the absorbed power can also be determined analytically. In Sec. II the numerical results of the model will be analyzed as a function of the sonication parameters, bubble size, and content. Section III includes a discussion of the model limitations and of the potential of this model to improve therapeutic focused ultrasound treatments.

II. MODEL DESCRIPTION

A. Biomechanics of capillary blood vessels in the mesentery

Blood is a mixture of blood plasma and blood cells (mainly red cells).[43] Blood is a non-Newtonian fluid, because its coefficient of viscosity as measured in a viscometer varies with the strain rate.[44] Normal plasma alone however behaves like a Newtonian fluid. Therefore the non-Newtonian nature of blood is due to the presence of blood cells. The viscosity of blood varies with the *hematocrit*, the percentage of the total volume of blood occupied by the cells. Typically, arterial hematocrit is 45%–50% and the hematrocrit in the capillaries (smallest blood vessels) varies from 10% to 26%, with an average of 18%.[45] In a viscometer only the relative viscosity, i.e., the ratio of viscosities between the test liquid and for example water can be measured accurately. The relative viscosity of blood is between 3 and 4 for a normal hematocrit of 45%–50% in humans and increases with increasing hematocrit.[43]

As long as the diameter of the capillary tube used in a viscometer is more than 1 or 2 mm the relative viscosity of blood is the same, whatever the size of the tube used. When, however tubes of narrower diameter are used, the value of relative viscosity is found to be less (*Fahraeus–Lindqvist effect*).[46] The resistance is however expected to increase with decreasing diameter when the tube is smaller than the red cell.[47] This is the reverse of the of the Fahraeus–Lindqvist effect. The measurements of blood viscosity in the microvessels *in vivo* are extremely difficult due mainly to the difficulty of measuring accurately the vessel internal diameter and the velocity and pressure fields. (For a review on the subject of how the effective viscosity of blood depend on the vessel diameter, hematocrit and flow velocity see, for example, Refs. 48, 49.) The situation is further complicated from the fact that the effective viscosity of blood changes from one microvessel to another in the microvasculature. When one examines microcirculation in a living preparation the red blood cells are not uniformly distributed. In a sheet of mesentery sometimes a long segment of capillary is seen without blood cells; at another instant cells are seen tightly packed together. For the purpose of illustration in this study we have chosen an effective viscosity of 2 times the water viscosity, valid experimentally with blood flow forced through micropipettes.[43]

Each organ has a unique microvasculature bed,[50] with common features. For example, the wall of the capillary blood vessel consists of a single layer of endothelium cells lying on a basement membrane which occasionally splits to enclose the pericytes and lacks of any elastic tissue. In this investigation we consider a relatively simple situation in which an artery supplies a number of parallel microvessels that drain into a vein. In particular the mesentery capillaries are going to be considered. This because in the mesentery the capillaries are long thin tubes embedded in tissue and are rather rigid. *In vivo* observation of the elasticity of capillary blood vessels in isolated preparation can be made under varying perfusion pressure without flow. Burton,[51] in summarizing Jerrad's unpublished data, stated that frog mesentery capillaries behave, to increase in transmural pressure (i.e., internal−external pressure), like almost completely rigid tubes. Jerrard found that the distensibility of the capillaries was certainly less than 0.2% per mm Hg. This lack of distensibility can be explained in terms of the Laplace law $\Delta P = T/R$, where ΔP is the transmural pressure, R is the radius of the tube, and T is the circumferential tension in the wall, required to resist the transmural pressure. For example, the aorta with a radius of 1.25 cm and mean ambient pressure of about 100 mm Hg is required to develop a tension of 170 g/cm in order to balance the transmural pressure. But a capillary, having a much smaller radius (about 4 μm in the mesentery) requires only a tension of 14 mg/cm to resist a transmural pressure of about 25 mm Hg.

A more sophisticated mathematical theory to describe the behavior of the capillaries in the mesentery have been developed by Fung[52,53] who proposed that capillaries behave like tunnels in gel and that their behavior cannot be tested independently of this surrounding gel. It follows that the compliance of the capillaries depends on the amount of surrounding tissue that is integrated with the blood vessel and to the degree the surrounding tissue is stressed. If the surrounding tissue is large compared with the capillary, and it is stressed to the degree used in most physiological experiments, then the capillary is rather rigid because is supported by the surrounding gel. The capillary blood vessels in a bat's wing are fairly distensible because the surrounding tissue is relatively small.[54]

Our model consists of an cylindrical blood capillary of diameter $D = 8\ \mu$m, length $L = 1$ mm, and mean ambient pressure of 25 mm Hg (3.3 kPa) above the atmospheric pressure (101.3 kPa). These data are typical for the capillaries of the mesenteric vascular bed of dogs.

Taking also into account that we consider only a weak

acoustic field, as described in more details below, we can approximate the capillary as a rigid tube. While a capillary acts a rigid tube to a distending pressure, it may dilate readily to chemical action. This aspect has not been considered in the present investigation.

B. Mathematical model

The linear steady-state response of a gas bubble contained in a small-blood capillary driven by a weak acoustic field up to a frequency of 3 MHz is considered. Several idealizations have been made. The basic idea is to study the linear response of a system consisting of two liquid columns in a small vessel, separated by a gas bubble (Fig. 1). Our investigation is based on a model which has been developed by Chen and Prosperetti[55] for applications in microfluidic devices.

A gas bubble acoustically driven immersed in an unbounded liquid, loses energy by heat transfer and frictional dissipation across the gas–liquid interface, as well as sound emission. In water, acoustic losses only dominate for bubble radii larger than several millimeters.[56] In this study we neglect the sound emitted by the microbubbles.

In the case of bubbles oscillating in bounded regions however, a new energy mechanism is present, namely viscous dissipation due to the liquid flow along the surface of the surrounding vessel. The typical ambient radius R_B of a U.S. contrast agent is between 1–5 μm and hence comparable in size to the radius of the capillary. Therefore an obvious approximation is to take the bubble to occupy an entire region of the capillary. We can adjust the axial length $2L_B$ of this region, so to give the same volume as the real bubble, namely

$$L_B = \frac{(4/3)\pi R_B^3}{2S}, \tag{1}$$

where S is the vessel cross sectional area. If L_1 is the distance of the bubble center to one end and $L_2 = L - L_1$ from the other end, then an amount L_B has to be subtracted from both L_1 and L_2 in order to preserve volume. Another correction, due to the presence of the surroundings, needs to be made. For a circular tube with a thin wall this adjustment amounts to add a correction of 1.22 R to the tube length L, where R is the tube radius. This correction is however tiny, because R is much smaller than L.[57] ΔL is however, a tiny correction, because the radius of the vessel R is much smaller than its axial length L. Thus the effective lengths of the two liquids columns ($i = 1,2$) are given by

$$L_i^{\text{eff}} = L_i - L_B + \Delta L. \tag{2}$$

We assume that the system is subject to a sound field, which may be expressed in complex notation as

$$p(t) = p_0 a e^{i\omega t}, \tag{3}$$

where p_0 is the average ambient pressure defined above, and a is the dimensionless amplitude of the pressure field, which is supposed to be small.

Let $x_1(t)$ and $x_2(t)$ denote the time dependent position of the two gas–liquid interfaces, both measured from the midpoint of the undisturbed bubble. We assume that under the effect of the acoustic field, the two interfaces undergo linear oscillations around their equilibrium positions, respectively $x_{20} = L_B$ and $x_{10} = -L_B$, according to

$$(x_2(t) - x_{20}) - (x_1(t) - x_{10}) = 2L_B X(t), \tag{4}$$

where $X(t)$ is a dimensionless parameter which represents the bubble oscillatory motion.

In their work on thermal processes in the oscillations of gas bubbles in tubes, Chen and Prosperetti,[55] noticed that the gas pressure in a linear problem, can be written without loss of generality as

$$p_B(t) = p_0(1 - X(t)\Phi), \tag{5}$$

where Φ is a constant, which can be regarded as a complex frequency dependent polytropic index and p_0 is the ambient pressure. Equation (5) can be regarded as the linearization of a relation $pV^{\Phi} = \text{const}$, where V is the bubble volume.

The real part of Φ determines the natural frequency of oscillation of the system and its imaginary part is responsible for thermal dissipation. At the free ends of the vessel the pressure is

$$p(t) = p_0(1 + a e^{i\omega t}). \tag{6}$$

The two liquids columns experience therefore a difference in pressure, $\Delta p = |p(t) - p_b(t)|$ which determines the Newton's equations of motion

$$\begin{aligned} &\rho L_1^{\text{eff}} \ddot{x}_1 + 2\rho L_1^{\text{eff}} b_v \dot{x}_1 - p_0 \Phi X = p_0 a e^{i\omega t}, \\ &\rho L_2^{\text{eff}} \ddot{x}_2 + 2\rho L_2^{\text{eff}} b_v \dot{x}_2 + p_0 \Phi X = -p_0 a e^{i\omega t}, \end{aligned} \tag{7}$$

where $L_{1,2}^{\text{eff}}$ have been defined in Eq. (2), and ρ is the plasma density, $p_B(t)$ and $p(t)$ are given, respectively, by Eqs. (5) and (6). b_v is the viscous damping and it will be derived below. The thermal damping is in the expression for $p_B(t)$ and will also be discussed below.

Equations (7) are the equations of two forced coupled harmonic oscillators. Their steady-state solutions, i.e., the solutions obtained after the transients effects have subsided, can be written as

$$x_1 - x_{10} = A_1 a \sin(\omega t - \delta), \tag{8a}$$

$$x_2 - x_{20} = -A_2 a \sin(\omega t - \delta), \tag{8b}$$

with amplitudes A_1 and A_2,

$$A_1 = \frac{p_0}{\rho L_1^{\text{eff}}} \frac{1}{\sqrt{(\omega^2 - \omega_0^2)^2 + 4b^2\omega^2}}, \tag{8c}$$

$$A_2 = \frac{p_0}{\rho L_2^{\text{eff}}} \frac{1}{\sqrt{(\omega^2 - \omega_0^2)^2 + 4b^2\omega^2}}, \tag{8d}$$

and phase δ,

$$\tan\delta = \frac{\omega^2 - \omega_0^2}{2b\omega}, \tag{8e}$$

where ω_0 is the natural frequency of the system

$$\omega_0^2 = \frac{p_0}{2L_B\rho}\left(\frac{1}{L_1^{\text{eff}}} + \frac{1}{L_2^{\text{eff}}}\right)\text{Re}\,\Phi \tag{9}$$

and b is the total damping coefficient (viscous plus thermal)

$$b = b_v + \frac{\omega_0^2}{2\omega}\frac{\mathrm{Im}\,\Phi}{\mathrm{Re}\,\Phi}. \tag{10}$$

The total damping coefficient b has a viscous and a thermal part. It determines the amount of energy absorbed from the external acoustic field which goes to increase the random motion and internal molecular energies of the system.

The system of Eqs. (7) has two degrees of freedom and therefore two natural frequencies of oscillations. The one, given by Eq. (9), is associated with the relative motion of the system, the other one is associated to the center of mass motion. However in our case, the center of mass natural frequency is not excited, because we assume the same pressure at each free end of the tube and zero initial velocities for the two bubble interfaces.

The bubble motion can be obtained by substituting Eqs. (8) into Eq. (4) and one obtains

$$X = -A_b a \sin(\omega t - \delta), \tag{11a}$$

$$A_b = \frac{p_0}{\rho 2 L_B}\left(\frac{1}{L_1^{\mathrm{eff}}} + \frac{1}{L_2^{\mathrm{eff}}}\right)\frac{1}{\sqrt{(\omega^2-\omega_0^2)^2 + 4b^2\omega^2}}. \tag{11b}$$

C. Polytropic index Φ and viscous damping

In order to calculate the natural frequency ω_0 and the damping coefficient b the polytropic index Φ needs to be evaluated. The general evaluation of Φ is not possible, however for the case of small-amplitude oscillations of a perfect gas with a spatially uniform internal pressure it is possible to derive some analytical expressions for Φ.[58] In particular for a circular tube, it has been found the following expression:[55]

$$\Phi = \frac{\gamma}{1+(\gamma-1)G}, \tag{12a}$$

γ is the ratio of specific heats, and G is defined by

$$G = 1 + i\Omega\sum_{n=1}^{\infty}\left(\frac{(2/\alpha_n)}{k_n}\right)^2\left[\frac{\tanh k_n \mathcal{A}}{k_n \mathcal{A}}\right], \tag{12b}$$

where α_n are the zeros of the zero order Bessel function of the first kind J_0 and the other quantities are defined by

$$\Omega = \omega\frac{l^2}{D}, \quad l = \frac{RL_B}{R+2L_B}, \quad \mathcal{A} = 1 + \frac{2L_B}{R},$$

$$k_n = \sqrt{\left(\alpha_n\frac{l}{R}\right)^2 + i\Omega}, \tag{12c}$$

where D is the gas thermal diffusivity and L_B is obtained from Eq. (1), once the radius of the bubble R_B is given. It is important to point out here that Eqs. (12) have been obtained with another assumption, which is also standard for a gas bubble in an unbounded region, i.e., that the surface delimiting the gas remains at the undisturbed temperature of the system. The justification of this assumption lies in the much larger heat capacity per unit volume of most liquids and solids than gases. Thus, amounts of heat sufficient to cause significant temperature changes in the gas are too small to cause any appreciable temperature changes in the materials surrounding the bubble.

The evaluation of Eq. (10) also requires the knowledge of the viscous damping coefficients b_v. The details of the mathematical derivation of b_v are tedious and are omitted in this study, but the final result is

$$b_v = \frac{4\nu}{R^2}\frac{R_\omega}{16}\frac{I}{I_1^2+I_2^2}, \tag{13a}$$

where ν is the blood viscosity, $R_\omega = \omega R^2/\nu$ is a dimensionless parameter, and I, I_1, and I_2 are integrals containing zero and first order Bessel's functions of the first kind (J_0, J_1), which can be evaluated only numerically

$$I = \int_0^1 dx x[A\,\mathrm{Re}[cJ_1(c\sqrt{R_\omega}x)] + B\,\mathrm{Im}[cJ_1(c\sqrt{R_\omega}x)]]^2 + \int_0^1 dx x[B\,\mathrm{Re}[cJ_1(c\sqrt{R_\omega}x)] - A\,\mathrm{Im}[cJ_1(c\sqrt{R_\omega}x)]]^2, \tag{13b}$$

$$I_1 = \int_0^1 dx x(A^2+B^2-A\,\mathrm{Re}[J_0(c\sqrt{R_\omega}x)] - B\,\mathrm{Im}[J_0(c\sqrt{R_\omega}x)]), \tag{13c}$$

$$I_2 = \int_0^1 dx x(B\,\mathrm{Re}[J_0(c\sqrt{R_\omega}x)] - A\,\mathrm{Im}[J_0(c\sqrt{R_\omega}x)]), \tag{13d}$$

where $c = e^{-i(\pi/4)}$, $A = \mathrm{Re}[J_0(c\sqrt{R_\omega})]$, $B = \mathrm{Im}[J_0(c\sqrt{R_\omega})]$.

For the blood we have chosen an effective viscosity of twice the water viscosity, valid in fine blood vessels, i.e., $\nu = 2\times10^{-6}\,\mathrm{m/s^2}$.

It is interesting to point out that the velocity field required to calculate Eqs. (13) has been obtained by an exact solution of the Navier–Stokes equation for parallel oscillatory flow in an infinitely long circular channel.[59]

D. Average absorbed power

It is well known from the theory of mechanical vibration that when the frequency of the applied force is equal to the natural frequency of the system, the velocity and kinetic energy of the oscillator are maximum and it is said there is energy resonance. These are the most favorable conditions for transfer of energy to the oscillator. The average power, transferred to the oscillator from the applied force can also be calculated. For example by taking the time derivative of Eq. (8a), one obtains the velocity v_1 for the liquid column L_1^{eff}. The average power absorbed is obtained by averaging in time over a period $T = 2\pi/\omega$ the power $P = Fv_1 = S\,\mathrm{Re}(p(t))v_1$, where S is the cross sectional area and $p(t)$ is the applied pressure defined in Eq. (3). The result can be written as

$$P_{\mathrm{ave}} = \langle Fv_1\rangle_{\mathrm{ave}} = \frac{1}{2}\frac{Sp_0^2a^2}{\rho L_1^{\mathrm{eff}}}\frac{2b}{\left(\frac{\omega_0^2}{\omega}-\omega\right)^2+4b^2}. \tag{14}$$

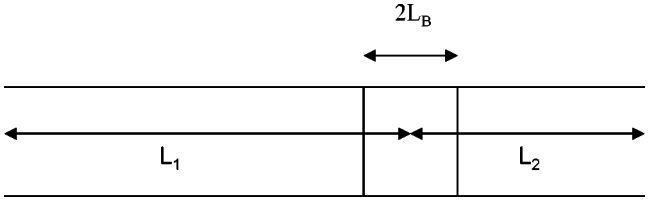

FIG. 1. Gas bubble of axial length $2L_B$. L_1 is the distance from the bubble center to one end and L_2 is from the other end.

At the energy resonance $\omega=\omega_0$ and the average power reduces to

$$(P_{\text{ave}})_{\text{res}}=\frac{1}{2}\frac{Sp_0^2a^2}{\rho L_1^{\text{eff}}}\frac{1}{2b}. \tag{15}$$

The ratio between P_{ave} and $(P_{\text{ave}})_{\text{res}}$ simplifies to

$$\frac{P_{\text{ave}}}{(P_{\text{ave}})_{\text{res}}}=\left(\frac{2b}{\sqrt{\left(\frac{\omega_0^2}{\omega}-\omega\right)^2+4b^2}}\right)^2. \tag{16}$$

This result does not depend on the L_1^{eff} and therefore is true for the entire system, bubble plus two liquid columns.

III. RESULTS

In this section the numerical predictions of the mathematical model described above will be illustrated.

A. Natural frequency of oscillation

The natural frequency of oscillation of the system bubble plus vessel is expressed by Eq. (9). In order to evaluate this equation, the real part of the polytrophic index Φ needs to be determined. Φ is a function of the microbubble radius, the type of gas considered, as well as the driving frequency. In this investigation we have considered frequencies up to 3 MHz and bubble radius range between 1 and 4 μm. The real part of Φ determines the isothermal and/or adiabatic behavior of the gas bubbles. It is possible to see that the isothermal behavior prevails for small gas bubbles and low frequencies. On the other hand, the rate of heat transfer is intermediate between isothermal and adiabatic for frequencies above 1 MHz and larger size bubbles (4 μm). This general behavior is true for all the types of gases (air, C_3F_8, C_4F_{10}) considered, but it is more accentuated for the higher molecular weight molecules.

The natural frequency f_0 depends on the driving frequency through the real part of the polytrophic index. However, in the range of frequencies of interest in this study, f_0 as function of the driving frequency is nearly constant. There is a slightly more marked dependence on the frequency for larger size bubble (4 μm) and frequencies higher than 1 MHz, as it has been shown in Fig. 2. For air this frequency dependence is stronger than for C_3F_8, C_4F_{10}.

For a fixed value of the driving frequency, f_0 depends on the bubble radius thorough Eq. (1) and on the bubble position in the vessel.

In Fig. 3 we have plotted the natural frequency f_0, as given by Eq. (9) as a function of the microbubble radius R_B for a fixed value of the driving frequency. The gas considered in the plot is octafluoropropane, but air and perflurobutane give very similar plots. For the purpose of illustration we have considered three different lengths for L_1:$L/2$ (solid line), $L/5$ (dashed line), and $L/10$ (dotted line), which correspond, respectively, to a distance of the bubble center from one end to be 500, 200, 100 μm. For a given position of the bubble in the tube, the resonance frequency increases for decreasing bubble radius. Moreover the resonance frequency decreases as the bubble gets closer to the center of the vessel.

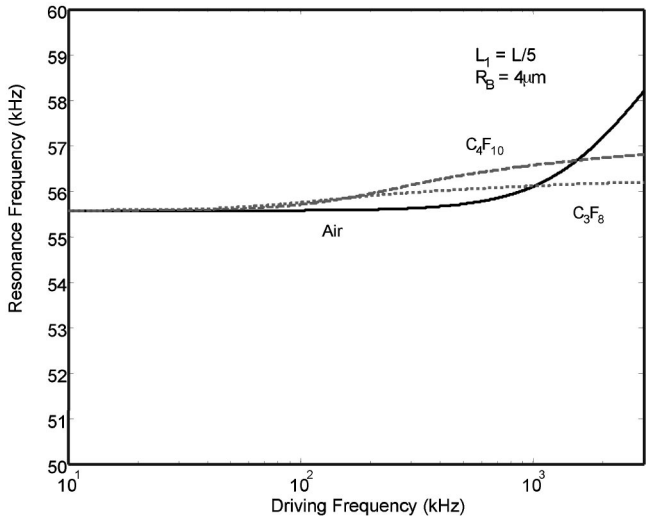

FIG. 2. Natural frequency of oscillation as a function of the driving frequency up to 3 MHz for a bubble at a distance of $L/5$ from one end and radius $R_B=4$ μm. The solid line corresponds to a bubble containing air, the dashed line to one containing octafluropropane, and the dotted line to a perflurobutane gas bubble.

The natural frequency of oscillation of a bubble confined in a narrow region is therefore affected by the presence of the boundary and it is different from its resonance frequency in an unbounded region. This consideration is true in general any time the bubble size is not small with respect to the container dimension and not only for bubbles driven in the linear regime. However only in the linear regime one can

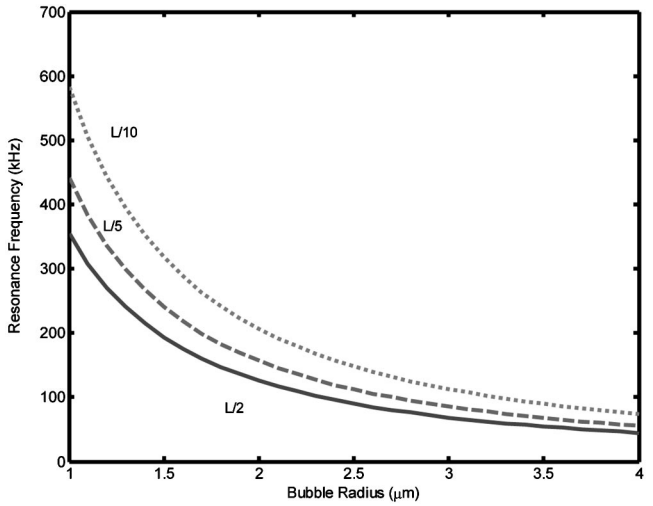

FIG. 3. Natural frequency of oscillation as a function of the bubble radius for three different positions of the bubble in the blood vessel. The solid line corresponds to a bubble at a distance of $L/2$ from one end, the dashed line to a distance of $L/5$, and the dotted line to a distance of $L/10$.

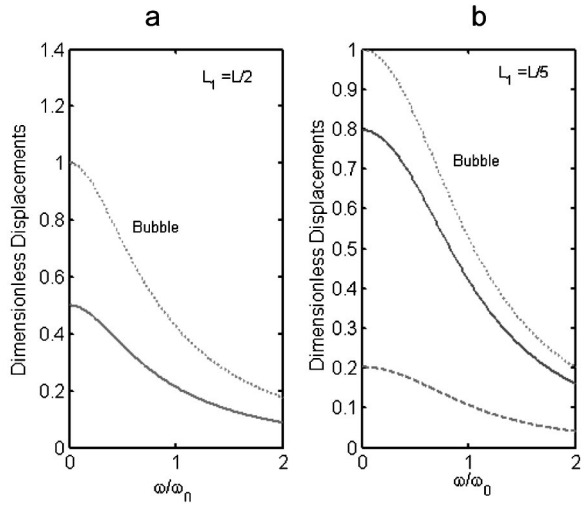

FIG. 4. (a) Displacements of the two liquid interfaces (solid line) and of the bubble (dotted line) as a function of the dimensionless frequency ω/ω_0 for a bubble of radius $R_B=3\ \mu$m at the center of the vessel. (b) Displacements of the shorter liquid column (solid line), longer liquid column (dashed line), and bubble (dotted line) as a function of the dimensionless frequency ω/ω_0 for a bubble of radius $R_B=3\ \mu$m at a distance $L/5$ from one end.

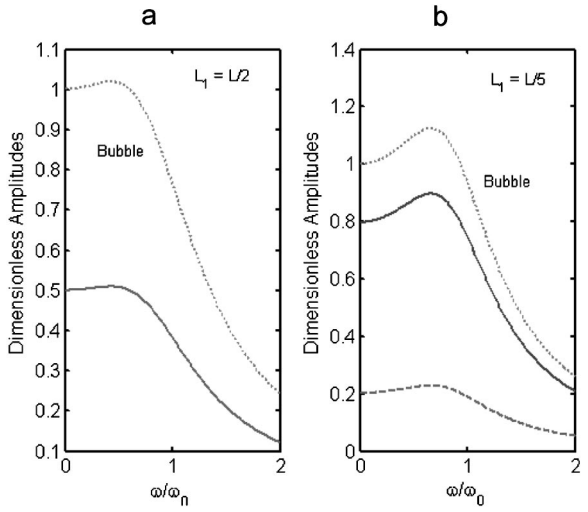

FIG. 5. (a) Bubble (dotted line) and liquid interface dimensionless displacements (solid line) as a function of the dimensionless frequency ω/ω_0 for a bubble of radius $R_B=2\ \mu$m at the center of the vessel. (b) Displacements of the shorter liquid column (solid line), longer liquid column (dashed line), and bubble (dotted line) as a function of the dimensionless frequency ω/ω_0 for a bubble of radius $R_B=2\ \mu$m at a distance $L/5$ from one end.

find analytical expressions for the natural frequency. For example, for a bubble in a unbounded liquid, driven by an external acoustic field into linear steady oscillations, the equation for the resonance frequency, neglecting surface tension is[58]

$$\omega_{0\mathrm{unb}}^2=\frac{p_0}{\rho R_B^2}3\ \mathrm{Re}\,\Phi. \tag{17}$$

The ratio between the two natural frequencies, given, respectively, by Eqs. (9) and (17) is

$$\frac{\omega_0^2}{\omega_{0\mathrm{unb}}^2}=\frac{S}{4\pi R_B}\left(\frac{1}{L_1^{\mathrm{eff}}}+\frac{1}{L_2^{\mathrm{eff}}}\right). \tag{18}$$

In deriving the above equation we have made use of Eq. (1). Equation (18) shows clearly how the confinement of the bubble in a narrow region affects its resonance frequency. However it is important to point out here once again, that this particular formula is valid when the bubble undergoes steady linear oscillations.

B. Amplitude resonance

We now consider the displacements of the two liquid column interfaces and the bubble. These amplitudes depend on the resonance frequency ω_0 as well as the total damping coefficient b, defined by Eq. (10). It is possible to see that for the range of parameters of interest in this study the viscous coefficient is much larger than the thermal coefficient.

The dimensionless amplitudes $A_1/2L_B$, $A_2/2L_B$, A_b, given by Eqs. (8c), (8d), and (11b) are plotted as a function of the dimensionless frequency ω/ω_0, where ω_0 is the resonance frequency as determined above. These amplitudes have a very rich structure, which is very sensitive to the values of the bubble size and columns lengths.

In Fig. 4(a) we show the three dimensionless amplitudes for $R_B=3\ \mu$m and the bubble at the center of the tube. In this case the displacements of the two liquid interfaces are equal, however they are small. The displacement of the bubble also remains relatively small except at very small frequencies. The reason why the displacements are larger in the limit of very small frequencies can be explained as follows. The maximum for these amplitudes takes place when their denominators $\sqrt{(\omega^2-\omega_0^2)^2+4b^2\omega^2}$ has a minimum. For the case of Fig. 4(a) the term $4b\omega$ is much larger than the term $|(\omega^2-\omega_0^2)|$, which can be neglected, therefore giving a maximum for the displacements in the limit of $\omega\to 0$.

Hence, for $R_B=3\ \mu$m and the bubble at the center of the vessel, the so-called *amplitude resonance* occurs for very small frequencies. The fact that the amplitude resonance does not take place at the natural frequency ω_0 is due to the fact the damping coefficient b is very large. The smaller the damping, the more pronounced the resonance, and when b is zero, the resonance amplitude is infinite and occurs exactly at the natural frequency ω_0. In Fig. 4(b) the bubble center is at a distance $L_1=L/5$ from one end. Also in this case the amplitude resonance takes place in the limit $\omega\to 0$ and the bubble displacement is much larger than the liquid ones. The shorter column however undergoes larger oscillations than the longer one.

In Figs. 5(a) and 5(b) we consider a 2 μm radius bubble, respectively, at a distance $L/2$ and $L/5$ from one end. In this case the amplitude resonance takes place at a frequency of about $0.5\omega_0$ for the bubble at a distance $L/2$ and at a frequency of about $0.7\omega_0$ for the one at a distance of $L/5$. This is due to the fact the natural frequency for smaller bubbles is comparable in value to the damping coefficient b.

The plots for the dimensionless displacements for a 1 μm radius bubble, shown in Figs. 6(a) and 6(b), are the most interesting ones. In Fig. 5(a) the bubble is at a distance $L/5$ from one end and in Fig. 5(b) is at a distance $L/5$. In both cases the amplitude resonance takes place very close to the energy resonance. The gas considered in plots given by Figs.

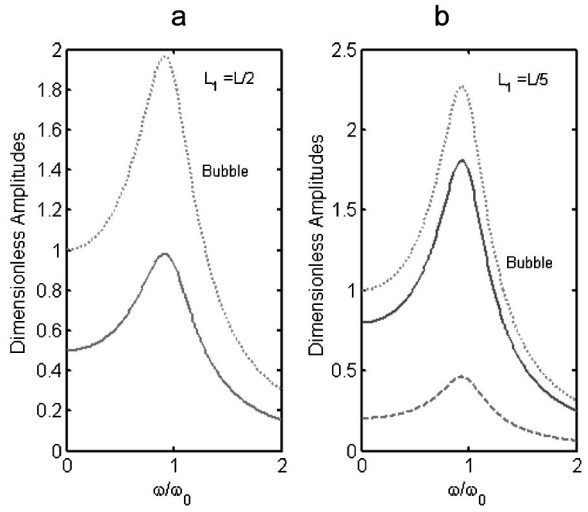

FIG. 6. (a) Bubble (dotted line) and liquid interface dimensionless displacements (solid line) as a function of the dimensionless frequency ω/ω_0 for a bubble of radius $R_B=1$ μm at the center of the vessel. (b) Displacements of the shorter liquid column (solid line), longer liquid column (dashed line), and bubble (dotted line) as a function of the dimensionless frequency ω/ω_0 for a bubble of radius $R_B=1$ μm at a distance $L/5$ from one end.

4, 5, and 6 is C_3F_8, however, similar plots are obtained for air and C_4F_{10}.

C. Energy resonance

At energy resonance the energy transfer from the applied force to the system is at its maximum. In Fig. 7 we have plotted the ratio between P_{avc} and $(P_{\text{avc}})_{\text{res}}$, given by Eq. (16), as a function of the normalized frequency ω/ω_0 for $R_B=3$, 2, 1 μm and $L_1=L/5$.

As it can seen from the plot the maximum absorption of energy takes place at the natural frequency of oscillation. The width of the resonance however is strongly dependent on the bubble size and the 1 μm radius bubble has the sharpest resonance.

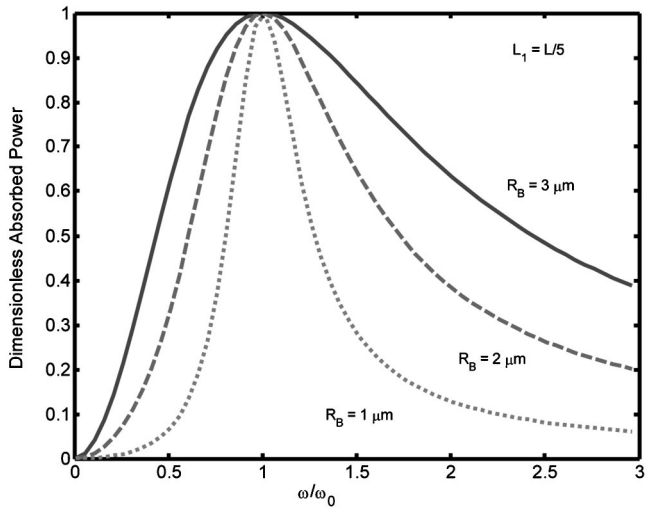

FIG. 7. The ratio between the average absorbed power and the average absorbed power at resonance for a bubble at a distance $L/5$ from one end as a function of the dimensionless frequency ω/ω_0 for $R_B=3$ μm (solid line), 2 μm (dashed line), and 1 μm (dotted line).

Only when the damping coefficient b is much smaller than the natural frequency ω_0 there is no great differences between the frequencies corresponding to the amplitude resonance and to the energy resonance. In this condition the energy absorbed from the external field produces the macroscopic motion of the system and very little is dissipated as internal friction. In this study only for bubbles with radius of the order 1 μm the frequency corresponding to the amplitude resonance amplitude is practically equal to the natural frequency. Therefore only for the case of smaller bubbles, more absorbed energy is available to sustain the motion of the system and less is dissipated as internal friction. In general most of the absorbed energy is dissipated as internal friction and this dissipation is maximum at the natural frequency of oscillation.

IV. DISCUSSION AND CONCLUSION

Before starting any discussion, it is important to keep in mind that the present model is only a first approach to a highly complex process and therefore it should be considered in this context. Several approximations have been made. We have ignored the presence of the bubble shell for U.S. contrast agents, by assuming that those bubbles simply act as nucleation sites. We have neglected the blood flow speed of in the capillaries, which is very slow, by assuming that once the steady-state oscillations are established, they are the dominant effect. The gas bubbles have a transient nature, which has not been considered in this study. More precisely the effects of gas diffusion, vapor contribution to the gas internal pressure and phase changes processes have not been taken into account, as it is also usually done for bubbles pulsating in unbounded liquids. The presence of more than one bubble in the vessel has been neglected. The assumption of a rigid capillary may be justified in the presence situation, because we consider mesentery capillaries and pressures of the order of the local ambient pressure. However for bubbles driven in the nonlinear regime the properties of the vessel wall and surrounding tissues have to be taken into account. Each organ has a unique capillary network and its characteristics should be incorporated in any realistic model of microbubble behavior in the microvasculature. The non-Newtonian nature of blood, which is important for small blood vessels, should be taken into consideration in a more general way than it has been done here, where we have supposed an effective relative viscosity of two.

Many capillary blood vessels in a number of organs have diameters smaller than the diameter of red cells at rest. It is extremely difficult to make *in vivo* measurements of the velocity and pressure fields in these small blood vessels, as well as to check the bubble dynamics. To obtain some knowledge, two alternative approaches may be undertaken: mathematical modeling at the microscale, as it has been done in this study, or larger-scale model testing. This last approach has been applied by Geng *et al.*[60] to study the forced oscillations of a gas bubble in liquid filled tubes, having dimension of a few mm. The results of their experiment is in excellent agreement with the theory developed by Prosperetti and co-workers.[55,61] In the context of biomedical applications of ultrasound, the method of larger scale model testing

has been utilized by Roy *et al.*[62] in a vascularized tissue phantom, obtaining very useful insights into the problem.

We have considered several aspects of the forced linear oscillations of microbubbles in fine capillary blood vessels in the parameter range of interest in medicine. We have established their behavior which is isothermal at low frequencies and for small bubbles and between isothermal and adiabatic for larger bubbles and higher frequencies. We have estimated their damping coefficient, which is dominated by viscous losses. These losses increase the internal molecular energies of the blood and surrounding tissues. The natural frequency of oscillation is affected by the presence of the blood wall, as well as bubble size and position. Moreover, the displacements of the two liquid–gas interfaces and of the bubble show a rich variety of behaviors. For smaller bubbles (1–2 μm) more energy is going into the macroscopic motion and less is dissipated as internal friction.

This model suggests the possibility to use ultrasound in a range of frequency and power which is in general lower than the one is used now for therapeutic ultrasound treatments. The microbubbles injected in the blood stream will be acoustically driven at the natural frequency of oscillation of the blood capillary plus bubble in order to get the maximum absorption of energy. This energy can be used to increase tissue temperature, for drug delivery or gene therapy.

ACKNOWLEDGMENTS

E. Sassaroli gratefully acknowledges funding by NIH training Grant No. T32-EB002177. The authors would like to thank the referee for his/her very useful comments, which have greatly improved the paper quality.

[1] R. E. Apfel, ''Acoustic cavitation: A possible consequence of biomedical uses of ultrasound,'' Br. J. Cancer Suppl. **45**, 140–146 (1982).
[2] H. G. Flynn, *Physical Acoustics, Principles and Methods*, edited by W. P. Mason (Academic, New York, 1964), pp. 57–172.
[3] T. Leighton, *The Acoustic Bubble* (Academic, San Diego, 1994).
[4] D. L. Miller and R. M. Thomas, ''Ultrasound contrast agents nucleate inertial cavitation *in vitro*,'' Ultrasound Med. Biol. **21**, 1059–1065 (1995).
[5] S. Z. Child, C. L. Hartman, L. A. Schery, and E. L. Carstensen, ''Lung damage from exposure to pulsed ultrasound,'' Ultrasound Med. Biol. **16**, 817–825 (1990).
[6] D. Dalecki, C. H. Raeman, S. Z. Child, D. P. Penney, R. Mayer, and E. L. Carstensen, ''The influence of contrast agents on hemorrhage produced by lithotripter fields,'' Ultrasound Med. Biol. **23**, 1435–1439 (1997).
[7] A. F. Tarantal and D. R. Canfield, ''Ultrasound-induced lung hemorrhage in the monkey,'' Ultrasound Med. Biol. **20**, 65–72 (1994).
[8] J. F. Zachary and W. D. O'Brien, Jr., ''Lung lesions induced by continuous- and pulsed-wave (diagnostic) ultrasound in mice, rabbits, and pigs,'' Vet. Pathol. **32**, 43–54 (1995).
[9] P. P. Lele, *Thresholds and Mechanisms of Ultrasonic Damage to "Organized" Animal Tissues*, DHEW publication FDA 78-8048, edited by D. G. Hazzard and M. L. Litz (U.S. Department of Heath, Education, and Welfare, Rockville, MD, 1977), pp. 224–239.
[10] G. R. ter Haar, S. Daniels, K. C. Eastaugh, and C. R. Hill, ''Ultrasonically induced cavitation *in vivo*,'' Br. J. Cancer **45**, 151–155 (1982).
[11] J. Y. Chapelon, J. Margonari, Y. Theillere, F. Gorry, F. Vernier, E. Blanc, and A. Gelet, ''Effects of high-energy focused ultrasound on kidney tissue in the rat and the dog,'' Eur. Urol. **22**, 147–152 (1992).
[12] L. A. Frizzell, ''Threshold dosages for damage to mammalian liver by high intensity focused ultrasound,'' IEEE Trans. Ultrason. Ferroelectr. Freq. Control **35**, 578–581 (1988).
[13] F. J. Fry, G. Kossoff, R. C. Eggleton, and F. Dunn, ''Threshold ultrasonic dosages for structural changes in the mammalian brain,'' J. Acoust. Soc. Am. **48**, 1413–1417 (1970).
[14] K. Hynynen, ''The threshold for thermally significant cavitation in dog's thigh muscle *in vivo*,'' Ultrasound Med. Biol. **17**, 157–169 (1991).
[15] P. P. Lele, *Effects of Ultrasound on Solid Mammalian Tissues and Tumors in vivo*, edited by M. H. Repacholi, M. Gandolfo, and A. Rindi (Plenum, New York, 1987), pp. 275–306.
[16] F. Prat, J. Y. Chapelon, A. el Fadil, A. Sibille, Y. Theilliere, T. Ponchon, and D. Cathignol, ''Focused liver ablation by cavitation in the rabbit: a potential new method of extracorporeal treatment,'' Gut **35**, 395–400 (1994).
[17] N. T. Sanghvi, R. S. Foster, R. Bihrle, R. Casey, T. Uchida, M. H. Phillips, J. Syrus, A. V. Zaitsev, K. W. Marich, and F. J. Fry, ''Noninvasive surgery of prostate tissue by high intensity focused ultrasound: an updated report,'' Eur. J. Ultrasound **9**, 19–29 (1999).
[18] F. G. Sommer and D. Pounds, ''Transient cavitation in tissues during ultrasonically induced hyperthermia,'' Med. Phys. **9**, 1–3 (1982).
[19] N. I. Vykhodtseva, K. Hynynen, and C. Damianou, ''Histologic effects of high intensity pulsed ultrasound exposure with subharmonic emission in rabbit brain *in vivo*,'' Ultrasound Med. Biol. **21**, 969–979 (1995).
[20] S. Bao, B. D. Thrall, and D. L. Miller, ''Transfection of a reporter plasmid into cultured cells by sonoporation *in vitro*,'' Ultrasound Med. Biol. **23**, 953–959 (1997).
[21] A. A. Brayman, M. L. Coppage, S. Vaidya, and M. W. Miller, ''Transient poration and cell surface receptor removal from human lymphocytes *in vitro* by 1 MHz ultrasound,'' Ultrasound Med. Biol. **25**, 999–1008 (1999).
[22] M. Fechheimer, J. F. Boylan, S. Parker, J. E. Sisken, G. L. Patel, and S. G. Zimmer, ''Transfection of mammalian cells with plasmid DNA by scrape loading and sonication loading,'' Proc. Natl. Acad. Sci. U.S.A. **84**, 8463–8467 (1987).
[23] H. R. Guzman, D. X. Nguyen, S. Khan, and M. R. Prausnitz, ''Ultrasound-mediated disruption of cell membranes. I. Quantification of molecular uptake and cell viability,'' J. Acoust. Soc. Am. **110**, 588–596 (2001).
[24] H. J. Kim, J. F. Greenleaf, R. R. Kinnick, J. T. Bronk, and M. E. Bolander, ''Ultrasound-mediated transfection of mammalian cells,'' Hum. Gene Ther. **7**, 1339–1346 (1996).
[25] S. Koch, P. Pohl, U. Cobet, and N. G. Rainov, ''Ultrasound enhancement of liposome-mediated cell transfection is caused by cavitation effects,'' Ultrasound Med. Biol. **26**, 897–903 (2000).
[26] J. Liu, T. N. Lewis, and M. R. Prausnitz, ''Noninvasive assessment and control of ultrasound-mediated membrane permeabilization,'' Pharm. Res. **15**, 918–924 (1998).
[27] D. L. Miller and R. M. Thomas, ''The role of cavitation in the induction of cellular DNA damage by ultrasound and lithotripter shock waves *in vitro*,'' Ultrasound Med. Biol. **22**, 681–687 (1996).
[28] K. Tachibana, T. Uchida, K. Ogawa, N. Yamashita, and K. Tamura, ''Induction of cell-membrane porosity by ultrasound,'' Lancet **353**, 1409 (1999).
[29] W. G. Greenleaf, M. E. Bolander, G. Sarkar, M. B. Goldring, and J. F. Greenleaf, ''Artificial cavitation nuclei significantly enhance acoustically induced cell transfection,'' Ultrasound Med. Biol. **24**, 587–595 (1998).
[30] K. Hynynen, N. McDannold, N. Vykhodtseva, and F. A. Jolesz, ''Noninvasive MR imaging-guided focal opening of the blood-brain barrier in rabbits,'' Radiology **220**, 640–646 (2001).
[31] D. L. Miller, A. R. Williams, J. E. Morris, and W. B. Chrisler, ''Sonoporation of erythrocytes by lithotripter shockwaves *in vitro*,'' Ultrasonics **36**, 947–952 (1998).
[32] M. W. Miller, E. C. Everbach, C. Cox, R. R. Knapp, A. A. Brayman, and T. A. Sherman, ''A comparison of the hemolytic potential of Optison and Albunex in whole human blood *in vitro*: Acoustic pressure, ultrasound frequency, donor and passive cavitation detection considerations,'' Ultrasound Med. Biol. **27**, 709–721 (2001).
[33] R. J. Price, D. M. Skyba, S. Kaul, and T. C. Skalak, ''Delivery of colloidal particles and red blood cells to tissue through microvessel ruptures created by targeted microbubble destruction with ultrasound,'' Circulation **98**, 1264–1267 (1998).
[34] R. V. Shohet, S. Chen, Y. T. Zhou, Z. Wang, R. S. Meidell, R. H. Unger, and P. A. Grayburn, ''Echocardiographic destruction of albumin microbubbles directs gene delivery to the myocardium,'' Circulation **101**, 2554–2556 (2000).
[35] A. R. Williams, G. Kubowicz, E. Cramer, and R. Schlief, ''The effects of the microbubble suspension SH U 454 (Echovist) on ultrasound-induced cell lysis in a rotating tube exposure system,'' Echocardiography **8**, 423–433 (1991).
[36] B. C. Tran, J. Seo, T. L. Hall, J. B. Fowlkes, and C. A. Cain, ''Microbubble-enhanced cavitation for noninvasive ultrasound surgery,''

IEEE Trans. Ultrason. Ferroelectr. Freq. Control **50**, 1296–1304 (2003).
[37] J. B. Keller and M. J. Miksis, ''Bubble oscillations of large amplitude,'' J. Acoust. Soc. Am. **68**, 628–633 (1980).
[38] F. Chavrier, J. Y. Chapelon, A. Gelet, and D. Cathignol, ''Modeling of high-intensity focused ultrasound-induced lesions in the presence of cavitation bubbles,'' J. Acoust. Soc. Am. **108**, 432–440 (2000).
[39] C. C. Church, ''The effects of an elastic solid surface layer of the radial pulsations of gas bubbles,'' J. Acoust. Soc. Am. **97**, 1510–1521 (1995).
[40] J. B. Fowlkes and M. Averkiou, ''Contrast and Tissue Harmonic Imaging. *In 2000 Categorial Course in Diagnostic Radiology Physics: CT and US Cross-Sectional Imaging*, Eds. L. W. Goldman and J. B. Fowlkes (RSNA, Oak Brook, IL) 77–95 (2000).
[41] J. E. Kennedy, G. R. ter Haar, and D. Cranston, ''High intensity focused ultrasound: Surgery of the future?'' Br. J. Radiol. **76**, 590–599 (2003).
[42] D. L. Miller, S. V. Pislaru, and J. E. Greenleaf, ''Sonoporation: Mechanical DNA delivery by ultrasonic cavitation,'' Somatic Cell Mol. Genet. **27**, 115–134 (2002).
[43] A. C. Burton, *Physiology and Biophysics of the Circulation* (Yearbook medical publishers, 1972).
[44] S. Chien, S. Usami, H. M. Taylor, J. L. Lundberg, and M. I. Gregersen, ''Effects of hematocrit and plasma proteins on human blood rheology at low shear rates,'' J. Appl. Physiol. **21**, 81–87 (1966).
[45] B. Klitzman and B. R. Duling, ''Microvascular hematocrit and red cell flow in resting and contracting striated muscle,'' Am. J. Physiol. **237**, H481–H490 (1979).
[46] R. H. Haynes, ''Physical basis of the dependence of blood viscosity on tube radius,'' Am. J. Physiol. **198**, 1193–1200 (1960).
[47] Y. C. Fung, *Biomechanics: Mechanical Properties of Living Tissues* (Springer-Verlag, New York, 1993).
[48] A. R. Pries, T. W. Secomb, and P. Gaehtgens, ''Biophysical aspects of blood flow in the microvasculature,'' Cardiovasc. Res. **32**, 654–667 (1996).
[49] R. Skalak, ''Poiseuille Medal lecture. Capillary flow: Past, present, and future,'' Biorheology **27**, 277–293 (1990).
[50] G. Kaley and B. M. Altura, *Microcirculation* (University Park Press, Baltimore, 1977).
[51] A. C. Burton, ''Role of geometry, of size and shape, in the microcirculation,'' Fed. Proc. **25**, 1753–1760 (1966).
[52] Y. C. Fung, *Microscopic Blood Vessels in the Mesentery*, edited by Y. C. Fung (New York, ASME. Biomechanics, Proc.Symp., 1966), pp. 151–166.
[53] Y. C. Fung, ''Theoretical considerations of the elasticity of red cells and small blood vessels,'' Fed. Proc. **25**, 1761–1772 (1966).
[54] E. Bouskela, and C. A. Wiederhielm, ''Microvascular myogenic reaction in the wing of the intact unanesthetized bat,'' Am. J. Physiol. **237**, H59–H65 (1979).
[55] X. M. Chen and A. Prosperetti, ''Thermal processes in the oscillation of gas bubbles in tubes,'' J. Acoust. Soc. Am. **104**, 1389–1398 (1998).
[56] M. S. Plesset and A. Prosperetti, ''Bubble dynamics and cavitation,'' Annu. Rev. Fluid Mech. **9**, 145–185 (1977).
[57] H. Levine and J. Schwinger, ''On the radiation of sound from an unflanged circular pipe,'' Phys. Rev. **73**, 383–406 (1948).
[58] A. Prosperetti, ''The thermal behavior of oscillating gas bubbles,'' J. Fluid Mech. **222**, 587–616 (1991).
[59] L. G. Leal, *Laminar Flow and Convective Transport Processes* (Butterworth–Heinemann, Boston, 1992).
[60] X. Geng, H. Yuan, N. Oguz, and A. Prosperetti, ''The oscillations of gas bubbles in tubes: Experimental results,'' J. Acoust. Soc. Am. **106**, 674–681 (1999).
[61] H. N. Oguz and A. Prosperetti, ''The natural frequency of oscillation of gas bubbles in tubes,'' J. Acoust. Soc. Am. **103**, 3301–3308 (1998).
[62] R. A. Roy, J. Huang, and R. G. Holt, ''A quantitative comparison of theory and experiments on high intensity focused ultrasound (HIFU) induced heating in a vascularized tissue phantom,'' Abstract from a program at the 144th meeting of the Acoustical Society of America, Vol. 112, p. 2369, 2002.

Errors in ultrasonic scatterer size estimates due to phase and amplitude aberration

Anthony Gerig[a] and James Zagzebski
Department of Medical Physics, University of Wisconsin—Madison, 1300 University Ave., Rm. 1530, Madison, Wisconsin 53706

(Received 16 October 2003; revised 15 March 2004; accepted 18 March 2004)

Current ultrasonic scatterer size estimation methods assume that acoustic propagation is free of distortion due to large-scale variations in medium attenuation and sound speed. However, it has been demonstrated that under certain conditions in medical applications, medium inhomogeneities can cause significant field aberrations that lead to B-mode image artifacts. These same aberrations may be responsible for errors in size estimates and parametric images of scatterer size. This work derives theoretical expressions for the error in backscatter coefficient and size estimates as a function of statistical parameters that quantify phase and amplitude aberration, assuming a Gaussian spatial autocorrelation function. Results exhibit agreement with simulations for the limited region of parameter space considered. For large values of aberration decorrelation lengths relative to aberration standard deviations, phase aberration errors appear to be minimal, while amplitude aberration errors remain significant. Implications of the results for accurate backscatter and size estimation are discussed. In particular, backscatter filters are suggested as a method for error correction. Limitations of the theory are also addressed. The approach, approximations, and assumptions used in the derivation are most appropriate when the aberrating structures are relatively large, and the region containing the inhomogeneities is offset from the insonifying transducer. © *2004 Acoustical Society of America.* [DOI: 10.1121/1.1738455]

PACS numbers: 43.80.Vj, 43.80.Qf [FD] Pages: 3244–3252

I. INTRODUCTION

The estimation and imaging of tissue parameters using ultrasound has proven to be useful in the diagnosis and monitoring of disease.[1–7] Scatterer size estimation and imaging, in particular, has been thoroughly investigated as a source of additional information beyond what is currently provided by clinical ultrasound machines.[8–12] However, the methods currently used to estimate scatterer size assume that the interrogating acoustic field is well characterized and free of distortion. They ignore aberration in the phase and amplitude of the field due to inhomogeneities located between the transducer and the region of interest. Although neglecting aberration is often appropriate and results in no significant consequences, it has been demonstrated that in certain cases, such distortion can lead to the significant deterioration of B-mode images.[13–17] Consequently, there may be instances where failing to account for aberration results in noticeable scatterer size estimation errors.

A significant amount of work has been done on the quantification of aberration, and the characterization of its effects upon ultrasonic fields. In particular, Waag *et al.* developed a theoretical scattering model which incorporates the effects of phase aberration, and relates the physical characteristics of inhomogeneities to aberration quantifiers.[18] O'Donnell looked at the effects of phase aberration upon backscatter measurement,[19] and Smith, Trahey *et al.* investigated the properties of B-mode speckle in the presence of phase aberration.[13,14] Recent work has focused primarily upon compensating for errors due to phase aberration through the incorporation of appropriate time delays in array transducer processing.[20–23] Varghese *et al.*, however, recently investigated the implications of phase aberration for elastographic imaging.[24]

In this work we extend the basic model published by Waag *et al.*[18] to include amplitude aberration due to variations in inhomogeneity attenuation with respect to the background, and investigate the effects of both aberration types (amplitude and phase) upon scatterer size estimation. In particular, aberration quantification is briefly discussed before inclusion in the general expression for Fourier-transformed rf-data segments. This expression is then used to calculate the errors in both backscatter coefficient and size estimates resulting from phase and amplitude aberration. These results are subsequently partially verified by simulations that address the two types of aberration separately. Only the limiting case, where aberration is invariant over the space occupied by an individual scatterer, is investigated. After a brief discussion of the results, possible correction filters are proposed. Finally, the limitations of the theoretical model are discussed.

II. THEORY

The following analysis closely follows the theoretical work done by Waag for phase aberration,[18] and is therefore subject to the same constraints. Namely, in order to properly apply his geometric ray/perturbation theory formalism, it must be assumed that the scale of the distorting inhomogeneities, or aberrators, are larger than the insonifying wavelength. According to Waag, the amount of phase distortion

[a]Corresponding author. Electronic mail: algerig@wisc.edu

associated with any given point in space can be characterized by a path length correction which is associated with a phase change.[18]

$$l(\mathbf{r}) = -\int_C \gamma_c(\mathbf{r}')\, d\,\mathbf{r}', \tag{1}$$

where $\mathbf{r}$ is a point in space, γ_c is the fractional variation in sound speed at any given location from the average, c_0, and C is the straight line path from the acoustic source to the point $\mathbf{r}$, which is an approximation to the actual ray path that neglects refraction. For the sake of later analysis, the path length correction (i.e., phase aberration) will be treated as a random variable. This work will follow Waag *et al.* in assuming a zero-mean Gaussian distribution for the correction, which should be approximately valid and become moreso, according to the central limit theorem, as the number of aberrators between the source and $\mathbf{r}$ increases. In order to assure a zero-mean distribution, it will be assumed that the aberrating region is homogeneous, and that its thickness, if it does not extend throughout the entire medium, remains relatively constant across the acoustic beam.

Amplitude aberration due to attenuation variation is handled in a similar fashion. The attenuation between an acoustic source and any point in space can be expressed by

$$A(\mathbf{r},\omega) = e^{-\int_C f[\alpha(\mathbf{r}')+\alpha_0]d\,\mathbf{r}'}, \tag{2}$$

where α_0 is the average attenuation in nepers per unit distance per unit frequency, α is the deviation from this value at $\mathbf{r}'$, ω is the acoustic angular frequency, and f is the acoustic frequency. This quantity can be simplified to

$$A(\mathbf{r},\omega) = e^{-f\alpha_0|\mathbf{r}-\mathbf{r}_0|} e^{-f\psi(\mathbf{r})}, \tag{3}$$

where $\mathbf{r}_0$ is the location of the acoustic source, and

$$\psi(\mathbf{r}) = \int_C \alpha(\mathbf{r}')\, d\,\mathbf{r}'. \tag{4}$$

The first term contained in Eq. (3) is generally measured and compensated for in scatterer size estimation. In particular, the estimation method described in this work will use a point correction technique, which accounts for medium attenuation as quantified by the point approximation described below. The second term is the source of amplitude aberration, and will therefore be the focus of what follows. For the reasons mentioned previously, it will be assumed that ψ is also a zero-mean, Gaussian distributed, random variable.

In general form, the Fourier transform of a windowed ultrasonic rf data segment is given by[25]

$$V(\omega) \approx T(\omega)B(\omega)\omega^2 e^{-2f\alpha_0 z} \int_{\Delta\Omega} d\,\mathbf{r}\, \gamma(\mathbf{r}) A_t(\mathbf{r},\omega) A_r(\mathbf{r},\omega), \tag{5}$$

where aberration effects have been excluded, and gating effects have been approximated by a restriction, represented by $\Delta\Omega$, on the limits of integration over the scatterer field. The restriction includes positions in space for which $2|\mathbf{r}|/c_0$ falls within the time interval of the gate, and is most accurate when the system response for a single scatterer is short in comparison to the gate duration. $T(\omega)$ is the complex transfer function for the system transducer, $B(\omega)$ is the complex superposition coefficient corresponding to the insonifying pulse, and A_t and A_r are the field integrals for transmit and receive, respectively. $\gamma(\mathbf{r}) = [\kappa(\mathbf{r}) - \kappa_0]/\kappa_0 - [\rho(\mathbf{r}) - \rho_0]/\rho(\mathbf{r})$ is the spatially dependent reflectivity of the scattering medium, where κ and ρ are compressibility and density, and κ_0 and ρ_0 are their corresponding mean values. $e^{-2f\alpha_0 z}$ is a point approximation of the medium attenuation, where z is the distance from the transducer aperture to the point in space perpendicular to the aperture which corresponds to the middle of the time gate, and is most accurate when z is greater than the width of the active transducer aperture.[25]

To generate a size estimate for a gated segment, the Fourier transform of the segment, given by Eq. (5), is used to produce a corresponding spectral estimate. The result is divided by the magnitude squared of the appropriate point attenuation correction term and a type of system transfer function, which is, in most cases, measured using a planar reflector or reference phantom.[26,27] What remains, assuming that z is much larger than the characteristic length of the spatial autocorrelation function for the scatterers, is a backscatter estimate for the medium. This function is subsequently fit to a theoretical curve, whose frequency dependence is defined solely by scatterer size, to produce a size estimate. Several different theoretical models have been used to estimate scatterer size in tissue,[4] however, the Gaussian model for spatial autocorrelation functions will be considered exclusively here. For this case, the size estimate corresponding to an individual backscatter estimate is given by[28]

$$\hat{a}^2 = \frac{-d_1^2 c_0^2 \sum_{\omega_{\min}}^{\omega_{\max}} (y(\omega)\omega^2 - \overline{y}\,\overline{\omega^2})}{80 \sum_{\omega_{\min}}^{\omega_{\max}} (\omega^2 - \overline{\omega^2})^2}, \tag{6}$$

where $y(\omega) = 10\ln(\hat{\mathrm{BSC}}(\omega)/\omega^4)$, $d_1 \approx 3.1$ is a constant, and the summation is over discrete frequency values, correlated or uncorrelated, within the bandwidth of the transducer.

In order to discern how phase and amplitude aberration effect scatterer size estimates, aberration terms must be included in the signal equation, Eq. (5), and propagated through the mathematical machinery of size estimation described above. The resulting changes to the signal equation appear in the field integrals, and are outlined below:

$$A_{t'}(\mathbf{r},\omega) = \int_S d\,\mathbf{r}' K_t(\mathbf{r}') \frac{e^{ik|\mathbf{r}-\mathbf{r}'|}}{|\mathbf{r}-\mathbf{r}'|} e^{ikl(\mathbf{r}-\mathbf{r}')-f\psi(\mathbf{r}-\mathbf{r}')},$$

$$A_{\mathbf{r}'}(\mathbf{r},\omega) = \int_S d\,\mathbf{r}' K_r(\mathbf{r}', |\mathbf{r}-\mathbf{r}'|) \frac{e^{ik|\mathbf{r}-\mathbf{r}'|}}{|\mathbf{r}-\mathbf{r}'|} \times e^{ikl(\mathbf{r}-\mathbf{r}')-f\psi(\mathbf{r}-\mathbf{r}')}, \tag{7}$$

where the final exponential terms are the additions, S is the face of the transducer, K_t contains transmit phase and amplitude modifying terms, such as those for apodization and transmit focusing, and K_r contains analogous receive terms, including those for dynamic receive focusing, dynamic aperture, and apodization. Given these changes, the periodogram spectral estimate for a gated segment is expressed by

$$S(\omega,z)=\langle V(\omega)V^*(\omega)\rangle$$
$$=|T(\omega)B(\omega)|^2\omega^4 e^{-4f\alpha_0 z}\int\int_{\Delta\Omega} d\mathbf{r}_1\, d\mathbf{r}_2\langle \gamma(\mathbf{r}_1)\times\gamma^*(\mathbf{r}_2)\rangle\langle A_{t'}(\mathbf{r}_1,\omega)A_{r'}(\mathbf{r}_1,\omega)A^*_{t'}(\mathbf{r}_2,\omega)\times A^*_{r'}(\mathbf{r}_2,\omega)\rangle, \quad (8)$$

where it has been assumed that the aberrators and scatterers are independent, i.e. that they are not the same objects. Making the change of variable $\mathbf{r}_2=\mathbf{r}_1+\Delta\mathbf{r}$ yields

$$S(\omega,z)=|T(\omega)B(\omega)|^2\omega^4 e^{-4f\alpha_0 z}\int\int_{\Delta\Omega} d\mathbf{r}_1\, d\Delta\mathbf{r} R(\Delta\mathbf{r})\times\langle A_{t'}(\mathbf{r}_1,\omega)A_{r'}(\mathbf{r}_1,\omega)A^*_{t'}\times(\mathbf{r}_1+\Delta\mathbf{r},\omega)A^*_{r'}(\mathbf{r}_1+\Delta\mathbf{r},\omega)\rangle, \quad (9)$$

where $R(\Delta\mathbf{r})=\langle\gamma(\mathbf{r}_1)\gamma^*(\mathbf{r}_1+\Delta\mathbf{r})\rangle$ is the spatial autocorrelation function (SAF) for the scatterer field,[29] and is assumed to be statistically stationary.

Assuming that the characteristic length of the spatial autocorrelation function is small, the far-field approximation can be introduced, $k|\mathbf{r}-\mathbf{r}'+\Delta\mathbf{r}|\approx k|\mathbf{r}-\mathbf{r}'|+\mathrm{k}\cdot\Delta\mathbf{r}$ and $|\mathbf{r}-\mathbf{r}'+\Delta\mathbf{r}|\approx|\mathbf{r}-\mathbf{r}'|$, giving

$$S(\omega,z)=|T(\omega)B(\omega)|^2\omega^4 e^{-4f\alpha_0 z}\int_{\Delta\Omega} d\mathbf{r}_1 A_t(\mathbf{r}_1,\omega)\times A_r(\mathbf{r}_1,\omega)A^*_t(\mathbf{r}_1,\omega)A^*_r(\mathbf{r}_1,\omega)\times\int_{\Delta\Omega} d\Delta\mathbf{r} R(\Delta\mathbf{r})D(\mathbf{r}_1,\Delta\mathbf{r},\omega)e^{-2i\,\mathbf{k}\cdot\Delta\mathbf{r}}, \quad (10)$$

where

$$D(\mathbf{r}_1,\Delta\mathbf{r},\omega)=\langle e^{2ikl(\mathbf{r}_1)-2f\psi(\mathbf{r}_1)}e^{-2ikl(\mathbf{r}_1+\Delta\mathbf{r})-2f\psi(\mathbf{r}_1+\Delta\mathbf{r})}\rangle, \quad (11)$$

and two additional assumptions have been made. First, the direction of the vector $\mathbf{k}$ has been approximated by the direction of $\mathbf{r}_1$ rather than the true direction of $\mathbf{r}_1-\mathbf{r}'$, which is accurate given that that the distance to the gated region is larger than the size of the active area of the transducer. Second, and most importantly, it has been assumed that both forms of aberration are effectively independent of $\mathbf{r}'$, the variable of integration over the transducer surface, in order to achieve results that are both simple and field, and thus system, independent. This approximation may not always hold true, but should be acceptable when aberrator size is on the order of the transducer's active area, or the aberrating region is far from the transducer face.

If the further assumption is made that the aberration is either negligible or not present in the gated region, which is consistent with small gates or aberration due to intervening layers such as a bodywall, it follows that aberration values are invariant along the direction of the beam (approximately $\mathbf{r}_1/|\mathbf{r}_1|$) within the gated region (Fig. 1 displays the geometry for an aberrating layer). This assumption, together with the earlier homogeneity assumption, implies both that aberration variances, $\sigma_l^2(z)$ and $\sigma_\psi^2(z)$, are dependent solely upon gate position, and that correlations between aberration quantities are functions of the angular separation between their associated spatial vectors and gate position alone. For example, $\langle\psi(\mathbf{r}_1)\psi(\mathbf{r}_1+\Delta\mathbf{r})\rangle/\sigma_\psi^2(z)$ is a function of z and $\Delta\theta$, the angular separation between $\mathbf{r}_1$ and $\mathbf{r}_1+\Delta\mathbf{r}$. It therefore becomes possible to demonstrate, given the previous Gaussian distribution assumption for aberration values, that

$$D(\mathbf{r}_1,\Delta\mathbf{r},\omega)\Rightarrow D(z,\Delta\theta,\omega)=e^{4[f^2\sigma_\psi^2(z)+f^2\sigma_\psi^2(z)\rho_\psi(\Delta\theta/\theta_\psi,z)-k^2\sigma_l^2(z)+k^2\sigma_l^2(z)\rho_l(\Delta\theta/\theta_l,z)]}, \quad (12)$$

regardless of the correlation between values of l and ψ, where

$$\rho_\psi\left(\frac{\Delta\theta}{\theta_\psi},z\right)=\frac{\langle\psi(\mathbf{r}_1)\psi(\mathbf{r}_1+\Delta\mathbf{r})\rangle}{\sigma_\psi^2(z)},$$
$$\rho_l\left(\frac{\Delta\theta}{\theta_l},z\right)=\frac{\langle l\mathbf{r}_1)l(\mathbf{r}_1+\Delta\mathbf{r})\rangle}{\sigma_l^2(z)},$$

and θ_ψ and θ_l are characteristic decorrelation values similar to the decorrelation lengths of scatterer spatial autocorrelation functions. These values may be related to one another if the sources of the two types of aberration are identical, i.e., the same inhomogeneities are both phase and amplitude aberrators. If amplitude aberration is excluded, Eq. (12) is identical to the result presented by Waag *et al.* for Gaussian distributed phase aberration.[18]

Arbitrarily setting the Δz axis direction to match that of $\mathbf{r}_1$, the approximation

$$\frac{\Delta\theta}{\theta_{\psi,l}}\approx\frac{\tan\Delta\theta}{\theta_{\psi,l}}=\frac{\sqrt{\Delta x^2+\Delta y^2}}{\theta_{\psi,l}(|\mathbf{r}_1|+\Delta z)}\approx\frac{\sqrt{\Delta x^2+\Delta y^2}}{\theta_{\psi,l}|\mathbf{r}_1|} \quad (13)$$

can be used given that the integrand of Eq. (10) is suppressed by the scatterer spatial autocorrelation function for all but the smallest values of $\Delta\mathbf{r}$. Assuming a short gate and relatively narrow acoustic field such that $|\mathbf{r}_1|\approx z$, Eq. (12) can be recast:

$$D(z,\Delta\theta,\omega)\Rightarrow D(z,\omega,\sqrt{\Delta x^2+\Delta y^2})=e^{4[f^2\sigma_\psi^2(z)+f^2\sigma_\psi^2(z)\rho_\psi(\sqrt{\Delta x^2+\Delta y^2}/w_\psi)-k^2\sigma_l^2(z)+k^2\sigma_l^2(z)\rho_l(\sqrt{\Delta x^2+\Delta y^2}/w_l)]}, \quad (14)$$

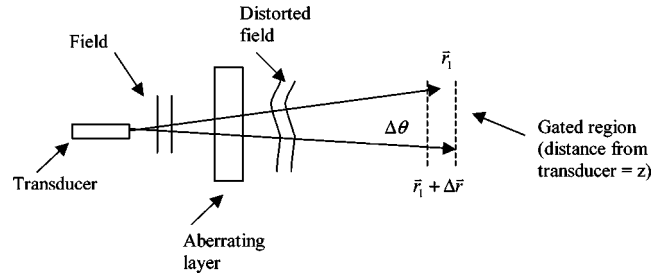

FIG. 1. Geometry for an aberrating layer. Aberration variances are independent of z for such cases as long as the gated region lies beyond the aberrating layer.

where $w_\psi = \theta_\psi z$ and $w_l = \theta_l z$ are amplitude and phase decorrelation lengths, respectively. Assuming a Gaussian form for the aberration correlation functions yields

$$D(z,\omega,\sqrt{\Delta x^2+\Delta y^2}) = e^{4[f^2\sigma_\psi^2(z)+f^2\sigma_\psi^2(z)\exp\{-(\Delta x^2+\Delta y^2)/w_\psi^2\}]} \times e^{4[-k^2\sigma_l^2(z)+k^2\sigma_l^2(z)\exp\{-(\Delta x^2+\Delta y^2)/w_l^2\}]}. \quad (15)$$

Because aberrator size must be much larger than scatterer size for the theoretical approach to be valid, the aberration decorrelation lengths must also be much larger than the characteristic length of the spatial autocorrelation function.[30] As a result, the exponential terms within the exponents of Eq. (15) will be small for nonzero values of the spatial autocorrelation function. These terms can therefore be legitimately approximated by their first-order expansions to yield

$$D(z,\omega,\sqrt{\Delta x^2+\Delta y^2}) = e^{8f^2\sigma_\psi^2-4f^2\sigma_\psi^2[(\Delta x^2+\Delta y^2)/w_\psi^2]}e^{-4k^2\sigma_l^2[(\Delta x^2+\Delta y^2)/w_l^2]}. \quad (16)$$

Using this result in Eq. (10) for a Gaussian spatial autocorrelation function, and correcting for the system response and attenuation gives

$$\langle \hat{\mathrm{BSC}}(\omega)\rangle = \mathrm{BSC}(\omega)\frac{e^{8f^2\sigma_\psi^2}}{1+2d^2/w^2}, \quad (17)$$

where d is the characteristic length of the scatterer spatial autocorrelation function, and

$$w^2 = \frac{w_\psi^2 w_l^2}{4f^2\sigma_\psi^2 w_l^2 + 4k^2\sigma_l^2 w_\psi^2}. \quad (18)$$

By inserting Eq. (17) into Eq. (6), size estimation errors can be calculated. Results are plotted in Figs. 2 and 3, where the effects of the two types of aberration have been isolated by setting the variance of the excluded type in Eq. (17) to zero. In both cases, the scatterer diameter is 80 microns, which is representative for scatterer size estimation at diagnostic frequencies, the bandwidth is 50 percent, the center frequency is set such that[9] $k_{\mathrm{cent}}a = 0.8$, and the interval between summed frequencies corresponds to the decorrelation distance for a 5 mm Hanning window. For Fig. 2, the fractional error in scatterer size is displayed as a function of w_l/σ_l, while for Fig. 3, it is plotted versus σ_ψ for several values of w_ψ, the amplitude decorrelation length. Results for lower values of the aberration decorrelation lengths should be regarded with caution given the earlier restriction that $w_{l,\psi} \gg \lambda \gg a$. As the aberration decorrelation lengths both increase and decrease, errors approach limiting values that become relatively insensitive to changes in the lengths. For example, for decreasing values of these parameters, the frequency dependence of $\langle \hat{\mathrm{BSC}}(\omega)\rangle$ approaches $\mathrm{BSC}(\omega)f^{-2}e^{8f^2\sigma_\psi^2}$, which dominates the behavior of Figs. 2 and 3 for small aberration decorrelation lengths, yet is independent of these values.

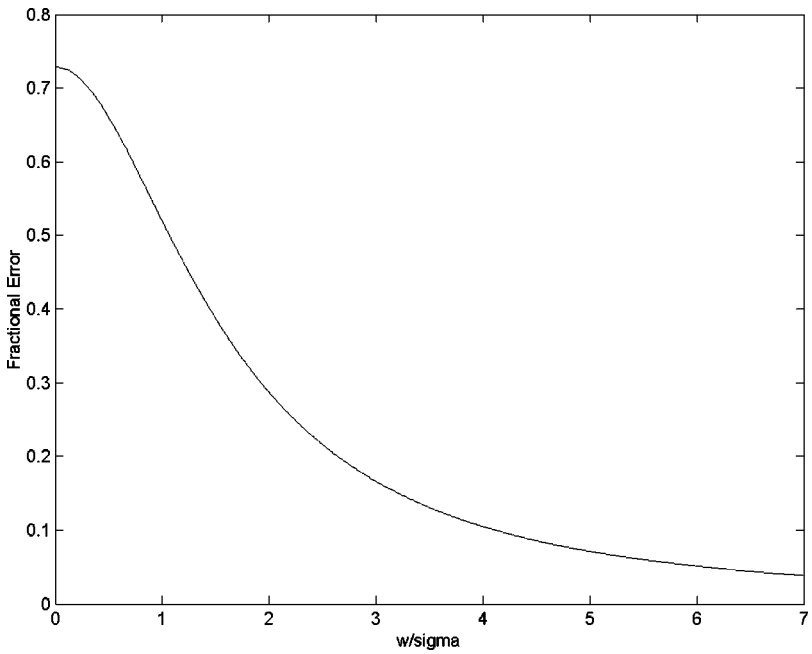

FIG. 2. Theoretical fractional error in size estimates due to phase aberration. Fractional error is plotted as a function of the ratio of phase decorrelation length to phase aberration standard deviation, w_l/σ_l.

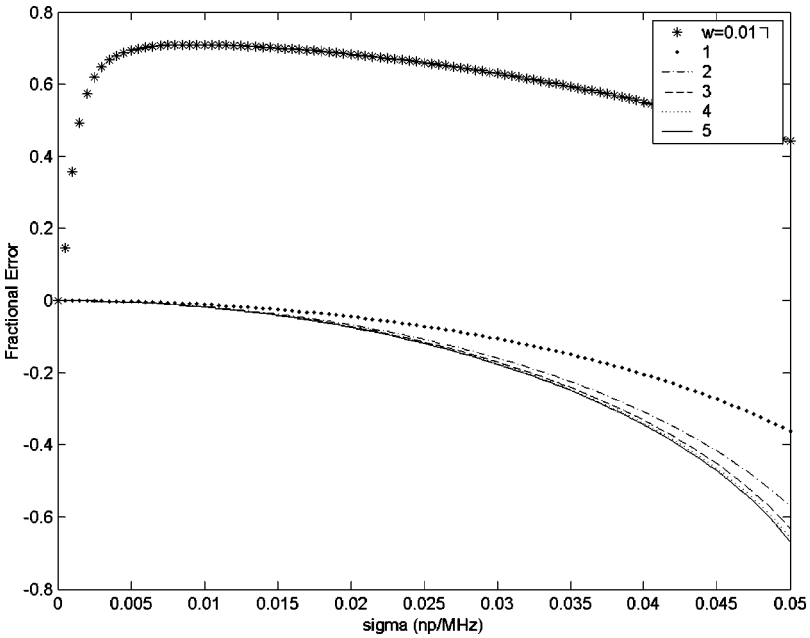

FIG. 3. Theoretical fractional error in size estimates due to amplitude aberration. Different values of amplitude decorrelation length, w_ψ (i.e., w in the legend), correspond to the different line types and are given as a fraction of scatterer radius. The fractional error is plotted as a function of amplitude aberration standard deviation, σ_ψ, which is shown in units of nepers/MHz.

III. METHOD

Verification focused upon the opposing region of parameter space where w [see Eq. (18)] is large, since, as will become evident, it can be explored without simulations that employ a high degree of complexity. Within this region, Eq. (17) can be approximated by

$$\langle \hat{\mathrm{BSC}}(\omega)\rangle \approx \mathrm{BSC}(\omega) e^{8f^2\sigma_\psi^2}, \tag{19}$$

which indicates that while amplitude aberration remains a source of error, phase aberration does not. This result is equivalent to what is obtained when it is assumed that aberration values are effectively invariant over the characteristic length of the spatial autocorrelation function. Under this assumption, the correlation functions of Eq. (12) can be replaced by unity, leaving a quantity that can be extracted from the integrals of Eq. (10) to yield an expression that reduces to Eq. (19).

Simulated rf data were generated using code[31] that artificially implements a Gaussian spatial autocorrelation function by multiplying the frequency-dependent scattered amplitude from randomly distributed point-like scatterers by the square root of the form factor for a Gaussian spatial autocorrelation function, $e^{-k^2d^2}$. Typically, such an implementation would be inadequate for studying aberration effects since it cannot incorporate effects due to changing aberration values over the dimension of a spatially extended scatterer. However, because size estimate errors in the region of parameter space under consideration are equivalent to those obtained under the assumption of aberration invariance on the scale of scatterer size as described above, it can be appropriately used. Aberration effects were included by multiplying the frequency dependent scattered amplitude for each scatterer by either

$$e^{-2f\sigma_\psi(z)n} \quad \text{or} \quad e^{2ik\sigma_l(z)n}, \tag{20}$$

for amplitude and phase aberration respectively, where n is a random number drawn from a zero-mean, unity-standard deviation Gaussian probability distribution.

Several independent planes of rf data (300 acoustic lines per plane) were generated for a simulated linear array transducer (0.15 mm by 10 mm elements with 0.2 mm spacing; 5 cm transmit and elevational foci; 10 elements active during transmit; dynamic receive focus, dynamic aperture, and apodization active). In all cases, the average speed of sound was set to 1540 m/s, the average attenuation to 0, the scatterer density to 4000 per cubic cm, the transducer center frequency to 7 MHz, and the bandwidth to 5.5 MHz. The sampling frequency was set by the code to be approximately 38 MHz. 17 aberration-free reference planes were generated for backscatter estimation, where the scatterer diameter was 50 microns. Planes that included aberration were generated in sets of two across multiple values of aberration variance. Each set incorporated only one type of aberration, and all scatterer diameters were 75 microns. Backscatter estimates were produced for each of the 300 acoustic lines using the reference phantom method,[27] where the necessary power spectral estimates were drawn from 1 cm data segments centered about a depth of 4 cm. Sample power spectral estimates were averaged across each 2-plane set, and reference power spectral estimates across all 17 planes. The results were used to generate size estimates using the method described previously. The fractional error was calculated for each size estimate, and mean and standard deviation point estimates of the fractional error were produced for each value of aberration variance.

IV. RESULTS

Figures 4 and 5 display the results for phase and amplitude aberration, respectively. In both cases, the mean fractional error is plotted as a function of the aberration standard deviation. Error bars correspond to the approximate standard error of the mean, and theoretical values were generated nu-

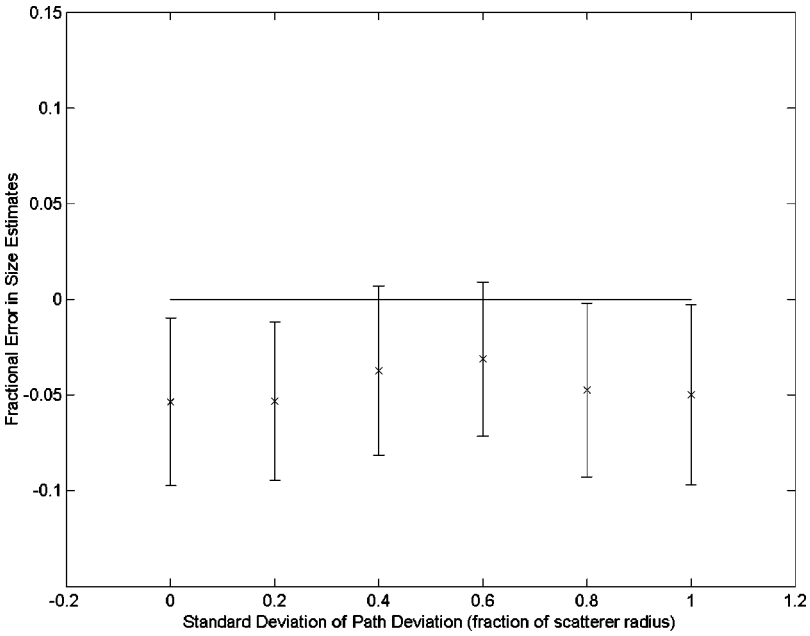

FIG. 4. A comparison of theoretical and simulation size estimate fractional errors as a function of path deviation (i.e., phase aberration) standard deviation when the phase decorrelation length is much larger than the phase aberration standard deviation.

merically according to Eqs. (19) and (6). All values, including the phase aberration control, are biased low. This error appears to be the result of an inherent bias in the backscatter coefficient estimation technique, although bias in the size estimator could also be a contributing factor. The more noise contained in the reference spectral estimate, the worse the bias of the reference phantom method. Otherwise, the agreement between simulation and theoretical values appears to be good.

V. DISCUSSION

According to the results contained in Fig. 4, phase aberration should have a minimal effect upon size estimates for typical values of the phase decorrelation length unless the aberration standard deviation is high. As a result, corrections should only be necessary under this condition, given that the stated assumptions of the theoretical section hold. Figure 5, on the other hand, indicates that amplitude aberration can cause significant errors for modest values of aberration standard deviation, regardless of the value of the amplitude decorrelation length. Errors, in fact, appear to be maximal for larger values of the decorrelation length. However, the form of Eqs. (17) and (19) suggests a relatively simple method to correct for amplitude aberration. Assuming that σ_ψ is known and that w_ψ, the amplitude decorrelation length, is comparatively large, the filter

$$H(\omega) = e^{-8f^2\sigma_\psi^2}, \tag{21}$$

can be applied to backscatter estimates before size estimation to effectively eradicate any detrimental aberration effects. Notice that according to Eqs. (17) and (18), the filter can be

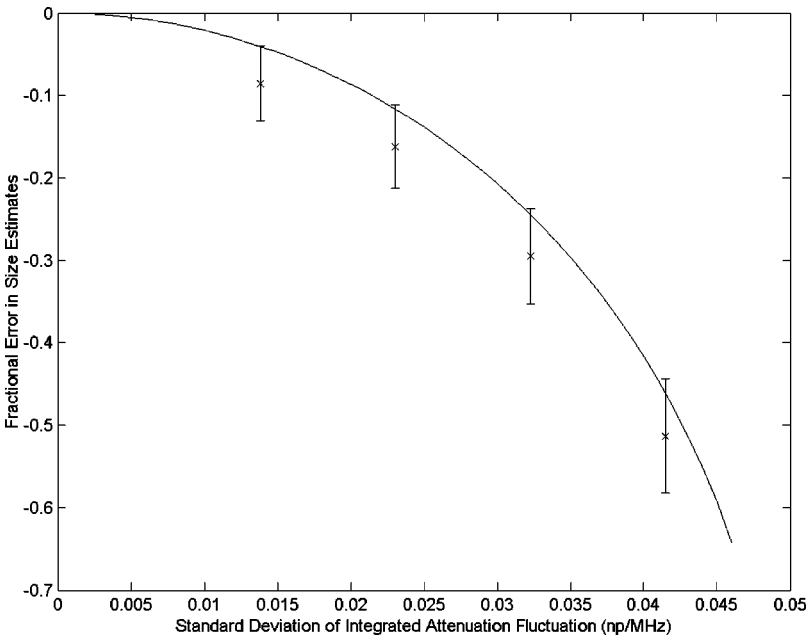

FIG. 5. A comparison of theoretical and simulation size estimate fractional errors caused by amplitude aberration when the amplitude decorrelation length is much greater than the amplitude aberration standard deviation. Fractional error is plotted as a function of amplitude aberration standard deviation in units of nepers/MHz.

adapted to account for both amplitude and phase aberration when aberration standard deviations are higher. However, an approximate *a priori* knowledge of scatterer size and aberration decorrelation lengths is necessary in order to make the appropriate adjustments.

Although the effects of phase and amplitude aberration upon size estimation have been adequately characterized under the stated restrictions, the assumption that both forms of aberration are independent of $\mathbf{r}'$, which was made in order to arrive at Eqs. (10) and (11), excludes aberration due to moderately sized inhomogeneities close to the active face of the transducer. If this assumption is withdrawn, the expected value of Eq. (9), rather than simplifying to the form found in Eq. (10), becomes

$$\int_{S^{(1)}}\int_{S^{(2)}}\int_{S^{(3)}}\int_{S^{(4)}} K_t(\mathbf{r}^{(1)})K_{\mathbf{r}}(\mathbf{r}^{(2)},|\mathbf{r}_1-\mathbf{r}^{(2)}|)K_t^*(\mathbf{r}^{(3)})K_r^*(\mathbf{r}^{(4)},|\mathbf{r}_1+\Delta\,\mathbf{r}-\mathbf{r}^{(4)}|)$$
$$\times\frac{e^{ik|\mathbf{r}_1-\mathbf{r}^{(1)}|}e^{ik|\mathbf{r}_1-\mathbf{r}^{(2)}|}e^{-ik|\mathbf{r}_1+\Delta\,\mathbf{r}-\mathbf{r}^{(3)}|}e^{-ik|\mathbf{r}_1+\Delta\,\mathbf{r}-\mathbf{r}^{(4)}|}}{|\mathbf{r}_1-\mathbf{r}^{(1)}||\mathbf{r}_1-\mathbf{r}^{(2)}||\mathbf{r}_1+\Delta\,\mathbf{r}-\mathbf{r}^{(3)}||\mathbf{r}_1+\Delta\,\mathbf{r}-\mathbf{r}^{(4)}|}\langle e^{ikl(\mathbf{r}_1-\mathbf{r}^{(1)})-f\psi(\mathbf{r}_1-\mathbf{r}^{(1)})}e^{ikl(\mathbf{r}_1-\mathbf{r}^{(2)})-f\psi(\mathbf{r}_1-\mathbf{r}^{(2)})}$$
$$\times e^{-ikl(\mathbf{r}_1+\Delta\,\mathbf{r}-\mathbf{r}^{(3)})-f\psi(\mathbf{r}_1+\Delta\,\mathbf{r}-\mathbf{r}^{(3)})}e^{-ikl(\mathbf{r}_1+\Delta\,\mathbf{r}-\mathbf{r}^{(4)})-f\psi(\mathbf{r}_1+\Delta\,\mathbf{r}-\mathbf{r}^{(4)})}\rangle. \tag{22}$$

Not only is this expression extremely complex, but it also implies that backscatter and size estimation errors will be field dependent, given that the aberration term is a function of the field integration variables. As a result, characterization of the error will be both difficult and system specific. The one case that is easily calculable is the limit where the correlation between aberration values approaches zero, such that

$$\langle e^{ikl(\mathbf{r}_1-\mathbf{r}^{(1)})-f\psi(\mathbf{r}_1-\mathbf{r}^{(1)})}e^{ikl(\mathbf{r}_1-\mathbf{r}^{(2)})-f\psi(\mathbf{r}_1-\mathbf{r}^{(2)})}e^{-ikl(\mathbf{r}_1+\Delta\,\mathbf{r}-\mathbf{r}^{(3)})-f\psi(\mathbf{r}_1+\Delta\,\mathbf{r}-\mathbf{r}^{(3)})}e^{-ikl(\mathbf{r}_1+\Delta\,\mathbf{r}-\mathbf{r}^{(4)})-f\psi(\mathbf{r}_1+\Delta\,\mathbf{r}-\mathbf{r}^{(4)})}\rangle$$
$$\approx\langle e^{ikl(\mathbf{r}_1-\mathbf{r}^{(1)})-f\psi(\mathbf{r}_1-\mathbf{r}^{(1)})}\rangle\langle e^{ikl(\mathbf{r}_1-\mathbf{r}^{(2)})-f\psi(\mathbf{r}_1-\mathbf{r}^{(2)})}\rangle\langle e^{-ikl(\mathbf{r}_1+\Delta\,\mathbf{r}-\mathbf{r}^{(3)})-f\psi(\mathbf{r}_1+\Delta\,\mathbf{r}-\mathbf{r}^{(3)})}\rangle\langle e^{-ikl(\mathbf{r}_1+\Delta\,\mathbf{r}-\mathbf{r}^{(4)})-f\psi(\mathbf{r}_1+\Delta\,\mathbf{r}-\mathbf{r}^{(4)})}\rangle$$
$$=e^{2\,f^2\sigma_\psi^2-2k^2\sigma_l^2}. \tag{23}$$

Because this result is independent of all integration variables, given the previous assumptions of the theoretical section, its associated backscatter error can be obtained immediately:

$$\langle\hat{\mathrm{BSC}}(\omega)\rangle=\mathrm{BSC}(\omega)e^{2\,f^2\sigma_\psi^2-2k^2\sigma_l^2}. \tag{24}$$

However, for this limit to be remotely applicable to physical cases, aberrating inhomogeneities must be small in comparison to the active area of the transducer, a condition which may rarely be met by objects which must also meet a minimum size requirement for the theory to be accurate.

VI. CONCLUSION

Expressions for the errors in ultrasonic backscatter coefficient and size estimates due to phase and amplitude aberration were derived based upon the theoretical framework described by Waag *et al.*[18] For large values of aberration decorrelation lengths relative to aberration standard deviations, theoretical results compared favorably with simulations. Under these conditions, phase aberration errors appear to be minimal, while amplitude aberration errors remain significant. However, a simple filter can be applied to backscatter estimates, assuming that the amplitude aberration variance is known to correct for the error. When aberration standard deviations are comparatively large, the filter can be modified to correct for higher order phase and amplitude aberration given that prior knowledge of the approximate scatterer size and aberration decorrelation lengths is available.

Although the results of the aberration error characterization are relatively simple, their applicability is somewhat limited by the assumptions that were made in their derivation. Namely, they are accurate only in cases where the aberrating inhomogeneities are large in comparison to and/or distant from the insonifying transducer.

ACKNOWLEDGMENTS

This work was supported in part by NIH Grants No. R01CA39224, No. R21EB002722, and No. T32CA09206.

TABLE OF SYMBOLS

A	attenuation between an acoustic source and a point in space
A_r	receive acoustic field integral
$A_{r'}$	receive acoustic field integral including aberration effects
A_t	transmit acoustic field integral
$A_{t'}$	transmit acoustic field integral including aberration effects
a	scatterer size (radius)
$\hat{a}$	scatterer size estimate (radius)
α_0	average attenuation for a medium
α	deviation from the average attenuation at a point in space
B	complex superposition coefficient corresponding to an insonifying pulse
BSC	backscatter coefficient
$\hat{\mathrm{BSC}}$	backscatter coefficient estimate

C	straight line path from an acoustic source to a spatial point
c_0	average speed of sound for a medium
d	characteristic length of a scatterer spatial autocorrelation function
d_1	a constant
$\Delta\Omega$	spatial approximation of a temporal gate
$\Delta\theta$	angular separation between spatial vectors
f	acoustic frequency
γ_c	fractional variation in sound speed from the average
γ	reflectivity
H	aberration correction filter
$k,\mathbf{k}$	acoustic wave number
k_{cent}	wave number corresponding to a transducer center frequency
κ	compressibility
κ_0	average compressibility for a medium
K_r	signal processing term included in the receive acoustic field integral
K_t	signal processing term included in the transmit acoustic field integral
l	path length correction associated with phase aberration
λ	acoustic wavelength
n	random variable
ρ	mass density
ρ_0	average mass density for a medium
ρ_l	phase aberration correlation
ρ_ψ	amplitude aberration correlation
ψ	integrated (along the path from transducer to scatterers) deviation from the average attenuation
$\mathbf{r},\mathbf{r}',\mathbf{r}_0$	spatial variables/vectors
$\mathbf{r}_1,\mathbf{r}_2,\Delta\mathbf{r},\mathbf{r}^{(n)}$	
R	spatial autocorrelation function (SAF) for a scatterer field
S	transducer surface periodogram spectral estimate
σ_l^2	phase aberration variance
σ_ψ^2	amplitude aberration variance
T	the complex transfer function for a system transducer
θ_l	phase aberration decorrelation angle
θ_ψ	amplitude aberration decorrelation angle
V	Fourier transform of a windowed ultrasonic rf data segment
w	a combination of aberration decorrelation lengths and variances
w_l	phase aberration decorrelation length
w_ψ	amplitude aberration decorrelation length
ω	acoustic angular frequency
$\omega_{\min}$	lower limit of transducer bandwidth
$\omega_{\max}$	upper limit of transducer bandwidth
y	transformed backscatter coefficient estimate
z	perpendicular distance from a transducer aperture to the middle of a gated region

[1] S. L. Bridal, P. Fornes, P. Bruneval, and G. Berger, "Parametric (integrated backscatter and attenuation) images constructed using backscattered radio frequency signals (25–56 MHz) from human aortae in vitro," Ultrasound Med. Biol. **23**, 215–229 (1997).

[2] E. J. Feleppa, F. L. Lizzi, D. J. Coleman, and M. M. Yaremko, "Diagnostic spectrum analysis in ophthalmology: A physical perspective," Ultrasound Med. Biol. **12**, 623–631 (1986).

[3] M. Insana and T. Hall, "Parametric ultrasound imaging from backscatter coefficient measurements: Image formation and interpretation," Ultrason. Imaging **12**, 245–267 (1990).

[4] M. Insana, R. Wagner, D. Brown, and T. Hall, "Describing small-scale structure in random media using pulse-echo ultrasound," J. Acoust. Soc. Am. **87**, 179–192 (1990).

[5] R. Kuc and M. Schwartz, "Estimating the acoustic attenuation coefficient slope for liver from reflected ultrasound signals," IEEE Trans. Sonics Ultrason. **26**, 353–362 (1979).

[6] F. Lizzi, M. Ostromogilsky, E. Feleppa, M. Rorke, and M. Yaremko, "Relationship of ultrasonic spectral parameters to features of tissue microstructure," IEEE Trans. Ultrason. Ferroelectr. Freq. Control **34**, 319–328 (1987).

[7] P. Stetson and G. Sommer, "Ultrasonic characterization of tissues via backscatter frequency dependence," Ultrasound Med. Biol. **23**, 989–996 (1997).

[8] T. Hall, M. Insana, L. Harrison, and G. Cox, "Ultrasonic measurement of glomerular diameters in normal adult humans," Ultrasound Med. Biol. **22**, 987–997 (1996).

[9] M. Insana and T. Hall, "Characterising the microstructure of random media using ultrasound," Phys. Med. Biol. **35**, 1373–1386 (1990).

[10] M. Insana, T. Hall, J. Wood, and Z.-y. Yan, "Renal ultrasound using parametric imaging techniques to detect changes in microstructure and function," Invest. Radiol. **28**, 720–725 (1993).

[11] M. L. Oelze, J. F. Zachary, and J. William D. O'Brien, "Parametric imaging of rat mammary tumors *in vivo* for the purposes of tissue characterization," J. Ultrasound Med. **21**, 1201–1210 (2002).

[12] R. L. Romijn, J. M. Thijssen, and G. W. J. V. Beuningen, "Estimation of scatterer size from backscattered ultrasound: A simulation study," IEEE Trans. Ultrason. Ferroelectr. Freq. Control **36**, 593–606 (1989).

[13] S. W. Smith, G. E. Trahey, and S. M. Hubbard, "Properties of acoustical speckle in the presence of phase aberration Part II: Correlation lengths," Ultrason. Imaging **10**, 29–51 (1988).

[14] G. E. Trahey and S. W. Smith, "Properties of acoustical speckle in the presence of phase aberration Part 1: First order statistics," Ultrason. Imaging **10**, 12–28 (1988).

[15] W. A. Smith, R. C. Waag, and D. Dalecki, Assessing the limits of ultrasonic focusing through tissue from scattering measurements, *Ultrasonics Symposium* (IEEE, Chicago, 1988), pp. 809–814.

[16] L. M. Hinkelman, T. D. Mast, L. A. Metlay, and R. C. Waag, "The effect of abdominal wall morphology on ultrasonic pulse distortion. Part 1. Measurements," J. Acoust. Soc. Am. **104**, 3635–3650 (1998).

[17] T. D. Mast, L. M. Hinkelman, M. J. Orr, and R. C. Waag, "The effect of abdominal wall morphology on ultrasonic pulse distortion. Part II. Simulations," J. Acoust. Soc. Am. **104**, 3651–3664 (1998).

[18] R. C. Waag, J. P. Astheimer, and G. W. Swarthout, "A characterization of wavefront distortion for analysis of ultrasound diffraction measurements made through an inhomogeneous medium," IEEE Trans. Sonics Ultrason. **32**, 36–48 (1985).

[19] M. O'Donnell, "Quantitative ultrasonic backscatter measurements in the presence of phase distortion," J. Acoust. Soc. Am. **72**, 1719–1725 (1982).

[20] S. W. Flax and M. O'Donnell, "Phase-aberration correction using signals from point reflectors and diffuse scatterers: Basic principles," IEEE Trans. Ultrason. Ferroelectr. Freq. Control **35**, 758–767 (1988).

[21] M. O'Donnell and S. W. Flax, "Phase-aberration correction using signals from point reflectors and diffuse scatterers: Measurements," IEEE Trans. Ultrason. Ferroelectr. Freq. Control **35**, 768–774 (1988).

[22] S. Krishnan, P.-C. Li, and M. O'Donnell, "Adaptive compensation of phase and magnitude aberrations," IEEE Trans. Ultrason. Ferroelectr. Freq. Control **43**, 44–55 (1996).

[23] D.-L. Liu and R. C. Waag, "Estimation and correction of ultrasonic wavefront distortion using pulse-echo data received in a two-dimensional aperture," IEEE Trans. Ultrason. Ferroelectr. Freq. Control **45**, 473–489 (1998).

[24] T. Varghese, M. Bilgen, and J. Ophir, "Phase aberration effects in elastography," Ultrasound Med. Biol. **27**, 819–827 (2001).

[25] J.-F. Chen, J. Zagzebski, F. Dong, and E. Madsen, "Estimating the spatial autocorrelation function for ultrasound scatterers in isotropic media," Med. Phys. **25**, 648–655 (1998).

[26] E. L. Madsen, M. F. Insana, and J. A. Zagzebski, ''Method of data reduction for accurate determination of acoustic backscatter coefficients,'' J. Acoust. Soc. Am. **76**, 913–923 (1984).
[27] L. X. Yao, J. A. Zagzebski, and E. L. Madsen, ''Backscatter coefficient measurements using a reference phantom to extract depth-dependent instrumentation factors,'' Ultrason. Imaging **12**, 58–70 (1990).
[28] A. Gerig, J. Zagzebski, and T. Varghese, ''Statistics of ultrasonic scatterer size estimation with a reference phantom,'' J. Acoust. Soc. Am. **113**, 3430–3437 (2003).
[29] M. Insana and D. Brown, ''Acoustic scattering theory applied to soft biological tissues,'' in *Ultrasonic Scattering in Biological Tissues*, edited by K. Shung (CRC Press, Boca Raton, FL, 1993), pp. 75–124.
[30] R. C. Waag and D. Dalecki, ''Estimates of wavefront distortion from measurements of scattering by model random media and calf liver,'' J. Acoust. Soc. Am. **85**, 406–415 (1988).
[31] Y. Li and J. A. Zagzebski, ''A frequency domain model for generating B-mode images with array transducers,'' IEEE Trans. Ultrason. Ferroelectr. Freq. Control **46**, 690–699 (1999).

Erratum: Propagation of quasiplane nonlinear waves in tubes and the approximate solutions of the generalized Burgers equation [J. Acoust. Soc. Am. 112, 91–98 (2002)]

M. Bednarik and P. Konicek
Czech Technical University in Prague, FEE, Technicka 2, 166 27 Prague, Czech Republic

(Received 19 October 2001; revised 11 April 2002; accepted 4 May 2002)

[DOI: 10.1121/1.1747990]

PACS numbers: 43.25.Cb, 43.25.Jh, 43.10.Vx [MFH]

In our paper, Eq. (30) should read

$$V(\sigma,\theta)=\mathrm{Im}\left\{\sum_{n=1}^{\infty} a_n \exp[j(n\theta-D_0\sqrt{n}\sigma)]\right\}.$$

The inner pair of brackets is missing in the equation given in our paper.

 © 2004 Acoustical Society of America